AGARD-CP-571

AGARD

ADVISORY GROUP FOR AEROSPACE RESEARCH & DEVELOPMENT
7 RUE ANCELLE, 92200 NEUILLY-SUR-SEINE, FRANCE

AGARD CONFERENCE PROCEEDINGS 571

Loss Mechanisms and Unsteady Flows in Turbomachines

(les Mécanismes des pertes et les écoulements instationnaires dans les turbomachines)

Papers presented at the Propulsion and Energetics Panel (PEP) 85th Symposium held in Derby, United Kingdom, 8-12 May 1995.

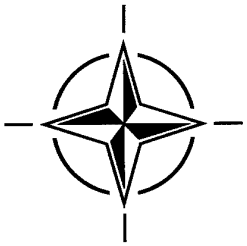

NORTH ATLANTIC TREATY ORGANIZATION

Published January 1996

Distribution and Availability on Back Cover

DISCLAIMER NOTICE

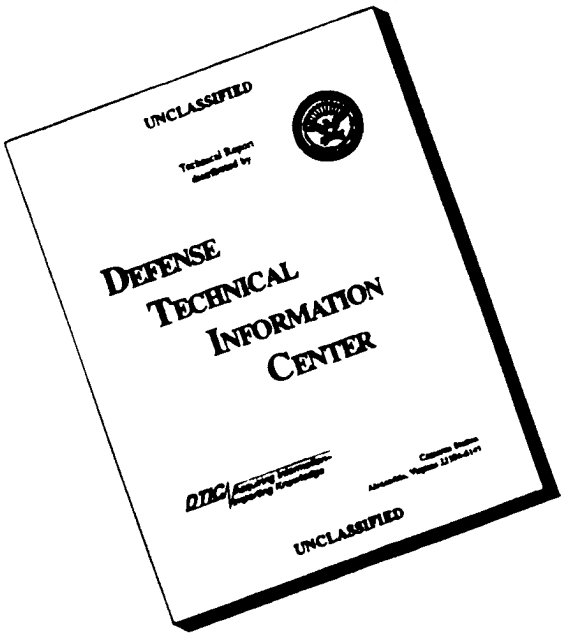

THIS DOCUMENT IS BEST QUALITY AVAILABLE. THE COPY FURNISHED TO DTIC CONTAINED A SIGNIFICANT NUMBER OF PAGES WHICH DO NOT REPRODUCE LEGIBLY.

AGARD-CP-571

AGARD

ADVISORY GROUP FOR AEROSPACE RESEARCH & DEVELOPMENT
7 RUE ANCELLE, 92200 NEUILLY-SUR-SEINE, FRANCE

AGARD CONFERENCE PROCEEDINGS 571

Loss Mechanisms and Unsteady Flows in Turbomachines

(les Mécanismes des pertes et les écoulements instationnaires dans les turbomachines)

Papers presented at the Propulsion and Energetics Panel (PEP) 85th Symposium held in Derby, United Kingdom, 8-12 May 1995.

North Atlantic Treaty Organization
Organisation du Traité de l'Atlantique Nord

The Mission of AGARD

According to its Charter, the mission of AGARD is to bring together the leading personalities of the NATO nations in the fields of science and technology relating to aerospace for the following purposes:

- Recommending effective ways for the member nations to use their research and development capabilities for the common benefit of the NATO community;
- Providing scientific and technical advice and assistance to the Military Committee in the field of aerospace research and development (with particular regard to its military application);
- Continuously stimulating advances in the aerospace sciences relevant to strengthening the common defence posture;
- Improving the co-operation among member nations in aerospace research and development;
- Exchange of scientific and technical information;
- Providing assistance to member nations for the purpose of increasing their scientific and technical potential;
- Rendering scientific and technical assistance, as requested, to other NATO bodies and to member nations in connection with research and development problems in the aerospace field.

The highest authority within AGARD is the National Delegates Board consisting of officially appointed senior representatives from each member nation. The mission of AGARD is carried out through the Panels which are composed of experts appointed by the National Delegates, the Consultant and Exchange Programme and the Aerospace Applications Studies Programme. The results of AGARD work are reported to the member nations and the NATO Authorities through the AGARD series of publications of which this is one.

Participation in AGARD activities is by invitation only and is normally limited to citizens of the NATO nations.

Published January 1996

ISBN 92-836-0020-7

Printed by Canada Communication Group
45 Sacré-Cœur Blvd., Hull (Québec), Canada K1A 0S7

Loss Mechanisms and Unsteady Flows in Turbomachines

(AGARD CP-571)

Executive Summary

Today's military aviation relies crucially on the turbine engine, in particular on the turbo jet for propulsion. Besides striving for less weight and better economy new standards are being set for more reliable operation under off design conditions. Flight envelopes are constantly being expanded and there are also new tasks for propulsion engines such as providing part or full lift in manoeuvering or in take off and landing. As has been demonstrated recently in the X-31, the engine will even be used for direct physical control of the aircraft which pushes the flight envelope, as well as the degree of necessary reliability, to new extremes.

Achieving efficiency and operating stability in off-design conditions depends on the control of loss mechanisms and small scale flows in the machine. Experimental and computational analysis is extremely difficult and very expensive and has been worked on for about two decades. Academia and laboratories, as well as the turbine industry itself, have invested large amounts of labour and money indicating the importance of the work and they have already achieved excellent results. The pace has been determined both by the effort which could be invested and by the available computer technology which in turn has received a major impulse from the fluid dynamics field's requirements.

AGARD's Propulsion and Energetics Panel has promoted the field with three previous Symposia at roughly five-year intervals. The most recent of these in 1989 marked a major milestone. It was found that Computational Fluid Dynamics (CFD) already provided useful design guidance but that improvement of the quantitative analysis and data was now to be achieved. The present Symposium reviewed in forty-two papers the state of the quantitative knowledge on secondary flow losses gathered from both experimental work and computational analysis and the state-of the-art of applicable CFD.

It was found that codes incorporating all fluid dynamic conditions are meanwhile being widely applied. They are still limited to stage-by-stage computation though, and they are much more complex than had been anticipated earlier. Yet they provide the base for future multistage codes with the goal of optimizing the machine as a whole. In the nearer term it will be possible to incorporate loss management already in the design stage which so far had to be done at great expense during development testing. However, sufficiently highly developed computer technology must be available. First approaches to designing for loss and flow management were demonstrated in single papers and systematic general approaches will be developed in the immediate future. The next generation of engines and any upgrades of existing designs will benefit from better economy as well as from much improved operating characteristic filling the future requirements for military aircraft engines.

Les mécanismes des pertes et des écoulements instationnaires dans les turbomachines

(AGARD CP-571)

Synthèse

Pour l'aviation militaire moderne, les turbomachines, et en particulier les turboréacteurs, sont l'élément clé de la propulsion. En plus de la recherche d'une diminution de masse et d'une meilleure rentabilité, de nouvelles normes sont en cours d'établissement en vue d'assurer la fiabilité du fonctionnement dans des conditions hors normes de conception. Les domaines de vol sont en évolution constante et de nouvelles tâches ont été assignées aux propulseurs, tel que l'apport partiel ou intégral de la sustentation demandée en manœuvre, au décollage ou à l'atterrissage. A l'instar de l'exemple récent fourni par le X31, le propulseur sera même utilisé pour assurer le contrôle physique direct de l'aéronef, ce qui poussera le domaine de vol, ainsi que le niveau de fiabilité exigé, vers de nouvelles limites.

L'obtention d'un régime stable et efficace dans des conditions hors normes de conception dépend de la maîtrise des mécanismes des pertes et des écoulements d'ordre mineur dans le réacteur. L'analyse expérimentale numérique, dont les origines datent de vingt ans, s'avère très difficile et très coûteuse. Les sommes d'argent et les heures de travail considérables déjà consacrées à ce domaine par les universités, les laboratoires et l'industrie des turbomachines elle-même, donnent une indication de l'importance accordée aux travaux, et des excellents résultats obtenus. Le rythme d'avancement a été dicté par l'effort qui a pu être consacré aux travaux d'une part, et par les possibilités des technologies de l'informatique d'autre part, qui ont d'ailleurs pris un nouvel essor sous l'influence des besoins exprimés par les spécialistes en dynamique des fluides.

Le Panel AGARD de propulsion et d'énergétique a contribué au développement du domaine par l'organisation de trois symposia, tenus à des intervalles de cinq ans environ. Le plus récent de ceux-ci, qui a eu lieu en 1989, a marqué un tournant décisif. Il a été constaté que l'aérodynamique numérique CFD représentait déjà une source de renseignements utiles pour la conception des turbomachines, mais qu'une amélioration des données et des analyses quantitatives était toujours souhaitable. En quarante deux présentations, le symposium a fait le point des connaissances quantitatives actuelles dans le domaine de pertes des écoulements secondaires y compris les études expérimentales, les analyses informatiques et l'état de l'art du CFD applicable.

Il a été constaté que des codes, incorporant l'ensemble des conditions aérodynamiques sont déjà employés de façon quasi général. Cependant, le calcul de ces codes est toujours effectué phase par phase, et ils sont beaucoup plus complexes qu'initialement prévu. Néanmoins, ils constituent la base de futurs codes multiphase à élaborer en vue de l'optimisation globale des turbomachines. Dans un avenir plus proche, la gestion des pertes pourra être incorporée dès la phase de conception, alors que jusqu'à présent cette fonction a dû être intégrée, à grands frais, lors des essais de développement. Il faudra toutefois disposer de technologies informatiques hautement développées. Des communications sur les premières approches de conception intégrant la gestion des pertes et des écoulements ont été présentées et il a été affirmé que des méthodes générales systématiques seraient développées très prochainement. La prochaine génération de propulseurs, ainsi que d'éventuelles revalorisations de moteurs existants, seront plus économes, avec des caractéristiques de fonctionnement améliorées, répondant aux cahiers de charges des futurs propulseurs des avions militaires.

Contents

Recent Publications of the Propulsion and Energetics Panel

CONFERENCE PROCEEDINGS (CP)

Interior Ballistics of Guns
AGARD CP 392, January 1986

Advanced Instrumentation for Aero Engine Components
AGARD CP 399, November 1986

Engine Response to Distorted Inflow Conditions
AGARD CP 400, March 1987

Transonic and Supersonic Phenomena in Turbomachines
AGARD CP 401, March 1987

Advanced Technology for Aero Engine Components
AGARD CP 421, September 1987

Combustion and Fuels in Gas Turbine Engines
AGARD CP 422, June 1988

Engine Condition Monitoring — Technology and Experience
AGARD CP 448, October 1988

Application of Advanced Material for Turbomachinery and Rocket Propulsion
AGARD CP 449, March 1989

Combustion Instabilities in Liquid-Fuelled Propulsion Systems
AGARD CP 450, April 1989

Aircraft Fire Safety
AGARD CP 467, October 1989

Unsteady Aerodynamic Phenomena in Turbomachines
AGARD CP 468, February 1990

Secondary Flows in Turbomachines
AGARD CP 469, February 1990

Hypersonic Combined Cycle Propulsion
AGARD CP 479, December 1990

Low Temperature Environment Operations of Turboengines (Design and User's Problems)
AGARD CP 480, May 1991

CFD Techniques for Propulsion Applications
AGARD CP 510, February 1992

Insensitive Munitions
AGARD CP 511, July 1992

Combat Aircraft Noise
AGARD CP 512, April 1992

Airbreathing Propulsion for Missiles and Projectiles
AGARD CP 526, September 1992

Heat Transfer and Cooling in Gas Turbines
AGARD CP 527, February 1993

Fuels and Combustion Technology for Advanced Aircraft Engines
AGARD CP 536, September 1993

Technology Requirements for Small Gas Turbines
AGARD CP 537, March 1994

Erosion, Corrosion and Foreign Object Damage Effects in Gas Turbines
AGARD CP 558, February 1995

Environmental Aspects of Rocket and Gun Propulsion
AGARD CP 559, February 1995

ADVISORY REPORTS (AR)

Producibility and Cost Studies of Aviation Kerosines *(Results of Working Group 16)*
AGARD AR 227, June 1985

Performance of Rocket Motors with Metallized Propellants *(Results of Working Group 17)*
AGARD AR 230, September 1986

Recommended Practices for Measurement of Gas Path Pressures and Temperatures for Performance Assessment of Aircraft Turbine Engines and Components *(Results of Working Group 19)*
AGARD AR 245, June 1990

The Uniform Engine Test Programme *(Results of Working Group 15)*
AGARD AR 248, February 1990

Test Cases for Computation of Internal Flows in Aero Engine Components *(Results of Working Group 18)*
AGARD AR 275, July 1990

Test Cases for Engine Life Assessment Technology *(Results of Working Group 20)*
AGARD AR 308, September 1992

Terminology and Assessment Methods of Solid Propellant Rocket Exhaust Signatures *(Results of Working Group 21)*
AGARD AR 287, February 1993

Guide to the Measurement of the Transient Performance of Aircraft Turbine Engines and Components *(Results of Working Group 23)*
AGARD AR 320, March 1994

Experimental and Analytical Methods for the Determination of Connected — Pipe Ramjet and Ducted Rocket Internal Performance *(Results of Working Group 22)*
AGARD AR 323, July 1994

Recommended Practices for the Assessment of the Effects of Atmospheric Water Ingestion on the Performance and Operability of Gas Turbine Engines *(Results of Working Group 24)*
AGARD AR 332, September 1995

LECTURE SERIES (LS)

Engine Airframe Integration for Rotorcraft
AGARD LS 148, June 1986

Design Methods Used in Solid Rocket Motors
AGARD LS 150, April 1987
AGARD LS 150 (Revised), April 1988

Blading Design for Axial Turbomachines
AGARD LS 167, June 1989

Comparative Engine Performance Measurements
AGARD LS 169, May 1990

Combustion of Solid Propellants
AGARD LS 180, July 1991

Steady and Transient Performance Prediction of Gas Turbine Engines
AGARD LS 183, May 1992

Rocket Motor Plume Technology
AGARD LS 188, June 1993

Research and Development of Ram/Scramjets and Turboramjets in Russia
AGARD LS 194, December 1993

Turbomachinery Design Using CFD
AGARD LS 195, May 1994

Mathematical Models of Gas Turbine Engines and their Components
AGARD LS 198, December 1994

AGARDOGRAPHS (AG)

Measurement Uncertainty within the Uniform Engine Test Programme
AGARD AG 307, May 1989

Hazard Studies for Solid Propellant Rocket Motors
AGARD AG 316, September 1990

Advanced Methods for Cascade Testing
AGARD AG 328, August 1993

REPORTS (R)

Application of Modified Loss and Deviation Correlations to Transonic Axial Compressors
AGARD R 745, November 1987

Rotorcraft Drivetrain Life Safety and Reliability
AGARD R 775, June 1990

Theme

A key factor for future improvements in turbomachinery is a detailed understanding of loss generation in the presence of the unsteady effects induced by the machine environment. Better understanding of loss mechanisms, and thus of general flow characteristics, is essential for the optimisation of turbomachines, particularly at off-design conditions, and in the unsteady flow prevailing in multi-blade row machines. This symposium will present experimental data on loss generation, as well as numerical models and their validation. Time averaged flows and unsteady flows (periodic or not) in single rows, single stage and multi-stage configurations will be discussed. Topics include boundary layer transition, separation and post-separation behavior, shock/boundary layer interactions, clearance effects, surge and stall, and secondary flows, especially at off-design and unsteady periodic conditions. The work presented at this meeting will help pave the way for improved design and analysis techniques which explicitly incorporate the management of loss generation and unsteady flow effects, based upon a more complete understanding of flow physics.

Thème

Un facteur clé des progrès futurs en turbomachines réside dans la compréhension de la génération des pertes en présence des effets instationnaires induits par l'environnement machine. Une meilleure connaissance des mécanismes à l'origine des pertes et donc des mécanismes généraux de l'écoulement est essentielle pour l'optimisation des turbomachines. C'est particulièrement vrai pour le fonctionnement en dehors des conditions nominales et dans l'écoulement à dominante instationnaire qui règne dans les machines multiètage.

Ce symposium est consacré à la présentation de résultats expérimentaux sur les mécanismes de génération de pertes ainsi qu'à la description de modèles mathématiques et numériques correspondants et à leur validation.

On présentera des approches moyenniées dans le temps et des approches instationnaires, périodiques ou non, pour la caractérisation des écoulements dans les rangées d'aubes isolées et en configurations mono et multiétage. On traitera, en particulier, de la transition, du décollement et du comportement après décollement des couches limites, des interactions ondes de choc couche limite, des effets de jeu, du décrochage tournant et du pompage, des écoulements secondaires. Les travaux présentes à ce symposium aideront à ouvrir la voie vers des techniques de conception et d'analyse des turbomachines incorporant explicitement la génération des pertes et les effets instationnaires.

Propulsion and Energetics Panel

Technical Evaluation Report
Loss Mechanisms and Unsteady Flows In Turbomachines

CC Koch
GE Aircraft Engines
1 Neumann Way
MS A-411
Cincinnati, Ohio 45215-6301
USA

Overview

This symposium was the 85th sponsored by the Propulsion and Energetics Panel of AGARD and was held in Derby, England, May 8 - 12, 1995. The primary focus of the symposium was on steady and unsteady-flow loss sources in gas turbine engine compressors and turbines. An additional related topic covered compressor stall and overall engine surge phenomena. In total, 42 technical papers were presented in nine sessions. The papers were about evenly divided between experimental studies of turbomachinery flowfields and loss-producing mechanisms, and analytical studies using computational fluid dynamic methods. Most papers generated several questions from the audience, and the resulting discussions added substantially to the value of the symposium.

The conference was very well attended, with nearly 270 persons being identified in the list of participants. This large participation reflects the high interest generated by the rapid pace of development in this area. The last 3-5 years have seen powerful CFD analytical methods achieve a high degree of maturity and acceptance. Three-dimensional, viscous, time-steady, single-bladerow codes are now well-enough validated (although "calibrated" is perhaps more accurate) that these are used routinely by gas-turbine manufacturers for virtually all new fan, compressor and turbine designs. Multi-bladerow, steady-state codes are now coming into use to better refine the upstream and downstream boundary conditions for each airfoil and to reflect the influence of any secondary flows, separation regions and wakes of adjacent airfoils. It is expected that these codes will come into widespread use in industry within the next few years. And finally, fully 3-D, viscous, time-unsteady 2-bladerow turbomachinery analysis codes are currently being developed and evaluated. These sophisticated codes have already seen limited practical use in analyzing certain cases where unsteady-flow effects have caused performance or durability problems. Clearly, their frequent use for design and development is not far in the future. These powerful CFD tools are taking the place of exploratory or prototype testing in guiding designers toward product configurations. With these analytical methods, substantial gains in performance have been achieved compared to designs done using 2-D inviscid methods. The viscous codes now used can identify regions of high loss and can thus lead designers to configurations that avoid flow separations, etc. As a result, recent CFD-based designs are much more likely to meet performance goals on the first try, without requiring lengthy and costly development testing.

In view of this rapid progress in the development and application of new analytical methods, this symposium was particularly timely. It provided specialists in turbomachinery research and design an opportunity to assess what is known, and not adequately known, about turbomachinery loss and compressor stall mechanisms. It was particularly valuable for assessing the capabilities, strengths and weaknesses of the newest CFD codes.

The keynote address by John Dunham, on Aerodynamic Losses in Turbomachines, was especially useful in highlighting both the progress made in the last two decades in aerodynamic design and performance prediction, and also in pointing out that there are numerous turbomachinery loss sources which have not had adequate experimental or analytical treatment. Designers must therefore make configuration selections based on experience or empiricism rather than firm knowledge of the performance impact of these design choices. Dunham concluded by providing a list of 20 key questions about turbomachinery loss mechanisms that need to be answered in order to advance the state-of-the-art. While few of these questions were answered by the papers presented at this symposium, the analytical means to answer many of them is clearly developing rapidly. Thus Mr. Dunham's address provides a useful agenda for future experimental and analytical studies; efforts to address his questions will direct future research toward topics of maximum practical value.

Topics Presented

The 42 papers presented in the symposium can be grouped into 6 broad subject areas. These are listed below, along with the paper numbers relating to that subject and the sessions in which these subjects were addressed:

- Secondary And Endwall Flows
  Paper No.'s 1, 7, 8, 9, 18
  Session No.'s I, II, IV

- Tip Clearance Effects
  Paper No.'s 10, 11, 12, 13, 41
  Session No.'s III, IX

- Airfoil Boundary Layers In Steady Flow
  Paper No.'s 2, 3, 4, 6, 14, 15, 18, 21
  Session No.'s I, II, III, IV, V

- Bladerow Unsteady Interactions
  Paper No.'s 5, 19, 20, 22, 23, 24, 34, 35, 36, 37, 38, 39, 40, 42
  Session No.'s V, VII, VIII, IX

- Shock Waves In Airfoil Cascades
  Paper No.'s 16, 17, 18, 36, 42
  Session No.'s IV, VIII, IX

- Compressor Stall And Surge
  Paper No.'s 25, 26, 28, 29, 30, 33
  Session No. VI

The following sections summarize the key findings presented in each of these subject areas, attempt to draw some conclusions about the state-of-the-art in these areas and make recommendations for future work and symposia.

Secondary And Endwall Flows

Five papers were presented on this topic, three of which were primarily experimental and two primarily analytical. Useful, high-quality experimental data were presented in Papers No. 1 (Stark and Bross) and No. 8 (Moore and Gregory-Smith) for linear turbine and compressor cascades. Progress in the ability of CFD codes to calculate endwall and secondary flows were illustrated in Papers No. 7 (Bassi and Savini) and No. 18 (Tinaztepe, Akmandor and Ucer). The possibility of controlling secondary flows via innovative design features and achieving significant loss reductions was shown in Paper No. 9 (Tikhomirov). Further analytical and experimental work along these lines should be encouraged in order to obtain the maximum practical benefit from the increased physical understanding and modeling capability we now have for such flows.

Tip Clearance Effects

Five papers were also presented on this topic, two experimental and three analytical. The interesting experimental data presented in Papers No. 12 (Peters and Moore) and No. 41 (Granovskii, et.al) quantified the losses produced as a result of tip clearance leakage flows. Paper No. 13 (Kameier and Neise) showed that large tip clearances could also produce increases in fan noise as well as loss increases. Very detailed CFD modeling of tip clearance leakage flows was presented in Paper No. 10 (Kang and Hirsch). A semi-empirical analytical model of clearance effects on loss and turning and on the formation of the leakage vortex was presented in Paper No. 11 (Nikolos, Donvikas and Papailion) which could improve the ability to represent complex, multi-stage flowfields using axisymmetric flow models. With the increased ability to model these complex flows with CFD techniques, it should be possible to evaluate creative design concepts that might lead to a reduction in clearance losses. More effort in this direction should be encouraged.

Airfoil Boundary Layers In Steady Flow

A total of 8 papers were presented on this topic, evenly divided between primarily experimental and analytical studies. Essentially all the papers explored details of airfoil boundary layer development, transition and loss. The analytical papers document the current state-of-the-art in CFD turbulence models. Paper No. 3 (Chen, Lien and Leschziner) in particular showed that significant progress can be made in turbulence modeling. Transition of airfoil boundary layers was shown to be critical to understanding and modeling turbomachinery losses, and modeling and predicting the onset of separation is critical to predicting off-design performance and aeroelastic behavior. Improved turbulence models for complex turbomachinery flows are clearly required in order to capitalize on the growing power of CFD solvers, and this may in fact be the final barrier problem for aero design, off-design performance prediction, prediction of flutter and forced response, and aero-acoustics. A very high priority needs to be placed on making progress in this area.

Bladerow Unsteady Interactions

Sixteen papers were presented on this topic, and much insight was gained on a variety of unsteady interaction effects. Some quite substantial unsteady effects were seen on blade forces, heat transfer coefficients and airfoil boundary layer development. Sometimes the effect on losses was shown to be substantial, as in Paper No. 23 (Hodson, et.al), although in many of the papers the magnitude of unsteadiness-induced losses was not quantified. The impressive 3-D, viscous, unsteady CFD analyses presented in Paper No. 37 (Dawes) show that practical CFD tools are becoming available to deal with unsteady interactions. The industry will quickly adopt these tools and will use them in the design process whenever experience suggests that unsteadiness effects are large. More studies to identify when this added complexity in the design process is justified should be encouraged.

Shock Waves In Airfoil Cascades

Four papers, two experimental and two analytical, were presented on this general topic. Some interesting, quite detailed data was given in Paper No. 17 (Schreiber) showing how cascade pressure rise capability is limited by shock/boundary layer interaction and separation. This could form the basis for a stall prediction model for transonic fans whose stall limits don't appear to correlate with traditional airfoil surface diffusion or endwall loading criteria. The ability of CFD codes to address shock/boundary layer interactions was illustrated in Paper No. 18 (Tinaztepe et.al), although the accuracy of such calculations is probably limited by the relatively simple turbulence models currently available. Progress in semi-empirical modeling of transonic compressor shock losses was shown in Paper No. 16 (Bloch et al), and more work along these lines should be encouraged in order to improve preliminary

performance estimates. Finally, some valuable studies on the impingement of shocks generated in other blade rows moving relative to the airfoil in question were shown in Papers No. 36 (Liamis, Bacha and Burgaud) and No. 42 (Doughty and Schetz).

Compressor Stall And Surge

There were six papers presented on this subject, five of which, were experimental. Studies to identify stall precursors, presented in Papers No. 26 (Breuer and Servaty) and No. 30 (Riess and Walbaum), show some promise and could possibly lead to an active stall control system. The onset of rotating stall and the flow details associated with rotating stall cells were documented in Papers No. 25 (Borys and Moffatt), No. 28 (Owen) and No. 29 (Cousins, et al). Progress in modeling compressor and full engine stall and surge was demonstrated in Papers No. 26 (Breuer and Servaty) and No. 33 (Davis et al). It is encouraging that stall precursor studies are now being published that address the real-word cases of high-speed, multistage compressors with variations in stage matching and with inlet distortions. Yet this author suspects that infallible, fail-safe, lightweight, cheap and durable stall control systems are still far in the future. It seems, instead, that there might be a greater chance for success, and possibly a greater near-term payoff to the industry, to devote more effort to devising a reliable way of predicting stall in advance. Developments in CFD methods are such that it may soon be possible to predict stall limits knowing only the compressor geometry and its operating conditions. Unfortunately, no work along these lines was presented.

Conclusions

The past few years have seen the rapid development and validation of powerful analytical methods capable of providing great insight into complex turbomachinery flows and loss mechanisms, including time-unsteady processes. This progress has been brought about by a concerted effort on the part of both code developers and experimentalists, and a good overview of this work was presented at this symposium. These codes are now well-enough developed to be used in industry for nearly all design work, so that it now appears that further progress in predicting exact magnitudes of losses may be paced primarily by development of better boundary layer turbulence models.

The turbomachinery field may thus be reaching the point where the emphasis can shift from developing better tools, to one of better utilizing these tools. Researchers could now begin to conduct "electronic experiments" on key problems, such as answering all of John Dunham's 20 questions. Priority could be placed on evaluating innovative design features so that significant advances in the state-of-the-art might be realized. Perhaps, therefore, the next AGARD PEP Symposium on turbomachinery performance should focus on practical demonstrations of advancements in the state-of-the-art due to application of advanced analytical design methods and experimental research. Topics could include:

- improvements in efficiency
- increases in stall margin and loading limits
- reduced sensitivity to clearance changes
- reduced sensitivity to inlet distortions
- lower turbomachinery-generated noise
- resistance to airfoil flutter

Technology advances such as these are, after all, expected by those industrial firms and government agencies that have invested heavily in research and the development of advanced CFD codes for the past 10-15 years; in many cases these "investors" are becoming impatient to see some substantial returns on their investment.

Aerodynamic losses in turbomachines

J.Dunham
Defence Research Agency, Pyestock,
Farnborough, Hampshire, GU14 0LS, United Kingdom

SUMMARY

During the early decades of aero engine gas turbine development, aerodynamic losses were predicted by means of empirical correlations of experimental results, and these predictions were used to optimise new designs. Nowadays, the physical mechanisms by which the losses are generated are understood in much more detail, leading to correspondingly complex mathematical models, although they still embody some empiricism. CFD codes solving the steady Reynolds-averaged Navier-Stokes equations are now available, and designers are beginning to use them to arrive at good designs. This paper assesses the extent to which knowledge of loss mechanisms is adequate for design purposes, and the extent to which better understanding is needed. Design methods have almost invariably assumed that the incoming flow to each row is the mixed-out average of the flow leaving the preceding row. The escalating power of computers is enabling the adequacy of that assumption to be critically examined, both experimentally and computationally. In the course of this review of the state-of-the-art in loss prediction, some important questions for research workers in this field are suggested.

1. INTRODUCTION

In preparing this keynote address, the aim has been to review the present state of knowledge in this field, so as to identify critical questions for research to answer. Section 2 outlines why engine designers need to predict losses. For some project studies, very simple pitchline efficiency estimates are sufficient, which are commented on in Section 3, but the rest of the paper is concerned with the loss predictions needed in designing an axial compressor or turbine.

Denton[1] undertook a comprehensive review of loss mechanisms in compressors and turbines; readers wishing to see what is known about loss mechanisms should refer to that paper, which also contains some new analytical insights. The present paper is more concerned with what is *not yet* known and needs to be found out. The need to understand loss mechanisms is evident when the design procedure is based upon some kind of throughflow calculation, in which mathematical models of the various types of loss are incorporated. It might be thought that, if designers are moving towards unsteady three-dimensional Reynolds-averaged Navier-Stokes codes, in which all the various losses are automatically accounted for, the only loss model needed is the turbulence model. But it is hard to see how the designer, however well he can predict the efficiency of his design, will be able to perceive how to improve it without grasping the physical reasons underlying what the code tells him. The number of design choices is virtually infinite, far too large to undertake a purely-computational optimisation.

Section 4 looks at the definition of aerodynamic losses, drawing attention to "accountancy" problems. Sections 5 and 6 look at profile and secondary losses respectively, and Section 7 addresses the effect of adjacent rows - that is, the effect on losses of the passage of upstream and downstream rows. Section 8 discusses turbulence modelling in the turbomachinery context. Section 9 reviews the extent to which, using a better understanding of loss mechanisms, losses have been reduced. Section 10 looks briefly at the increased losses seen as an engine gets older.

Finally, the concluding Section 11 draws together the various issues which the author considers of particular importance.

2. THE NEED FOR LOSS PREDICTION

The primary need for loss prediction is of course to predict compressor or turbine efficiency, but aerodynamic losses also affect the outlet gas angle from a blade row (or deviation), the matching of rows (through endwall "blockage"), and they control the surge line of a compressor. In a turbine, the aerodynamics of losses are closely linked to (and sometimes predicted by the same computations as) the heat transfer.

Engine manufacturers use these efficiency predictions during two distinct phases of engine design. In the first phase, the project designer has to select the overall architecture of the engine; spool layout, mass flows, pressure ratios and temperatures, bypass ratio, shaft speeds and so on. There are many considerations which have to be taken into account, of which component aerodynamic efficiency is only one, but nevertheless the trade-off between, for example, four or five or six LP turbine stages is critically dependent on how the turbine efficiency drops with loading. Details of the blading are of course unknown at this time; the designer wants to know how efficient a turbine will be possible (in several years' time) at the conditions envisaged in the design study.

When the time comes to design the compressor or turbine in detail, loss predictions are needed, firstly to guide the designer towards the optimum choice of velocity triangles, and such features as aspect ratio, leading to the choice of aerofoil shapes, and secondly to estimate the overall performance characteristics of the unit. It is necessary to check not only that the design point performance satisfies requirements, but also that the off-design performance (such as the high speed and low speed surge margin of a compressor) is acceptable.

Paper presented at the AGARD PEP 85th Symposium on "Loss Mechanisms and Unsteady Flows in Turbomachines", held in Derby, United Kingdom, 8-12 May 1995, and published in CP-571.

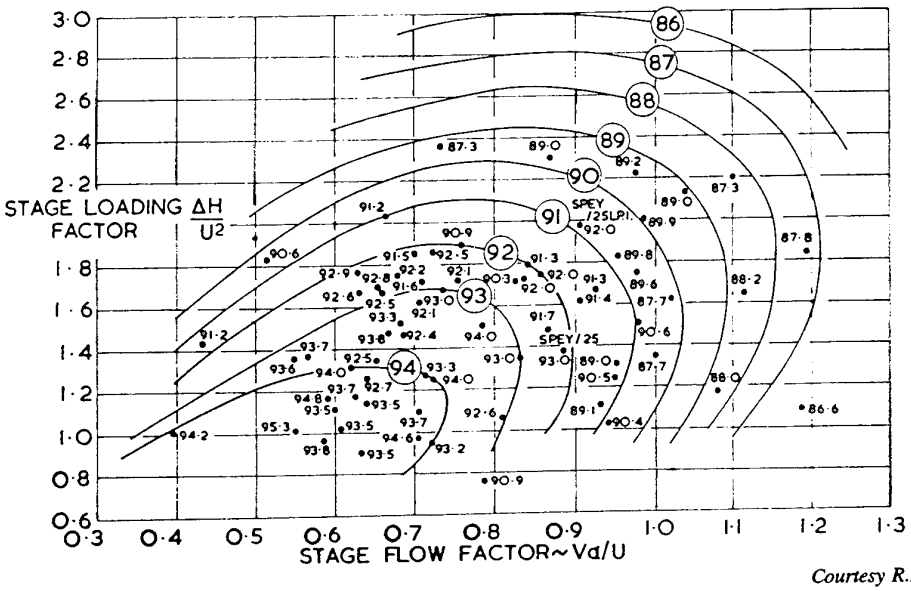

Courtesy R.Ae.S.

Fig.1 Rolls-Royce turbine efficiency correlation (1965)

3. PITCHLINE EFFICIENCY PREDICTIONS

This class of methods is exemplified by the Smith chart[2] (Fig.1) which shows contours of turbine efficiency (for zero tip clearance) as a function of stage loading and flow coefficient. The diagram was constructed from the measured efficiencies of Rolls-Royce turbines. As Smith recognised, a diagram of this type can only be valid for high aspect ratio blading; and as a way of selecting optimum flow coefficient it is probably now misleading. Diagrams of this type - but taking account of more of the relevant parameters - can be constructed for turbines using updates[3,4] of the original Ainley and Mathieson method[5] for turbines, and using a method such as those of Howell and Calvert[6] or Casey[7] or Wright and Miller[8] for compressors. As a way of estimating the flow and efficiency variation over the full range of running conditions, such methods are still useful, but as a way of selecting optimum flow coefficient or aspect ratio they are generally inadequate. Koch and Smith[9] undertook a much more detailed scheme for predicting the design point efficiency of a well-designed compressor, for the purpose of preliminary design, and this scheme also enables the leading design parameters to be optimised on a pitchline basis.

So what is the project engine designer to do to obtain approximate performance estimates (including surge pressure ratio) and to select optimum stage loading, hub and tip diameters and axial length in the initial phase of a design, when they represent only one element amongst many others, such as safety, weight and cost? Probably the best system for the experienced manufacturers is to employ the Kacker and Okapuu[4] or the Howell and Calvert[6] or the Koch and Smith[9] method (or some equivalent scheme) but to use the actual achievements of the Company for a similar class of turbomachine to anchor the predictions.

The first question addressed to research workers is therefore:

Q1 What methods do you recommend for project designers, and what allowance (efficiency improvement) should they make for potential improvements due to more recent research developments such as "endbends" and "3D design"?

4. DEFINITION OF LOSS COEFFICIENTS

Although Denton[1] advocates the use of entropy loss coefficient or energy loss coefficient, usually loss coefficient is defined in cascade tests as the loss of stagnation pressure along a streamline (P_{t1}-P_{t2}), divided by q, the inlet dynamic head (for a compressor) or outlet dynamic head (for a turbine). In a turbomachine, it is necessary to adopt the more careful definition (P_{t2is}-P_{t2})/q, where P_{t2is} is the outlet stagnation pressure resulting from an isentropic process from inlet to the outlet stagnation temperature, and all quantities are relative to the blade row. This definition caters for a rotor row in which the stream surface changes radius, so that the rotor outlet relative stagnation temperature T_{t2} is not the same as the inlet value T_{t1}.

The concept of loss coefficient rests on the idea of a "stream surface" passing through a blade row, containing the same fluid at outlet as at inlet. It is now recognised that in a real turbomachine spanwise mixing occurs; that is, fluid is exchanged across the stream surfaces assumed in a throughflow calculation. This raises "loss accounting" questions. Looking at the simple case of a stator, or a rotor with no change in streamline radius, it would normally be assumed that $T_{t2} = T_{t1}$ so that $P_{t2is} = P_{t1}$. However, if a spanwise temperature redistribution occurs, this is no longer true, and the "cascade" definition of loss coefficient no longer agrees with the "turbomachine" definition. Fig.2 illustrates the difference for the particular case of a low speed research compressor[10]. The measured stator loss coefficient in stage 3, using the "cascade" definition, is compared with predictions (by a spanwise mixing

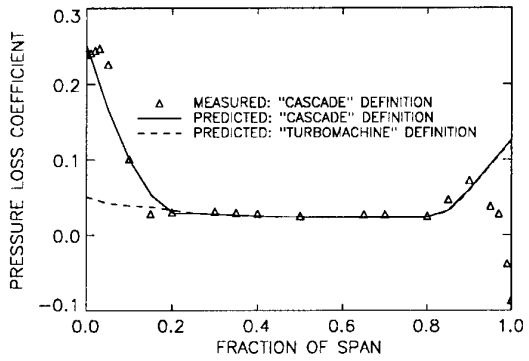

Fig.2 The effect of spanwise mixing on the apparent loss coefficient

throughflow code[11]) using the two alternative definitions. There is a marked difference near the inner wall, where, because the stator is unshrouded, there is a radial stagnation temperature gradient and hence some turbulent diffusion. The stagnation temperature drops only about 0.2° across the stator but this is enough to make the difference. This is a warning to research workers attempting to correlate secondary losses from measured stagnation pressures.

Another "loss accounting" issue arises from the unsteady nature of the real flow; every row after the first row receives a succession of wakes from the previous rows, and the customary assumption that its aerodynamic performance is the same as it would have been had its inflow been steady at the mixed-out value of the incoming flow is open to question. This is discussed in Section 7.

It is also worth noting that the overall efficiency of a turbomachine measured on a test rig is often quoted assuming that the inlet flow is uniform in stagnation temperature and pressure; the losses along the annulus wall boundary layers upstream of the blading are debited to the turbomachine.

The absolute accuracy with which losses need to be predicted is not unusually high. For a turbomachine having 90% efficiency, a 10% error in loss prediction causes a 1% error in efficiency prediction, around the best level of absolute efficiency measurement. A better standard of efficiency *change* prediction, say 0.2%, is needed for a design procedure being used to optimise blading. A specific example is given in Section 5.

Loss coefficients are divided, for convenience, into profile losses, associated with the blade-to-blade flow, and secondary losses, associated with the endwalls. These categories will now be considered separately.

5. PROFILE LOSSES

Profile losses are caused by the development of the aerofoil boundary layers along the surfaces, including any separated regions; by shock waves; by trailing edge base pressure; and by mixing in the wake. In a turbine, the discharge of cooling air into the mainstream also causes losses (though if it increases the base pressure it may have a favourable effect[12]). In principle these phenomena are understood and should be predictable; in practice some difficulties are well-known.

The boundary layer starts as a laminar boundary layer at the leading edge, but at high incidence, or if the leading edge is sharp, transition may occur almost immediately. This transition may occur naturally but, more often, it is seen as a laminar separation bubble, leading to a turbulent reattachment. The prediction of the length of the transition region and the momentum thickness of the emerging turbulent boundary layer remains difficult[13]. Then in the case of a transonic compressor, the boundary layer will be disturbed by the leading edge or passage shock. There or later on, the turbulent boundary layer may separate (and possibly reattach). If the surface is locally concave, Görtler vortices may develop. At the trailing edge, the separation will leave a base region at what is still an unpredictable pressure - at least for a turbine in supersonic flow where trailing edge shock waves are found, and perhaps cooling air is discharged.

There are four ways of predicting these effects: correlation, boundary layer calculations, viscous-inviscid interaction, and Navier-Stokes computations. AGARD-PEP Working Group 12 reviewed[14] those available in 1978-81. The oldest is of course by correlating experimental results. Correlations have been published for "classical" aerofoil families such as the NACA-series, but it is well-known that modern tailored aerofoil shapes produce lower losses[15] and the correlation approach may be misleading for them. Also, for a modern supersonic section of a transonic fan, the location of the shock, and hence the deviation and loss, is critically dependent on the streamtube shape, which no cascade correlation can take into account. The second way is to compute the inviscid flow around the aerofoil and then calculate the resulting boundary layers. This does not work if the boundary layers block the passage significantly or if either boundary layer approaches separation. In that case, a viscous-inviscid interaction scheme is essential. Koch and Smith[9] adopted an intermediate approach in which boundary layer computations were done on a wide range of typical compressor blade pressure distributions, and the results of those computations were correlated. The fourth method is a quasi-two-dimensional Navier-Stokes computation of the entire flow field.

Q2 How accurate is 2D Navier-Stokes compared with viscous-inviscid interaction?

In an engine compressor or turbine, there is sometimes a significant radial pressure gradient. The boundary layer on a rotor blade is subject to centrifugal forces. So for one reason or another, the aerofoil surface boundary layers and wakes may move radially, the fluid crossing the stream surfaces of the mainstream flow. The first good experimental evidence of how large this effect can be in a turbine was published by Herzig and Hansen in 1955[16]. In their turbine, fluid initially on the casing wall was swept on to the aerofoil, and down the blade or perhaps down the base region at the trailing edge to around mid-height before being discharged in the wake. Much more recently, Dominy and Kirkham[17] have published the interesting result of an experiment on a swan-necked annular duct, in

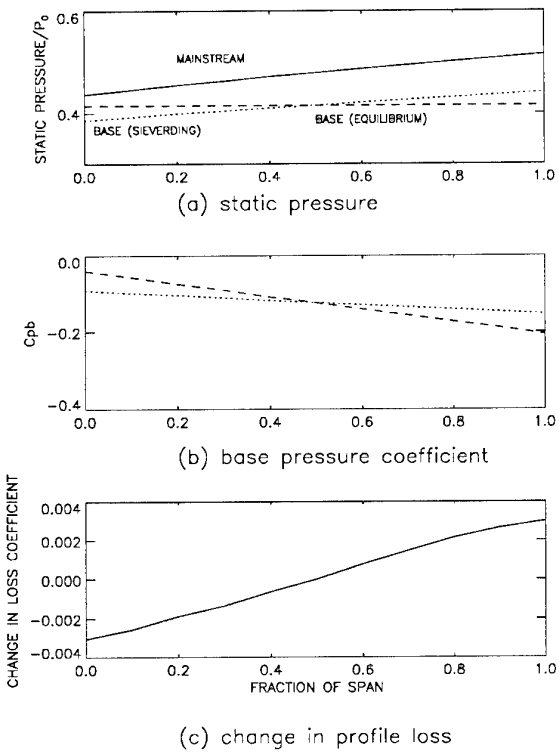

Fig.3 Nozzle guide vane base pressure

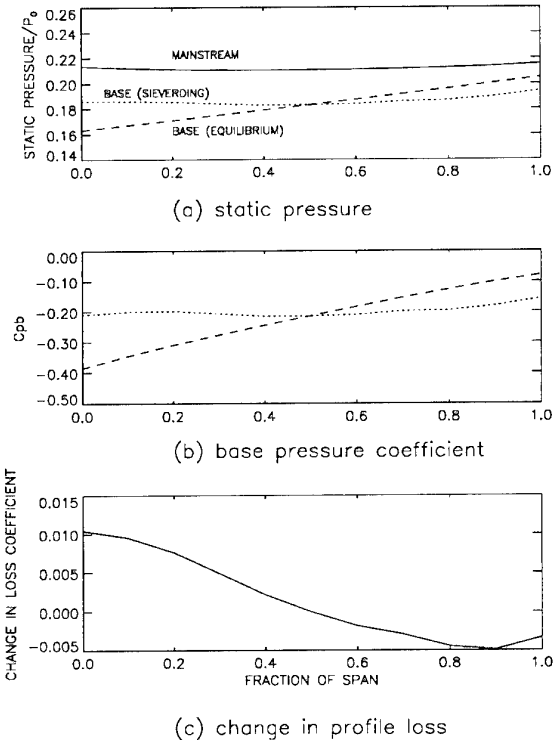

Fig.4 Rotor base pressure

which they found that the inner wall boundary layer approaching the first bend was swept outwards up the wake of an uncambered vane placed at that location, so that the inner wall boundary layer became much thinner and the outer wall boundary layer much thicker. Mathematical models have been proposed for these boundary layer and wake migrations[18,19,20] but they have not been widely adopted by turbomachinery analysts. Clearly, this creates a "loss accounting" problem, as mentioned in Section 4.

The base pressure is very important for a turbine blade because the trailing edge is relatively thick, and contributes typically one third of the profile loss[1], but it is not known how to predict it. Correlations by Hart et al[21] and Sieverding et al[22] can be used to predict base pressure at subsonic and transonic speeds respectively. How good this prediction is in the context of an actual turbine is uncertain. In the author's opinion, the problem lies in an essentially three-dimensional consideration: there must be some kind of radial equilibrium within the base region of the whole blade, which means that the base pressure at a particular radius is not determined solely by the aerofoil flow at that radius only. Radial flows within the base region, as described in the previous paragraph, may be needed to put the radial pressure variation into equilibrium.

To illustrate this some approximate calculations have been done for one particular single stage turbine[23] representative of an aero engine high pressure turbine. Fig.3a shows the pitchwise mean static pressure distribution in the mainstream at the nozzle guide vane (ngv) trailing edge plane, normalised by the upstream stagnation pressure P_0. Because of the swirl, it increases with radius. Fig.3a also shows the base pressure predicted by the Sieverding correlation; it too increases with radius. But if the air in the base region is actually stagnant, it cannot sustain any radial pressure gradient, so it must be at a constant static pressure; suppose that is the Sieverding mid-height value. Fig.3b shows the base pressure coefficients corresponding to those alternative base pressures, and Fig.3c shows the difference in loss coefficient between the "equilibrium" base pressure and the Sieverding base pressure, using equation (26) of Ref 1 which applies only if there is no radial flow redistribution in the base region. It will be seen that the loss reduces below mid-height and increases above mid-height. The estimated total profile loss coefficient for these ngvs is around 0.15, so the change is not great. Fig.4 shows the corresponding calculations for the rotor. In this case, the mainstream static pressure is fairly constant across the span, because the swirl is low. But if the air in the base region is stagnant with respect to the blades, it has a tangential velocity equal to the blade speed, so if it is in equilibrium without radial flow, the base pressure must increase with radius as shown; again, the mid-height Sieverding pressure is assumed correct. Fig.4b shows the base pressure coefficients, and Fig.4c shows the corresponding change in loss coefficient. This time, the loss increases at the hub end and decreases at the tip end. The changes are larger in magnitude, the predicted total profile loss coefficient being also around 0.15.

The author is unaware of specific experimental evidence as to whether the base pressure conforms in practice to the Sieverding value or to the "equilibrium" value - or at which spanwise position they match. In principle, a 3D Navier-Stokes computation should reveal the correct answer, but computations can produce dubious results in the base region because of the proximity of trailing edge shocks. The AGARD-PEP WG18 test cases[24] include just one case in which ngv surface static pressures were

measured in detail, and in that case extrapolation suggests that there is a considerable radial static pressure gradient in the base region.

If, as seems likely, the base pressure is not in radial equilibrium with zero radial flow, then there must be sufficient radial flow up or down the base region to satisfy equilibrium. Adkins and Smith[18] and Whitfield and Keith[19] have proposed ways of predicting radial flows within blade surface boundary layers and wakes in the context of compressors, but the author is not aware of radial flow predictions in the base region of turbine blades, where the trailing edge shock pattern is a serious complication. Of course, any radial flow not only changes the relationship between base pressure coefficient and loss coefficient; it also transfers fluid, and entropy, from one radius to another, invalidating the whole approach to profile loss prediction by correlation.

Q3 How good a prediction of base pressure is possible, with or without a Navier-Stokes code?

A cooled turbine blade has two additional complications. One is that the heat transfer from the gas to the aerofoil alters the boundary layers. The other is that cooling air discharge changes the boundary layer directly. Since cooling air comes out of holes not two-dimensional slots, any model other than a fully-three-dimensional model involves some form of local spanwise averaging. Recent research has shown that the shape of the cooling air discharge hole matters; a rounded edge is better[25]. So the prediction of cooling air effects is far from simple. "Momentum box" methods have been proposed by Barnes[26] and Hartsel[27] which are in common use.

Q4 How accurate are the Barnes and Hartsel methods?

When the blade wake has left the trailing edge, it gradually mixes out; the additional loss due to wake mixing (to the extent that it occurs before the next blade row) is well established[1,28].

A key feature in predicting compressor or turbine performance is the relative gas outlet angle just after the trailing edge. The computation of this angle is done at the same time as the loss calculation, and of course they are interlinked, especially if there is a separation of the boundary layer well before the trailing edge.

Last year, ASME organised a "blind" test case, in which research workers were invited to predict the performance of an isolated transonic fan rotor ("Rotor 37") using 3D Navier-Stokes computations. In an isolated rotor like this, the complications of unsteady flow or blade row interactions are absent, and the overall performance prediction accuracy is dominated by the two factors of deviation and profile loss. NASA had previously measured its performance in great detail, but the measurements were not disclosed until the predictions had been received. The purpose of the exercise was to help the research community to advance the state of the art by exposing the weaknesses of their present codes, and to give other people a yardstick to assess the sometimes over-optimistic claims of code developers. Entrants were asked to predict the overall characteristics at the design speed, from stall to choke, but

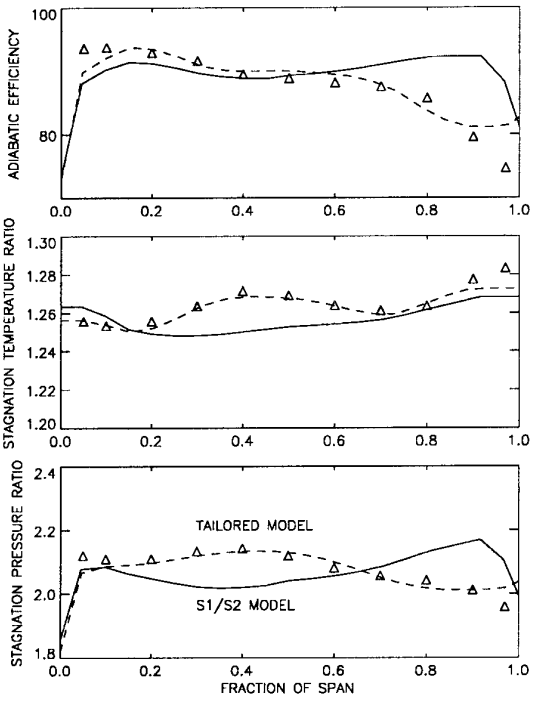

Fig.5 Rotor 37 modelling

to concentrate on two particular mass flows - 92% and 98% of the choking flow. The predictions of flow range from choke to stall were good although the stall point was judged by failure of the codes to converge.

The present author has used a revised version of his throughflow code[11] to study the 98% flow point to clarify the level of accuracy of loss prediction needed, and the level of accuracy achieved by entrants. Firstly, the assumed radial distributions of profile loss and deviation were tailored until the calculated radial distributions of stagnation pressure and temperature matched the measured values fairly well. In Fig.5, the broken lines showing this "tailored" model are close to the measured values, shown by symbols. The overall pressure and temperature ratios and efficiency were almost exactly matched. Then first the deviation was reduced by 1° at all radii, and later the loss coefficient was increased by a uniform 0.01, to establish the sensitivity of the overall performance to such changes. Fig.6 shows the results diagrammatically. It shows the measured values (with NASA's estimated measurement accuracy), and the range of predictions of all 11 entrants. It also shows the much smaller range predicted by most of the entrants, which is fairer; a coding error had been discovered in the worst prediction. It is noticeable that most of the predictions overestimated the temperature and pressure ratio, though not the efficiency. The temperature ratio prediction is very sensitive to deviation but is little affected by small changes in the assumed losses. It can be seen that the predictions imply errors of several degrees in deviation, and that an accuracy better than ½° is needed to predict the work level to 2%. The efficiency prediction is sensitive to the loss coefficient, of course, but is little affected by small changes in the assumed deviation. The

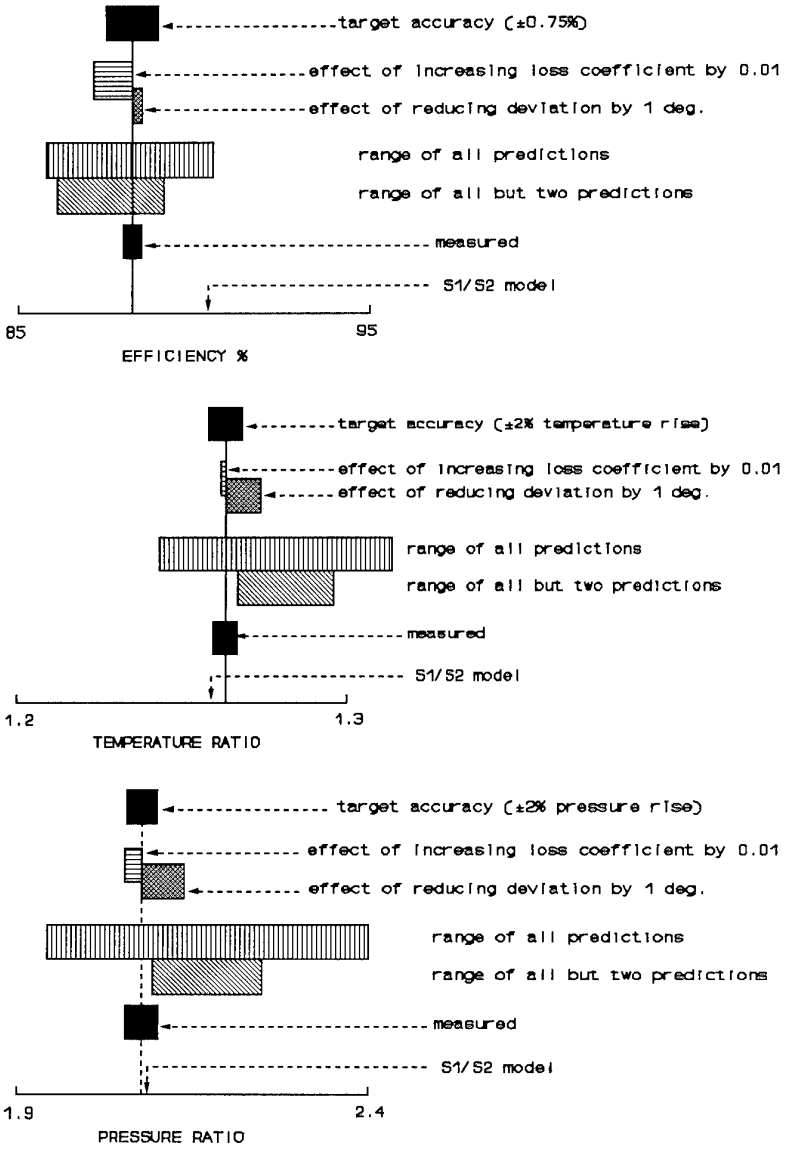

Fig.6 Sensitivity of Rotor 37 overall performance to profile loss and deviation

predicted loss coefficient varied over a range of about 0.04, which is around 40% of the mean value, whereas to achieve 1% accuracy in efficiency the loss coefficient needs to be within 0.01. Of course these figures only apply to this particular case but they do give an indication of the levels of accuracy typically needed.

The radial distribution of stagnation temperature ratio, pressure ratio and efficiency also proved illuminating. The DRA's S1/S2 code[29], employing a viscous-inviscid interaction method[30] to predict the profile loss and deviation, was used in 1993 to predict the performance of Rotor 37 over a range of speeds. It produced a reasonable prediction at 90% speed, but at design speed it would only converge at the choking flow and predicted a pressure ratio of 2.022 at an efficiency of 87.7%. Reducing the flow provoked a major separation around 40% span and the S1/S2 iteration diverged. So the profile loss and deviation at the converged point were inserted into the author's code (which predicts the endwall region effects internally). This calculation produced quite different radial distributions, also shown in Fig.5 (labelled "S1/S2 model" for brevity), with overall predictions marked on Fig.6. The predicted profile loss and deviation distribution is shown in Fig.7 along with the values tailored (as described earlier) to the observed pressure and temperature profiles. It will be seen that the S1/S2 method predicts a large increase in deviation around 40% span, as a result of premature separation of the suction surface boundary layer. The experiment, on the other hand, if reconstructed correctly by the throughflow code, shows that the high losses occur near the outer casing.

It has been shown that the predictions are very sensitive to the assumed deviation. Examination of the deviation predictions produced by the viscous-inviscid blade-to-blade code[30] shows that they depend on whether the average mainstream value of outlet angle is used, or the wakes are taken to be fully mixed out. The value the code actually uses is the fully mixed out value referred to the trailing

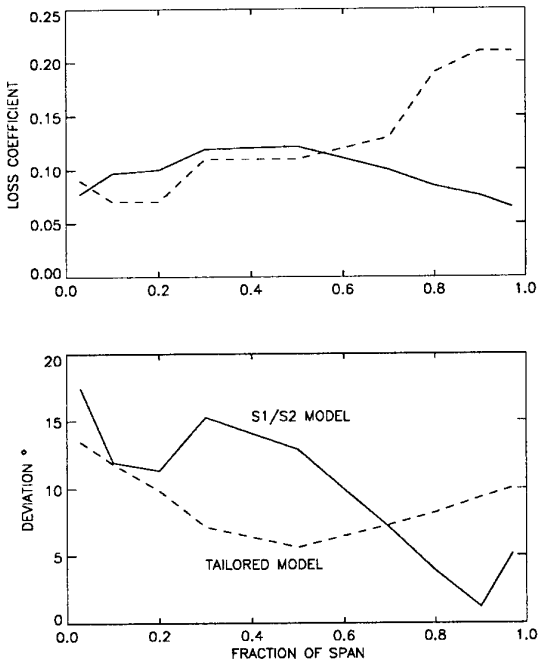

Fig.7 Rotor 37 loss and deviation estimates

edge plane radius and area, but the values differ by several degrees, especially if the loss is high.

Referring back to the 3D Navier-Stokes predictions of the entrants, most of the predicted temperature and pressure profiles are similar in shape to the S1/S2 predictions in Fig.6, so it appears that they too predict high values of deviation and loss around 40% but not 80% span.

What the exercise suggested is that, even for an isolated row, current 3D Navier-Stokes codes need to be improved before they can be relied upon to predict deviation and losses, although they have been shown to predict surface static pressures well in easier test cases. The Rotor 37 case is clearly difficult and hence a most suitable basis for further study. AGARD-PEP has set up Working Group 26 to pursue it in more detail.

Q5 How accurately can outlet relative gas angle be predicted?

6. SECONDARY LOSSES

The original definition of secondary losses was "what is left over when profile losses have been allowed for", but secondary losses are now taken to refer to the additional losses arising from the two endwall effects: the interaction of the endwall boundary layers and the blade passages, and tip clearances.

If there is no tip clearance, the incoming annulus wall boundary layer is swept partly, or fully in the case of a turbine, across the passage and on to the suction surface. A streamwise vortex is formed in accordance with the classical ideas of "secondary flow". Losses arise from the development of the annulus wall boundary layer, from the interaction between the low energy fluid convected on to the suction surface and the existing boundary layer on that surface, and from the mixing of the streamwise vortices (dissipating their kinetic energy[31]). These physical processes are now quite well understood, but the prediction of the resulting losses is far from easy.

Q6 How accurately can this type of secondary loss be predicted (a) without recourse to 3D Navier-Stokes computations and (b) using them?

If there is a tip clearance, air is driven through it by the pressure difference from the pressure surface to the suction surface, helped or hindered by any relative movement between wall and blade. This tip leakage rolls up into streamwise vortices. The physical processes are becoming much better understood[32,33], but again the quantitative accuracy of loss prediction is still poor.

Q7 How accurately can tip clearance loss be predicted (a) without recourse to 3D Navier-Stokes computations and (b) using them?

Reference has already been made to spanwise mixing. This occurs as a result of three physical phenomena: turbulent diffusion (Gallimore and Cumpsty[34]), turbulent convection[11,18], and spanwise migration of blade surface boundary layer and wake fluid[18]. By turbulent convection, in this context, is meant the radial transfer of fluid by the streamwise vortices (due to classical secondary flow or to tip clearance flow) described in the previous paragraphs[35]. The transferred fluid takes with it momentum, energy, and entropy. So in effect it may transfer aerodynamic losses from one stream surface of the main flow to another. Attempts have been made to model spanwise mixing in the context of throughflow calculations (Adkins and Smith[18], Whitfield and Keith[19], Gallimore and Cumpsty[34], de Ruyck and Hirsch[20], Howard and Gallimore[36], Dunham[11,37,38], Lewis[39]), but the level of success is not well established. Dring has shown experimentally that the radial transfers of momentum near the endwalls in both a compressor[40] and a turbine[41] are sufficient to upset the application of the angular momentum equation (change of angular momentum = torque on rotor) to an assumed stream surface. This radial transfer is particularly strong in a compressor if a corner stall occurs. Corner stall is a three-dimensional separation in the corner between the suction surface and the endwall, which has now been widely observed in fairly highly loaded cascades and compressors[42]. In so far as this phenomenon sets a limit to the achievable pressure rise in a blade row (further throttling would lead to surge?) its prediction must be an important research target. There is no simple prediction method yet available, though Howard and Gallimore[36] refer to a correlation (not specified in detail). A three-dimensional Navier-Stokes computation should be capable of predicting the corner flow, and may be successful in predicting corner stall.

Q8 Can the onset and consequences of corner stall be predicted?

An alternative method for predicting the first two of these steady secondary flow effects in compressors has been proposed[11]. This method calculates the pitchwise-average flow by a streamline curvature method. The annulus wall boundary layers are calculated by Hirsch and de Ruyck's

method (Chap.II.2.3 of Ref 14), which needs empirically-based expressions for the forces exerted by the blades on the annulus wall boundary layer fluid. When combined with calculations of secondary flow, turbulent diffusion, and turbulent convection, this method replaces purely empirical expressions for these endwall effects. It can give good predictions; Fig.2 is an example. In this method, the choice of the empirically-based expressions referred to is crucial. The formulae chosen in Ref 14 were justified by physical arguments, but direct experimental evidence was not available.

An alternative approach is now becoming available for choosing the mathematical model in such circumstances - numerical "experiments". A Navier-Stokes code selected to model the loss in question is applied to a representative configuration, and the parameters believed to be relevant are varied systematically. The CFD results, even if quantitatively indifferent, should at least guide the research worker to the correct choice of non-dimensional parameters on which to base his model, and to the nature of the relationship (for example, linear or logarithmic) to be postulated. This may leave empirical constants to be chosen to fit a very small range of experimental data, but with far more confidence than without the numerical experiment.

In addition to an endwall loss, the annulus wall boundary layers also constitute an effective blockage of the annulus (the sum of their displacement thicknesses). This blockage can be critical in controlling stage matching, especially in a transonic compressor. Currently, designers tend to rely on empirical blockage estimates, based on their past experience.

Q9 How well can "blockage" be predicted?

The concept of a pitchwise average annulus wall boundary layer is open to question for a compressor. It seems unlikely that an equivalent mathematical model could be at all realistic for a turbine, because experimental evidence shows clearly that the incoming wall boundary layer fluid is swept completely off the endwall and replaced by mainstream fluid.

In some turbomachines there are additional endwall complications, not at all well understood, which cannot yet be predicted quantitatively. One arises from cooling air discharge. Another arises from the leakage of air into or out of the mainstream at seals. (In an engine, air is extracted from the core compressor, used to cool the discs, and then it escapes back into the turbine flow.) Some low pressure turbines, especially large steam turbines, have steps in the annulus wall at the trailing edges of blade rows, which may have a favourable effect on performance; but it is not known how to predict their effect. It has been found that "tip treatments", in the form of overtip cavities of some kind, alter the surge margin and efficiency of a compressor. The aerodynamic mechanism has been shown[43] to involve air entering the wall cavity as the pressure surface of a blade passes, and then being blown back into the main stream as the suction surface passes. The prediction of resulting changes in loss, in the annulus wall boundary layer, and in the surge margin, presents another challenge to research workers.

7. UNSTEADY EFFECTS

In a compressor stage, for example, the aerodynamic losses generated within the rotor give rise to wakes and vortices, which arrive at the stator leading edges as an unsteady flow. When each wake enters a stator passage, it interacts with the stators and influences what emerges from the stator row as a stator wake. So the losses observed by a stator outlet traverse incorporate some rotor wake effects, and it is not necessarily true (as most design methods assume) that the stator loss is the same as it would have been had its inflow been steady and axisymmetric at the mixed-out value of the rotor outlet flow. The potential flow field effects of adjacent rows also influence the row. At present, turbomachinery design methods explicitly ignore unsteady effects, although probably some of the rules-of-thumb adopted by manufacturers in selecting aerofoil solidity allow, implicitly, for the effects of unsteadiness. Improved experimental techniques now enable the time-resolved flow fields to be measured[42], so as such measurements are acquired a better understanding of their effects will emerge and a demand to predict them will arise.

The intermittent arrival of the wakes from an upstream blade row interferes with the boundary layers; specifically an incoming wake may trigger immediate transition[44]. As the effect of that transition passes further along the surface, the boundary layer may revert to laminar until the next wake arrives. The first and simplest way of representing the effect of incoming wakes is to treat them as "high freestream turbulence". There is of course a rather high level of random turbulence within any turbomachine, but this approach may be too simplistic. A better approach to predicting such effects is the concept of "intermittency"[45,46]. This concept models the boundary layer by assuming it spends some fraction of the time in a fully-laminar state and the rest of the time in a fully-turbulent state.

Fan and Lakshminarayana[47] discussed the unsteady effects thoroughly. They presented an unsteady viscous-inviscid interaction method for incompressible flow which gives an indication of their magnitude. They used a specially-developed low Reynolds number form of the k-ε model, which reproduced the observed physical phenomena well. They found that the velocity changes in the boundary layer lagged behind the mainstream velocity changes, and that the time-average intermittency increased with frequency, implying that the quasi-steady equations would not be adequate. They showed how the increase in time-averaged loss coefficient over that calculated for steady flow depended on the axial gap and the wake-passing frequency. Increases around 10% were typical.

Clearly, the secondary flow is also seen by the next row as unsteady. A start has been made by Dawes[48] on understanding the consequences of that form of interaction.

Imanari[49] proposed a theoretical model for the spanwise mixing effects caused by unsteadiness, based on corresponding steady flow models.

There is one turbomachinery analysis scheme which specifically allows for blade-passing effects and for

random turbulence effects in the context of a steady flow computation. This is Adamczyk's method[50,51]. In his computational scheme, all the unsteady terms in the fluid dynamic equations are written down, and then formal spatial and time averages are derived. In this way, extra terms appear in the computation of the steady 3D Navier-Stokes equations for a single row which represent, to some approximation, the presence of all the other blade rows in the machine. Some of these extra terms can be computed directly, but others have to be modelled. Last year, Adamczyk et al presented an example[52], comparing computations of blade row interference by different methods.

It is clear that computers will have to be improved by around three orders of magnitude before the unsteady 3D Reynolds-averaged Navier-Stokes equations can be solved in a routine way for a multistage turbomachine with a different number of blades in every row. Adamczyk has proposed and recently implemented[53] one approach (an extension to the steady-flow method outlined above) to obtaining an acceptable approximation to the full solution with today's best computers. He[54] and Giles[55] have adopted other approaches.

The key questions are:

Q10 Can the unsteady 2D effects be predicted adequately by quasi-steady equations?

Q11 Is the profile loss coefficient of an isolated blade row increased by running it ahead of or behind another row?

Q12 Can this change be predicted by an unsteady 2D Navier-Stokes code?

Q13 Could the change be predicted in a simpler way, using intermittency in the boundary layer predictions, perhaps?

Q14 And what about unsteady 3D effects?

Q15 Are the Adamczyk, He and Giles approaches good enough to improve significantly on steady codes?

8. TURBULENCE MODELLING

The increasing use of Reynolds-averaged Navier-Stokes solvers in predicting turbomachinery flows means that the loss predictions depend on the turbulence modelling employed, and how transition is predicted. Moore and Moore[56] have given a detailed account of the relevant equations.

Turbulence modelling is recognised by all aerodynamicists - not just in the engine context - as a key research topic. Various turbulence models have been tried by turbomachinery specialists; the Baldwin-Lomax model seems the most popular. It is generally agreed, however, that while there are several models which give very good predictions of attached boundary layers, no one has confidence that any model yet proposed can be relied upon to predict separated flows, especially in three dimensions. One reason for the uncertainty is that, when a code produces a poor prediction, its author is often unsure whether to blame the type or distribution of his computational grid, or to blame the turbulence model, which many research workers find to be a convenient scapegoat!

Turbulence models predict Reynolds stresses, as well as the usually-measured parameters of a turbomachine flow. Only a small number of experimental measurements of Reynolds stresses have been made in the classes of separated flow which are most difficult to predict. Gregory-Smith and Biesinger[57] made measurements of turbulence equation terms in a low speed turbine cascade, and compared them with some predictions; there were large differences.

Q16 Are more measurements of that kind needed; if so, what is the most important type of flow to set up?

It does seem clear that better turbulence modelling must be the key to obtaining satisfactory predictions of aerodynamic losses. For corner flows, it is probably essential to have a turbulence model which does not use the "distance to the nearest wall". A new approach called Renormalisation Group Theory has recently shown promise of improved predictions for swept wings[58], and could help with three-dimensional separations.

Q17 Can any clear guidance as to the merits or drawbacks of currently-used turbulence models be given?

9. LOSS REDUCTION

To what extent have aerodynamic losses been reduced in modern designs, and has that been done as a result of better physical understanding, or of better computational fluid dynamics (CFD)?

History reveals that over the years the in-engine efficiency levels have not changed dramatically. What has happened is that the aerodynamic loading level at which a good efficiency is possible has progressively increased. Coplin[59], for example, showed the history of Rolls-Royce civil fans (Fig.8); every manufacturer no doubt has similar histories showing the evolution in time of compressor and turbine efficiency versus aerodynamic loading. In general, improvements have been achieved through better understanding of loss mechanisms.

It is clear that losses at high aerodynamic loading levels have been greatly reduced over the years. Each major step has been achieved by the application to design of an improved CFD method[60], but all the successful methods have so far been coded in the form of mathematical models expressing in quantitative terms an improved physical understanding of the fluid flow phenomena. Progress has not been achieved by coding the basic fluid flow equations and then searching systematically for the highest efficiency the computer could light upon. Denton[1] made the point strongly that *understanding* is the key to reducing losses.

Historically, the first CFD success in the UK was the use of the "Prescribed Velocity Distribution" method[61] to tailor turbine blade shapes for the Olympus 593 engine which powers Concorde. The early improvements in transonic fan design shown in Fig.8 were made using the (then new) streamline curvature method[62] to blade along stream surfaces. But it was not possible to tailor fan and compressor blade shapes in the way turbine aerofoils were tackled; only when an inviscid-viscous interaction scheme

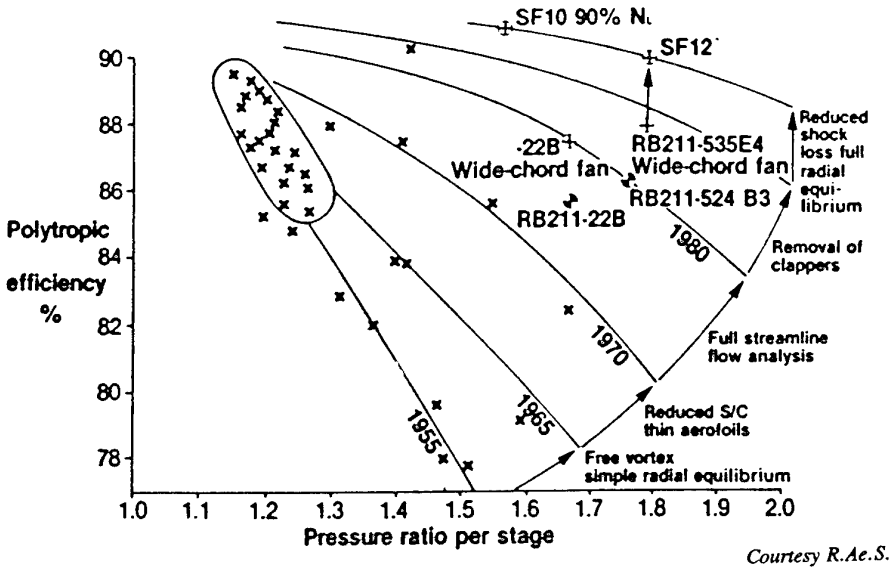

Courtesy R.Ae.S.

Fig.8 Rolls-Royce single stage fan progress (1984)

was formulated[30] could that be done. In a review of compressor technology in 1981, Kerrebrock[63] drew attention to the need to improve the low efficiency levels achieved at that time by the supersonic sections of transonic fans. The tailoring of transonic profiles to minimise separation and shock losses made a big improvement to engine fans and compressors.

An interesting experiment by Paige[64], however, serves as a warning against over-confidence. He redesigned the profile of a turbine blade, tailoring it so as to reduce the boundary layer momentum thicknesses reaching the trailing edge, and tested it in a cascade against the original shape. He succeeded in thinning the boundary layers, but the overall loss coefficient proved to be no lower because the base pressure was slightly lower!

Turbomachinery designers are generally agreed that there are two ways, in broad principle, of reducing secondary losses. One way is to tailor the aerofoil shapes ("endbends") or the endwall shapes. Such ideas were first tried as far back as 1949[65]! But a satisfactory understanding of how best to do the tailoring, and how to predict the improvements, is yet to be produced. The other way is to tailor the *radial* pressure gradient, by means of blade lean[66] or sweep[67] or wall shaping[68], so influencing the radial movement of aerofoil surface boundary layers, and the radial location of secondary vortices. As with endbends, modifications of this type have been widely reported when they were successful, but in other cases they have only moved losses from one place to another, with no overall improvement. In the case of compressors, of course, these imperfectly understood phenomena are also seen as ways of delaying stall and surge.

Q18 To what level can secondary losses eventually be reduced?

Improved turbomachinery technology has been used to design efficient compressors and turbines at higher and higher loading levels, and hence to reduce the number of stages and the number of aerofoils in an engine - with obvious savings in weight and cost. Looking ahead, designers face two immense challenges in the next century. The first, already a key one, is how to achieve acceptable low pressure turbines with very high stage loadings so as to build low specific thrust engines without too many (heavy) stages and without a gearbox. The second arises from the fact that any further increases in military engine thrust/weight ratio will soon require a solution to the problem of achieving adequate operating range and efficiency in fully supersonic fan and compressor stages. Massive research efforts in the 1950s failed to solve this problem. Can it be solved in the coming decades?

Q19 What has to be done to make a supersonic compressor feasible?

10. IN-SERVICE CHANGES

When a newly-made engine enters service, its performance deteriorates as the blading gets worn, dirty or damaged, and seal clearances increase. When the engine is cleaned, some but not all the new engine performance is recovered. If designers understood in more detail why the deterioration occurs, it might be possible to design the blading in such a way that its aerodynamic performance is less sensitive to dirt or damage or larger tip clearances.

Increases in aerodynamic losses while an engine is in service have been ascribed to foreign object damage, to dirt and dust, to erosion and corrosion, to the increase in running clearances as a result of wear and the engine casing losing concentricity, and to the opening up of gaps at shaft seals. When an engine is washed, the dirt is removed but not of course any surface roughness. When the engine is overhauled, damaged blades are replaced or carefully "dressed" until they appear smooth. The initial profile is of course carefully designed, and manufactured

to tight tolerances, to which the dressed aerofoils no longer conform; but the performance satisfies the airline's needs. So how close a manufacturing tolerance is really needed, and which aspects of the shape are most important to get right?

It is not only in an engine that losses increase; if a newly-made compressor is tested its performance is seen to deteriorate gradually over the first few hundred hours of testing, as the blading gets dirty and eroded by dust particles. Surface finish is specified in manufacture; how important is it?

Performance prediction methods have always considered the blading to be new; no one has proposed a "loss increase with time" model. Research has been done on the effect of surface roughness on turbomachinery boundary layers[9,69,70], and when the Reynolds number is in the region of 10^4 to 10^5 (based on chord) both compressor and turbine efficiencies have been seen to drop significantly when the aerofoil surfaces were rough. But no papers have been published until recently in which systematic studies were done to establish which regions of which blades are most critical.

Last year, however, Suder et al[71] published the results of some systematic experiments conducted on the same isolated transonic fan rotor (Rotor 37) as was used for the ASME test case, at NASA Lewis. They added thickness, with or without roughness, to various areas of the aerofoil surface, and also, in effect, damaged the leading edge region. What they found was that serious efficiency losses occurred only when the relative inlet flow was supersonic, and that they occurred only when the leading edge itself was damaged. They were unable to predict their results fully using CFD, but assuming immediate transition at the leading edge showed the right trend. The large increases in loss they observed may perhaps be explained as follows. Transonic fan blades have a thin leading edge. Walraevens and Cumpsty[72] measured the leading edge bubbles and the reattachment momentum thickness θ_R for a range of thin leading edge shapes. They found that quite small changes in leading edge shape can cause large changes in θ_R. The suction surface boundary layer is then disturbed by the shock system and whether it separates or not depends on its thickness. It would not be surprising if a damaged leading edge gave rise to a higher θ_R and an earlier or more severe separation. Whether that is true or not, more research into the phenomena exposed by Suder's tests could be very helpful in guiding both manufacturing tolerances and overhaul procedures.

Q20 What follow-up to Suder's tests is recommended?

11. CONCLUSIONS

Efficiency estimates are needed at the earliest phase in engine design, in order to enable the optimum engine architecture to be selected. At this phase, there are no component designs to analyse; recourse must be made to empiricism guided by previous achievements. Then, at the component design phase, loss estimates are needed to guide the choice of loading parameters, numbers of blades, and velocity triangles, and later to shape the aerofoil profiles. Finally, an estimate of overall mass flow, pressure ratio, efficiency and (for a compressor) surge margin is needed over the working range. Such information can be obtained using empirical correlations of various categories of loss inserted into a pitchline model or a throughflow model, or by some kind of 3D Navier-Stokes computation, probably linked by throughflow calculations. For the future, the research route is clear; 3D unsteady Navier-Stokes codes must be developed and applied in sufficiently finely gridded regions to produce acceptably accurate loss predictions. At present, the best today's computers can attempt (other than using Adamczyk's approach) is a steady throughflow computation linked to steady 3D Navier-Stokes or viscous-inviscid interaction computations for each row. How good the mathematical models of loss generation are in this context is not clear.

Assuming that throughflow codes will remain a major design tool for some years to come, the need to improve the loss modelling incorporated in them is generally agreed. In the past, the main way of devising and developing better models has been experiments - first to identify and then to quantify the significant parameters. The use of a Navier-Stokes code to fulfil that role is now becoming available.

It is being widely suggested that the unsteady effects of the passage of neighbouring blade rows increase the aerodynamic losses, and ways of predicting and accounting for this effect need to be found. What is intuitively likely, but cannot be proved as yet, is that a better understanding of these unsteady effects will allow new designs to be improved.

At present, Navier-Stokes codes have proved unreliable in respect of loss and efficiency predictions, and although in some cases the gridding details may be at fault there is general agreement that better turbulence modelling is needed, especially where there are three-dimensional separations.

Profile losses have been reduced, probably as far as possible, by tailoring aerofoil shapes under the guidance of blade-to-blade computations. There must be scope for reducing secondary losses if equally reliable computations of endwall effects can be made; at present this has not, in the author's opinion, been achieved.

There is a case for careful research on the reasons why efficiency decreases as blading gets dirty or damaged, with a view to designing blading which is less sensitive.

Engines have improved enormously during the last twenty years in respect of the number of stages. Further reductions pose immense aerodynamic difficulties; efficient supersonic compressors will be needed. Will this ever be possible?

The process of improving turbomachinery performance has passed the point where the intelligent application of trial-and-error changes guided by intuitive understanding of fluid flow phenomena can bring big returns. The key approach must be first to understand the loss mechanisms, then express that understanding as a mathematical model within a CFD code, then to use that model to suggest

improvements. It will then be essential to evaluate them in a research or demonstrator trial before committing them to an engine.

ACKNOWLEDGEMENTS

The author is grateful to his colleague Mr W.J.Calvert, who supplied his S1/S2 computations for Rotor 37, and to Dr A.J.Strazisar of NASA Lewis Research Centre, who supplied a copy of the Rotor 37 test case vufoils shown during the ASME meeting in the Hague last year.

REFERENCES

1. Denton, J.D., "*Loss mechanisms in turbomachines*", Trans ASME, J Turbomachinery, v.115 no.4, p.621-656, 1993
2. Smith, S.F., "*A simple correlation of turbine efficiency*", J.R.Ae.S. v.69, no.655, 1965
3. Dunham, J., Came, P.M., "*Improvements to the Ainley-Mathieson method of turbine performance prediction*", Trans ASME (A) v.92, no.3, p.252, July 1970
4. Kacker, S.C., Okapuu, U., "*A mean line performance prediction method for axial flow turbine efficiency*", ASME paper 81-GT-58, 1981
5. Ainley, D.G., Mathieson, G.C.R., "*A method of performance estimation for axial flow turbines*", Aeronautical Research Council R&M 2974, 1951
6. Howell, A.R., Calvert, W.J., "*A new stage stacking technique for axial-flow compressor performance prediction*", ASME paper 78-GT-139, 1978
7. Casey, M.V., "*A mean line prediction method for estimating the performance characteristic of an axial compressor stage*", I.Mech.E. Conference paper C264/87, 1987
8. Wright, P.I., Miller, D.C., "*An improved compressor performance prediction model*", I.Mech.E. Conference paper, 1991
9. Koch, C.C., Smith, L.H., "*Loss sources and magnitudes in axial-flow compressors*", Trans ASME, J Engg for Power, p.411, July 1976
10. Howard, M.A., Ivey, P.C., Barton, J.P., Young, K.F., "*Endwall effects at two tip clearances in a multi-stage axial flow compressor with controlled diffusion blading*", ASME paper 93-GT-299, 1993
11. Dunham, J, "*A new endwall model for axial compressor throughflow calculations*", ASME paper 94-GT-75, 1994
12. Denton, J.D., Xu, L., " *The trailing edge loss of transonic turbine blades*", ASME paper 89-GT-278, 1989
13. Calvert, W.J., "*An inviscid-viscous method to model leading edge separation bubbles*", ASME paper 94-GT-247, 1994
14. Hirsch,Ch., Denton, J.D.(eds.),"*Through flow calculations in axial turbomachines*", AGARD AR-175, 1981
15. König, W.M., Hennecke, D.K., Fottner, L., "*Improved blade profile loss and deviation angle models for advanced transonic compressor bladings*", ASME papers 94-GT-335 and 336, 1994
16. Herzig, H.Z., Hansen, A.G., "*Visualization studies of secondary flows with applications to turbomachines*", Trans ASME, v.77, p.249, 1955
17. Dominy, R.G., Kirkham, D.A., "*The influence of blade wakes on the performance of inter-turbine diffusers*", ASME paper 94-GT-207, 1994
18. Adkins, G.G., Smith, L.H., "*Spanwise mixing in axial-flow turbomachines*", Trans ASME, J Engg for Power, v.104, p.97, 1982
19. Whitfield, C.W., Keith, J.S., "*Spanwise redistribution of energy and loss in an axial flow compressor by wake centrifugation*", Report AFWAL-TR-84-2109, 1984
20. de Ruyck, J., Hirsch, Ch., "*A radial mixing computation method*", ASME paper 88-GT-68, 1988
21. Hart, M., Hall, D.M., Singh,G., "*Computational methods for the design of large steam turbines*", I.Mech.E. Conference paper C423/009, 1991
22. Sieverding, C.H., Stanislas, M., Snoek,J. "*The base pressure problem in transonic cascades*", Trans ASME, J Engg for Power, v.102, p.711, 1980
23. Kingcombe, R.C., Harasgama, S.P., Leversuch, N.P., "*Aerodynamic and heat transfer measurements on blading for a high rim speed transonic turbine*", ASME paper 89-GT-228, 1989
24. Fottner, L. (ed.), "*Test cases for computation of internal flows in aero engine components*", AGARD AR-275, 1990
25. Hay, N., Lampard, D., Khaldi, A., "*The coefficient of discharge of 30° inclined film cooling holes with rounded entries or exits*", ASME paper 94-GT-180, 1994
26. Barnes, J.F., Came, P.M., "*Some aerodynamic aspects of turbine blade cooling*", ASME paper 69-GT-15, 1969
27. Hartsel, J.E., "*Prediction of the effects of mass transfer cooling on the blade-row efficiency of turbine aerofoils*", AIAA paper 72-11, 1972
28. Stewart, W.L., Whitney, W.J., Wong, R.Y., "*A study of boundary layer characteristics of turbomachine blade rows and their relation to overall blade loss*", Trans ASME, J Basic Engg, v.82, ser.D, p.588, 1960
29. Calvert, W.J., Ginder, R.B., "*A quasi-three dimensional calculation system for the flow within transonic compressor blade rows*", ASME paper 85-GT-22, 1985
30. Calvert, W.J., "*An inviscid-viscous interaction treatment to predict the blade-to-blade performance of axial compressors with leading edge normal shock waves*", ASME paper 82-GT-135, 1982
31. Moore, J., Adhye, R.Y., "*Secondary flows and losses downstream of a turbine cascade*", ASME paper 85-GT-64, 1985
32. Moore, J.G., Tilton, J.S., "*Tip leakage flow in a linear turbine cascade*", ASME paper 87-GT-222, 1987
33. Bindon, J.P., "*The measurement of tip clearance flow structure on the end-wall and within the clearance gap of an axial turbine cascade*", I.Mech.E.Conference paper C273/87, 1987
34. Gallimore, S.J., Cumpsty, N.A., "*Spanwise mixing in multistage axial flow compressors*", Trans ASME, J Turbomachinery, v.108, p.2, 1986
35. Leylek, J.H., Wisler, D.C., "*Mixing in axial-flow compressors: conclusions drawn from 3-D Navier-Stokes analyses and experiments*", ASME J Turbomachinery, v.113, no.2, p.139, 1991
36. Howard, M.A., Gallimore, S.J., "*Viscous throughflow*

modelling for multi-stage compressor design", ASME paper 92-GT-302, 1992

37. Dunham, J, "*A new approach to predicting annulus wall boundary layers in axial compressors*", Proc I Mech E, v.207, p 413, 1993
38. Dunham, J., "*Analysis of high speed multistage compressor throughflow using spanwise mixing*", ASME paper 92-GT-13, 1992.
39. Lewis, K.L., "*Spanwise transport in axial-flow turbines*", ASME papers 93-GT-289 & 290, 1993
40. Dring, R.P., "*Radial transport and momentum exchange in an axial compressor*", ASME paper 92-GT-364, 1992
41. Dring, R.P., "*Radial mixing in an axial turbine*", ASME paper 94-GT-137, 1994
42. Cherrett, M.A., Bryce, J.D., Ginder, R.B., "*Unsteady 3D flow in a single stage transonic fan*", ASME papers 94-GT-223 and 224, 1994
43. Crook, A.J., Greitzer, E.M., Tan, C.S., "*Numerical simulation of compressor endwall and casing treatment flow phenomena*", ASME paper 92-GT-300, 1992
44. Hodson, H.P., "*Boundary layer and loss measurements on the rotor of an axial-flow turbine*", ASME paper 83-GT-4, 1983
45. Doorly, D.J., "*Modelling the unsteady flow in a turbine rotor passage*", Trans ASME, J Turbomachinery, v.110, p.27, 1988
46. Hodson, H.P., "*Modelling unsteady transition and its effects on profile loss*", AGARD CP-468, paper 18, 1990
47. Fan, S., Lakshminarayana,B., "*Computation and simulation of wake-generated unsteady pressure and boundary layers in cascades*", ASME papers 94-GT-140 & 141, 1994
48. Dawes, W.N., "*A numerical study of the interaction of a transonic compressor overtip leakage vortex with the following stator blade row*", ASME paper 94-GT-156, 1994
49. Imanari, K., "*Theoretical model of the spanwise mixing caused by periodic incoming wakes*", ASME paper 94-GT-153, 1954
50. Adamczyk, J.J., "*A model equation for simulating flows in multi-stage turbomachinery*", ASME paper 85-GT-226, 1985
51. Adamczyk, J.J., Celestina, M.,Mulac, R.A., "*A model for closing the inviscid form of the average passage equations*", Trans ASME, J Turbomachinery, v.108, n.2, p.180, 1986
52. Adamczyk, J.J., Celestina, M.L., Chen, J.P., " *Wake-induced unsteady flows: their impact on rotor performance and wake rectification*", ASME paper 94-GT-219, 1994
53. Chen, J.J., Celestina, M.L., Adamczyk, J.J., "*A new procedure for simulating unsteady flows through turbomachinery blade passages*", ASME paper 94-GT-151, 1994
54. He, L., "*Some recent developments in calculation of unsteady turbomachinery flows*", I.Mech.E. Seminar, 7 Oct 1993
55. Giles, M.B., "*An approach for multi-stage calculations incorporating unsteadiness*", ASME paper 92-GT-282, 1992
56. Moore, J., Moore, J.G., "*Osborne Reynolds - Energy methods in transition and loss production - a centennial perspective*", ASME paper 94-GT-225
57. Gregory-Smith, D.G., Biesinger, T., "*Turbulence evaluation within the secondary flow region of a turbine cascade*", ASME paper 92-GT-60, 1992
58. Ashworth, R., "*A renormalisation group turbulence model for three-dimensional wall-bounded flows*", Proc 8th Int.Conf.on Numerical Methods in Laminar and Turbulent Flows, July 1993
59. Coplin, J.F., "*The accelerating pace of advancing aero engine technology*", Aerospace, v.11, no.2, p.17, 1984
60. Dunham, J., "*The role of flow field computation in improving turbomachinery*", AIAA paper ICAS-86-3.7.3, 1986
61. Stanitz, J.D., "*Design of two-dimensional channels with prescribed velocity distributions along the channel walls*", NACA TNs 2593 & 2595, 1952
62. Silvester, M.E., Hetherington, R., "*Three-dimensional compressible flow through axial flow turbomachines*", in Numerical Analysis - An Introduction, Ch.II, Pt.III, p.182, Academic Press, New York, 1966
63. Kerrebrock, J.L., "*Flow in axial compressors*", AIAA J, v.19, no.1, p.4, 1981
64. Paige, R.W., "*A computational method for the aerodynamic design of turbine blades*", Cambridge Univ.Ph.D.Thesis, 1983
65. Jeffs, R.A., "*Preliminary note on the performance of axial compressor blading designed to operate in a radially varying axial velocity distribution*", unpublished NGTE memorandum, 1949
66. Liu, H.C., Booth, T.C., Wall, W.A., "*An application of three-dimensional viscous flow analysis to the design of a low aspect-ratio turbine*", ASME paper 79-GT-53, 1979
67. Tweedt, D.L., Okiishi, T.H., Hathaway, M.D., "*Stator endwall leading edge sweep and hub shroud influence on compressor performance*", ASME paper 86-GT-197, 1987
68. Atkins, M.J., "*Secondary losses and endwall profiling in a turbine cascade*", I.Mech.E.Conference paper C255/87, 1987
69. Schäffler, A., " *Experimental and analytical investigation of the effects of Reynolds number and blade surface roughness on multistage axial flow compressors*", ASME paper 79-GT-2, 1979
70. Tabakoff, W., Balan, C., "*A study of the surface deterioration due to erosion*", ASME paper 83-GT-213, 1983
71. Suder, K.L., Chima, R.V., Strazisar, A.J., Roberts, W.B., "*The effect of adding roughness and thickness to a transonic axial compressor rotor*", ASME paper 94-GT-339, 1994
72. Walraevens, R.E., Cumpsty, N.A., "*Leading edge separation bubbles on turbomachine blades*", ASME paper 93-GT-91, 1993

ENDWALL BOUNDARY LAYER SEPARATIONS AND LOSS MECHANISMS IN TWO COMPRESSOR CASCADES OF DIFFERENT STAGGER ANGLE

U. Stark
Technische Universität Braunschweig
Institute Fluid Mechanics
Bienroder Weg 3, 38106 Braunschweig
Germany

S. Bross
KSB AG
Div.: New Technologies
Johann-Klein-Straße 9, 67227 Frankenthal
Germany

1. SUMMARY

The paper describes experimental and theoretical investigations on the effect of stagger angle on the endwall flow in two compressor cascades, one with a low stagger angle (λ = 30°) and one with a high stagger angle (λ = 50°). The results of flow visualization tests, wake measurements and inviscid secondary flow calculations are shown for both cascades. The more important differences between the two sets of results are discussed with particular attention to 3D endwall boundary layer separations and loss mechanisms.

2. INTRODUCTION

The AVR (axial velocity ratio) characteristics of compressor cascades generally show a remarkable change with increasing stagger angle (see, for example, Rhoden, 1956; Hebbel, 1964; Starke, 1979). For low stagger cascades ($\lambda \approx 30°$), the AVR characteristics are usually flat, while they are highly progressive for high stagger cascades ($\lambda \approx 50°$). In the first case, the AVR values are often not much above unity, while they are much higher in the second case. This is due to different blockage effects of the endwall boundary layers at different stagger angles. To the authors knowledge, these effects, together with their associated losses, have been investigated so far in low stagger cascades only (see, for example, Horlock et. al., 1966; Papailiou, 1975; Dring et. al., 1982; Dong et. al., 1987). There is no work known on endwall flows in high stagger cascades.

In the present investigation, two compressor cascades of different stagger angle (λ = 30° and 50°), but otherwise of identical geometry, were tested in order to qualify and to quantify the different features of the endwail flow at lower and higher stagger angles. Special emphasis was placed on getting high quality oil flow pictures, from which the important informations on shape and location of the 3D separation and attachment lines as well as on the location of the associated singular points could be deduced. The conclusions drawn were supported by the results of spanwise wake measurements and secondary flow calculations.

As usual, the inlet boundary layers on the endwalls were collateral. Therefore, important effects of skewing of the inlet boundary layers on the endwall flow and loss are missing in the results of the present investigation. However, the tests will be repeated with skewed inlet boundary layers and then, by comparison of the results, it will be possible to determine the skewing effects very accurately.

3. CASCADE TUNNEL

The present investigations were carried out in the low-speed cascade tunnel of the Institute of Fluid Mechanics, Technical University of Braunschweig. The horizontal test section width (blade span) of the wind tunnel is h = 600 mm, its vertical height varies between 340 and 915 mm depending on inlet angle (β_1), solidity (l / t), and blade number. The inlet angle can be changed continuously, while the stagger angle is usually held constant at some prescribed value.

A periodic cascade flow is achieved by boundary layer suction devices at the ends of the horizontal test section walls, just above and below the end blades of the cascade. The suction mass flow is controlled by the requirement of a constant static pressure distribution in a plane about one chord upstream of and parallel to the cascade front. The boundary layers on the vertical test section walls (endwalls) may not be withdrawn by suction in an investigation like this.

4. CASCADE GEOMETRY AND TEST PROGRAM

Two compressor cascades of different stagger angles (see Fig. 1) were tested in the cascade tunnel described before. The more important details of the blade section and of the cascade geometry may be summarized as follows:

i) Blade section: 9 C 7 / 32.5 C 50
ii) Solidity: l / t = 1.0
iii Stagger angle: λ = 30° and 50°
iv) Aspect ratio: h / l = 5.0

The blade section (chord length: l = 120 mm) with the notation 9 C 7 / 32.5 C 50 has a British C7 base profile with 9% maximum thickness/chord ratio and a circular arc camber line with a camber angle of φ = 32.5°.

Results will be described of the following measurements and investigations:

i) Wake measurements downstream of the cascade at midspan position for a number of inlet angles between positive and negative stall.
ii) Wake measurements downstream of the cascade at various spanwise positions between midspan position and one endwall for one selected inlet angle each, at nearly the same loading (static pressure rise).
iii) Endwall boundary layer measurements upstream of the cascade for the inlet angles mentioned under ii).
iv) Flow visualization tests using a surface film technique for a number of inlet angles between positive and negative stall.

Paper presented at the AGARD PEP 85th Symposium on "Loss Mechanisms and Unsteady Flows in Turbomachines", held in Derby, United Kingdom, 8-12 May 1995, and published in CP-571.

5. EXPERIMENTAL PROCEDURE AND DATA REDUCTION

The Reynolds number based on chord length and inlet velocity was $Re_1 = W_1 l / \nu = 3.5 \cdot 10^5$ for all measurements and investigations. The corresponding inlet velocity was 44 m / sec.

As reference quantities, the following quantities of the inlet flow were chosen: the total pressure p_{t1}, the static pressure p_1, and the dynamic pressure $q_1 = p_{t1} - p_1$. The total pressure p_{t1} was measured as an average value of ten Pitot probes in the settling chamber of the wind tunnel. A conventional static pressure probe in front of the cascade (more than one chord axial upstream and somewhat outside the test section centre plane) was used to measure the static pressure.

The inlet boundary layers on the endwalls of the test section were measured at an axial distance of 40 and 50 mm upstream of the cascade for the low ($\lambda = 30°$) and high ($\lambda = 50°$) stagger cascade, respectively. A calibrated five hole probe (probe head diameter: 2.0 mm) was used to traverse the cascade exit flowfield. The axial distance between the cascade outlet and the measuring plane was 40 ($\lambda = 30°$) and 50 mm ($\lambda = 50°$), and the downstream guidance of the exit flow was 34 and 48 mm, respectively.

Introducing a rectangular x, y, z - (left hand) coordinate system with z pointing in the spanwise direction and z = 0 at midspan (see Fig. 2), the spanwise position of the various traverse planes between z = 0 mm (midspan) and z = 300 mm (endwall) can be specified: Starting with the following traverse planes at z = 0, 200, 220 and 296 mm, the position of the other planes may be found by adding to these numbers an increasing multiple of the respective spacings $\Delta z = 10, 4, 2$ and 1 mm.

Without going into detail with the measurement equipment it shall be mentioned that with the calibrated five hole pressure probe six pressure differences were measured from which two local flow angles, β (y, z) and γ (y, z), see Fig. 2, and two local pressure differences, p_2 (y, z) - p_1 and $p_{t1} - p_{t2}$ (y, z), were determined. The two flow angles β and γ describe (here as well as in the calibration procedure) the geometrical relationship between the probe and the (exit) velocity vector.

From these results two further flow angles, β_2 (y, z) and γ_2 (y, z), this time describing the geometrical relationship between the cascade (x, y, z - coordinate system) and the exit velocity vector, and several local nondimensional pressure differences, $(p_2 (y, z) - p_1) / q_1$ and $(p_{t1} - p_{t2} (y, z)) / q_1$, and velocity ratios W_2 / W_1, W_{2x} / W_1, W_{2y} / W_1, W_{2z} / W_1, W_{2x} / W_{1x} = AVR (all depending on y and z) were calculated, see Fig. 2. By integrating the local data across one pitch, so-called mass-averaged performance parameters were determined for every traverse plane: i) outlet angle β_2 (z), ii) yaw angle γ_2 (z), iii) static pressure difference Δp (z) / q_1, iv) total pressure difference Δp_t (z) / $q_1 = \zeta_{v1}$ (z), and v) axial velocity ratio AVR (z).

6. RESULTS AND DISCUSSION

6.1 Performance Parameters at Midspan

For both cascades the midspan performance parameters are presented in Fig. 3. It shows the turning angles ($\Delta \beta$) and the loss coefficients (ζ_{v1}), usually regarded as the most important performance parameters, together with the nondimensional values of the static pressure rise ($\Delta p / q_1$) and the axial velocity ratios (AVR), parameters of special importance for the present investigation. The abscissa in Fig. 3 is the angle of attack (α), as defined in Fig. 1.

A comparison of the two data sets in Fig. 3 leads to the conclusion, that the turning angles and losses are similar for both cascades, while the axial velocity ratios and the static pressure differences are highly different. For the low stagger cascade, the AVR increases very slowly with angle of attack and the resulting curve is very flat. Most of the values are not much above unity, thus indicating that the displacement effect of the endwall phenomena is comparatively small in a configuration like this. For the high stagger cascade, the AVR increases very rapidly with angle of attack and the resulting curve is highly progressive, leading to a maximum value of about 1.5 for the highest angle of attack. This indicates that this time the displacement effect of the endwall phenomena is very large.

Closely coupled with the AVR is the static pressure rise of a compressor cascade. With an AVR always close to unity, the pressure rise of the low stagger cascade is nearly two-dimensional. Then, as shown in Fig. 3, the peak pressure rise is obtained, when the profile losses start to increase and when the profile boundary layers begin to separate (blade stall). However, with an AVR rapidly increasing with angle of attack, the peak pressure rise of the high stagger cascade is obtained much earlier, that is at some intermediate angle of attack of the low loss range, see Fig. 3 (wall stall). The profile boundary layers are then attached.

Although the cascades stall in a different manner, it is interesting to see, that the stalling pressure coefficients are not so much apart, that is 0.435 in the low stagger and 0.46 in the high stagger case. These values are also close to the limit (0.44) suggested by de Haller (1953). The de Haller criterion is one of the many stalling criteria for compressor cascades. It applies to the endwall boundary layers and predicts the beginning of massive endwall boundary layer separation (wall stall), without qualifying the characteristic features of the stalling process. The more recent correlation methods for estimating the stalling pressure rise of compressor stages (see, for example, Koch, 1981; Schweitzer and Garberoglio, 1984) are also wall stall criteria essentially. They predict the stall onset somewhat more precise than the older criteria, but again do not give the details of the stalling process.

6.2 Oil Flow Pictures

Oil flow pictures are photographs of especially prepared surfaces showing the surface pattern of the shear stress lines. The directions of these lines are nearly identical with the flow directions of the fluid particles next to the surface. Following the criteria described by Tobak and Peake (1982), the more important features of the endwall flow

may be identified, as for example: i) three-dimensional separation lines (convergence of the shear stress lines), ii) three-dimensional (re) attachment lines (divergence of the shear stress lines) and iii) so-called singular points (saddle and nodal points, foci). Having these features, a first idea of the flow field may be developed.

Oil flow pictures were prepared by coating one endwall and two blade surfaces (all painted black) with a mixture of fluorescent powder, petroleum, and benzine, before the wind tunnel was taken in operation. After each wind tunnel run detailed photographs of the coated surfaces were taken. Mixture bubbles in separated flow regions were sucked off early in the tests, avoiding thus a bubble burst and a spread out of mixture at a later instant.

From the many pictures produced, only a few can be presented in the present paper. A typical set of results for the low stagger cascade is given with Figs. 4, 5, 6 and 7. All figures are for $\alpha = 18°$ and show i) the wall streamlines on the endwall, when the whole endwall was coated at the beginning of the test (Fig. 4), ii) the endwall flow characteristics (Fig. 5), iii) the wall streamlines on the endwall, when only a strip was coated in front of the cascade at the beginning of the test (Fig. 6) and iv) the wall streamlines on the blade suction surface. A description of the more important features of the endwall flow starts best with the forward saddle-points in front of the profiles near the leading edges. There are always two different lines running through each saddle-point, that is: one attachment line (diverging shear stress lines) and one separation line (converging shear stress lines). An attachment line comes from upstream infinity, passes through the saddle-point and proceeds in a direction onto a profile. A separation line consists of two branches: The suction side branch turns around the profile leading edge, continues downstream in the immediate vicinity of the profile suction side, and becomes finally part of a focus near the profile trailing edge, after first having surrounded a region of back flow (corner stall region). The pressure side branch of the separation line runs across the passage between two blades and hits a (rear) separation line near the exit of the blade passage. Then, the character of the line has already changed from a separation to an attachment line, the line turns around the profile trailing edge and enters a neighbouring passage from behind. The rear separation line is roughly in line with the profile and may be followed into a focus on one side and down to infinity on the other side.

The described connexion of two saddle-points, to be seen in Figs. 4, 5 and 6, theoretically is an exception and experimentally, within the present investigation, a result for $\alpha = 18°$ only. For other angles of attack, there are always two lines crossing the passage, that is i) a separation line through the leading edge saddle-point and ii) a nearly parallel attachment line through the rear saddle-point. Figs. 12 and 13 show an example for $\alpha = 22° > \alpha = 18°$. In this case the separation line is in front of the attachment line. Things are vice versa for $\alpha < \alpha = 18°$.

For the high stagger cascade, Figs. 8, 9, 10 and 11 represent a typical set of results for $\alpha = 10°$. To be seen are, similar to the low stagger case, i) the wall streamlines on the endwall (Fig. 8), ii) the endwall flow characteristics (Fig. 9), iii) the wall streamlines on the endwall in a strip-coating technique (Fig. 10), and iv) the wall streamlines on the blade suction surface. An inspection of Figs. 8 and 10 leads to the conclusion that the endwall flow characteristics (Fig. 9) are basically the same as in Fig. 5 for the low stagger cascade. What is different, and important, is the position and the change of position of the characteristics with angle of attack. In the low stagger cascade, for example, the pressure side branch of the forward separation line is a cross passage line with the actual position depending on angle of attack, see Figs. 4 and 12. The corresponding line of the high stagger cascade, however, is a line that stays next to the profile, all along the profile, for low and medium angles of attack, see Figs. 8 and 9. Further, the rear separation lines, nearly parallel with the profiles in Figs. 4 and 5 for the low stagger cascade, are now cross passage lines, see Fig. 8 and 9 for the high stagger cascade. In accordance with previous experiences, the wall streamlines (wall shear stress lines) of the low stagger cascade are highly overturned, see Figs. 4 and 12. Surprisingly, this is not the case with the high stagger cascade, where the wall streamlines are very nearly potential flow streamlines up the rear separation lines, see Fig. 8.

Finally, the most important feature of the endwall flow of the high stagger cascade shall be mentioned: While the position of the rear separation lines in the low stagger cascade remains unchanged with increasing angle of attack, the position of the corresponding lines in the high stagger cascade is highly dependent on angle of attack. These lines, beginning with a rear position for a low angle of attack, travel upstream through the cascade with increasing angle of attack, until they finally join to a single separation line in front of the cascade, see Fig. 14, which is for $\alpha = 20°$. This line may best be seen in Fig. 15, where a strip coating technique was used to produce the picture.

A comparison of the two sets of oil flow pictures leads to the following observations and conclusions:

i) The overturning of the endwall flow in the low stagger cascade indicates a classical secondary flow and a well defined passage vortex (see Figs. 4 and 7).On the contrary to this,there is little evidence for a cross flow component in the high stagger cascade (see Fig. 8). Therefore, a secondary flow in a classical sense may not be expected.

ii) In the low stagger cascade a considerable part of the endwall boundary layer concentrates and separates in a vortex, to be seen in Figs. 4, 5 and 6 as a focus in the streamline pattern on the endwall in the suction surface endwall corner. Further to be seen in this corner are an ordinary 3D separation of the endwall boundary layer in Fig. 6 and an ordninary 3D separation of the blade suction surface boundary layer in Fig. 7. All three phenomena are in strong interaction and together constitute the wellknown corner stall, usually responsible for most of the blockage (see Fig. 3) and most of the secondary losses in low stagger cascades.

iii) At the rear separation lines (see Fig. 5 and 9), the endwall boundary layers of two neighbouring channels

get into contact. The following interaction seems to be weak in case of the low stagger cascade and strong in case of the high stagger cascade. A strong interaction in the latter case may well be suspected, because in this case the rear separation lines are cross channel lines with forward flow on the left side and backward flow on the right side. As a consequence, the boundary layers separate, thus creating regions of high blockage in every channel, on the endwall, between the blades. It is this feature of the endwall flow of the high stagger cascade, that is probably responsible for most of the blockage (see Fig. 3) and most of the secondary losses. This process, described for $\alpha = 10°$, exaggerates with increasing angle of attack (to be seen in a number of oil flow pictures, not included in the present paper).

6.3 Spanwise Distribution of the Performance Parameters

Wake measurements downstream of the cascades were performed at various spanwise positions between the midspan plane and one endwall for one selected angle of attack each, $\alpha = 18°$ for the low stagger cascade and $\alpha = 10°$ for the high stagger cascade. The measurements were then evaluated to give the spanwise distributions of the performance parameters.

The results of wake measurements do not only depend on the actual geometry of a cascade, but also on the thickness and velocity distribution of the upstream endwall boundary layer. The measured velocity profiles for the two cases under consideration are shown in Fig. 16 together with a power law approximation of the form $W_1(z') / W_{1\delta} = (z' / \delta)^{1/n}$, with z' measured positive from the endwall, $1/n = 1/7$ and $\delta = 22.2$ mm. Calculated values for the displacement thickness (δ^*), the momentum thickness (Θ), and the shape factor (H) are also shown in Fig. 16 for the measured velocity distributions. A value of 1.3 for the shape factor H is characteristic for a turbulent flat plate boundary layer.

The spanwise distributions of the mass-averaged performance parameters β_2, γ_2, $\Delta p / q_1$, ζ_{v1} and μ, defined in section 4, are shown in Figs. 17 and 18 for the low ($\lambda = 30°$) and high ($\lambda = 50°$) stagger cascade, respectively. In both cases, $\Delta\beta$ has been plotted instead of β_2. Reference quantities (β_1, p_{t1}, p_1, q_1, $= p_{t1} - p_1$, W_1) are midspan (MS) values of the inlet flow.

The spanwise distributions of three parameters ($\Delta\beta$, ζ_{v1} and μ) shall be discussed. The first parameter is the turning angle $\Delta\beta$, which is constant in both cases for the first 200 mm of the span. Then, within the rest (100 mm) of the span, the low stagger cascade shows the usual underturning/overturning of the flow in Fig. 17, while the high stagger cascade demonstrates an unusual underturning only, see Fig. 18. A comparison of measured and predicted $\Delta\beta$ - distributions using classical inviscid secondary flow theory (Hawthorne, 1955; Came and Marsh, 1974; Marsh, 1974; Glynn et. al. 1977) is shown in Figs. 19a and 19b for the low and high stagger cascade, respectively. As may be seen, the agreement between theory and experiment is fairly good in Fig. 19a and completely insufficient in Fig. 19b.

The second parameter to be discussed is the loss coefficient ζ_{v1}, defined in section 4. By definition, this coefficient includes the losses of the upstream endwall boundary layer as well as the cascade losses. The former, if measured separately, may be subtracted from the total losses (ζ_{v1}) and the resulting cascade losses may be split into profile- and secondary-losses. This was proceeded for both cases, and two completely different secondary-loss distributions (with the higher losses for the high stagger cascade) were obtained at nearly the same loading ($\Delta p / q_1 \approx 0.41$ for the low stagger cascade and $\Delta p / q_1 = 0.435$ for the high stagger cascade), and with nearly identical velocity and total pressure distributions of the upstream boundary layers.

Finally, the AVR-distributions shall be discussed, where AVR is the axial velocity ratio, defined in section 4. These distributions are different, especially between z = 250 and 300 mm, where the AVR-values of the high stagger cascade are considerable below the AVR-values of the low stagger cascade. Between z = 0 and 250 mm the differences are small, and the AVR-values of the high stagger cascade are now above the AVR-values of the low stagger cascade. This result implies that, for nearly identical loadings and inlet velocity profiles, the blockage effects of the endwall flow phenomena are much higher in the high stagger cascade than in the low stagger cascade. The associated contractions of the main stream, however, measured by the AVR-values at midspan, are not very different. But this changes with angle of attack.

6.4 Secondary Flows and Losses

For a large number of selected points of the y, z - measuring plane (Fig. 2), the secondary velocity vectors, as defined by Marchal and Sieverding (1977), were experimentally and theoretically determined. Figs. 20 and 21 show the results for the low stagger cascade and Figs. 22 and 23 those for the high stagger cascade.

The wake measurements were carried out across one pitch only. However, because of the fairly good periodicity achieved, the evaluated results could be doubled, and this is how Figs. 20 and 22 were constructed. Now the complete secondary flow motion of one channel between two blades can be observed (between the marks PS / SS with PS for pressure side and SS for suction side) and compared with the corresponding theoretical results in Figs. 21 and 23.

Fig. 20 shows a classical secondary flow motion downstream of the low stagger cascade with a typical cross channel endwall flow from the pressure to the suction side of the channel, thus confirming all indications of a developed passage vortex mentioned before. Moreover, the measured results of Fig. 20 are fairly well reproduced by classical inviscid secondary flow theory in Fig. 21. Differences exist with respect to the position of the vortex cores and with respect to the direction of the trailing edge flows close to the wall.

The measured secondary flow for the high stagger cascade (see Fig. 22) is not a secondary flow in a classical sense and has therefore no similarity with the predicted secondary flow in Fig. 23. As shown in Fig. 8, the wall streamlines of

the high stagger cascades are nearly potential flow streamlines with vanishing cross flow components up to the rear separation line. Thus the main feature of a classical secondary flow is missing. This leads to the conclusion that the secondary flow in Fig. 22 is mainly determined by the endwall flow phenomena downstream of the rear separation line. Indeed, as indicated in Fig. 8 and to be seen in Fig. 22, a strong and extended endwall/trailing edge flow is the dominating feature of the secondary flow in the high stagger cascade. This endwall/trailing edge flow is so strong that, on the contrary to all previous results, the secondary flow direction on the endwall is from the suction to the pressure side of the channel (see Fig. 22) and not vice versa.

In addition to the oil flow pictures and secondary flow charts, so-called loss contour plots were prepared, because they also may contribute to a better understanding of the endwall flow phenomena in low and high staggered compressor cascades. Iso-loss lines, obtained by linear interpolation between the measured local total pressure losses, were plotted for $(p_{t1} - p_{t2}(y, z)) / q_1 = 0.05, 0.1, 0.15$ and so on for the low stagger cascade ($\lambda = 30°$, $\alpha = 18°$) in Fig. 24 and for the high stagger cascade ($\lambda = 50°$, $\alpha = 10°$) in Fig. 25.

Due to the overturning of the endwall flow, high loss material accumulates in the corner regions of the low stagger cascade. This has already been mentioned in section 5.2 and is now confirmed by Fig. 24, showing the loss contours with the highest loss coefficients in the corner regions. For the high stagger cascade, it has been speculated in section 5.2 that high loss material will accumulate between the blades, on the endwall, and not so much in corner regions as with the low stagger cascade. This turns out to be true, as may be seen in Fig. 25, where the loss contours with the highest loss coefficients are, indeed, between the blades, on the endwall.

7. CONCLUSIONS

Two compressor cascades of different stagger angle ($\lambda = 30°$ and $50°$), but otherwise of identical geometry, were experimentally and theoretically investigated, in order to evaluate the effects of stagger angle on endwall boundary layer development, 3D boundary layer separations (including blockage effects), and loss mechanisms.

To this end the following experiments and calculations were carried out: i) wake measurements at midspan (all inlet angles), ii) wake measurements at various spanwise positions between midspan and one endwall for one selected inlet angle each, iii) endwall boundary layer measurements upstream of the cascades for the inlet angles mentioned before, iv) flow visualization tests (all inlet angles), and v) inviscid secondary flow calculations.

The results turned out to be quite different. Only those of the low stagger cascade show similarity with existing experimental results and agreement with predictions of the classical inviscid secondary flow theory, including the well-known overturning and underturning of the flow at the end of the blades. The blockage effects of the endwall separation and corner stall phenomena grow with increasing angle of attack, but remain comparatively small. Nevertheless, corner stall is the main 3D feature of the low stagger cascade, responsible for most of the blockage and most of the secondary losses.

The results of the high stagger cascade do not show the classical overturning and underturning of the flow. Instead, only a severe underturning and a considerable disagreement with the predictions is to be seen. Moreover, the oil flow pictures of the endwall flow do not show any significant cross flow towards the suction surface of the blades. Indeed, the wall streamlines (wall shear stress lines) are very nearly potential flow streamlines up to a rear cross channel separation line (so far unknown), where two endwall boundary layers of different blade channels collide. The backward flow behind this separation line acts as a barrier for the passage (forward) endwall boundary layer in front of the separation line. In this way an interaction process is initiated, which leads to high blockage and to high mixing losses on the endwall between the blades (and not so much in the suction surface endwall corner). The rear separation lines move upstream with angle of attack and join to a single separation line in front of the cascade at some special angle of attack.

8. ACKNOWLEDGEMENT

The authors would like to acknowledge the contributions of their former students Christian Fiedler, Volker Gümmer and Jürgen Hübner.

9. REFERENCES

Came, P. M., and Marsh, H., 1974, "Secondary flow in cascades: two simple derivations for the components of vorticity," *Journal of Mechanical Engineering Science*, Vol. 16, pp. 391-401.

Dong, Y., Gallimore, S. J., and Hodson, H. P., 1987, "Three-dimensional flows and loss reduction in axial compressors," *ASME Journal of Turbomachinery*, Vol. 109, pp. 354-361.

Dring, R. P., Joslyn, H. D., and Hardin, L. W., 1982, "An investigation of axial compressor rotor aerodynamics," *ASME Journal of Engineering for Power*, Vol. 104, pp. 84-96.

Glynn, D., Spurr, A., and Marsh, H., 1977, "Secondary flow in cascades," *Secondary Flows in Turbomachines, AGARD CP*, No. 214.

de Haller, P., 1955, "Das Verhalten von Tragflügelgittern in Axialverdichtern und im Windkanal," *VDI-Berichte*, Band 3, pp. 27-31.

Hawthorne, W. R., 1955, "Some formulae for the calculation of secondary flow in cascades," *ARC RM*, No. 17, 519.

Hebbel, H. H., 1964, "Untersuchungen über den Einfluß der Profilwölbung auf die Strömung durch ebene Verdichter-Schaufelgitter bei hohen Unterschall-geschwindigkeiten. Teil 2: Untersuchungen bei kompressibler Strömung," *DFL Braunschweig*, Bericht Nr. 0269.

Horlock, J. H., Louis, J. F., Percival, P. M. E., and Lakshminarayana, B., 1966, "Wall stall in compressor cascades," *Journal of Basic Engineering*, Vol. 88, pp. 637-648.

Koch, C. C., 1981, "Stalling pressure rise capability of axial flow compressor stages," *ASME Journal of Engineering for Power*, Vol. 103, pp. 645-655.

Marchal, P., and Sieverding, C. H., 1977, "Secondary flows within turbomachinery bladings," *Secondary Flows in Turbomachines, AGARD CP*, No. 214.

Marsh, H. 1974, "Secondary flows in cascades," *Journal of Mechanical Engineering Science*, Vol. 16, pp. 402-407.

Papailiou, K., 1975, "Secondary flows in axial compressors," *Secondary Flows in Turbomachines, VKJ Lecture Series* 72.

Rhoden, H. G., 1956, "Effects of Reynolds number on the flow of air through a cascade of compressor blades," *ARC RM*, No. 2919.

Schweitzer, J. K., and Garberoglio, J. E., 1984, "Maximum loading capability of axial flow compressors", *Journal of Aircraft*, Vol. 21, pp. 593-600.

Starke, J., 1979, "Der Einfluß des axialen Stromdichteverhältnisses auf die aerodynamischen Beiwerte ebener Verdichtergitter", *Dissertation Technische Universität Braunschweig*.

Tobak, M., and Peake, D. J., 1982, "Topology of three-dimensional separated flows," *Ann. Rev. Fluid Mech.*, Vol. 14, pp. 61-85.

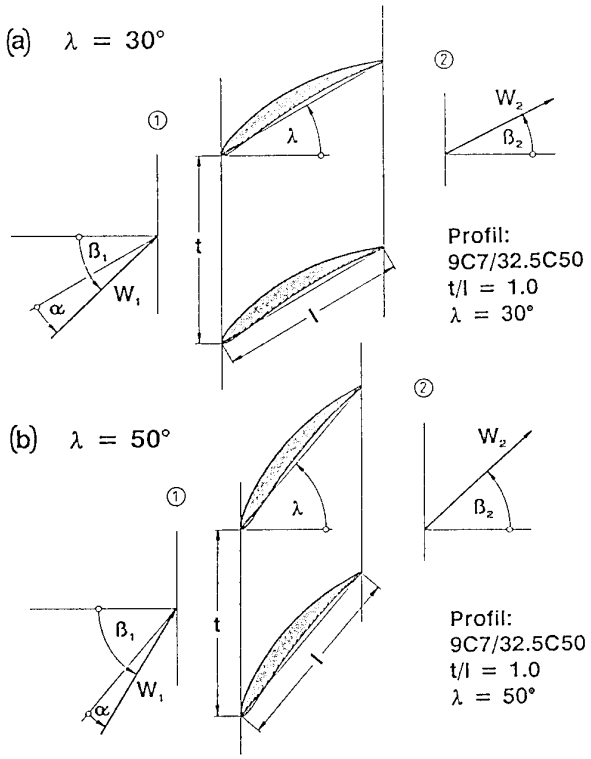

Figure 1: Compressor cascade
a) Low stagger cascade
b) High stagger cascade

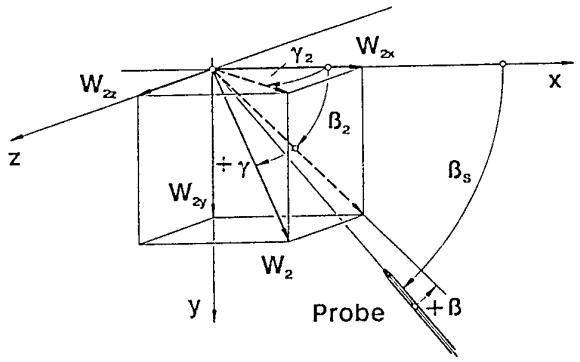

x,y - plane ≡ midspan section
y,z - plane ≡ measuring plane
positiv y - direction pointing from profile pressure to profile suction side

Figure 2: Angle definitions

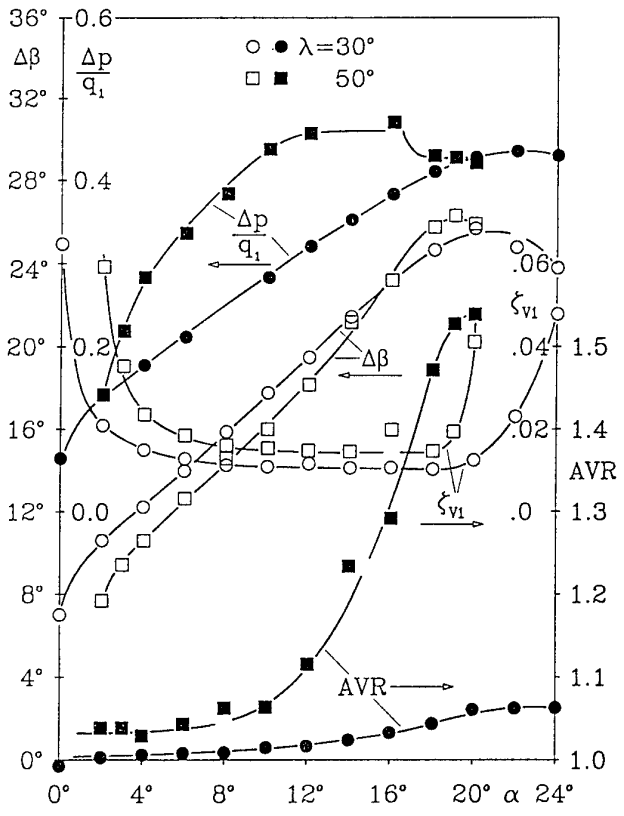

Figure 3: Performance parameters at midspan

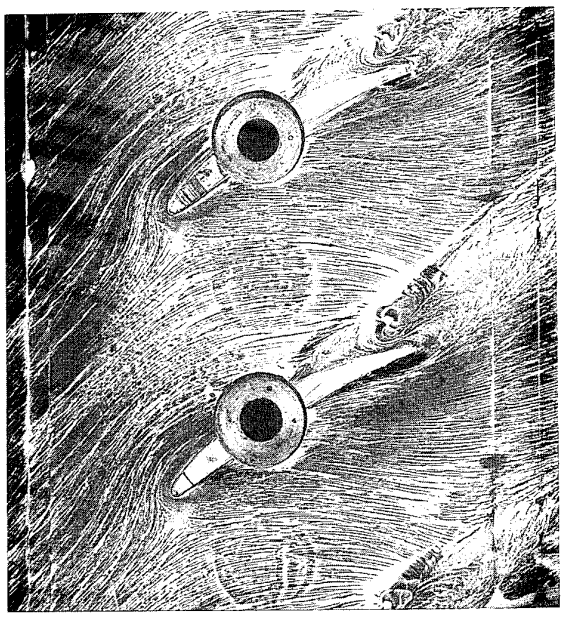

Figure 4: Wall streamlines on endwall:
$\lambda = 30°$, $\alpha = 18°$

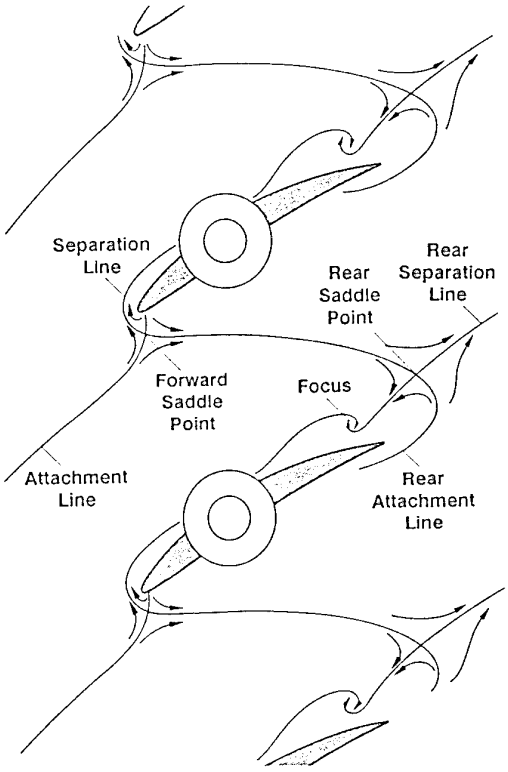

Figure 5: Endwall flow characteristics:
$\lambda = 30°$, $\alpha = 18°$

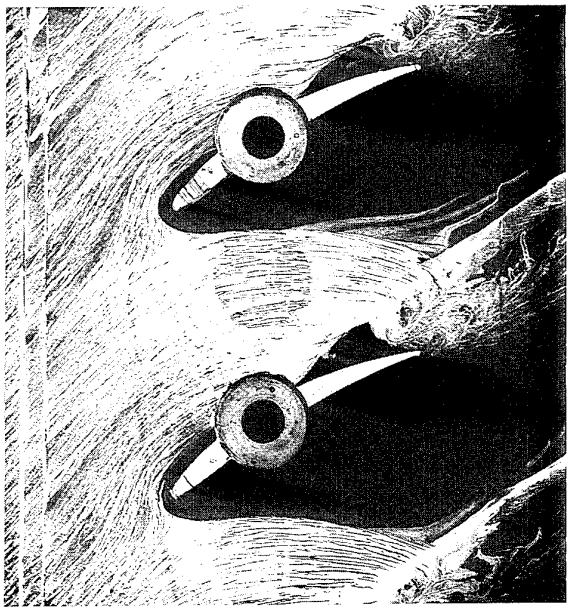

Figure 6: Wall streamlines on endwall by strip coating technique
$\lambda = 30°$, $\alpha = 18°$

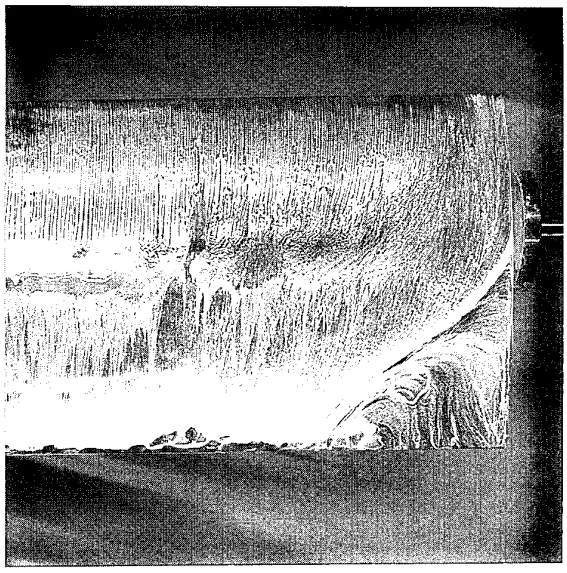

Figure 7: Wall streamlines on blade suction surface
$\lambda = 30°$, $\alpha = 18°$

Figure 8: Wall streamlines on endwall:
$\lambda = 50°$, $\alpha = 10°$

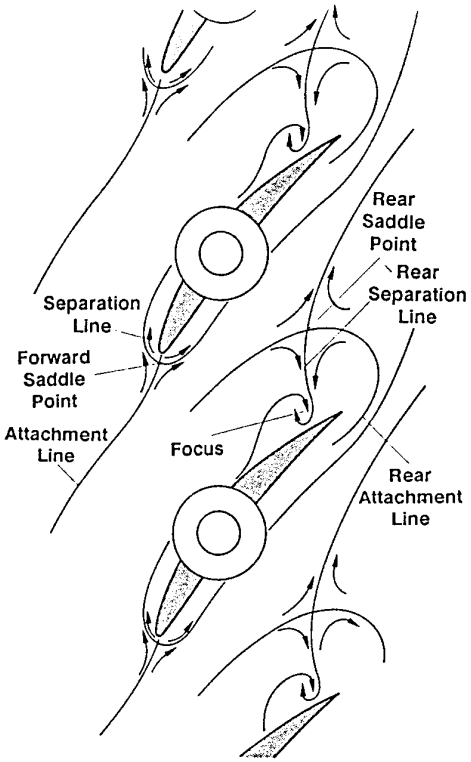

Figure 9: Endwall flow characteristics:
$\lambda = 50°$, $\alpha = 10°$

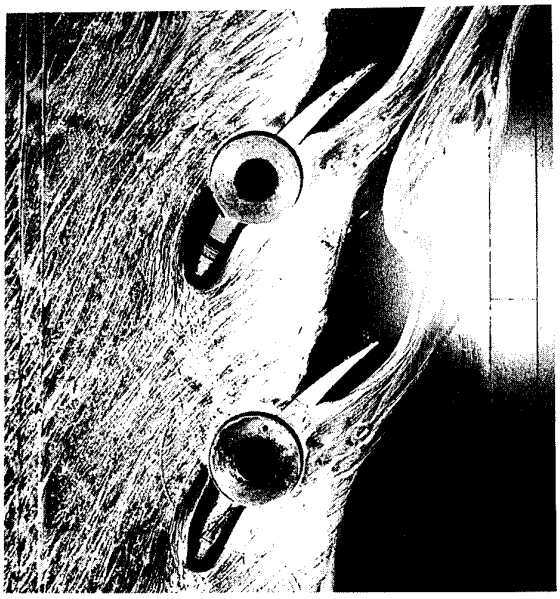

Figure 10: Wall streamlines on endwall
by strip coating technique
$\lambda = 50°$, $\alpha = 10°$

Figure 11: Wall streamlines on blade
suction surface
$\lambda = 50°$, $\alpha = 10°$

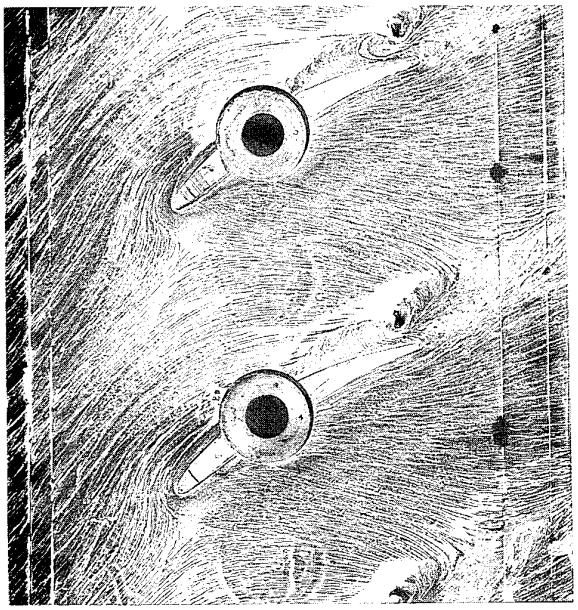

Figure 12: Wall streamlines on endwall:
$\lambda = 30°$, $\alpha = 22°$

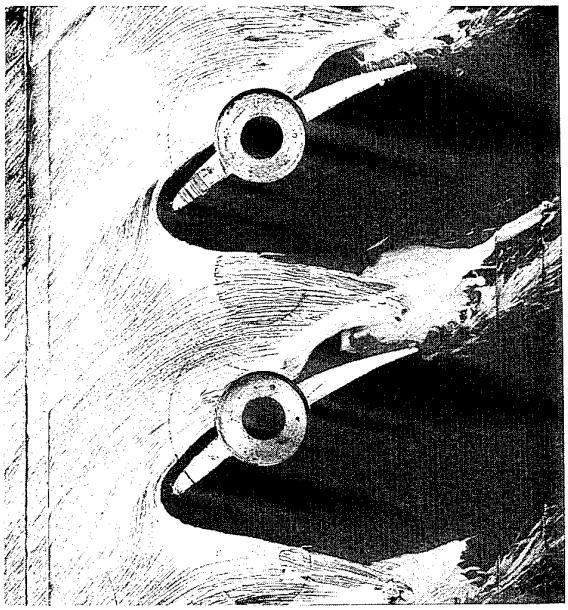

Figure 13: Wall streamlines on endwall
by strip coating technique
$\lambda = 30°$, $\alpha = 22°$

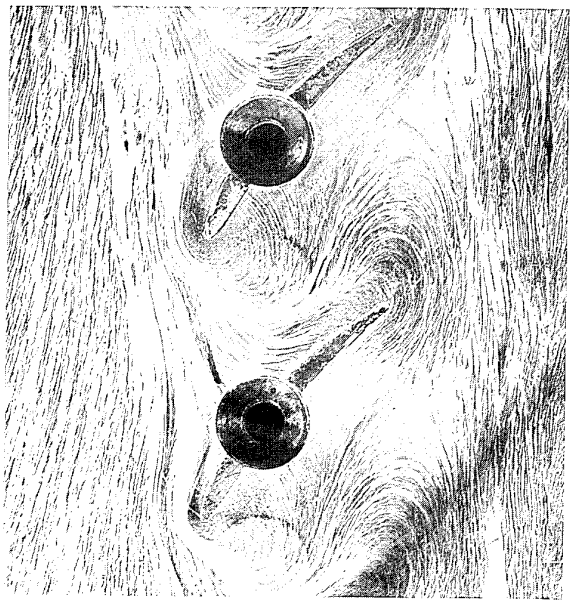

Figure 14: Wall streamlines on endwall:
$\lambda = 50°$, $\alpha = 20°$

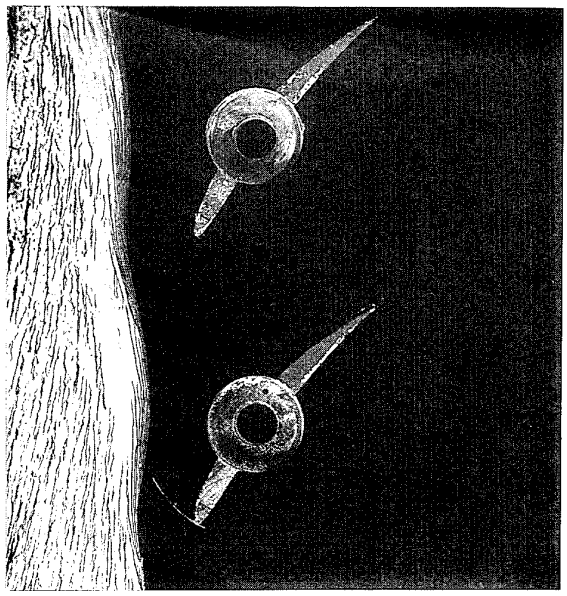

Figure 15: Wall streamlines on endwall
by strip coating technique
$\lambda = 50°$, $\alpha = 20°$

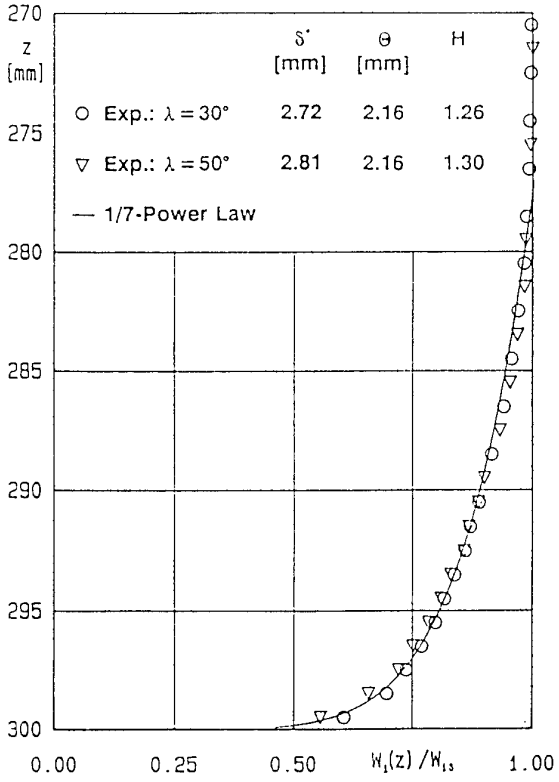

Figure 16: Upstream wall boundary layer

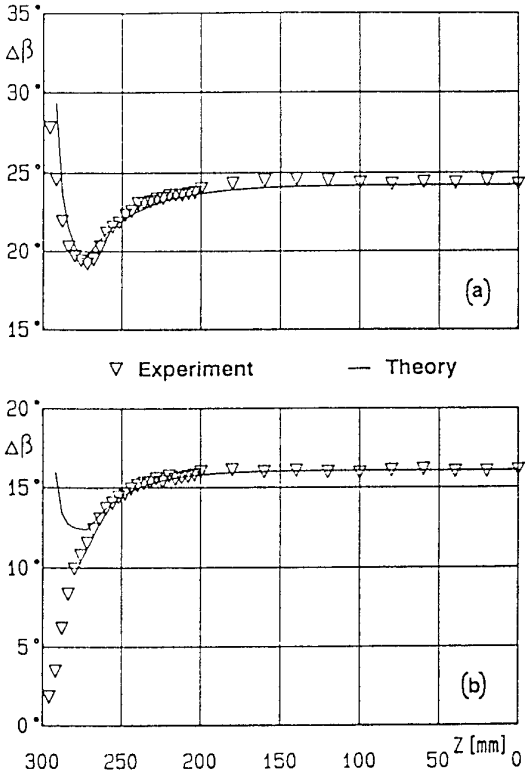

Figure 19: Measured and predicted turning angles a)λ=30° b)λ=50°

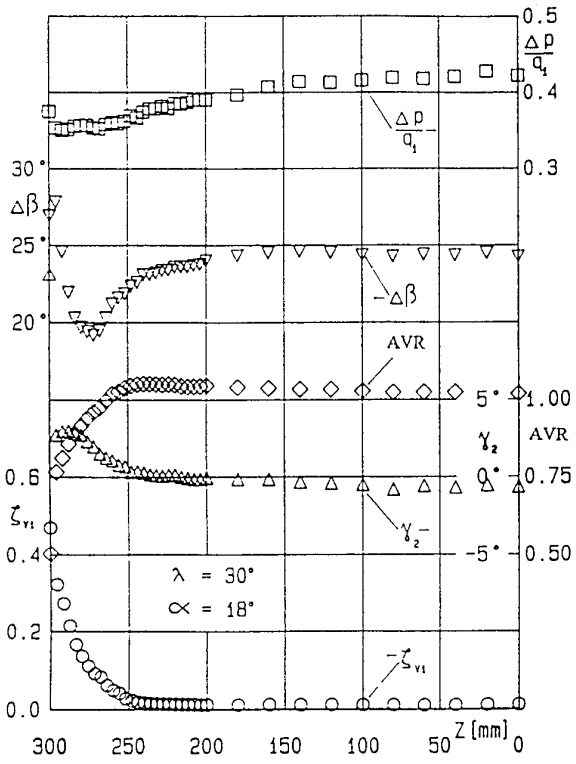

Figure 17: Spanwise distribution of performance parameters: λ = 30°, α = 18°

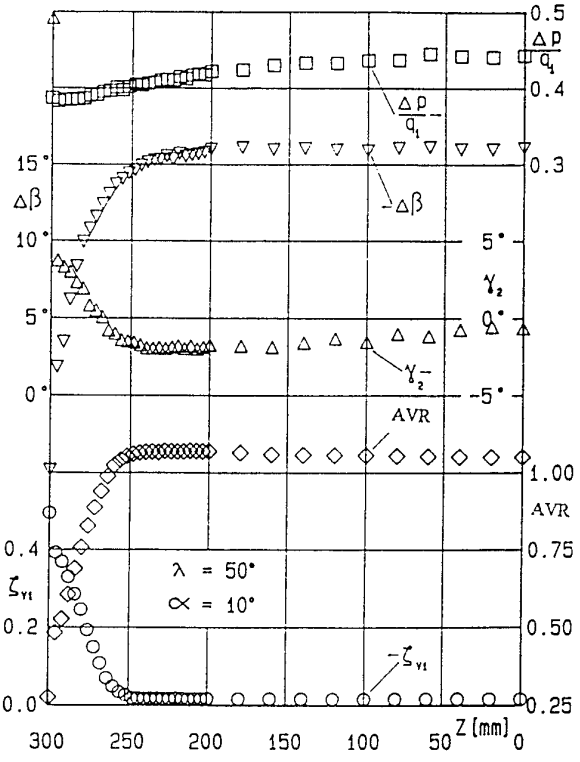

Figure 18: Spanwise distribution of performance parameters: λ = 50°, α = 10°

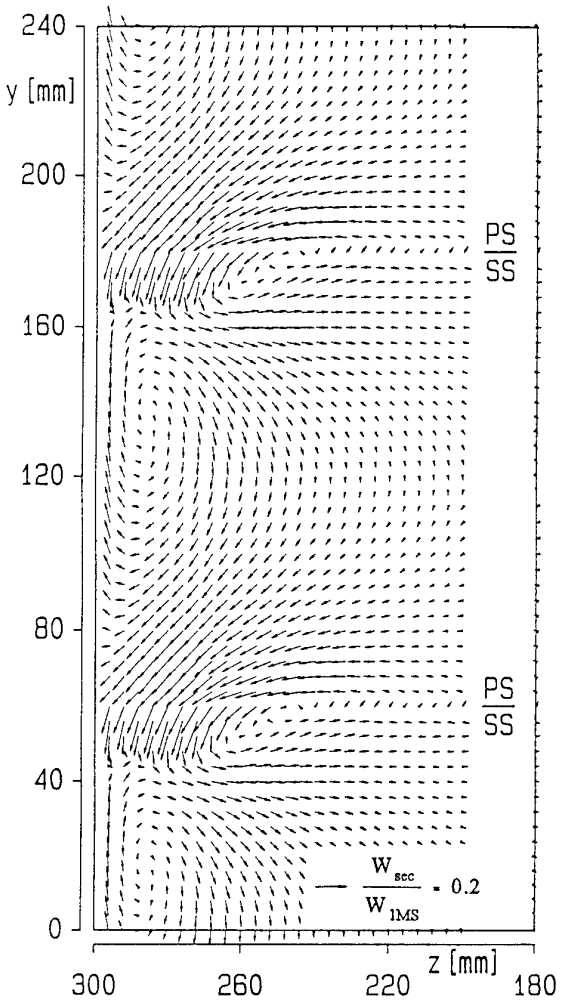

Figure 20: Secondary flow chart,
measured: $\lambda = 30°$, $\alpha = 18°$

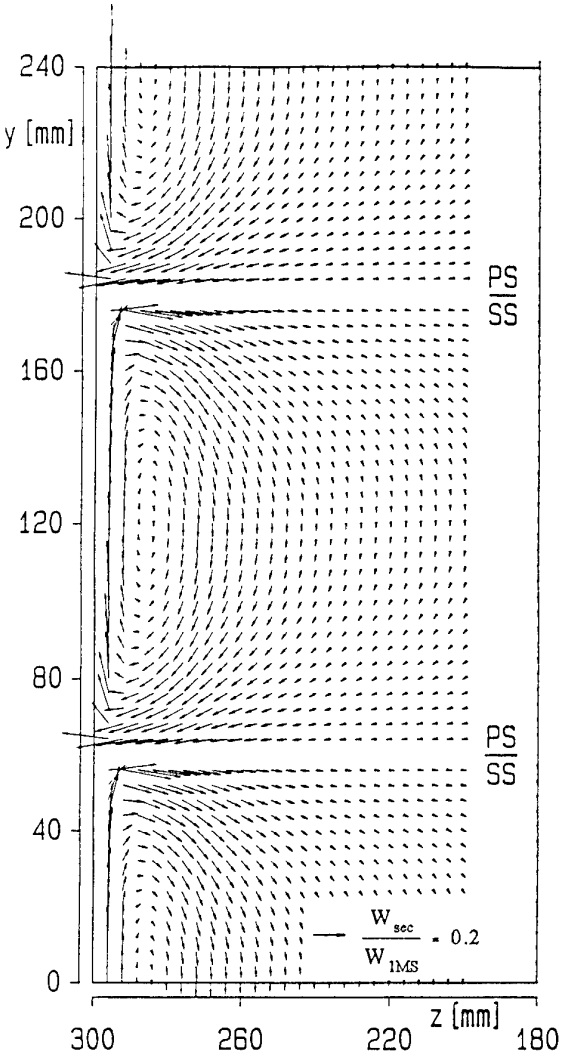

Figure 21: Secondary flow chart,
predicted: $\lambda = 30°$, $\alpha = 18°$

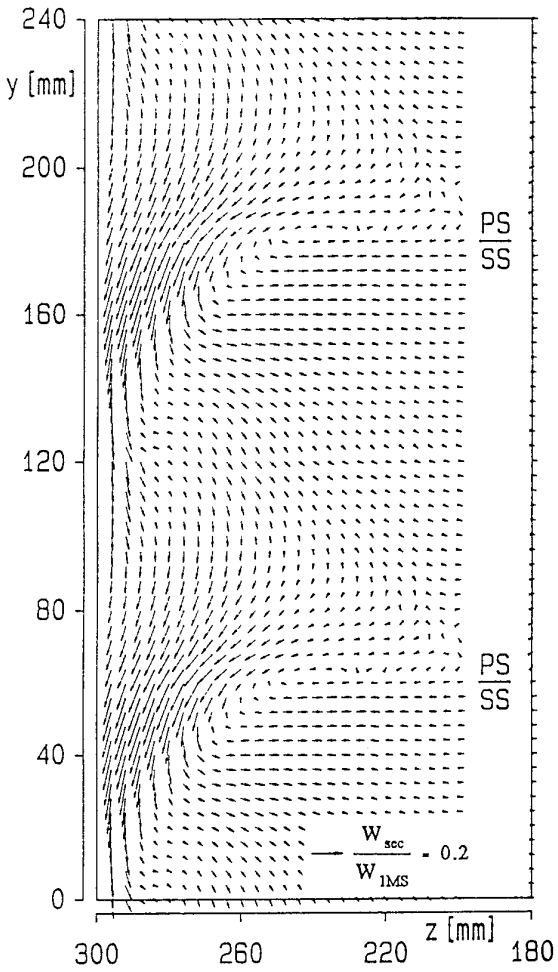

Figure 22: Secondary flow chart, measured: $\lambda = 50°$, $\alpha = 10°$

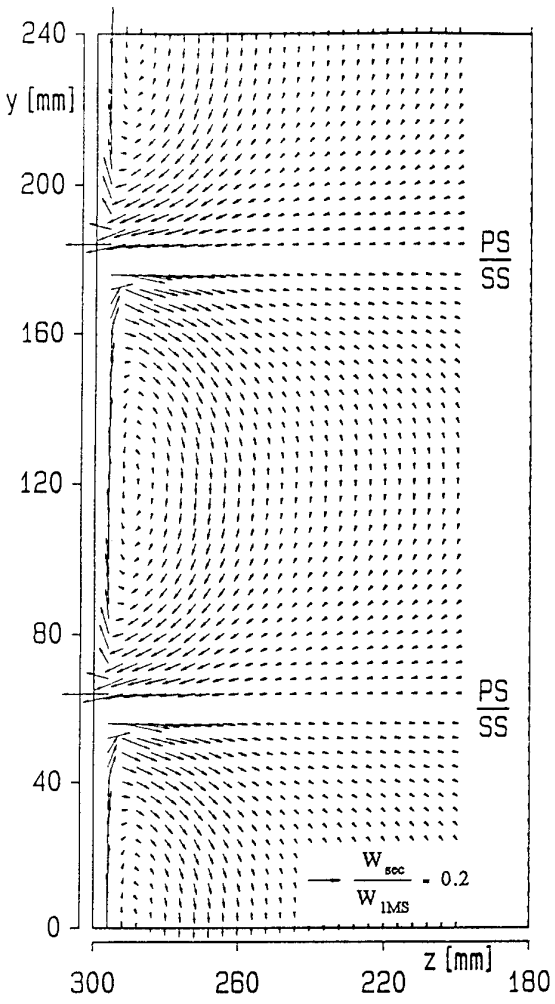

Figure 23: Secondary flow chart, predicted: $\lambda = 50°$, $\alpha = 10°$

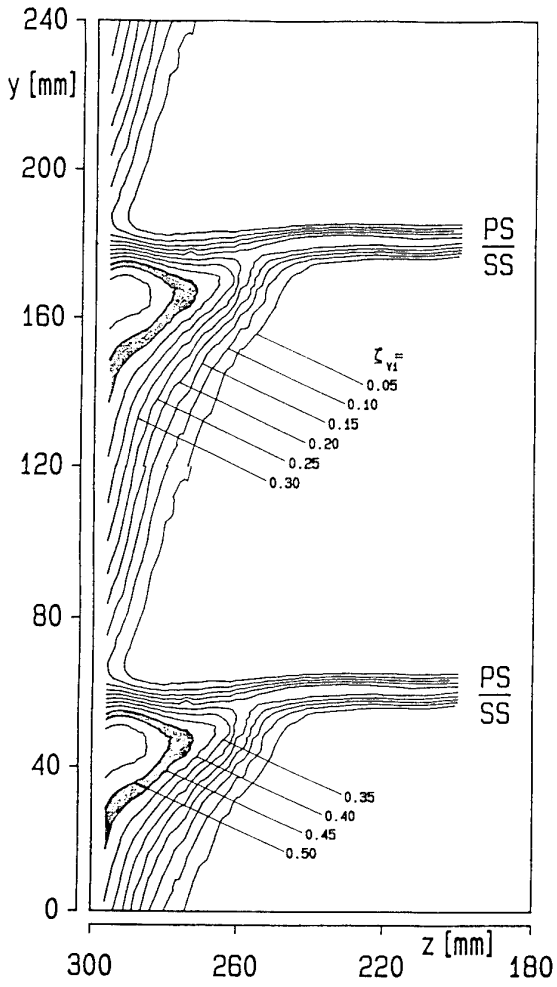

Figure 24: Loss contour plot:
$\lambda = 30°$, $\alpha = 18°$

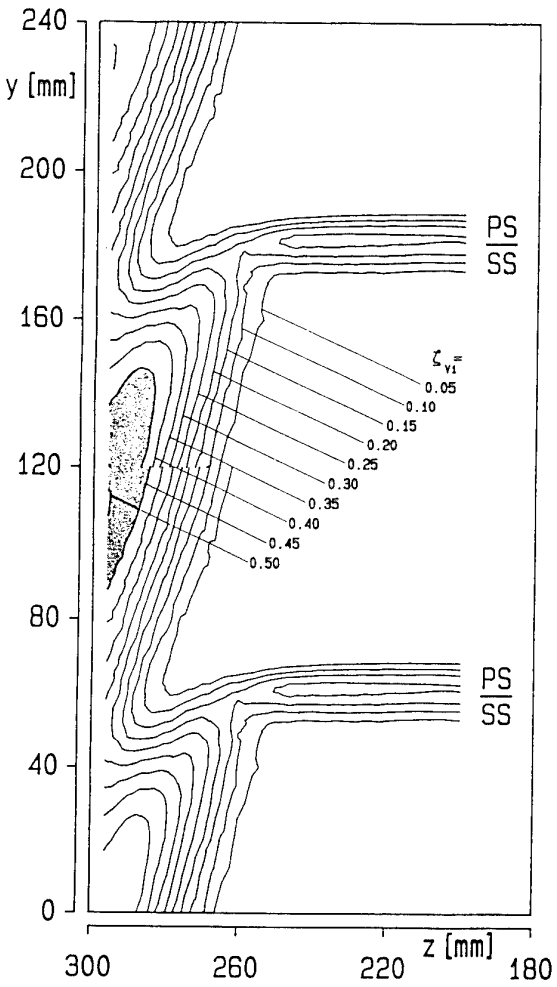

Figure 25: Loss contour plot:
$\lambda = 50°$, $\alpha = 10°$

REFERENCE NO. OF THE PAPER: 1

DISCUSSOR'S NAME: M.G. Rose, Rolls-Royce, U.K.

AUTHOR'S NAME: Stark & Bross

Q.: The endwall flow-visualization showed an endwall separation upstream of the leading edge for the higher stagger cascade. I would like to ask: Where does the inlet boundary layer go?

A: For the high stagger ($\lambda = 50°$) cascade, beginning with an angle-of-attack of $\alpha = 15°$, the endwall boundary layers separate in front of the cascade, first along a wave-like line and later along a nearly straight line (see Fig. 15 for $\alpha = 20°$). The separated boundary layers probably enter the cascade at a certain distance from the endwalls and then become part of highly three-dimensional flows, for which the details presently are unknown.

REFERENCE NO. OF THE PAPER: 1

DISCUSSOR'S NAME: Kang Shun, Univ. Brussels, Belgium

AUTHOR'S NAME: Stark & Bross

Q.: According to topological theory, two saddle points cannot be connected directly. But in your Fig. 5, the saddle point in front of the leading edge is directly connected to the saddle behind the trailing edge. How do you explain it?

A: The direct connection of two saddle-points, to be seen in Fig. 5 (derived from Fig. 4), is theoretically an exception (see Perry and Chong in Ann. Rev. Fluid Mech. 1987) and experimentally a result of $\alpha = 18°$ only. For other angles-of-attack, there are always two lines crossing the passage: i) a separation line through the leading edge saddle-point, and ii) a nearly parallel attachment line through the rear saddle-point. Fig. 12 shows an example of $\alpha = 22°$ ($\alpha > 18°$); in this case, the separation line is in front of the attachment line. Things are vice versa for $\alpha < 18°$ (not shown in the paper, but nevertheless available). For $\alpha = 18°$, both lines are simply at the same position.

REFERENCE NO. OF THE PAPER: 1

DISCUSSOR'S NAME: I.H. Skoe, IA-T, Norway

AUTHOR'S NAME: U. Stark and S. Bross

Q.: From the loading point of view, it is somewhat unfair to compare the same solidity and camber airfoil at stagger angles of 30° and 50°. What are the achieved diffusion factors, and do the losses correlate with equivalent diffusion ratio (D_{eq} of NASA)?

A: The present work is part of a parametric investigation. The usual way to carry out such investigations is to change only one parameter at a time and to keep the others constant. This was done. The results of an investigation like this may be used to analyze variable stator flows, with the low and high stagger cascade simulating a design (or near-design) and off-design condition, respectively.

For $\alpha = 20°$ ($\lambda = 30°$) and $\alpha = 18°$ ($\lambda = 50°$), the equivalent diffusion ratios ($D_{eq} \approx V_{max,\,S}/V_2$) were calculated to be $D_{eq} \approx 1.93$ in the first case and $D_{eq} \approx 1.85$ in the second case. Both values are below $D_{eq} = 2.0$ (the blade stall limit), up to which a strong correlation between the losses and the diffusion ratios exists (see Lieblein in Trans. ASME J. of Basic Eng. Vol. 81 (1959), pp. 387-397,Fig. 9).

LOSSES PREDICTION IN AXIAL FLOW COMPRESSOR CASCADES USING AN EXPLICIT k-ε NAVIER-STOKES SOLVER

C. VASSILOPOULOS, G. SIMANDIRAKIS, K.C. GIANNAKOGLOU, K.D. PAPAILIOU
Laboratory of Thermal Turbomachines
National Technical University of Athens, P.O. Box 64069
15710 Athens, Greece

ABSTRACT

Flow patterns and losses prediction in a controlled diffusion airfoil cascade of an industrial axial compressor are demonstrated by means of a two-dimensional, explicit, time-marching fractional-step solver. The fractional-step algorithm presents certain advantages which are mainly related to its simplicity and the fact that greater time-steps are allowed, in comparison to other explicit solvers. In the present analysis, turbulence is modeled through both a low-Reynolds k-ε model and the algebraic Baldwin-Lomax one. The former is combined with an efficient artificial viscosity scheme, leading thus to a smooth ε-field close to the solid walls. From a numerical point of view, the Baldwin-Lomax model cooperates perfectly with the basic numerical kernel. The k-ε model, when used in conjuction to an explicit solver, is prone to instabilities and a particular semi-implicit treatment of the source terms is required. On the basis of the examined cases, differences in the predictive capabilities of the two turbulence models are presented and discussed.

NOMENCLATURE

AVDR	axial-velocity-density-ratio
$c_{\epsilon 1}, c_{\epsilon 2}, c_\mu$	empirical constants for the k-ε model ($c_{\epsilon 1}=1.57$, $c_{\epsilon 2}=1.92$, $c_\mu=0.09$)
E_t	total energy per unit volume ($E_t=\rho e+\frac{1}{2}\rho V^2+\rho k$)
f_2, f_μ	empirical functions for the k-ε model
g^{ij}	contravariant metric tensor
h	channel thickness
J	Jacobian
k	turbulent kinetic energy
k_2, k_4	artificial dissipation constants ($k_2=0.25$, $k_4=0.01$)
n	normal to the wall direction
M	Mach number
p	static pressure
p_{eff}	effective pressure ($p_{eff}=p+\frac{2}{3}\rho k$)
q,Q	dependent variable arrays
P	production term in the k-ε equations
$Pr, Pr_t, Pr_k, Pr_\epsilon$	Prandtl numbers ($Pr=0.72$, $Pr_t=0.9$, $Pr_k=1.0$, $Pr_\epsilon=1.3$)
Re	Reynolds number
T	temperature
u_τ	friction velocity
u,v	Cartesian velocity components
V	local velocity magnitude
V^1, V^2	contravariant velocity components
x,y	Cartesian coordinates
y^+	dimensionless distance from the wall ($y^+=\rho u_\tau y/\mu$)
ε	isotropic turbulent energy dissipation
μ, μ_t, μ_{eff}	molecular, turbulent and effective viscosity coefficients
ξ,η	curvilinear coordinates
ρ	density
τ_{ij}	Cartesian stress tensor components
ω	total pressure loss coefficient

Subscripts

1	inlet
2	exit
is	isentropic flow

INTRODUCTION

A major performance parameter for industrial compressors is their efficiency. During the last years, a considerable amount of work has been invested in improving the efficiency of the existing compressors. Due to the high efficiency of modern compressors, further improvements are quite difficult. Both experiments and calculation methods of various complexities are in use for this reason. Besides, computational methods, performing either in the direct or in the inverse mode, have led to an improved understanding of the flow in compressor stages. Software development is facilitated a lot by the modern computer architectures which make these runs affordable, in the design departments of compressor industries.

As a consequence, the design and analysis of turbomachinery components has become increasingly dependent on the solution of the Navier-Stokes equations. The accuracy with which a computational method models a physical problem depends on various parameters. From a numerical point of view, an important parameter is the allowed discretization error in space or in time (for time accurate calculations). From a physical point of view, the accuracy of the numerical model depends on the successful selection of the incorporated turbulence model.

In the present paper, an explicit fractional step code with a two-equation k-ε low-Reynolds closure (Jones and Launder, 1972) will be used for the prediction of losses in a controlled diffusion airfoil cascade of an industrial axial compressor. The examined cascade consists of blades designed using an inverse full potential code and tested in a windtunnel. Apart from the k-ε model, the Baldwin-Lomax turbulence model will be used in parallel, for the sake of comparison. Among other things, the algebraic turbulence model is more flexible in incorporating various transition models or even fixing the transition point at any grid node along the airfoil, which is not the case if the k-ε model is used.

The present Navier-Stokes method has been previously

Paper presented at the AGARD PEP 85th Symposium on "Loss Mechanisms and Unsteady Flows in Turbomachines", held in Derby, United Kingdom, 8-12 May 1995, and published in CP-571.

used to perform various turbomachinery calculations (Simandirakis, 1992, Giannakoglou et al., 1991). According to the fractional step algorithm, the conservative two-dimensional Navier-Stokes equations are split in a sequence of one-dimensional operators for the inviscid part, the viscous part and the source terms. Thus, instead of applying a pure two-dimensional scheme, a number of one-dimensional steps are executed, with less strict stability constraints. For each one-dimensional step, an explicit predictor-corrector MacCormack scheme is used, with the exception of the semi-implicit treatment of source terms. A second- and fourth-order dissipation scheme is added to prevent odd-even uncoupling, in a modified form in order to account for the turbulence equations. The latter are solved in a coupled way with the mean flow equations.

GOVERNING EQUATIONS

Since, in the present study, both an algebraic and a two-equation turbulence model are in use, governing equations will be presented for the more general case, that of the k-ε model. As it will be discussed, in more detail, in the Results section, the compressor cascade will be examined by imposing a variable channel thickness distribution h = h(x) between the leading and the trailing edges. The corresponding unsteady, Favre-averaged Navier-Stokes equations, with a low-Reynolds k-ε closure are written in the form

$$\frac{\partial \vec{q}}{\partial t}+\frac{\partial \vec{f}}{\partial x}+\frac{\partial \vec{g}}{\partial y}=\vec{s} \qquad (1)$$

where the unknown variable vector $\vec{q}$, which consists of mean-flow and turbulence quantities, is given by

$$\vec{q}= h[\rho,\rho u,\rho v,E_t,\rho k,\rho \varepsilon]^T$$

The flux vectors f and g are written in the form

$$\vec{f}= h\Big[\rho u,\rho u^2+p_{eff}-\tau_{xx},\rho uv-\tau_{xy},$$
$$u(E_t+p_{eff})+q_x-u\tau_{xx}-v\tau_{xy}-\frac{\mu_t}{Pr_k}\frac{\partial k}{\partial x},$$
$$\rho uk-\left(\mu+\frac{\mu_t}{Pr_k}\right)\frac{\partial k}{\partial x},\rho u\varepsilon-\left(\mu+\frac{\mu_t}{Pr_\varepsilon}\right)\frac{\partial \varepsilon}{\partial x}\Big]^T \qquad (2)$$

$$\vec{g}= h\Big[\rho v,\rho uv-\tau_{xy},\rho v^2+p_{eff}-\tau_{yy},$$
$$v(E_t+p_{eff})+q_y-u\tau_{xy}-v\tau_{yy}-\frac{\mu_t}{Pr_k}\frac{\partial k}{\partial y},$$
$$\rho vk-\left(\mu+\frac{\mu_t}{Pr_k}\right)\frac{\partial k}{\partial y},\rho v\varepsilon-\left(\mu+\frac{\mu_t}{Pr_\varepsilon}\right)\frac{\partial \varepsilon}{\partial y}\Big]^T$$

and the effective stress tensor is given by

$$\tau_{xx}= \mu_{eff}\left[2\frac{\partial u}{\partial x}-\frac{2}{3}\frac{1}{h}\left(\frac{\partial (hu)}{\partial x}+\frac{\partial (hv)}{\partial y}\right)\right]$$

$$\tau_{xy}= \mu_{eff}\left(\frac{\partial u}{\partial y}+\frac{\partial v}{\partial x}\right)$$

$$\tau_{yy}= \mu_{eff}\left[2\frac{\partial v}{\partial y}-\frac{2}{3}\frac{1}{h}\left(\frac{\partial (hu)}{\partial x}+\frac{\partial (hv)}{\partial y}\right)\right]$$

$$\tau_{zz}= \mu_{eff}\left[2\frac{u}{h}\frac{dh}{dx}-\frac{2}{3}\frac{1}{h}\left(\frac{\partial (hu)}{\partial x}+\frac{\partial (hv)}{\partial y}\right)\right]$$

where p_{eff} should be replaced by p if the Baldwin-Lomax model is used. The heat flux vector is given by

$$(q_x\ ,\ q_y)= \left(-Pr_{eff}^{-1}\frac{\partial e}{\partial x}\ ,\ -Pr_{eff}^{-1}\frac{\partial e}{\partial y}\right)$$

where the effective Prandtl number Pr_{eff} is defined as

$$Pr_{eff}^{-1} = \gamma\left(\frac{\mu}{Pr}+\frac{\mu_t}{Pr_t}\right)$$

The use of a variable channel (i.e. streamtube) thickness results to a non-zero r.h.s. term in the x-momentum equation. When the Jones and Launder (1972) low-Reynolds k-ε turbulence model is used, non-zero source term entries for the k and ε equations also appear. Thus, the source term vector $\vec{s}$ takes the form

$$\vec{s}= [0,\ s_x,\ 0,\ 0,\ s_k,\ s_\varepsilon]^T$$

with

$$s_x=p_{eff}\frac{dh}{dx}-\tau_{zz}\frac{dh}{dx}$$

$$s_k=h\ \left(\ P-\rho\varepsilon-2\mu\left(\frac{\partial\sqrt{k}}{\partial n}\right)^2\ \right) \qquad (3)$$

$$s_\varepsilon=h\ \left(\ c_{\varepsilon_1}P\frac{\varepsilon}{k}-c_{\varepsilon_2}f_2\rho\frac{\varepsilon^2}{k}+2\frac{\mu\mu_t}{\rho}\left(\frac{\partial^2 V}{\partial n^2}\right)^2\ \right)$$

The production term P, is given by

$$P = \mu_t\left(\frac{\partial u}{\partial y}+\frac{\partial v}{\partial x}\right)^2+2\mu_t\left[\left(\frac{\partial u}{\partial x}\right)^2+\left(\frac{\partial v}{\partial y}\right)^2\right]$$
$$-\frac{2}{3}\mu_t\left(\frac{\partial u}{\partial x}+\frac{\partial v}{\partial y}\right)^2-\frac{2}{3}\rho k\left(\frac{\partial u}{\partial x}+\frac{\partial v}{\partial y}\right)$$

and the turbulent viscosity μ_t is obtained from the Prandtl-Kolmogorov relation,

$$\mu_t=c_\mu f_\mu\frac{\rho k^2}{\varepsilon}$$

For the selected model, the constants and functions used are given by

$$f_2=1-0.3\exp(-Re_t^2) \quad , \quad f_\mu=\exp\left[\frac{-3.4}{\left(1+\frac{Re_t}{50}\right)^2}\right]$$

$$Re_t=\frac{\rho k^2}{\mu\varepsilon}$$

The Baldwin-Lomax model is applied following the two-layer approach presented in the original paper (Baldwin and Lomax, 1970). Nevertheless, important modifications are encountered concerning (a) the calculation of the wall shear stress close to the separation point, (b) the calculation of the maximum of the function F(y) when the latter displays two peaks and (c) the prediction of transition. For the aforementioned modifications the reader should turn to a previous publication by the authors (Giannakoglou et al, 1991).

GRID GENERATION AND GEOMETRICAL TRANSFORMATION

Governing equations are discretized using a structured H-type grid which extend about one chord upstream and downstream of the airfoil. The grid, being common for all runs, was numerically generated using a system of elliptic equations, enhanced with appropriate source terms (Sorenson, 1980) which allow a direct control of grid lines stretching and orthogonality, close to the solid boundaries.

All governing equations are transformed to the body-fitted coordinate system (ξ,η) defined by the grid lines of the generated grid. It must be said that the use of a precisely orthogonal grid is not necessary, since all cross-derivatives are retained during the discretization. However, both the calculation of the low Reynolds terms in the k-ε equations and the practical implementation of the Baldwin-Lomax model recommend the use of a grid which should be as orthogonal as possible. The governing equations (1) are transformed in the computational plane (ξ,η) and the resulting equations may be cast in the following conservative form

$$\frac{\partial\vec{Q}}{\partial t}+\frac{\partial\vec{F}}{\partial\xi}+\frac{\partial\vec{G}}{\partial\eta}=\vec{S} \qquad (4)$$

where

$$\begin{aligned}\vec{Q} &= J\,\vec{q}\\ \vec{F} &= J\left[\xi_x\vec{f}+\xi_y\vec{g}\right]\\ \vec{G} &= J\left[\eta_x\vec{f}+\eta_y\vec{g}\right]\\ \vec{S} &= J\,\vec{s}\end{aligned} \qquad (5)$$

BOUNDARY CONDITIONS

In the examined cases which are characterized by a subsonic axial velocity component at the inlet, all but one dependent variables need to be specified at the inlet. The stagnation pressure and temperature of the working fluid entering the flow field, as well as the inlet flow angle must be imposed. At the exit boundary, the static pressure is given, which is used to specify the mass flow rate. The non-specified dependent variables, at both inlet and exit, are extrapolated from the interior nodes. Unfortunately, in the aforementioned procedure, the precise inlet Mach number is an outcome of the calculation, depending upon the imposed exit pressure level. So, runs at the desired inlet Mach number have been carried out using a trial and error procedure.

With respect to turbulence quantities, the turbulence intensity level at the inlet along with an arbitrary but reasonable μ_t/μ ratio is specified. The inlet values of k and ε are calculated directly calculated from the previously mentioned quantities. When the Baldwin and Lomax model is used, this is either left free to form the transition point according to a built-in transition criterion, or transition is imposed at a specified grid node along the airfoil walls.

Along solid walls the velocity components are set to zero and the pressure is calculated through the normal momentum equation. If the low-Re k-ε model is used, zero Dirichlet conditions for both k and ε are imposed at the solid walls. A zero heat flux condition is imposed. Finally, periodicity conditions are imposed at each step of the algorithm.

NUMERICALPROCEDURE

The fractional-step concept implies that the finite-difference form of the discretized equation (4) split into a sequence of multiple single-directional operators (Laval, 1983). Each operator corresponds to a different physical component of the equation. The 1-D operators are denoted by L and are superscribed by H, P or ST in order to distinguish the part of the governing equations which is resolved by each operator. Thus, an L^H operator represents the scheme used to resolve the inviscid part of the equations (H=Hyperbolic), an L^P operator solves for the viscous part (P=Parabolic), while the L^{ST} operator is the one which handles the source terms in the equations. All operators are also subscribed by either ξ or η, depending on whether sweeps are performed along the η or ξ=constant grid lines respectively.

According to the fractional-step concept, the time evolution of the unknown vector array Q, is obtained by applying the sequence of operators, which may be cast in the following symbolic form

$$\vec{Q}^{n+2}=L_\xi^H L_\eta^H L_\xi^P L_\eta^P L^{ST} L^{ST} L_\eta^P L_\xi^P L_\eta^H L_\xi^H \vec{Q}^n \qquad (6)$$

A double and inverse sequence of the one-dimensional operators leads to a second order accuracy in time, while the calculated quantities have a physical meaning only at the expiration of a $2\Delta t$ time interval (i.e. from n to n+2 iteration level) (Abarbanel and Gottlieb, 1981). The predictor-corrector MacCormack scheme is used to handle the hyperbolic and parabolic operators (MacCormack, 1988).

A common time step is used for all L operators and this is the minimum of the time steps which result from the stability analysis performed for each operator separately. The total time-increment per time-step is less strict compared to that dictated by any explicit two-dimensional stability criterion.

With regard to the treatment of the source terms, a semi-implicit scheme is used to ensure numerical stability. Thus, for the solution of the intermediate step, corresponding to the L^{ST} operator, namely

$$\frac{\partial \vec{Q}}{\partial t} = \vec{S} \tag{7}$$

the right-hand-side array S splits in S_+ (which contains the positive source terms) and S_- (with the negative ones). The negative part is Newton linearized and the delta form of equation (7) can be written as

$$\left[I - \Delta t^* \left(\frac{\partial \vec{S}_-}{\partial \vec{Q}} \right)^{n+\frac{4}{5}} \right] \Delta \vec{Q}^{\,n+\frac{4}{5}} = \Delta t^* \vec{S}^{\,n+\frac{4}{5}} \tag{8}$$

ARTIFICIAL DISSIPATION

Extra dissipation terms are explicitly added to the solution array $\vec{Q}$ at the end of a complete calculation period, corresponding to a time interval of $2\Delta t$, as follows

$$\vec{Q}^{\,n+2} = \vec{Q}^{\,n+2} + \vec{D}_\xi + \vec{D}_\eta \tag{9}$$

The quantity $D_\xi + D_\eta$ represents a blend of second- and fourth-order derivatives of the solution array scaled by the inverse of the Jacobian J. For the ξ-direction, the artificial dissipation term D_ξ yields

$$\begin{aligned} \vec{D}_\xi = & \nabla_\xi \left[2\ \Sigma_\xi (\sigma\ J) \varepsilon_\xi^{(2)} \Delta_\xi \left(\frac{\vec{Q}^{\,n+2}}{J} \right) \right] \\ & - \nabla_\xi \left[2\ \Sigma_\xi (\sigma\ J) \varepsilon_\xi^{(4)} \Delta_\xi \nabla_\xi \Delta_\xi \left(\frac{\vec{Q}^{\,n+2}}{J} \right) \right] \end{aligned} \tag{10}$$

where ∇_ξ, Δ_ξ are the backward and forward difference operators in the ξ-direction and Σ_ξ is the forward averaging operator in the same direction.

The amount of extra diffusion added is controlled (Jameson et al, 1981) using two coefficients $\epsilon_\xi^{(2)}$ and $\epsilon_\xi^{(4)}$, namely

$$\begin{aligned} \epsilon_\xi^{(2)} &= k_2 \Delta t\ \max_\xi(Y) \\ \epsilon_\xi^{(4)} &= \max(0, k_4 \Delta t - \epsilon_\xi^{(2)}) \end{aligned} \tag{11}$$

where $\max_\xi()$ stands for the local maximum value of () in the ξ-direction. For the mean flow equations, the sensor Y is based on static pressure variations

$$Y = \frac{|\nabla_\xi \Delta_\xi P|}{|4\bar{P}|} \tag{12}$$

where $\bar{P}$ is the local average of the pressure P, in the ξ-direction and σ stands for the sum of the two one-dimensional spectral radii. Similar analysis is valid for the η-direction as well.

For the turbulence equations the added artificial dissipation is still given by (10), but the stability analysis of the k and ε equations, suggests the use of unequal time-steps for the mean flow and the turbulence equations, provided that a common CFL number is used. Alternatively, a consistent time evolution of mean flow and turbulence quantities would require the use of a dual CFL number. In the present work, a common CFL number is used, for all equations.

In the k-ε equations, the parameters σ in (10) and the control coefficients (11) are still defined in the same way, but the sensor Y which influences the second-order term only, is given by (Simandirakis, 1992, Dejean et al, 1994)

$$Y = \frac{|\nabla_\xi \Delta_\xi \varepsilon|}{|4\bar{\varepsilon}|} \tag{13}$$

RESULTS AND DISCUSSION

The method which was previously analysed was applied in a two-dimensional controlled diffusion airfoil cascade which is representative for the first rotor hub section of an industrial axial compressor. This cascade was designed using an inverse full potential code, in order to make full allowance of a controlled diffusion along the blade surfaces and was tested in a cascade windtunnel. The whole analysis of the cascade is described in an ASME Paper (Steinert, 1990).

The profile coordinates are given in the cited reference; the pitch-to-chord ratio was 0.68 and the stagger angle equal to -30 deg. Design conditions correspond to inlet flow angle $\alpha_1 = 47$ deg and inlet Mach number equal to $M_1 = 0.62$. According to the experiments, the axial-velocity-density-ratio (ADVR) was equal to 1.1 and this was taken into account by allowing a variation of the channel thickness $h = h(x)$ between the leading and trailing edges of the order of -10%. Upstream of the leading edge and downstream of the trailing edge, the channel or streamtube thickness remained constant and equal to the corresponding values of h at the leading and trailing edges, respectively. Numerical tests have shown that the non-unit ADVR value had to be taken into account in order to capture the correct pressure distribution over the profile. Losses were secondarily influenced by this parameter.

For the present analysis, a H-type grid, having 170×71 nodal points, was used; the leading edge was located at the 40th node while the trailing edge corresponds to the 125th one. The grid was stretched close to the solid walls in order to ensure the well known requirement for calculations carried out using a low-Re k-ε model. An elliptic grid generator was used for this purpose and the non-dimensional distance of the first node off the wall was less than 1. Figure (1a) illustrates the computational grid as a whole, while figures (1b) and (1c) provide a detailed view of the grid in the region close to the leading and trailing edges. In figure (1c) the reduced rear thickness of the blade is clearly shown; the blade was designed in such a way in order to allow higher diffusion and thicker boundary layers.

The compressor cascade was tested at four different inlet flow angles $\alpha_1 = 40, 43, 47$ and 52 deg, corresponding to a wide range of incidence angles, from i = -7 deg up to i = +5 deg. The exit pressure was calculated by the known P_2/P_1 ratios (which for the four aforementioned cases were equal to $P_2/P_1 = 1.0619$, 1.0948, 1.221, 1.1459, respectively) in combination with the desired inlet Mach number $M_1 = 0.62$. All four cases were examined by means of both the low-Re k-ε model and the Baldwin-Lomax one. For the latter, transition was imposed by applying the criterion of Baldwin

et al (1978); according to that criterion, the eddy viscosity coefficient was set equal to zero everywhere in a profile where its maximum tentatively computed value was less that 14 μ, where μ is the bulk viscosity, as provided by the Sutherland law. The Reynolds number in the four examined cases was equal to

$$Re = 8.61\times10^5 \text{ , for } \alpha_1 = 40 \text{ deg}$$
$$Re = 8.59\times10^5 \text{ , for } \alpha_1 = 43 \text{ deg}$$
$$Re = 8.41\times10^5 \text{ , for } \alpha_1 = 47 \text{ deg}$$
$$Re = 7.63\times10^5 \text{ , for } \alpha_1 = 52 \text{ deg}$$

Figures (2) and (3) present the calculated iso-Mach fields in the two cases which correspond to the minimum and maximum examined incidences. A common plotting increment dM=0.1 was used and it must be pointed out that in the i=-7 deg (α_1=40 deg) case, the flow is almost chocked, as may be seen from figure (2). It must be also kept in mind that figure (2) shows results from the k-ε model; the existence of a sonic line which almost closes the passage is more clear in the flow field calculated by the Baldwin-Lomax model (not shown). With the k-ε model, the maximum Mach number was 1.1 (α_1=40 deg), while the maximum Mach number in the i=+5 deg (α_1=52 deg) case was equal to 0.815 and a purely subsonic flow field was obtained.

Figure (4) illustrates the calculated isentropic Mach number distributions along the pressure and suction sides of the blade. Mach distributions using both turbulence models are presented and compared against experimental data. At least in three cases (α_1=40, 43 and 47 deg) which correspond to non-positive incidences, the Baldwin-Lomax model is in better agreement with measurements, especially in the suction side of the blade. For the design conditions (α_1=47 deg), this could be attributed to the fact that an extended laminar boundary layer at the first part of the suction surface does exist and this was better captured through the Baldwin-Lomax model, where the incorporated transition model allowed the exact formation of this laminar region.

In the positive incidence case (α_1=52 deg) the maximum velocity appears very close to the leading edge where the transition point is also located. According to the transition criterion incorporated in the Baldwin-Lomax model, only a very small laminar region of approximately 5% of the chord length is calculated. On the other hand, the k-ε model predicts a turbulent boundary layer which starts from the leading edge. Consequently, both models are predicting an almost identical distribution of the isentropic Mach number along the blade surface, with a slightly different behaviour at the last 20% of the suction side. In the α_1=40 deg and α_1=43 deg cases, the Baldwin-Lomax results are much closer to the experiments and correspond to higher Mach number peaks on the suction side. In the α_1=40 deg case, the negative incidence of the flow leads to an almost chocked field, especially as it is predicted by the Baldwin-Lomax model.

Cascade losses are put in the form of a total pressure loss coefficient defined as

$$\omega = \frac{p_{t1} - p_{t2}}{p_{t1} - p_1}$$

and are tabulated below

α_1(deg)	40	43	47	52
i	-7	-4	0	+5
ω(exp)	0.0466	0.0232	0.0186	0.0417
ω(k-ε)	0.045	0.0254	0.023	0.0419
ω(B.L.)	0.0370	0.0163	0.0131	0.0185

Table 1

The k-ε model predicts a loss level which is too close to the measured one and this prediction is even better in off-design conditions (see also figure 5b). The Baldwin-Lomax model underpredicts the cascade losses in all cases, but it has of course the correct qualitative behaviour versus the incidence (see figure 5a). By further examining the calculated flow fields, it may be seen that the predicted losses are almost exclusively profile losses which are not affected by the artificial dissipation scheme used to provide stability. The reduced losses predicted by the Baldwin-Lomax model can be attributed to the lower level of losses which occur in the rear half part of the suction side of the airfoil.

Figures (6a) and (6b) present the calculates exit flow angles for different inlet angles, using both models. The calculated exit flow angles are also included in Table 2

α_1(deg)	40	43	47	52
i	-7	-4	0	+5
α_2(exp)	21.5	20.2	20.2	22.8
α_2(k-ε)	22.2	21.4	21.7	23.6
α_2(B.L.)	21.5	20.2	20.2	22.3

Table 2

The Baldwin-Lomax model predicts accurately the exit flow angles, while with the k-ε model differences of approximately one degree between predictions and measurements exist.

CONCLUSIONS

A parametric investigation of an industrial axial flow compressor cascade by means of an explicit time-marching Navier-Stokes equations was carried out. Turbulence was modelled using the low-Reynolds version of the k-ε model. The Baldwin-Lomax was also used and the obtained results from both models are compared to the available measurements.

The k-ε model reproduces exactly the measured cascade loss coefficient, but underestimates the flow turning by approximately one degree. On the other hand, the Baldwin-Lomax model leads to lower losses along with a very accurate prediction of the exit flow angle. The differences in the prediction of the exit flow angle which exist between the two models are in full compatibility with the calculated isentropic Mach number distributions along the pressure

and the suction side of the blade. The Baldwin-Lomax model results, are affected by the incorporated transition criterion. With the original criterion proposed by Baldwin and Lomax, transition is predicted more downstream than expected, especially in off-design conditions and this influences the predicted cascade loss coefficient.

From a numerical point of view, the method presents certain advantages, like its simplicity and friendliness to the user. Thus, the presented method should be considered as a useful tool for the prediction of flow patterns and loss levels in compressor cascades.

REFERENCES

Abarbanel, S. and Gottlieb, D., 1981, "Optimal Time Splitting for Two- and Three-Dimensional Navier-Stokes Equations with Mixed Derivatives", Journal of Computational Physics 41.

Baldwin, W.S. and Lomax, H., 1978, "Thin-Layer Approximation and Algebraic Model for Separated Turbulent Flows", AIAA Paper 78-257.

Dejean, F., Vassilopoulos, C., Simandirakis G., Giannakoglou, K. and Papailiou, K.D., 1994, "Analysis of Transonic Turbomachinery Flows Using a 2-D Explicit Low-Reynolds k-ε Navier-Stokes Solver",ASME Paper 94-GT-63.

Giannakoglou, K., Simandirakis and G., Papailiou, K.D., 1991, "Turbine Cascade Calculations Through a Fractional Step Navier-Stokes Algorithm", ASME Paper 91-GT-55.

Jameson, A., Schmidt, W. and Turkel, E., 1981, "Numerical Solutions of the Euler Equations by Finite Volume Methods Using Runge-Kutta Time Stepping Schemes", AIAA Paper 81-1259.

Jones, W.P. and Launder, B.E., 1972, "The Prediction of Laminarization with a Two-Equation Model of Turbulence", Int. Journal Heat Mass Transfer, Vol. 15, pp. 301-314.

Laval, P., 1983, "Nouveaux Schémas de Désintégration pour la Résolution des Problèmes Hyperboliques et Paraboliques Non Linéaires: Application aux Equations d' Euler et de Navier-Stokes", Recherche Aérospatiale, No 4.

MacCormack, R.W., 1988, "On the Development of Efficient Algorithms for Three-Dimensional Fluid Flow", Recent Developments in Computational Fluid Dynamics, T.E. Tezchigar et al., ed., ASME AMD-Vol. 95, pp.117-138.

Simandirakis, G., 1992, "Numerical Solution of Navier-Stokes Equations for Transonic Flows Inside Turbine Bladings", PhD Thesis, NTUA, Athens, February 1992.

Sorenson, R.L., 1980, "A Computer Program to Generate Two-Dimensional Grids About Airfoils and Other Shapes by the Use of Poisson Equations", NASA TM/81198.

Steinert, W., Eisenberg, B. and Starken, H., 1990, "Design and Testing of a Controlled Diffusion Airfoil Cascade for Industrial Axial Flow Compressor Application", ASME Paper 90-GT-140.

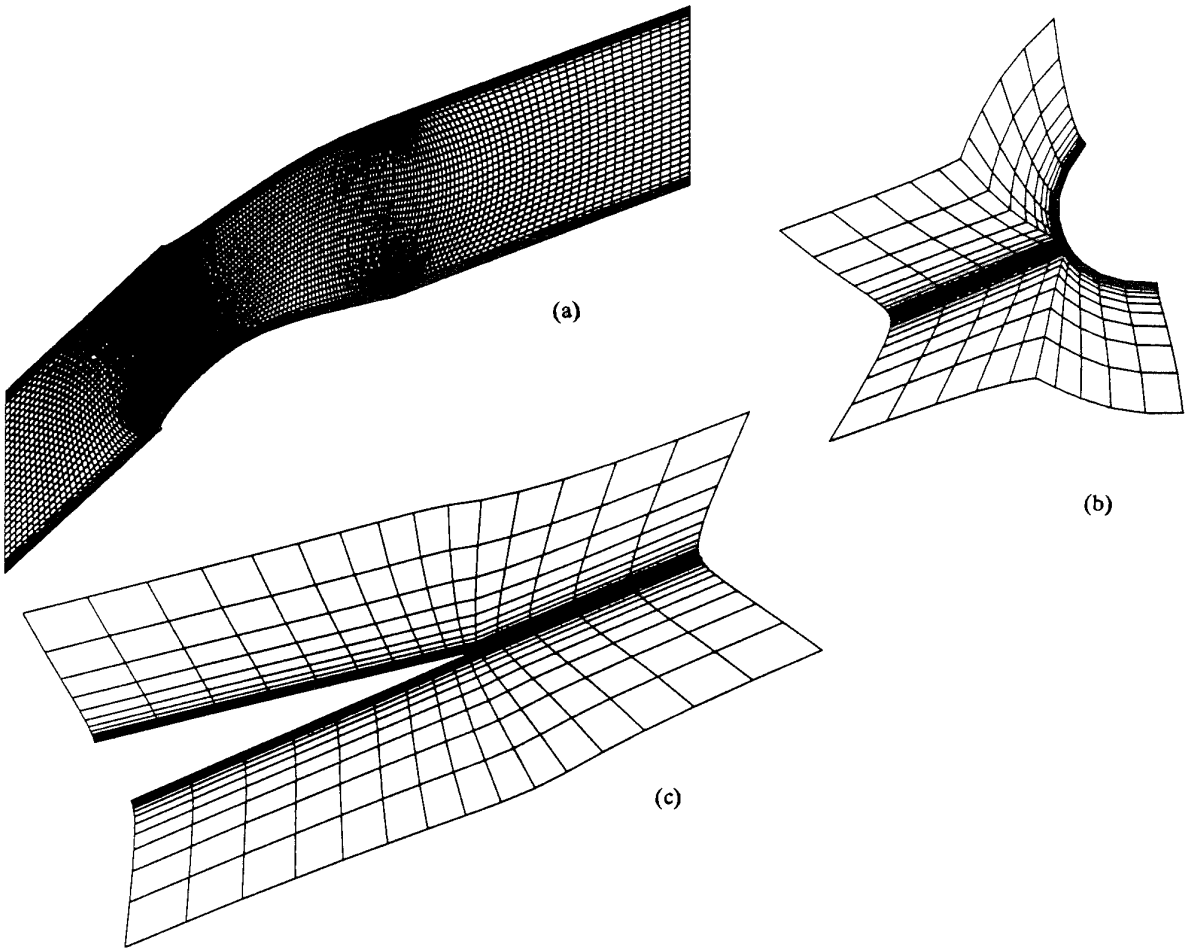

Figure 1: Computational Grid (a) the whole grid, (b) blow-up close to the leading edge and (c) blow-up close to the trailing edge.

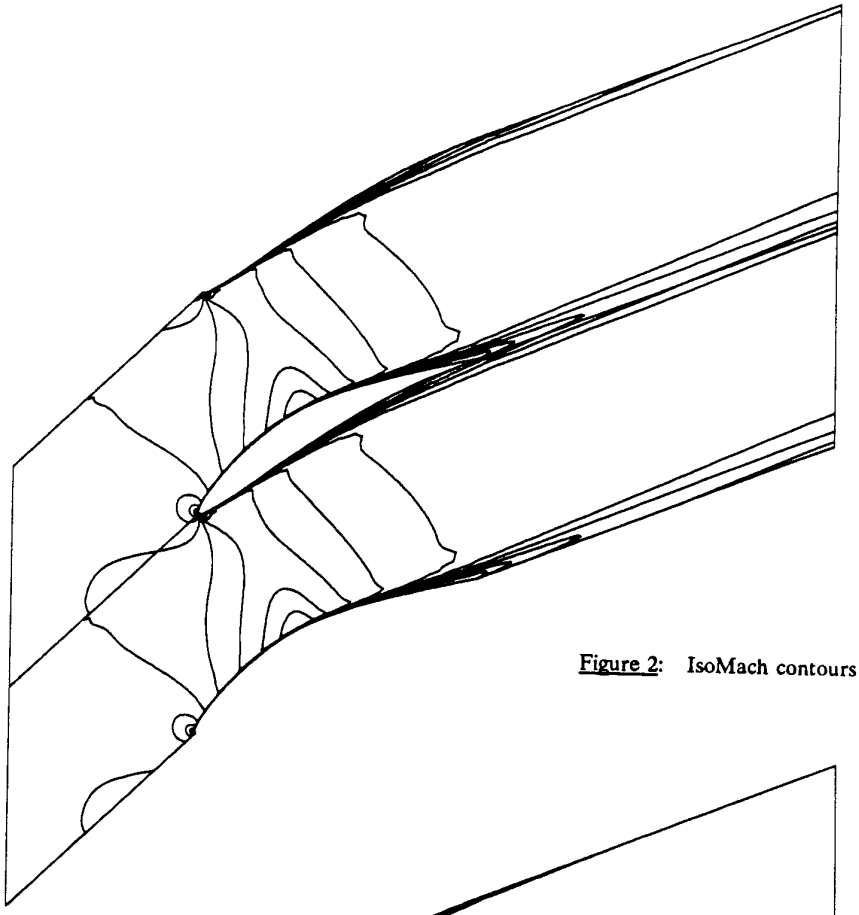

Figure 2: IsoMach contours ($\alpha_1 = 40$ deg).

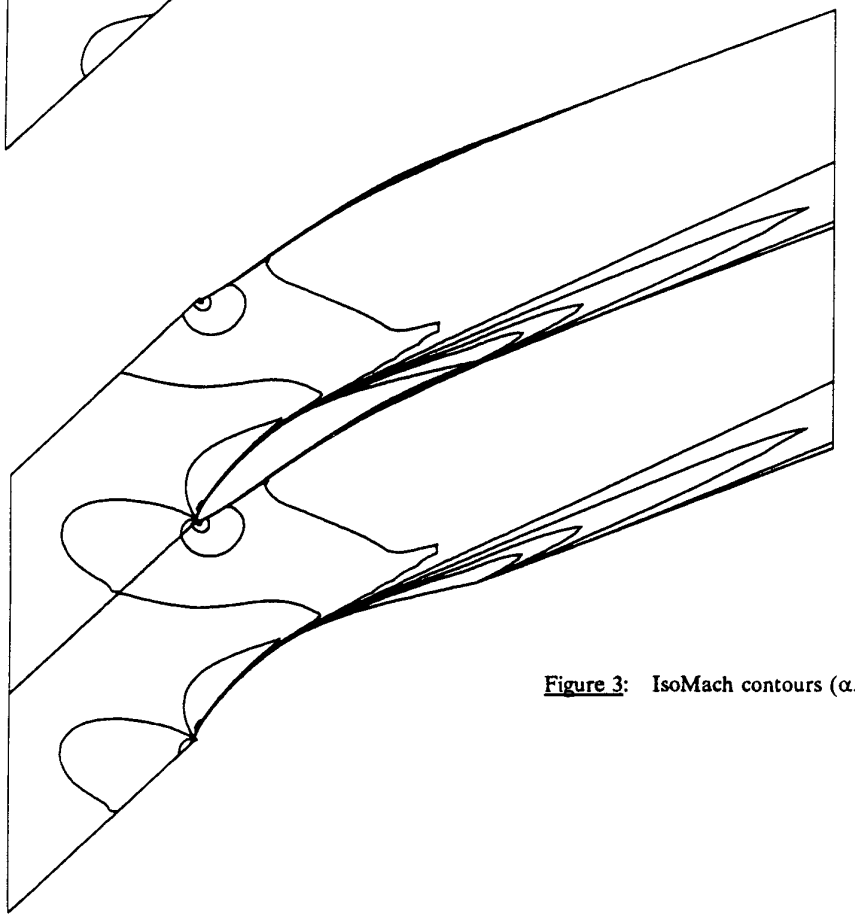

Figure 3: IsoMach contours ($\alpha_1 = 52$ deg).

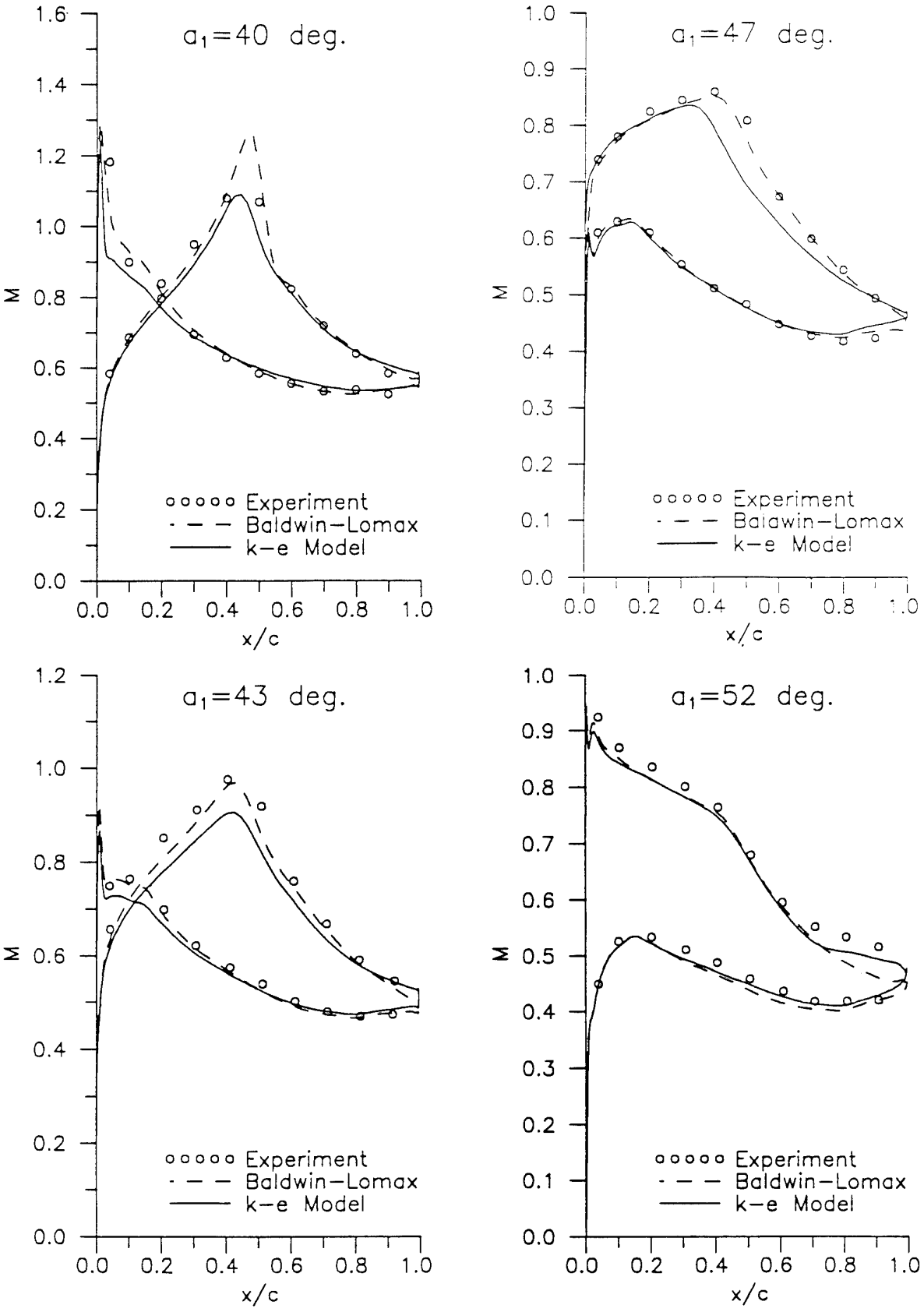

Figure 4: Isentropic Mach Distribution.

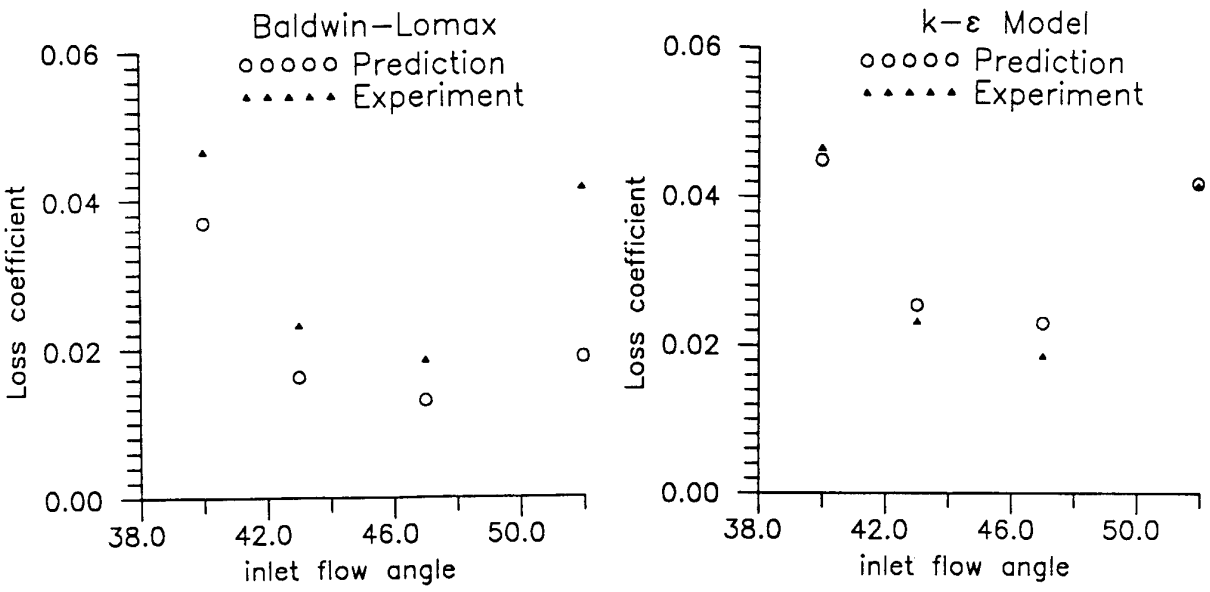

Figure 5: Loss coefficient versus inlet flow angle.

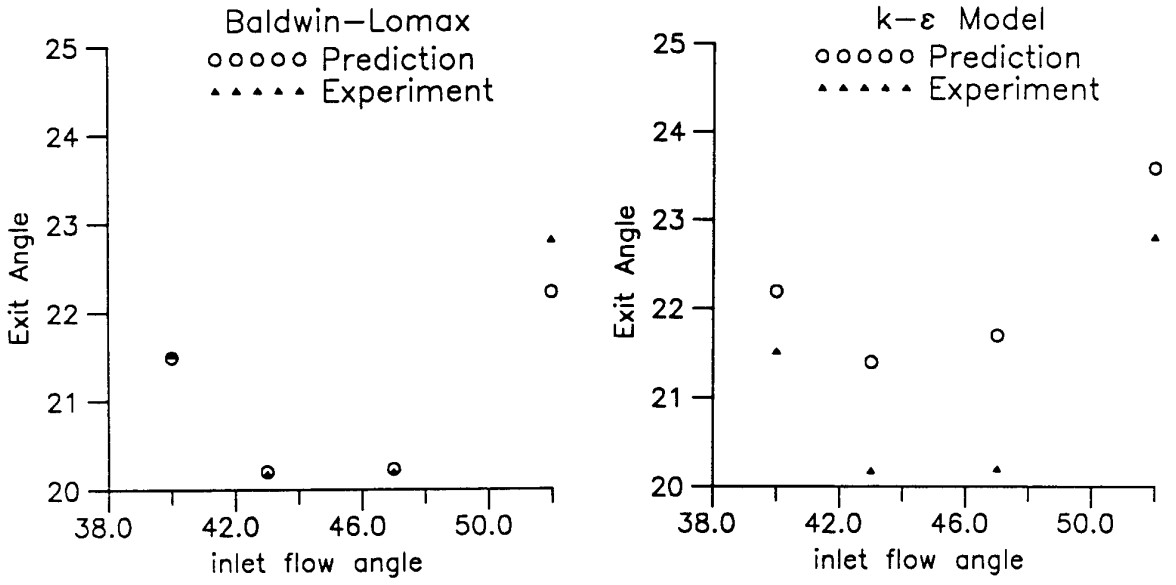

Figure 6: Exit flow angle versus inlet flow angle.

REFERENCE NO. OF THE PAPER: 2

DISCUSSOR'S NAME: H.A. Schreiber, DLR, Germany

AUTHOR'S NAME: C. Vassilopoulos, G. Simandirakis, K. Giannakoglou, K.D. Papailiou

Q: A comment concerning the flow angle accuracy of the experiments. The cascade tests have been run parallel to numerical blade calculations, and immediately compared to each other. Therefore the accuracy of the inlet flow angle should be half a degree or even better.

A: The authors were involved only in the numerical study of the cascade flow problems; inlet conditions were those provided in the cited reference describing the experiments.

REFERENCE NO. OF THE PAPER: 2

DISCUSSOR'S NAME: L.A. Povinelli, NASA, United States

AUTHOR'S NAME: C. Vassilopoulos, G. Simandirakis, K. Giannakoglou, K.D. Papailiou

Q: The evaluation of turbulence modeling effects need to be performed very carefully.
1) Was a grid dependency study carried out?
2) Were values of y+ less than 1 used?
3) What was the convergence behavior for your numerical code?

A: 1) Yes a grid dependency analysis has been carried out. Especially for the k-ε model, this analysis has shown that the correctness of the results is very sensitive to the distribution of grid lines within the boundary layer region. In order to obtain accurate results, it is recommended that approximately 30 grid points must be placed within the boundary layer. Misleading conclusions can be drawn if less grid nodes are used. Any further increase in grid nodes does not alter the quality of the results.
2) Yes, everywhere along the solid wall the non-dimnensional distance y+ was kept less than 1, since a low-Re k-ε model was used.
3) For a typical 2-D cascade problem, like those included in this paper, approximately 10,000 iterations are required for the covergence of all equations within 4-5 orders of magnitude (which is enough for engineering purposes). Convergence is always better in transonic cases than in subsonic ones. No important differences between the convergence behavior of the k-ε model and that of the Baldwin-Lomax model should be reported.

COMPUTATIONAL MODELLING OF CASCADE-BLADE FLOW WITH LINEAR AND NON-LINEAR LOW-RE EDDY-VISCOSITY MODELS

W.L. Chen
F.S. Lien
M.A. Leschziner
Department of Mechanical Engineering
University of Manchester Institute of Science and Technology, P.O. Box 88
Manchester, M60 1QD, UK

SUMMARY

A computational study is presented of the flow around a controlled-diffusion compressor-cascade blade at design as well as off-design conditions. In this flow, features associated with by-pass transition close to the leading edge - probably including laminar leading-edge separation - contribute significantly to the evolution of the boundary layer on the blade surface. This has motivated the additional investigation of transition in a number of flows which are highly pertinent to the principal blade flow: two flat-plate boundary layers, a flow over a curved blade-like bump in a channel, and a flow past a rounded leading edge involving laminar separation and transitional reattachment. It is demonstrated that conventional eddy-viscosity models, based on the linear Bousinesq stress--strain relations, are able to capture by-pass transition in simple shear, but are unable to resolve transitional features in complex strain, especially those associated with leading-edge separation, unless a mechanism is introduced to suppress excessive normal-strain-induced production of turbulence energy. The non-linear model is shown to return a considerably improved reperesentation of the blade flow, resolving the leading-edge processes and returning a much improved variation of the loss as a function of the inlet angle of incidence.

1 INTRODUCTION

Although the pressure distribution around turbomachine blades - and with it, the primary operational performance - are govered by inviscid processes, some influential flow characteristics and parameters are materially affected by turbulence transport and its manifestations. Examples are total pressure loss due to dissipation in the boundary layers and wakes, reduced static pressure recovery, enhancement of wall heat-transfer rate and the influence of wake mixing on transition and the boundary layer structure on rear-ward rotor or stator blades. Even in design conditions, the boundary layer developing on a blade can grow rapidly as a consequence of adverse pressure gradients, and this will induce losses as well as affect the pressure field in the passage. More seriously, in off-design or high-load conditions, the boundary layer may separate, in which case pressure recovery may collapse. The response of the boundary to the pressure gradient depends sensitively on transition which may be induced either by laminar leading-edge separation or diffusion of free-stream turbulence into the boundary layer triggering turbulence (so-called by-pass transition). It is evident, therefore, that a realistic representation of turbulence effects is an important contributor to the predictive capabilities of any numerical procedure for turbomachinery flows. The quality of this representation is the focus of the present paper.

In complex flow conditions in which shear, normal strain and curvature coexist, the minimum level of turbulence closure offering any prospect of generality is one which is based on transport equations for appropriate turbulence parameters. The simplest closure variants in this category are based on the eddy-viscosity concept, applied in conjunction with the linear stress-strain relations, and involving transport equations for the turbulence energy 'k' and its rate of dissipation 'ε'. This approach is relatively simple, numerically advantageous and can give a credible representation of turbulence effects in many flows. Yet, it is also known to suffer from a number of important weaknesses, including an insufficient sensitivity to curvature, grossly excessive generation of turbulence due to normal straining (especially close to stagnation points),

Paper presented at the AGARD PEP 85th Symposium on "Loss Mechanisms and Unsteady Flows in Turbomachines", held in Derby, United Kingdom, 8-12 May 1995, and published in CP-571.

an over-estimation of turbulence transport in boundary layers subjected to adverse pressure gradient, and an incorrect representation of by-pass transition, especially if this follows a region of complex strain. A fundamentally superior modelling strategy is *second-moment closure* which is based on the solution of transport equations for all Reynolds stresses. This is now being applied, with considerable advantage, to many complex 2D and even 3D flows (Leschziner [1,2], but is computationally demanding and thus rather unattractive for routine industrial applications. An intermediate route increasingly favoured as a compromise between the needs for simplicity and predictive realism is one in which the eddy-viscosity concept is retained, but in which the stresses are related to non-linear expansions of the strain and, in some model variants, vorticity components (Shih et al [3], Craft et al [4]). This approach aims to return, at least in some measure, the anisotropy of turbulence and its interaction with curvature, normal strain and swirl.

Amongst the many processes affecting the predictive capabilities of a turbulence model in the turbomachine environment, transition poses perhaps the biggest challenge. No model is capable of resolving natural transition, but some return, more or less correctly, the sensitivity of by-pass transition to free-stream turbulence, at least in simple boundary-layer flows (Savill [5]); it is the latter type of transition which is most pertinent to turbomachine aerodynamics, and this makes it imperative to identify those model variants which not only correctly predict the flow behaviour in fully turbulent conditions, but also return a credible representation transitional features.

In the present paper, computational solutions obtained with three low-Re two-equation models are reported for the controlled diffusion (CD) compressor cascade of Elazar & Shreeve [6]. Two models (Launder & Sharma [7] and Lien & Leschziner [8]) are linear, while the third (Craft et al [4]) involves cubic stress-strain/vorticity relations. It turns out that the resolution of transitional features close to the leading edge of the blade is an important issue in this flow. Therefore, special consideration is being given to the performance of the turbulence models in two additional test flows in which the prediction of transition is the principal objective.

2 TURBULENCE MODELS

Within the low-Re k-ε eddy-viscosity framework, the turbulent viscosity μ_t and transport equations of k and ε can be written, in general form, as follows:

$$\nu_T = c_\mu f_\mu \frac{k^2}{\tilde{\varepsilon}} \tag{1}$$

$$\frac{\partial u_i k}{\partial x_i} = \frac{\partial}{\partial x_i}\left[(\nu + \nu_T)\frac{\partial k}{\partial x_i}\right] + P_k - \varepsilon \tag{2}$$

$$\frac{\partial u_i \tilde{\varepsilon}}{\partial x_i} = \frac{\partial}{\partial x_i}\left[(\nu + \frac{\nu_T}{1.3})\frac{\partial \tilde{\varepsilon}}{\partial x_i}\right] + \frac{\tilde{\varepsilon}}{k}(C_{\varepsilon 1}P_k - C_{\varepsilon 2}\tilde{\varepsilon}) + E \tag{3}$$

where

$$P_k = c_\mu f_\mu \tilde{\varepsilon} S^2,\ S = \frac{k}{\tilde{\varepsilon}}\sqrt{0.5(\frac{\partial U_i}{\partial x_j} + \frac{\partial U_j}{\partial x_i})^2}\ , \tag{4}$$

$$\tilde{\varepsilon} = \varepsilon - D.$$

Three model variants are adopted in the present study. The first two involve the linear stress-strain relations:

$$\frac{\overline{u_i u_j}}{k} = \frac{2}{3}\delta_{ij} - \frac{\nu_t}{k} S_{ij} \tag{5}$$

in conjunction with the following terms:

- The Launder & Sharma model [7]:

$$c_\mu = 0.09$$

$$f_\mu = \frac{-3.4}{(1 + \tilde{R}_t/50)^2},\quad D = 2\nu(\partial\sqrt{k}/\partial x_i)^2, \tag{6}$$

$$E = 2\nu\nu_T(\frac{\partial^2 U_i}{\partial x_j \partial x_k})$$

$$C_{\varepsilon 1} = 1.44,\quad C_{\varepsilon 2} = 1.92[1 - 0.3\exp(-\tilde{R}_t^2)]$$

• The Lien & Leschziner model [8]:

$$c_\mu = 0.09$$

$$f_\mu = \frac{1-\exp(-0.016y^*)}{1-\exp(-0.263y^*)}, \quad D = 0, \quad E = 0. \qquad (7)$$

$$C_{\varepsilon 1} = 1.44(1+\frac{P'_k}{P_k}),$$

$$C_{\varepsilon 2} = 1.92[1-0.3\exp(-\tilde{R}_t^2)]$$

where $y^* = y\sqrt{k}/\nu$, $\tilde{R}_t = k^2/\nu\tilde{\varepsilon}$ and

$$P'_k = \frac{0.544[1-0.3\exp(-\tilde{R}_t^2)]k^{3/2}}{y[1-\exp(-0.236y^*)]\exp(-0.00222y^{*2})} \qquad (8)$$

The third model, by Craft et al [9], adopts a cubic relationship between stresses and strain/vorticity components:

$$\begin{aligned}\frac{\overline{u_iu_j}}{k} &= \frac{2}{3}\delta_{ij} - \frac{\nu_t}{k}S_{ij} \\ &-0.1\frac{\nu_t}{\tilde{\varepsilon}}(S_{ik}S_{kj} - \frac{1}{3}S_{kl}S_{kl}\delta_{ij}) \\ &+0.1\frac{\nu_t}{\tilde{\varepsilon}}(\Omega_{ik}S_{kj} + \Omega_{jk}S_{ki}) \\ &+0.26\frac{\nu_t}{\tilde{\varepsilon}}(\Omega_{ik}\Omega_{jk} - \frac{1}{3}\Omega_{ik}\Omega_{ik}\delta_{ij}) \\ &-10c_\mu^2\frac{\nu_t}{\tilde{\varepsilon}^2}\frac{k}{\tilde{\varepsilon}^2}(S_{ki}\Omega_{lj} + S_{kj}\Omega_{li} - \frac{2}{3}S_{km}\Omega_{lm}\delta_{ij})S_{kl} \\ &-5c_\mu^2\frac{\nu_t}{\tilde{\varepsilon}^2}\frac{k}{\tilde{\varepsilon}^2}S_{ij}S_{kl}S_{kl} + 5c_\mu^2\frac{\nu_t}{\tilde{\varepsilon}^2}\frac{k}{\tilde{\varepsilon}^2}S_{ij}\Omega_{kl}\Omega_{kl}\end{aligned} \qquad (9)$$

where

$$S_{ij} \equiv \frac{\partial U_i}{\partial x_j} + \frac{\partial U_j}{\partial x_i}, \quad \Omega_{ij} \equiv \frac{\partial U_i}{\partial x_j} - \frac{\partial U_j}{\partial x_i}$$

$$c_\mu(\tilde{S},\tilde{\Omega}) = \frac{0.3[1-\exp\{\frac{-0.36}{\exp[-0.75\max(\tilde{S},\tilde{\Omega})]}\}]}{1+0.35\{\max(\tilde{S},\tilde{\Omega})\}^{1.5}} \qquad (10)$$

$$f_\mu = 1-\exp\{-(\frac{\tilde{R}_t}{90})^{\frac{1}{2}} - (\frac{\tilde{R}_t}{400})^2\}$$

$$E = 0.0022\frac{\tilde{S}\nu_t k^2}{\tilde{\varepsilon}}(\frac{\partial^2 U_i}{\partial x_k \partial x_l})^2, \tilde{R}_t \le 250$$

$$D = 2\nu\,(\partial\sqrt{k}/\partial x_i)^2$$

$$C_{\varepsilon 1} = 1.44, \quad C_{\varepsilon 2} = 1.92[1-0.3\exp(-\tilde{R}_t^2)]$$

$$\tilde{\Omega} = \frac{k}{\tilde{\varepsilon}}\sqrt{0.5\Omega_{ij}^2}$$

The Launder-Sharma model is well established and generally held to be among the best of the conventional low-Re k-ε variants, especially in respect of capturing relaminarisation and by-pass transition. The Lien-Leschziner model has been formulated so as to adhere, very close to the wall, to the turbulent length-scale prescribed by the one-equation model of Wolfshtein [9], the objectives being to improve performance in adverse pressure gradients, to increase numerical stability and to reduce the grid density required in the semi-viscous sublayer. The cubic model has arisen from a related Reynolds-stress-transport closure, and it allows effects arising from curvature, normal strain and swirl to be captured. This is a new model which has not previously been applied to the type of geometries considered herein.

3 NUMERICAL APPROACH

Calculations have been performed with the general non-orthogonal fully collocated finite-volume approach 'STREAM' (Lien & Leschziner [10]). Single- and multi-block versions are available (Chen et al [11]), and both have been used herein to identify any dependence of the solution to grid disposition, in particular skewness at the leading and trailing edges. Convection is represented by the quadratic 'QUICK' scheme (Leonard [12]) and by the second-order TVD approximation 'UMIST' (Lien & Leschziner [13]). Any solution is iterated to convergence using a pressure-correction approach, which is applicable to both incompressible and compressible conditions, the latter including shocks. Versions of the procedure apply to 2D and 3D conditions and embody a variety of turbulence closures, including a non-linear 'RNG' k-ε model and second-moment

closure (Lien & Leschziner [14]).

4 RESULTS and DISCUSSION

Because of the importance of transition to the prediction of the flow around the highly-loaded CD compressor blade of Elazar & Shreeve [6], which is the main focus of this paper, calculations have been performed first for several test flows specifically designed to yield a data-base for validating the performance of turbulence models in transitional conditions. These test cases, ranging from a flat-plate boundary layer in zero pressure-gradient to the flow past a rounded leading edge with laminar separation and reattachment transition, have been examined experimentally at the laboratories of Rolls Royce Aeroengines in Derby, UK, and feature in an extensive collaborative validation exercise coordinated by Savill [5] under the ERCOFTAC umbrella.

The first case examined is a transitional flow over a flat plate with a sharp leading-edge - referred to as **Case T3A** - in which the free-stream turbulence intensity, Tu, is 3%, while the dissipation length scale, L_ε, is 10 mm. The calculation domain has been extended upstream of the leading edge, and elliptic pressure effects at the leading edge as well as at the transition locations (the latter arising from a jump in displacement thickness) are fully accounted for. Results obtained for the skin friction with Launder & Sharma's and Craft et al's models over a 157x52 grid are shown in Figure 1. Both models yield a similar representation of the transition process, with the non-linear model returning a somewhat superior transition position but producing an overshoot following the transition process. A similar behaviour is observed in the more challenging case of higher free-stream turbulence intensity (Tu=6%) (with L_ε=30 mm) - referred to as **Case T3B** - as is conveyed by Figure 2. While there are insignificant differences between the velocity fields returned by the two models - both agree closely with experimental data - reference to the turbulence-intensity profiles given in Figure 3 for **Case T3B** appears to show that the non-linear model yields better agreement with the measured data, especially close to the wall. It must be noted, however, that the Launder-Sharma model is inherently unable to account for anisotropy so that it is bound to underestimate the streamwise normal stress. Figure 3 thus demonstrates, principally, that the non-linear model resolves anisotropy and returns an elevated stream-wise normal stress values. It is appropriate to remark here that this type of transition calculation is extremely sensitive to a whole host of computational issues, among them the type of solution method (parabolic or elliptic), the starting position of the calculation (at the leading edge or upstream of it), the grid density, and the order of approximation adopted for mean as well as turbulence convection.

The third preliminary test case - referred to as **Case T3C** - is the transitional flow over a arched bump in a channel (Figure 4). Experimental results are here available for 5 flow conditions, in terms of free-stream turbulence parameters and Reynolds number. Results for skin friction in one case, T3C1, are shown in Figure 5. Here again, the non-linear model returns later transition, but clearly, the improvement relative to the linear model is modest, which highlights the formidable challenge of capturing transition in complex conditions.

An especially interesting case is the flow past the rounded leading edge of a flat plate, shown in Figure 6 together with part of the 293x81 grid used for its computation. Results for this case have been obtained with the Lien-Leschziner model and with a variant of that same model but with the strain S^2 in the turbulence production term P_k (equation 4) replaced by:

$$S^2 \leftarrow S\,[\alpha S + (1-\alpha)\Omega]; \quad \alpha=0.15 \qquad (11)$$

This replacement follows a suggestion by Kato and Launder [15] and has the benefit of substantially reducing the entirely unphysical high level of turbulence energy production at the stagnation region, which leads to immediate transition, in contrast to actual transition occurring as a consequence of laminar leading-edge separation. Figure 7 compares contours of turbulence energy arising with and without modification (11) above, and the velocity profiles in Figure 8 demonstrate that a suppression of turbulence production at the leading edge is crucially important if the laminar leading-edge separation is to be resolved. No non-linear model results are available at the time of writing.

The principal test case in this study is the flow past a CD compressor cascade examined experimentally by Elazar & Shreeve [6]. The blade and the four-block mesh, containing 13100 nodes, is shown in Figure 9, with the leading- and trailing-edge regions magnified. Computations have been performed for various incidence angles ranging from 25°-46°.

Of greatest interest to the designer in the variation of the loss coefficient as a function of incidence, and this is shown in Figure 10. As seen, different models return significantly different loss levels, especially in off-design conditions. The origin of this behaviour is revealed upon reference to Figure 11 which shows variations of boundary-layer thickness, displacement thickness and momentum thickness along both the suction and pressure sides at an incidence angle of 46° - the most challenging operational condition. It is noted, as an aside, that the determination of the boundary-layer thickness, δ, which is the limit of the integrals involved in determining the boundary-layer parameters is not trivial for a curved surface. Here, the approach proposed by Stock & Haase [16] has been adopted. This assumes $\delta=1.93\ y_{max}$, with y_{max} corresponding to the wall-normal distance where $y|\partial u/\partial y|$ reaches its maximum. As seen from Figure 11, the crucial issue is the response of the performance of the turbulence models during the initial development phase of the boundary layer over the suction side. Evidently, the leading-edge boundary is either separated or almost separated, probably due to a laminar or transitional state of flow. The linear model entirely fails to resolve this feature, while the non-linear model responds much more sensitively, predicting a much more rapid thickening of the boundary layer at the leading edge and hence higher losses in the fully turbulent state.

Consistent with the above is the behaviour of the pressure distribution along the suction side, shown in Figure 12. The tendency towards separation at the leading edge is accompanied by a more gentle increase in pressure in this region. Moreover, the pressure plateau on the suction-side base is captured, suggesting a tendency towards stall as the trailing edge is approached.

The predicted boundary-layer structure is conveyed in Figures 13 and 14 which show, respectively, selected profiles of velocity and turbulence energy in the suction-side boundary layer. Clearly, none of the models returns an entirely satisfactory flow structure, but it is recognised that the non-linear model gives a better representation at the leading edge flow and a much thicker boundary layer further downstream. The very different behaviour returned by the models is rooted, principally, in large difference in the turbulence levels in different parts of the boundary layer. The non-linear variant tends to initially seriously under-predict the turbulence activity in the outer part of the boundary layers - a behaviour also observed in other transition test cases considered earlier. This defect favours a rapid thickening of the leading-edge boundary layer which is subjected to the strongly adverse pressure gradient. Once the boundary layer has been displaced, turbulence transport is excessively elevated in the central boundary-layer region, which enhances inflexion and steers the lower part of the boundary towards stall.

Results at other incidence angles (40° and 43.4°) are broadly consistent with those given above, though at the design condition of 40° differences between the models are fairly small. This is exemplified by the suction-side velocity profiles finally shown in Figure 15.

5. CONCLUSIONS

The paper investigated the flow around a cascade blade and several related flows in which by-pass transition plays an important role in the mix of processes that turbulence models must resolve. The test calculations permit the following conclusions to be drawn:

- A satisfactory prediction of highly-loaded turbomachine blades depends both on the quality with which the turbulence model represents the fully turbulent boundary layer, especially its response to adverse pressure gradient, and on its ability to resolve transitional features at the leading edge.

- Turbulence models of the eddy-viscosity type are capable, in principle, of resolving by-pass transition in relatively simple boundary-layer flows. Of the models

examined, the non-linear variant returned the best performance, although significant differences between calculations and experiments remain.

- In the case of impingement preceding the formation of the boundary-layer, as arising in a rounded or blunt leading edge, no conventional eddy-viscosity model is able to predict laminar leading-edge separation because of excessive normal-strain induced generation of turbulence energy.

- In order to overcome this deficiency, it is essential to depress the turbulence energy in the vicinity of leading edge. This has been achieved here by using a modification in the turbulence production term. Whether the non-linear eddy-viscosity model or second-moment closure are able to return the correct response is currently under investigation.

- In design conditions, all models return similar levels of predictive realism. In off-design conditions, however, the linear models fail. In contrast, the non-linear variant captures the leading-edge flow, predicts the rapid thickening of the boundary layer in this region, as well as the tendency of the base flow towards stall, and returns a credible variation of the loss with the inlet-flow incidence angle.

- Multi-block grids are advantageous in resolving blade flows, for they allow a combination of O- and H-type grids to be used, with consequent reduction in grid skewness at the leading and trailing edges and, hence, improved accuracy.

ACKNOWLEDGEMENTS

Part of the work documented herein was supported by Rolls Royce (Aeroengines) plc, Derby, and the UK Defence Research Agency (DRA). The authors are grateful for this support.

REFERENCES

1. Leschziner, M.A., (1990), "Modelling Engineering Flows with Reynolds-Stress Turbulence Closure", J. Wind Eng. Ind. Aerodyn., Vol. 35, pp. 21-47.

2. Leschziner, M.A., (1994), "Computation of Aerodynamic Flows with Turbulence-Transport Models Based on Second-Moment Closure", to appear in Computers and Fluids.

3. Shih, T.H., Zhu, J. and Lumley, J.L., (1993), "A Realisable Reynolds Stress Algebraic Equation Model", NASA TM-105993.

4. Craft, T.J., Launder, B.E. and Suga, K., (1993), "Extending the Applicability of Eddy Viscosity Models Through the Use of Deformation Invariants and Non-Linear Elements", Proc. 5th Int. Symp. on Refined Flow Modelling and Turbulence Measurements, Paris, p. 125.

5. Savill, A.M. (1993, ed.), "Further Progress in the Turbulence Modelling of By-Pass Transition", in Engineering Turbulence Modelling and Experiments 2 (eds. W. Rodi & F. Martelli) Elsevier, pp. 583.

6. Elazar, Y. and Shreeve, R.P. (1989), "Viscous Flow in Controlled Diffusion Compressor Cascade With Increasing Incidence", ASME Paper 89-GT-131.

7. Launder, B.E. and Sharma, B.I. (1974), "Application of the Energy-Dissipation Model of Turbulence to the Calculation of Flow Near a Spinning Disc", Letters in Heat and Mass Transfer, Vol. 1, p. 131.

8. Lien, F.S. and Leschziner, M.A. (1993a), "Computational Modelling of 3D Turbulent Flow in S-Diffuser and Transition Ducts", Engineering Turbulence Modelling and Experiments 2 (W. Rodi and F. Martelli, ed.),p. 217.

9. Wolfshtein, M.W., (1969), "The Velocity and Temperature Distribution in One-Dimensional Flow with Turbulence Augmentation and Pressure Gradient", Int. J. Heat Mass Transfer, Vol. 12, p. 301.

10. Lien, F.S. and Leschziner, M.A. (1993b), "A General Non-Orthogonal Finite-Volume Algorithm for Turbulent Flow at All Speeds Incorporating Second-Moment Closure, Part

1: Numerical Implementation and Part 2: Application", Comp. Meth. Appl. Mech. Eng., Vol. 114, p. 123 and p. 149.

11. Chen, W.L., Lien, F.S. and Leschziner, M.A. (1994), "Multi-Block Algorithm for General Turbulent Flows", 6th Biennial Colloquium on CFD, Dept. of Mech. Engrg., UMIST.

12. Leonard, B.P. (1979), "A Stable and Accurate Convective Modelling Procedure Based on Quadratic Upstream Interpolation", Comp. Meth. Appl. Mech. Eng., Vol. 19, p. 59.

13. Lien, F.S. and Leschziner, M.A. (1994), "Upstream Monotonic Interpolation for Scalar Transport With Application to Complex Turbulent Flows", Int. J. Num. Meths. in Fluids, Vol. 19, pp. 527-548.

14. Lien, F.S. and Leschziner, M.A. (1994), "Assessment of Turbulence-Transport Models Including Non-Linear RNG Eddy-Viscosity Formulation and Second-Moment Closure for Flow Over a Backward-Facing Step", Computers Fluids, Vol. 23, No. 8, pp. 983-1004.

15. Kato, M. and Launder, B.E. (1993), "The Modelling of Turbulent Flow Around Stationary and Vibrating Square Cylinders", Proc. 9th Symp. Turbulent Shear Flows, Kyoto, p. 10-4.

16. Stock, H.W. and Haase, W. (1989), "Determination of Length Scales in Algebraic Turbulence Models for Navier-Stokes Methods. AIAA J., Vol. 27, No. 1, pp. 5-14.

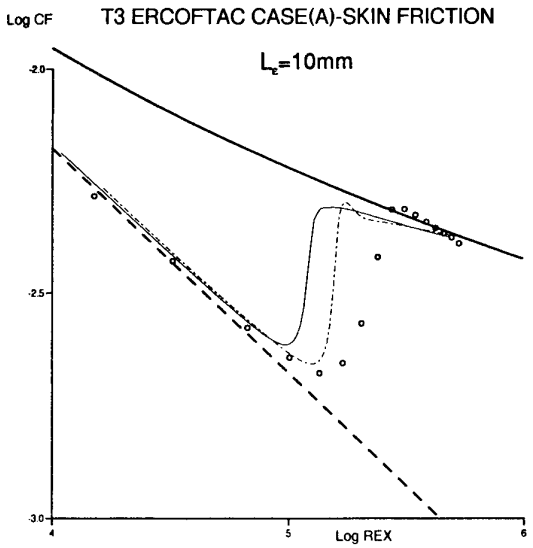

Figure 1. Case T3A: skin friction

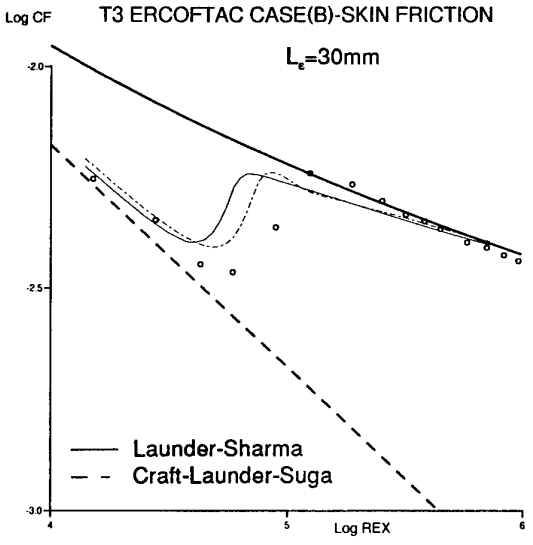

Figure 2. Case T3B: skin friction

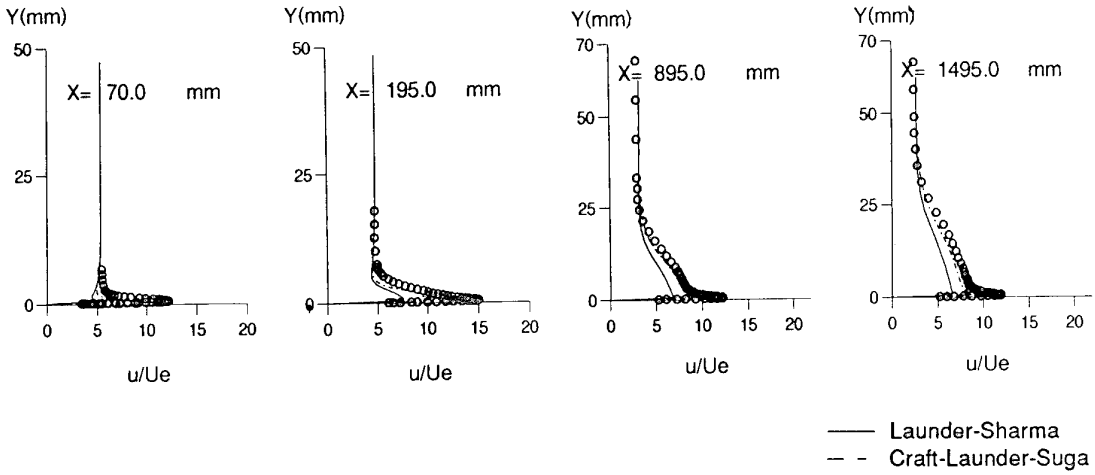

Figure 3. Case T3B: streamwise turbulence intensity

Figure 4. Case T3C: geometry and grid (220x102)

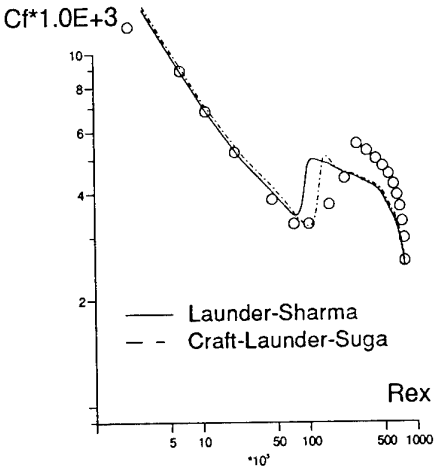

Figure 5. Case T3C1: skin friction

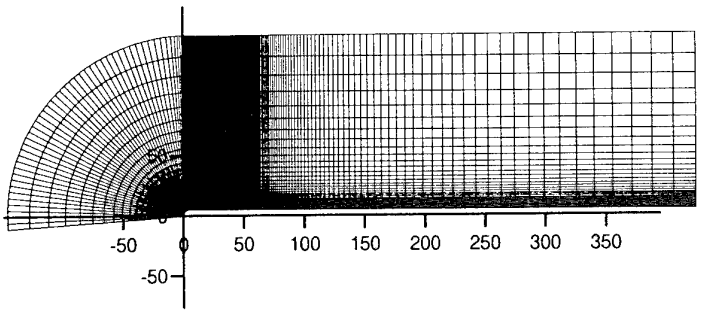

Figure 6. Case T3L: geometry and grid (293x81)

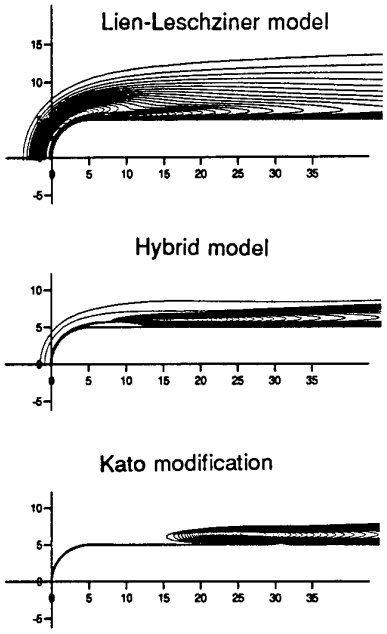

Figure 7. Case T3L: turbulence intensity contours

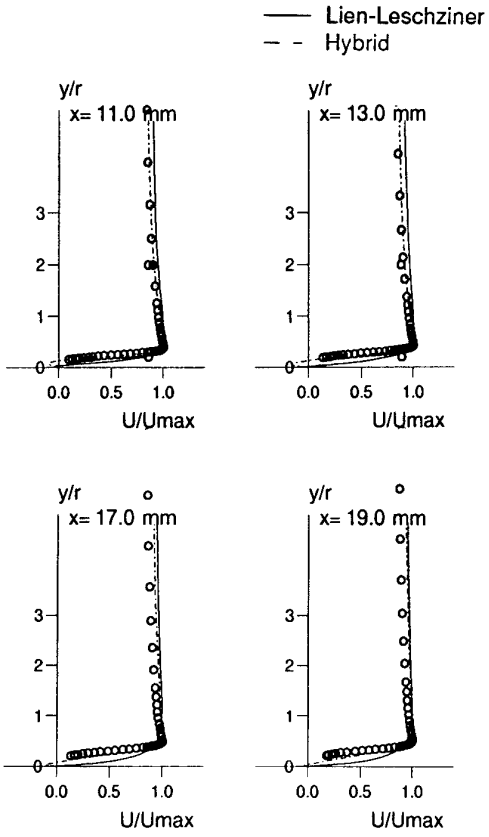

Figure 8. Case T3L: velocity profiles

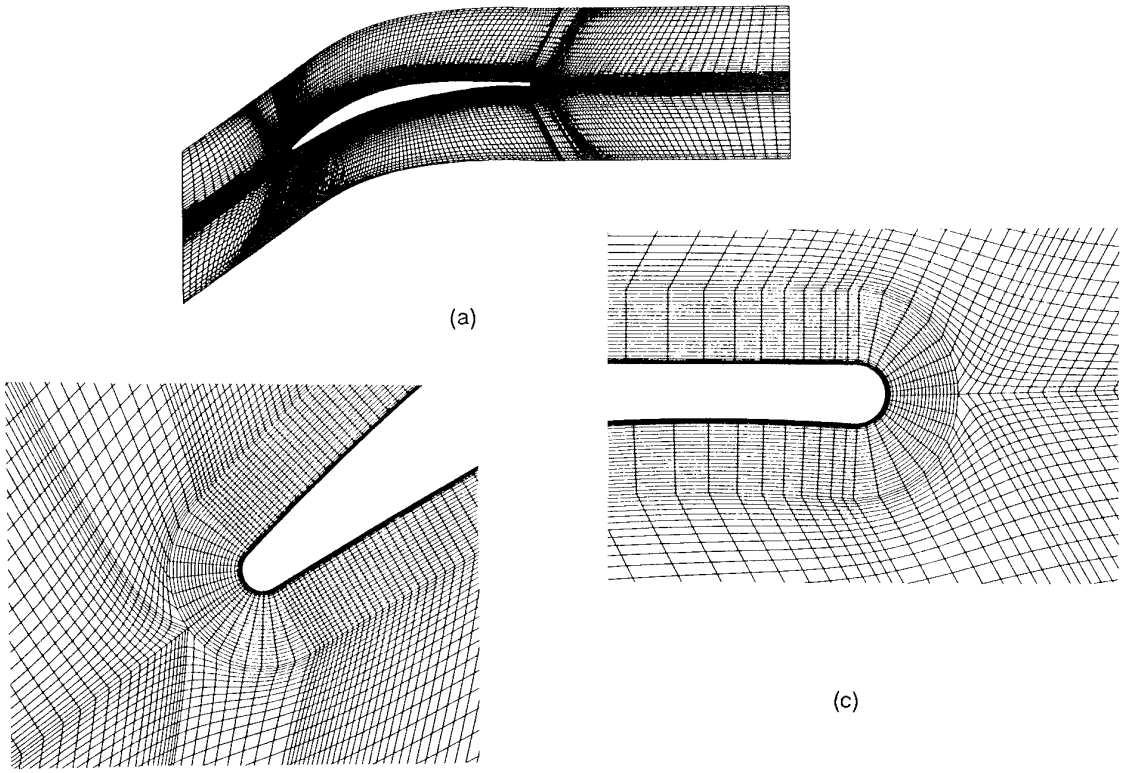

Figure 9. CD compressor blade: multi-block mesh;
(a) overall mesh, (b) leading-edge, (c) trailing-edge

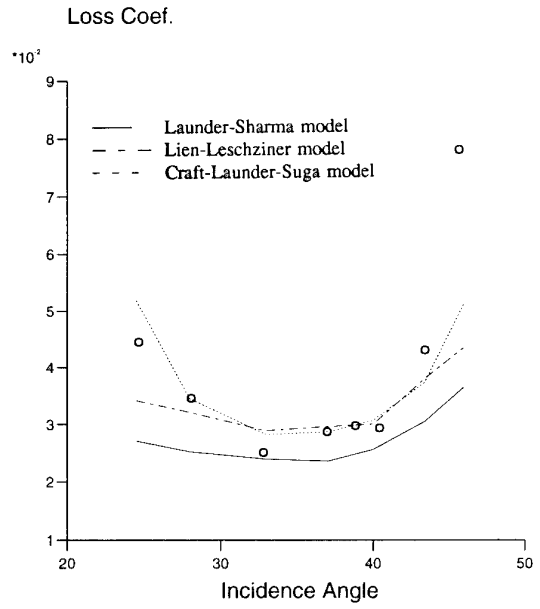

Figure 10. CD compressor blade: loss-coefficient distributions

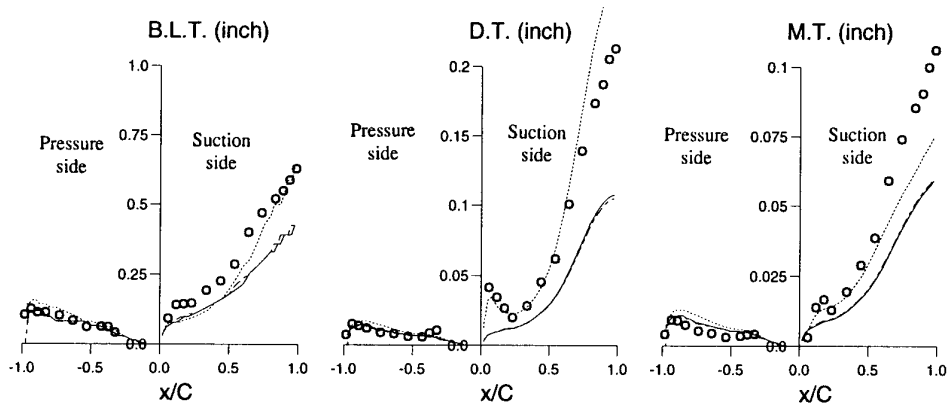

Figure 11. CD compressor blade: boundary-layer-, displacement- and momentum-thickness-distributions;

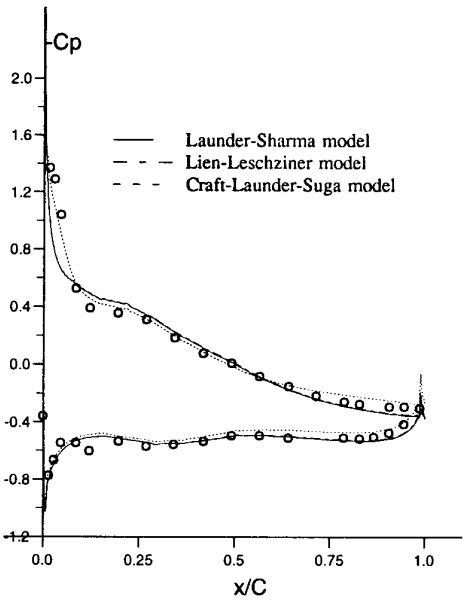

Figure 12. CD compressor blade: pressure distributions

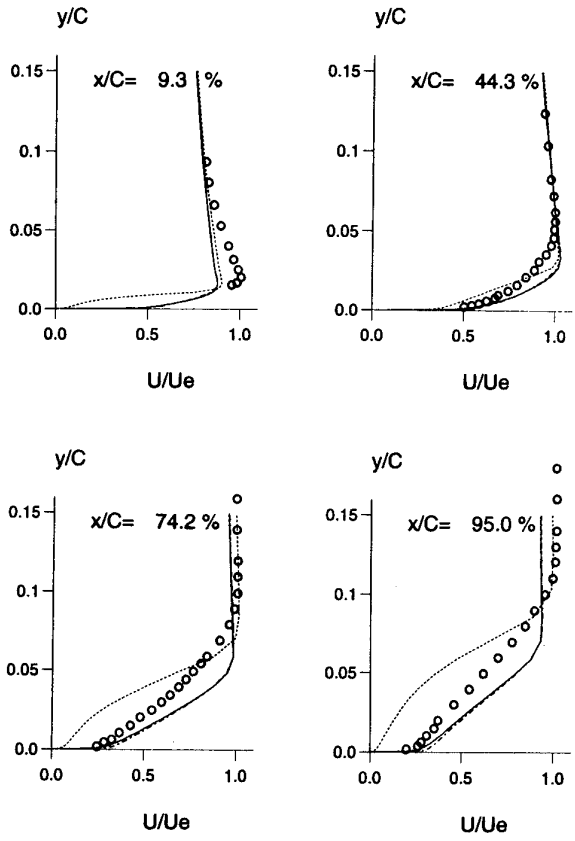

Figure 13. CD compressor blade: streamwise-velocity profiles on suction-side, β=46°

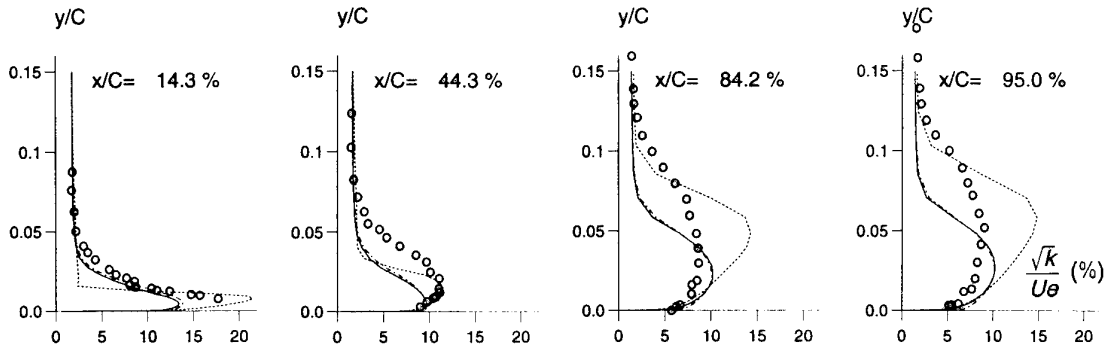

Figure 14. CD compressor blade: turbulence-intensity profiles on suction-side, β=46°

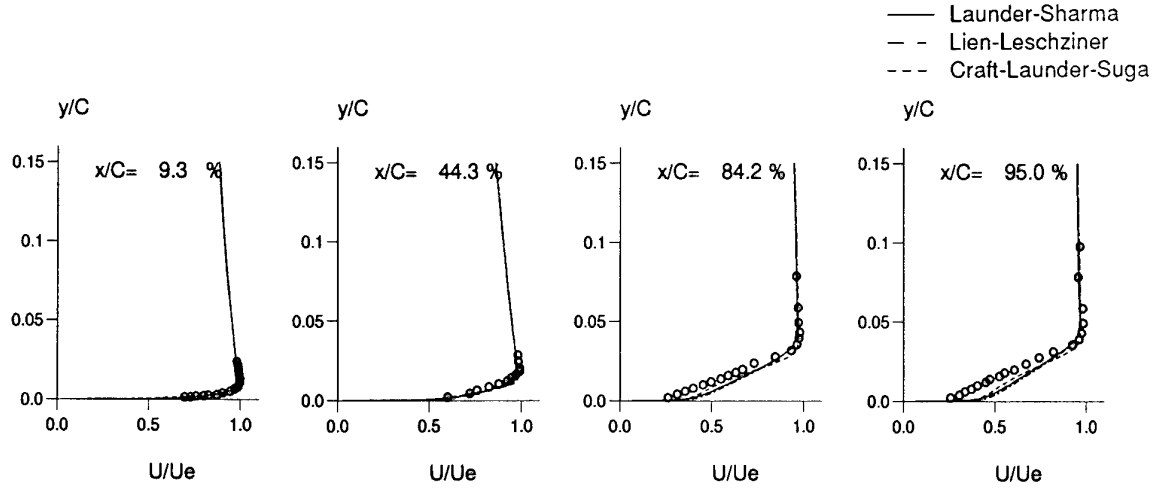

Figure 15. CD compressor blade: streamwise-velocity profiles on suction-side, β=40°

REFERENCE NO. OF THE PAPER: 3

DISCUSSOR'S NAME: J-F. Chevalier, SNECMA, France

AUTHOR'S NAME: M.A. Leschziner

Q: You have shown an excessive level of sensitivity to adverse pressure gradient. Are you confident that the experimental conditions are two-dimensional?

A: The degree of two-dimensionality is usually measured by the ratio of mean axial velocity at exit (based on the mid-span profile) to mean velocity at inlet. In the experiment, this was 1.05. So the flow was not far from a 2D state, and numerical experiments with a quasi-3D treatment (2D plus bulk correction) showed no significant differences to the 2D calculations. Of course, our calculations could not take into account any effects arising from traverse circulation and associated momentum redistribution. It is accepted, however, that the experiments are close to 2D.

REFERENCE NO. OF THE PAPER: 3

DISCUSSOR'S NAME: F. Eulitz, DLR, Germany

AUTHOR'S NAME: M.A. Leschziner

Q:1 You mentioned that higher-order turbulence modelling is computationally costly. What is the extra computation time of a non-linear model application when compared to an algebraic model, e.g. Baldwin-Lomax?

A:1 We have no experience with zero-equation models of the Baldwin-Lomax type. The non-linear model uses non-linear stress-strain relationships and evaluates the eddy viscosity from the k and ε transport equations. The additional effort relative to the linear (Boussinesq viscosity) k-ε model is negligible.

Q:2 The boundary layer traverses you have shown of the compressor blade indicate a fine grid. What was the average y+ value?

A:2 The average minimum y+ value close to the wall was between 0.1 and 0.5.

Q:3 What is the Reynolds number?

A:3 The Reynolds number, based on chord, was 7×10^5.

BOUNDARY LAYER AND LOSS STUDIES ON HIGHLY LOADED TURBINE CASCADE

A. Smolny, J. Blaszczak
Institute of Turbomachinery
Technical University of Lodz
90240 Lodz
POLAND

Summary

The test results of a boundary layer developing on the suction side of the highly loaded turbine vane are presented. The tests of the boundary layer development were performed with hot film transducers deposited on a polyimide foil and glued to the profile wall. Special attention was paid to a formation of a separation region. Total pressure losses with regard to the boundary layer condition on the suction side of the profile were determined.

Nomenklature

b	blade axial chord
c	chord length
C_p	pressure coefficient
e	unsteady a-c thin-film signal
E	time averaged thin-film signal
Eo	time averaged thin-film signal, no flow
p	local static pressure
p_t	stagnation pressure
Re	Reynolds number
S	surface coordinate from trailing edge
S_c	circumference of the vane
t	blade pitch
ξ	total pressure loss coefficient
x,y,z	coordinate system

Introduction

The efficiency of an advanced turbine is considerably affected by the aerodynamic characteristics of the turbo components. However, flow investigations in turbomachinery are usually carried out only at the inlet and outlet of a given flow duct. The investigations inside the flow duct are very difficult to perform or - most often - even impossible. Particularly, a reduction in the solidity of turbine blading leads to an increase in the load of turbine blading without detriment to its performance. Obtaining high efficiency in this case depends mainly on the behaviour of the boundary layer on the suction side of the vane.
This layer develops in conditions similar to the extreme ones. In such conditions, a separation of the boundary layer and its reattachment can occur. A mutual arrangement of a laminar, a transitional, with separation and reattachment and a turbulent flow regions influences greatly the total pressure losses. The increase in the turbine performance can be achieved if the data concerning the locations of these regions are known.

Investigations of the behaviour of the boundary layer from the leading edge to the trailing edge, especially in the leading edge region, are very difficult and sometimes even impossible with traditional measurement techniques. A changing thickness of the boundary layer and a curvature of vane profiles makes it impossible to apply ordinary measurement probes because of their insufficient spatial resolution and high level of blockage. An investigation of the development of the boundary layer and flow structures connected with it can be performed by means of special measurement methods, in which hot film sensors deposited on a polyimide foil and glued to the wall are applied. The development and conditions of the boundary layer are determined on the basis of an analysis of the output signals generated by sensors connected to a constant temperature anemometer (CTA) [3], [5], [6]. Dynamic properties of the sensors are very good, their frequency response limit is in the range 15 - 20 kHz [3]. Thus, an unsteady character of the flow in the boundary layer can be taken into account during the measurements.
The aim of this investigation was to analyse a development of the boundary layer on the suction side of the highly loaded turbine vane by means of this measurement technique. Particularly, we were interested in the possibilities of following the changes in the total pressure losses, caused by different conditions of the development of the boundary layer. It was investigated how disturbances of the boundary layer generated by a trip wire affected the separation of the boundary layer and flow losses connected with its development. This paper presents the results of the experiments which were carried out at the Institute of Turbomachniery, Technical University of Łódź in a turbine cascade.

Experimental Facilities

The investigation was conducted in a low- speed cascade wind tunnel. The tunnel is an open cycle configuration exhausting to atmosphere at the exit of the test section. The cascade consisting of nine blades is shown in Fig. 1. The blades have an aspect ratio of 1.44 and the central blade was provided with 60 static pressure taps partly arranged (on the suction side) in the blade height direction. The blade with holes for pressure measurements could be moved along the blade span. Measurements of the static pressure distribution were performed with a single transducer and a Scanivalve system, which made it possible to minimise the measurement errors related to the transducers calibration. Measurements of the pressure distribution in

Paper presented at the AGARD PEP 85th Symposium on "Loss Mechanisms and Unsteady Flows in Turbomachines", held in Derby, United Kingdom, 8-12 May 1995, and published in CP-571.

a wake behind the cascade were carried out with a conical five-hole probe of the diameter of 1.5 mm [8]. The probe was calibrated up to ± 25° in pitch and yaw angles in an open air jet tunnel.
The signals from the transducers were fed to the Keithley 500A system which controlled and managed the operation of the whole cascade.
The blade-surface boundary layer was tested with special multisensor probes on a polyimide foil. These transducers were manufactured at the Institute of Turbomachinery, TU Lodz. The foil with the transducers is shown in Fig. 2a. The sensors were made by means of a vapour deposition of a nickel film onto a high quality polyimide foil. To simplify the design, it was decided to use a uniform track geometry for each sensor. The sensor to sensor spacing was specified to be 4 mm. The span-wise lenght of the sensors was limited to 1.5 mm. The width of the nickel deposited track in the flow direction was 0.1 mm. The sensors resistance was designed for 10-15 ohms to be compatible with an anemometer bridge
Scheme of the vane with the transducers glued to it is shown in Fig. 2b, while the arrangement of the transducers was shown in Fig. 1. The transducers were connected via coaxial cable and a multiway rotary switch to a single channel constant temperature anemometer. The data provided by the hot films were digitised at the maximum rate of 50 kHz and then stored in the computer memory and on the hard disk. In order to avoid Nyquist folding of these data, a low pass, 10 kHz filter was used prior to the acquisition (Fig. 2b).
The output signals from the sensors depend on the rate of heat transfer of the heated sensor into the colder boundary layer and the heat of the sensor lost to the surface. Flow regions can be analysed as it was shown in [5], [6], [7], on the basis of comparisons between distributions of signals coming from different transducers glued to the vane.
The results of the thin film measurements are evaluated separately according to the d-c and a-c voltage. The d-c voltage marked as E corresponds to the time-averaged heat transfer, whereas the a-c voltage marked by e represents the unsteady part of the heat transfer. The outlet signals from the transducers (d-c and a-c) were referred to the value of the signal Eo (the heat transfer dissipated without the flow), or E which decreased the effects caused by non-uniformity in the manufacturing and in the overheat used film to film [5], [6] occuring in the subsequend sensors.

Cascade Test Results

Upstream Boundary Layer The inlet flow condition to the cascade was obtained by performing the boundary layer traverse 125 mm (1.5 cascade width) upsteam of the leading edge of the middle blade The experiment was conducted with a small total pressure probe (0.5 mm o.d.). The investigations showed that at the inlet there was a thick turbulent boundary layer. The integral values of the inlet boundary layer are presented in Fig. 1.

Static Pressure Measurement

The results of the static pressure distributions on the suction and pressure sides of the blade at 1 and 50 percent of the span are shown in Fig. 3. The results of calculations of two-dimensional potential pressure distribution by means of the method developed by Kazimierski [1] are also shown in this figure. The consistence of the potential pressure distribution and both cases of measured distributions on the pressure side is excellent. There is no such an agreement on the suction side. The pressure distribution at the endwall is a little different from that one measured for the midspan. Also in the region on the right from the minimum in the pressure distribution there is a divergence of the calculated and measured distributions for the midspan, which indicates that the boundary layer can have been separated in this region.

Secondary Flow Plots

In Fig. 4 the measurement results of the total pressure losses in the cascade outlet plane are shown (z/b =1.5). A large region in which losses have a two- dimensional character is easily observable. Three- dimensional structures are focused near the end wall. The wide region, where the two- dimensional flow prevails makes it possible to separate the losses and to consider further only the changes of losses in the midspan of the vane.

Boundary Layer Investigation

A diagram of the CTA measurement system for the investigation of the boundary layer is shown in Fig. 2b. The preliminary investigations of the boundary layers on the vane were performed for several Reynolds numbers of untripped boundary layer and then, the investigation of the tripped boundary layer were performed for the maximum Reynolds number. In Fig.5 distributions of d-c and a-c signals measured and referred to the value Eo (d-c) and E (a-c) for the untripped layer on the profile were presented. It was decided to refer the nonstationary signal e_{RMS} rather to E because a slightly smaller scattering of the e_{RMS}/E value in the relation to e_{RMS}/E_o in the distribution of this signal in the boundary layer was observed (Fig. 5 and Fig. 7).
The oil-lampblack visualisation made on the profile showed that there was a separation in the boundary layer in the region marked in Fig. 5 and 7.
The results were consistent with the investigation [6].
The maximum fluctuation level occurs at the end of the separation region. On the other hand, the maximum in the averaged signal distribution occurs at the beginning of the reattachment region. Further experiments carried out for smaller values of the Reynolds number (Fig.7) confirmed these observations, while following the location of the maximum of the fluctuation signal turned to be the best way for observing the changes in the separation region. This maximum was clearly seen for

high and small Reynolds numbers, which is easily observable in Fig. 7 and which always corresponded to the end of the separation. Supplementary tests of flow visualisation made it possible to state that the beginning of the separation had the same location independent of the Re number. Similar conclusions concerning the beginning of the separation region can be drawn from [2]. Hence, the development of the separation region can be investigated in an actual case by means of the observation of the displacement of the maximum in the fluctuation signal.

In the second part of the research project we carried out the tests of the separation region in case when the boundary layer was tripped. Two locations of the trip wire on the suction side of the vane were considered: the first one (marked by the letter A) was close to the leading edge, while the second one (marked by the letter B) was in the middle of the pressure decrease region (Fig. 6).

The results of the investigations are presented in Fig. 8-12. Pressure distributions for the untripped boundary layer for various Re numbers are shown in Fig. 6, and for a constant Re number for the untripped and tripped boundary layers - in Fig. 8. In both the figures one can see a separation region, although pressure differences for all the cases considered are small in this region.

The observation of signal distributions coming from individual transducers and frequency domains in this signal allows to determine when this boundary layer becomes turbulent. In Fig. 9 it is shown how the nonstationary signal from transducers changes along the vane surface. For the untripped layer, an increase in the fluctuations, initially in the low frequency range and then in the higher frequency range, is observable (Fig. 10). In the case of the tripped layer A, an initial signal distribution for both the amplitude and frequency is similar as for the untripped layer. Differences occur in the drop of the fluctuation intensity for the maximum of the signal (sensor 23) and downstream in the transitional to turbulent range or at the beginning of the reattachment region. In this region the most significant changes in the case of the tripped A layer are visible as it is shown in Fig. 9 and 10. This region is the most sensitive one to disturbances occurring in the boundary layer. In the case of the tripped layer B one can see significant changes in comparison to the untripped layer. If the untripped layer is treated as a reference case, then a full range of frequencies up to 10 kHz occurs just before the separation. Then, a region of low frequencies occurs (sensor 26) in the direct neighbourhood of the beginning of the separation of the untripped layer. This can be treated as remains of the laminar and turbulent transition region, or rather the transitional to turbulent region. The tripped layer B is fully turbulent in the remaining part.

It is evident from Fig. 10 that the most significant differences between the untripped and tripped layer take place in the low frequency range (a bandwidth 0-2 kHz). The e_{RMS} part of the nonstationary signal measured in the bandwidth 0-2 kHz is presented in Fig. 11. For the untripped layer the distribution of e_{RMS} in the range of 2 kHz is close to the distribution of e_{RMS} in the full range. If we treat the untripped layer as a reference case, then it is characteristic that the fluctuation level before the separation and during the separation in the range of low frequencies is the same for both the untripped and tripped layers.

As far as the laminar-turbulent range with the separation is concerned, the decrease in the maximum of the fluctuation intensity and its migration towards the separation line are observed.

Similar conclusion (migration reattachment towards separation line) can be drawn from [2], where the influence of the external turbulence on the boundary layer with the separation was investigated. It can be stated that irrespective of an influence on the boundary layer, the separation is cancelled by the migration of the attachment line to the separation line.

Total Pressure Losses

It is interesting to see how this migration of the maximum in the signal fluctuation distribution on the blade is reflected by the total pressure losses. The test results of total pressure losses for three cases as untripped and tripped a function of the Reynolds number are presented in Fig. 12. For low and high Re numbers the tripped layers cause the increase in the losses.

Short bubbles are an effective way to force the turbulent flow and they do not appear clearly in the level of total pressure losses. It can be considered that they will be a good way to control the performance of turbomachines.

Conclusions

The measurement methods developed and thin film transducers are suitable for an analysis of the boundary layer conditions.

Nonstationary part of the signal from the transducers provides most valuable information concerning the boundary layer conditions. However, further investigations are needed to provide a full identification of the boundary layer with the separation and transition on the basis of nonstationary part of the signal. The maximum which occurs in the nonstationary signal distribution is connected with the laminar and turbulent transition and with the end of the separation. In the investigation presented here the location of the RMS maximum was correlated very well with the end of the separation.

For small Reynolds numbers the decrease in the level of maximum values of RMS fluctuations and their displacement downstream is observed, which means widening and dissipation of the laminar-turbulent transition region and the separation region.

Turbulisation of the boundary layer causes the decrease in the maximum values of RMS fluctuations and their displacement upstream.

Turbulisation of the boundary layer with a local separation showed an increase in the losses for low and high Reynolds numbers. A small close separation is not more evident in the level of losses, thus it can be treated as an effective way of turbulising the flow.
Further investigations of thin film signals and their correlation with the investigation of other parameters in the boundary level are still needed so that a correct interpretation of outlet signals for different conditions of the developing boundary layer could be possible.

Literature

[1] Kazimierski Z. : Two-Dimensional Flow Through an Axial Stage of Turbomachine of Any Geometric Parameters. Archiwum Budowy Maszyn, t. XIII, 1966, issue 2 pp 213-232.

[2] Haas W., Rodi W., Schonung B., Swamy N.V.C. : Experimentelle Untersuchung von lokalen Abloseblasen an Gasturbinenschaugeln. Z.Flugwiss. Weltraumforsch. 1987, Vol. 11, p.261-270.

[3] Hodson H. P. : Boundary - Layer and Loss Measurements on the Rotor of an Axial-Flow Turbine. Journal of Engineering for Gas Turbines and Power, April 1984, Vol. 106, p.391

[4] Hoheisel H., Kiock R., Lichtfuss H. J., Fottner L. : Influence of Free - Stream Turbulence and Blade Pressure Gradient on Boundary Layer and Loss Behavior of Turbine Cascades. Translations of the ASME, April 1987, Vol. 109, p.210.

[5] Oldfield M. L. G., Kiock R., Holmes A. T., Graham G. G. : Boundary - Layer studies on highly loaded cascades using heated thin-films and a traversing probe. ASME, Journal of Engineering for Power, 1981, Vol. 103, p.237-246.

[6] Pucher P., Gohl R. : Experimental Investigation of Boundary Layer Separation with Heated Thin-Film Sensors. Journal of Turbomachinery, April 1987, Vol. 109, p.303.

[7] Schulz H. D. : Experimentelle Untersuchung der Dreidimensionalen Abgelosten Stromung in einem Axialverdichterring gitter. RWTH Aachen, Ph. Doctor Thesis 1989.

[8] Sitaram N., Treaster A. L. : A Simplified Method of Using Four-Hole Probes to Measure Three-Dimensional Flow Fields. Journal of Fluids Engineering, March 1985, Vol. 107, p.31.

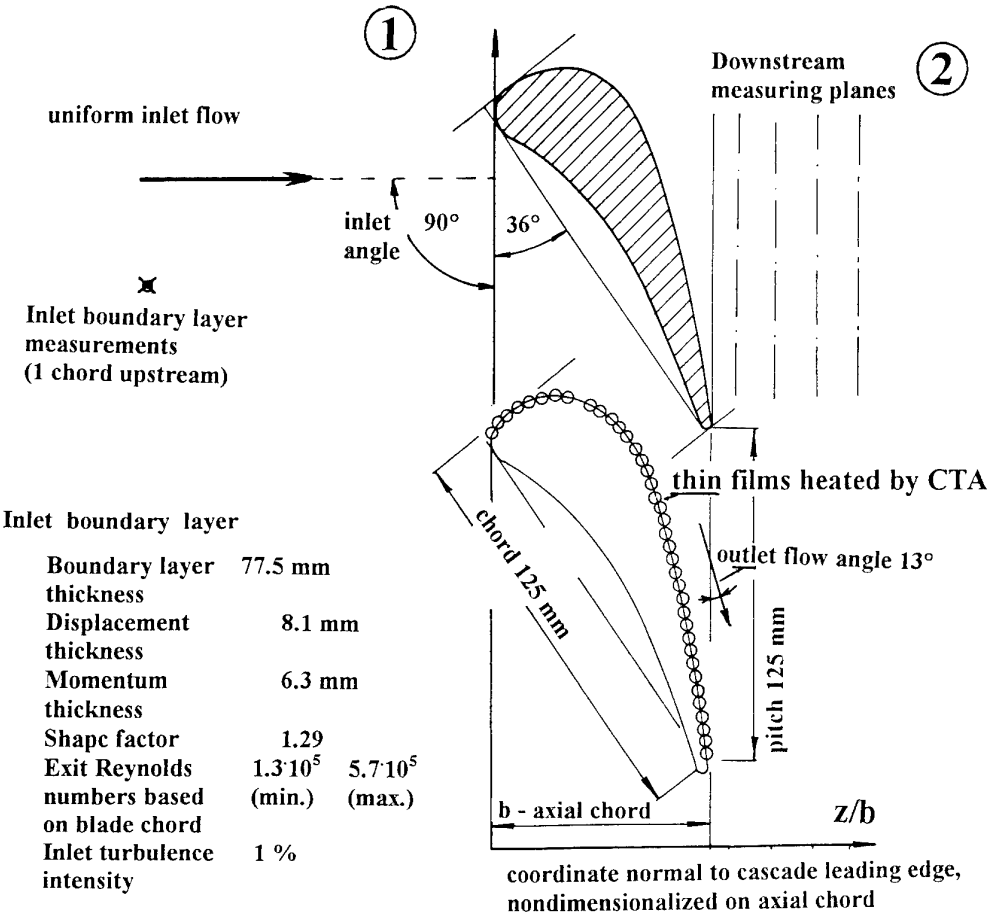

Fig. 1 Cascade geometry

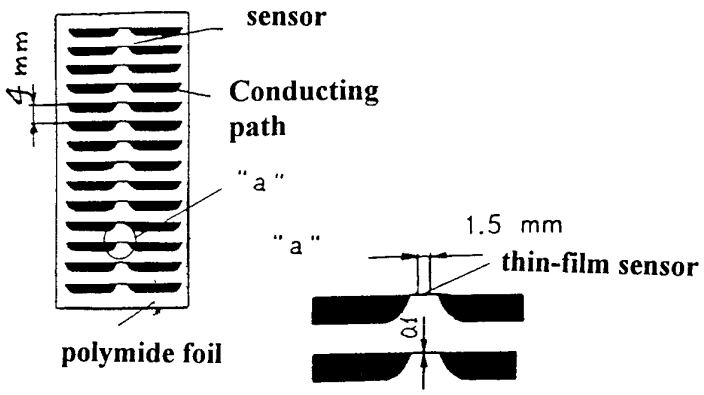

Fig. 2a Hot film sensors, multielement array

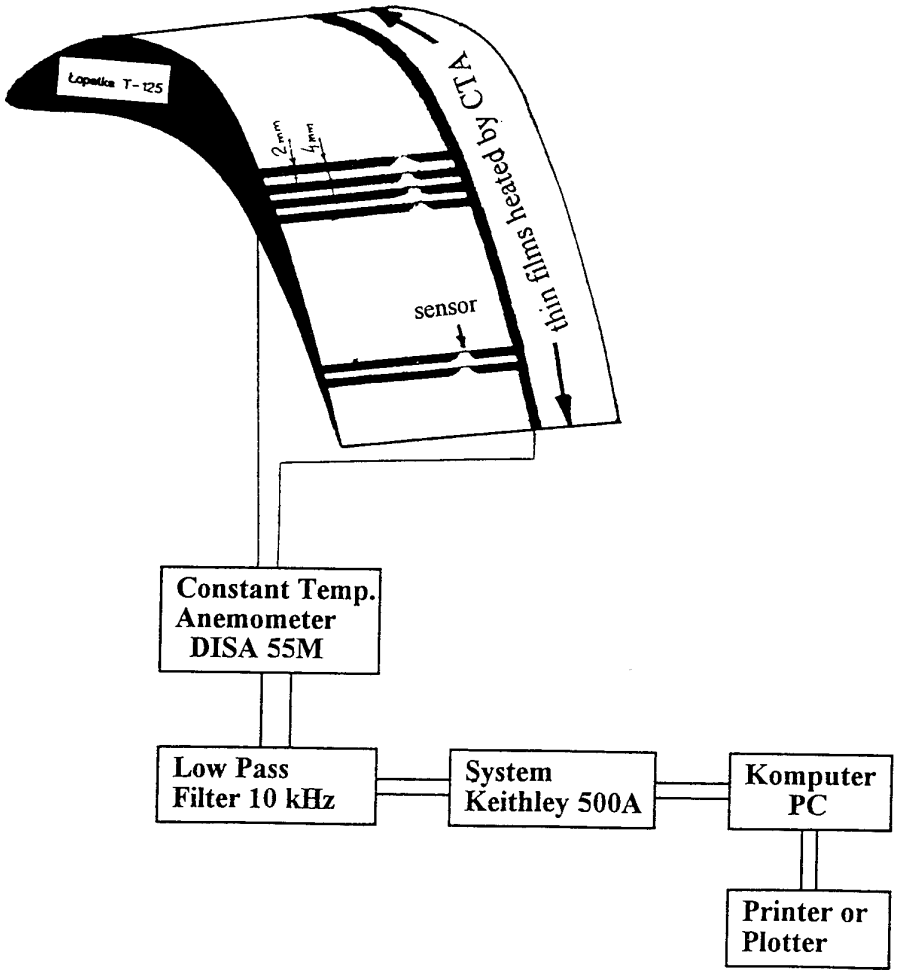

Fig. 2b Instrumentation for heated thin film technique

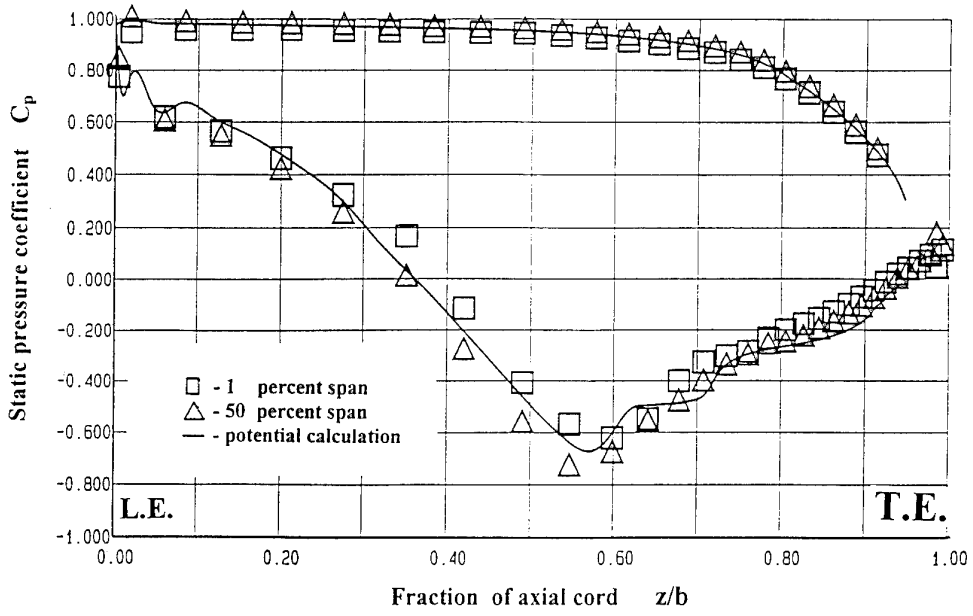

Fig. 3 Static pressure distributions around the middle vane at two spanwise locations measured from enddwall

Re = 5.7·10^5

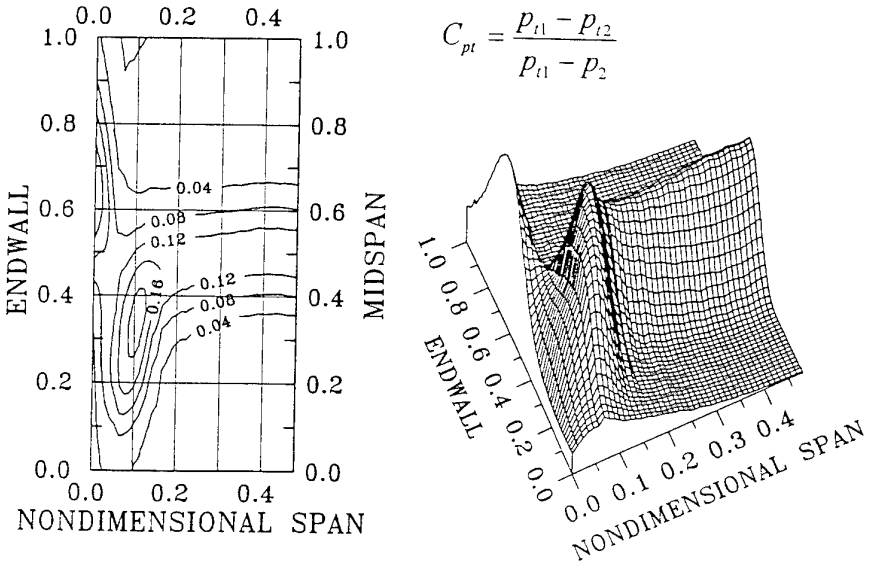

Fig. 4 Contours of total pressure loss coefficient Cpt at downstream measuring plane, z/b=1.5

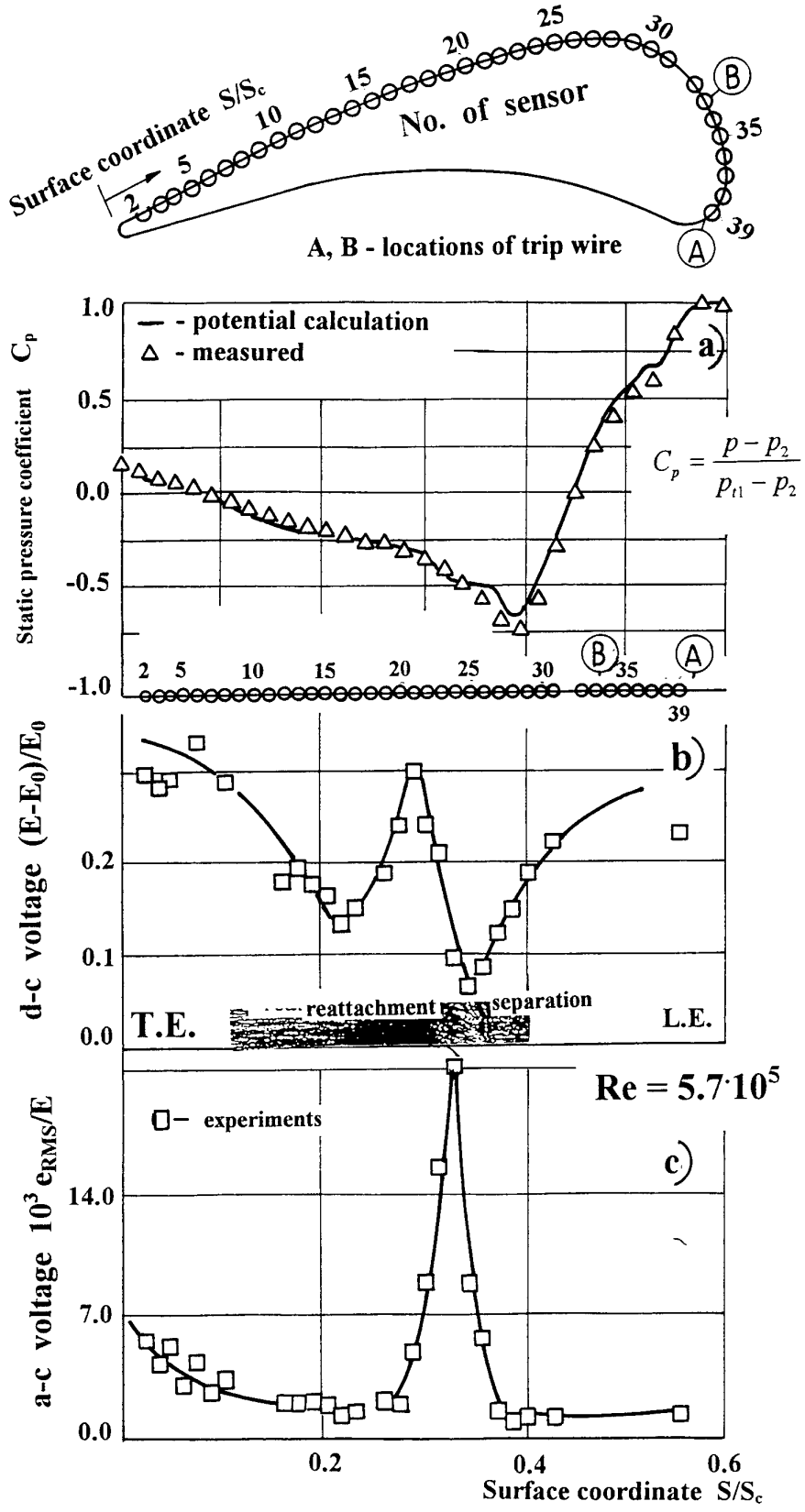

Fig. 5a Pressure distribution on suction side of the vane
5b,c Thin-film signals from the suction side of the vane

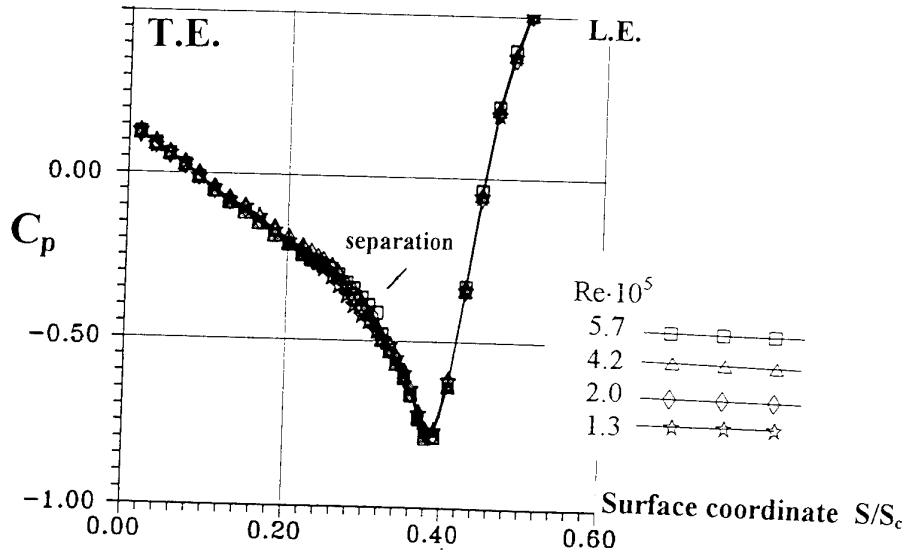

Fig. 6 Pressure distribution on suction side of the vane at different Reynolds numbers

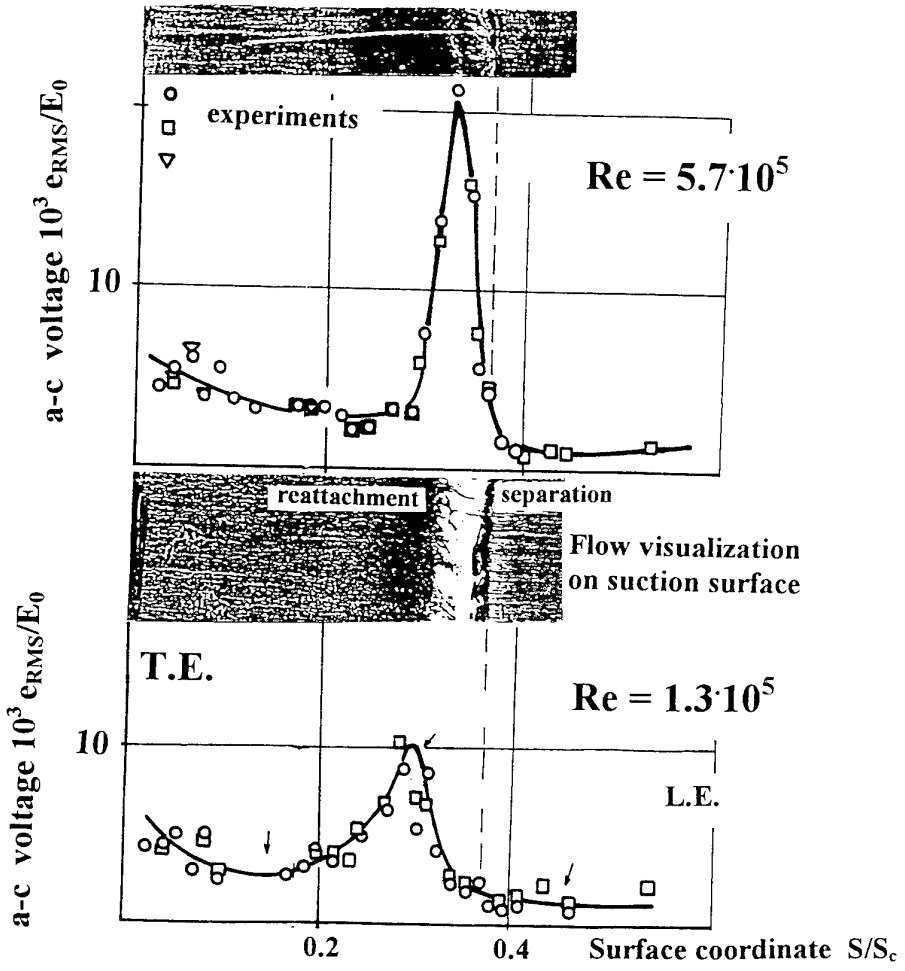

Fig. 7 Thin-film signals distributions from suction side of the vane at different Reynolds numbers

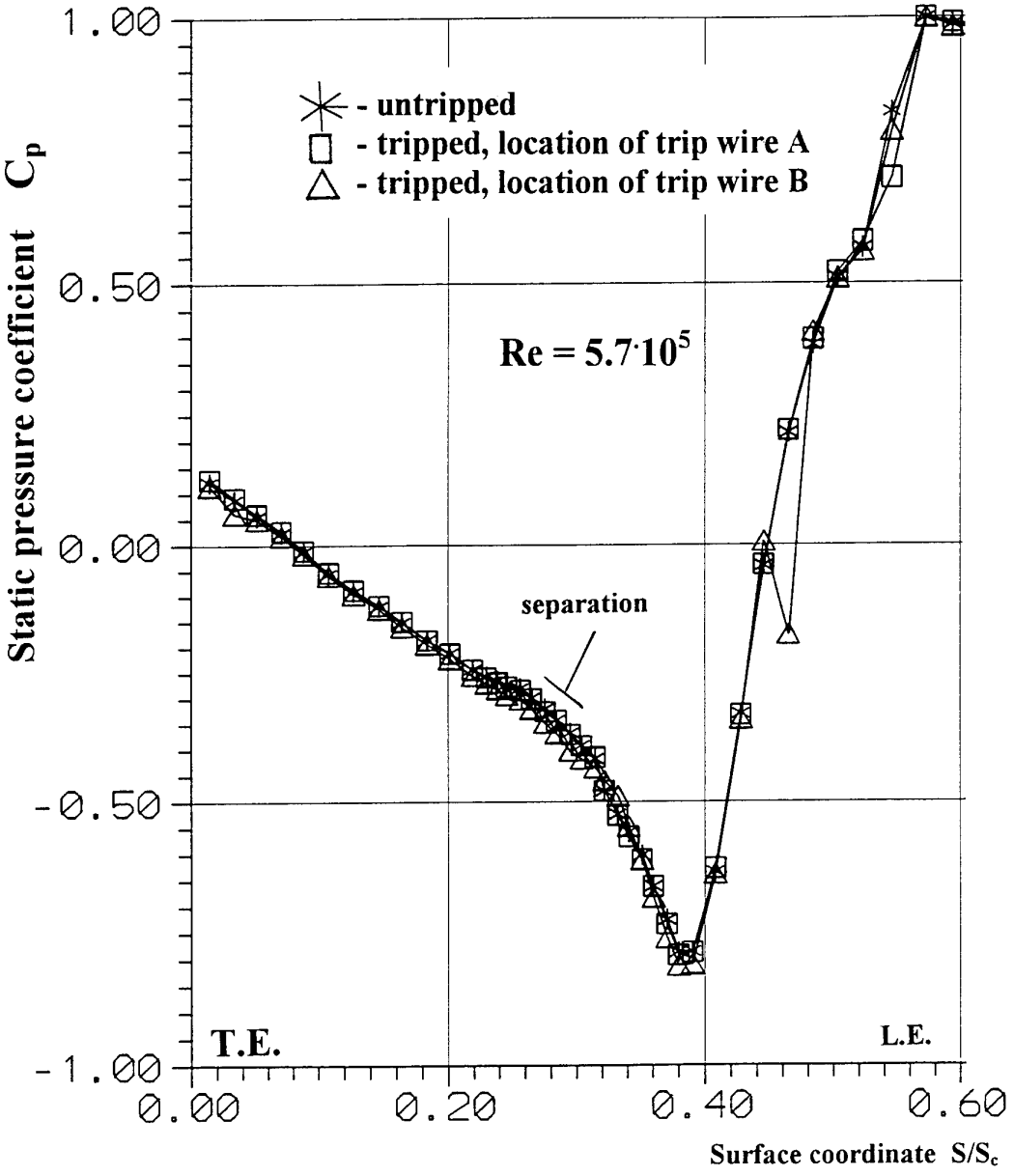

Fig. 8 Pressure distribution on suction side of the vane at different trip wire locations

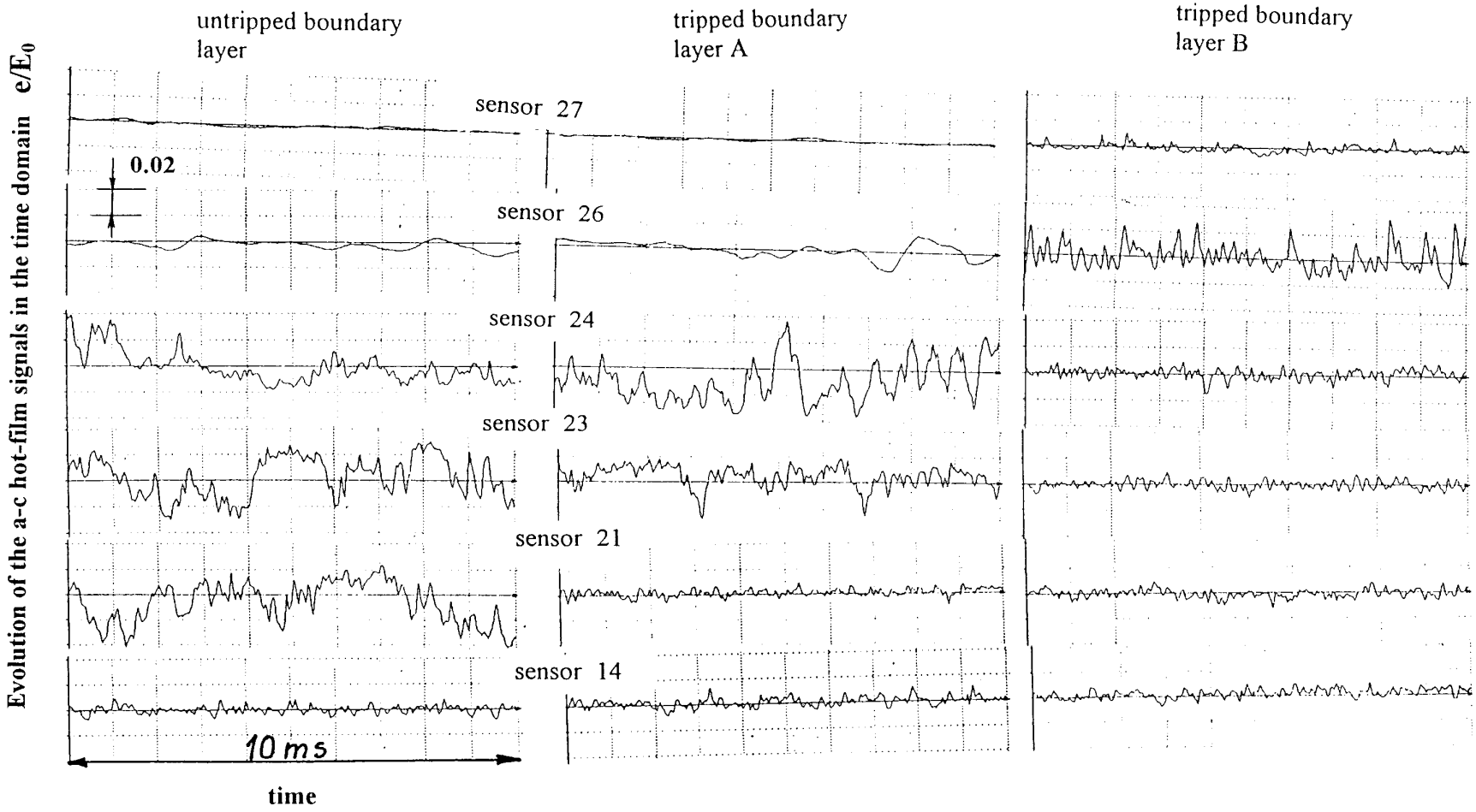

Fig. 9 Unsteady thin-film signals from suction side, untripped and tripped boundary layers

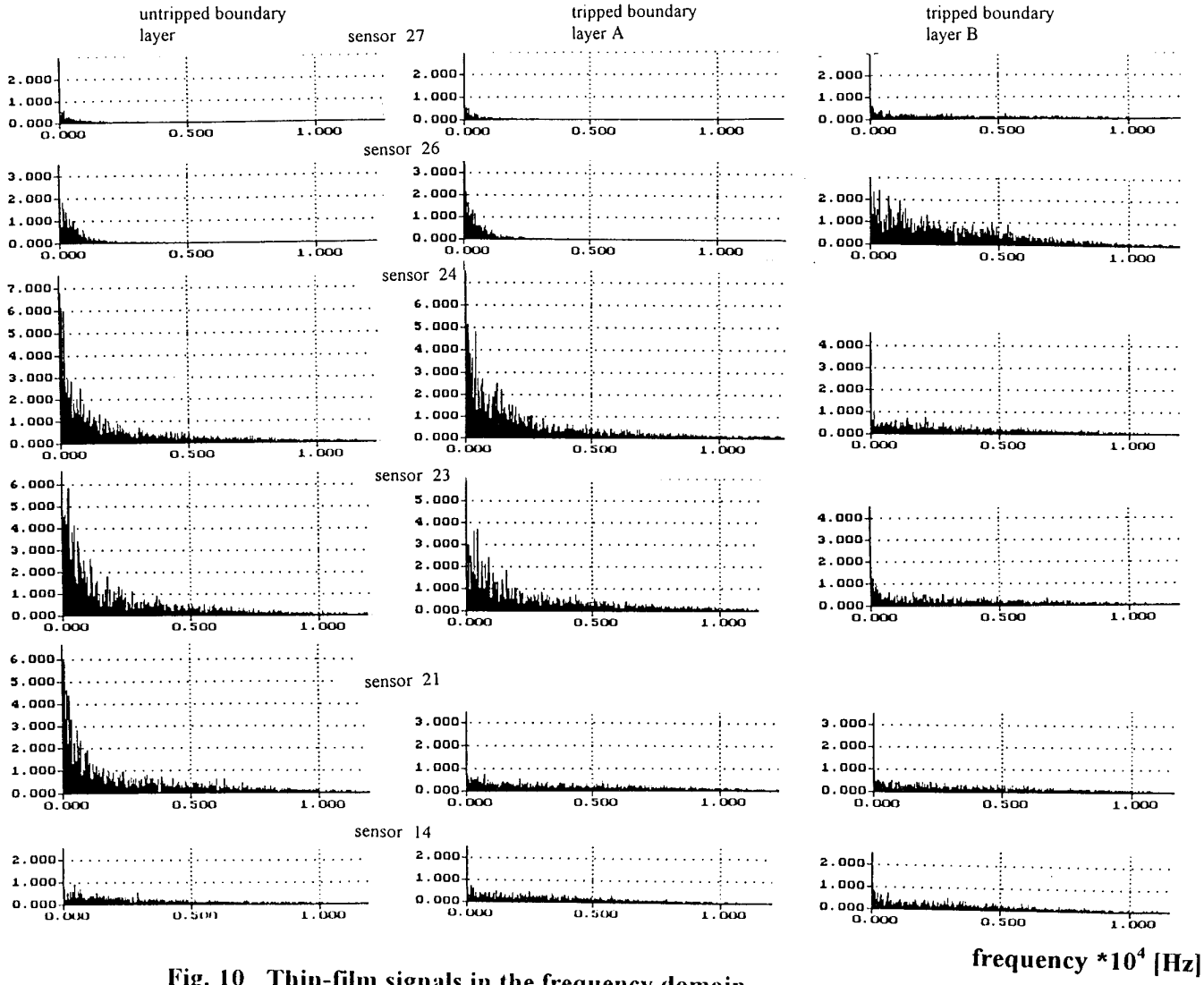

Fig. 10 Thin-film signals in the frequency domain, untripped an tripped boundary layer

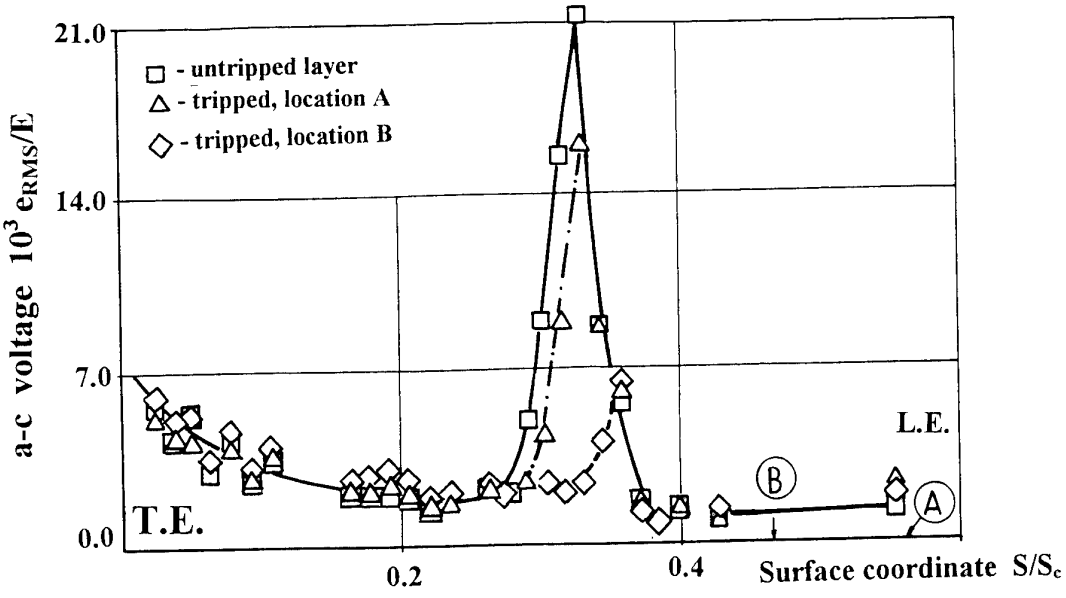

Fig. 11 Thin-film signals distributions from suction side of the vane at different trip wire locations (0-2 kHz bandwidth)

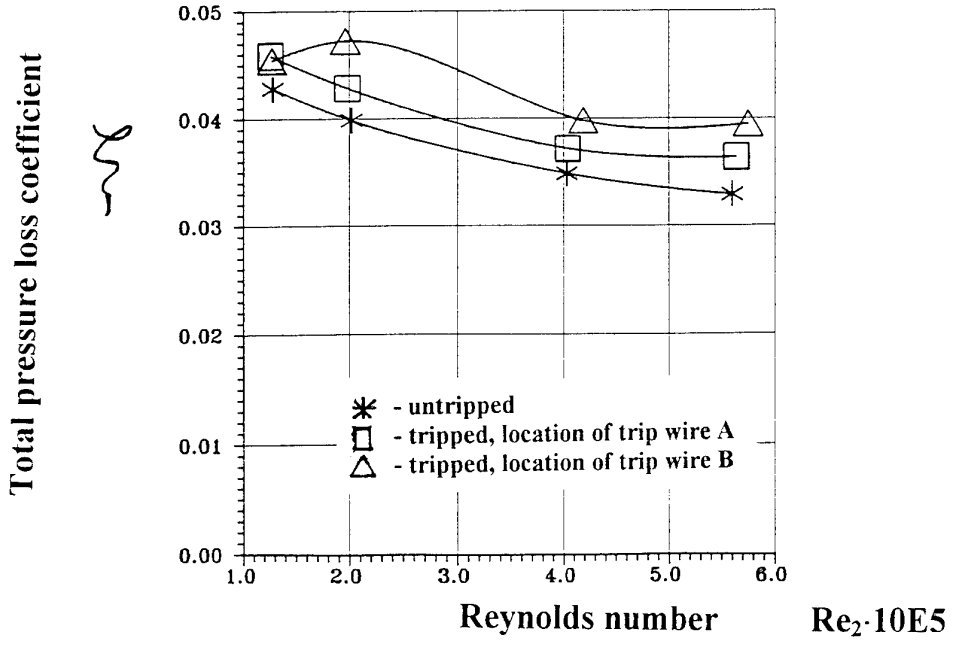

Fig. 12 Loss coefficient untripped and tripped boundary layer on suction side versus Reynolds number

REFERENCE NO. OF THE PAPER: 4

DISCUSSOR'S NAME: H.B. Weyer, DLR, Germany

AUTHOR'S NAME: A. Smolny, J. Blaszczak

Q.: What is the thickness of the trip wire compared to the boundary layer, and did you account for the losses generated by the trip wire in your loss analysis?

A: The thickness of the trip wire was 0.4 mm and was bigger than the boundary layer thickness near the leading edge and at position A. As to position B of the trip wire, these two values were comparable. In our experiment only the total pressure losses were considered.

REFERENCE NO. OF THE PAPER: 4

DISCUSSOR'S NAME: D.G. Gregory-Smith, Univ. of Durham, U.K.

AUTHOR'S NAME: A. Smolny, J. Blaszczak

Q: What was the inlet turbulence level? What were inlet and exit-flow angles for the cascade at mid-span?

A: The inlet turbulence level was 1 %. Inlet flow angle was 90° and the exit (outlet) flow angle was 13°. All the values were measured at the mid-span of the cascade.

The Effect of Vane-Blade Spacing on Transonic Turbine Stage Performance

F.J. Kelecy, J.W. Griffin, and R.A. Delaney
Allison Engine Company
Speed Code T14A
P.O. Box 420
Indianapolis, IN 46206-0420
USA

SUMMARY

This paper presents the results of a computational study on the effect of axial spacing between the vane and blade rows of a transonic turbine stage. The study was performed on the mid-span section of a high-pressure turbine stage using a quasi-3D, unsteady Navier-Stokes solver that provides a fully interactive vane-blade unsteady flow solution [7]. Three different cases were considered, corresponding to axial spacings of 20%, 40%, and 60% of the vane axial chord. The calculated vane and blade pressure distributions for the 40% case were found to compare favorably with experimental measurements acquired in a short-duration shock tunnel [6]. In addition, the analysis shows a marked increase in the amplitude of the unsteady pressure fluctuations on the vane and blade surfaces as the spacing decreases. Time-averaged stage adiabatic efficiency predictions for each case are presented to show the effect of spacing on aerodynamic performance.

LIST OF SYMBOLS

M	absolute isentropic Mach number
p	pressure
T	temperature
η_{ad}	adiabatic efficiency
α	absolute flow angle
γ	specific heat ratio

Subscripts

ex	stage exit
in	stage inlet
ir	inter-blade-row
t	turbulent or total

1 INTRODUCTION

Over the last decade, designers of gas turbine engines have made extensive use of computational fluid dynamics (CFD) to provide aerodynamic performance predictions for specific engine components. In high pressure turbine design, such predictions can provide valuable information to assist in the optimization of stage efficiency, component weight, and other design parameters.

With the advent of powerful supercomputers and workstations, single row, steady-state solutions to both the Euler and Navier-Stokes equations can now be obtained on a routine basis. In addition, methods for computing steady flows through multiple stages have appeared in the literature, where adjacent blade rows are accounted for by either a mixing plane model [1] or a more sophisticated average passage model [2]. While these steady flow approaches have proven useful, it is well known that unsteady interactions can have significant impact on the performance of turbomachinery blading, particularly blade loading, stage efficiency, heat transfer, aeromechanics, and noise [3]. Accordingly, multiple stage calculations are now beginning to employ time-accurate flow solvers in order to accurately model the unsteady interactions between the stator (vane) and rotor (blade) of a given stage [4],[5].

The principal sources of the unsteadiness associated with turbine vane-blade interaction can be grouped into three broad categories: (1) subsonic

Paper presented at the AGARD PEP 85th Symposium on "Loss Mechanisms and Unsteady Flows in Turbomachines", held in Derby, United Kingdom, 8-12 May 1995, and published in CP-571.

potential interactions, (2) shock wave interactions, and (3) wake interactions. Subsonic potential interactions arise due to the relative motion of the stator and rotor blades within the turbine stage, and are manifested primarily as unsteady pressure waves which travel both unstream and downstream relative to a given blade row. If the flow becomes supersonic at the blade trailing edge, then the resulting shock system will interact with the leading edge of the downstream blade, giving rise to large amplitude pressure fluctuations. Wake interactions result from the convection of viscous wakes from an upstream blade into a downstream blade row. The wake structure itself may also involve vortex shedding and thus lead to high frequency unsteadiness. All of these interactions are strongly affected by the axial spacing between blade rows.

The present work is part of an on-going effort to study the effects of unsteadiness on high pressure turbines. The main thrust of this research involves an extensive analytical and experimental investigation of the unsteady flow within a high pressure research turbine stage [6]. This turbine was developed specifically to obtain rotor-stator interaction data in a short-duration shock tunnel facility. The stage was constructed to allow different rotor-stator axial spacings to be tested. Flow through the stage was controlled by setting the vane in either a closed position, producing a transonic vane exit flow ($M = 1.1$), or an open position, producing a high subsonic vane exit flow ($M = 0.9$).

This paper documents results obtained from a numerical study of the effect of vane-blade axial spacing on the unsteady aerodynamics of the VBI turbine at transonic conditions. In the sections which follow, the computational methodology will be briefly reviewed, followed by a presentation of results for spacings of 20%, 40%, and 60% of the vane axial chord. Comparisons of the numerical solutions with available experimental data will also be made for the 40% spacing case.

2 NUMERICAL APPROACH

The aerodynamic analysis was performed using a quasi-3D vane-blade interaction code developed by Rao and Delaney [7]. A brief description of the methodology employed in the code is provided in this section. For additional information, the reader should consult the paper by Rao and Delaney [7] and the references cited below.

The unsteady flow field is modeled using the Reynolds-averaged Navier-Stokes equations for flow on a blade-to-blade stream surface of revolution. The blade geometry is defined on a quasi-three-dimensional stream surface which passes through the blade midspan and has a prescribed streamtube thickness. The differential equations are discretized using central-difference approximations for the convective fluxes in conjunction with an artificial dissipation model which blends second and fourth-order differences. The viscous fluxes are also discretized with central differences for both first and second derivative terms. The resulting semi-discrete system is then integrated in time using a five-stage Runge-Kutta scheme.

For the Reynolds-averaged equations, the effects of the turbulent stresses on the mean flow are modeled using the Baldwin-Lomax two-layer algebraic turbulence model Ref. [8]. The current version of the vane-blade interaction code implements this model in the near-wall regions only (neglecting the wake). Transition from laminar to turbulent flow along the airfoil surface is simulated using the practice suggested in Ref. [8]. Essentially, this model sets $\mu_t = 0$ everywhere in a profile in which $\mu_t/\mu < 14$.

The grid system used in the present work is shown in Fig. 1. Each row (vane or blade) employs a single airfoil-conforming O grid embedded in a periodic background H grid. The transfer of information between the O and H grids is handled using the Chimera approach of Benek et. al. [9]. In the Chimera approach, dependent variables are interpolated at the interface boundary points using precomputed interpolation stencils. Points on the H grid which are covered by the O grid are excluded from the computation by setting the solution update at those points equal to zero. On the O grid, points are clustered near the airfoil surface in order to provide adequate resolution of turbulent boundary layers. Typically, a spacing which yields a y^+ value of approximately one or less at each near-wall point is required for the Baldwin-Lomax turbulence model. The vane and blade H grids are overlapped at the vane exit-blade inlet boundaries so that information can be transferred (by interpolation) from one row

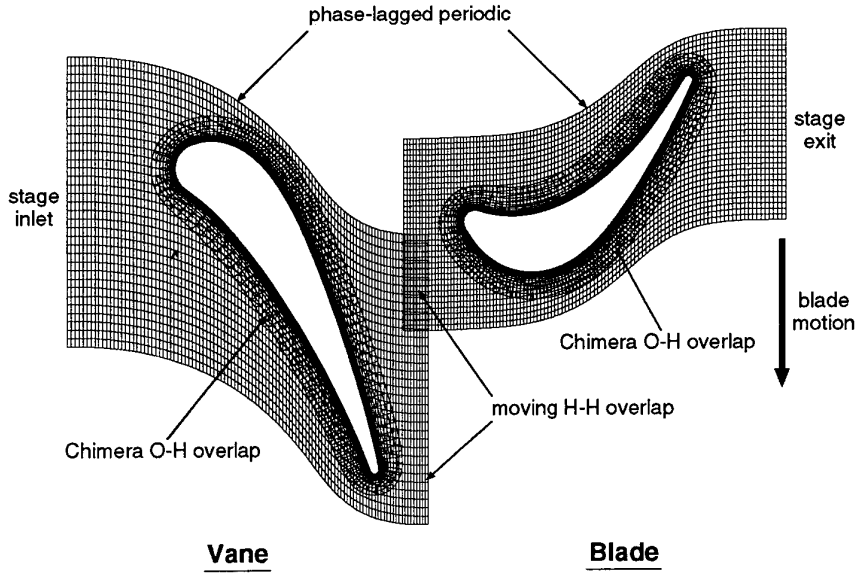

Figure 1: Illustration of O-H grid systems and boundary conditions used in VBI calculations.

to the next. The relative positions of the H grids can be easily varied to accommodate arbitrary axial spacings between the vane and blade rows.

Figure 1 also illustrates the types of boundary points encountered in the present analysis. At the stage inflow and exit boundaries, nonreflecting boundary conditions are used which are based on the original method of characteristics approach of Erdos et. al. [10]. At the airfoil surface, a no slip boundary condition is invoked along with either a constant wall temperature or adiabatic wall thermal boundary condition.

In order to model blade rows with unequal airfoil counts, the phase-lagging method of Erdos et. al. [10] is used, following the implementation developed by Lewis et. al. [11]. With this procedure, the solution domain for a given row need only span one pitch rather than multiple pitches as is required for spatial periodicity. The solution at a point outside the periodic boundary is derived from the solution one pitch away at an earlier time step. The temporal period needed to retrieve the data from the time-storage arrays is a simple function of the airfoil count and the rotor speed. This requires storing (in main memory) the time-history of dependent variables at points adjacent to the periodic boundaries.

At the vane exit-blade inlet boundary, dependent variables are transferred from one grid to another by interpolation. Since, in general, the airfoil pitch will vary from one row to the next, only certain sections of each grid will physically overlap. For the overlap sections, a simple bilinear interpolation is used to transfer variables between grids. The non-overlapped sections are treated using a phase-lagging procedure similar to that described above for the periodic boundary.

3 RESULTS

The present study employed the geometry and nominal stage data for the turbine stage described in Ref. [6]. Key parameters associated with the turbine geometry and stage aerodynamics are summarized in Tables 1 and 2. The grids were constructed to model the closed vane setting, which produces transonic flow conditions within the turbine stage. The working fluid was assumed to be air with a specific heat ratio of 1.4, gas constant of 55.3 $ft-lb/lbm-R$, and Prandtl number of 0.72.

Three axial spacings of 20%, 40% (the nominal case) and 60% of axial chord were investigated. The grid sizes used for these three cases are given in Ta-

Table 1: VBI turbine stage geometry

Parameter	Stator	Rotor
Number of airfoils	30	45
Chord (in)	2.66	1.87
Spacing (in)	2.03	1.34
Chord/spacing	1.32	1.39
Mean radius (in)	9.73	9.70
Aspect ratio	0.72	1.10
Leading edge radius (in)	0.18	0.09
Trailing edge radius (in)	0.03	0.03
Hub/tip radius ratio	0.82	0.81
Tip radius (in)	10.64	10.64
Trailing edge blockage (%)	9.44	10.32

Table 2: VBI turbine stage aerodynamics

Parameter	Stator	Rotor
Rotor speed (rpm)	—	11400
Stage equivalent work (Btu/lb)	—	33.7
Stage expansion ratio (p_t/p_s)	—	4.07
Inlet relative Mach number	0.164	0.483
Exit relative Mach number	1.121	1.054
Inlet relative flow angle (deg)	0.0	-49.18
Exit relative flow angle (deg)	-72.66	62.22
Inlet total presure $(psia)$	44.0	—
Inlet total temperature (R)	940	940
Corrected flow (lb/sec)	22.57	—
Inlet Reynolds number	8×10^5	—
Inlet turbulence intensity (%)	5.0	—
Reduced frequency	7.8	8.5
Vane setting angle (deg)	-61.0	—

ble 3. A fourth case was also run at 40% axial spacing using a refined H grid in order to examine the effect of grid resolution on the numerical results. Both the vane and blade rows utilized identical O and H grid sizes.

For the bulk of the results presented below, the calculations employed the constant wall temperature boundary condition ($T_{wall} = 530\ R$). However, in order to determine the adiabatic efficiency for the stage, a corresponding set of runs was made using the adiabatic wall boundary condition. A comparison of the constant temperature and adiabatic wall solutions showed essentially no difference in the lift histories and unsteady pressure envelopes for the corresponding cases.

The unsteady calculations were initialized with isolated steady-state solutions obtained for each row using the stage data in Table 2 for boundary conditions. A fixed time step was derived from these steady-state solutions and adjusted so that both the vane and blade passing periods (defined as the pitch divided by the wheel speed) were integer numbers. A time-accurate solution was then carried out using this fixed time step. Converged time-periodic solutions were usually achieved in a time period corresponding to about one revolution of the rotor.

3.1 Unsteady Lift

The convergence of the unsteady lift coefficient for the three axial spacings is shown in Figs. 2 – 5. In each case, the amplitude of the unsteady lift grows steadily, eventually leveling off as a time-periodic solution is approached. In comparing the three solutions, it can be seen that the amplitude of the unsteady lift decreases rapidly as the spacing is increased from 20 to 60 % of axial chord. For the blade in particular, the amplitude drops by a factor of two from 20 to 40 %, and by a smaller factor from 40 to 60%. Also notable in these plots are the sharp peaks in the blade lift, which arise from the unsteady interaction of the vane wake and shock system with the leading edge of the blade.

The effect of grid resolution can be seen by comparing the lift history for the baseline grid 40% spacing case (Fig. 3) with that for the fine grid (Fig. 5). In particular, the fine grid solution contains sharp peaks in lift at higher harmonics which are not present in the baseline grid solution. This behavior is consistent with the ability of the fine H grid to resolve small scale features of the flow (such as vortex shedding).

3.2 Surface Pressure Distributions

Additional insight into the nature of the unsteady pressure fluctuations is provided by the surface pressure envelopes plotted in Figs. 6 – 13. These figures show the minimum-maximum surface pressure distributions, along with the computed time-mean and steady-state (isolated airfoil) distributions. From

Table 3: Case summary of VBI numerical calculations.

Spacing (%)	Grid Type	Grid Size
40	H/O	107×35 / 161×25
20	H/O	107×35 / 161×25
60	H/O	107×35 / 161×25
40	H/O	235×91 / 161×23

these plots, it is seen that the vane is operating at a choked condition, since no unsteadiness propagates upstream of the throat location on the suction surface. The pressure distribution on the blade, however, is unsteady over the entire blade surface. Moreover, the magnitude of the unsteady pressure fluctuations near the blade leading edge are nearly as large as the time-mean and steady-state levels.

A comparison of the numerical solution for the 40% spacing case (fine grid) with the data reported in Ref. [6] is presented in Figs. 14 – 17. Figures 14 and 15 show the computed unsteady surface pressure envelopes for the vane and blade plotted with the experimental data. It can be seen that the computed envelopes are in reasonable agreement with the data for the blade, but that the level of vane unsteadiness appears to be overpredicted. The computed time-mean and steady-state pressure distributions are compared with the experimental data in Figs. 16 and 17. Here, the agreement is good for both the vane and blade. It should be noted that the present model only partially accounts for three-dimensional effects (through the variation of the stream tube thickness). Therefore, the present results will probably not match the experimental data in the inter-blade-row regions, where three-dimensional effects are important.

3.3 Mach Number and Static Pressure Contours

Details of the unsteady flow through the turbine stage can be seen in the contour plots of instantaneous absolute Mach number and static pressure shown in Figs. 18 – 25. Two vane and three blade passage solutions are plotted in each case. These figures show the interaction of the vane trailing edge shock system and wake with the leading edge of the blade. The interaction is clearly strongest for the 20% spacing, and diminishes as the spacing is increased.

The effect of grid refinement is readily observed by comparing the baseline and fine grid Mach number plots (Figs. 19 and 21, respectively). The fine grid solution, for example, shows a train of vortices being shed from both the vane and blade trailing edges. This behavior is not present in the baseline grid solution, although the baseline grid wake appears to convect in generally the same direction.

3.4 Time-Averaged Stage Data

Stage data for the VBI turbine were derived from the adiabatic wall solutions by averaging the flow variables in time and space at three axial locations: (1) the vane inlet, (2) the inter-blade row station (taken to be the average between the vane exit and blade inlet), and (3) the blade exit. The time and space-averaged total pressures and temperatures at the vane inlet and blade exit were used to determine the adiabatic stage efficiency as follows:

$$\eta_{ad} = \frac{T_{t,ex} - T_{t,in}}{T_{t,in}\left[1 - \left(\frac{p_{t,ex}}{p_{t,in}}\right)^{\frac{\gamma-1}{\gamma}}\right]} \qquad (1)$$

In the above, the subscripts in and ex denote the stage inlet and exit stations, respectively.

The computed stage data are presented in Table 4. It can be seen that the largest total pressure and temperature drops occur across the rotor, with virtually no total temperature drop across the vane. The stage efficiencies, which vary from 92.9% to 93.2%, show little variation with increased spacing. The slightly lower efficiency at 20% spacing is expected since the interaction is strongest at this spacing. Of course, the two-dimensional analysis considered here neglects losses due to secondary flows and endwall boundary layers. These losses would tend to reduce the stage efficiency at larger spacings. One could conclude, therefore, that an optimum spacing exists for which the sum of the losses due to interaction, secondary flows, and endwall boundary layers is a minimum.

Table 4: VBI turbine stage data and adiabatic efficiencies for 20%, 40%, and 60% axial spacings.

	20%	40%	60%
$p_{t,ir}/p_{t,in}$	0.963	0.971	0.957
$T_{t,ir}/T_{t,in}$	1.001	1.001	1.001
M_{ir}	1.072	1.033	1.046
α_{ir} (deg)	-70.7	-71.8	-72.1
$p_{t,ex}/p_{t,in}$	0.310	0.320	0.312
$T_{t,ex}/T_{t,in}$	0.736	0.741	0.735
M_{ex}	0.486	0.494	0.485
η_{ad} (%)	92.9	93.2	93.1

4 CONCLUDING REMARKS

A series of 2D vane-blade interaction calculations were carried out for the VBI high pressure turbine stage to investigate the effect of axial spacing on the unsteady stage aerodynamics. The calculations performed to date have shown that the amplitude of the unsteady pressure fluctuations which arise due to the interaction decrease rapidly as the spacing is increased. In addition, the present results were found to be in reasonable agreement with available experimental data, indicating that the CFD analysis is capable of providing realistic results. The computed stage efficiencies show little variation over the range of spacings considered, with a small decrease at 20% spacing due to the more intense interaction of the vane shock and wake structures with the leading edge of the blade.

Acknowledgements

This work was supported by the NASA Lewis Research Center under NASA Grant NAG3-1645, with Calspan-University of Buffalo Research Center. The authors wish to thank the Allison Engine Co. for granting permission to publish this work, and Dr. Chan Kim of the NASA Lewis Research Center for his guidance and support of the present research effort.

References

[1] Dawes, W.N., 1991, "Multi-Blade Row Navier-Stokes Simulations of Fan Bypass Configurations," ASME 91-GT-148.

[2] Adamczyk, J.J., Celestina, M.L., and Chen, J.P., 1989, "Simulation of Three-Dimensional Viscous Flow Within a Multistage Turbine," ASME-GT-152.

[3] Hodson, H.P., "Measurements of Wake-Generated Unsteadiness in the Rotor Passages of Axial Flow Turbines," ASME Paper 84-GT-189.

[4] Rangwalla, A.A., Madavan, N.K., and Johnson, P.D., 1991, "Application of Unsteady Navier-Stokes Solver to Transonic Turbine Design," AIAA Paper 91-2468.

[5] Sharma, O.P., Pickett, G.F., and Ni, R.H., 1992, "Assessment of Unsteady Flows in Turbines," *ASME Journal of Turbomachinery*, Vol. 114, January 1992, pp. 79 – 90.

[6] Delaney, R.A., Helton, D.J., Bennett, W.A., Dunn, M.G., Rao, K.V., and Kwon, O., "Turbine Vane-Blade Interaction," WRDC-TR-89-2154, Vol. I, March, 1990.

[7] Rao, K.V., Delaney, R.A., "Investigation of Unsteady Flow Through a Transonic Turbine Stage: Part I - Analysis," AIAA Paper 90-2408, Orlando, FL, 1990.

[8] Baldwin, B.S., and Lomax, H., "Thin-Layer Approximation and Algebraic Model for Separated Turbulent Flows," AIAA Paper 78-0257, 1978.

[9] Benek, J.A., Buning, P.G., and Steger, J.L., "A 3-D Chimera Grid Embedding Technique," AIAA Paper 85-1523, Cincinnati, OH, 1985.

[10] Erdos, J.I., Alzner, E., and McNally, W., "Numerical Solution of Periodic Transonic Flow through a Fan Stage," *AIAA Journal*, Vol. 15, 1977, pp. 1559 - 1568.

[11] Lewis, J.P., Hall, E.J., and Delaney, R.A., "Numerical Prediction of Turbine Vane-Blade Aerodynamic Interaction," *ASME Journal of Turbomachinery*, Vol. 111, 1989, pp. 387 - 393.

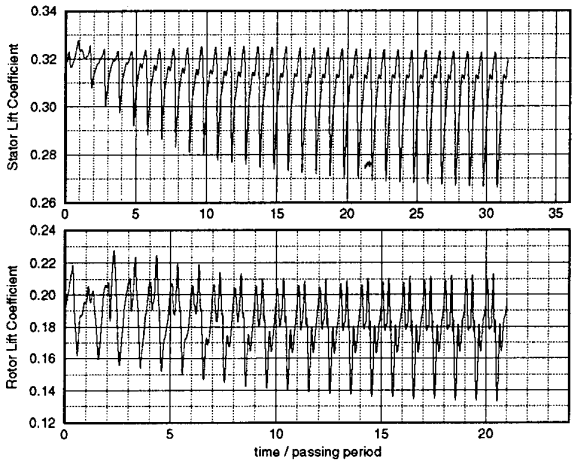

Figure 2: Lift history for VBI turbine stage: 20% spacing, baseline grid.

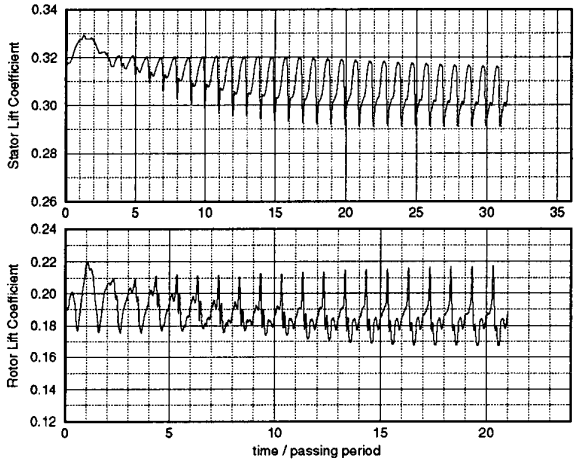

Figure 4: Lift history for VBI turbine stage: 60% spacing, baseline grid.

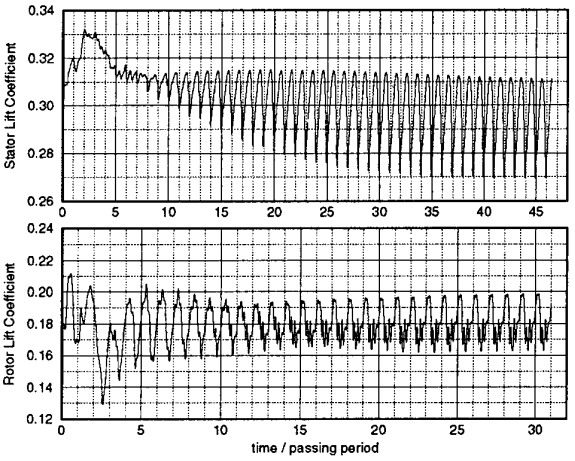

Figure 3: Lift history for VBI turbine stage: 40% spacing, baseline grid.

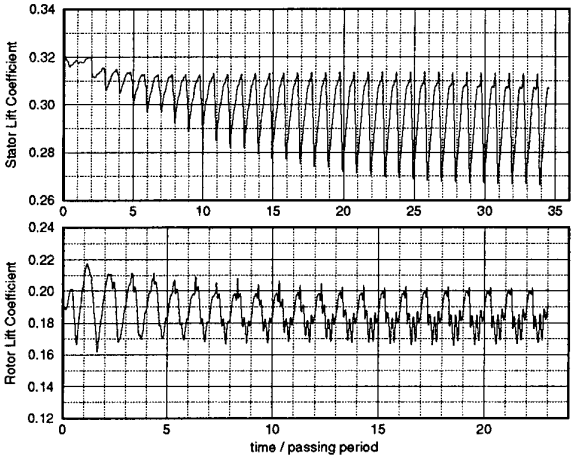

Figure 5: Lift history for VBI turbine stage: 40% spacing, fine grid.

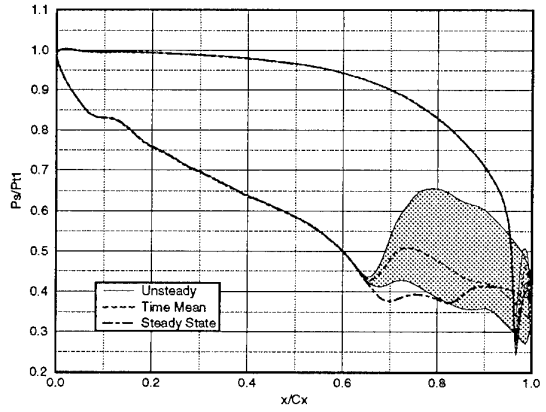

Figure 6: Vane surface pressure distribution: 20 % spacing, baseline grid

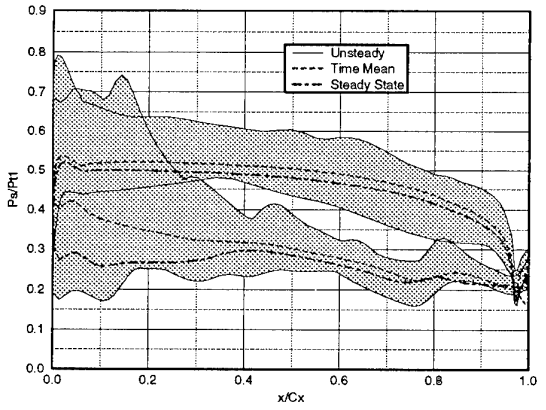

Figure 7: Blade surface pressure distribution: 20 % spacing, baseline grid

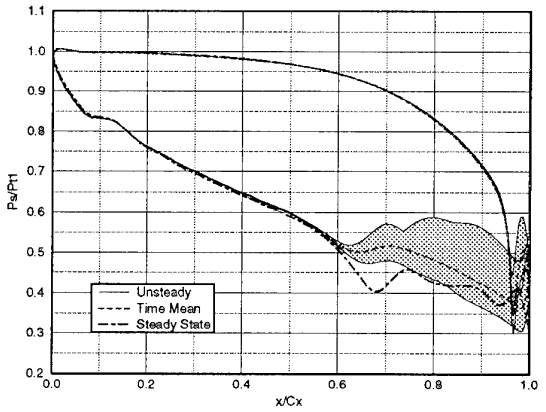

Figure 8: Vane surface pressure distribution: 40 % spacing, baseline grid

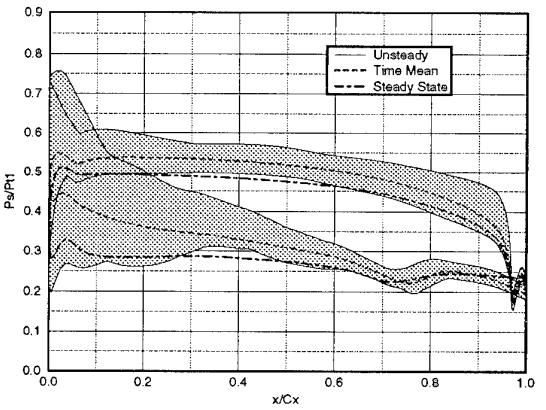

Figure 9: Blade surface pressure distribution: 40 % spacing, baseline grid

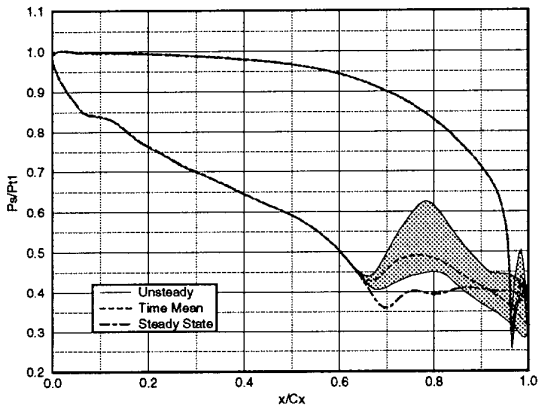

Figure 10: Vane surface pressure distribution: 60 % spacing, baseline grid

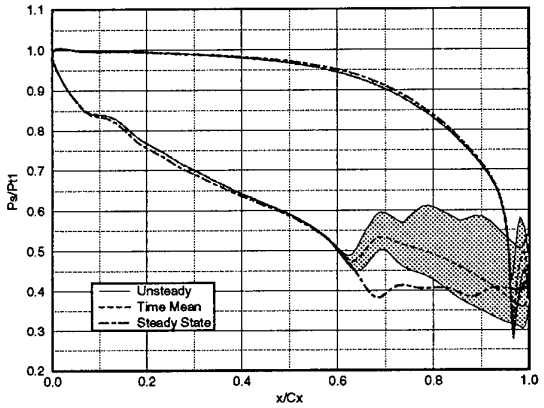

Figure 12: Vane surface pressure distribution: 40 % spacing, fine grid

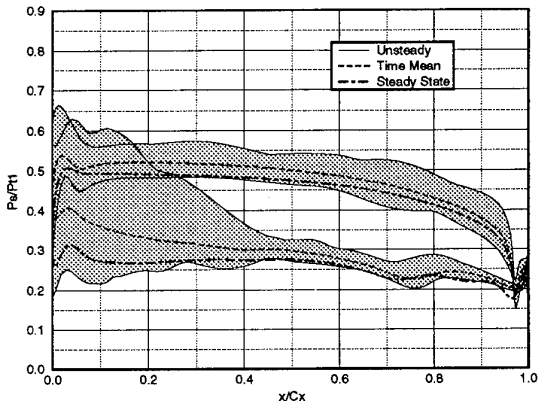

Figure 11: Blade surface pressure distribution: 60 % spacing, baseline grid

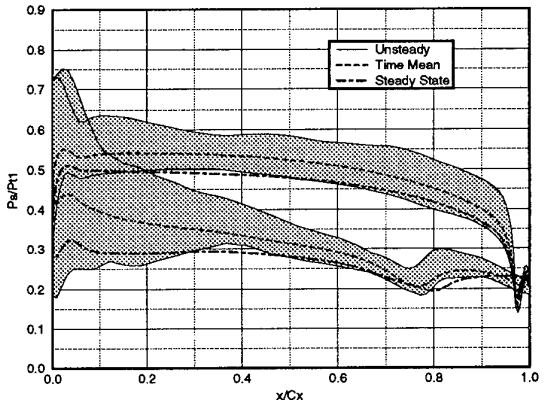

Figure 13: Blade surface pressure distribution: 40 % spacing, fine grid

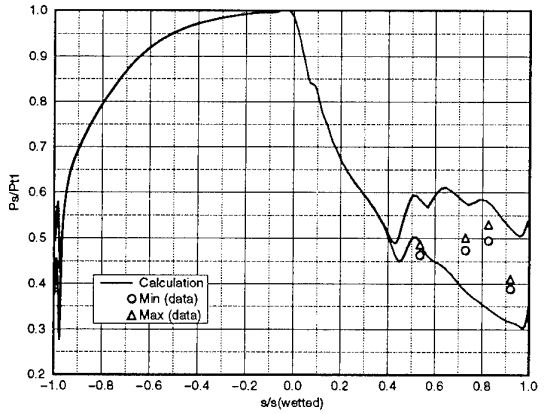

Figure 14: Comparison of computed vane surface pressure envelope with Calspan data: 40 % spacing, fine grid

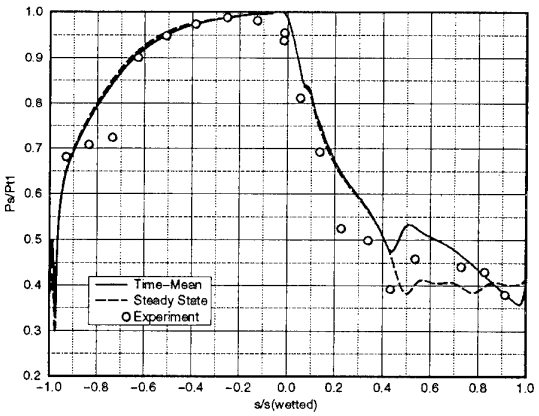

Figure 16: Comparison of computed time-averaged vane surface pressure distribution with Calspan data: 40 % spacing, fine grid

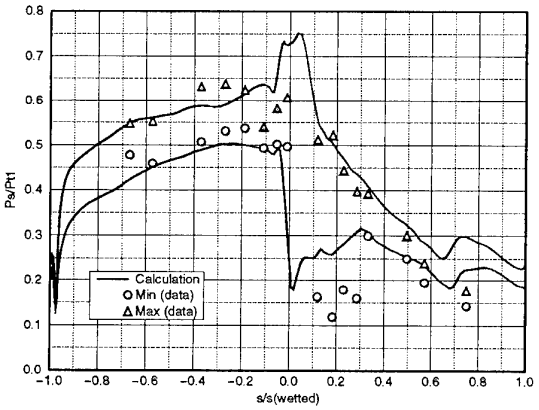

Figure 15: Comparison of computed blade surface pressure envelope with Calspan data: 40 % spacing, fine grid

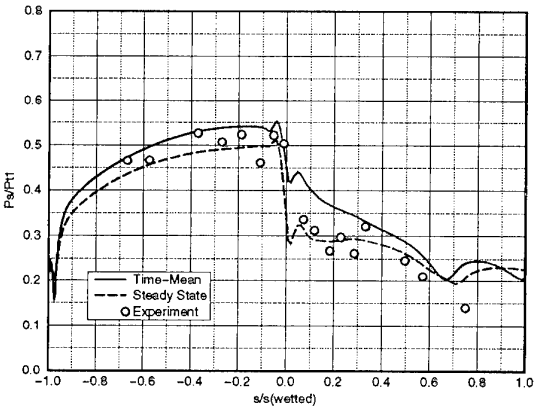

Figure 17: Comparison of computed time-averaged blade surface pressure distribution with Calspan data: 40 % spacing, fine grid

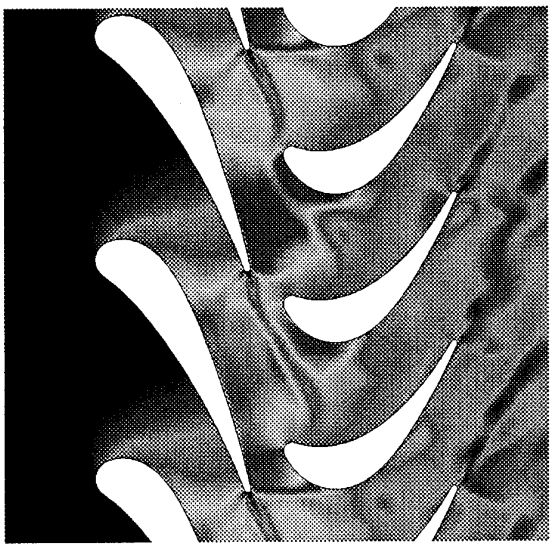

Figure 18: Shaded contour plot of instantaneous absolute Mach number: 20% spacing, baseline grid.

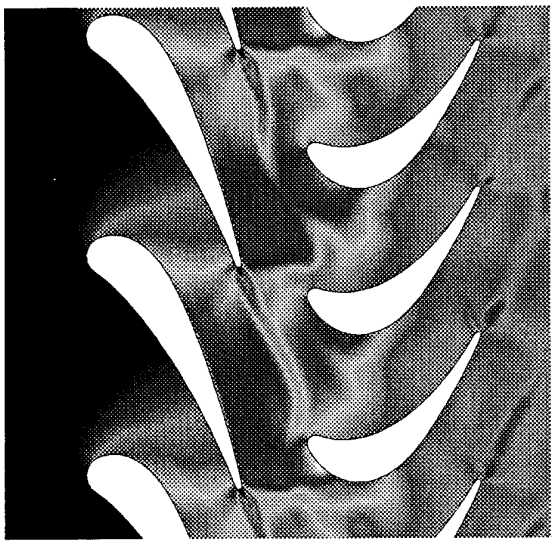

Figure 19: Shaded contour plot of instantaneous absolute Mach number: 40% spacing, baseline grid.

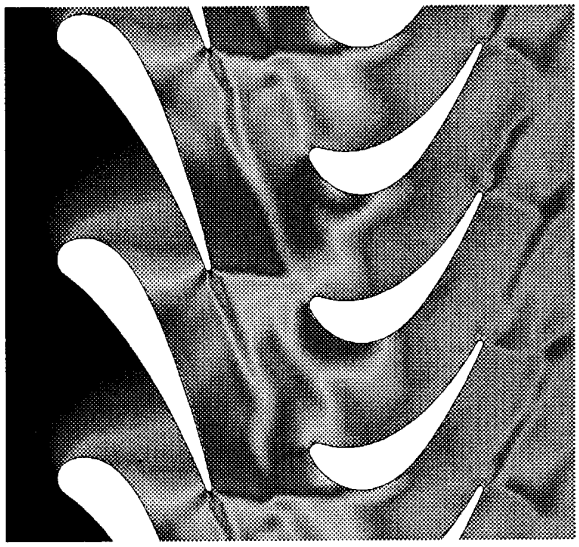

Figure 20: Shaded contour plot of instantaneous absolute Mach number: 60% spacing, baseline grid.

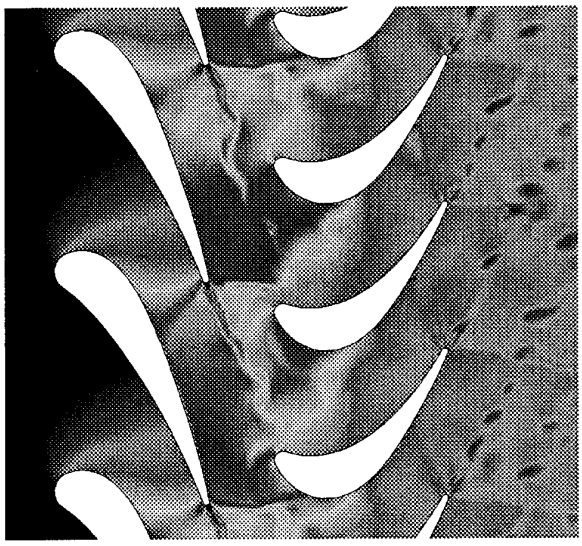

Figure 21: Shaded contour plot of instantaneous absolute Mach number: 40% spacing, fine grid.

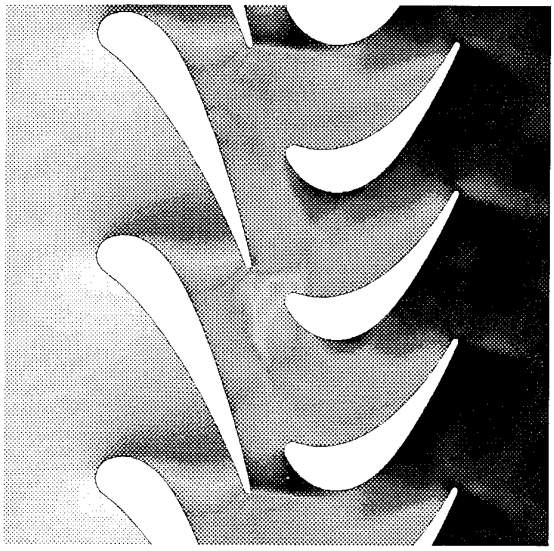

Figure 22: Shaded contour plot of instantaneous static pressure: 20% spacing, baseline grid.

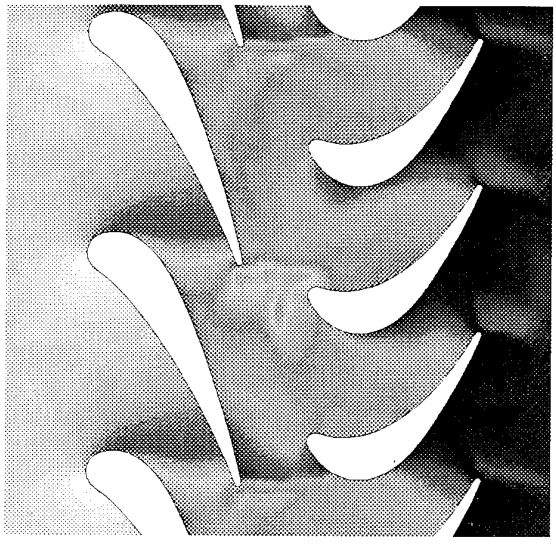

Figure 23: Shaded contour plot of instantaneous static pressure: 40% spacing, baseline grid.

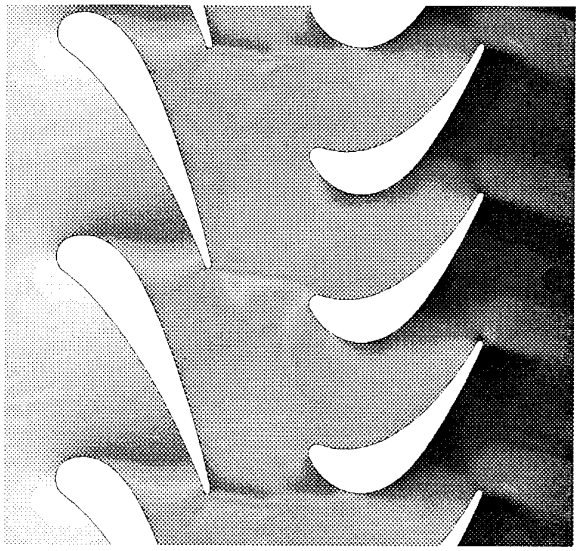

Figure 24: Shaded contour plot of instantaneous static pressure: 60% spacing, baseline grid.

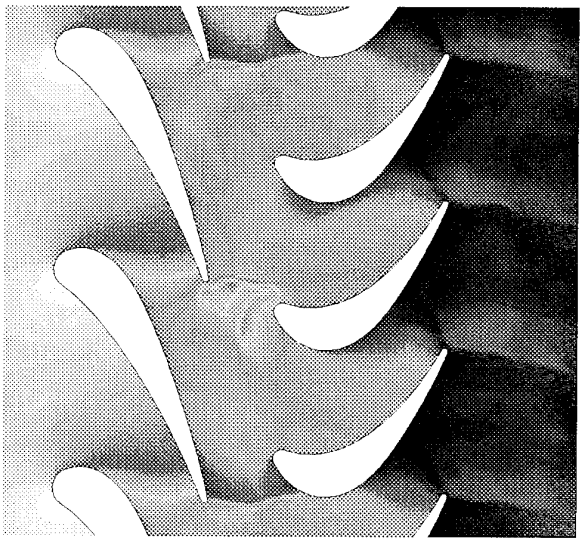

Figure 25: Shaded contour plot of instantaneous static pressure: 40% spacing, fine grid.

REFERENCE NO. OF THE PAPER: 5

DISCUSSOR'S NAME: F. Leboeuf, ECL, France

AUTHOR'S NAME: JW Griffin, FJ Kelecy, RA Delayney

Q: If the code would have run in an Euler mode, would you expect similar amplitude for the pressure fluctuation on the suction side of the vane?

A: Our experience with our Euler version of the code suggests that the pressure fluctuations would be greater than with the Navier-Stokes code.

REFERENCE NO. OF THE PAPER: 5

DISCUSSOR'S NAME: NW Harvey, Rolls-Royce, U.K.

AUTHOR'S NAME: JW Griffin, FJ Kelecy, RA Delayney

Q: Can you comment on the component of the loss specifically attributable to unsteadiness? For instance, have you calculated the separate steady vane and blade row efficiencies, combined them into a stage efficiency and compared that with the time-averaged value from the unsteady calculation?

A: No, we haven't done that, but your point is well taken. It would be interesting to compare those two efficiencies.

REFERENCE NO. OF THE PAPER: 5

DISCUSSOR'S NAME: C.H. Sieverding, VKI, Belgium

AUTHOR'S NAME: JW Griffin, FJ Kelecy, RA Delayney

Q:1 Between the axial planes x/Cx=0.2 and 0.6, the outlet flow angle changes from 70.7 deg to 72.1 deg. Can you comment on this change?

A:1 That change appears to be consistent with the change in loading on the vane at those two spacings. It is not surprising that the loading changes on the vane as a result of the change in strength of the interaction at those spacings.

Q:2 Did the authors compare the blade interference effects with both Navier-Stokes and Euler calculations? If so, which effects were the most important: those induced by the wake, or those due to the inviscid gradient field?

A:2 We did not perform direct comparisons with Euler and Navier-Stokes calculations for this study, but previous experience with Euler computations for this case suggests that the effect of the shock (inviscid effect) on the unsteady pressures is substantially larger than the effect of the wake.

Q:3 At x/Cx = 0.6, the difference between the steady state calculation and the time-averaged unsteady calculation is large. Is there an explanation for this? Did you perform calculations with even bigger differences?

A:3 I would not expect the time-mean of the unsteady solution and the steady state prediction to agree even at large spacings. This is because the steady solutions were obtained using vector diagram information from our turbine design system which accounts for loss by adjusting the streamtube thickness. Since loss is automatically predicted with the Navier-Stokes code, we are in effect accounting twice for the loss using the design system streamtube data. A better approach to obtaining a steady state prediction would be to assume no streamtube thickness variation and to use the predicted vane exit conditions as inlet conditions to the blade.

A Review of the Research on Unsteady Turbine Blade Wake Characteristics

G. Cicatelli **C.H. Sieverding**

von Karman Institute
72 Chaussée de Waterloo
B-1640 Rhode St. Genèse
Belgium

1. SUMMARY

The research on unsteady wake flows behind turbine blades is the orphan of turbomachinery research. The statement that blade wake flows are characterised by the presence of so-called von Karman vortex streets, is a common-place, but yet, only very few researchers concluded that this phenomenon deserved their attention. The paper attempts to summarise the available bits and pieces and provides the reader with the state of art of our present knowledge in this domain. In many circumstances, the authors have to rely on research results on flows behind cylinder.

Schlieren, interferometry and smoke visualisations are used to illustrate the existence of vortex street in a wide variety of cascade and flow conditions. The difference in the Strouhal number describing the vortex shedding frequency behind turbine blades and cylinders is explained and the effect of the vortical motion on the base pressure is discussed. A description of the vortex generation mechanism and the wake structure, developed for flows over cylinders, proves useful in the interpretation of the instantaneous stream lines in time varying turbine blade wakes containing large coherent structures.

2. INTRODUCTION

Turbine wakes occupy a central place in turbine stage flows. On one side the wake is the ultimate development stage of the blade boundary layers, and mirrors therefore the entire past history of their evolution along the blade suction and pressure side, their separation from the blade trailing edge and their subsequent merging process. On the other side the wake mixing process determines the inlet conditions to the following blade row which is exposed to important time varying variations of inlet pressure and temperature, of the flow angle and wake associated turbulence. The correct prediction of the wake evolution is evidently a pre-requisite for any trust-worthy calculation of blade row interference effects and therefore it is surprising to note that, compared to the research on the wake blade interference and the wake mixing process has received much less extension. The literature shows only a few examples of systematic studies of the wake evolution behind turbine blades: Raj and Lakshminarayana [1], Kiock [2], Mee et al. [3], Stastny and Safarik [4], Kapteijn et al. [5] Sieverding et al. [6]. Except for the first reference, reporting incompressible flow experiments, all the others investigations were done at transonic outlet Mach numbers. Stastny, Kapteijn and Sieverding find that the wake profiles follow very closely Gaussian distributions and are self-similar in the far wake. For the near wake, it is advantageous to adopt different wake shape factors for the pressure and suction sides of the wake. The afore mentioned investigations, however, do not provide any key to the understanding of the highly turbulent wake mixing process in which large scale coherent structures, the well known von Karman vortex street, play a dominant role as regards turbulence production, diffusion and dissipation. The development of fast response measurements techniques and "pattern recognition methods" allow at present a new look at the wake flow patterns.

This new experimental approach comes most timely as regards recent developments in viscous flow calculations. It is notorious that Navier-Stokes calculations using conventional mixing-length and 2-equations turbulence models fail to correctly predict the wake evolution behind turbomachinery bladings. The reason is their inability to deal with the highly non-isotropic character of turbulent separated flows and wake flows. Non-linear 2-equation models, Reynolds stress models and LES techniques are presently investigated with respect to their capability to deal with these types of flows. The assessment of these methods requires detailed information on turbulent wake characteristics. The combination of advanced numerical and experimental methods promises for the near future real progress in the understanding of unsteady blade wake flows. This moment appears to be appropriate to review our present knowledge in this domain. Over the years several singular attempts have been made to gain some inside into unsteady trailing edge flow characteristics, but apart from a few exceptions, the tests were done on relatively small size turbine blades with trailing edge dimensions too small for detailed investigation. Luckily the turbomachinery researches can benefit from the intense research on wake flow behind cylinders which is much less affected by geometrical constraints and the authors will also refer to those results.

Paper presented at the AGARD PEP 85th Symposium on "Loss Mechanisms and Unsteady Flows in Turbomachines", held in Derby, United Kingdom, 8-12 May 1995, and published in CP-571.

3. VISUALISATION OF THE VON KARMAN VORTEX STREET IN TURBINE BLADE WAKES

The unsteady character of turbine blade wakes is best illustrated by flow visualisation. Various techniques have been used: smoke visualisation at low speed, schlieren and interferometry at high speed. Lawaczeck and Heinemann [7] were probably the first to reveal the existence of von Karman vortices behind turbine blades. The authors observed vortex street behind very different types of blade shapes and over a wide range of Mach numbers from subsonic to supersonic flows, Fig. 1-a,b,c. The chord length is about 60 mm for all the blades and the trailing edge thicknesses are respectively 2,5 and 1 mm. The visualisation of these high frequency phenomena (the frequency of the vortex shedding in Fig. 1-c is of the order of 50 kHz), was made possible through the use of a flash light of 20 nano-seconds only.

Up to the subsonic Mach number range, the photos show the familiar alternating vortex street known from the flow behind cylinders. For blade 3, with a normal trailing edge shock system, the vortex street looks somewhat different. In the far-wake field the vortices form the usual alternating vortex pattern, i.e. pressure side and suction side vortices are 180° out of phase, while right behind the shock the first vortices appear to be in phase.

Carscallen and Gostelow [8], publishing recently a series of schlieren photographs behind a relatively large scale transonic nozzle blade with a thick trailing edge (c=175 mm, te/c=0.03), shed light upon 4 different vortex patterns for transonic downstream conditions referred to by the authors as:

a) von Karman: vortices are shed from pressure and suction surfaces 180° out of phase, Fig. 2-a.

b) Couples: vortex couples shedding in phase from blade surfaces, Fig. 2-b.

c) Doublets: vortices are shed 180°out of phase, but as doublets, Fig. 2-c

d) Hybrids: vortices are shed from the pressure side as twice the rate as from the suction side, Fig. 2-d.

These different patterns seem to occur over a Mach range in which the trailing edge shock system changes gradually from a normal to a fully developed oblique trailing edge shock with a closed triangular trailing edge base region, at which the emission of large vortices ceases.

The near wake flow patterns for the transition from a normal to an oblique shock system is described by Benelmouffok and Beretta-Piccoli [9] for a single airfoil in Fig. 3:

a) an open wake with no dead air zone and vortices shed from the blade surfaces,

b) a semi-triangular region with a dead air zone and vortices issuing in the recompression region,

c) a stable, closed dead air region,

Configuration (b) is said to be very unstable and may be the reason for the different vortex pattern in Fig. 2.

The visual spatial resolution of the vortex patterns depends of course on the size of the vortices (i.e. on the trailing edge thickness), on their frequency (function of the trailing edge thickness and velocity) and the exposure time of the schlieren system. Details of the enrolment of the trailing edge shear layers, their shedding from the trailing edge and

Fig. 1-a: Schlieren picture of a L.P. steam turbine rotor blade section with a thin trailing edge (from Lawaczeck and Heinemann) [7]

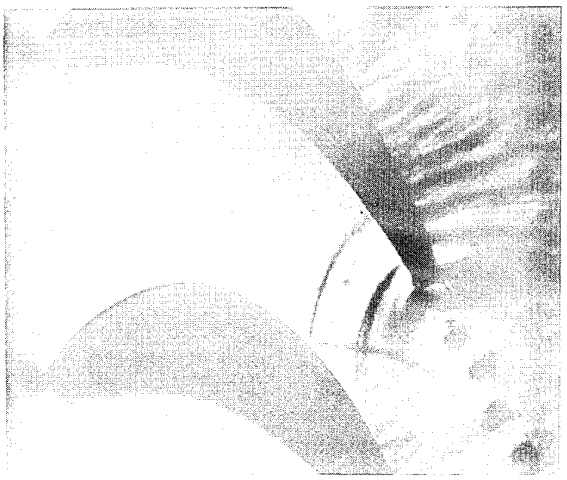

Fig. 1-b: Schlieren picture of a H.P. gas turbine rotor blade section with high deflection M_2=0.8 (from Lawaczeck and Heinemann) [7]

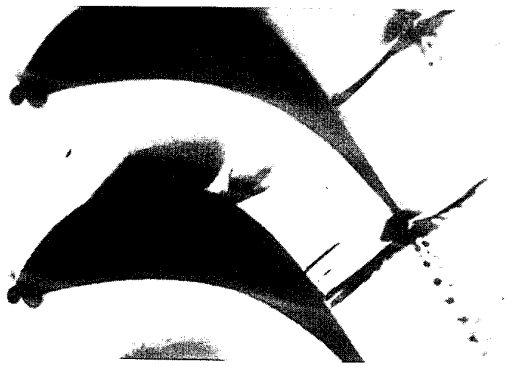

Fig. 1-c: Schlieren picture of a high turning steam turbine rotor blade section with thin trailing edge M_2=0.95 (from Lawaczeck and Heinemann) [7]

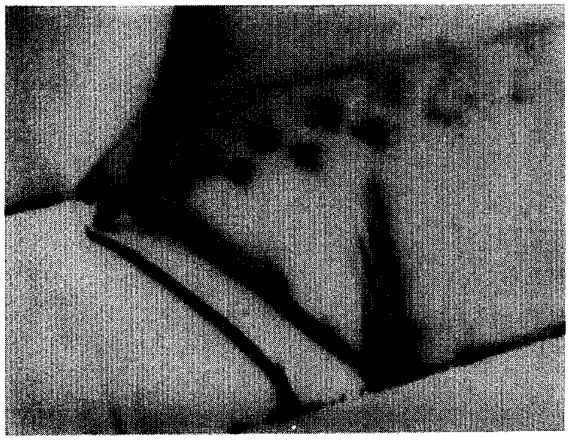

Fig. 2-a: von Karman: vortex shed from pressure and suction surface 180° out of phase (from Carscallen and Gostelow) [8]

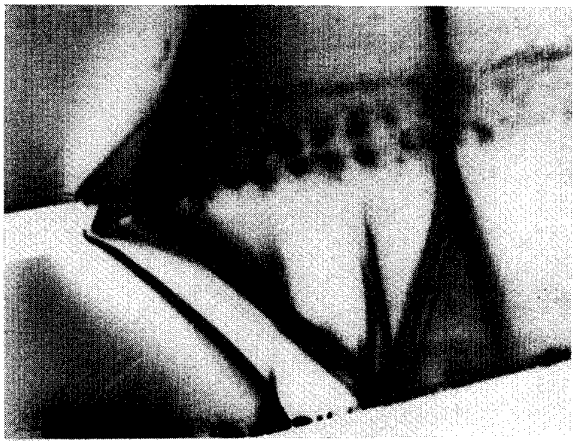

Fig. 2-b: Couples: vortex couples shed in phase from blade surfaces (from Carscallen and Gostelow) [8]

Fig. 2-c: Doublet: vortex shed 180° out of phase but as doublets (from Carscallen and Gostelow) [8]

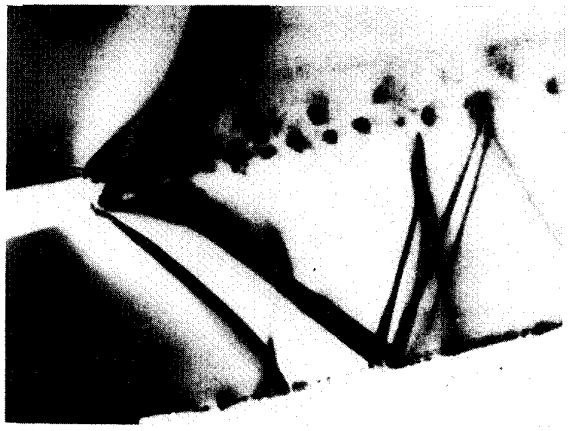

Fig. 2-d: Hybrids: vortices from the pressure side as twice the rate as from the suction side (from Carscallen and Gostelow) [8]

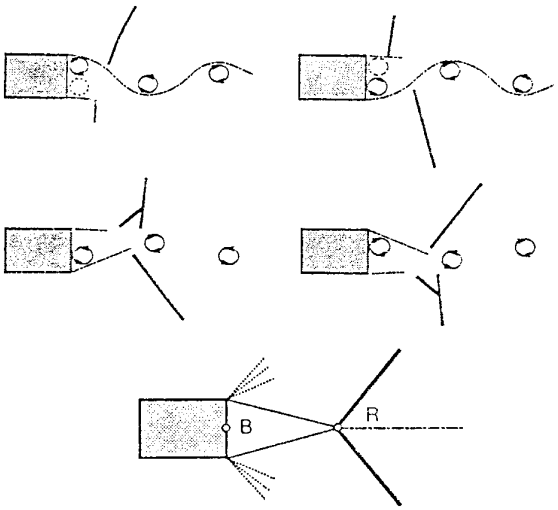

Fig. 3: Transition from a normal to an oblique trailing edge shock system (from Benelmuffok and Beretta-Piccoli)[9]

their downstream evolution are dramatically demonstrated in the schlieren picture in Fig. 4 taken at von Karman Institute on a blade model simulating the overhang section of a transonic turbine cascade. The trailing edge thickness was 6 mm, the time duration of the flash lamp was 8-10 nano-seconds.

Similar details as in Fig. 5 were obtained by Han and Cox [10], with a smoke visualisation on a very large scale nozzle blade (c=533 mm or 21 inch) at low speed. The authors found much sharper and well defined contours of the vortices issued from the pressure side and concluded that this implied stronger vortex shedding from this side and attributed this to the circulation around the blade. A difference in the intensity of the vortex shedding from the suction side and pressure side had already been observed before by Lawaczeck and Heinemann [7], who measured the vortex intensity in the two vortex rows and found a higher intensity for the pressure side than for the suction side.

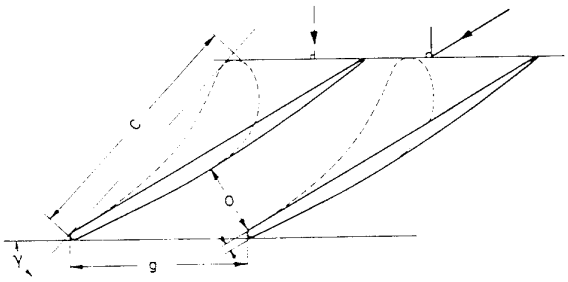

Fig. 4: Schlieren picture of the von Karman vortex street behind a large scale turbine blade cascade model at transonic outlet Mach number

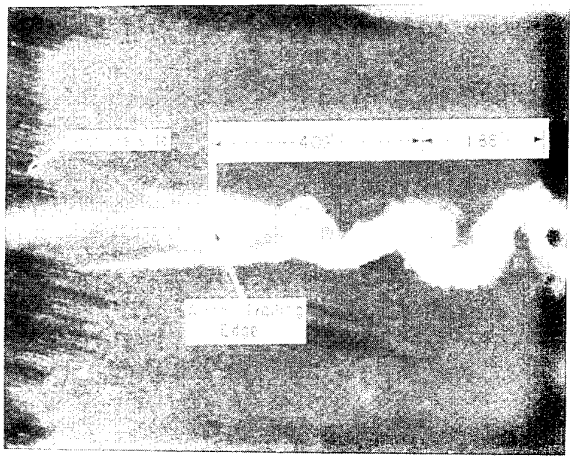

Fig. 5: Smoke visualisation of the von Karman vortex street behind a large scale low speed nozzle blade (from Han and Cox) [10]

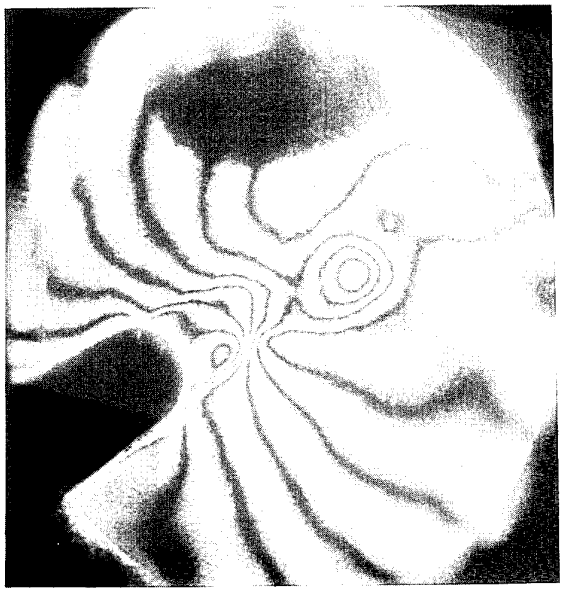

Fig. 6: Interferogram of the von Karman vortex street behind a large scale turbine guide vane at outlet Mach number M_2=0.4

Interferometry has frequently been used for visualisation and quantitative analysis of vortex patterns behind flat plates and cylinders but rarely for wake flow studies behind turbine blades. Either the trailing edges were so small that interferograms did not give more than a faint hint to the existence of the vortex street, Sari [11], or the interferograms are taken at high supersonic outlet Mach numbers, at which conditions vortices do not appear in the wake (Bryanston Cross et al. [12]).

As part of a BRITE EURAM project on "Time varying wake flow characteristics behind flat plates and turbine blades" the von Karman Institute attempts to obtain decent interferograms of the vortex patterns behind a large scale turbine blade at a downstream Mach number of 0.4 with holographic interferometry. Using the infinite fringe technique the density variations are too small for a clear description of the vortex pattern, Fig 6. Better results are expected through the use of the differential interferometry technique developed at IMFL (Institut de Mechanique de Fluides de Lille, France) and used very successfully in the low subsonic Mach range for the flow behind flat plates, Desse [13].

4. VORTEX SHEDDING FREQUENCY

The vortex shedding frequency "f" is usually expressed under the form of the Strouhal number:

$$St = \frac{f \cdot d}{u}$$

In cascades, the reference velocity "u" is typically taken equal to the downstream velocity, for cylinders "u" represents the upstream velocity and for flat plates, the free stream velocity at the trailing edge or something similar.

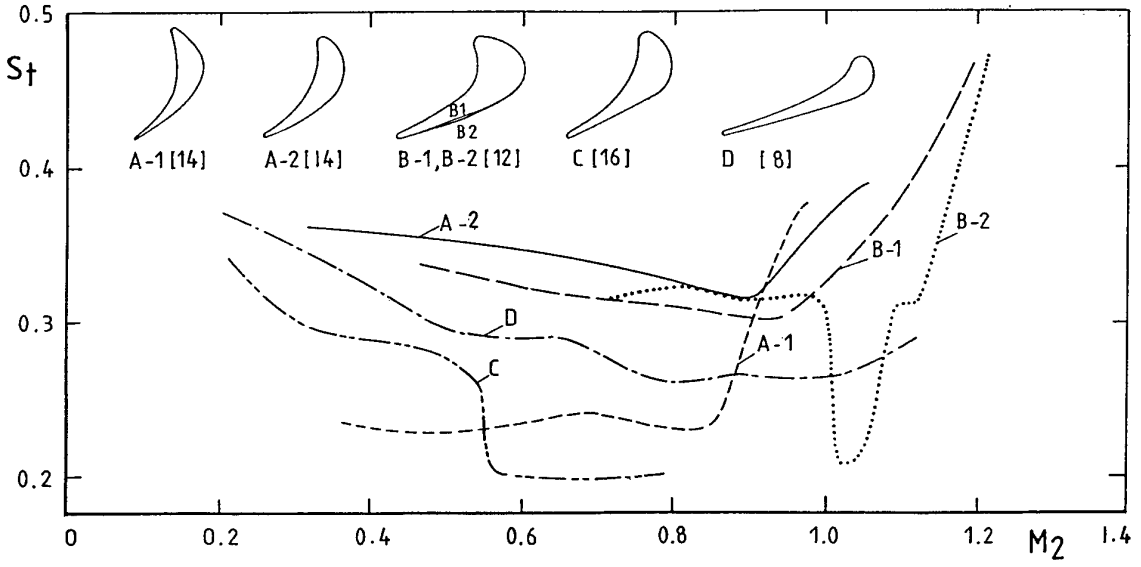

Fig. 7: Strouhal numbers for various turbine cascades over a large range of Mach numbers

The most important data set were provided by Heinemann and Butefish [14], 8 cascades ranging from low turning tip sections to high turning hub sections, Bryanston-Cross and Camus [15], 2 two highly turning rotor blades differing by their rear suction side curvature, Sieverding and Heinemann [16], 1 nozzle guide vane and 2 higher turning rotor blades selected for the differences of their load distribution, and Carscallen and Gostelow [8], 1 high turning nozzle guide vane. All blades were tested over a wide range of Mach numbers extending from the low subsonic into the transonic domain. Except or the tests of Bryanston-Cross and Camus, who performed all tests at constant Reynolds number, all other tests were conducted with the Reynolds number increasing with the downstream Mach number. None of the authors provided measurements of the blade boundary layer characteristics.

Six blades have been selected for comparison in Fig. 7 to provide an idea of the wide range of Strouhal numbers one may encounter on turbine blades (for clarity the original data points have been omitted from the curves). Note, that the profiles, denoted as A1 and A2 from Heinemann and Butefish correspond to the schlieren photographs in Fig. 1-b and 1-c, respectively. Table I provides additional information on blades characteristics and Reynolds numbers.

Irrespective of the large differences between the curves, one observes two general trends: (a) a decreasing or constant St number in the subsonic domain and (b) an increase of the St number in the transonic domain.

Sieverding and Heinemann [16] explained the wide range of Strouhal numbers in the subsonic range by differences in the boundary layer state of the trailing edge. The authors arrived at this conclusion through flat plate tests which not only allowed them to measure the boundary layer characteristics but also to modify them. The flat plate model was designed to preserve natural laminar boundary layer all along its surface, but trip wires allowed to change the shape factor from H=2 for a natural boundary layer development, to H=1.4 with trip wires. The Strouhal number changed accordingly from St=0.31 for the laminar state to St=0.24 for the turbulent state and an intermediate value for a mixed configuration, i.e. a laminar boundary layer on one side and a turbulent on the other side. The latter case is frequently encountered on turbine blades. For example, the suction side boundary layer of a front loaded blade like that of Fig. 1-c is likely to transition already at relatively low Reynolds number while the pressure side boundary layer may remain laminar to considerable higher Reynolds numbers. The lesson learned from these flat plate tests then enabled the authors to interpret the wide variations of Strouhal numbers observed in subsonic cascade tests as changes due to differences in the blade boundary layer characteristics. As regards the subsonic range in Fig. 7 one can say with some degree of confidence that:

a) St numbers of the order of St=0.2-0.23 indicate that the boundary layers at the trailing edge are turbulent on both the pressure and suction side.

b) Strouhal numbers St>0.35 indicate a laminar boundary layer state on both sides.

c) Strouhal numbers between these two limits indicate a transitional boundary layer on one or both sides.

Blade C is a good example for the latter. Its suction side velocity distribution is characterised by a very strong front velocity peak leading inevitably to a fast transition and a full turbulent boundary layer on the rear suction side. The initial smooth variation of St up to an outlet Mach number of M_2=0.54 is then an indication of the progressive change from a laminar to a transitional state of the pressure side

Authors	Chord [mm]	te/c	Re_c	Re_d
Heinemann Butefish [14]	60 60	0.052 0.014	$4\cdot10^5 - 9\cdot10^5$	$2\cdot10^4 - 4.7\cdot10^4$ $5.6\cdot10^3 - 1.2\cdot10^4$
Bryanston-Cross Camus [15]	--	0.04 0.04	$7.1\cdot10^5$ constant over the entire Mach range	$2.8\cdot10^4$
Carscallen Gostelow [8]	175.3	0.036	$2.5\cdot10^5$ at M=1.2 For inlet conditions	--
Sieverding Heinemann [16]	100	0.045	$0.4\cdot10^6 - 1.6\cdot10^6$	$1.8\cdot10^4 - 7.2\cdot10^4$

Table I

boundary layer, while the sudden drop at M_2=0.54 indicates the sudden change to a full turbulent boundary layer.

The increase of the Strouhal number in the transonic domain is probably related to the strong modification of the base flow region during the formation of the trailing edge shock system, see Fig. 3, and is therefore mainly a Mach number effect. The local sudden drop in the Strouhal number for blade B2 between M_2=1.0 and 1.1, however, is apparently linked to the occurrence of a boundary layer separation from the rear suction side as explained by the authors of this particular study.

The Strouhal numbers in turbine cascades are often compared to those measured for flows over cylinders. Basing the Reynolds number of turbine blades on their trailing diameter the values for nearly all cascades lie in the range $10^4 < Re_d < 2\cdot10^5$, (except for low speed conditions). The Strouhal numbers for cylinders over this range are typically of the order of St=0.18-0.21, see Fig. 8, compared to St numbers between 0.2 and 0.45 for cascades. The difference is due to the entire different flow conditions for both cases.

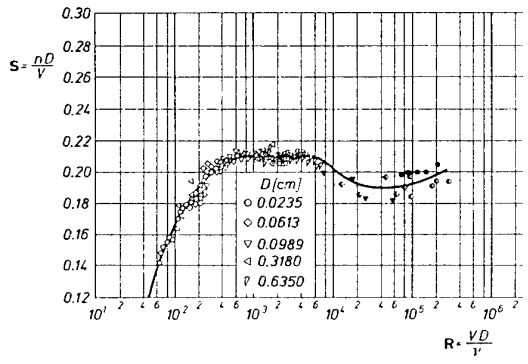

Fig. 8: Strouhal numbers in sub-critical Reynolds number range for flow over cylinders (from Schlichting) [32]

In the so-called sub-critical Reynolds number range for cylinders, i.e. $Re_d < 2.5\cdot10^5$, the boundary layers separate in a laminar state at about 80° from the forward stagnation point but the shear layers have a defined turbulent character due to the strong velocity peak preceding the separation. Hence it is the state of the state of the shear layers and not the state of the boundary layers which determines the vortex shedding frequency. Sieverding and Heinemann [16] come to a similar conclusion by comparing Strouhal numbers for blades and plates with rounded and sharp cut trailing edges. The much lower Strouhal numbers for the latter geometry are attributed to the early transition of the starting shear layers induced by the trailing edge discontinuity.

5. VORTEX SHEDDING AND BASE PRESSURE

The best way to elucidate the relation between the vortical activity in the wake and the base pressure is to inhibit or delay the formation of the large coherent wake structures. Splitter plates are a classical mean to destroy coherent wake structures as demonstrated by Morkovin [17] for flows over a wedge profile at a Mach number M=0.55 and a Reynolds number based on the base height of $Re_d = 2.7\cdot10^5$, by

(a) allowing the separation shear layer to grow increasing thus the local vorticity in the shear layer in comparison with the net vorticity across the wake and

(b) allowing 3-d effects to grow within the shear layers.

Roskho [18] showed that a splitter plate fixed to the rear of the cylinder resulted in a decrease of the base pressure coefficient from 1.4 to 0.6 thus reducing considerably the drag.

Besides splitter plates, trailing edge blowing was found to be an efficient mean for delaying or inhibiting vortex formation in wakes behind bluff bodies (see e.g. Bearman [19] and Wood [20]). This method is of particular interest to turbine designers because of its practical use for blade trailing edge cooling.

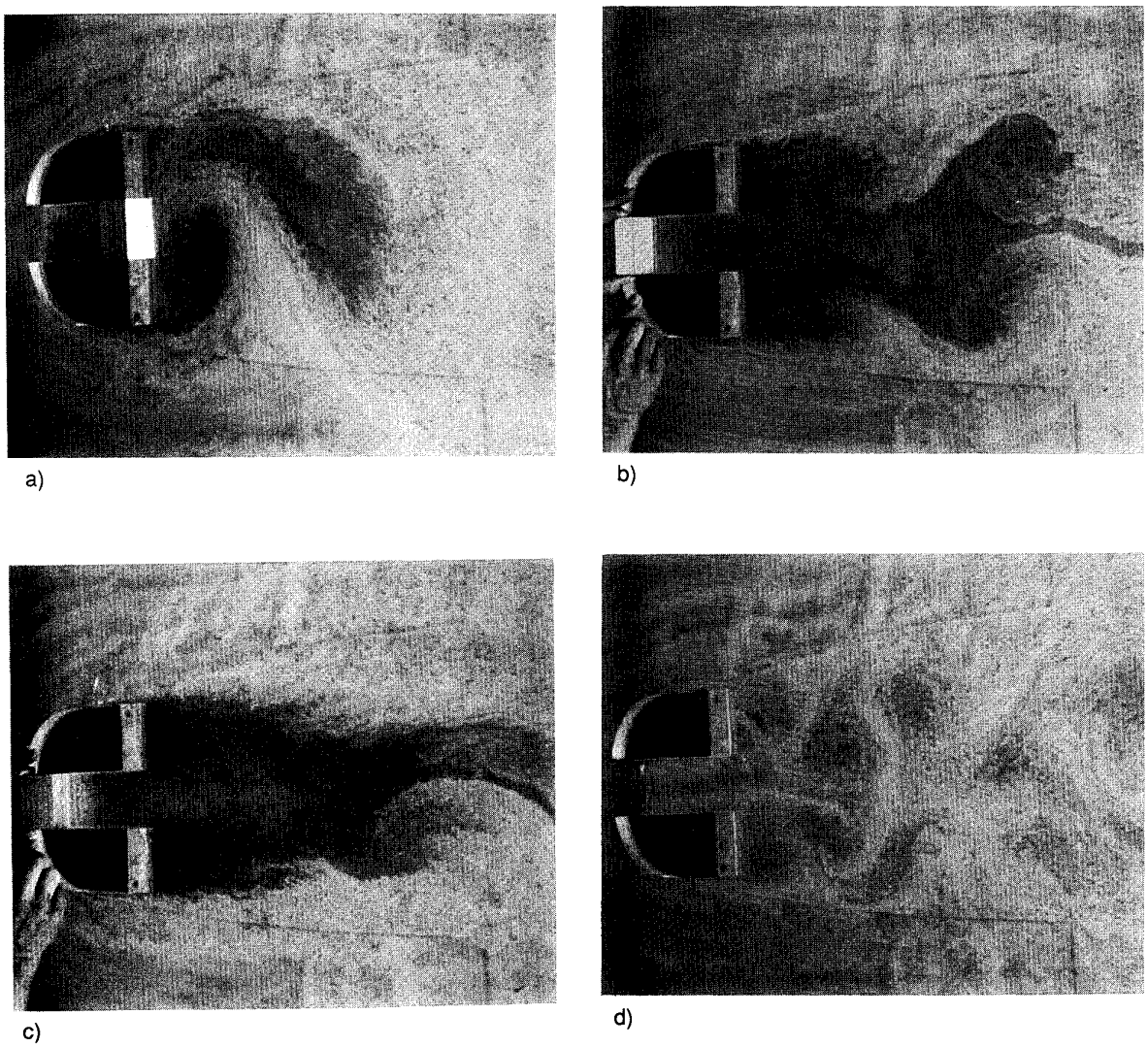

Fig. 9: Water table tests demonstrating the effect of trailing edge ejection on vortex formation behind a bluff body

The effect of trailing edge ejection on the wake structure behind a bluff body was studied at VKI first in water table tests, Fig. 9. The model consisted of two halves separated by a central passage closed by a movable block. The effect of fluid ejection from the base region is obtained by lifting slightly this block allowing water to pass through the centre of the model and mix with the wake. The photographs are taken with a slight oblique view onto the model base.

It is evident from Fig. 9-b that even small fluid ejection rates have already a stabilising effect on the oscillating wake structures: the lateral displacements are reduced, the vortex size shrinks and the vortex formation is delayed. Fig. 9-c presents the maximum length of the stabilised wake region. Any further increase of the ejected fluid velocity will result in a situation similar to that in Fig. 9-d, for which the central block has been entirely removed. In this case the fluid velocity through the model base is of the same order of magnitude as the outer flow and each model half sets up its own vortex street but with a much higher frequency as in Fig. 9-a due to the smaller trailing edge thickness.

Very similar visualisations were obtained recently at VKI by Cicatelli on the before mentioned blade model simulating the overhang section of a transonic turbine blade. Schlieren photographs taken with a nano-light source are shown in Fig. 10. At low ejection rates (Fig. 10-a) the wake opens and the shear layers extend much further downstream allowing the vortex layers to get thicker relative to their lateral distance and more distorted. The vortex formation appears to be entirely inhibited at this ejection rate. Only small scale random turbulence is still present. The disappearance of the large scale vortices also leads to a stabilisation of the shock waves.

At very high ejection rates with coolant ejection velocites equal to the main stream velocity, Fig. 10-b, new vortex streets are formed individually behind the pressure side and suction side.

Results confirming the effect of coolant flow ejection on the base pressure of turbine blades are reported by Michel and Kost [21] and Sieverding [22]. Both sources demonstrated a strong increase of the base pressure at low coolant flow rates

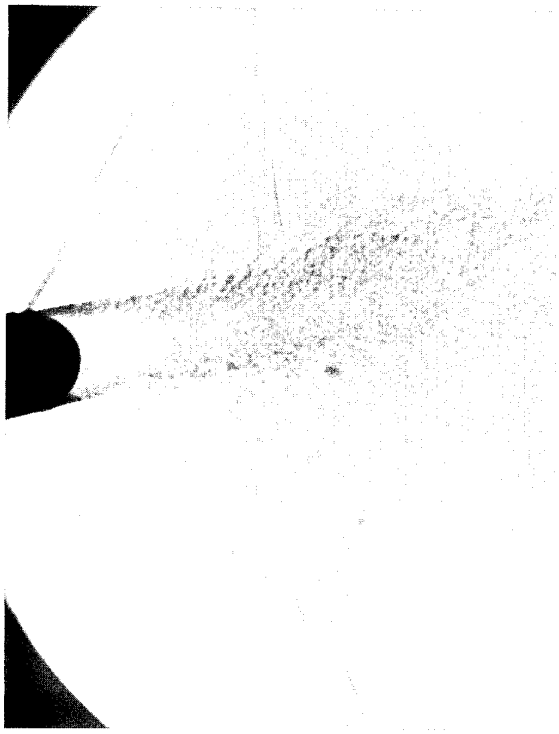

Fig. 10-a: Wake behind large scale turbine blade cascade model (Fig. 4) at low trailing edge ejection rate

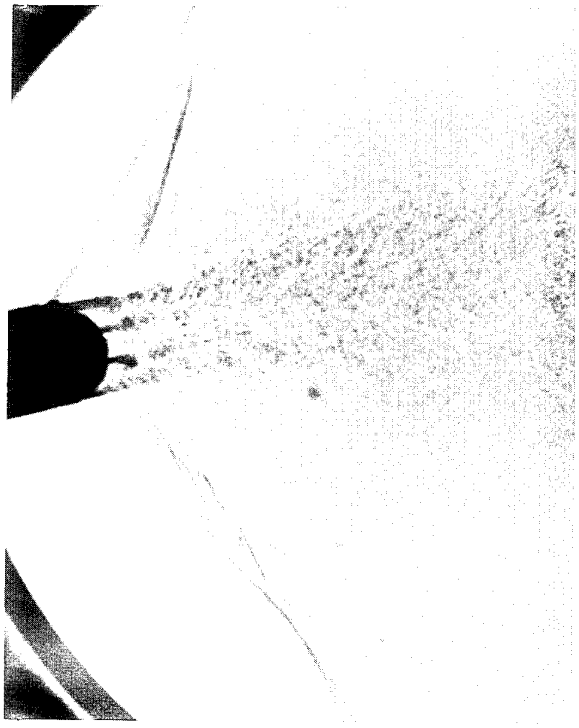

Fig. 10-b: Wake behind large scale turbine blade cascade model (Fig. 4) at high trailing edge ejection rate

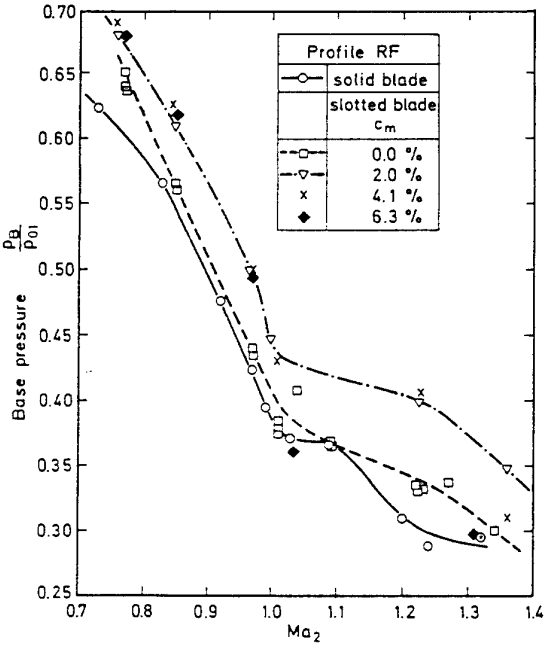

Fig. 11-a: Base pressure variation in function of outlet Mach number and coolant flow rates (from Michel and Kost) [21]

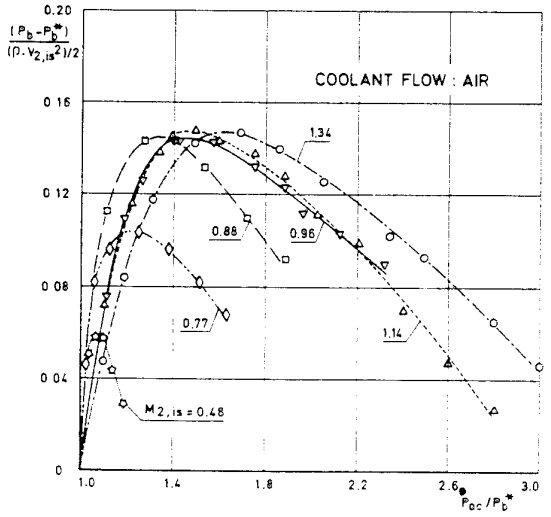

Fig. 11-b: Base pressure rise in function of coolant flow ejection pressure ratio from subsonic to supersonic outlet Mach numbers(from Sieverding) [22]

C_m, respectively low coolant pressure ratios π (total pressure of coolant flow P_{0c} non-dimensionalized by base pressure in absence of coolant ejection P_b^*), followed by a gradual decrease of the base pressure with higher coolant flows, Fig. 11-a,b.

6. VORTEX FORMATION MECHANISM AND WAKE STRUCTURE

For a description of the generation of the vortical wake structures and their role as regards turbulent production, diffusion and dissipation, we have to rely entirely on the large amount of research work on flow over cylinders.

Following Gerrard [23] the vortex formation mechanism involves a relationship between the size of the formation region, the strength of the vortices and the vortex shedding frequency. The author defines the end of the formation region as the point on the wake axis closest to the trailing edge where a hot wire signal shows a clear defined peak, characteristic of the vortex shedding. The model proposed is illustrated in Fig. 12 where the arrows show the path of the fluid: it is partly entrained by the growing vortex and partly by the shear layer upstream the vortex. The growing vortex is fed by the circulation existing in the oncoming shear layer until the vortex is strong enough to entrain fluid from the other shear layer bearing vorticity of opposite circulation. When the quantity of entrained fluid is sufficient to cut off the supply of circulation to the growing vortex (because of the cancellation of vorticity by the oncoming fluid marked with opposite vorticity) than the vortex is shed. The formation region length is determined by the amount of fluid crossing the wake; in turn this length is directly related to the vortex shedding frequency. Increasing the Reynolds number, the rate of entrainment of fluid crossing the wake tends to increase and this tendency determines a shrinkage of the formation region length.

Parallel, there is another characteristic length that plays a key role in determining the shedding frequency: the shear layer thickness or following Gerrard "the diffusion length". The importance of the shear layer thickness has been recognised also by Berger [24]. A turbulent shear layer results is being more diffuse, then it takes longer for the circulation to be carried across the wake in a sufficient concentration to determine the beginning of the shedding. It may be suggested that the shedding frequency is the result of the balance between a shrinkage in the formation region size and an increase of diffusion length. The final result is the constancy of the Strouhal number for cylinders for the entire sub-critical regime. Moreover if the state of the shear layer is modified, it results in a drop of the Strouhal number.

During the last decade several researchers attempted the interpretation of the physics of the wake using the concept of coherent structures. The case of cylinders is again the only one for which an in-depth investigation has been made.

The attempts to perform a clear eduction of large scale structures in the wake started with Cantwell [25] following the growing interest in coherent structures related to turbulent phenomena. The first complete study on this problem is due to Cantwell and Coles [26]. Hussain and Hayakawa [27] performed eduction of large scale structures in the wake of a cylinder for a Reynolds number of $1.3 \cdot 10^4$ based on the cylinder diameter.

Since a coherent structure is a large organised motion of turbulent fluid with coherent vorticity concentration, then the vorticity is the optimal quantity needed to identify coherent structures.The following discussion refers to Fig. 13.

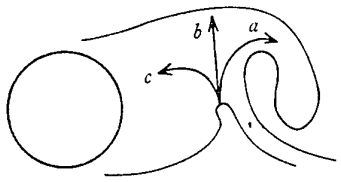

Fig. 12: Vortex formation mechanism (from Gerrard)[23]

In terms of vorticity the wake can be described using the topological notation as a set of centres which characterise the location of a peak of coherent spanwise vorticity and saddles located between coherent vorticity structures and defined by a minimum of coherent spanwise vorticity. Further information on the evolution of the wake can come from the estimation of Reynolds stresses and turbulence production contours, in comparison with a topological description of the wake. Incoherent turbulence intensity has its maximum near the centre. The intensity is higher at the back than at the front of the structure. This is explained with the fact that the turbulence is produced around the saddle point and then accumulated at the back of the structure. The distribution of incoherent Reynolds stresses shows a peak around the saddle point with the contour shape somewhat aligned with the braid or the diverging separatrix at the saddle. The strain rate <S> has also the highest value around the saddle point. This can be explained as a direct consequence of the intense stretching process induced by the predominant spanwise vortices. But because there is not sufficient spanwise vorticity in the saddle region, than the vorticity here should be aligned mostly in the longitudinal direction. Thus the successive spanwise vortices seem to be connected by ribs, that are longitudinal smaller scale vortices of alternated sign. Kiya and Matsumura [28] through frequency analysis of the wake signal concluded that the ribs between spanwise rolls must be responsible for the distribution of frequency in the different random contribution.

Fig. 13 provides a reasonable explanation for most experimental data available up to now. The predominant spanwise vorticity of the primary structures induces motion of the external fluid toward the wake region along the converging separatrix (solid arrows in Fig. 13-a). The fluid advected to the saddle, picks up the rotation of the ribs and is subjected to the vortex stretching along the diverging separatrix: this is the way by which smaller scale (almost incoherent) turbulence is produced in the saddle region. The turbulence production is related to the stretching of these ribs by adjacent (nominally spanwise) rolls that would increase the spinning of the ribs (Fig. 13-b). This hypothesis is in contrast to the accepted notion that turbulence production first occurs in the longitudinal (u) component, then is convected into transverse (v,w) components by the influence of static pressure fluctuations (Tennekes and Lumley [29]).

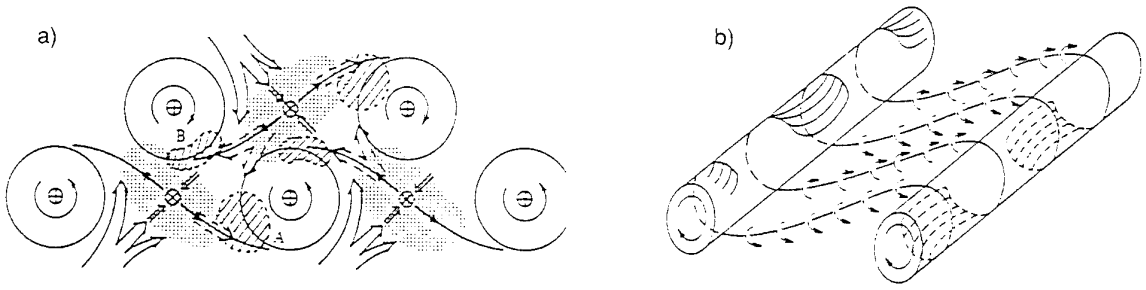

Fig. 13: Pictorial description of the wake structure (from Hussain and Hayakawa) [27]

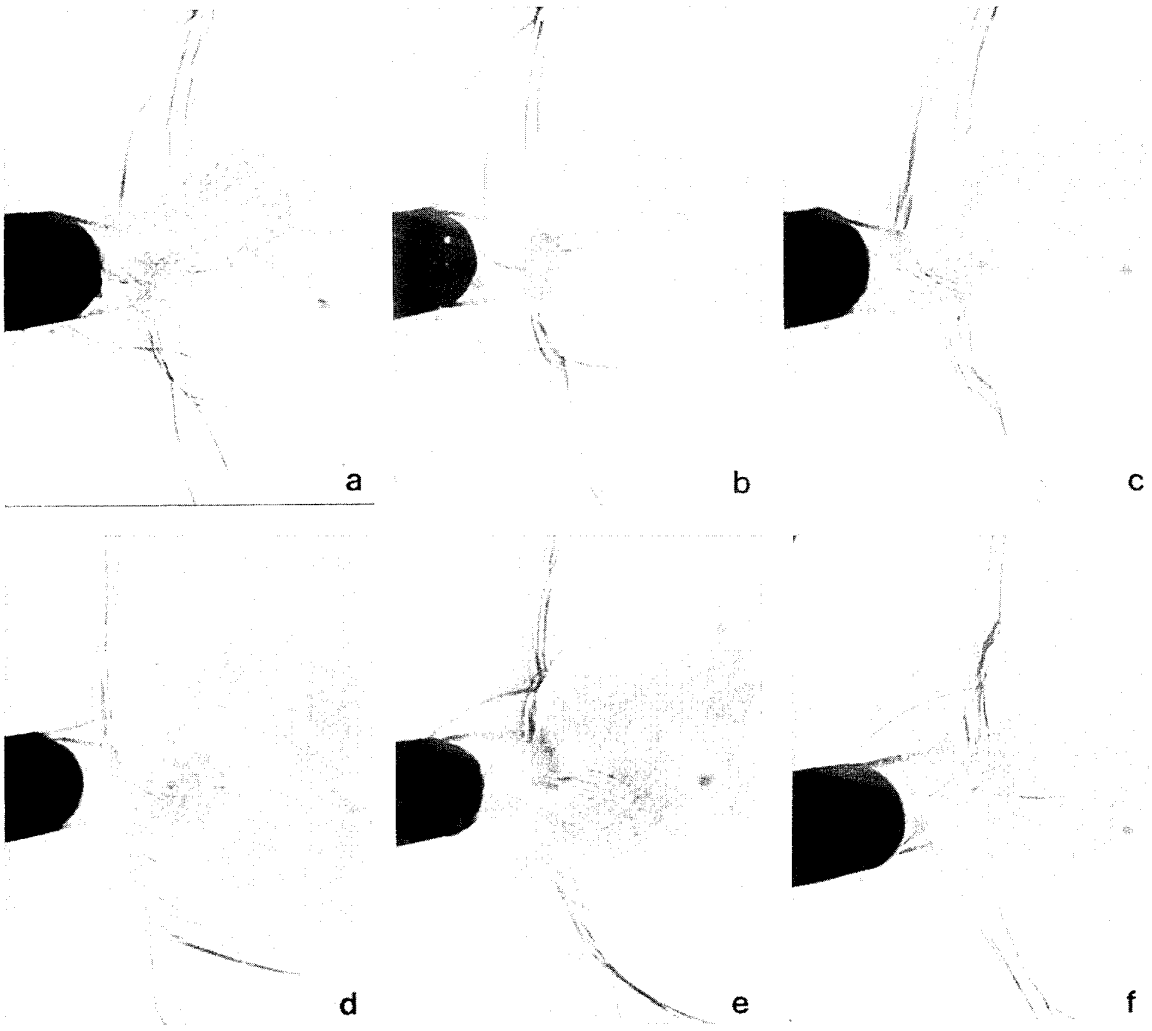

Fig. 14: One half vortex shedding cycle behind transonic turbine blade model (Fig. 4).

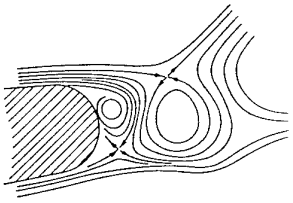

Fig. 15: Sketch of the instantaneous streamlines in the near wake region (corresponding to Fig. 14-d).

7. INTERPRETATION OF TURBINE BLADE WAKE VISUALISATIONS

The topological description of the wake flow patterns in the previous section is useful in the interpretation of the schlieren photographs in Fig. 14 showing one half cycle of the vortex shedding process behind the transonic turbine blade model of Fig. 4. The photographs were taken randomly and are arranged in sequential order following the growth of the pressure side vortex (pressure side up).

Let us first comment briefly on the most striking flow features:

- The pressure side shear layer angle is varying from about -18° to about +4° with respect to the pressure surface. The suction side shear layer angle variations are of the same order of magnitude but 180° and off phase.
- Although the shear layers do not necessarily separate tangential from the blade surface, their angle is certainly a measure for the local static pressure at the point of separation, i.e. high negative angles indicate a low local static pressure, positive angles a high static pressure. The implication is that the time varying base pressure distribution around the trailing edge is not uniform since the pressure in the separation regions fluctuate with opposite signs.
- The outwards moving shear layers generate sound waves which interact with the trailing edge shocks i.e. Fig. 14-d,e,f.
- The shock waves stands approximately on the centre of the vortex and moves downstream with the growing vortex until the formation of a new vortex.

The enrolment of the shear layer into a vortex drains free shear fluid far beyond the wake centre line.

- The schlieren photographs disclose the existence of embedded shocks in the wake.

Based on the topological description of the vortex patterns in the previous chapter, Fig. 15 presents the instantaneous streamlines corresponding to the schlieren picture in Fig. 14-d. Centres and saddles as loci of minimum and maximum pressure are clearly indicated. The instantaneous streamlines define the "alleyway" of fluid crossing the wake. In this virtual "channel", defined by two centres, the fluid is accelerated and then recompressed by the following saddle point. This recompression process starts with a normal shock as a proof that the transverse velocities through the wake can be of the same order of magnitude of the free stream flow. The original photographs show clearly that the embedded shock moves downstream with the vortices.

Apart from the embedded wake shocks another interesting observation is the presence of high frequency large eddies in the shear layers. These structures are very clearly visible on the original photographs of Fig. 14-d, but do not show up on the print. Similar observations were made by Dymant and Gryson [30] for the flow behind a flat plate at Mach 0.6, Fig. 16. The authors ascribe their origin to the instability of the free boundary which follows separation. The emitted eddies undergo successive coalescence the process of which is explained by a simplified theory.

Unal and Rockwell [31] in their studies on absolute and convective instability in the wake of cylinders have detected the existence of two well defined frequencies: one related to

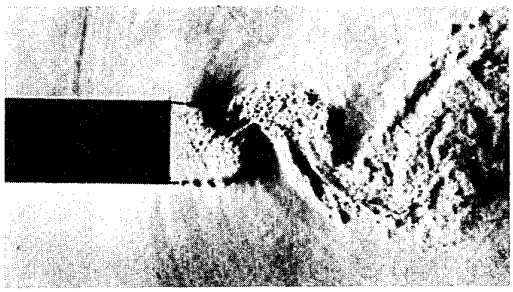

Fig. 16: Large eddies in separating shear layer behind flat plate (from Dymant and Gryson) [30]

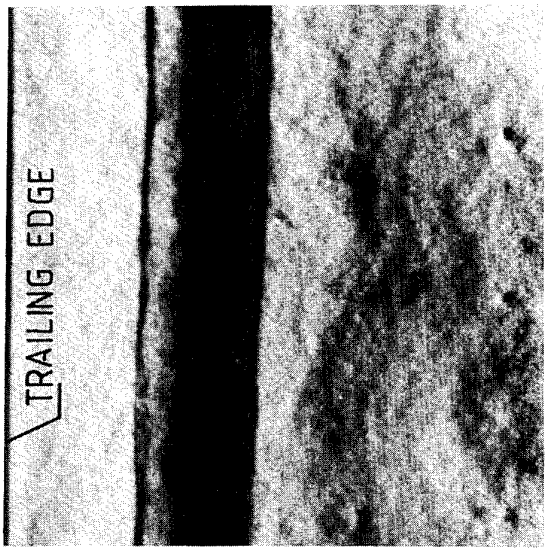

Fig. 17: Enlarged schlieren top view corresponding to Figure 14

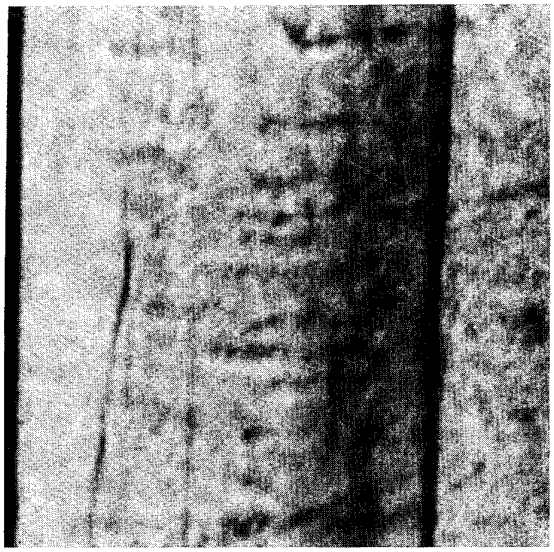

Fig. 18: Schlieren top view showing longitudinal vortex structures

the large vortical structures, another one that seems related to the small structures. The observations suggested to the authors that, when large scale anti symmetrical vortex formation occurs, the selected frequency characteristics of the phenomenon dominate the other components in the spectrum of frequency, precluding successive coalescence of small-scale vortex frequencies. In practice, once the large-scale vortex is allowed to form downstream of the body, there is predominance of fluctuation energy at large-scale frequency component. This observation is consistent with the existence of an absolute instability in the near wake region: the global resonance of this type of instability apparent overwhelms the multiple frequency characteristics of the purely convective shear layer. In conclusion, in the shear layer coexist instabilities causing both large-scale vortices and small-scale vortices, only the former seems to have an absolute character.

In addition to the normal lateral views it was also attempted to take top view schlieren photographs for the same blade Fig. 17. In the pictures the direction of the flow is from the left to right. Close to the trailing edge the traces of shock waves and the vortical structures are visible. In the region where the two structures are superposed it is not possible to clarify the exact behaviour of the wake.

Several top views have been taken and in one of these small regular stream wise structure were found, Fig. 18. It may be daring to give an explanation for these patterns, but it can not be excluded that they present the streamlined ribs which interconnect the spanwise vortices as explained in Fig. 13-b.

8. CONCLUSION

The experimental research on time varying wake flow characteristics behind turbine blades is still in its initial stage.

Only time resolved wake flow field measurements will also allow to improve our understanding of the wake dynamics. The measurements and data acquisition techniques must allow the separation of periodic and random fluctuating components. Large scale models appear to be the best solution to provide sufficient spatial resolution.

Compared to flow over cylinders the flow behind turbine blades appears to be much more difficult to understand due to the different boundary layer states on both blade surfaces and the effect of the blade circulation on the wake structure.

9. REFERENCES

1. RAJ, R. and LAKSHMINARAYANA, B.: Characteristics of the wake behind a cascade of airfoils. J. Fluid. Mech. Vol. 61, Pt. 4 pp. 707-730.

2. KIOCK, R.: Experimental investigation of the flow field downstream of a plane turbine cascade in transonic flow. Proceedings of Symposium on Measuring Techniques in Transonic and Supersonic Cascades and Turbomachines. Lausanne, Nov. 1976.

3. MEE, D.J.; BAINES, N.C.; OLDFIELD, M.L.G.; DICKENS, T.E.: An estimation of the contributions to loss on a transonic turbine blade cascade. ASME Journal of Turbomachinery Vol. 109.

4. STASTNY, M. and SAFARIK, P.: Boundary layer effects on the transonic flow in straight turbine cascade.

5. KAPTEIJN, C.; AMECKE, J.; MICHELASSI, V.: Aerodynamic performance of a transonic turbine guide vane with trailing edge coolant ejection. Submitted to IGTI Conference 1994

6. SIEVERDING, C.H.; ARTS , T.; DENOS, R.; MARTELLI, F.: Investigation of the flow field downstream of a turbine trailing edge cooled nozzle guide vane. ASME 94-GT-209.

7. LAWACZECK, O.and HEINEMANN, J. : von Karman vortex street in the wake of subsonic and transonic cascades. AGARD Conference Proceedings N. 177 on Unsteady Phenomena in Turbomachinery AGARD CP-177.

8. CARSCALLEN, W.E. and GOSTELOW, J.P.: Observation of vortex shedding in the wake from transonic turbine nozzle vanes. Fifth International Symposium on Transport Phenomena and Dynamics of Rotating Machinery. (ISROMAC-5) Kaanapali,Hawaii, U.S.A. May 8-10, 1994

9. BENELMUFFOK, A.and BERETTA-PICCOLI F.: Etude de l'ecoulements subsonique et transonique au bord de fuite epais d'un profile isole'. Rapport N.: EPFL-LTT -86-31,1986.

10. HAN, L.S. and COX W.R. 1982: A visual study of turbine blade pressure side boundary layer. ASME paper 82-GT-47

11. SARI, O.: Etude experimentale et teorique d'ecoulements supersoniques aux bord de fuite d'aubes de turbines.Rapport de these, Ecole Polytechnique Federale de Lausanne, Lausanne 1988.

12. BRYANSTON-CROSS, P.J.; OLDFIELD, M.L.G.: Interferometric measurements in a turbine cascade using image-plane holography. Transaction of ASME Vol. 103 January 1981.

13. DESSE, J.M. and PEGNEAUX, J.C.: Whole-field measurement of gas density from two simultaneously recorded interferograms. Exp. in Fluid Vol.12 pp.1-9. 1991.

14. HEINEMANN, J.and BUTEFISH, K.A.: Determination of the vortex shedding frequency of cascades with different trailing edge thicknesses. AGARD CP-227, Paper 11, 1977.

15. BRYANSTON-CROSS, P.J. and CAMUS, J.J.: Auto and cross correlation measurements in a turbine cascade using a digital correlator. ASME 82-GT-132.

16. SIEVERDING, C.H. and HEINEMANN, H.: The influence of boundary layer state on vortex shedding from flat plates and turbine cascades. ASME 89-GT-296.

17. MORKOVIN, M.V.: Aerodynamic loads on bluff bodies at low speeds. AIAA J. Vol. 2 N. 11. 1964.

18. ROSKHO, A.: On the Wake and Drag of Bluff Bodies. Aeronautical Science Vol. 22

19. BEARMAN, P.W.: The effect of base bleed on the flbw behind a two-dimensional model with a blunt trailing edge; The Aeronautical Quarterly, August 1967.

20. WOOD, C.J.: Visualization of an incompressible wake with base blade; J. Fluid Mech. Vol 29, part 2, pp 259-272, 1967.

21. MICHEL, G.W.and KOST, F.H.: The effect of coolant flow on the efficiency of a transonic HP turbine profile suitable for a small engine. ASME 82-GT-63.

22. SIEVERDING, C.H.: The influence of trailing edge ejection on the base pressure in transonic turbine cascades. ASME 82-GT-50.

23. GERRARD, J. H.: The mechanism of the formation region of vortices behind bluff bodies. J. of Fluid Mech. Vol. 25 Part. 2 pp 401-413.

24. BERGER., E.: Jahr. Wis. Ges. L.&R. Berlin.

25. CANTWELL, B.: A flying hot wire study of the turbulent near wake of a circular cylinder at Re=140000. Ph.D. Thesis Cal. Inst. Tech. 1976.

26. CANTWELL, B. and COLES, D.: An experimental study of entrainment and transport in the turbulent near wake of a circular cylinder J. of Fluid Mech. Vol. 136 pp321-374, 1983

27. HUSSAIN, A.K.M.F. and HAYAKAWA, M.: Eduction of large-scale organised structures in a turbulent plane wake. J. of Fluid Mech. Vol. 180 pp. 193-229, 1983

28 .KIYA, M. and MATSUMURA, M.: Incoherent turbulence structure in the near wake of a normal plate. J. of Fluid Mech. Vol 190 pp343-356, 1988

29. TENNEKES, H. and LAMLEY, J.L.: A first course in turbulence. MIT Press

30. DYMANT, A. and GRYSON,P.: Etude d'ecoulements turbulents subsoniques et supersoniques par visualisation ulta-rapide. AGARD CP-227 Paper 28, 1977.

31. UNAL, M.F. and ROCKWELL, D.: On vortex formation from a cylinder. Part 1: The initial instability. J. of Fluid Mech. Vol. 190 pp. 491-512, 1988.

32. SCHLICHTING, H.: Boundary layer theory. McGraw-Hill. 7th Edition. 1979

Secondary Flows in a Turbine Cascade at Off-Design Conditions

F. Bassi[1] and M. Savini[2]
[1]Dipartimento di Energetica
Università di Ancona
via Brecce Bianche, 60100 Ancona, Italy
[2]Università di Bergamo
Viale G. Marconi 5, 24044 Dalmine (BG), Italy

1. SUMMARY

In this work a finite volume full 3-D Navier-Stokes solver equipped with the two equation k-ω turbulence model is described. The code is applied to the analysis of the secondary flows occurring in a low aspect ratio turbine cascade both at design and at highly off-design incidence angle. Numerical results and experimental data concerning loss, flow angle, and turbulent kinetic energy distributions are compared and discussed. Aim of the work is to investigate the capability of the physical models, namely of the turbulence model, to simulate the marked three-dimensional flow features that characterize the secondary flows at off-design conditions.

2. INTRODUCTION

During the last ten years the use of computer codes for the numerical solution of the Reynolds-Averaged Navier-Stokes (RANS) equations has remarkably spread both at the research and at the industrial level. This is due both to the improvement of numerical techniques and to the impressive progress in computer performances. Nowadays the RANS equations equipped with some kind of turbulence model can be considered the state-of- the-art of fluid dynamic simulations in turbomachinery. Despite the undoubtful progress achieved, the validation of the physical models (essentially the turbulence and transition modelling) is still far from giving a fully satisfactory answer about the capabilities of simulating the effects of turbulence on the mean flow field. This is especially true when considering complex flow situations (secondary flows, tip clearance effects, coolant ejection, off-design conditions, unsteadiness) or when studying the development of mean turbulent quantities such as turbulent kinetic energy or Reynolds stresses. In this work we try to simulate the development of secondary flows in a turbine cascade both at design and off-design conditions. Moreover we compare numerical results and experimental data not only in terms of mean quantities (losses, flow angles, blade pressure distributions) but also in terms of turbulent kinetic energy distributions. We implemented in our Navier-Stokes solver, Ref. [2], the k-ω model developed by Wilcox, Ref. [8], which is numerically less stiff than more widely used k-ϵ models and, in the standard version, can be integrated to the wall without making use of near-wall damping functions. An appealing feature of this model with regard to 3-D computations is that it is not required the specification of the distance from solid walls. The test cases used for comparison are presented in Ref. [1] and refer to low subsonic flow through a linear turbine cascade at different pitch-chord ratios and/or incidence angles. The complete set of experimental data contains also the distribution of the components of the Reynolds stress tensor and of the turbulent kinetic energy.

3. MATHEMATICAL MODEL AND NUMERICAL SOLUTION

3.1 Governing Equations

The governing equations are the Favre mass-averaged Navier-Stokes equations. The averaging process generates the Reynolds stresses as additional unknowns in the equations of conservation of momentum and energy. By making the Boussinesq approximation that the Reynolds stress tensor is proportional to the mean strain-rate tensor and by using the two-equation k-ω turbulence model, the complete set of equations of motion and of the turbulence model reads as

$$\frac{\partial \rho}{\partial t} + \frac{\partial}{\partial x_j}(\rho u_j) = 0 \tag{1}$$

$$\frac{\partial}{\partial t}(\rho u_j) + \frac{\partial}{\partial x_j}(\rho u_j u_i) = -\frac{\partial p}{\partial x_i} + \frac{\partial \hat{\tau}_{ji}}{\partial x_j} \tag{2}$$

$$\frac{\partial}{\partial t}(\rho E) + \frac{\partial}{\partial x_j}(\rho u_j H) = \frac{\partial}{\partial x_j}\left[u_i \hat{\tau}_{ij} - q_j\right] + \frac{\partial}{\partial x_j}\left[(\mu + \sigma^* \mu_t)\frac{\partial k}{\partial x_j}\right] \tag{3}$$

$$\frac{\partial}{\partial t}(\rho k) + \frac{\partial}{\partial x_j}(\rho u_j k) = \tau_{ij}\frac{\partial u_i}{\partial x_j} - \beta^* \rho \omega k + \frac{\partial}{\partial x_j}\left[(\mu + \sigma^* \mu_t)\frac{\partial k}{\partial x_j}\right] \tag{4}$$

Paper presented at the AGARD PEP 85th Symposium on "Loss Mechanisms and Unsteady Flows in Turbomachines", held in Derby, United Kingdom, 8-12 May 1995, and published in CP-571.

$$\frac{\partial}{\partial t}(\rho\omega)+\frac{\partial}{\partial x_j}(\rho u_j\omega)=\frac{\gamma\omega}{k}\tau_{ij}\frac{\partial u_i}{\partial xj}-\beta\rho\omega^2 +\frac{\partial}{\partial x_j}\left[(\mu+\sigma\mu_t)\frac{\partial\omega}{\partial x_j}\right] \quad (5)$$

where t is time, x_i position vector, u_i velocity vector, ρ density, p pressure, μ and μ_t molecular and eddy viscosity coefficients, $\hat{\tau}_{ij}$ the sum of the viscous and Reynolds stress tensors, and q_j the sum of the viscous and turbulent heat flux vectors. The quantities $E = e + u_i u_i/2 + k$ and $H = h + u_i u_i/2 + k$ are total internal energy and enthalpy, respectively; e and h denote internal energy and enthalpy, and $h = e + p/\rho$. The turbulent mixing energy k and the specific dissipation rate ω define the eddy viscosity coefficient:

$$\mu_t = \gamma^* \frac{\rho k}{\omega} \quad (6)$$

The total stress tensor is given by

$$\hat{\tau}_{ij} = 2\mu\left[S_{ij} - \frac{1}{3}\frac{\partial u_k}{\partial x_k}\delta_{ij}\right] + \tau_{ij} \quad (7)$$

where the mean strain-rate S_{ij} is

$$S_{ij} = \frac{1}{2}\left[\frac{\partial u_i}{\partial x_j} + \frac{\partial u_j}{\partial x_i}\right] \quad (8)$$

The Boussinesq hypothesis assumes that the Reynolds stress tensor is proportional to the mean strain-rate tensor, that is

$$\tau_{ij} = 2\mu_t\left[S_{ij} - \frac{1}{3}\frac{\partial u_k}{\partial x_k}\delta_{ij}\right] - \frac{2}{3}\rho k\delta_{ij} \quad (9)$$

The total heat flux vector is given by

$$q_j = -\left(\frac{\mu}{\mathrm{Pr}} + \frac{\mu_t}{\mathrm{Pr_t}}\right)\frac{\partial h}{\partial x_j} \quad (10)$$

where Pr and $\mathrm{Pr_t}$ are the laminar and turbulent Prandtl numbers and have been assumed equal to 0.72 and to 0.9, respectively. The values of the closure coeficients β, β^*, γ, γ^*, σ, σ^* that appear in the equations have been established by Wilcox, Ref. [8], and are given by:

$$\beta = 3/40, \quad \beta^* = 9/100, \quad \gamma = 5/9, \quad \gamma^* = 1, \quad \sigma = 1/2, \quad \sigma^* = 1/2 \quad (11)$$

As almost all two-equation turbulence models, also the k-ω model includes an evolution equation for the turbulent kinetic energy. The other equation of the model can be interpreted as the evolution equation for the ratio of the turbulence dissipation rate ϵ to the turbulent mixing energy k. A distinctive feature of the k-ω model is that it does not require damping functions in the viscous sublayer and that the equations are less stiff near the wall; this is very useful because it is possible to extend the model down to the wall without introducing wall functions that could be questionable for general flows and without suffering too much from the stability problems typical of other models near the wall.

3.2 Numerical Solution

We use a finite volume discretization, whereby the computational domain is partitioned into hexaedral cells and the integral form of Eqs. (1)–(5) is applied to each cell. By taking advantage of the divergence theorem the volume integral of spatial derivatives reduces to the surface integral of fluxes, which need to be evaluated at cell interfaces. The convective fluxes in Eqs. (1)–(3) are evaluated at each face as the arithmetic mean of the fluxes in the cells which share that face. This is equivalent to a centered discretization of first order derivatives that can decouple the solution and induces oscillations near shock waves and stagnation points; following Jameson's approach, Ref. [3], we add a controlled amount of non-linear artificial dissipation given by a blend of second and fourth order spatial differences of conservative variables: in this work particular attention was devoted to limit the amount of added artificial viscosity in order to do not alter the computed total pressure losses. The main advantage of Jameson's approach is that it is very efficient, especially if one uses the convergence acceleration techniques that have been proposed in the literature.

On the other hand, we found that the centered scheme plus artificial viscosity is not best suited for the discretization of the convective terms in the turbulence model equations: when using such an approximation, in fact, it can happen that the k and ω distributions in the outer part of the boundary layer are slightly oscillatory. Hence, a more robust upwind scheme has been used to discretize the convective fluxes in Eqs. (4) and (5): even if the upwind scheme that has been implemented can be higher-order accurate, we did not really found worth to go beyond first order accuracy. The simple, Lax-Friedrichs type, numerical flux that has been used reads as

$$\hat{f} = \frac{1}{2}\left[f\left(w^+\right) + f\left(w^-\right) - \lambda\left(w^+ - w^-\right)\right]$$

$$\lambda = \max\left(\left|\lambda^+\right|, \left|\lambda^-\right|\right)$$

where λ is the maximum absolute eigenvalue of the Jacobian matrices of $f(w^+)$ and $f(w^-)$; on account of the weak coupling between Eqs. (4) and (5) and Eqs. (1)–(3), λ is taken equal to the convective velocity. If a first order scheme is employed, w^+ and w^- are equal to the average values in the cells sharing the face.

To compute the surface integral of diffusive fluxes we need to evaluate the derivatives of velocity components, temperature, k and ω on the cell faces; for this purpose the derivatives components are computed at cell centers, by using the divergence theorem, and averaged to get surface cell values; however, the surface values so obtained are used only to evaluate the derivatives along the two logic directions on the surface whilst the derivatives along the logic direction which crosses the cell surface are computed by using directly the cell values; the derivatives along the three

logic directions are then combined to get the cartesian components of derivatives on cell faces.

The time integration of the discretized form of Eqs. (1)–(5) is performed by an explicit multistage Runge-Kutta algorithm; in this work we have used the three stage scheme with the coefficients advised by Jameson, Ref. [4]. The convergence toward steady state is improved by using the local time step and the variable coefficients implicit residual smoothing, described in Refs. [6] and [5]. The source terms in Eqs. (4) and (5) are evaluated implicitly and the Jacobian matrix of the source terms with respect to ρk and $\rho\omega$, resulting from the linearization process, is computed at the beginning of the multistage algorithm. As a result of these implementations solutions can be marched with a local CFL number up to 3. Each computation takes about 10,000 Runge-Kutta multistage cycles to reduce the RMS of the density time derivative of about four orders of magnitude; the convergence of the k-ω model is checked looking at the maximum modulus and at the RMS of the eddy viscosity time derivative. Marching with the k-ω model the code requires 30% more CPU time per cycle than with an algebraic turbulence model, as for example the Baldwin-Lomax one. In all the computations we start the turbulent computation from a roughly converged turbulent 2-D solution. In our experience this crude initialization has always been sufficient to start the computations without compromising the stability of the coupled solution.

3.3 Boundary Conditions

At the inflow boundary the flow is subsonic and four independent variables have to be specified: these are the total enthalpy, the entropy, and the flow direction; the last variable is computed using the Riemann variable associated with the characteristic running from inside the domain, assuming that the flow is locally one-dimensional in the axial direction. The input entropy distribution in the spanwise direction is such that, by assuming constant total enthalpy and pressure, the computed velocity profile matches the measured one; the entropy distribution is held fixed during the unsteady phase of computation, hence the velocity profile agrees with the experimental one only at the steady state.

At the outflow the static pressure, corresponding to the prescribed isentropic outlet Mach number, is set. The numerical boundary conditions are computed by extrapolating from the interior the characteristic variables of the flow, assumed locally one-dimensional in the axial direction.

At solid walls the velocity is zero and, by neglecting the pressure gradient in the normal direction, the pressure is set equal to that of the first cell adjacent to the surface; moreover adiabatic wall condition is assumed.

At the midspan simmetry conditions are set and periodicity conditions are enforced along the periodic boundaries.

The boundary conditions for the k-ω model must be provided at inflow and solid wall boundaries; at the outflow k and ω are freely convected out.

At the inflow boundary k is computed from the prescribed spanwise distribution of turbulence intensity. The value of ω at midspan is prescribed by giving the ratio between the turbulent and the laminar viscosity coefficients. Lacking any experimental data about the spanwise distribution of ω (or of some related variable), it was decided to relate the variation of ω to that of k in order to obtain roughly the same rate of turbulence decay in the axial direction along the span.

At solid walls k is zero and ω is computed by following the approach suggested by Wilcox in Ref. [9]; in this paper the wall value of ω is written as

$$\omega = \frac{u_\tau^2}{\nu} S_R \tag{12}$$

where $u_\tau^2 = \tau_w/\rho$ is the friction velocity, ν is the kinematic viscosity and the function S_R is related to the non-dimensional relative surface roughness $k_R^+ = k_R u_\tau/\nu$ through the correlation

$$S_R = \begin{cases} \left(50/k_R^+\right)^2 & k_R^+ < 25 \\ 100/k_R^+ & k_R^+ \geq 25 \end{cases}$$

where, according to Wilcox, $k_R^+ \leq 5$ for hydraulically smooth surfaces. Eq. (12) is more general than the original analytical formula, Ref. [8], because it does not make any reference to geometrical quantities such as the distance from the wall and can be easily applied in three-dimensional geometries.

4. COMPUTATIONAL RESULTS

The above described solver has been used to compute the three-dimensional flow field in a linear turbine cascade for which a set of detailed measurements, both at design and at off-design conditions, is available. The computational results presented below are compared to the experimental data looking not only at the mean-flow variables but also at the turbulent kinetic energy field, which is much more difficult to simulate with a two-equation turbulence model, especially at off-design conditions.

Fig. 1 and Table 1 present the cascade geometry and the relevant geometrical data. The 3-D measurements were taken in a plane located at 22% of axial chord downstream of the trailing edge, by means of a five hole pressure probe and a hot wire anemometer. Two tests have been selected for the purpose of comparison, namely 0° and 30° of incidence angle. The outlet isentropic Mach number is $M_{2is} = 0.3$ and the Reynolds number based on the downstream isentropic conditions and the chord length is $Re_{2is} = 3.7 \times 10^5$.

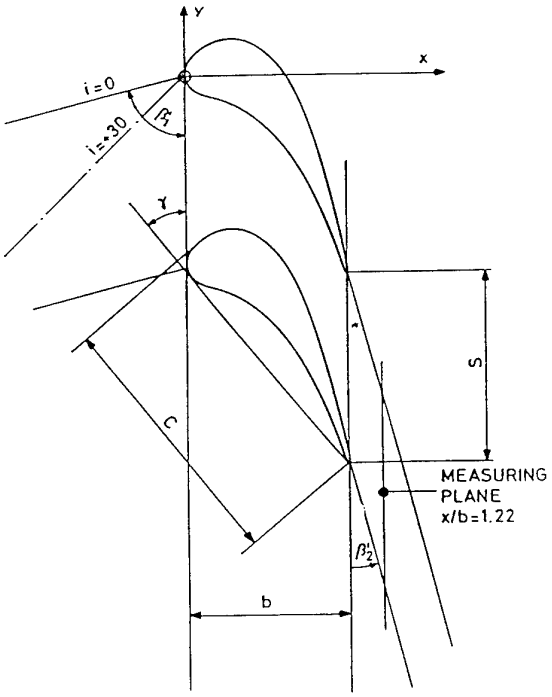

Figure 1: Cascade geometry

More informations about the experimental apparatus and the performed tests can be found in Ref. [1].

The 3-D computational grid, displayed in Fig. 2 with every other line removed, contains 240 × 36 × 36 cells and is obtained by stacking the same 2-D C-type mesh in the spanwise direction; the density of grid points can be considered medium for this type of computations with a second order accurate scheme. The non-dimensional distance y^+ of the cell centers nearest to the blade surface and to the endwall is roughly included between 1 and 2; in terms of blade chord the minimum distance is about 1.5×10^{-4} in the blade-to-blade surfaces and is 2×10^{-4} at the endwall.

Table 1: Cascade geometrical data

Chord length	c	55.2 mm
Axial chord	b	34.0 mm
Pitch to chord ratio	s/c	0.87
Aspect ratio	h/c	0.91
Inlet blade angle	β_1'	76.1°
Outlet blade angle	β_2'	14.5°
Blade turning angle	$\Delta\beta'$	89.4°
Stagger angle	γ	39.9°

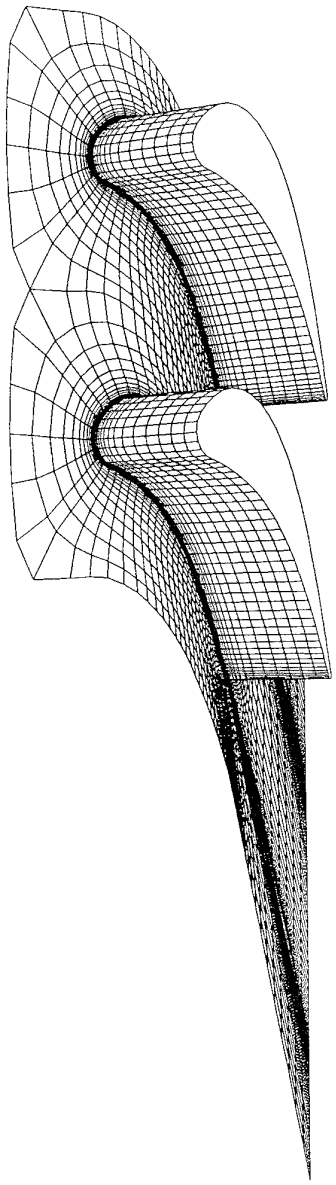

Figure 2: Computational grid

4.1 Computational results, $i = 0°$ incidence angle

The flow field at midspan is summarized in Figg. 3 and 4, which put in evidence the good agreement between the experimental and the computed blade pressure distributions, and the marked difference between the boundary layer development on the suction and pressure side of the blade; the favourable pressure gradient on the blade pressure side suggests that, although the numerical simulation predicts an early transition, the flow could actually be laminar up to the trailing-edge.

The Figg. 5 and 6 show the kinetic energy loss and the turbulent kinetic energy contours on a sequence of tangential planes inside the blade passage: the phenomena of the passage vortex formation and the migration of the low-energy fluid away from the pressure side towards the suction side seem to be well described by the numerical simulation. The evolution of the turbulent kinetic energy inside the passage displays some features similar to that of the losses, the turbulent flow at the endwall being swept under the action of the crossflow. However, in the first part of the blade passage the convection of the turbulent flow is predominant and there is a low production of turbulence on the pressure side and at the endwall. In the second part of the channel the production of turbulent kinetic energy due to the mean velocity gradients is able to sustain relevant turbulence intensities in the rapidly growing suction side boundary layer and in the core of the passage vortex. Moreover, note that at $x/b = 0.66$ the blade pressure side boundary layer has already become turbulent and its content of k rises considerably up to the trailing edge.

The numerical and experimental results, concerning the losses, the turbulent kinetic energy and the secondary velocity vectors in a plane at $x/b = 1.22$, are shown in Figg. 7 and 8; note that the slightly different position of the plots with respect to the y/s axis is not meaningful and is due to the different origin of the axis. From the comparison of Figg. 7 and 8 one can observe that:

- the computed loss region at the endwall is more confined than in the experimental data;
- the computed secondary velocity vectors are slightly smaller than the experimental ones; this could be due to the spanwise grid discretization which is not sufficiently fine to avoid some numerical diffusion away from the endwall;
- the smaller extension of the computed shed vortex is probably responsible for the spanwise shift of the loss peak ($z/h = 0.3$ instead of 0.25) and of the passage vortex core ($z/h = 0.2$ instead of 0.15);
- the two-dimensional losses at midspan are much higher in the computations than in the experiments and attain a peak value that is twice the

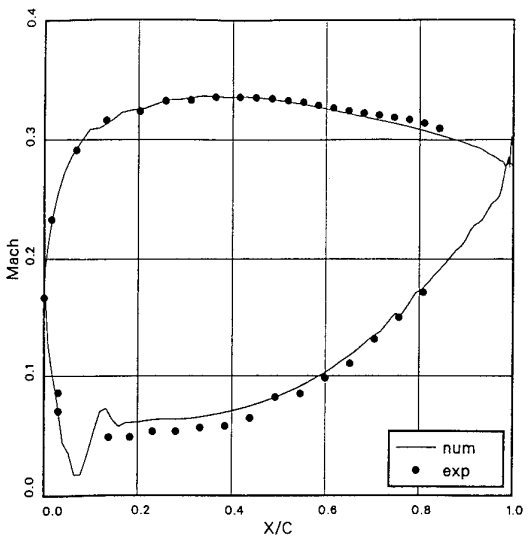

Figure 3: Blade isentropic Mach number, $i = 0°$ incidence angle

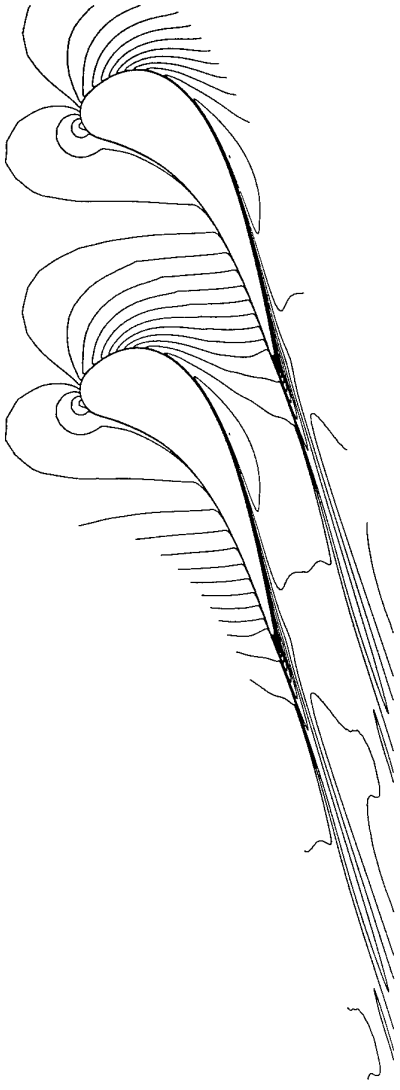

Figure 4: Mach contours at mid-span, $i = 0°$ incidence angle

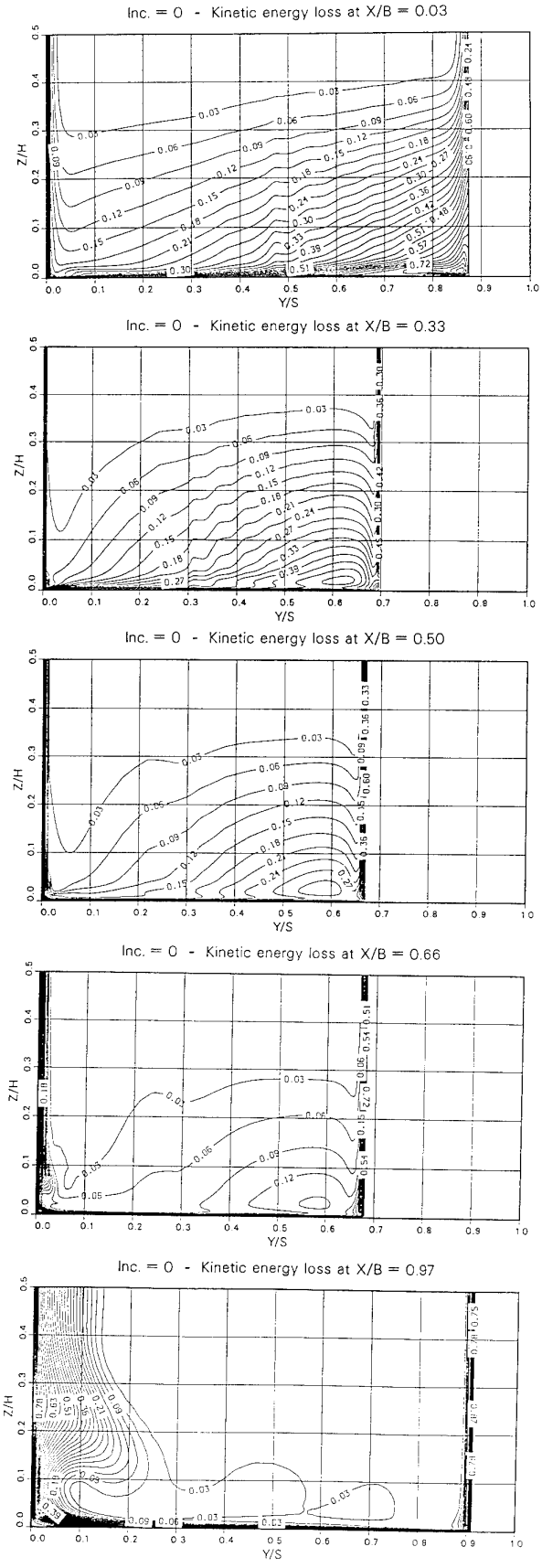

Figure 5: Kinetic energy loss inside the blade passage, $i = 0°$ incidence angle

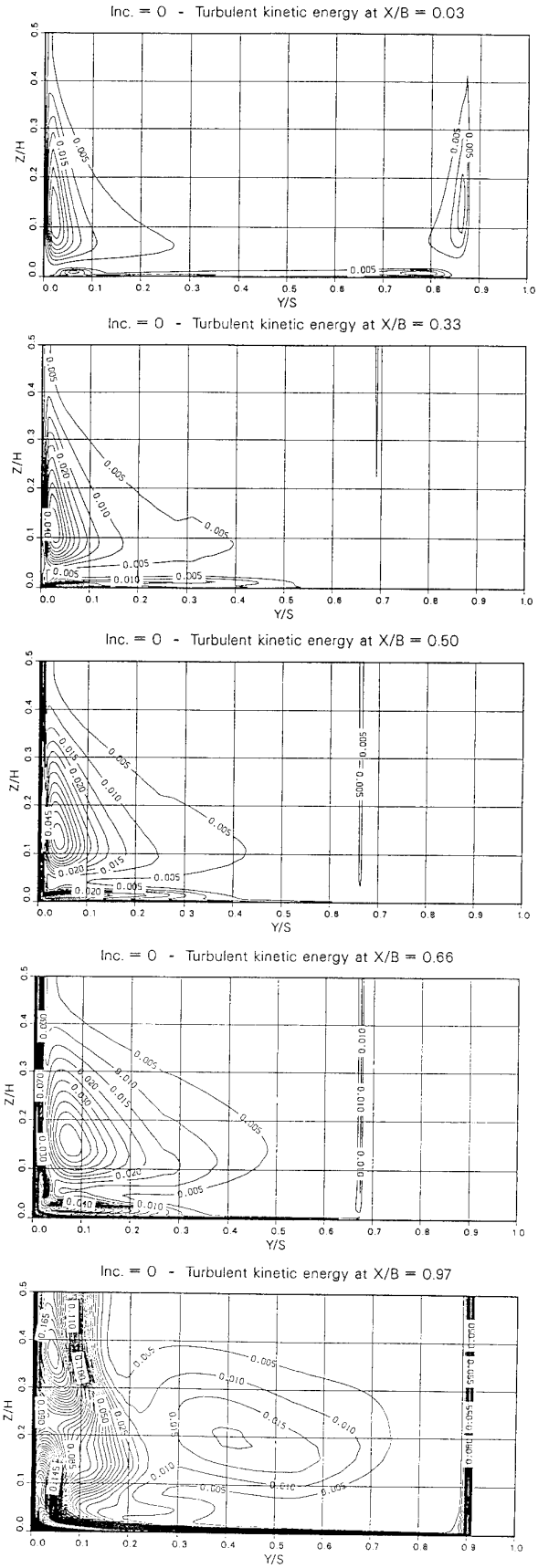

Figure 6: Turbulent kinetic energy inside the blade passage, $i = 0°$ incidence angle

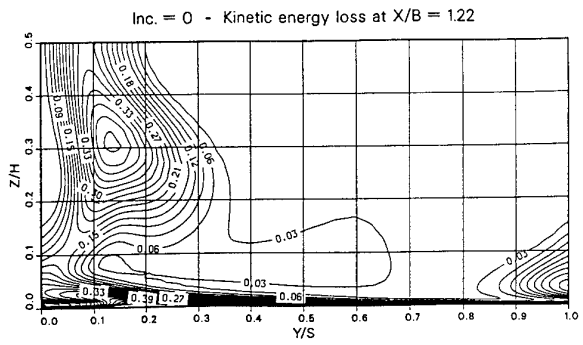

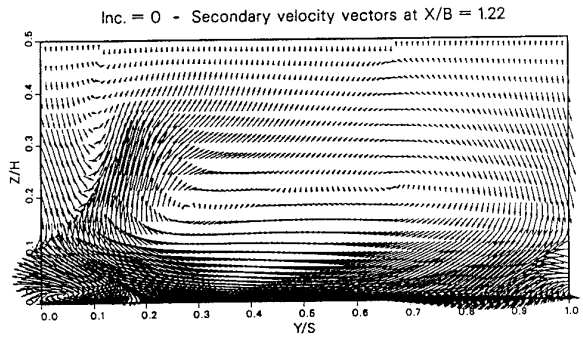

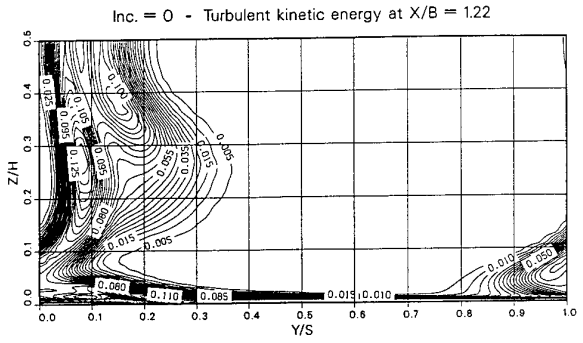

Figure 7: Numerical results at $x/b = 1.22$, $i = 0°$ incidence angle

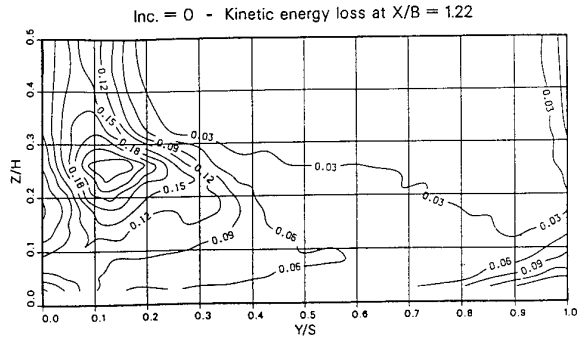

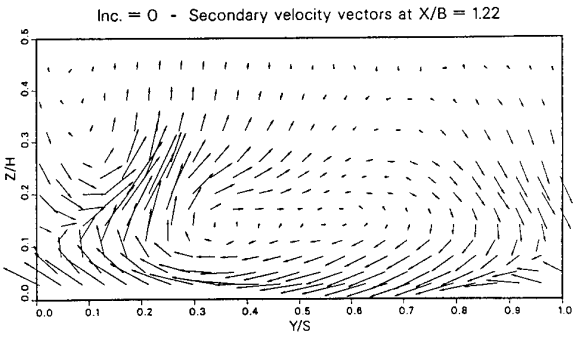

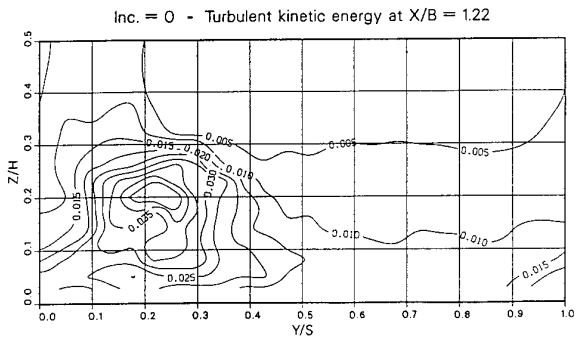

Figure 8: Experimental results at $x/b = 1.22$, $i = 0°$ incidence angle

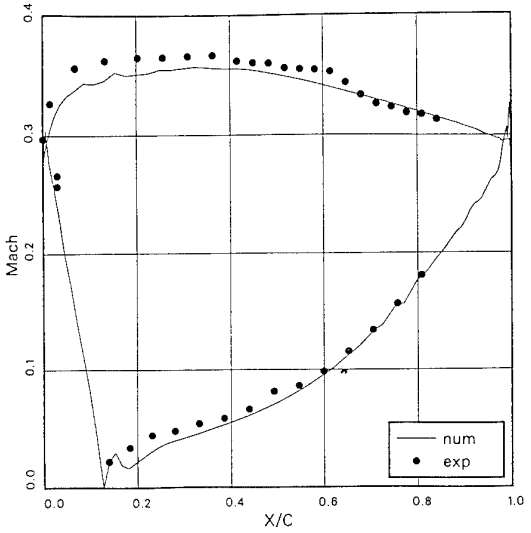

Figure 9: Blade isentropic Mach number, $i = 30°$ incidence angle

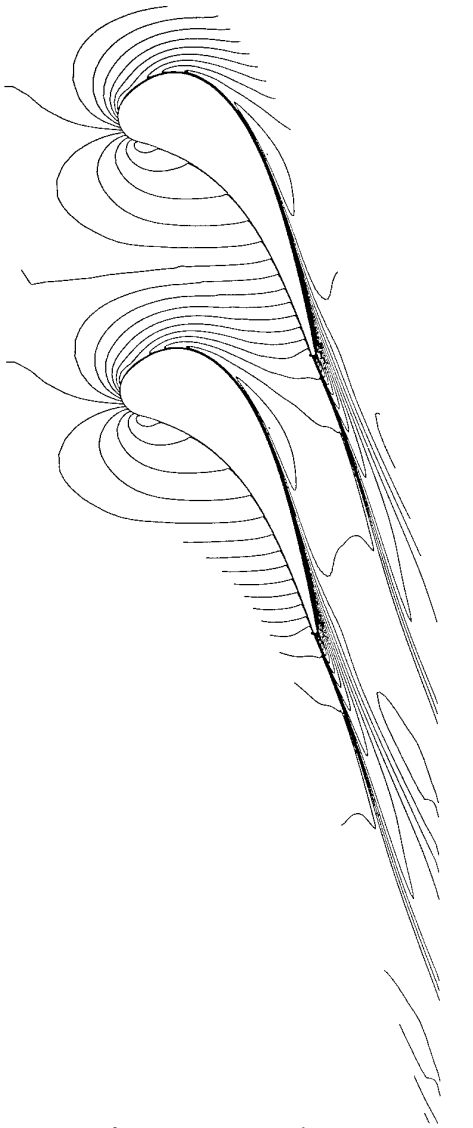

Figure 10: Mach contours at mid-span, $i = 30°$ incidence angle

Table 2: Mass-averaged quantities

		ζ_{ms}	β_{2ms}	ζ_{ov}	SKE
$i = 0°$	exp	.0275	17.4	.0542	.0311
	num	.0329	17.4	.0657	.0298
$i = 30°$	exp	.0879	23.0	.1134	.1792
	num	.0887	19.8	.0849	.0684

measured one (0.3 versus 0.15); this explains also the difference in the region of interaction between passage and shed vortex where the maximum loss core (0.45 versus 0.27) is found. We believe that the discrepancy is mainly a two-dimensional effect due to the incorrect modelling of boundary layer transition and is reflected in the difference of the overall losses reported in Table 2.

These observations and the mass-averaged results reported in Table 2 allow to conclude that, apart from the differences observed at the endwall, the 3-D effects and the dynamic of the passage vortex are well captured by the numerical simulation.

Different conclusions stem from the analysis of the turbulent kinetic energy contours. The numerical computation does not simulate the rapid decay of turbulence in the wake (even keeping in mind the difference between numerical and experimental levels of turbulence at the trailing edge), whereas the turbulence peak located near the passage vortex core is rapidly damped in the numerical simulation, maybe owing to insufficient grid resolution.

4.1 Computational results, $i = 30°$ incidence angle

Fig. 10 shows the Mach contours at midspan. Comparing these isolines with those at 0° incidence angle one can notice the greater acceleration on the blade suction side, the shift of the stagnation point on the pressure side and the significant thickening of the suction side boundary layer. The isentropic Mach number distribution, displayed in Fig. 9, is in good agreement with the experiment even if at a slightly lower level. The behaviour of the secondary flows inside the blade channel, not shown here, is qualitatively similar to that of the previous case, but the region of flow affected by dissipation and turbulence is larger and displaced closer to the midspan.

Comparing the numerical and experimental results at $x/b = 1.22$, Figg. 11 and 12, the first three observations of the previous case apply also in this case. However, unlike the 0° incidence case, the flow field at midspan is strongly affected by the interaction between the passage vortices that develop in the upper and lower part of the channel. Looking at the flow

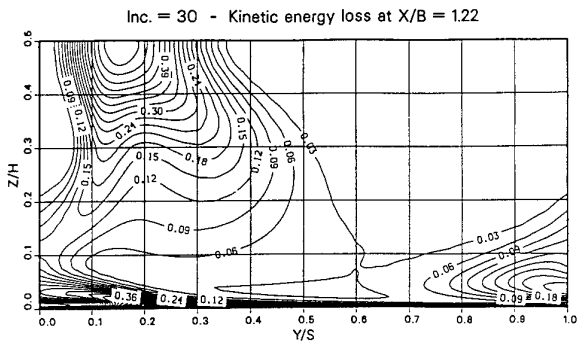

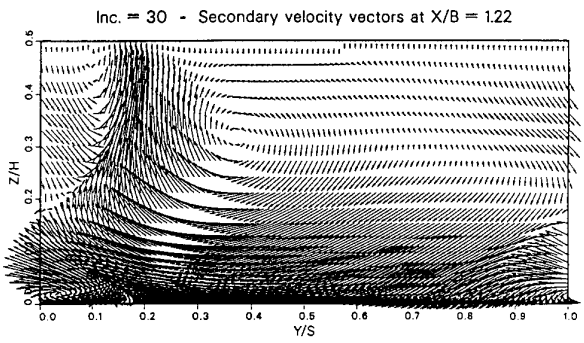

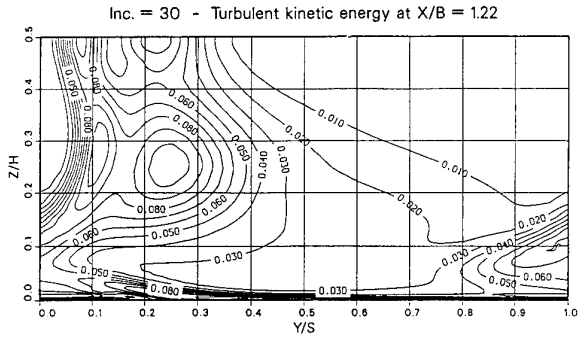

Figure 11: Numerical results at $x/b = 1.22$, $i = 30°$ incidence angle

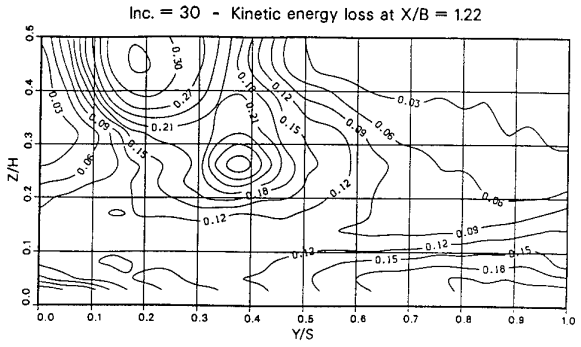

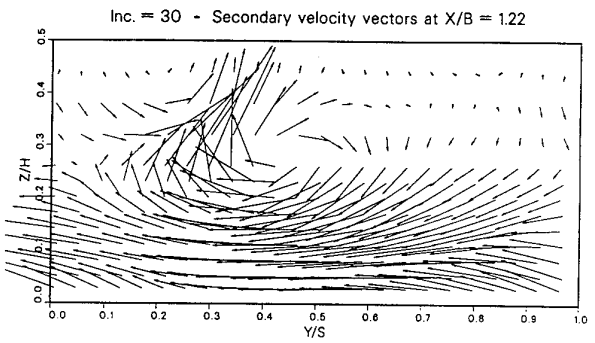

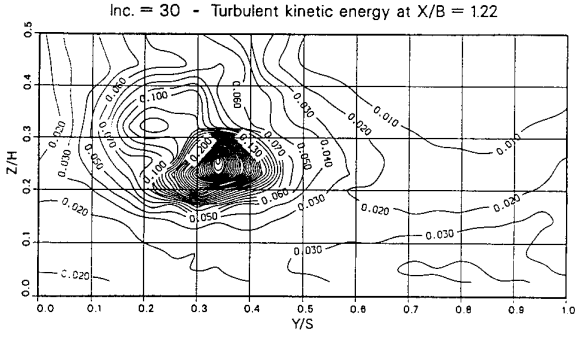

Figure 12: Experimental results at $x/b = 1.22$, $i = 30°$ incidence angle

angles reported in Table 2 one can notice both the large variation with respect to the 0° incidence case, and the marked discrepancy between numerical and experimental results. The presence of the passage vortices at midspan is certainly the main responsible for the variation with respect to the design conditions, but the disagreement with the experiment could also be ascribed to a boundary layer separation, not predicted by the computation. Whether or not this separation actually occurs is an issue about which we have no information from the experiments. The computed loss contours display a peak loss region at midspan as in the experiments; unlike the experimental loss contours, only a vague hint at a second peak loss can be seen in the computed loss isolines. The large low-energy flow region near the endwall is markedly underestimated in the computations and this results in a mass-averaged overall loss lower than that at midspan.

The difference between computed and measured turbulent kinetic energy in the wake region at midspan is lower than at 0° incidence angle possibly because of a different development of the suction side boundary layer. The bigger spraeding of the measured k isolines as well as the distortion of the passage and shed vortices in pitchwise direction seem to be connected to the larger flow deviation. Unlike the 0° incidence angle case, the peak of turbulence in the passage vortex is now present in the numerical results, but its intensity is largely underestimated. Finally the computed secondary kinetic energy is much lower than the experimental one suggesting that a finer grid resolution should be advisable to properly simulate the complex flow features of this case.

5. CONCLUSIONS

A 3-D solver for the RANS equations using the k-ω turbulence model has been presented and applied to the analysis of secondary flows in a turbine cascade both at design and off-design incidence condition. The results presented confirm that state-of-the-art numerical simulations are useful to investigate complex flow fields, but also stress the deficiencies of the turbulence model and mark the areas of possible improvement. At design conditions the simulation of the mean flow field is basically correct and the only relevant misprediction is thought to be ascribed to the lack of a suitable model of transition from laminar to turbulent motion. On the contrary the turbulent flow field, here analyzed in term of turbulent kinetic energy distribution, is still far from being satisfactory when strong three-dimensional effects and flow distorsion are present. In such a condition the turbulence may also have a marked influence on the mean-flow quantities so that its correct simulation seems unavoidable in order to obtain a good quantitative agreement with the experiments. The discrepancies found especially in the endwall boundary layer behaviour strengthen the above comment. The computational grid employed is probably not fine enough throughout the whole domain; the results suggest that more spatial resolution is needed when the gradients of flow quantities are not confined in restricted regions. From a numerical point of view is interesting to assess the accuracy of the predictions on denser computational meshes. Finally two-equations eddy-viscosity turbulence models may not contain enough physics for their use in complex flows and one could be pushed toward algebraic or differential Reynolds stress models. These are aspects that surely deserve a deeper investigation and our work in the near future is pointed along these directions.

REFERENCES

[1] Dossena, V., Perdichizzi, A., Ubaldi, M., Zunino, P., "Turbulence Measurements Downstream of a Turbine Cascade at Different Incidence Angles and Pitch-Chord Ratios", ASME paper no. 93-GT-52, 1993.

[2] Bassi, F., Savini, M., "Secondary Flows in a Transonic Cascade: Validation of a 3-D Navier-Stokes Code", ASME paper no. 92-GT-62, 1992.

[3] Jameson A., Schmidt, W., Turkel, E., 1981, "Numerical Solutions of the Euler Equations by Finite-Volume Methods Using Runge-Kutta Time-Stepping Schemes", AIAA paper no. 81-1259.

[4] Jameson A., 1984, "Transonic Flow Calculations", Dept. of Mechanical and Aerospace Engineering, Princeton Univ., Princeton, NJ, MAE Rept. 1651.

[5] Swanson, R.C., Radespiel, R., 1991, "Cell Centered and Cell Vertex Multigrid Schemes for the Navier-Stokes Equations", AIAA Journal, vol. 29, no. 5.

[6] Martinelli, L., 1988, "Validation of a Multigrid Method for the Reynolds-Averaged Equations", AIAA paper no. 88-0414.

[7] Gregory-Smith, D.G., Graves, C.P., Walsh, J.A., Fulton, K.P., "Turbulence Measurements and Secondary Flows in a Turbine Rotor Cascade ", ASME paper no. 88-GT-244, 1988.

[8] Wilcox, D.C., "Reassessment of the Scale-Determining Equation for Advanced Turbulence Models", AIAA Journal, vol. 26, no. 11, 1988.

[9] Wilcox, D.C., "A Half Century Historical Review of the k-ω Model", AIAA paper no. 91-0615, 1991.

TURBULENCE AND TRANSITION IN SECONDARY FLOWS IN A TURBINE CASCADE

H. Moore and D. G. Gregory-Smith
School of Engineering
University of Durham
South Road
Durham, DH1 3LE
United Kingdom

ABSTRACT

The accurate prediction of flows in turbomachinery blade rows requires realistic modelling of turbulence and transition, particularly for loss estimation. The complex secondary flow within a large scale cascade of turbine rotor blades has been measured in detail. In particular hot wire measurements have been made close to the end walls in order to characterise the three-dimensional boundary layers.

Although at inlet on the end-wall there is a well developed turbulent boundary layer, this is rolled up into a loss core by the secondary velocities and a new highly skewed boundary layer is formed which exhibits significant laminar characteristics. The physical insights gained by this work have implications for the development of turbulence and transition modelling as well as providing test data for the verification of CFD codes.

1. INTRODUCTION

An important area of work in the development of Navier-Stokes computational codes is the production of suitable models for turbulence and transition. Detailed experimental data is required, related to the application of the code, in order to guide the development of the models and also to test their validity. This paper concerns the flow in a simple geometry, that is a linear turbine cascade, but with a very complex flow due to the development of strong secondary flows caused by the end wall boundary layers. This cascade ('the Durham Cascade') has been extensively investigated with respect to the bulk flow and has been used already as a test case for CFD code validation, see for instance Gregory-Smith (1993) regarding the ERCOFTAC series of turbomachinery CFD workshops.

The most dominant feature within the blade row is the passage vortex generated by the action of the cross-passage pressure gradient on the boundary layer fluid on the end walls. Where the end wall boundary layer meets the leading edge of each blade, a horseshoe vortex is formed with a leg that runs down the end wall on each side of the blade. The pressure side leg rotates in the same direction as the passage vortex and crosses the blade passage causing a three-dimensional separation line. It then appears to merge with the passage vortex. The suction side leg rotates in the opposite sense and hugs the blade before climbing up the suction surface, giving rise to a separation line on the suction surface. These secondary flow features have been extensively investigated by many other authors, and Sieverding (1985) gives a comprehensive review. Since then investigations of the highly turbulent features of the flow have received attention, for instance Zunino et. al. (1987), Gregory-Smith and Cleak (1992).

The effect of the secondary flows on the boundary layers is considerable, particularly on the end wall and suction surface as indicated above. On the end wall, the initial relatively thick boundary layer is completely stripped away by the passage vortex and rolled up to form a loss core. Behind the horseshoe pressure side leg separation line, a new thin highly skewed boundary layer is formed. Although most workers have found this to be too thin to determine its state, measurements by Harrison (1989) using film gauges have shown it be substantially laminar, except close to the suction surface.

Measurements of the suction surface boundary layer have also been carried out by various researchers. Halstead et. al. (1990) found that for a low level of inlet turbulence (Tu<1%) the boundary layer was laminar until shortly after the point of maximum free stream velocity where laminar separation followed by turbulent re-attachment took place. This was also found for the Durham cascade with low inlet turbulence, see Walsh and Gregory-Smith (1987).

In a real turbine turbulence levels are much higher

Paper presented at the AGARD PEP 85th Symposium on "Loss Mechanisms and Unsteady Flows in Turbomachines", held in Derby, United Kingdom, 8-12 May 1995, and published in CP-571.

(Tu=4-7%), as well as periodic unsteadiness being present. Halstead et. al. (1990) also reported results at a higher turbulence level and found that the initial laminar boundary layer underwent natural transition rather than producing a separation bubble. Again, this was also observed in the Durham cascade, Gregory-Smith and Cleak (1992). Measurement of suction surface profiles by Mee et. al. (1990) showed similar results, but with an indication of a small unsteady separation bubble.

A study of the importance of transition in gas turbines has been presented by Mayle (1991) and has further been discussed by Walker (1992). Both highlight the importance of transition and its effect on heat transfer and loss generation. Cleak et. al. (1991) have also shown that the assumed location of transition has a large effect on the results of computations of the flow in the Durham cascade. There is however relatively little detailed data on the state of the boundary layers within turbine blade rows with which to compare the results of CFD calculations.

Thus a programme of work has been undertaken to investigate in detail the flows near the end wall and suction surface of the Durham cascade to provide further data in this area. This paper reports the results of hot wire anemometry studies close to the end wall. As already indicated, the overall aim is to guide the development of turbulence and transition modelling in the highly three-dimensional flows typical of turbines, and to provide data for code validation.

2. APPARATUS

The geometry of the Durham cascade is shown diagrammatically in Figure 1 and has been described in detail earlier, see for instance, Walsh and Gregory-Smith (1987) and Gregory-Smith and Cleak (1992). The cascade consists of six blades which have a profile typical of a high pressure turbine rotor, with over 110° of turning. A turbulence intensity of about 4.5% at inlet to the cascade is achieved by a grid of bars 1400 mm upstream of the cascade.

For this work two minor modifications were made, one of which may be seen in Figure 2. Three slots upstream of the cascade and parallel with the inlet flow were made in order to allow traversing to determine the decay rate of the inlet turbulence. They also permitted measurement of the end wall boundary layer profile sufficiently far upstream to be unaffected by the presence of the blades. Previous data had been obtained from slot 1, but this is too close to the blades to be a convenient inlet plane for CFD

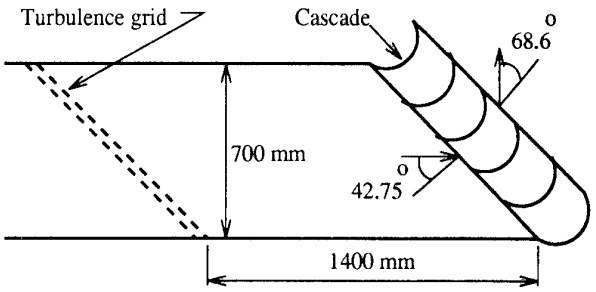

Fig 1: Diagram of the apparatus.

modelling. As indicated in Figure 1 the upstream slots were positioned to be aligned with either a bar edge, gap centre or bar centre, so as to determine whether there was any variation due to the pitching of the bars (109 mm).

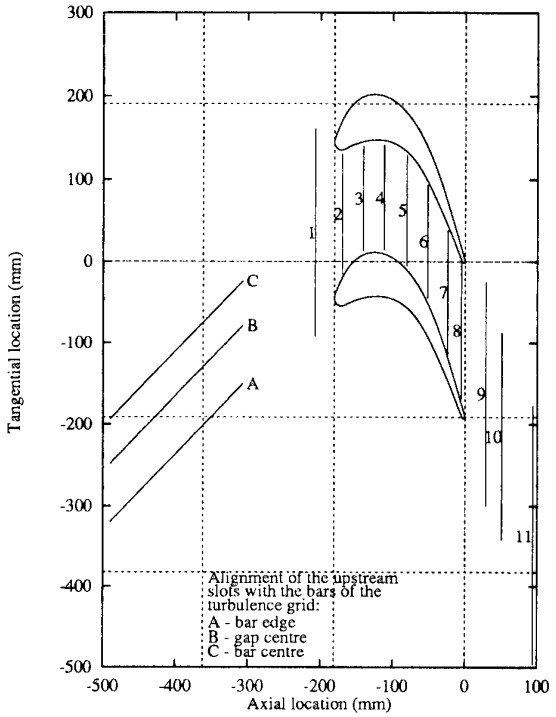

Fig 2: Location of the traverse slots.

The second modification was the removal of the moving belt used by Walsh and Gregory-Smith (1987) to investigate the effect of inlet skew. There was a possibility that the flexible surface, although taped down for later work, might have affected the end wall flow slightly. Since the interest of this work was on the detail of the end wall flow, it was decided to remove this possibility by inserting a solid wall.

The main design features of the cascade are given in Table 1. The actual flow angle upstream of the

cascade is about 43.5° (Angles are measured from the axial direction).

Design Inlet Flow Angle	42.75°
Blade Exit Angle	−68.7°
Blade Chord	224mm
Blade Axial Chord	181mm
Blade Pitch	191mm
Blade Half-Span	200mm
Reynolds Number (C_{ax} and V_{exit})	4.0×10^5

Table 1: Cascade design data

2.1 Hot Wire Anememometry

The measurements of the flow were made using hot wire anemometry designed to give the mean velocity components and also the six components of the Reynolds stresses. The technique uses a double traverse with a slant wire and a normal wire, each rotated to a number of positions relative to the flow vector. The method is similar to that described by Perdichizzi et. al. (1990).

The Jørgensen equation (Jørgensen (1971)) may be written in the form:

$$U_{eff}^2 = A_{11}U_1^2 + A_{22}U_2^2 + A_{33}U_3^2 + A_{12}U_1U_2 + A_{13}U_1U_3 + A_{23}U_2U_3 \quad (2.1)$$

Where:

$$\begin{aligned} A_{11} &= \cos^2\alpha + k^2\sin^2\alpha \\ A_{22} &= \cos^2\theta(\sin^2\alpha + k^2\cos^2\alpha) + h^2\sin^2\theta \\ A_{33} &= \sin^2\theta(\sin^2\alpha + k^2\cos^2\alpha) + h^2\cos^2\theta \\ A_{12} &= (1-k^2)\sin 2\alpha\cos\theta \\ A_{13} &= (k^2-1)\sin 2\alpha\sin\theta \\ A_{23} &= \sin 2\theta(-\sin^2\alpha - k^2\cos^2\alpha + h^2) \end{aligned} \quad (2.2)$$

Here U_1, U_2 and U_3 are the three mutually perpendicular components of velocity (U_1 is parallel to the probe axis). The angle α is that which the wire makes with the normal to the probe axis and θ is the angle between the plane of the wire and the direction of U_2.

For a non-steady flow each component of velocity can be split up into a steady, $\overline{U}$, and fluctuating, u, component where $U = \overline{U} + u$. Inserting this into (2.2) and multiplying out gives:

$$\begin{aligned} &(\overline{U}_{eff} + u_{eff})^2 = \\ &\left.\begin{aligned} &A_{11}\overline{U}_1^2 + A_{22}\overline{U}_2^2 + A_{33}\overline{U}_3^2 + \\ &A_{12}\overline{U}_1\overline{U}_2 + A_{13}\overline{U}_1\overline{U}_3 + A_{23}\overline{U}_2\overline{U}_3 + \end{aligned}\right\}\overline{\mathrm{X}}^2 \\ &\left.\begin{aligned} &2A_{11}\overline{U}_1u_1 + 2A_{22}\overline{U}_2u_2 + 2A_{33}\overline{U}_3u_3 + \\ &A_{12}(\overline{U}_1u_2 + \overline{U}_2u_1) + A_{13}(\overline{U}_1u_3 + \overline{U}_3u_1) + \\ &A_{23}(\overline{U}_2u_3 + \overline{U}_3u_2) + \end{aligned}\right\}\overline{\mathrm{Y}}\mathrm{y} \\ &\left.\begin{aligned} &A_{11}u_1^2 + A_{22}u_2^2 + A_{33}u_3^2 + \\ &A_{12}u_1u_2 + A_{13}u_1u_3 + A_{23}u_2u_3 \end{aligned}\right\}\mathrm{z}^2 \end{aligned}$$

Or in shorthand form:

$$(\overline{U}_{eff} + u_{eff})^2 = \overline{\mathrm{X}}^2 + \overline{\mathrm{Y}}\mathrm{y} + \mathrm{z}^2 \quad (2.3)$$

Taking square roots of both sides and expanding the R.H.S. using a power series gives:

$$\overline{U}_{eff} + u_{eff} = \overline{\mathrm{X}}\left[1 + \frac{1}{2}\frac{(\overline{\mathrm{Y}}\mathrm{y} + \mathrm{z}^2)}{\overline{\mathrm{X}}^2} - \frac{1}{8}\left(\frac{(\overline{\mathrm{Y}}\mathrm{y})^2}{\overline{\mathrm{X}}^4} + \frac{2\overline{\mathrm{Y}}\mathrm{y}\mathrm{z}^2}{\overline{\mathrm{X}}^4} + \frac{\mathrm{z}^4}{\overline{\mathrm{X}}^4}\right) + \ldots\right] \quad (2.4)$$

Neglect terms with triple or higher order fluctuating velocity correlations (e.g. $u_1u_2u_3$ or $u_1^2u_2$) gives:

$$\overline{U}_{eff} + u_{eff} = \overline{\mathrm{X}}\left[1 + \frac{(\overline{\mathrm{Y}}\mathrm{y} + \mathrm{z}^2)}{2\overline{\mathrm{X}}^2} - \frac{(\overline{\mathrm{Y}}\mathrm{y})^2}{8\overline{\mathrm{X}}^4}\right] \quad (2.5)$$

Time averaging (2.5):

$$\overline{U}_{eff} = \overline{\mathrm{X}}\left[1 + \frac{\overline{\mathrm{z}^2}}{2\overline{\mathrm{X}}^2} - \frac{1}{8\overline{\mathrm{X}}^4}\overline{(\overline{\mathrm{Y}}\mathrm{y})^2}\right] \quad (2.6)$$

Squaring and again neglecting terms with triple or higher order fluctuating velocity correlations:

$$\overline{U}_{eff}^2 = \overline{\mathrm{X}}^2 + \overline{\mathrm{z}^2} - \frac{1}{4\overline{\mathrm{X}}^2}\overline{(\overline{\mathrm{Y}}\mathrm{y})^2} \quad (2.7)$$

Time averaging (2.3):

$$\overline{U}_{eff}^2 + \overline{u_{eff}^2} = \overline{\mathrm{X}}^2 + \overline{\mathrm{z}^2} \quad (2.8)$$

Subtracting (2.7) from (2.8):

$$\overline{u_{eff}^2} = \frac{1}{4\overline{X}^2}\overline{(Yy)^2} \qquad (2.9)$$

Multiplying out $\overline{(Yy)^2}$ gives an expression with 45 terms. Rearranging this and factorizing yields:

$$\overline{u_{eff}^2} = \frac{1}{\overline{X}^2}\left(B_1^2\overline{u_1^2} + B_2^2\overline{u_2^2} + B_3^2\overline{u_3^2} + 2B_1B_2\overline{u_1u_2} + 2B_1B_3\overline{u_1u_3} + 2B_2B_3\overline{u_2u_3}\right) \qquad (2.10)$$

where:

$$B_1 = A_{11}\overline{U}_1 + \frac{1}{2}A_{12}\overline{U}_2 + \frac{1}{2}A_{13}\overline{U}_3$$
$$B_2 = \frac{1}{2}A_{12}\overline{U}_1 + A_{22}\overline{U}_2 + \frac{1}{2}A_{23}\overline{U}_3$$
$$B_3 = \frac{1}{2}A_{13}\overline{U}_1 + \frac{1}{2}A_{23}\overline{U}_2 + A_{33}\overline{U}_3 \qquad (2.11)$$

Equations 2.10 & 2.11 have been derived by previously by Perdichizzi et. al. (1990). Given a sufficient number of readings from the wires, equations 2.7 and 2.10 provide a solution for both the mean flow and Reynolds stresses. Since they are dependent on eachother an iterative solution is used based on the steps below;

Step 1 Guess a solution for U_1, U_2 & U_3 and calculate k^2, h^2 and the 'A' coefficients.

Step 2 Solve $\overline{U}_{eff}^2 = \overline{X}^2$ to give a first approximation of U_1, U_2 & U_3.

Step 3 For this solution recalculate k^2, h^2 and the 'A' coefficients and calculate the 'B' coefficients.

Step 4 Solve eqn. (2.10) for the Reynolds stresses.

Step 5 Solve eqn. (2.7) for U_1, U_2 & U_3.

Step 6 Repeat from Step 3 until the mean flow and Reynolds stress solutions have converged.

In practice 12 readings are taken with the wires rotated to different angles (7 readings with the slanted wire and 5 with the normal wire). This yields an over-determined set of equations which both reduces the sensitivity of the solution to experimental errors and allows an estimate to be made of the likely accuracy.

3. RESULTS

3.1 Upstream Slots

The midspan traverses at the upstream slots showed no significant variations in the flow that could be attributed to the pitching of the grid of bars. There were some differences in the mean flow due probably to the flow adjustment following the slight deflection caused by the angled positioning of the bars to the free stream. The differences in velocity magnitude were typically ±1.5% and in angle ±0.4° in yaw and ±0.5° in pitch. Details of the inlet turbulence (measured at one axial chord upstream of the leading edge) are given in table 2.

Streamwise turbulence intensity	5.12%
Normal turbulence intensity	4.95%
Spanwise turbulence intensity	5.62%
Turbulent k.e.	6.44%
Freestream length scale	9.358mm
Turbulent dissipation rate	32.65 m^2/s^3

Table 2: Inlet flow conditions.

The boundary layer profiles at one axial chord upstream of the blades are shown in Figure 3. Slight differences are seen between the three slots, but they are acceptably small. The average boundary layer parameters are given in Table 3, and these may be compared with the pitch averaged data obtained at Slot 1 obtained by Cleak (labelled JGC), and that from this work (labelled HM). The growth of the end wall boundary layer can be seen.

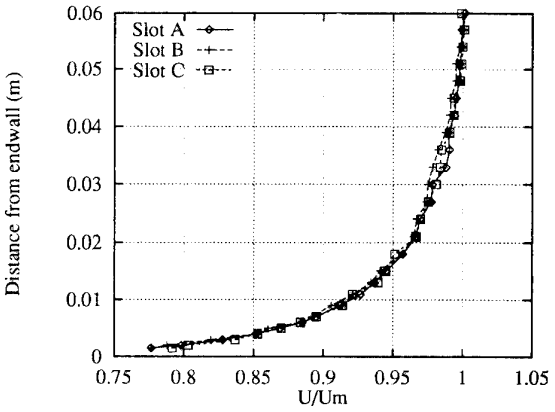

Fig 3: Inlet boundary layer velocity profiles.

The profiles of turbulent kinetic energy coefficient are shown in Figure 4. The scatter is similar to that seen at mid-span.

	$-1.0C_{ax}$	Slot 1	
		HM	JGC
99% thickness	40mm	42mm	43mm
Displacement thickness	2.8mm	2.9mm	3.7mm
Momentum thickness	2.3mm	2.4mm	3.1mm
Shape factor	1.22	1.18	1.20

Table 3: End wall boundary layer parameters

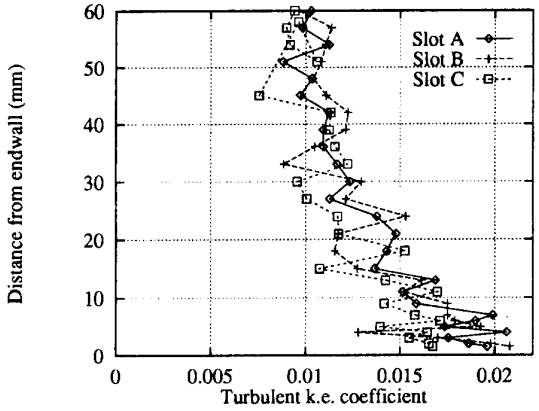

Fig 4: Inlet boundary layer kinetic energy profiles.

3.2 Tangential Slot Traverses

Using 21 locations, the spanwise extent of the all the traverses reported here was 60 mm (0.3 of half-span), which was sufficient to include the end wall flow features of interest to this work. The nearest location was 1.5 mm from the end wall. At Slot 1, the tangential extent covered about 1.5 *(blade pitch), with 17 locations, which was the same as earlier work, e.g. Gregory-Smith and Cleak (1992). At the traverse slots used within the blade row (3, 5, 6 & 8), 16 equally placed tangential locations were used. A complete area traverse was performed at the downstream slot 10 using the same grid of traverse points as used by Gregory-Smith and Cleak (1992). Thus the nearest location to the end wall was 5 mm for that traverse.

Slot 1 (-9% Cax).

Figure 5 shows the velocity magnitude contours and the secondary velocity vectors. The upstream potential effect of the blades can be seen away from the wall, while closer to the wall the effect of the horseshoe vortex can be seen, causing flow towards the end wall. The turbulence quantities (not shown) show away from the wall the expected decay in turbulence from the upstream traverse position. Pitch averaging the velocity to find the boundary layer profile gives the boundary layer parameters shown in Table 3. It would appear that replacing the moving belt wall by a solid wall has slightly reduced the

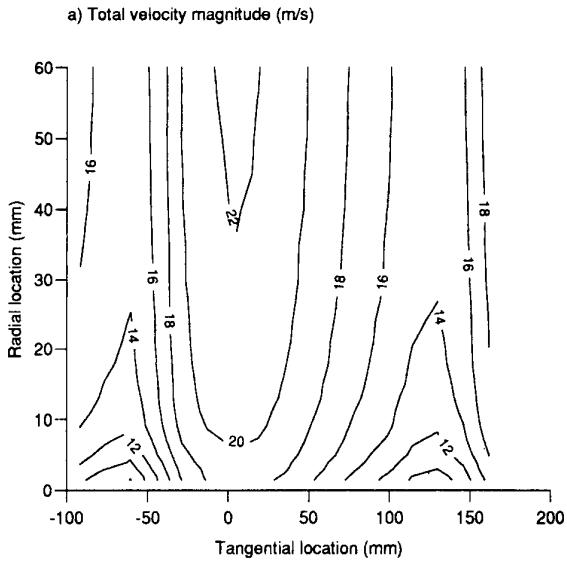

Fig 5a: Slot 1 Total velocity magnitude.

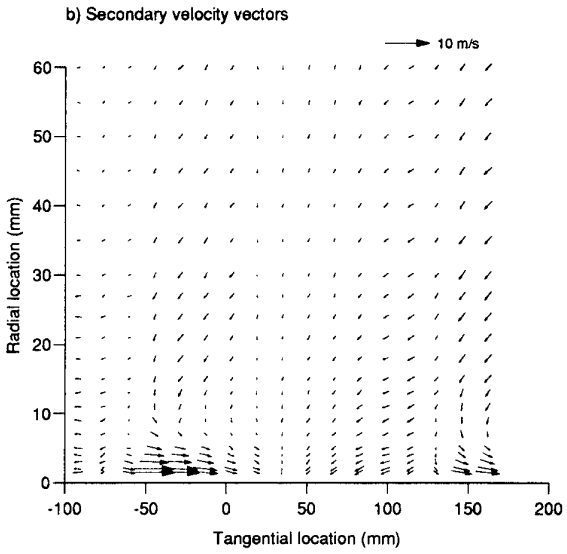

Fig 5b: Slot 1 Secondary velocity vectors.

boundary layer growth from the upstream to the Slot 1 position.

Slot 3 (26% Cax).

The velocity magnitude and secondary velocity vectors are shown in Figure 6. The cross passage velocity gradient is now well established, being distorted near the pressure surface and end wall corner by the formation of the passage vortex, clearly visible in the secondary velocity vector arrows. It should be noted that the vertical scale is magnified relative to the horizontal scale, so that the secondary vor-

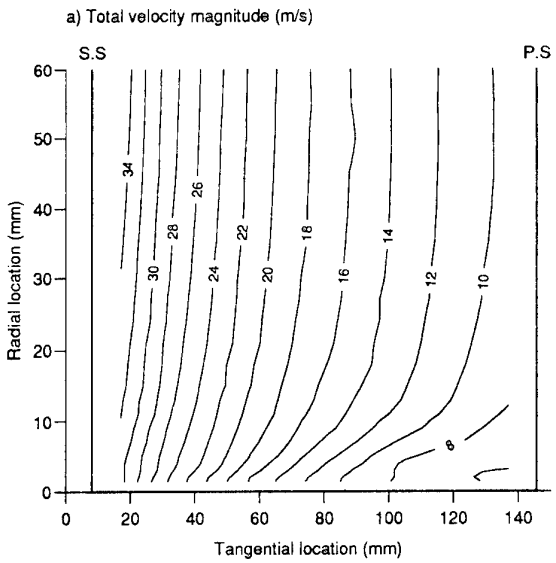

Fig 6a: Slot 3 Total velocity magnitude.

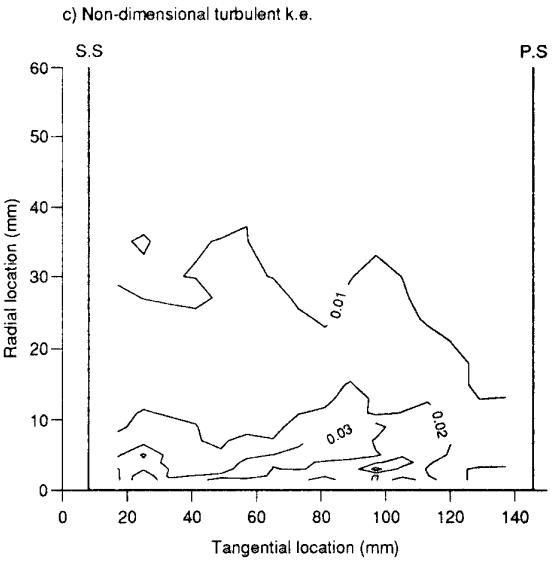

Fig 6c: Slot 3 Turbulent kinetic energy.

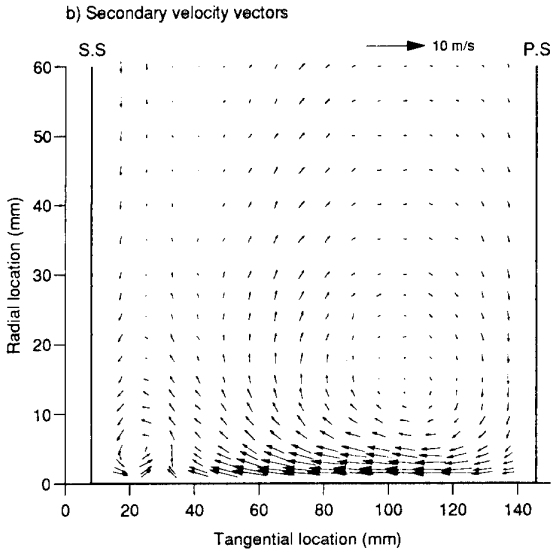

Fig 6b: Slot 3 Secondary velocity vectors.

tex is much more 'squashed' than it appears here. The suction side leg of the horseshoe vortex is also clearly visible very close to the suction surface corner. Figure 6 also shows the dimensionless turbulent kinetic energy contours also being distorted by the passage vortex, as it starts to induce low turbulence mainstream fluid down the pressure surface.

Slot 5 (55% Cax).

A large amount of blade turning occurs between slot 3 and 5 so that the passage vortex has crossed the passage, and is now located nearer the suction surface, as can be seen in Figure 7. The highly skewed nature of the flow at this slot near the end wall is indicated by the yaw angle contours. There is a considerable increase in the turbulent kinetic energy in the region of the vortex. However the near the end wall towards the pressure surface, the turbulent energy is quite low. The shear stresses (not shown) have also increased considerably in the region of the vortex.

Slot 6 (71% Cax).

Figure 8 shows that the passage vortex is beginning to move outwards along the suction surface and there is an indication of a corner vortex in the suction surface and endwall corner. As with slot 5, the turbulent kinetic energy is high in the region of the vortex and low away from it on the end wall. The $\overline{uv}$ (streamwise–cross passage) correlation shows mainly positive values in the passage vortex region, with some negative values (positive shear stress) above it, presumably due to the suction surface boundary layer. The $\overline{uw}$ (streamwise–spanwise) correlation is almost always negative, but on the end wall the values are very low, except in the region of the corner vortex. A turbulent boundary layer on the end wall would, of course, give negative values.

Slot 8 (97% Cax).

Slot 8 is just before the trailing edge, and the results are shown in Figure 9. The passage vortex has moved much further up the suction surface, so that much of it has not been captured in the traverse as seen by the turbulent kinetic energy contours. The $\overline{uv}$ correlation is now almost entirely negative as is

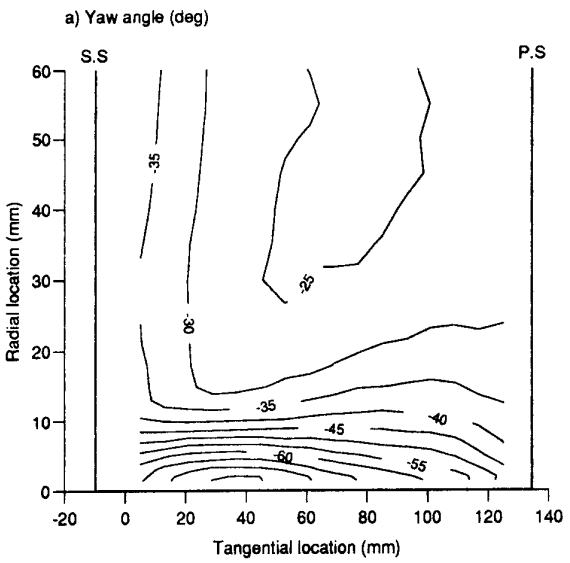

Fig 7a: Slot 5 Yaw angle.

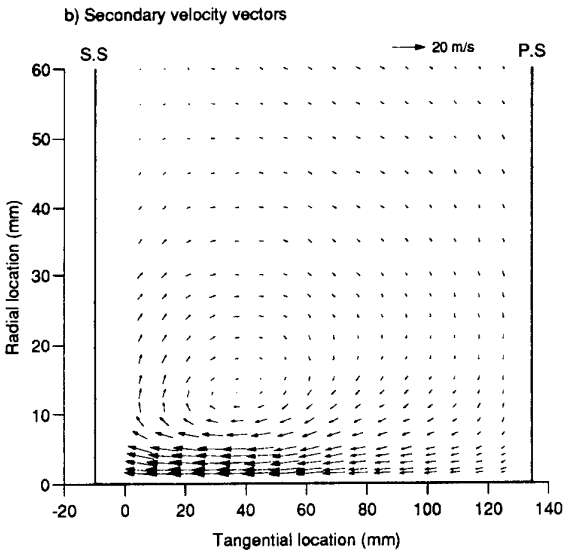

Fig 7b: Slot 5 Secondary velocity vectors.

the $\overline{uw}$ correlation. The latter still does not show significant values on the end wall attributable to a turbulent boundary layer.

Slot 10 (128% Cax).

This traverse yielded data generally similar to that presented by Gregory-Smith and Cleak (1992). Thus only the three shear stress correlations are presented here in Figure 10. The $\overline{uv}$ correlation shows the expected sign change across the wake and large negative and positive values in the vortex region, which are also seen for the $\overline{uw}$ correlation. The latter also

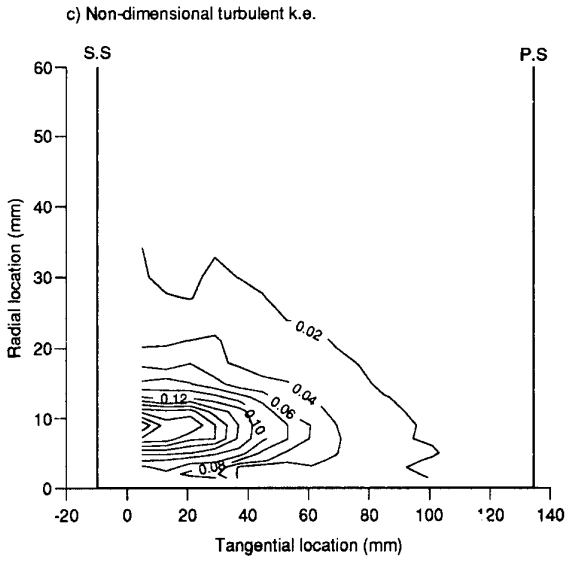

Fig 7c: Slot 5 Turbulent kinetic energy.

continues to show high negative values in the passage vortex region, now extending to about half the blade pitch. The $\overline{vw}$ correlation generally shows low values for most of the flow except in the region of the passage vortex, which also has a sign change across it.

3.3 End Wall Values

The data 1.5 mm from the end wall obtained by the above tangential traverses has been replotted as carpet plots. The secondary velocity vectors are shown in Figure 11. The highly skewed nature of the end wall flow can be seen in the later part of the passage, downstream of the pressure side leg separation line. The contours of turbulent kinetic energy in Figure 12 show clearly the high turbulence in the suction surface and end wall corner caused by the counter vortex, and relatively low values elsewhere. (The data in Figure 12 have been repeated to the adjacent blade passages – only one blade passage was traversed.)

4. DISCUSSION

The flow at the new upstream slots provide data suitable for an inlet plane for a CFD simulation with freestream values of turbulent components, decay rate and length scale having been determined. The boundary layer on the end wall shows a rather low value of shape factor compared to a standard flat plate boundary layer, where a value of 1.28 corresponds to a 1/7th power law profile. The flow has

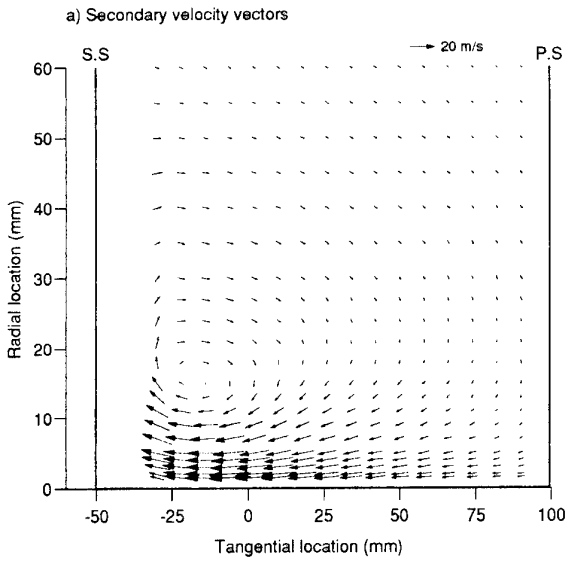

Fig 8a: Slot 6 Secondary velocity vectors.

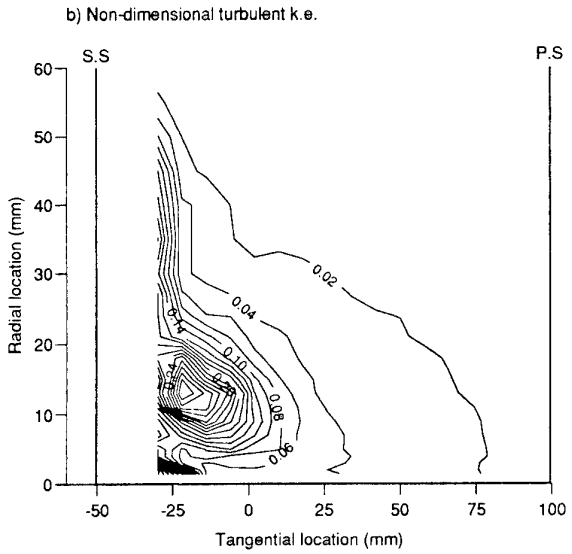

Fig 8b: Slot 6 Turbulent kinetic energy.

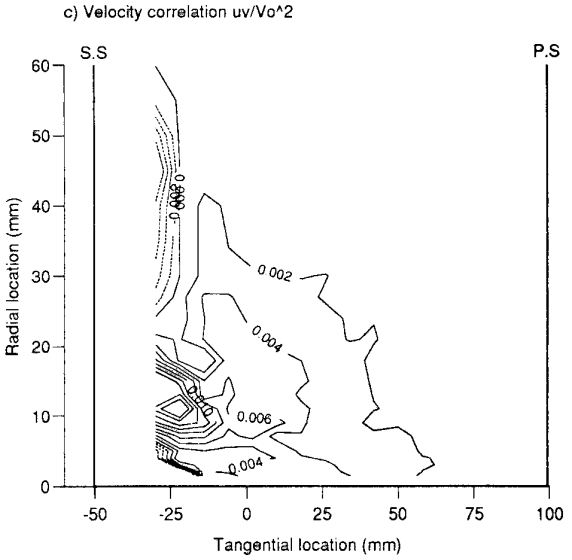

Fig 8c: Slot 6 $\overline{uv}$ velocity correlation.

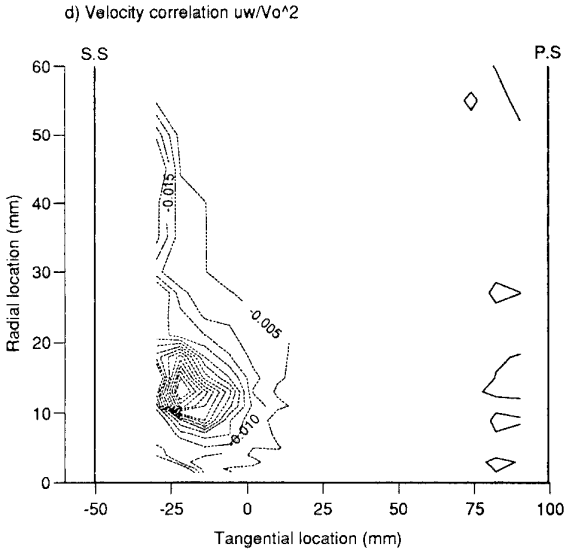

Fig 8d: Slot 6 $\overline{uw}$ velocity correlation.

been disturbed by the upstream grid of bars, and also the boundary layer bleed at the start of the end wall may have affected the profile. The growth up to slot 1 appears reasonable, although the agreement with previous work is only fair for displacement and momentum thickness. The newer end wall may have eliminated unevenness in the taped down flexible wall used previously.

The flow within the blade passage exhibits many of the features observed previously in this cascade and by many other workers investigating turbine secondary flows. The development of the horseshoe vortex legs and the passage vortex are clearly seen, with the movement of the passage vortex, first from pressure to suction surface, and then outward along the suction surface. The flow is seen to be highly turbulent within the passage vortex, particularly from slot 5 (55% C_{ax}) onwards. One difference from the data presented by Gregory–Smith and Cleak (1992) is in the sign of the $\overline{uv}$ correlation in the vortex region. They found the in vortex region the sign was positive at slot 8, but by slot 10 it was negative. In this

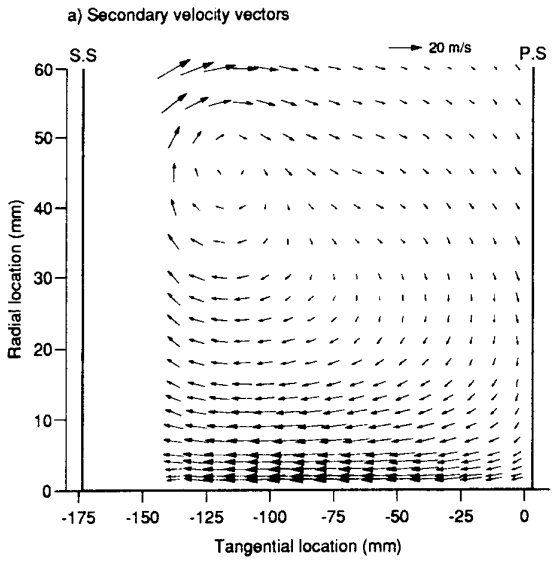

Fig 9a: Slot 8 Secondary velocity vectors.

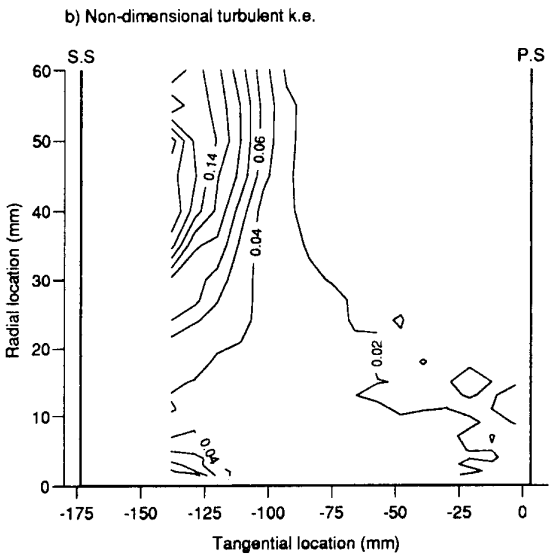

Fig 9b: Slot 8 Turbulent kinetic energy.

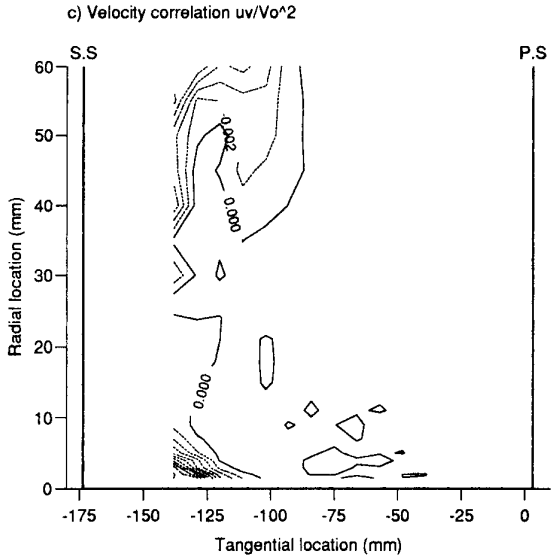

Fig 9c: Slot 8 $\overline{uv}$ velocity correlation.

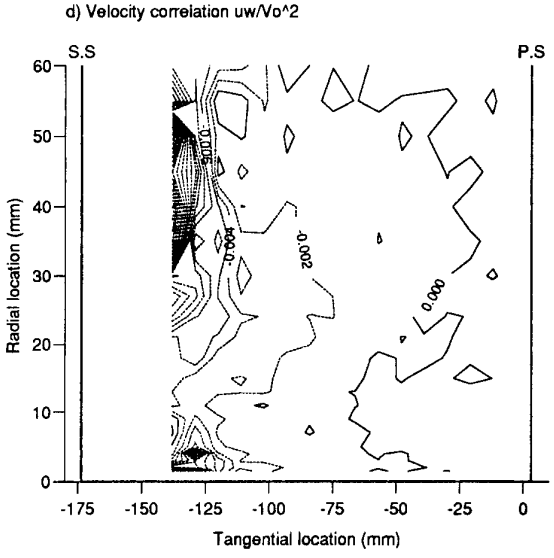

Fig 9d: Slot 8 $\overline{uw}$ velocity correlation.

work at slot 6 it is seen to be positive, but by slot 8 it appears negative (although not all the vortex region has been measured here at slot 8) and the negative value continues to slot 10, as seen previously. The sign change was discussed by Gregory–Smith and Cleak (1992), who indicated a possible mechanism. Here the sign change appears earlier, although further investigation of this is really required.

The state of the flow close to the end wall can be seen to show little evidence of turbulent behaviour except close to the suction surface where the counter vortex develops, as well illustrated by Figure 12. The $\overline{uw}$ correlation values which would be expected to be negative in a turbulent boundary layer are very low, again except close to the suction surface, although by the downstream slot 10, there are higher values beginning to appear over more of the end wall. These results agree with the conclusions presented by Harrison (1989) using film gauges on the end wall. It would be desirable to extend these investigations using a similar technique. A further development would be to study the intermittency close to the end wall, thus also indicating areas of transition.

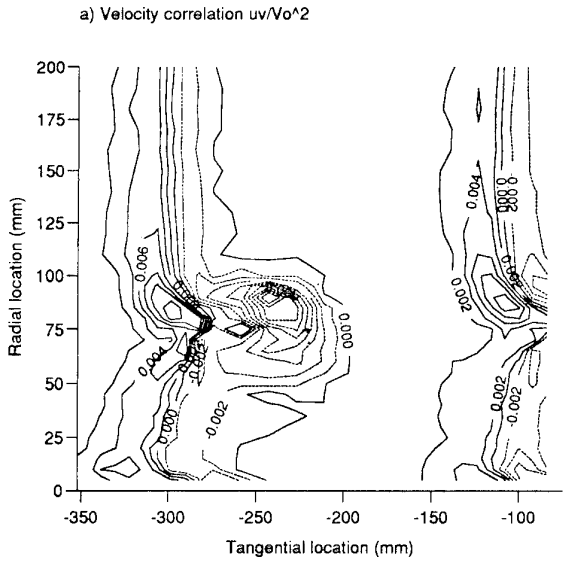

Fig 10a: Slot 10 $\overline{uv}$ velocity correlation.

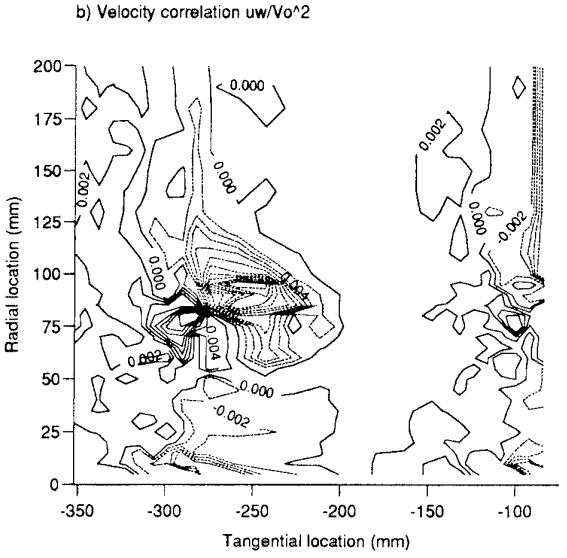

Fig 10b: Slot 10 $\overline{uw}$ velocity correlation.

In general the traversing did not go very close to the blade suction surface due to the probe shape, although it is rather closer than, for instance, Figure 9 would suggest, since the traverse plane is steeply inclined to the blade surface (Figure 2). However it would appear that in the secondary flow region, the flow is highly turbulent near the suction surface by slot 5, although further away from the end wall the flow may be laminar. By slot 6, the negative $\overline{uv}$ correlation well above the vortex region suggests that the mid-span flow on the suction surface

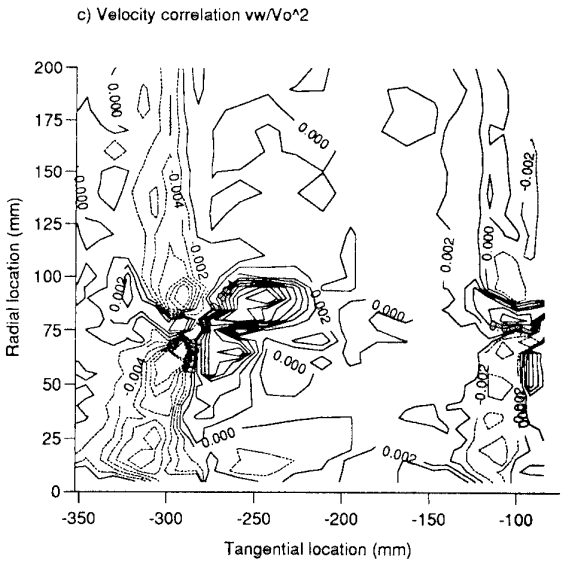

Fig 10c: Slot 10 $\overline{vw}$ velocity correlation.

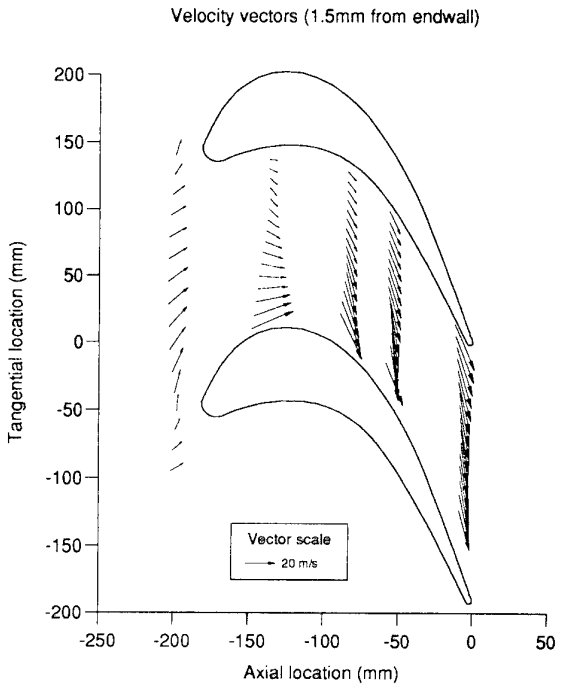

Fig 11: Secondary velocity vectors.

may now be turbulent. Previous surface flow visualisation by Beisinger and Gregory-Smith (1993) has shown turbulent flow on the suction surface behind and below the separation line that runs diagonally up the suction surface due to the suction side leg of the horseshoe vortex. Without the turbulence grid, a laminar separation bubble had been observed at 80% C_{ax} (slot 6 is at 71% C_{ax}), and this disappeared

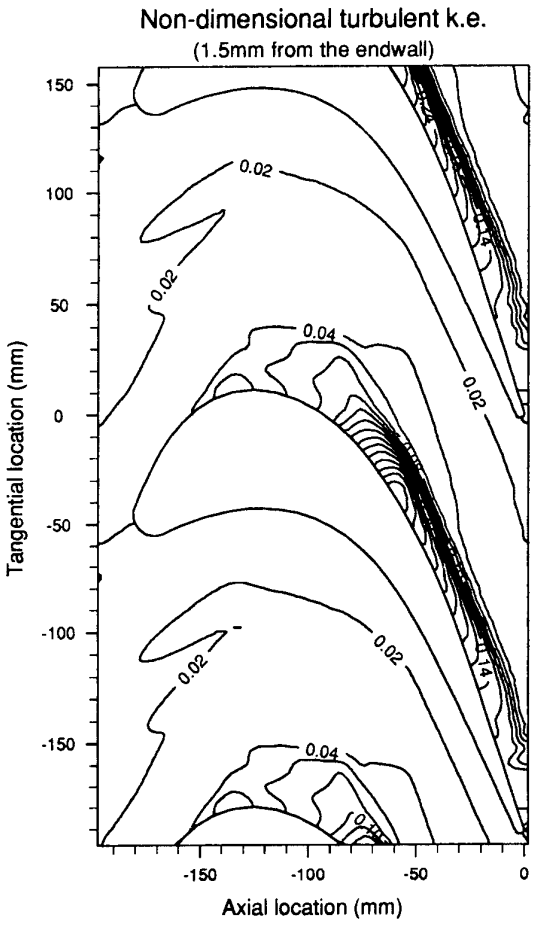

Fig 12: Turbulent k.e. 1.5mm from the endwall.

with the high inlet turbulence. The results presented here confirm the earlier flow visualisation findings. However there is clearly a greater need for traversing closer to the suction surface, which will require modification to the present instrumentation.

5. CONCLUSIONS

Detailed measurements of the flow close to the endwall have been made on six axial planes through the cascade. The following points are the main conclusions that have been drawn from this work.

- The initially thick, turbulent endwall boundary layer is rolled up into a loss core and replaced by a thin, highly skewed boundary layer.
- The low $\overline{uw}$ shear stress and turbulent k.e., at least up until slot 10 (128% C_{ax}), suggest that this new boundary layer is mainly laminar.
- There is a region of high turbulece levels in the endwall and syction surface corner, suggesting turbulent flow associated with the corner vortex.
- Although the traverses do not go very close to the suction surface, it appears that transition in the suction surface boundary layer, away from the passage vortex, occurs between slot 5 (55% C_{ax}) and slot 6 (71% C_{ax}).
- Measurements of intermittency and/or wall shear stress in both the suction surface and endwall boundary layers would help confirm these results. It would be particularly useful if they could be taken at more axial locations.

ACKNOWLEDGEMENTS

The authors gratefully acknowledge support from Rolls–Royce plc and their permission to publish this paper. The authors are also gratefull for additional support from the Engineering and Physical Sciences Research Council.

REFERENCES

Biesinger T.E. and Gregory–Smith D.G., Reduction in secondary flows and losses in a turbine cascade by upstream boundary layer blowing., ASME Paper No. 93–GT–114, (1993)

Cleak J.G.E., Gregory–Smith D.G. and Birch N.T., Experimental verification of a 3D turbulent flow calculation in an axial turbine cascade., AGARD PEP Symposium oc Computational Fluid Dynamics in Propulsion, AGARD–CP–501, Paper No. 8, (1991)

Gregory–Smith D.G. and Cleak J.G.E., Secondary flow measurements in a turbine cascade with a high inlet turbulence., Trans. ASME, J. Turbomachinery, 114, pp 173–183, (1992)

Gregory–Smith D.G., The ERCOFTAC seminar and workshop on 3D turbomachinery flow predictions., ASME Paper No. 93–GT–423, (1993)

Halstead D.E., Okiishi T.H. and Wisler D.C., Boundary layer transition and separation on a turbine blade in plane cascade., AIAA/SAE/ASME/ ASEE 26th Joint Propulsion Conference, Orlando, Fl., (1990)

Harrison, S., Secondary loss generation in a linear cascade of high–turning turbine blades., ASME Paper No. 89–GT–47, (1989)

Jørgensen F.E., Directional sensitivity of wire and fiber film probes: An experimental study., DISA Information, No. 11, (1971)

Mayle R.E., The role of laminar–turbulent transition

in gas turbine engines., ASME Paper No. 91-GT-261, (1991)

Mee D.J., Baines N.C. and Oldfield M.L.G., Detailed boundary layer measurements on a transonic turbine cascade., ASME Paper No. 90-GT-263, (1990)

Perdichizzi A., Ubaldi, M. & Zunino P., A hot-wire measuring technique for mean velocity and Reynolds stress components in compressible flow., Measurement techniques for transonic and supersonic flows in cascades and turbines, Proceedings of 10th symposium, VKI, (1990)

Sieverding C.H., Recent progress in the understanding of basic aspects of secondary flows in turbine blade passages., Trans. ASME, J. Eng. Gas Turbines and Power, 107, pp 248-252, (1985)

Walker G.J., he role of laminar-turbulent transition in gas turbine engines - a discussion., ASME Paper No. 92-GT-301, (1992)

Walsh J.A. and Gregory-Smith D.G., The effect of inlet skew on the secondary flows in a turbine cascade., Proc. I. Mech. E., Turbomachinery - Efficiency Prediction and Improvement, Paper C275/87, pp 15-28, (1987)

Zunino P., Ubaldi M. & Satta A., Measurements of secondary flows and turbulence in a turbine cascade passage., ASME Paper No. 87-GT-132, (1987)

REFERENCE NO. OF THE PAPER: 8

DISCUSSOR'S NAME: G.D. Willis, GEC-Alsthom, U.K.

AUTHOR'S NAME: D.G. Gregory-Smith, H. Moore

Q: Was the turbulence grid a single or bi-planar grid, and how did you maintain a high level of turbulence (4.5%) at cascade inlet, 1400 mm downstream of the turbulence grid?

A: The grid consisted of two rows of 25mm diameter bars. One row had the axes horizontal, and the other bars were inclined vertically to be parallel to the cascade inlet (Figure 1). The large scale meant that from one chord upstream to the inlet plane the turbulence intensity decayed from 6% to 4.5%, approximately.

THREE DIMENSIONAL MODELLING AND SECONDARY FLOWS CONTROL IN GAS TURBINES.

B.A. Tikhomirov
J.M. Pogodin
Marine Technical University
3, Lotsmanskaja str.
190008 St. Petersburg
Russia

SUMMARY

Three-dimensional model of vortex Flow in a passage is based on Clebsh's Transformation. The associated computer codes consist of the following modules: finite elements mesh automatical generation, finite elements optimum renumberation, calculation of flow, processing of results, analysis of losses . Losses analysis uses typical elements losses models:friction, turn, expansion losses and losses due to equalization throughout the flow. Two last components of losses are calculated by use of integrating throughout the streamlines of the passage element where the results of 3-D flow calculations are known.

The model of mass flux averaged flow in turbine rows with end wall inclination, tangential lean or curvature of the blades has been developed. It is made due to the additional boundary condition along geometrical throats line of blade to blade passage. The boundary condition is radial distribution of meridional stream lines inclination which is based on the principle of flow mass flux maximum. Correlations between different flow models has been developed.

Research of secondary flows control problem focuses on the effect of end wall fences, wall and blade ledges use for cross flows limitation. Combination of wall ledge and suction from ledge surface, blade through slots and holes used for gas transportation from pressure to suction blade surface in secondary flows area are also experimentally studied in axial turbines.

LIST OF SYMBOLS

a,r,u	axial, radial, tangentional coordinates
B	end wall fence axial width
Bt	stator blade axial size from leading edge to the blade passage throat section
b	blade profile chord
C,Ca	velocity and its axial component
Cs	secondary flow velocity
D	stator row mean diameter
F	body force per unit mass
fs	dissipative force per unit mass
g_a,g_e	defined by equation (6) and (7) factors
h	end wall fence radial length
i	enthalpy
K	proportional thinckness of blade factor
l	stator blade length
n_a, n_r, n_u	components of a normal to stream surface
p	pressure
q	defined by equation (1) parameter
s	end blade ledge surface size
$(t/b)p$	periphery pitch to chord ratio
α_s	angle defined by equation (9)
α_1	stator blade mean diameter discharge angle
γ	end wall fence lean angle to radial direction
γ_s	meridional streamlines lean angle to axial direction
δ	end wall ledge maximum radial size, tip clearance
δ_s	angle defined by equation (10)
δ_0^*	inlet displacement thickness
ς	total pressure loss factor
η	stage efficiency based on the total inlet and outlet parameters for heat drop analysis
η_e	energy factor
θ	periphery wall angle
μ	mass flux factor
ρ	density
φ	velocity factor

Superscripts

—	averaged, relative value
~	mass flux averaged parameter by equation (1)
$\rightarrow$	vector

BACKGROUND

Vaneless spacings including intakes and discharges, turbomachinery blade spacings are being considered in the paper. Untill recently different vaneless spacings have been designed with experimental methods or calculations derived from the empirical models of energy losses [1],[2]. Now there are real possibilities of three-dimensional flow models use for complicated structures of turbomachinery intakes and discharges design. Among the models of flow calculation it should be mentioned the viscous flow models [3],[4] and also inviscid flow models and components of losses analysis procedures with use of empirical models based on experimental data [5].

Paper presented at the AGARD PEP 85th Symposium on "Loss Mechanisms and Unsteady Flows in Turbomachines", held in Derby, United Kingdom, 8-12 May 1995, and published in CP-571.

Flow mathematical modelling in turbomachinery blading spaces have a long way of development from axisymmetrical models and iterative procedures of inviscid flow calculation on stream surfaces [6],[7], [8] to viscous flow three-dimensional models [9],[10]. Such type of analysis procedures doesn't make it possible to use simple computer techniques and require significant time to prepare and for calculations. Alternative as in the vaneless spacings is turbomachinery blades row profiling based on simpler inviscid flow models and current concepts and generalization on energy losses experimental data. Use of limited numbers of blade area calculation sections can make it possible to approach the flow pattern performance in case of complicated structures as blade rows with leaned or curved blades. Computer codes based on the simple flow models with high accuracy of performance analysis due to experimental data in the energy losses can provide operational use for the preliminary design of turbomachinery elements , reduce the terms and expences for their development. In the paper this approach to turbomachinery flow modelling is considered.

Secondary flow modelling in turbomachinery blade to blade passage has also a long history where the early models were based on the inviscid flow end wall inlet vorticity development. The later are three-dimensional viscous flow models for the blading space of the row taking into account end wall secondary flows. The secondary flows mathematical modelling doesn't have practical use. Experimental results generalization of parameters measurements in secondary flows area and associated data on end wall losses are more popular. Another part of secondary flows study is development of end wall losses reduction methods, which have several effect schemes of the influence on the secondary flows on the turbine level, on the stage, row and finally blade to blade passage levels. As to the turbine design level it is reduction of the blade rows inlet vorticity with choice of turbine end wall shapes, dividing the heat drop among the stages and blades length determination. Influence on the secondary flows in the stage can be provided with the choice of meanflow parameters and angles, radial distribution of the mass flux and circulation in the row to row gap. The secondary flows limitation on the blade row level concerns the choice of pitch to chord ratio, aspect ratio, profiles and passages shapes, end wall profiling. The methods of direct secondary flow control in the blade passage are high efficient and considered in this paper.

The problem of secondary flows control in passages of axial flow turbines was being studied in limited number of researches. The methods of secondary flows control are being classified in two types. The first is the method of structural effect with additional elements located on the passage surfaces as obstacles for secondary flows development. The second are the mass and energy flux effects based on the reduction of passage surfaces boundary layer thickness with suction of low velocity gas or on the change of flow parameters with additional energy supply to the secondary flow area. Among researches of structural effects it should be mentioned blade fences [13],[14] ledges [14], and grooves [18], wall fences [17],[18], [19] , ledges [17] and grooves [15] in the secondary flow area.

Several works are devoted to the mass flux effect on the secondary flows. For example effect of suction is studied in [12],[18], effect of energy supply to the secondary flow area with jet stream is investigated in [16], [17],[18]. An attempt to summarize and to get an generalization of the effect of secondary flows control methods is made in this paper.

THREE-DIMENSIONAL FLOW MODELLING in TURBOMACHINERY INTAKE and DISCHARGE PASSAGES

Three-dimensional model of inviscid fluid vortex flow in a passage is based on applying of the variational principles to the system of governing equations where the Clebsh's transformation for a velocity is used to introduce new variables such as the potential and vortex function. The associated computer codes consist of the next modules: finite elements system automatical generation, finite elements number optimum renumberation, three-dimensional flow calculation and results processing. The main problem of finite elements automatical generation is setting of mesh coordinates, directions of finite elements round-about paths and mesh visualization. Structure analysis of turbomachinery shows that in some cases for example for turbine exhaust systems and others the passages can be represented as a system of regular subareas having similar restricting surfaces and sections. Renumberation finite elements numbers is iteractive procedure which can be stopped when condition of minimum numbers value of touching finite elements is achieved. The comparison of model calculating results to accurate solutions and Stanitz's curved rectangular-sectioned passage experimental research data shows good accuracy. Under confidence probability 0.95 mean value of confidence interval of model calculated pressure in Stanitz's passage is 1.3 %.

The numerical analysis of the flow in circular-sectioned bend has been carried out. Different inlet conditions on velocity profile (symmetrical and nonsymmetrical) have been considered (Fig.1). It made possible to find out interaction effects of main and secondary flows. Pressure distribution along the bend depends on the inlet velocity profile. Minimum pressure gradient from external to internal surface has been received for the maximum of inlet velocity displacement to the external surface (*c*). It leads to the secondary flows energy χ reduction. The secondary flow is developed in maximum rate for inlet velocity maximum displacement to the internal surface of the bend (*b*). The main and secondary flow interaction leads to more uniform outlet velocity profile and it can be used for the solution of such problems in gas pipe system design.

Axial Flow turbine intake passage of Diesel Turbocharges has been calculated. It is a complicated design of limited sizes volute casing with one or two sides of tangential flow supply and outlet axial annular stator blade row. The satisfactory coincidence with the experimental values of velocity distribution in tangential and less in spanwise direction at the passage outlet has been shown for volute casing of one side of flow supply . The calculation is made for intake passage without stator blade row and give a reasonable approach of flow outlet tangential ununiformity and stator blades incidence angle. Two sides flow supply intake passage provide more uniform in tangential direction velocity profile. One of the basic problems of intake passages numerical modelling is outlet boundary conditions on streamlines lean angle due to the stator blades back influence. Empirical data based on the experiments has been used in the calculation procedure. One and two sides flow supply intake passages have been tested for different inlet and outlet values of stator blades angle. The generalizations of the velocity as functions of incidence angle is received for positive and negative angles and this boundary condition is automatically being corrected in iterative scheme of calculation.

In addition to the three-dimensional flow modelling the energy losses model and computer programm for discharge passages have been developed on the basis of the experimental data generalizations for typical components of energy losses: friction losses, turn losses, expansion losses and losses due to parameters equalization throughout the flow. Two last components of losses are being calculated with integrating throughout the stream-lines of passage element where the results of three-dimensional flow calculations are known. Validation of efficient and accurate analysis procedure has been made with comparison of calculation data to the results of experimental study of annular axial, axial and radial flow diffusers and passages with diffuser and collecting chamber of one side flow outlet. The axial diffuser angle, expansion rate (Fig.2) and collecting chamber diameter influence on the passage efficiency have been analysed. Standard relative deviation of loss calculation is 5% for the axial and radial flow diffusers and 7% for passage as a whole. The computers codes have been used for exhaust passages design of aeroderived gas turbine for power and mechanical drive.

THE MASS FLUX AVERAGED AXISYMMETRICAL FLOW in MULTISTAGE TURBINES with STATOR BLADES TANGENTIAL LEAN or CURVATURE

During prelimitary design of multistage turbines axisymmetrical flow models in the space between blade rows are widely used to coordinate the cascades operation conditions. It is a first approach to quasi-3D models. Axisymmetrical models of inviscid compressible flow including empirical correlation for several viscous phenomena has been developed [7], [8], [9] and been used for the stage design for many years.

Some important improvements of the axisymmetrical flow model in the space between blade rows will be discussed in the paper. The purposes of the improvements are as follows:

- Development of the correlations between integral cascade parameters that are determined with 1,2,3-D models, experimentally determined parameters and reversible adiabatic flow parameters with traditional mass flux μ, velocity or momentum φ, and energy η_c factors.

- An empirical-analytical simple model development for approximate analysis of blades tangential lean or curvature and also end wall inclination influence on the flow parameters in the space between blade rows. It should be considered as an approach to 3-D models having fast solution.

The particular features of improved models are the following:

1. Inviscid flow is being analysed in the blade sections along geometrical throats, leading and trailing edges and in the sections of space between blade rows. The space between leading edges and throat lines is approximated with actuator discs. The model equations are represented in terms of averaged parameters. The velocity components, enthalpy, stagnation enthalpy are mass flux rate through the section across passage averaged parameters with the equation

$$\tilde{q} = \left(\int_0^{2\pi K} q c_a \rho dr \right) / \left(\int_0^{2\pi K} c_a \rho dr \right) \qquad , (1)$$

where $\tilde{q}$ is mass flux averaged parameter , K is proportional thickness of blades or other structures coefficient.

Pressure is the section across passage area averaged parameter. Resulting pressure force acting on the elements of blade surface is represented as distributed body force and the force components normal to the mean stream surface $\overline{F}$ are determined.

The small perturbations were neglected. They represent the difference of mass flux factor in section elements normal to axial and radial direction. The small perturbations will be equal to zero if the equations are being integrated throughout the section. As a result the main equations in stationary co-ordinate system are as follows:

- continuity

$$\nabla\left(g_a \cdot K \bar{\rho} \vec{\bar{C}} \right) = 0 \qquad , (2)$$

- motion

$$g_a \left(\vec{\bar{C}} \nabla \right) \vec{\bar{C}} + \frac{\nabla \bar{p}}{\bar{\rho}} - \vec{\bar{F}} - \vec{f}_s = 0 \qquad , (3)$$

energy

$$\nabla\left(\tilde{i}+g_e\frac{\tilde{C}^2}{2}\right)=0 \qquad ,(4)$$

-state $\quad \bar{\rho}=f\left(\bar{p},\tilde{i}\right) \qquad .(5)$

The parameters g_a and g_e in the equations (2)-(4) estabish equivalence between the mass flux and kinetic energy of real flow and flow where properties are calculated with averaged velocity $\tilde{C}$. The parametres g_a and g_e can be determined with traditional mass flux, velocity and energy factors

$$g_a=\frac{\mu}{\varphi}\frac{\bar{\rho}_t}{\bar{\rho}} \qquad ,(6)$$

$$g_e=\frac{\eta_e}{\varphi^2} \qquad ,(7)$$

where $\bar{\rho}_t$, $\bar{\rho}$ are averaged densities determined in reversible adiabatic and real flows.

It should be noted that the value of parameters g_a, g_e are almost equal to 1 when the flow properties gradients in averaging direction are moderate and g_a, g_e aren't equal to 1 when the gradients are large.

2. The influence of blades tangential lean or curvature and end wall inclination are being modeled approximately with the additional boundary conditions placed along the geometrical throats line of turbine blade to blade passage [11].

The additional boundary conditions are radial distribution of angles of meridional streamlines to axial direction γ_s. The angles are determined with solving the system of equations which represents the principle of mass flux maximum through geometrical throats section of the blade passages. This solution for every point of throat section is

$$tg\gamma_s=-\frac{tg\delta_s ctg\alpha_s}{1+tg^2\delta_s} \qquad ,(8)$$

where the angles α_s and δ_s are determined as

$$ctg\alpha_s=-\frac{n_a}{n_u} \qquad ,(9)$$

$$tg\delta_s=-\frac{n_r}{n_u} \qquad ,(10)$$

and n_a ,n_r ,n_u are the components of a normal to mean stream surface.

If the hub or tip angles γ_s aren't equal to the wall angle, the angle γ_s is being corrected in space near walls to satisfy boundary conditions on the walls.

The additional boundary conditions in geometrical throats section are used to approximate the meridional streamlines and provide the influence on a streamlines curvature.

3. The loss, velocity and mass flux factors analysis models are based on empirical data obtained from experimental study of cascades, blade rows and turbine stages. The objects of experiments have radial, tangentialy leaned, curved end-adapted stator blades and different angles of tip wall inclination.

Several test calculations of blade rows and turbine stages of different tangential lean angle and curved blades have shown acceptable accuracy of flow characteristics prediction in comparison to the experiments at and off design conditions. An example of calculation and experimental analysis of angle α_s radial distribution at the different sections of outlet of turbine stator row with tangential lean and radial blades is in Fig.3. Calculation and experimental analysis results of stator blades tangetial curvature [angle δ_s is determined from equation (8)] influence on the efficiency of turbine stage of different end wall lean angle γ_s are presented in Fig. 4.

The computer codes have been used for 2 stages power turbine design of 60 MW aeroderived gas turbine power unit. The recomendations on the parameters radial distribition for the blading profiling have been worked out. Use of tangential curvature stator blades made it possible to increase turbine stage efficiency by 0.8% in comparision to the stage with radial stator blades efficiency which was 92.5%.

SECONDARY FLOWS CONTROL in AXIAL FLOW TURBINES

The Structural Means of Effect on The Secondary Flows

The research results of this type of secondary flows control means focuses on the study of end wall fences, ledges and end blade ledges influence on the turbine stages efficiency. The fences are located on the stator row periphery wall in each blade passage along mean line of the passage. Several examples of end wall fences influence on the turbine stage efficiency are presented in the paper (Fig.5). Optimum fences geometry experimental analysis includes *h/l, B/Bt* and γ optimum values determination. The part of results has been got by dynamic test of the stages ($\Delta\eta_h$). For confidence probability 0.95 confidence interval of stage efficiency η experimental determination is 0.3%. The other results (*B/Bt*, γ influence) were received by means of the static test of cascades. Data base for the fences influence analysis consists of the results of experimental study of 13 turbine stages. The range of stage geometry change is as follows:

D/l = 3.18 - 19 ; $\alpha_1=10^0-45^0$; $\theta=0^o-49^o$;

l/b = 0.36 - 2.5 ; $(t/b)p$ = 0.65 -1.075 .

Statistic generalizations take into account the optimum relative fence length $\overline{h} = h/b$, width $\overline{B} = B/Bt$, lean angle to radial direction and relative efficiency growth

$$\Delta\overline{\eta}_h = (\eta - \eta_{h=0})/\eta_{h=0}$$

under the optimum fence sizes and stage velocity ratio.

$$\overline{h} = 0.11\left[\left(D/l\right)^{0.5}(l/b)^{-0.9}\eta^{0.4}\cos\theta\cdot\sin\alpha_1\right]^{-1},$$

$$\overline{B} = 0.384\cdot\left(t/b\right)+0.6,$$

$$\gamma = \arcsin(tg\theta\cdot tg\alpha_1),$$

$$\Delta\overline{\eta}_h = 0.034(D/l)\left[(l/b)^{-0.2}(t/b)_p^2\eta^{1.6}\cos\theta\sin^{1.1}\alpha_1\right]^{-1}$$

The experimentally set fact that if the secondary flows are more developed and stage efficiency is less the positive fences effect is higher was used in statistic generalization. The use of stage efficiency unital value η in regression equation helped to take into account the operation parameters (*M, Re* , incidence), inlet vorticity and turbulence influence. Cosideration of geometry effects on the secondary flows development provides necessary regression accuracy. The experimentally set correlations $\Delta\overline{\eta}$ from $\overline{h},\overline{B},\gamma$, are of extremum type. The optimum values $\overline{h},\overline{B},\gamma$ and matching maximum values $\Delta\overline{\eta}$ are used in generalization. The fences optimum sizes and lean angle corresponds to the more favourable combination of losses components due to the secondary flow velocity reduction and additional fences surface friction, free end and trailing edge wake vorticity.

The end wall ledges are also located on the stator row periphery wall in blade passages in the passage part between pressure side of the blade and mean line of the passage (Fig.6). The ledge geometry configuration is smoothly coordinated with the wall in the inlet and outlet passage parts and in the part close to the blade. The example of turbine stage dynamic test with ledges and comparison of results to fences influence on the stage efficiency are shown in the paper (Fig. 6). Periphery end wall ledges positive effect is less then fences effect. The data base for end wall ledges influence analysis consists of the results of experimental study of 8 turbine stages. The range of stages geometry change is as follows:

D/l = 3.18 - 19 ; α_1 = 10° - 30° ; θ = 0 - 40° ;

l/b = 0.36 - 2.95 ; $(t/b)p$ = 0.65 - 1.075

Statistic generalizations for optimum value of the ledge relative radial depth $\overline{\delta} = \delta/b$ and relative efficiency growth $\Delta\overline{\eta}_\delta = (\eta - \eta_{\delta=0})/\eta_{\delta=0}$ under the optimum ledge depth and stage velocity ratio are as follows:

$$\overline{\delta} = 0.22\eta^{0.5}\cos\theta\cdot\left[(D/l)(t/b)_p^{0.5}\sin^{0.8}\alpha_1\right]^{-1},$$

$$\Delta\overline{\eta}_\delta = 0.31\sin^{0.2}\alpha_1\cdot(t/b)_p^2(D/l)\cos\theta\cdot\left[(l/b)^{-0.8}\eta^{0.2}\right]^{-1}$$

The nature of ledge effect on the secondary flow is close to the effect of fence but result is less because of limited ledge radial depth in comparison to the fence radial length. The ledges effect doesn't depend on the ledge design where the wall step along mean passage line can be provided with the cavity between passage mean line and blade pressure side or the bulge between passage mean line and blade suction line.

The end blade ledges are located on the stator row blades suction side close to the periphery wall (Fig.7) and are being used for partial localisation of secondary flow vortex in the blade wake. The data base for the end blade ledges influence analysis consists of the results of experimental study 6 linear cascades. The range of cascades geometry change is the following: *(t/b)p* = 0.6 - 1.2; $\alpha_1 = 10^0 - 45^0$. Verification of end blade ledges effect has been conducted with the test of 2 stages *D/l*= 7.0 and 4.4 , α_1= 17° and 27° , *(l/b)* = 0.9 and 1.43. The result of turbine stage test is on Fig.7. Optimum relative ledge high $\overline{c}$ = 0.1 -0.12 and the size along suction side $\overline{S} = S/b$ have been got due to the experimental results generalization

$$\overline{S} = \left[\begin{array}{l} 0.81(t/b)_p + 0.2(t/b)_p^{-1} - 2.73\alpha_1 + \\ 7.05\alpha_1^2 - 5.7\alpha_1^4 - 0.42\alpha_1^2(t/b)_p^{-1} - 0.46 \end{array}\right] tg^{-1}\alpha_1$$

For confidence probability 0.95 confidence interval of $\overline{h},\overline{B},\gamma,\overline{\delta},\overline{S}$ analysis is 10% and confidence interval for the stage with stator row fences and ledges efficiency η is 0.3% that corresponds to the confidence interval of η experimental determination.

The Mass Flux Effect on The Secondary Flows

In this papers only one method of mass flux effect on the secondary flows is considered. It is the use of blade through slots and holes for gas transportation from high pressure blade surface part to blade suction side. The location of the slot and hole exit in the end zone of the blade provides high energy jet effect on the secondary flow. The slot or hole exit is located between the point of maximum curvature of the blade suction side and throat line (Fig.8). The small energy supply to the secondary flow area is capable to reduce the pulsations in passage vortex zone or even to exclude vortex generation and unsteadiness that provide the main component of the end wall losses. The mouth of the slot or the hole can be located in the high pressure zone on the blade pressure side or upstream on the suction side.

The energy supply to the secondary flow area on the blade suction side has been studied for the stator blades periphery slots arrangement. The examples of turbine stages test results are on Fig.8. Inlet displacement thickness variation have been got due to the different angles of inlet diffusers. The data base

consists of the results of experiments with the linear cascades and several turbine stages. The range of stage geometry performance change is as follows:

D/l = 4.12 - 8.02 ; $(t/b)p$ = 0.87 - 1.2 ; l/b = 0.83 - 1.2.

The optimum relative slot high $\bar{e} = e / b$ generalization and associated relative stage efficiency growth

$$\Delta\bar{\eta}_e = (\eta - \eta_{e=0}) / \eta_{e=0}$$

are the following:

$$\bar{e} = 0.08\cos\theta\left(\eta^{2.5}\sin^{0.4}\alpha_1\right)^{-1} \quad ,$$

$$\Delta\bar{\eta}_e = 0.52(t/b)_p\left(\eta^4\sqrt{\sin\alpha_1}\right)^{-1}$$

In addition to the slots influence generalization several experiments have been carried out for limited number of turbine stages which were devoted to the study of stator blade through holes in the secondary flow area and rotor blade periphery slots effects . Turbine stage with stator blade through holes (Fig. 9) has D/l = 19 and $(t/b)p$ = 0.65 . The hole in the secondary flow area is of variable section and the hole axis has minimum angle to the blade suction surface in the exit point. The hole is located between upstream and downstream points of the blade suction side. The optimum ratio of the hole exit area value to the passage throat area value is 0.012. The relative growth of the stage efficiency is about 1.5% . It is less than the slots positive effect.

Rotor end blade slots use (Fig. 10) can be considered as a method of end blade area reduction. Study of turbine stage with geometry D/l = 8 , l/b = 1.2 and different tip clearance values has shown positive effect of slots up to 2% of stage efficiency relative increasing. Tip clearance increasing provides higher slots effect. The combination of end wall ledge and suction from the ledge surface has been studied with the stage of D/l = 3.9 , α_1= 30° testing. This method provides interception of the gas part participating in the secondary flow. The suctioned gas is being directed with the system of internal ducts to the annular space and then to the tip clearance zone (Fig. 11). The ledge relative radial size $\bar{\delta} = \delta / b = 0.05$ The hole area value for the gas suction was changed. The optimum ratio of hole area value to the passage throat area value is f / f_t=0.025 and associated relative growth of stage efficiency is about 2.2% for the suction from ledges step surface and about 1.5% for the suction from the wall without ledges. The main effect here is the secondary flows limitation with ledges because of the ledges effect without suction for this experiment is 1.5%.

CONCLUSION

1. The 3-D model of inviscid flow and associated computer codes of turbomachinery passages based on the energy losses experimental data generalization are of good accuracy of passage performances prediction and can provide operational use for turbine preliminary design with minimum PC time expenditure.

2. The flow model based on the energy losses experimental data provides calculations of tangential lean or curved blades of axial flow multistage turbine. Computer codes providing fast solution and sufficient accuracy of results are recomended for use in turbomachinery preliminary design.

3. The turbomachinery secondary flows limitation and associated losses reduction are usually achieved with the methods of blade design or stage and blade row geometry and parametres choice. The means of straight influence on the secondary flows in a passage considered in this paper are more complicated for the design and manufacture but their positive influence on the turbomachinery efficiency can be high and some means of the set studied in the paper can be used.

REFERENCES

1. Deitch, M.E., Zarjankin, A.E., " Gas Dynamics of Turbomachinery Diffusers and Exhaust Passages". Moscow, USSR, Energy, 1970, Rus.

2. Migay, V.K., Goudkov, E.I., " Design and Calculation of Turbomachinery Exhaust Diffusers", Leningrad, Engineering, 1981,Rus.

3. Moore, J., Moore, J.G., "A calculation Procedure For Three-Dimensional Viscous Compressible Duct Flow", Trans. ASME,J.Fluid Eng., 101, 4, 1979, p.p.415-428.

4. Ecer, A., Akay, H.U., Rubek, V., Gurdogan, O., "Computation of Three-Dimensional Viscous Flows Through a Curved Duct",AIAA Pap., 1353, 1987, pp.1-6.

5. Moshkov, E.F., Tikhomirov, B.A., "Numerical Modelling of Marine Turbines Exhaust Passages", Krilov's Science and Technology Society publication, St.Petersburg, 520, 1991, pp.15-24. Rus.

6. Denton, J.D., "Through Flow Calculation for Transonic Axial Flow Turbines", Trans. ASME,J.Engineer.for Power, 100, 2, 1978,pp.21-29.

7. Sirotkin, Y.A., "Aerodynamic Computation of Axial Turbomachines Blades", Moscow, Engineering, 1972, Rus.

8. Horlock, J.H., Marsh, H.,"Flow Models For Turbomachines" J,Mech. Engin. Science, 13,5, 1971, pp.358-368.

9. Denton, J.D., "The Calculation of Three-Dimensional Viscous Flow Through Multistage Turbomachineres", Trans. ASME, J., Turbomach., 114, 1,1992, pp.18-26.

10. Dawes, W.N.,"Toward improved through flow Capability: The Use of Three -Dimensional viscous flow Solvers in a Multistage enviroument", Trans.ASME,J.,Turbomach., 114, 1, 1992, pp.8-17.

11. Topounov, A.M., Pogodin, J.M., Shoupovalenko, K.V. "The Application of Mass Flux Maximum Principle to Flow Parameters Computation at The Outlet of Tangential Leaned Blades Cascade",Trans. Leningrad Shipbilding Inst., 1987, pp.107-113. Rus.

12. Herzig, H.Z., Hansen, A.G. "Visualisation Studies of Secondary Flow with Applications to Turbomachines", Trans. ASME, 77. 3. 1955.

13. Prumper,H., "Methoden zur Verminderung der Secondarverluste in Axialen Turbinenstufen", Flugwiss, 20, 1/2, 1972, pp.60-70.

14. Whitney, W.T., Szanza, E.M., Moffit,T.P., Monroe, D.E., "Cold-Air Investigation of a Turbine for High Temperature Engine Application", NASA TN. D-3757, 1967.

15. Likherzak, E.E., Lev S.G., "End wall Area Pattern in a Turbine Stator Row under Different Boundary Layer Effects",Trans. NAMI, Moscow, 118, 1969, pp.76-91, Rus.

16. Beknev, V.S., Toumashev, R.Z., Shkourichin, I.J., "End wall Losses Reduction in Converging Passage Cascades", High School News, Engineering, USSR, 8, 1972, Rus.

17. Topounov, A.M., Tikhomirov, B.A., "Flow Control in Heat Turbines", Leningrad,USSR, Engineering, 1979. Rus.

18. Topounov, A.M., Tikhomirov, B.A., Chernish, A.A., Chernousenko, A.G., Lebedev, J.I.,"Secondary Flows Control in Axial Turbines Blade Rows", Power Enrgetics, USSR, 5, 1991, pp.60-64, Rus.

19. Kawai, T., "Effects of End wall Boundary Layer Fences on The Aerodynamic Performance at a Turbine Cascade", Exp. and Comp. Aerothermodyn. Intern. Flows, Proc. Ist Int. Symp., Beijing, July, 1990, pp.171-179.

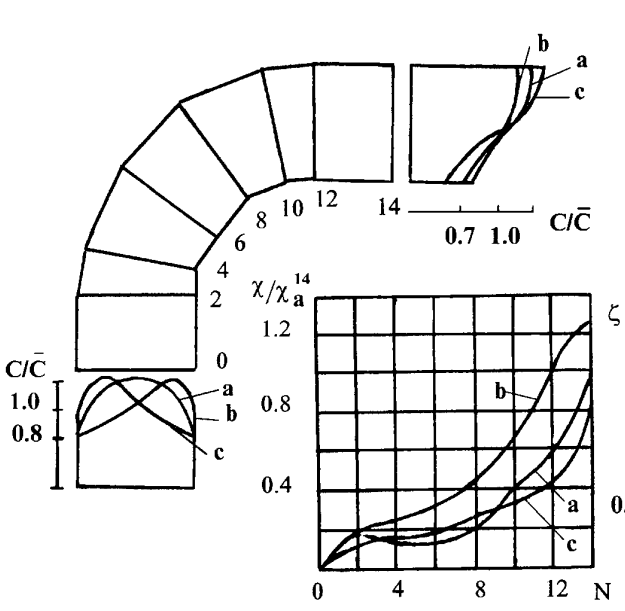

Fig.1 Calculation results of energy of secondary flows $\chi = \int_F C_s C_a \rho dF \Big/ \int_F C_a \rho dF$ change along the bend and outlet velocity C distribution. **a,b,c**-different inlet velocity profile.

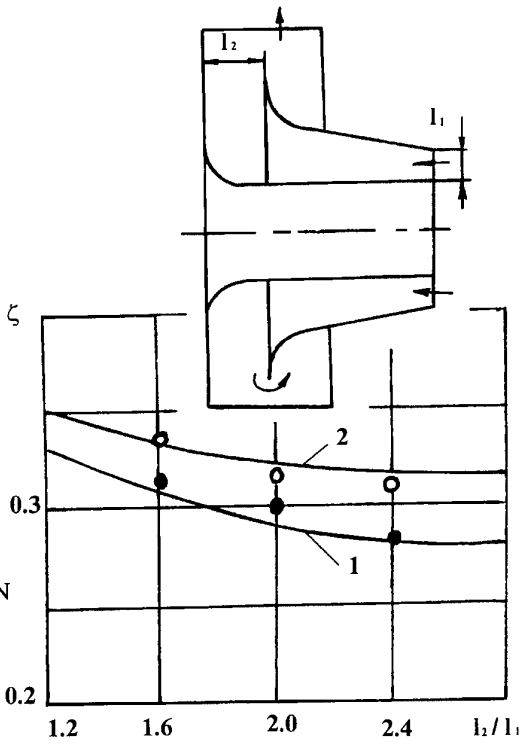

Fig.2. Experimental and calculation results of total pressure loss factor analysis in exhaust passage.
1- Annular diffuser, 2- exhaust passage with diffuser,
— experiment, o,• -calculation.

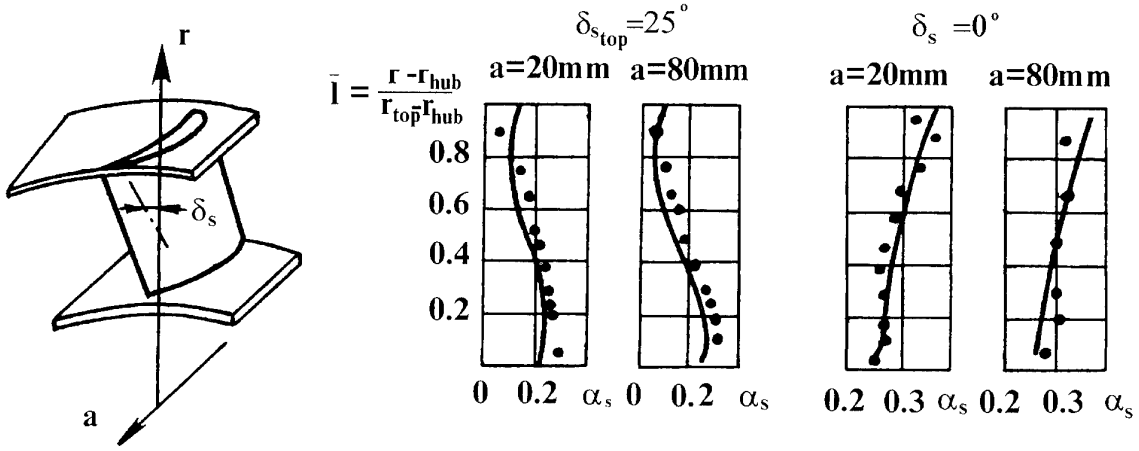

Fig.3.Spanwise distribution of the parameters at the outlet sections of turbine stator row of different blade tangential lean.
— calculation, • - experiment.

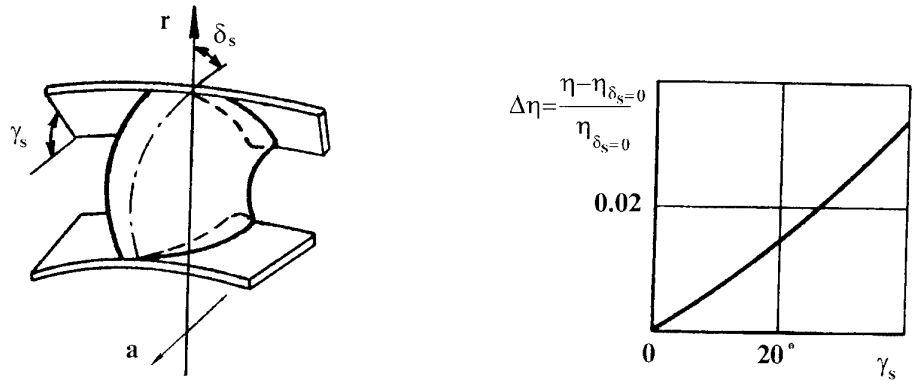

Fig.4. Stator blade tangential curvature influence on turbine stage (*D/l*=4) efficiency at different end wall lean angle γ_s: η - stage efficiency at stator blade angle δ_s calculated with (8);
$\eta_{\delta_s=0}$ -radial stator blades stage efficiency.

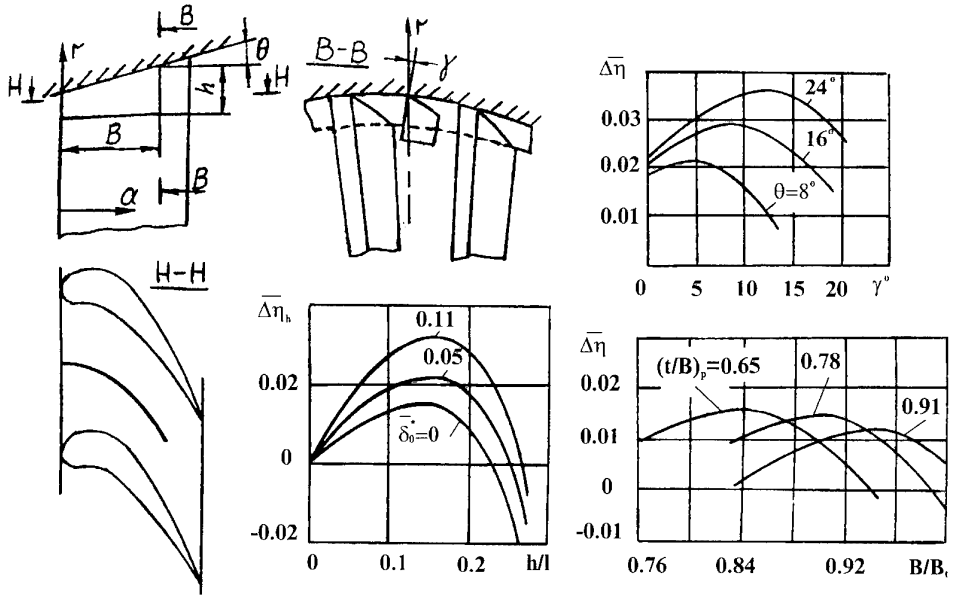

Fig.5. Geometry of stator passages periphery end wall fence andtest results:
- of turbine stage *D/l*=4.4, α_1=27°, *l/b*=1.43, θ=10°, *(t/b)p*=0.76 with the fences radial length *h* variation.
- of cascade (α_1=25°) with the fences width *B* and angle γ variation.

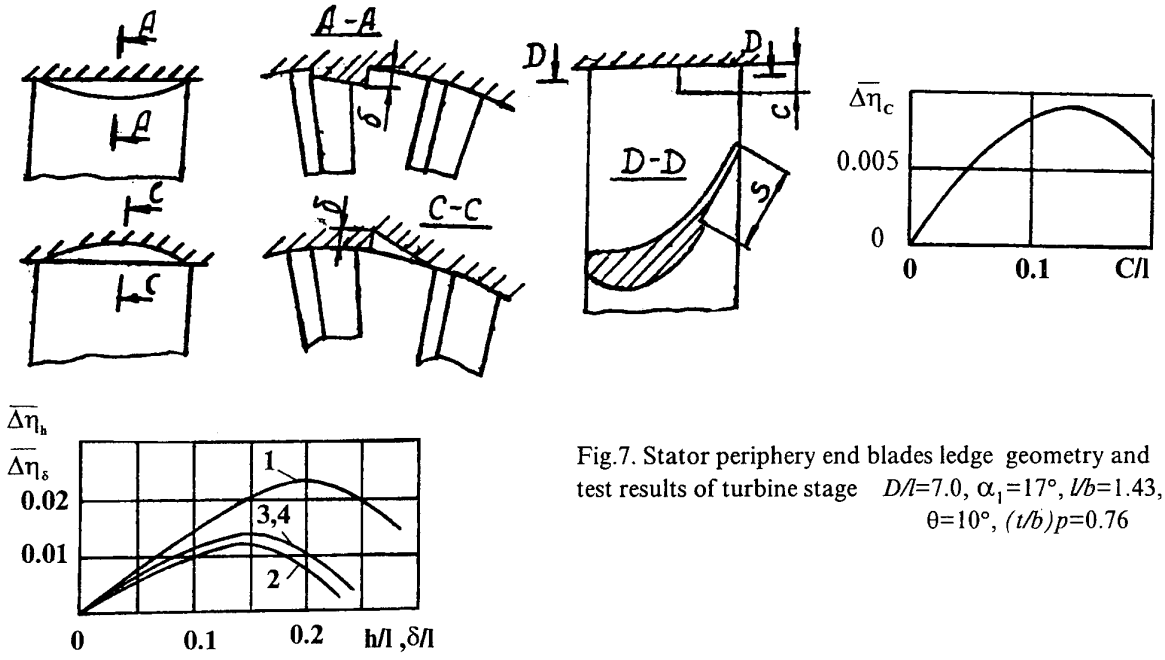

Fig.7. Stator periphery end blades ledge geometry and test results of turbine stage D/l=7.0, α_1=17°, l/b=1.43, θ=10°, $(t/b)p$=0.76

Fig.6. Stator passages periphery end wall ledge geometry and test results of turbine stage D/l=7.0, α_1=17°, l/b=0.9, θ=0°, $(t/b)p$=0.76.

1 - periphery fences, **2** - hub fences, **3, 4** - periphery internal and external ledges.

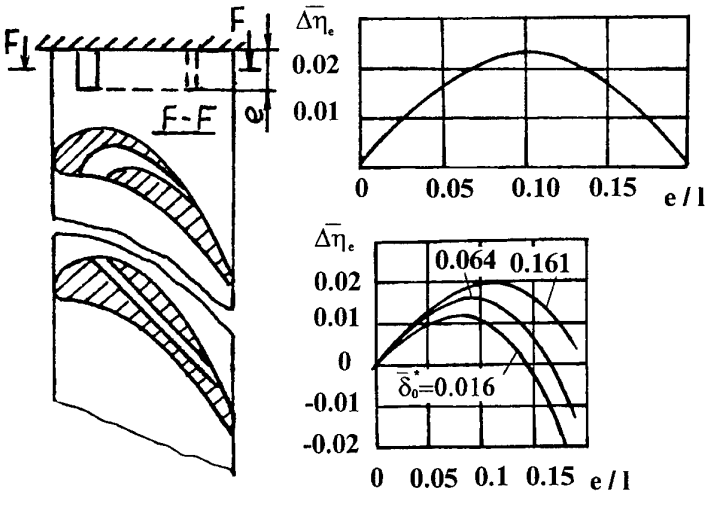

Fig.8. Stator blades periphery slot geometry and test results of turbine stage:
— slot from pressure to suction side
D/l=4.15, α_1=30°, l/b=2.3, θ=28°, $(t/b)p$=0.92
— slot from suction to suction side
D/l=4.9, α_1=23°, l/b=1.6, θ=11°, $(t/b)p$=1.0

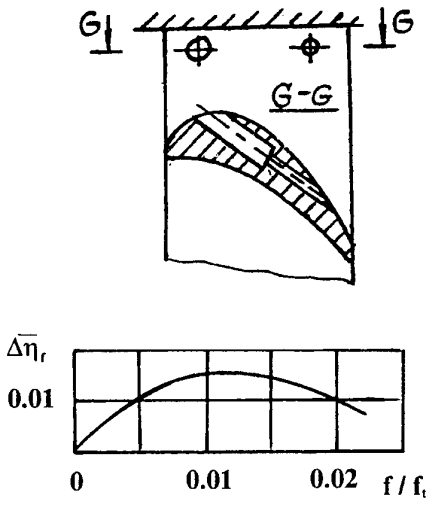

Fig.9. Stator periphery end blades hole geometry and test results of turbine stage D/l=19, α_1=10°, l/b=0.36, θ=0°, $(t/b)p$=0.65.

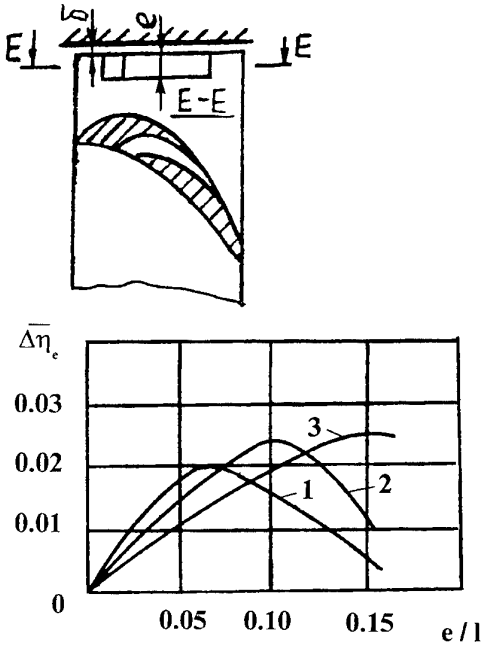

Fig.10. Rotor blades tip slot geometry and test results of turbine stage
D/l=8, α_1=19°, l/b=1.2, θ=0°.
1 - $\bar{\delta}$=0.0075; **2** - $\bar{\delta}$ = 0.0125; **3** - $\bar{\delta}$ = 0.025.

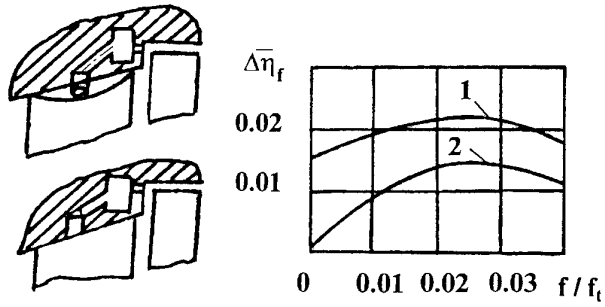

Fig.11. Stator passages periphery end wall suction means geometry and test results of turbine stage
D/l=3.9, α_1=30°, l/b=3, θ=0°, $(t/b)p$=0.71
1 - ledge,step surface suction,
2 - end wall suction.

REFERENCE NO. OF THE PAPER: 9

DISCUSSOR'S NAME: H.B. Weyer, DLR, Germany

AUTHOR'S NAME: Tikhomirov

Q.: All concepts of secondary flow control you tested revealed the same effect of about 2% in efficiency. What is the reason behind this?

A: The effect of the various secondary flow control means is different. We have a maximum stage efficiency improvement in the case of endwall fences. The effect of endwall ledges and end blade slots and holes is less. The effect of end blade ledges is less than 1%. The effect of secondary flow control means cannot be more than 2% to 3% because secondary flows in good turbine axial stages are rather weak. In some tests of less-efficient turbine stages, with significant value of periphery endwall angle, relative efficiency improvement was about 4-5%.

REFERENCE NO. OF THE PAPER: 9

DISCUSSOR'S NAME: D.W. Beckert, DLR, Germany

AUTHOR'S NAME: Tikhomirov & Pagodin

Q.: Would some of your suggestions also work in compressors?

A: Some of the secondary flows control means we studied could be used in axial compressors. It depends on the rate of secondary flow development in blade-to-blade passages. Maximum effect is expected in stages with highly-developed secondary flows. Several research works on the problem of secondary flow control by endwall fences have been published.

REFERENCE NO. OF THE PAPER: 9

DISCUSSOR'S NAME: L.A. Povinelli, NASA, USA

AUTHOR'S NAME: B. Tikhomirov

Q.: Have any of the concepts shown in figs. 8, 9, and 10 been applied in turbine engines? If so, have efficiency improvements been observed?

A: The idea of fences and endwall ledges was used in turbine engines (Fig. 5, 6). It was impossible to directly measure the effect of the secondary flow control methods used, but tests of engines have shown the output increasing.

REFERENCE NO. OF THE PAPER: 9

DISCUSSOR'S NAME: J-F Chevalier, SNECMA, France

AUTHOR'S NAME: B. Tikhomirov

Q.: How do you explain the different degrees of success of secondary flow reduction means on actual engines?

A: The success of secondary flow control means in axial turbines is usually a favorable balance between positive (reduction of the secondary flow) and negative (additional surface friction and vorticity) factors. For secondary flow control use, the stages should be selected which have more developed secondary flows, such as stages with short blades, with significant values of periphery endwall angle, or with thick inlet wall boundary layers etc.

TIP CLEARANCE FLOW AND LOSS IN AXIAL COMPRESSOR CASCADES

Shun Kang and Charles Hirsch
Dept. Fluid Mechanics, Vrije Universiteit Brussel
Pleinlaan 2, 1050 Brussels, Belgium

ABSTRACT

The tip clearance flow and loss production in a low speed linear compressor cascade with a moving endwall is investigated. The analysis is based on numerical computations with a 3D viscous code, at one tip clearance level. Comparisons with experimental data are given for the stationary wall case. The moving wall modifies significantly the secondary flow field near the wall, by generating the skewing of the inlet endwall boundary layer and dragging the tip leakage vortex towards the pressure side. It is found that the leakage flow near the wall is collateral over most of the chord. Close to the tip surface, however, the flow is highly skewed due to the vena contracta. With the moving wall, the leakage mass flow and pressure drop are noticeably increased.

NOMENCLATURE

c	blade chord
C_f	friction
C_p	static pressure coefficient
C_{pt}	total pressure coefficient
D_c	discharge coefficient
Lz	pitchwise coordinate of tip leakage vortex core
m	mass
PS	pressure side
s	pitch
SS	suction side
$\bar{u}$	averaged gap exit velocity
U	endwall moving speed
u_m	moving wall induced velocity
V	velocity
x, y, z	axial-, span- and pitchwise coordinates
β	flow angle
β_m	mean flow angle
σ	contraction coefficient
ϕ	flow coefficient
ρ	density
τ	gap height
τ_b	blade thickness

Subscripts

1	cascade inlet
p	pressure side
s	suction side
t	stagnation value

TABLE of CONTENT

1. INTRODUCTION

In turbomachines, a gap is commonly present between blade tip and casing in an unshrouded rotor or between blade end and hub in an unsealed stator. Due to the sudden discharge of blade loading, a large pressure difference, directed from the pressure side to the suction side, exists across the tip gap. The pressure difference will drive the fluid in the pressure side / endwall corner to the suction side / endwall corner and thus produces a pressure-driven leakage flow.

The leakage flow structure and loss production mechanism have been extensively studied for many years. Great progresses have been made, especially over the last few years, Bindon (1986), Moore & Tilton (1988), Heyes et al. (1991), Storer & Cumpsty (1993), and our previous works (Kang & Hirsch, 1993 & 1994). It is now understood that the gap flow is strongly three-dimensional, especially close to the blade tip surface due to the generation of a tip separation vortex, or vena contracta (Fig.1). The vena contracta may include more than one vortex under certain conditions (Sjolander & Cao, 1994). The flow above the vena contracta, or jet flow, is almost isentropic and tends to be mixed with the flow behind the vena contracta, or the wake flow. Due to mixing, the static pressure is significantly recovered (Fig.1). Downstream of the exit, i.e., in the suction side corner, the leakage flow rolls up into the tip leakage vortex.

Most of the above mentioned flow phenomena came from the observations in linear cascades. In a real machine, however, the leakage flow would be much more complex. One of the most important effects come from the relative motion between blade and endwall. Due to viscosity, the moving wall will drag the fluid close to

Paper presented at the AGARD PEP 85th Symposium on "Loss Mechanisms and Unsteady Flows in Turbomachines", held in Derby, United Kingdom, 8-12 May 1995, and published in CP-571.

it, similar to a Couette flow. Hence, the leakage mass is in general increased in a compressor and reduced in a turbine. This influences the peripheral blade force, clearance loss and discharge coefficient. However, all known theories for leakage loss neglect the relative motion influence, due to the difficulties in obtaining measurements within the small dimensions of tip gap. The effect of the relative motion in turbine blades has been investigated by Morphis & Bindon (1988) and Yaras et al. (1991) Through experiments, they found that the general flow pattern over the tip was not greatly affected by relative motion and that the relative motion increases the pressure on the suction side of the clearance gap, resulting in reduction of the leakage mass and loss.

In this paper, the tip leakage flow and loss production in a low speed, linear cascade with moving endwall is presented, with an attempt to address the influence of relative motion on the leakage flow in an axial compressor. The discussions will be based on numerical results from a 3D viscous code computation, at one tip clearance level with moving and stationary walls. Comparisons with experimental data are only given for the stationary wall case.

The numerical methods and flow conditions are described in section 2. In section three, the 3D flow structure is shown by 3D streamline patterns and static pressure contours. The trajectory of the tip vortex is analyzed in section 4. In the fifth section, the averaged leakage flow quantities are presented. Some discussions on the loss production due to tip clearance are given in section six.

2. NUMERICAL METHOD

2.1 BRIEF DESCRIPTION OF THE CODE

The Navier-Stokes code, developed by Hirsch et al. (1991), solves the time-dependent Reynolds averaged Navier-Stokes equations, with the algebraic turbulence model of Baldwin-Lomax or the two-equation k-ε turbulence model for closure. It is based on a multiblock/multigrid approach and incorporates various numerical schemes, based on either central or upwind discretization.

For the present calculations, the algebraic turbulence model of Baldwin-Lomax is selected. The calculations were performed with a central scheme, setting the second order dissipation coefficient to zero. and the fourth order to 0.1, with a V-cycle multigrid technique. The numerical procedure applied a five-stage Runge-Kutta scheme with coefficients of (1/4, 1/6, 3/8, 1/2, and 1). Incorporating implicit residual smoothing, the calculations were performed at a CFL number of 7, requiring close to 300 iterations for a residual reduction of three orders of magnitude.

2.2 COMPUTATIONAL GRIDS

The cascade blades are NACA 65-1810 with a chord of 20cm. Pitch and span of the cascade are respectively 18cm and 20cm, and the stagger angle is 10°. See Kang & Hirsch (1991) for the details of the cascade geometry.

Body-fitted grids with two calculation domains, shown in Fig.2, were made by the Interactive 3D Geometry Modeling and Grid Generation System (IGG) developed by Dener & Hirsch (1992), to represent the cascade geometry. The first domain with a H-H mesh is limited in the region with one pitch in tangential direction and half span in height, since the existence of the tip gap produces little influence on the midspan flow field based on the experimental observations in Kang and Hirsch (1993). In the axial direction, the mesh extends from 1.5 chord upstream to 1.5 chord downstream. The second domain occupies the space in the tip gap with a O-H mesh.

The mesh consists of 97x41x45, in the axial, blade to blade and spanwise directions, in domain 1 and 97x13x13 in domain 2 with 195,358 points in total, as shown in Fig.2. There are 13 H-lines over the gap and 13 O-lines leading to 25 points across the blade profile in the gap.

For comparing, another mesh with 49x21x37 in domain 1 and 49x13x17 in domain 2 was also computed. For presentation, the first mesh is named as mesh I and the second mesh II. It was expected that the first mesh would produce high accuracy inside the passage, but the second one would show more details of the gap flow.

2.3 BOUNDARY CONDITIONS

In the inlet plane, three velocity components and static pressure are given. At this location the flow is collateral and the spanwise velocity is zero. The profiles of the pitchwise and axialwise velocity components employed in the calculation were calculated from the measured velocity (Kang & Hirsch, 1993) at 40% chord upstream of the leading edge and from the flow angles around midspan. The pressure in the inlet plane was considered uniform and also taken from the measured data at midspan. Riemann boundary treatment was employed for the inlet boundary. Hence the real imposed parameters in the inlet are entropy (first characteristic variable), axial velocity (second characteristic variable), and pitchwise and spanwise velocity components.

No-slip boundary conditions were used on the blade surfaces and endwalls. Periodic conditions were enforced along the boundaries upstream and downstream of the passage, and also in the gap. A symmetric (or mirror) boundary condition was used at the midspan. In the outlet plane, uniform static pressure was imposed with the averaged midspan value, measured at 25% chord downstream.

2.4 FLOW CONDITIONS

Only one clearance level with 4mm, or 2.0% chord, was run. In the stationary case, two inlet flow angles, β_1=29.3° (design condition) and 36.5° (off-design condition) were simulated with both mesh I and II. The inlet flow velocity V_1=23.5m/s, the Reynolds number, based on the velocity and blade chord, is about 3.0 x 10^5; The inlet boundary layer is turbulent with a shape factor of about 1.22 and a displacement thickness of 0.014 chord. For the moving wall cases, two moving speeds, corresponding to flow coefficients of 0.5 and 0.7, were performed with mesh I, keeping the inlet flow condition the same as the design one.

Although the blade surface boundary layer may have laminar and transition states, as observed in the experiments (Kang & Hirsch, 1991), the calculations was undertaken with the supposition that all the boundary layers of the blade surfaces and endwall are in a turbulent state.

3. THE 3D ENDWALL FLOW

3.1 STATIONARY ENDWALL

It is necessary, before presenting the moving wall effects, to briefly review the 3D flow structure in the linear cascade with stationary endwall. More detailed data can be found in the previous papers (Kang & Hirsch, 1994a&b), on both experimental and numerical observations.

Figure 3 shows the predicted surface flow pattern, or limiting streamline patterns, on the endwall at the off-

design condition, compared with the experimental observations obtained by Kang & Hirsch (1993) with a paint-trace visualization technique. The prediction was done with mesh I (Hereafter, if no indication, the computational data will be always referred to mesh I). Streamlines passing through the mesh points close to a solid wall are considered limiting streamlines in this study. It is seen from Fig.3b that the code predicts the endwall flow phenomena observed in the visualizations, such as the reattachment line (from which streamlines diverge) in the pressure side and the separation line (to which streamlines converge) of the tip leakage vortex in the suction side. However, the predicted separation line is closer to the midpassage downstream of the midchord than in the experiments. In addition, the calculated streamlines under the blade are almost straight over the whole chord, there are no turns as in Fig.3a before midchord.

Figure 4 shows the predicted flow structure around the tip and the midpassage close to the endwall at the off-design condition. Static pressure isolines on the blade surfaces are also shown in Fig.4. It includes a tip separation vortex (TSV), a tip leakage vortex (TLV), two secondary vortex (SV1 and SV2), and a passage vortex (PV). The tip vortices located at the suction side are produced by the flows coming from upstream and passing through the tip gap. Downstream, the small size vortices, TSV and SVs, are going to be engulfed into the larger one, TLV, and tend to be mixed with it. The passage vortex (PV), however, keeps independent from the tip leakage vortex even far downstream. One of the secondary vortices was also observed in the experimental studies (Kang & Hirsch, 1993a).

Due to the tip leakage vortex, the contours of wall static pressure just under the vortex core should exhibit a pressure trough, as shown by Inoue et al. (1991) and Moyle et al (1991). It is seen clearly from Fig.5 that the pressure trough is well predicted with the calculation.

Figure 6 represents the predicted limiting streamline patterns on the tip surface at the design condition with both mesh I and II, compared with the ink-trace visualization (Kang & Hirsch, 1993a). It is seen that the main features of the flow, observed in the visualization, are reproduced in Fig.6b&c. Comparing to mesh I (13 points over the gap height), the reattachment line of the tip separation vortex (TSV) predicted with mesh II (17 points over the gap height) is closer to the experiments.

The leakage flow varies in direction from the parallel pattern on the endwall (Fig.3) to the divergence pattern on the tip surface (Fig.6). This variation can be clearly viewed from Fig.7 which presents the three-dimensional velocity vectors through the tip clearance in the section No.6, 44% of chord, indicated in Fig.1. Close to the endwall the flow is collateral.

Comparisons of the wall pressure distributions between the calculations and the experiments are presented in Fig.8, for the sections No.6 and No.8 (66%c) at the design condition. In the experiments, the pressure reaches its minimum just inside the gap, being related to the tip separation vortex (TSV). After the vortex, the wall pressure starts recovering from its minimum value. With the recovery process, the leakage flow would be mixing. But due to the relatively thin blade thickness in the present case, the mixing process is not completed at the gap exit (Kang & Hirsch, 1994a). It is seen that, over most of the chord, the calculated data are reasonable. A large difference between the experimental and the calculated results occurs behind the midchord and under the blade profile, in connection with the underestimated tip blade loading and the vena contracta (Kang & Hirsch, 1994b). The underprediction may be related to the simple turbulence model and the mesh which is not fine enough. With the mesh II, the variation of the pressure under the blade in the section No.8 is predicted, but larger discrepancy occurs downstream of the gap exit.

3.2 MOVING ENDWALL

Numerical simulations with the moving wall have been performed for two moving speeds, corresponding to flow coefficients of 0.5 and 0.7. As the flow structure, observed from the numerical computation, is quite similar for the two speeds, the 3D streamline pattern and the endwall static pressure contours presented in Figs.9 and 10 are only shown for the flow coefficient of 0.5. Static pressure isolines on the blade surfaces are also shown in Fig.9. Comparing to Figs.4 and 5, following observations can be made.

Due to the motion, the flow close to the wall is highly skewed, giving rise to a spanwise (radial) variation of incidence. The incidence increases through the boundary layer as the wall is approached in an axial compressor blade, and reversely in a turbine. Hence, the minimum pressure under the blade (Fig.10) is reduced about 30%, compared to the stationary case (Fig.5), while at the pressure side the pressure is nearly unchanged, resulting in an increasing of the pressure difference over the gap.

The structure and location of the tip leakage vortex core are significantly different from the stationary cases. The pressure trough in the stationary case stretches towards downstream just close to the passage suction side. With the wall moving, however, the pressure trough, indicated by line A in Fig.10, is swept strongly from the suction side corner towards the pressure side. The green lines in Fig.9 coming from upstream and passing through the tip gap near the leading edge, form the tip leakage vortex (TLV). The vortex trajectory, stretching across the passage towards the pressure side close to trailing edge, can be clearly observed. Behind the cascade, the vortex trajectory follows the mainstream direction. The start location of the vortex at stationary case in Fig.4 is at about a quarter of chord from the leading edge. But in fact, the vortex at the moving wall condition does appear around the leading edge (Fig.9). The shift of the tip leakage vortex towards the leading edge also results from the inlet flow skewing which tends to increase the incidence. Consequently the minimum of the wall pressure in the suction side (Fig.10) occurs about 15% chord closer to the leading edge than that in Fig.5 for collateral inlet flow.

The other observations from Figs.9 and 10 are a secondary tip vortex (SV) and trailing edge separation vortex. The secondary tip vortex (SV) is also generated near the leading edge and has the same rotation sense as the tip leakage vortex (TLV), but with very small size. This vortex trajectory can also be recognized from the wall pressure contour with a relative small pressure trough, as indicated by line B in Fig.10. The short pressure trough close to the suction side near the trailing edge, indicated by line C in Fig.10, however, is related to the trailing edge vortex (Fig.9). It is seen from Fig.9 that the red streamlines, coming from upstream along the pressure side near midspan, turn around the trailing edge and form the trailing edge separation vortex in the suction side. This vortex moves up along the spanwise direction towards the tip. Close to the wall, it turns forward into the passage a short distance and then backward towards downstream, generating a very complex flow structure in the suction side and endwall corner. In addition, no scraping vortex is found from the present numerical simulations.

Figure 11 presents the three-dimensional velocity vector inside the gap at the section No.6 (44%c) for ϕ=0.7. The strong skewing near the blade tip surface is associated with the tip separation vortex. Figure 12 shows the predicted blade tip streamline patterns for the two studied flow coefficients. The reattachment line of the vortex can be recognized at the higher flow coefficient. At the lower flow coefficient, however, the divergence line disappears, since the higher wall moving speed has greatly enhanced the gap flow volume.

4. TIP LEAKAGE VORTEX LOCI

Figure 13 presents the computed tangential coordinate L_Z of the tip leakage vortex core center at different moving speeds, compared with the experimental data of the stationary case (Kang & Hirsch, 1993b). The zero point of L_Z inside the passage is the suction side; behind the trailing edge it is on the mesh line from the trailing edge in the axial direction. It is seen that in the stationary case, the coordinate almost obeys a linear relation with axial distance and the computational data compare very well with the experiments.

The influence of relative motion on the trajectory is clearly seen from Fig.13. Reducing the flow coefficient, i.e., increasing the moving wall speed, the trajectory shifts far away from the suction side. Its variation in axial direction is close to a linear relation over the region of the first half of chord. Just behind the midchord, however, its slope changes. The slope discontinuity was also observed from visualizations of the tip vortex cavitation by Rains (1954) and Zierke, et al. (1994) in axial flow compressors, but much closer to the trailing edge than the present computation performed in a linear cascade.

Based on similarity analysis, Chen et al. (1991) set up a simple model for predicting the tip leakage vortex trajectory L_Z inside a compressor passage. On the supposition that the main factors affecting the trajectory are tip gap height, pressure difference, and time, they gave

$$\frac{L_Z / s}{x / c} = A \sqrt{\frac{c\,(\tan\beta_1 - \tan\beta_2)}{s\cos\beta_m}} \qquad (1)$$

where A=0.46. To present the influence of relative motion on the trajectory explicitly, the authors have modified Eq.(1) by replacing the factor A with

$$A = A_o + A_u \frac{U}{V_x} \qquad (2)$$

in the Authors' Closure of Kang & Hirsch (1993b). Based on the experimental data in the present cascade and the compressor rotors of Inoue et al. (1991) and Moyle et al. (1992), Ao and Au were suggested to be 0.19 and 0.27 respectively.

Comparisons of the model to the computations are also presented in Fig.13. It is seen that the modified model predicts the variation, observed from the computations, with flow coefficient. For the stationary case, the model compares very well with the computation.

5. AVERAGED QUANTITIES OF GAP FLOW

5.1 STATIONARY ENDWALL

Figure 14 shows the predicted chordwise distribution of the averaged gap exit (Suction Side) velocities for the design and off-design conditions with both mesh I and II, compared with the experimental data at the off-design condition. The prediction compares well with the experimental data around and after the midchord with mesh I, while a larger discrepancy exits near the leading edge. Similar comparison of predicted Reynolds number to experiment can be found from Fig.15.

5.2 MOVING ENDWALL

Lakshminarayana(1970) indicated that not all the bound circulation in the blade tip was shed downstream into the tip leakage vortex, part of the vorticity near the tip was believed to jump over the gap to the endwall in the form of a vortex sheet. In other wards, the fluid moving within the gap is experiencing a lift force. This lift, called retained lift, is shown in Fig.16. This figure presents the loading acting on the gap leakage flow. The loading is normally calculated by the pressure difference between the pressure side a certain distance away from the tip and the suction side. For the present linear cascade, the loading in Fig.16 is calculated from the difference between the pressures of midspan pressure side and the mass averaged gap exit. It is seen that for a stationary endwall, the loading is lower, about 7%, than the midspan loading. With the wall moving, the loading is increased near the leading edge, resulting in an averaged increment of 5% from stationary to ϕ=0.7 (see Table-1). Reducing flow coefficient from 0.7 to 0.5, the averaged loading increases about 2%.

Figure 17 and 18 shows the distribution of gap mass flow and velocity along the chord. Even the gap flow velocity has a strong variation in axial direction, the mass is nearly constant over a wide range.

Table 1 Tip gap total averaged-quantities

	ϕ=0.5	ϕ=0.7	U=0,design	U=0,off-design
ΔC_p	0.6987	0.6844	0.6363	0.6886
ΔC_{pt}	0.0721	0.1095	0.2281	0.2378
m, Eq.(3)	0.0760	0.0752	0.0725	0.0754
$m-m_{U=0}$	0.0344	0.0182	0	0
m	0.0869	0.0707	0.0525	0.0605

The quantitative effect of the moving wall on the gap mass flow can be seen from Fig.17 and Table 1. Moving the wall with ϕ=0.7, the gap mass flow increases about 27%. Increasing the wall speed, the mass flow increases about 20%.

If one separates the leakage flow as pressure-driven flow and moving-wall induced flow, the mass difference, $m-m_{U=0}$, may be approximately considered as the moving wall induced mass flow, neglecting the effects of the moving wall on the gap pressure difference. It is 0.034 and 0.018 for ϕ=0.5 and 0.7, respectively.

The pressure-driven leakage flow can also be determined with the known pressure difference in Table 1. For potential flow, the gap leakage mass flow is proportional to the square root of the pressure drop, as

$$m = \tau c \rho V_1 \sqrt{\Delta C_p} \qquad (3)$$

The mass flow calculated with Eq.(3) is also listed in Table 1. It is seen that the potential flow model overpredicts the mass flow by about 2%.

6. TIP CLEARANCE LOSS

6.1 STATIONARY ENDWALL

Figure 19 shows the isolines of the calculated total pressure loss coefficient in the sections No.4, No.6 and No.8, with some profiles through the gap in the section No.6, at the design condition. The occurrence of the tip

separation vortex can be recognized by the contour loops, with high loss, just inside the gap inlet (PS). The viscous layer is thin near the wall but thick close the tip due to the wake behind the separation. The mixing of the wake with the core flow can be understood by viewing the plots from pressure side to suction side. But the predicted leakage flow seems fully mixed at the gap exit due to the underprediction of the tip separation vortex (Fig.6)

Figure 20 shows the averaged gap internal loss distribution along the axial direction, calculated by the difference between the pressure and suction sides. This loss, with an averaging of 0.23 (Table 1), is in general created by the leakage flow mixing and the boundary layer. Based on mesh II, it seems that the internal loss is almost constant over most of the chord.

6.2 MOVING ENDWALL

Figure 21 presents the isolines of predicted total pressure loss coefficient, with some profiles inside the tip gap from entrance to exit, for ϕ=0.5, 0.7 at the section No.6. In the other sections the contours are quite similar. The influence of the moving wall on the profiles seems limited to the region close to the wall, especially at the high flow coefficient. Since the moving wall adds a certain energy to the near-wall flow, the total pressure coefficient is lower, or even negative at ϕ=0.5, close to the wall. It follows from Fig.21 that just inside the gap entrance, the isolines in the blade tip side are quite similar to the stationary case (Fig.19), showing the effect of the separation (vena contracta). The mixing seems to be completed earlier than the stationary case as the profiles, except the inlet one, remain stable shape over the gap passage.

Figure 22 shows the axial distribution of the averaged gap internal loss for different flow coefficients, compared with the stationary wall condition. It is seen that the energy loss has been significantly reduced by the moving wall, about 10% at ϕ=0.7 (see Table 1). This may be explained by the fact that the moving wall weakens the tip separation vortex, as one has seen from Fig.12. Hence the mixing loss is reduced.

6.3 SUMMARY ON TIP CLEARANCE LOSS

The tip leakage flow can be divided into three regions with distinct natures: the inviscid flow around the midgap, the viscous flow near the endwall and the tip surface. The viscous flow near the wall is the development of the endwall boundary layer in the pressure side of the passage and occupies a relatively thin layer. Flows inside this layer are collateral over most of the chord. The high potential flow around the midgap behaves like a jet flow. The flow near the tip surface separates from the tip edge immediately inside the gap and forms the tip separation vortex. Downstream of the vortex, the flow behaves like a wake and tends to be mixed with the jet flow. The mixing process may depend on the ratio of gap height to blade thickness and the strength of the tip separation vortex, or blade tip loading.

In general, the energy losses created by a tip gap leakage in a low speed machine can be classified as follows

i) shear stress loss, due to the existence of endwall and blade tip surface shear stresses.

ii) mixing loss, due to the mixing of the jet flow with the wake flow,

iii) secondary flow loss, due to the creation of the tip leakage vortex. and

iv) mixing loss, due to the mixing of the leakage flow with the mainstream.

The first two losses may also be considered together as gap internal loss. The level of the different energy losses depends on the geometry (including blade thickness, gap size and tip shape), the blade tip loading, Reynolds number, and relative motion. If the ratio of blade thickness to gap height is more than 4, as is usually the case for turbines and low speed compressor, mixing inside the gap will occur with a consequent increase in static pressure and entropy. But in most of the practical cases, the mixing process will not be completed up to the gap exit (Heyes et al., 1991, Storer & Cumpsty, 1991, Kang & Hirsch, 1993, and Sjolander & Cao, 1994).

Since the leakage flow differs from the mainstream, in both direction and magnitude, a significant loss, category iv, will be produced by the mixing of the two flows (Denton, 1993), which occurs in any turbomathine. This mixing process may continue for a long distance even through next blade row. The secondary flow loss, category iii, may also be included in the mixing loss, which neglects the details of the tip leakage vortex. Comparing to other losses, the shear stress loss is normally smaller due to the relatively thin endwall boundary layer and the short distance of the gap passage.

7. CONCLUSIONS

A numerical investigation of the influence of endwall motion on tip clearance flow in an axial compressor cascade has been presented. The numerical solution, from a 3D turbulent flow solver, have been validated by extensive comparisons with detailed experimental data for the stationary wall case.

The effects of relative motion on tip leakage vortex, leakage mass flow and leakage losses are discussed and compared with the general fields observed in axial compressors and turbines.

The calculations provide informations on the leakage flow structure and the mixing process in the gap.

Most of the observed properties compares well with available data, but more work is needed to establish validated quantitative results and influences of turbulence model on tip clearance flow predictions

8. REFERENCES

Bindon, J. P., 1986, "Visualization of Axial Turbine Tip Clearance Flow Using a Linear Cascade," CUED/A-Turbo/TR 122.

Chen, T. G., Greitzer, M. E., Tan, C. S., and Marble, F. E., 1991, "Similarity Analysis of Compressor Tip Clearance flow Structure," ASME J. of Turbomachinery, Vol.113, pp.260-271.

Dener C. and Hirsch, Ch., 1992, "IGG - An Interactive 3D Surface Modeling and Grid Generation System," AIAA-92-0073, in AIAA 30th Aerospace Sciences Meeting, Reno, Nevada, Jan. 1992.

Denton, J., D., 1993, "Loss Mechanisms in Turbomachines," ASME Paper No. 93-GT-435.

Heyes, F. J. G., Hodson, H. P., and Dailey, G. M., 1991, "The Effect of Blade Tip Geometry on the Tip Leakage Flow in Axial Turbine Cascades," ASME Paper No.91-GT-135.

Hircsh, Ch., Lacor, C., Dener, C., and Vucinic, D., 1991, "An Intergrated CFD System for 3D Turbomachinery Applications," AGARD-CP-510.

Inoue, M., Kuroumaru, M., Iwamoto, T., and Ando, Y., 1991, "Detection of a Rotating Stall Prediction in Isolated Axial Flow Compressor Rotors," ASME J. of Turbomachinery, Vol. 111, pp.281-289.

Kang, S., and Hirsch, Ch., 1991, "Three Dimensional Flows in a Linear Compressor cascade at design conditions," ASME paper No.91-GT-114.
Kang, S., and Hirsch, Ch., 1993a, "Experimental Study on the Three Dimensional Flow within a Compressor Cascade with Tip Clearance: Part I -- Velocity and Pressure Fields," J. of Turbomachinery, Vol.115, pp.435-443.
Kang, S., and Hirsch, Ch., 1993b, "Experimental Study on the Three Dimensional Flow within a Compressor Cascade with Tip Clearance: Part II-- The Tip Leakage Vortex," J. of Turbomachinery, Vol.115, pp.444-452
Kang. S., and Hirsch, Ch., 1994a, "Tip Leakage Flow in a Linear Compressor Cascade," J. of Turbomachinery, Vol. 116, pp.657-664.
Kang. S., and Hirsch, Ch., 1994b, "Numerical Simulation of 3D Viscous Flow in a Linear Compressor Cascade with Tip Clearance," ASME GT-94-364, (To be published in J. of Turbomachinery, 1995)
Lakshminarayana, B., 1970, "Method of Predicting the Tip Clearance Effects in Axial Flow Turbomachinery," ASME J. of Basic Eng. Vol. 92, pp. 467-480.
Milne-Thomson, L. M., 1968, "Theoretical Hydrodynamics, MacMillan, 5th ed., pp.332-334.
Moore, J., and Tilton, J. S., 1988, "Tip Leakage Flow in a Linear Turbine Cascade," J. of Turbomachinery, Vol. 110, pp.18-26.
Morphis, G.. and Bindon, J. P., 1988, "The Effects of Relative motion, Blade Edge Radius and Gap Size on the Blade Tip Pressure Distribution in an Annular Turbine Cascade with Tip Clearance," ASME Paper No.80-GT-256.
Moyle, I. N., Walker, G. J., and Shreeve, R. P., 1991, "Stator Averaged, Rotor Blade-to-Blade Near Wall Flow in a Multistage Axial Compressor with Tip Clearance Variation," ASME Paper No.91-GT-30.
Rains, D. A., 1954, "Tip Clearance Flow in Axial Compressors and Pumps," California Institute of Technology, Mech. Eng. Laboratory, Report 5.
Sjolander, S. A., and Cao, D., 1994, "Measurements of the Flow in an Idealized Turbine Tip Gap," ASME Paper No. 94-GT-74.
Storer, J. A., and Cumpsty, N. A., 1991, "Tip Leakage Flow in Axial Compressors," ASME J. of Turbomachinery, Vol.113, pp.252-259.
Storer, J. A., and Cumpsty, N. A., 1993, "An Approximate Analysis and Prediction Method for Tip Clearance Loss in Axial Compressors," ASME Paper No. 93-GT-140.
Yaras, M. I., and Sjolander, S. A., 1991, "Effects of Simulated Rotation on Tip Leakage in a Planar Cascade of Turbine Blades; Part I: Tip Gap Flow," ASME Paper No. 91-GT-127.
Zierke, W. C., Farrel, K. J., and Straka, W. A., 1994, "Measurements of the Tip Clearance Flow for a High Reynolds Number Axial-Flow Rotor: Part 1 --- Flow Visualization," ASME Paper No.94-GT-453.

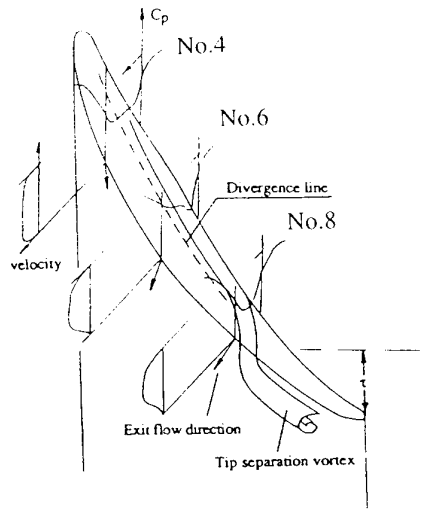

Fig.1 Schematic of tip leakage flow pattern, with the pitchwise profiles of wall static pressures and the spanwise profiles of exit velocities, Kang & Hirsch (1994a)

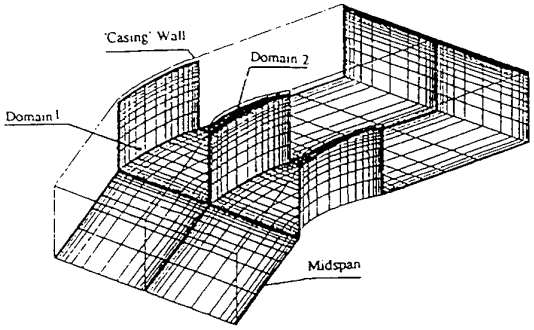

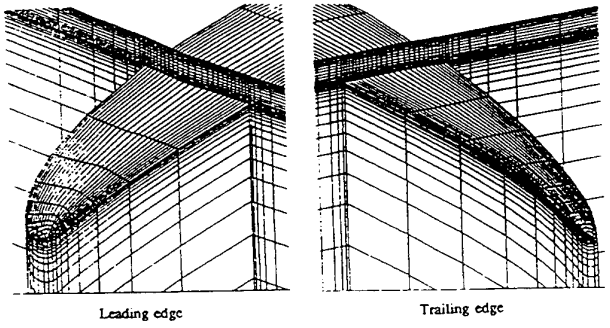

Fig.2 Coarse mesh with tip clearance, two domains included.

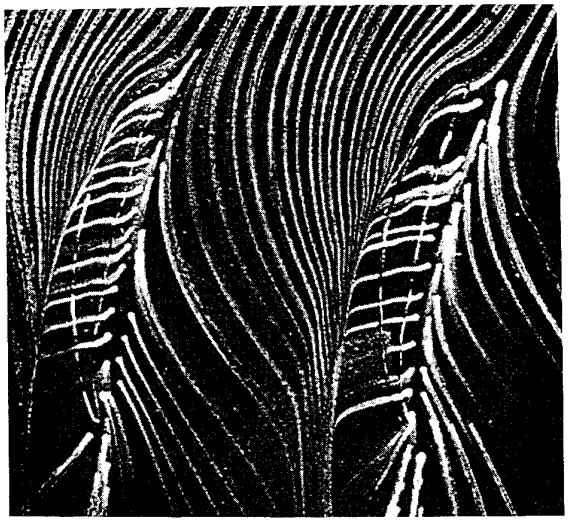

a)

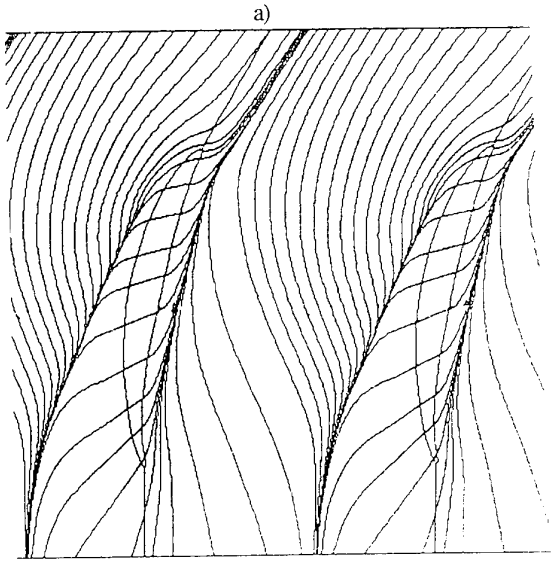

b)

Fig.3 a) paint-trace visualization and b) predicted limiting streamlines on the stationary endwall at off-design condition

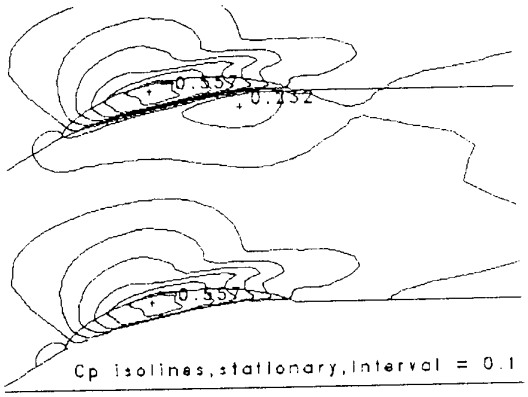

Fig.5 Contours of static pressure on the stationary endwall at the design condition

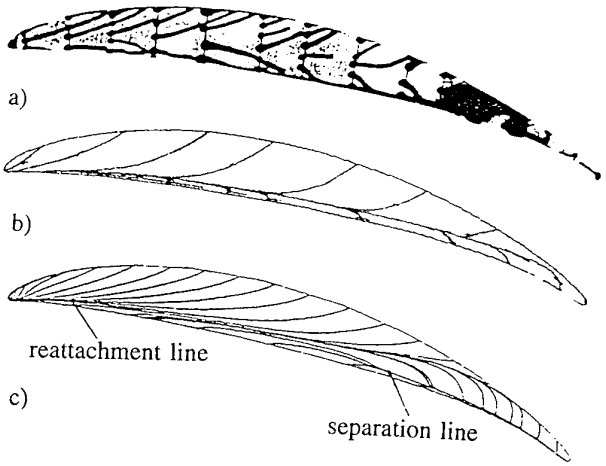

Fig.6 a) ink-trace visualization and b) predicted limiting streamlines (I) and c) predicted limiting streamlines (II) on the tip surface with stationary wall at off-design condition

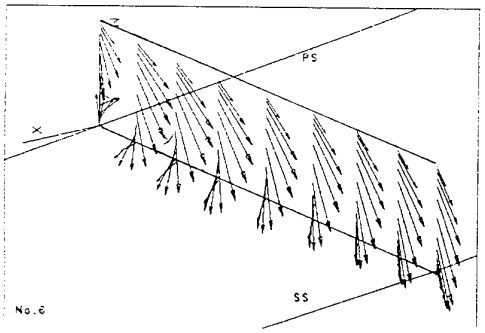

Fig.7 Predicted 3D velocity vectors inside the gap with stationary wall at the location of No.6 (44%c)

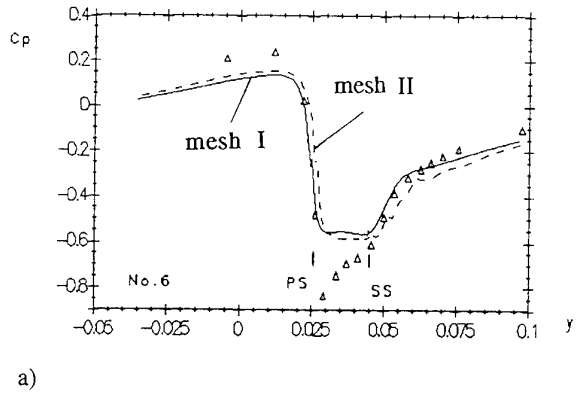

a)

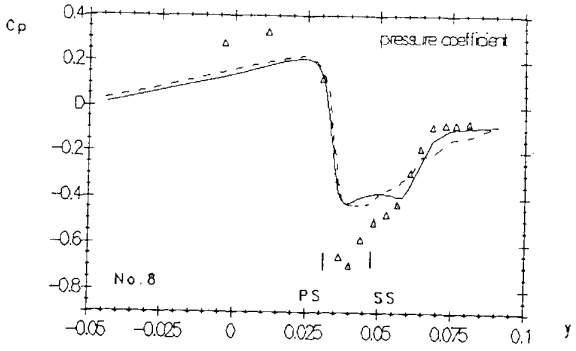

b)

Fig.8 Comparison of wall static pressure under the blade with stationary wall at design condition at the location a) No.6 (44%c) and b) No.8 (66%c)

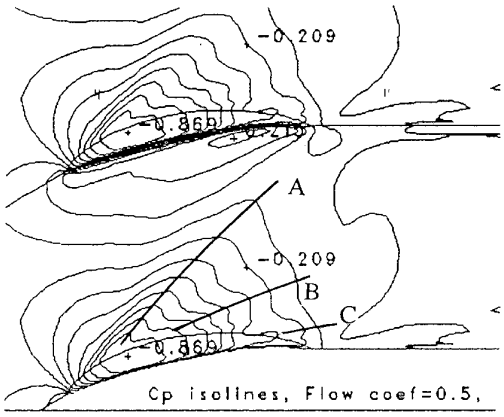

Fig.10 Contours of static pressure on the moving wall at ϕ=0.5

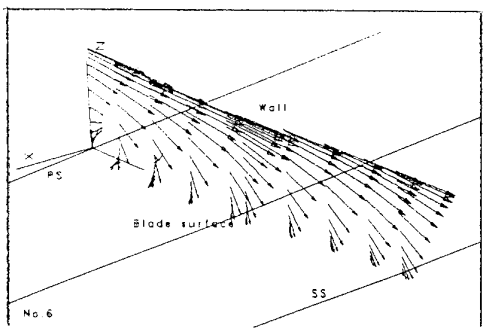

Fig.11 3D velocity vectors inside gap with moving wall at ϕ=0.7

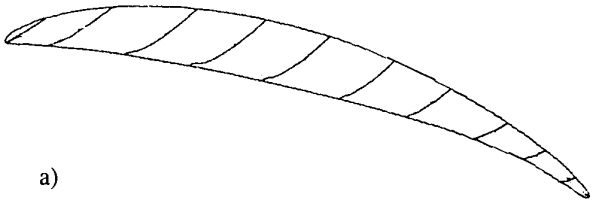

a)

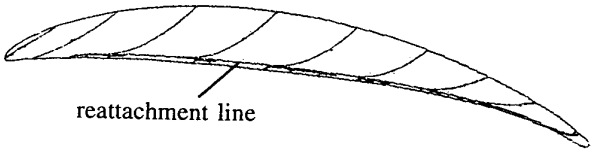

b)

Fig.12 Predicted limiting streamlines on tip surface with moving wall at a) ϕ=0.5 and b) ϕ=0.7

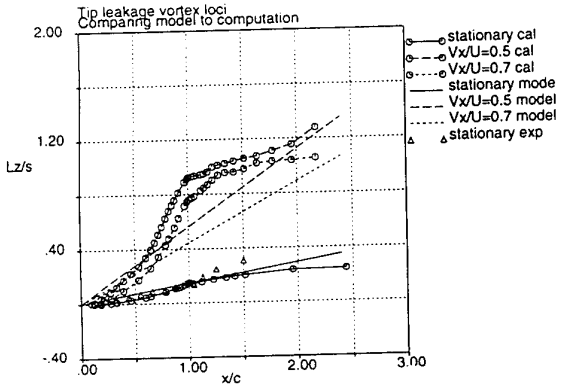

Fig.13 Evolution of tip leakage vortex core location in axial direction

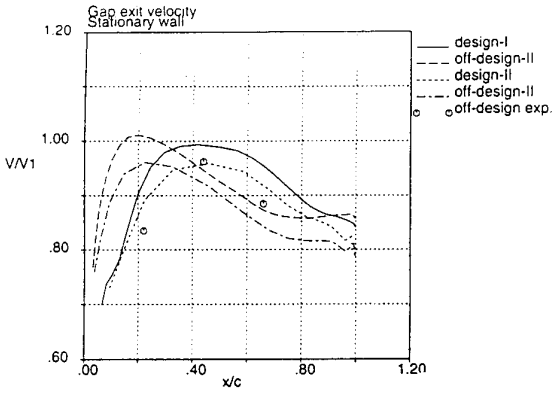

Fig.14 Chordwise distribution of averaged gap exit velocities of mesh I and II with stationary wall, compared with experimental data

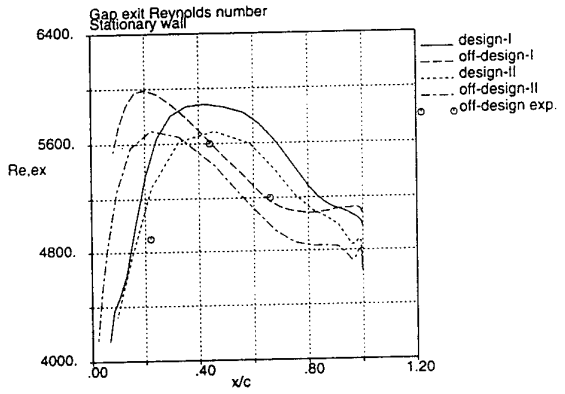

Fig. 15 Chordwise distribution of averaged gap Reynolds numbers of mesh I and II with stationary wall, compared with experimental data

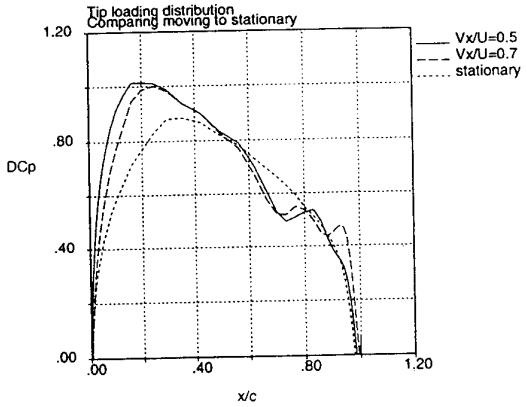

Fig.16 Chordwise distribution of averaged gap loading of mesh I and II with stationary wall

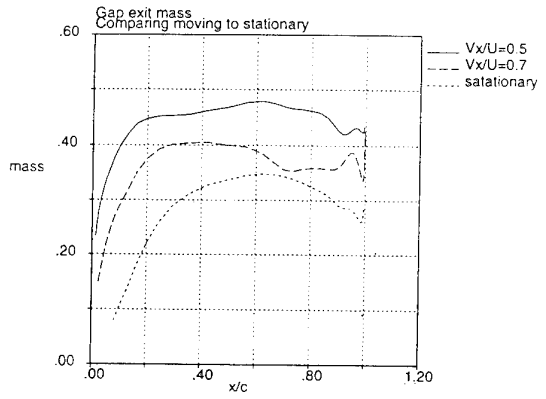

Fig.17 Chordwise distribution of averaged gap mass flow for different moving conditions

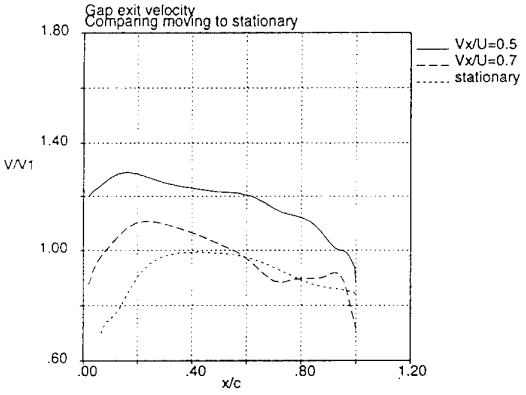

Fig.18 Chordwise distribution of averaged gap exit velocity for different moving conditions

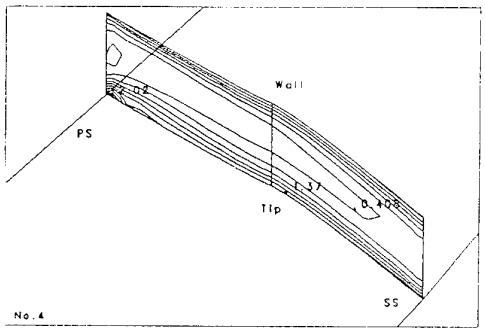

a)

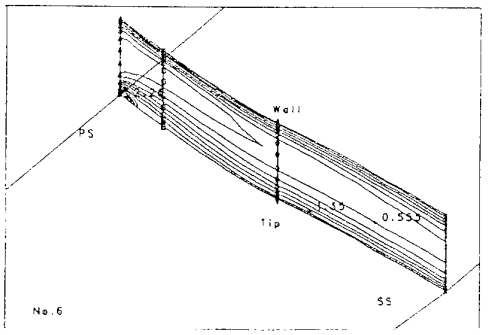

b)

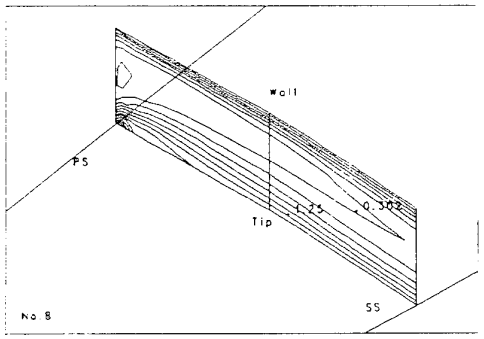

c)

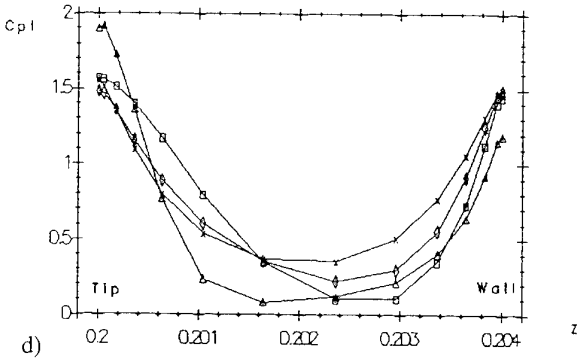

d)

Fig.19 Predicted total pressure isolines inside the gap with stationary wall at design condition at the sections a) No.4 (22%c), b) No.6 (44%c), c) No.8 (66%c), and d) profiles in the section No.6

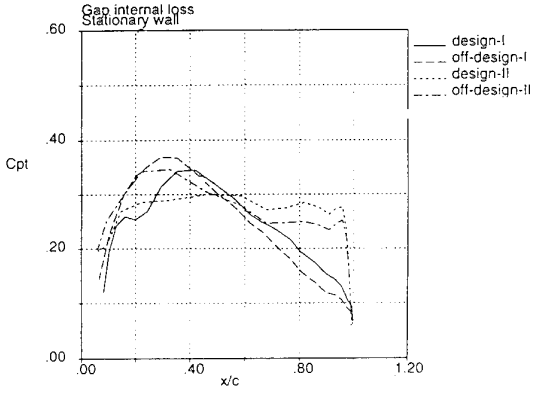

Fig.20 Chordwise distribution of averaged internal loss, obtained with mesh I and II for stationary wall

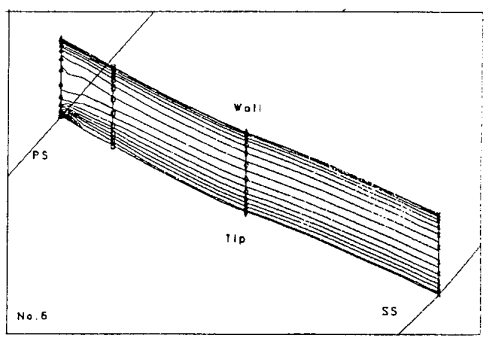

a)

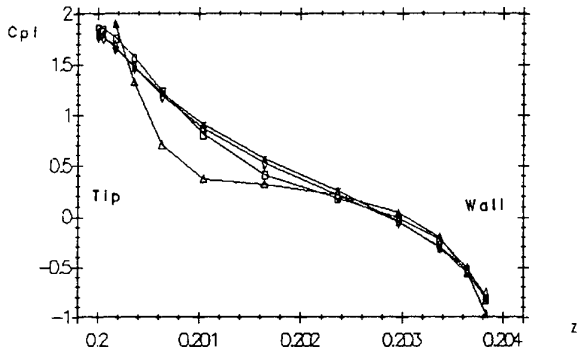

b)

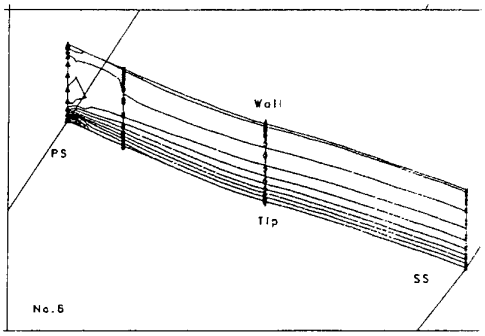

c)

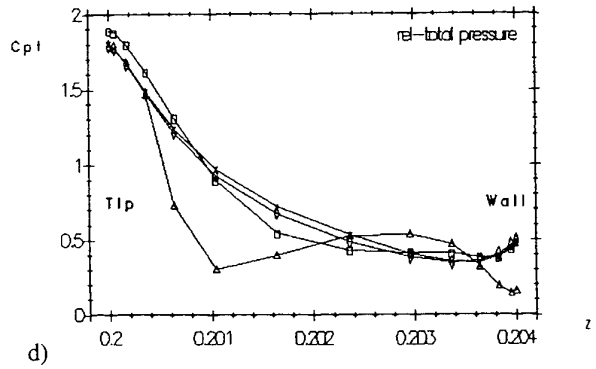

d)

Fig.21 Predicted total pressure isolines and profiles inside the gap with moving wall at the location of No.6 (44%c) for a) and b) ϕ=0.5, c) and d) ϕ=0.7

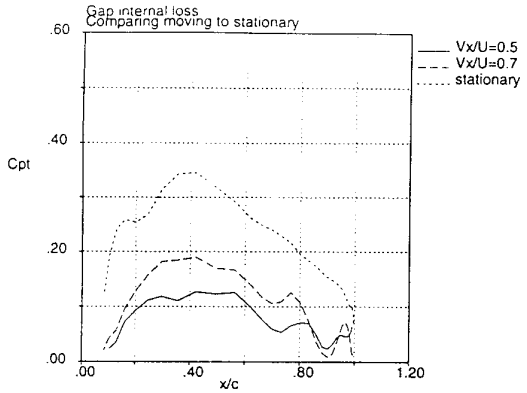

Fig.22 Chordwise distribution of averaged gap internal loss for different moving conditions

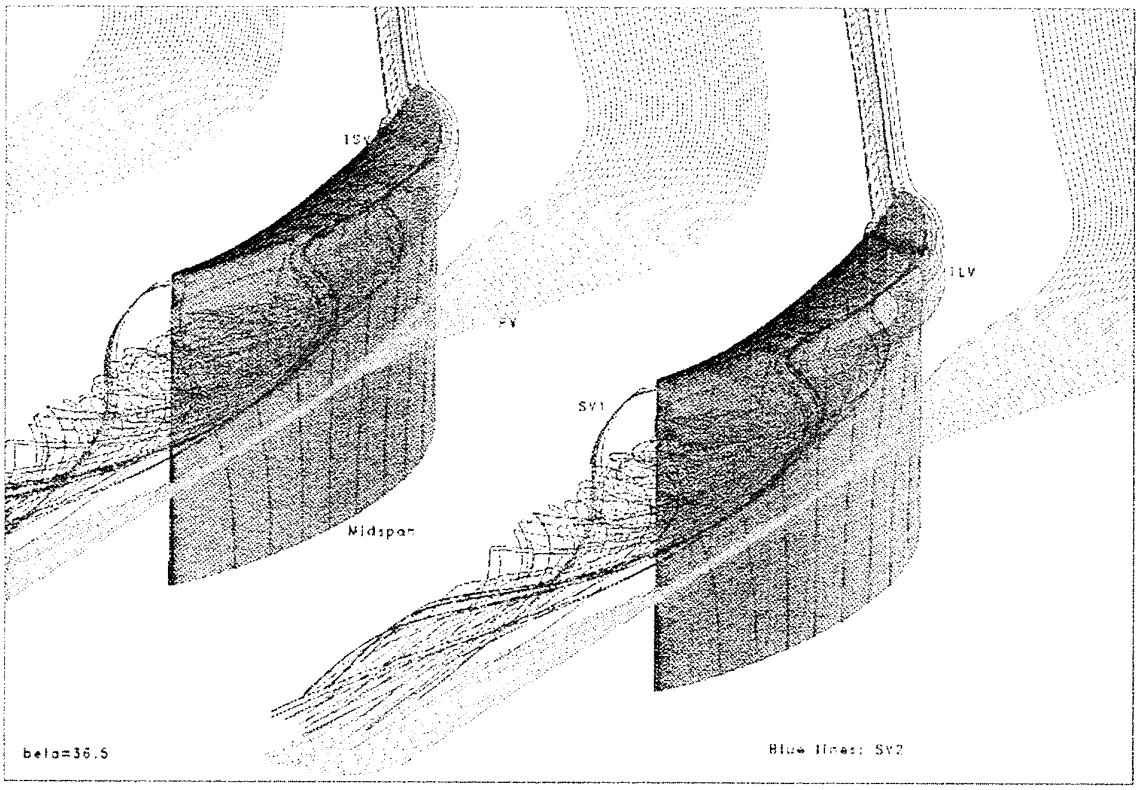

Fig.4 Streamline pattern close to the stationary wall at off-design condition (in color), with contours of static pressure

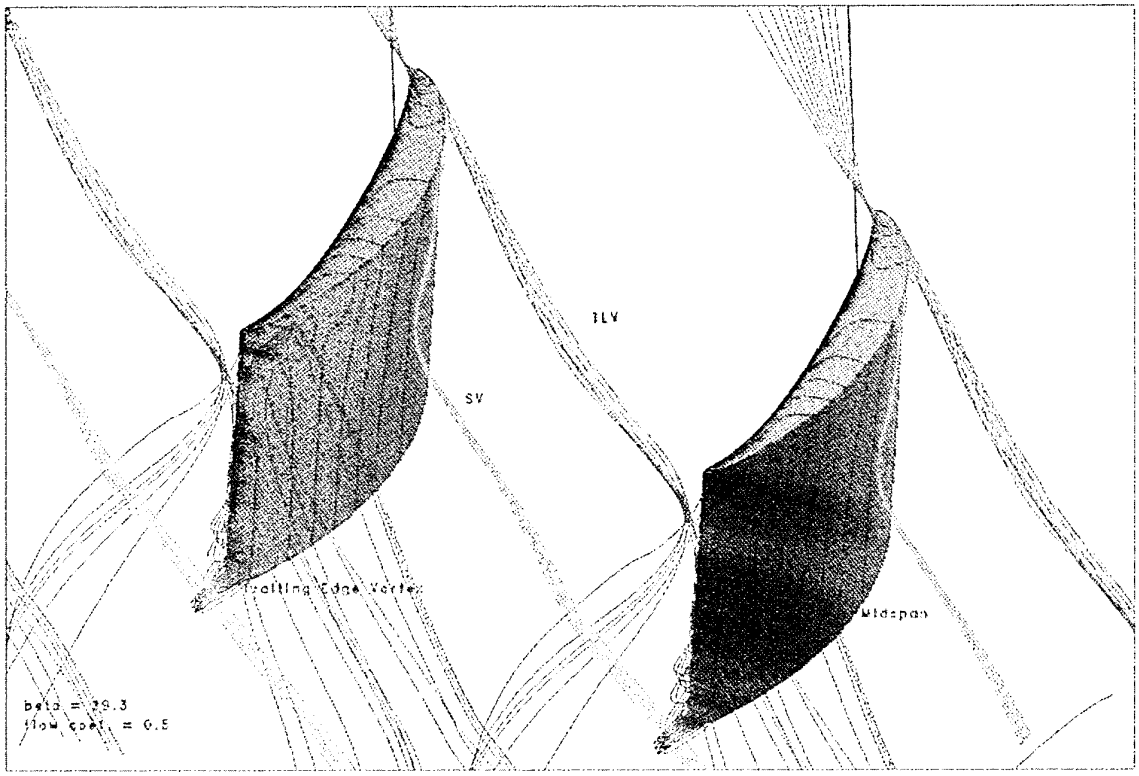

Fig.9 3D streamline pattern close to the moving wall and the trailing edge at ϕ=0.5 (in color), with contours of static pressure

REFERENCE NO. OF THE PAPER: 10

DISCUSSOR'S NAME: D.G. Gregory-Smith, Univ. of Durham, U.K.

AUTHOR'S NAME: S. Kang, C. Hirsch

Q: How far does the moving endwall extend upstream? This relates to the question of how much the effect of the endwall movement is due to the skewing of the inlet boundary layer or due to the relative motion of the wall over the blade tip.

A: The computational domain extends from 1.5 chords upstream to 1.5 chords downstream, and in the moving wall cases, the whole wall is moving.
Figure 23 shows the 3D velocity vectors near the endwall at a few axial sections, from the inlet of the computation domain, I=1, to 12% chord behind the trailing edge, I=82, where I=25 is the leading edge section. The imposed 2D velocity profile and wall speed can be seen in the section of I=1. Skewing of the profile of the boundary layer occurs in all other sections.

As mentioned in the paper, the moving wall results in an increase of tip leakage mass flow and a shift of the tip leakage vortex trajectory towards the pressure side, which may be explained by the following two reasons:

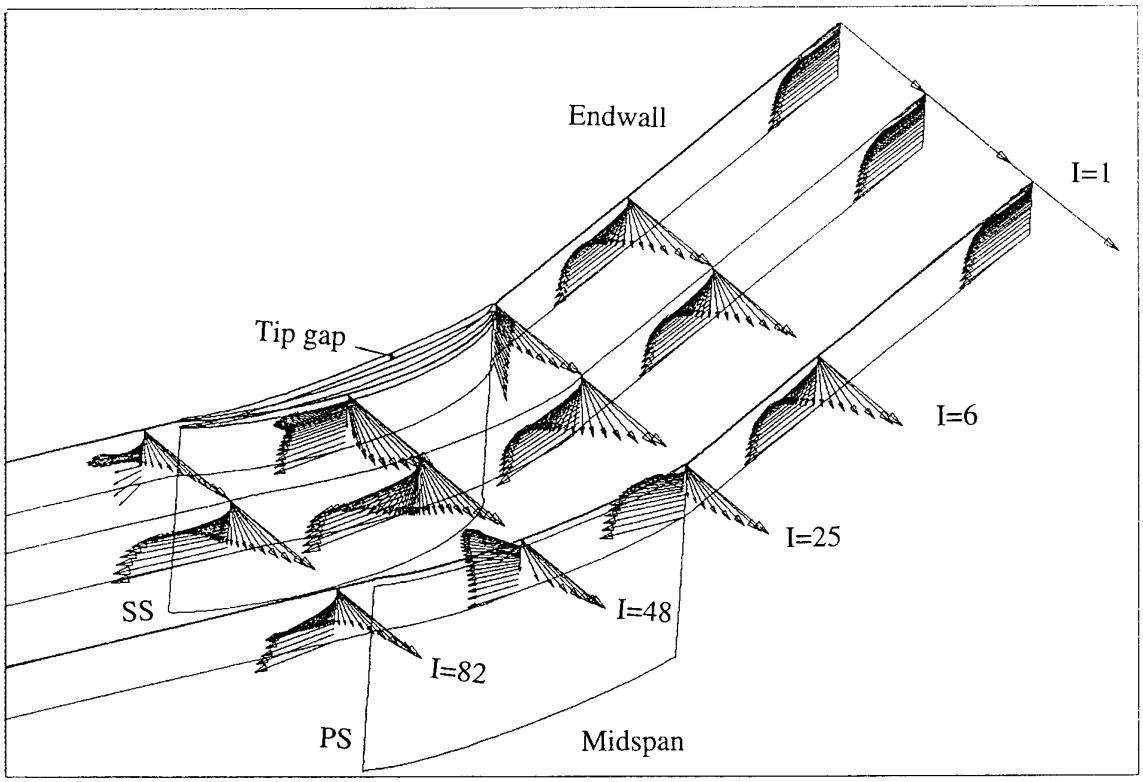

Fig.23 3D velocity vectors near the endwall at few axial sections from the inlet of computation domain, I=1, to 12% chord behind trailing edge, I=82, for ϕ=0.7

1) Skewing of the inlet boundary layer. The skewing of the inlet boundary layer gives rise to an increase of incidence through the boundary layer, resulting in an increase of tip blade loading. Based on the studies of the design and off-design conditions with a stationary endwall, it can be deduced that due to the skewing, the tip leakage mass flow will be enhanced (Table 1) and the tip leakage vortex will shift slightly away from the suction side (Kang & Hirsch, 1994a).
2) Moving wall induced flow just over the blade tip. Skewing of an endwall boundary layer depends on both the wall speed and the boundary layer thickness. Since this thickness in general remains constant up to near the leading edge, the skewing of the inlet boundary layer will not greatly affect the skewing downstream of the leading edge. In other words, the global flow phenomena downstream the leading edge will not be significantly affected by the extension of the moving wall upstream.

REFERENCE NO. OF THE PAPER: 10

DISCUSSOR'S NAME: H.B. Weyer, DLR, Germany

AUTHOR'S NAME: S. Kang, C. Hirsch

Q: In the stationary wall case, what happens to the horse-shoe vortex? Did you calculate that the relatively large clearance of 4 mm (2% of chord) will most likely swallow the horse-shoe vortex at the leading edge?

A: The formation of the horse-shoe vortex, in a cascade with tip clearance, depends not only on the clearance size but also on the inlet flow angle and the ratio of gap size to the thickness of the endwall boundary layer.

In the experiments, we did observe the horseshoe vortex at 1% clearance and saw an indication of its presence at 2% clearance at the design condition. With increasing inlet flow angle, the vortex was also observed at the 2% clearance (Kang & Hirsch, 1994b). Increasing the tip size to 3.3%, no sight of the vortex was observed (Kang & Hirsch, 1993a). The computation at both design and off-design conditions confirms the presence of the horseshoe vortex at the 2% clearance.

REFERENCE NO. OF THE PAPER: 10

DISCUSSOR'S NAME: F. Leboeuf, ECL, France

AUTHOR'S NAME: S. Kang, C. Hirsch

Q: What is the relative part of the internal losses compared to the overall losses associated with tip leakage flow?

A: For the stationary wall case, the overall losses associated with the presence of tip clearance are 1.6% and 2.1% of the inlet dynamic pressure at the design and off-design conditions, respectively. These values are the differences between the overall losses with and without tip clearance. The loss inside the tip gap, i.e., the internal loss, accounts for about 77% and 69% of the overall loss associated with the presence of tip clearance at the design and off-design conditions, respectively.

REFERENCE NO. OF THE PAPER: 10

DISCUSSOR'S NAME: G.D. Willis, GEC-Alsthom, U.K.

AUTHOR'S NAME: S. Kang, C. Hirsch

Q: Did you use the standard Baldwin-Lomax model, or a modified version; and did you have any implementation difficulties?

A: In this comparison we used the standard Baldwin-Lomax turbulence model. The wake coefficient C_{wk} in the Baldwin-Lomax model was taken as 0.25. We did not have any difficulty.

PREDICTION OF LOSSES DUE TO THE TIP CLEARANCE PRESENCE IN AXIAL FLOW MACHINES.

I.K. Nikolos, D.I. Douvikas, K.D. Papailiou
Lab. of Thermal Turbomachines
National Technical University of Athens
P.O. Box 64069, 157 10 Athens, Greece

1. SUMMARY

Theoretical models for the investigation of the phenomena connected with the tip clearance are presented. A model was developed for the description of the flow through the gap, which recognizes the basic flow characteristics inside the gap. The mass flow rate as well as the pressure losses inside the gap are predicted with sufficient accuracy.

A new method, based on the moment of momentum equation, is proposed for the calculation of the shed vorticity and the formation of the leakage vortex. A diffusion model for the vorticity distribution is used for the calculation of the pressure deficit field, so that the total pressure loss profile due to the presence of the leakage vortex, is derived.

An algorithm is being set up for the implementation of the above models in a secondary flow calculation method. A complete theoretical procedure was developed, which calculates the circumferentially averaged flow quantities and their radial variation due to the tip clearance effects. The calculation takes place in successive planes, where a Poisson equation is solved, in order to provide the kinematic field. The self induced velocity is used for the positioning of the leakage vortex. The calculated pressure deficit due to the vortex presence is used, through an iterative procedure, in order to modify the pressure difference in the tip region.

Calculation results are compared to experimental ones for axial flow machines. The agreement between theory and experiment is good.

2. LIST OF SYMBOLS

A	constant of integration (equations (20,21))
B	gap loss coefficient (equation (5))
C_D	discharge coefficient (equation (9))
Cp_s	static pressure coefficient (equation (8))
c	chord
e	tip clearance
h_1	characteristic length of vortex core control volume (figure (2))
i,j,k	orthogonal Cartesian coordinates (figure (2))
l	characteristic length of vortex core control volume (figure (2))
P	static pressure
P_t	total pressure
r	radial position
R	vortex core radius
t	time
u,v,w'	vortex radial, peripheral and axial velocity components
V	flow velocity at the control volume of the vortex core
W	flow velocity inside the tip gap
W	free stream axial velocity
w	w = W-w'
z	distance along vortex axis

Greek symbols

Γ	leakage vortex circulation
ΔE	rate of gap losses (equation (4))
Δs	finite length along the blade camber line
Λ	Owen's constant for the calculation of the eddy viscosity
ν	kinematic viscosity
ν_e	eddy viscosity
ρ	density
σ	contraction ratio (equation (1))
ϕ,θ	angles of vector n_3 (figure (2))
Ψ	Stream Function
ω	vorticity

Subscripts

i,j,k	orthogonal Cartesian coordinates (figure (2))
n	normal to the surface direction
N	normal to the blade camber line direction
p	pressure side
s	suction side
S	direction along the blade camber line
S	surfaces of the control volume of figure (2)
1,2,3,4	positions along the blade passage (figure (1)), or surfaces of the control volume of figure (2)
∞	free stream conditions

3. INTRODUCTION

Extensive experimental and theoretical investigations have been carried out in order to gain a better understanding of the flow inside and downstream of the tip clearance, in either compressor or turbine configurations. The prediction of the losses associated with the tip clearance, as well as the estimation of the induced kinematic field, is essential in the matching of the successive stages of the machine, in order to optimize its performance. Although different approaches have been adopted for the modelling of tip clearance effects, most of the researchers have emphasized the dominance of the pressure difference across the blade tip in

Paper presented at the AGARD PEP 85th Symposium on "Loss Mechanisms and Unsteady Flows in Turbomachines", held in Derby, United Kingdom, 8-12 May 1995, and published in CP-571.

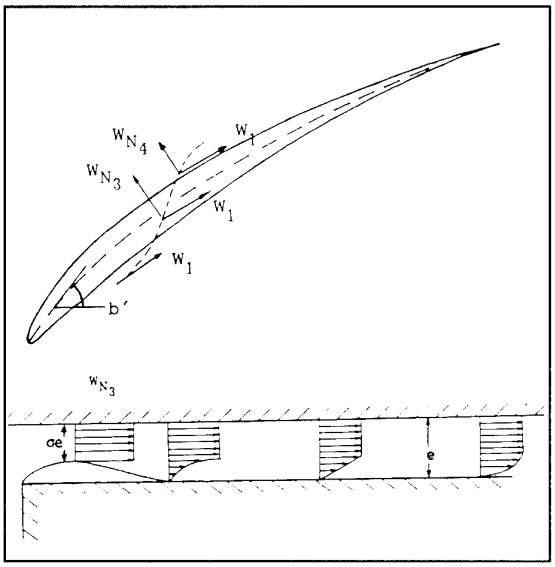

FIG.(1): PROPOSED MODELLING OF THE FLOW INSIDE THE TIP CLEARANCE .

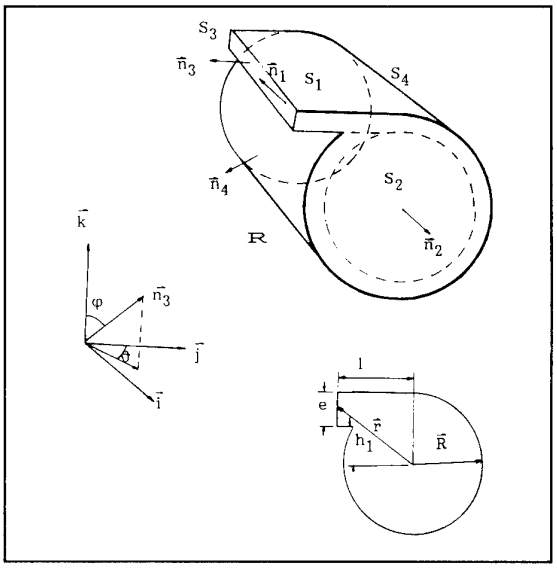

FIG.(2): TIP CLEARANCE VORTEX MODELLING AND THE CORRESPONDING CONTROL VOLUME FOR THE APPLICATION OF THE MOMENT OF MOMENTUM EQUATION.

driving the leakage flow through the gap.

Rains [1] first realized that the pressure difference across the blade tip was dominant compared to the one along the blade on both surfaces. An expression for the losses due to the tip clearance presence was obtained assuming that all the secondary kinetic energy of the leakage flow would be dissipated during the mixing processes.

Lakshminarayana and Horlock [2] used the lifting line theory to predict tip clearance effects. Their observation that the strength of the trailing vortex is less than the blade's bound vorticity, resulted in the adoption of an empirical relation between the retained lift at the blade tip and the tip clearance height. Vavra [3] extended Rains method to a more general form. Booth et al [4] used Rains basic assumptions to propose a tip gap model employing an iterative procedure for the calculation of the tip clearance jet magnitude and angle.

A combined two dimensional potential flow and mixing model was proposed by Tilton [5] for the calculation of the pressure distribution through the gap and the evaluation of the discharge coefficient. Yaras et al [6] used a variation of Rains' model to determine the magnitude and the direction of the leakage jet. Midspan pressure differences, shifted rearward, along with a linear rise in pressure difference at the leading edge, are used as an input to the calculation. A loss model (Yaras et al. [7]) was developed as an extension to Vavra's method [3].

Chen et al [8] adopted a slender body approximation for the decomposition of the tip clearance velocity field into independent through-flow and cross-flow, based in the dominance of normal pressure gradients as Rains [1] proposed.

The present work presents theoretical models for the investigation of the phenomena related to the tip clearance presence. In order to develop a calculation method for the prediction of the tip clearance effects, it is assumed that those effects are considered as a perturbation with respect to the rest of the flow. The principle of superposition is applied, for the tip clearance flow and the rest of the flow. The procedure is an iterative one due to the mutual interdependence of the boundary conditions of the two respective problems. The complete computational procedure and the corresponding algorithm will be described, which permits the numerical calculation of the flow, when tip clearance effects are present.

4. GAP FLOW MODEL

Rains [1] introduced the assumption that the flow through the tip gap of a compressor blade may be simulated on the basis of two-dimensional considerations. A vena contracta is formed at the gap entrance and its presence has been identified among others by the experimental investigations of Sjolander and Amrud [9] and Yaras et al. [6] for turbine blades. Storer's [10] experiments on a compressor cascade suggest that the length scale of reattachment inside the clearance gap depends heavily on height of the tip gap. Similar results were obtained by Moore et al [11] by performing laminar and turbulent flow calculations for an idealized two-dimensional tip gap geometry. These results, compared with Graham's [12] measurements for different gap heights, suggest that the ratio of the tip gap height to blade thickness could be a useful criterion for the reconstruction of the jet profile at the tip clearance exit.

The basic flow model developed previously by the authors (Nikolos et al [13]) presented in figure (1), uses Rains'[1] basic assumptions in order to calculate both the mass flow rate through the gap and the corresponding total pressure losses. Following the formation of the vena contracta, a loss producing region appears, characterised by one of the simple profiles present in figure (1). The profile shape at different gap positions is assumed to depend on the value

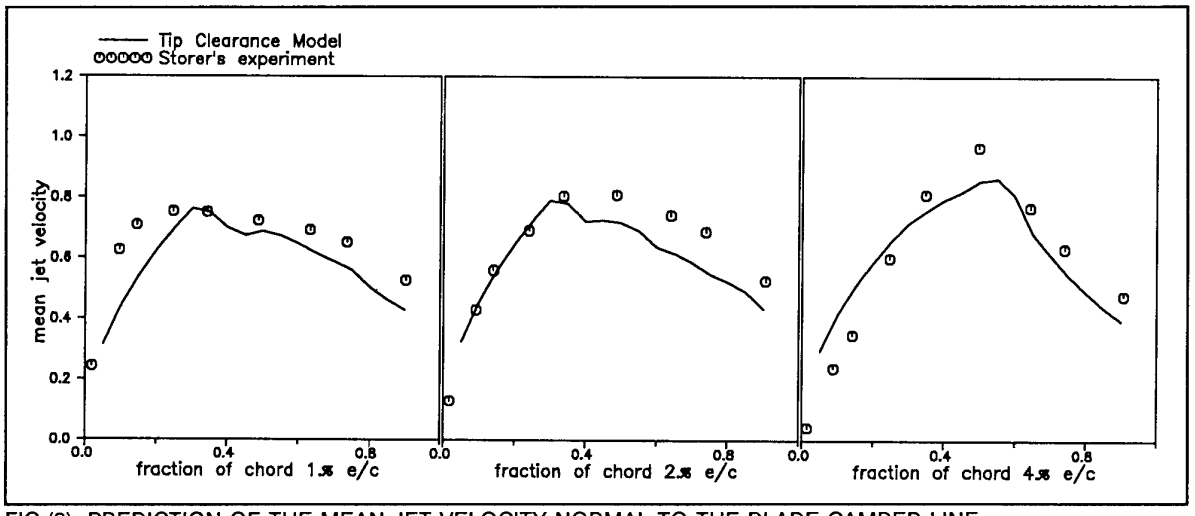

FIG.(3): PREDICTION OF THE MEAN JET VELOCITY NORMAL TO THE BLADE CAMBER LINE.

of the dimensionless distance (normalized with the gap height) from the entrance of the gap.

The gap flow model permits calculation of the discharge coefficient at the gap exit, shown as station 4 in Figure (1). The model gives the following expression for the gap-average velocity of the jet normal to the blade meanline at a particular chordwise location ($\bar{W}_{N4}$) :

$$\frac{\bar{W}_{N4}}{W_1} = C_D\sqrt{-Cp_{S4}} \tag{1}$$

where

$$Cp_{S4} = \frac{P_4 - P_1}{1/2\rho W_1^2} \tag{2}$$

and C_D is the discharge coefficient.The values of C_D depend on the assumed shape of the discharge jet velocity profile and vary along the blade chord with the local blade thickness-to-clearance ratio. For the profile shapes considered (Figure (1)) the calculated values for C_D are the following:

Profile Shape	C_D	t/e
uniform	0.84	>6
parabolic	0.80	2 - 6
triangular	0.76	.8 - 2
inverse parabolic	0.72	<.8

(3)

The pressure difference used for the calculation of the mass flow rate through the gap is the one modified by the presence of the leakage vortex. It is further modified near the leading edge region of the blade using a linear variation of the pressure difference for the first thirty percent of the blade chord.

In order to calculate the losses inside the gap it is assumed that the loss production is occurring at the mixing region downstream the vena contracta. Then, one gets for the losses

$$\Delta\dot{E} = \left[\frac{1}{2}\Delta s\int_{0_4}^{e} W_{N_4} W_4^2 dy - \frac{1}{2}\Delta s\sigma e[W_{N_3}{}^3 + W_{S_3}{}^2 W_{N_3}]\right] + \left[\int_{0_4}^{e}\frac{P_4}{\rho}W_{N_4}\Delta s dy - \frac{P_3}{\rho}\Delta s\sigma e W_{N_3}\right] \tag{4}$$

where Δs is a finite distance along the mean camber line of the blade. The work due to the stresses in the shear layers near the wall has been ignored in the above equation.Taking into account the moment of momentum equation and the conservation of momentum in the direction of the blade camber line for the various adopted simple velocity profiles, equation (4) finally yields

$$\Delta\dot{E} = \frac{1}{2}\Delta s e W_1^3 B(-Cp_{S_4})^{3/2} \tag{5}$$

where B is a coefficient depending on the profile shape. Values of B for the various profile shapes are shown below

Profile shape	B
uniform	-0.24
parabolic	-0.19
triangular	-0.15
inverse parabolic	-0.11

(6)

The losses inside the tip clearance can be computed using equation (5) with constant B taking the above values, according to the local blade thickness to clearance ratio.

5. VORTEX MODEL

The calculation of the induced kinematic field as well as the estimation of the losses downstream of the gap exit is based mainly on the correct computation of the strength and position of the leakage vortex. The formation and the evolution of this vortex is quite similar to that of the finite wing case and previous researchers insisted on using prediction methods tailored to this last case.

Various experiments exist which confirm that the circulation of the leakage vortex is a fraction of the blade's bound circulation but do not indicate directly the validity of the

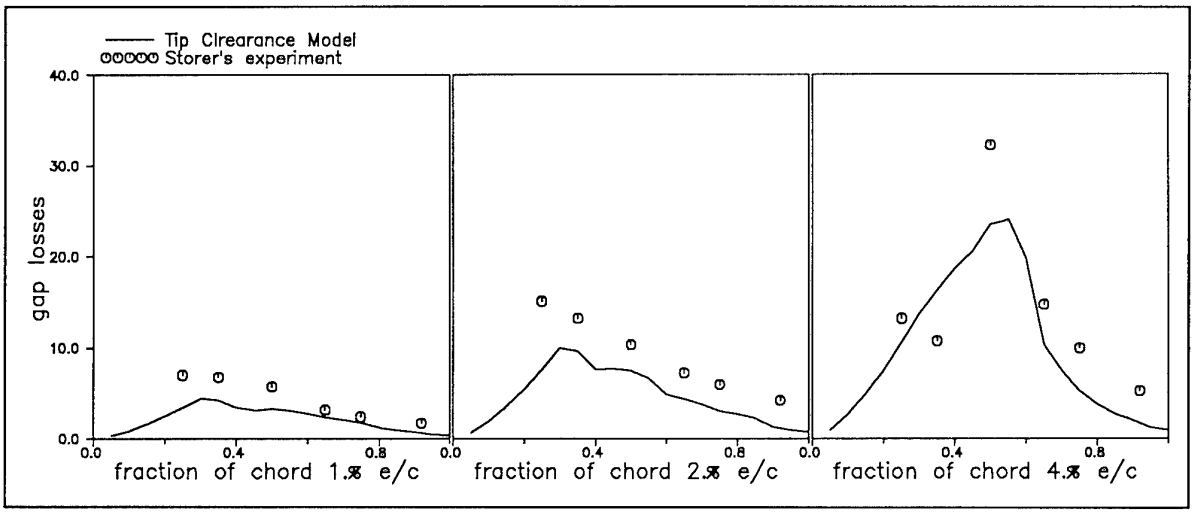

FIG.(4): CALCULATION OF THE LOSSES INSIDE THE TIP CLEARANCE.

"retained lift" theory, which stipulates that the shed out vorticity is produced by part of the vortex lines of the blade, the rest going towards the endwall and producing the existing pressure difference along the gap. On the other hand various researchers, such as Yamamoto [14], Inoue and Kurumaru [15], Sjolander and Amrud [9] demonstrated that the strength of the leakage vortex seems to increase with increasing tip clearance height. This increase in the amount of vorticity of the leakage vortex is followed by an increase of the vortex diameter. The above experimental evidence seems to suggest that the key factor for the determination of the amount of shed out vorticity is the mass flow rate through the tip clearance.

The flow field near the endwall is characterised by the interaction of two opposing flows. The secondary flow, having a direction from the pressure to the suction side of the passage, and the leakage jet flow, coming out of the gap at an angle to the main flow. As a result, the leakage flow rolls down away from the endwall, along a separation line, and forms the leakage vortex. In the outer flow, this vortex interacts with the tip-side passage vortex, rotating contrary to the leakage vortex. At the same time, as we march downstream, the additional mass from the tip clearance jet, entering the vortex, increases both its radius and its strength. The complexity of this flow situation suggests that some drastic assumptions should be adopted in order to derive a simple model. Flow visualisation suggests that the mass leaving the gap exit enters in its quasi-totality inside the leakage vortex. The performed measurements (Lakshminarayana [16]), Inoue et al [15], Yaras et al [17], etc) indicate that the vortex nearly has a solid body rotation structure. These features are retained in the adopted model and it is assumed that the mass flow coming out of the gap is wrapped around the existing solid body rotation vortex, increasing its radius and moment of momentum component in the direction of the vortex axis. The most elementary form of this model is schematically presented in figure (2), where, at the same time, an elementary control volume between two successive computational stations is defined. From inlet to exit inside the control volume, the flow quantities are assumed to vary linearly. As it will be seen below, this model presents an alternative mechanism for specifying the strength of the vortex, which depends heavily on the mass flow rate coming out of the tip clearance.

According to the assumptions outlined above, we apply the moment of momentum theorem to the control volume **R** of figure (2), for steady state conditions and ignoring gravity effects. Considering the component of the moment of momentum equation in the direction of the axis of the solid body rotating vortex and neglecting the contribution of the shear stresses we have

$$\omega_1\int_0^{2\pi}\int_0^{R_1}\rho r^3 V_{1_i}\,dr\,d\phi-\omega_2\int_0^{2\pi}\int_0^{R_2}\rho r^3 V_{2_i}\,dr\,d\phi+\int_0^{\Delta s}\int_{h_1}^{h_1+e}\rho V_{3_n}V_{3_j}\,h\,dh\,ds = \int_0^{\Delta s}\int_{R_1}^{R_1+e}(l\cos\phi+h\sin\phi\cos\theta)P\,dh\,ds \tag{7}$$

with V_{3_n} being the velocity component in the direction of n_3. The mass balance for the control volume **R** reads

$$\left|\int_{(S_1)}\rho ds_1\vec{n}_1\cdot\vec{V}_1\right|+\left|\int_{(S_3)}\rho ds_3\vec{n}_3\cdot\vec{V}_3\right|=\left|\int_{(S_2)}\rho ds_2\vec{n}_2\cdot\vec{V}_2\right| \tag{8}$$

Assuming that the density is constant and uniform distributions for the velocity magnitude on the surfaces (S_1) and (S_2), the following equations are derived from equations (7) and (8) respectively

$$\rho\left[\omega_1 V_{1_i}\pi\frac{R_1^4}{2}-\omega_2 V_{2_i}\frac{\pi R_2^4}{2}-V_{3_n}V_{3_j}\Delta s\frac{(h_1+h_2)}{2}e\right]= P_3\int_0^{\Delta s}s\left[\int_{h_1}^{h_1+e}(l\cos\phi+h\sin\phi\cos\theta)dh\right]ds \tag{9}$$

$$\pi R_2^2 V_{2_i}=\pi R_1^2 V_{1_i}+V_{3_n}\Delta s e \tag{10}$$

The circulation at a radius R, associated with a solid body rotation of speed ω is

$$\Gamma=\oint_C d\vec{r}\vec{V}=2\pi\omega R^2 \tag{11}$$

Combining eqs (9), (10), (11) yields the expression for the

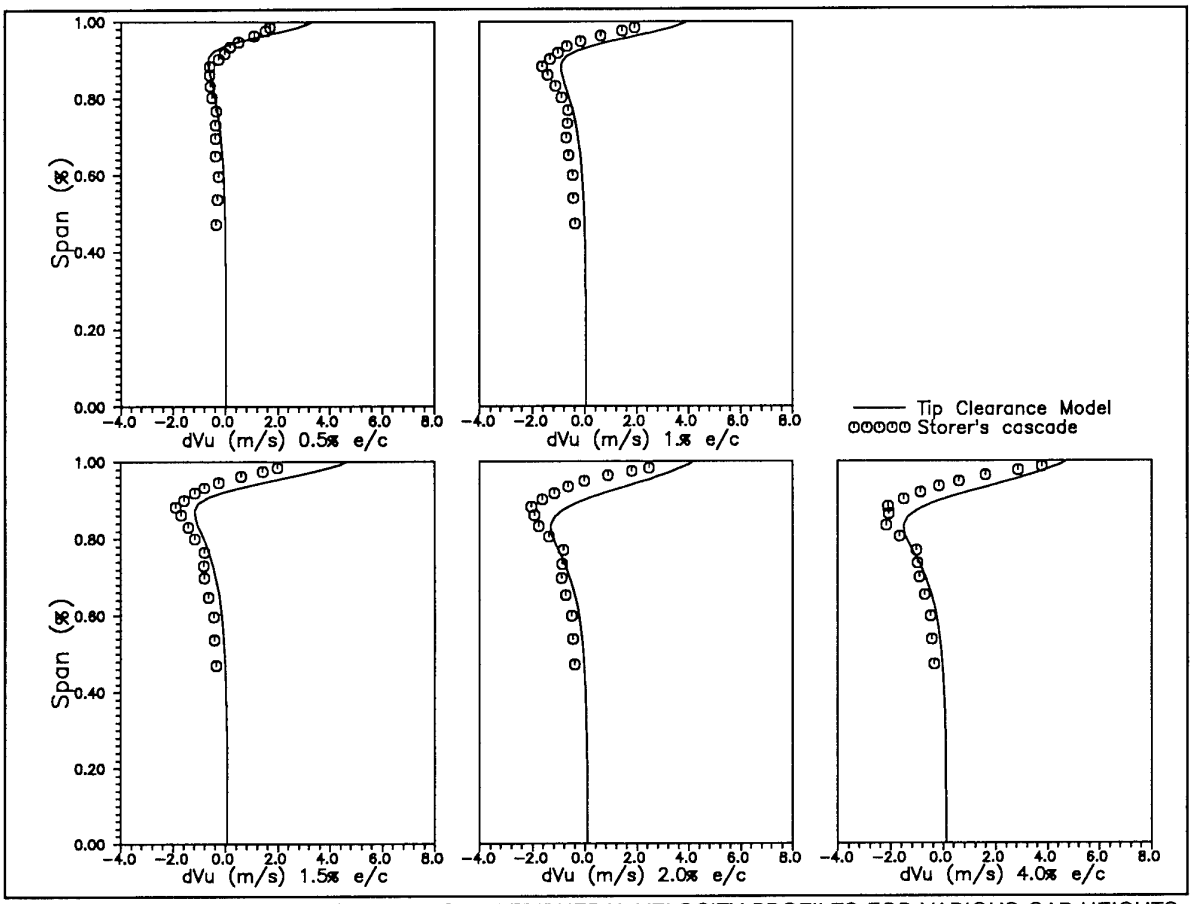

FIG.(5): PERIPHERALLY AVERAGED INDUCED PERIPHERAL VELOCITY PROFILES FOR VARIOUS GAP HEIGHTS.

vortex strength at station 2 Γ_2, expressed in terms of the conditions at station 1

$$\Gamma_2=\frac{1}{V_{2_i}R_2^2}[\Gamma_1 V_{1_i}R_1^2+2V_{3_a}V_{3_j}\Delta_s(h_1+h_2)e]- \\ -\frac{4}{V_{2_i}R_2^2}\frac{P_3}{\rho}\int_0^{\Delta s}\int_{h_1}^{h_1+e}(l\cos\phi+h\sin\phi\cos\theta)dhds \qquad (12)$$

While equation (12), may be used for the calculation of the strength of the vortex, the mass balance equation (10) provides a basis for the calculation of the vortex core radius.

6. THE DIFFUSIONOF THE LEAKAGE VORTEX

The rolling up of the tip clearance jet and the formation of the leakage vortex is followed by a diffusion of vorticity, leading to an increase of the vortex radius and a reduction of the maximum value of vorticity downstream the trailing edge.

During the evolution of the leakage vortex, a reduction of static pressure is produced inside it. This modification of the pressure field can be easily distinguished in the measured static pressure difference distributions at the tip region of the blade suction side. The diffusion of the leakage vortex produces a rise in the static pressure along the centerline of the vortex and the pressure deficit is reduced downstream of the trailing edge (Yaras et al. [17], Inoue et al. [15]).

The models developed by Lamb [18] and Newman [19] for the diffusion of a line vortex are used in the present work to simulate the diffusion of the leakage vortex and predict the pressure disturbance as well as the total pressure loss distribution due to the tip clearance presence.

Lamb's solution to the diffusion of a line vortex gives the distribution of vorticity in successive planes as

$$\omega(r,t)=\frac{\Gamma}{4\pi\nu t}\exp\left(-\frac{r^2}{4\nu t}\right) \qquad (13)$$

where ν is the kinematic viscosity, r is the radial distance from the vortex axis and t is the time measured from the beginning of the diffusion process. The vortex core radius is given

$$R=\sqrt{4\nu t} \qquad (14)$$

We consider the problem not as a three-dimensional steady one but as a two-dimensional unsteady one, assuming that the time steps of the diffusion process correspond to distances Δz between successive planes normal to the vortex axis, fulfilling the relation

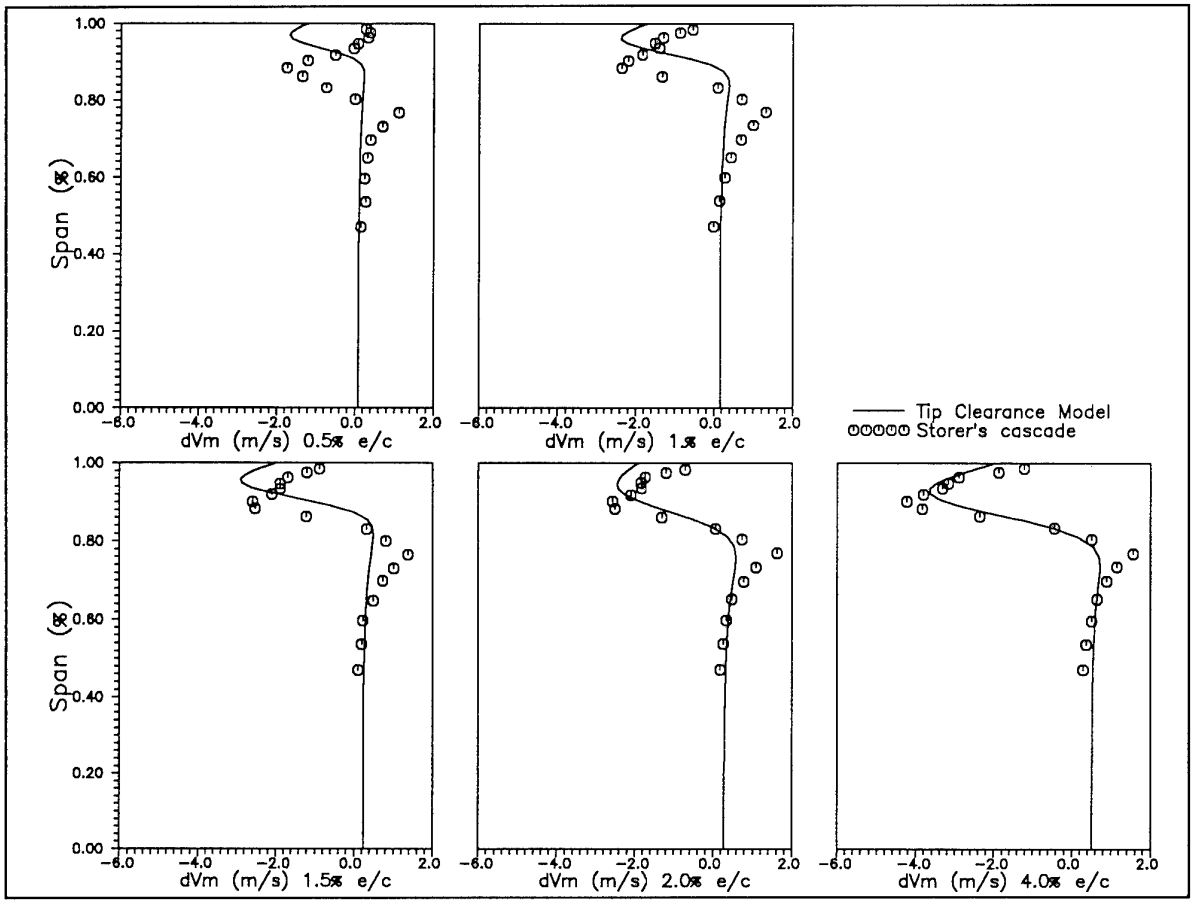

FIG.(6): PERIPHERALLY AVERAGED INDUCED MERIDIONAL VELOCITY PROFILES FOR VARIOUS GAP HEIGHTS.

$$\Delta z=\Delta t\cdot W \tag{15}$$

where W is the velocity of the mainstream along the vortex axis.

From equation (14) we have for two successive time steps

$$R_2^2-R_1^2=\Delta R^2=4\nu(t_2-t_1) \Rightarrow$$
$$\Rightarrow \Delta R^2=4\nu\Delta t \tag{16}$$

or from equation (15)

$$\Delta R^2=4\nu\frac{\Delta z}{W} \tag{17}$$

The turbulent nature of the tip vortex flow can be incorporated by replacing viscosity ν with $\nu+\nu_e$ where ν_e is the appropriate eddy viscosity value. Yaras and Sjolander [17] use Owen's [20] modelling for ν_e,which reads

$$\frac{\nu_e}{\nu}=\Lambda^2\sqrt{\frac{\Gamma}{\nu}} \tag{18}$$

with Λ taking values between 0.7 and 1.2. The value of 0.95 has consistently been used throughout the present work.

Equation (17) provides a way of estimating the expansion of the leakage vortex core due to the diffusion of its vorticity.

A similar solution to the problem of a line vortex diffused radially was proposed by Newman [19]. Denoting the radial velocity by u, the rotational velocity by v and the longitudinal by w' and putting w' = W-w where W is the axial velocity in the undisturbed fluid, the following relation is derived

$$v=\frac{\Gamma}{2\pi r}\left[1-\exp\left(-\frac{r^2}{R^2}\right)\right] \tag{19}$$

The two other velocity components may be finally expressed as

$$w=\frac{A}{z}\exp\left(-\frac{r^2}{R^2}\right) \tag{20}$$

$$u=-\frac{A}{2z^2}\exp\left(-\frac{r^2}{R^2}\right) \tag{21}$$

where A is the constant of integration.

The expression for the static pressure reads

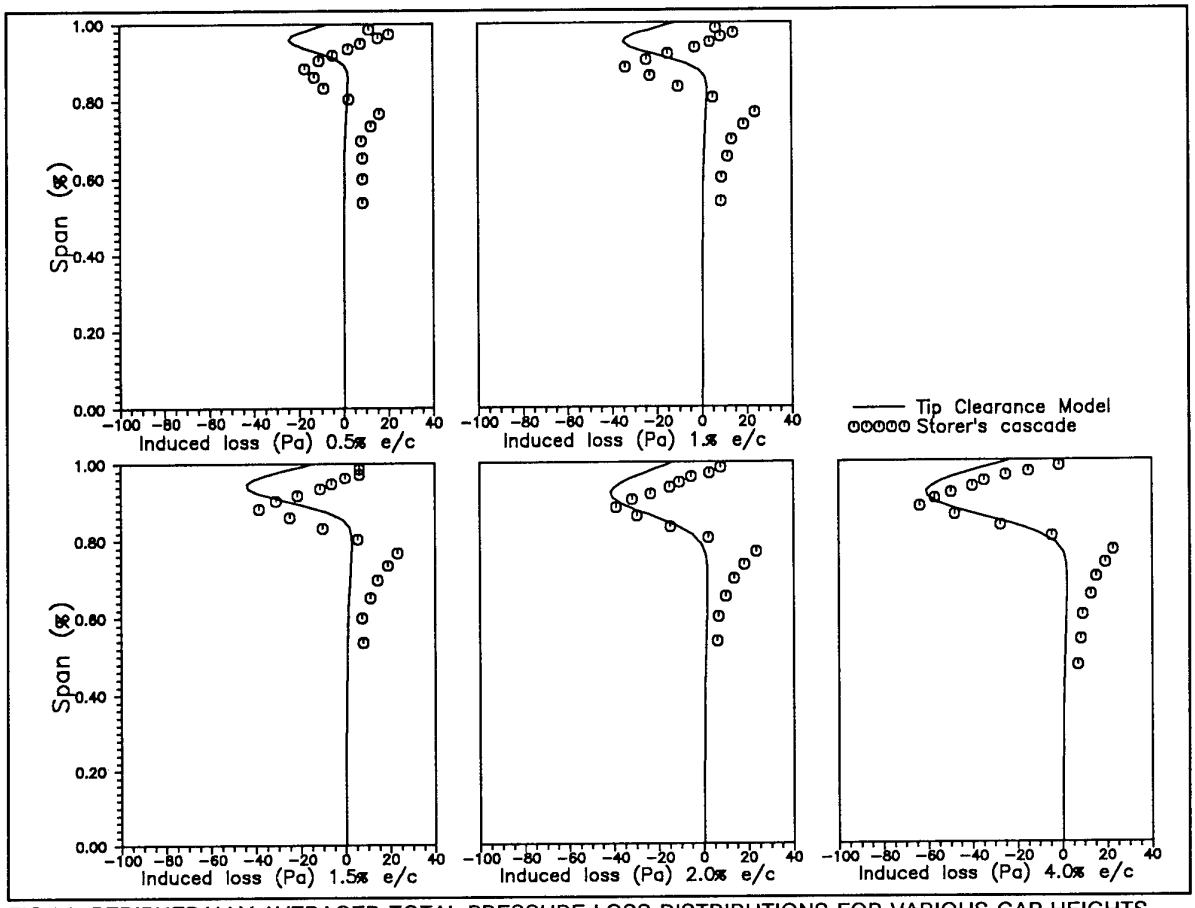

FIG.(7): PERIPHERALLY AVERAGED TOTAL PRESSURE LOSS DISTRIBUTIONS FOR VARIOUS GAP HEIGHTS.

$$\frac{\partial P}{\partial r}=\frac{\rho\Gamma^2}{4\pi^2 r^3}\left[1-2\ \exp\left(-\frac{r^2}{R^2}\right)+\exp\left(-\frac{2r^2}{R^2}\right)\right] \qquad (22)$$

The numerical integration of the above equation provides the distribution of pressure inside the vortex using as boundary condition the value of the undisturbed free stream static pressure.

If $P_{t\infty}$ and P_t are the total pressure in the free stream and inside the vortex respectively we have that

$$P_{t_\infty}-P_t=P_\infty-P+\frac{1}{2}\rho[W^2-(w'^2+v^2+u^2)] \qquad (23)$$

Substituting w' in the above equation the total pressure loss is expressed as

$$\Delta P_t=\Delta P+\frac{1}{2}\rho[2Ww-w^2-v^2-u^2] \qquad (24)$$

7. THE CALCULATION PROCEDURE

The already described model of the tip clearance gap, provides us with the mean jet velocity magnitude and direction at the gap exit, as well as the total pressure loss occurring inside the gap. For this calculation, the static pressure difference between pressure and suction sides at the tip level is needed, as this is modified by the tip clearance vortex presence. As the jet velocity is the key element for the vorticity shed from the gap inside the leakage vortex and its computation must be done accurately, the complete calculation must necessarily be iterative.

The second model provides the necessary elements for the leakage vortex formation, its strength, its evolution characteristics and total pressure losses, but it does not provide its position in space.

In the present work the formation of the leakage vortex and the calculation of the induced kinematic field is treated also in successive planes adopting the decomposition assumption of Chen et al [8]. In order to provide a better cooperation between a meridional flow calculation procedure and the tip clearance model, the successive calculation planes are normal to the axis of the machine. In this way, each plane corresponds to a specific axial position and the peripherally mean values can be easily calculated.

The computation of the shed out vorticity is performed between two successive planes. A linear variation of the leakage mass flow rate is assumed between the two planes. The resulting vortex strength corresponds to a vorticity distribution in the second of the two successive planes. Equation (13) is used for the distribution of the vorticity in the current calculation plane in the following form

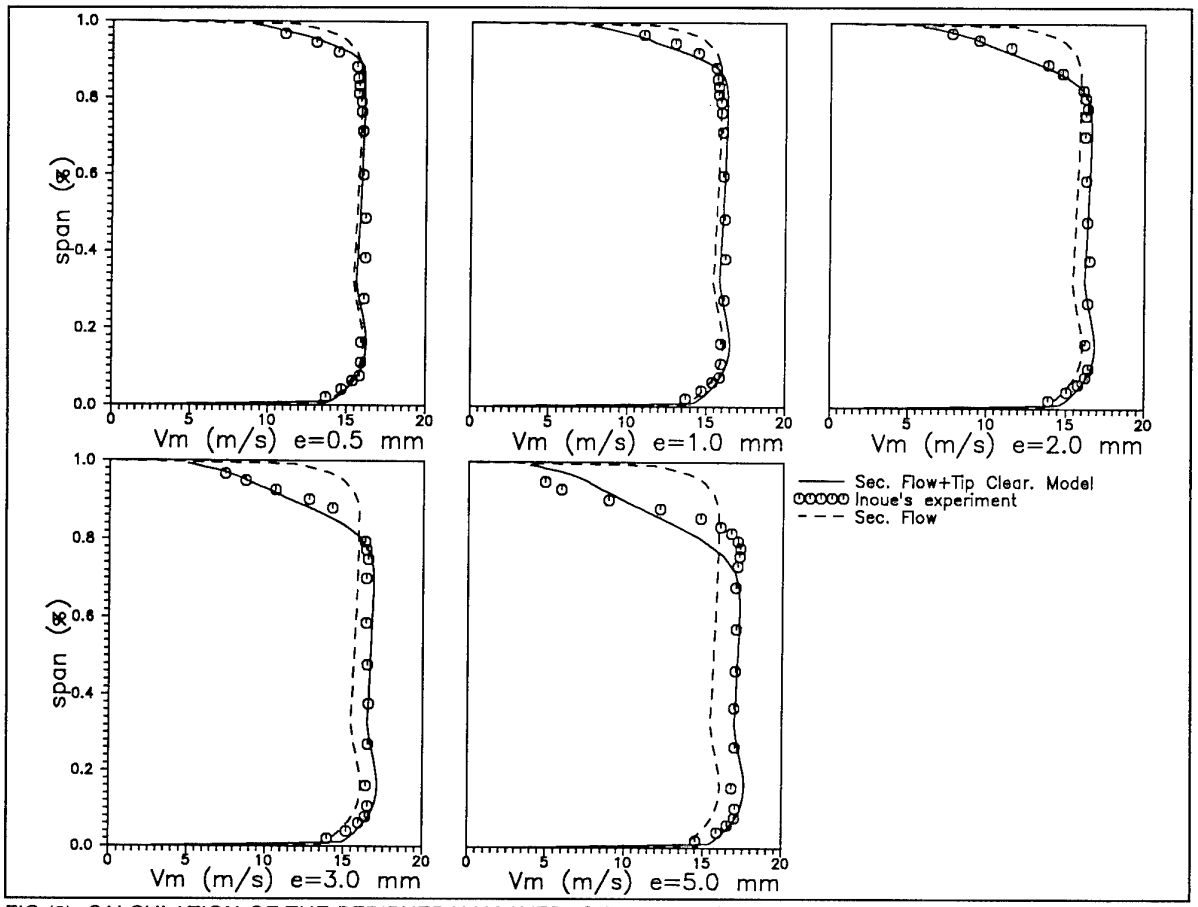

FIG.(8): CALCULATION OF THE PERIPHERALLY AVERAGED MERIDIONAL VELOCITY DOWNSTREAM THE ROTOR TRAILING EDGE WITH AND WITHOUT THE TIP CLEARANCE INFLUENCE.

$$\omega(r,R)=\frac{\Gamma}{\pi R^2}\exp\left(-\frac{r^2}{R^2}\right) \qquad (25)$$

where R is the radius of the leakage vortex. This vortex radius is calculated using the mass balance equation (eq.10) and taking into account the diffusion process (eq. 17). However, the axis of the leakage vortex is not perpendicular to the calculation planes, so that the angle of the vortex trace must be taken into account.

The vortex trace and the peripheral position of the vortex centre at the current calculation plane are computed using the self induced velocity field in the previous plane. The time step resulting from the flow velocity at the vortex centre, considered in the absence of tip clearance effects, and the distance between the calculation planes are used in order to compute the peripheral displacement of the vortex centre. The radial position is estimated by assuming that the vortex core edge lies between the endwall and the blade tip.The computation of the induced velocity field necessitates the solution of a Poisson equation of the following form

$$\Delta\Psi=-\omega \qquad (26)$$

For calculation planes inside the blade passage a zero normal to the wall velocity is used as boundary condition, for all the boundary nodes except those at the tip clearance exit, where the leakage mass flow rate determines the boundary values of the stream function. The zero normal to the wall velocity condition is used at planes downstream the trailing edge, only for the hub and tip boundaries. At the other two boundaries periodic conditions are used.

The complete calculation procedure will be described with the remark that the tip clearance flow will be introduced as a modification to the basic flow, existing in the absence of tip clearance effects. Consequently, the tip clearance flow is introduced as a third zone in the already existing two-zone model, which is used for the calculation of the secondary flow effects. The implementation of the complete calculation procedure in a secondary flow method is discussed by Nikolos et al [21]. The secondary flow method which is used is discussed in detail by Douvikas et al [22].

The flow field without tip clearance effects is established through the meridional flow calculation procedure, including secondary flow effects [22]. Peripherally mean flow quantities are calculated and, it is possible to compute, through momentum considerations, the forces acting on the blade surface (per unit surface). The pressure differences (P_p-P_s) can be computed if it is assumed that the shear stresses at the blade surfaces can be neglected. This pressure difference provided by the secondary flow

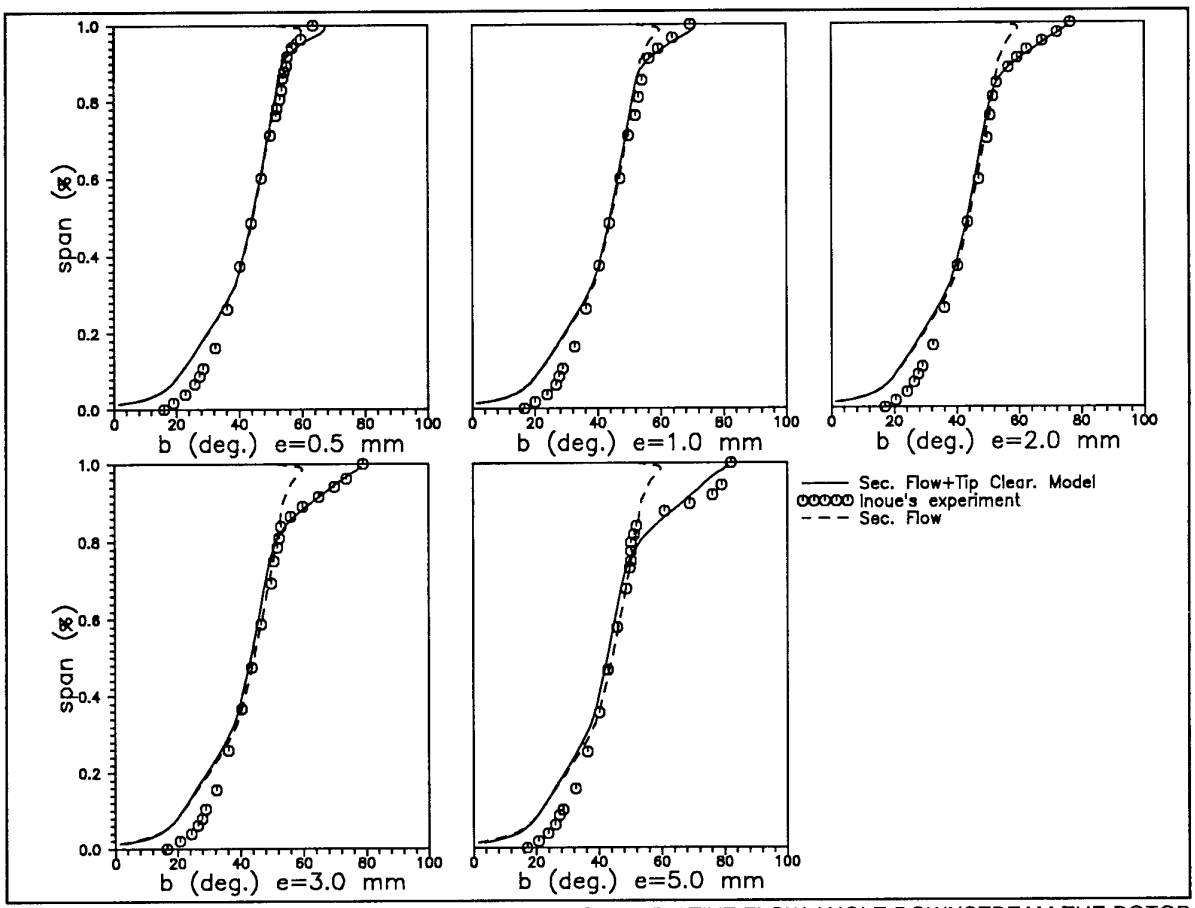

FIG.(9): CALCULATION OF THE PERIPHERALLY AVERAGED RELATIVE FLOW ANGLE DOWNSTREAM THE ROTOR TRAILING EDGE WITH AND WITHOUT THE TIP CLEARANCE INFLUENCE.

calculation procedure, does not include the contribution of the leakage vortex. This contribution may be computed integrating equation (22), using the undisturbed flow value for the static pressure at the boundary. The vortex strength is required for this computation, so that an iterative procedure must be set up in order to provide the various flow quantities, which need for their calculation the modified pressure difference at the blade tip. Convergence is established when the assumed and computed pressure difference between pressure and suction sides are found to be the same.

At the considered station the blade thickness is known and a first guess for the static pressure difference may be made from the results of the secondary flow calculation procedure. Then according to the ratio of the local blade thickness to tip gap height, a simple exit velocity profile is adopted and the mean jet velocity and the total pressure losses occurring inside the gap are calculated. The conservation of the longitudinal component of momentum through the gap provides also the angle of the velocity of the jet. The peripherally mean value of the longitudinal component of the velocity at the tip clearance height, provided by the secondary flow calculation, is used for this purpose. A linear variation of the jet velocity component, between the previous and the considered station is assumed for the calculation of the mass flow rate through the corresponding part of the gap. This flow rate is used to evaluate the expansion of the vortex core between two successive stations, assuming that the complete leakage flow enters the leakage vortex.

The vortex model is then applied providing the amount of vorticity at the considered axial position. The vortex trace at the previous calculated position is used in order to determine the direction of the vortex axis. The calculation of the induced kinematic field is then carried out. The total pressure loss profile is then estimated. In particular, equation (24) is used to provide the total pressure difference profile between the cases with and without tip clearance effects.

8. RESULTS AND DISCUSSION

In order to validate the proposed calculation procedure, the experimental data of Storer [10] and Inoue et al [23] were used. The first case (Storer [10]) concerns a linear compressor cascade with a circular arc camber line and 5% maximum thickness-to-chord ratio. The inlet velocity of 24m/s corresponds to an inlet Mach number of 0.03. Five different tip gap heights (besides zero clearance) were measured, with the smallest being 0.5% of the chord and the largest 4% of the chord. The mean jet velocity distributions normal to the blade's camber, are available only for three clearances (1% e/c, 2% e/c and 4% e/c) and these are used for the validation of the gap flow model. The

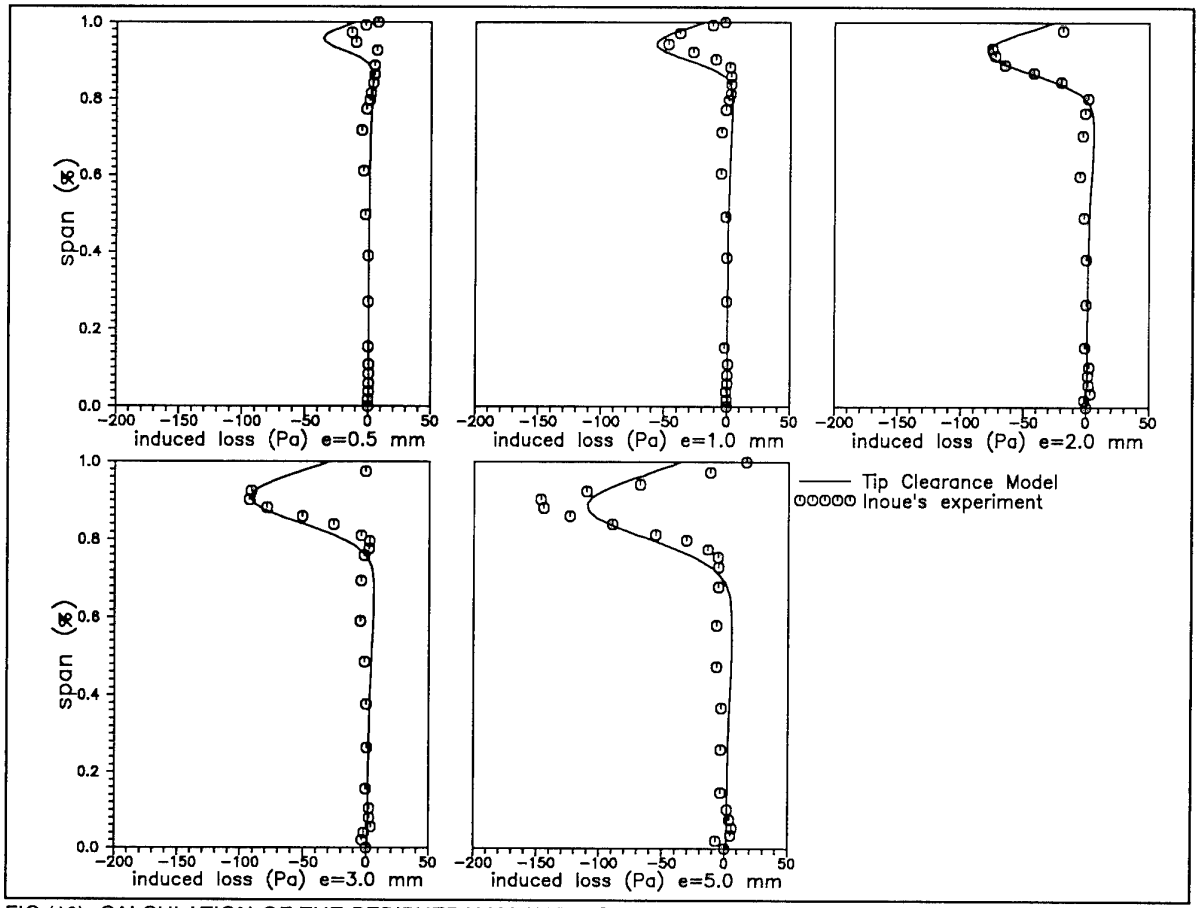

FIG.(10): CALCULATION OF THE PERIPHERALLY AVERAGED INDUCED TOTAL PRESSURE LOSS DISTRIBUTION.

comparison presented in figure (3), between theory and experiment for the mean jet velocity distribution normal to the blade's camber line is good. The adoption of linear variation of pressure for the first thirty percent of the chord had a positive influence especially in the case of 2% e/c. Storer's [10] experimental data were also used in order to compare calculated and measured total pressure loss through the gap, defined as

$$\int_0^e W_{N_4}(s)\cdot(P_{t_4}(s)-P_{t_1})ds \qquad (27)$$

Comparisons between theory and experiment are presented in figure (4). The existing differences can be partially explained by the fact that the present model does not include the losses due to the endwall boundary layer inside the gap. However, the trends are well predicted and the fact that this part of the losses is small compared to the total losses attributed to tip clearance effects, renders this level of comparison adequately accurate for the complete calculation.

Circumferentially averaged distributions of the peripheral and meridional components of the vortex flow field, for various tip clearances, are presented in figures (5) and (6) respectively. They are compared with measured distributions of the mass averaged peripheral velocity components for every tip clearance height, minus the corresponding distribution for the case with zero clearance (the computation is based on a secondary flow calculation, thus the peripheral variations of the flow quantities are not available).

Figure (7) presents comparisons between mass averaged experimental data and peripherally mean predictions of total pressure losses for the Storer's [10] experiment. The experimental total pressure losses, due to the clearance presence, were obtained by subtracting the losses for the zero clearance case. In this way the vortex model itself, as well as the adopted in the present work superposition principle, are validated. Although the estimation of the radial position of the leakage vortex is fairly correct for the small clearances, the shape of the loss profile confirms the validity of the adopted model. However, considering the simplicity of the models and the assumptions adopted, comparisons are quite good.

The isolated rotor experiment of Inoue et al [23] was used next, which comprises 12 blades of the NACA 65 series with 6% maximum thickness at the tip and 10% at the hub. Five different tip clearances were examined (0.5 mm, 1.mm, 2.mm, 3.mm, 5.mm). Figure (8) contains the calculation results for the meridional velocity, with and without the tip clearance effect, compared with the corresponding experimental data. The strong blockage due to the leakage vortex presence is clear especially for the large clearances. Figure (9) contains the corresponding relative flow angle

calculations, with and without the clearance effects, compared with experimental data. The agreement is very good for both axial velocity component and relative flow angles, for all gap heights.

Figure (10) contains the predictions of the peripherally mean total pressure loss profiles for the various gap heights, compared with the corresponding experimental data. In order to distinguish the losses due to the tip clearance presence, the secondary losses at the tip region were taken to be equal with those at the hub. The errors introduced by this assumption seem to be negligible, as the secondary flow losses are small compared to those due to the tip clearance effects, especially for the large clearance cases. Looking at the variation of the total pressure loss profile with the gap height it may be seen that the position and strength of the leakage vortex is sufficiently predicted for a wide variety of gap heights.

The magnitude as well as the shape of the calculated total pressure loss profiles in both cases for all the clearances tested, demonstrate the ability of simple modelling to predict quite complicated phenomena with sufficient accuracy.

9. CONCLUSIONS

Basic theoretical models for the prediction of the tip clearance effects and especially the total pressure losses inside and downstream the tip gap,were examined and presented in this paper along with a complete calculation procedure.

The first model concerned the flow inside the tip clearance gap. A simple modelling of the loss production mechanism inside the gap enables the model not only to predict the gap losses but also to calculate the gap exit jet velocity with reasonable accuracy. The satisfactory prediction of the mass flow rate through the gap is emphasized, as this quantity monitors the shed vorticity from the gap into the leakage vortex.

The second model concerned the formation and the development of the leakage vortex. An alternative and simple way of describing the process of the rolling up of the jet issued from the gap in order to form the leakage vortex is presented, which predicts correctly the vortex strength. The proposed model was improved by introducing a mechanism of vorticity diffusion. This provides the model with the ability to predict correctly not only the shed out vorticity, but also the distribution of the static pressure deficit and the total pressure loss profile due to the leakage vortex presence.

The superposition principle adopted was proved to be adequate for setting up the complete calculation procedure, for a wide variety of gap heights. The proposed tip clearance method can cooperate quite satisfactory with a secondary flow calculation method, used in order to provide the basic flow field without the tip clearance effects.

Finally, the present work demonstrates the ability of simple modelling to predict quite complicated phenomena, so that fast computational tools may be developed, particularly attractive for industrial purposes.

ACKNOWLEDGEMENTS

The Authors would like to express their thanks to SNECMA, Rolls-Royce, Turbomeca and MTU for permitting them to publish this work, as well as for the discussions that they had with the engineers of the above mentioned companies and the colleagues from the Cranfield Institute of Technology participating to this project. The authors also wish to express their thanks to the European Community which funded this project (AER2 CT92-0039-AC3A) and to Mr W. Borthwick, who acted as Technical Monitor.

10. REFERENCES

1. Rains D.A., 1954, "Tip Clearance Flow in Axial flow Compressors and Pumps", California Institute of Technology, Hydrodynamics and Mechanical Engineering Laboratories Rep. No 5.
2. Lakshminarayana B., Horlock J. H., 1965, "Leakage and Secondary Flow in Compressor Cascades", ARC R&M 3483.
3. Vavra M.H., 1960, "Aerothermodynamics and Flow in Turbomachines", John Wiley and Sons Inc., New York.
4. Booth T.C., Dodge P.R., Hepworth H.K., 1982, "Rotor-Tip Leakage: Part I - Basic Methodology", ASME Journal of Eng. for Power, *104*, pp 154-161.
5. Tilton J.S., 1986, "Tip Leakage Flow in a Linear Turbine Cascade", M.Sc. Thesis, Virginia Polytechnic Institute and State University.
6. Yaras M.I., Yingkang Z., Sjolander S.A., 1989, " Flow Field in the Tip Gap of a Planar Cascade of Turbine Blades", ASME Journal of Turbomachinery, *111*, pp 276-283.
7. Yaras M.I., Sjolander S.A., 1990a, "Prediction of Tip Leakage Losses in Axial Turbines", ASME paper 90-GT-154.
8. Chen G.T., Greitzer E.M., Tan C.S., Marble F.E., 1990, "Similarity Analysis of Compressor Tip Clearance Flow Structure", ASME paper 90-GT-153.
9. Sjolander S.A., Amrud K.K., 1986, "Effects of Tip Clearance on Blade Loading in a Planar Cascade of Turbine Blades", ASME paper 86-GT-245.
10. Storer J.A., 1991, "Tip Clearance Flows in Axial Compressors", Ph.D. Thesis Dept. of Engineering University of Cambridge.
11. Moore J., Moore J.G., Henry G.S., Chaudhry U., 1989, "Flow and Heat Transfer in Turbine Tip Gaps", ASME Journal of Turbomachinery, *111*, pp 301,309.
12. Graham J.A.H., 1985, "Investigation of a Tip Clearance Cascade in a Water Analogy Rig", ASME paper 85-IGT-65.
13. Nikolos I.K., Douvikas D.I., Papailiou K.D., 1993a, "A Method for the Calculation of the Tip Clearance Flow Effects in Axial Flow Compressors, Part I: Description of Basic Models", ASME paper 93-GT-150.
14. Yamamoto A., 1989, "Endwall Flow/Loss Mechanisms in a Linear Turbine Cascade With Blade Tip Clearance", ASME Journal of Turbomachinery, vol. 111, pp. 264-275.
15. Inoue M., Kurumaru M., 1989, "Structure of Tip Clearance Flow in an Isolated Axial Compressor

Rotor", ASME Journal of Turbomachinery, *111*, pp 250-256.

16. Lakshminarayana B., 1970, " Methods of Predicting the Tip Clearance Effects in Axial Turbomachinery", ASME Journal of Basic Eng., Ser. D., *92*, 3, pp 467-482.
17. Yaras M.I., Sjolander S.A., 1990, "Development of the Tip Leakage Flow Downstream of a Planar Cascade of Turbine Blades: Vorticity Field", ASME Journal of Turbomachinery, *112*, pp 609-617.
18. Lamb H., 1932, "Hydrodynamics", 6th Edition, Dover Publications.
19. Newman B.G., 1959, "Flow in a Viscous Trailing Vortex", The Aeronautical Quarterly pp 149-162.
20. Owen P.R., 1970, "The Decay of a Turbulent Trailing Vortex", Aeronautical Quarterly, *XX*, pp 69-78.
21. Nikolos I.K., Douvikas D.I., Papailiou K.D., 1993b, "A Method for the Calculation of the Tip Clearance Flow Effects in Axial Flow Compressors, Part II: Calculation Procedure", ASME paper 93-GT-151.
22. Douvikas D., Kaldellis J., Papailiou K.D., 1989, "A Secondary Flow Calculation Method for One Stage Centrifugal Compressor", 9th ISABE, Athens.
23. Inoue M., Kuroumaru M., Fukuhara M., 1985, "Behaviour of Tip Leakage Flow Behind an Axial Compressor Rotor", ASME paper 85-GT-62.

REFERENCE NO. OF THE PAPER: 11

DISCUSSOR'S NAME: C.H. Sieverding

AUTHOR'S NAME: I.K. Nikolos, D.I. Douvikas, K.D. Papailiou

Q.: The comparison of the induced losses in Fig. 7 and 10 with the experiments of Storer and Inoue, respectively, shows overall a fairly good prediction capability of your method, but Storer's data show between 75 and 80% span an important positive induced loss peak, which does not show up with calculations. Do the authors have an explanation for these differences?

A.: The experimental data for the total pressure losses due to the tip clearance presence were obtained in the Storer's cascade by subtracting the losses for the zero clearance case. The positive induced loss peak is connected with a similar peak in the meridional induced velocity profiles (Fig. 6). Storer's experiment is the only case from those we have examined, that has such a strong positive pressure loss peak and we cannot give an explanation for this phenomenon.

REFERENCE NO. OF THE PAPER: 11

DISCUSSOR'S NAME: P.M. Came

AUTHOR'S NAME: I.K. Nikolos, D.I. Douvikas, K.D. Papailiou

Q.: You have achieved good agreement between your predictions and two sets of compressor blading experimental data. Have you any experience of comparing predictions with unshrouded turbine blade data and, if so, how good was the agreement'?

A.: We have applied the method only in turbine cascade cases. Concerning the gap flow model, it can predict with good accuracy the mass flow rate through the gap [1,2]. The application of the vortex model gave also good results in the turbine cascade case we have considered [3]. The scarcity of available experimental data in the open literature, concerning total pressure losses, did not give us the opportunity of testing the methods ability in predicting the loss distribution in turbine cases.
However, in both turbines and compressors, tip clearance phenomena exhibit strong similarities, the only difference being the relative wall motion effect, which in the compressor case is enhancing the leakage flow, while the opposite is the case for turbines. Consequently, we expect, from the indications we have from applying our model to turbine test cases, that reasonable predictions will be possible using the proposed model.

An additional model has been developed by the authors, which deals with this wall motion effect on leakage flow for both compressor and turhine cases and has been applied with success to both cases [3].

REFERENCE NO. OF THE PAPER: 11

DISCUSSOR'S NAME: F. Kameier, BMW-RR

AUTHOR'S NAME: I.K. Nikolos, D.I. Douvikas, K.D. Papailiou

Q.: With a large tip clearance gap reversed flow conditions are possible in the gap. Could you calculate this flow with your model'?

A.: No case with reversed flow conditions has been considered up to now, as the interest is for rather small clearances. However we think that the proposed calculation procedure has the potential to deal with such cases with minor modifications.

REFERENCE NO. OF THE PAPER: 11

DISCUSSOR'S NAME: H. Weyer, DLR

AUTHOR'S NAME: I.K. Nikolos, D.I. Douvikas, K.D. Papailiou

Q.: Blade loading is the drive factor for clearance flow. How do you calculate the associated pressure difference at off-design operation?

A.: Calculations have been performed, up to now, using the quasi-3D computation procedure. Blade to blade calculation at different radial positions may give the profile losses and deviation at the corresponding conditions. The calculated deviation and loss profiles are imposed at the blade trailing edge in the meridional flow calculation. The meridional flow code, using a proper distribution of the imposed losses and deviation along the blade chord provides the resulting pressure difference, used in the tip clearance calculation.

REFERENCE NO. OF THE PAPER: 11

DISCUSSOR'S NAME: F. Leboeuf

AUTHOR'S NAME: I.K. Nikolos, D.I. Douvikas, K.D. Papailiou

Q.: Can you comment about the origin of the tip leakage vortex and how it is linked to the bound vorticity which is included inside of the blade and associated to the blade load?

A.: In the present work we tried to disconnect the calculation of the vortex strength from the blade bound circulation. Considering the overall effect of the shed

vorticity on the leakage vortex formation and taking into account the available experimental evidence (solid body rotation, near conical vortex shape) a simple model was constructed, using the integral form of the equations of motion.

Generally, the rate of generation of vorticity is equal to the relative tangential acceleration of fluid in respect to the boundary and the generation mechanism, therefore, involves either the tangential to the flow direction pressure gradient within the fluid or the external acceleration of the solid boundary [4]. The vorticity decay results from cross-diffusion of two fluxes of opposite sense and takes place in the fluid interior.

Especially in the tip clearance gap we have the case of pressure gradient across the gap, which accelerates the fluid normal to the blade camber and, therefore, is responsible for the vorticity production inside the gap. This pressure difference is obviously dependent on blade loading. Vorticity of opposite sense is produced inside the gap at the casing region but of smaller magnitude due to the different acceleration of the flow. The cross-diffusion of the two fluxes of opposite sense may take place inside the leakage vortex, as the leakage jet wraps around the already existing leakage flow increasing its radius. The net amount of the vortex circulation is assumed to result from this cross-diffusion of vorticity of opposite sense. In the case of a very large clearance, where no interaction is observed with the endwall region the leakage vortex circulation reaches asymptotically the blade bound circulation.

References

1. Nikolos I.K., Douvikas D.I., Papailiou K.D., 1993, "A Method for the Calculation of the Tip Clearance Flow Effects in Axial Flow Compressors, Part I: Description of Basic Models", ASME paper 93-GT-150.

2. Nikolos I.K., Douvikas D.I., Papailiou K.D., 1993, "A Method for the Calculation of the Tip Clearance Flow Effects in Axial Flow Compressors, Part II: Calculation Procedure", ASME paper 93-GT-151.

3. Nikolos I.K., Douvikas D.I., Papailiou K.D., 1995, "Theoretical Modelling of Relative Wall Motion Effects in Tip Leakage Flow", ASME paper 95-GT-88.

4. Morton B.R.,1984, "The Generation and Decay of Vorticity", Geophys. Astrophys. Fluid Dynamics, 1984, vol. 28, pp. 277-308.

TIP LEAKAGE LOSS DEVELOPMENT IN A LINEAR TURBINE CASCADE

by

David W. Peters
Turbine Specialties, Inc.
Salina, KS 67401
U.S.A.

John Moore
Mechanical Engineering Department
Virginia Polytechnic Institute and State University
Blacksburg, VA 24061-0238
U.S.A.

ABSTRACT

Tip leakage losses were studied in a large-scale linear turbine cascade with a tip clearance gap equal to 2.1% of blade height. The cascade was located at the exit of a low speed wind tunnel; the blade exit Reynolds number based upon blade axial chord was 4.5×10^5. The flow was measured at a plane 0.96 axial chords downstream from the blade leading edge. Earlier studies performed at the tip gap exit and at a downstream plane 1.4 axial chords from the blade leading edge were utilized with the present study to understand loss development better. The effect of tip leakage and the corresponding loss production mechanisms involved as the flow mixes out were analyzed.

The flow properties at the measurement plane were numerically integrated. To estimate the maximum potential loss of the cascade, the flow was mixed-out through a momentum analysis. The loss at the measurement plane due to tip leakage was found to be equal to the sum of the total pressure loss within the tip gap and the dissipated tip gap secondary kinetic energy. As the flow proceeded downstream, losses were attributed to dissipation of secondary kinetic energy, trailing edge wake mixing, endwall losses, and primary flow mixing.

NOMENCLATURE

C_{ps}	static pressure coefficient, Eq. 2
C_{pt}	total pressure loss coefficient, Eq. 1
P	static pressure
P_{s0}	cascade inlet static pressure
P_t	total pressure
P_{t0}	cascade inlet total pressure
u	velocity component in primary direction
U_0	cascade inlet free stream velocity
v	velocity component orthogonal to u and w
V	velocity at measurement plane
V_n	velocity component normal to meas. plane
w	velocity component in the spanwise direction
X,Y,Z	cascade coordinates, Fig. 1
X/c	axial distance from blade leading edge/axial chord
ΔY	blade pitch
ΔZ	blade span
β	flow angle with respect to pitchwise direction
δ_{99}	boundary layer thickness
δ^*	displacement thickness of boundary layer
ρ	fluid density

Subscripts

0	upstream of cascade, reference
d	mixed-out plane
n	normal
sp	sphere static pressure probe
t	total conditions
x	axial direction
y	pitchwise direction

Superscripts

—	area average
=	mass average

INTRODUCTION

Tip leakage flow and loss production within and downstream of unshrouded turbine rotor blade rows is a practical problem in turbomachinery performance prediction [Hourmouziadis and Albrecht, [1987]. It also provides an interesting area of fluid mechanics and thermodynamics research.

Flow through and within the clearance gap between the rotor blade and the stationary shroud wall has received much attention; see for example, Bindon [1987], Moore et al. [1989], and Yaras et al. [1989]. It is generally found that the flow separates from the blade tip at the tip gap entrance and a vena contracta is formed. After about two tip gap heights, the flow, which has a strong component normal to the camber line, reattaches and begins a mixing process to fill the gap. Losses are thus produced within the gap; and both Dishart and Moore [1990] and Yaras and Sjolander [1992] found that for a typical tip clearance of two percent of blade height, the losses in the gap represented about 30 percent of the total mixed-out tip leakage loss.

The leakage flow then exits the tip clearance gap on the suction side of the blade with a strong velocity component normal to the suction surface. And further losses are produced as the tip leakage mixes with the primary throughflow. It is this extra loss production, that represents about 70 percent of the total leakage loss (for a two percent tip clearance), which is the subject of the present paper. Two aspects of loss production are of concern, understanding the loss production mechanisms and the rate at which they occur. These considerations are important for the designer who wishes to predict the flow at the entrance to the next blade row and for the turbulent flow modeller who wishes to accurately predict the flow development [Moore et al., 1991].

Paper presented at the AGARD PEP 85th Symposium on "Loss Mechanisms and Unsteady Flows in Turbomachines", held in Derby, United Kingdom, 8-12 May 1995, and published in CP-571.

Models of Overall Tip Leakage Losses

There are several approaches to modelling the extra losses due to tip leakage:

a) models based on momentum and an induced drag force on the blade;
b) models which consider the flux of kinetic energy associated with the flow normal to the blade to be eventually dissipated without recovery;
c) a sudden-mixing analysis which assumes the leakage jet mixes as it leaves the clearance gap on the suction side of the blade.

Yaras and Sjolander [1992] have reviewed the drag force models, including the relatively successful model of Ainley and Mathieson [1951]. They also reviewed energy methods and developed an improved version of a method used by Rains [1954] and adapted by Vavra [1960]. Denton [1993] made simple estimates of tip leakage losses using a mixing analysis due to Shapiro [1953].

These overall-loss models are used to predict the fully mixed-out value of the losses and they give little insight into the rate of loss production. Thus they cannot predict the losses at the trailing edge plane of a rotor blade or at the entrance to a close-coupled downstream stator. Also, only Yaras and Sjolander [1992] directly account for the loss production in the tip clearance gap.

Loss Development

Since losses in the mixing process between the leakage jet and the primary flow are mainly produced by the energy cascade from mean kinetic energy to turbulence kinetic energy, and thence to internal energy and entropy, it appears that energy methods are most appropriate for studying the production of tip leakage losses and the development of the turbine rotor exit flow distribution. Dishart and Moore [1990] used this approach to relate the measured losses at an axial plane 0.4 axial chords downstream of the trailing edges of a linear turbine cascade to the flow at the exit of the tip clearance gap. They found that the additional loss due to tip leakage was equal to the sum of the internal tip gap losses and the tip leakage secondary kinetic energy which had been dissipated. The results of Yaras and Sjolander [1989] show similar behavior at their downstream planes, one axial chord downstream. But at their trailing edge plane Yaras and Sjolander found a surprising result. The sum of the measured total pressure losses and secondary kinetic energy had dramatically decreased. And it appeared that much of the gap kinetic energy had been recovered by the time the flow reached the trailing edge; subsequently this recovery was apparently negated, possibly due to a combination of vortex mixing with the surrounding free stream fluid and higher shear stresses and loss production at the endwall. This possible scenario has not to the present authors' knowledge received confirmation in the literature. And there is a need for more data showing the development of tip leakage losses and endwall loss distributions. This paper contributes a data set near the trailing edge plane of the cascade used by Dishart and Moore, and it offers a different picture to that suggested by Yaras and Sjolander.

APPARATUS

A linear turbine cascade with a tip gap was used to simulate and study tip leakage flow in an actual turbomachine. The blades of the cascade have a turning angle of 109.3°. The aspect ratio is 1.0 with an axial chord length of 235.2 mm. The tip gap is nominally 5 mm, 2.1% of blade span.

The cascade was located within a low speed wind tunnel. The cascade consists of five blades with six corresponding flow passages. Adjustable end bleeds along the outer passages are positioned to insure uniform flow conditions through each passage conforming to an infinite cascade case. The inlet boundary layer upstream of the cascade is bled off in order to reduce secondary flow effects due to horseshoe and passage vortices. Trip wires located on the inlet endwall and near the blade leading edges insure that the inlet boundary layers on all surfaces were turbulent.

This study was performed in the passage between blades 2 and 3. The passage dimensions and the coordinate system are shown in the top view in Figure 1. Measurements were made at an axial plane 0.96 blade axial chords downstream of the blade leading edge, X/c = 0.96.

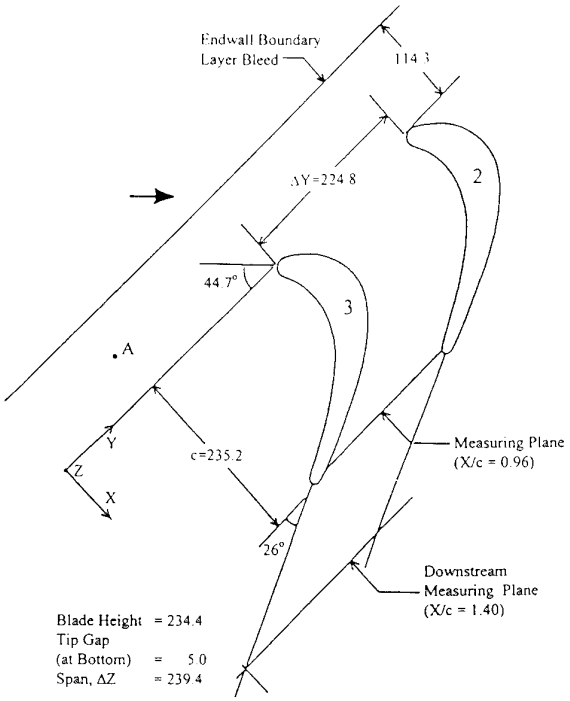

Fig. 1. Cascade Passage, Top View: All dimensions in mm

Pressure Measuring Equipment

Pressure taps and several pressure probes were used in order to obtain velocity vectors and static and total pressure coefficients throughout the whole plane. Pressures from the probes were monitored by a computerized data acquisition system described in the next section.

A total pressure probe, which was inserted at location A of Figure 1, served to define the inlet total pressure. An endwall pressure tap located in front of blade 3 served to define the inlet static pressure. Four additional pressure probes were traversed in the measurement plane: a five hole probe, two three-hole probes, and a spherical pressure probe.

A United Sensor five hole probe, which had a tip diameter of 3.18 mm, was traversed in the pitchwise and spanwise directions by a traversing gear mounted on top of the flow tunnel. The probe holder permitted rotation in yaw in order to null the probe. Both the traversing and yaw angle movement were controlled by the data acquisition system. The probe was calibrated in order to determine the static pressure, the total pressure, and the velocity components from the five probe pressures and the inlet reference pressures. The probe was inserted into the passage through a slot in the top endwall. The five hole probe was used throughout the inner region of the measurement plane.

A long three hole probe with tip dimensions of .89mm thickness and 1.93mm width was used to obtain total pressure and the flow angle in the probe yaw direction near the blade and bottom endwall surfaces. The probe was also calibrated in order to determine static pressure. The probe proved capable of determining static pressure at wall surfaces and thus was used along the top endwall and blade suction surface for that purpose.

A shorter three hole probe with tip dimensions of .8mm thickness and 3.7mm width was used to determine the total pressure and the flow angle in the probe yaw direction along the top endwall.

A Flow Corporation spherical pressure probe was utilized in order to determine the nature of the static pressure variation along the blade suction surface as well as to verify the static pressure measured by the five hole probe in the tip leakage vortex. The tip of the probe has a head diameter of 3.3 mm.

Positioning of the long and short three hole probes and the spherical pressure probe was performed by a simple traversing gear. A dial gage readable to 0.025 mm (0.001 in.) was used for position measurement in the traverse direction. The probe holder permitted rotation in yaw; the yaw angle could be read to within 0.2 degrees. The three hole probes were manually nulled in yaw for each test location. The spherical pressure probe was aligned with the flow orientation determined from the other probes.

Pressure taps with 1.0 mm holes are located along the bottom endwall of the measurement plane. In addition, pressure tappings are located along the blade surfaces.

A Tel Tru micromanometer with a pressure range of 0-5 in . of H_2O was used to calibrate the pressure measuring system, to obtain static pressure tap readings, and to measure the inlet velocity head during the five hole probe measurements.

Data Acquisition System

The data acquisition system had two main functions: pressure data acquisition and probe movement control. The pressure data from the pressure probes were acquired digitally through a 12-bit data acquisition board. Pressure signals were generated by Statham strain-gage type pressure transducers, model PM5TC. The transducers have a rated differential pressure range of ± 0.3 psi (2.07 kPa). The pressure signal was amplified by a circuit designed to use the full voltage range of the data acquisition board. Each amplifying circuit was zeroed before each test to correct for the inherent offset signal associated with the transducers. Multiple data points were taken and averaged at each measurement location.

The five hole probe movement was controlled by the data acquisition system. Stepper motors mounted on the traversing gear and on the probe holder controlled the spanwise and pitchwise motion and the probe yaw angle, respectively. The stepper motors located on the traversing system had a movement sensitivity in the pitchwise and spanwise directions of 0.0016 mm and 0.0013 mm, respectively. The stepper motor controlling the yaw angle had a movement sensitivity of 0.09 degrees. Once the probe was positioned in a particular location, the probe was either manually or automatically nulled in yaw.

Further details of the measurement apparatus are given by Peters [1992].

MEASUREMENTS AND PROCEDURE

The five hole probe was used extensively in the measurement plane, covering the inner rectangular flow region. Along the bottom endwall and also along the blade surfaces, the long three hole probe was used. The top endwall measurements were obtained by applying the short three hole probe.

Five Hole Probe Traverses

Five hole probe data was acquired at specified grid locations within the passage. A grid with Y and Z direction measurements of 0.5 in. (12.7 mm) and 0.875 in. (22.2 mm), respectively, covers most of the five hole probe measurement region. In the vortex regions a finer square grid of 0.25 in. (6.4 mm) was used to define the flow characteristics better.

The five hole probe, was traversed to within 0.94 in. (23.8 mm) of the top endwall. Along the blade suction surface, the probe was traversed to a location 21.6 mm from the blade surface to the probe center in the Y axis direction. At this position, the probe side was 2.1 probe diameters, 7.9 mm, from the blade in a direction normal to the blade surface. Along the blade pressure surface, the five hole probe was traversed to within 10.2 mm of the blade surface in the Y axis direction, which corresponds to 2.2 probe diameters from the probe side to the blade surface. Along the bottom endwall, the five hole probe was traversed normal to the surface to within a distance from the probe side to wall of 0.7 diameters.

Three Hole Probe Traverses

At the top endwall surface, the short three hole probe was traversed and nulled in yaw. Because of the presence of the slot in the top endwall, the probe traverses were performed slightly upstream at X/c = 0.91 and projected downstream to X/c = 0.96. At the bottom endwall, the long three hole probe was inserted in the top endwall slot and traversed using the simple traversing gear. Along the blade surfaces, the long three hole probe was used by projecting the probe from a downstream location and traversing in the Y axis direction. Along the suction side of the blade, the probe was positioned normal to the blade. Similarly, along the blade pressure surface, the long three hole probe was positioned at an angle typical of the velocity vector angles along the nearby five hole probe data boundary (40°).

The long three hole probe results from traverses along the blade suction surface showed that static pressure values compared well with blade surface pressure taps. Thus, this probe was used along the top pressure surface to determine static pressure there by inserting the probe in the top slot and nulling in yaw.

Spherical Pressure Probe Traverses

The spherical pressure probe was traversed at the same locations and probe yaw angle positions of the three hole probe traverses. Using the three hole probe total pressure results, static pressure was determined by the spherical pressure probe.

Tip Leakage Vortex Core Measurements

The low static pressure conditions at the tip leakage vortex core were seen as a test case of the capabilities of the five hole probe. Thus, both the three hole probe and the spherical pressure probe were positioned in the core in order to verify the five hole probe static pressure results. The spherical pressure probe and the long three hole probe were positioned at the low static pressure core position defined by the five hole probe.

RESULTS, ANALYSIS, AND DISCUSSION

Inlet Flow Conditions

The inlet flow conditions of the cascade have been determined by previous studies. Dishart and Moore found an average inlet freestream velocity of 20.5 m/s at the standard conditions of 94.9 kPa and 299 K. They found the blade exit Reynolds number based upon blade axial chord to be 4.5×10^5. Moore and Tilton [1988] measured the inlet endwall boundary layer thickness 0.30 axial chords upstream of the blade leading edge. They found the boundary layer thickness, δ_{99}, equal to 2.18 mm ($\pm$ 0.13) and a corresponding displacement thickness, δ^*, of 0.29 mm ($\pm$ 0.02).

Measurement Plane

Three main properties were the basis for the present study at X/c = 0.96: the velocity, the total pressure loss, and the static pressure. In order to generate contour plots of total pressure loss and static pressure and to calculate area and mass average properties, it was necessary to define the flow properties for all Y and Z measurement locations to create a rectangular grid. A grid was generated and linear interpolation was applied to determine the property values at non-data point positions as described in the following sections.

The three hole probes, which were used near the passage boundaries, do not provide all of the property information necessary for the analysis. This is due to the inability of the probe to determine the probe pitchwise component of velocity and to adequately determine static pressure. Therefore, interpolation schemes were again applied to generate values in these regions. The corner regions required more detailed analysis as discussed in Peters [1992].

Total Pressure Loss

The total pressure loss coefficient is defined by:

$$C_{pt} = \frac{P_{t0} - P_t}{\frac{1}{2}\rho U_0^2} \qquad (1)$$

Contours of C_{pt} at the measurement plane are shown in Figure 2. The maximum C_{pt} value in the measurement plane, 3.0, occurred within the tip leakage vortex core. The top passage vortex and the bottom passage vortex had C_{pt} core measurements of 1.4 and 1.9, respectively. Another region of high loss fluid is in the wake region along the blade pressure surface. Within this wake region, C_{pt} is nearly uniform at 3.2 and reaches a maximum value of 3.3. As shown in Figure 1, the measurement plane intersects the trailing edge at the blade pressure surface. As would be expected, boundary layer separation was evident at this trailing edge location. However, the three hole probe was able to distinguish this stagnant flow condition. Although the fluid has a higher loss than the tip leakage core, the influence of this high loss fluid on the mass averaged properties presented later is minimal because of the stagnant flow condition.

The contours of C_{pt} found by Dishart and Moore at X/c = 1.4 are shown in Figure 3; the contour intervals are the same as those used at X/c = 0.96. Table 1 shows a comparison of the maximum core measurements between this study at X/c = 0.96 and the previous study at X/c = 1.4. Although there is evidence of flow mixing within the passage vortices between the two planes, the level of total pressure loss remains relatively high in the tip leakage vortex. The bottom passage vortex appears to be dissipating at a much more rapid rate than the others. This may be due to the enhanced mixing and entrainment of low loss fluid between the bottom passage and tip leakage vortices.

Table 1. Total Pressure Loss Coefficient Maxima, C_{pt}

Vortex	X/c = 0.96	X/c = 1.4
Top Passage	1.4	1.1
Bottom Passage	1.9	1.3
Tip Leakage	3.0	2.8

Static Pressure

The static pressure coefficient is defined by:

$$C_{ps} = \frac{P - P_{s0}}{\frac{1}{2}\rho U_0^2} \qquad (2)$$

C_{ps} contours at the measurement plane are shown in Figure 4. In the regions of low total pressure loss, nearly two-dimensional C_{ps} gradients in the blade to blade direction are seen. Regions of low C_{ps} are located in the top passage vortex at -2.5 and in the tip leakage vortex at -3.3. No region of low C_{ps} is apparent for the bottom passage vortex. The variation of C_{ps} through the tip leakage vortex in the pitchwise direction is nearly identical to the variation along the bottom endwall.

The contours of C_{ps} found by Dishart and Moore at X/c = 1.4 are shown in Figure 5; the contour intervals are the same as those used at X/c = 0.96. At X/c = 1.4, C_{ps} was more uniform at -2.0 with a tip leakage core value of -2.3. Unlike at X/c = 0.96, the pitchwise variation of C_{ps} through the tip leakage vortex core is not similar to C_{ps} along the bottom endwall at X/c = 1.4. This is probably due to the cessation of tip leakage flow beyond the blade passage.

Use Of 3 Hole Probe To Find Wall Pressure

The three hole probe traverses near the blade suction surface included a position at which the probe was touching the wall. The C_{ps} values determined at this wall position compared well with those determined by five blade static pressure taps and one bottom endwall tap. Thus, it became apparent that the long three hole probe was a viable device to determine C_{ps} at flow surfaces. The C_{ps} values determined by the long three hole probe at the blade suction surface were used in conjunction with static pressure tap values to define a surface relationship.

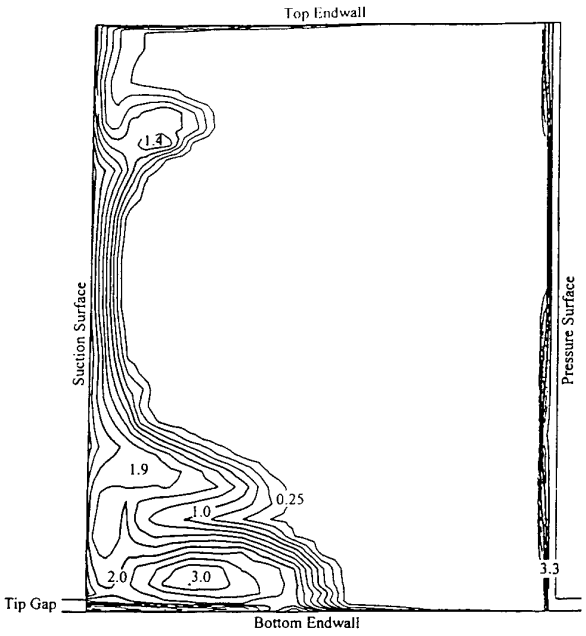

Fig. 2. Contours of Total Pressure Loss Coefficient: Measurement Plane at X/c = 0.96

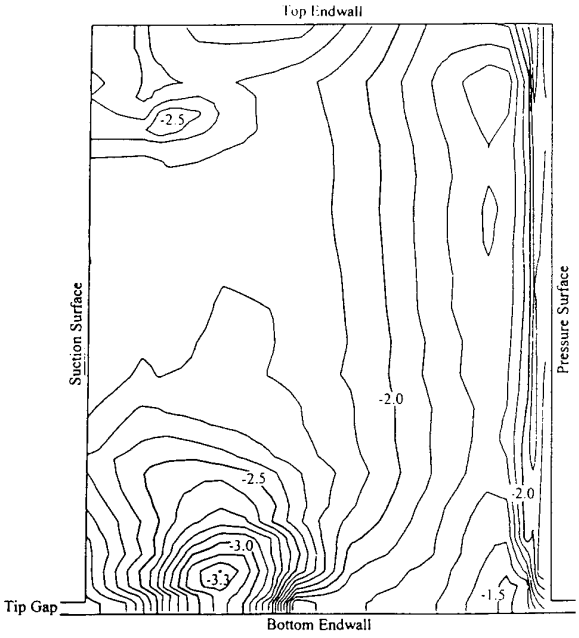

Fig. 4. Contours of Static Pressure Coefficient: Measurement Plane at X/c = 0.96

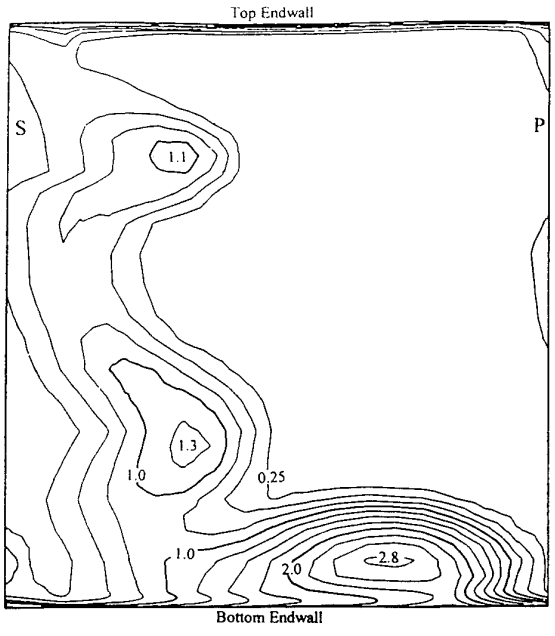

Fig. 3. Contours of Total Pressure Loss Coefficient Measured by Dishart and Moore at X/c = 1.4: __ projections downstream of blades in direction of mean camber lines at trailing edges; S - downstream of blade 3, P - downstream of blade 2

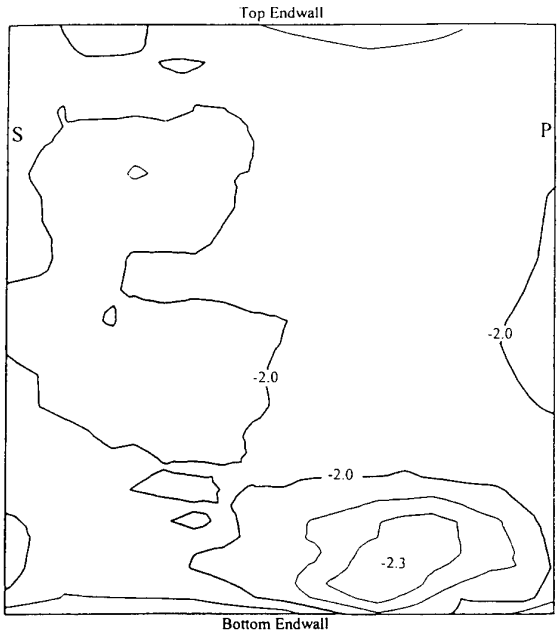

Fig. 5. Contours of Static Pressure Coefficient Measured by Dishart and Moore at X/c = 1.4

The ability of the long three hole probe to determine wall C_{ps} allowed a more detailed study to be performed along the blade suction surface. In particular, the three hole probe was positioned against the blade wall just above the tip gap exit, 0.25 in. (6.4 mm) from the bottom endwall. The result, -1.96, was nearly identical to the endwall pressure tap value of -1.95. This confirmed the validity of a Dishart and Moore's assumption that static pressure was constant across the gap exit. That assumption was applied in order to analyze their tip gap exit measurements.

Applying the ability of the long three hole probe to determine wall static pressure, the long three hole probe was also used at the top endwall surface to establish C_{ps} there.

Tip Leakage Vortex Core

To verify the accuracy of the five hole probe in regard to C_{ps}, the long three hole probe and the spherical pressure probe were inserted into the tip leakage vortex core. The C_{ps} results for each probe are listed in Table 2.

Table 2. Probe Comparison in the Tip Leakage Core

Probe	C_{ps}
Five Hole	-3.31
Long Three Hole	-3.37
Spherical Pressure	-3.35

The good agreement between the probes confirms the accuracy of the five hole probe in a vortex region.

Determination Of Static Pressure Near Surfaces

Two methods were attempted to find static pressure near the blade suction surface. Both the spherical pressure probe and the three hole probe were traversed in the region between the blade wall and the five hole probe data boundary. As discussed above, the static pressure from the three hole probe when touching the wall compared well with the wall static pressure taps. But, the resulting static pressure from the three hole probe when traversed to the five hole probe data boundary did not match the five hole probe results. The spherical pressure probe static pressure neither matched the wall nor the five hole probe data. However, both probes did confirm the expected trend in a static pressure rise from the vortices towards the blade suction surface. An explanation for the static pressure discrepancy is that both the three hole probe and the spherical pressure probe had high pitch angle sensitivity, becoming inaccurate in regions of strong secondary flow. The good agreement between the spherical pressure probe and the five hole probe in the tip leakage core was most likely due to the uniform flow conditions there.

Fortunately, the C_{ps} results from the long three hole and spherical pressure probe near the blade suction surface were not needed. C_{ps} was well defined by the wall static pressure taps and the long three hole probe surface measurements. Thus, static pressure could be determined by horizontal linear interpolation between the surface and the five hole probe data region.

Similarly, C_{ps} was measured at the top endwall using the long three hole probe. C_{ps} was then determined in the top endwall region by vertical linear interpolation between the top endwall surface and the five hole probe data boundary.

Near the bottom endwall, the five hole probe data boundary C_{ps} results at 0.175 in. (4.4 mm) from the endwall compared well with the C_{ps} at the static pressure taps in the endwall. Therefore, C_{ps} was determined by projecting the five hole probe results downward towards the wall.

Along the blade pressure surface, C_{ps} was determined by the results from the long three hole probe horizontal traverses. The C_{pt} and C_{ps} values determined by the three hole probe compared well with the results found by the five hole probe at the common boundary. This agreement offered validity to the usage of the three hole probe to determine C_{ps} at the blade pressure surface despite the discrepancies between the pressure probes found in other regions. Vertical linear interpolation was used between the horizontal traverses to establish C_{ps} for non-data point grid values.

Secondary Flow

The primary flow direction is defined as the direction parallel to the trailing edge mean camber line, $\beta_2 = 26^\circ$. The secondary flow directions are normal to the primary flow direction. Figure 6 shows the primary and secondary flow components. The u component of the velocity is the primary flow component and the v and w components are the secondary flow velocity components.

The secondary velocity components determined for the X/c = 0.96 plane are shown in Figure 7. The vectors are the projection of the secondary velocities on a cross sectional plane as shown in Figure 6. As expected, a tip leakage vortex and a top passage vortex are well defined. In addition, a bottom passage vortex is also defined, a flow feature which was not as apparent for Moore and Dishart's study at the downstream location of X/c = 1.4. The approximate centers of the vortices are listed in Table 3 as ratios of the passage flow region measurements with the origin at the bottom endwall-blade suction surface boundary.

Table 3. Vortex Centers

Vortex	$\frac{Y}{\Delta Y}$	$\frac{Z}{\Delta Z}$
Top Passage	0.15	0.86
Bottom Passage	0.28	0.23
Tip Leakage	0.28	0.07

The secondary velocity vectors in the tip leakage vortex region are expanded for clarity in Figure 8. The maximum secondary velocity was found near the bottom endwall in the tip leakage vortex region. The maximum secondary velocity magnitude was 34.6 m/s, which was 1.7 times the cascade inlet velocity, U_0. In comparison, the maximum secondary velocity found at X/c = 1.4 was 11.2 m/s, 0.55 U_0.

The secondary velocity components found at X/c = 1.4 by Dishart and Moore are shown in Figure 9; the velocity scale is the same as used in Figure 7. Between the two measurement planes, the strength of the secondary flow is clearly decreasing. The tip leakage vortex is also convecting away from the trailing edge camber line of blade 3 towards the trailing edge camber line of blade 2.

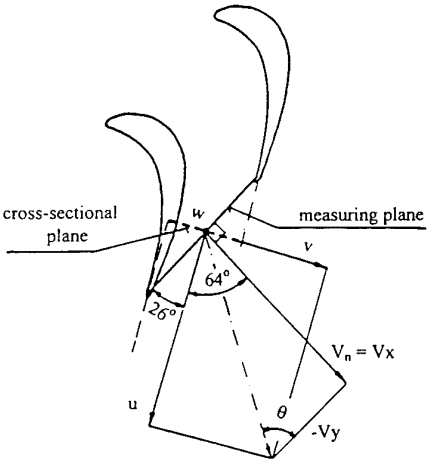

Fig. 6. Flow Coordinate System at Measuring Plane
Secondary velocity vectors are projected on the cross-sectional plane and viewed looking upstream along the trailing edge camber line.

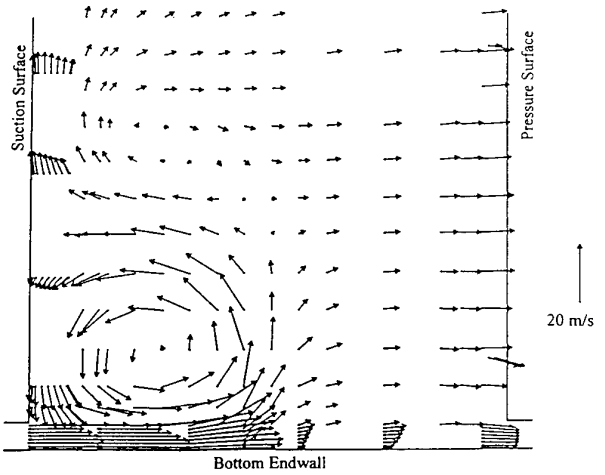

Fig. 8. Secondary Velocity Vectors in Tip Gap Region

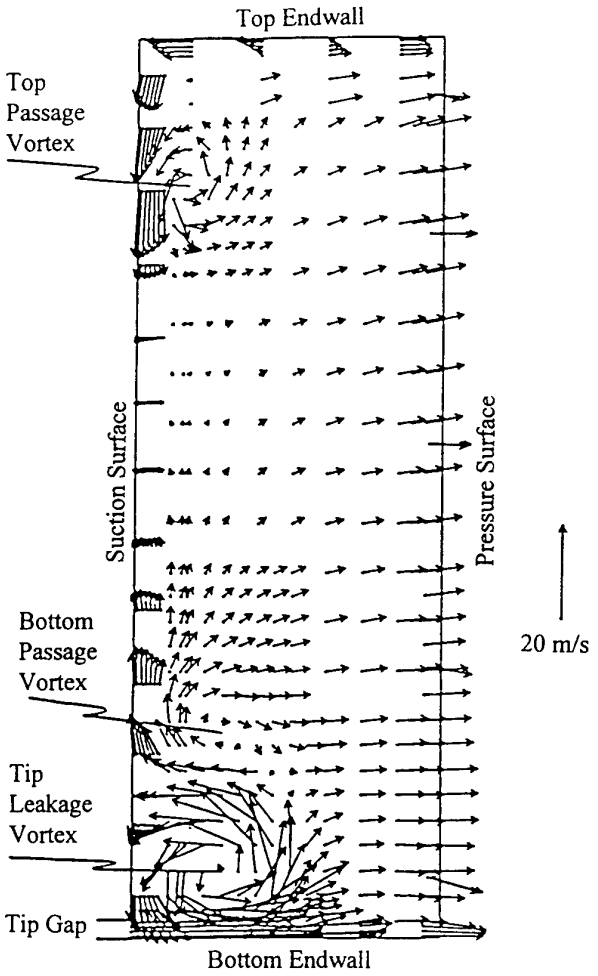

Fig. 7. Secondary Velocity Vectors in the Cross-sectional Plane at X/c = 0.96

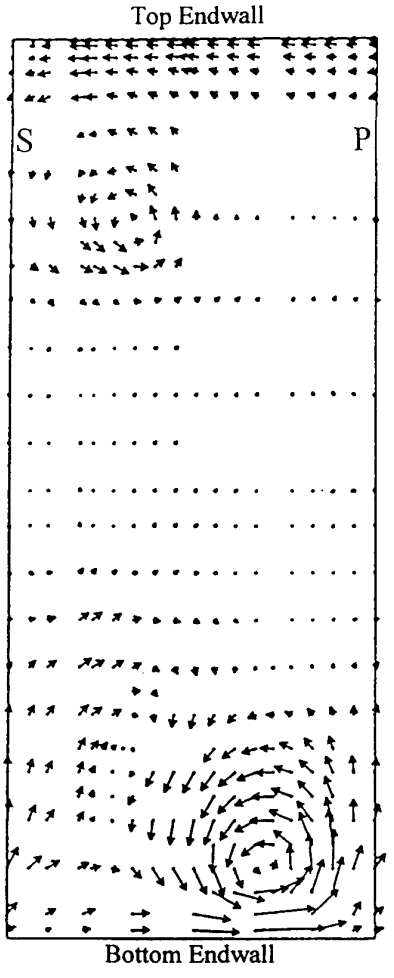

Fig. 9. Secondary Velocity Vectors Measured by Dishart and Moore at X/c = 1.4

Determination Of Velocity Near Surfaces
A three hole probe is unable to distinguish the probe pitchwise component of velocity. Thus, along the top and bottom endwall surfaces, the w component of velocity is interpolated vertically from the five hole probe region to a value of zero at the wall. Similarly, along the blade suction surface, the v component of velocity is linearly interpolated horizontally from the five hole probe region to a value of zero at the wall.

Near the blade pressure surface, the boundary layer separates requiring special consideration for the probe pitchwise component of velocity. The separated flow precludes the use of horizontal linear interpolation to a zero velocity at the wall as was used on the blade suction surface. In order to determine the three hole probe pitchwise component of velocity, the nearby five hole probe yaw angle results were projected horizontally. Note that since the probes were traversed normal to each other, the five hole probe yaw angle is in the same plane as the three hole probe pitch angle.

The tip gap exit velocity profile was determined by applying Dishart's nearby suction side, tip gap exit measurements. Measurements performed by Dishart at axial downstream distances of X/c = 0.938 and X/c = 0.996 were linearly interpolated to determine C_{pt} and the yaw angle at the measurement plane, X/c = 0.96. Note that C_{ps} was determined from the blade suction surface relationship defined by the long three hole probe and static pressure taps. Therefore, velocity could then be determined by setting the inlet velocity.

Averaged Flow Properties
The flow properties found at X/c = 0.96 were averaged on a mass and area basis. Finite difference type numerical integration was applied in order to evaluate the relationships. The area-averaged normal velocity and static pressure takes the form

$$\overline{V}_n = \frac{\int_0^{\Delta Y}\int_0^{\Delta Z} V_n dz dy}{\Delta Y\, \Delta Z} \qquad (3)$$

The mass averaging for the velocity components, total pressure, and kinetic energies takes the form

$$\bar{\bar{X}} = \frac{\int_0^{\Delta Y}\int_0^{\Delta Z} \rho V_n X dz dy}{\int_0^{\Delta Y}\int_0^{\Delta Z} \rho V_n dz dy} \qquad (4)$$

The averaged flow angles were defined by

$$\overline{\beta} = \tan^{-1}\left[\frac{\overline{V}_x}{-\bar{\bar{V}}_y}\right] \qquad (5)$$

$$\bar{\bar{\beta}} = \tan^{-1}\left[\frac{\bar{\bar{V}}_x}{-\bar{\bar{V}}_y}\right] \qquad (6)$$

Conservation Of Mass Flow
In order to validate the data measurements, the mass flow exiting the measurement plane was compared with the blade inlet flow and found to be within 0.6 percent. In comparison, Dishart found that for his measurements at X/c = 1.4 the mass flow was within 6 percent of the blade inlet mass flow, a yaw angle correction of 1.85 degrees was applied to the X/c = 1.4 data in order to obtain continuity. In this present study, a similar yaw correction of 0.2 degrees would be needed to achieve continuity. Since this is certainly within experimental error, a correction was not made to the measurement plane data.

Indirectly, a continuity correction had been made to the present data by an adjustment made to the velocity data to be consistent with Dishart's data for comparative purposes. Dishart found an average inlet velocity component, U_0 of 20.5 m/s. The local velocity magnitude was normalized by applying this specified inlet velocity along with the local pressure coefficients to calculate velocity components. The smallest and largest correction factor applied was 1.005 and 1.047, respectively. The majority of the discrepancy can be attributed to the variation in inlet velocity. The additional error was attributed to measurement error and different methods of calculating velocity magnitude used in the analysis programs. Considering that different data acquisition systems were utilized, the error can be considered reasonable.

An attempt was made to correct Dishart's mass flow rate at X/c = 1.4 by making the inlet velocity magnitude uniform as described above. The results, however, showed little improvement and the correction was not applied.

Tip Gap Flow
The measurements taken between the endwalls and blade surfaces provided an incomplete analysis of the flow at X/c = 0.96 in that the flow in the tip gap was not included. No means existed to establish the flow conditions under the blade. Dishart and Moore had measured the properties of the tip leakage flow at the gap exit. From the tip gap exit measurements, it was estimated that less than 1 percent of the flow was unaccounted for. This could be considered insignificant, but the tip gap flow properties were calculated by the following method.

Assuming minimal dissipation of properties occurs in the tip gap near the trailing edge, the tip gap exit properties around the trailing edge were used to define the properties at the measurement plane. Dishart had made vertical traverses near the blade boundary at a pressure surface location of X/c = 0.96 and at suction surface locations X/c = 0.938 and X/c = 0.996. The blade suction side traverses were linearly interpolated in the axial direction in order to determine the conditions at the measurement plane location, X/c = 0.96. Thus, a grid was formed between the vertical traverses at the pressure side X/c = 0.96 location, the suction side X/c = 0.996 location, and the interpolated suction side X/c = 0.96 location. Numerical integration was performed on this grid to determine the contribution of the tip gap flow to the area and mass property averages.

Measurement Plane Averages
The results of the area and mass averages are listed in Table 4. These results were obtained by numerical integration over the entire measurement plane including the tip gap flow as

described previously. The velocity magnitudes are based upon the blade inlet area. The measurement plane area is less than the blade inlet area due to the blade thickness. By basing the velocity magnitudes upon the blade inlet area, comparisons can be made with results found at the downstream plane of X/c = 1.4 by Dishart and Moore, which are also presented in Table 4.

Table 4. Flow Property Averages

Property	X/c = 0.96	X/c = 1.4
$\overline{V}_n$	14.4	14.4
$\bar{V}_x$	15.6	14.6
$\bar{V}_y$	-28.2	-29.3
$\overline{\beta}$	27.2°	26.2°
$\bar{\beta}$	28.9°	26.6°
$\bar{C}_{pt}$	0.249	0.378
$\frac{\bar{u}^2}{U_0^2}$	2.717	2.594
$\frac{\bar{v}^2}{U_0^2}$	0.088	0.010
$\frac{\bar{w}^2}{U_0^2}$	0.013	0.006
$\frac{\bar{v}^2 + \bar{w}^2}{U_0^2}$	0.101	0.016
$\bar{C}_{pt} + \frac{\bar{v}^2 + \bar{w}^2}{U_0^2}$	0.350	0.394
$\bar{C}_{ps}$	-2.11	-1.99
$\overline{C}_{ps}$	-2.06	-1.99

The area averaged normal velocity is 14.4 m/s as required for mass conservation. Clearly, the flow is mixing as it progresses downstream as seen by the dissipation of secondary kinetic energy. Most of the dissipation occurs to the secondary kinetic energy term associated with the velocity component v, which is defined in Figure 6.

Top and Bottom Halves

Insight into the effects of tip leakage flow can be gained by dividing the flow into top and bottom halves of equal area and performing property averages over the respective regions. This flow division gives a basis for analyzing loss production.

The property averages for the passage halves are presented in two different ways, the reasons for which will become apparent in the discussion of loss. In Table 5, the property averages for the passage halves are based upon the mass flow in the entire plane. Thus, the property averages for the entire measurement plane may be determined by addition of the property averages for two passage halves. In contrast, the property averages in Table 6 are presented on the basis of mass flow in the particular passage half. Thus, the properties for the entire measurement plane may be determined by mass averaging the passage halves' properties. The area averaged normal velocity is included in Table 6 in order to determine the respective mass flow in each half. For both tables, Dishart and Moore's results at X/c = 1.4 are presented as well.

Table 5. Partial Flow Properties Based Upon Total Flow

	X/c = 0.96		X/c = 1.4	
	Top	Bottom	Top	Bottom
$\bar{C}_{pt}$	0.060	0.189	0.101	0.276
$\frac{\bar{v}^2 + \bar{w}^2}{U_0^2}$	0.028	0.074	0.002	0.013

Table 6. Partial Flow Properties Based Upon Half Area Flow

	X/c = 0.96		X/c = 1.4	
	Top	Bottom	Top	Bottom
$\bar{C}_{pt}$	0.117	0.386	0.201	0.558
$\frac{\bar{v}^2 + \bar{w}^2}{U_0^2}$	0.054	0.151	0.005	0.027
$\overline{V}_n$	14.76	14.13	14.51	14.24

Mixing Analysis

To determine the maximum possible loss and the mechanisms involved with loss production, the flow at the measurement plane was mixed-out. By considering a downstream plane at which there are fully mixed-out uniform flow properties with no secondary velocity components, loss generation can be determined downstream of the measurement plane through a momentum analysis.

At the upstream plane the control surface of the momentum analysis control volume coincides with the blade surface near the trailing edge. Neglecting blade shear stresses, the blade forces were determined by static pressure along the blade. The resultant blade force in the Y axis direction was assumed minimal. The blade force in the X axis direction was determined by calculating an average static pressure for the blade surface. The static pressures measured along both the suction and pressure surface of the blade at X/c = 0.96 were averaged in the spanwise direction. These two values were further averaged with a static pressure measurement at a pressure tap located at the trailing edge near midspan.

Through the use of the adjustable end bleeds on the cascade, which when adjusted assures equal mass flow through each cascade passage, an infinite cascade is simulated. Thus, the camber line momentum components would be equal and opposite, subsequently canceling from the momentum analysis. Further simplification is made to the analysis by neglecting shear stress along the top and bottom endwalls to the mixed-out plane.

The resulting momentum equations are listed below. Note that the integrations over the measurement plane included the tip gap area.

Continuity:

$$V_{n,d} = V_{n,u}\left(\frac{A_u}{A_d}\right) \qquad (7)$$

X-momentum:

$$F_x + \int_u PdA + \int_u \rho V_n V_x dA = [\, P_d + \rho \overline{V}^2_{n,d}] \, A_d \quad (8)$$

Y-momentum:

$$\int_u \rho V_n V_y dA = \int_d \rho V_n V_y dA = \rho \overline{V}_{n,d} \overline{V}_{y,d} A_d \quad (9)$$

The mixed-out flow properties for the measurement plane, X/c = 0.96, as well as Dishart and Moore's results at X/c = 1.4 are presented in Table 7. The mixing analysis was also performed for the top and bottom flow areas, separately, using the mass flow in the particular passage half per the discussion on Top and Bottom Halves.

The total pressure loss at the mixed-out plane is defined as

$$\overline{C}_{pt,d} = \frac{P_{t0} - P_{t,d}}{\frac{1}{2}\rho U_0^2} \quad (10)$$

where

$$P_{t,d} = P_d + \frac{1}{2}\rho(\overline{V}^2_{n,d} + \overline{V}^2_{y,d}) \quad (11)$$

Table 7. Downstream Mixed-Out Total Pressure Loss, $\overline{C}_{pt,d}$

X/c = 0.96		X/c = 1.4	
0.452		0.438	
Top Half	Bottom Half	Top Half	Bottom Half
0.222	0.681	0.215	0.655

Loss Production

An understanding of the mechanisms involved with loss production can be gained by considering the top half region as representative of the conditions in the bottom half if no tip gap were present. Thus, if the top half conditions are subtracted from the actual bottom half conditions, then the tip leakage effects will be apparent. This superposition is not strictly valid in that the secondary flow, namely the passage vortices, develop differently. Unlike in the top half, no horseshoe vortex is generated at the blade leading edge - bottom endwall boundary. Also, in the bottom half, the tip leakage vortex and the passage vortex interact. However, the similarity in strength and form of the measured bottom and top passage vortices offers validity to the superposition method. In addition, the passage halves can be considered isolated since at midspan total pressure loss is minimal.

Another important aspect to the study of loss is the concept that all secondary kinetic energy is dissipated, not recovered. Moore and Adhye's [1985] study of losses in a cascade with no tip gap resulted in this finding. For their cascade, the mass averaged total pressure loss was similar to that found at the planes measured for this cascade. However, in the present flow, the gradients of total pressure loss were much more severe and the primary velocity distribution was made more nonuniform by the tip leakage flow. Therefore, primary flow mixing can be expected to contribute significant additional losses as discussed by Dishart and Moore.

Three loss production studies will be presented. The first study will determine the effects of tip leakage flow at the measurement plane. The second study will determine the loss mechanisms involved as the flow proceeds downstream and mixes out. The third and final study will determine the overall loss contributions in the bottom half mixed-out plane.

Extra Loss Due To Tip Leakage

At the X/c = 1.4 plane, Dishart and Moore found that the extra total pressure loss in the bottom half was equal to the sum of the total pressure loss incurred within the tip gap and the dissipation of the tip gap exit secondary kinetic energy. The secondary direction at the tip gap exit was defined as the direction normal to the blade surface.

For the present measurement plane, X/c = 0.96, the extra total pressure loss in the bottom half of the plane can be determined by subtracting the top half loss from the bottom half loss as shown in Table 8. These values are based upon the entire mass flow.

Table 8. Extra Total Pressure Loss in Bottom Half, $\overline{\overline{C}}_{pt}$

Bottom Half	0.189
Top Half	0.060
Difference	0.129

Similarly, the extra secondary kinetic energy in the bottom half can be determined as listed in Table 9. The extra secondary kinetic energy can be considered the residual tip gap secondary kinetic energy.

Table 9. Residual Tip Gap Secondary Energy, $\frac{\overline{\overline{v}}^2 + \overline{\overline{w}}^2}{U_o^2}$

Bottom Half	0.074
Top Half	0.028
Residual	0.046

Dishart and Moore measured the total pressure loss and the kinetic energy of the flow exiting the tip gap. These measurements were mass averaged on a total passage flow basis. The resulting mass averaged coefficient for the component of the kinetic energy normal to the blade surface was termed NKEC by Dishart and was found to be 0.109. The component of the kinetic energy exiting the gap normal to the blade will be referred to as the tip leakage secondary kinetic energy. The resulting mass averaged coefficient for the tip gap total pressure loss was termed TPLC and was found to be 0.071.

The amount of tip leakage secondary kinetic energy, NKEC, which has dissipated by X/c = 0.96 can be estimated by subtracting the residual secondary kinetic energy from the tip leakage secondary kinetic energy as listed in Table 10. Nearly 58 percent of the tip leakage secondary kinetic energy has been dissipated by the X/c = 0.96 measurement plane.

Table 10. Dissipated Tip Leakage Secondary Kinetic Energy

NKEC	0.109
Residual at X/c = 0.96	0.046
Dissipated (by difference)	0.063

Finally, the extra loss in the bottom half due to tip leakage can be estimated by the sum of the tip leakage total pressure loss

and the dissipated secondary kinetic energy as listed in Table 11.

Table 11. Extra Tip Leakage Loss, X/c = 0.96

Tip Gap Total Pressure Loss, TPLC	0.071
Dissipated NKEC	0.063
Extra Loss (by summation)	0.134

The extra loss due to tip leakage, 0.134, is very similar to the extra total pressure loss found in the bottom half, 0.129. Dishart and Moore found at X/c = 1.4 a corresponding extra tip leakage loss of 0.169 and an extra total pressure loss in the bottom half of 0.174. These results confirm the validity of attributing extra loss in the bottom half to tip leakage as originally proposed by Dishart and Moore.

Downstream Loss

The loss development as the flow proceeds downstream from the X/c = 0.96 measurement plane to the mixed-out plane will be discussed. Dishart and Moore's results at X/c = 1.4 will be applied to determine the dominant loss mechanisms between the respective plane regions. This analysis is approximate due to the slightly different mass flow rates between the top and bottom halves at the X/c = 0.96 and X/c = 1.4 axial planes , as seen in Table 6.

$\overline{C}_{pt,d}$ was higher for the X/c = 0.96 plane than for the X/c = 1.4 plane as listed in Table 7. The opposite trend would be expected due to irreversibility from the second law of thermodynamics associated with endwall friction between the two measurement planes. Endwall friction, which wasn't considered in the mixing analysis, would increase the total pressure loss at X/c = 1.4 and subsequently increase the downstream loss for that plane. Perhaps, this suggests the insignificance of endwall friction between the two planes in comparison to other loss production mechanisms.

However, $\overline{C}_{pt,d}$ values determined for the top and bottom halves of the measurement planes were within 2 percent of the average between the planes. Considering that different data acquisition systems were used, the agreement can be considered good. Thus, the average $\overline{C}_{pt,d}$ values for the top and bottom halves, 0.219 and 0.668, respectively, will be used for this study. All values used for this study are based upon the mass flow in the respective region of flow, either the top or bottom.

The results of the loss study in the top half as the flow mixes out are tabulated in Table 12. Between planes X/c = 0.96 and 1.4 the loss mechanisms involve dissipation of secondary kinetic energy, which dominates, as well as an additional extraneous loss contribution. This extraneous loss is probably due to endwall flow losses and to trailing edge wake and primary flow mixing. As the flow proceeds downstream of X/c = 1.4 to the mixed-out plane, the remaining secondary kinetic energy is dissipated. However, primary flow mixing contributes the largest share of loss generation. Endwall losses are not included due to the nature of the momentum analysis.

Dishart and Moore did not find that there was a primary flow mixing contribution between X/c = 1.4 and the mixed-out plane for the top half. Their findings were based upon numerical integration results which did not include the entire flow plane. The region between the endwalls and the nearest endwall data points was not used. This oversight, compounded with the present averaging of $\overline{C}_{pt,d}$, resulted in the different finding. Since the endwall flow region constituted only a small fraction of the flow, the other flow properties were only slightly affected. However, those changes are reflected in the X/c = 1.4 results presented in this paper.

Table 12. Top Half Downstream Loss Model

$\overline{\overline{C}}_{pt}$ at X/c = 0.96	0.117
$\Delta\frac{\overline{\overline{v}}^2 + \overline{\overline{w}}^2}{U_0^2}$, X/c = 0.96 to 1.4	0.049
Extraneous Loss	0.035
$\overline{\overline{C}}_{pt}$ at X/c = 1.4	0.201
$\frac{\overline{\overline{v}}^2 + \overline{\overline{w}}^2}{U_0^2}$ at X/c = 1.4	0.005
Primary Flow Mixing (by difference)	0.013
$\overline{C}_{pt,d}$	0.219

Conclusions similar to those made for the top half can also be made for the bottom half flow as it mixes out. The results of the bottom half study are presented in Table 13. Between plane X/c = 0.96 and 1.4, dissipation of secondary kinetic energy dominates loss production. Again, an additional extraneous loss mechanism, which probably includes similar contributors for both flow halves, was present. Downstream of X/c = 1.4, primary flow mixing dominates loss production in comparison to the remaining secondary kinetic energy dissipation.

Table 13. Bottom Half Downstream Loss Model

$\overline{\overline{C}}_{pt}$ at X/c = 0.96	0.386
$\Delta\frac{\overline{\overline{v}}^2 + \overline{\overline{w}}^2}{U_0^2}$, X/c = 0.96 to 1.4	0.124
Extraneous Loss	0.048
$\overline{\overline{C}}_{pt}$ at X/c = 1.4	0.558
$\frac{\overline{\overline{v}}^2 + \overline{\overline{w}}^2}{U_0^2}$ at X/c = 1.4	0.027
Primary Flow Mixing (by difference)	0.083
$\overline{C}_{pt,d}$	0.668

Mixed-Out Loss

The overall loss contributions to the differences between the top and bottom halves mixed-out loss are tabulated in Table 14. The baseline flow to which the tip leakage effects will be added to obtain the bottom half mixed-out loss is represented by the top half mixed-out loss. The top half mixed-out loss accounted for 33 percent of the final loss in the bottom half.

The tip leakage flow property coefficients NKEC and TPLC measured by Dishart and Moore and converted to the bottom half mass flow basis are applied. The tip gap secondary kinetic

energy, NKEC = 0.223, completely dissipates by the mixed-out plane resulting in 33 percent of the loss. The total pressure loss within the tip gap, TPLC = 0.145, resulted in 22 percent of the loss. Together, these direct tip leakage effects resulted in 55 percent of the final loss. The remaining extra loss in the bottom half, 12 percent, is probably due to primary flow mixing of the tip leakage vortex and extra trailing edge wake mixing and endwall loss.

Table 14. Mixed-out Flow Analysis

Top Half Loss, $\overline{C}_{pt,d}$	0.219	33 %
Dissipated Tip Gap NKEC	0.223	33 %
Tip Gap Total Pressure Loss, TPLC	0.145	22 %
Extraneous Loss (by difference)	0.081	12 %
Bottom Half Loss, $\overline{C}_{pt,d}$	0.668	100 %

CONCLUSIONS

An experimental investigation of the effects of tip leakage flow on loss production was performed in a linear turbine cascade with a tip gap equal to 2.1 percent of blade height. A comprehensive study was made over an entire cross-sectional plane located 0.96 axial chords downstream of the blade leading edge. Earlier studies performed at the tip gap exit and at a plane 1.4 axial chords downstream of the blade leading edge were utilized with the present study to gain a better understanding of loss production.

Measurements were performed with pressure probes. A five hole probe was used to define the flow in most of the plane region. Three hole pressure probes and a spherical pressure probe were also used near the walls and in the tip leakage vortex.

Property Averaging and Mixing Analysis

The results from a flow property averaging using numerical integration and from a mixing analysis using a momentum analysis are summarized below.

The extra total pressure loss in the bottom half of the passage was found to be equal to the sum of the total pressure loss incurred within the tip gap and the dissipated tip gap exit secondary kinetic energy. This further supports the same conclusion made experimentally by Dishart and Moore and numerically by Moore and Moore at X/c = 1.4.

Nearly 58 percent of the tip leakage secondary kinetic energy had dissipated by the measurement plane, X/c = 0.96. Dishart and Moore found that 90 percent had dissipated by X/c = 1.4. The large percentage of loss by the trailing edge plane suggests that minimal improvement could be made by trying to recover secondary kinetic energy downstream of a blade row.

As the flow proceeded from the present measurement plane, X/c = 0.96, to the downstream measurement plane previously studied, X/c = 1.4, the total pressure loss development was dominated by secondary kinetic energy dissipation. The loss development appears to also involve primary kinetic energy dissipation as well as trailing edge wake mixing and endwall effects. As the flow then mixed-out, total pressure loss development involved secondary kinetic energy, but was dominated by primary mixing loss. These loss contributors were present in both halves of the flow even in the top half where tip leakage effects were not present.

Of the total pressure loss in the bottom half of the mixed-out plane, 22 percent was due to losses within the tip gap and 33 percent was due to dissipated tip gap secondary kinetic energy. Together, these direct tip leakage effects accounted for 55 percent of the bottom half loss. The baseline level, which would be present without a tip gap, is represented by the top half mixed-out loss and accounts for 33 percent of the bottom half mixed-out loss. The remaining 12 percent probably consists of primary flow mixing of the tip leakage vortex and extra trailing edge mixing and endwall loss.

The present study showed no evidence of recovery of the tip gap exit secondary kinetic energy as suggested by Yaras and Sjolander [1989] for their trailing edge plane. As a result, enhanced endwall friction did not appear to be a major contributor to the tip leakage losses in the present study.

Acknowledgments

The authors wish to thank Rolls-Royce plc, Aero Division, for supporting this work under a cooperative agreement with Virginia Polytechnic Institute and State University.

References

Ainley, D.G., and Mathieson, G.C.R., 1951, "A Method of Performance Estimation for Axial-Flow Turbines," ARC R&M 2974.

Bindon, J.P., 1987, "Measurement of Tip Clearance Flow Structures on the End-Wall and within the Clearance Gap of an Axial Turbine Cascade," I. Mech. E. 1987-6, pp.43-52, Int. Conf. on "Turbomachinery - Efficiency Prediction and Improvement," Cambridge, England.

Denton, J.D., 1993, "Loss Mechanisms in Turbomachines", ASME Journal of Turbomachinery, Vol. 115, pp. 621-656.

Dishart, P.T., and Moore, J., 1990, "Tip Leakage Losses in a Linear Turbine Cascade," ASME Journal of Turbomachinery, Vol. 112, No. 4, October, pp. 599-608.

Hourmouziadis, J., and Albrecht, G., "An Integrated Aero/Mechanical Performance Approach to High Technology Turbine Design," AGARD Conference Proceedings No. 421 on Advanced Technology for Aero Gas Turbine Components, Paris, France, May 1987.

Moore, J., and Adhye, R.Y., 1985, "Secondary Flows and Losses Downstream of a Turbine Cascade," ASME Journal of Engineering for Gas Turbines and Power, Vol. 107, No. 4, October, pp. 961-968.

Moore, J., Moore, J.G., Henry, G.S., and Chaudhry, U., 1989, "Flow and Heat Transfer in Turbine Tip Gaps," ASME Journal of Turbomachinery, Vol. 111, No. 3, July, pp. 301-309.

Moore, J. and Moore, J. G., 1991, "A Computational Study of Tip Leakage Flow and Losses in a Linear Turbine Cascade," AGARD Conference Proceedings No. 510 on CFD Techniques for Propulsion Applications, San Antonio, Texas, May.

Moore, J. and Tilton, J.S., 1988, "Tip Leakage Flow in a Linear Turbine Cascade," ASME Journal of Turbomachinery, Vol. 110, January, pp. 18-26.

Peters, D.P., 1992, "Tip Leakage Loss Development in a Linear Turbine Cascade," M.S. Thesis, Virginia Polytechnic and State University, Blacksburg, Virginia, February.

Rains, D.A., 1954, "Tip Clearance Flows in Axial Flow Compressors and Pumps," California Institute of Technology, Hydrodynamics and Mechanical Engineering Laboratories, Report No. 5, June.

Shapiro, A.H., 1953, The Dynamics and Thermodynamics of Compressible Fluid Flow, Wiley, New York.

Vavra, M.H., 1960, Aero-Thermodynamics and Flow in Turbomachines, Wiley, New York.

Yaras, M.I. and Sjolander, S.A., 1989, "Losses in the Tip Leakage Flow of a Planar Cascade of Turbine Blades," AGARD Conference Proceedings No. 469 on Secondary Flows in Turbomachines, Luxembourg, August.

Yaras, M.I., and Sjolander, S.A., 1992, "Prediction of Tip-Leakage Losses in Axial Turbines," ASME Journal of Turbomachinery, Vol. 114, pp. 204-210.

Yaras, M.I., Zhu, Y., and Sjolander, S.A., 1989, "Flow Field in the Tip Gap of a Planar Cascade of Turbine Blades," ASME Journal of Turbomachinery, Vol. 111, pp. 276-283.

REFERENCE NO. OF THE PAPER: 12

DISCUSSOR'S NAME: N.W. Harvey, Rolls-Royce, U.K.

AUTHOR'S NAME: J. Moore

Q: What difference do you think inclusion of the casing relative motion (of a rotating turbine rotor) would make to your results?

A: In an unshrouded turbine, the wall friction on the stationary casing will probably act to reduce the flow through the tip clearance gap. The extent of the reduction will depend on the blade geometry and the magnitude of the tip clearance. The additional loss due to tip leakage will probably still be well modelled as the sum of the losses in the tip gap plus the dissipated tip gap exit secondary kinetic energy.

REFERENCE NO. OF THE PAPER: 12

DISCUSSOR'S NAME: MG Rose, Rolls-Royce, U.K.

AUTHOR'S NAME: J. Moore

Q: In your loss analyses you have looked at each loss source directly. Is it possible that there may be losses due to the interaction of the flow features? For example, the leakage vortex may cause blockage on the suction surface, higher velocities and hence higher loss.

A: The wall boundary layers are modified by the presence of the tip leakage flow. For example, there is a reattachment line on the suction surface where the recirculating tip leakage flow impinges on the wall. There is also an important region of turbulence production as the tip leakage flow separates from the endwall. This turbulence is convected around the tip leakage vortex core, leading to further dissipation of mean kinetic energy, as shown by Moore, et al.

Reduction of Tip Clearance Loss and Tip Clearance Noise in Axial-Flow Machines

by
Frank Kameier and Wolfgang Neise+)

BMW Rolls-Royce AeroEngines,
Abteilung ET 44
Eschenweg 11,
15827 Dahlewitz, Germany

+)*Deutsche Forschungsanstalt für Luft- und Raumfahrt e.V.,*
Abteilung Turbulenzforschung Berlin
Müller-Breslau-Straße 8, 10623 Berlin, Germany

Abstract

An experimental study is described to investigate the negative effects of the tip clearance gap on the aerodynamic and acoustic performance of axial turbomachines. In addition to the increased broadband levels reported in the literature when the tip clearance is enlarged, significant level increases were observed within narrow frequency bands below the blade passing frequency. Measurements of the pressure and velocity fluctuations in the vicinity of the blade tips reveal that the tip clearance noise is associated with a rotating flow instability at the blade tip which in turn is only present under reversed flow conditions in the tip clearance gap. A turbulence generator inserted into tip clearance gap is found to be effective in eliminating the tip clearance noise and in improving the aerodynamic performance.

1. Introduction

This paper is concerned with the negative effects of the radial clearance between the casing wall and the blade tip upon the aerodynamic and acoustic performance characteristics of axial turbomachines like jet engines, axial compressors, and axial fans. It is well known that a small tip clearance is beneficial for both the aerodynamic performance and the noise characteristic of axial turbomachines. The pressure rise increases and the onset of rotating stall moves to lower flow rates as the clearance is reduced, compare Hutton (1955) and Cumpsty (1989). Tip clearance noise can be a significant source of noise when the tip clearance exceeds a certain limit. While Marcinowski (1953), Longhouse (1978), Stütz (1988) and Fukano et al.(1986) reported increased broadband noise levels as a result of an enlarged tip clearance, Kameier et al. (1992) observed, on top of the higher broadband noise drastic level increases within limited almost narrow-band frequency regions below the blade passing frequency. This narrow-band noise component was found when the dimensionless gap width became larger than τ=s/D=0.0027 (D=impeller diameter) and at flow rates equal to or smaller than the optimum. The generation mechanism of the tip clearance noise, however, is yet widely unknown.

To investigate the unsteady flow processes in the blade tip region that are responsible for the aerodynamic losses as well as for the generation of the tip clearance noise, measurements are made in this study of the pressure fluctuations at the casing wall in the vicinity of the impeller, of the pressure fluctuations on the impeller blades, and of the steady and

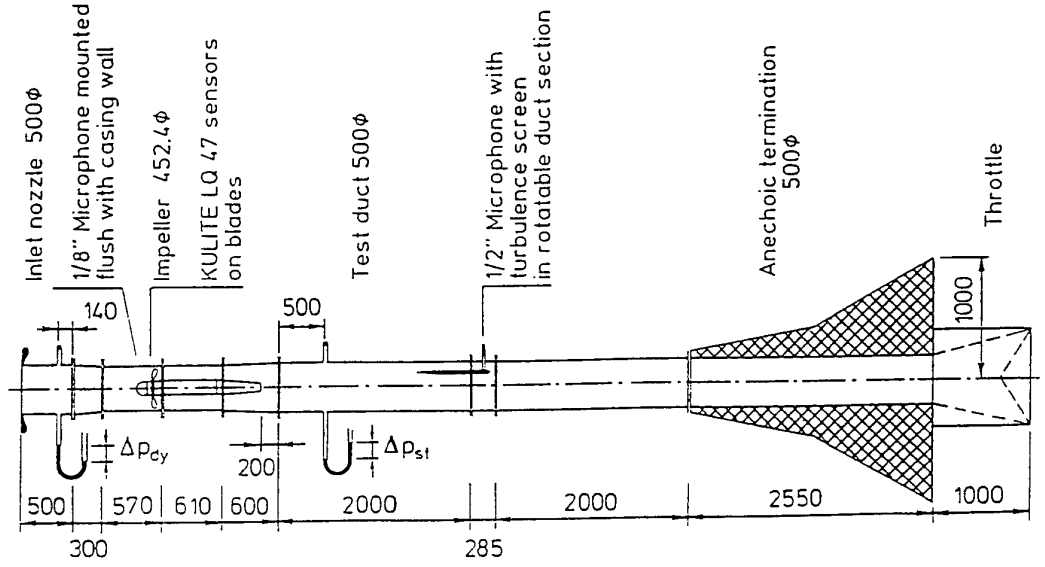

Figure 1: Schematic of the experimental set-up (dimensions in mm).

Paper presented at the AGARD PEP 85th Symposium on "Loss Mechanisms and Unsteady Flows in Turbomachines", held in Derby, United Kingdom, 8-12 May 1995, and published in CP-571.

unsteady velocity fluctuations around the blade tips as well as in the tip clearance gap itself. These measurements reveal that the tip clearance noise is associated with rotating flow instability at the blade tip which in turn is only present under reversed flow conditions in the tip clearance gap. A simple method is described to diminish the negative effect of the tip clearance gap while maintaining its nominal width.

Finally, a comparison with a multi stage high-pressure compressor shows similar spectral characteristics of wall pressure fluctuations in the low-speed and in the first stage of a high-speed compressor.

2. Experimental Apparatus

The test fan is low-speed high-pressure axial fan with outlet guide vanes. The design is similar to an axial fan manufactured by J.M. Voith GmbH, Heidenheim, Germany (now Voith Howden GmbH) who kindly supplied the impeller blades. The impeller diameter was kept constant throughout all experiments; the tip clearance was varied by changing the casing diameter: Four different casing segments were used to give gap widths of 0.3, 0.6, 1.2, and 2.4mm which correspond to tip clearance ratios of τ=s/D= 0.00066, 0.0013, 0.0027, and 0.0053. The principal impeller dimensions are: diameter D=452.4mm, hub-to-tip ratio ε=0.62, blade number Z=24, blade chord length at the tip c=43mm, blade stagger angle at the tip θ=27°, blade profile NACA 65. The stator row comprises V=17 non-profiled vanes.

Figure 1 shows the experimental set up along with its major dimensions. The measurement facility meets the requirements of DIN 24 163 (1985) for measurement of the aerodynamic fan performance. On the inlet side there is a short duct section with a bellmouth nozzle. The anechoically terminated outlet duct is in accordance with the standardised in-duct method (DIN 45 635 Part 9 (1989), ISO 5136 (1990)). A 1/2-inch microphone equipped with a turbulence screen is mounted in a rotatable duct section to measure the circumferentially averaged sound pressure level at a specified radial distance from the duct axis. The pressure fluctuations on the interior casing wall are monitored by using 1/8-inch Microphones (Brüel&Kjaer type 4138) which are mounted flush with the inner wall. To measure the unsteady blade pressures, four miniature pressure sensors (Kulite type LQ 47-5-SG) are mounted in small recesses of the impeller blades so that the original outer blade contour is retained. The low-voltage output signals of the sensors are amplified within the rotating system and then transmitted into the fixed frame of reference via a two-channel Datatel telemetry-system. A special hot-wire probe is used to measure the flow field in the blade tip region as well as in the 2.4mm wide tip clearance gap. More details about the experimental equipment and measurement techniques are given by Kameier (1994).

3. Effect of the Tip Clearance on the Fan Performance

In Figure 2 are shown the aerodynamic and acoustic fan performance curves for four tip clearance ratios in terms of the total pressure coefficient $\Psi=2\Delta p_t/\rho U^2$, efficiency $\eta=Q\Delta p_t/P_{imp}$, and specific sound power level $L_{Ws}= L_W-20$ lg $\Delta p_t/\Delta p_0-10$ lg Q/Q_0 as functions of the flow coefficient $\Phi=4Q/D^2U$ (Δp_t=total fan pressure, Δp_0=1Pa, ρ= density, U= impeller tip speed, Q = volume flow, Q_0=1m^3/s, L_W=sound power level, P_{imp}=power transmitted by impeller). Except for the largest tip clearance, the fan performance curves are characterized by pronounced hysteresis loops with sudden drops in flow rate, fan pressure, and efficiency and accompanying increases in the specific sound power level when the fan is throttled into the stall

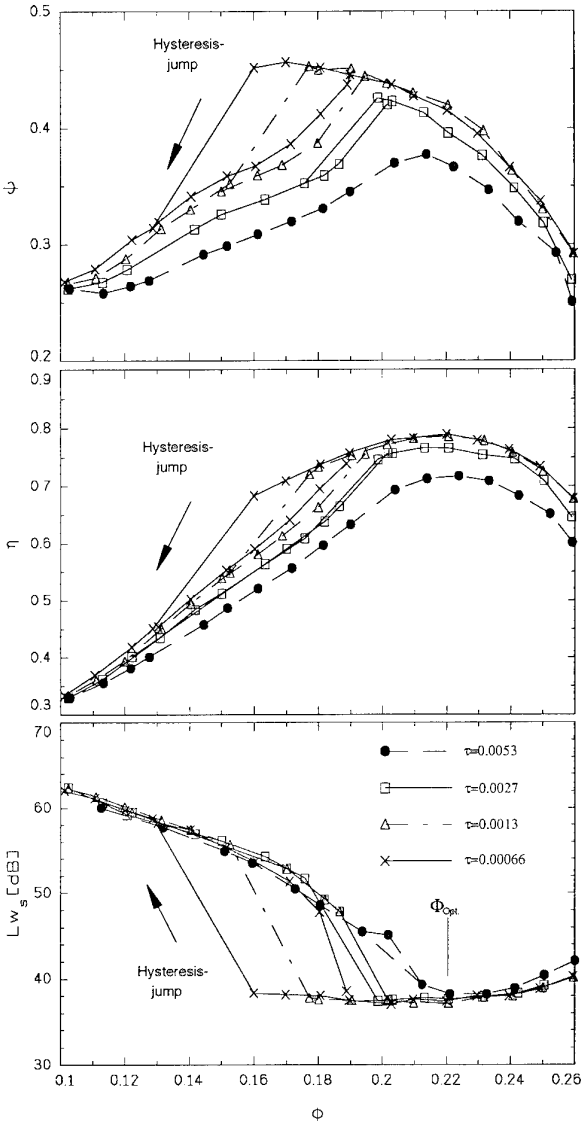

Figure 2: Effect of tip clearance on the aerodynamic and acoustic fan performance

region. The larger the hysteresis loop, the larger the drop in fan pressure and efficiency, as was demonstrated earlier by Hutton (1955). Note that the rise in specific sound power level is as much as 20dB at small tip clearances. The smaller the tip clearance, the further the fan can be throttled before the blade flow is stalled but, on the other hand, the stronger the hysteresis type behaviour. At the largest tip clearance (τ= 0.0053), the hysteresis loop is reduced to a very small regime which is visible only in the specific sound power level distribution, while there is only a discontinuous change in the fan pressure and efficiency curve.

The hysteresis loop is always fairly close to the point of maximum efficiency. Decreasing the tip clearance ratio from τ=0.0053 to τ=0.00066 increases the optimum efficiency by as much as 7 percent points. On the other hand, there is hardly any change in the specific sound power level with tip clearance at optimum fan operation. Incidentally, the efficiency data shown in Figure 2 are somewhat lower than commonly found in these types of flow machines, but this is due to the fact that the stator vanes were designed for a higher impeller speed (n=3000/min).

4. Pressure Spectra in the Acoustic Far Field and Near Field

In earlier papers by Marcinowski (1953), Longhouse (1978), Fukano et al.(1986), and Stütz (1988), increases in broadband noise are reported as the result of an enlarged tip clearance. The sound pressure spectra depicted in Figure 3, which were measured in the fan outlet duct, support this finding. The bottom diagram shows only the low frequency range of the spectra with enhanced frequency resolution; there it is obvious that enlarging the tip clearance results in drastic level increases of the radiated sound pressure within limited, almost narrow-band frequency regions. A particularly steep level increase of 15dB occurs at 370 Hz when the tip clearance is raised from τ=0.0027 to τ=0.0053.

Nawrot (1991) and Kameier et al. (1992) performed measurements with the short inlet duct shown in Figure 1 replaced by an anechoic test duct which had about the same dimensions as the outlet duct. The various fan performance curves measured with this arrangement were slightly different from the ones reported here, but the effect of the tip clearance was found to be unaltered. This statement holds also true for the sound spectra radiated. From these results it appears that tip clearance effects discussed here are largely independent of the flow conditions at the fan inlet.

In Figure 4 pressure spectra are compared which were measured in the outlet duct (acoustic far field, curves labelled "B") and at the casing wall at an axial location ζ=z/D=–0.007 upstream of the leading edge of the impeller blades (acoustic near field, curves labelled "A").

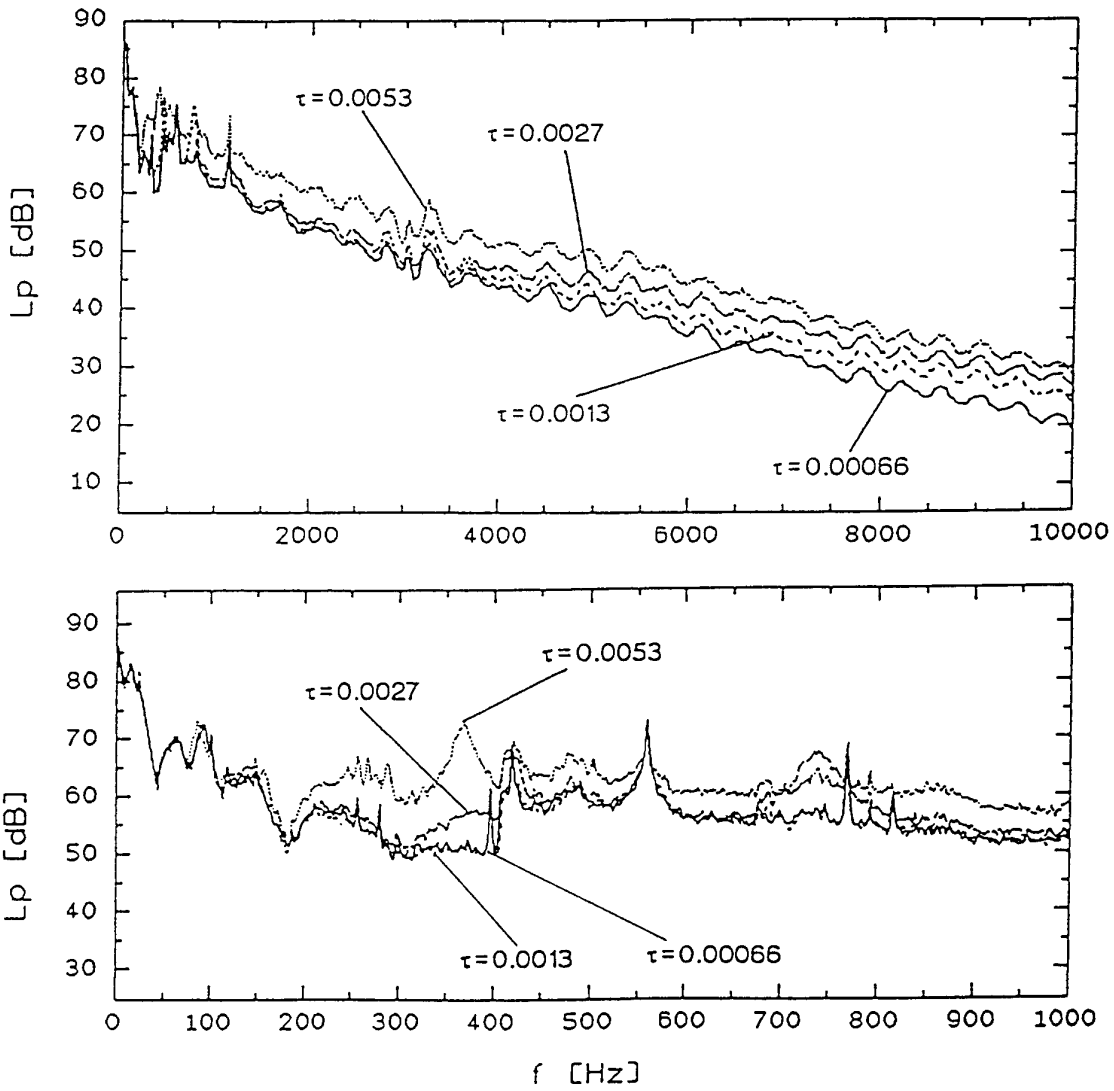

Figure 3: Sound pressure spectra in the fan outlet duct; Φ/Φ_{opt}=1, n=1400/min.

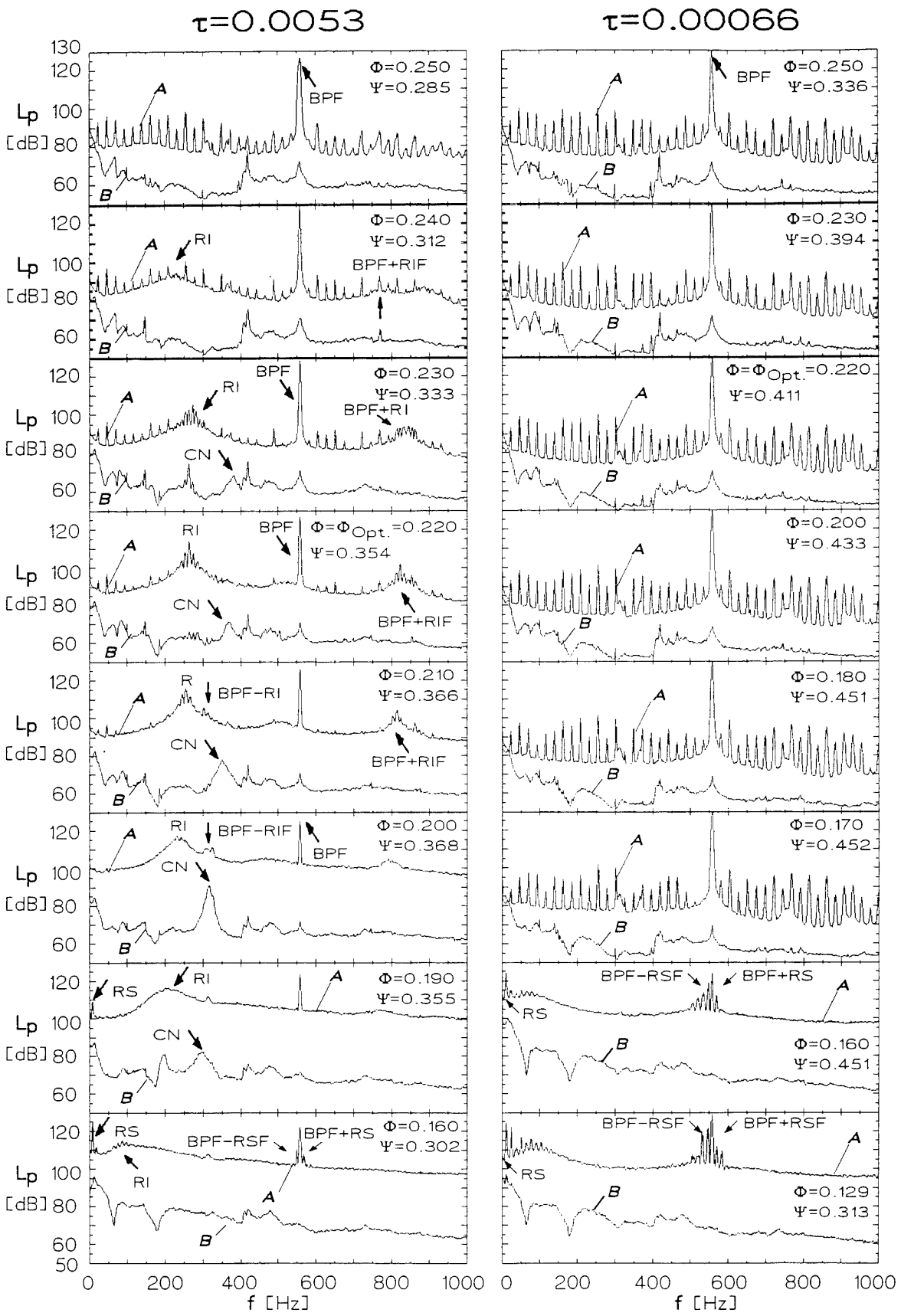

Figure 4: Pressure spectra in the outlet duct ("B") and at the casing wall ("A", ζ=–0.007) for various operating conditions; n=1400/min.

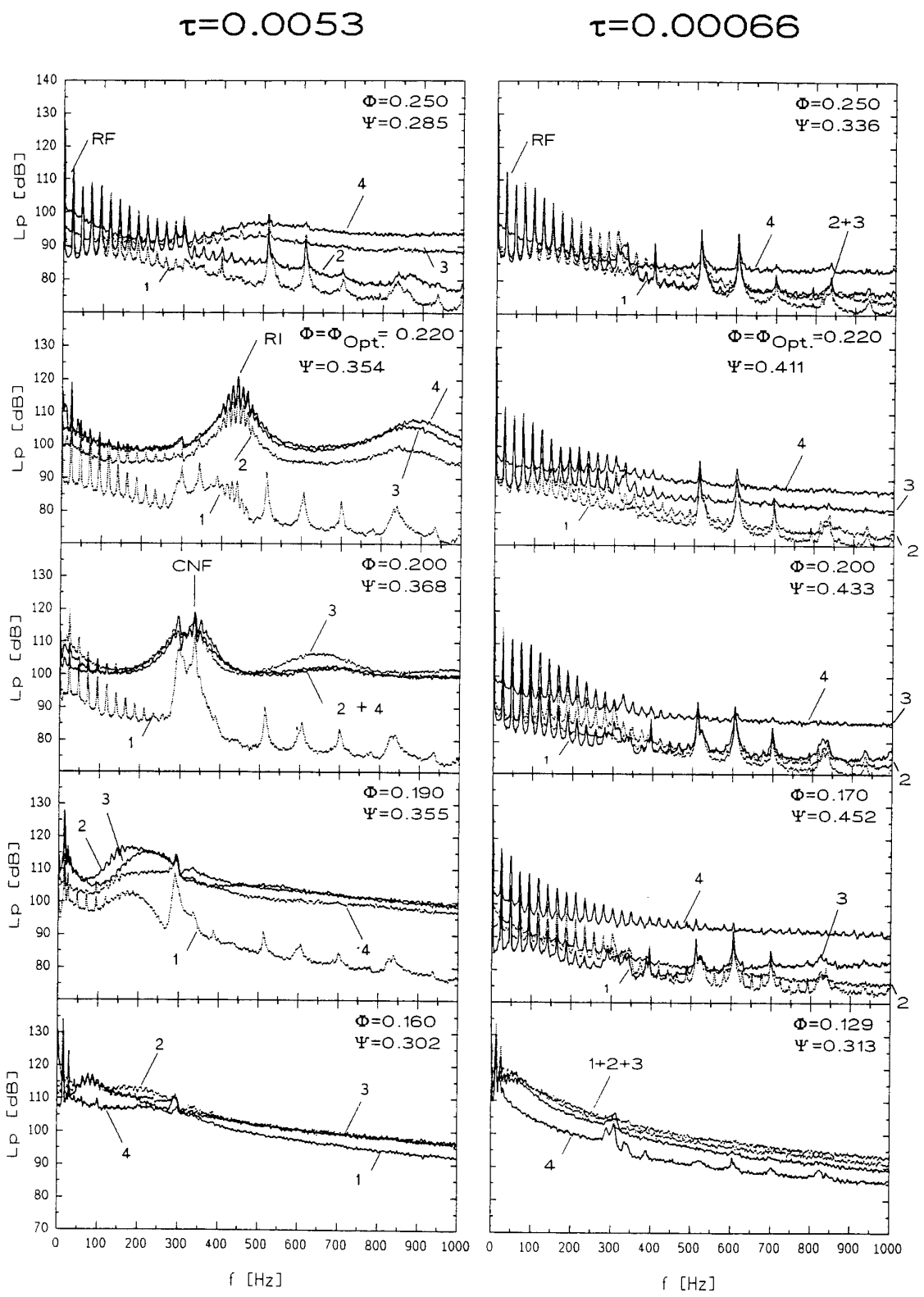

Figure 5: Spectra of the impeller blade pressures for various operating conditions; n=1400/min.

The diagrams in the left column show the results for the largest tip clearance ratio (τ=0.0053) where the tip clearance noise is most prominent in the spectrum, and the right column is for the smallest tip clearance ratio (τ=0.00066). The outlet duct spectra were obtained as before by using a 1/2-inch slit-tube microphone, and 1/8-inch microphones mounted flush with the inner duct wall were used to measure the near-field pressures, compare Figure 1. The flow coefficient Φ is reduced from the top to the bottom diagram. The blade passing frequency component (BPF) is clearly visible in the wall pressure spectra, and multiples of the rotor frequency (RF) appear to both sides of this component.

The tip clearance noise component (CN) measured for τ=0.0053 in the duct is shifted towards lower frequencies as the flow rate is reduced. In the wall pressure spectra another component termed rotating instability (RI) appears, which increases in level as the flow rate is throttled. At some operating conditions, tone components exist at frequencies equal to the sum or difference of the blade passing frequency and the frequency of the rotating instability component, i.e., at BPF+RIF and BPF-RIF. The tip clearance noise reaches its highest level at Φ= 0.200 (3rd diagram from the bottom). At flow rates below Φ=0.200, the fan operation becomes unstable, and a tonal component below the rotor shaft frequency is generated in the outlet duct spectra as well as in the wall pressure spectra which is associated with rotating stall (RS). This also results in a frequency modulation of the blade passing frequency, and consequently side bands at BPF+RSF and BPF-RSF appear in the wall pressure spectrum.

With a tip clearance ratio of τ=0.00066 (right column in Figure 4), the clearance noise component and rotating instability component are missing in the spectra throughout the range of operating conditions. Rotating stall occurs at much lower flow rates than before, i.e., $\Phi \leq 0.16$.

5. Pressure Fluctuations on the Impeller Blades

A series of pressure spectra measured with flush mounted pressure transducers on the impeller blades is shown in Figure 5, where the left column is again for the largest tip clearance (τ=0.00053) and the right column for the smallest (τ=0.00066). From the top to the bottom, the flow rate is reduced. In each diagram, four spectra are shown which were measured at the following blade positions: #1: r/R=0.88, x/c=0.3, suction side; #2: r/R=0.99, x/c=0.3, suction side; #3: r/R=0.99, x/c=0.6, suction side; #4: r/R=0.99, x/c=0.44, pressure side (r=radial distance from the axis, R=impeller diameter, x=axial distance from the leading edge, c=blade chord).

The upper three diagrams in the left column (τ=0.0053) correspond to stable fan operating conditions, and the lower two to the rotating stall regime. At all four meas-urement positions the spectra are dominated by spikes at the rotor shaft frequency and multiples thereof which indicates that the flow environment of the rotor is not quite uniform. Since the tone levels are highest at the rotor shaft frequency Ω and decrease monotonously with increasing frequency, it is concluded that these tones are generated by the interaction of the rotor with inlet flow distortions. For most of the flow rates tested, the "stator passing frequency" $V \cdot \Omega$=397 Hz is not visible but buried in the random noise. When the fan is operated just near the maximum efficiency point (Φ= 0.220), a broad band hump with superimposed multiple peaks appears in the spectrum which moves to lower frequencies when the flow is further throttled. This behaviour is similar to that of the rotating instability component in the wall pressure spectra, compare Figure 4. The frequencies measured in the fixed and in the rotating frame of reference are different. Closer to the hub (r/R=0.88, sensor #1), the pressure fluctuations of the rotating instability component are much lower in level than at the blade tip which reveals that the cause for this phenomenon lies in the tip flow region. Mongeau (1991), Bent et al. (1992), and Mongeau et al. (1993) reported similar pressure spectra on the blades of a casingless centrifugal pump impeller and interpreted them as the result of a rotating "almost-frozen" discharge flow instability pattern, which rotates relative to the blades just like the cells of separated flow in case of rotating stall. The term rotating flow instability is also used in the present paper, however, it was shown by Kameier (1994) that the rotating instability components found in the blade tip region of axial fans are not caused by a frozen flow disturbance but rather by a rotating source or vortex mechanism.

Like in the case of the wall pressure spectra shown in Figure 4, the rotating instability component is missing in the blade pressure spectra when the tip clearance is small, compare the diagrams in the right column of Figure 5. With the onset of rotating stall, the low frequency random noise levels are increased, and the harmonics of the stator frequency are masked. The spectra are now dominated by the rotating stall component with the highest levels at sensor location #2 and #3, i.e., on the blade suction side at a radial distance from the axis of r/R=0.987. This indicates that the blade flow is stalled first at the tip. When the flow is further reduced, the stalled flow regime extends deeper down to the hub. Note that the frequency of the rotating stall component is now different from the one found in the wall pressure fluctuations (see Figure 4); the sum of the two frequencies is, of course, equal to the rotor shaft frequency.

6. Azimuthal Propagation of the Rotating Instability Component

Bendat and Piersol (1980) describe a source location method which is adapted here to determine the azimuthal propagation velocity of the rotating instability component. On the premises that auto power spectra of the pressure signals measured at two different locations have the same magnitude (G_{11}= G_{22}), the cross-spectrum G_{12} between the two signals can be written as

$$G_{12}(\omega) = G_{11}(\omega)\, e^{i\,\omega\,\Delta t} \qquad (1)$$

Here G_{11} is the auto power spectrum at the location 1, ω the angular frequency, and Δt the time delay between the two signals. In equation (1) the phase angle of the cross-spectrum is expressed as a function of the propagation time:

$$\hat{\varphi}_{12} = \omega\,\Delta t\,. \qquad (2)$$

The speed of propagation is determined by the displacement between the sensors and the delay time Δt. In the present experiments, the azimuthal propagation velocity Ω_{RI} is determined by using two azimuthally spaced sensors in the casing wall and two sensors mounted on adjacent impeller blades. The angular displacement is $\Delta\varphi$=15° in both cases. The azimuthal propagation velocity Ω_{RI} is given by the following relation:

$$\Omega_{RI} = \Delta\varphi/\Delta t = \Delta\varphi\,\omega/\hat{\varphi}_{12} \qquad (3)$$

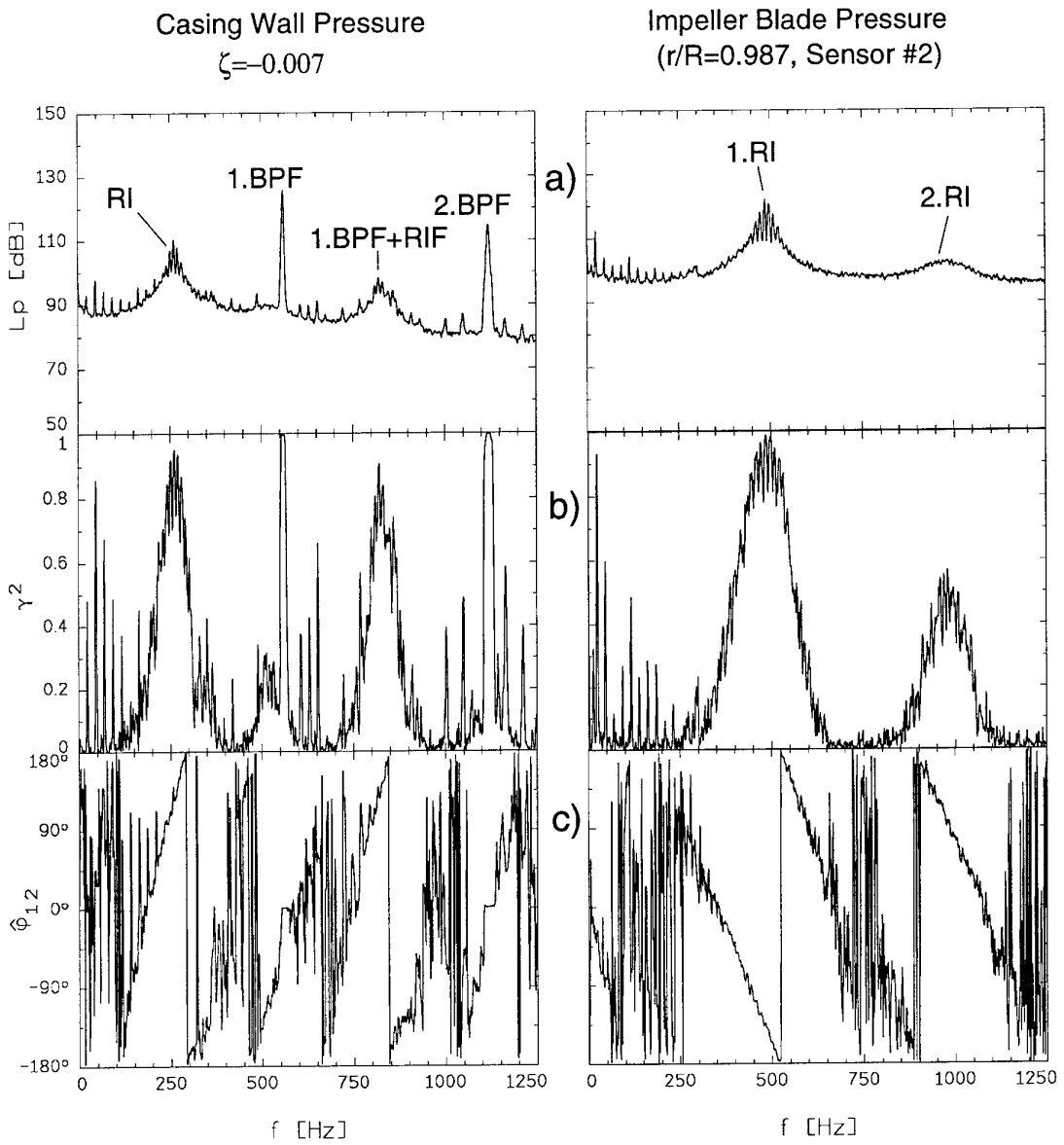

Figure 6: Comparison of the pressure fluctuations at the casing wall and on the impeller blades; Φ/Φ_{opt}=1, τ=0.0053, n=1400/min; a) pressure spectra, b) coherence, c) phase angle of the cross-spectrum.

The power spectrum of one of the two sensors, the coherence of the two sensor signals, and the phase angle of the cross spectrum are shown in Figure 6 for the best efficiency point and the tip clearance ratio τ=0.0053; the diagrams on the left are for the casing wall pressures and the ones on the right for the impeller blade pressures. Clearly, the frequencies of the rotating instability component are different in the fixed and in the rotating frame of reference. The coherence of the signals of the two microphones or, respectively, the two pressure pressure sensors on the blades, is high in the frequency range of the rotating instability component. The gradient of the phase angle in that frequency range is different for the fixed and the rotating system which indicates that the propagation velocity of the rotating instability component is positive in one coordinate system and negative in the other.

The angular propagation velocity is now determined by applying equation (3) to the spectral line with the highest coherence. This was done for different operating conditions, and the result is plotted in Figure 7 for the tip clearance ratios τ=0.0027 and τ=0.0053; the rotating instability phenomenon does not exist at the two other, smaller tip clearances.

The data in Figure 7 reveal that the rotating instability components move relative to the impeller blades as well as relative to the fixed coordinate system. Note that differently from the rotating stall case, the sum of the frequencies of the various spikes measured in the fixed and the rotating frame of reference is not equal to the rotor shaft frequency. On the other hand, the sum of the magnitudes of the propagation velocities in the two coordinate systems is equal to the impeller angular velocity or, in other words:

$$\Omega_{RI}^{F} = \Omega_{RI}^{R} + \Omega \quad (4)$$

where the superscripts F and R denote the fixed and the rotating frame of reference, respectively. Since the angular displacement of the two sensors $\Delta\varphi$ is the same in the fixed and in the rotating frame of reference, a simple relation can

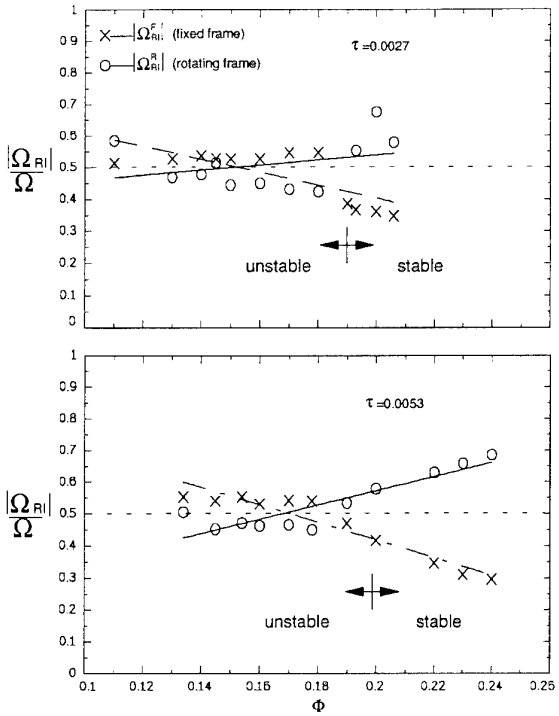

Figure 7: Normalized angular propagation velocity of the rotating instability components.

be derived for the frequencies of the rotating instability component measured in the two coordinate systems:

$$f^F/\hat{\varphi}^F_{12} - f^R/\hat{\varphi}^R_{12} = \Omega/2\pi\,\Delta\varphi \qquad (5)$$

7. Modification of the Tip Clearance Gap

Up to this point, the experimental results do not give a decisive clue as to what the exact relation is between the tip clearance noise and the rotating instability component found in the impeller blade pressures and the casing wall pressures. To examine if the tip clearance noise is generated by the flow over the blade tip, i.e., by the blade tip vortex, which is driven by the pressure difference between the pressure and the suction side of the blade profile, a thin self adhesive plastic tape was wrapped around the impeller from blade to blade to suppress the flow over the blade tip. The tape formed a polygon with the impeller blades placed in the corners. With this configuration, however, the tip clearance noise level was higher than before, despite the fact that the flow rate and the fan pressure were reduced (Kameier (1994)).

From the above result it was concluded that it is not the blade tip flow that generates the tip clearance noise but rather the secondary flow through the gap which is driven by the static pressure difference between inlet and outlet of the impeller disk and extends over the entire circumference. To help block or at least impede this gap flow, a tape of 2mm thick Velcro tape material was inserted into the 2.4mm wide tip clearance gap (τ=0.0053), see the schematic presentation shown in Figure 8. The Velcro tape is bonded to the inner casing wall; its axial width is 15mm, and its axial position is that of the maximum thickness of the impeller blade profile. Incidentally, in experimental fluid dynamics such a Velcro tape is frequently used as a tripping device for the generation of turbulent boundary layers.

In Figure 9 is shown a comparison of the sound pressure spectra in the fan outlet duct and the pressure spectra at the casing wall for the cases with and without the Velcro tape. The fan operating point is that of maximum tip clearance noise (Φ=0.200). The effect of the Velcro material is to diminish the tip clearance noise component by more than 30dB which practically eliminates this component from the radiated far field spectrum. The rotating instability component in the near field pressures is suppressed as well. At the same time the fan pressure coefficient is improved from Ψ= 0.368 to 0.419. A comparison of the aerodynamic and acoustic fan performance curves is depicted in Figure 10. Clearly, the fan with the modified tip clearance gap reaches a distinctly higher fan pressure and widens the useful range of operating conditions. The hysteresis loop is comparable to that of a fan with about half the gap width, and the stall behaviour is similar to that with the two smallest tip clearance ratios τ=0.0013 and τ= 0.00066, compare Figure 2.

To investigate the influence of the Velcro tape on the flow conditions in the blade tip region and in the tip clearance gap, hot-wire measurements were made in that area with a special hot-wire probe. Figure 11 shows the radial distribution of the axial and the azimuthal velocity component in the tip

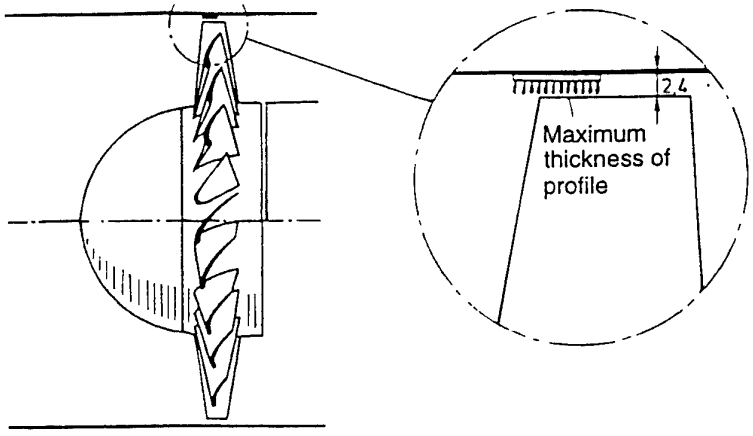

Figure 8: Schematic of tip clearance gap with Velcro tape inserted.

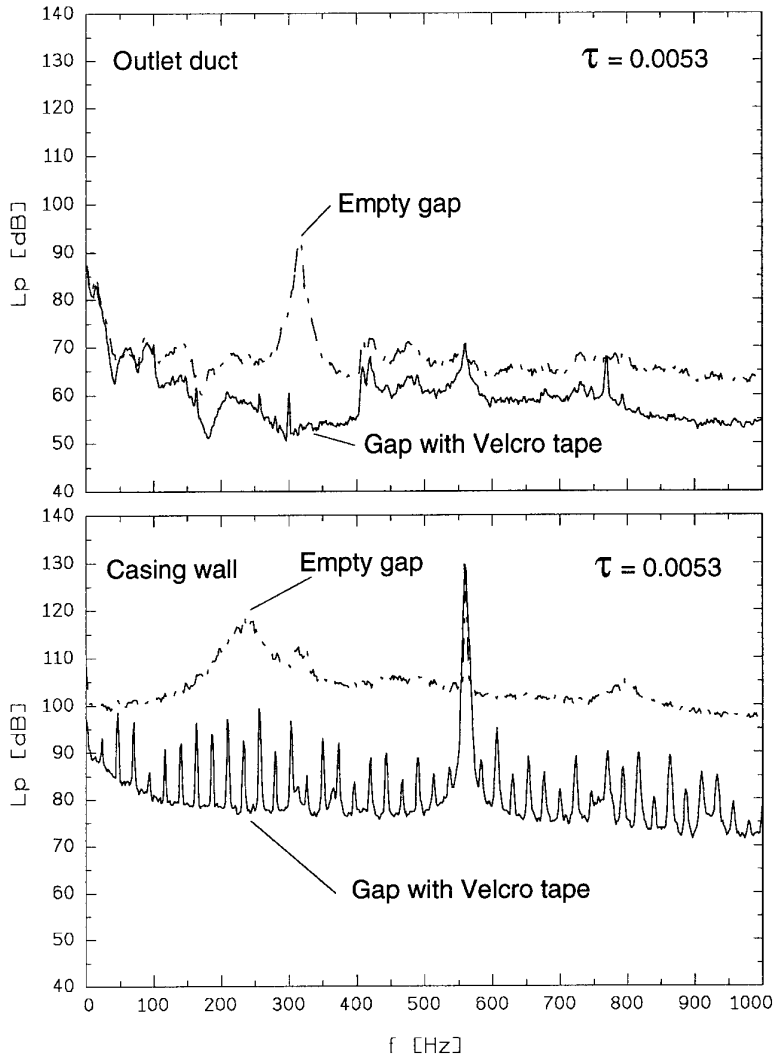

Figure 9: Pressure spectra in the outlet duct and on the casing wall at the flow rate of maximum tip clearance noise Φ=0.20, n=1400/min.

clearance gap at an axial position downstream of the blade tip (ζ=z/D=0.009). The azimuthal component is normalized by the impeller tip speed U and the axial component by the average flow velocity $\overline{C_z}$ in the fan annulus. The azimuthal velocity component increases when the flow rate is reduced while the axial component is reversed. The more the fan is throttled, the higher the reversed flow velocity. In conclusion we note that reversed flow conditions exist at those operating conditions where the tip clearance noise appears in the sound pressure spectrum. Note that the data shown in Figure 11 were obtained by continuous time averaging of the hot-wire signals and therefore represent the flow components averaged over the impeller circumference. Hence, the reversed flow in the tip clearance gap at flow rates $\Phi/\Phi_{opt} \leq 1$ extends over the entire circumference. When the Velcro tape is inserted into the gap, the flow reversal in the gap is suppressed. At this point it worth mentioning that large measurement errors may have occurred in the determination of the magnitude of the axial velocity component downstream of the Velcro tape due to the increased turbulence intensity. In particular the data for Φ/Φ_{opt}=0.9 are probably in error because they show values larger than the average flow velocity in the fan annulus.

8. Comparison to a High-Speed Axial Compressor

The rotating instability phenomenon was also observed in the first stage of a multi stage high-speed axial compressor. Figure 12 shows spectra of the wall pressure fluctuations measured close to the leading edge of the (first) rotor. The low-speed compressor was operating at the point of maximum efficieny (Φ=0.22) and the multi stage high-speed compressor at off-design condition (n=83 %). The rotating instability components (RI) and the results of a frequency modulation of the blade passing frequency with the rotating instability frequencies (BPF±RIF) are clearly visible. Recent tests (Baumgartner et al. 1995) revealed that vibrations of the first stage rotor blades were caused by pressure fluctuations in the frequency region below the blade passing frequency which show a spectral characteristic similar to the rotating instability components described here. Parker et al. (1985) have also found frequency spectra with signature similar to the rotating instability in a single stage, low speed, axial flow compressor. The pressure fluctuations which are propagating as rotating waves are inducing blade vibrations with different frequencies of pressure fluctuations and blade vibrations. It is possible that these pressure fluctuations induced significant forced vibrations of the rotor blades.

9. Conclusions

An experimental study is described to investigate the negative effects of the tip clearance gap on the aerodynamic and acoustic performance of axial turbomachines. The experiments were made with a high-pressure low-speed axial fan with D=452mm impeller diameter, ε=0.62 hub-to-tip ratio, Z=24 blades (NACA 65 profile), and V=17 outlet guide vanes. The impeller diameter was kept constant throughout the tests, and the tip clearance was varied in the range s= 0.3 to 2.4 mm by using casing segments of different size.

In the published literature higher broad band levels were reported when the tip clearance was enlarged. The present result show that in addition to that, significant sound pressure level increases occur within limited, almost narrow frequency bands in a region below the blade passing frequency component. This tip clearance noise component which is a particularly effective noise source was observed when the tip clearance ratio was larger than or equal to τ=s/D=0.0027 and if there is a high enough pressure difference between suction and pressure side of the impeller, i.e., at flow rates equal to or smaller than the design flow rate.

Measurements of the pressure fluctuations on the casing wall close to the impeller and on the rotating blades have shown that a flow instability mechanism occurs at the blade tip which is associated with the tip clearance noise. These rotating instability components move in azimuthal direction, relative to the impeller blade row. Hot wire measurements in the tip region have shown that this rotating instability only occurs if a reversed flow condition exists in the tip clearance gap. The effect of the reversed flow is to increase the thickness of the casing wall boundary layer at the rotor intake and to eliminate the axial component of the absolute flow

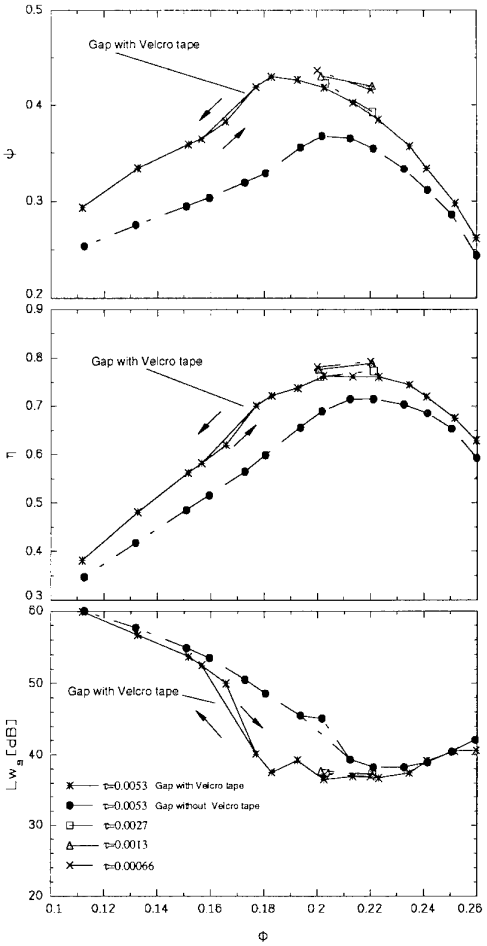

Figure 10: Influence of the Velcro tape on the aerodynamic and acoustic fan performance

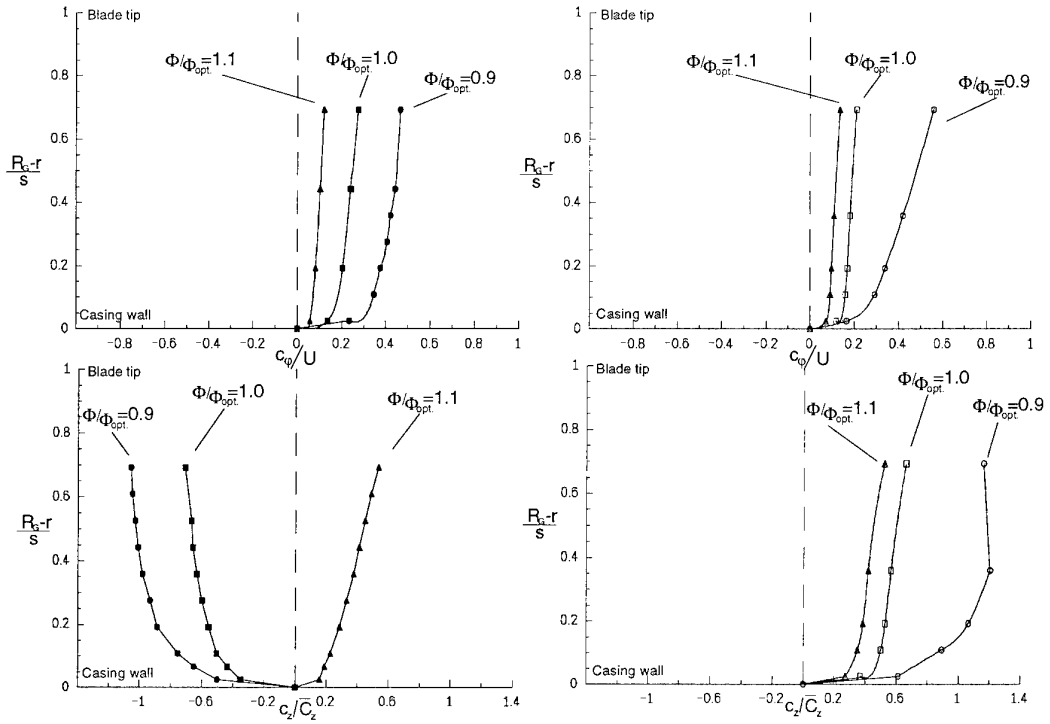

Figure 11: Radial distribution of the axial and azimuthal velocity componets in the tip clearance gap; left column: empty gap; right column: gap with velcro tape.

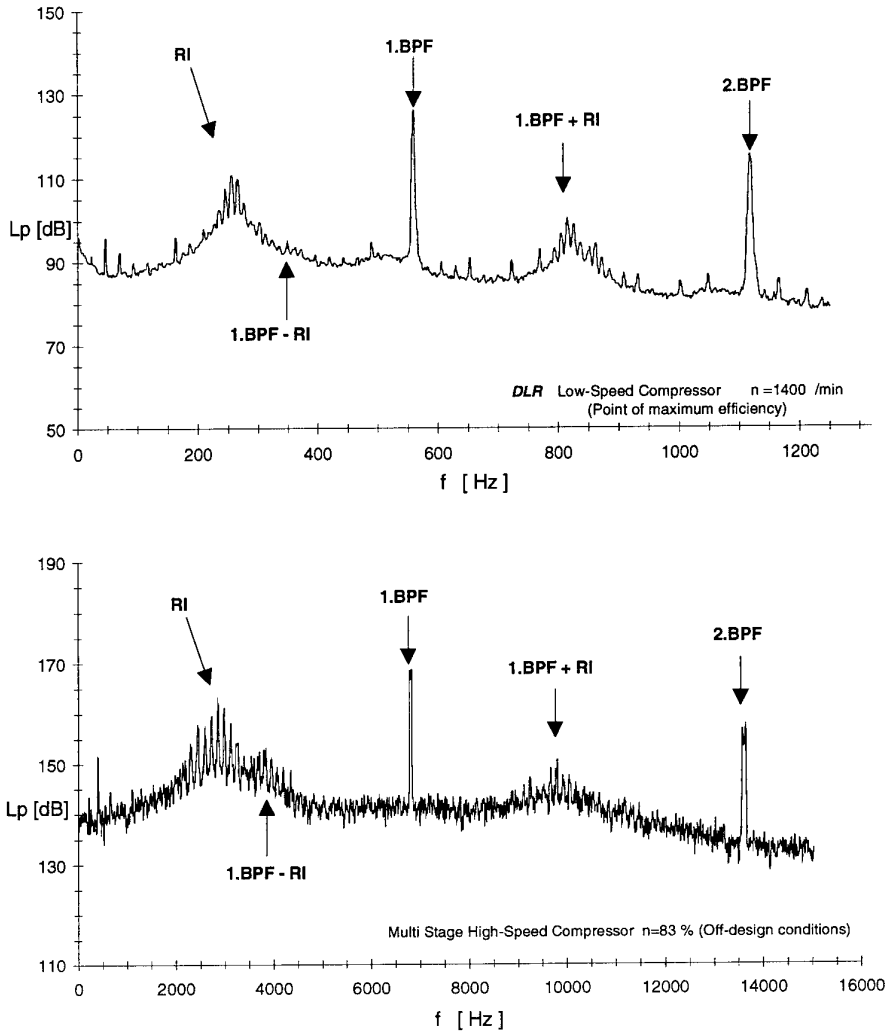

Figure 12: Pressure spectra at the casing wall, upstream the leading edge of the rotor; upper diagram: low-speed compressor of the present investigation; lower diagram: first stage of a multi stage high-speed compressor.

velocity in the gap. As a result, vortex separation takes place at the blade tip. If the azimuthal wavelength of the shed vortices is equal to the blade spacing, a strong interaction of the vortex separation on individual blades occurs which results in drastic increases of the radiated noise. When the mean flow is throttled even further, the blade flow is separated over the entire radial span over part of the impeller circumference, which is the well known phenomenon of rotating stall.

The rotating flow instability phenomenon found in the present study was also observed in other low-speed axial compressors and in a high-speed axial compressor. The pressure fluctuations which are propagating as rotating waves can induce blade vibrations at frequencies which are different from the frequencies of the pressure fluctuations. The wall pressure fluctuations are in the range of the half blade passing frequency.

As a modification of the tip clearance geometry, a turbulence generator (Velcro tape) is inserted into the 2.4mm wide tip clearance gap (τ=0.0053) to obstruct the secondary flow through the gap. With this device, the tip clearance noise component is diminished in the acoustic far field spectrum by more than 30dB at the operating point where maximum tip clearance noise is found otherwise. At the same time the fan pressure is improved by 14%, the fan efficiency by 7 percent points, the specific sound power level is reduced by 11 dB(A), and the onset of rotating stall is shifted to lower flow rates so that the useful range of the characteristic curve is comparable to the case of a much smaller tip clearance ratio, i.e., τ=0.0013 and τ=0.00066. The turbulence generator device is suggested for fan installations where the tip clearance cannot be reduced further for reasons like blade stagger angle variation, relative motion between impeller and casing, blade deformation under thermal or acceleration forces, or spark generation; it can be used for retrofitting existing axial turbomachines as well as for new installations.

10. Acknowledgments

This work was supported in part by the Technische Universität Berlin, Hermann-Föttinger-Institut für Thermo- und Fluiddynamik.

11. References

Baumgartner, M., Kameier, F. and Hourmouziadis, J. 1995: Non Engine Order Blade Vibration in a High Speed Compressor. *Twelfth International Symposium on Airbreathing Engines,* Melbourne, Australia, 10-15 Sep. 1995.

Bendat, J.S. and Piersol, A.G., 1980: *Engineering applications of correlation and spectral analysis.* John Wiley & Sons, New York.

Bent, P.H., McLaughlin, D.K., and Thompson, D.E.: The Influence of Discharge Configuration on the Generation of Broadband Noise in Centrifugal Turbomachinery. *Proc. 14th DGLR/AIAA-Aeroacoustics Conference Aachen,* DGLR Bericht 92-03, 607-614, Paper 92-02-099, Bonn, Germany.

Cumpsty, N. A., 1977: Review – A Critical Review of Turbomachinery Noise. T*ransactions of the ASME, J. Fluids Engineering* **99**, 278-293.
Cumpsty, N. A., 1989: Compressor Aerodynamics. Longman Scientific & Technical, 343-345.

DIN 24 163, Parts 1, 2 and 3, 1985: Ventilatoren, Leistungsmessung: German Standard, Deutsches Institut für Normung, Berlin, Germany.

DIN 45 635, Part 9, 1989: Geräuschmessungen an Maschinen, Luftschallmessung, Kanal-Verfahren, Rahmen-Meßverfahren für Genauigkeitsklasse 2. German Standard, Deutsches Institut für Normung, Berlin, Germany

Fukano, T., Takamatsu, Y, and Kodama, Y., 1986: The Effect of the Tip Clearance on the Noise of Low Pressure Axial and Mixed Flow Fans. *J. Sound and Vibration* **105**, 291-308.

Hutton, S. P., 1955: Three-dimensional Motion in Axial Flow Impellers. *Proc. Institution Engineers Mechanical* **170**, 863-873.

ISO/DIS 5136, 1990: Acoustics - Determination of Sound Power Radiated into Duct by Fans - In-duct Method. Int. Standard, International Organisation for Standardization.

Kameier, F., 1994: Experimentelle Untersuchung zur Entstehung und Minderung des Blattspitzen-Wirbellärms axialer Strömungsmaschinen. *Fortschritt Berichte VDI Reihe 7*, Nr. **243**, Verein Deutscher Ingenieure, VDI Verlag GmbH, Düsseldorf, Germany (Doctoral Dissertation, Technische Universität Berlin).

Kameier, F., Geuer, U., and Neise, W., 1991: Untersuchung zur Entstehung des Blattspitzen-Wirbellärms an einer axialen Strömungsmaschine. *VDI Berichte* Nr. **872**, 343-358.

Kameier, F., Nawrot, T., and Neise, W., 1992: Experimental Investigation of Tip Clearance Noise in Axial Flow Machines. *Proc. 14th DGLR/AIAA-Aeroacoustics Conference Aachen,* DGLR Bericht **92-03**, 250-259, Paper 92-02-040, Bonn, Germany.

Longhouse, R.E, 1978: Control of Tip-Vortex Noise of Axial Flow Fans by Rotating Shrouds. *J. Sound and Vibration* **58**, 201-214.

Marcinowski, H., 1953: Einfluß des Laufradspaltes und der Luftführung bei einem Kühlgebläse axialer Bauart: *Motortechnische Zeitschrift (MTZ)* **14**, 259-262.

Mongeau, L., 1991: Experimental Study of the Mechanism of Sound Generation by Rotating Stall in Centrifugal Turbomachines. PhD-thesis, Penn State University. University park, Pennsylvania, USA.

Mongeau, L., Thompson, D.E., and McLaughlin, D.K., 1993: Sound Generation by Rotating Stall in Centrifugal Turbomachines. *J. Sound and Vibration* **163**, 1-30.

Parker, R., Stoneman, S.A.T. 1985: An Experimental Investigation of the Generation and Consequences of Acoustic Waves in an Axial Flow Compressor: Large Axial Spacing between Blade Rows. *J. Sound and Vibration* **99**, 169-182.

Nawrot, T., 1992: Experimentelle Untersuchung zum Entstehungsmechanismus des Spitzenwirbellärms an einer axialen Strömungsmaschine. Diploma-thesis; Hermann-Föttinger-Institut, Technische Universität Berlin, Germany.

Stütz, W., 1988: Experimentelle Untersuchung zum Radialspalteinfluß auf das aerodynamische und akustische Verhalten eines Axialventilators. S*trömungsmechanik und Strömungsmaschinen* **39**, Verlag G. Braun, Karlsruhe, Germany, 153-160.

Discussion:

H.A.Schreiber, DLR Germany: Could you please comment on the difference between the rotating instability and the rotating stall. What is the physical driving mechanism for the observed rotating instabilities?

The best known rotating flow instability in turbomachines is rotating stall. Rotating stall can be regarded as a special case of a rotating aerodynamic instability. Unlike in the rotating stall case, the pressure generated by the rotating instability is unsteady, even in a frame rotating with this instability pattern. An observer moving with the instability cell would measure a discrete frequency signal associated with the pressure fluctuation whereas when moving with the rotating stall cell he would not detect unsteady signals due to the stall.

The physical driving mechanism of the rotating flow instability is not yet fully understood. Further investigations into the nature of this flow phenomenon are presently underway at DLR Berlin and BMW-RR.

F. Eulitz, DLR Germany: The effects of the Velcro tape on noise reduction is impressive. Will this simple and effective device as a turbulence generator be applied to real-life engines? Or has it already been applied?

An application of Velcro tape has been carried out in a low speed ventilation fan of 1.8 m in diameter and a blade number of 8. In this fan, both tip clearance noise and rotating blade flow instability were found to be very weak. Nevertheless, the noise reduction due to the insertion of the Velcro tape was about 2 dB in overall sound pressure level, and the improvement of efficiency reached up to 2 percent points. More details are not available because of the customer restrictions for this evaluation.

J.F. Chevalier, SNECMA France: You said that the effect of Velcro tape is through turbulence creating and not gap fullfilling. In order to be some of that, did you try to test with thinner Velcro?

The mean effect of the Velcro tape is not the blockage although the fullfilling of the gap has only positive influence on performance. With the Velcro tape, the performance curve of the fan is totally changed especially the hysteresis region is nearly disappear and moved to lower flow rates at high pressure rise.

Experiments with thinner Velcro have not been realised.

REFERENCE NO. OF THE PAPER: 13

DISCUSSOR'S NAME: H.A. Schreiber, DLR, Germany

AUTHOR'S NAME: F. Kameier & W. Neise

Q.: Could you please comment on the difference between the rotating instability and the rotating stall. What is the physical driving mechanism for the observed rotating instabilities?

A: The best known rotating flow instability in turbomachines is rotating stall. Rotating stall can be regarded as a special case of rotating aerodynamic instability. Unlike in the rotating stall case, the pressure generated by the rotating instability is unsteady, even in a frame rotating with this instability pattern. An observer moving with the instability cell would measure a discrete frequency signal associated with the pressure fluctuation, whereas when moving with the rotating stall cell he would not detect unsteady signals due to the stall.

The physical driving mechanism of the rotating flow instability is not yet fully understood. Further investigations into the nature of this flow phenomenon are presently underway at DLR Berlin and BMW-RR.

REFERENCE NO. OF THE PAPER: 13

DISCUSSOR'S NAME: F. Eulitz, DLR, Germany

AUTHOR'S NAME: F. Kameier & W. Neise

Q.: The effects of the Velcro tape on noise reduction is impressive. Will this simple and effective device as a turbulence generator be applied to real-life engines? Or has it already been applied?

A: An application of Velcro tape has been carried out in a low speed ventilation fan of 1.8 m in diameter and a blade number of 8. In this fan, both tip clearance noise and rotating blade flow instability were found to be very weak. Nevertheless, the noise reduction due to the insertion of the Velcro tape was about 2 dB in overall sound pressure level, and the improvement of efficiency was up to 2 percentage points. More details are not available because of customer restrictions on the data from this evaluation.

REFERENCE NO. OF THE PAPER: 13

DISCUSSOR'S NAME: J-F Chevalier, SNECMA, France

AUTHOR'S NAME: F. Kameier & W. Neise

Q.: You said that the effect of Velcro tape is through turbulence creation and not gap filling. In order to be sure of that, did you try to test with thinner Velcro?

A: The mean effect of the Velcro tape is not the blockage, although filling of the gap has a positive influence on performance. With the Velcro tape, the performance curve of the fan is totally changed; the hysteresis region, especially, nearly disappears and is moved to lower flow rates at high pressure rise. Experiments with thinner Velcro have not been realized.

WAKE DEVELOPMENT DOWNSTREAM OF A TRANSONIC TURBINE INLET GUIDE VANE WITH TRAILING EDGE EJECTION

Cornelis Kapteijn
Institut für Strömungsmechanik
Deutsche Forschungsanstalt für Luft- und Raumfahrt e.V.
Bunsenstrasse 10
37073 Göttingen, Germany

ABSTRACT

The temperature at the inlet of modern high pressure turbines requires an effective cooling of the nozzle guide vanes. This project investigates an annular cascade of internally cooled nozzle guide vanes with bleeding through a slot at the pressure side near the trailing edge. Purpose of the actual work is the determination of the downstream flow field undisturbed by the presence of the rotor with emphasis on the mixing process between main flow and coolant flow. During the second part of this project the investigation of a complete stage will take place, where the present results will enable the elucidation of the flow field deviations due to the rotor presence.

NOMENCLATURE

b_{th}	throat width
c	chord
c_m	coolant mass flow rate
d	width of the coolant slot
M	Mach number
p	pressure
T	temperature
Tu	turbulence degree
g	pitch of the cascade
te	trailing edge thickness
v	velocity
x	coordinate in axial direction
y	coordinate in circumferential direction
α	angle between flow direction and axial direction
δ	trailing edge wedge angle
γ	stagger angle
θ	count rate of particles
ρ	density
σ	standard deviation
subscripts	
0	total (pressure, density or temperature)
1	homogeneous flow upstream
2	homogeneous flow downstream
2y	measuring plane downstream
ax	axial
is	isentropic
u	longitudinal direction
v	transverse direction

INTRODUCTION

The experiments were carried out in the rotating cascade windtunnel (RGG) at DLR Göttingen. This continuous operating windtunnel is of the closed circuit type, enabling Reynolds number variation by change of the total pressure in the settling chamber independent of Mach number variation. Figure 1 shows schematically the layout of the windtunnel; the measurement chamber in Fig. 2 with its cylindrical test section enables a blade height of 36 mm . A description of the RGG windtunnel was written by Amecke and Kost [1].

An annular cascade of inlet guide vanes of a high pressure turbine stage was investigated. The blades are hollow to enable internal cooling, with a coolant supply at the hub through one radially mounted tube; the bleeding of coolant takes place through a slot at the pressure side near the trailing edge. The slot, which extends from hub to tip, is generated by cutting off blade material at the pressure side over the last 10 % of the chord.

Main flow and coolant air had the same total temperature, i.e. $T_0 = 305$ K, the total pressure in the settling chamber was at $p_0 = 1,32.10^5$ Pa, resulting in $Re_2 = 9,52.10^5$ at a homogeneous downstream isentropic Mach number of $Ma_{2,is} = 1.05$. Fig. 3 shows a picture of the cascade at midspan and table 1 presents a list of characteristic data.

isentropic outlet Mach no.	$M_{2,is}$	=	1.05
inlet flow angle	α_1	=	90.0 °
outlet flow angle	α_2	=	70...75 °
pitch-to-chord ratio	g/c	=	0.75
chord length	c	=	49.92 mm
axial chord length	c_{ax}	=	29.86 mm
throat width	b_{th}	=	10.6 mm
stagger angle	γ	=	51.9 °
trailing edge thickness	te	=	1.18 mm
width of the coolant slot	d	=	0.4 mm
trailing edge wedge angle	δ	=	6.4 °
number of blades	N		43.

Table 1: Cascade parameters

MEASUREMENT SYSTEM

A twodimensional laser-two-focus measurement system was used in two different ways, i.e. as a velocity measurement system , resulting in local Mach number, flow angle,

Paper presented at the AGARD PEP 85th Symposium on "Loss Mechanisms and Unsteady Flows in Turbomachines", held in Derby, United Kingdom, 8-12 May 1995, and published in CP-571.

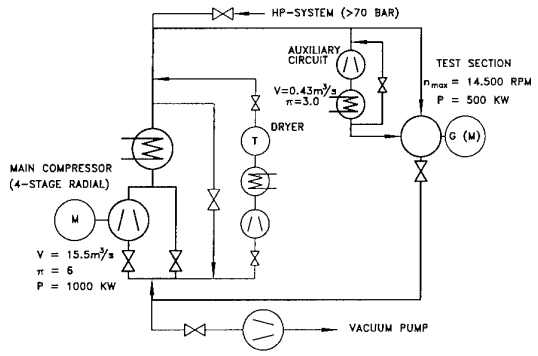

Figure 1: Windtunnel for rotating cascades with ejection system.

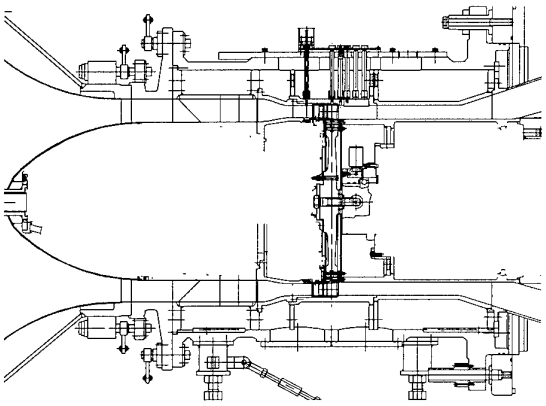

Figure 2: Measurement chamber of annular cascade windtunnel.

turbulence intensities in main stream - and in transverse direction and Reynolds' shear stress, or as a particle counter. A detailed description of the l2f-measurement system was written by Schodl [3], in Kost [2] the application to an annular cascade windtunnel was treated.

For the use as a particle counter one of the systems two photomultipliers suffices. These count rates visualize the mixing process between main stream and coolant air in the wake of the cascade using only a fraction of the measurement time needed for standard l2f-velocity-measurements, as the stepwise variation of the angle between the two focus points is abandoned. In both cases the experiments were done at midspan in the wake of the cascade, taking traverses parallel to the cascade exit plane. The laser beam was directed in radial direction, the radial component of the particle velocity therefore could not be detected.

Either the main flow was seeded in the settling chamber or seeding of the coolant air took place in the supply tube. Oil particles, the diameter of which was typically $0,1\mu m$ with a maximum of $0,3\mu m$, were used as seeding material.

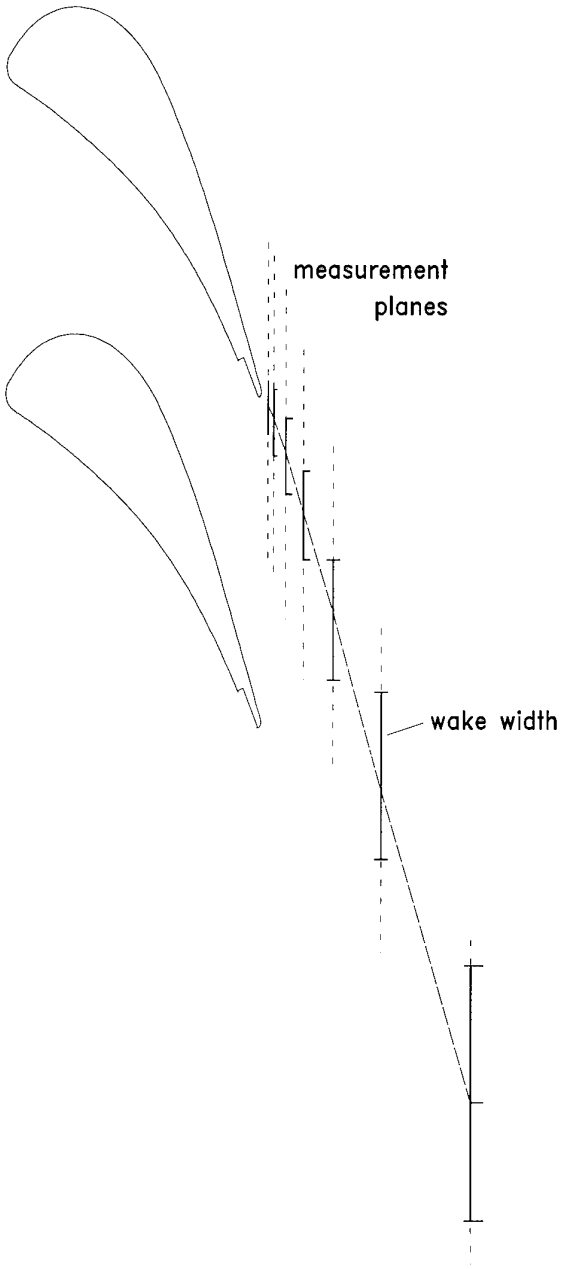

Figure 3: Cascade of nozzle guide vanes with coolant slot at the pressure side. The dashed lines parallel to the cascade exit plane mark the measurement traverses. The solid lines indicate the growth of the mixing area.

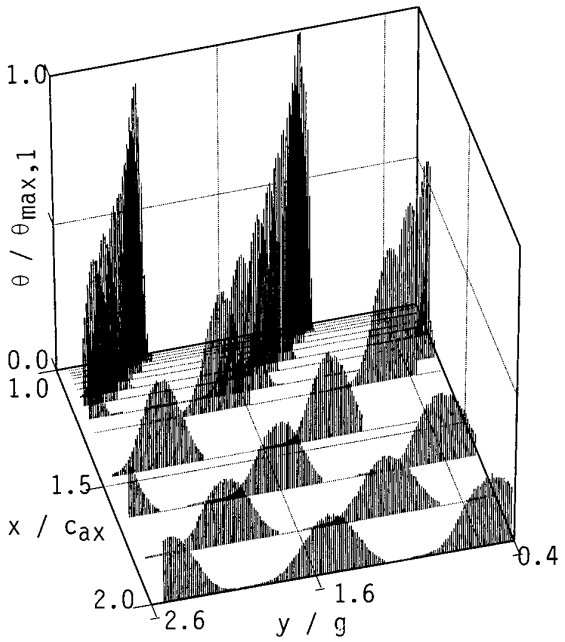

Figure 4: Distribution of particle count rate measured in 14 traverses between x/c_{ax} = 0.012 and x/c_{ax} = 1.000.

- Seeding of the coolant flow: count rates were measured in 14 planes at distances x/c_{ax} between 1.01 and 2.00 . l2f-velocity-measurements took place in 4 planes at distances x/c_{ax} between 1.02 and 1.16 . The step in circumferential direction was chosen 0.1°, i.e. 83 points per pitch, enabling detailed information about rise and fall of the count rate in the wake.
- Seeding of the main flow: l2f-measurements were carried out in 9 measurement planes at distances x/c_{ax} between 1.02 and 2.00 . The traversing mechanism of the stator enabled the investigation of two passages; the density of the measurement points was fixed at 16 per passage.

MEASUREMENT RESULTS

In Fig. 4 the results of the particle counting experiments in the wake of the cascade are drawn. Close to the cascade exit plane the axial distance between adjacent measurement planes is much less than farther downstream, as the strong gradients occur close to the blades. The comparability between the count rates of neighbouring blades is good, although the maximum count rate of the lower blade (at left) in the first measurement plane is about 10 % less than the maximum of the upper blade. The distances among the measurement planes are small enough to visually connect the maxima of the traverses into a gradually decaying curve.

Fig. 5 shows an example of the results of the l2f-system at x/c_{ax} = 1.023 and a coolant mass flow rate of 3 %. The dimensionless coordinate in circumferential direction y/g is 0 at the leading edge of the upper blade in Fig. 9, the leading edge of the lower blade is at y/g = -1. The seeding particles in the coolant air reach at this axial position only a small fraction of the pitch, the results in case of coolant flow seeding therefore only cover the pressure side part of the wake. The Mach number curves generally show a good agreement between both ways of seeding, with only a slight deficit in Mach number for the seeded coolant flow. The flow angle of the coolant flow on the other hand significantly differs from the flow angle of the seeded main flow. Only at one measurement point both happen to be identical; this point, at y/g = -1.1, is lying straight downstream of the trailing edge of the blade. The turbulence intensities outside of the wake are about 2%. The rise of the turbulence levels in the wake is remarkable, reaching a maximum of almost 30 % in longitudinal and 17 % in lateral direction. The change of sign in Reynolds shear stress is evoked by vortex shedding at the trailing edge of the turbine blade.

WAKE MIXING PROFILES

The mixing profiles of a plane jet and a uniform velocity field are expected to behave as gaussian curves with a standard deviation that is growing with axial distance. In the wake of the cascade main flow and coolant flow mix in a similar way. Because of the differences in flow parameters between pressure side and suction side of the passage flow the gaussian curve is divided in a suction side and a pressure side part, with separate parameters:

$$\theta_{ss} = \theta_{max} \exp\left(-\frac{(y-\bar{y})^2}{2\sigma_{ss}^2}\right) \quad (1)$$

and

$$\theta_{ps} = \theta_{max} \exp\left(-\frac{(y-\bar{y})^2}{2\sigma_{ps}^2}\right) \quad (2)$$

for suction and pressure side of the wake, respectively. In these equations, θ denotes the count rate of oil particles, θ_{max} the maximum in a particular traverse.

The parameters θ_{max}, $\bar{y}$, σ_{ss} and σ_{ps} for every measurement traverse were deduced as follows: θ_{max} and its position $\bar{y}$ were determined by a paraboloid through the 3 measurement points at the maximum count rate. Integration of the exponential function and comparison with the area under the measured curve, carried out separately for suction and pressure side, led to σ_{ss} and σ_{ps}.

Two examples of measured count rate curves and corresponding gaussian curves are shown in Fig. 6. The discrepancy at x/c_{ax} = 1.01 at the suction side of the curve is generated by the position of the coolant slot at the pressure side of the blade, i.e. the interaction between wake and oil particle jet is still taking place. Farther downstream at x/c_{ax} = 2.00 the count rate profile behaves as a gaussian curve.

The downstream development of the position of the maximum count rate in a measurement traverse (i.e. x/c_{ax} = const.) in relation to the centre of the wake was investigated.

The wake centre can be detected by the minimum in Mach number, the maximum in the turbulence intensities or the point of zero Reynolds shear stress between minimum and maximum (Fig. 5). However Mach number and turbulence intensity in main flow direction usually are strongly influenced wenn a shock crosses the measurement traverse. For this comparison therefore the turbulence intensity in lateral direction marked the centre of the wake. In Fig. 8 it is visible that the maximum count rate lies at the pressure side of the wake centre between trailing edge ($x/c_{ax} = 1$) and $x/c_{ax} = 1.6$. At larger distances from the cascade there exists hardly any difference between both curves. At $x/c_{ax} = 2$ the count rate maximum and wake centre do not separate again, which might be concluded from the graph. The rather large distance in circumferential direction between adjacent l2f measurement points in combination with the very smooth behaviour of the turbulence in lateral direction enlarge the error in the determination of the wake centre in the last measurement plane.

Fig. 7 shows the dependence of θ_{max}, σ_{ss} and σ_{ps} on the axial distance to the cascade. In the upper graph $\theta_{max,1}$ denotes the maximum count rate in the measurement plane closest to the cascade. The continuous decay in the maximum count rate with axial distance is accompanied with a steadily rising standard deviation of the gaussian distribution. The differences between the standard deviation on suction and pressure side are rather small; close to the cascade, i.e. at $x/c_{ax} < 1.1$, the count rate distribution exhibits a more gradual decay at the suction side. As 3σ may be interpreted as the limit of the particle distribution, the jet at $x/c_{ax} = 2.0$ covers about 80 % of the pitch.

In Abramovich [4] the maximum concentration in a plane jet as a function of the distance $s - s_0$ from the injection point is described as:

$$\frac{\theta_{max,s}}{\theta_{max,s_0}} = \frac{const}{\sqrt{(s - s_0)}} \tag{3}$$

A least square fit resulted in the second line in the upper graph of Fig. 7. In this picture s is taken in axial direction, resulting in a constant of 0.219 and a start of the mixing process at $x/c_{ax} = 0.971$. The onset of mixing downstream of the slot position ($x/c_{ax} = 0.9$) may be caused by the vicinity of the pressure side of the trailing edge, which retards the mixing. Usually s is taken in main flow direction, which means downstream of the cascade an angle α_2 with respect to the axial direction. In that case the constant has to be divided by $cos(\alpha)$.

The validity of the measurement results can be checked by integrating in circumferential direction the number of oil particles in the wake of one turbine blade:

$$I = \int \theta cos(\alpha) dy \tag{4}$$

Neglecting threedimensional effects, i.e. gradients in particle count rate and flow angle in radial direction, this result must correspond with the output of particles from the blade and be equal in every measurement plane. As the variation in α is rather small in the region of high particle count rates, a global check of the number of particles in the wake gives the term $\theta_{max}(\sigma_{ss}+\sigma_{ps})$. The maximum in the relative variation of $\theta_{max}(\sigma_{ss} + \sigma_{ps})$ among the measurement traverses was 26 %. Close to the trailing edge ($x/c_{ax} < 1.2$) the relative variation typically was about 1%, the larger deviations occured farther downstream. One explanation for this discrepancy is the gradual reduction of the hub diameter at $x/c_{ax} > 1.25$. The design rotor, that is to be installed in future, with a conical hub prescribes the downstream duct area of the stator as well. The enlarged flow area reduces the particle count rates farther downstream of the cascade. Another explanation is the appearance of threedimensional effects in the annular cascade. The pressure drop from the outher cascade casing to the hub forces oil particles to be deviated into the hub direction.

Interpolation in axial direction of the count rate maximum and the standard deviations followed by calculation of the count rate in circumferential direction generated a detailed equidistant grid, which formed the basis for Fig. 9, showing the continuous mixing process between main flow and coolant jet.

CONCLUSION

The mixing process between main flow and coolant flow ejected from a slot at the pressure side of a transonic turbine inlet guide vane was experimentally investigated in an annular cascade windtunnel. The mixing process can be described using gaussian curves with separate standard deviations for pressure and suction side of the jet.

ACKNOWLEDGEMENTS

The author is grateful to the European Community for support of this research under contract IMT Area 3 Turbine Project AER2-CT92-0044.

REFERENCES

[1] Amecke, J. and Kost, F. III/.1 Rotating Annular Cascades. In Hirsch Ch. (Ed.) Advanced Methods for Cascade Testing, AGARD AG 328, 1993 .

[2] Kost, F. Längswirbelentstehung in einem Turbinenlaufrad mit konischen Seitenwänden, Dissertation Universität Göttingen, DLR-Forschungsbericht DLR-FB 93-13, Köln (1993).

[3] Schodl, R. Verfahren und Programm zur Auswertung der von einem L2F-Geschwindigkeitsmeßgerät gelieferten Meßdaten, DFVLR interner Bericht IB 352/2 (1981).

[4] Abramovich, G. N. The Theory of Turbulent Jets, English translation, Cambridge MA, The MIT Press (1963).

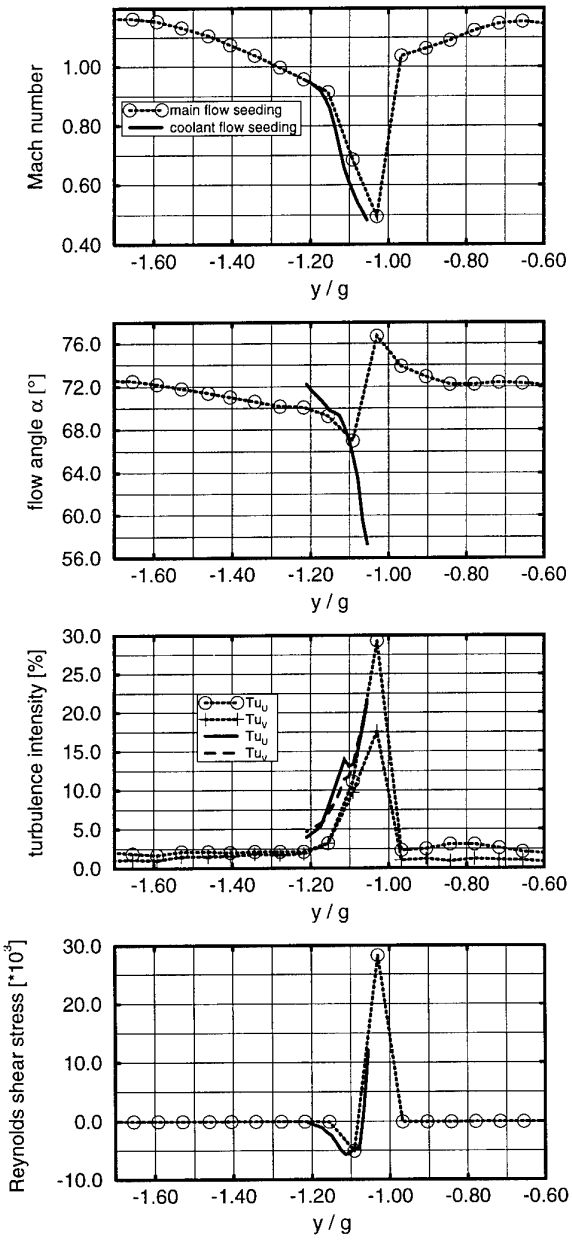

Figure 5: 12f measurement results with both seeding alternatives at $x/c_{ax} = 1.023$

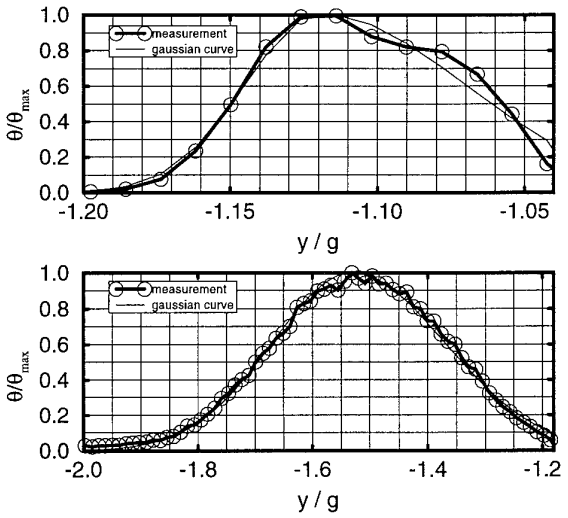

Figure 6: Distribution of particle count rate and corresponding gaussian curve at $x/c_{ax} = 1.012$ and at $x/c_{ax} = 2.000$ (lower picture)

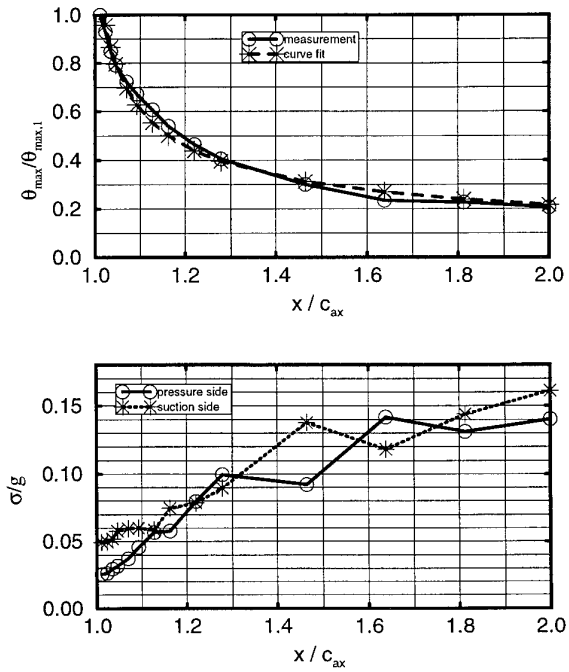

Figure 7: Development of maximum particle count rate and standard deviation (lower picture) of gaussian curves with axial distance.

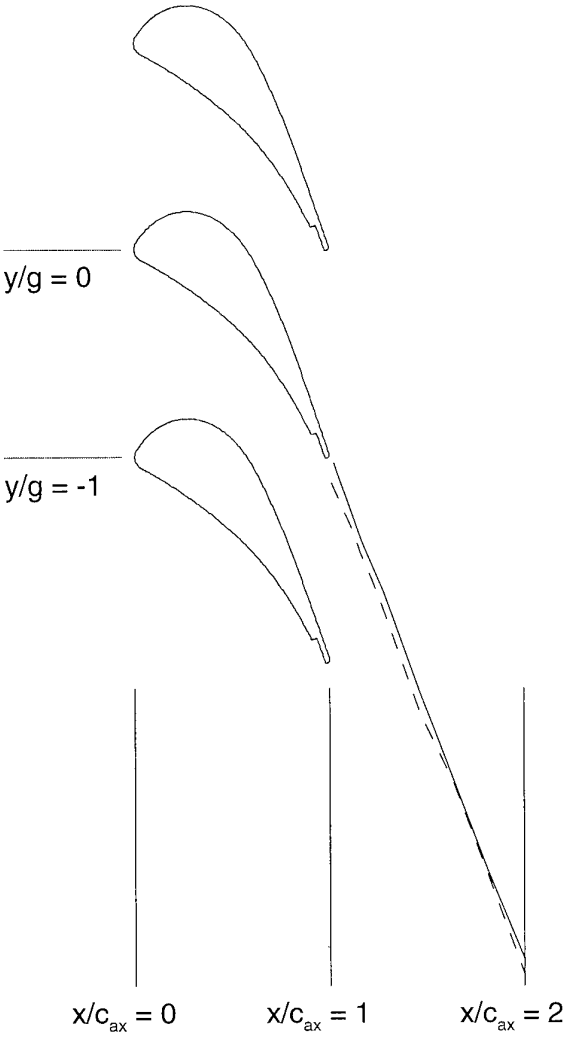

Figure 8: Position of the wake centre (—) and of the maximum count rate in a measurement traverse (- - -).

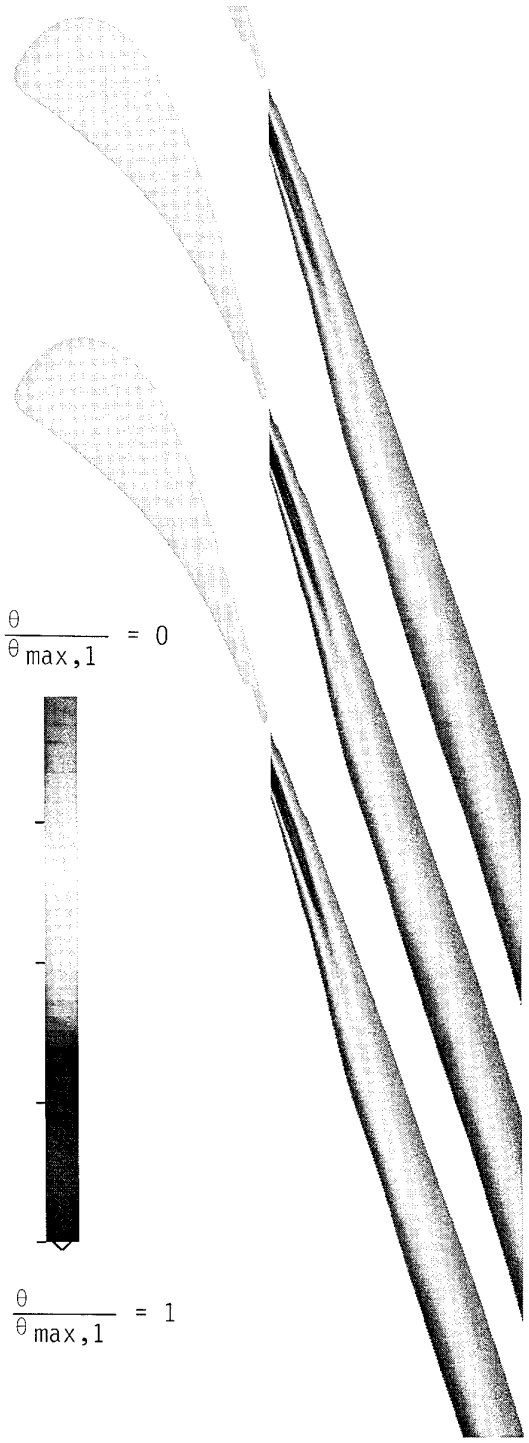

Figure 9: Interpolated particle count rate distribution downstream of the cascade at $M_{2,is} = 1.05$ and at $c_m = 3\%$.

REFERENCE NO. OF THE PAPER: 14

DISCUSSOR'S NAME: J. Dunham, DRA, U.K.

AUTHOR'S NAME: C. Kapteijn

Q: Did you also make any pressure measurements?

A: In a previous project, blade pressure distributions using pressure tappings and total and static pressure measurements with a wedge-type probe in the wake of this nozzle guide vane were carried out in a plane cascade wind tunnel.

In the rotating cascade facility, the total pressure was investigated in the wake of this cascade at 4 axial distances x/C_{ax} between 1.25 and 2.0.

FLOW PREDICTIONS IN TRANSONIC TURBINES USING NONPERIODIC GRIDS

A. Hamed, J.J. Yeuan and W. Tabakoff

Department of Aerospace Engineering and Engineering Mechanics
University of Cincinnati MS70
Cincinnati, Ohio, 45221-0070 USA

SUMMARY

Numerical results are presented for viscous flow through transonic turbine blades using different turbulence models and H-type grids. The numerical schemes for the solution of the compressible Navier-Stokes equations are developed with an option of conservative zonal approach for interpolation across non-periodic boundaries to minimize numerical errors. This makes it possible to use nonperiodic type grids which are more orthogonal and less skewed for improved accuracy in the prediction of turbine blade performance. The results obtained using traditional and nonperiodic H-type grids are compared with the experimental results for transonic turbine cascades and turbine stator vanes.

INTRODUCTION

Transonic turbine performance predictions is very challenging because of their high flow turning and the complexities associated with shock boundary layer interactions on the blade surface. In addition, the shock structure at the blade trailing edge which is determined by the viscous flow in the base region and the mixing losses generated immediately downstream of the trailing edge [Mee et al. (1990)] further complicate their flow fields at supersonic exit Mach numbers. Under these conditions, the traditional periodic grids commonly used in turbomachinery flow computations become highly sheared on the blade surface and in the wake region leading to inaccuracies due to numerical dissipation.

In the present investigation, numerical solutions are obtained for the compressible Navier-Stokes equations in conservation law form and general curvilinear coordinates using traditional and nonperiodic H-type grids. The computational results for the complete Navier-Stokes equations with algebraic and two equation turbulence models are presented for the flow field and compared with the experimental results in a transonic turbine cascade tested in four European wind tunnels (Kiock et al., 1986). Computational results for the two different H-type grids (traditional and nonperiodic) are also presented for a turbine stator and are compared with the experimental results of Goldman et al. (1975, 1982). Both the two dimensional results for the transonic turbine cascade and the 3-D results for the turbine stator indicate improved predictions with the latter grid type. The improvements are especially noticeable toward the trailing edge of the suction surface where a near orthogonal mesh replaces the highly skewed mesh of the traditional H-type grid.

COMPUTATIONAL METHOD

Numerical solutions are obtained for the Reynold's time averaged Navier-Stokes equations in conservation law form and general curvilinear coordinates. Two turbulence closure models are considered, first an algebraic turbulence model [Baldwin and Lomax (1978)] in the blade passage and a formulation by Thomas (1979) beyond the trailing edge, which does not require the determination of the wake centerline in the unbounded flow regions. In addition, the low Reynold's number k-ε turbulence model of Nichols (1990) for compressible flow was considered since it was found to give better agreement with the experimental data for shock boundary layer interactions [Hamed (1992)].

At inlet, the total pressure and the total temperature are specified while the density and energy are calculated from isentropic relations, and Riemann invariant is used to update the inlet meridional velocity. At exit, the static pressure is specified at the hub, and the radial pressure distribution is obtained from the integration of the radial momentum equation. Other flow quantities are obtained using first order extrapolation. The normal momentum equation based on first order accurate one sided differencing is used to calculate the blade surface pressure. The periodic boundary conditions require special treatment in the

Paper presented at the AGARD PEP 85th Symposium on "Loss Mechanisms and Unsteady Flows in Turbomachines", held in Derby, United Kingdom, 8-12 May 1995, and published in CP-571.

nonperiodic type grid in order to insure that the interpolation is conservative. Rai (1986) proposed an interpolation scheme for Euler equation based on the contravariant flux vectors that satisfies the global conservation properties of the flux vectors across the zonal boundaries. Since the flux vectors are generally not perpendicular to the control volume boundaries in the present investigation, the interpolation scheme is applied directly to the state vectors to preserve the local conservation properties. Linear interpolation along the periodic boundaries is used to update the state vector at grid points on the coarse side, while cubic spline-fit of the coarse side state vector is used to update the grid points on the dense side boundaries. This treatment has previously been verified in inviscid transonic turbine cascade flow solutions [Yeuan, Tabakoff and Hamed (1992)].

The three dimensional flow solutions in the transonic turbine stator were obtained using an implicit solver based on Pulliam's diagonalized numerical algorithm [Pulliam and Steger (1980)]. Jameson-style second order damping was implemented and local time stepping was used to speed up the convergence.

The two dimensional flow solutions in the transonic turbine cascade were obtained by advancing the numerical solution in time using the explicit five stage cell centered Runge-Kutta scheme [Holmes et al. (1985, 1989)]. The explicit Runge Kutta was used in turbomachinery flow computations by Chima (1986, 1988, 1992), Jennions and Turner (1993), Turner et al. (1993), Arnone (1993) and Dawes (1991) because of the flexibility it offers in implementing different computational strategies such as multiple, adaptive and unstructured grids. Second and fourth difference smoothing are applied with the switching of second difference smoothing controlled by second derivative pressure differences in the Navier-Stokes and k-ε equations [Shih et al. (1994)]. Local time stepping with a constant Courant number of 0.95, is used to obtain the steady solutions.

RESULTS AND DISCUSSIONS

Computational results are presented for the two dimensional flow in a transonic turbine cascade and compared with the experimental results obtained by Kiock et al. (1986), at inlet turbulence level of 1%. Three dimensional computational results are presented for the turbine stator vanes designed and tested by Goldman et al. (1975, 1982).

Turbine Stator Vanes

An annular cascade of constant profile turbine stator vanes was developed and tested at NASA Lewis by Goldman and Seasholtz (1982) and Goldman and McLallin (1975). The annular ring has 36 vanes with a hub-tip radius ratio of 0.85 and a tip diameter of 508 mm. The vanes have an axial chord of 38.23 mm and a blade height of 38.10 mm. Design flow conditions are for a fully axial inflow with a hub-static to inlet-total pressure ratio of 0.6705 with an average inlet and exit Mach number of 0.665. The Reynolds number based on axial chord is 1.73×10^5. The implicit three dimensional flow solution in the turbine stator was obtained using the algebraic turbulence closure model Baldwin and Lomax (1978), without modeling the experimentally measured boundary layer at the vane inlet. The 99x51x33 periodic and nonperiodic H-type grids used in the numerical solution for the turbine stator are shown in Figs. 1 and 2. One can see that the nonperiodic H-type is near orthogonal from the throat to the trailing edge and is less skewed over the rest of the blades. The initial spacing at the wall was equal to 0.03% of the axial chord in both grids. Starting from freestream conditions, all 3-D computations converged within 1500 iterations based on maximum pressure and density changes of 1.0×10^{-4}.

Figures 3 and 4 show the calculated blade surface pressure distributions and the experimental data obtained by Goldman and Seasholtz at 13.3, 50.0 and 86.6 percent span. According to these results, much better agreement with the experimental data is obtained with the nonperiodic grid, especially over the last 40% of the axial chord on the suction surface. The nonperiodic grid requires further refinement, however to improve the grid placement on the suction surface between 30% and 50% of the axial chord. No attempt was made to compare the computational results with the experimental data for the efficiency contours downstream of the trailing edge, since the inlet boundary layers whose thicknesses were measured to be 1.9% and 71.1% of the span at the hub and tip, were not simulated in the current solution.

Transonic Turbine Cascade

The design parameters and flow conditions for the transonic cascade are summarized in Tables (1) and (2). The computations were performed for two

types of H grids with the same number of mesh points (222x51). The traditional H-type mesh shown in Fig. 5 has 236 points on blade surface, while the nonperiodic H-type grid mesh shown in Fig. 6 has 139 points on the blade suction surface and 61 points on the blade pressure surface. The first grid point next to the blade was at Y^+ between 0.5 to 2.5 over most of blade surface except in the leading edge region. The convergence criteria was based on local maximum pressure error of $1x\ 10^{-4}$ and RMS residual of 10^{-6}. Approximately 1500 iterations were sufficient to achieve this level of convergence. The computed results are presented in Figs. 7 through 12.

Comparing Figs. 7 and 8 for the Mach number contours, one can observe improved flow resolution over the second half of the blade suction surface and downstream of the blade with the nonperiodic grid. This is especially clear in capturing the shock near the suction surface trailing edge which is very crisp in the predictions with the nonperiodic H-type grid. Thicker boundary layers and wakes can be observed in the results obtained using the traditional H-type grid (Fig. 7) due to numerical dissipation in the highly skewed grid in these regions. This leads to overpredicting the losses as discussed later in connection with Fig. 12.

The results for the surface isentropic Mach number are presented and compared with the experimental results in Figs. 9 and 10. One can see better agreement between experimental and computed results with the nonperiodic type grid in terms of the local peak in the isentropic Mach number on the suction surface at x/c=0.61. The figures further indicate no major improvement in the predictions with the k-ε turbulence model over the algebraic turbulence model.

The predicted exit flow angles and loss coefficients at one subsonic and one transonic condition are compared with the experimental data at 0.5 chord length downstream of trailing edge are in Figs. 11 and 12. The largest difference in the computed exit flow angles is observed in transonic flow predictions with the Baldwin-Lomax model and traditional grid. Figure 12 shows that the computations based on the traditional type grid grossly overpredict the loss coefficient by a factor of more than 2. This can be attributed to the inferior modeling of the shock boundary layer interactions over the blade surface and to the numerical dissipation associated with the highly skewed grid over the blade suction surface and downstream of the trailing edge. The predicted loss coefficient using the nonperiodic type grid are generally much closer to the experimental results, and are within 10% in the transonic case with the k-ε model.

CONCLUSIONS

Numerical solutions to the compressible Navier-Stokes equations were obtained in transonic turbine cascades and stator turbine vanes using traditional and nonperiodic H-type grids. The results indicate that grid skewness in the traditional H-type grid adversely affects the prediction of loss coefficient, and smear the large flow gradient in the aft part of the suction surface and the shock at the trailing edge. The solutions obtained with the nonperiodic H-type grid are in closer agreement with the measured surface pressure distribution, especially on the pressure surface, near the trailing edge. The closest agreement with the experimental losses and exit flow angles are obtained with the compressible k-ε turbulence closure model but the algebraic model results are not too different in the case of nonperiodic H-type grid.

REFERENCES

Arnone, A. (1993), "Viscous Analysis of Three-Dimensional Rotor Flows Using a Multigrid Method," ASME Paper No. 93-GT-19.

Baldwin, B. and Lomax, H. (1978), "Thin-Layer Approximation and Algebraic Model for Separated Turbulent Flows," AIAA Paper 78-257.

Beam, R. and Warming, R.F. (1976), "An Implicit Finite Difference Algorithm for Hyperbolic System in Conservation Law Form," Journal of Computational Physics, Vol. 22, No. 1, pp. 87-110.

Chima, R.V. (1986), "Development of An Explicit Multigrid Algorithm for Quasi-Three-Dimensional Viscous Flows in Turbomachinery," NASA TM 87128, Jan..

Dawes, W.N. (1991), "The Development of a Solution Adaptive 3D Navier-Stokes Solver for Turbomachinery," AIAA Paper 91-2469.

Goldman, L.J. and McLallin, K.L. (1975), "Cold-Air Annular Cascade Investigation of Aerodynamic Performance of Core-Engine-Cooled Turbine Vanes.

1: Solid-Vane Performance and Facility Description," NASA TM X-3224.

Goldman, L.J. and Seasholtz, R.G. (1982), "Laser Anemometer Measurements in an Annular Cascade of Core Turbine Vanes and Comparison with Theory, NASA TP 2018.

Hamed, A., (1992), "An Investigation of Oblique Shock/Boundary Layer Interaction Control," Progress Report on AFOSR Contract No. 91-0101.

Holmes, D.G. and Tong, S.S. (1985), "A 3-D Euler Solver for Turbomachinery Blade Rows," ASME Journal of Engineering for Gas Turbines and Power, Vol. 107.

Holmes, D.G. (1989), "Numerical Methods for Flows in Turbomachinery - Inviscid 3D Solution Methods," von Karman Institute for Fluid Dynamics, Lecture Series 1989-06.

Jennions, I.K. and Turner, M.G. (1993), "Three Dimensional Navier-Stokes Computations of Transonic Fan Flow Using an Explicit Flow Solver and an Implicit k-ε Solver," Tans. of ASME, Journal of Turbomachinery, Vol. 115, pp. 261-272.

Kiock, R., Lehthaus, F., Baines, N.C. and Sieverding, C.H. (1986), "The Transonic Flow Through a Plane Turbine Cascade as Measured in Four European Wind Tunnels," Journal of Engineering for Gas Turbines and Power, Vol. 108, pp. 277-284.

Mee, D.J., Baines, N.C., Oldfield, M.L.G. and Dickens, T.E., (1990) "An Examination of the Contributions to loss on a Transonic turbine Blade in Cascade," ASME Paper 90-GT-264, June.

Nichols, R.H. (1990), "A Two-Equation Model for Compressible Flows," AIAA-90-0494.

Pulliam, T. and Steger, J. (1980), "Implicit Finite-Difference Simulations of Three-Dimensional Compressible Flow," AIAA Journal, Vol. 18, pp. 159-167.

Rai, M.M. (1986), "A Conservative Treatment of Zonal Boundaries for Euler Equation Calculations," Journal of Computational Physics, Vol. 62, pp 472-503.

Shih, S.H., Hamed, A. and Yeuan, J.J. (1994), "Unsteady Supersonic Cavity Flow Simulation Using k-ε and Navier-Stokes Equations," AIAA Journal, Vol. 32, No. 10, October, pp. 2015-2021.

Thomas, P.D. (1979), "Numerical Method for Predicting Flow Characteristics and Performance of Nonaxisymmetric Nozzles-Theory," Langley Research Center, NASA CR 3147, September.

Turner, M.G., Liang, T. and Jennions, I.K. (1993), "The Use of Orthogonal Grids in Turbine CFD Computations," ASME Paper No. 93-GT-38.

Yeuan, J.J., Tabakoff, W. and Hamed, A. (1992), "Inviscid Quasi 3D Flow Solutions in a Transonic Turbine Cascade Using Conservative Zonal Boundaries for a Nonperiodic H-type Grid," The Foruth International Symposium on Transport Phenomena and Dynamics of Rotating Machinery, Honolulu, Hawaii.

Table 1

Spacing / Chord (S/C):	0.71
Exit Blade Angle (arc cos(O/S)):	67.8
Inlet Blade Angle:	33.3 deg.
Inlet Flow Angle:	30.0 deg.
Chord Length:	60.0 mm

Table 2

	Transonic
Inlet Flow Angle	30.000
Inlet Mach Number	0.282
Exit Flow Angle	67.020
Exit Mach Number	0.957
Exit Reynold Number	8.8 x 105

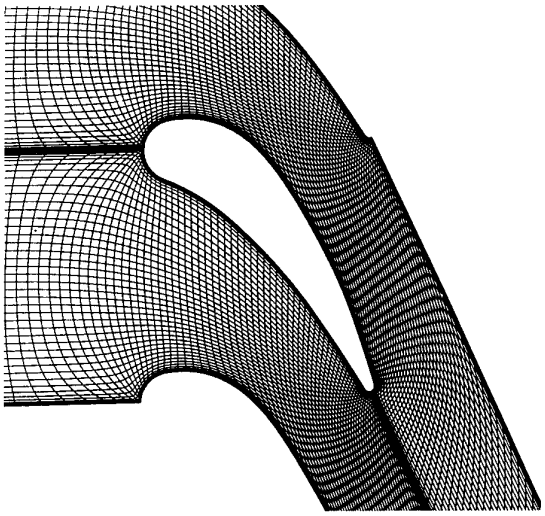

Fig. 1. Traditional H-Type Grid for Turbine Stator

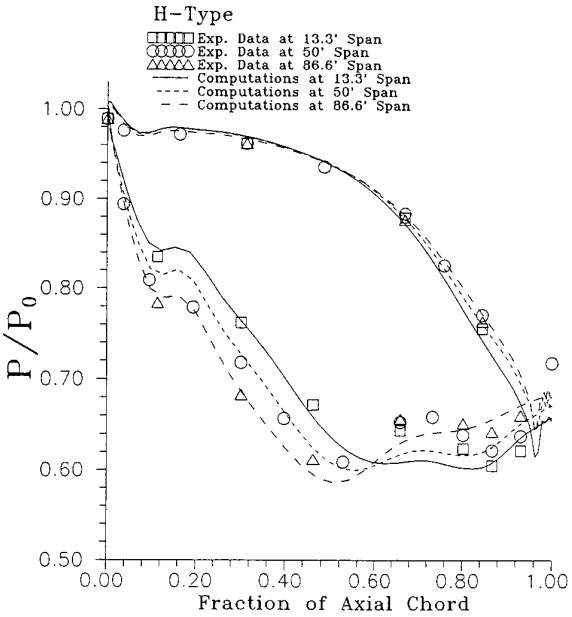

Fig. 3. Vane Surface Pressure Distribution for Turbine Stator (Traditional H-Type Grid).

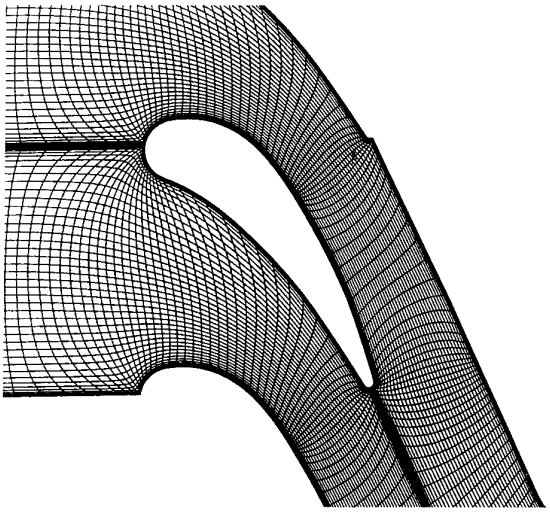

Fig. 2. Nonperiodic H-Type Grid for Turbine Stator.

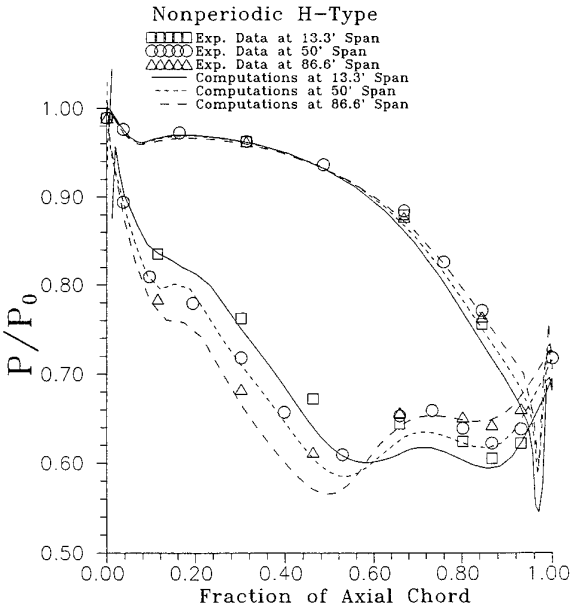

Fig. 4. Vane Surface Pressure Distribution for Turbine Stator (Nonperiodic H-Type Grid).

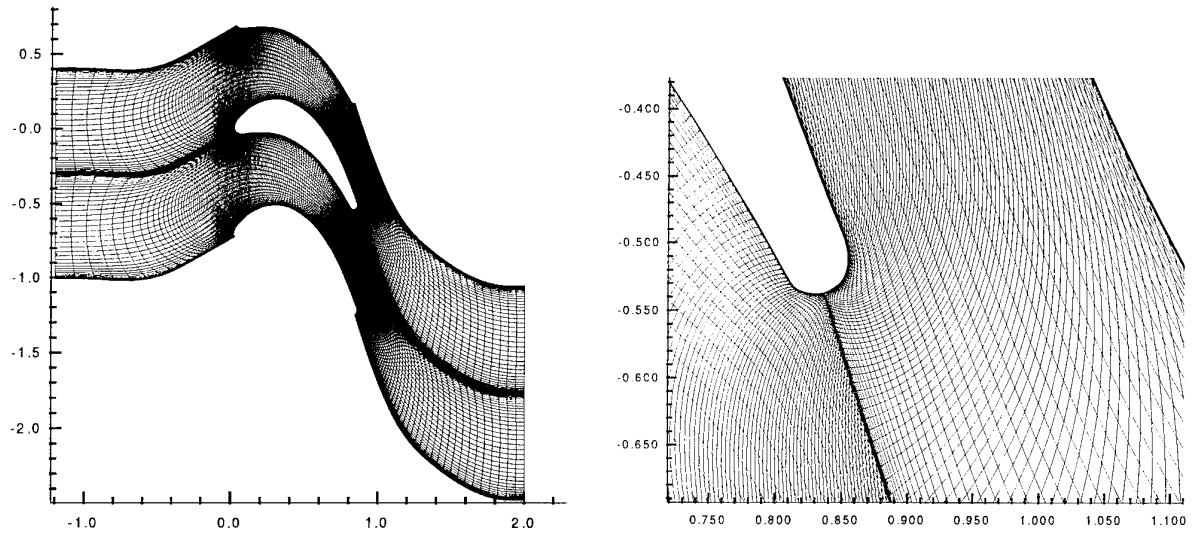

Fig. 5. Traditional H-Type Grid for Transonic Cascade.

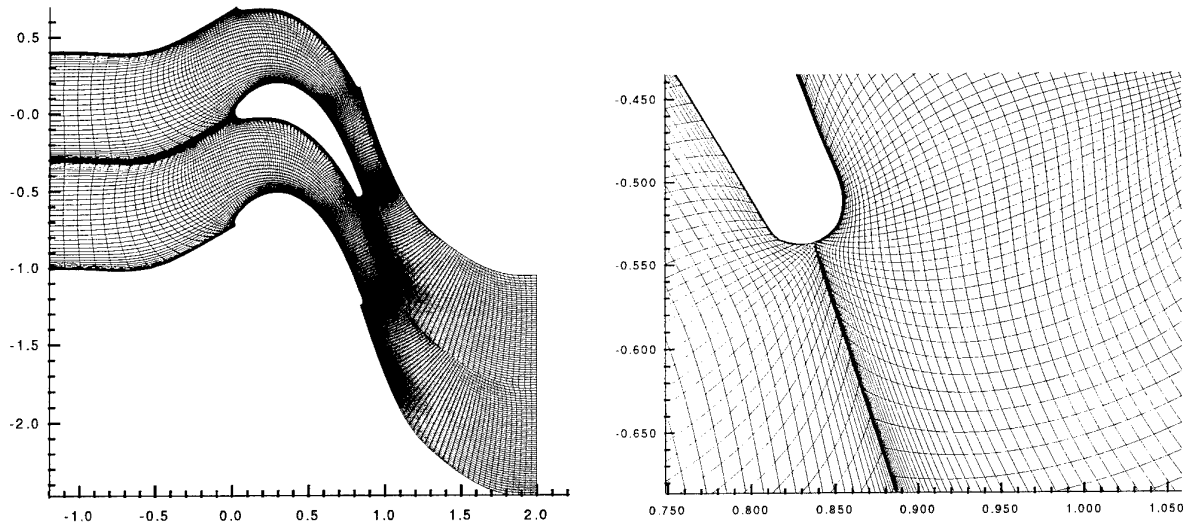

Fig. 6. Nonperiodic H-Type Grid for Transonic Cascade.

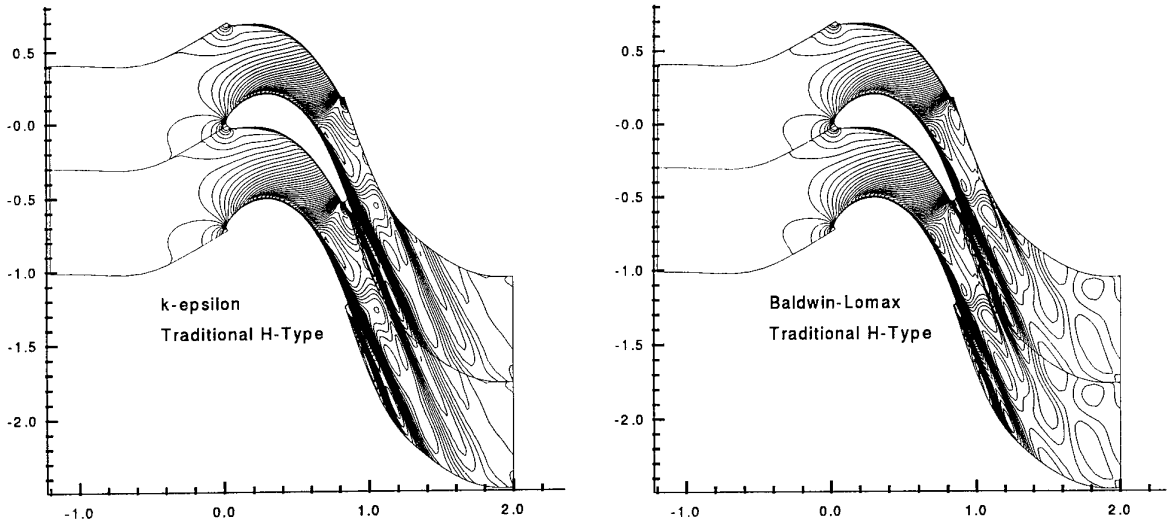

Fig. 7. Mach Number Contours Obtained from Traditional H-Type Grid for Transonic Cascade (M_{max} = 1.14, M_{min} = 0.14, Increment = 0.02).

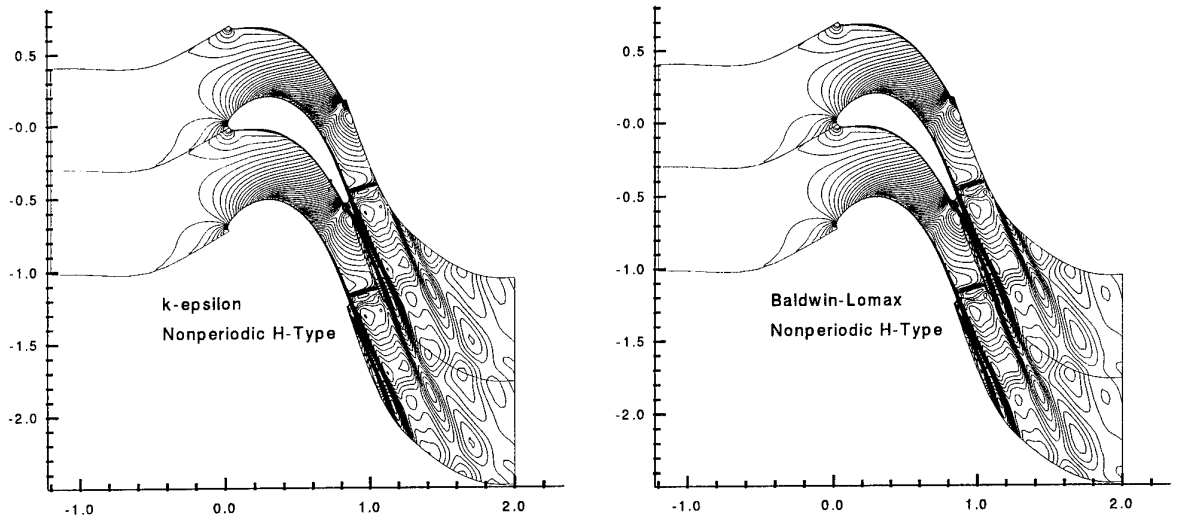

Fig. 8. Mach Number Contours Obtained from Nonperiodic H-Type Grid for Transonic Cascade (M_{max} = 1.14, M_{min} = 0.14, Increment = 0.02).

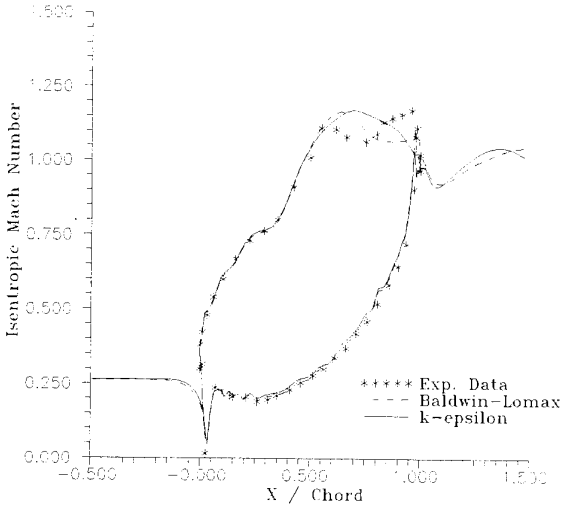

Fig. 9. Surface Isentropic Mach Number (Traditional H-Type Grid).

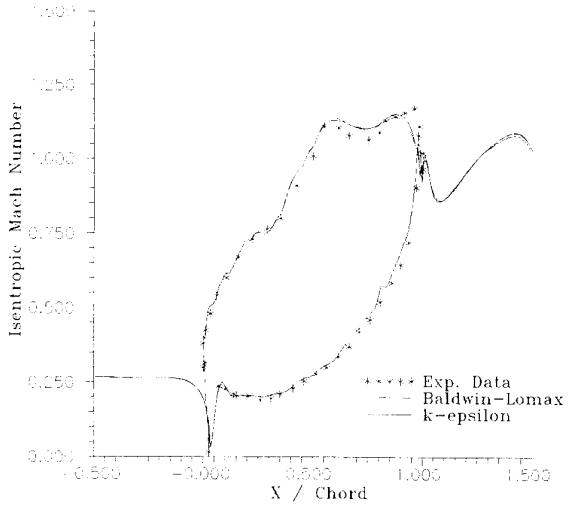

Fig. 10. Surface Isentropic Mach Number (Nonperiodic H-Type Grid).

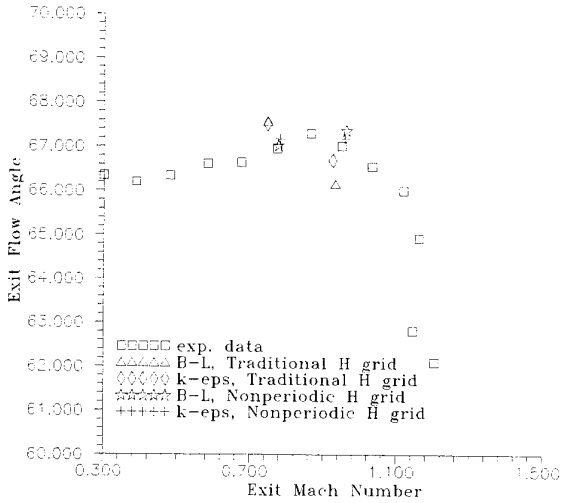

Fig. 11. Exit Flow Angle.

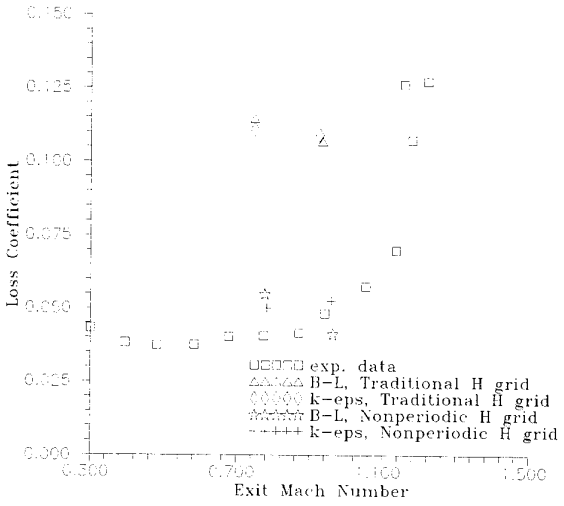

Fig. 12. Loss Coefficient.

REFERENCE NO. OF THE PAPER: 15

DISCUSSOR'S NAME: F. Eulitz, DLR, Germany

AUTHOR'S NAME: A. Hamad

Q:1 In the introductory remarks, you mentioned among other turbulence models the k-ω model. Have you gained any experience with the k-ω model for the present application?

A:1 We have not used the k-ω model in the current application. However, we had experience applying it to oblique-shock/turbulent boundary layer interactions over a flat plate. This was done in an extensive investigation of different algebraic and two-equation (k-ε and k-ω) turbulence models to assess and validate the computational results. Comparisons were made with the experimental data for surface static pressure distribution and the location of the separation and reattachment points.

Q:2 You applied an implicit solver to the first (subsonic) test case. What was the reason for applying an explicit time marching scheme to the transonic case which seems to be a greater challenge to numerical stability?

A:2 The transonic cascade simulations were conducted first, and at that time we had not completed the development of the implicit scheme which we are currently using in turbomachinery flow simulations.

Development of an Off-Design Loss Model for Transonic Compressor Design

Gregory S. Bloch
William W. Copenhaver
WL/POTF Bldg. 18
1950 Fifth Street
Wright-Patterson AFB, OH 45433-7251
USA

Walter F. O'Brien
Mechanical Engineering Dept.
Virginia Tech
Blacksburg VA 24061-0238
USA

Summary

A numerical investigation has been conducted to determine the changes in shock geometry that will occur with throttle setting for a modern transonic fan. The passage shock was found to be approximately normal near stall, with increasing obliqueness at higher mass flows. At peak efficiency, the shock system consists of an oblique passage shock followed by a normal shock, with the 2 shocks coalescing near the suction surface. As the back pressure is reduced further, the rotor becomes completely choked and the second shock moves downstream, becoming a separate, full-passage shock. The Mach number upstream of the second shock increases steadily as the shock moves downstream with decreasing back pressure. For all values of back pressure, the second passage shock is approximately normal to the predominant flow direction. Because the flow is supersonic downstream of the first passage shock, there are no changes in the first passage shock along this portion of the characteristic.

A simple, but fundamentally based model has been developed which captures the qualitative trends of shock performance over the entire range of design-speed mass flows for a transonic fan. Model predictions are compared with measured data at multiple spanwise locations. The results of the comparison suggest that shock losses contribute a significant share of the total loss, but other mechanisms must also be considered.

List of Symbols

c constant in profile loss correlation
i incidence angle
M Mach number
p static pressure
P total pressure
PR total pressure ratio
T temperature
U wheel speed
V absolute velocity
W relative velocity

GREEK SYMBOLS
α absolute flow angle
β relative flow angle
ε angle by which flow is turned by oblique shock
ϕ angle between flow direction and normal to shock surface
γ ratio of specific heats
η isentropic efficiency
ψ angle between flow direction and shock surface
ω cascade loss coefficient, $\left(P_{01} - \overline{P}_{02}\right)/\left(P_{01} - p_1\right)$

SUBSCRIPTS
N normal to the shock
R relative frame
x axial direction
θ tangential direction
0 total property
1 blade inlet station
2 blade exit station

Introduction

The detailed design of transonic compressors is typically performed using a streamline curvature method of solution of the equations of fluid motion. The flow is assumed to be axisymmetric, and the effects of entropy generation are included as total pressure losses determined from loss models. These types of models can be used either as analytical tools to predict the flow field from a known geometry, or in an inverse mode to predict the blade shape needed to generate a desired flow. While a direct solution of the Navier-Stokes equations can yield a more detailed description of the flow field for a known geometry, these methods are quite expensive in terms of computer resources and time required for solution. Also, such methods are not presently used in an inverse mode to provide the blade design required to generate a desired flow field.

It is generally accepted that streamline curvature methods will provide a satisfactory prediction of compressor performance as long as the losses and blockage are predicted accurately. In a transonic compressor, these are

Paper presented at the AGARD PEP 85th Symposium on "Loss Mechanisms and Unsteady Flows in Turbomachines", held in Derby, United Kingdom, 8-12 May 1995, and published in CP-571.

produced by casing and blade boundary layers, shocks, tip-leakage flows, secondary flows, and interactions among them. It is clearly beyond the scope of any single paper to address all of these areas, so discussion will be limited to profile and shock loss models.

Profile Loss

By considering only well designed blade shapes operating at minimum-loss incidence, Kqch and Smith (1976) developed a semiempirical correlation between cascade diffusion and trailing edge boundary layer parameters that accounts for blade thickness and has approximate corrections for compressibility and streamtube contraction. A compressible-flow mixing calculation similar to that of Stewart (1955) is then used to calculate the fully mixed profile loss coefficient. The model of Koch and Smith is generally accepted as the most fundamentally based profile loss model in the open literature, as it rationally accounts for many of the real-fluid phenomena that exist in a transonic compressor (Hirsch and Denton, 1981; Çetin, et al 1987), but application of the model is restricted to minimum-loss operation of well-designed airfoils.

For off-design operation of low-speed machines, the method of Lieblein (1957) can be used with reasonable accuracy. But for transonic compressors, the profile loss is typically assumed to vary in a parabolic fashion:

$$\omega = \omega_{DESIGN} + c\left(i - i^*\right)^2 \qquad (1)$$

where c is a function of inlet relative Mach number, blade profile shape, and whether the blade is operating at greater or less than design incidence. A substantial amount of empiricism is involved in this method, as the user must specify the range of incidence between design and stall, between design and choke, and the magnitude of loss at stall and choke. Curves obtained from this method for a given blade will not, in general, be the same as those for a different blade.

Shock Loss

Wennerstrom and Puterbaugh (1984) assumed that the passage shock in a transonic fan operating at the design point is a normal shock attached to the blade leading edge, after Miller, et al. (1961). Since the cascade stagger increases from hub to tip, the locus of points where the shock impinges on the suction surface is calculated for each streamline. This line is typically swept back relative to the flow as one proceeds from hub to tip, and the suction surface spanwise obliqueness angle is determined from the slope of this line. The Mach number on the suction surface is then calculated from a Prandtl-Meyer expansion from the upstream conditions to the suction surface blade angle. On the pressure surface, the shock sweep angle is assumed to be the leading edge sweep angle and the Mach number is assumed to be the upstream Mach number. The Mach number and sweep angle are assumed to vary linearly from pressure to suction surface, and a 3-point integration of shock loss is performed across the passage. Because this model does not include any change in shock geometry with throttle setting, its application is limited to design-point operation.

Prediction of off-design shock losses requires an accurate *a priori* knowledge of the shock geometry and Mach number (Balzer, 1970) or of flow angle significantly downstream of the shock (Freeman and Cumpsty, 1992). In both cases, the models are limited to the operating region between design point and surge. To the best of the authors' knowledge, none of the shock loss models in the open literature is applicable in the "unique incidence," or choked region of operation, and none are capable of predicting the performance of cascades with multiple shocks in the passage.

To summarize, presently used loss models do not include accurate, fundamentally based off-design prediction methods. While thoughtful application of these tools can estimate design-point operation with sufficient accuracy, as shown in Figure 1, off-design operation is predicted poorly for transonic machines. The off-design loss model used for this comparison was that of Lieblein (1957).

Although the fraction varies by aircraft mission, all man-rated aircraft spend a significant amount of their operating life away from the design point. To ensure meeting overall aircraft mission requirements, engine cycle decks must be used to perform mission analyses, engine operability studies must be performed, and engine control logic must be developed *before* the compression system hardware is tested. For each of these endeavors, the accuracy of the stage characteristics used as inputs to the prediction methods is critical to their ability to obtain meaningful information about engine performance (Saravanamutto and Fawke, 1970; Boyer and O'Brien, 1989; Dowler, et al., 1989). Therefore, the ability to meet overall propulsion system goals hinges on the ability to generate accurate off-design compressor stage characteristics rapidly, reliably, and early in the design cycle.

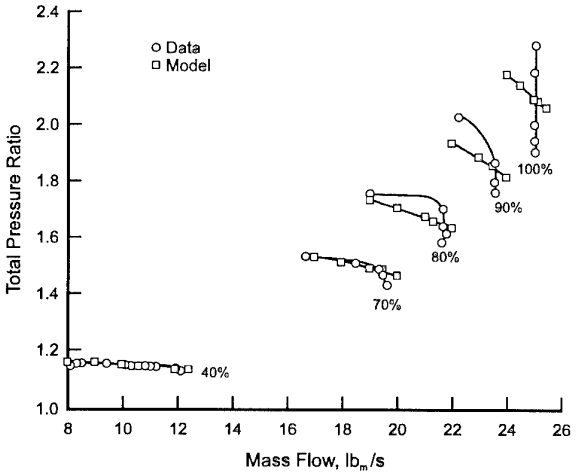

Figure 1. Predicted and measured performance for the first stage of a 3-stage transonic compressor.

One of the limitations of using Equation 1 to predict transonic compressor characteristics is a result of the condition described as "unique incidence". The discussion that follows is admittedly oversimplified because it ignores the effects of shock-boundary layer interaction and assumes that the leading edge radius is sufficiently small to allow an attached shock, but it serves to illustrate the point. For a blade section operating with supersonic relative inflow, there is typically a critical back pressure for which the passage shock can be closely approximated as being attached to the blade leading edge. As the back pressure is reduced, the shock may move farther back in the passage, but the flow upstream of the passage shock has the same Mach number and incidence, and application of Equation 1 will yield the same value of loss coefficient. But a larger value of loss coefficient must be generated to allow calculation of the lower downstream total pressures. This paper will present the foundation of a simplified shock loss model that will enable streamline curvature models to predict the choked portion of a transonic compressor characteristic more accurately.

Experimental Procedure

Test Article

The experiment was performed at the Wright Laboratory Compressor Aero Research Lab. This facility is configured for closed-loop testing of high-speed, high-specific-flow fans and compressors with a maximum power requirement of 2000 horsepower. A schematic of the compressor test rig is shown in Figure 2. Note that there are no inlet guide vanes or upstream struts in this test configuration. Details of the test facility are provided by Law and Wadia (1993) and Copenhaver, et al. (1993).

The rotor that is the subject of the current study, denoted "Rotor 4", is a low-aspect-ratio, high-through-flow, highly loaded configuration. Detailed design information on Rotor 4 was provided by Parker and Simonson (1982). The rotor overall performance was studied in detail by Copenhaver, et al. (1993) and Wadia and Copenhaver (1994). The stator configuration was designed through a computational fluid dynamics (CFD) technique as was reported by Copenhaver, et al. (1993).

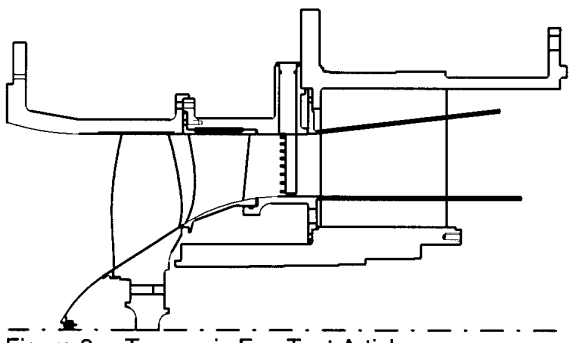

Figure 2. Transonic Fan Test Article.

Nominal stage performance and geometric information for Rotor 4 are given below:

Pressure ratio	2.00
Isentropic efficiency	88.7%
Corrected flow per annulus area (lbm/sec-ft^2)	43.0
Corrected tip speed (ft/sec)	1500
Approximate tip relative Mach number	1.6
Mean rotor aspect ratio	1.320
Rotor inlet hub/tip ratio	0.312
Mean tip clearance (% of tip chord)	0.5%

Rotor Exit Measurements

To establish rotor pressure ratio and efficiency, rotor exit total pressures and temperatures were obtained with calibrated wedge and thermocouple probes traversed in the spanwise direction through two two-axis actuators mounted on the casing. Traverse resolution in the radial direction is 0.01mm with a repeatability of 0.025mm and an overall accuracy in position of $\pm$0.05mm. Data were obtained at 24 discrete spanwise locations for three operating back pressures at 100% speed. In the yaw direction, both resolution and repeatability is 0.1degrees with an accuracy of $\pm$0.25degrees. The wedge probe was autonulled by the actuator to ensure accurate alignment with the flow. The thermocouple probe followed the flow angle established by the wedge probe. Both probes were calibrated prior to the test for total pressure and temperature recovery versus Mach number and pitch angle. These calibrations, based on pitch angle from a third probe, were applied to the raw total pressure and temperature measurements. Measurement uncertainty in the total pressure and total temperature were $\pm$0.05psi and $\pm$1.97°F, respectively, with a 95% confidence interval.

Shock Structure in a Transonic Fan

A numerical investigation was conducted into the changes in shock structure that will occur with throttle setting for Rotor 4. To establish the shock structure changes with operating point (back pressure), fully 3-D Navier-Stokes numerical solutions were obtained through the methods described by Hah (1987) for 7 operating points on the 100% speed line for the rotor only configuration. The grid was a 52 x 46 x 152 (circumferential x spanwise x axial) I-grid, and is shown in Figure 3. Of the 46 spanwise grid points, 40 are used to describe the blade and 6 are located in the tip clearance region. Other details of the CFD method can be found in Hah (1987), Hah and Wennerstrom (1991), and Copenhaver, et al. (1993). The numerical results at 18% rotor immersion were considered in this study to minimize the effects of the tip clearance flows. From a similar numerical study Puterbaugh (1994) reported for this rotor that the clearance flows influence the tip most 15% span. All results reported here are for 18% rotor immersion and greater, and are designated as the "free-stream region".

When this transonic fan rotor is operating near stall, the passage shock in the free-stream supersonic region is approximately straight, nearly normal to the mean flow direction and slightly detached from the blade leading edge, as shown in Figure 4. This and the following figures are for the 18% rotor immersion. As the back pressure is reduced, the shock becomes attached to the leading edge and is swept back into the passage.

Near peak efficiency, the passage shock has reached its maximum amount of obliqueness near the pressure surface, and is approximately straight from the pressure surface to a point very near the suction surface, as shown in Figure 5. The flow downstream of the oblique passage shock is still supersonic in the relative frame until encountering a second passage shock. The second shock is approximately normal to the mean flow direction, and coalesces with the first passage shock near the suction surface. This peak efficiency shock structure supports Denton's (1993) conclusion that a smaller entropy rise will occur if the same pressure rise is accomplished with 2 weak shocks, rather than 1 strong shock. At this flow condition, the rotor is almost choked.

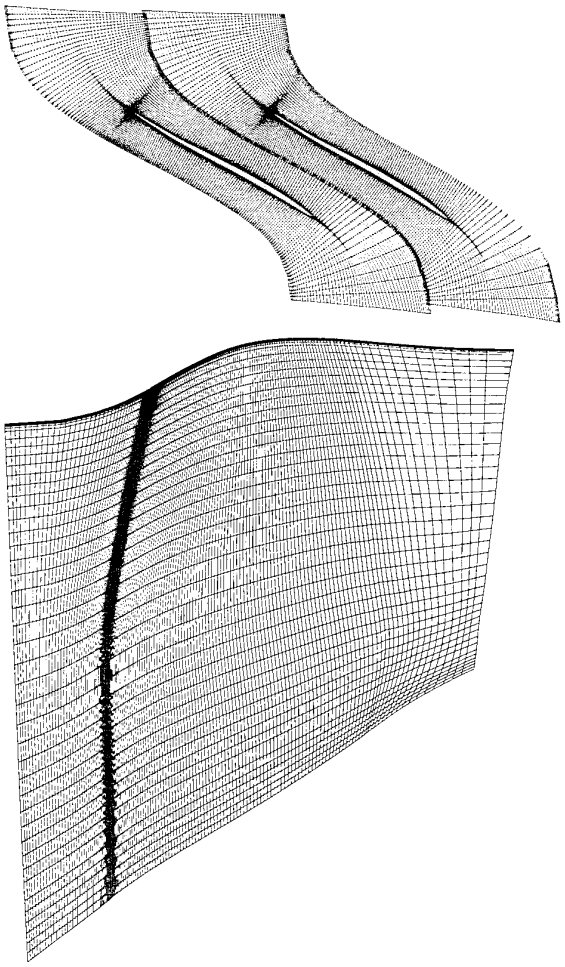

Figure 3. Grid Used for Numerical Investigation.

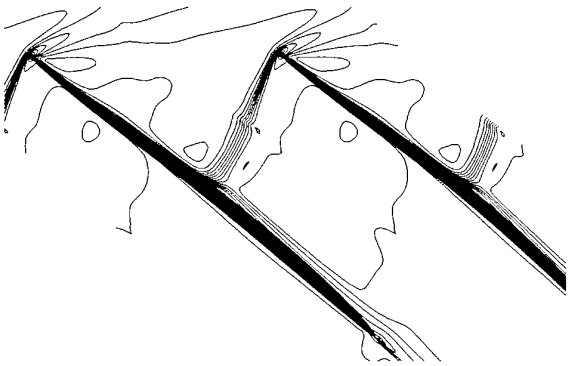

Figure 4. Mach Number Contours Near Stall in a Transonic Fan.

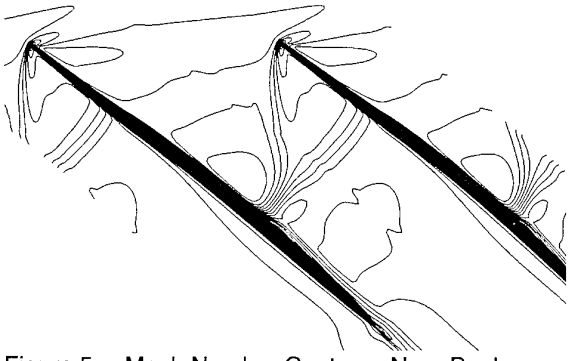

Figure 5. Mach Number Contours Near Peak Efficiency in a Transonic Fan.

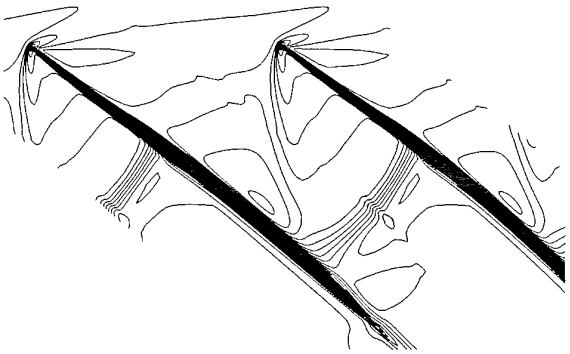

Figure 6. Mach Number Contours for Back Pressure Slightly Below the Maximum Choked Value.

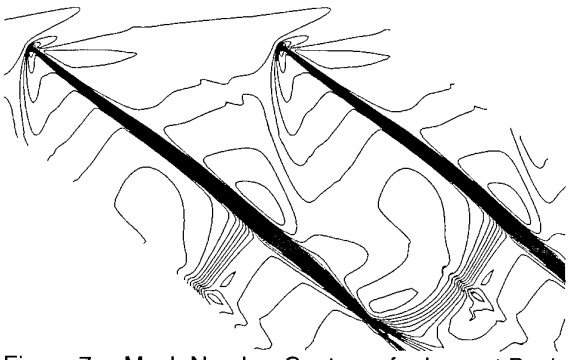

Figure 7. Mach Number Contours for Lowest Back Pressure Operating Point.

As the back pressure is reduced further, the rotor becomes completely choked and the second shock moves downstream, becoming a separate, full-passage shock, as shown in Figure 6. Because the flow downstream of the first passage shock is still supersonic, the camber in the aft portion of the blade causes the flow to accelerate before encountering the second shock. The Mach number upstream of the second shock increases steadily as the shock moves downstream with decreasing back pressure, as shown in Figure 7. Because the flow is still supersonic downstream of the first passage shock, there are no changes in the first passage shock along this portion of the characteristic. For all values of back pressure, both choked and unchoked, the second passage shock is approximately normal to the predominant flow direction.

These numerical results are in excellent qualitative agreement with the sparse experimental measurements of off-design shock structure available in the open literature. Chima and Strasizar (1983) used laser anemometry to measure shock structures in a full-span supersonic compressor rotor operating near stall and at maximum flow. The measurements presented in that study for 15% rotor immersion, reproduced in Figure 8, are nearly identical to those of the current investigation.

Pierzga and Wood (1985) used laser anemometry to measure shock structures in a different transonic fan, and their results for 30% rotor immersion are reproduced in Figure 9. The similarity between those measurements and the current numerical results is clear. In that study, however, a single, mildly oblique passage shock was measured at the 10% rotor immersion near peak efficiency (the shock structure at maximum flow was not presented for the 10% immersion). In the current numerical investigation, the peak efficiency passage shock structure was found to vary continuously from that shown in Figure 5 in the free-stream region to a single nearly normal shock near the casing. This transformation of the shock structure was determined to be a result of the interaction between the shock and the tip-leakage flow. Both the spanwise and streamwise extent of the interaction varied with throttle setting, but further discussion of this interaction is beyond the scope of the current paper.

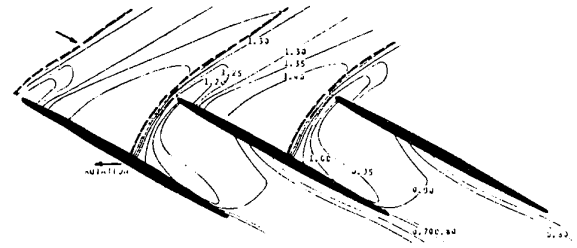

a) Near-Stall Condition

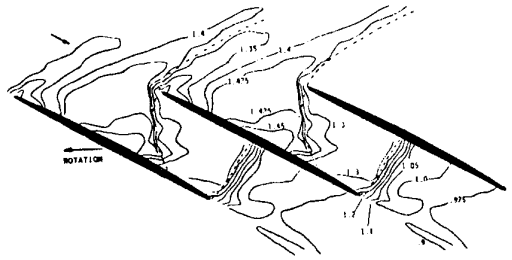

b) Maximum Flow Condition

Figure 8. Measured Shock Structure for 15% Rotor Immersion (Chima and Strasizar, 1983).

Sellin, et al. (1993) used casing static pressure measurements to determine the tip shock structure for 3 parametrically dissimilar transonic rotors, 1 of which is the subject of the current study. In that investigation, significant parametric variations of rotor leading edge sweep, throat margin, and suction surface shape were determined to have little effect on the tip-region shock structure. The casing shock structures calculated by the current numerical experiment are compared to those determined from the static pressure measurements in Figures 10 and 11. The agreement at the near-stall condition is clear, with a pronounced nearly normal shock standing ahead of the blade leading edge. At peak efficiency, the shock-vortex interaction causes the dual-shock system shown in Figure 5 (for the 18% immersion) to coalesce into a single nearly normal shock near the casing, and the extent of this interaction increases with decreasing back pressure. As mentioned above, the interaction between shock and tip flow is beyond the scope of the current paper, but the favorable agreement noted in this highly complex region adds to the credibility of the observations made in the free stream.

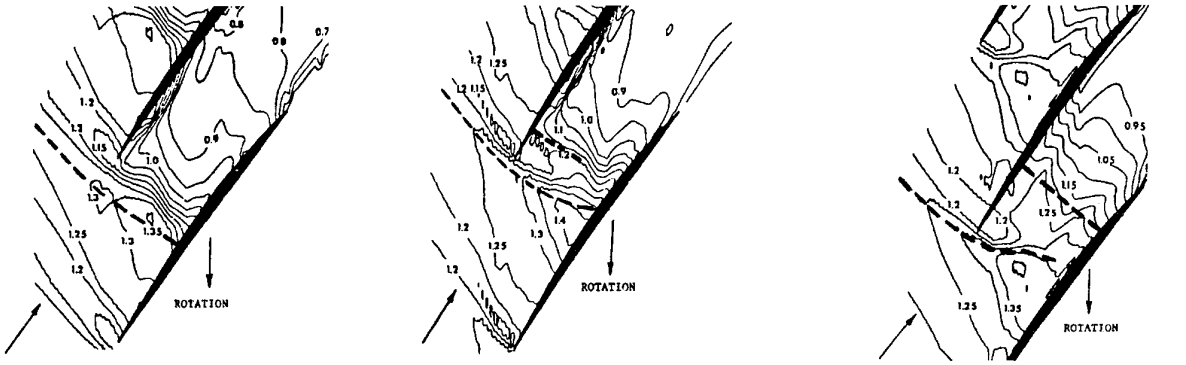

a) Near-Stall b) Peak Efficiency c) Maximum Flow

Figure 9. Measured Shock Structure for 30% Rotor Immersion (Pierzga and Wood, 1985).

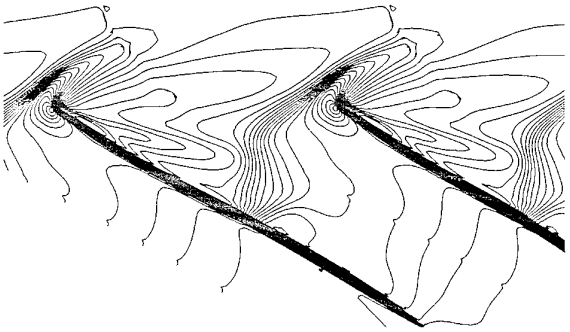

a) 3-D Navier-Stokes Solution

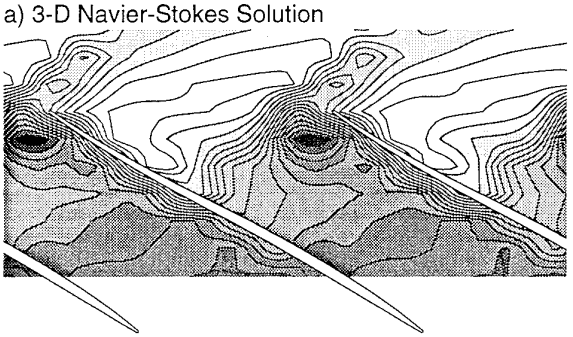

b) Measurements

Figure 10. Rotor 4 Near-Stall Casing Static Pressure Contours.

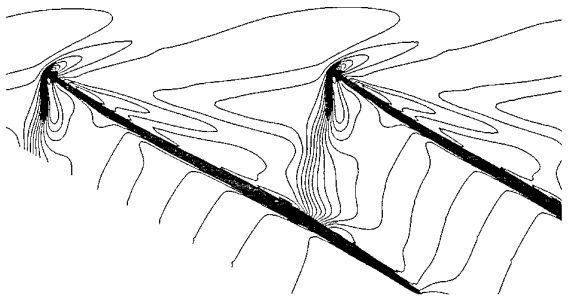

a) 3-D Navier-Stokes Solution

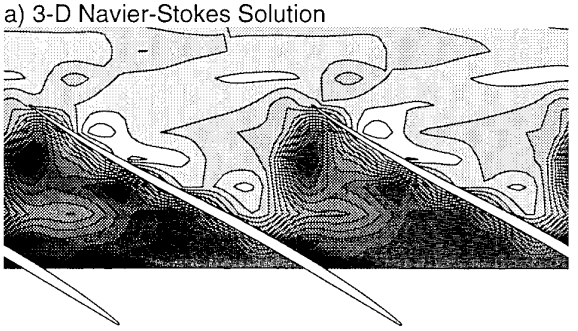

b) Measurements

Figure 11. Rotor 4 Peak-Efficiency Casing Static Pressure Contours.

Development of a Simplified Shock Model

It is generally accepted that much of the pressure rise that occurs in the supersonic region of a transonic fan rotor is the result of diffusion across the shock, and not from turning within the blade passage. Obviously, the shock will have a larger contribution near the tip where the relative Mach number is higher, and a smaller contribution near the sonic radius where more of the work input is from blade camber. So although the shock is responsible for much of the entropy production within the passage, it is also responsible for much of the work input. The development of simplified model to account for work input and total-pressure loss as a result of typical transonic compressor shock systems is presented here.

Consider the supersonic blade section in Figure 12 operating with an oblique passage shock. To clarify the point that only the contribution from the shock is being considered, and not the turning due to curvature of the blade passage, Figure 12 shows a cascade of flat plates. No expansion or precompression prior to the flow encountering the first shock is considered for this example. This is equivalent to considering the flow at the end of the Prandtl-Meyer expansion, while ignoring the blading and flow conditions upstream which would be required to produce this flow. The flow is also assumed to have a negligible radial velocity. While this assumption clearly does not hold for a general turbomachine, it is a special case for which the spanwise sweep of the shock can be ignored. It is desirable to make this assumption to avoid confusing the effects of the spanwise shock obliquity with the effects of the passage shock obliquity.

The conditions upstream of the shock are indicated by the subscript 1 and downstream conditions by the subscript 2. Unless explicitly identified, i.e., containing the subscript "*R*", quantities will be considered in the absolute reference frame. An aero-thermodynamic analysis of the flow will be developed which will provide the absolute (laboratory frame) total pressure ratio and efficiency due solely to the shock as a function of upstream conditions. It is assumed that the total pressure and total temperature in the absolute frame, circumferential velocity, wheel

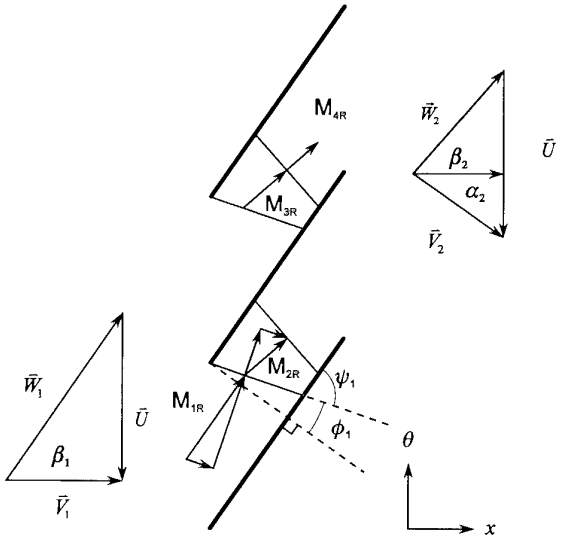

Figure 12. Simplified Model of Stationary Shock in the Relative Frame.

speed, and relative Mach number are all known upstream of the shock (T_{01}, P_{01}, $V_{\theta 1}$, M_{1R}, U).

To obtain an expression for static temperature, identities from the velocity triangle can be substituted into the relation for relative Mach number to obtain:

$$M_R^2 = \frac{V_x^2 + (V_\theta - U)^2}{\gamma RT} \tag{2}$$

Mach number in the absolute frame is given by:

$$M^2 = \frac{V_x^2 + V_\theta^2}{\gamma RT} \tag{3}$$

Therefore $$M_R^2 = M^2 - \frac{2V_\theta U - U^2}{\gamma RT} \tag{4}$$

The total-to-static temperature ratio (in the absolute frame) can be rearranged:

$$M^2 = \frac{2}{\gamma - 1}\left(\frac{T_0}{T} - 1\right) \tag{5}$$

Substituting this relation into Equation 4 and rearranging, an expression for T is obtained:

$$T = \frac{2T_0/(\gamma - 1) - (2V_\theta U - U^2)/\gamma R}{M_R^2 + 2/\gamma - 1} \tag{6}$$

This gives static temperature as a function of total temperature, whirl velocity, blade speed, and relative Mach number and is applicable at either the upstream or downstream station. At the upstream station, the static pressure can now be determined from isentropic relations; the upstream condition is fully defined.

The above statements concerning the upstream conditions are subject to an additional trigonometric constraint. For a fixed whirl velocity and wheel speed, there is a certain minimum value of M_{1R} for which the following identity is defined. From trigonometry:

$$\beta_1 = \sin^{-1}\left(\frac{V_{\theta 1} - U}{M_{1R}\sqrt{\gamma RT_1}}\right) \tag{7}$$

For relative Mach numbers lower than the minimum value, the tangential component of relative velocity will be less than the difference between wheel speed and whirl velocity, and the arc sine function will be undefined. In a similar fashion, if whirl velocity and relative Mach number are held fixed, there is a certain maximum wheel speed for which the trigonometric identity is satisfied. (For both cases, it was assumed that total temperature was fixed.)

Once the upstream condition has been fully defined, oblique shock theory is used to obtain normal Mach number, static temperature, and static pressure downstream of the shock. Recall that static quantities are reference frame independent, and that they are uniquely defined by the normal Mach number upstream of the shock. Discussion of the value to be used for the shock obliqueness angle, ψ_1, is delayed until the next section; for the time being, consider it to be a known value.

$$M_{1N} = M_{1R}\sin\psi_1 \tag{8}$$

$$M_{2N}^2 = \frac{1 + [(\gamma - 1)/2]M_{1N}^2}{\gamma M_{1N}^2 - (\gamma - 1)/2} \tag{9}$$

$$\frac{p_2}{p_1} = 1 + \frac{2\gamma}{\gamma + 1}\left(M_{1N}^2 - 1\right) \tag{10}$$

$$\frac{T_2}{T_1} = \left[1 + \frac{2\gamma}{\gamma + 1}\left(M_{1N}^2\right)\right]\left[\frac{2 + (\gamma - 1)M_{1N}^2}{(\gamma + 1)M_{1N}^2}\right] \tag{11}$$

To compute pressure ratio and efficiency, the downstream total temperature and total pressure in the absolute reference frame must be determined. Before these can be established, the angle through which the flow is turned by the oblique shock and the Mach number downstream of the oblique shock must be determined:

$$\tan\varepsilon = 2\cot\psi_1\left[\frac{M_{1R}^2\sin^2\psi_1 - 1}{M_{1R}^2(\gamma + \cos 2\psi_1) + 2}\right] \tag{12}$$

The relative flow angle downstream of the shock is given by:

$$\beta_2 = \beta_1 - \varepsilon \tag{13}$$

And the relative Mach number downstream of the shock is given by:

$$M_{2R} = \frac{M_{2N}}{\sin(\psi_1 - \varepsilon)} \tag{14}$$

Total temperature can now be determined by rearranging Equation 6:

$$T_{02} = \frac{\gamma - 1}{2}\left[T_2\left(M_{2R}^2 + \frac{2}{\gamma - 1}\right) + \frac{2V_{\theta 2}U - U^2}{\gamma R}\right] \tag{15}$$

Total pressure can then be determined from the isentropic relations. Note that the equation for T_{02} requires that downstream tangential velocity be known. This can be obtained from the velocity triangle as follows:

$$V_{\theta 2} = M_{2R}\sqrt{\gamma RT_2}\sin\beta_2 + U \tag{16}$$

Because the oblique shock deflects the flow toward the suction surface by an angle ε, there must be some mechanism that realigns the flow with the blade passage. If the flow downstream of the shock is subsonic, the flow will realign itself without a shock. But if the oblique shock angle is sufficiently large that the downstream flow is supersonic, another mechanism will be required to realign the flow.

There are 4 possibilities for realigning the supersonic flow downstream of the oblique passage shock. The first 2 possibilities are that a reflected shock may occur at the location where the first oblique shock intersects the suction surface of the blade to realign the flow. If this were the case, Equation 12 could be used to determine the shock angle, and both a weak shock and strong shock solution would potentially be possible. It is also possible that, for the low supersonic Mach number downstream of the first shock, a second shock may not be able to turn the flow all the way back to realign it with the blade passage. The third possibility is for a second shock to decelerate the flow to a subsonic Mach number, so the flow can realign itself with the blade passage for the remainder of the blade chord. The fourth possibility would be for the passage shock to change from an oblique shock to a normal shock near the suction surface impingement point.

To determine which of the above methods to use in this performance calculation, the CFD solutions mentioned previously were studied. These solutions indicated that the oblique passage shock becomes nearly normal in the immediate vicinity of the suction surface. In addition, any supersonic flow downstream of the oblique passage shock is terminated by a shock that is nearly normal to the predominant flow direction.

Because the first shock is normal to the flow in only a small region, this effect is ignored and the shock is approximated as straight and oblique across the entire passage. If the flow downstream of the oblique shock is still supersonic, a normal shock is calculated to decelerate the flow to a subsonic value. After the changes across the (possible) second shock have been calculated, the usual performance parameters can be computed:

$$PR = \frac{P_{02}}{P_{01}} \tag{17}$$

and

$$\eta = \frac{PR^{[(\gamma-1)/\gamma]} - 1}{T_{02} / T_{01} - 1} \tag{18}$$

This analysis only considers the effect of 1 or 2 homogenous oblique shocks at a single spanwise location. Obviously, suction surface curvature of an arbitrary rotor blade will cause variations in shock Mach number between the pressure and suction surfaces. In addition, many other factors, such as profile loss, tip clearance loss, secondary flows, and shock-boundary layer interaction, influence the performance of a real turbomachine. What is given here is an upper bound, the best that can be expected from the process associated with compression due to a moving shock, which is only one portion of the compression process that occurs in a transonic or supersonic compressor rotor.

Application of Simplified Shock Model

The results of this shock loss model are highly dependent on the angle of the oblique passage shock. In general, supersonic compressor blading has some finite leading edge radius for damage tolerance. Therefore, the shock angle cannot be determined from classical oblique shock analysis for wedges. Moeckel (1949) determined that the shape of a blunt body in a supersonic stream has only a secondary effect on the shape of the detached shock that will stand ahead of it. The sonic line was approximated as a straight line extending from the point where the contour of the body is inclined at the wedge angle corresponding to shock detachment, as shown in Figure 13. The shock was then approximated as a hyperbola that is normal to the body at the vertex of the imaginary wedge and asymptotically approaches the free-stream Mach lines.

Although experimental results indicated that the shape of the sonic line may depend considerably on the shape of the nose, this variation was found to be unimportant in determining the shape of the shock. Since this method was developed for isolated objects, it cannot account for the changes in shock shape that will occur with increased back pressure inside a turbomachine. It should, therefore, only be used to predict the shock angle at peak efficiency and higher flow rates. Although this approximation is less than exact, it does produce the correct trends of shock shape and detachment distance with both relative Mach number and leading edge radius. These trends include increased shock detachment distance with either increased leading edge radius or decreased Mach number, and increased shock obliqueness angle with increased Mach number, as measured by Kim (1956).

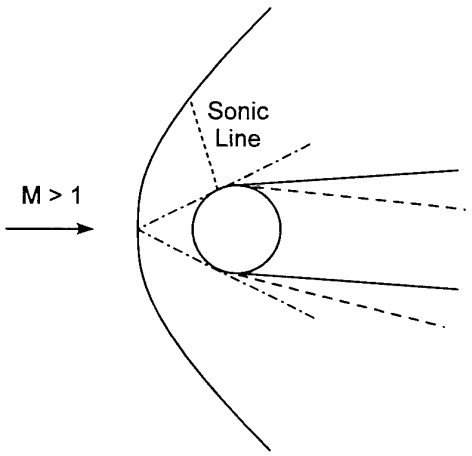

Figure 13. Detached Bow Shock Ahead of Blades at Zero and Nonzero Angles of Attack.

This method can be applied to objects at nonzero angle of attack by considering the upper and lower portions of the body separately. Because the extreme leading edge of an actual blade is a cylinder, essentially the same shock shape relative to the incoming flow is predicted for both zero and nonzero angles of attack. What changes at nonzero angle of attack is simply the orientation of the blade relative to the incoming flow, as shown by the dashed airfoil in Figure 13. The angle of the first passage shock predicted by this method was within approximately 2° of the angle obtained from the numerical experiment for each of the 6 spanwise locations considered.

With the oblique shock angle established through the method of Moeckel, the bounds for shock pressure rise and loss between the peak-efficiency and fully choked operating points can be determined. At peak efficiency, the Mach number of the second shock is established by the conditions immediately behind the oblique shock with no supersonic flow acceleration prior to encountering the second shock. For the fully choked operating condition a duct flow calculation can be used to compute the Mach number to which the supersonic flow behind the oblique shock would accelerate if the back pressure were low enough for the second passage shock to stand at the blade trailing edge.

To develop a better understanding of the significance of the passage shock(s) to transonic rotor performance, the method developed in the previous section was applied to Rotor 4. For simplicity, information from the CFD solutions was used to establish the Mach number entering the second shock for the high-flow operating points rather than the duct flow calculation mentioned above. At peak efficiency, the Mach number for the second passage shock was assumed to be the oblique shock exit Mach number with no acceleration. The method presented here does not allow for first-principle prediction of the characteristics for flows lower than peak efficiency where typically a detached shock occurs. For the portion of the characteristic at flows lower than the peak efficiency point, the computational study was used to establish the single shock angle and thereby pressure rise and loss. The low-flow portion of the characteristic is provided to demonstrate the differences in shock loss characteristics between the high-flow and low-flow regions of compressor operation. It should also be noted that the comparisons in this section are only qualitatively correct, as the spanwise sweep of the shock that exists in a transonic rotor has not been addressed in this application.

The pressure ratio attributed solely to the shock, and not from turning in the blade passage, is shown in Figure 14 for 2 spanwise locations of Rotor 4. In addition, the measured performance at the same spanwise locations is shown for comparison. The measurements were obtained from total pressure traverses at the rotor exit as discussed previously. The trends presented for the model predictions are consistent for all radii calculated, but it was felt that presenting more spanwise comparisons

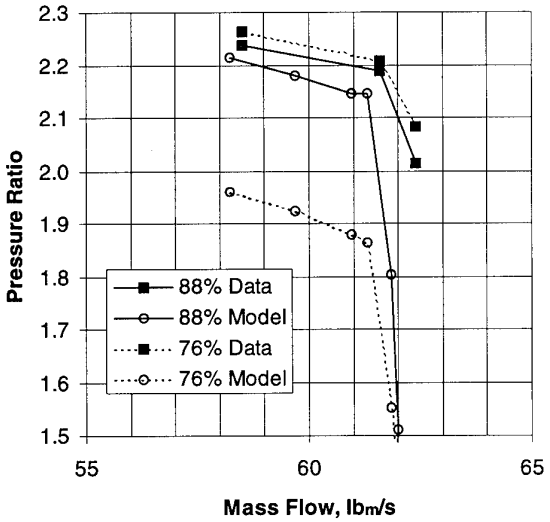

Figure 14. Predicted and Measured Pressure Ratio at 2 Spanwise Locations.

would clutter the figure without adding additional information. For the model predictions, the mass flow values plotted on the abscissa are the values for the entire annulus calculated from the CFD solutions at the same shock Mach number and obliqueness angle. The model results clearly show that the pressure rise generated by the shock system increases with increasing radius. This is because of the higher relative Mach number ahead of the passage shock at larger radii. The pressure rise due to the shock also becomes a larger fraction of the overall pressure rise across the blade passage as radius increases. This is why the modeled results approach the measured results at greater radii. Although not shown in the figure, the modeled pressure ratio across the shock above 88% span actually exceeds the measured pressure ratio for like spanwise locations. In the tip region, shock pressure rise gains are reduced by the large losses from the tip leakage flow. This finding supports the notion put forth by Puterbaugh (1994) that tip flowfields are significantly impacted by clearance flows.

Figure 15 shows the modeled and measured efficiency for Rotor 4 at the same 2 spanwise locations shown in the previous figure. The modeled efficiencies based on shock losses alone are considerably higher than those measured, but follow the same general trends. The figure suggests that the shock system establishes the shape of the efficiency curve and plays a significant role in the magnitude. The figure also supports the notion that loss mechanisms other than shocks (profile loss, shock-boundary layer interaction, etc.) contribute to the overall loss since the measured efficiencies are lower than the model predictions. In addition, these mechanisms generate loss at the same magnitude as generated by the passage shocks.

The shock loss coefficients predicted by the current model are shown in Figure 16 for 4 spanwise locations. On the unchoked portion of the loss curves, the well-known

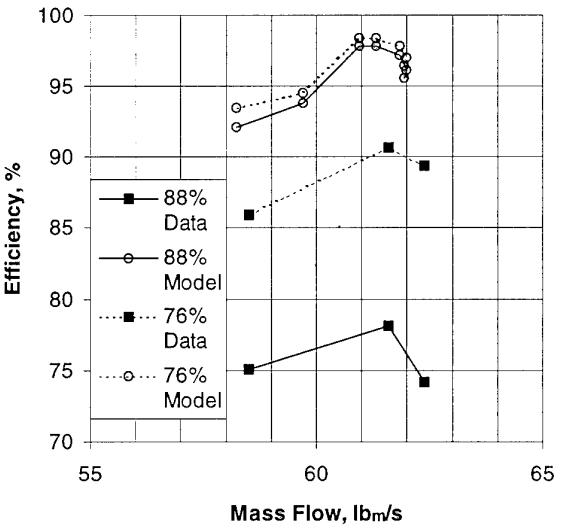

Figure 15. Predicted and Measured Efficiency at 2 Spanwise Locations.

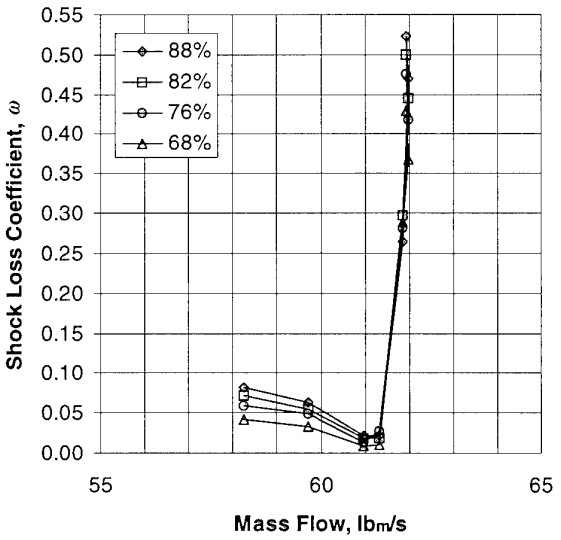

Figure 16. Shock Loss Coefficients Predicted by Simplified Model.

trends of increased shock loss coefficient with increased radius (relative Mach number) or decreased mass flow are predicted. This figure demonstrates the dramatic increase in loss calculated on the choked portion of the curve. The figure also suggests that two fundamentally different flow conditions, which converge at the peak efficiency point, dictate shock loss from choke to stall.

Conclusions

A numerical investigation has been conducted to determine the changes in shock geometry that will occur with throttle setting in the region not influenced by tip clearance flows for a modern transonic fan. The passage shock was found to be approximately normal near stall, with increasing obliqueness at higher mass flows. At peak efficiency, the shock system consists of an oblique passage shock followed by a normal shock, with the 2 shocks coalescing near the suction surface. As the back pressure is reduced further, the rotor becomes completely choked and the second shock moves downstream, becoming a separate, full-passage shock. The Mach number upstream of the second shock increases steadily as the shock moves downstream with decreasing back pressure. For all values of back pressure, the second passage shock is approximately normal to the predominant flow direction. Because the flow is supersonic downstream of the first passage shock, there are no changes in the first passage shock along this portion of the characteristic.

These numerical results are in excellent qualitative agreement with measured results (Chima and Strasizar, 1983; Pierzga and Wood, 1985; Sellin, et al., 1993). Although the blade shapes were significantly different in these experiments, the shock structures produced by them were qualitatively similar over the entire range of design-speed mass flows. The current authors suggest that the compressor operating point and the blade leading edge radius are the primary factors that determine the design-speed passage shock structure. Curvature of the suction surface will influence the strength of the passage shock, but the small amount of entrance-region curvature typical of modern transonic blading makes this a secondary effect.

A simplified shock loss model that accounts for the variation of shock geometry with mass flow has been developed for design-speed application. The model is based on the conservation of mass, momentum, and energy, and captures the qualitative trends of shock performance over the entire range of design-speed operation of a transonic fan. The following general conclusions can be drawn from the model and comparisons with measured results:

1. The model, when compared with measured results, supports the notion that tip region losses are influenced greatly by the clearance flows.

2. The model demonstrates a distinct difference in the shape of the loss characteristic shape for back pressures greater than and less than the peak efficiency level.

3. The model suggests that shock systems are the primary mechanism for establishing the shape of the efficiency characteristic.

4. Loss from sources other than shocks have magnitudes similar to the shock loss.

5. Shock losses, although not the sole contributor to loss in transonic compressor, are a factor that must be considered in off-design performance predictions.

Acknowledgments

The authors would like to express their thanks to Dr. Chunill Hah for providing the CFD solutions used in this investigation. In addition, the authors would like to thank the members of the Compressor Aero Research Lab team who were instrumental in obtaining the measured data presented here. Finally the authors thank the management at Wright Laboratory and Air Force Office of Scientific Research for their continued support of our research efforts.

References

Balzer, R. L., "A Method of Predicting Compressor Cascade Total Pressure Losses When the Inlet Relative Mach Number is Greater than Unity," ASME *Journal of Engineering for Power*, Vol. 93, No. 1, pp. 119-125.

Boyer, K. M., and O'Brien, W. F., 1986, "Model Predictions for Improved Recoverability of a Multistage Axial-Flow Compressor," AIAA-86-2687.

Çetin, M., Üçer, A. Ş., Hirsch, C., and Serovy, G. K., 1987, "Application of Modified Loss and Deviation Correlations to Transonic Axial Compressors," AGARD R-745.

Copenhaver, W. W., Hah, C., and Puterbaugh, S. L., 1993, "Three-Dimensional Flow Phenomena in a Transonic, High-Throughflow, Axial-Flow Compressor Stage," ASME *Journal of Turbomachinery*, Vol. 115, No. 2, pp. 240-248.

Denton, J. D., 1993, "Loss Mechanisms in Turbomachines," ASME *Journal of Turbomachinery*, Vol. 115, No. 4, pp. 621-656.

Dowler, C. A., Boyer, K. M., Poti, N., 1986, "Model Predictions of Fan Response to Inlet Temperature Transients and Spatial Temperature Distortion," AIAA-86-2686.

Freeman, C., and Cumpsty, N. A., 1992, "A Method for the Prediction of Supersonic Compressor Blade Performance," AIAA *Journal of Propulsion and* Power, Vol. 8, No. 1, pp. 199-208.

Hah, C., 1987, "Calculation of Three-Dimensional Viscous Flows in Turbomachinery With an Implicit Relaxation Method," AIAA *Journal of Propulsion and Power*, Vol. 3, No. 5, pp. 415-422.

Hah, C., and Wennerstrom, A. J., 1991, "Three-Dimensional Flowfields Inside a Transonic Compressor With Swept Blades," ASME *Journal of Turbomachinery*, Vol. 113, No. 2, pp. 241-251.

Hirsch, C.; and Denton, J. D., 1981, "Propulsion and Energetics Panel Working Group 12 on Through Flow Calculations in Axial Turbomachines," AGARD AR-175.

Kim, C. S., 1956, "Experimental Studies of Supersonic Flow Past a Circular Cylinder," Journal of the Physical Society of Japan, Vol. 11, pp. 439-445.

Koch, C. C., and Smith, L. H., 1976, "Loss Sources and Magnitudes in Axial-Flow Compressors," ASME *Journal of Engineering for Power*, Vol. 98, pp. 411-424.

Law, C. H., and Wadia, A. R., 1992, "Low Aspect Ratio Transonic Rotors: Part I - Baseline Design and Performance," ASME *Journal of Turbomachinery*, Vol. 115, pp. 218-225.

Lieblein, S., 1957, "Analysis of Experimental Low-Speed Loss and Stall Characteristics of Two-Dimensional Compressor Blade Cascades," NACA RM E57A28.

Miller, G. R., Lewis, G. W., Hartman, M. J., 1961, "Shock Losses in Transonic Compressor Blade Rows," ASME *Journal of Engineering for Power*, Vol. 83, pp. 235-242.

Moeckel, W. E., 1949, "Approximate Method for Predicting Form and Location of Detached Shock Waves Ahead of Plane or Axially Symmetric Bodies," NACA TN 1921.

Parker, D. E., and Simonson, M. R., 1982, "Transonic Fan/Compressor Rotor Design Study, Volume V," AFWAL-TR-82-2017, ADB-69405, Air Force Wright Aeronautical Laboratories, Wright-Patterson AFB, Ohio.

Pierzga, M. J., and Wood, J. R., 1985, "Investigation of the Three-Dimensional Flow Field Within a Transonic Fan Rotor: Experiment and Analysis," ASME *Journal of Engineering for Gas Turbines and Power*, Vol. 107, pp. 436-449.

Puterbaugh, S. L. 1994, "Tip Clearance Flow-Shock Interaction in an Advanced, Transonic, Axial-Flow Compressor Rotor," Doctoral Dissertation, University of Dayton.

Saravanamuttoo, H. I. H., and Fawke, A. J., "Simulation of Gas Turbine Dynamic Performance," ASME Paper 70-GT-23.

Stewart, W. L., 1955, "Analysis of Two-Dimensional Compressible-Flow Loss Characteristics Downstream of Turbomachinery Blade Rows in Terms of Basic Boundary-Layer Characteristics," NACA TN 3515.

Wadia, A. R., and Copenhaver, W. W., 1994, "A Numerical and Experimental Investigation of the Effect of Throat Margin and Internal Contraction on Transonic Compressor Performance," ASME Paper No. 94-GT-286.

Wennerstrom, A. J., and Puterbaugh, S. L., 1984, "A Three-Dimensional Model for the Prediction of Shock Losses in Compressor Blade Rows," ASME *Journal of Engineering for Gas Turbines and Power*, Vol. 106, No. 2 pp. 295-299.

Discussion

G. Schulze:
Do you have an idea about the losses due to boundary layer separation after the shock-boundary layer interaction? Are they included in your model?

Authors' Reply:
The CFD solutions indicate that the boundary layer thickens at the point where the passage shock impinges on the suction surface. Some personal interpretation would be involved in saying that the boundary layer separates, but it clearly thickens. This shock-boundary layer interaction is a significant mechanism in transonic turbomachinery, but is beyond the scope of the current paper.

J. P. Gostelow:
The casing flowpath seemed quite exciting. Could you give me an idea of the design diffusion factor in this region?

Authors' reply:
The blade tip design diffusion factor for this rotor is 0.5 (Parker and Simonson 1982). As stated in the paper, this is a high-performance fan with an overall pressure ratio of 2. This is rather aggressive when compared to the fans found on flight-rated engines.

J. Dunham:
Please would you indicate the numerical differences in shock loss coefficient between your new method and the "classical" Miller, Lewis, and Hartmann (1961) method?

Authors' reply:
The method of Miller, et al. (1961) approximated the design-point passage shock system as a single shock which was nearly normal to the blade suction surface. We now believe that a single normal shock is typical of a near-stall operating condition, and that a dual-shock system exists at peak efficiency. Approximate comparisons of the design-point loss coefficients predicted by Miller, et al. and by the current method can be made, however, by ignoring the mass flow values in Figure 16. The values plotted as the near-stall condition for each radius are for shock obliqueness angles not greater than 12° and are very nearly the values which would be predicted by the normal-shock method of Miller, et al.

The design-point loss coefficients shown in Figure 16 represent the loss associated with a fluid particle which passes through the nearly homogeneous portion of the dual-shock system. As shown in Figure 13, however, a small region near the blade leading edge will have a strong shock and a correspondingly larger local loss coefficient. To obtain the correct overall loss coefficient, the loss must be integrated across the passage to include this effect. Although this is the subject of continuing work, the current authors believe that the integrated loss coefficient determined by this method will be significantly less than the value calculated by the method of Miller, et al.

REFERENCE NO. OF THE PAPER: 16

DISCUSSOR'S NAME: G. Schulze, Tech. Hochschule Darmstadt, Germany

AUTHOR'S NAME: Bloch/Copenhaver/Law/O'Brien

Q.: Do you have an idea about the losses due to boundary layer separation after the shock-boundary layer interaction? Are they included in your model?

A: The CFD solutions indicate that the boundary layer thickens at the point where the passage shock impinges on the suction surface. Some personal interpretation would be involved in saying that the boundary layer separates, but it clearly thickens. This shock-boundary layer interaction is a significant mechanism in transonic turbomachinery, but is beyond the scope of the current paper.

REFERENCE NO. OF THE PAPER: 16

DISCUSSOR'S NAME: J.P. Gostelow, Univ. of Leicester, U.K.

AUTHOR'S NAME: Bloch/Copenhaver/Law/O'Brien

Q.: The casing flowpath seemed quite exciting. Could you give me an idea of the design diffusion factor in this region?

A: The blade tip design diffusion factor for this rotor is 0.5 (Parker and Simonson 1982). As stated in the paper, this is a high-performance fan with an overall pressure ratio of 2. This is rather aggressive when compared to the fans found on flight-rated engines.

REFERENCE NO. OF THE PAPER: 16

DISCUSSOR'S NAME: D.J. Dunham, DRA, U.K.

AUTHOR'S NAME: Bloch/Copenhaver/Law/O'Brien

Q.: Please would you indicate the numerical differences in shock loss coefficient between your new method and the "classical" Miller, Lewis, and Hartmann (1961) method?

A: The method of Miller, et al. (1961) approximated the design-point passage shock system as a single shock which was nearly normal to the blade suction surface. We now believe that a single normal shock is typical of a near-stall operating condition, and that a dual-shock system exists at peak efficiency. Approximate comparisons of the design-point loss coefficients predicted by Miller, et al. and by the current method can be made, however, by ignoring the mass flow values in Figure 16. The values plotted as the near-stall condition for each radius are for shock obliqueness angles not greater than 12° and are very nearly the values which would be predicted by the normal-shock method of Miller, et al.

The design-point loss coefficients shown in Figure 16 represent the loss associated with a fluid particle which passes through the nearly homogeneous portion of the dual-shock system. As shown in Figure 13, however, a small region near the blade leading edge will have a strong shock and a correspondingly larger local loss coefficient. To obtain the correct overall loss coefficient, the loss must be integrated across the passage to include this effect. Although this is the subject of continuing work, the authors believe that the integrated loss coefficient determined by this method will be significantly less than the value calculated by the method of Miller, et al.

Shock-Wave Turbulent Boundary Layer Interaction in a Highly Loaded Transonic Fan Blade Cascade

Heinz-Adolf Schreiber
Deutsche Forschungsanstalt für Luft- und Raumfahrt e.V.
Institut für Antriebstechnik
Linder Höhe
D-51140 Köln
Germany

SUMMARY

Results of experimental investigations on strong shock-wave turbulent boundary layer interactions in a transonic compressor cascade are presented. The tests have been conducted in a linear cascade facility at inlet Mach numbers, ranging from 1.37 to 1.59, for freestream Reynolds numbers of about 2.7×10^6. The cascade tested is typical for a fan blade tip section with little flow turning, providing a static pressure ratio of more than 2.0 .

Main interest is concentrated on the blade suction surface, where the oblique extension of the bow shock of the neighbouring blade forms a Mach reflection in combination with a boundary layer separation. Structure and loss mechanism of the shock system within the blade passage is discussed. Detailed measurements of the boundary layer within the interaction region and the rear part of the blade were performed. The results show that shock induced boundary layer separation on the tested blade can be controlled for inlet Mach numbers up to 1.42 . At preshock Mach numbers of 1.32 to 1.44, there are only local boundary layer separations with reattachments. Complete boundary layer separation cannot be avoided beyond inlet Mach numbers of 1.45. However, the magnitude of the separation and thus the total pressure losses can be controlled by increasing the axial stream sheet contraction of the blade channel.

LIST OF SYMBOLS

AVDR	-	axial velocity density ratio $= \rho_2 w_2 \sin\beta_2 / (\rho_1 w_1 \sin\beta_1)$
c	mm	chord length
H_{12}	-	$= \delta_1 / \delta_2$ boundary layer shape factor
H_{32}	-	$= \delta_3 / \delta_2$ boundary layer shape factor
M	-	Mach number
M_{is}	-	isentropic Mach number = f (p/p_{t1})
p	N/m^2	static pressure
p_2 / p_1	-	static pressure ratio across cascade
p_t	N/m^2	total pressure
R_{ss}	mm	radius of curvature on blade suction surface
Re	-	Reynolds number, $w_1 c / \nu_1$
Re_δ	-	Reynolds number, $w_\delta \cdot \delta / \nu_\delta$
t	mm	blade spacing
w	m/s	flow velocity
x	mm	coordinate along blade chord
y	mm	coordinate normal to chord
β	deg	flow direction with respect to cascade front
β_s	deg	stagger angle
δ	mm	boundary layer thickness
δ_1	mm	displacement thickness
δ_2	mm	momentum thickness
δ_3	mm	energy loss thickness
φ		ramp angle
η	-	coordinate in tangential direction
ν	m^2/s	kinematic viscosity
ω	-	total pressure loss coefficient $= (p_{t1} - p_{t2}) / (p_{t1} - p_1)$
ρ	kg/m^3	density

INDICES

0	condition just upstream of interaction region
1	uniform inlet conditions
2	uniform exit conditions (mixed out)
i	incompressible
is	isentropic
LE	leading edge
δ	condition at outer edge of boundary layer

1. INTRODUCTION

Fan and compressor designs are constantly being pushed to higher pressure ratios and lower weigth. This leads to a considerable increase of the flow velocities relative to the blades with supersonic speeds and shock-waves in front of and within the blade passages. To realize the full benefit of such high speed compressors for pressure increase and reduction of the number of stages without compromising the efficiency level, a profound understanding of the flow phenomena and loss mechanism of the transonic blade to blade flow is necessary.

The aerodynamic performance of such transonic blades is essentially dependent on both, the total pressure losses of the imbedded shock-waves and the momentum losses and the displacement effects of the blade surface boundary layers. Thereby, the interaction of the shock-waves with the boundary layer becomes an aerodynamic problem of paramount importance. The shock-waves with their strong adverse pressure gradients cause considerable modification of the boundary layer itself, as well as of the flow field external to the boundary layer. Shock induced boundary layer thickening for example can change the blade passage throat area and may even cause unexpected choking.

The most detrimental effect, however, is a shock induced flow separation, which leads to poor pressure recovery and a dramatic increase in turbulence intensity.

Many of the highly loaded compressor rotors operate with supersonic relative flows and preshock Mach numbers on the blade surface, in which boundary layer separation cannot be

Paper presented at the AGARD PEP 85th Symposium on "Loss Mechanisms and Unsteady Flows in Turbomachines", held in Derby, United Kingdom, 8-12 May 1995, and published in CP-571.

avoided. Designing such blade elements, there is a strong motivation to understand the basic physics of the strong interaction mechanism, in order to control the interaction and the associated separation.
Recent progress in computational fluid dynamics allows the engineer to use numerical methods as an analysis tool for a better understanding of the blade to blade flow or as a design tool to improve the blade geometries. But still the transonic flow fields with imbedded shock-waves create tremendous difficulties, and especially the strong shock-wave boundary layer interactions with separation are not accurately predictable.
Detailed experimental data of such highly loaded configurations can help to improve and validate the numerical models (for example Kunz and Lakshminarayana, 1992).
In the past, several investigators have studied the interaction between a normal shock-wave and a turbulent boundary layer. This, however, has been performed in simplified experimental arrangements such as flat plates (Seddon, 1960, Koi, 1978), rectangular nozzles or windtunnel sections (for example Sawyer and Long, 1982), axisymmetric sections (Mateer et.al. 1976) or bumps on windtunnel walls (Alber et.al., 1973, Delery, 1978, Liu and Squire, 1988). A report of Atkin and Squire (1992) gives an excellent discription of the flow physics of normal shock-wave boundary layer interaction for pre-shock Mach numbers from 1.3 to 1.55.
Furthermore, methods are described to control the shock-interaction by vortex generators or cavities underneath the shock (Mc Cormick, 1993, Schnerr et.al., 1993).
However, very few experimental data are available from setups, relevant for real turbomachinery flows, especially from highly retarded flows in compressor blades.
The present paper discribes results, obtained in a transonic/ supersonic cascade, in which real compressor blade element flow could be simulated. Thereby, the boundary layer development upstream, across and behind the shock-waves, corresponds to the boundary layer behaviour in real blade configurations. This is especially important since the interaction mechanism with boundary layer separation is essentially influenced by the flow in the rear blade passage and the free trailing edges. First results of these experiments are given in a previous paper (Schreiber and Starken, 1992), in which especially the shock structure and boundary layer was analysed with a laser anemometer (L2F) at a cascade inlet Mach number of 1.5. The present paper provides experimental results, showing primarily the influence of the inlet Mach number on the interaction process, the loss mechanism, and the boundary layer development.

2. EXPERIMENTAL ARRANGEMENT

2.1 Cascade Blade Design

The cascade was especially designed for these investigations on strong shock-wave boundary layer interaction. The geometry is typical for a tip section of a highly loaded transonic fan operating with an axial Mach number of 0.6 and a relative inlet Mach number of 1.5. The cascade had to provide a static pressure ratio of more than 2.0 with relatively little flow turning. In order to reduce the Mach number incident to the shock-wave at the blade passage entrance, the profile was designed with a negative suction surface camber along the cascade entrance portion (about 5 degrees within 18% of chord). Thereby, the surface velocity is reduced isentropically to a Mach number level of around 1.4 over the main part of the blade passage entrance. This so-called pre-compression design allows a considerable reduction of the losses, resulting from the detached

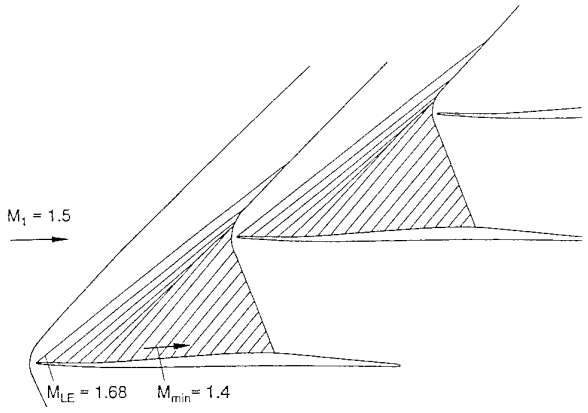

Fig. 1: Design inlet wave pattern

bow-shock and the first shock at the blade passage entrance. The design was performed by prescribing the supersonic Mach number distribution on the blade suction surface entrance region up to a position, where the oblique passage shock meets the blade surface.
Figure 1 shows the approximate design wave pattern in the entrance region. A unique feature of the pre-compression airfoil is the coalescence of the left-running characteristics, emanating from the concave forward portion of the blade surface, which overlap and form a so-called pre-compression shock-wave, which inturn intersects the detached bow shock of the adjacent blade. The pre-compression shock is relatively weak, but it reduces the Mach number ahead of the leading edge and the covered passage.
The first passage shock was designed to be oblique with a deflection of 8.4 degrees and a deceleration to nearly sonic velocities in case of a weak oblique shock solution. Figure 1 shows the approximate position of the passage shock wave if a strong oblique shock is assumed.
In reality, the prescribed back pressure behind the cascade and in the rear part of the blade passage determines the formation of the passage shock waves. A sketch of the real shock-wave pattern, which establishes at design pressure ratio is shown in Fig. 2. Thereby, the relatively strong first oblique passage shock induces a boundary layer separation on the blade suction surface, forming a lambda shock system above the separation region. The pressure surface shows a slight reacceleration along the front portion up to a Mach number of almost 1.3 ahead of the second nearly normal passage shock, which meets the pressure surface at about 35% of chord.

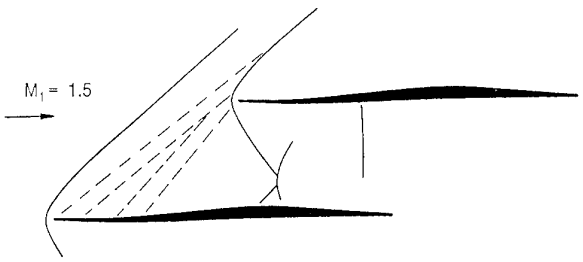

Fig. 2: Shock-wave pattern at design pressure ratio

Supersonic cascade inlet flows with a subsonic axial velocity component involve a dependency of the inlet flow direction on

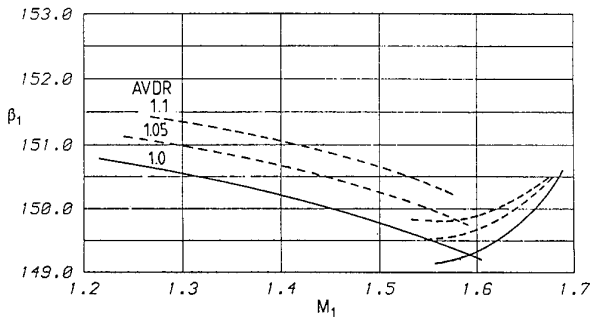

Fig. 3: Inlet flow angle versus inlet Mach number, unique incidence

the inlet Mach number, often called unique incidence (Lichtfuß and Starken, 1974). The present pre-compression cascade with its concave suction surface camber of the blade front portion shows an interesting feature of the "unique incidence" relation, as it is shown in Fig. 3. With increasing inlet Mach number the inlet flow angle β_1 (or incidence) decreases continously until a minimum is reached at about $M_1 \sim 1.56$. Beyond $M_1 \sim 1.56$ the axial component of the inlet Mach number reaches its maximum value of about $M_{1ax} = 0.82$. Within this range, the inlet flow turns to higher incidences, when the inlet Mach number is further increased but the axial Mach number component nearly remains constant (Starken et.al., 1984). The unique incidence curves shown in Fig. 3 are obtained by an approximate one/two-dimensional method. They additionally indicate the influence of the axial stream sheet convergence (AVDR) on the inlet flow direction. Some geometrical data are summarized in table 1.

Table 1: Cascade PAV -1.5

Chord	c	= 170 mm
Thickness	d_{max} / c	= 0.03
Leading edge	R_{LE} / c	= 0.0023
Gap-chord ratio	t/c	= 0.65
Stagger angle	β_s	= 148.1°

2.2 Test Facility and Test Conditions

The investigations were performed in the supersonic cascade facility of the DLR in Cologne. This windtunnel is a closed loop, continuously running facility with a test section area of 152 x 240 mm, equipped with an adjustable converging-diverging nozzle, allowing Mach number variations from 1.3 to 2.4.

Due to the need of great chord length, in order to get high resolution of the shock-wave boundary layer interaction region and the boundary layer, the cascade was built with three blades, having a chord length of 170 mm. The center blade was instrumented on the suction side and the neighbouring blade on the pressure side. A cross-sectional drawing of the test section is shown in Fig. 4.

In the exit area of the cascade tailboards were hinged to the trailing edges of the upper and lower most blades, in order to guide the exit flow and allow an independent throttling for the desired backpressure and shock-wave position. Using the combination of tailboard and throttle system at the downstream end of the tailboards, a stable shock-wave pattern could be achieved. Only a slight, natural shock oscillation with streamwise amplitudes in the order of 1.5 δ_0 was observed. Because of the relatively small blade aspect ratio, the influence of the incoming windtunnel sidewall boundary layers and their thickening within the highly loaded blade passage, creates considerable problems in establishing a two-dimensional, or at least a quasi two-dimensional flow field. To overcome this problem, at least partly, a sidewall boundary layer suction was applied in the area, where the strong passage shock interacts with the endwall boundary layer. Furthermore, this suction allowed a certain control of the axial stream sheet contraction which results from the endwall boundary layer thikkening throughout the blade passage.

The test were run with a total pressure in the settling chamber of 1.1 - 1.2 bar and a total temperature of about 315-320 K. The freestream Reynolds number, based on chord length, was around 2.5 - 2.8 x 10^6 and the Reynolds number, based on the boundary layer thickness at the beginning of the strong interaction region on the blade suction side, was about $Re_{\delta 0} = 0.3 \cdot 10^5$. Cascade overall performance at midspan position with total pressure losses and shock losses were determined by traversing a combination probe for static pressure, total pressure, and flow direction at an axial distance of 15 mm (ξ_2/C_{ax} = 0.167) downstream of the cascade exit plane.

The development of the suction surface boundary layer across the strong interaction region and the rear part of the blade was analysed with a flattened Pitot tube of about 0.17 mm height, and a static needle probe. Thereby, the boundary layer properties are computed from the measured Pitot pressure and the corresponding blade surface pressure, assuming a constant static pressure throughout the boundary layer. The boundary layer traverses and cascade overall performance measurements

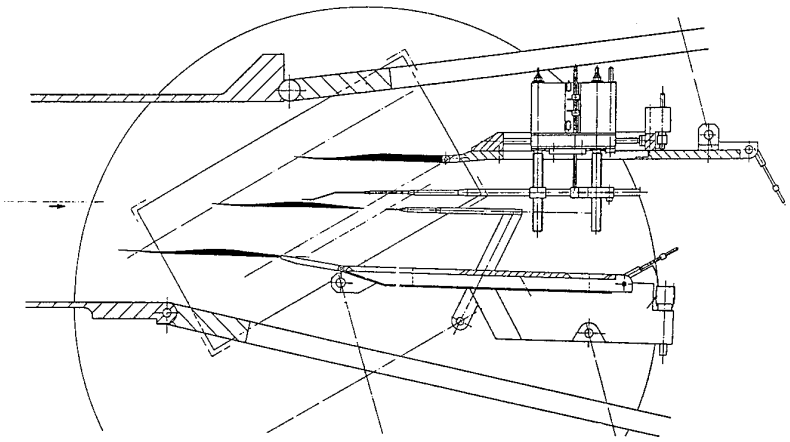

Fig. 4: Cascade windtunnel test section

obtained from wake traverse, were performed immediately after each other, to guarantee identical test conditions.
A Schlieren system was used to monitor the shock-wave pattern and probe position, although the sidewall suction system and the static pressure instrumentation severely restricted visual access to the flow field.

3. RESULTS

3.1 Cascade Blade Performance

Tests were performed at cascade inlet Mach numbers, ranging from 1.37 to 1.60. At these supersonic Mach numbers, the cascade inlet flow is independent on the exit flow conditions, and only the wave pattern at cascade entrance region establishes the 'unique incidence' condition shown in Fig. 3 . For most of the test, a nearly maximum attainable backpressure was established at which the cascade operates with nearly minimum losses and a shock wave pattern similar to those shown in Fig. 10. Figure 5 provides the measured static pressure ratios and the corresponding total pressure loss coefficient, as well as the shock losses for the investigated inlet Mach numbers. Thereby, the shock losses are analysed from the downstream measured total pressures by subtracting the amount of viscous losses, which are concentrated in the wake, corresponding to an empirical model given in Schreiber (1987). Due to the precompression design with its low preshock Mach numbers , the cascade has relatively low losses, ranging from $\omega = 0.08$ to

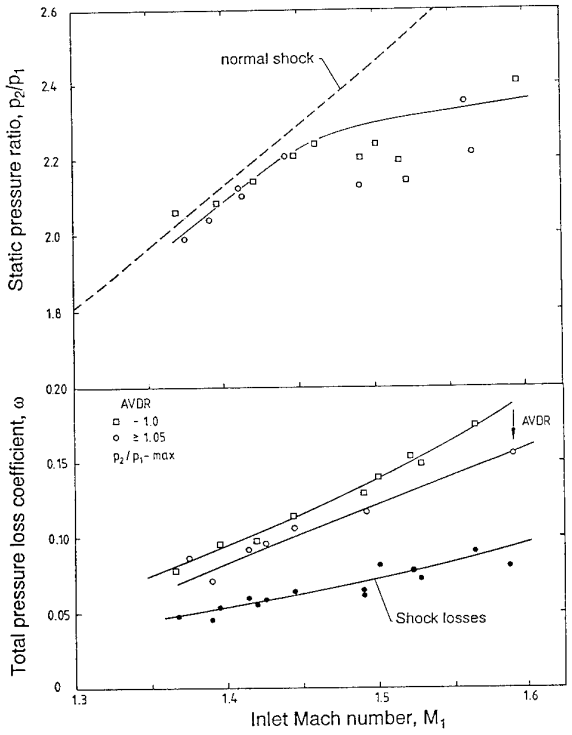

Fig. 5: Influence of inlet Mach number on static pressure ratio, total pressure losses and shock losses

0.17 for the investigated Mach number range. Nevertheless, the level of the shock losses is dominant. It exceeds more than about 50% of the overall losses, and also the gradual rise of the losses with increasing inlet Mach number is primarily a function of shock strength. A slight scatter in the loss level is caused by different AVDR values, of which the influence is discussed later. The measured flow turning is about 0.5 degree for nearly 2-dimensional conditions, but as flow turning is sensitive to AVDR it increases to about 3 degrees for an AVDR of 1.1.

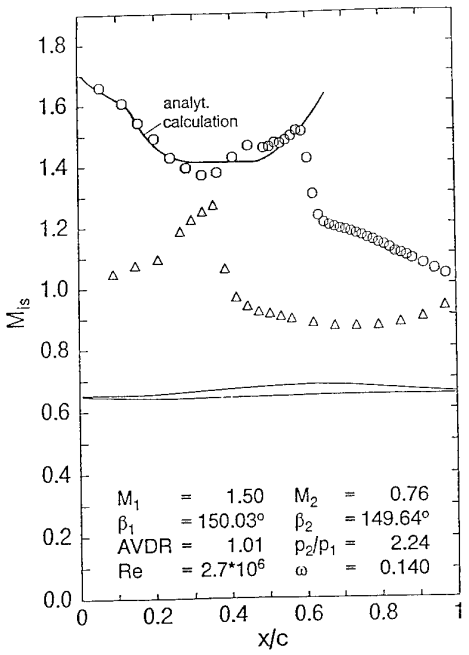

Fig. 6: Isentropic blade Mach number distribution $M_1 = 1.5$

3.2 Cascade Flow Field at Design Condition

Typical for the pre-compression design with a concave suction surface front portion is that the peak Mach number is attained immediately at the leading edge (Fig. 6), followed by a strong deceleration up to about 30% of chord. Within this precompression region a natural boundary layer transition is forced between 15 to 20%, which is confirmed by surface flow visualisations, using an oil streak technique as well as liquid crystal coatings, which indicate a streaky surface temperature distribution between the laminar and turbulent boundary layer. Due to this design with its front deceleration, a fully developed turbulent boundary layer is guaranteed before the strong first passage shock wave meets the blade suction surface. This early enforced transition is possibly one of the essential advantages of the precompression designs by which a strong *laminar* shock boundary layer interaction with its severe boundary layer separation and detrimental loss rise can be avoided.
The measured isentropic blade surface Mach number distribution at the design inlet Mach number of 1.5 and a static pressure ratio of 2.2 is shown in Fig. 6. The suction surface Mach number shows a slight reacceleration, due to the convex blade curvature downstream of 49% of chord up to a maximum isentropic Mach number of 1.52 incident to the strong passage shock. At about 60% of chord, the steep pressure rise indicates the onset of strong interaction with separation, which occurs near the inflection point at approximately 63% of chord. Downstream of this inflection point a further considerable flow deceleration is measured although the suction surface boundary layer remains fully separated. This rear deceleration is enforced by the prescribed back pressure and a second nearly normal shock wave, that develops within the covered blade passage (Fig. 2). The pressure surface Mach number distribution shows this second passage shock wave, when it meets the blade contour at about 35% of chord.

Concerning the measured blade Mach number distribution shown in Fig. 6, it should be mentioned that there exist some discrepancies between the initial design and the finally measured Mach number distribution from 28 to 48 % of chord of the suction side. These discrepancies are caused by some disturbances, emanating from the blade leading edge sidewall corner region, where the detached bow shock interacts with the incoming sidewall boundary layer (Schreiber, 1988). These disturbances (weak three-dimensional compression and expansion waves) fade away towards the blade center, but a slight influence on the blade suction surface flow remains. However, the impuls of the supersonic flow and the turbulent suction surface boundary layer is so high that these disturbances have only a minor influence on the strong shock-wave boundary layer interaction mechanism further downstream.

3.3 Flow Structure of Strong Interaction

The first oblique passage shock, that runs from the leading edge of the neighbouring blade into the covered passage, was designed with a flow deflection of about 8.4 degrees. At operating conditions with back pressures lower than design, this shock would meet and reflect from the blade suction surface at about 69% of chord. With increasing back pressure this shock near the blade surface is slightly being pushed upstream; it becomes steeper and induces a boundary layer separation (Fig. 2). Beyond a certain intensity or deflection angle, this oblique shock cannot reflect from the surface and associated boundary layer in a regular oblique shock reflection, but it forms a so-called Mach reflection with a quasi normal shock near the blade contour. Due to its strong interaction with the boundary layer, however, this normal shock in turn splits into a lambda shock system with its leading oblique shock and rear quasi normal shock. The corresponding strong flow deflection, which is necessary to enforce the Mach reflection of the oblique passage shock, is caused by the wedge-type displacement effect of the severe boundary layer separation. The principal features of this Mach reflection from the separated boundary layer is illustrated in Fig. 7. Figure 8 shows a Schlierenpicture for a similar flow condition with an inlet Mach number of 1.5 and a cascade static pressure ratio of 2.2. Characteristic for this type of strong interaction is the formation of two shock bifurcation points, from which the upper one belongs to the Mach reflection and the lower one to the lambda shock system.

Downstream of the two shock bifurcation points slip lines or vortex sheets develop, which devide the flow behind the nearly normal shock from the flow downstream of the two upper and lower oblique shock-waves. Concerning the loss mechanism of this flow structure, it is interesting to note that most of the cascade shock losses are concentrated behind the normal part of this bifurcated shock system, which is about 20-35% of blade channel height away from the surface. The shock losses slighly decrease, when approaching the lambda shock and the edge of the boundary layer. This is clearly shown by the pitot probe data from the boundary layer measurements (Fig. 13), as well as by the wake traverse data, recorded approximately 17% of chord downstream of the trailing edge plane (Figure 17).

Generally, the strong interaction is dominated by the separating boundary layer underneath the bifurcated shock. Thereby, the displacement of the boundary layer forms a ramp, by which the outer supersonic flow is turned away from the blade surface. Near the front part of the wedge, when the boundary layer begins to thicken, a series of compression waves coalesce and form the leading oblique shock, across which the flow is deflected by about 8.5 degrees (for $M_0 \sim 1.5$).

Analysing the measured boundary layer, the displacement thickness shows a nearly linear increase, from which a "ramp"-angle of about $\varphi = 7°$ is derived. This derived flow deflection is quite similar to the findings of Alber et.al. (1973), who observed that incipient separation occurs with an external flow deflection of 6.6 degrees. This happens, when the Mach number just upstream of the shock is $M_0 = 1.32$ and a supersonic compression with a flow deflection of 6.6 degrees leads to sonic flow conditions, associated with a pressure rise of 1.50. Furthermore, it was oberserved that with increasing preshock Mach numbers and more significant separations, this flow deflection remains nearly constant and does not exceed values of about 6.8 degrees (Atkins and Squire, 1992).

The blade surface pressure rise across the shock boundary layer interaction is directly coupled to this flow deflection behaviour near the edge of the boundary layer. For the present experiments, the interaction pressure rise is plotted in Fig. 9. It shows the static pressure increase between the minimum pressure p_0 and the so-called kink pressure p_K, which is observed underneath the main shock. Thereby, the kink in the blade

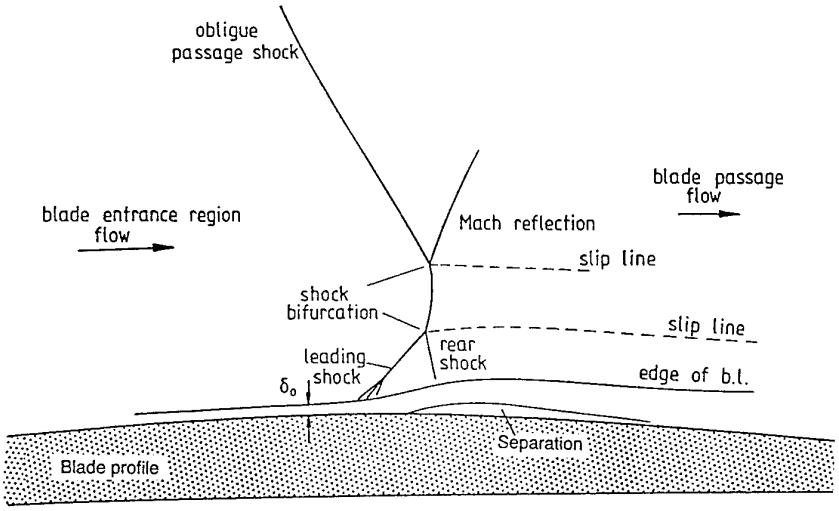

Fig. 7: Flow structure of strong interaction in a cascade blade passage

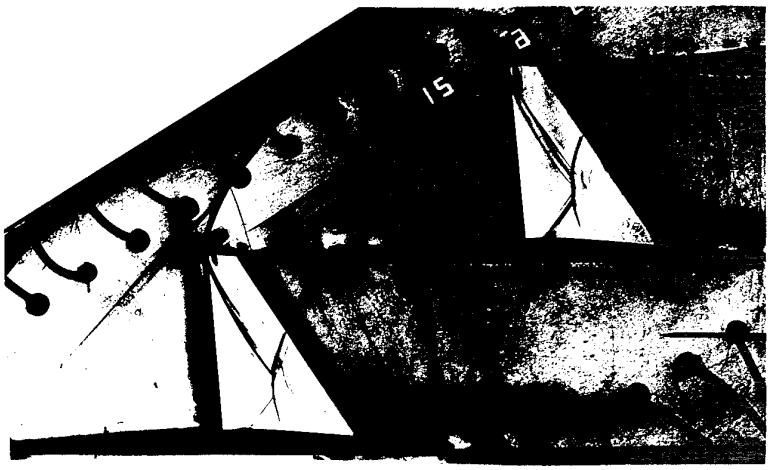

Fig. 8: Schlieren photograph at $M_1 = 1.5$

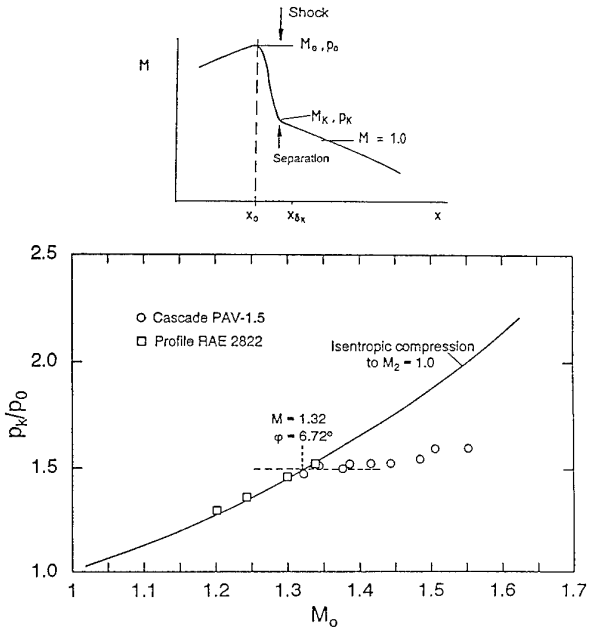

Fig. 9: Kink pressure rise at strong interaction

pressure distribution nearly corresponds to the point of boundary layer separation.

The cascade data show that beyond a certain preshock Mach number M_0 the kink pressure ratio does not considerably increase above values of 1.5-1.55. In Fig. 9 the experimental kink pressure rise data are compared to the theoretical pressure rise, which is obtained by an isentropic compression, due to a negative flow deflection away from the surface, that leads to sonic velocities. The data follow the theoretical curve up to a Mach number of about 1.32, beyond of which the kink pressure rise nearly remains constant. At $M_0 = 1.32$ the isentropic compression with a flow deflection of $\varphi = 6.72°$ achieves a pressure ratio of 1.5. For higher Mach numbers the boundary layer separation becomes more severe, but the nearly linear pressure increase within the supersonic part of the interaction, caused by the 'viscous ramp', remains practically constant.

The observed phenomenon of the constant kink pressure rise at significant separation was already hypothesized and discussed with earlier experiments (i.e. Alber, Delery, Atkin), but again it makes clear that, due to strong boundary layer separation, a certain physical limit in cascade blade passage pressure rise cannot be exceeded without an essential loss in pressure recovery. The slight change in cascade static pressure increase, which is oberserved beyond cascade inlet Mach numbers of 1.42 in Fig. 5, corresponds to the above physical behaviour.

3.4 Influence of Inlet Mach Number

The back pressure essentially influences the rear blade passage flow field and the position of the passage shock-wave, but because the shock meets the blade suction side on a curved surface ($R_{ss}/c \sim 1.0$) with an essential flow accaleration the back pressure indirectly also influences the level of the preshock Mach number.

However, primarily the cascade inlet Mach number and the associated preshock Mach number are the driving parameters for pressure rise and total pressure loss development. Figure 10 shows sketches of the shock wave pattern, which are derived from Schlieren photographs at inlet Mach numbers from 1.37 to 1.49, and figure 11 provides the corresponding isentropic blade Mach number distributions along with the measured performance data. The cascade backpressure, thereby again, is enforced in such a way that relatively high, nearly maximum pressure ratios are obtained. At the inlet Mach number of 1.37 the first, main passage shock is relatively steep and slightly curved, when approaching the blade surface. A bifurcation of this shock into a lambda shock is hardly visible. At an actual, not isentropic preshock Mach number of about 1.34 the thikkening of the boundary layer gives rise to compression waves, which join the main passage shock before they coalesce and do not form a single leading oblique shock. With increasing Mach number and associated shock strength the boundary layer separation becomes more severe, the displacing 'ramp' angle increases and the foot of the main passage shock clearly begins to bifurcate into the lambda shock. Furthermore, the height of the bifurcation in the lambda shock increases from about 3 to roughly 5 initial boundary layer thicknesses above the blade surface and it becomes 6.6 δ_0 at a cascade inlet Mach number of nearly 1.6.

When analysing the measured suction surface boundary layer, the "viscous ramp" angle, which is derived from the linear displacement thickness variation, also increases with the shock-

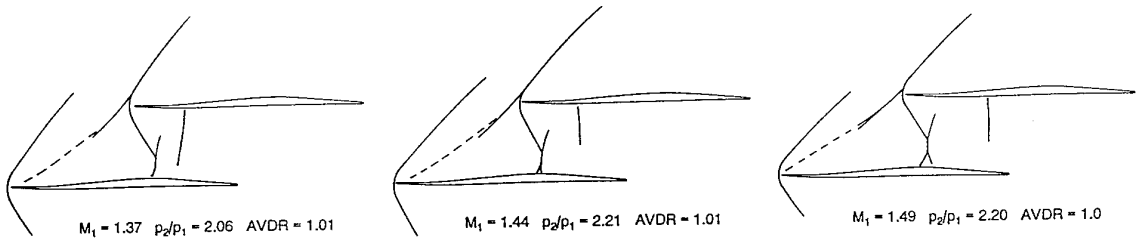

Fig. 10: Shock-wave pattern at M_1= 1.37, 1.44 and 1.49

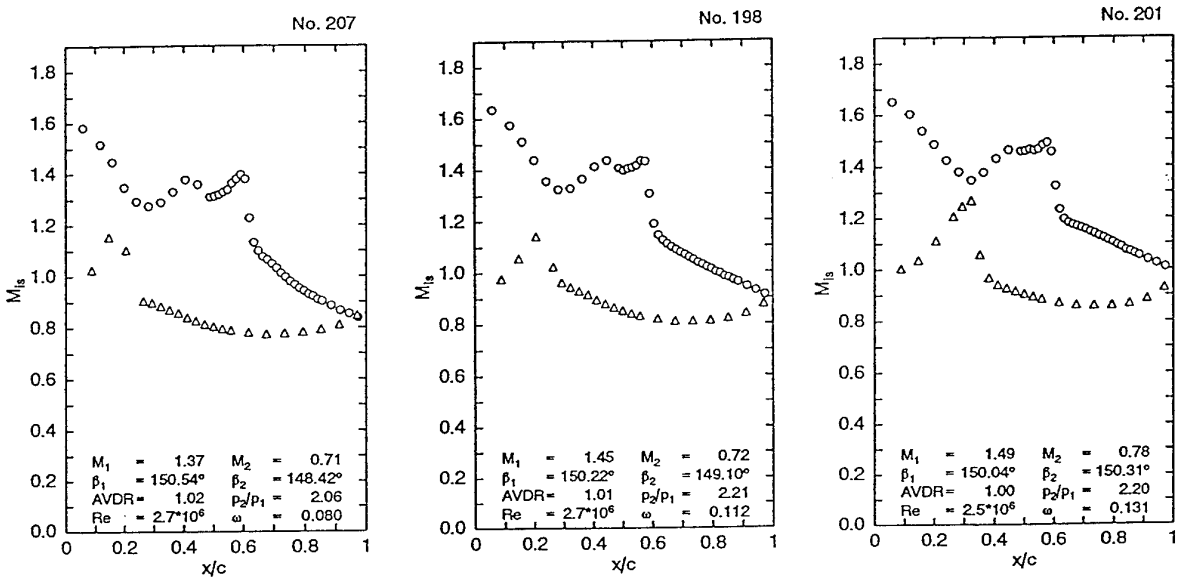

Fig. 11: Isentropic blade Mach number distributions at M_1 = 1.37, 1.44 and 1.49

upstream Mach number from about 3.3 degrees to roughly 7 degrees (M_0 = 1.34 to 1.45). However, it should be mentioned here that the displacementeffect and herewith the ramp angle, additionally depend on the flow confinement effect behind the interaction, which is caused by overall stream tube contraction, due to the thickening side wall boundary layers. Its effect on the interaction mechanism and the resulting losses will be discussed in the overnext section.

Figure 11 shows the Mach number influence on the blade pressure distribution. For all these tests, the distributions are qualitatively similar and the kink pressure rise underneath the strong shock, which was discussed above, is nearly the same. Differences occur, due to a different position and strength of the second quasi normal shock, that meet the pressure surface. All three test points have a complete suction surface separation at about 62-63% of chord and no reattachment could be observed. This was confirmed by injecting a tiny stream of ink through static taps within the separated region. In case of separation, the coloured fluid spreads in spanwise direction and shows the separation line, as wells as regions of reverse flow. It should be mentioned here that the tests, shown in Figure 11 and those, which are discussed in the following section, are run with AVDR-values around 1.0 (approximately 2-dimensional), which is why the aerodynamic loading is relatively high.

3.5 Boundary Layer Development

Velocity profiles of the suction surface boundary layer are provided in Fig. 12 for M_1 = 1.41, 1.44 and 1.49 together with the corresponding integral parameters. Some basic data of the undisturbed boundary layer are given in table 2. The presented velocity profiles clearly show the influence of the inlet Mach number on boundary layer growth and increase of separation intensity across the interaction. The strong passage shockwave, thereby, is located at 62 to 64% of chord. At the end of the displacement phase of the strong interaction (viscous ramp with a streamwise extension of about 25 - 50δ_{1o} or 4.5 to 9δ_0), the form factor H_{12i} reaches a local maximum. However, as the aerodynamic loading in the rear blade passage is extremely high, the form parameter H_{12i} shows no essential boundary layer recovery. When discussing the measured boundary layer and the derived parameters, it must be considered that the probe readings in the vicinity of separation and within the separated region must be considered with caution. Since the flow in the interaction region can no longer be regarded as steady, and since reverse flow does accur, the readings are erroneous, particularly close to the wall, so the derived integral parameters are approximations, showing only trends rather than absolute values.

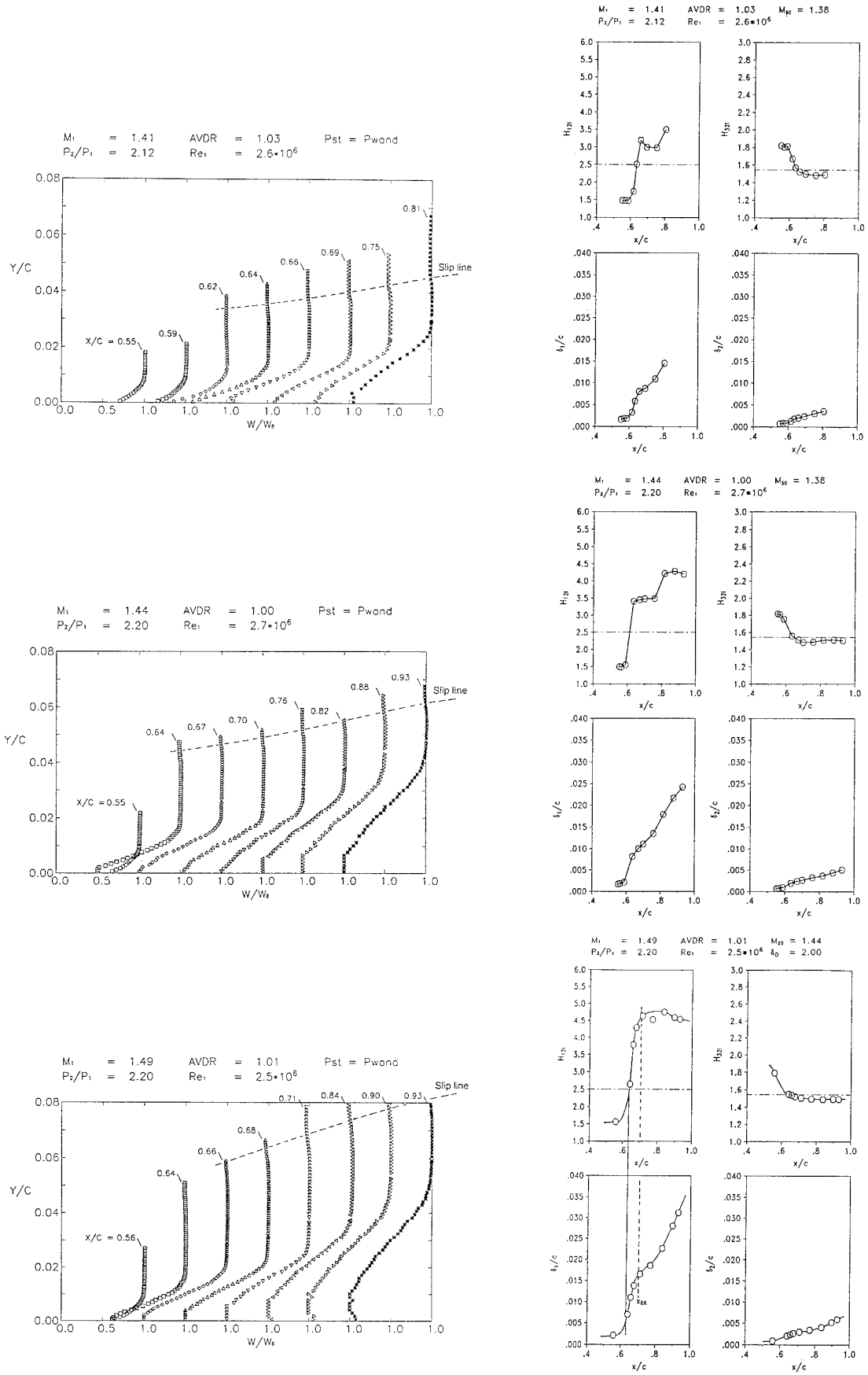

Fig. 12: Suction surface boundary layer development at strong interaction for inlet Mach numbers of 1.41, 1.44 and 1.49

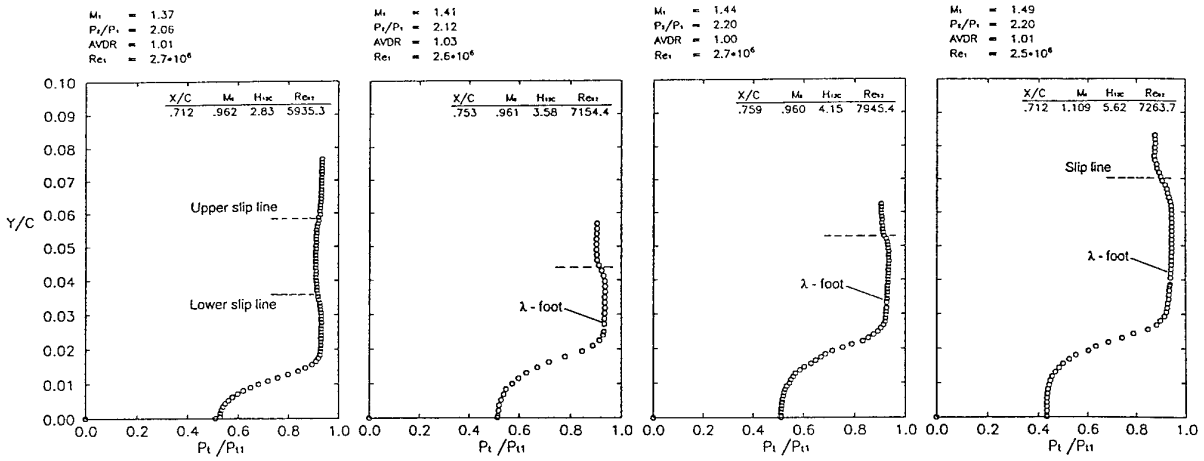

Fig. 13: Total pressure profiles downstream of the lambda shock

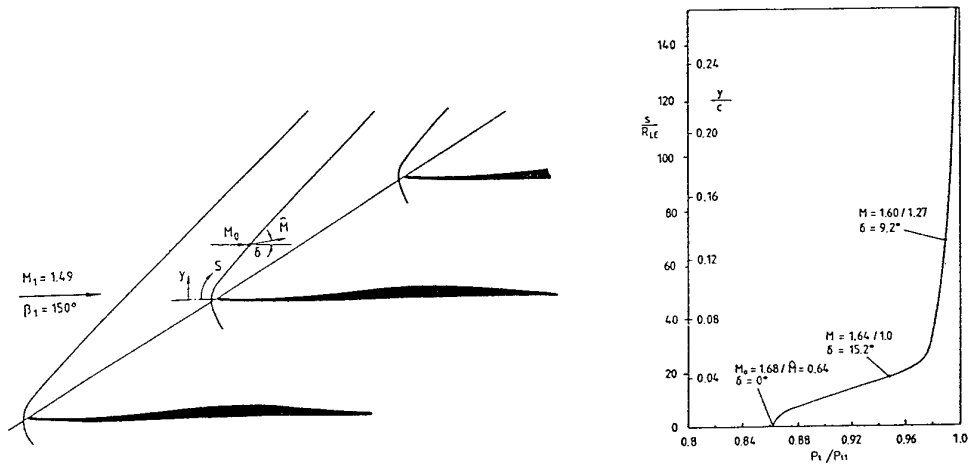

Fig. 14: Theoretical total pressure profile behind the detached bow shock at $M_1 = 1.49$

Table 2:
Test condition and boundary layer parameters ahead of interaction

M_1	= 1.37 - 1.49
p_2/p_1	~ 2.0 - 2.2
Re	~ 2.5 - 2.7·10^6
$M_{\delta o}$	~ 1.32 - 1.48
δ_0	= 1.75 - 2.0 mm
$Re_{\delta 1o}$	= 4400 - 5500
H_{12i}	= 1.5 - 1.6
Blade surface curvature at interaction R_{ss}/c	~ 1.0,
R_{ss}/δ_0	~ 80-85

All velocity profiles downstream of 64% chord show clearly the characteristic feature of the lambda shock with its slip line behind the bifurcation point. Again its height and intensity increases with the inlet Mach number. Figure 13 shows this influence on the total pressure profiles immediately behind the shock system. It is conspicuous that the total pressure ratio at the boundary layer edge is not 1.0, but does not exceeds values in the order of 0.93 to 0.94. This is due to the pressure loss of the detached bow shock, that stands ahead of the blade leading edge. Its loss distribution normal to the blade surface, was approximately calculated and plotted in Fig. 14.

3.6 Influence of AVDR

Axial stream sheet contraction, expressed by the AVDR can have an essential influence on blade element performance, especially on flow turning, but also on the loss mechanism, associated with shock boundary layer interaction. Thereby, it must be considered that the special feature of started supersonic flow into a cascade allows a variation of AVDR, while keeping the static pressure ratio and with it the overall retardation constant. This means that under these conditions, AVDR does not really relief the cascade deceleration as it is the case with unstarted transonic or subsonic cascade flows.
Tests with increased AVDR values, but constant static pressure ratios showed less intensive boundary layer separations, smaller lambda shocks with lower bifurcation points, and slightly lower overall losses. Even a reattachment of the separated boundary layer can be achieved, as long as the cascade inlet Mach number does ot exceed values beyond 1.45. Figure 15 shows such an example with the measured suction surface boundary layer profiles and the integral parameters at $M_1 = 1.42$. At an AVDR value of 1.06, the formfactor H_{12i} shows a clear maximum and an essential boundary layer rehabilitation. Surface flow visualisation confirmed a reattachment at about 80% of chord.

For higher inlet Mach numbers, however, separation cannot be avoided. But increasing AVDR helps to control boundary layer separation and the associated loss rise. Figure 16 provi-

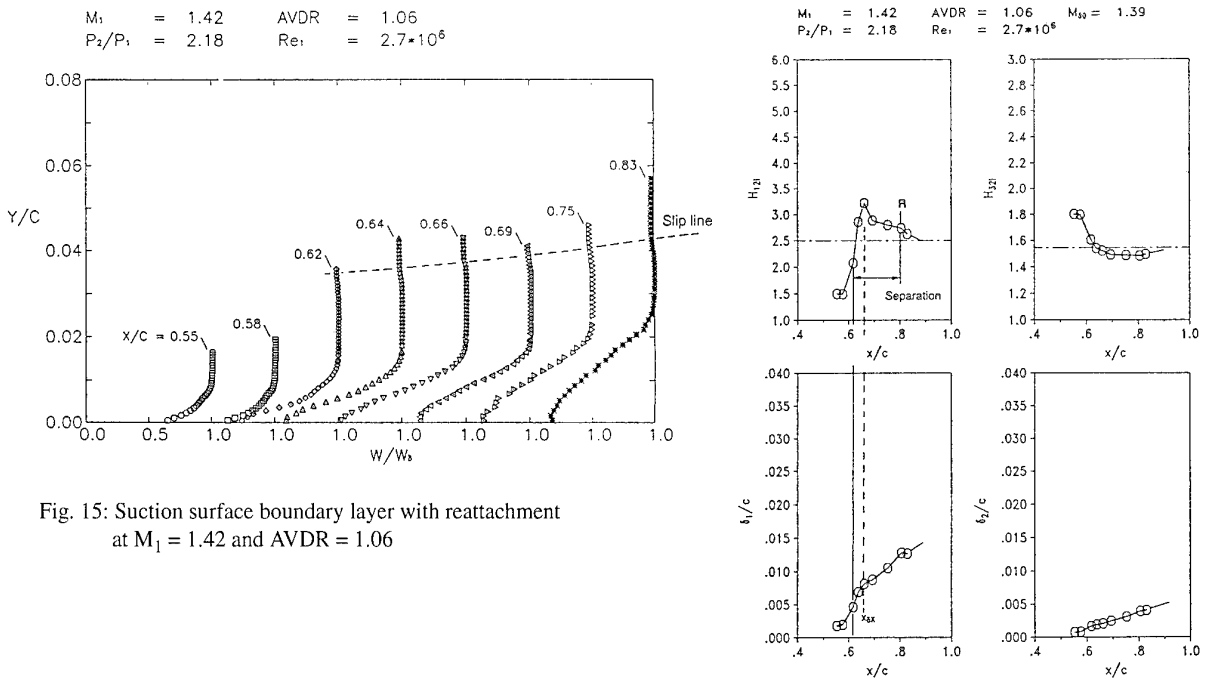

Fig. 15: Suction surface boundary layer with reattachment at $M_1 = 1.42$ and AVDR = 1.06

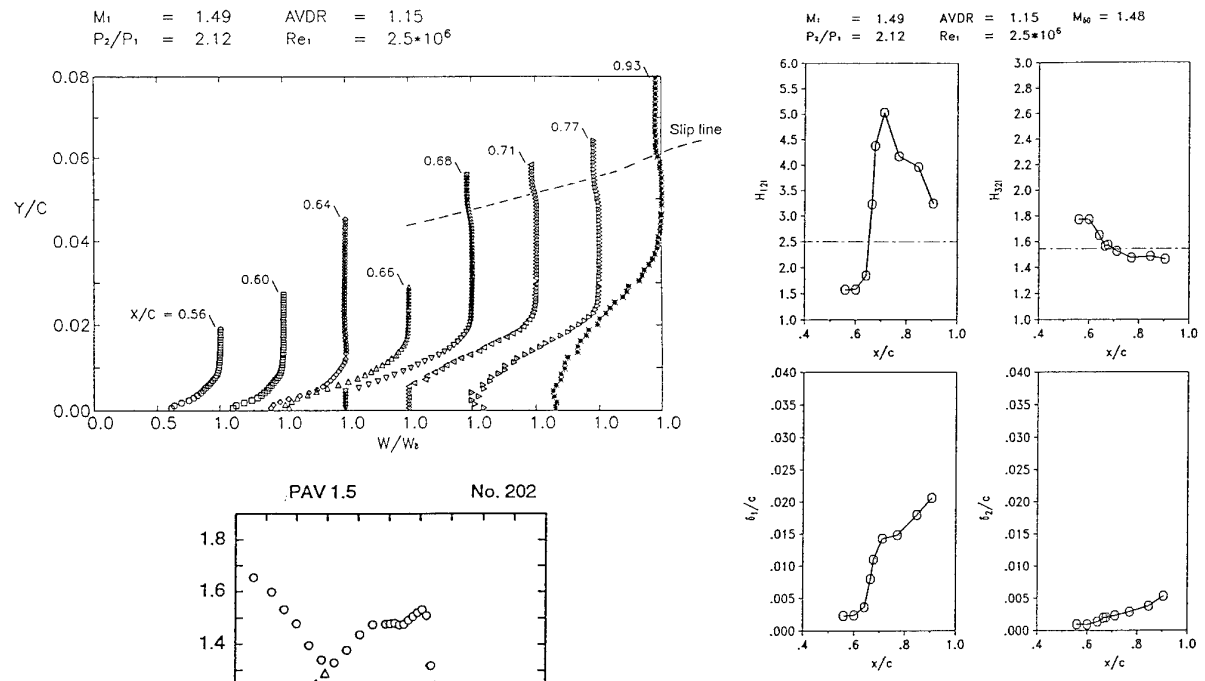

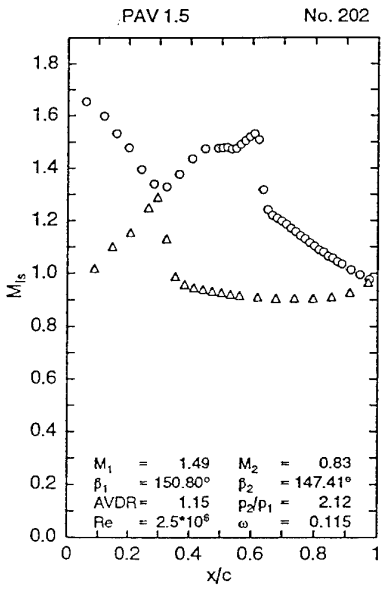

Fig. 16: Suction surface boundary layer data and blade Mach number distribution at $M_1 = 1.49$ with increased AVDR

des data of such a test point at $M_1 = 1.49$, which corresponds to the test with low AVDR, shown in Fig. 11c. Less boundary layer thickening, a lower shock bifurcation point, and a clear boundary layer rehabilitation in the rear blade

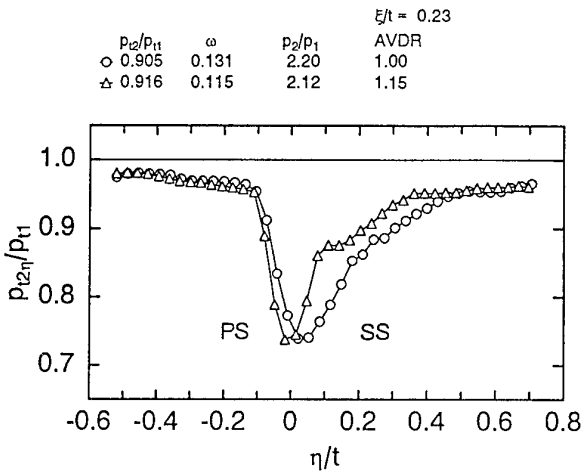

Fig. 17: Influence of axial stream sheet convergence (AVDR) on wake total pressure distribution

passage could be observed at the higher AVDR value of 1.15. A corresponding overall loss reduction from $\omega = 0.131$ to 0.115 was confirmed by the wake traverse data shown in Fig. 17.

Increasing stream tube contraction (higher AVDR) causes a slight upstream shifting of the passage shock waves, when the back pressure is forced to be constant. Thereby, the shock strength decreases, resulting in a considerable relief of the strong interaction process.

4. CONCLUSIONS

The fluid dynamic behaviour and the loss mechanism of shock-wave turbulent boundary layer interaction with separation was experimentally investigated on the suction surface of a fan-blade cascade with pre-compression profiles. The presented results provide a comprehensive picture of the flow structure, associated with the strong oblique blade passage shock-wave, which reflects from the blade surface in form of a Mach reflection, inducing a severe boundary layer separation. The results show clearly that the inlet and preshock Mach numbers are the driving parameters for pressure rise and loss production. Blade passage pressure rise, associated with strong shock-wave boundary layer interaction, is limited to the onset of significant separation underneath the main shock, which particularly becomes clear for inlet Mach numbers beyond 1.42 to 1.44 of the present cascade. The intensity of the strong interaction with separation can be controlled by an increase of the axial stream sheet contraction, causing a slight reduction of shock, as well as viscous losses.

Acknowledgements

This work was partially supported by Arbeitsgemeinschaft Hochtemperatur Gasturbine - AG Turbo, German Bundesministerium für Forschung und Technologie and German Bundesministerium der Verteidigung. The author gratefully acknowledges the permission for publishing the results.

REFERENCES

1) Alber, I.; Bacon, J.W.; Masson, B.S.; Collins, D.J.
An experimental investigation of turbulent transonic viscous/ inviscid interactions.
AIAA Journal, 11, 620-627, 1973

2) Atkin,C.J.; Squire, L.C.
A study of the interaction of a normal shock wave with a turbulent boundary layer at Mach numbers between 1.3 and 1.55.
European Journal of Mechanics, B/Fluids, Vol. 11, No 1, pp.93-118, 1992

3) Delery, J.
Analyse du decollement resultant d'une interaction choc-couche limite turbulente en transsonique.
La Recherche Aerospatiale, No. 1978-6, pp. 305-320, English Translation ESA-TT 560,1978

4) Kooi, J.W.
Influence of the Free-Stream Mach Number on Transonic Shock-Wave/Boundary Layer Interaction, NLR MP-78013 U, May 1978

5) Kunz, R.F.; Lakshminarayana,B.
Explicit Navier-Stokes Computation of Cascade Flow Using the k-ε Turbulence Model.
AIAA Journal, Vol. 30, No. 1, 13-22 Jan. 1992

6) Lichtfuß, H.J. Starken, H.
Supersonic Cascade Flow.
Progress in Aerospace Science, Vol. 15, D. Kuchemann, ed., Pergamon Press Ltd., New York, pp. 37-149, 197

7) Liu, X. Squire, L.C.
An Investigation of Shock/Boundary Layer Interaction on Curved Surfaces at Transonic Speeds.
J. Fluid Mech., Vol. 187, pp. 467-486, 1988

8) Mateer, F.G.; Brosh,A; Viegas, J.R.
A Normal Shock-Wave Turbulent Boundary-Layer Interaction at Transonic Speeds.
AIAA Paper no. 76-161, 1976

9) Mc Cormick, D.C.
Shock/Boundary Layer Interaction Control with Vortex Generators and Passive Cavity.
AIAA Journal, Vol. 31, No. 1, pp. 91-96, January 1993

10) Sawyer W.G., Long, C.J.
A study of normal shock wave/turbulent boundary-layer interaction at Mach numbers of 1.3, 1.4 and 1.5 .
RAE TR 82099, 1982

11) Schnerr, G.H.; Dohrmann, U.; Zierep, J.
Passive Control of the Shock-Boundary Layer Interaction in a Transonic Compressor Cascade.
2nd International Symposium on Experimental and Computational Aerothermodynamics of Internal Flows, Prague, July 12-15, 1993

12) Schreiber, H.A.
Experimental Investigation on Shock Losses of Transonic and Supersonic Compressor Cascades.
AGARD-CP-401, Transonic and Supersonic Phenomena in Turbomachines, paper No. 11, 1987

13) Schreiber, H.A.; Starken, H.
An Investigation of a Strong Shock-wave Turbulent Boundary Layer Interaction in a Supersonic Compressor Cascade.
ASME Journal of Turbomachinery, Vol. 114, pp. 494-503, July 1992

14) Schreiber, H.A.
Three-Dimensional Endwall Disturbances in the Entrance Region of a Supersonic Cascade.
Proceedings to the 9th Symposium on Measuring Technique for Transonic and Supersonic Flows in Cascades and Turbomachines, Oxford, 21-22 March, 1988

15) Seddon, J.
The Flow Produced by Interaction of a Turbulent Boundary-Layer with a Normal Shock-Wave of Strength Sufficient to cause Separation.
ARC R&M 3502, 1960

16) Starken, H.; Zhong, Y.; Schreiber, H.A.
Mass Flow Limitation of Supersonic Blade Rows due to Leading Edge Blockage.
ASME Paper 84-GT-233, 1984

REFERENCE NO. OF THE PAPER: 17

DISCUSSOR'S NAME: C.H. Sieverding, VKI, Belgium

AUTHOR'S NAME: H.A. Schreiber

Q.: Referring to your boundary layer measurements, the data show constant zero velocity through the separation bubble. Did you observe any backflow in this region?

A: The boundary layer measurements have been performed using a pitot probe. In the separated region the velocities obtained from probe readings are erroneous and artificially set to zero when the pitot pressure was less than the corresponding wall pressure.

REFERENCE NO. OF THE PAPER: 17

DISCUSSOR'S NAME: G. Schulze, Tech. Hochschule Darmstadt, Germany

AUTHOR'S NAME: H.A. Schreiber

Q: Do you know how stable the shock position is?

A: The main passage shock wave in this investigation is relatively stable. Only a slight shock oscillation with amplitudes in the order of 1.5 boundary layer thicknesses ahead of the interaction was observed. However, we observed shock instabilities, especially at transonic flow conditions (M1 = 0.8 - 1.2), when the incidence angle to the cascade was high. Such unstationary shock/boundary layer interactions can show streamwise shock amplitudes in the order of 5-20% of chord.

REFERENCE NO. OF THE PAPER: 17

DISCUSSOR'S NAME: I.H. Skoe, IA-T, Norway

AUTHOR'S NAME: H.A. Schreiber

Q: Did your experiment confirm the findings of Seddon (Your Ref 15), or were the differences in geometry and TBLx characteristics sufficient to cause significant differences?

A: The intention of the present experiment was to provide data for a realistic compressor blade element by using the cascade model. The shock wave/boundary layer interaction mechanism is strongly influenced by the flow within the downstream blade passage and the flow around the free trailing edge. Nevertheless, the present results qualitatively correspond to the findings of Seddon. However, his experiment with a normal shock on a flat plate showed a different reattachment behavior, because there was no reverse pressure gradient downstream. The conditions in Seddon's test upstream of the shock were M0 = 1.47, $Re_{\delta o} \simeq 0.5x10^5$ and $H_{12c} \simeq 2.1$.

LOSS PREDICTION IN AXIAL FLOW CASCADES USING A NAVIER - STOKES SOLVER

H. Tuğrul TINAZTEPE,
ROKETSAN A, Ş.,
P.K. 30, Elmadağ,
06780 Ankara,
TURKEY

İ. Sinan AKMANDOR,
Middle East Technical University,
Aeronautical Eng. Dept.
06531 Ankara,
TURKEY

Ahmet Ş. ÜÇER,
Middle East Technical University,
Mechanical Eng. Dept.
06531 Ankara,
TURKEY

SUMMARY

In this paper, results of a 3D Navier-Stokes flow solver which uses cell vertex finite volume method are given. The code uses Lax-Wendroff time integration method and Baldwin-Lomax turbulence model. Validation of the code are presented briefly in terms of modeling accuracy due to viscous effects. An attempt is made to predict shock boundary layer interaction on an airfoil. The paper also gives loss distributions. Effects like separation and secondary flow due to a high turning turbine cascade are discussed. Physical aspects of secondary flow and loss generation mechanisms are investigated in the predicted flow field.

LIST OF SYMBOLS

U	:	conservative variables
F, G, H	:	flux vector
ρ	:	density
u	:	velocity along x-direction
v	:	velocity along y-direction
w	:	velocity along z-direction
p	:	pressure
Re	:	Reynolds Number (based on axial chord)
τ	:	shear stress
T	:	temperature
μ	:	viscosity
l	:	length (chord)
a	:	speed of sound
M	:	Mach Number
Pr	:	Prandtl Number

1. INTRODUCTION

The time marching explicit Lax-Wendroff solver has already been adopted for the calculation of inviscid 3-D turbomachine flow [1]. However relevant viscous effects including the effect of end wall boundary layer development, viscous layer, blade loading, shock and boundary layer interaction are important in turbomachine flows. It is well known that a boundary layer like inlet velocity profile due to total pressure loss at the upstream through a high turning blade row will lead to the generation of secondary flows. Two main mechanisms will lead to the complicated flow structure at the exit of such cascades.

1. Secondary flow due to turning which cause the flow with an initial vorticity to develop a streamwise component of vorticity. This contributes strongly to the formation of passage vortex.
2. Horse shoe vortex flow due to the presence of end wall boundary layer flow . The blade leading edge causes the vortex filament to bend on each side of the blade and the created vortices interact with the passage vortex.

With regard to secondary flows, Euler solvers have already been used in the redistribution of prescribed upstream boundary layer loss profile. However the use of Navier-Stokes solutions should be an improvement in the calculation of the magnitude and the location of the loss.

Many loss mechanisms exist: Secondary flow losses, incidence losses, tip clearance losses, profile, end wall, and mixing losses. With the advent of high performance turbomachines, shock losses also gain importance. The most important loss contributions are closely linked to the vortex structure and their effects on the boundary layers present within the passage. Some of them can be stated as follows:

a) stagnant separation bubble at the leading edge of the blades
b) growth of the end wall boundary layer at the hub and the tip
c) loss due to the shear action on blade surfaces
d) corner losses in both pressure and suction side end wall corners, the latter being most important
e) mixing loss between secondary and 3-D primary flow
f) dissipation loss of all vortices and complete mixing of the non-uniform outlet flow

The present paper will address only a few of these loss mechanisms. However a systematic approach will be adopted to illustrate and quantify the basic loss mechanisms. To this end, the flat plate viscous solution has been firstly investigated in order to validate the Navier-Stokes code. Then the solver has been adopted to the flow about NACA 0012 airfoil. This is a well established external flow test case. The shock boundary interaction has been illustrated in a lambda mode for flow around NACA 0012 airfoil section. Finally 3-D inviscid and viscous flow in the Durham low speed high turning turbine cascade is investigated. Comparisons are presented between computed and experimental results. Comparisons are also made between Euler and Navier-Stokes solutions.

2. GOVERNING EQUATIONS

The system of time dependent three-dimensional Navier-Stokes equations to be solved for a perfect gas are written in conservative form using Cartesian coordinate system as:

$$\frac{\partial U}{\partial t}+\frac{\partial (F-F_v)}{\partial x}+\frac{\partial (G-G_v)}{\partial y}+\frac{\partial (H-H_v)}{\partial z}=0 \qquad (1)$$

where

Paper presented at the AGARD PEP 85th Symposium on "Loss Mechanisms and Unsteady Flows in Turbomachines", held in Derby, United Kingdom, 8-12 May 1995, and published in CP-571.

$$U=\begin{bmatrix}\rho\\ \rho u\\ \rho v\\ \rho w\\ e\end{bmatrix}$$

$$F=\begin{bmatrix}\rho u\\ \rho uu+p\\ \rho uv\\ \rho uw\\ \rho uH\end{bmatrix}\quad G=\begin{bmatrix}\rho v\\ \rho uv\\ \rho vv+p\\ \rho vw\\ \rho vH\end{bmatrix}\quad H=\begin{bmatrix}\rho w\\ \rho uw\\ \rho vw\\ \rho ww+p\\ \rho wH\end{bmatrix}$$

$$F_v=\frac{1}{\mathrm{Re}_0}\begin{bmatrix}0\\ \tau_{xx}\\ \tau_{xy}\\ \tau_{xz}\\ \tau_{xx}u+\tau_{xy}v+\tau_{xz}w-\left(\frac{\mu}{\mathrm{Pr}}\right)\frac{1}{(\gamma-1)}T_x\end{bmatrix}$$

$$G_v=\frac{1}{\mathrm{Re}_0}\begin{bmatrix}0\\ \tau_{yx}\\ \tau_{yy}\\ \tau_{yz}\\ \tau_{yx}u+\tau_{yy}v+\tau_{yz}w-\left(\frac{\mu}{\mathrm{Pr}}\right)\frac{1}{(\gamma-1)}T_y\end{bmatrix}$$

$$H_v=\frac{1}{\mathrm{Re}_0}\begin{bmatrix}0\\ \tau_{zx}\\ \tau_{zy}\\ \tau_{zz}\\ \tau_{zx}u+\tau_{zy}v+\tau_{zz}w-\left(\frac{\mu}{\mathrm{Pr}}\right)\frac{1}{(\gamma-1)}T_z\end{bmatrix}$$

Where

$$\mathrm{Re}_0=\frac{\rho_0 a_0 l_0}{\mu_0}=\frac{\mathrm{Re}_\infty}{M_\infty}$$

Where M_∞ is the free stream Mach number and Re_∞ is the free stream Reynolds number. Another useful non-dimensional number appearing in the non-dimensionalization procedure is the Prandtl Number.

In the above (Reynolds averaged) form of governing Navier-Stoke's equations, μ is the sum of laminar and turbulent (eddy) viscosity coefficients. The variation of laminar viscosity coefficient for air is taken into account using the Sutherlands formula.

Thermal conductivity is obtained from the Prandtl Number. Total effective conductivity in the heat flux term is obtained by summing up the laminar and turbulent conductivity by using the Prandtl's relation.

The total energy e is related to the other variables by the equation of state for perfect gas:

$$p=(\gamma-1)(e-\frac{1}{2}\rho(u^2+v^2+w^2))$$

Total enthalpy per unit mass is calculated from;

$$H=\frac{(e+p)}{\rho}$$

Turbulence Model

The Baldwin-Lomax [2] model which is a two-layer algebraic model is used for calculating turbulent viscosity. The model is adopted to non-dimensional formulation of the present code. Inner layer eddy viscosity is found from the Prandtl mixing length theory as follows,

$$(\mu_t)_{inner}=\mathrm{Re}_0\,\rho l^2|\omega|$$

where mixing length l is defined as,

$$(l)_{inner}=0.4y\left[1-e^{\frac{-y^+}{26}}\right]$$

The non-dimensional wall distance y^+ is defined as follows,

$$y^+=\sqrt{\frac{\mathrm{Re}_0\,\rho_\omega\tau_\omega}{\mu_l{}^2}}\,y$$

The outer region where $y\geq y_{crossover}$, the turbulent eddy viscosity is calculated from

$$(\mu_t)_{outer}=\mathrm{Re}_0\cdot 0.0168\cdot C_{cp}\cdot\rho\cdot F_{WAKE}\cdot F_{KLEB}$$

where F_{WAKE} is obtained from

$$F_{WAKE}=\min(y_{\max}F_{\max},C_{WK}y_{\max}\frac{u_{DIF}^2}{F_{\max}})$$

In this equation the first formula is valid for attached boundary layers and the second formula is valid for separated boundary layers where $C_{cp}=1.6$ and $C_{WK}=0.25$. The velocity difference u_{DIF} is the difference between the maximum and the minimum total velocity in the shear layer. The vorticity moment is calculated by:

$$F(y)=y\cdot|\omega|\cdot\left[1-e^{\frac{-y^+}{26}}\right]$$

The Klebanoff intermittency factor F_{KLEB} makes the outer eddy viscosity vanish as moving far away from the wall.

3. DISCRETIZATION OF *GOVERNING EQUATIONS*

A second order accurate one step Lax-Wendroff type integration scheme due to Ni [3] has been employed to discretize the Navier- Stokes equations. The solution of any grid point at time level n+1 can be expressed in terms of the solution at time level n,

$$U^{n+1}\approx U^n+\Delta t\cdot(\frac{\partial U}{\partial t})^n+\frac{\Delta t^2}{2}\cdot(\frac{\partial^2 U}{\partial t^2})^n \qquad (2)$$

The time derivatives in above equation are evaluated in terms of the spatial derivatives from equation (1) and defining the following terms

$$\delta U=U^{n+1}-U^n$$

$$\Delta U_i^n=-\Delta t(\frac{\partial F}{\partial x}+\frac{\partial G}{\partial y}+\frac{\partial H}{\partial z})^n \qquad (3)$$

$$\Delta U_v^n=\Delta t(\frac{\partial F_v}{\partial x}+\frac{\partial G_v}{\partial y}+\frac{\partial H_v}{\partial z})^n$$

$$\Delta F^n=(\frac{\partial F}{\partial U})\Delta U_i^n,\Delta G^n=(\frac{\partial G}{\partial U})\Delta U_i^n,\Delta H^n=(\frac{\partial H}{\partial U})\Delta U_i^n$$

then

$$\delta U=\Delta U_i^n+\Delta U_v^n+\frac{\Delta t}{2}\cdot\left(\frac{\partial}{\partial x}(\Delta F^n)+\frac{\partial}{\partial y}(\Delta G^n)+\frac{\partial}{\partial z}(\Delta H^n)\right) \qquad (4)$$

Where ΔU_i^n is the inviscid and ΔU_v^n is the viscous first order changes. Current implementation corresponds to second order time accurate inviscid and first order time accurate viscous discretization. Eqn. (4) is integrated using finite volume

method. And change associated with each cell is distributed according to Ni's formula.

Local Time Stepping

Local time stepping accelerates convergence to steady state by advancing the solution at each cell in time at the prescribed CFL number. The technique was successfully used for flat plate and NACA 0012 transonic turbulent test cases. However the local time stepping was found to produce unwanted effects in NACA 0012 laminar separated flow test case and in high turning Durham turbine cascade.

Artificial Smoothing

Because the scheme is second order accurate, it generates oscillations around sharp discontinuities. Especially in transonic flows, existing shocks away from viscous dominant wall regions cause sharp discontinuities in density and pressure. Therefore numerical smoothing is needed to stabilize the flow around shocks and in parts of skew grids.

Artificial smoothing is based originally on Ni's formulation [3] which is a second difference operator for smoothing shocks. The smoothing operator implements the distribution of property change calculated in a cell. It is defined as follows:

$$\delta U = \delta U^* + \frac{1}{8}\mu (U_c - U_i) \qquad (5)$$

This is a smoothing operator for the distribution of the change calculated for a cell using Eqn. 4. Where subscript i indicates the property at the node and subscript c indicates the average value of that property at that cell. δU^* is the change before smoothing and μ is the artificial viscosity coefficient of smoothing . The local first order smoothing coefficient can be scaled by the square of the ratio of local cell Mach Number (M) to free stream Mach number (M_∞) ratio. This scaling provides the reduction of smoothing in viscous regions and provide a control over the artificial numerical dissipation in order to avoid numerical corruption.

4. BOUNDARY CONDITIONS

All boundary conditions are of characteristic type. The free stream boundary which is used in the solution of external flow test cases are of characteristic type. In the case of cascade flow the inlet and exit boundary conditions are specified by giving Mach number and flow directions. At the solid wall boundaries flow tangency condition is used for Euler solution and non-slip condition for the Navier-Stokes solution. At the midspan of linear cascade, flow symmetry is imposed by slip boundary condition. At the sides of the cascade periodic boundary condition is used.

5. TEST CASES AND DISCUSSION OF RESULTS

For verifying the Navier-Stokes solver primarily the two dimensional laminar flat plate problem is solved. . The free stream Reynolds number of the flow is 35 000 and the free stream Mach number is 0.3. For such flows the external velocity is independent from the streamwise space variable and such flows are also mentioned as constant pressure flow. An H-grid of 121x80 points (5 chords length and 3 chords of height) is used. First Δy is 0.0006 and exponentially grows towards the top boundary. Δx is clustered algebraically at the leading edge with an hyperbolic function, the minimum value is 0.0025. Similarity parameter $\eta = \frac{y}{5x}\sqrt{\mathrm{Re}_x}$ is used. Self similar Blasius solution results of u compares well with the laminar numerical solution at x/c=0.5 as seen in Fig. 1. v velocity is also found to be in good agreement with the Blasius self similar profile. A comparison of local skin friction C_f with the finite length expression as given by [4];

$$C_f = 0.664 \cdot \mathrm{Re}_x^{-0.5} + 1.334 \cdot \mathrm{Re}_x^{-0.875}$$

revealed the code as successful in computing the analytical results. Artificial smoothing coefficient is 0.001 and it is minimized by mach number scaling as explained above.

Second test case is a laminar - transition fixed - turbulent flow flat plate problem [5]. The free stream Reynolds number of the flow is 6 000 000 and the free stream Mach number is 0.3. A similar H-grid of 181x80 points of above is used. First Δy is 0.00015 and exponentially grow to the top. Δx is clustered at the leading edge and at the transition location (x/c=0.054) with minimum of 0.0025. Local skin friction coefficient is in good agreement in laminar ($C_f = 0.664 \cdot \mathrm{Re}_x^{-0.5}$) and turbulent regions with the Prandtl 1/5 law ($C_f = 0.0592 \cdot \mathrm{Re}_x^{-0.2}$). Laminar Blasius solution results of u compares well with the laminar numerical solution at x/c=0.04 as seen in Fig.3.a. Turbulent solution is compared with the turbulent 1/7 power law $(u/U) = (y/\delta)^{1/7}$ at several streamwise locations in Fig.3.b. There are 4 grid points in the laminar sublayer ($y_+ \le 5$) and around 25 points in the boundary layer. Turbulent similarity profiles are given in Fig. 4. In this figure calculated laminar sublayer, logarithmic and wake regions are presented at several streamwise locations along the flat plate.

Third test case is a numerical test case. The Laminar separation on a NACA 0012 airfoil which was attempted by several code developers was of interest [6,7,8,9,10,11]. A two dimensional laminar flow solution is obtained on the NACA 0012 airfoil at zero angle of attack with 0.5 free stream Mach number. The challenge is to calculate the laminar separation at the trailing edge due to the adverse pressure gradient. The free stream Reynolds Number of the flow is 5000. A C-type grid of 257x65 points is used. Farfield is at 6 chords away from the airfoil. For this grid 129 points are on the airfoil and 65 points are on the wake. Δx at the leading edge and trailing edge are 0.001 and 0.005 respectively. First Δy is 0.0006 . Global time step and artificial smoothing scaling are used as explained above. Local skin friction and static pressure coefficient results on the airfoil are given in Fig. 5. Flow separation is obtained at 55% chord. Other authors calculated the separation around 80-82 % chord. In the solution, complete airfoil is used and symmetric separation is obtained without enforcing symmetry condition. It is believed that the location of separation is sensitive to adverse pressure gradient which starts at 25% chord in our calculation. Accurate modeling of viscous effects with minimum numerical smoothing in the viscous layer is needed in order to obtain laminar separation due to existing adverse pressure gradient. Computed total pressure loss is given in Fig. 6. The figure shows that the maximum total pressure loss is in the viscous layer at the first half of the airfoil. There is a loss core in the separated region down the trailing edge. A close up view of the flow at the trailing edge and in the wake is given in Fig. 7. Velocity profiles and streamlines are illustrated in the recirculation region.

There are sources of loss associated with shock waves in both compressors and turbines because of the interaction of shock wave and the boundary layer. A boundary layer separation bubble is usually formed at the foot of the shock and extra dissipation is likely to occur within the downstream of the bubble. If the boundary layer is laminar the bubble will almost certainly cause transition. Strong shock waves may cause complete boundary layer separation.

The next test case is a transonic test of the Baldwin- Lomax turbulence model on a well established external flow over NACA 0012 [12]. The free stream Reynolds Number is 9 000 000 and Mach Number is 0.799. The angle of attack is 2.26 degrees (experimental angle of attack is 2.86). A C-type grid of 257x65 points is used. Farfield is at 6 chords away from the airfoil. For this grid 192 points are on the airfoil and 32 points are on the wake. Δx at the leading edge and trailing edge are 0.001 and 0.005 respectively. First Δy is 0.0001 . Fig. 8 shows the grid as clustered at 55% chord where the shock wave is expected. Fig. 9 shows the Mach Number contours. The strongest shock forms approximately at 58% chord at the suction side above the boundary layer. The upstream Mach Number of the shock is 1.25. The shock is curved to upstream about 45% close to the surface due to viscous effects. Flow separates at the downstream of the shock, does not reattach on the blade but merge into the wake. Mach Number outside the separated region again reach to supersonic speeds at approximately 95% chord showing a sign of a second shock as the other leg of the lambda shock. Fig. 10 illustrates the variation of total pressure loss around the airfoil. The maximum loss occurs in the boundary layer at the downstream of the shock. Iso-total pressure lines extend around the shock indicating the entropy increase across the shock. The high loss fluid is accumulated on the upper side of the airfoil.

Durham Turbine Cascade

This cascade is a test case of ERCOFTAC and extensive research is being carried out [13,14]. The Durham turbine blade section is representative of a high pressure turbine rotor blade. Details of the experimental facility are given in references [15,16]. The cascade turns the flow 110 degrees and produces a strong secondary flow. Upstream velocity is 19.1 m/s which corresponds to an approximately incompressible flow. At the cascade inlet, end wall boundary layer measurement is available; the static pressure is taken as constant and the total pressure is calculated from the measured velocity profile. This gives a total pressure and velocity distribution at the inlet. A mean velocity is calculated at the outlet using the inlet mass flow rate and blade angles assuming incompressible flow.

The high turning linear turbine cascades vortex structures and loss have been investigated by various authors [17,18,19,20,21]. The approaching end wall boundary layer towards the cascade leading edge produces the two counter-rotating branches of the horseshoe vortex. Namely the pressure side and suction side horse shoe vortices. Because of the turning, the well known passage vortex also forms. Pressure side horseshoe vortex rotates in the same direction as the passage vortex. These two vortices merge as the flow proceeds through the blade row. The suction side branch of the horseshoe vortex convects towards the midspan. The position of this vortex depends on the cascade geometry and overall flow conditions. There might be a suction side corner vortex rotating in the same direction as the suction side horse shoe vortex. This vortex forms as the pressure side limiting streamlines come in contact with the suction side of the adjacent blade. The corner vortex occurs inside end wall boundary layer.

The present solution is performed only up to the mid span position because of the symmetrical flow of this linear turbine cascade. The flow is initially analyzed by the Euler version of the Navier-Stokes code. Then the same geometry is run with the laminar flow throughout. An H-type grid (81x33) has been used in the blade to blade plane. In the streamwise direction there are; 14 grid points in the upstream, 48 in the bladed section and 19 in the downstream. The same 2-D grid have been stacked 30 times in the spanwise direction in order to obtain the 81x33x30 grid for the computation. The code is run at an elevated Mach number. Average inlet Mach Number used is 0.148 instead of the actual 0.055. One expects in this case some convective errors that might affect the computed total pressure distribution. Reynolds Number of the flow is $4x10^5$ The experimental velocity profile given at slot 1 of the data is applied to the upstream boundary condition. During computations maximum Mach Number experienced in the flow is 0.35.

The mass averaged total pressure distribution in the streamwise direction was monitored in order to reduce the numerical viscosity in the case of Euler solution. Mass averaged total pressure change in the streamwise direction never exceeded 0.6 percent of the inlet mass averaged total pressure in the Euler computations. The Navier-Stokes solution was restarted from the converged Euler solution. The solution is considered converged as the residuals reduce by 3 orders.

Fig. 11 shows the limiting streamlines obtained by taking a cut at 1.0% halfspan. Fig. 11 shows the limiting streamlines near the leading edge, the well known saddle point flow pattern is observed as a result of Navier-Stokes computations. This is generated due to viscous hub and the prescribed inlet velocity profile. In this figure at the downstream of saddle point the flow is pushed towards the suction side due to the pressure side horseshoe vortex which can easily turn the flow inside the end wall boundary layer. This end wall boundary layer cause the pressure side horse shoe vortex to lift off from the hub along the streamwise direction. As a result of this lift off, the cross flow from pressure side to suction side increase.

The total pressure contours at x=47.8 mm downstream of the trailing edge (Fig. 12), show the accumulation of the loss near the suction side. A low energy flow region is seen at the end wall. The end boundary layer loss is slightly swept from the end wall leaving a thinner loss layer at the hub mid pitch region. The high loss core near half pitch, quarter span develops almost at the measured position. Distribution of loss is in agreement with those presented in reference [13]. The loss magnitude is high, but maximum values are very close to the hub, below 5 mm span. Fig.13 displays the secondary velocity field and the secondary streamlines at the same axial position. Passage vortex can be seen clearly. Bottom half of the passage is dominated by a large passage vortex, whose core is located at the mid pitch close to the end wall. A smaller vortex core exists below mid span near the suction surface, which is the rolled up suction side horse shoe vortex. In this plane the pressure surface is unloaded with the flow directed - by the merged pressure side horse shoe and passage vortices - away from the pressure side.

Pitch averaged data for the total pressure and yaw angle are presented in Fig.14 a and b. Fig. 14.a shows spanwise pitch averaged loss distribution which resembles qualitatively to the experimental data. However the magnitude of loss is predicted higher as it has been pointed out by other authors[16,21]. The

discrepancy is attributed to the numerical dissipation due to grid quality. The overturning of flow near the end wall and the underturning of flow between the vortex core and the mid span are observed. The mid span turning is over predicted (approximately 67 degrees) as compared to the measured value of 66.7 degrees. Fig. 15 shows the two legs of the hub leading edge horseshoe vortex, looking upstream from a location just downstream of the leading edge. The clockwise rotating pressure side and counter-clockwise rotating suction side vortices are clearly visible in the figure.

5. CONCLUSION

An explicit time-marching, hexahedral 3D Navier-Stokes solver which uses cell vertex one-step Lax-Wendroff scheme with Ni - type distribution have been applied to two and three dimensional flow problems. The laminar "Blasius" and turbulent type solutions over a flat plate and the laminar trailing edge separation past a NACA 0012 airfoil have been successfully calculated. The shock boundary layer interaction and resulting loss has also been given for the aforementioned airfoil- but this time - at an angle of attack. The turbine cascade test case treats the loss distribution under the presence of secondary incompressible flows. Despite the wide range in the Reynolds Numbers (5 000 - 9 000 000) and in the inlet Mach Numbers (0.148 - 0.799), the calculated flow field loss structure and magnitude agree with analytical, numerical and experimental results.

ACKNOWLEDGMENT

This work is partially supported by ROKETSAN and it is a part of the ongoing research within METU Aerospace Design Technology Group.

REFERENCES

1. Oktay, E., Akmandor, İ.S. and Üçer, A.Ş., "Three Dimensional Solution of Internal Flows Using a Cell Vertex Finite Volume Method", AGARD-CP-510, February 1992, Paper 27.
2. Baldwin, B.S. and Lomax, H., "Thin-Layer Approximation and Algebraic Model for Separated Turbulent Flows", AIAA Paper, 78-257, 1978.
3. Ni, R.H., "A Multiple Grid Scheme for Solving the Euler Equations", AIAA Journal , Vol. 20, No. 11, pp. 1565-1571, 1982.
4. Schlichting, H., "Boundary-Layer Theory", McGraw-Hill Book Company, 7th edition, 1987, (ISBN 0-07-055334-3), pp. 147-148.
5. Liu, F., and Jameson, A., "Multigrid Navier-Stokes Calculations for Three-Dimensional Cascades", AIAA Journal, Vol. 31, No. 10, pp. 1785-1791, 1993.
6. Swanson, R.C., and Turkel, E., "A Multistage Time-Stepping Scheme for the Navier-Stokes Equations", AIAA Paper, 85-0035, 1985.
7. Swanson, R.C., and Turkel, E., "Artificial Dissipation and Central Difference Schemes for the Euler and Navier-Stokes Equations", AIAA Paper, 87-1107, 1987.
8. Radespiel, R., "A Cell-Vertex Multigrid Method for the Navier-Stokes Equations", NASA Technical Memorandum 101557, 1989.
9. Tysinger, T.L., and Caughey, D.A., "Implicit Multigrid Algorithm for the Navier-Stokes Equations", AIAA Paper, 91-0242, 1991.
10. Mavriplis, D.J., and Jameson, A., "Multigrid Solution of the Navier-Stokes Equations on Triangular Meshes", AIAA Journal, Vol. 28, No. 8, pp. 1415-1425, 1990.
11. Crumpton, P.I., Mackenzie, J.A., and Morton, K.W., "Cell Vertex Algorithms for the Compressible Navier-Stokes Equations", Journal of Computational Physics, Vol. 109, pp. 1-15, 1993.
12. Holst, T.L., "Viscous Transonic Airfoil Workshop Compendium of Results", AIAA Paper, 87-01460, 1987.
13. Gregory-Smith, D.G., "The ERCOFTAC Seminar and Workshop on 3D Turbomachinary Flow Predictions-December 1992", Paper ASME 93-GT-423, 1993.
14. Cleak, J.G.E. and Gregory-Smith, D.G., "Experimental Verification of a 3D Turbulent Flow Calculation in an Axial Turbine Cascade", AGARD-CP-510, February 1992, Paper 8.
15. Gregory-Smith, D.G. and Cleak, J.G.E., "Secondary Flow Measurements in a Turbine Cascade with High Inlet Turbulence", Journal of Turbomachinary, Vol. 114, pp 173-183, January 1992.
16. Gregory-Smith, D.G., "Durham Low Speed Turbine Cascade: ERCOFTAC Turbomachinary Workshop Test Case No.3 ", Private Communication, April 1994.
17. Sieverding, C.H., "Secondary Flows in Straight and Annular Turbine Cascades", Thermodynamics and Fluid Mechanics of Turbomachinary, Vol. 2, pp 621-664, NATO ASI Series, Martin Nijhop Publishers, 1985.
18. Moore, J. and Moore, J.G., "Performance Evaluation of Linear Turbine Cascades Using Three-Dimensional Viscous Flow Calculations", Journal of Engineering for Gas Turbines and Power, Vol. 107, pp 969-975, October 1985.
19. Langston, L.S., "Research on Cascade Secondary and Tip-Leakage Flows- Periodicity and Surface Flow Visualization", AGARD-CP-469, February 1990, Paper 19.
20. Yaras, M.I. and Sjolander, S.A., "Losses in the Tip-Leakage Flow of a Planar Cascade of Turbine Blades", AGARD-CP-469, February 1990, Paper 20.
21. Hirsch , Ch., "CFD Methodology and Validation for Turbomachinary Flows", AGARD-LS-195, May 1994, Paper 5.

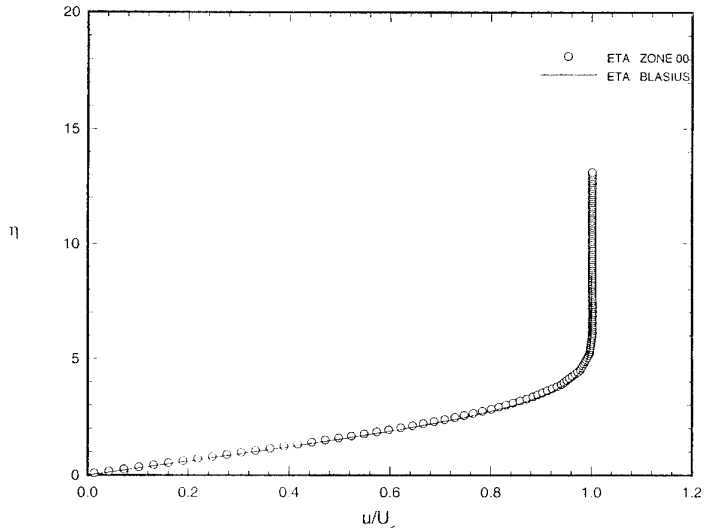

Fig. 1. u velocity profile at x/c=0.5

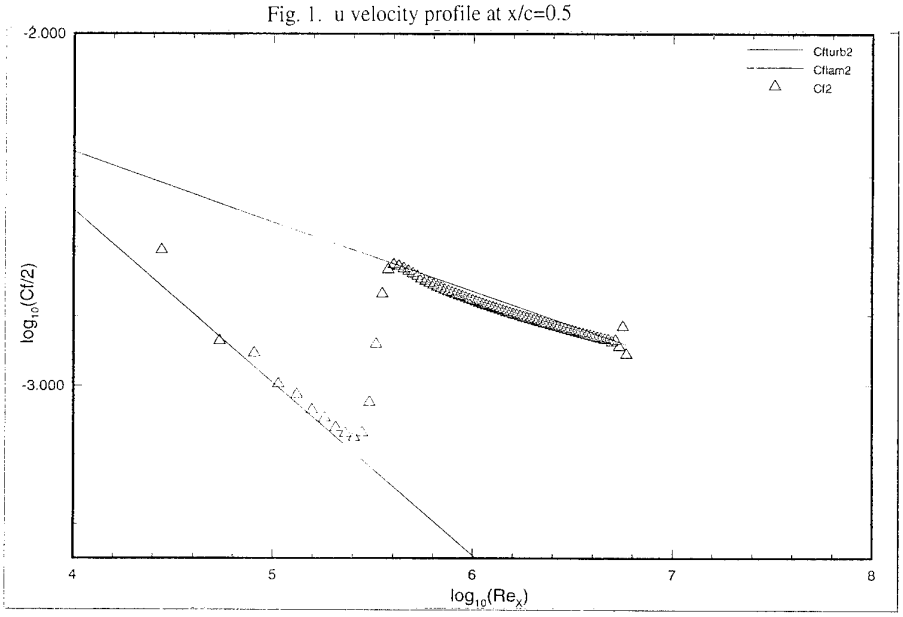

Fig. 2. Skin friction variation along the wall

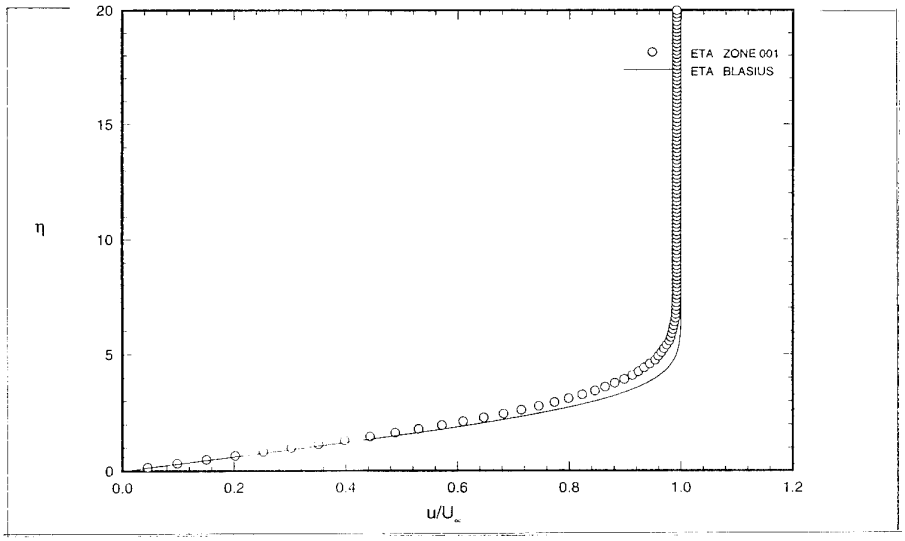

Fig. 3.a. Laminar u-velocity profile comparison at x/c=0.04

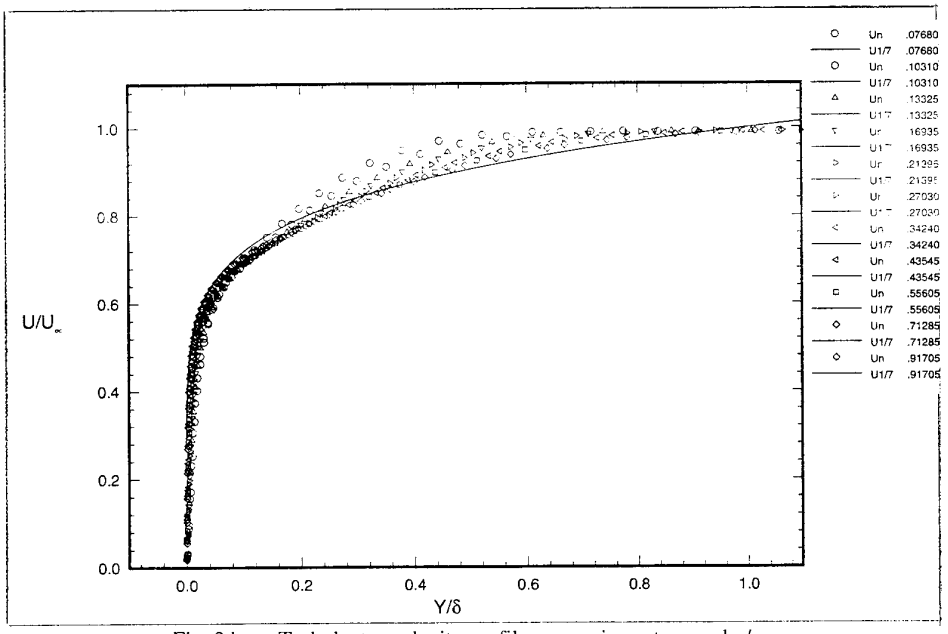

Fig. 3.b. Turbulent u-velocity profile comparison at several x/c

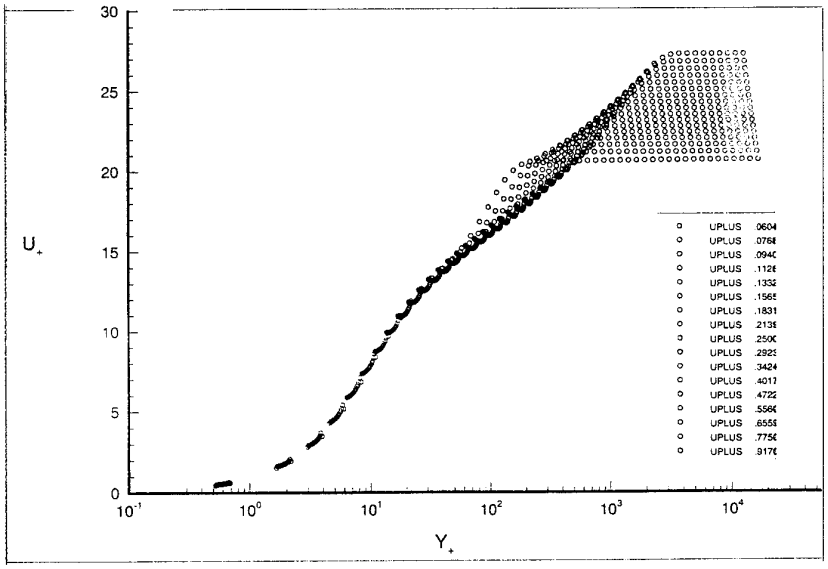

Fig. 4. Turbulent similarity profiles calculated at several x/c

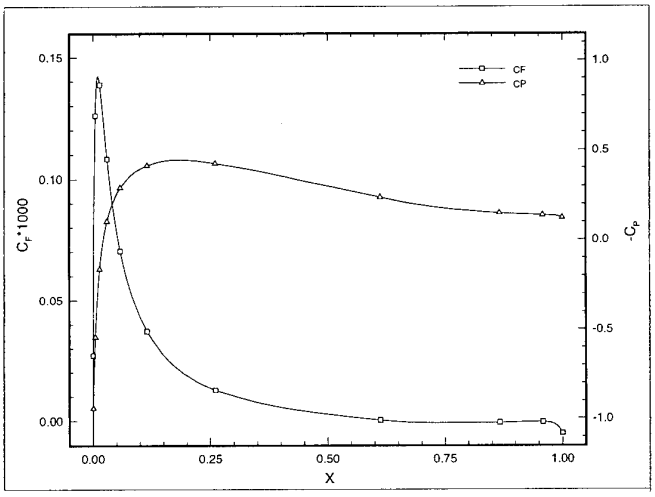

Fig. 5. Skin friction and static pressure coefficient variation along NACA 0012.

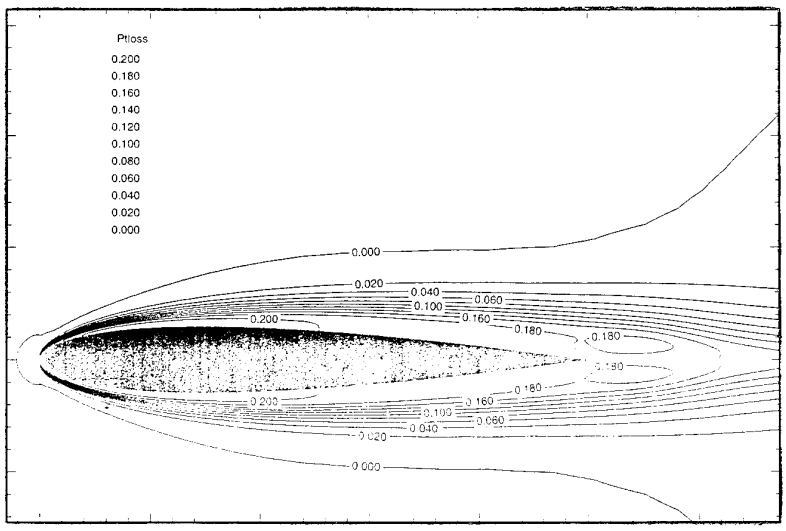

Fig. 6. Total pressure loss computed around NACA 0012.

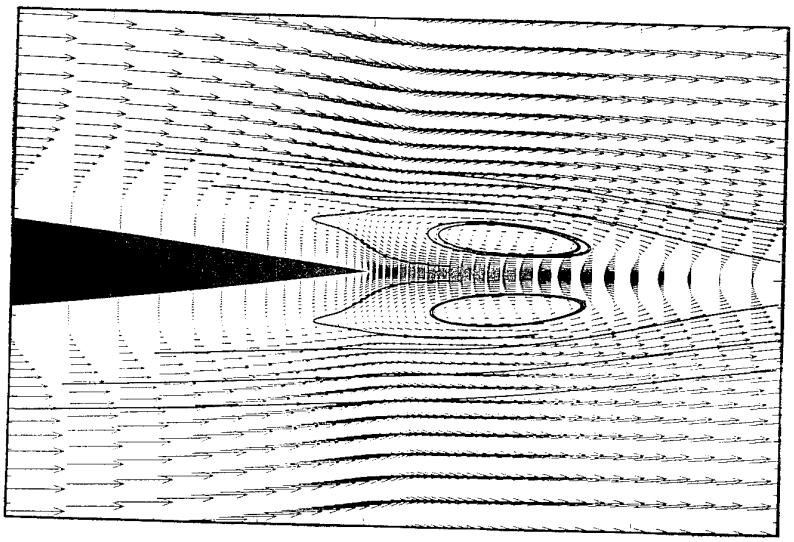

Fig. 7. Velocity vectors and streamlines computed around trailing edge of NACA 0012.

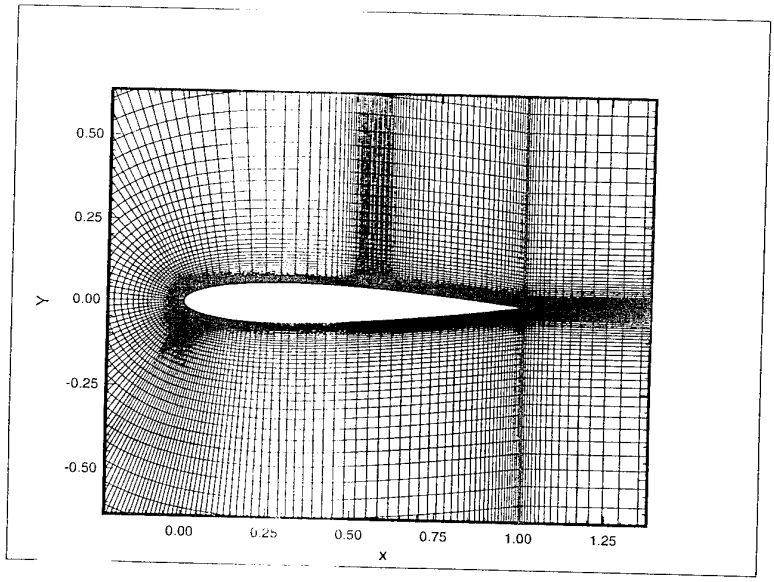

Fig. 8. Close up view of the grid used in transonic NACA 0012 computations.

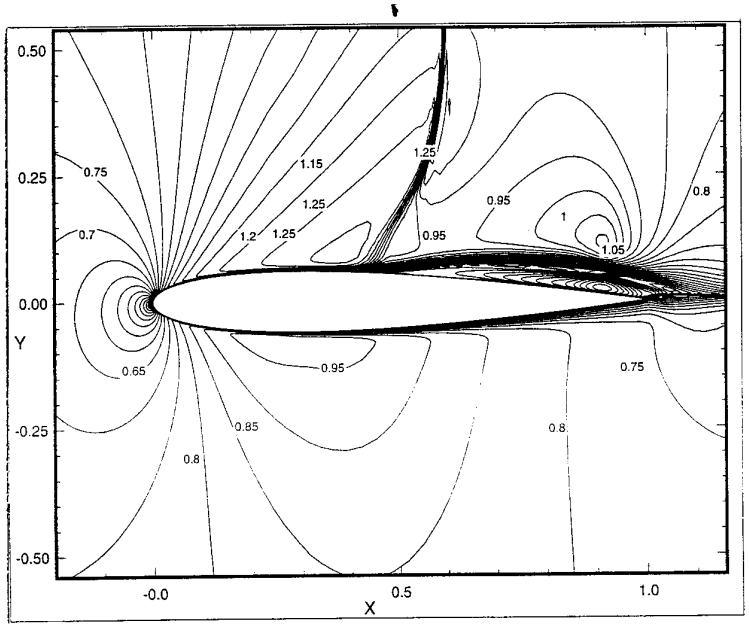

Fig. 9. Mach Number contours computed around NACA 0012.

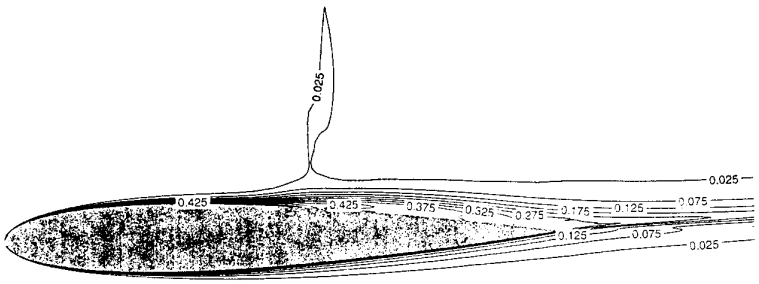

Fig. 10. Total pressure loss contours computed around NACA 0012.

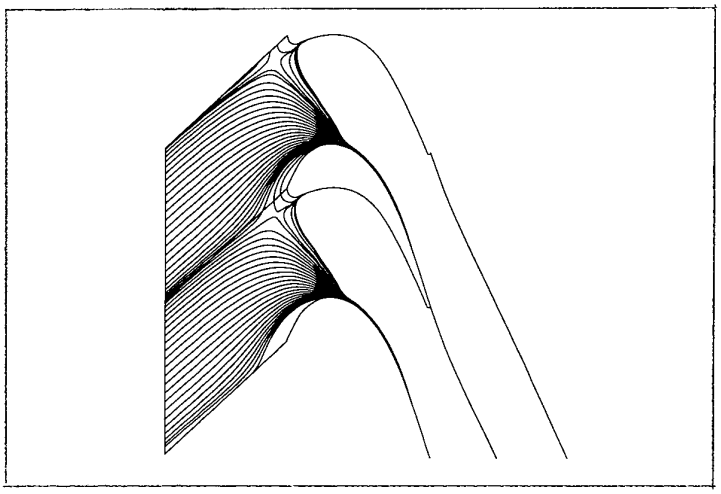

Fig. 11 Streamlines near hub for Navier-Stokes solutions.

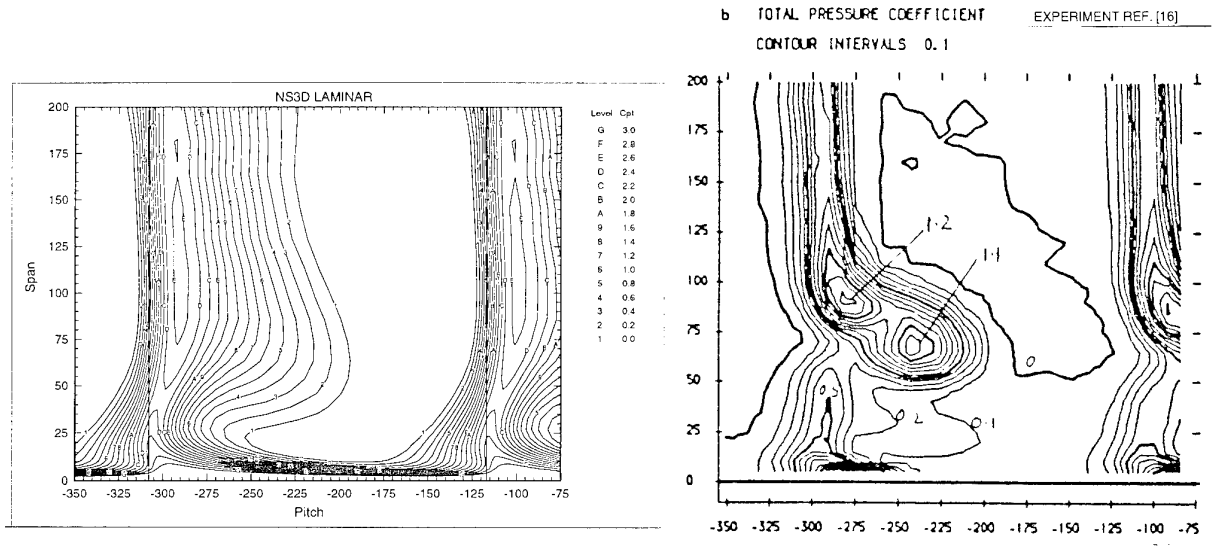

Fig. 12. Calculated total pressure loss coefficient distribution. Experimental data [16].

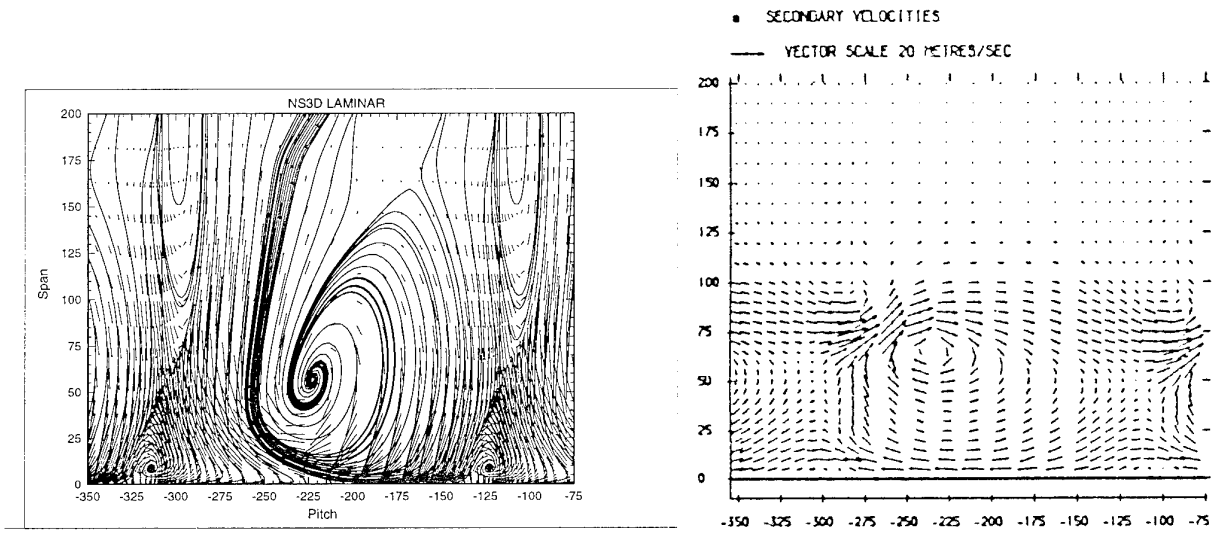

Fig. 13. Calculated secondary velocity vectors and streamlines at downstream of cascade. Experimental data [16].

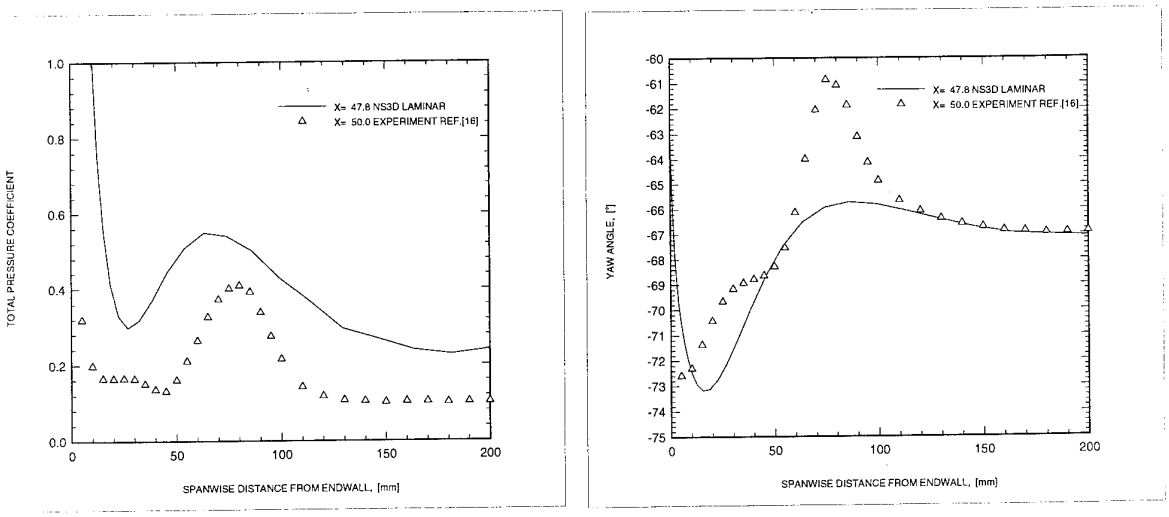

Fig. 14. Calculated pitch averaged total pressure loss coefficient and yaw angle.

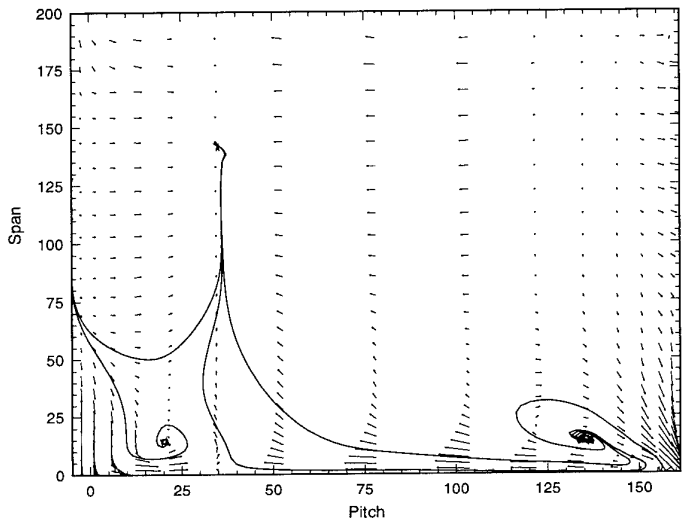

Fig. 15. Calculated secondary velocity vectors and streamlines inside the cascade passage near leading edge.

REFERENCE NO. OF THE PAPER: 18

DISCUSSOR'S NAME: G.D. Willis, GEC-Alsthom, U.K.

AUTHOR'S NAME: T. Tinaztepe

Q: Do you have plots of the turbulence visosity (or effective visosity) from the Baldwin-Lomax Turbulence Model?

A: No, instead we presented in Figure 4 the calculated turbulent similarity profiles at several axial locations. In regions like the laminar sublayer, the logarithmic law of the wall and the wake profiles are captured as a result of Baldwin-Lomax turbulence model.

REFERENCE NO. OF THE PAPER: 18

DISCUSSOR'S NAME: D.G. Gregory-Smith, Univ. of Durham, U.K.

AUTHOR'S NAME: T. Tinaztepe

Q: There seems to be too much loss at mid-span. This is similar to other computations with fully turbulent flow assumed. Often this results in too much loss and not enough secondary flow. Did you have fully turbulent flow, or did you fix a transition point? If it is a laminar calculation, this suggests a lot of numerical loss. What was your grid like? Did it have a lot of skew?

A: The presented solutions are obtained with full laminar flow assumption. The magnitude of loss is predicted too high, and this discrepancy is attributed to the numerical dissipation due to grid quality. An H-type grid is used in which there are 81, 33, and 30 grid points in the axial, blade to blade and spanwise directions, respectively. The blade boundary layer (or wake) was found to be thick compared to the experimental data, and this is due to the laminar flow assumption and the predicted flow separation on the suction side blade surface. Also, the coarse grid near the blade surface contributes to the flow separation. Increasing the grid points, especially near the blade surface, together with use of transition-fixed turbulent solutions is believed to be necessary to improve the computational results.

REFERENCE NO. OF THE PAPER: 18

DISCUSSOR'S NAME: NW Harvey, Rolls-Royce, U.K.

AUTHOR'S NAME: AS Ucer

Q: Computational results are greatly enhanced by including comparisons with experiment. Do you have any such comparisons?

A: Results of the first two test cases are compared with analytical Blasius solutions for laminar computations (see Figures 1, 2, 3a). Turbulent flat plate solutions are compared with Prandtl's Law in Figure 3b, and turbulent similarity profiles are obtained in Figure 4. NACA 0012 laminar separation is a numerical test case (M=0.5, Re=5000) and results are discussed in the paper. For the results of transonic turbulent flow over the above airfoil, the shock position agrees with the experimental position, and the other details are discussed in the paper. Durham turbine cascade results are compared with the experimental data at downstream plane and presented in Figures 12, 13, 14.

Rotor-Stator Interaction Effects On Turbulent Boundary Layers

R.L. Evans and R.M. Holland
Department of Mechanical Engineering
The University of British Columbia
Vancouver, B.C., V6T 1W5
Canada

1. SUMMARY

Compressor and turbine blade boundary layers in axial-flow turbomachines are subject to periodically disturbed flow. This study modelled these conditions in a wind tunnel with circular cylinders traversing in front of a flat plate. Turbulent boundary layer velocity profiles on the flat plate were measured with a hot-wire anemometer. The ensemble-averaged turbulence intensity in the boundary layer was found to be significantly increased by the unsteady free stream flow, resulting in increases in the characteristic boundary layer thicknesses and the skin friction coefficient. The vortex structure within the unsteady cylinder wakes was found to explain the behaviour of the velocity and phase angle profiles in the boundary layer.

2. INTRODUCTION

The unsteady phenomenon present in turbomachinery is due to the movement of upstream blades relative to downstream blades, creating periodic wakes that interact with the downstream blades. This unsteadiness may be of considerable interest in compressors because the blades tend to operate in near-stall conditions and may therefore be greatly affected by any change in the flow conditions. The study of turbomachine blade boundary layers has grown in interest due to the desire to continually improve the performance of axial flow gas turbine engines. Evans [1] studied the effects of rotor blade wakes on stator blade boundary layers of a large model axial-flow compressor. He found that the unsteady flow resulted in higher time-averaged boundary layer integral parameters such as δ^*, θ, and C_f. The higher momentum loss was found to be caused by the wake disturbance from the upstream blades influencing the boundary layer.

In a subsequent paper, Evans [2] found that the fluctuations were out of phase with the free stream throughout the boundary layer. Evans and Yip [3] studied the effects of periodic cylinder wake disturbances on a turbulent flat plate boundary layer. Their results showed that the unsteadiness caused by cylinders passing in front of the plate resulted in a dramatic increase in the displacement and momentum thicknesses in the foremost section of the boundary layer, but that the unsteady effects diminished downstream. A phase lag was noticed for the wake profile in the boundary layer as compared to the wake profile in the free stream, attributed to the generally lower convection velocity in the boundary layer. This study extends the analysis and amplifies the results of Evans and Yip [3]. In particular, the experimental apparatus was redesigned to provide true one-dimensional cylinder velocity while allowing unsteady measurements much further downstream. Analysis of the data focussed on the presence of discrete vortices in the cylinder wakes, and on their effect on the tubulent boundary layer.

3. EXPERIMENTAL DESIGN

In a turbomachine compressor or turbine the incoming flow is of velocity U_0, while the rotor blade is travelling perpendicular to the incoming fluid at velocity U_{rot}, as shown in Figure 1. Wakes created behind the rotors propagate downstream, and affect the boundary layers on subsequent blade rows. A periodic unsteadiness results due to the passage of these wakes over the downsream blade rows.

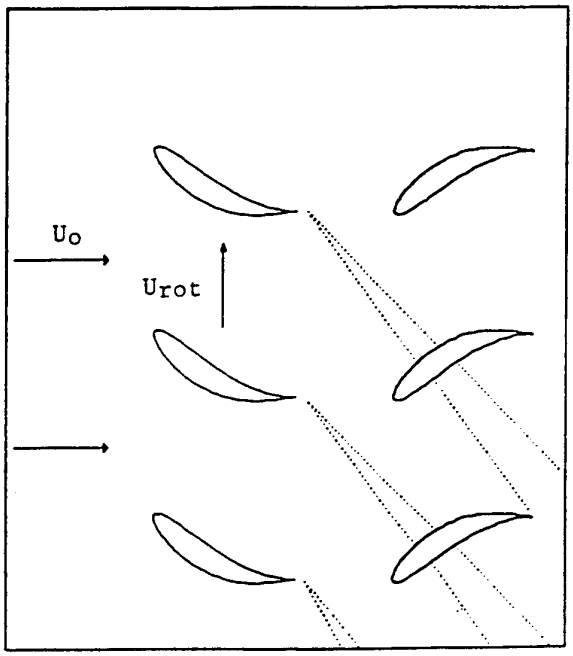

Figure 1. Schematic Drawing of Rotor/Stator Interactions inside Gas Turbine Compress Section

Paper presented at the AGARD PEP 85th Symposium on "Loss Mechanisms and Unsteady Flows in Turbomachines", held in Derby, United Kingdom, 8-12 May 1995, and published in CP-571.

In the experimental set-up used for this study, the incoming air travels at velocity U_0, as shown in Figure 2. A series of circular cylinders, modelling rotor blades, travel perpendicular to the incoming flow at velocity U_{cyl}, and a flat plate, representing a stator blade, is placed downstream of the cylinders in a wind-tunnel. The set-up duplicates the relative flow conditions present in axial flow turbomachinery but does not account for blade geometry or 3-dimensional effects. This was felt to be the simplest form of experimental set-up to model the very complicated unsteady boundary layer development on actual turbomachinery blades.

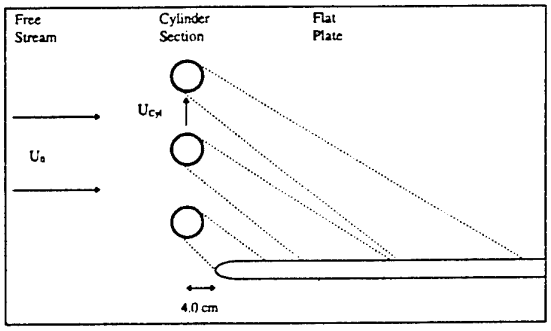

Figure 2. Schematic Diagram of Wind Tunnel Experiment to Model Axial Flow Compressor Rotor/Stator Interactions.

In order to simulate actual turbomachinery conditions in the experimental model, the wake strength of the cyliners and the flow coefficient were matched to typical turbomachine conditions. Wake strength, determined by multiplying the coefficient of drag, C_d, by the characteristic length, is used to compare the relative forces on the bodies that create the wake disturbances:

$$C_d(rot) \cdot L = C_d(cyl) \cdot D \qquad (1)$$

Duplicating the flow coefficient, defined as the ratio of free stream velocity to the velocity of the moving rotor blades, ensures that relative flow characteristics are maintained:

$$C_\theta = \left(\frac{U_0}{U_{cyl}}\right)_{wt} = \left(\frac{U_0}{U_{rot}}\right)_{comp} \qquad (2)$$

4. EXPERIMENTAL FACILITY

A two-dimensional model of the rotor-stator interaction process was constructed in an open-circuit wind tunnel, and the apparatus is shown in Figure 3. Rotor blades were simulated by a series of circular cylinders attached to an endless belt mechanism which passed through slots in the top and bottom walls of the wind tunnel. The cylinders, seven in number, were 1.27 cm in diameter and were spaced 21.5 cm apart. The first two and last two cylinders were used to establish consistent periodic wakes for the three centre cylinders, and these were used to generate wakes which then convected over the flat plate. Only one side of the belt mechanism contained the cylinders, so that just one row of blades passed in front of the flat plate when the pulleys holding the belt were rotated. Horizontal vibrations of the cylinders in motion were limited to an amplitude of less than 2.0mm. The wind tunnel test-section measured 20cm in height by 40cm in width. Free stream velocity ranged from less than 1.0 m/s to about 15.0 m/s, and the average free stream turbulence intensity was less than one percent. Typical flow coefficients inside an operating gas turbine engine can range from 0.5 to 4.0. The cylinder apparatus was limited to a maximum velocity of less than 5.0 m/sec, and therefore flow coefficients of 1.0 and 2.0, with cylinder velocities of 2.0, 3.0, and 4.0 m/s were used for the study.

The flat plate, placed 4.0cm downstream of the plane of the cylinders, had an elliptical leading edge to ensure smooth flow without separation or disruption. The plate extended 2.5 m downstream so that conditions in the boundary layer far downstream of the moving cylinders could be studied. The plate Reynolds number, based on distance from the leading edge, ranged from 10^5 to 10^6. A trip-wire was used near the leading edge of the plate to ensure turbulent flow over the entire length. The trip-wire, 0.8 mm in diameter, was taped to the top of the plate one centimetre downstream of the leading edge. A triggering mechanism, used to ensure that data acquisition began at the same point in each experimental cycle, consisted of a small magnet attached to the leading cylinder and a hall-effect switch to detect the passing of the magnet. In practice, this proved to be a very reliable triggering method. A Disa P15 hot wire probe, using 5μm platinum plated tungsten wire, along with a Disa C16 general purpose bridge, was used to measure fluid velocity in both the free stream and in the boundary layer. The hot wire was calibrated against steady-state flow conditions, using a correction for wall proximity effects described by Evans [1]. Although ambient temperature variations were considered negligible, the apparatus was frequently re-calibrated.

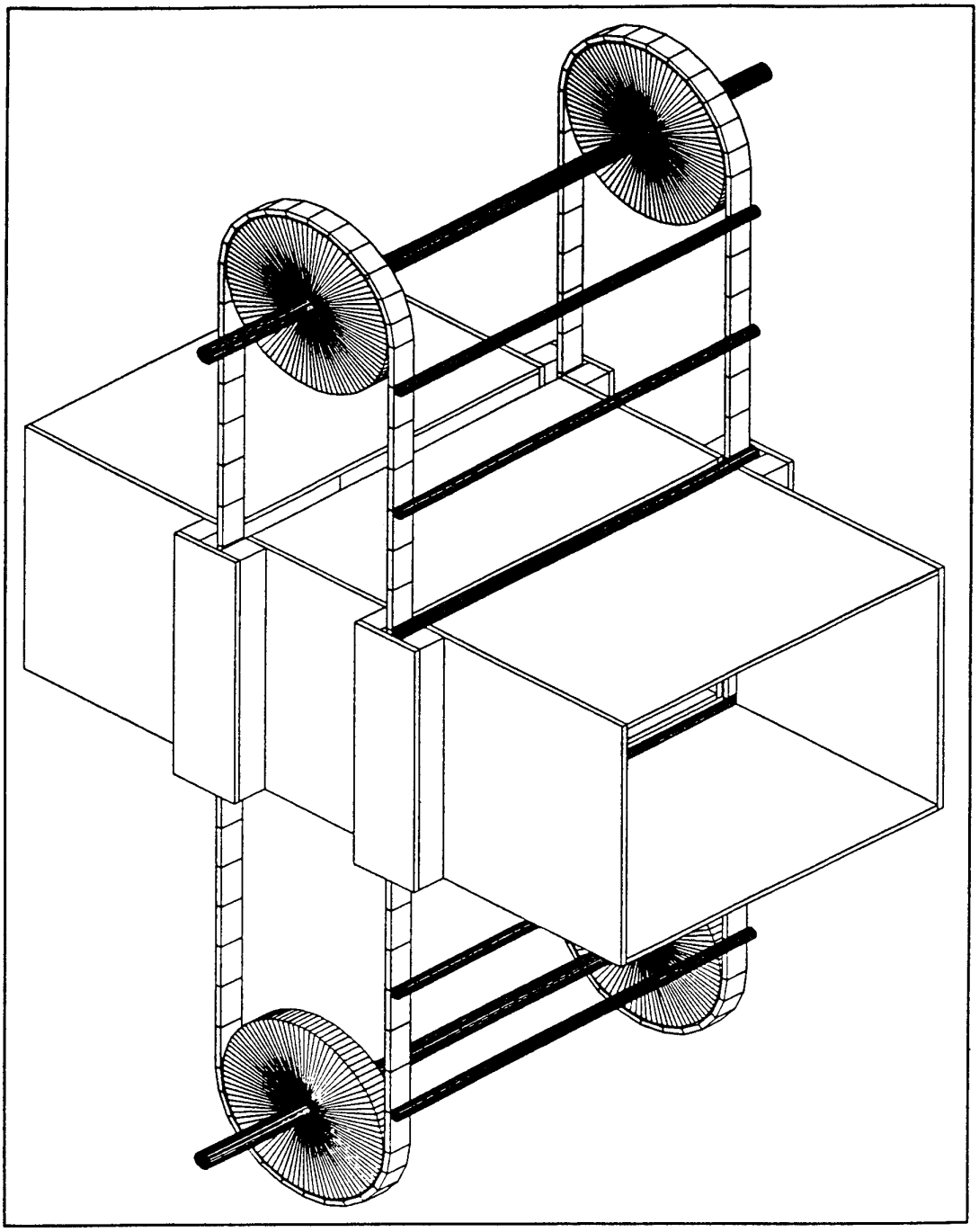

Figure 3. Rotating Cylinder Apparatus used to create Unsteady Periodic Wake Disturbances in the Wind Tunnel Test Section.

5. DATA ANALYSIS

The experimental velocity records contain both periodic unsteadiness and random turbulent fluctuations. It is therefore necessary to account for these effects when establishing velocity profiles and turbulence intensity distributions. An ensemble-averaging technique was therefore used, as shown schematically in Figure 4 for flow in the free steam downstream of the moving cylinders.

The ensemble-averaging procedure was begun by averaging the instantaneous velocity records for each point in time:

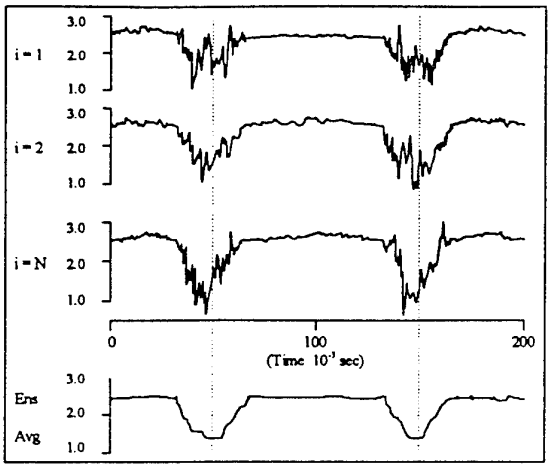

Figure 4. Graphical Representation of Ensemble-Averaging

$$\overline{U}(t) = \frac{\sum_{i=1}^{N} U_i(t)}{N} \qquad (3)$$

The number of instantaneous velocity records required to ensure consistency varied from a minimum of 50 in the free stream flow near the leading section of the flat plate to a maximum of 130 deep inside the boundary layer on the flat plate. Similarly, the ensemble-averaged turbulence intensity is defined by:

$$\overline{T_u}(t) = \left(\sum_{i=1}^{N} \left(U_i(t) - \overline{U}(t) \right)^2 / N \right)^{0.5} / \overline{U}(t) \qquad (4)$$

The velocity deficit is the difference between maximum and minimum ensemble-averaged velocities over one period. Phase angle defines the lead or lag of the ensemble-averaged velocity records throughout the profile. The reference velocity record, the outermost record, is arbitrarily assigned a phase angle of 0°. A positive phase angle corresponds to a velocity record which leads the reference velocity in phase, while a negative value represents a phase lag.

6. EXPERIMENTAL RESULTS

The ensemble-averaged free stream velocity records were compared to an analytical solution for a steady state wake developed by Reichardt [4]. The actual ensemble-averaged free stream velocity record does not completely coincide with the analytical solution, as seen in Figure 5. The size and shape of the characteristic free stream wake is very similar to the analytical solution, but differences are noted in the sudden rise in velocity just before the wake is encountered, and in the small velocity deficit after the wake.

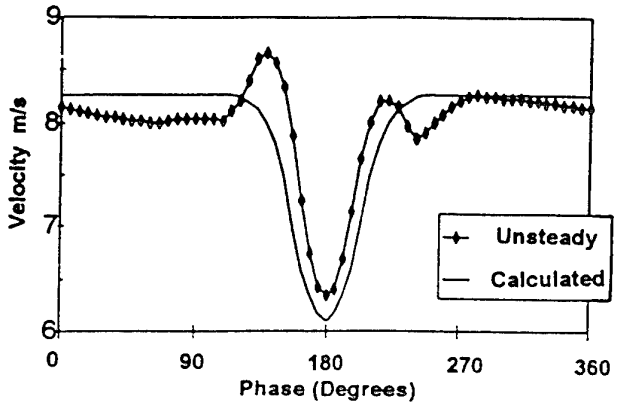

Figure 5. Ensemble-average Free Stream Velocity Record Compared to Analytical Solution of Reichardt [4].

For time-averaged unsteady results, the skin friction coefficient tends to diminish both with increasing downstream distance and with decreasing flow coefficient, $C\theta$. The skin friction coefficients were determined through the use of Clauser plots, using an estimated turbulent boundary layer thickness. For $C\theta$ = 1.0, the skin friction coefficient was 0.0054 for X = 0.12 m and 0.0047 for X = 0.66 m; for $C\theta$ = 2.0, it was 0.0048 for X = 0.12m and 0.0037 for X = 0.66m. The characteristic boundary layer thicknesses for unsteady flow were higher than those for steady flow, with a general trend showing the difference between these thicknesses for unsteady and steady flows diminishing as the flow proceeds downstream. Additionally, the ratio of unsteady to steady boundary layer thicknesses is greater for lower values of $C\theta$. The results suggest that the adverse effects are larger for lower values of $C\theta$, but that these effects generally tend to diminish as the flow proceeds downstream.

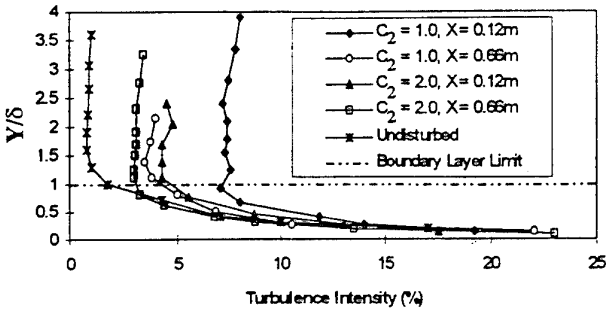

Figure 6. Ensemble-average Turbulence Intensity Profiles for $C\theta$=1.0 and $C\theta$=2.0.

Time-averaged turbulence intensity profiles are shown for both the steady and unsteady flow conditions in Figure 6. The difference between the steady and unsteady turbulence intensities diminishes as the flat plate is approached, suggesting that the turbulence in the boundary layer becomes predominant, and independent of the unsteady flow in the outer layer. The effect of flow unsteadiness on turbulence intensity decreases both with increasing $C\theta$ and increasing downstream distance. The velocity deficit varies throughout the boundary layer and the free stream, as shown in Figure 7. Moving from the flat plate out towards the free stream, the velocity deficit starts at a small value, builds up to a local maximum, and then decrease to a local minimum again, continuing in a cyclic fashion. This behaviour suggests the presence of periodic coherent structures in the wake.

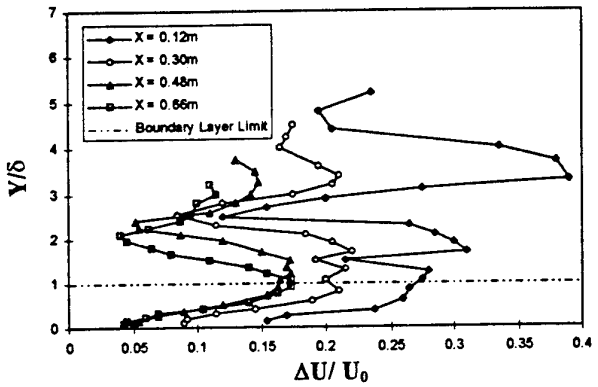

Figure 7. Boundary Layer Velocity Deficit Ratios for U_0=8.0 m/sec and U_{cyl} = 4.0 m/sec.

The phase-angle profiles through the boundary layer are shown for four different experimental conditions in Figure 8. The general trend of the phase angle profiles is a region of nearly constant phase angle as one moves towards the flat plate from the free stream, followed by a very sudden increase in the phase angle and then another region of constant phase angle. This trend continues until the boundary is reached.

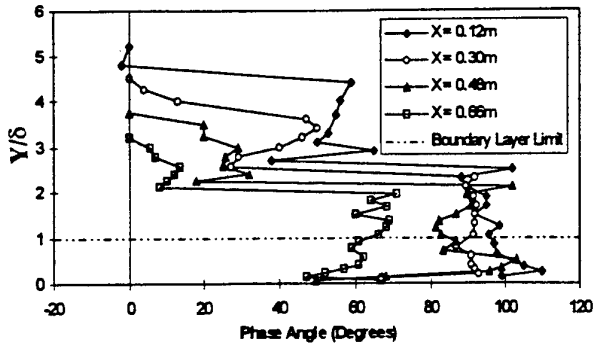

Figure 8. Boundary Layer Phase Angle Profiles for U_0=8.0 m/sec and U_{cyl}=4.0 m/sec

7. DISCUSSION

The results seen in this study suggest that unsteadiness may have a substantial effect on turbulent boundary layers. Among these effects are: increases in displacement and momentum thicknesses; an increase in turbulence intensity; cyclic variations in the velocity deficit; and step-like phase angle profiles. These effects are most prominent at lower values of the flow coefficient, and nearer to the plate leading edge. While the calculation of ensemble-averaged turbulence intensity is based on the wind tunnel free stream velocity U_0, the production of turbulence in the flow is based on the fluid velocity relative to the circular cylinder, U_{rel}. With constant U_0, U_{rel} increases with decreasing flow coefficient, $C\theta$. Therefore, the turbulence levels should be greater for flows with lower values of $C\theta$. Higher levels of turbulence in the flow with higher turbulent stresses tends to increase the local coefficient of skin friction and the characteristic boundary layer thicknesses.

The experimental results imply the presence of discrete structures, all being produced in phase, in the flow. The velocity deficit profiles suggest that subsequent structures grow, reach a maximum amplitude, and then diminish as the next structure starts its cycle. The phase angle profiles suggest that the structure is discrete, with subsequent structures occupying a given phase in the flow regime. In both cases, the structures appear to be dominant in the upstream portion of the flow, close to where the cylinder wakes are being generated. The results suggest that vortices shed from the moving cylinders tend to dominate the flow, at least near the plate leading edge. The size and shape of the discrete steps in the phase angle results suggest that the vortices are shed at a distinct frequency, are in phase with each other, and are aligned perpendicular to the wind tunnel free stream flow. In order to produce vortices that are in phase with each other, they must be triggered at the same time for each passing cylinder. This may be attributed to the passing of the cylinder in front of the flat plate. With a separation of only four cm between the cylinder centre-line and the flat plate, the leading edge of the plate may interact with the cylinder near-wake in such a way to ensure ordered triggering of vortices from the cylinder, thus ensuring the vortices remain in phase with each other. The frequency of vortex production should be directly related to the Strouhal number.

The cylinder wake velocity profiles are primarily influenced by the shed vortices, which leads to several simplifications in the overall flow regime. The time $t_{cyl} = 1/f_{cyl}$ represents one complete cycle of 360 degrees, as it is the time lapse between the appearance of two subsequent cylinders at any given position in the cycle.

The phase difference between the shedding of subsequent vortices from a cylinder would be governed by the time between the shedding of the first and second vortices from a cylinder, namely $t_{vor} = 1/f_{vor}$. This phase difference would be proportional to the vortex period divided by the cylinder period. Therefore, the phase angle profile could be predicted for this type of unsteady boundary layer. The frequency with which vortices are shed by a circular cylinder is:

$$\frac{f_{vor} \cdot D}{U_{rel}} = S \qquad (5)$$

where S is the Strouhal number. For the experimental conditions with Reynolds numbers between 600 and 9000, the Strouhal number may be assumed to remain constant at approximately 0.21, as indicated by Schlichting [6].

The relative velocity, the vector addition of the free stream and cylinder velocities, is:

$$U_{rel} = \sqrt{U_{cyl}^2 + U_0^2} \qquad (6)$$

Therefore, the flow coefficient C_θ can be used to give:

$$f_{vor} = \frac{S \cdot U_{cyl} \cdot \sqrt{1 + C_\theta^2}}{D} \qquad (7)$$

Assuming that the cylinder wakes are dominated by the vortices shed from the cylinder, the velocity profiles seen in the wake of the cylinder are determined by vortices shed at a frequency determined by the Strouhal number. The phase difference between subsequent vortices is determined by the ratio of cylinder passing frequency to vortex shedding frequency. Therefore, this phase difference is,

$$\Omega = \frac{f_{cyl}}{f_{vor}} \cdot 360^\circ \qquad (8)$$

where Ω is the phase difference between shedding of subsequent vortices. However, the cylinder passing frequency is;

$$f_{cyl} = \frac{U_{cyl}}{d} \qquad (9)$$

The phase difference can then be defined as,

$$\Omega = \frac{\Delta}{S \cdot \sqrt{1 + C_\theta^2}} \cdot 360^\circ \qquad (10)$$

where a geometrical coefficient, Δ, is defined as the ratio of the circular cylinder diameter, D, to the distance between centrelines of the circular cylinders, d. For fixed geometry and Strouhal number, phase difference is a function of the flow coefficient. With D = 0.0125m, d = 0.215m, and a Strouhal number of 0.21, the phase difference for C_θ = 1.0 would be 71.6 degrees and that for C_θ = 2.0 would be 45.3 degrees. The vertical distance that is traversed between the shedding of subsequent vortices, can be defined as:

$$d_\Omega = \frac{\Delta}{S \cdot \sqrt{1 + C_\theta^2}} \cdot d \qquad (11)$$

This must be divided by the boundary layer thickness to give the fraction of the boundary layer that is traversed by the cylinder during one vortex cycle. In this study the boundary layer thickness for U_{cyl} =4.0 m/s, U_0=8.0 m/s, and X=0.12 m was δ = 0.014 m. This equates to d_Ω = 1.77, suggesting that the cylinder travels 1.77 times the boundary layer thickness between subsequent shedding of vortices. This information can now be compared to the experimental results for the conditions stated. For U_{cyl} - 4.0 m/s, U_0 = 8.0 m/s, and X = 0.12 m, a comparison between the results obtained from the simple analytical procedure just described and the experimental results is shown in Figure 9. Overall, the comparison provides quite a good qualitative correlation between theory and experiment.

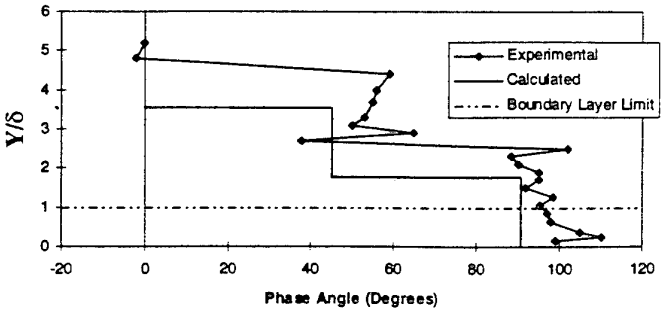

Figure 9. Kinematic versus Experimental Phase Angles for U_0=8.0 m/sec, U_{cyl}=4.0 m/sec and X = 0.12m.

8. CONCLUSIONS

The experimental evidence suggests that vortices dominate the flow structure in the cylinder wakes in the experiments described here. This is generally not the case, however, for axial-flow compressor or turbine blade wakes at or near design conditions. When approaching stall conditions, on the other hand, turbomachinery blade wakes may be subject to the onset of vortex production. The results of this study should therefore be relevant to the conditions under which turbomachines cease to operate efficiently. The knowledge gained from the study of such conditions should also provide insight into the flow conditions which result in flow-induced vibration failure of axial flow turbomachinery.

Vortices shed from the moving cylinders have a large effect on the turbulent flat plate boundary layer. The ordered triggering of these vortices seems to occur as the cylinder passes in front of the leading edge of the flat plate. The vortices are shed from the circular cylinder at a frequency determined by the Strouhal number, and are aligned perpendicular to the free stream velocity resulting in a step-like cylinder wake centreline. This wake structure tends to break down as it proceeds downstream and is affected by dissipation in the boundary layer. The boundary layer flow is controlled by the vortices inside the boundary layer, which are slowed relative to the vortices in the free stream. The boundary layer and free stream velocity profiles appear to be dominated by the vortex structure in the cylinder wake, the lower convection velocity caused by the boundary layer, and dissipation and re-orientation of the vortex structure as the flow proceeds downstream.

The boundary layer thickness, as well as the displacement and momentum thicknesses, in the unsteady boundary layer increase with decreasing flow coefficient. This seems to be a result of the increased turbulence intensity generated by the cylinder wake flows at lower values of the flow coefficient. Much more study is needed to fully understand the implications of vortices in unsteady periodic boundary layer flows. The triggering, vortex parameters (orientation, strength, shedding frequency), and dissipation must be understood in order to get a more complete picture of the complex effects.

Future work in this area should include the study of airfoil shapes passing in front of the flat plate to better model the actual conditions one would see in an axial flow turbomachine operating near the design point. The use of airfoils will enable a comparison of both streamlined body and vortex-induced wakes to be conducted, and permit a comparison of normal operating conditions with conditions near the stall point.

9. ACKNOWLEDGEMENTS

The authors would like to thank the Natural Sciences and Engineering Research Council of Canada for their support of this study.

10. REFERENCES

1. Evans, R.L., "Some Turbulence and Unsteadiness Effects in Turbomachinery", *in* "Turbulence in Internal Flows", ed. S.N.B. Murthy, Hemisphere Press, 1976, pp 485-516.
2. Evans, R.L., "Boundary Layer Development on an Axial-flow Compressor Stator Blade", ASME Journal of Engineering for Power, *100*, 1978, pp 287-293.
3. Evans, R.L. and Yip, R.S.K., "An Experimental Investigation of Unsteady Wake-Boundary Layer Interactions", Journal of Fluids and Structures 2, 1988, pp 313-322.
4. Reichardt,H., "GesetzmaBigkeiten der freien Turbulenz", VDI-Forschungsheft, VDI-Verlag, Dusseldorf, 1950, p 414.
5. Coles, D., "The Law of the Wake in the Turbulent Boundary Layer", Journal of Fluid Mechanics, *1*, 1956, pp 191-226.
6. Schlichting, H., "Boundary Layer Theory", 7th ed., McGraw-Hill, 1979.

11. NOMENCLATURE

C_d	Coefficient of drag
$C\theta$	Flow coefficient (= U_0/U_{rot} or U_0/U_{cyl})
d	Cylinder separation
D	Cylinder diameter
f	Frequency
L	Chord length of compressor rotor blade
N	Number of instantaneous velocity records
Re_x	Reynolds numbers based on X (= $U_\infty X/\mu$)
S	Strouhal number
$\overline{T}_{u(t)}$	Ensemble-averaged turbulence intensity at time t
U_0	Free stream velocity
U_{cyl}	Experimental cylinder velocity
$U_i(t)$	Instantaneous velocity in X-direction at time t
U_{rel}	Fluid velocity relative to the cylinder
U_{rot}	Compressor section rotor velocity
$\overline{U}$ (t)	Ensemble-averaged velocity at time t
X	Distance from flat plate leading edge
Δ	Cylinder geometrical coefficient (= D/d)
δ	Boundary layer thickness
δ^*	Displacement thickness
θ	Momentum thicknesses
Ω	Phase angle
d_Ω	Vertical Distance between the vortices

REFERENCE NO. OF THE PAPER: 19

DISCUSSOR'S NAME: W.B. de Wolf, NLR, The Netherlands

AUTHOR'S NAME: R.L. Evans & R.M. Holland

Q.: Could you comment on the relevance of your findings for rotor-stator wake interaction noise?

A: The phase-locked nature of the vortex shedding from the rotor would no doubt influence noise generation. We have not attempted to make any noise measurements, but we would like to add fast-response pressure measurement instrumentation for any subsequent work in this area.

REFERENCE NO. OF THE PAPER: 19

DISCUSSOR'S NAME: D.W. Bechert, DLR, Germany

AUTHOR'S NAME: R.L. Evans & R.M. Holland

Q.: Did you try to confirm your hypothesis on the vortex motion on the plate by flow visualization?

A: No, we did not do any flow visualization, but this is definitely something that we would like to try in our next set of experiments

REFERENCE NO. OF THE PAPER: 19

DISCUSSOR'S NAME: M.G. Rose, Rolls-Royce, U.K.

AUTHOR'S NAME: R.L. Evans & R.M. Holland

Q.: The vortices from the round bars will be of alternate sign. Did you try ensemble averaging for alternate vortices? One might find different response to vortices of different sign.

A.: That is a very interesting question! I believe that you are correct, but it would be interesting to see if the phase-locked vortices which are shed just as the bar passes the plate are always of the same sign. We could try ensemble averaging for vortices of alternate sign, as you suggest, but flow visualization may be another way of examining this phenomena.

EXPERIMENTAL AND NUMERICAL INVESTIGATION OF UNSTEADY FLOW PROPERTIES IN A STATOR OF MULTISTAGE AXIAL FLOW COMPRESSOR

Hubert MITON, Mustapha BELHABIB, Umit KUS

Université Pierre et Marie Curie
L.E.M.F.I. U.R.A CNRS 1504
Bdg. 511 , Campus Universitaire
91405 ORSAY - FRANCE

ABSTRACT

This analysis has been performed from tests realized in a four stage low speed axial flow compressor (4000 rpm). First, two unsteady velocities components has been measured, using hot wire anemometry, directly upstream and downstream of the first stage stator in the (r,θ) plane. Simultaneously, unsteady flow characteristics has been collected at four blade surfaces. Experimental techniques consisted first in pressure transducers fitted in the inner part of the profiles, then, in series of hot films (29), bounded, at two different radial positions, to the blade surfaces. These films were uniformly distributed orthogonaly to the axial direction, from leading to trailing edges. Data have been processed in view to identify the multiple origins of excitation from the other parts of the machine and to describe the behavior of the boundary layer along the blade surfaces. Comparison of the experimental results with the ones given by a two-dimensional blade to blade computation method, taking into account the development of the boundary layer, has been performed.

1. INTRODUCTION

Experimental investigations in turbomachinery components are frequently realized using models in which the operational conditions of machines are not accurately taken into account (isolated rotor, widely spaced blade rows). In such models the interactions between different blade rows are highly attenuated.
The present study have been carried out on an axial four stages compressor. In this machine, the spacing between the rotating and stationary blade rows is similar to one commonly used in aeronautical or industrial type of machines. The tests reported in the present paper concern the stator flow field of the first stage of this compressor.
A serie of unsteady velocity measurements have been carried out upstream and downstream the first stator using the hot film anemometry. Unsteady pressure and heat flux data have been recorded along the blade walls of the stator. Principal causes of the periodic component of the unsteadiness in the flow have been identified. Data concerning the boundary layer development on blade surfaces have been collected. These experimental data have been linked in order to use for the validation of codes.
In a first time, using these data, a comparison has been performed with a fast two-dimensional blade to blade computation method taking into account the boundary layer behavior, specially the effect of the upstream wake on the transition phenomenon. Experimental and computed characteristics of the flow are then compared.

2. EXPERIMENTAL EQUIPMENT

2.1. The Axial Compressor CME1

CME1 is a four stage axial flow compressor. A characteristic feature of this machine is the narrow spacing of the adjacent blades rows compared to the chord (10 mm vs 80 mm)); the interactions between stationary and rotating flow fields are reproduced in a realistic way. Such spacing is just sufficient to allow the use of probes between blade rows.

Total axial length of four stages is equal to 624 mm. The diameter of the casing is equal to 550 mm. On the hub, the diameter varies from 371 mm (inlet plane) to 410 mm (outlet plane) (see fig. 1).
The main characteristics of the first stage blades are given by the following table.

Paper presented at the AGARD PEP 85th Symposium on "Loss Mechanisms and Unsteady Flows in Turbomachines", held in Derby, United Kingdom, 8-12 May 1995, and published in CP-571.

	Radius	Chord (mm)	Thickness (mm)	Stagger Angle (°)	Camber Angle (°)
ROTOR	Hub	**82**	**7.4**	**44.77**	**51.65**
	Main	**82**	**6.4**	**55.17**	**37.12**
	Tip	**82**	**7.8**	**64.02**	**25.61**
STATOR	Hub	**88**	**5.2**	**19.67**	**75.30**
	Main	**88**	**5.2**	**16.72**	**71.55**
	Tip	**88**	**5.2**	**15.07**	**67.75**

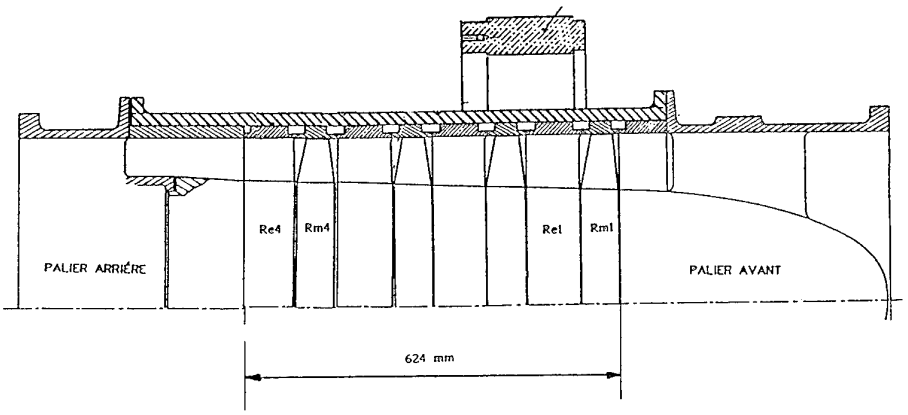

figure 1: Research Compressor CME1

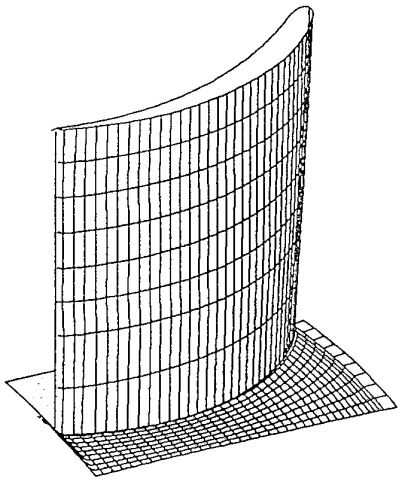

figure 2 : Stator Blade Geometry

The stator blade geometry is given below (figure 2)
For the stages 2 to 4 the blade geometries are identical to the previous one except for solidity. The values of this solidity at the hub is given below for all stages.

	Stages	Number of blades	Solidity
ROTORS	**1**	**17**	**1.027**
	2	**19**	**0.936**
	3	**19**	**0.950**
	4	**19**	**0.962**

STATORS	**1**	**24**	**0.682**
	2	**27**	**0.618**
	3	**27**	**0.626**
	4	**27**	**0.634**

The pressure ratio versus mass flow rate chart for this compressor is illustrated by figure 3.

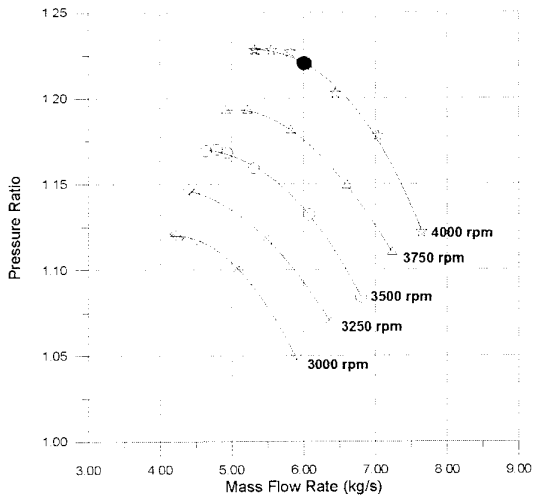

figure 3 : Characteristics Chart of Compressor CME1

2.2. Test Bed AX200

The main components of the experimental setup are represented in figure 4. It is a test rig aspirating and discharging in the atmosphere. The available power is 200 kW; the maximum rotational speed is 4500 rpm.
The mass flow rate of the compressor is regulated by axial displacement of the conical hub wall which is placed just downstream of the compressor outlet.

3. INSTRUMENTATION

3.1. "X" Hot Films Probes

"X" hot films probes, connected to a constant temperature anemometer, are used for unsteady velocity measurements (figure 5). Experimental investigations are carried out upstream and downstream of the first stage stator of the compressor.
On such way that the probe axis is parallel to the radial direction, probes measure the axial and tangential components of the flow velocity. They can be moved in planes orthogonal to the compressor axis (radial and tangential directions). A typical measurement grid (including 15x10 probe locations) is represented by figure 6. In each position of the probe, 4096 samples are acquired with a frequency of 10 kHz. In the operating condition (4000 rpm), the number of samples is about 150 per revolution.

3.2. Flush Surface Mounted Hot Films Probes

The development of the boundary layer along the surfaces of the stator is strongly affected by the rotating flow field associated to the adjacent blade rows. The relation between the wall shear stress and the rate of heat flux through the inner region of the boundary layer is well known. So the unsteady behavior of the boundary layer can be deduced from heat flux measurements using flush mounted hot films.

The suction side and pressure surface of two stator blades have been instrumented with multi-sensors array. It consists in 29 hot films equally spaced (3 mm), covering the blade surface from its leading to its trailing edge. Current is supplied by conductive tracks mounted on blade surface, along the spanwise direction. As a result, one can displace the array of sensors along the blade span (see figure 7).

However it is not possible to calibrate properly the films with respect to the shear stress; so one has to keep in mind that those probes provide mainly qualitative data, as pointed out by several authors.
For each sensor, 4096 samples are acquired with a sampling frequency of 15 kHz.

3.3. Wall Pressure Transducers

The suction and pressure sides of two stator blades have been instrumented with miniature pressure transducers. For each blade, 5 sensors are spaced along chordwise direction up to 70 % chord length. Each transducer is radially moved in order to investigate 7 positions from root to tip of the blade. The corresponding measurement grid is shown by figure 8.
Static and dynamic calibration of the whole device (including the transducer and the pressure orifice) has been performed. The static sensitivity of the transducers is about 38 mV/bar. Dynamic calibration curves (amplitude, phase) are plotted in figure 9 a and b . The cutting frequency of the device is pratically five times greater the blade passing frequency. In evidence, this system is also used to carry out steady pressure measurements.

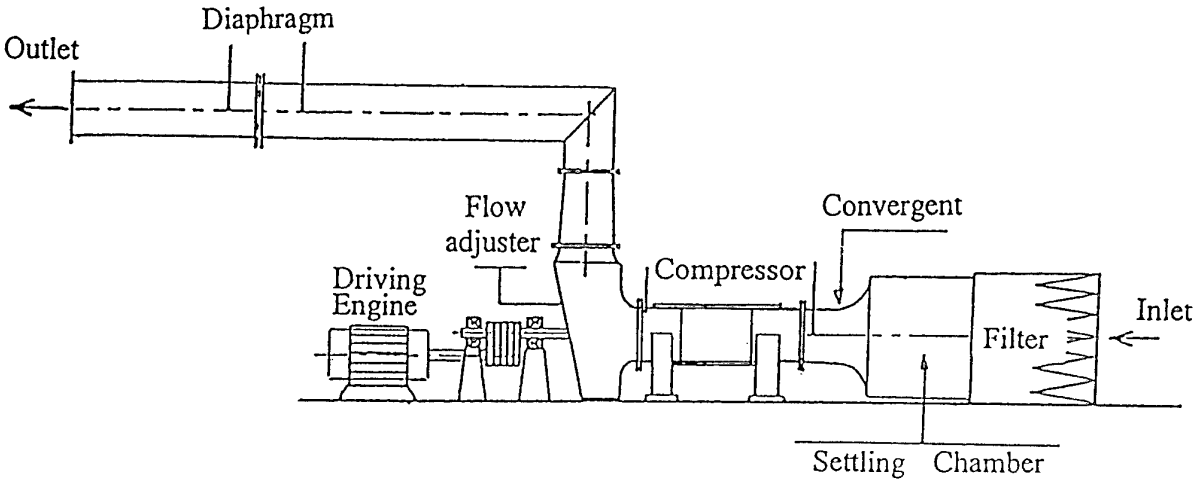

figure 4 : Test Bed AX200

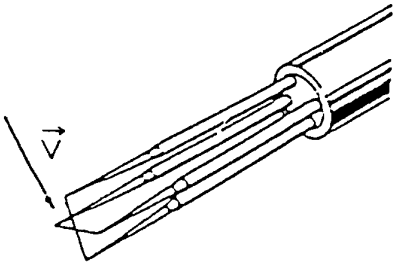

figure 5 :" X " Hot Films Probe

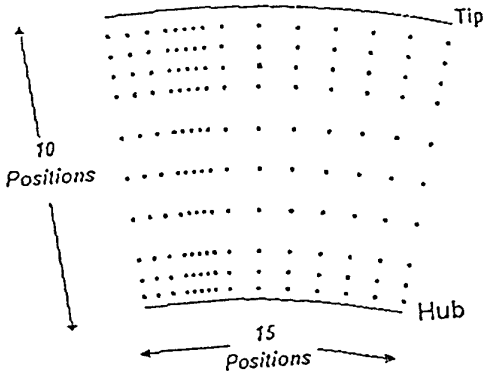

figure 6 : Measurement Grid in (r,θ) Plane

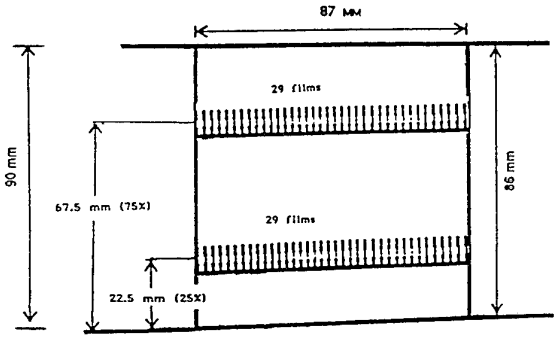

figure 7 : Flush Surface Mounted Hot Films Probes

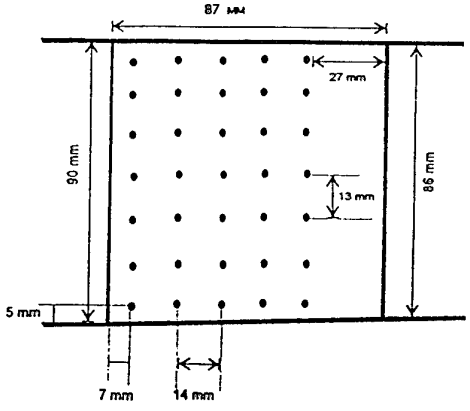

figure 8 : Pressure Measurement Grid on Blade Surfaces

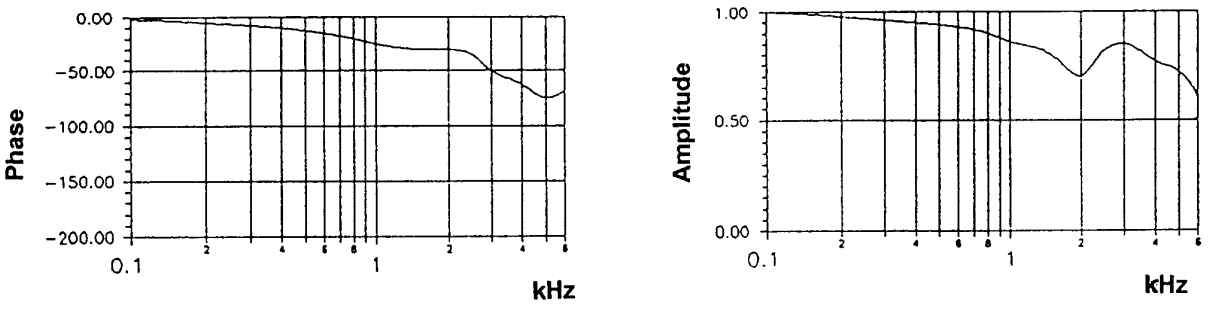

- a - - b -

figure 9 : Dynamic Calibration Curves of Pressure Transducer

4. DATA PROCESSING

The unsteady characteristics of the flow (velocity, heat flux etc..) are splitted in three components :

1) main value
2) periodic fluctuations
3) random fluctuations

A Fourier transform of 4096 samples is presented in figure 10. Two sort of harmonics (peaks and noise) can be observed in this spectrum. The peaks characterize the periodic fluctuations, while the noise is due to random fluctuations. Distinction between periodic and random fluctuations is performed by using a criterion based on the spectral energy distribution (Belhabib [1994] and [1995] , Miton et al. [1994]). Inverse Fourier transform gives separately periodic and random fluctuations in time domain. An equivalent method was developed recently (Camp et al.[1995]). This method suppose that the pick's frequencies corresponding to periodic fluctuations are well known. Which is not our case, where several picks exist in the spectrum induced by rotor /rotor interaction

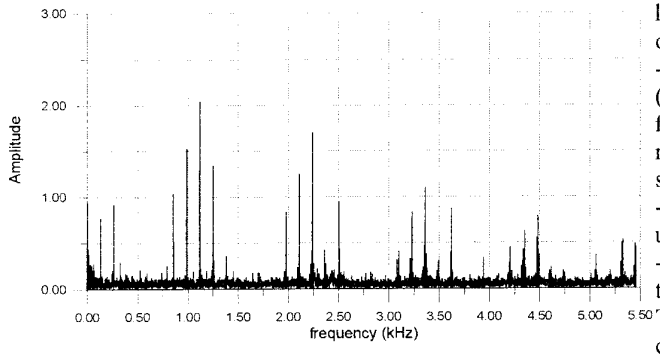

figure 10 : Velocity Spectrum Downstream of Rotor 1

5. FLOW CALCULATION METHOD.

The viscous-inviscid interaction method used in the present work was designed to model the phenomena typically occur in a subsonic, incompressible, steady flow in cascades of airfoils. The inviscid flow is simulated by a singularity method using the incompressible potential flow equations. The viscous solver is built up from integral models of the boundary layer development. These include:

- the laminar boundary layer development from the leading edge stagnation point up to the transition onset,
- the transitional boundary layer development (natural, by-pass, periodic unsteady or by the formation of a laminar separation bubble which may reattach after transition ends or burst into a separated flow region),
- the attached turbulent boundary layer development, until its separation if it occurs,
- the separated flow region which extends until the trailing edge, if it exists.

The laminar and turbulent boundary layers are computed by solving the Von Karman integral incompressible boundary layer equations using a theory formulated by Le Foll (1965). For the closure of the integral equations the Falkner-Skan laminar boundary layer and Le Foll's turbulent boundary layer profiles are used. For the turbulent separation, Jacob's simple free streamline theory (1982) is used. It consists in simulating the separated zone as an isobaric streamline, emanating from the separation point which is evaluated iteratively.

Four types of transition are considered : natural, by-pass, separated flow and wake-induced. For the two first type, the prediction of transitional flow is carried out in two steps: transition onset and transition

length. First the start of transition is predicted by using Wilkinson's onset criterion. Then Emmons' Intermittency concept (1951) is used in order to predict the transitional values of boundary layer integral parameters such as thicknesses and shape factors. An advanced type of Dhawan & Narasimha's criterion is used for predicting the intermittency distribution which corresponds to the transition length. The natural and bypass type of criteria have been discussed by Kus & Chauvin (1994).

Separated flow transition has been considered by computing laminar separation bubbles using the semi-empirical method developed by Roberts (1980). When laminar separation is detected, the location of transition, the boundary layer characteristics at transition and the reattachment point are determined from the value of δ_2 at separation, the semi-empirical theory of Roberts and the potential flow velocity distribution.

In order to simulate the unsteady effects of passing wakes, in the semi-steady form, Pfeil and Herbst 's "time-averaged condition" approach (1979) and Mayle and Dullenkopf 's "turbulent strip" theory (1990 and 1991) are used. From those, it can be deduced that the time-averaged wake-induced intermittency depends only on the reduced frequency which is an input for the problem, and the beginning of transition due to wakes which must be evaluated. It can be supposed in fact that the effect of the wake on the boundary layer is essentially due to the high-local instantaneous level of turbulence acting as a switch to generate turbulent spots and the beginning of transition due to the wakes is calculated by the steady flow approach mentioned above using a very high level of turbulence typically 5 to 10%.

The coupling method described above allows to obtain the local characteristics of the boundary layer as well as the global performance. The local performance are the local boundary layer thicknesses, shape factors, the
existence, position and length of laminar separation bubbles when appropriate, beginning of transition, length of transition region, the turbulent separation point when existing. The global performance are the exit angle and the loss coefficient. The exit angle is obtained from the calculated outlet flow angle at the end of the convergence process involving both potential and the boundary layer type of calculation. The loss coefficient is obtained by calculating the mass-weighted averaged total pressure at the cascade exit-plane, the reduction of the total pressure being due to the boundary layer and the separation region. For the latter, the boundary layer computation stops at the separation point. The value of the displacement thickness at the trailing edge is known as it is equal to the dividing streamline height from the blade surface, while the momentum thickness at trailing edge is obtained from the shape factor H_{12} which is calculated using an empirical model based on NACA results (NACA TN 3916). The applications of the actual flow method in turbomachinery environment have been discussed by Kus & Chauvin (1995).

6. RESULTS

All the following results have been obtained for a revolution speed equal to 4000 rpm and a mass flow rate equal to 6.0 kg/s (see figure 3)

6.1 Characteristics of the mean flow field upstream and downstream of the stator

First, upstream of the stator (inlet plane : see figure 11), the flow is essentially affected by the leading edge of the stator blades, as well as the hub and the casing. In the vicinity of the leading edge of the stator, a low axial velocity field is observed, extending from the hub up to the casing boundary layer. The thickness of the casing boundary layer is about15% of the blade height. Despite the fact that hot wire velocity measurements are not significant very close to the wall, it is observed that the velocity defect interest mainly the axial component; therefore the flow incidence with respect to the blade tip is high. In this region the level of turbulence is important (up to 6 %). Close to the hub, the tickness of boundary layer is less than on the casing. Also turbulence intensity is lightly lower (4.5%). In the region extending from 10% to 80% of the blade height, the velocity is quite uniform 68 m/s : except close to the leading edge). The level of turbulence in this region is about 3%. Downstream of stator (outlet plane : figure 2), the influence of the walls on flow (blades wakes and wall boundary layers) can be clearly distinguished. The velocity defect in the wakes of the stator blade is about 25%. Far from the wall, the velocity is fairly uniform. It can be observed that the tangential velocity component is always negative (opposite sense of rotation) or zero, except in the casing region.

6.2 Characteristics of the unsteady flow upstream and downstream of stator.

In the inlet plane, velocity defect in the wakes of the first rotor are quite weak. Then it is more interesting to use the turbulent intensity in order to identify the rotor blade passages. The pictures presented in figure 13 show the wakes prints with respect to the turbulence intensity at different times of a blade passing period. It can be observed that the center of the wake is slightly dephased with respect to the trailing edge of the rotor. This is due to the axial distance from the rotor trailing edge to the probe. Due to secondary flows, the width of the wake appear to be larger close to the hub and the casing than in the mid-span region. Downstream of the stator, the flow field is strongly influenced by the rotating velocity field relative to the second rotor blades. The potential "upstream influence" of this rotor propagates through the first stator and interact even with the wakes of the first rotor (see fig. 14 and 15).

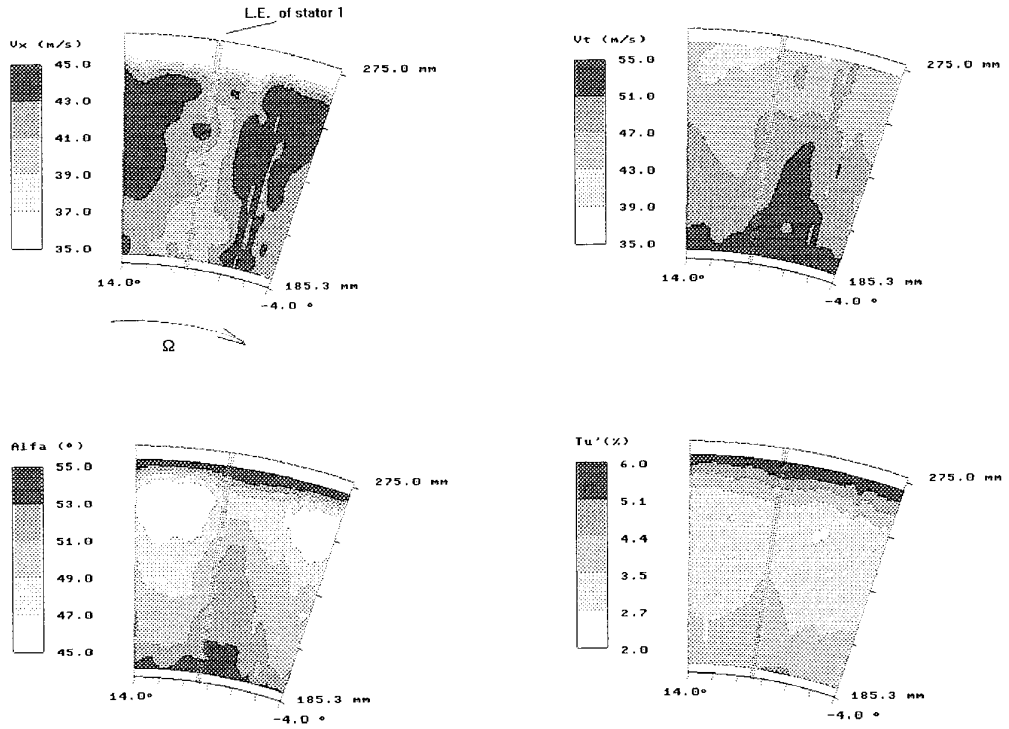

Inlet Plane

figure 11: Mean Flow Field Upstream of Stator 1

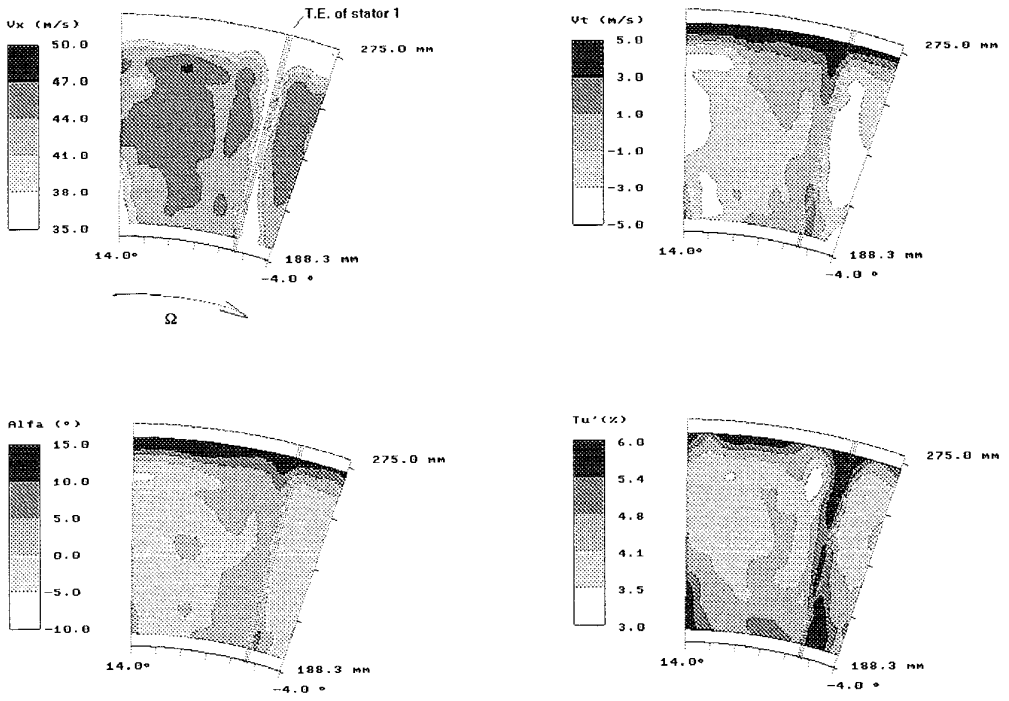

Outlet Plane

figure 12 : Mean Flow Field Downstream of Stator

6.3 Unsteady pressure field on the wall of stator

The unsteady static pressure fields on the wall of stator blades are plotted on figures 16 (pressure side) and 17 (suction side) for different instants of the blades passing period. A pseudo static pressure P^* deduced from the velocity measurements have been used to represent the flow at inlet and outlet planes, at the same instants. This pseudo static pressure is defined using the following way :

$$P^*(t) = Pi - \frac{1}{2} \cdot \rho \cdot \tilde{V}(t)^2$$

where Pi is the mean total pressure measured in the inlet plane using a pitot probe, $\tilde{V}(t)$ the unsteady velocity given by the hot films probes. This pseudo pressure is introduced only as an element of comparison between the pressure measurements on the blades surfaces and the velocity measurements at inlet and outlet planes.Those plots show the propagation of the pressure waves along the blade suction and pressure side of the blades. This phenomenom depends mainly on the location of the leading edge of the second rotor. Its period is equal to 0.88 T1 = 17/19 T1, where T1 represents the passing period of the first rotor, 17 and 19 being the number of blades in the first and the second rotor respectively. At the time t=0, a blade of the second rotor is just located behind the trailing edge of the stator.

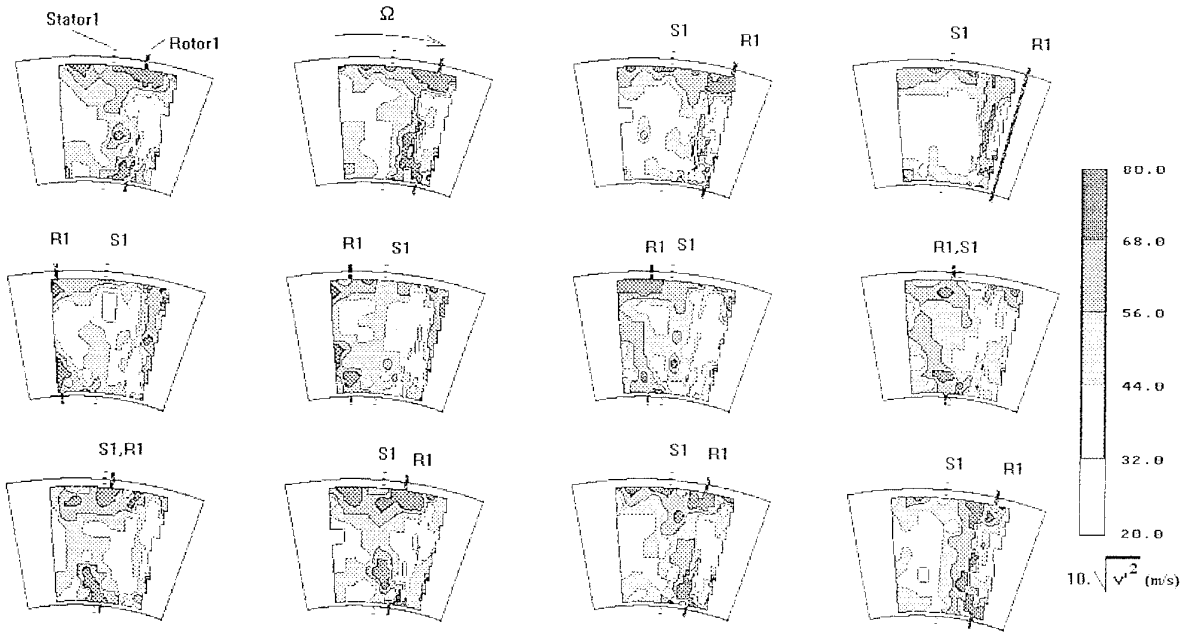

figure 13 : Unsteady Turbulence Intensity Fields Downstream of Rotor 1

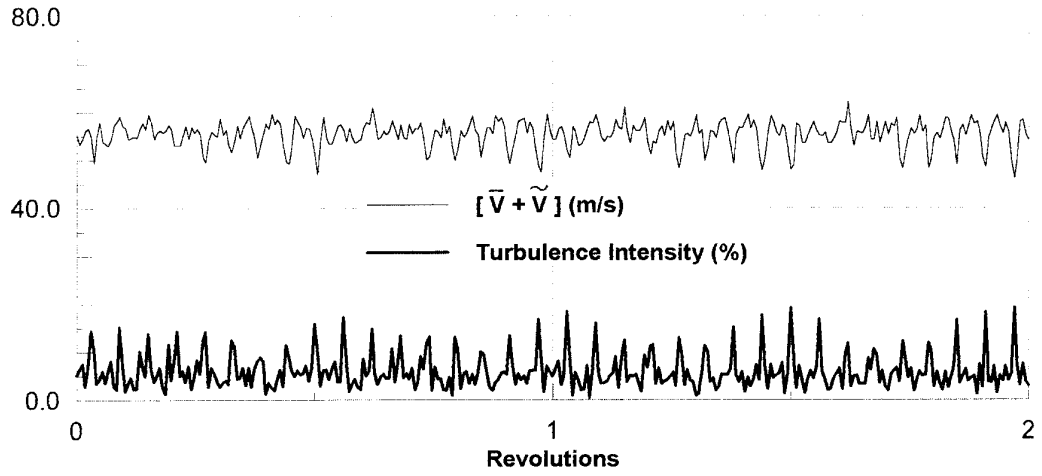

figure 14 : Periodic Signals of Absolute Velocity and Turbulence Intensity Downstream of Rotor1

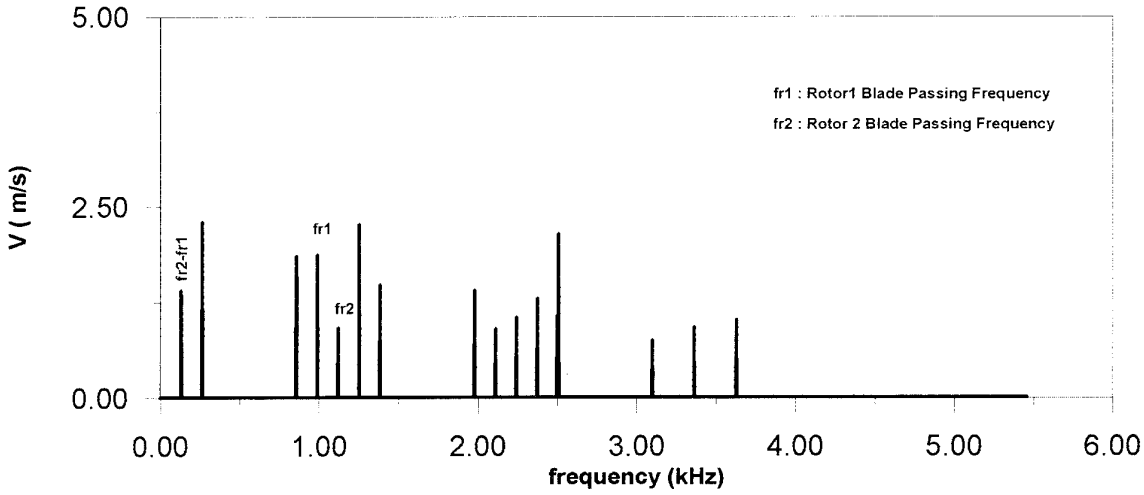

figure 15 : Spectrum of Periodic Velocity Downstream of Rotor 1

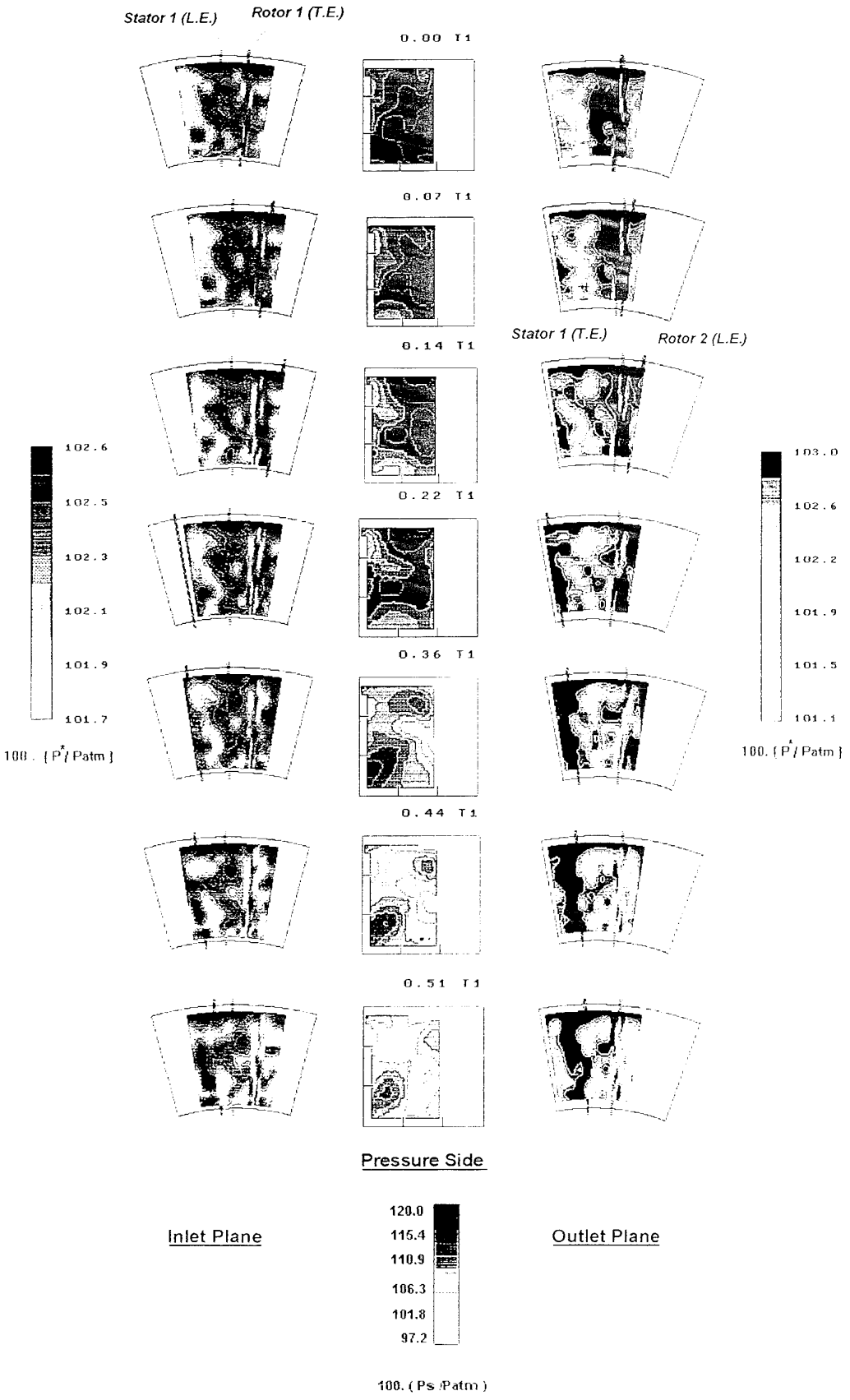

figure 16 : Effects of Neighbouring Rotors on Stator Surface Pressure Field (Pressure Side)

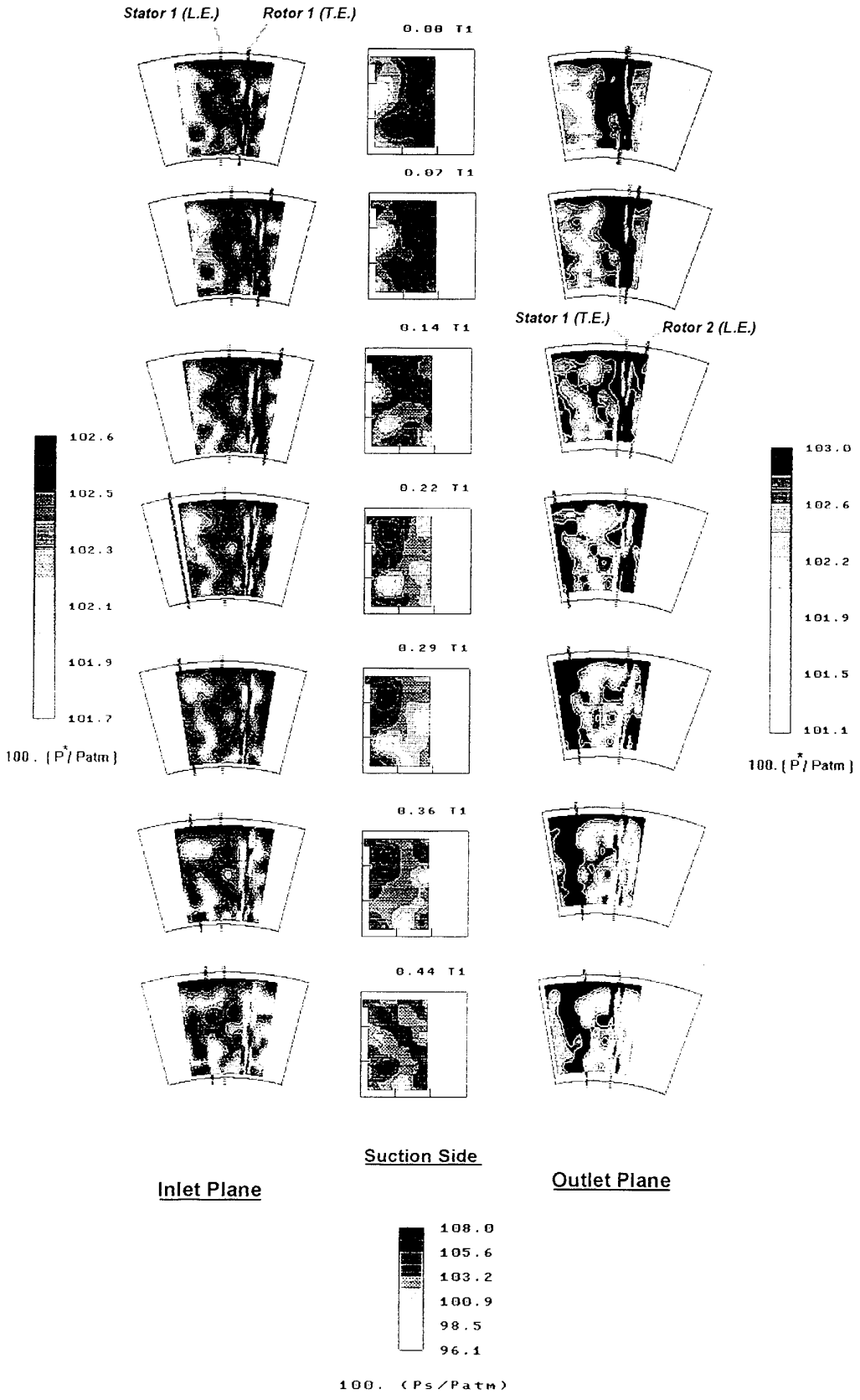

figure 17 : Effects of Neighbouring Rotors on Stator Surface Pressure Field (Suction Side)

7. COMPARISON BETWEEN FLOW METHOD AND EXPERIMENTAL INVESTIGATIONS

The flow method described above is used to a comparison with experimental investigations carried out on stator blade surface and on stator exit plane. Here are presented the results from 4000 RPM and 6.0 kg s^{-1} for two pre-selected blade height, one closer to the hub (R=208.1 mm) and another to the tip (R=252.7 mm).

The calculation begins using hot films results on stator inlet plane (plane 2) as initial conditions which are represented below :

nitial Conditions 4000 / 6.0	R = 208.1	R = 252.7
V_2 (ms^{-1})	64.6	60.4
α_2 (°)	50.2	45.0
M_2	0.185	0.174
$Re_{V_2, c_{stator1}}$	360000	337000
Tu (%)	4.2	4.0

7.1. Blade Boundary Layers

The coupling method has been used first to predict chordwise velocity distribution on suction and pressure sides. Figures below (18 a - b) represent a comparison between calculation and spatial-temporal values from static pressure measurements (BELHABIB [1995]) which have been carried out up to 70% chordlength..
These plots show that the pressure surface velocity distribution is reasonably well predicted while suction surface velocity distribution, although its slope is well captured, is highly underestimated

Results from surface mounted hot films give some information about global characteristics of the development of suction and pressure surface boundary layers. Below (figure 19 a - b and 20 a - b) are represented corresponding spatial-temporal results in form of plots of heat flux periodic and random fluctuations Tx (%).

Although those type of plots are difficult to interpret, it is interesting to give some possible physical approaches.

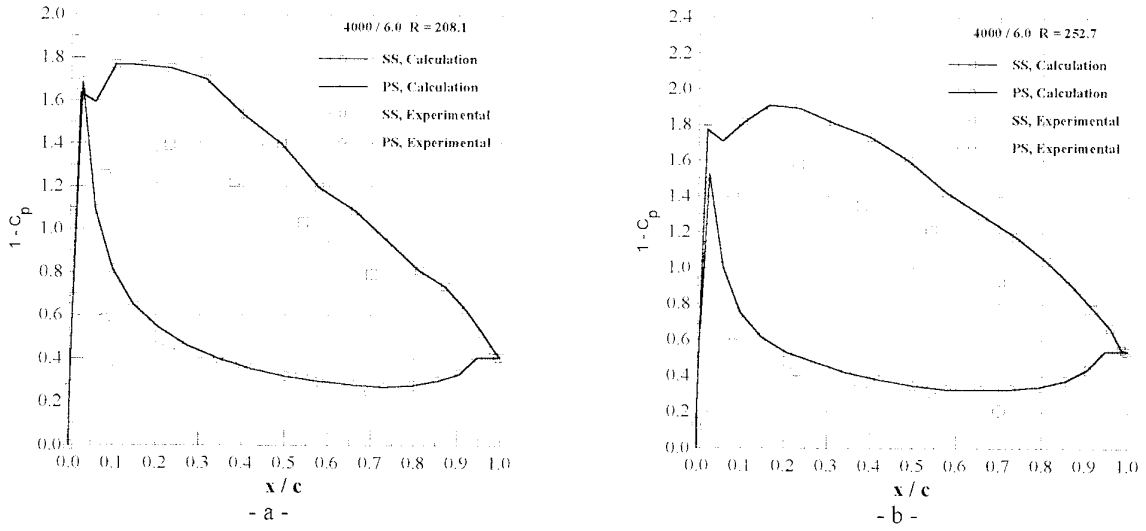

figure 18 : Chordwise Evolution of Pressure Coefficient at Two Radial Positions (Comparison Between Experimental Results and Calculation)

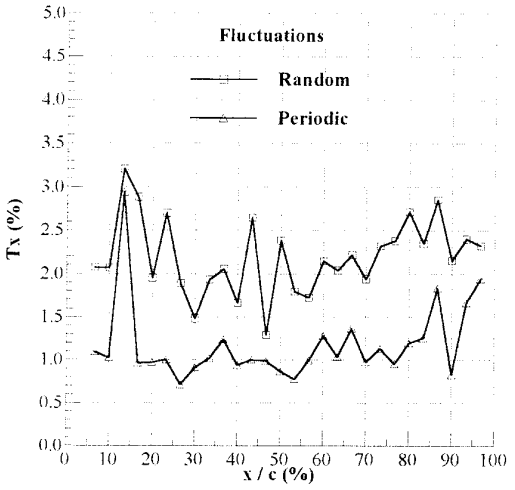

4000 / 6.0 R = 208.1 Suction Surface

- a -

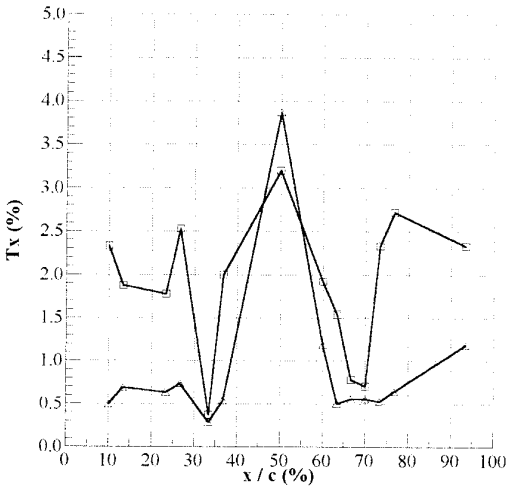

4000 / 6.0 R = 208.1 Pressure Surface

- b -

figure 19 : Chordwise Evolution of Random and Periodic Fluctuations Levels of Heat Flux (R=208.1 mm)

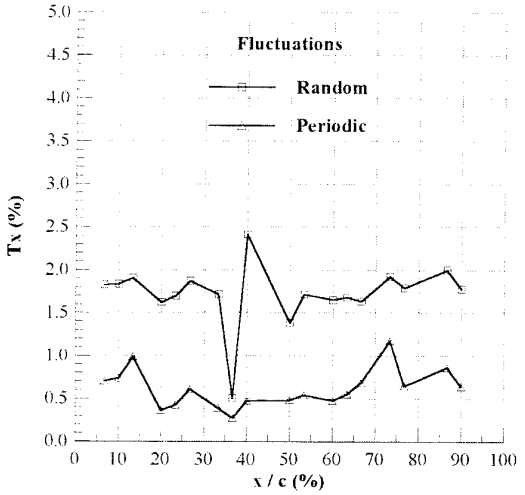

4000 / 6.0 R = 252.7 Suction Surface

-a -

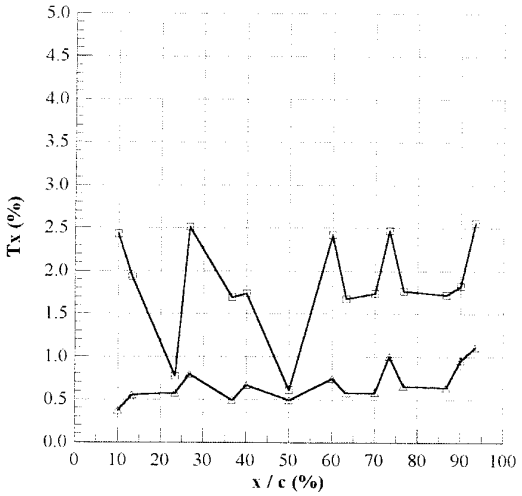

4000 / 6.0 R = 252.7 Pressure Surface

- b -

figure 20 : Chordwise Evolution of Random and Periodic Fluctuations Levels of Heat Flux (R=252.7 mm)

Pressure surface hot films results for R = 208.1 mm appear as the most clear in sense of transitional flow region. Two picks observed at the same position in RMS. and periodic fluctuations may probably correspond a natural type of transition region between 35 and 65 % chord. After this point boundary layer remains either fully turbulent or burst into a turbulent separation region. Suction surface hot films results of the same blade height give also a formation of two picks but this time closer to the leading edge (between 10 and 20 % chord). This may be explained either as a premature natural transition region or one may take into account the possibility of an abortive laminar separation bubble. One can not rule out the possibility that a bypass type of transition may occur due to the existence

of a double picks in RMS. values. Afterwards, the boundary layer seems to remain turbulent.

Heat flux plots for R = 252.7 mm are not only less significant but also more difficult to interpret than R = 208.1 mm. However, RMS. values may indicate a natural type of transition on each blade side. It is not evident to estimate any length of transition region. Even so, the transition onset seems to take place about 35 % chord on suction and 25 % chord on pressure side. With transition end boundary layers on each side may develop in fully turbulent.

Using flow properties on plane 2 as initial conditions the flow method is then used to predict boundary layer main features such as the location of laminar, transitional and turbulent regions as well as the existence and the location of laminar separation bubbles and turbulent separation. Below are presented for two pre-selected blade height the main features and global performance parameters such as total pressure loss coefficient, drug coefficient, outlet angle and mean outlet velocity.

4000 / 6.0	R = 208.1		R = 252.7	
Performance	SS	PS	SS	PS
LAMINAR (% x/c)	0 - 20	0 - 21	0 - 22	0 - 20
TRANSITION (% x/c)	20 - 90	21 - 46	22 - 82	20 - 48
TURBULENT (% x/c)	90 - 98	46 -100	82 - 100	48 - 100
BUBBLE (% x/c)	-	-	-	-
SEPARATION (% x/c)	98	-	-	-
$\overline{\omega}$ (%)	0.017		0.014	
C_D	0.017		0.015	
α_3 (°)	-3.2		-2.1	
V_3 (m/sec)	38.7		42.8	

As seen on this table, the calculation predicts practically the same behavior of transitional region on the same side whatever the blade height is chosen. This means that the onset and the end of transition are predicted practically at same locations (between 20 and 90 % chord on suction sides and between 20 and 50 % chord on pressure sides). The low level of total pressure loss and drug coefficients indicates that the thickness of boundary layer on each side is weak and gives evidence that there is neither large separated regions nor long bubbles in the vicinity of the leading edge region.

Comparison between measured and calculated transitional regions is schematically represented below(figure 21).

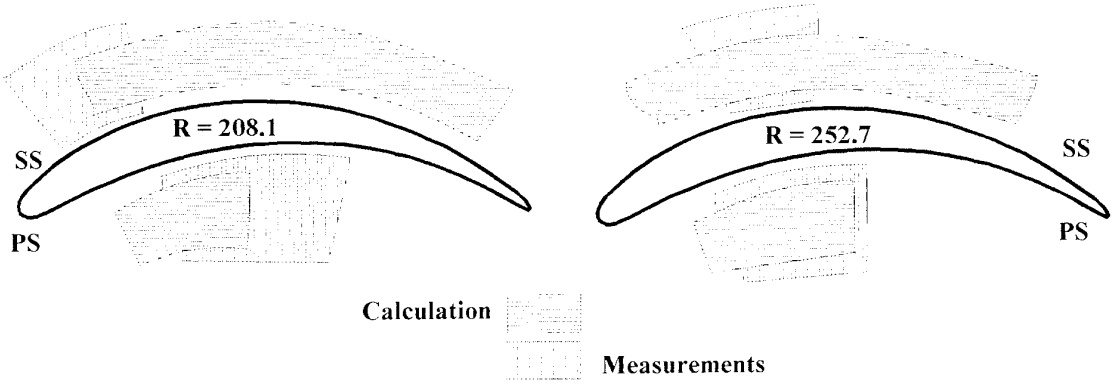

figure 21 : Boundary Layer Transition on Stator Surfaces
(Comparison Between Experimental Results and Culculation)

From this figure, it can be easily seen that transitional regions on pressure surfaces are relatively well predicted (differences on transition onset and its length are limited maximum to 20% chordlength). Calculation predicts always an advanced transition onset compared to measured one. While on suction surfaces, the most significant difference is the length of transition. Calculation predicts transition length nearly more than two times greater. Transition onset seems to behave a different role. At the time being, notwithstanding our efforts we are not able to explain why the calculation gives so different results on suction side transitional regions.

Wakes

The flow method is also able to predict the wake signature at trailing edge of blade rows. Using a wake development method based on experimental investigations of Lakshminarayana et al. (Kus, 1995), wake characteristics (deficit and width) on stator outlet plane (plane 3) have been obtained. Therefore, calculated wake profile is compared to experimental one for two blade height. These are shown by figures 22 a - b

These plots show that although wake deficit is well captured, wake width is widely underestimated for each blade height. Therefore calculated wake profiles on stator exit plane are highly different compared to experimental ones. This can be explained by the potential effect of downstream rotor considering the weak spacing of blade rows. It should also be reminded that the hot films results on stator exit plane and on blade surface showed the evidence of the potential effect of the second rotor even up to mid-chord distance on stator blade surface.

Finally, a comparison of stator outlet velocity and deviation angle has been carried out in order to check the agreement of mean values on stator outlet plane. This is given by the table below .

Notwithstanding the differences obtained by local characteristics of boundary layer and wake development, the mean values are reasonably well predicted.

case 4000 / 6.0	R = 208.1		R = 252.7	
COMPARISON	EXPERIENCE	LEMFI's CODE	EXPERIENCE	LEMFI's CODE
V_3 (ms^{-1})	33.0	35.6	40.5	39.7
δ (°)	-16.4	-17.8	-17.5	-20.9

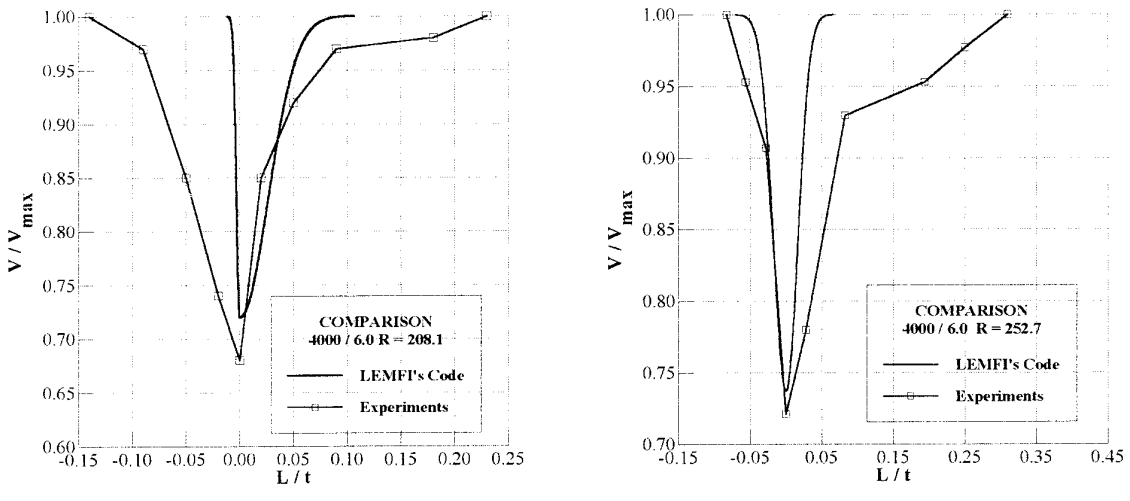

- a - - b -

figure 22 : Velocity Deficit in Stator Wakes
(Compa rison Between Experimental Results and Culculation)

CONCLUSION

An experimental investigation of the unsteady flow in the first stator of an axial four stages compressor has been performed. Unsteady velocity measurements have been carried out upstream and downstream of the stator blade row. These test permitted the identification of the sources of unsteadiness of the flow in the stator. It is evident from the results that the rotating flow field of the second rotor has a much greater influence than the first one, on the periodic unsteadiness of the flow. However, the first rotor act as a periodic (vs. time) source of turbulence interacting with the viscous layers along the surface of the stator. Unsteady pressure measurements realized on the pressure side as well on the suction side of the blade confirm these respective influences of the first and the second rotating blade rows on the flow.

Data concerning the development of the boundary layer along the walls of a blade in the stator have been collected from measurements using flush mounted hot films probes. These data have been compared with the ones furnished by a blade to blade computation method, taking into account the boundary layer behavior as well the wake development downstream of the blades. On the pressure surface, the transitional regions of the boundary layer are quiet well predicted by calculation. On the suction surface, the most significant differences between calculation and measurements concern the length off the transition region. The measured length is nearly more than two times shorter. It must be noticed that data obtained from such hot film measurements are very difficult to analyze. Questions occur, concerning the adequacy off the boundary layer model to represent the viscous layers along the blade walls in the presence of strong unsteady interactions between the relative moving blade rows flow fields. Concerning the development of the wakes of the stator blades, the velocity deficit at the center region of the wake is well predicted by the calculation, while the wake wide is greatly underestimated. Despite this fact, the mean flow characteristics downstream of the stator are fairly well predicted by the calculation.

ACKNOWLEDGEMENTS

The authors gratefully acknowledge the support of Direction des Recherches, Etudes et Techniques (G7) (Délégation Générale pour l' Armement), to the present research.

REFERENCES

BELHABIB M. [1995] Aérodynamique 3D instationnaire dans un compresseur axial multiétages - Etude expérimentale ' Ph. D thesis .Université Pierre et Marie Curie - Paris (Previoused to be presented on June 1995).

BELHABIB M. and MITON H. [1994] " Experimental Analysis of Blade Rows Interaction in Multistage Turbomachinery" Accepted to be published at Journal de Physique III, France (Reference N° 4-123).

CAMP. T.R. and H. -W. SCHIN [1995] " Turbulence Intensity and Length Scale Measurements in Multistage Compressors" ASME, Journal of Turbomachinery , Vol. 117 , January 1995.

EMMONS H.W. [1960] " The Laminar-Turbulent Transition in Boundary Layer Part - 1"
J. Aero. Sci. Vol. 18, %. 490-498

JACOB K. [1982] " Computation of the Flow Around Wings with Rear Separation" DFVLR-Bericht FB 82-22 , 1982.

KUS, U. [1995] "Contribution à la prédiction des performances globales et locales des grilles d'aubes", Ph. D. Thesis, Ecole Nationale Supérieure d'Arts et Métiers, March 1995, Paris.

KUS U. and CHAUVIN J. [1995] "Performance Prediction of Turbomachinery Cascade as Affected by Upstream Turbulence". (Accepted for Publication at Journal de Physique III, France (Reference N° 4-167).

LE FOLL J. [1965] " A Theory of representation of the Boundary Layer Properties on a Plane"
Paper, Seminar on " Advanced Problems in Turbomachinery", Brussels, Belgium, 1965.

MAYLE R.E. and DULLENKOPF K. [1990] "A Theory for Wake-Induced Transition"
ASME , Journal of Turbomachinery, Vol. 112, April 1990, %.188-195.

MAYLE R.E. and DULLENKOPF K. [1991] " More On The Turbulent-Strip Theory for Wake-Induced Transition"*ASME , Journal of Turbomachinery, Vol. 113, April 1991, %. 428-432.*

MITON H. and BELHABIB M. [1994] 'Effet de l'environnement machine sur le comportement des aubages de compresseurs axiaux - Etude expérimentale de l'intercation de couche limite d'aubage et sillage '
Contract Repport DRET N°91-173, December. 1994.

PFEIL H. and HERBST R. [1979] " Transition Procedure of Instationary Boundary Layers" *ASME Paper 79-GT-128*

ROBERTS W.B. [1980] " Calculation of Laminar Separation Bubbles and their Effect on Airfoil Performance"
AIAA Journal, Vol. 18,1980,%.25-31.

REFERENCE NO. OF THE PAPER: 20

DISCUSSOR'S NAME: F. Kameier, BMW-RR, Germany

AUTHOR'S NAME: H. Miton, M. Belhabib, U. Kus

Q:1 Figure 15 shows the difference of blade passing frequency of rotor 2 and rotor 1. Does the occurrence of this difference frequency depend on operating conditions of the compressor, and what is the explanation of the occurrence? I'm surprised that the rotor shaft frequency isn't visible.

A:1 On Figure 15 you can see, indeed, two low frequencies. The lower one corresponds to the difference between the blade passing frequency of rotor 2 (11 blades) and the blade passing frequency of rotor one (17 blades). The second frequency is equal to twice the lower one. Taking into account this difference between the numbers of blades (19 -17 = 2), these peaks correspond to frequencies equal to 2N and 4N, where N is the frequency of the rotor shaft. These peaks can be observed in the overall domain of operation of the compressor (from maximum pressure ratio to choke). I agree with your remark concerning the rotor shaft frequency, but I confirm that it has been never observed clearly in such velocity measurements. Perhaps a different result could have been obtained with a pressure rake fitted in the casing.

Q:2 The noise level in the wall pressure spectrum is zero (Figure 15). What kind of averaging method was used?

A:2 Figure 15 represents a spectrum in which noise has been removed. To realize such a "cleaning", we use a criterion based on the energy contained in the peaks: if the square of the amplitude is lower than a given level, the corresponding frequency is extracted from the spectrum. (i.e. replaced by "0": see 4 in the paper).

Q:3 What kind of pressure transducers have been used and what was the calibration procedure (Figure 9)?

A:3 The pressure transducers used in this study were piezo-resistant type (ENTRAN EPI series). They have been calibrated in the blade, using a shock tube giving pressure pulses of variable length.

The Effect of Incoming Wakes on Boundary Layer Transition of a Highly Loaded Turbine Cascade

M. Engber, L. Fottner
Institut für Strahlantriebe
Universität der Bundeswehr München
D 85577 Neubiberg, Germany

ABSTRACT

Extensive pressure and thin-film measurements have been performed on a linear turbine cascade with variations of inlet angle, inlet Reynolds number, and inlet turbulence intensity at homogeneous and inhomogeneous inflow conditions. Especially the occurrence of laminar separation bubbles was investigated. With both measuring techniques their existence could be verified and the characteristic points of a bubble could be located.

Incoming wakes similar to those in real turbomachines were simulated by a cascade of cylindrical bars which was positioned in front of the turbine cascade. Diameter and distance of the bars to the blades were chosen to produce non-uniformities in the cascade inlet plane similar to those in real engines. The wake impingement point could be varied by moving the cylindrical bars in circumferential direction parallel to the turbine cascade front. With this set-up the so called rotor-rotor or stator-stator interaction of a multistage turbine can be simulated.

Measurements of direction, quantity and fluctuation of the velocity inside the boundary layer have been conducted with a Laser-2-Focus measuring technique.

The analysis of the experiments results in a better understanding of the transitional phenomena on blade profiles and allows to improve empirical correlations for the calculation of transition in boundary layer.

NOMENCLATURE

Symbols

c	[m/s]	mean velocity
c'	[m/s]	velocity fluctuation
$c_{p,2th}$	[-]	pressure distribution coefficient
d	[mm]	diameter
E_0	[V]	time averaged anemometer output voltage at zero flow conditions
E_M	[V]	time averaged anemometer output voltage
E_{RMS}	[V]	Root-Mean-Square value of the voltage
h	[mm]	blade height
h_b	[mm]	height of the laminar separation bubble
l	[mm]	chord length
l_b	[mm]	length of the laminar separation bubble
Ma	[-]	Mach number
p	[hPa]	static pressure
p_t	[hPa]	total pressure
q	[hPa]	dynamic pressure
Re	[-]	Reynolds number
s	[mm]	surface coordinate
t	[mm]	pitch
T	[K]	Temperature
Tu	[%]	Turbulence level
u	[mm]	circumferential coordinate
v	[m/s]	velocity
x	[mm]	coordinate in chord direction
y	[mm]	coordinate perpendicular to the surface
β	[°]	flow angle
β_S	[°]	stagger angle
ω	[-]	pressure loss coefficient

Indices

FS	related to free-stream conditions
ges	maximum
K	related to the pressure tank of the wind tunnel
δ	at the boundary layer edge
1	upstream conditions
2	downstream conditions
2th	downstream condition for isentropic flow

Abbreviations

DP	design point
ET	end of transition
IP	impingement point of the wake
L2F	Laser-2-Focus
PS	pressure side
RP	(turbulent) reattachment point
SP	(laminar) separation point
SS	suction side
ST	start of transition
TP	transition point

INTRODUCTION

The profile losses of a turbine cascade are mainly influenced by the state of the suction side boundary layer. The mode and the position of the boundary layer transition from the laminar into the turbulent flow pattern are responsible for the amount of the losses. A long laminar boundary layer causes basically low losses. High pressure gradients and low Reynolds numbers, Mach numbers and turbulence levels can cause separation of the laminar boundary layer from the blade profile, and a strong increase of the losses. If the profile length downstream of the separation point is sufficient for changing the laminar separated boundary layer into the turbulent flow pattern and for reattaching of the high-energy turbulent boundary layer on the profile, the steep rise of the losses will be avoided. Between the separation point and the reattachment point of the boundary layer a self-contained unsteady recirculation area, the so-called laminar separation bubble, develops (Mayle (1991) [1]).

Paper presented at the AGARD PEP 85th Symposium on "Loss Mechanisms and Unsteady Flows in Turbomachines", held in Derby, United Kingdom, 8-12 May 1995, and published in CP-571.

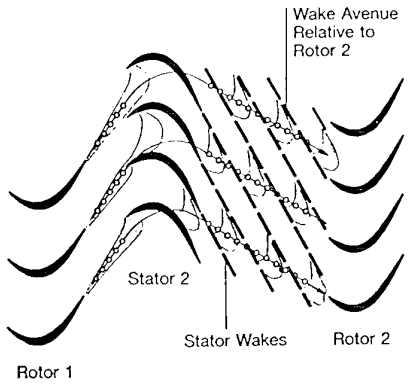

Fig. 1: Schematic illustration of the Rotor 2 inflow conditions

Real multistage turbomachines are marked by non-moving and rotating blade rows. Here the influence of a blade row on the downstream rows is of importance (Hodson (1990) [2], Walker et al. (1993) [3]). Wakes downstream of a blade row present a periodic unsteady inflow for the following blade row, which is in relative motion to the first one. The wakes are chopped by this cascade and hit the next blade row in a weakened form. Because this blade row is not in motion relative to the wake producing blade row the wakes build a steady non-uniformity in its inlet flow. This influencing is called the rotor-rotor (Fig. 1) or stator-stator interaction.

Measurements by Binder et al. (1988) [4], Schröder (1989) [5], Arndt (1991) [6] in a five stage low pressure turbine showed loss concentrations on specific circumferential positions behind the rotor 2, which are caused by different blade numbers of rotors 1 and 2. The wakes of rotor 1 hit the blades of rotor 2 on different circumferential positions (Fig. 1) and result in the development of different boundary layers on the blade profiles, so that local circumferential loss concentrations downstream of the rotor 2 could be observed.

The objective of this work is to enhance the influence of a steady non-uniform inlet flow on the boundary layer development and the profile losses of a highly loaded low pressure turbine cascade. The inhomogeneous inlet flow was generated by fitting a wake generator made of cylindrical bars in front of the turbine cascade. Moving the wake generator parallel to the turbine inlet plane allows different impingement points of the wakes on the turbine blades. In addition to the impingement point the Reynolds number Re_{2th} and the inlet angle β_1 were varied. The experimental examinations were carried out at the High Speed Cascade Wind Tunnel of the University of the Federal Armed Forces Munich.

TEST FACILITY AND MEASUREMENT TECHNIQUES

The High Speed Cascade Wind Tunnel (Fig. 2) is located inside of an evacuable pressure tank. By lowering the pressure level in the vacuum tank and by setting the temperature in the measurement area of the wind tunnel by means of an extensive cooling set-up an independent variation of the Reynolds number and the Mach number is possible. The turbulence level of the inflow can be increased by fitting a turbulence generator into the nozzle of the wind tunnel.

The mounting of the turbine cascade in the wind tunnel is shown in Fig. 3. For the achievement of a periodic inlet flow, guide plates were fixed to the upper and the lower wall of the test section which have the shape of the camber line of the turbine profiles. Thus a constant static pressure distribution in the inflow of the turbine cascade is achieved. The static pressure of the inflow p_1 as well as the total pressure p_{t1} are measured 100 mm in front of the turbine inlet plane with static wall tappings and a Pitot tube. The total temperature is determined as the mean value of four resistance thermometers in the settling chamber of the wind tunnel. With the assumption of an adiabatic flow this temperature corresponds to the total temperature in the cascade inlet plane T_{t1}.

UniBw München Institut für Strahlantriebe	High-Speed Cascade Wind Tunnel	1985

test section data:		supply units:		wind tunnel data:	
- Mach number	: 0.2 ≤ Ma ≤ 1.05	- evacuating unit	: P_1 = 30 kW	- AC electric motor	: P = 1300 kW
- Reynolds number	: $0.2 \cdot 10^6\ m^{-1} \le Re/l \le 16.0 \cdot 10^6\ m^{-1}$		P_2 = 20 kW	- axial compressor	: 6 stages
- degree of turbulence	: 0.4% ≤ Tu_1 ≤ 7.5%	- boundary layer suction	: P = 155 kW	air flow rate	: $\dot{V}_{max}$ = 30 m³/s
- upstream flow angle	: 25° ≤ β_1 ≤ 155°	(centrifugal compressor)		total pressure ratio	: $(p_{t1}/p_K)_{max}$ = 2.14
- blade height	: 300 mm	- additional air supply	: P = 1000 kW	number of revolutions	: n_{max} = 6300 min⁻¹
- test section height	: 235 mm - 510 mm	(screw compressor)		tank pressure	: p_K = 0.04 - 1.2 bar

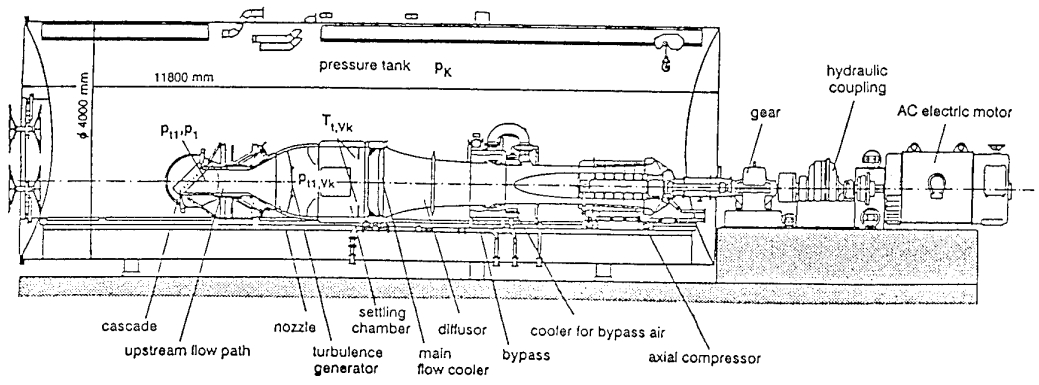

Fig. 2: High Speed Cascade Wind Tunnel

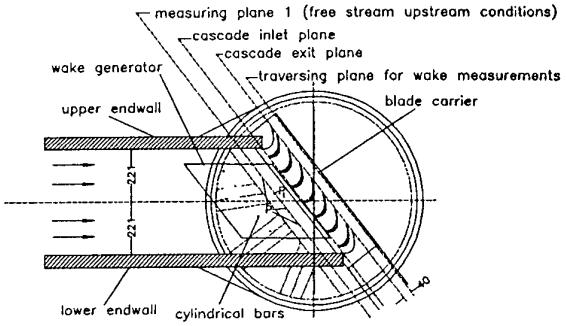

Fig. 3: Test-section of the wind tunnel with wake generator and turbine cascade

The linear turbine cascade used for these tests represents a modern design of a highly loaded uncooled low pressure turbine (Fig. 4). It consists of 7 blades with a chord length of l = 100 mm and a blade height of h = 300 mm.

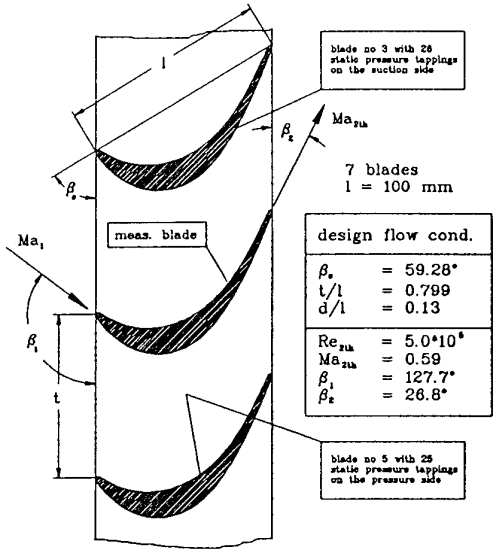

Fig. 4: Turbine cascade T106

For wake traverse measurements (total pressure, static pressure and outlet flow angle) a wedge probe was used downstream of the center blade at 40% of chord axially downstream of the blade trailing edge plane (Fig. 3). The measured inhomogeneous flow field is converted into an equivalent homogeneous flow field applying the laws of conservation of mass, momentum, and energy (Amecke (1967) [7], Ladwig (1989) [8]) leading to the total pressure loss coefficient:

$$\omega_{2th} = \frac{p_{t1} - p_{t2}}{p_{t1} - p_K}$$

Surface pressures were measured using 26 static pressure tappings on the suction side and 25 static pressure tappings on the pressure side of the blades adjacent to the center blade. The surface pressure distribution is applied in the form of the dimensionless coefficient

$$c_{p,2th} = \frac{p(x/l) - p_K}{p_{t1} - p_K}$$

and plotted versus the relative profile coordinate in the blade chord direction x/l.

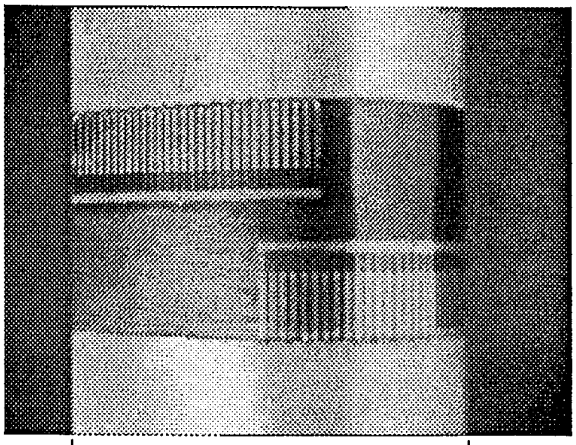

Fig. 5: Turbine blade with surface-mounted thin-film sensors

For the thin-film measurements the center blade is replaced by a blade equipped with thin film sensors. The sensors are made of nickel, evaporated on a polyamid foil and glued on the turbine blade in two sheets of 30 sensors each (Fig. 5). During measuring operation the sensors are heated in succession with a Constant-Temperature-Anemometer to a constant temperature level above the temperature level of the flow (ΔT = 30 K). The anemometer output signal is devided in the time averaged voltage E_M, which is proportional to the heat transfer from the sensor to the fluid and thus to the mean wall shear stress, and the RMS value of the voltage E_{RMS}, which is proportional to the fluctuating heat transfer (Römer (1990) [9], Schröder (1991) [10]). Both voltages are made dimensionless by dividing by the sensor voltage at zero flow conditions E_0 and are plotted versus the relative sensor position in blade chord direction x/l. E_0 corresponds to the heat flow due to free convection and heat conduction in the turbine blade.

Additional to mode and position of the transition area on the turbine profile it is possible to determine the flow values inside of the boundary layer (velocity vector, turbulence level) with the Laser-2-Focus measurement technique. The L2F velocimeter used for these measurements is a water cooled Argon Ion laser with an output power of 1 Watt in the single line operation. The L2F method is a non-intrusive measurement technique for establishing the velocity of small particles carried within the flow by using the light barrier principle (Schodl (1974) [11], Beeck (1992) [12]). The two parallel laser beams are focused in the measuring volume resulting in a very high intensity with a beam diameter of 8 µm and a distance of 168 µm. A particle passing through the focal volumes scatters the laser light in all directions . The scattered light is picked up by two photo detectors, amplified, and sent to the signal processor. The time between the two floodlight signals is equivalent to the time-of-flight of the particles. The velocity of the particles is fixed by the known distance of the two laser beams. Particles with a mean diameter of 0.3 µm are generated by spraying an aerosol liquid under pressure. Because start and stop impulse can be triggered by different particles, a huge number of measurements has to be conducted at one measuring point

and the result has to be evaluated statistically. For the determination of the flight direction the measuring plane which is spread by the two laser beams is scanned at varying angular positions. Thus for each measuring point a two-dimensional frequency distribution is obtained whose statistical evaluation delivers the amount, the direction, and the turbulence level of the flow vector at this measuring point.

The different modes of transition (laminar separation bubble and natural transition) can be visualised distinctly by means of oil-flow pictures. Besides the two-dimensional flow effects in the cross section of the turbine blades oil-flow pictures show in addition the three-dimensional flow field on the blade surface near the wall.

THE WAKE GENERATOR

For the simulation of steady non-uniformities in the inlet flow of the turbine cascade T106 cylindrical bars were used, because the macro structures of wake flows behind blades and cylindrical bars are nearly identical (Pfeil (1975) [13], Ladwig (1993) [14]). The bars are fitted in a cascade with the same pitch as the turbine cascade. The spacing between the bar plane and the turbine inlet plane and the diameter of the cylindrical bars had to be dimensioned to get wakes of definite width and definite maximum turbulence in the cascade inlet plane. The wake width should not exceed half of the pitch to allow a detailed examination of the dependency of the boundary layer development on the impingement point of the wakes when moving the bar cascade parallel to the blade cascade. The desired value for the maximum turbulence level inside the wake was 4%. This value corresponds to a turbulence level which is reached for homogeneous flow in the turbine inlet plane using the turbulence generator VI K and which occurs in low pressure turbines of real turbomachines as well (Hourmouziadis (1989) [15], Hoeger (1992) [16]).

Hot-film measurements for the determination of the turbulence level were carried out with a single sensor probe. The turbulence level is defined as the ratio of the velocity fluctuation and the mean velocity of the flow .

$$Tu_1 = \frac{\sqrt{\overline{c_1'^2}}}{c_1}$$

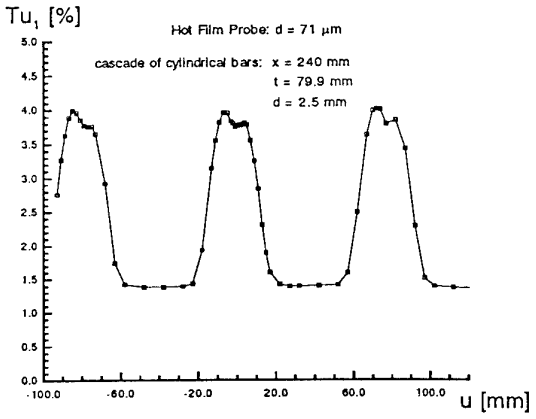

Fig. 6: Turbulence level distribution in the turbine cascade inlet plane using the wake generator

The results are shown in Fig. 6. The desired values were reached with bars of a diameter of d = 2.5 mm and a spacing in flow direction to the turbine inlet plane of 240 mm. For the variation of the wake impingement point on the turbine blades the bar cascade can be moved parallel to the fixed turbine cascade without removing the cascade from the test section (Fig. 3).

MEASUREMENTS AT THE DESIGN POINT OF THE T106

A detailed examination of the transition phenomena on the suction side of the turbine blade was conducted at the design point of the turbine cascade T106 at Mach number Ma_{2th} = 0.59, Reynolds number $Re_{2th} = 5*10^5$, and inlet angle β_1 = 127.7°.

Uniform Inlet Flow

Initially the boundary layer development was examined for homogeneous inlet flow and two different inlet turbulence levels. Without fitting a turbulence generator in the nozzle of the wind tunnel a turbulence level of Tu_1 = 1% exists in the turbine inlet plane. This low turbulence level permits the laminar boundary layer to separate in the deceleration part of the suction side before reaching the transition point. Transition occurs in the separated shear layer and the high-energy turbulent boundary layer reattaches further downstream of the transition point. Below the separated shear layer a self-contained, unsteady recirculation area, the laminar separation bubble, is formed.

In the profile pressure distribution this mode of transition can be recognised by the development of a plateau in the deceleration part of the suction side (Fig. 7). As shown by Rannacher (1982) [17] the laminar separation point (SP) can be assumed at the beginning of the constant pressure plateau and the transition point (TP) at the end. The reattachment point (RP) of the turbulent boundary layer corresponds to the point of intersection of the measured pressure shape with the potential pressure curve plotted with a dashed line.

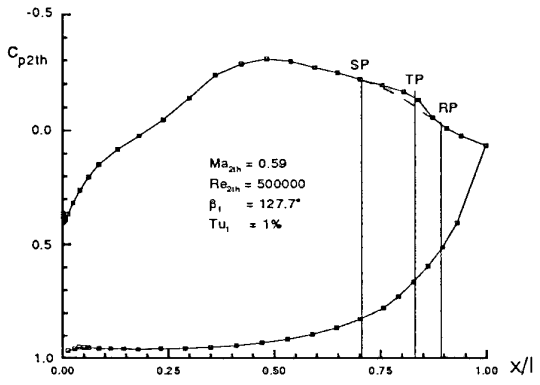

Fig. 7: Profile pressure distribution at low inlet turbulene level

Length and position of laminar separation bubbles can be determined with high accuracy by the thin-film signal. The averaged voltage E_M of the anemometer output signal, which

is proportional to the shear stress on the profile surface, drops in the laminar boundary layer area with increasing boundary layer thickness, rises steeply in the transition area and slopes again in the turbulent boundary layer area (Fig. 8). The transition point (TP) is defined as the location of the highest shear layer gradient. In the RMS voltage distribution it builds the maximum of a transition peak. If the curve contains a second smaller maximum in front of the big transition maximum (Fig. 8), this maximum marks the separation point (SP) of the laminar boundary layer. The reattachment point (RP) of the turbulent boundary layer is located at the end of the transition peak. Laminar and even turbulent boundary layers possess small values in the RMS distribution while the heat fluctuations rise in the transition area due to the continuous change of laminar and turbulent boundary layer segments.

The turbulence generator VI K in the nozzle of the wind tunnel increases the inlet turbulence level to 4% and leads to natural transition on the suction side of the turbine profile.

Natural transition can be detected in the profile pressure distribution only by a slight blip in the shape of the curve (Fig. 9). In the averaged voltage distribution E_M the minimum marks the starting of transition (ST), the highest gradient the transition point (TP) and the maximum the end of transition (ET) (Fig. 10). The RMS shape is dominated by a very distinct transition peak.

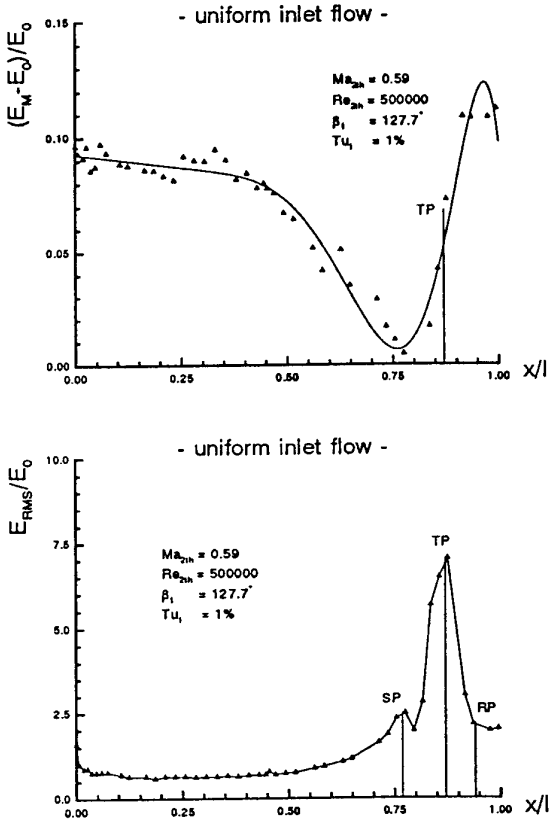

Fig. 8: Thin-film results at low inlet turbulence level

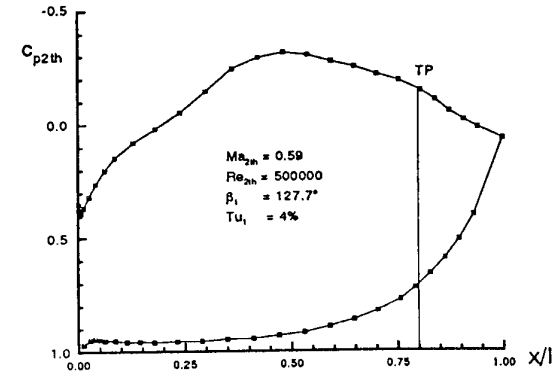

Fig. 9: Profile pressure distribution at high inlet turbulence level

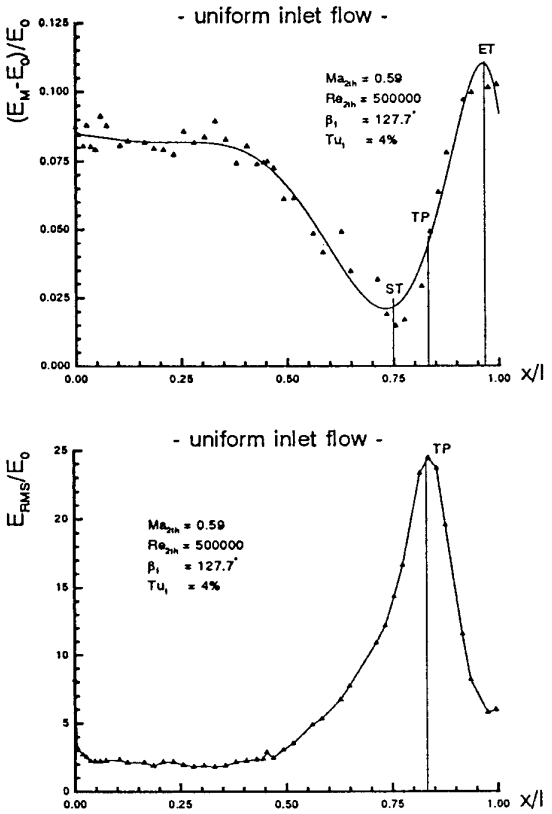

Fig. 10: Thin-film results at high inlet turbulence level

Non-uniform Inlet Flow

The impingement point of bar wakes on the turbine inlet plane has been varied in steps of 10 mm. An impingement point at the stagnation point of the turbine blades is distinguished with IP = 0 mm, impingement points at the pressure side with positive values and at the suction side with negative values.

The profile pressure distributions (Fig. 11) show, that an impingement point at IP = -10 mm, 0 mm and +10 mm causes natural transition on the suction side of the profile. A distance of 20 mm or more from the stagnation point to the suction side or the pressure side admits the development of a laminar separation bubble in the deceleration part of the suction side on the profile. Position and length of the separation bubbles are very similar to each other in all examined cases

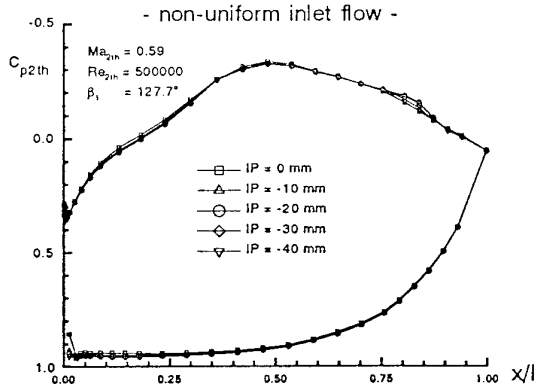

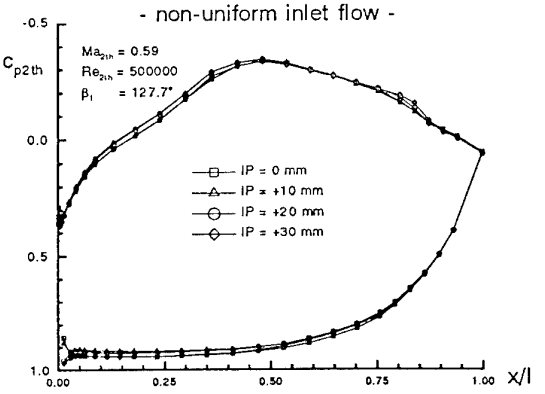

Fig. 11: Profile pressure distribution at different wake impingement points

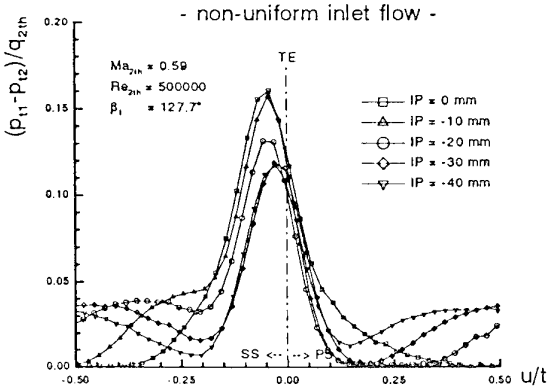

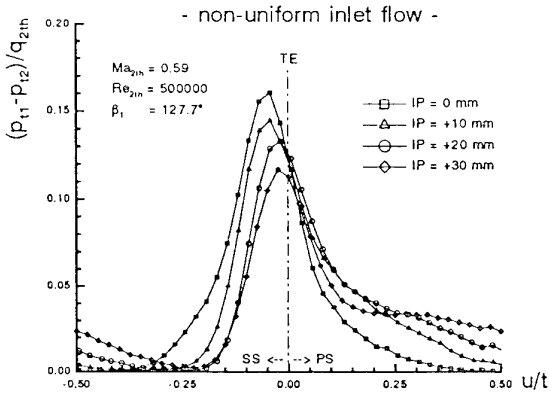

Fig. 12: Wake traverse measurements at different wake impingement points

because for these impingement positions the wakes have no influence on the development of the suction side boundary layer of the turbine blades. The separation bubbles extend from x/l = 0.7 to x/l = 0.9 with the transition point at x/l = 0.8. The exact listing of the separation, transition and reattachment points are given in Table 1.

Ma_{2th} = 0.59, Re_{2th} = 5*10^5, β_1 = 127.7°

	Profil Pressure M.			Thin-Film Meas.		
IP [mm]	SP	TP	RP	SP	TP	RP
Tu = 1%	**0.71**	**0.83**	**0.89**	**0.77**	**0.87**	**0.94**
- 40	0.73	0.83	0.90	0.77	0.86	0.94
- 30	0.72	0.83	0.90	0.77	0.87	0.95
- 20	0.73	0.83	0.89	----	0.86	----
- 10	----	----	----	----	0.83	----
Tu = 4%	----	**0.80**	----	----	**0.83**	----
0	----	----	----	----	0.76	----
+ 10	----	----	----	----	0.77	----
+ 20	0.72	0.81	0.87	----	0.82	----
+ 30	0.70	0.83	0.89	0.75	0.86	0.93

Table 1: Characteristic points of laminar separation bubbles at uniform and non uniform inlet flow conditions

The wake measurements (Fig. 12) show the highest peaks for impingement points near to the stagnation point, because an addition of the wakes of the cylindrical bar and the turbine blade occurs. With the deviation of the impingement point from the stagnation point a second small maximum builds up near the blade wake, which is caused by the wake generator. The widest loss curves are obtained for impingement points near the stagnation point. The high turbulence level inside the wakes shifts the transition area upstream. Thus the length of the turbulent boundary layer increases and the higher boundary layer thickness is responsible for the expanding loss curve. By transforming the measured non uniform outlet flow into an equivalent homogenuous flow, applying the laws of conservation, the distribution of the total pressure loss coefficient presented in Fig. 13 is achieved. Contrary to first impressions the maximum and the minimum of the losses could not be found at an impingement point of the wakes at the stagnation point and at the middle of the duct between the turbine blades respectively. The loss minimum is located at IP = -10 mm. This flow condition is characterised by the change of the mode of transition from a laminar separation bubble to natural transition. A further approach of the impingement point to the stagnation point moves the transition area upstream and extends the length of the turbulent boundary layer. The occurrence of a laminar separation bubble as well as the lengthening of the turbulent boundary layer cause increasing profile losses. The pressure side is not influenced by the wake and exhibits the laminar flow pattern on its whole length because of the low free stream turbulence level of 1%, which leads to a minimum of the pressure side profile losses too. A shifting of the impingement point to the pres-

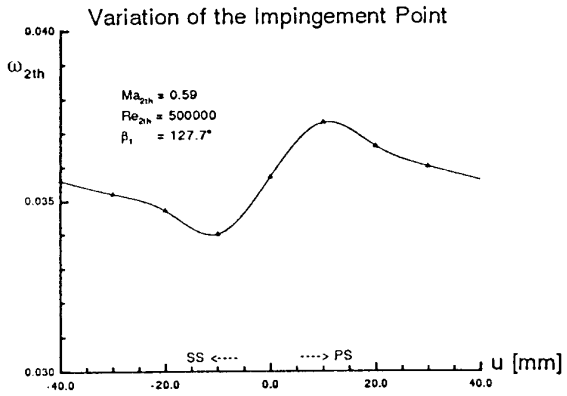

Fig. 13: Loss coefficient at different wake impingement points

sure side gives rise to a growing of the profile losses, which reach their maximum at IP = +10 mm. This is caused by the pressure side boundary layer, which feels the high turbulence level of the wake of 4% as free stream turbulence level and therefore changes just behind the leading edge into the turbulent flow pattern. The resulting thickening of the pressure side boundary layer can be seen clearly in Fig. 12. With a further drift of the impingement point off the stagnation point the influence of the wakes on the boundary layer decreases and the losses decline again. The minimum of the losses amounts to ω_{2th} = 0.0340, the maximum to ω_{2th} = 0.0373. An unfavourable impingement point of the wakes can lead to an increase of the total pressure losses of 10% at the design point of the turbine cascade T106.

The thin-film results (Fig. 14) confirm and complement the results of the profile pressure and wake measurements. Gluing the polyamid foil on the profile changes the surface roughness. Therefore the transition area is shifted slightly to the trailing edge for all examined cases. In addition the zone of natural transition is now located in a wider range of IP = -20 mm to IP = +20 mm. The remaining three cases with an impingement point near the middle of the blade passage show again nearly identical laminar separation bubbles at the deceleration part of the suction side. By moving the wake impingement point to the stagnation point the transition area is shifted upstream. The exact position of the transition points is given in Table 1. The high turbulence level in the wake causes an upstream drift of the transition point of 10% chord length.

Two cases have been examined in detail by the L2F measuring technique, the natural transition at IP = 0 mm and the laminar separation bubble at IP = 40 mm. Between x/l = 0.35 and the trailing edge the velocity profiles have been determined on 19 lines perpendicular to the blade surface. In the transition area the spacing of the lines is 2.5 mm. As a result, the velocity distributions shown in Fig. 15 are obtained. On the top an example of a laminar boundary layer profile is presented at x/l = 0.55 with a boundary layer thickness of 0.4 mm, down below the turbulent boundary layer profile at x/l = 0.975 with a boundary layer thickness of 1.9 mm. The big advantage of the L2F measuring technique is obvious. Because of the small measuring volume it is possible to carry out measurements up to 50 µm to the blade surface without disturbing the flow even very slightly.

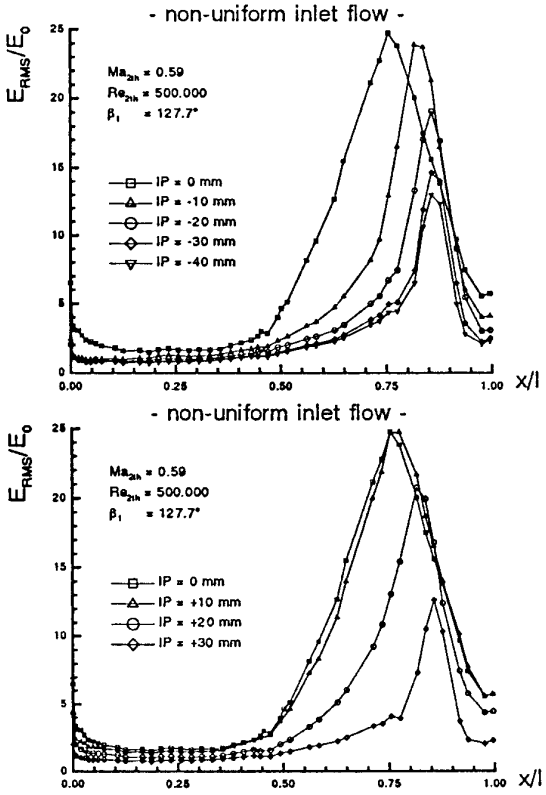

Fig. 14: E_{RMS} distributions at different wake impingement points

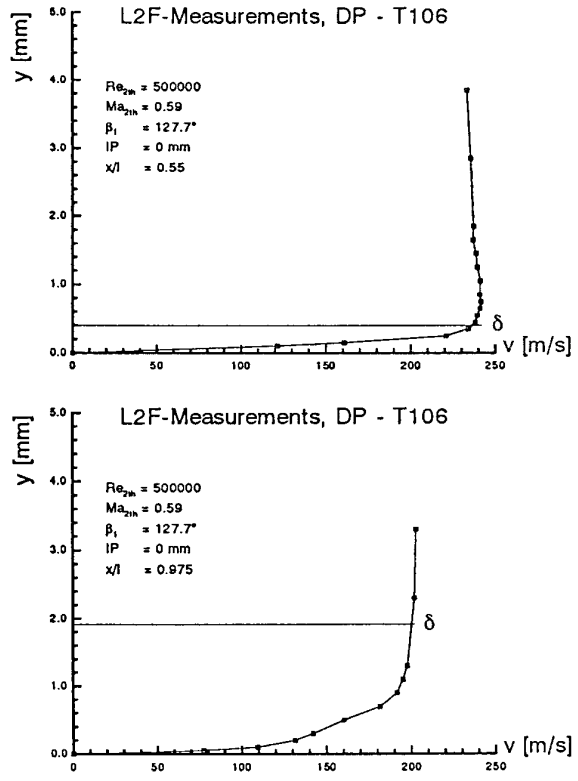

Fig. 15: Velocity distribution for a laminar and a turbulent boundary layer

For natural transition the velocities of all measuring points, normalized with the free stream velocity of each line, are shown in Fig. 16. The edge of the boundary layer is found according to the definition at 99% of the free stream velocity. The laminar boundary layer is very thin with 0.3 to 0.6 mm, while the turbulent boundary layer is thickening sharply and reaches 2 mm at the trailing edge. The position of the transition area can be inferred from the turbulence level distribution (Fig. 17). The slight increase of the turbulence level inside of the boundary layer behind s/s_{ges} = 0.5 (x/l = 0.45) corresponds to the occurrence of first instabilities (Tollmien-Schlichting-Waves) in the boundary layer. The transition area is marked by a high turbulence level in the immediate vicinity of the blade surface and extends from s/s_{ges} = 0.65 (x/l = 0.63) to s/s_{ges} = 0.96 (x/l = 0.97). The maximum at s/s_{ges} = 0.75 (x/l = 0.75) corresponds to the transition point itself.

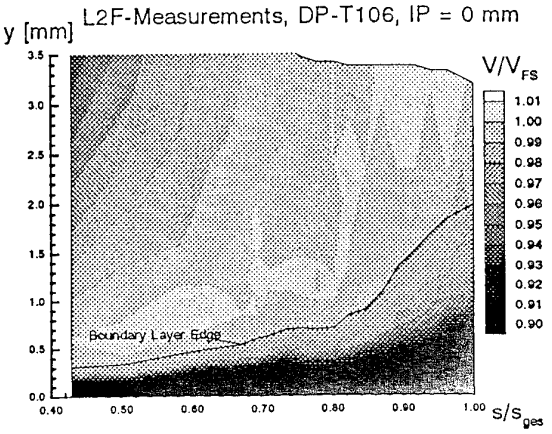

Fig. 16: Velocity distribution at IP = 0 mm

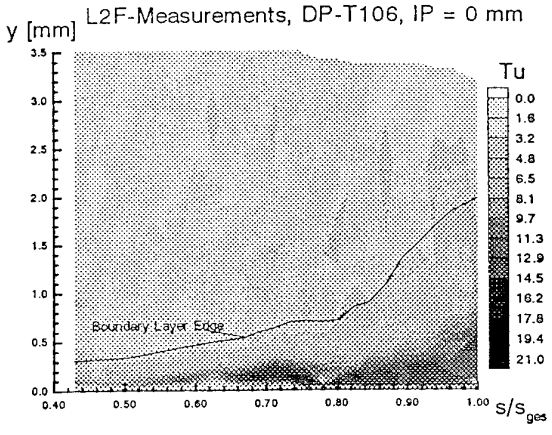

Fig. 17: Turbulence level distribution at IP = 0 mm

Measurements near the wall in the case of the laminar separation bubble at IP = 40 mm were more difficult to perform. Because of the low free stream turbulence level there were not enough particles for accurate L2F measurements in the lower part of the boundary layer and inside the laminar separation bubble. Nevertheless the edge of the boundary layer could be determined reliably from the measured velocity distribution (Fig. 18). The dimension of the laminar separation bubble can be derived from the turbulence level distribution (Fig. 19). The growing of the turbulence level at s/s_{ges} = 0.74 (x/l = 0.73) corresponds to the separation point (SP) of the laminar boundary layer, the maximum at s/s_{ges} = 0.85 (x/l = 0.85) to the transition point (TP) and the renewed in-

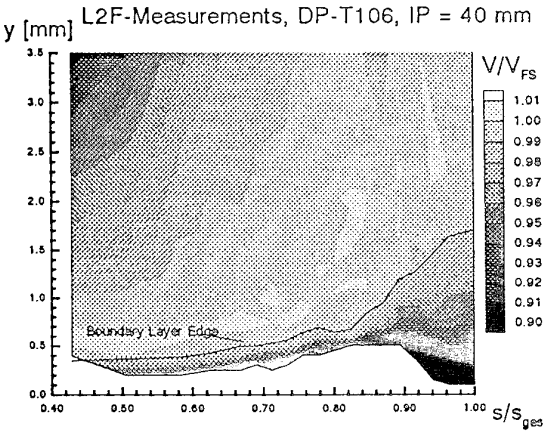

Fig. 18: Velocity distribution at IP = 40 mm

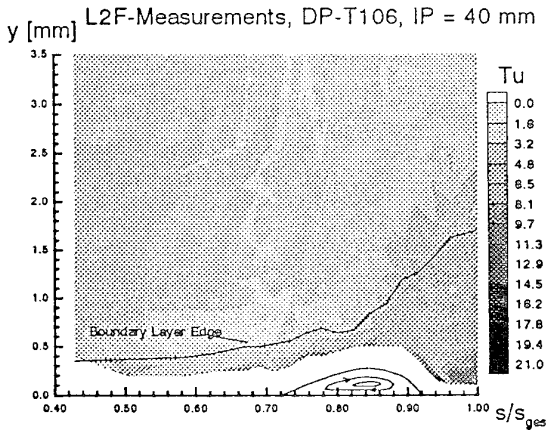

Fig. 19: Turbulence level distribution at IP = 40 mm

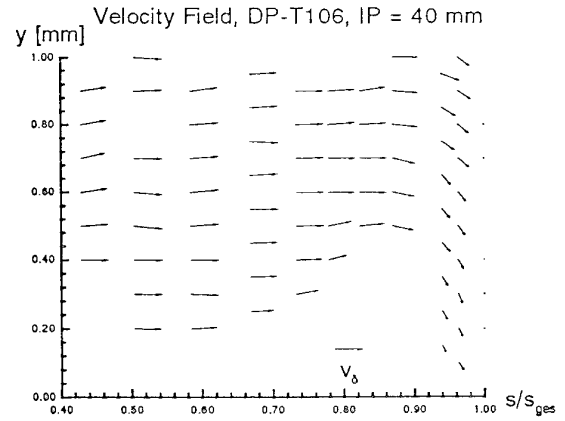

Fig. 20: Velocity field at IP = 40 mm

creasing at s/s_{ges} = 0.92 (x/l = 0.93) to the reattachment point (RP) of the turbulent boundary layer. The flow around the separation bubble can be seen more easily in the vector field of the measured velocity vectors (Fig. 20). It shows clearly the very flat rise of the vectors at the beginning of the laminar separation bubble and the sharp decay at the end of the bubble. Thus the overall dimension of the bubble is known and it can be drawn into Fig. 19, although no measurements inside the bubble could be performed. The laminar separation bubble has a length of l_b = 26 mm and a height of h_b = 0.3 mm. The ratio of length to height is: l_b/h_b = 86.

In addition to the L2F measurements oil flow pictures have been made for both cases. Before starting the wind tunnel a mixture of oil, turpentine and fluorescent powder is painted uniformly on the turbine blade. At the operating point of the wind tunnel the flow around the blade carries away almost all the paint in areas of fast adjacent flow, while in local areas of flow separation the paint accumulates because of the low shear stresses. Due to the high fluctuations less paint is removed from the blade surface in turbulent boundary layers than in laminar boundary layers. Thus the transition line at natural transition (IP = 0 mm) can be seen clearly in Fig. 21. It is located at x/l = 0.75 and agrees exactly with the other presented measuring techniques. For the impingement point of the wake in the middle between the turbine blades (IP = 40 mm) paint collects inside the laminar separation bubble. One has to wait until the paint at the separation line and the reattachment line dries up on the blade. After stopping the wind tunnel the paint from inside of the bubble flows over the blade. Nevertheless the separation line and the reattachment line can be seen clearly in the oil flow picture at x/l = 0.76 and at x/l = 0.91, respectively (Fig. 22). Besides the good agreement with the other measurement techniques oil flow pictures show vividly the two-dimensional character of the flow in a wide area around the cross section of the blades and the three-dimensional flow effects near the wall.

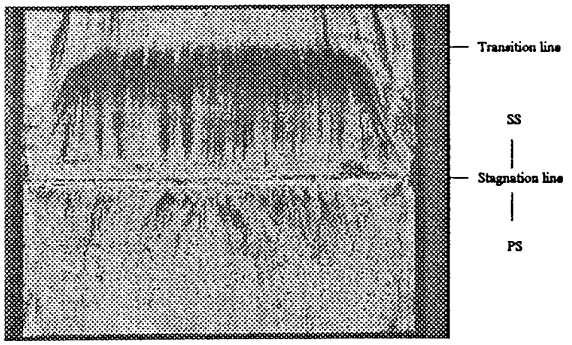

Fig. 21: Flow visualization at IP = 0 mm

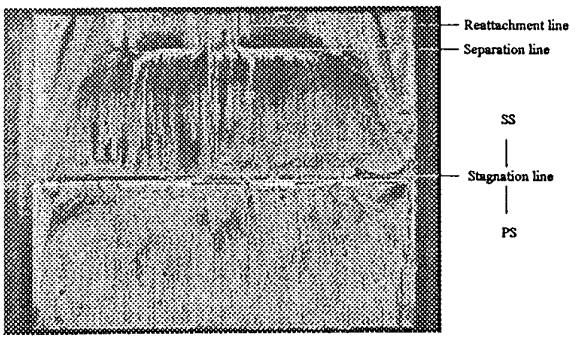

Fig. 22: Flow visualization at IP = 40 mm

MEASUREMENTS AT OFF-DESIGN POINTS OF THE T106

For the impingement points IP = -30 mm, -10 mm, +10 mm and +30 mm measurements have been conducted at Reynolds numbers $Re_{2th} = 3*10^5$, $5*10^5$and $7*10^5$ as well as at inlet angles β_1 = 115°, 127.7° and 137° (Mack (1993) [18]). Within the scope of this paper not all examined cases can be shown, but a few selected examples will demonstrate the influence of these parameters on the development of the boundary layer.

It can be seen that an increasing Reynolds number leads at first to a reduction of the size of the laminar separation bubble and afterwards to a changing from a laminar separation bubble to natural transition (Fig. 23). In the case of natural transition an increasing Reynolds number moves the transition area upstream and can force the turbulent boundary layer to separate before reaching the trailing edge (Fig. 24).

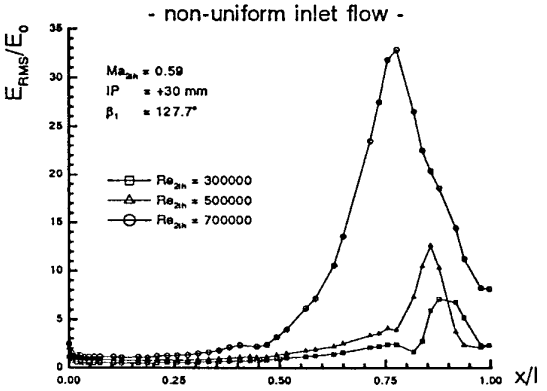

Fig. 23: E_{RMS} distribution at different Reynolds numbers

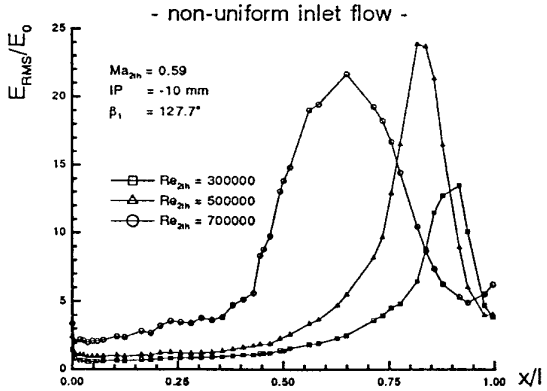

Fig. 24: E_{RMS} distribution at different Reynolds numbers

The raising of the inlet angle causes different profile velocity distributions but a similar transition behaviour as the increasing Reynolds number. After the disappearance of the laminar separation bubble the transition area is shifting upstream again (Fig. 25).

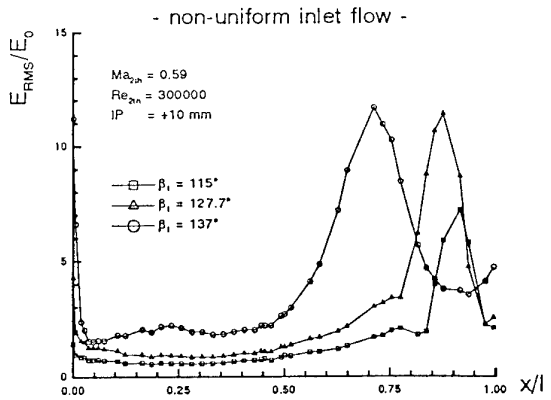

Fig. 25: E_{RMS} distribution at different inlet angles

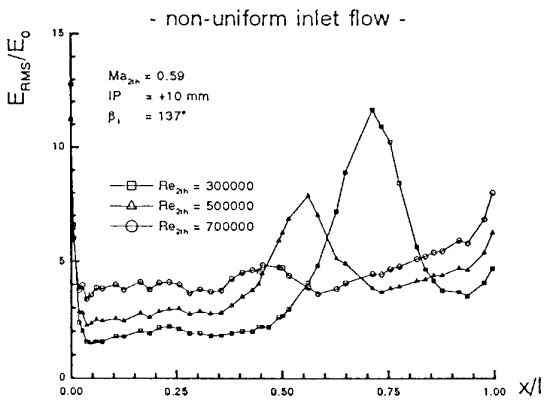

Fig. 27: E_{RMS} distribution at different Reynolds numbers

The influence of the wake impingement point depends strongly on both flow parameters. At low Reynolds numbers and inlet angles the impingement point is the major factor for the mode of transition on the profile suction side (see design point T106). A high inlet angle reduces the influence of the impingement point (Fig. 26). The additional increase of the Reynolds number leads to the disappearance of the laminar-turbulent boundary layer transition on the profile suction side (Fig. 27). Here the boundary layer is turbulent on its whole length.

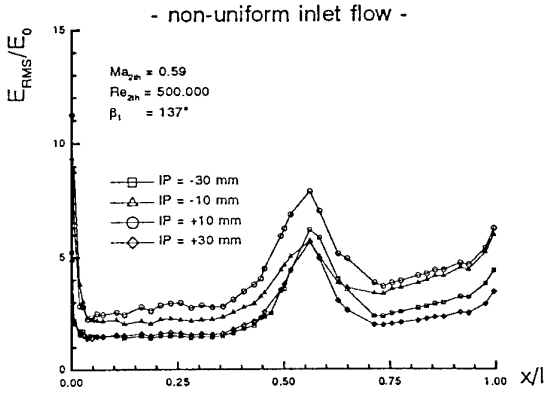

Fig. 26: E_{RMS} distribution at different wake impingement points

SUMMARY

With wake traverse, profile pressure, thin-film, Laser-2-Focus measuring techniques, and oil flow pictures the influence of a non uniform inlet flow on the boundary layer development and transition has been investigated on the low pressure turbine cascade T106. The non-uniform inlet flow was created by cylindrical bars, which produce wakes with a width of half a pitch and a maximum turbulence level of 4% in the turbine inlet plane. At the design point of the turbine cascade the approach of the impingement point to the stagnation point causes at first the disappearance of the laminar separation bubble from the profile suction side and afterwards an upstream shifting of the transition area (natural transition). The lowest profile losses exist at the suction side impingement point IP = -10 mm, where the change from a laminar separation bubble to natural transition has just happened. The highest losses (10% higher) occur at the pressure side impingement point IP = +10 mm, since there the pressure side has a turbulent boundary layer on its whole length, due to the high free stream turbulence level caused by the wake. While the mode and the position of the transition area could be determined by the profile pressure and the thin-film measurements, additionally the Laser-2-Focus measuring technique allows the examination of the boundary layer thickness and of the velocity and the turbulence level distribution inside the boundary layer. Although no measurements inside the laminar separation bubble could be performed, the overall dimensions and the exact position of the bubble were determined confidently from the measured data. Both modes of transition have been presented distinctly by means of oil flow pictures. All five measuring techniques show very good agreement, complement one another, and lead to a better understanding of the transition phenomena on blade profiles.

Supplementary off-design measurements of the turbine cascade have been conducted. An increase of the Reynolds number or of the inlet angle causes a reduction of the size of the laminar separation bubble, the disappearance of the bubble, an upstream shifting of the transition area at natural transition or the separation of the turbulent boundary layer before reaching the trailing edge. At the same time the influence of the wake impingement point on the mode and position of the transition area is reduced. A simultaneous rise of the Reynolds number, inlet angle and turbulence level (impingement point near the stagnation point) leads to a fully turbulent boundary layer on the whole profile length.

The objective of this experimental examination is to transfer the acquired measured data to a boundary layer calculation routine by improving the empirical correlations. The planned coupling of the boundary layer calculation with an Euler method (calculation of the inviscid main flow) will allow to calculate the cascade flow in turbomachines reliably, precisely and with small calculation effort.

ACKNOWLEDGEMENT

This research project in the scope of which the reported work was performed is part of a joint research program of 'Deutsche Forschungs Gemeinschaft'. The permission for publication is gratefully acknowledged

REFERENCES

[1] Mayle R.
The Role of Laminar-Turbulent Transition in Gas Turbine Engines
ASME, 91-GT-261 (1991)

[2] Hodson H. P.
Modeling Unsteady Transition and Its Effects on Profile Loss
Journal of Turbomachinery, Vol. 112, October 1990

[3] Walker G. J., Solomon W. J., Gostelow J. P.
Observations of Wake-Induced Turbulent Spots on an Axial Compressor Blade
ASME, 93-GT-378 (1993)

[4] Binder A., Schröder Th., Hourmouziadis J.
Turbulence Measurements in a Multistage Low-Pressure Turbine
ASME, 88-GT-79 (1988)

[5] Schröder Th.
Measurements with Hot-Film Probes and Surface Mounted Hot-Film Gauges in a Multistage Low-Pressure Turbine
Modern Techniques and Developments in Engine and Component Testing, European Propulsion Forum (1989)

[6] Arndt N.
Blade Row Interaction in a Multistage Low-Pressure Turbine
ASME, 91-GT-283 (1991)

[7] Amecke J.
Auswertung von Nachlaufmessungen an ebenen Schaufelgittern
Bericht 67 A 49, AVA Göttingen (1967)

[8] Ladwig M.
Auswertung von Nachlauf- und Druckverteilungsmessungen an ebenen Verdichter- und Turbinengittern im Hochgeschwindigkeits-Gitterwindkanal
Institutsbericht LRT-WE12-89/13, Inst. f. Strahlantriebe, UniBw München (1989)

[9] Römer N.
Untersuchungen zum Umschlagverhalten der Profilgrenzschicht an Verdichter- und Turbinengittern
Dissertation, Universität der Bundeswehr München (1990)

[10] Schröder Th.
Investigations of Blade Row Interaction and Boundary Layer Transition Phenomena in a Multistage Aero Engine Low-Pressure Turbine by Measurements with Hot-Film Probes and Surface Mounted Hot-Film Gauges
von Karman Institute for Fluid Dynamics, LS 1991-06 (1991)

[11] Schodl R.
On the Development of a New Optical Method for Flow Measurements in Turbomachines
ASME, 74-GT-157 (1974)

[12] Beeck A., Fottner L., Benz E., Wittig S.
The Aerodynamic Effect of Coolant Ejection in the Leading Edge Region of a Film-Cooled Turbine Blade
AGARD-CP-527 (1992)

[13] Pfeil H., Eifler J.
Messungen im Turbulenten Nachlauf des Einzelzylinders
Forsch. Ing.-Wes. 41, No 5, pp 137-168 (1975)

[14] Ladwig M., Fottner L.
Experimental Investigations of the Influence of Incoming Wakes on the Losses of a Laminar Turbine Cascade
ASME, 93-GT-394 (1993)

[15] Hourmouziadis J.
Blading Design for Axial Turbomachines
AGARD-LS-167 (1989)

[16] Hoeger M.
Theoretische und Experimentelle Untersuchungen an Schaufelprofilen mit Grenzschichtumschlag über eine laminare Ablöseblase
ZLR-Forschungsbericht 92-01, Inst. f. Strömungsmechanik, TU Braunschweig (1992)

[17] Rannacher J.
Vorgang des Grenzschichtumschlags in laminaren Ablösewirbeln und seine Berücksichtigung bei Grenzschichtrechnungen
Maschinenbautechnik 31, pp 322-326 (1982)

[18] Mack Th.
Ermittlung des Einflusses definierter Nachlaufdellen in der Zuströmung des Turbinenschaufelgitters T106 auf Art und Lage des laminar-turbulenten Grenzschichtumschlags
Diplomarbeit Nr. 93/4.12, Institut für Strahlantriebe, UniBw München (1993)

REFERENCE NO. OF THE PAPER: 21

DISCUSSOR'S NAME: J. Dunham, DRA, U.K.

AUTHOR'S NAME: M. Engber, L. Fottner

Q: Does the (slow) passage of the incoming wakes increase the profile loss of the cascade?

A: I made measurements with a fixed wake generator in front of the turbine cascade and simulated the rotor-rotor interaction in multistage turbines. The results cannot be transformed to the rotor-stator interaction with moving (periodic) incoming wakes. In that case unsteady flow effects influence the profile losses, but I cannot make any statement about the amount of these losses in comparison to the measured losses at steady inlet flow conditions.

REFERENCE NO. OF THE PAPER: 21

DISCUSSOR'S NAME: N. W. Harvey, Rolls-Royce, U.K.

AUTHOR'S NAME: M. Engber, L. Fottner

Q: You are specifically investigating stator-stator (or rotor-rotor) interaction. How significant are these effects relative to the effect of adjacent (Rotor/Stator, or Stator/Rotor) blade row interactions?

A: The main effect in multistage turbomachines is the rotor-stator interaction. But there are losses which occur due to the rotor-rotor interaction. I showed in my presentation that if you know where the losses come from, you may be able to avoid them by mounting the blades of two corresponding rotors in a favorable position.

REFERENCE NO. OF THE PAPER: 21

DISCUSSOR'S NAME: D.W. Bechert, DLR, Germany

AUTHOR'S NAME: M. Engber, L. Fottner

Q: Was there any frequency analysis made in the wake of the rod or on the airfoil?

A: I made no frequency analysis in the wake, but I made frequency analyses of the signals of some thin film sensors on the blade surface at different flow conditions. The results are available at the Institute for Jet Propulsion in Munich.

UNSTEADY PRESSURE AND HEAT TRANSFER MEASUREMENTS ON A ROTATING BLADE SURFACE IN A TRANSIENT FLOW FACILITY

by

R.W. Moss, C.D. Sheldrake, R.W. Ainsworth
University of Oxford
Dept. of Engineering Science
Parks Road
Oxford OX1 3PJ
United Kingdom

A.D. Smith, S.N. Dancer
Rolls-Royce plc (0/vr/SND)
P.O. Box 31
Derby DB2 8BJ
United Kingdom

Abstract

The Oxford rotating turbine facility has been used to obtain measurements of blade surface heat flux, static pressure and relative inlet velocity. The measurements provide time-resolved data which is compared with predictions from a two-dimensional unsteady flow calculation.

Nomenclature

c	Specific heat capacity of air
C_{ax}	Axial chord
corrf	Cross-correlation factor of unsteady vs ensemble averaged signals.
f_w	Wake passing frequency, Hz.
htc	Heat transfer coefficient, W/m^2K
k	Conductivity of air
LE	Leading edge
NGV	Nozzle Guide Vane
p	Static pressure, Pa
PSD	Power spectral density
PTOT	Stage inlet total pressure, Pa
q	Heat flux, W/m^2
ρ	Density
rms	Root-mean-square level of unsteady signal at frequencies > $f_w/2$
s	Length of blade surface (pressure or suction)
TE	Trailing edge
x	Perimeter from leading edge to transducer.
X	Axial distance from leading edge

Subscripts

g	gas
rel	In blade-relative frame
w	wall, wake
$\overline{q}$	time-mean value

Introduction

The development of unsteady flow prediction software for gas turbines offers the opportunity to calculate many time-unsteady rotor parameters in far greater detail than ever before. Unsteady effects arise from both the passage of nozzle guide vane wakes through the blade row and from the rotor blades chopping through the potential flow field from adjacent vane rows.

Unsteady CFD codes allow the variations in rotor incidence to be quantified and may be used to confirm that the aerofoils' off-incidence performance is satisfactory; the fluctuations in loading and surface pressure may be used to predict blade vibration levels and any transient component of the aerofoil losses; and an understanding of the variations in heat flux may allow a better prediction of both the mean heat flux and thermal fatigue effects.

The use of unsteady predictions in this manner requires them to have first been validated against experimental data.

Johnson et al (1988) developed a model for predicting the unsteady heat flux resulting from the impingement of shock waves on a boundary layer. The change in heat flux is assumed to consist of two components: one from the change in temperature of the boundary layer, resulting in one-dimensional heat conduction from the air to the wall, and a second term describing the increase in temperature gradients in the boundary layer due to its change in thickness, i.e.

$q = q_1 + q_2$

with

$$q_1(s) = \sqrt{(\rho ck)_g}\left(T_g(s) - T_w(s)\right)\sqrt{s}$$

(in the Laplace domain) and

$$q_2 = \overline{q}\left(\frac{p}{\overline{p}}\right)^{1/\gamma}$$

This model is referred to below as the "JRO" method.

Abhari et al (1991) have compared UNSFLO predictions with time resolved heat transfer data taken on the MIT rotor facility. They compared the measured heat flux signal with that predicted by UNSFLO: at some gauge positions their data agreed well with the prediction, while at others there was a discrepancy that could be explained in terms of the turbulence model or the shock strength. The UNSFLO-predicted signal was also found to agree well with that calculated from the predicted pressure field using the above Johnson and Rigby model. They were, however, unable to directly compare the predicted pressure field with experimental data.

Dunn (1989) used thin-film gauges on pyrex inserts to obtain phase-resolved blade heat flux measurements in a rotating turbine. He was able to show that the unsteady heat flux and pressure on the shroud ring were in phase, and that the presence of NGV cooling air raised the blade leading edge heat flux by approximately 11%.

Korakianitis et al (1993) studied the mechanisms of unsteady heat transfer on a rotor blade using UNSFLO and concluded that, at typical blade-passing frequencies, quasi-steady calculations were sufficient to predict the instantaneous heat transfer rate for subsonic flows in the absence of shock waves.

Paper presented at the AGARD PEP 85th Symposium on "Loss Mechanisms and Unsteady Flows in Turbomachines", held in Derby, United Kingdom, 8-12 May 1995, and published in CP-571.

The results presented here are intended to contribute to the unsteady CFD evaluation process by allowing comparison of the unsteady blade-relative inlet flow, surface pressure and heat transfer with UNSFLO predictions. All data is at the blade mid-height section.

Computational methods

UNSFLO is a 2-D viscous, time resolved code that has been developed by Giles (1988) to predict the interactions of both the stator pressure field and the stator wakes with the blade row. It can handle arbitrary ratios of rotor:stator pitch and incorporates highly accurate non-reflecting boundary conditions to minimise non-physical reflections at inflow and outflow boundaries.

The present study used a grid resolution of 120×30 points for each of the stator and rotor passages and was performed at representative Reynolds and Mach numbers. UNSFLO was run at realistic turbine conditions but no attempt has been made to tune the input parameters to match measured pressures or to assess grid sensitivity and one can, for instance, see that the blade inlet Mach number is slightly lower than measured. It seems appropriate at this stage to report the unsteady pressure predictions while omitting UNSFLO's Nusselt number predictions until a more thorough matching of overall conditions has been attained.

Experimental facility

The Oxford rotor facility (Ainsworth et al, 1988)) consists of a 0.6 m diameter isentropic light piston tube driving a shroudless turbine stage. The turbine discharges to an evacuated "dump tank" and is driven at 6000 rpm by an air motor prior to the run. Compressed air drives a free-sliding piston down the pump tube, compressing the air in front of it until the required pressure and temperature are achieved; at this moment a fast acting annular valve opens and the air passes through the turbine. The flow lasts for 200 ms and during this period the turbine accelerates to approximately 9000 rpm. Data is captured at a slow sampling rate throughout the run, to obtain accurate time-mean levels, and at a fast sampling rate for a 16 ms period during which the turbine is close to its design point.

The tunnel design parameters and operating conditions are listed in Table 1.

Rotor tip diameter	554 mm
Blade axial chord	24.35 mm
Design speed	8434 rpm
Temperature ratio T_{oref}/T_w	1.138
Blade Reynolds number Re_{Cax}	1.554×10^6
Blade exit Mn, isentropic.	0.959

Table 1. Rotor nominal operating point.

Signals from the rotor blade instrumentation pass through in-shaft conditioning electronics and a 24-channel slip ring to a 12-bit, 500 kHz data acquisition system.

Heat transfer data is obtained from thin-film platinum resistance gauges painted over an insulating enamel layer. Heat transfer occurs because the air from the piston tube rises in temperature as it is compressed while the turbine blades remain close to ambient temperature. The gauges are energised by a constant current source and the resulting voltage passes through a high frequency boosting circuit to improve the signal to noise ratio and allow accurate digitisation. Digital signal processing subsequently removes the effect of this circuit and, using the measured thermal properties and enamel thicknesses, converts the signal to heat flux.

Pressure data is obtained from sub-miniature Kulite pressure transducers. These are mounted flush with the blade surface (Dietz and Ainsworth, 1992) to give a frequency response of up to 200kHz with a diaphragm width of only 1mm.

A miniature hot wire probe has been developed (Sheldrake and Ainsworth, 1994; Sheldrake and Ainsworth, 1995) for mounting at the aerofoil leading edge. Both single and crossed hot wires have been used. A three-channel hot wire anemometer circuit is mounted inside the turbine shaft to avoid including a slip ring within the anemometer bridge. The hot wires provide blade-relative inlet Mach number and incidence angle data.

Rotor position is determined using shaft encoders so that signals may be ensemble averaged. A line-fitting algorithm is used for this ensemble averaging (Moss and Ainsworth 1993); this interpolates all the data onto the instant when the turbine passes through its design point.

There are considerable passage to passage variations in the time-resolved pressure and heat flux data. These result both from slight differences in NGV surface finish and trailing edge thickness and, more importantly, from the random nature of the flow in a turbulent boundary layer or wake region. Time-unsteady codes such as UNSFLO can only attempt to predict the periodic aspects of such signals and must therefore be compared with ensemble-averaged signals; one must remember, however, that the actual signal may show large fluctuations that are not seen in the ensemble average.

Figure 1 compares a pair of signals and their ensemble averages. The upper plot has only a small random component, and the correlation factor between the original signal and the average is 0.92, while the lower graph shows a highly random signal with a correlation factor of only 0.26.

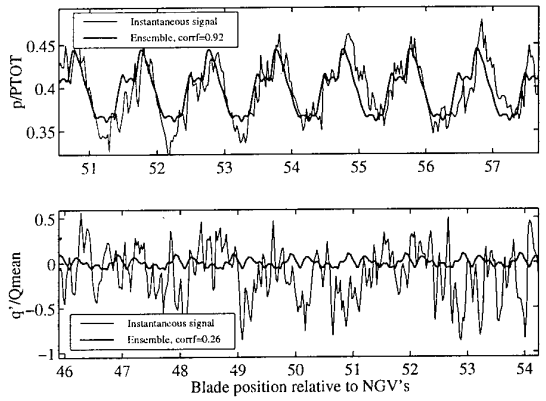

Figure 1. Ensemble averages of periodic (Kulite k003, top) and random (thin-film gauge B17, bottom) signals.

Figure 2. UNSFLO entropy contours.

Results

Hot wire.

Figure 2 shows UNSFLO entropy contours as a pair of NGV wakes propagate through the blade row. As the wake progresses it moves towards the suction surface and becomes wider on this side of the passage; after about 15% x/s it completely loses contact with the pressure surface.

The range of variation in surface static pressure can be seen in Figure 3; it is interesting to note that the blade pressure surface experiences significant pressure variations due to distortion of the flow field despite the fact that the wake does not impinge upon it.

Figure 4 compares crossed hot wire measurements of blade-relative inlet Mach number and relative inlet angle with the corresponding UNSFLO predictions. The sensing elements protruded approximately 3mm in front of the leading edge as shown by the "XHW" point on the aerofoil drawing, and UNSFLO predictions were obtained by filing the UNSFLO stripchart data after placing the cursor at this position. (The

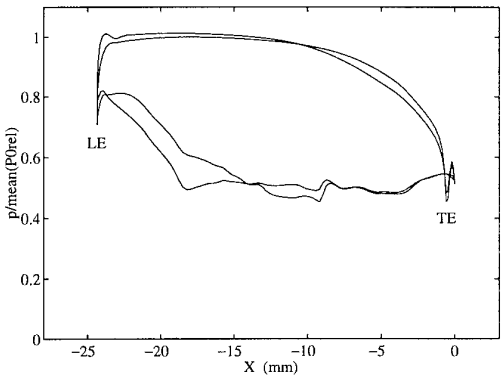

Figure 3. Extent of variation in blade pressure distribution predicted by Unsflo.

stripchart data must then be time-reversed for plotting against position).

The upper-left graph compares the experimental (ensemble averaged) inlet Mach number with the UNSFLO prediction over two wake-passing cycles. The shape and rms level are very similar, although the UNSFLO mean Mach number is 0.1 below the measured level; some adjustment of throat areas or hade may be necessary in future calculations to correct this. The relative inlet angles (lower left axes) also show similar levels of peak-to-peak variation, though the mean levels differ by some 9°. In each of these graphs the mean level has been adjusted to that given by velocity triangle calculations based on static pressures measured on the annulus walls at the NGV exit plane; it should be noted, however, that one would not expect the Mach number derived from time-mean pressure to be exactly the same as the mean of the instantaneous Mach numbers. The 9° difference between the UNSFLO and hot wire values for mean inlet angle may reflect the difficulty of calibrating a crossed wire for a flow where the peak-to-peak variation in blade-relative angle can be from 10° to 65°: data acquired earlier in the test at a mean inlet angle of 50° showed a much better agreement with the velocity triangle prediction.

The correlation coefficients of >60% in each case (shown as *corrf* on the bar charts) show the signals to be predominantly periodic, as can also be seen from the peaks on the power spectral density of the unaveraged signals (upper right) at multiples of the wake passing frequency F_w. No legend has been given as the higher power spectrum is clearly the one with the larger rms level, i.e. the inlet angle in this case. The *rms* barchart columns show the root-mean-square of the experimental data *before* ensemble averaging, at frequencies greater than half the wake passing frequency, i.e. the integrated area under the spectral density line above $F_w/2$.

Pressure and heat flux - suction surface.

Figure 5 shows measured pressure and heat flux traces on the early suction surface at x/s = 14%. The upper-left axes show the ensemble-averaged static pressure, normalised with respect to the stage inlet total pressure PTOT and compared with the UNSFLO prediction at this point. Note that (as in all such figures) the phase relationship between the traces has been chosen arbitrarily to maximise the correlation between them rather than being obtained from UNSFLO itself. The

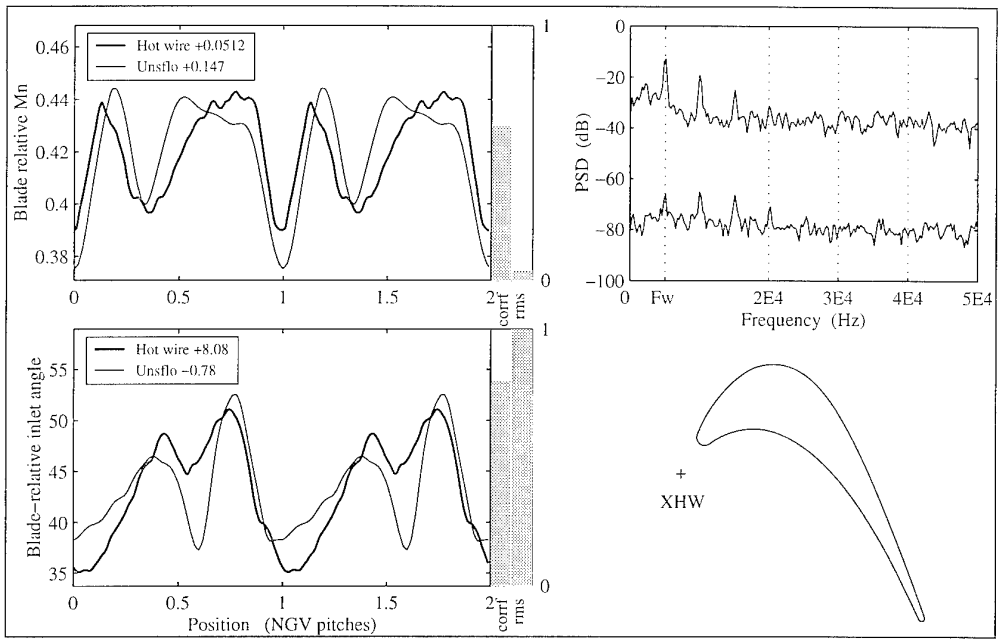

Figure 4. Comparison of hot-wire measurements and UNSFLO predictions of blade-relative inlet Mach number and angle.

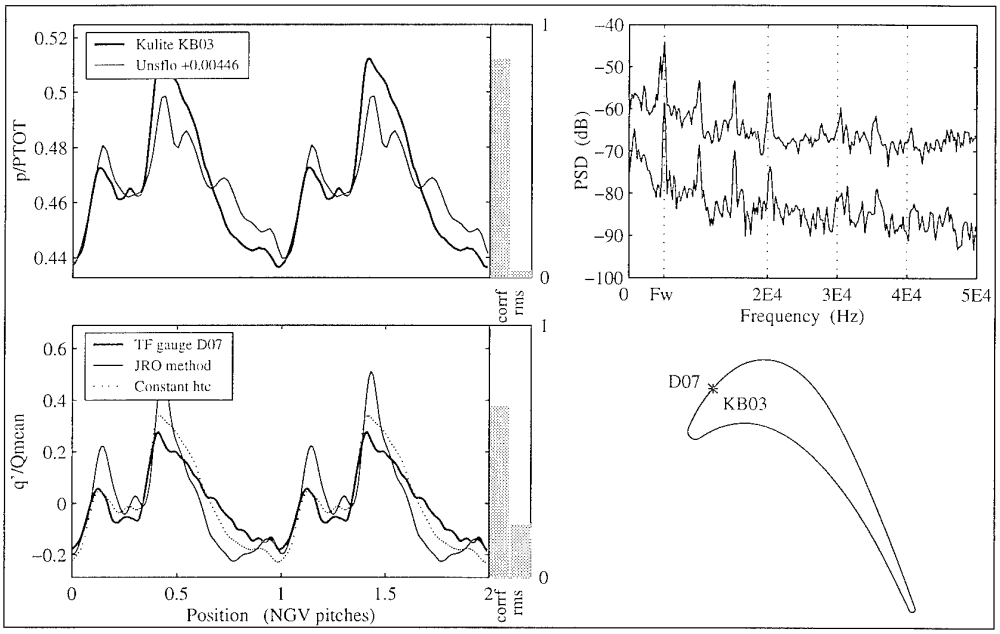

Figure 5. Suction surface x/s = 14%

agreement between the two traces is surprisingly good, both in terms of the shape and the mean and peak-to-peak levels. One can see from the high correlation coefficient that the signal is highly periodic here.

The measured unsteady heat flux is compared in the lower-left axes with two simple predictions, both of which use the measured static pressure signal from the axes above. The "JRO method" is based on the work by Johnson et al (1988) as described in the Introduction, while the "Constant htc" method simply assumes that the heat transfer coefficient is constant and that the change in heat flux can be calculated from the change in temperature, assumed to be isentropic, resulting from the change in static pressure. The JRO method assumes that the boundary layer thickness is greater than the penetration depth of these heat flux cycles into the air, and so would not be expected to give great accuracy in this region that will have a relatively thin boundary layer; one can see, however, that the simpler "constant htc" method gives a remarkably good prediction at this point.

A characteristic "double peak" can be seen in both the pressure and heat flux traces; this signature will persist

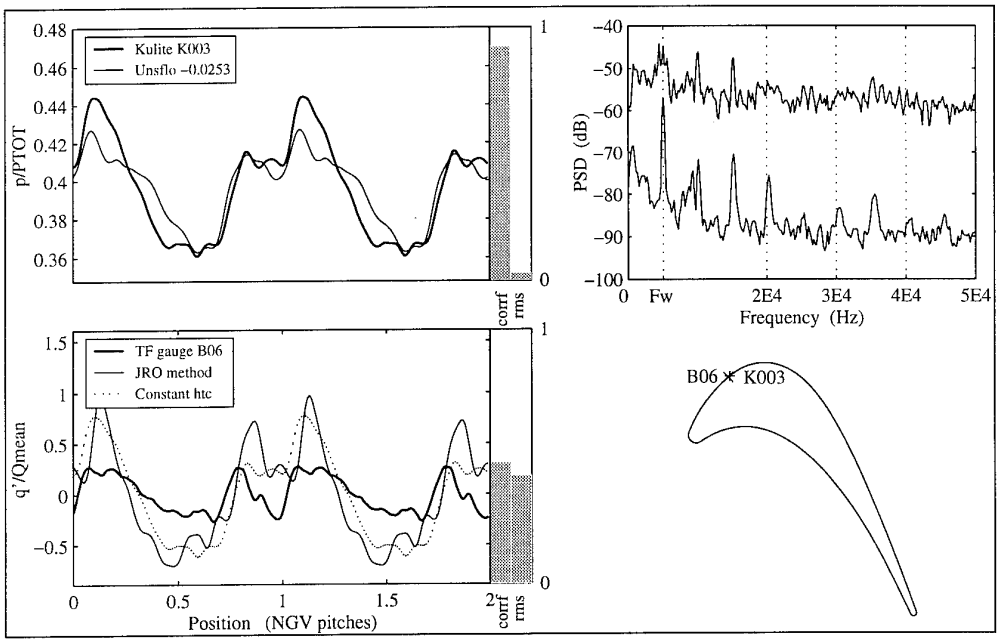

Figure 6. Suction surface at x/s = 19%.

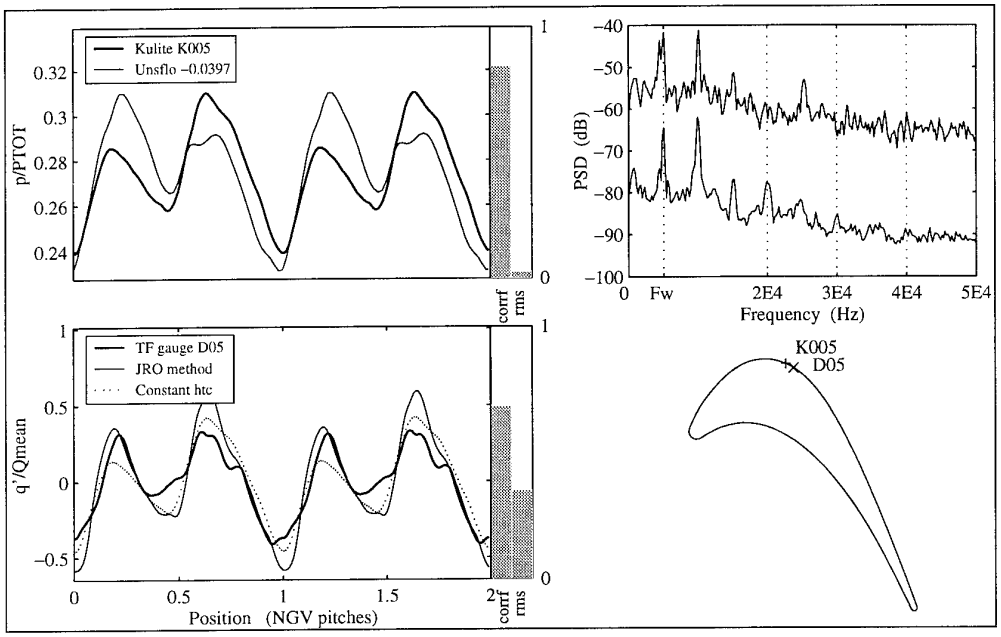

Figure 7. Suction surface at x/s = 34%.

around the front half of the suction surface and, at smaller amplitude, on the pressure surface also.

A comparison of the rms barcharts shows that the changes in non-dimensionalised heat flux are far larger than the changes in pressure. This is to be expected in the present turbine which has a small gas to wall temperature ratio.

Figure 6 shows the corresponding data at *x/s* = 19%. The UNSFLO pressure data still agrees well with the measurements, but both heat flux methods considerably overpredict the fluctuations: the reason for this is, at present, unknown.

Figure 7 shows the signals on the suction surface crown at *x/s*=34%. The double-peaked characteristic is particularly evident here; UNSFLO predicts that the first peak of each cycle should be the stronger, while the measurements show the second one to actually be the larger - but the peak to peak level appears to be correct. The UNSFLO predicted Mach number, both here and further down the surface, is lower than the measured level and it is conceivable that a more precise matching of the UNSFLO and test conditions would have reproduced the pressure profile more exactly.

On the late suction surface (Figure 8, x/s=69%; Figure 9, x/s=89%) the double-peaked characteristic disappears; one can see, both from the spectra and the traces themselves, that the fluctuations are predominantly at the wake-passing

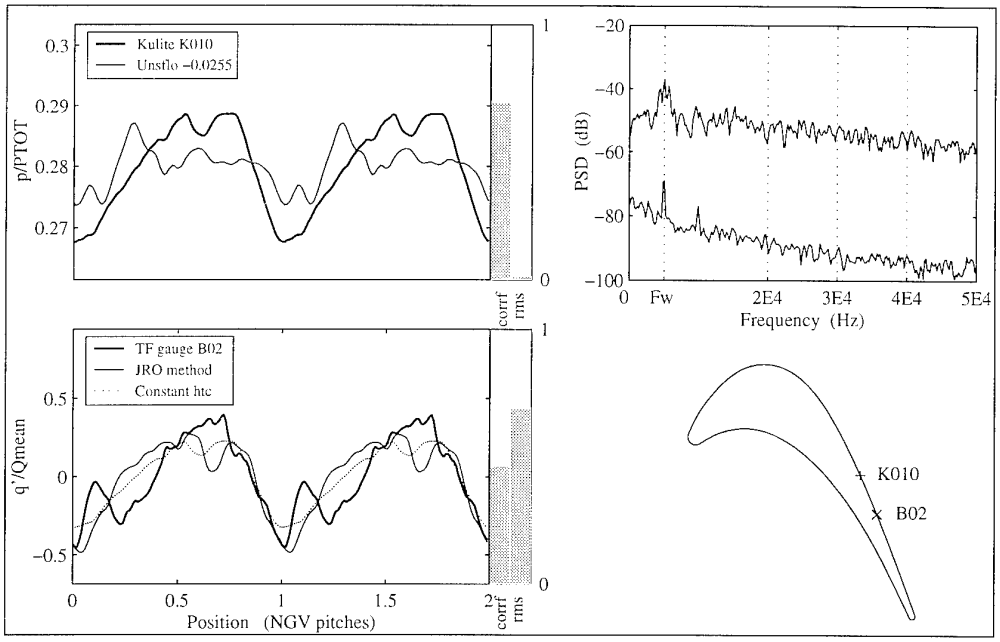

Figure 8. Suction surface at x/s=69%.

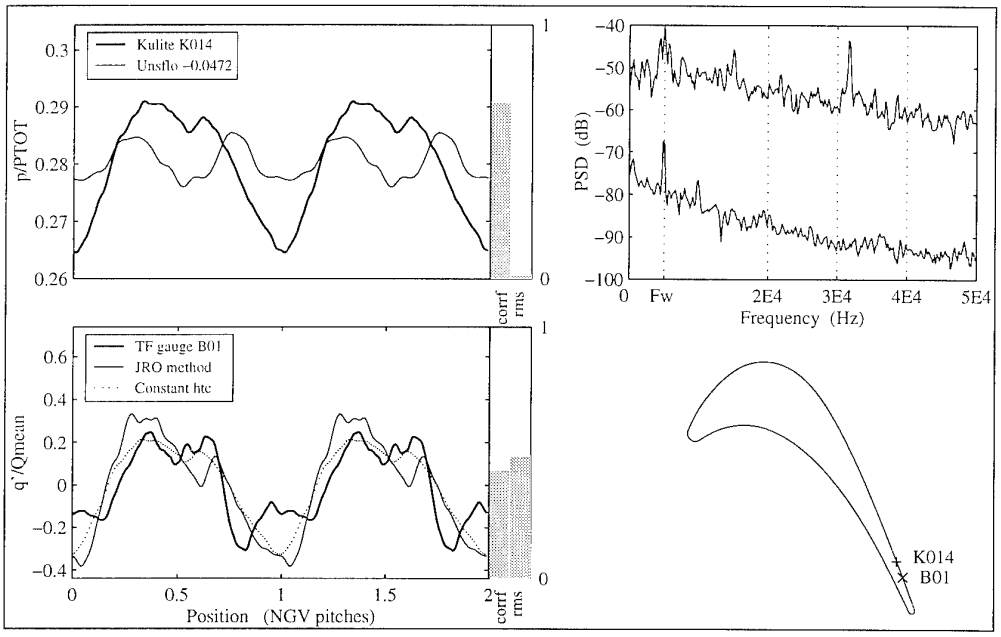

Figure 9. Suction surface at x/s = 89%

frequency. At both these positions UNSFLO underpredicts the pressure oscillation; this may be a Mach number effect as mentioned above. Both the heat flux predictions agree remarkably well with the measured levels.

Pressure and heat flux - pressure surface.

Figure 10 compares the signal from a leading edge Kulite with the UNSFLO prediction of total pressure at this point. The Kulite is mounted as a pitot device with a surrounding bell mouth to minimise incidence effects, and protrudes slightly from the leading edge. The mean levels agree very closely, though UNSFLO predicts a double-peaked appearance that is not seen experimentally. The appearance of the heat flux signal, however, suggests that the measured pressure is correct.

The predicted heat fluxes agree well with the measurement. The "constant htc" gives the best result here, as might be expected with a very thin boundary layer.

Kulite KA01 on the early pressure surface (Figure 11) does show a double-peaked signal that agrees closely with UNSFLO both in appearance and mean level. The UNSFLO trace shows four rather sharp peaks but these would probably, considering the passage to passage variation in conditions, be smoothed by the ensemble averaging into something very close to the observed signal.

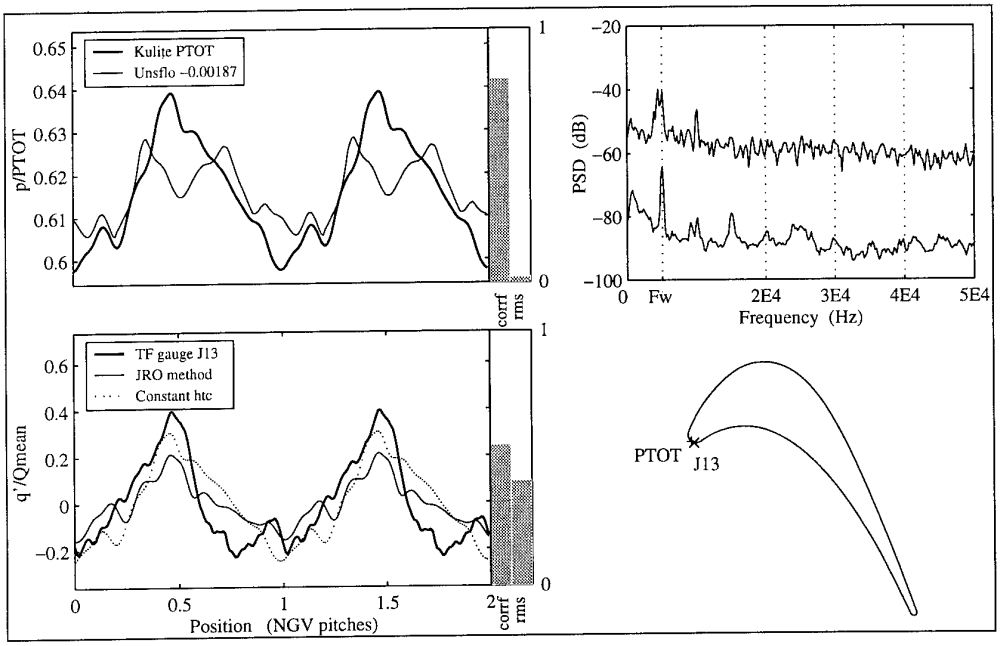

Figure 10. Pressure surface leading edge at x/s = -0.5%.

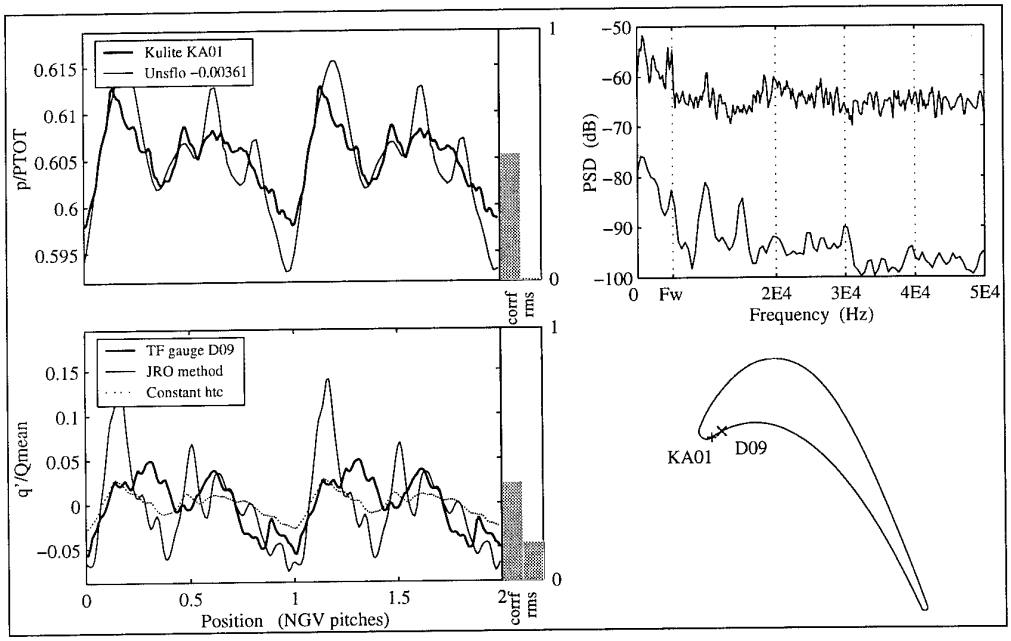

Figure 11. Pressure surface at x/s = -5%.

The heat flux from gauge D09 is not well modelled by either prediction method. This is unsurprising considering the low level of periodic fluctuation here and the low level of cross-correlation between the raw and ensemble-averaged data.

Figure 12 shows the signals around *x/s* = -61%. UNSFLO overpredicts the fluctuations here, though the mean level and the shape are in good agreement. The heat flux here has a double-humped appearance that is predicted by both models, though the JRO method overpredicts the amplitude.

The late pressure surface Kulite (Figure 13) shows most of the features predicted by UNSFLO, though the sudden dip at 0.2 pitch position appears to have been smoothed out by the ensemble averaging. The heat flux predictions (particularly JRO) match the data well over the first half of the cycle, but then show a large fluctuation that is not measured. Comparison with the previous figure shows both pressure and heat flux traces to have changed significantly over this region, and one may suppose that the agreement would have been better had the Kulites used for this comparison been nearer to the thin film gauges.

Comparison of rms levels.

Figure 14 compares the rms level of the UNSFLO-predicted pressure fluctuations with the measured (ensemble averaged) values. The UNSFLO prediction is typically 60% high on the pressure surface but approximately 40% low on the suction

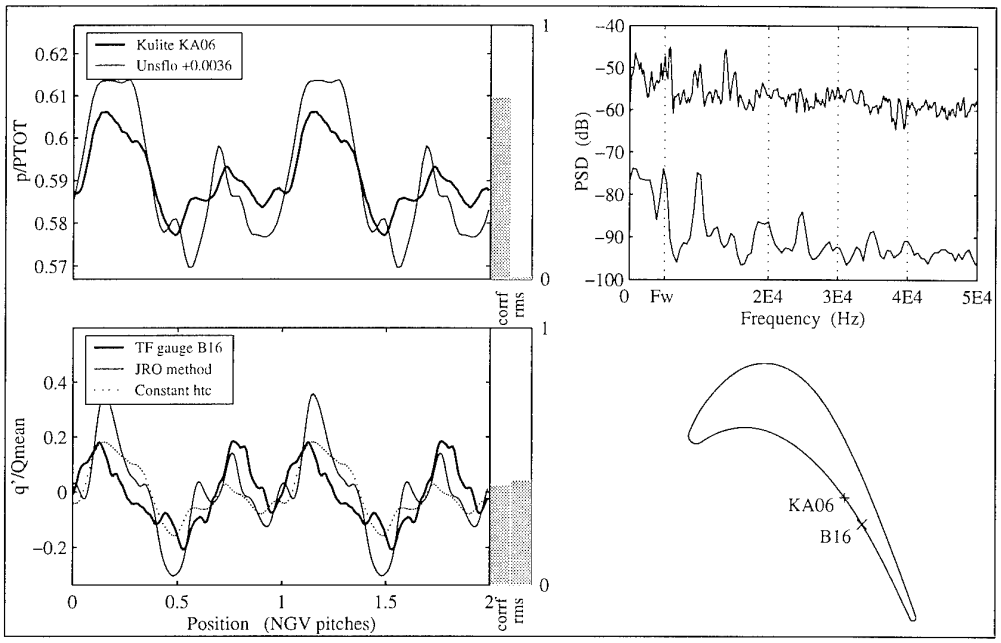

Figure 12. Pressure surface at x/s = -61%.

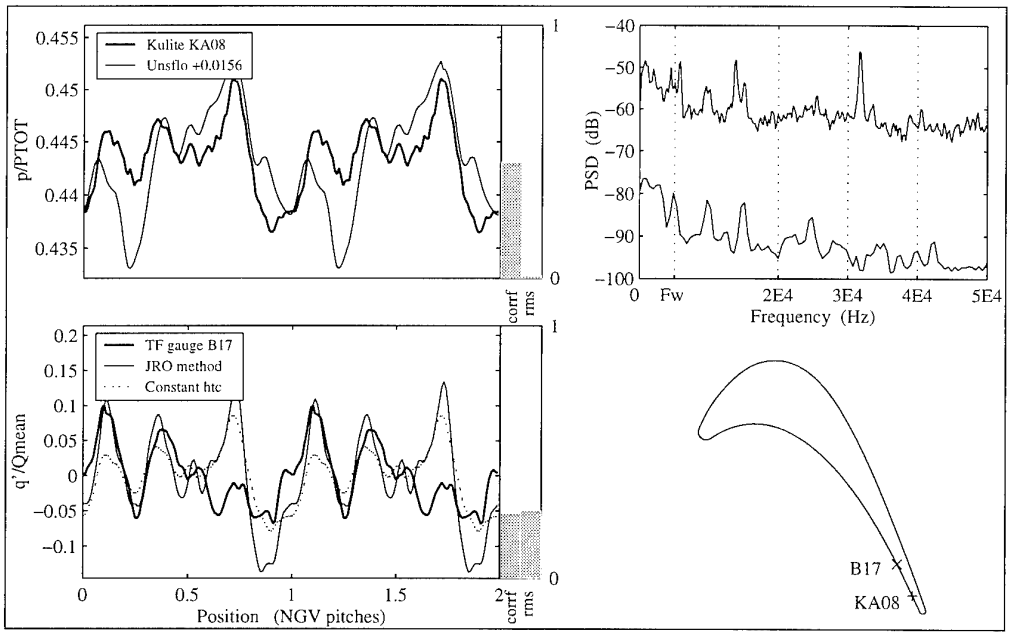

Figure 13. Pressure surface at x/s = -87%.

surface; the prediction on the suction surface crown, however, is roughly 15% high.

Conclusions.

Time resolved measurements of blade surface static pressure and heat flux have been obtained around the mid-height section of a rotating turbine blade at realistic Mach and Reynolds numbers.

The pressure traces are generally very similar in appearance to those predicted by UNSFLO; the predicted rms levels are typically 60% high on the pressure surface and 40% low on the suction surface.

The unsteady heat flux history may be predicted either using the Johnson et al boundary layer compression model or by simply assuming a constant heat transfer coefficient and an isentropic gas temperature change. The Johnon model tends to show sudden peaks and dips that are not apparent in the ensemble averaged data, but both models work surprisingly well considering their simplicity and the absence of wake turbulence terms.

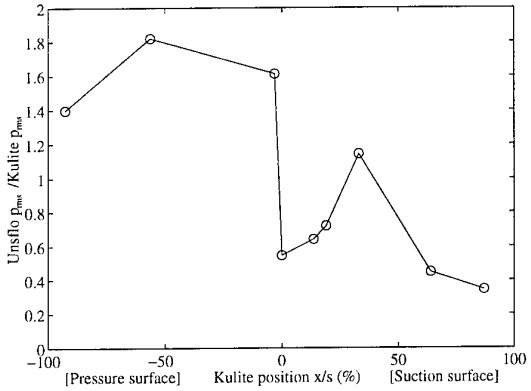

Figure 14. Ratio of UNSFLO-predicted to measured rms pressure fluctuation levels.

Acknowledgements.

The authors would like to thank Rolls-Royce plc, the Defence Research Agency (Pyestock), the Ministry of Defence and the Department of Trade and Industry for their support of this work.

References.

Abhari, R.S., Guenette, G.R., Epstein, A.H., and Giles, M.B., *Comparison of Time-Resolved Turbine Rotor Blade Heat Transfer Measurements and Numerical Calculations*, ASME 91-GT-268

Ainsworth, R.W., Schultz, D.L., Davies, M.R.D., Forth, C.P.J., Hilditch, M.A., Oldfield, M.L.G. and Sheard, A.G., *A Transient Flow Facility for the Study of the Thermofluid-Dynamics of a Full Stage Turbine Under Engine Representative Conditions.* ASME 88-GT-144

Dietz, A.J., and Ainsworth, R.W., *Unsteady Pressure Measurements on the Rotor of a Model Turbine Stage in a Transient Flow Facility.* ASME 92-GT-156

Dunn, M.G., *Phase and Time-Resolved Measurements of Unsteady Heat Transfer and Opressure in a Full-Stage Rotating Turbine*, ASME 89-GT-135

Giles, M.B., *Calculation of Unsteady Wake Rotor Interaction*, AIAA Journal of Propulsion and Power, Vol 4., pp356-362, 1988.

Moss, R.W. and Ainsworth, R.W., *A Transient Measuring Technique for Heat Transfer to Metallic Aerofoils*, Eurotherm 32 - Heat transfer in single phase flows, St Anne's College Oxford, July 1993.

Johnson, A.B., Rigby, M.J., Oldfield, M.L.G., Ainsworth, R.W., and Oliver, M.J., *Surface Heat Transfer Fluctuations on a Turbine Rotor Blade due to Upstream Shock Wave Passing*, ASME 88-GT-172

Korakianitis, T., Papagiannidis, P, and Vlachopoulos, N.E., *Unsteady-Flow/Quasi-Steady Computations on a Turbine Rotor and Comparison with Experiments.* ASME 93-GT-145

Sheldrake, C.D., and Ainsworth, R.W., *Hot-wire Anemometry Techniques on Rotating Turbine Experiments*, 12th Symposium on Measuring Techniques on Transonic and Supersonic Flow in Turbomachines, Prague, 1994.

Sheldrake, C.D., and Ainsworth, R.W., *The Use of Hot-Wires Applied to Aerodynamic Measurements in a Model Turbine Stage*, to be presented at the First European Conference on Turbomachinery Fluid Dynamic and Thermodynamic Aspects, Nuremberg, March 1995.

REFERENCE NO. OF THE PAPER: 22

DISCUSSOR'S NAME: F. Leboeuf, ECL, France

AUTHOR'S NAME: RW Moss, C. Sheldrake, RW Ainsworth, AD Smith, SN Dancer

Q: About the constant heat transfer model which is used for connection of the unsteady heat transfer to the unsteady pressure:
1) What does the constant coefficient mean? Is it constant from the point of view of steady flow?
2) This method uses an isentropic hypothesis to connect T(t) and P(t). Does it imply that the wake may be assumed as inviscid flow, which is difficult to understand as the wake is a region of high dissipation?

A: 1) Yes, the heat transfer coefficient is assumed to be a boundary layer property; I am trying to test the premise that one can explain the heat flux signal in terms of a boundary layer that does not (at most positions) undergo wake-induced transition. I am essentially assuming that the total unsteady heat flux is the sum of a change in heat flux due to a change in gas temperature plus any change in heat flux resulting from disturbances to the boundary layer structure. This implies that, if the gas temperature effect comes close to predicting the measured signal, the effects of wake turbulence and transition must be small - and if this is true, one can reasonably define a "heat transfer coefficient". This is not the same as saying that the coefficient pertains to some steady flow, merely that a mean coefficient defined as h=mean(Q)/mean(Tg-Tw) can be calculated, and will be close to the mean of the instantaneous heat transfer coefficient h(t) = Q(t)/(Tg(t) - Tw).

2) Yes, in so far as it assumes that there is no total pressure deficit in the wake and, more importantly, that the total temperature is unaffected by heat transfer to the nozzle guide vanes. This assumption is justified only by the fact that the predicted heat flux does resemble the measured data - it seems most unlikely (though not impossible) that the lower gas temperature in the wake would be exactly offset by a rise in h due to wake turbulence. It does not mean that the experiment is showing the wakes to be inviscid, merely that in this case the large heat flux fluctuations can be explained without assuming that they are due to transition or other changes in the boundary layer state.

REFERENCE NO. OF THE PAPER: 22

DISCUSSOR'S NAME: G.J. Walker, Univ. of Tasmania, Australia

AUTHOR'S NAME: RW Moss, C. Sheldrake, RW Ainsworth, AD Smith, SN Dancer

Q: Could the discrepancy between measured and predicted heat flux at x/s = 19% (Fig 6) be associated with periodic boundary layer transition phenomena induced by wake passing? Inspection of the heat flux PSD results for neighboring positions suggests that transition is occurring in this area. Wake induced transitional strips would convict at a slower rate than the free-stream and produce periodic effects on heat transfer which would be out of phase with the UNSFLO solution.

A: There may well be periodic transition here, although it is difficult to infer which phase position actually corresponds to the wake passing. The ensemble averaged heat flux variations in Figure 6 are smaller than predicted, and one could try to explain this in terms of the low pressure and temperature effects of the wake flow being counteracted by a rise in Nusselt number due to transition. Time mean Nusselt numbers however (not presented) suggest that transition may start around 10% x/s on the suction surface, although later on the surface the Nusselt numbers lie between expected laminar and turbulent levels and the boundary layer state is unclear. Previous measurements with reverse rotation that had no wake passing showed no significant change in mean heat flux, so it appears that the wake passing does not bring the transition point very far forward from where it would be in the absence of such disturbances. The PSD of the unaveraged signal in Figure 6 is certainly higher above 30 kHZ than in Figures 5 and 7; while this may well indicate transitional behavior, it does not necessarily imply that it is periodic or due to wake disturbances. The small gas to wall temperature ratio in this experiment makes temperature fluctuation effects much more significant than transition.

Wake Passing in LP Turbine Blades

M.R. Banieghbal, E.M. Curtis, J.D. Denton, H.P. Hodson, I. Huntsman, V. Schulte
Whittle Laboratory
University of Cambridge, Madingley Road
Cambridge, CB3 0DY
UK

N.W. Harvey, A.B. Steele
Rolls-Royce plc Olvr/NWH
P.O. Box 31
Derby, DB2 8BJ
UK

1. SUMMARY

A study of the effect of wake passing on the boundary layer of a modern LP turbine is presented. Typically, such blading operates at low Reynolds numbers. As a consequence, significant regions of laminar flow might be expected to occur together with transition via laminar separation bubbles.

The paper examines the behaviour of the surface boundary layers in environments typical of modern low pressure turbines. Results were obtained from arrays of surface-mounted hot-film anemometers in the 3rd stage stator of a LP turbine. The results are considered in relation to more detailed experiments carried out in a steady flow high-speed linear turbine cascade and also with reference to tests carried out in a low-speed linear turbine cascade fitted with a mechanism that simulates the presence of upstream rotor wakes.

It is found that, although there are some differences in details, the results from the turbine are consistent with the cascade observations. The suction surface boundary layer is little affected by wakes over the forward half of the surface and remains laminar. Downstream of peak suction, laminar separation occurs and the main effect of the wakes appears to be to promote transition in the separated region. Nevertheless, even in the presence of wakes, laminar flow persists for part of the time right up to the trailing edge. Over most of the Reynolds number range, the wake effects add to the loss, but at the lowest Reynolds numbers ($Re<1x10^5$), the wakes reduce the profile loss as compared to the steady flow situation, probably by assisting reattachment. The large element of laminar flow, even though there is considerable diffusion over the rear part of the suction surface, leads to low losses for this profile.

2. INTRODUCTION

The emerging generation of large thrust civil engines feature fans of a larger diameter that demand more power from the Low Pressure (LP) turbine at a lower rotational speed. Since present day LP turbines already operate with aerodynamic efficiencies above 90 percent, the quest for further increases in efficiency and performance has become progressively more difficult. Consequently, attention must be focused on the details of the flow and particularly the loss generation processes that arise in actual turbines.

The aspect ratios in the new generation of LP turbines and the very low cruise Reynolds numbers (typically $1\text{-}3x10^5$) are such that the development of the blade surface boundary layers assumes an overwhelming importance. Accurate prediction of the development of these boundary layers is vital if performance targets are to be met. This is because the low Reynolds numbers mean that an inability to accurately predict how the boundary layers undergo transition from laminar to turbulent flow often limits the degree of certainty associated with a given design. For example, the lift coefficient may be constrained by concerns over whether or not a laminar separated flow will reattach to the blade surface to give a closed separation bubble.

One of the issues confronting the designer of LP turbines is the effect of upstream wakes on the transition process. In recent years, the problem of wake-boundary layer interactions has received much attention. The investigations carried out by Hourmouziadis et al[3], Binder et al[4] and Schröder[5] in cold-flow LP turbines have shown that separation bubbles exist on the rear part of the suction surfaces of many of the blade rows. Arndt[6] showed that the reattachment process is influenced by free-stream disturbances such as wakes.

In the presence of wakes, a laminar boundary layer begins to undergo transition nearer to the leading edge than would otherwise be the case. As turbulent boundary layers usually produce more loss than laminar ones, the profile loss might be expected to increase. The level of increase would depend on how far transition is moved upstream and how often the wakes arrive (Hodson[1]). At low Reynolds numbers it is possible that the wakes may reduce the profile loss to below the steady flow level by promoting transition and therefore reattachment (Schulte and Hodson[2]). This effect is of particular interest in the present study since laminar flow is more likely to exist in LP turbines.

It is an objective of the current work to quantify the significance of the effects of wake-generated unsteadiness on the development of the blade surface boundary layers. This paper is specifically concerned with an investigation of the type of blading used in the Rolls-Royce Trent 700 turbofan engine reported by Hodson et al[7]. As in all studies of boundary layer transition in actual turbomachines, the physical size of the airfoils, the time-scales of phenomena, the harsh environment of the flow, problems of accessibility and cost all conspire against a complete analysis of the problem. In this paper, laboratory studies in a steady flow, high-speed linear cascade and a larger scale, low-speed linear cascade fitted with a mechanism to simulate the presence of upstream wakes are used to provide a more detailed examination of the problem in simplified environments.

Paper presented at the AGARD PEP 85th Symposium on "Loss Mechanisms and Unsteady Flows in Turbomachines", held in Derby, United Kingdom, 8-12 May 1995, and published in CP-571.

3. TEST FACILITIES AND INSTRUMENTATION

3.1 Cold-Flow LP Turbine Test Facility

The design of the LP turbine has been described by Scrivener et al[8]. The new aerofoils were intended to control the development of the boundary layers on the suction and pressure surfaces and to provide an improved tolerance to changes in incidence. Three-dimensional design methods were used to determined the stacking of the aerofoils and the vortex distributions to limit the spanwise migration of the viscous flows.

The tests were conducted at Rolls-Royce in a cold-flow facility using engine-size components. The facility uses a pressurised air supply in conjunction with an exhaust extraction system and a variable speed brake. Fig. 1 illustrates the LP turbine.

The present paper is mainly concerned with the development of the suction-side boundary layer on the stator of the third stage of the LP turbine. It was investigated using a multi-sensor array of surface mounted hot-film anemometers. The array consisted of 18 individual sensors at approximately 60 percent of span. The line of the sensors was aligned with the predicted streamwise direction. With a height-axial chord ratio of 7.5, the array is far from the regions of secondary flow.

A once-per-revolution sensor enables the use of phased-locked ensemble averaging. Data logging and processing was carried out on-line under software control. Further details are given by Hodson et al[7].

3.2 High-Speed Linear Cascade Test Facility

The experimental results described in this report were obtained in the transonic cascade facility of the Whittle Laboratory, Cambridge[9]. This is a closed circuit wind tunnel in which the Mach number ($Ma < 1.25$) and the Reynolds number ($0.4x10^5 < Re < 13x10^5$) can be varied independently. The facility is provided with a fully automated and computer controlled data acquisition system. Automatic scanning of pressures is, for example, provided by a Scanivalve system whilst probes can be traversed using a mechanism that provides linear movement in three independent directions as well as rotation about the spanwise axis.

The cascade consisted of six blades that exhausted into a large plenum chamber. Tailboards were not used because experience has shown that they are unnecessary in subsonic exit flows.

The cascade is shown schematically in fig. 2. The two-dimensional cascade was designed to obtain the same Mach number distribution and exit flow angle as in the cold-flow turbine. Due to the absence of stream-tube divergence, the air inlet angle is slightly different to that in the cold-flow turbine. Table 1 provides further details of the high speed cascade.

At mid-span, the central passage of the cascade was instrumented with 0.2 mm diameter static pressure tappings. To minimise any disturbances of the instrumented surfaces, the static pressure tappings were connected, where possible, to the pressure measurement system by internal spanwise pathways that had been drilled into the blades. When this was not possible, hypodermic tubing was laid in slots that were cut into the blade surface before being covered by a layer of epoxy resin.

The static pressure at the inlet to each passage was measured one half of a chord length upstream of the leading edge plane at the cascade endwall. A conventional Pitot-probe was placed in the tunnel so that the inlet stagnation pressure could be measured. The inlet stagnation temperature, (typically 15°C to 35°C) was measured using a thermocouple that was placed within the inlet ducting, upstream of the working section.

Downstream of the cascade, a fixed-direction 4-hole Neptune probe similar to that described by Sieverding[10] was used to measure the exit flow field. The traverse plane was located at 0.4 chords downstream of the trailing edge plane of the cascade. The probe was operated in a fixed orientation with its axis parallel to the mean flow direction.

The local mean flow angle, Mach number and total pressure were determined from the calibration. Integration of these local values was then carried out using a constant area mixing calculation to provide the mixed-out values of the cascade loss and other quantities.

Visualisation of the blade surface and endwall flows were obtained using a mixture of fluorescent powder and silicone oil. This mixture was applied to the surfaces before the passage of the flow through the cascade. The viscosity of the mixture and the duration of the experiments were chosen so that the patterns were unaffected by the starting and stopping of the airflow.

Development of the suction-side boundary layer was investigated using multi-element hot-film sensors. Using the technique described by Hodson[11], these were fitted into pockets that had been machined out of the blade surfaces so that there was no disturbance to the geometry of the finished surface.

3.3 Low-Speed Moving-Bar Linear Cascade Test Facility

Fig. 3 shows the cascade wind tunnel that was used for this more detailed investigation of unsteady flow effects. The cascade consists of 7 blades.

The design of the two-dimensional low-speed cascade was such that its non-dimensional velocity distribution and exit flow angle matched the normalised Mach number distribution and exit flow angle of the cold-flow turbine. The air inlet angle is slightly different to that in the cold-flow turbine. Table 2 provides further details of the cascade.

The bars are driven by a variable-speed DC motor. The bar speed is continuously monitored during the experiment. A once-per-revolution sensor enables the use of phased-locked (ensemble) averaging.

The inlet stagnation temperature was measured using a thermocouple that was placed within the inlet plenum. A Pitot probe placed downstream of the moving bars provided the reference cascade inlet stagnation pressure. By traversing the Pitot in the axial direction in the absence of the cascade, it was shown that the effects of unsteadiness on the readings from this Pitot probe were not significant at the selected measurement location.

Pitch-wise traverses were performed at mid-span to measure the profile loss of the three blades at the centre of the cascade. The traverse was performed at a distance 0.25 axial chords downstream of the trailing edge plane of the cascade. A fixed-direction 4-hole Neptune probe was used for these mid-span traverses. The local mean flow angle, static pressure and total pressure were determined from the calibration. Integration of these local values was then carried out using a constant area mixing calculation to provide the mixed-out values of the cascade efficiency, exit flow angle, exit velocity etc.

As in the other investigations, development of the suction-side boundary layer was investigated using multi-element hot-film sensors. These were fitted to the blade surface using adhesive tape. Previous investigations had shown that the effect on transition of the thickness of the array and adhesive (72 μm), was negligible.

The cascade geometry and flow conditions that are reported here are summarised in table 2.

3.3.1 Bar Characteristics

To achieve a realistic simulation of wake-blade interactions, several similarity parameters must be correctly matched. The correct kinematics of the interaction is achieved by matching the velocity triangles. In this case, with 50% reaction stages, the flow-coefficient

$$\phi = \frac{V_x}{U_{bar}} \tag{1}$$

was set so that in the moving frame of reference, the flow angle at the bars was equal to the absolute exit flow angle of the cascade. Having selected the flow-coefficient, the reduced frequency

$$\bar{f} = f\frac{C}{V_2} \tag{2}$$

is set by the spacing of bars. The velocity defect, the turbulence intensity and the wake width must then be matched.

Pfeil and Eifler[12] showed, that the structure of the far wake of an airfoil and that of a cylindrical body of the same drag is almost the same. If the pressure loss coefficient of the turbine blade is defined by

$$Y_p = \frac{\Delta p_0}{\frac{1}{2}\rho V_2^2} \tag{3}$$

where V_2 denotes the exit velocity, then the loss coefficient is related to the drag coefficient c_d according to the equation

$$Y_P = \frac{c_d d}{s_{bar}\cos\beta}. \tag{4}$$

where β is the flow angle relative to the cascade of moving bars and s_{bar} is the distance between bars. With a drag coefficient of approximately unity, the values for s_{bar} and β being given by the reduced frequency, and the flow coefficient, one can determine the bar diameter d that is necessary to simulate a turbine blade with a certain wake defect.

During this study, bar diameters of 1 mm and 2 mm were employed with spacings of 68 mm and 136 mm respectively. The smaller bars were used to simulate upstream stator wakes. The larger bars were used to simulate upstream rotor wakes. These sizes were chosen to simulate specific conditions in a 1.5-stage low-speed research turbine in the Whittle Laboratory, where a parallel investigation of LP turbine aerodynamics is underway. The size of the bars was selected by matching the velocity defect of the rotor in the low-speed 1.5-stage LP turbine using equation (4).

To check the quality of the simulation, the velocity and the RMS intensity were measured in the absolute frame of reference downstream of the rotor in the low-speed LP turbine and downstream of the bars in the moving bar cascade. The measurements were performed at the scaled distance downstream of the bars and the rotor trailing edge. The distance corresponded to $x/d = 30$.

Fig. 4a shows the ensemble averaged velocity and the ensemble averaged RMS intensity for three blade passing periods. The largest velocity deficit is about 22%. The peak RMS intensity is about 11%. It is noted that between the wake passing a second peak in the RMS and a second dip in the velocity occurs. This is caused by the upstream stator wakes. This type of multi-stage interaction cannot be simulated with the moving bar cascade.

Fig. 4b presents the equivalent data for the moving bar cascade. The velocity defect amounts to 21%. The agreement with the measurements from the turbine rig was expected in this point, since the bar has been specifically selected to match this criterion. In terms of wake width, both measurements yield similar non-dimensional values. The RMS intensity shows peak values of 13%, which exceeds the 11% measured in the turbine. The small difference may arise because of relatively low frequency fluctuations caused by mechanical flutter of the moving bars. Between the wakes the flow is smooth and has low RMS intensity (below 1%). To achieve a more realistic simulation in terms of the turbulence intensity between the wake-passing, future work will use a turbulence grid.

3.4 Surface Mounted Hot-Film Anemometers

3.4.2 Psuedo-Calibration

The similarity between the velocity profile adjacent to the wall and the temperature profile of the thermal boundary layer, generated by the heated sensor, leads to a relationship between the rate of heat transfer to the fluid and the wall shear stress of the form[13]

$$\tau_w = k\left(\frac{E^2 - A^2}{\Delta T}\right)^3 \tag{5}$$

where k is a constant, ΔT is the temperature difference between the air and the heated sensor, E is the instantaneous output voltage from the constant temperature anemometer bridge and the constant A represents the heat lost to the substrate. The constants A and k in equation (5) may be determined by calibration. In the present investigation, this was not possible since the array was permanently fixed to the blade. However, un-calibrated hot-films can provide qualitative or semi-quantitative data about the state of the boundary layers.

Semi-quantitative data can be obtained because the rate of heat lost to the substrate, which is proportional to A^2 (equation (5)), is approximately proportional to the square

of the voltage E_0 measured under zero-flow conditions[9]. Furthermore, if the bulk temperature of the blade is equal to the air temperature, which will normally be the case, then the temperature difference ΔT is proportional to E_0^2 and so the data may be presented in the form

$$\tau_w \propto \left(\frac{E^2 - E_0^2}{E_0^2} \right)^3 \qquad (6)$$

This form allows us to attach significance to the relative magnitude of the hot-film output signals. Of course, the units associated with the quantity τ_w are arbitrary. Other effects on the calibration, such as changes in density, should also be considered but this is usually unnecessary.

In the cold-flow turbine, the E_0-temperature characteristic of each sensor was obtained in an oven. In the high speed cascade heating was applied after shutdown and the E_0-temperature characteristic of each sensor was obtained in situ as the rig cooled. In the low-speed cascade, the temperature remained constant and so the zero-flow voltage could be measured just before or just after the run data were obtained.

3.4.2 Data Acquisition and Processing

The upper frequency limit of the sensors, as indicated by 'square-wave' tests, was of the order of 20 kHz to 30 kHz. The upper frequency limit is such that only the lowest frequencies of the spectra associated with turbulent flow were detected in the high-speed facilities. It will be seen below that the frequency response was found to be adequate for the purposes of the present investigation. The blade passing frequency was of the order of 3 kHz in the cold-flow turbine and 200 Hz in the moving bar cascade.

Each anemometer output signal was recorded at a logging frequency of 30-100 kHz using a computer controlled 12 bit transient-capture system. Nine channels of data could be logged simultaneously. Therefore, the signals were often digitised in two batches. During each experiment, the output signal from each hot film anemometer was acquired as a DC-coupled signal and then as an amplified, AC-coupled signal (1 Hz cut-off). An anti-aliasing filter was also used. Each anemometer output signal was re-composed by adding the mean value determined from the DC-coupled data to the AC-coupled data. All the measured voltages were converted according to equation (6) before the determination of the most common statistical quantities. References [7] and [9] contain further details.

In the cold-flow turbine and the moving bar cascade, the acquisition of data was triggered using a once-per-revolution signal.

4. RESULTS & DISCUSSION

4.1 Mach Number Distributions

4.1.1 Cold-Flow Turbine, Ma_2=0.6

The array of hot-film sensors was located at approximately 60 percent of span. The predicted Mach number distribution corresponding to this location is presented in fig. 5. It shows that the maximum velocity on the suction surface is located near 0.52 s* and that there is a 12 percent reduction in Mach number over the rear half of the suction surface. Steady-flow predictions of the boundary layer development suggest that laminar separation will occur at 0.62 s* on the suction surface.

4.1.2 High-Speed Linear Cascade, Ma_2=0.6

Fig. 6 presents the measured Mach number distribution of the high speed cascade in comparison with the inviscid prediction for the measured cascade geometry.

In the inviscid prediction, the location of maximum velocity is at 0.54 s*, with a 16 percent reduction in velocity over the rear half of the suction surface. The suction side distribution is very similar to that predicted for the cold-flow turbine. The predicted pressure side distributions are also similar.

A comparison of the measured and predicted Mach number distribution in fig. 6 indicates that the high speed cascade has a pressure surface separation bubble. On the upstream half of the pressure surface, the measured velocity is significantly higher than predicted. On the downstream part of the pressure surface the measured and predicted distributions meet again and agree fairly well. The velocity distribution shows a smooth acceleration towards the exit value. Since the separation occurs in a region of low free-stream velocity, it might be expected that the subsequent acceleration is likely to decrease the boundary layer thickness from mid-chord towards the trailing edge and so reduce its overall significance.

On the suction surface, the maximum measured Mach number is lower than that predicted . There is approximately 13 percent deceleration to the exit velocity from the maximum value. Apart from this difference, the measurements also show that at approximately 0.65 s*, the shape of the measured suction-side Mach number distribution deviates from that of the inviscid prediction. The measured velocity is slightly higher than the prediction over the whole rear part of the suction surface towards the trailing edge. This deviation from the inviscid distribution may be due to the presence of laminar separation (see below).

4.1.3 Low-Speed Bar-Passing Cascade

Fig. 7 presents the measured Mach number distribution of the low speed cascade. A comparison of this figure with the predictions for the cold flow turbine (fig. 5) and with the data and predictions from the high-speed cascade (fig. 6) shows that the distributions are very similar. Maximum velocity occurs at 0.56 s*, with a ratio of maximum velocity to exit velocity of 15 percent. Using the measured data, laminar separation is predicted to occur at 0.62 s*. On the pressure surface, a separation bubble is again present, the scatter in the data being believed to be associated with unsteadiness in the separation bubble, or with errors in measurement of the low velocities in this region.

4.2 Cold-Flow Turbine

4.2.1 Hot-Film Data - Re_x=1.8x10^5, Ma_2=0.6

In this section, the main results obtained from the cold flow turbine are summarised. More information is provided by Hodson et al[7].

Fig. 8 presents a selection of the raw hot-film data traces. When following the development of individual events through successive raw data signals, it should be noted that data obtained using the sensors located between the leading

edge and 0.48 s* were obtained at a different time to data from the remainder of the sensors.

The most important aspect in fig. 8 is provided by the trace at 0.75 s*. The form of this trace is typical of those observed in an intermittently separated flow. The base-line of the signal is almost equal to zero which indicates a very low level of shear stress. Upstream, at 0.64 s*, the minimum level of the signal is slightly greater than at 0.75 s*, suggesting that separation occurs between 0.64 s* and 0.75 s*. Steady flow predictions indicate that separation might occur at 0.62 s*. This discrepancy is not unreasonable. It is unfortunate that one of the few gauges to fail was located between 0.64 s* and 0.75 s*.

In the signal at 0.75 s*, the intervals of laminar separated flow are punctuated by upward spikes and longer duration events of an intermediate height. These spikes are probably individual spots or, small collections of coalesced spots. They tend to occur just after a period when the level of the shear stress indicates that separation has occurred, though not exclusively so. They also tend to occur at preferred parts of the wake-passing cycle but not appear every cycle. Transition is more likely to occur in a separated flow.

The longer duration events noted above tend to appear at preferred parts of the wake-passing cycle. Like the spikes, they do not appear every wake-passing cycle. The longer duration events are thought to be associated with wake-induced transition. Wake-induced transition begins near 0.4 s*.

Further analysis of the data showed that the wake-induced transitional flow is, on an ensemble-average basis, more laminar than turbulent. Bypass transition correlations (e.g. [14], [15]) for steady flow suggest that if transition began near 0.4 s*, the intermittency would be approximately 50 percent just before separation. Wake-induced transitional flow will have a much lower intermittency[16]. When the wake-induced transitional flow reaches the neighbourhood of the separation zone (i.e., 0.75 s*), it occupies approximately 40 percent of the wake-passing interval. In between the wakes, the flow begins to undergo transition following laminar separation. Indeed, it is believed that separated flow persists even within that part of the flow that, on average, is affected by the wake-induced transition. Turbulent flow will not separate from this blade.

Downstream of 0.75 s*, fig. 8 reveals that the spikes which first appeared in the trace at 0.75 s* have increased in duration. Also, apparently new, shorter duration spikes appear for the first time. Since data were only obtained at one spanwise location, it is impossible to determine if the shorter duration spikes have formed between adjacent measurement locations or if they are associated with the spanwise spreading of spots that originated upstream at a different spanwise location. Whatever the case, it is clear from fig. 8 that the rate of transition is such that laminar flow persists as far as 0.96 s*.

Even though laminar flow exists at 0.96 s*, this should not be regarded as indicating that time-mean re-attachment has not occurred. At the trailing edge, the minimum level of shear stress is usually approached in the raw traces only occasionally. This indicates that although the flow may be laminar at times, it is usually attached when in that state. This behaviour is believed to be a consequence of the high-shear nature of the calmed zone that trails a turbulent spot. This is further discussed in the examination of the moving bar data.

In practice, it would seem most appropriate to visualise the transition process on this blade as proceeding by way of one of two mechanisms. Either, the passing of a given wake creates a turbulent spot or series of spots at or near the spanwise location in question or it does not. If it does not, the persisting laminar flow probably separates and undergoes transition as a result. In fact, the published data show that the most active region of transition occurs when the wake meets the separated flow. This is the dominant mechanism of transition. Thus it seems that the wakes modify the separated flow transition process even when they do not cause transition at an upstream location. The most turbulent flow is to be found downstream of the separation zone within the flow that is affected by the wake.

4.2.2 Effect of Reynolds number, Ma_2=0.6

Fig. 9 presents the results that were obtained at a Reynolds number of 0.9×10^5. The conditions are otherwise the same as for the data presented in fig. 8.

At the lower Reynolds number, the traces at 0.75 s* and beyond indicate that there are very few turbulent events. Consequently, the most common state of the boundary layer appears to be that of separated laminar flow. Unfortunately, the instrumentation associated with the gauge at 0.96 s* temporarily malfunctioned during the acquisition of this data so that the DC-coupled values were unavailable. However, the character of the data at 0.96 s* was very similar to that at 0.91 s*. This indicates that re-attachment of the flow was unlikely. In all other respects, the nature of the flow at the lowest Reynolds number was found to be similar to that described above for the Reynolds number of 1.8×10^5. In particular, transition began as a result of wake-boundary layer interactions and separation of the laminar flow. The most turbulent flow was found to be associated with the passing of the wakes over the separated flow.

4.2.3 Concluding remarks

The results suggest that boundary layer transition takes place in two ways. Over the range of Reynolds number investigated, the wakes of the upstream rotor cause the onset of periodic transition near 40 percent of surface distance. When viewed on an ensemble-averaged basis, this interaction will result in a zone of flow that grows in streamwise extent as it moves downstream. The zone contains intermittently laminar and turbulent flow. If the flow is laminar within this zone when it encounters the adverse pressure gradient over the rear of the surface, then the data suggest that the flow will separate. In between these zones of transitional flow, the flow that is unaffected by the wakes is also laminar and separates near the same location. The separation of the flow also leads to transition. Even though two modes of transition are possible, the resulting time-mean boundary layer remains transitional up to the trailing edge at all the Reynolds numbers investigated. Transition thus occurs as a result of laminar separation both inside and outside the wake-affected transitional flow. There is evidence to suggest that the process of transition in the separated flow region is influenced by the presence of the wakes.

4.3 High Speed Cascade

4.3.1 $Re=1.9x10^5$, $Ma_2=0.6$

Fig. 10 shows the result of a flow visualisation experiment at the design condition for the high speed cascade. The pictures show the view of the rear of the suction surface looking upstream. The flow over the upstream half of the suction surface is laminar and a leading edge separation bubble does not occur. The patterns show that the secondary flow has a limited extent, so that the flow in the centre of the passage can be expected to be not perturbed by secondary effects. A separation line on the rear of each blade surface is visible at 0.65- 0.70 s*.

Fig. 11 presents the surface distributions of the time-mean shear stress, its RMS and the skew. The results from the final gauge are not shown because the zero-flow voltages were found to be incorrect during post-processing. Nevertheless, the fluctuating component of the signal (see fig. 12) can still be used to assess the state of the boundary layer. Between 0.70 s* and 0.80 s*, fig. 11 shows that the shear stress is at its lowest value. Unfortunately, it is not possible to state absolutely that the boundary layer is time-mean reattached at the trailing edge, though the data would suggest that this is the case. However, even if the boundary layer is separated and a long, perhaps open, separation exists, it does not seem to have a significant impact on the pressure distribution.

Fig. 12 presents the raw hot-film traces. The time-base of fig. 12 is similar to that used for presentation of the cold-flow turbine data. Up to 0.80 s*, the signals are characterised by relatively low-amplitude, low-frequency disturbances typical of a laminar boundary layer in this facility. At 0.84 s*, the separated flow has begun to undergo transition. At 0.89 s*, the boundary layer is clearly transitional. At 0.94 s*, the amount of turbulent flow has increased but the character remains more laminar than turbulent. The plots of the RMS and the skew in Fig. 11 also suggest that the boundary layer is transitional at the trailing edge. In particular, the rms has its maximum at 0.89 s* and the skew just starts dropping from its maximum positive value at 0.84 s* to a lower value, which is still positive at 0.89 s*.

The hot-film data has shown that there is a very low shear stress level over the rear of the surface. This is believed to explain why reattachment is not clearly indicated in the photograph of fig. 10. It seems that the boundary layer is very close to a state where a small separation is not significantly different from attached flow. It is believed that very small differences between passages may have an *apparently* large effect on the flow visualisation patterns.

A comparison of the data from the high-speed cascade (fig. 12) and from the cold-flow turbine (fig. 8) indicates that in the turbine, transition has begun sooner and is relatively more complete. This suggests that the disturbance environment and particularly the wakes may be important, at least in so far as the nature of the trailing edge boundary layer is concerned. Whatever the situation, laminar flow persists to the trailing edge in both series of tests.

4.3.2 Effect of Reynolds Number, $Ma_2=0.6$

The cascade performance was investigated over a range of conditions. Fig. 13 reveals how the measured energy loss coefficient varies with Reynolds number.

At the lowest Reynolds number, the hot-film data indicated that transition began between 0.85 s* and 0.90 s*. Consequently, the flow is more laminar at the trailing edge than at higher Reynolds numbers. It is not clear if the boundary does reattach on a time-mean basis. At the highest Reynolds number shown ($1.9x10^5$), laminar separation occurs but time-mean reattachment is probably complete before 0.95 s*.

4.3.3 Concluding remarks

It is evident from the above discussion that a proper assessment of the state (separated or attached) of the high speed cascade boundary layer is difficult. However, whether the high speed cascade boundary layer is separated or not over large parts of the rear suction surface, does not seem to be of particular importance for the cascade performance. The surface velocity data indicate that the separation is very small in its extent normal to the blade surface. Thus it might be best to regard the rear part of the suction surface as an area with very low skin friction. Furthermore, given the aft-loaded nature of the profile, transition onset is very late. Consequently, a large part of the suction surface is covered with laminar flow. This is obviously responsible for the low loss coefficient.

It seems that a velocity distribution of this type may keep the boundary layer laminar on a large part of the surface. Since the amount of diffusion governs the displacement effect of a separation bubble, it might be concluded that the velocity distribution is close to an optimum concerning the suction surface boundary layer development under steady flow conditions in the low Reynolds number regime.

A comparison between the high-speed cascade and the cold-flow turbine hot film data reveals distinct similarities in boundary layer behaviour. Only the effect of the wakes appears to be absent from the steady flow high speed cascade. As a result, transition is more advanced in the cold flow turbine.

4.4 Moving Bar Cascade

The moving bar cascade was configured in such a way that the bars represented a stator blade row and the cascade, a rotor row. Bars of 1 mm were used rather than the 2 mm bars for which fig. 4 was obtained. The spacing was also half that of the 2 mm bars. It should be noted that the axial separation of the bars and cascade was also reduced by the appropriate amount. Under these circumstances, the peak intensity of the wakes, which is believed to be the most important parameter will be unchanged. Thus, a greater impact of wake-passing might be expected since the reduced frequency is approximately double that seen by a stator row although the duration of each wake passing event is reduced by about half.

4.4.1 Effect of Reynolds Number and Wakes on Loss

The performance of the low-speed cascade was investigated over a range of Reynolds numbers with and without wakes present. Fig. 13 reveals how the measured energy loss

coefficient varies with Reynolds number. The data for the high speed cascade have been discussed above. A comparison between the two sets of steady flow data shows good agreement, indicating the validity of using the low speed experiment in the present context.

Fig. 13 shows that the effect of the wakes is to increase the profile loss at the higher Reynolds numbers. Given that the behaviour of the low speed cascade without unsteadiness is similar to that of its high speed counterpart, it is expected that the efficiency of the cold flow turbine is reduced because of wake-induced transition. At design Re, the loss increases by about one-third due to the wakes. At the lowest Reynolds number ($Re = 1x10^5$), the wakes appear to have no effect on the loss. The trends shown suggest that the wakes may even reduce the loss at still lower Reynolds numbers. In LP turbine cascades, Schulte and Hodson[2] found a similar result on a more highly loaded suction surface. The Reynolds number at which the benefit began was about $1.2\text{-}1.5x10^5$. The benefit of wakes has also been demonstrated by Ladwig[17] using a wake produced by a stationary bar. This effect may be important in conjunction with the unexpected magnitude of the effects of rotor-rotor and stator-stator interactions that have been shown by Schroeder[5] and Arndt[6].

4.4.2 Boundary Layer Data

Fig. 14 presents the raw hot-film data obtained in the moving bar rig at a Reynolds number of $2.0x10^5$. When following the development of individual events through successive raw data signals, it should be noted that data obtained using the sensors located between the leading edge and 0.61 s* were obtained at a different time to data from the remainder of the sensors.

Flow visualisation using an oil-and-dye technique indicated that separation occurred near 0.6 s*. Fig. 14 shows that upstream of this location, there is very little evidence of wake induced transition. Perturbations due to the fluctuations in the free-stream velocity exist and, as a consequence, the separation line (zero wall shear stress) oscillates slightly. This situation is not dissimilar to that in the cold-flow turbine, where only a low intermittency flow is associated with the wake upstream of separation. Differences between the results from the two facilities may be associated with configuring the moving bar cascade to study stator-rotor rather than rotor-stator interactions. However, the absence of multistage effects from the cascade experiments may also contribute.

It is possible to trace the development of the transitional flow perturbations from 0.70 s* to the trailing edge. Just as in the cold-flow turbine, transition appears at preferred parts of the wake passing cycle but not every cycle during the early stages of transition. The absence of transition during certain cycles is primarily associated with a spanwise non-uniformity of the transition process (Howell[19]). Clearly, the wakes modify the transition process. Though not shown here, hot-film data taken without wakes indicate a less complete transition by the trailing edge. However boundary layer traverses indicate that the boundary layer is attached in the time-mean.

Fig. 14 also shows that, just as in the cold-flow turbine, a significant amount of laminar flow persists to the trailing edge. Following a period of high shear stress and turbulent flow, a relatively slow return to laminar separated flow takes place. This decay pattern is very like the high-shear region of laminar like flow (the becalmed region) which follows a turbulent spot (see Schubauer and Klebanoff[20]). Once the shear stress has returned to the undisturbed, separated value, oscillations develop which mark the onset of transition in the separated flow. This is consistent with the observations made above regarding transition in the cold flow turbine. Thus, although the wakes promote earlier transition and so increase the loss at the higher Reynolds numbers, they may not promote as big an increase as might be expected. Pfeil et al[20] noted a similar behaviour in attached flow situations. At even lower Reynolds numbers, there appears to be an overall benefit due to the wakes.

Apart from the hot-film data, the suction and pressure side boundary layers were traversed at 0.98 s*. The data were used to produce the integral parameters and therefore the shape factors ($H=\delta^*/\theta$) which are given in table 3. Without wakes, it can be seen that the suction side boundary layer is not completely separated nor is it fully turbulent. In the presence of upstream wakes, the profile has a lower shape factor, suggesting a more complete transition and reattachment of the boundary layer by the trailing edge. The steady flow hot-film data (not shown) present an identical impression.

4.4.3 Breakdown of Losses

Using the integral thicknesses of measured boundary layer profiles, and following the approximate method outlined by Denton and Cumpsty[18], a breakdown of the contributions to the overall 2-dimensional loss may be derived. It is acknowledged that more exact methods exist for this type of calculation but the present method provides sufficient accuracy to demonstrate the principal features.

Whether the incoming flow is steady or unsteady, table 4 reveals good agreement between the overall loss calculated from the sum of the measured components and the values measured directly. The table also shows that the combined effect of the base-pressure and trailing edge blockage accounts for about 20% of the total loss and that the pressure side loss also account for about 20% of the total loss in the case of steady flow. The values of the above components are unchanged by the presence of the wakes. However, the total loss is increased by 37% when the wakes are present and all the increase is attributable to the changes that take place in the suction side boundary layer. Thus, compared to the steady flow case, the suction side boundary layer assumes a greater importance in the case of unsteady flow.

4.4.4 Concluding Remarks

It has been observed that, just as in the high speed cascade, the low loss of the profile under steady flow conditions can be attributed to the predominantly laminar or transitional flow on the suction surface. However, the predominantly laminar nature of this flow and the small effect that the extended suction side separation bubble has on the overall loss, means that the loss is significantly increased by wake-induced transition at the higher Reynolds numbers. It is therefore possible that whereas the velocity distribution is close to an optimum concerning the suction surface boundary layer development under steady flow conditions in

the low Reynolds number regime, this may not be the case in the presence of wakes.

5. CONCLUSIONS

A number of investigations have been performed which collectively aim to improve the understanding of the dominant loss mechanisms in LP turbines.

Data were obtained from a cold-flow turbine, a high speed steady flow linear cascade and a low speed linear cascade fitted with moving bars. To ensure similarity between the different configurations the same Reynolds numbers and non-dimensional Mach number distributions were employed in each case. Experimental evidence suggests that this approach was successful. In addition, it is seen that simple rotor-stator interactions can be simulated in a moving bar cascade experiment at low speed. The significance of multi-stage effects (like stator-rotor-stator interactions) is not yet clear, but it is likely to be much less important then the primary stator-rotor interaction.

The experimental data obtained using hot-films reveal that in each facility, and without incoming wakes, laminar separation occurs on the rear of the suction surface and that this is responsible for the commencement of transition. However, the transition process is gradual and is not complete by the trailing edge. Given the low loss and small displacement effect of the separation bubble, it might be concluded that the velocity distribution is close to an optimum concerning the suction surface boundary layer development under steady flow conditions in the low Reynolds number regime.

In the cold flow turbine, the upstream wakes sometimes cause transition to begin upstream of separation but in general, the most significant impact of the wakes seems to be in promoting transition with the separated flow region. In the steady flow high and low speed cascades, transition begins later than in the unsteady cold flow turbine and low speed cascade. Even though two modes of transition are possible, the resulting time-mean boundary layer remains transitional up to the trailing edge at all the Reynolds numbers investigated. Transition occurs as a result of laminar separation both inside and outside the wake-affected transitional flow. The effect of the wakes is to increase the loss at Reynolds numbers greater than 1.0×10^5, the increase being entirely attributable to the change in nature of the suction side transition process.

6. ACKNOWLEDGEMENT

The authors also wish to thank Rolls-Royce plc. and the Defence Research Agency, Pyestock, for their support of the project and their permission to publish this paper

7. REFERENCES

[1] Hodson, HP, 1989, "Modelling Unsteady Transition and Its Effects on Profile Loss", Proceedings, AGARD Conf. PEP 74a on Unsteady Flows in Turbomachines, AGARD CP 468

[2] Schulte, V, and Hodson, HP, 1994, "Wake-Separation Bubble Interaction in Low Pressure Turbines", AIAA-94-2931, AIAA/SAE/ASME/ASEE 30th Joint Propulsion Conference & Exhibit

[3] Hourmouziadis, J, Buckl, F, and Bergmann, P, 1986, "The Development of the Profile Boundary Layer in a Turbine Environment", ASME Paper 86-GT-244.

[4] Binder, A, Schröder, T, Hourmouziadis, J, 1988, "Turbulence measurements in a multistage low-pressure turbine", ASME paper 88-GT-79.

[5] Schröder, T, 1991, "Investigations of blade row interaction and boundary layer transition in a multistage aero engine low pressure turbine by measurements with hot-film probes and surface mounted hot-film gauges", VKI Lecture Series 1991-06, Sept 2-6.

[6] Arndt, N, 1991, "Blade row interaction in a multistage low-pressure turbine", ASME paper 91-GT-283.

[7] Hodson, HP, Huntsman, I, Steele, AB, 1993, "An investigation of boundary layer development in a multistage LP turbine", ASME 93-GT-310

[8] Scrivener, CTJ, Connolly, CF, Cox, JC, and Dailey, GM, 1991, "Use of CFD in the design of a modern multistage aero engine LP turbine design", Paper No. C423/056, IMechE.

[9] Hodson, HP, 1985, "Boundary Layer Transition and Separation near the Leading Edge of a High Speed Turbine Blade", ASME Jnl. Engineering for Gas Turbines and Power, Vol. 107, Jan.

[10] Sieverding, C, et al, 1974, "Design and Calibration of Four Probes for use in the Transonic Turbine Cascade Testing", VKI TN 100, May

[11] Hodson, HP, 1983, "The Detection of Boundary Layer Transition and Separation in High Speed Turbine Cascades", presented at *8th Int. Symp. on Measurement Techniques in Transonic and Supersonic Flows*, Aachen, Sep.

[12] Pfeil, H, Eifler, J, 1976,"Turbulenzverhältnisse hinter rotierenden Zylindergittern", Forschung im Ingenieurwesen, Vol. 42, 1976, pg 27-32.

[13] Bellhouse, BJ, and Schultz, DL, 1968, "The measurement of fluctuating skin friction in air with heated thin-film gauges", JFM, Vol 32, No 4.

[14] Narasimha, R, 1985, "The Laminar-Turbulent Transition Zone in the Boundary Layer", Progress in Aerospace Science, Vol 22, pp 29-80.

[15] Mayle, RE, 1991, " The role of laminar turbulent transition in gas turbine engines" ASME paper 91-GT-261

[16] Hodson, HP, Addison, JS, and Shepherdson, C. A, 1992, "Models for unsteady wake induced transition in axial turbomachines", Jnl Phys III, France 2, pp 545-574

[17] Ladwig, M, 1991, "Experimentelle Untersuchung zum Einfluß einer inhomogenen Zuströmung auf die Entwicklung des Strömungfeldes in Turbinenschaufelgittern", Ph.D. Thesis, Universität der Bundeswehr München

[18] Denton, J, D, and Cumpsty, N, A, 1987 , "Loss mechanisms in turbomachines", Proc. I. Mech. E.,

Turbomachinery - Efficiency and Improvement, Paper C260/87, Robinson College, Cambridge, Sept.

[19] Howell, R.J., Private communication

[20] Schubauer, G.B., and Klebanoff, P.S., "Contributions on the Mechanics of Boundary Layer Transition," NACA TN 3489 (1955) and NACA Rep. 1289 (1956)

[21] Pfeil, H., Herbst, R. and Schröder, T., 1982, "Investigation of Laminar-Turbulent transition of boundary layers disturbed by wakes", ASME paper No. 82-GT-124.

8. NOMENCLATURE

A	Calibration constant
C	Chord
E	Anemometer voltage
E_0	Anemometer voltage under zero-flow conditions
f	Wake-passing frequency
k	Calibration constant
Ma	Mach number
p	Pressure
Re	Reynolds number based on chord and exit conditions
Re_x	Reynolds number based on axial chord and exit conditions
RMS	Root-Mean-Square
s	Surface distance
s*	Fractional surface distance = s/s_{max}
T	Periodic time
t	Time measured from once-per-revolution trigger
t*	Fractional time = t/T
U	Freestream velocity
V	Freestream velocity
Y_p	Stagnation Pressure Loss Coefficient = $\frac{P_{01} - P_{02}}{P_{01} - p_2}$
τ_w	Pseudo wall shear stress (equation (6)), arbitrary units.
ω	Energy Loss Coefficient = $1 - \frac{V_2^2}{V_{2,s}^2}$ ($\omega = Y_p$ for incompressible flow)

Subscripts

0	denotes Stagnation
1	denotes Inlet Plane
2	denotes Traverse Plane
s	denotes Isentropic Property

Chord	54.09 mm
Pitch-Chord Ratio	0.699
Aspect Ratio	1.87
Air Inlet Angle (from axial)	36.9°
Design Exit Angle (from axial)	-59.8°
Exit Mach number	0.64
Lift Coefficient	0.819
Inlet Free-stream turbulence intensity.	0.5 %

Table 1 High speed cascade geometry

Chord	150 mm
Axial Chord	126.7 mm
Pitch-Chord Ratio	0.68
Aspect Ratio	2.5
Air Inlet Angle (from axial)	30.4°
Design Exit Angle (from axial)	-62.8°
Bar Pitch/Cascade Pitch (1mm bars)	0.667
Bar Passing Frequency (1mm bars)	200 Hz
Axial Distance: Bars-Cascade L.E.	0.5 C_x
Lift Coefficient	0.819
Inlet Free-stream turbulence intensity.	see text

Table 2 Low speed cascade geometry

Component	Steady	Unsteady
Pressure Side	2.42	2.51
Suction Side	2.6	1.75

Table 3 Trailing edge boundary layer shape factors ($H=\delta^*/\theta$) for Low Speed Cascade at $Re=2.0x10^5$

Component	Definition	Steady	Unsteady
Pressure Side Boundary Layer	$\frac{2\theta_{ps}}{s\cos\alpha_2}$	0.005	0.005
Suction Side Boundary Layer	$\frac{2\theta_{ss}}{s\cos\alpha_2}$	0.015	0.022
Base Pressure	$\frac{p_2 - p_{base}}{p_{01} - p_2}\frac{t}{s\cos\alpha_2}$	0.001	0.001
Trailing Edge Blockage	$\left(\frac{\delta^*_{ss} + \delta^*_{ps} + t}{s\cos\alpha_2}\right)^2$	0.004	0.004
Total of above Losses	$\frac{P_{01} - P_{02}}{P_{01} - p_2}$	0.024	0.033
Measured Loss	$\frac{P_{01} - P_{02}}{P_{01} - p_2}$	0.022	0.030

Table 4 Breakdown of low speed cascade losses at $Re=2.0x10^5$

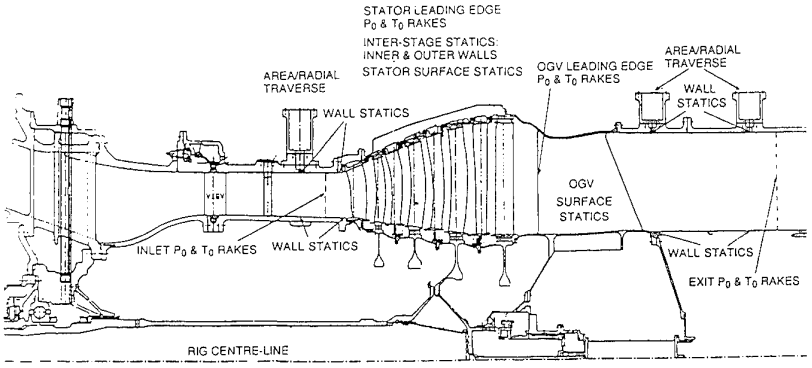

Fig. 1 Schematic of Trent 700 LP Turbine Parts Rig as configured for present investigation

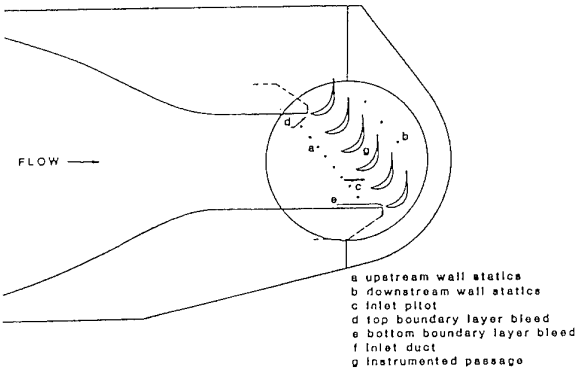

Fig. 2 Transonic wind tunnel

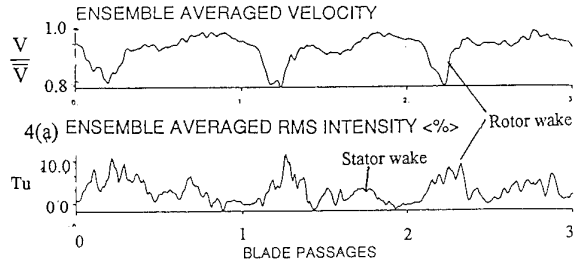

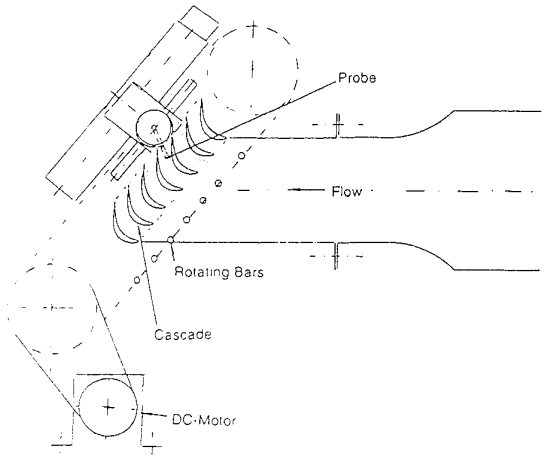

Fig. 3 Moving-bar cascade wind tunnel

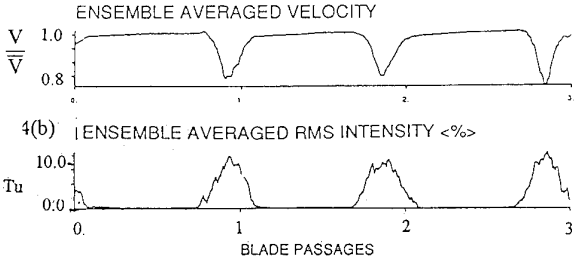

Fig. 4 Absolute frame ensemble-average velocity and RMS downstream of (a) rotor blades in low speed 1.5 stage turbine, (b) moving bars in cascade

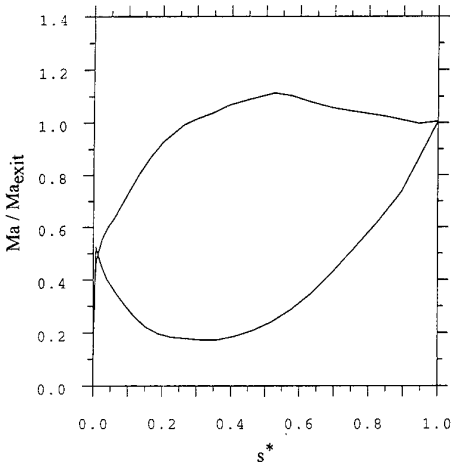

Fig. 5 Predicted inviscid blade-surface Mach number distributions for the cold flow turbine

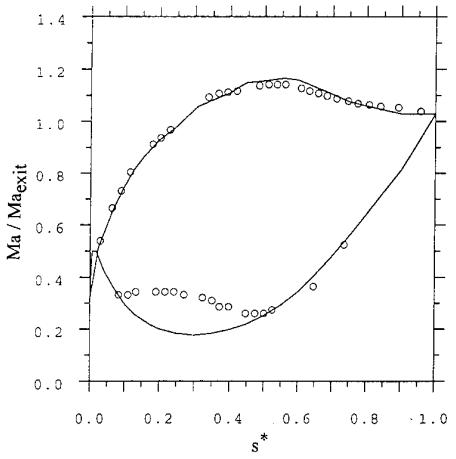

Fig. 6 Predicted inviscid and measured Mach-number distribution for the high speed cascade, Re = $1.9x10^5$

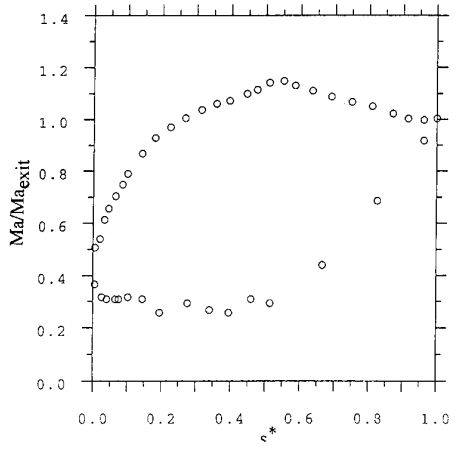

Fig. 7 Measured Mach-number distribution for the moving bar cascade, Re = $1.9x10^5$

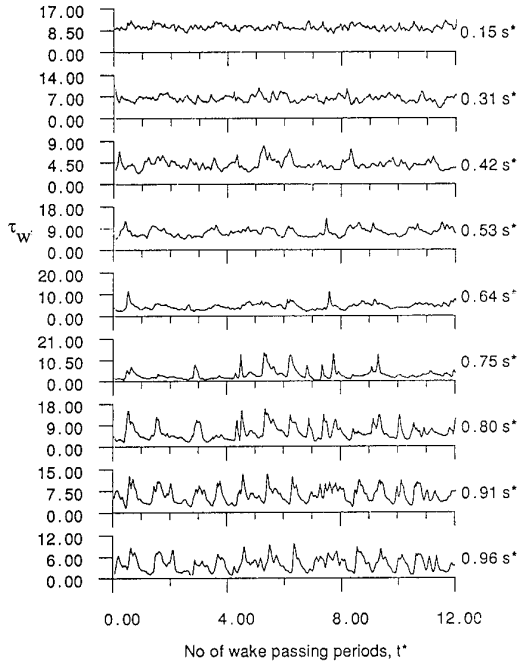

Fig. 8 Raw hot-film traces for the cold-flow turbine, Re_x = $1.8x10^5$

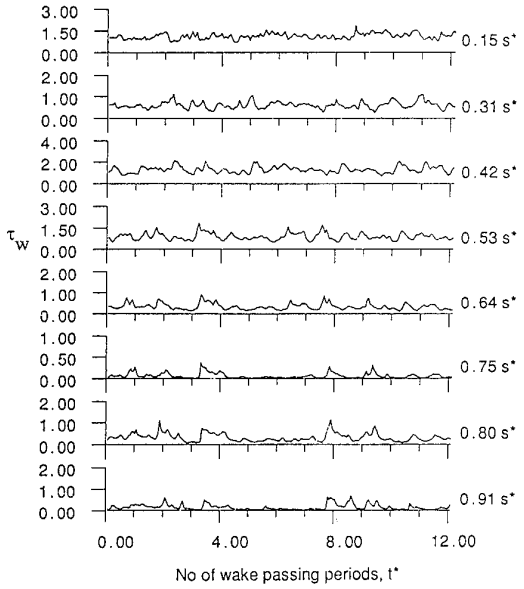

Fig. 9 Raw hot-film traces for the cold-flow turbine, Re_x = $0.9x10^5$

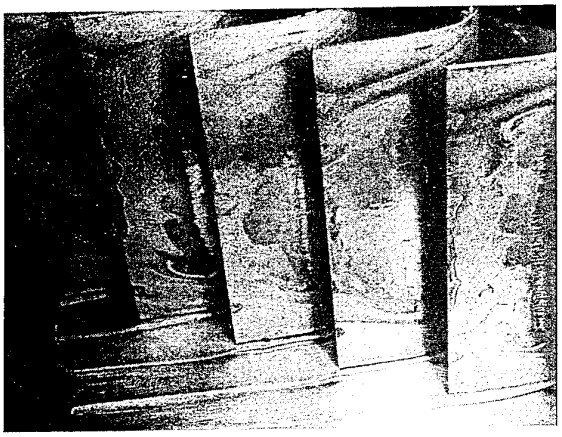

Fig. 10 Flow visualization the high speed cascade, Re = $1.9x10^5$

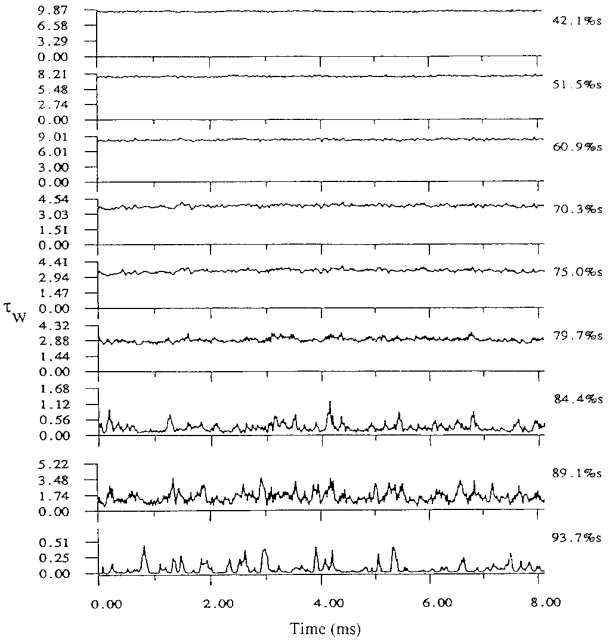

Fig. 12 Raw hot-film output $\tau_w(t)$ for the high speed cascade, Re = $1.9x10^5$

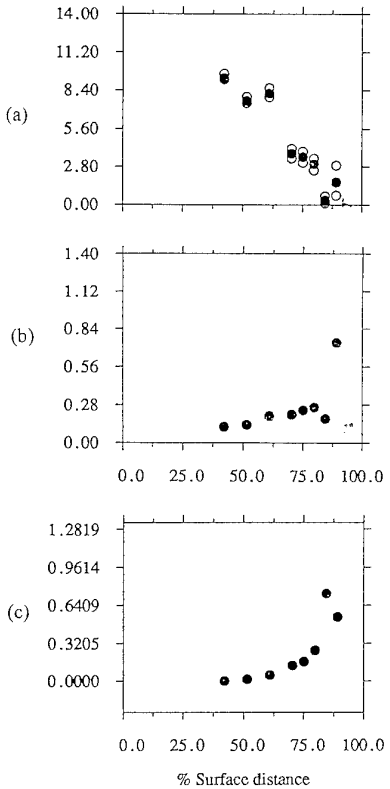

Figure 11 Raw signal τ_W

Re = $1.9x10^5$ (a) max, min, mean (b) rms (c) skew

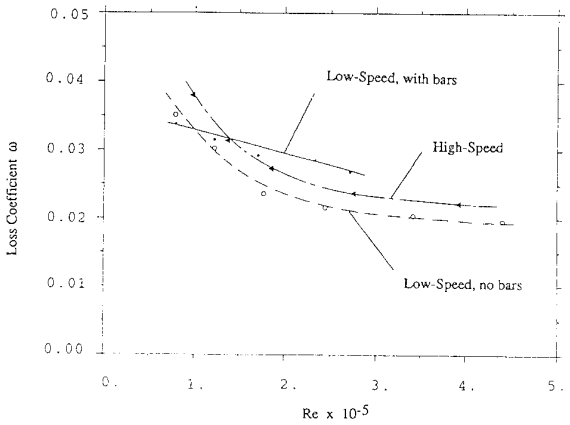

Fig. 13 Effect of Reynolds-number and wakes on kinetic energy loss coefficient ω of the moving bar cascade and high-speed cascade at design incidence

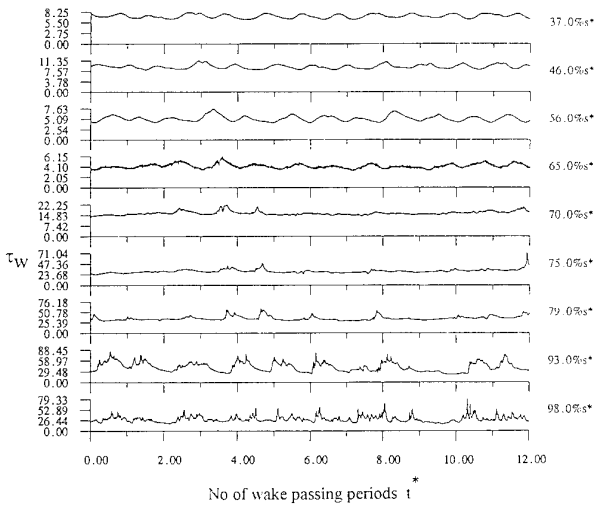

Fig. 14 Raw hot-film output $\tau_w(t)$ for the moving bar cascade, Re = $2x10^5$

UNSTEADY MEASUREMENTS IN AN AXIAL FLOW TURBINE

M. A. Hilditch, G.C. Smith, S.J. Anderson and K.S. Chana
Defence Research Agency, Pyestock, Farnborough, Hampshire, GU14 OLS
UK

T.V. Jones, R.W. Ainsworth and M.L.G. Oldfield
Department of Engineering Science, University of Oxford,
Parks Road, Oxford, OX1 3PJ
UK

1. SUMMARY

Fast response instrumentation has been used to measure the unsteady flow field in an axial flow turbine mounted in a transient test facility. The results show significant fluctuations in static pressure and heat transfer rate at mid-span on the rotor blade. The rotor is shown to have a limited influence on the heat transfer to the ngv at mid-span.

2. INTRODUCTION

The flowfield in a high pressure gas turbine is inherently unsteady. The most important source of unsteadiness is the relative motion of the fixed and moving blade rows. Each rotor blade cuts periodically through the wake and shock structure of the upstream ngv row. In addition, the potential flowfield around each aerofoil is continually modulated by the movement of adjacent blade rows.

This unsteady behaviour is of interest to turbine designers for several reasons: fluctuations in surface pressure and hence aerodynamic loading may cause vibration and affect the structural integrity of the blading; variations in heat flux can give rise to thermal fatigue and substantially affect the mean heat transfer level and the constantly changing incidence angle on to a rotor blade mean that it could be operating off design for most of the time.

Time accurate calculations of the unsteady flowfield are under development, but not yet available to the engine designer. Instead the design process relies on the results of time averaged calculations to establish the distribution of heat transfer and pressure about the blading. This approach has been highly successful and enabled a significant reduction in both the timescale and cost of developing an engine.

The technical and commercial constraints currently imposed on designers demand further improvements from the design and analysis systems. Time resolved measurements taken at engine representative conditions are needed both to increase fundamental understanding of the turbine flowfield and to provide test cases against which new time accurate calculations can be validated.

A programme of measurements to fulfil these requirements is underway at DRA Pyestock and this paper describes some of the first results.

3. THE EXPERIMENTAL FACILITY

The measurements described in this paper were made in the Isentropic Light Piston Facility (ILPF) at DRA Pyestock[1]. This is a transient facility which gives engine representative conditions for a fraction of a second. The blading is representative of a modern high pressure turbine and the turbine operating conditions are summarised in Table 1.

Inlet total pressure	4.6 bar
Reynolds number (ngv exit)	2.6 E6
Ngv exit Mach number (isentropic)	0.94
Steady rotational speed	9500 rpm
Ngv gas to wall temperature ratio	1.624
Run time	400 ms
Rotor blade mid-height radius	0.275 m
Rotor blade axial chord	27.1 mm

Table 1 Turbine operating conditions

The facility is shown schematically in Figure 1 and consists of a large diameter tube containing a lightweight piston which is separated from the working section by a fast acting valve. To initiate a test the working section is evacuated and the turbine assembly spun up to the design speed. High pressure air is let in behind the piston causing it to compress and heat the air in front of it. At a predetermined pressure the fast acting valve opens and a steady flow of air passes through the turbine for approximately 400ms.

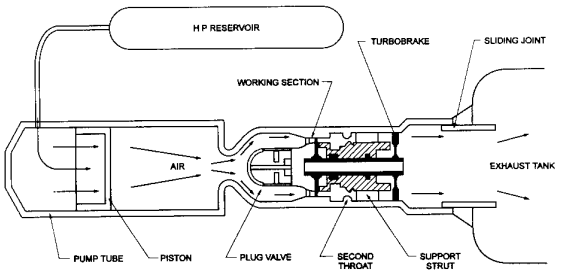

Figure 1 The Isentropic Light Piston Facility

Paper presented at the AGARD PEP 85th Symposium on "Loss Mechanisms and Unsteady Flows in Turbomachines", held in Derby, United Kingdom, 8-12 May 1995, and published in CP-571.

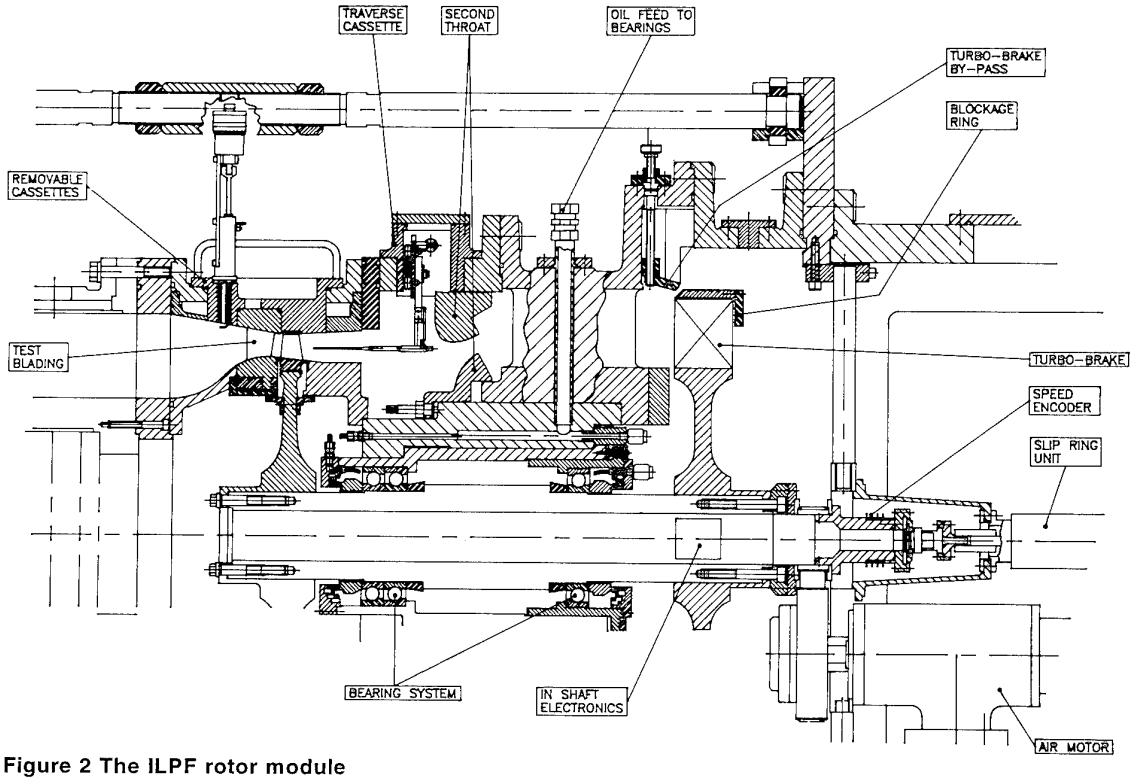

Figure 2 The ILPF rotor module

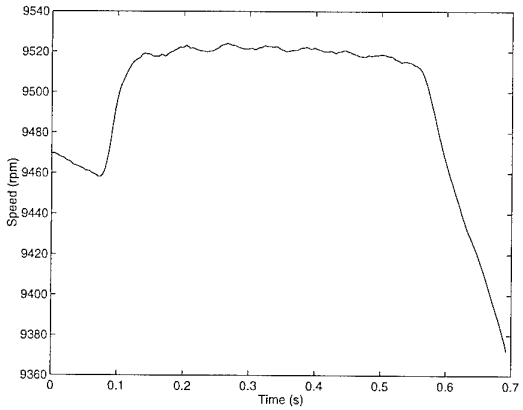

Figure 3 Turbine speed during test run

A novel feature of the Pyestock facility (Figure 2) is the aerodynamic turbobrake which is tuned to hold the turbine speed to within 0.5% of the design speed throughout the run (Figure 3).

Time averaged pressure readings are recorded on a Scanivalve Hyscan ZOC system and other time averaged measurements are recorded at 555 Hz on a PDP 11/23 data acquisition system. Typical time averaged pressure readings from ngv inlet, ngv exit and rotor exit for two test runs are plotted in Figure 4. This plot shows the duration of a test run and demonstrates the quality and repeatability of time averaged pressure measurements which are achieved. The low frequency oscillations are a well documented feature of this type of facility[2] and can be easily allowed for in the data processing.

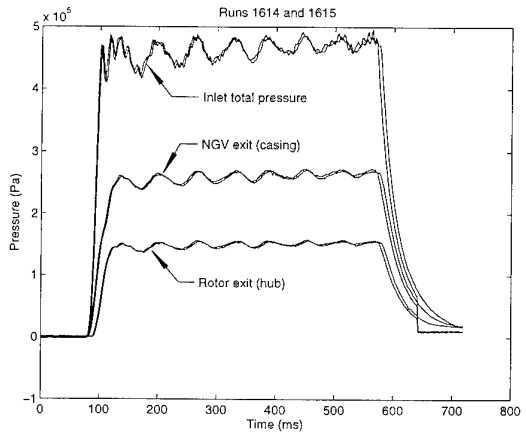

Figure 4 Measured pressures during two runs

Time resolved measurements were recorded on a Prosig AD3000 high performance data acquisition system capable of taking 20 channels of data at one million samples per second for one second. In all cases the unsteady data was passed through a 200 kHz low pass filter before being sampled at the maximum rate of 1 MHz. This gave approximately 6000 data points per

revolution. Typically the whole run was captured by sampling at the maximum rate for 700ms. The useful part of the run lasts approximately 400 ms during which the rotor completes 60 revolutions.

4. NGV HEAT TRANSFER MEASUREMENTS

Heat transfer measurements on the ngv were made using platinum thin film heat transfer gauges painted on vanes manufactured from machineable glass ceramic[3]. The signals are passed through an electrical analogue which models the behaviour of the gauge and gives an output directly proportional to heat transfer rate[2]. The bandwidth of the gauge and analogue was designed to be in excess of 100 kHz so that fluctuations in heat transfer rate occurring at the blade passing frequency of 9.5 kHz could be resolved.

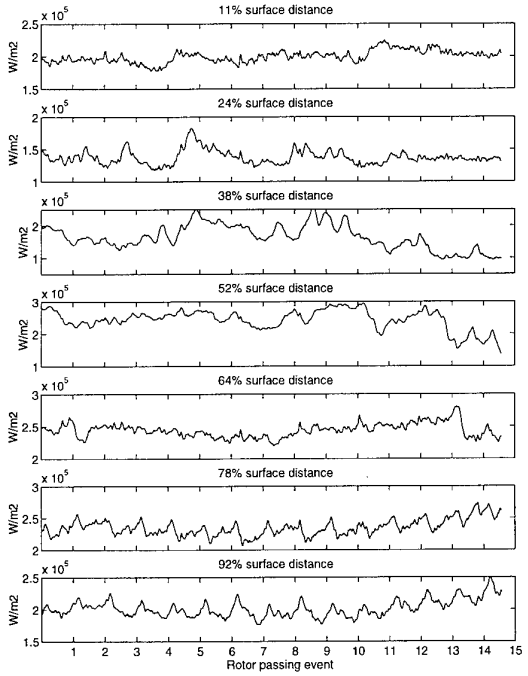

Figure 5 Unsteady heat transfer signals - ngv suction surface

The unsteady heat transfer signal was captured on the AD3000 system as described above. Measurements made around the vane midspan are shown in Figures 5 & 6. On the suction surface the gauge at 11% surface distance shows a low level of unsteadiness. Comparisons of this signal with those from gauges at 24-64% surface distance show some features which are propagated downstream. This behaviour is consistent with the boundary layer being transitional[2]. The periodic motion of the rotor appears to influence only the heat transfer measured at 78% and 92% surface distance.

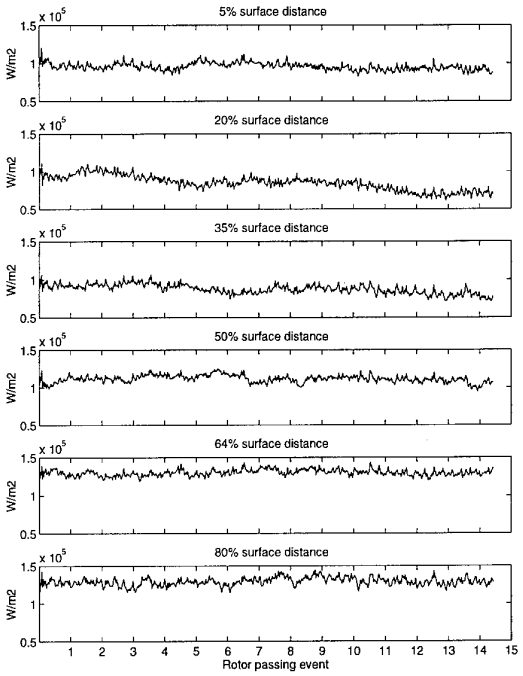

Figure 6 Unsteady heat transfer signals - ngv pressure surface

On the pressure surface a low level of unsteadiness can be seen on the signal from all gauges. Fluctuations at rotor passing frequency are not seen on the early pressure surface, but could possibly be detected at 64% and 80% surface distance.

These observations have been further investigated by calculating the power spectral density of each signal (Figures 7 and 8) and it can be seen that the signals from gauges located at 64, 72 and 89% on the suction surface and 64 and 80% on the pressure surface show significant components at multiples of the rotor passing frequency (9.5kHz).

The average magnitude of fluctuations at rotor passing frequency were then calculated and are shown in Figure 9. The points represent the mean time averaged heat transfer level and the bars represent the fluctuation amplitude. Again, fluctuations of a significant magnitude are only seen at gauges on the late suction surface and near the trailing edge on the pressure surface.

This result was expected as the vane is almost choked and hence much of the unsteadiness at the trailing edge is not able to propagate upstream beyond the throat. Similar results have been reported by Rao, Delaney and Dunn for another transonic turbine stage[4].

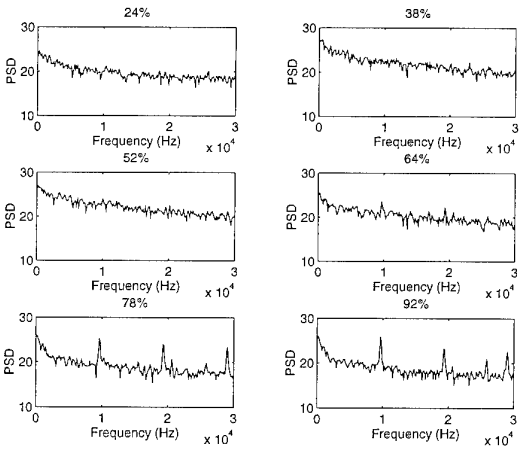

Figure 7 **Power spectrum of heat transfer signals - ngv suction surface**

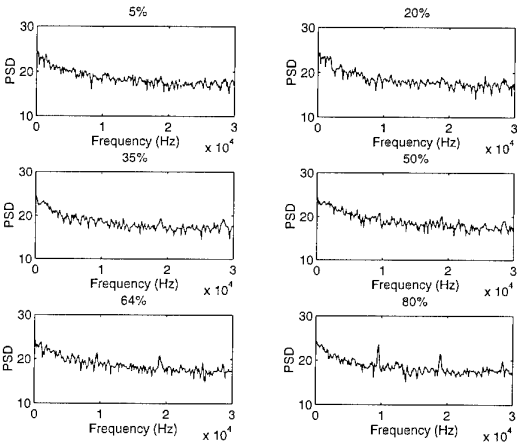

Figure 8 **Power spectrum of heat transfer signal - ngv pressure surface**

The heat transfer to this vane row has previously been measured in a stator only experiment[5,6]. These earlier measurements were carried out at a slightly different operating point, but a useful comparison can still be made to investigate the influence of the rotor on ngv heat transfer. Both experiments were conducted at the same Reynolds Number, but the peak Mach number on the aerofoil surface was 1.1 for the ngv alone tests and only 1.05 for the full stage tests. The gas to wall temperature ratio was 1.3 for the ngv alone tests compared with 1.624 for the full stage tests.

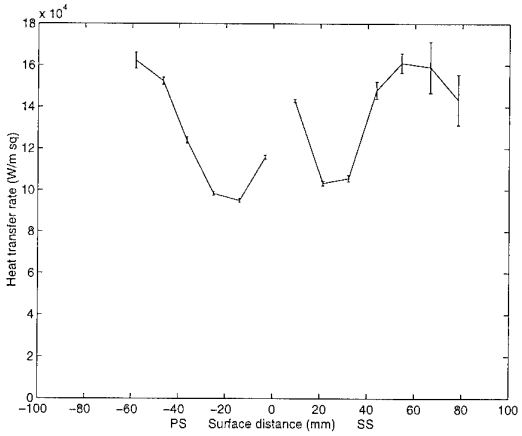

Figure 9 **Fluctuations in heat transfer rate measured at ngv mid-height**

A comparison of the time mean Nusselt number calculated from measurements taken at mid-span during the two tests has been made in Figure 10. In both cases Nusselt number was calculated as given by Equation 1 and there has been no attempt to correct for the differences in running conditions between the two tests.

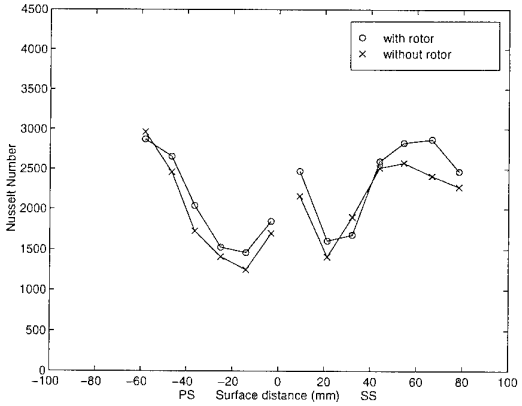

Figure 10 **Ngv Nusselt number at mid-span with and without rotor**

$$Nusselt\ Number = \frac{\dot{q}C}{(T_0 - T_w)\,k} \qquad (1)$$

where $\dot{q}$ = heat transfer rate

C = mid-span true chord

T_0 = measured inlet total temperature

Tw = surface temperature at the measure point

k = conductivity of air at the measured inlet total temperature

The Nusselt numbers from the two tests are very similar. Transition is seen at approximately 20mm surface distance on both pressure and suction surfaces in each case. The only major difference is that on the late suction surface the Nusselt numbers from tests with the rotor present are higher than those for the stator alone. This is consistent with the results shown in Figures 5-9 and confirms that for this turbine operating at the conditions given in Table 1, the presence of the rotor only influences the heat transfer to the ngv aerofoil downstream of the throat.

5. ROTOR PRESSURE MEASUREMENTS

Static pressure measurements have been made around the mid-span of the rotor blade using sub-miniature Kulite pressure transducers. This technique has been developed at Oxford University and is described by Ainsworth, Allen and Dietz[7]. One of the rotor blades instrumented with pressure transducers is shown in Figure 11. The transducer is mounted in a pocket machined in the blade surface and then covered with a thin layer of silastomer to restore the surface and protect the transducer. The frequency response of this type of transducer mounted in this way is 200 kHz.

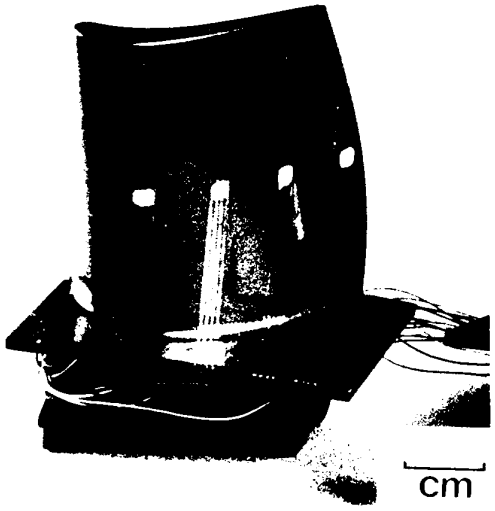

Figure 11 **Rotor blade instrumented for pressure measurement**

The output from the pressure transducers can be used to calculate both the time mean static pressure around the blade and the unsteady component. The unsteady signal has been ensemble averaged on a ngv passage to ngv passage basis and at each position around the blade fluctuations of a significant amplitude were calculated. These results are shown in Figure 12, the time mean static pressure is represented by crosses and the magnitude of the fluctuations is shown by dotted lines. The fluctuations are greatest near the leading edge and the amplitude here is almost equal to the mean pressure level. On the suction surface the fluctuations become smaller towards the trailing edge, whereas on the pressure surface the same level of activity persists along the entire surface.

This figure illustrates the average magnitude of the pressure fluctuations. The peak fluctuations in the raw signals were even larger. This level of static pressure variation will give rise to large fluctuations in lift and a periodic change in structural loading. The current design process assumes that the flowfield is steady and allows for the unsteadiness only by ensuring large margins of safety on all components.

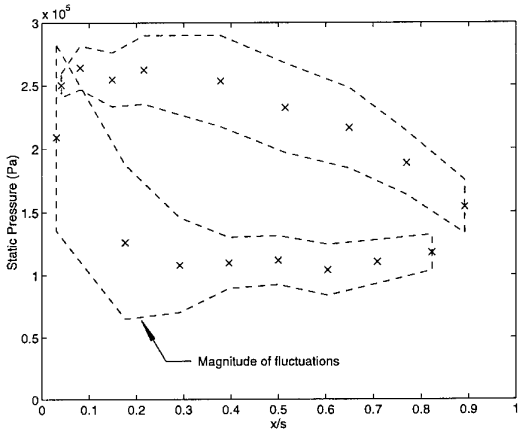

Figure 12 **Fluctuations in static pressure measured at rotor mid-span**

A similar observation has been made by Rao, Delaney and Dunn[8] who measured the unsteady pressure at mid-span of the vane and blade of a transonic turbine operating in a shock-tunnel and compared the results with predictions from a two-dimensional unsteady Navier-Stokes code. They suggest that the unsteadiness on the pressure surface stays at a uniform level because the entire pressure surface is exposed to the vane trailing edge activity. On the suction surface the unsteadiness decreases because the rear part of the suction surface is hidden from the vane trailing edge.

6. ROTOR HEAT TRANSFER MEASUREMENTS

Heat transfer measurements have been made around the rotor blade at mid-span using thin film gauges. The stress levels occurring in a rotating blade preclude the use of machineable glass ceramic and an alternative technique of painting the gauge on to the surface of a metal rotor blade coated with a layer of vitreous enamel has been adopted[9]. A rotor blade instrumented in this way is shown in Figure 13. The electrical analogue used for the ngv heat transfer measurements does not exactly model the behaviour of a thin film gauge mounted on a two

layer substrate; instead the output is preferentially amplified by electronic circuits mounted in the shaft before being transmitted through the slipring to the data acquisition systems. The signals are then digitally processed to recover the heat transfer rate[10].

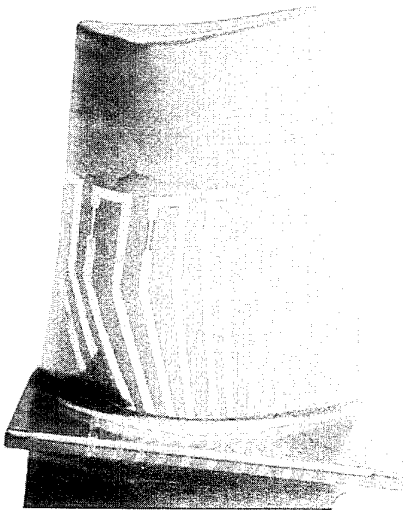

Figure 13 Rotor blade instrumented with thin film heat transfer gauges

The bandwidth of the thin film gauges and conditioning electronics is in excess of 100kHz and the system can be used to measure both time averaged and unsteady heat transfer rates. The unsteady component of each signal was recorded on the AD3000 system at a rate of one million samples per second. As with the rotor pressure and ngv heat transfer time resolved signals the data was filtered using a 200 kHz low pass filter before digitization.

To calculate the time mean heat transfer rate it is necessary to process the entire time history and for this purpose the signal is recorded at 555Hz on the PDP 11/34 data acquisition system. To calculate the fluctuations in heat transfer signal it is only necessary to process a portion of the time history and the calculation will then give the change in heat transfer signal since the beginning of that time record. The present digital processing system imposes a limit on the length of signal which can be processed in one calculation. So although data was taken at a fast rate throughout the run the procedure adopted for processing the unsteady component of heat transfer rate has been to choose a 25000 point record from approximately halfway through the run. The processing is carried out as detailed by Hilditch[11,12].

The unsteady heat transfer signals have been ensemble averaged at ngv passing frequency to allow comparison with the results of other researchers. The results are presented in Figure 14. The largest fluctuations are seen near the leading edge and significant fluctuations persist all along both surfaces. The single rounded peak recorded at the leading edge is replaced at x/s = 5.1% by a sharp spike embedded in a blunt peak. Two features of unequal magnitude are seen at x/s = 15.3 %, but further along the suction surface at x/s = 27.8 %, two distinct features are seen per vane passing event. A single event is again seen at x/s = 49 % on the suction surface, which appears narrower at x/s = 69.4% and has almost died away at the trailing edge.

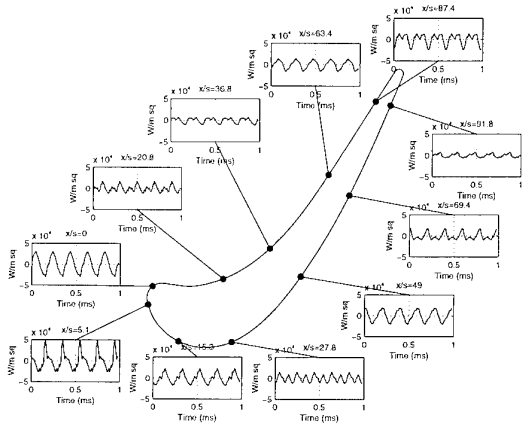

Figure 14 Ensemble averaged heat transfer fluctuations at rotor mid-span

On the pressure surface two distinct events are seen at x/s = 20.8 %. The fluctuation level at x/s = 36.8 % is very low and appears to consist of a broad peak with a second embedded dip. The signature seen at the trailing edge is similar but of a higher level, whereas the signal at x/s = 63.4% shows only a single peak.

Very similar behaviour has been seen in other experiments. Heat transfer fluctuations recorded on the Oxford transient turbine facility have been reported by Allan[13] and are reproduced in Figure 15. Allan also reported the highest level of fluctuations at the leading edge and his results show a single event at ngv passing frequency. On the early suction surface a sharp spike is seen which merges into another feature. Allan's results show the double peak feature dying out before 50% surface distance on the suction surface and a fairly low level of activity along the middle of the suction surface. However, there is a high level of activity on the remainder of the suction surface and the signals in this region show predominantly a single feature per ngv passing event.

Allan's results show a low level of activity on most of the pressure surface and only at the leading edge and towards the trailing edge is there much evidence of periodic activity at ngv passing frequency.

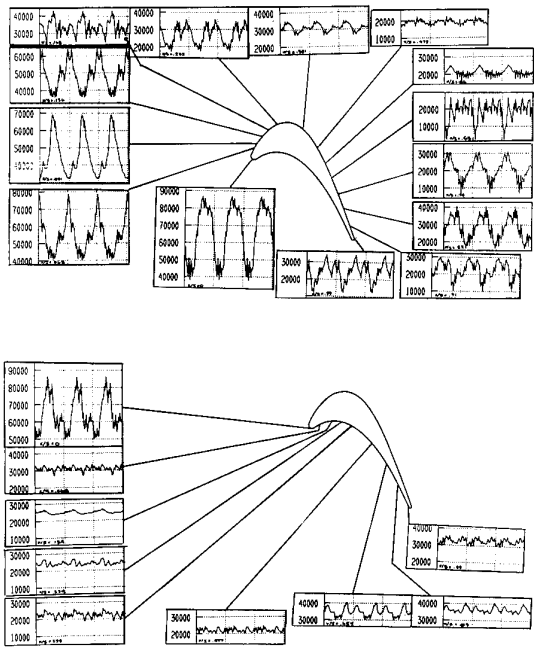

Figure 15 Heat transfer measurements made at Oxford (from Allan[13])

Unsteady heat transfer measurements have also been made in the blowdown facility at MIT and reported by Guennette et al[14]. Their results, Figure 16, show a large spike embedded in another feature on the early suction surface, a signal with multiple peaks on the crown of the suction surface and a general reduction in fluctuation level with distance along the remainder of the suction surface. On the pressure surface there is evidence of periodic activity along the whole surface. The largest fluctuations are found at approximately 10% surface distance. The magnitude then decays slowly towards the trailing edge.

One difference between the Oxford and Pyestock results and those from MIT is the low level of fluctuation measured by MIT at the leading edge. One suggestion put forward is that the thin film heat transfer gauges used in the MIT experiments are broader than those used at Oxford and Pyestock and therefore average the heat transfer signal in the chordwise direction.

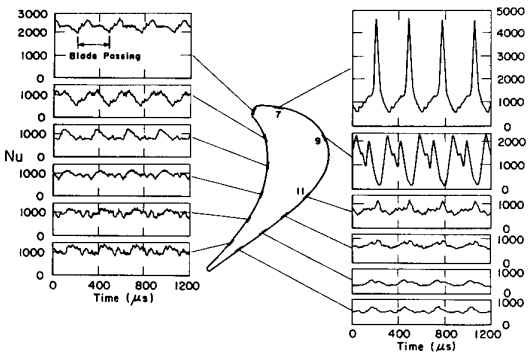

Figure 16 Heat transfer measurements made at MIT (from ref 14)

Abhari, Guennette, Epstein and Giles[15] at MIT have carried out unsteady numerical modelling which has enabled them to explain the pattern of heat transfer fluctuations seen around their blade. The UNSFLO[16] code was used to predict the unsteady flow field at mid-height and showed that there could be up to six shock waves in the rotor passage at any one time. Some of the shock waves were moving upstream and others downstream. Simultaneously there were interactions between the ngv wakes and the rotor. Abhari et al were able to relate many of the features seen in the rotor heat transfer measurements with the calculated shock and wake patterns.

7. CONCLUSIONS

A variety of unsteady measurements have been made in a transonic turbine stage. Measurements at mid-span on the ngv have shown that the downstream rotor only influences the heat transfer rate to the vane aerofoil downstream of the throat.

On the rotor, time resolved pressure measurements have shown the magnitude of the unsteady blade loading. Heat transfer signals measured on the rotor have been ensemble averaged to show distinct fluctuations at ngv passing frequency around much of the profile. The observed patterns are similar to those found by other researchers.

8. ACKNOWLEDGEMENTS

This work was funded by the DTI and MoD and the European Commission's BRITE EURAM initiative. Their permission to publish this paper is gratefully acknowledged.

The measurements described in this paper were acquired with the assistance of Mr. I. J. Carwithen. Thanks are also due to the staff and students of the Osney Laboratory, University of Oxford, for their help in manufacturing and calibrating some of the instrumentation and for their many helpful discussions.

9. REFERENCES

1 Hilditch, M.A., Fowler, A., Jones, T.V., Chana, K.S., Oldfield, M.L.G., Ainsworth, R.W., Hogg, S.I., Anderson, S.J. and Smith, G.C., 1994, "Installation of a turbine stage in the Pyestock Isentropic Light Piston Facility", ASME paper 94-GT-277

2 Jones, T.V., Oldfield, M.L.G., Ainsworth, R.W. and Arts, T, 1993, "Transient cascade testing", *Advanced Methods for Cascade Testing*, ed C Hirsch, AGARDograph 328

3 Oldfield, M.L.G., Jones, T.V. and Schultz, D.L., 1978, "On-line computer for transient turbine cascade instrumentation", IEEE Transactions on Aerospace and Electronic Systems, Vol AES-1

4 Rao, K.V., Delaney, R.A. and Dunn, M.G., 1994, "Vane-blade interaction in a transonic turbine, part II, heat transfer", AIAA Journal of Propulsion and Power, Vol. 10, No 3, pp 312-317

5 Harvey, N.W., Z. Wang, P.T. Ireland and T.V. Jones., 1989, "Detailed heat transfer measurements in nozzle guide vane passages in linear and annular cascades in the presence of secondary flows", AGARD-CP-469

6 Harvey, N.W., 1991, "Heat transfer on nozzle guide vane endwalls", D. Phil thesis, University of Oxford

7 Ainsworth, R.W., Dietz, A.J., and Nunn T.A., 1991, "Use of semiconductor sensors for blade surface pressure measurements in a model turbine stage",ASME Journal of Engineering for Gas Turbines and Power, Vol. 113, pp 261-269

8 Rao, K.V., Delaney, R.A. and Dunn, M.G., 1994, "Vane-blade interaction in a transonic turbine, part I: aerodynamics", AIAA Journal of Propulsion and Power, Vol. 10, No 3, pp 305-311

9 Ainsworth, R.W., Allen, J.L., Davies, M.R.D., Doorly, J.E., Forth, C.J.P, Hilditch, M.A., Oldfield, M.L.G. and Sheard, A.G., 1989, "Developments in heat transfer and processing for transient heat transfer measurement in a full stage model turbine", ASME Journal of Turbomachinery, Vol. 111, pp. 20-27

10 Doorly, J.E., 1987, "Procedures for determining surface heat flux using thin film gauges on a coated metal model in a transient test facility", ASME paper 87-GT-95

11 Hilditch, M.A., 1989, "Unsteady heat transfer measurements in a rotating gas turbine stage" D. Phil thesis, University of Oxford

12 Hilditch, M.A. and Ainsworth R.W.," Unsteady heat transfer measurements on a rotating gas turbine blade", 1990, ASME paper 90-GT-175

13 Allan, W.D.E., "Heat transfer and instrumentation studies on rotating turbine blades in a transient facility", 1990, D. Phil thesis, University of Oxford

14 Guenette, G.R., Epstein, A.H., Giles, M.B., Haimes, R. and Norton, R.J.G., 1989, "Fully scaled transonic turbine rotor heat transfer measurements", ASME Journal of Turbomachinery, Vol. 111, pp 1-7

15 Abhari, R.S., Guenette, G.R., Epstein, A.H. and Giles, M.B., 1992, "Comparison of time-resolved turbine rotor blade heat transfer measurements and numerical calculations", ASME Journal of Turbomachinery, Vol. 114, pp. 818-827

16 Giles, M.B., 1988, "Calculation of unsteady wake rotor interactions", AIAA Journal of Propulsion and Power, Vol. 4, pp 356-362

REFERENCE NO. OF THE PAPER: 24

DISCUSSOR'S NAME: J.P. Gostelow, Univ. of Leicester, U.K.

AUTHOR'S NAME: M.A. Hilditch

Q.: A number of excellent but expensive experimental investigations like this one are being made at present. In general, data are being taken with quite high acquisition rates. It is usual for time-resolved traces to be related to a primary blade passing frequency. One needs to see results presented in the frequency doman as well as the time domain and in reasonable detail. Where transition is involved one needs to have an appreciation of the most damaging frequency - usually the Tollmien-Schlichting frequency. Thus, my comment is more of a plea for all researchers presenting unsteady data from turbomachines to relate their data to the governing aerodynamic frequencies.

A: Thank you for your comment. I am quite aware that we have acquired sufficient data for a lifetime's analysis. The investigations that you suggest are some of the many things that we intend to do with the data.

REFERENCE NO. OF THE PAPER: 24

DISCUSSOR'S NAME: K. Broichhausen, MTU, Germany

AUTHOR'S NAME: M.A. Hilditch

Q: There are different tendencies regarding the decay of pressure fluctuations in your paper and the Oxford turbine. Have you an explanation for that?

A: I have not made a detailed comparison between the pressure fluctuations measured in the turbine experiment at Oxford University (paper 22) and those presented in this paper. However, the two turbines are of different geometry and operating point. I would therefore expect the velocity distribution about each aerofoil to be different, and this could produce significant differences in the levels of pressure fluctuations measured on the blades.

Rotating Stall in Turbojet Engine Compressors

W.J. Borys
W.C. Moffatt[1]
Department of Mechanical Engineering
Royal Military College of Canada
Kingston, Ont.
K7K 5L0
Canada

1. SUMMARY

Losses in an axial compressor are generally ascribed to the effects of shock waves or viscosity, the latter including boundary layer growth, separation, wakes, and secondary flows. Rotating stall is a viscosity-related phenomenon whose effects are well understood, but whose origins and prediction have defied definitive analysis. Experimental approaches to understanding such stalls have for very practical reasons been performed primarily on laboratory scale compressors; there is little information in the open literature on installed units. This paper presents the results of several studies of rotating stall characteristics for a compressor in a turbojet engine, including determination of the conditions in which stall is found, the characteristics of the stall pattern, some details of the flows within the cells, and the effects of inlet distortions on the nature of the stall. Flow characteristics were found using hot film anemometer probes for all the tests. Also included is a brief description of an experimental evaluation of the effects of temperature changes within the compressor on the accuracy of constant temperature hot film anemometer measurements.

2. INTRODUCTION

For well over half a century rotating stall has intrigued designers, users and researchers of turbomachines. It, and its associated phenomenon surge, are the most important limitations on the performance of pumps and compressors, yet the origins and details of the flow are still far from being well understood. Comprehensive reviews of the current knowledge regarding stall and surge, such as Ref. 1, make clear the enormous long term effort that has been expended on attempts to understand, predict, and mitigate the effects of these instabilities.

Analytical efforts aimed at modelling rotating stall, for example those of Emmons et al (2), Stenning and Kriebel (3), Cumpsty and Greitzer (4), Moore (5) and (6), and Takata and Nagano (7) have met with only mixed success; this is not surprising given the limitations of the models used and the apparent complexity of the flow phenomena involved. Even the qualitative model put forward by Emmons et al in Ref. 2 that has been widely used to describe rotating stall is suspect. The representation is two-dimensional, whereas experiments have clearly shown that stall is a three-dimensional phenomenon. For example, casing treatment has been shown to have a profound effect on the nature of rotating stall, but the model of Ref. 2 takes no account of this. McDougall et al (8) present an alternative based on the interaction between blade tip clearance flow and the endwall boundary layer blockage. This model, given its three-dimensionality, is more complex than that of Ref. 2, but is more credible, particularly for high hub-tip ratio machines.

A truly comprehensive theory should allow prediction of the global conditions under which rotating stall will occur for a particular compressor, the number and extent of the cells which will be present, and their rotative speed. To date, no such model exists, nor is it likely to in the near future. The situation with respect to surge is somewhat more positive. The methods of Greitzer (9) and (10) and Moore and Greitzer (11), while dependent upon an empirical factor representative of the entire compression system, have given credible results for isolated compressors. It remains to be seen whether this model can be adapted to a compressor operating as part of a gas turbine engine.

Given the difficulties of modelling rotating stall analytically, it is not surprising that the principal research efforts to understand the phenomenon have been experimental. Perusal of Ref. 1 gives some idea of the extent of the effort that has been expended. Unfortunately, despite the vast amount of data that have been collected, it is very difficult to draw general conclusions. Each compressor test setup displays different rotating stall characteristics, which leads us to conclude that the exact nature of the stalls is dependent on many geometric and operating variables. The number of cells, their rotative speed, their radial and axial location in the annulus, the degree to which the annulus is blocked, and the nature of

[1]For 1994-95, Dept. of Aerospace & Mechanical Engineering, Australian Defence Force Academy, Canberra ACT 2600

Paper presented at the AGARD PEP 85th Symposium on "Loss Mechanisms and Unsteady Flows in Turbomachines", held in Derby, United Kingdom, 8-12 May 1995, and published in CP-571.

the onset of the stall are all important parameters in describing the stall, but all defy prediction, and may vary widely even for a particular compressor, depending upon its operating conditions.

In spite of these difficulties, Pampreen (1) has drawn several conclusions from the large amount of experimental data available: (i) In many machines, as the mass flow rate is reduced for a particular rotor speed, the stall cells occupy only a part blade span. Further reduction in mass flow rate lowers the number of stall cells, but each extends over the full blade span. (ii) While there are many exceptions, the general trend of the data indicate that the cell pattern rotates at roughly 50 per cent of the rotor speed.

While these conclusions are useful, they are unfortunately based on data from lab compressors having only one or a few stages. The same can be said for a large number of other interesting investigations, which have sought to shed light on stall inception, the nature of the flow through stall cells, the effects of inlet flow distortions, etc. Both stall and surge are reflections of instabilities in the operating regime of the compressor and as such are inextricably linked. However, as Greitzer has shown (10), surge is strongly dependent on the nature of the flow passages downstream of the compressor. It is therefore essential to test any conclusions drawn from lab-scale investigations on full scale multistage compressors operating in realistic environments. For understandable reasons, there is a paucity of such information. Investigations on large multistage compressors were undertaken by Huppert et al (12), and Lucas and Filippi (13) in the 1950s, and more recently by Gorell et al (14). None of these studies however was performed on an engine.

Huppert et al (15) and Calvert et al (16), explored flows in engine compressors but focused mainly on confirming the existence of rotating stall and its frequency of rotation. There have been intensive investigations performed by the major engine companies but generally the results are not, to the authors' knowledge, in the public domain.

Acquisition and operation of an engine facility is costly. Furthermore, the investigation is constrained by the operating line of the engine to unique speed/mass flow rate combinations. A normal compressor performance map is not obtainable. Nevertheless, the behaviour of the compressor *as installed* is of interest, and it was for this reason that the investigations described in this paper were carried out.

The aims of the work were therefore to establish, for a typical installed turbojet engine compressor, the following:

(1) the overall character (number, rotational speed, radial and axial extent) of rotating stall at selected rpm settings in the front stages

(2) the two-dimensional internal flow within the cells

(3) the changes in the nature of the stall resulting from distortion of the inlet flow

An ancillary, but important part of the overall program was to establish the sensitivity of the velocity measurements to changes in gas temperature through successive stages of the compressor. The details of various aspects of the program are described in more detail in Refs. 17 – 19.

3. EQUIPMENT AND PROCEDURE

3.1 Compressor

The RMC experiments were performed on an Orenda 10 gas turbine engine having a rated thrust of 27 kN. The engine had a fixed geometry ten stage compressor having a design overall pressure ratio of 5:1 at 7800 rpm. The hub/tip ratios of the first four stages were respectively 0.66, 0.71, 0.73, and 0.76. Corresponding mid-span rotor solidities were 0.78, 1.37, 1.59, and 1.52. The internal diameter of the stator casing at the first stage inlet was 80.8 cm reducing to 70.0 cm at the last stage. The compressor was 80.3 cm long from inlet to exit. Bleed air ducts at the third, sixth and eighth stage rotors removed a small percentage of the air flow for use outside the compressor. Unfortunately, a performance map for the compressor was not available.

As was noted above, the use of an engine-mounted compressor constrained the tests to operating conditions applicable along the running line for the engine, either steady-state or transient. As anticipated, stage mismatch at part speed operation led to stalling in the front stages. Furthermore, early results showed that part-speed steady-state results were virtually identical to those for transient operation and therefore only steady-state data were acquired.

3.2 Instrumentation

The characteristics of the flow were measured using Dantec 55R52 crossed-film probes; these consisted of a quartz-coated nickel film mounted on a quartz substrate and had a frequency response of 175 kHz. Five access holes were drilled in the compressor casing to permit insertion of the sensors. Two holes were located between the first stage rotor and stator and were tangentially displaced by 77 deg. Single holes were located between the rotor and the stator of the second, third and fourth stages. When in use, each probe was mounted on an external support bracket designed to permit rotation of the probe about its own axis and also radial positioning of the sensors between the compressor hub and casing. The probe signals were fed to appropriate Dantec signal conditioning equipment, which for all flow measurements was operated in the constant-temperature anemometer

(CTA) mode. Constant-current mode was used only during the temperature calibration studies described below. Since the highest cell passing frequency anticipated in the tests was approximately 250 Hz, low pass filters operating in the range 500–1000 Hz were incorporated in the circuitry.

4. EXPERIMENTAL RESULTS

4.1 Stall Cell Configuration

The presence, number, rotational speed, and radial and axial extent of the rotating stall cells were of primary interest in these investigations. In the initial phases of this work (Ref. 17), analog signals recorded simultaneously at the two tangentially displaced probe positions behind the first rotor were digitized, and then analyzed for cell passing frequency using Fourier analysis. Knowing the time delay between passage of a cell from one probe to the next, the number and speed of the cell pattern could be inferred. Cross-correlation between the two probe signals also gave a clear picture of the nature of the cell pattern; in every case the two techniques gave results that were entirely consistent. In the subsequent studies (Ref. 18 and 19), direct a-to-d conversion was utilized, and autocorrelation methods were employed to permit additional consistency in the inferences drawn. Typical FFT results are shown in Ref. 18. An alternative representation, which displays significant frequencies more clearly than a simple FFT, is the spectral power density. Borys (19) utilised this quantity to characterize his data; a typical example is shown in Fig. 1.

Fig. 2 (taken from Ref. 18) shows a representative autocorrelation plot. Examination of Fig. 2 shows that two similar peaks (A and B) are separated by five cycles and that the time between them is 25 ms. This signal is appropriate for a five-cell pattern rotating at 40 Hz, which for this particular experiment was 51 percent of the rotor rotational frequency.

The data gathered with respect to stall cell configuration as reported in Refs. 17–19 were acquired over several years with a variety of instrumentation packages. To ensure consistency of techniques and interpretation, there was considerable overlap in operating conditions, probe location, etc. between successive experimenters, but the stall characteristics proved to be remarkably reproducible.

The results of all three investigations are summarized in Table 1. The notations "Up" and "Down" in the table refer to the two different tangential locations of the probes that were used in the first stage; percent rpm refers to the percentage of full design speed of 7800 rpm

It is evident from the table that full-span stall occurred in the first stage only and that the extent of the blockage due to the cells increased from hub to tip. In the third and fourth stages, stall was confined to the tip region only, with roughly the same blockage at each stage. At 70% rpm

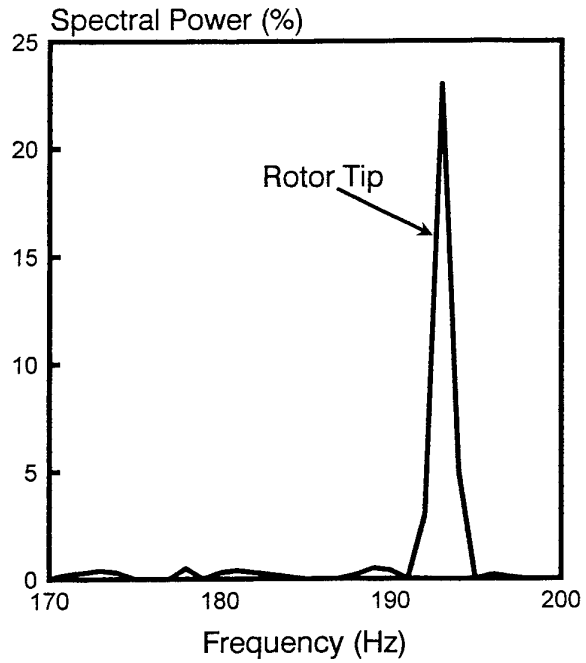

Fig. 1 Typical spectral power density as percent of total for rotating stall - 1st stage (Ref. 19)

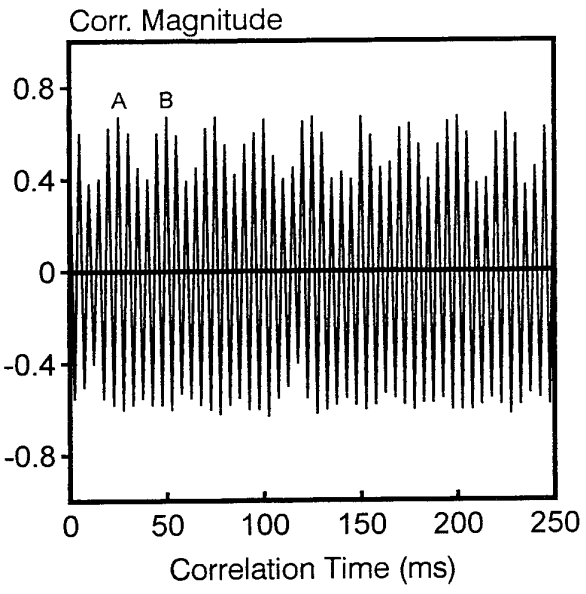

Fig. 2 Typical autocorrelation plot for rotating stall (Ref. 18)

Rotor Speed		STAGE 1		STAGE 2	STAGE 3	STAGE 4
		Up	Down			
40 %	Hub	5	5	-	-	-
	Mean	5 (9)	5	5 (9)	-	-
	Tip	5 (14)	5	5 (18)	5 (17)	5 (16)
50 %	Hub	5	5	-	-	-
	Mean	5 (10)	5	5 (9)	-	-
	Tip	5 (14)	5	5 (18)	5 (17)	5 (16)
60 %	Hub	4	4	-	-	-
	Mean	4 (8)	4	4 (11)	-	-
	Tip	4 (14)	4	4 (18)	4 (18)	4 (20)

Table 1 Number of rotating stall cells and location. Parenthesized numbers indicate circumferential extent of the cells expressed as a percent. All cell patterns rotated at half the rotor speed. Based on data from Refs. 17-19

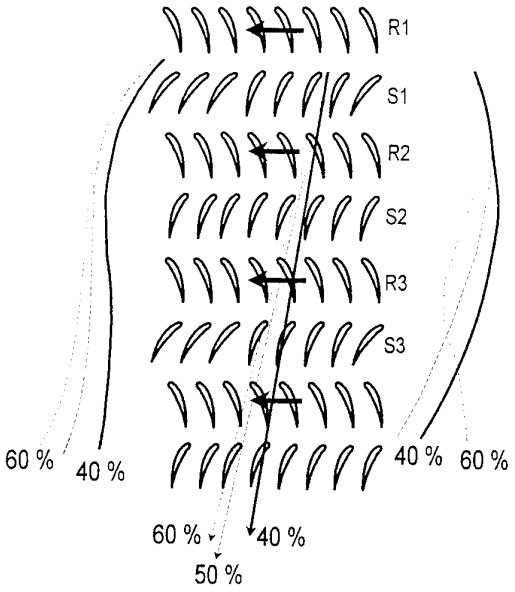

Fig. 3 Axial configuration of the stall cell through the first four stages at the tip, measured in the absolute reference frame (Ref. 17)

there was some evidence of rotating stall, but it was not sufficiently well-established to be conclusive.

The axial configuration of the rotating stall pattern, as shown in Fig. 3 was obtained by simultaneously recording data at more than one axial probe position. The overall pattern indicates the establishment of stall in the first two stages (thus the increased width in the second stage) and a slight decrease in stall extent in the third and fourth stages. The overall axial nature of the cell pattern as it passes through the machine is consistent with the observations reported by Day and Cumptsy (20).

It was reported in Ref. 18 that under some circumstances, a low frequency phenomenon exhibiting some of the characteristics of surge was observed. Borys (19) conducted an exhaustive experimental examination of this phenomenon, using cross-correlations of signals from multiple probes arranged both tangentially and axially in the compressor, but was unable to find any corroborating data. The conclusion therefore is that the low frequency phenomenon, while perhaps present locally within the compressor, was not surge.

4.2 Flow Within the Cells

The nature of the flow (ie. speed and direction) within the

stall cells is of interest and has been investigated by a number of authors (Refs. 20-22 for example). The general conclusion is that the flow is highly three-dimensional, with spanwise flows within the blade rows (typically outward in rotors and inward in stators) resulting from centrifugal effects and the necessity for adjustment to requirements of continuity. The flow in the z–θ plane has been a matter of some conjecture, although most experimenters have found clear evidence of strong reverse flows within the cells. There is less agreement as to whether unstalled flow passes tangentially through the stall cells in the gaps between rotor and stator rows.

In the course of the present investigations (Ref. 17), crossed hot film anemometer measurements were made between blade rows and the results suitably averaged to provide a picture of the flow in the z–θ plane. The results are shown in Figs. 4–6.

Comparison of Figs. 4 and 5 reveals that the intensity of the stall decreases sharply from the tip to mid-span. Furthermore, Fig. 6 clearly illustrates the decreasing strength of the stall with progression through the third and fourth stages of the compressor. The presence of reverse axial flow is evident for the strong stall appearing in Fig. 4. At the cell boundaries in all instances, the flow appears to cross in the direction of rotor rotation. In the regions of weak stall, the flow inside the cell generally deflects in the direction of rotor rotation or shows little change of direction. These observations are consistent with those of other studies, and lead us to conclude that the details of the stall cell flow in lab compressors are similar to those for full-scale machines.

4.3 Effects of Inlet Flow Distortions

Given the asymmetric nature of rotating stall, it is not surprising that stalls can be initiated in a susceptible compressor by spatial distortions of the flow at the inlet. These may be distortions of pressure, temperature, or flow speed, and may be circumferential, radial, or a combination of the two. Temporally varying distortions may also be present. However, circumferential total pressure distortions have received the greatest attention, because these are the easiest to simulate in the lab, and because they are representative of many in-service situations. References 23–26 typify the analytical and experimental effort this aspect of rotating stall has attracted.

The initial RMC work in this area is described in Ref. 18. Circumferential total pressure distortions were generated

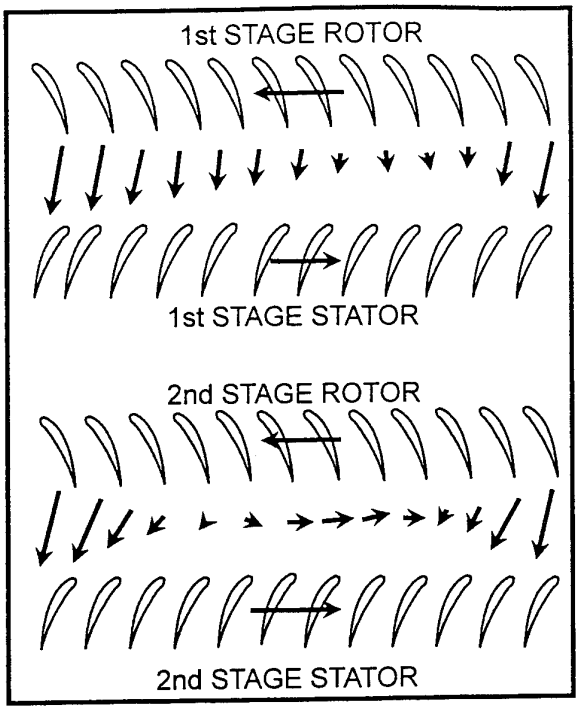

Fig. 4 Stall cell velocity vectors behind first and second stage rotor tip at 40% rpm measured in reference frame of the cell (Ref. 17)

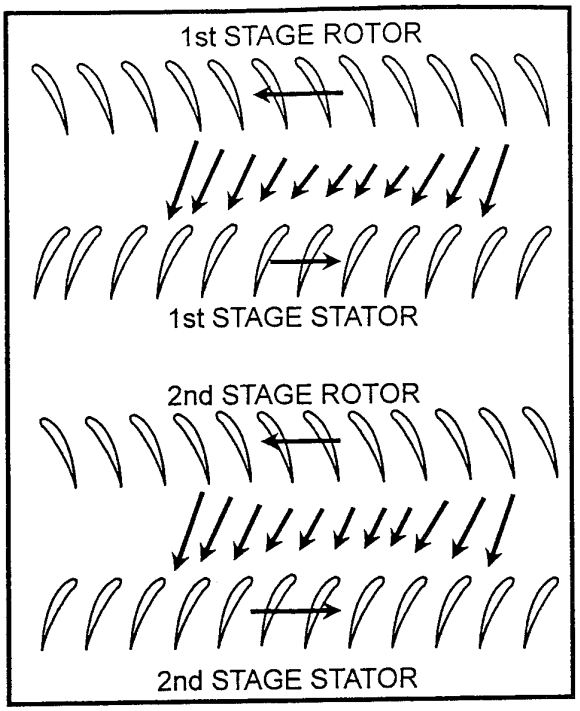

Fig. 5 Stall cell velocity vectors behind first and second stage rotor mid-span at 40 % rpm measured in reference frame of the cell (Ref. 17)

by means of screens mounted at the compressor inlet. These screens were manufactured from metallic plate and were either solid or were perforated with 3 mm diameter holes uniformly placed to provide a 51 per cent open area. Each screen covered a 30 degree sector of the inlet annulus and various combinations of the screens were installed to yield a total of seven different configurations as illustrated in Fig. 7. (Note that Configuration 1 is the undistorted flow case.) The nature of the stall pattern and its rotational speed were ascertained using hot film probes as described earlier.

In some cases during the early studies, anomalous results were found. For example, for four of the inlet distortion configurations (nos. 3, 4, 5, and 8) under some running conditions, the number of stall cells was found to differ radially ie. from hub to tip. Also, in several instances, a low frequency phenomenon was detected which suggested the presence of surge, although the evidence was inconclusive. In an effort to resolve these issues, Borys (19) repeated many of the experiments using significantly refined instrumentation and data reduction techniques. These results are presented in the following sections.

4.3.1 Radial discrepancy in number of cells

With regard to the unlikelihood of the number of stall cells being simultaneously different at two different radial positions, two explanations were considered. Firstly, the earlier data reported in Ref. 18 were acquired over an extended period of time. In particular, for practical reasons, data were taken at each radial position for a number of rotor speeds, and then the probe was moved to a new radial position. This procedure masked the possibility that the number of cells was the same spatially for any particular speed, but changed with time. The second possibility was that there was a hysteresis associated with the development of the cells, depending upon whether the engine was accelerating to the nominal speed or decelerating to it.

The time-dependence issue was addressed by acquiring data simultaneously with two probes, one at each of the two tangential positions behind the first rotor, and each being at a different radial location. Extreme care was used to ensure that the nominal speed (eg. 50 % rpm) was approached deliberately either from a lower or a higher speed, so that any hysteresis could be detected. These tests were run for all inlet distortion configurations which had given anomalous results (nos. 3,4,5, and 8) as well as the clean inlet arrangement.

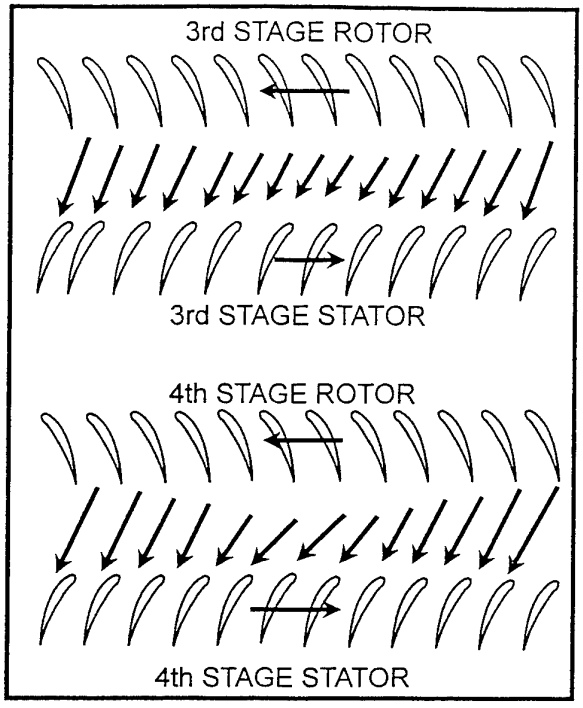

Fig. 6 Stall cell velocity vectors behind third and fourth stage rotor tip at 40 % rpm measured in reference frame of the cell (Ref. 17)

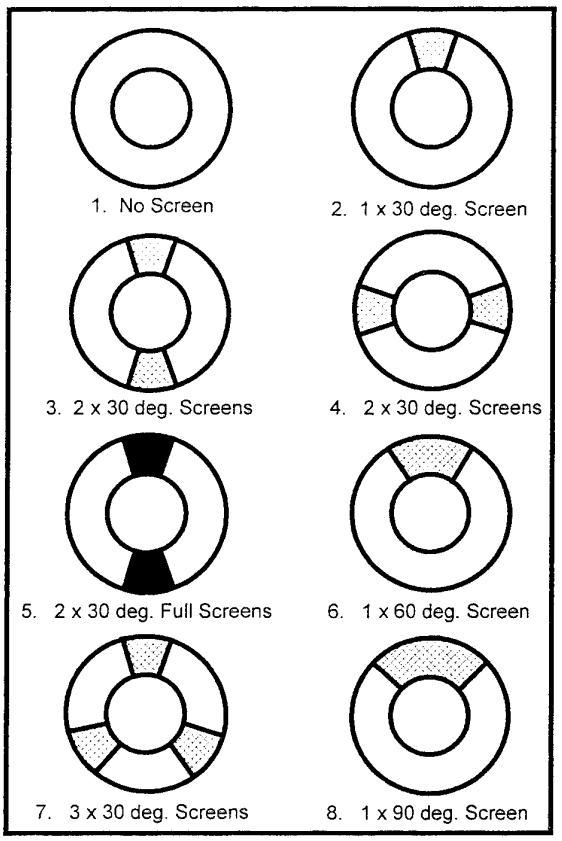

Fig. 7 Inlet distortion screen configurations

Rotor Speed		DISTORTION CONFIGURATION NUMBER							
		1**	2	3**	4	5**	6	7	8**
	Hub	5	5	5	5	5	5	5	5
40 %	Mean	5	5	5	5	5	5	5	5
	Tip	5	5	5	5	5*	5	5	5
	Hub	5	5	5	5	5	5	5	5
50 %	Mean	5	5	5	5	5	5	5	5
	Tip	5	5	5	5	5*	5	5	5
	Hub	4	4	4	4	5	5	5	4
60 %	Mean	4	4	4	4	5	5	5	4*
	Tip	4	4	4	4	5	5	5	4*
	Hub	-	-	-	-	-	-	-	-
70 %	Mean	-	-	-	-	-	-	-	-
	Tip	2	-	2	2	2	-	-	-

* Multiple cell patterns evident; only predominant shown
** From Ref. 19; remainder from Ref. 18

Table 2 Effect of inlet flow distortion on rotating stall cell pattern behind the first rotor. All cell patterns rotated at half rotor speed. Configurations are as identified in Fig. 7.

The results of the 144 data runs can be summarized as follows:

3 runs (2%)	no rotating stall
19 runs (13%)	rotating stall indicated by one probe only
122 runs (85%)	both probes yielded the same result

Of the 22 runs in which only one or neither probe detected stall, 17 were at 70 % rpm, an indication that at this relatively high speed, the strength of the stall was becoming insignificant.

In 28 of the 122 runs in which both probes yielded the same result, two or more distinct stall cell passing frequencies were present. However, careful examination of the raw data revealed that the number of stall cells was fluctuating with time. For example, for inlet flow distortion configuration 5, with the compressor decelerated to 50 % rpm, and with both probes at the tip, the predominant pattern consisted of five cells. Nevertheless, there was evidence that for short periods of time there were four or six cells present as well. The inference from this result is that the stall cell pattern was time-dependent under some circumstances, although the data showed clearly that there was a predominating pattern present in every case.

In none of the runs was there conclusive evidence of a hysteresis effect in development of the stall cell pattern. In other words, the general patterns observed under any particular operating condition were similar, irrespective of whether the engine was accelerated or decelerated to the rotor speed in question.

4.3.2 Low frequency phenomenon

In order to resolve the low frequency phenomenon

question, probes were placed behind the first and fourth stage rotors and signals acquired simultaneously from both probes. The tests were run at the same operating conditions and with the same flow distortion screens as were used in the experiments described in Ref. 18. It was anticipated that if the low frequency phenomenon was indeed surge, then both probes would register signals in the three to ten Hz range with a short time lag between the signals. However analysis of the signals revealed that a low frequency signal at one probe was never accompanied by a similar signal at the other. Further, a cross-correlation of the signals showed no discernible trend.

Additionally, cross-correlations of data obtained from two probes located at the same axial position yielded little evidence that an axisymmetric disturbance was present.

It was noted above that in some circumstances, the nature of the cell pattern was time-dependent. Unfortunately it was not possible to ascertain the frequency of the pattern fluctuations, or indeed if they occurred at regular intervals. It was observed however that for all the data reported on Ref. 18, in only one instance did the low frequency phenomenon coincide with radially-inconsistent stall cell numbers. Our conclusion is therefore that the low frequency phenomenon is not related to the fluctuating cell pattern described above.

4.3.3 Discussion

The final results of the investigation of stall cell patterns in the presence of inlet flow distortions, an amalgamation of the data presented in Refs. 18 and 19, are shown in Table 2. It is evident from the Table that the inlet flow distortions used had relatively little effect on the presence or nature of the rotating stall. It must be assumed that the distortion screens reduced the compressor stall margin, but once stall had occurred, the screens had no significant effect in comparison with the cell pattern in the undistorted inlet flow.

4.4 Temperature Corrections

An issue which clouds any anemometric investigation is the effect of fluid temperature on the signal obtained. While uncorrected velocity signals were acceptable for determining the qualitative aspects of stall cell behaviour, one of the objects of this experimental program (Section 4.2) was to obtain moderately reliable estimates of the flow speeds and angles within the stall cells. Since the estimated temperature increase per stage was roughly 15 K, the effect of temperature increases within the compressor on the output of a constant temperature (ie. velocity-measuring) anemometer was considered important enough to merit special attention.

4.4.1 Preliminary measurements

To ascertain the nature of the problem, a set of preliminary measurements was made behind the first rotor at five nominal rotor speeds at the hub and mid-span positions. Two crossed hot film probes were used, with the two probes tangentially displaced by 77 deg. The probes were operated in the constant-current anemometry (CCA) mode, and therefore the output from the associated bridges, which had been calibrated simultaneously, was a measure of the gas temperature.

Two significant results were obtained from this preliminary study: (1) It was found that both films on a probe gave very similar outputs, even though the flow behind the rotor was highly time-dependent. The conclusion was that since the films were oriented at 90 deg. to one another, temperature measurement by CCA probes is relatively independent of the flow direction. (2) While the standard deviations of the signals were small (typically 0.5 C), the temperatures measured by two tangentially displace probes differed on the average by approximately 3 C, and in some cases by as much as 7 C.

4.4.2 Laboratory investigations

As a result of the foregoing, a series of tests was conducted under controlled conditions in the lab using Dantec flow calibration equipment. The test confirmed that the probe output was indeed relatively independent of the flow direction for a particular speed. However a significant speed effect was observed. As the flow speed increased, the apparent temperature of the gas dropped. Typically, as

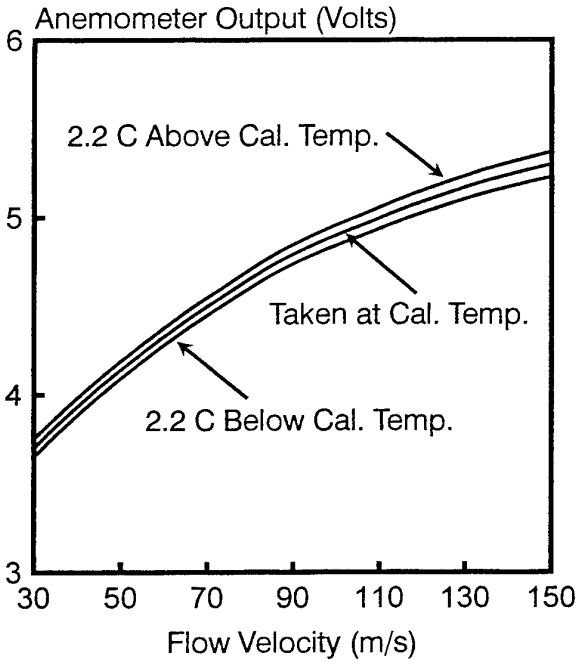

Fig. 8 Effect of temperature difference on measured flow speed for a constant temperature anemometer

the speed increased from 40 to 140 m/s, the measured temperature dropped from the nominal value by about 3 C. Introduction of a conventional recovery factor r, in the relationship

$$\frac{T_R}{T_O} = \frac{1 + r\frac{k-1}{2}M^2}{1 + \frac{k-1}{2}M^2}$$

where T_R and T_O are the measured and stagnation temperatures respectively, and M is the Mach Number of the flow, satisfactorily accounted for the velocity dependence of the temperature measurement. For the probes used in these tests, a value of 0.7 for r yielded good results.

Thermal stability of the bridges used in the anemometry equipment was also of some concern. However, on the basis of measurements made in still air, it was concluded that over the temperature range 20–40 C, the temperature could be reliably measured within ± 2.2 C provided the bridges were adjusted to a predetermined output corresponding to the ambient temperature at the beginning of a test.

Fig. 8 illustrates the effect of a temperature error of ± 2.2 C on the velocity calibration curve of the CTA setup used to measure flow velocities in the compressor. Not surprisingly, the error is speed dependent, being a maximum of ± 5 m/s at 140 m/s, or about ± 3 percent.

It is of interest to apply these results to those given in Section 4.2 above. The latter data were acquired under conditions when the gas temperatures could have been as much as 15 C higher than the calibration temperature. Using an analysis similar to that which led to Fig. 8, it is concluded that the speeds reported in Ref. 17 may be too high by as much as 20 percent. The qualitative results presented in Figs 4-6 should remain unaffected.

4.4.3 Final compressor tests

As a measure of the effectiveness of the laboratory investigations described above, a series of tests on the engine compressor was run to determine the consistency of the CCA temperature measurements. Each anemometer bridge was set to deliver the correct voltage in still air corresponding to the ambient temperature as determined by a thermocouple in the test cell. Care was also taken to ensure the bridges were maintained at roughly the same temperature in the cell as had prevailed in the lab during the earlier tests. Tests were run at all four engine speeds, with the two tangentially displaced probes located at each of the hub, mid-span, and tip positions. Data were passed through a 1000 Hz low pass filter and acquired at 500 Hz. For the 18 tests run, the average difference between the two probe temperatures was 1.3 C. This was within the 99 percent confidence limit for all but four of the samples. This result, in combination with Fig. 8 leads us to the conclusion that this technique for measuring temperatures in the compressor gas path has acceptable accuracy.

As a final check on the reliability of the CCA temperature data, signals from the two tangentially displaced probes were cross-correlated, and the resulting time lags compared with those expected for the appropriate stall cell pattern rotating at half rotor speed. The agreement was good and might reasonably be expected to be better had a higher sampling rate been used to acquire the temperature data.

5. CONCLUSIONS

The conclusions to be drawn from this work can be summarized as follows:

1. In general, the nature of rotating stall found in these investigations is consistent with that observed by other investigators on laboratory compressors. Reviews of the literature however indicate quite clearly that stall is highly compressor–specific. It is risky to attempt to draw generalized conclusions about such features as number of cells or radial and axial extent from a set of experiments on a particular compressor, be it in the lab or installed in an engine. Even cell rotative speed, which was consistently 50 percent of the rotor speed in these investigations (and therefore also 50 percent of the speed of the stators relative to the cell pattern) is not universally observed.

2. While fundamentally instability–related, rotating stall has proven to be a highly reproducible phenomenon. The experiments were performed over several years, and yet there was little observable change in the stall characteristics. Hysteresis was not a factor in the development of the cell patterns.

3. Stall tended to be strongest and most evident at the tip, weakest at the hub. Also, as anticipated, the strength of the stall decreased at successive stages through the compressor.

4. Axial flow reversal was observed at the second stage tip location, consistent with that found by several other experimenters. A reversal of tangential flow direction, when observed in the cell reference frame, indicated the presence of a circulatory flow with radial components within the stall cell.

5. The overall axial configuration from stage to stage through the compressor showed only slight inclination from the axial direction; this is consistent with the straight through model observed by others.

6. At the lower speeds (40 % and 50 % rpm) the presence of distortion screens at the inlet had little apparent effect on the stall pattern. At the higher speeds there was a tendency toward more cells as the angular extent and blockage of the distortion increased.

7. The presence of the distortion did not affect the rotational speed of the cell pattern.

8. Careful reruns of the distorted-inlet experiments revealed the occasional presence of a low frequency phenomenon, as observed in earlier work. Because of the localized nature of the signals we conclude they are not indicative of surge.

9. There was very clear evidence that, while the rotational speed of the cell pattern remained constant for a particular run, the number of cells was time-dependent, particularly with inlet flow distortion present.

10. The measurement of gas temperature is important for the proper interpretation of constant-temperature anemometer outputs. In a compressor, this is of some relevance, since in a typical machine, the stage temperature rise is in the order of 15 C. Errors in measured gas temperature of the order of 2 C can give gas speed errors of approximately 3 percent.

11. Temperature measurements using constant-current anemometers are not sensitive to probe orientation with respect to the flow, but for reliable measurements it is important to ensure that the bridges are set to deliver the correct voltage corresponding to the still air temperature at the outset of the run.

In summary, rotating stall and surge are the ultimate vestiges of losses in compressors. Thanks to the work of many investigators surge has yielded some of its secrets, but rotating stall, as a reproducible instability, remains a paradox . Even the most fundamental processes involved are not well understood, in spite of intense experimental and analytical efforts. Attempts to mitigate its effects during operation are likely to be beneficial, but changes in gas path design methods to alleviate its consequences await much greater in-depth understanding of its causes and associated flows.

6. ACKNOWLEDGEMENTS

The authors wish to acknowledge the invaluable assistance of the members of the technical staff of the RMC Department of Mechanical Engineering for their assistance in the conduct of this investigation. The work was supported by the Department of National Defence through the Academic Research Program and a number of research contracts.

7. REFERENCES

1. Pampreen, R.C., "Compressor Surge and Stall", Concepts ETI, Inc. Norwich, VT, 1993

2. Emmons, H.W., Pearson, C.E., and Grant, H.P., "Compressor Surge and Stall Propagation", Transactions of the ASME, Vol. 77, No. 4, May 1955, pp 455-467.

3. Stenning, A.H., and Kriebel, A., "Stall Propagation in Axial Compressors", Transactions of the ASME, Vol. 80, May 1958, pp. 777-790.

4. Cumpsty, N.A., and Greitzer, E.M., "A Simple Model for Compressor Stall Cell Propagation", Transactions of the ASME - Journal of Engineering for Power, Vol. 104, January 1982, pp. 170-176.

5. Moore, F.K., "A Theory of Rotating Stall of Multistage Axial Compressors: Part I - Small Disturbances", Transactions of the ASME - Journal of Engineering for Gas Turbines and Power, Vol. 106, No. 2, April 1984, pp. 313-320.

6. Moore, F.K., "A Theory of Rotating Stall of Multistage Axial Compressors: Part II - Finite Disturbances", Transactions of the ASME - Journal of Engineering for Gas Turbines and Power, Vol. 106, No. 2, April 1984, pp. 321-326.

7. Takata, H., and Nagano, S., "Nonlinear Analysis of Rotating Stall", Transactions of the ASME - Journal of Engineering for Power, October, 1972, pp.279-293.

8. McDougall, N.M., Cumpsty, N.A., and Hynes, T.P., Stall Inception in Axial Compressors, ASME Paper 89-GT-63, Presented at Gas Turbine and Aeroengine Congress, Toronto, 1989.

9. Greitzer, E.M., "Surge and Rotating Stall in Axial flow Compressors, Part I: Theoretical

Compression System Model", Transactions of the ASME - Journal of Engineering for Power, Vol. 98, April 1976, pp. 190-198.

10. Greitzer, E.M., "Surge and Rotating Stall in Axial flow Compressors, Part II: Experimental Results and Comparisons with Theory", Transactions of the ASME - Journal of Engineering for Power, Vol. 98, April 1976, pp. 199-217.

11. Moore, F.K., and Greitzer, E.M., "A Theory of Post-Stall Transients in Multistage Axial Compression Systems", NASA CR 3878, March 1985.

12. Huppert, M.C., Costilow, E.L., and Budinger, R.E., "Investigation of a 10-Stage Subsonic Axial-Flow Research Compressor. III - Investigation of Rotating Stall, Blade Vibration and Surge at Low and Intermediate Speeds", NACA RM E53C19, 1953.

13. Lucas, J.G., and Filippi, R.E., "Multiple Over-all Performance and Rotating Stall Characteristics of a 15-Stage Experimental Axial-Flow Compressor at an INtermediate Speed", NACA RM E54C29, 1954.

14. Gorell, S., Copenhaver, W., and O'Brien, W., "Stall Cell Blockage in a High-Speed Multistage Axial-Flow Compressor", AIAA 90-1913, Presented at AIAA/SAE/ASME/ASEE 26th Joint Propulsion Conference, Orlando, 1990.

15. Huppert, M.C., Calvert, H.F., and Meyer, A.J., "Experimental Investigation of Rotating Stall and Blade Vibration in the Axial Flow Compressor of a Turbojet Engine", NACA RM E54A08, 1954.

16. Calvert, H.F., Braithwaite, W.M., and Madeiros, A.A., "Rotating-Stall and Rotor Blade Vibration Survey of a 13-Stage Axial-Flow Compressor in a Turbojet Engine", NACA RM E54J18.

17. Best, R.C., LaFlamme, J.G.C., and Moffatt, W.C., "Flow Measurements in Rotating Stall in a Gas Turbine Engine Compressor", ASME Paper No. 88-GT-219, Presented at Gas Turbine and Aeroengine Congress, Amsterdam, 1988.

18. Fortin, J. and Moffatt, W.C., "Inlet Flow Distortion Effets on Rotating Stall", ASME Paper No. 90-GT-215, Presented at Gas Turbine and Aeroengine Congress, Brussels, 1990.

19. Borys, W.J., "An Experimental Investigation of Axial Compressor Instabilities", MEng. Thesis, Department of Mechanical Engineering, Royal Military College of Canada, Kingston, May, 1994.

20. Day, I.J. and Cumpsty, N.A., "The Measurement and Interpretation of Flow Within Rotating Stall Cells in Axial Compressors", Journal of Mechanical Engineering Science, Vol. 20, No. 2, April, 1978.

21. Mathioudakis, K. and Breugelmans, F.A.E., "Three-Dimensional Flow in Deep Rotating Stall Cells of an Axial Compressor", Journal of Propulsion, Vol. 4, No.3, May-June, 1988.

22. Gamache, R.N. and Greitzer, E.M., "Reverse Flow in Multistage Axial Compressors", Journal of Propulsion, Vol. 6, No. 4, July-August, 1990.

23. Cossar, B.F.J., Peacock, R.E., and Moffatt, W.C., "Compressor Rotating Stall in Uniform and Nonuniform Flow", Transactions of the ASME – Journal of Engineering for Power, Vol. 102, 1980, pp. 762-769.

24. Stenning, A.H.," Inlet Distortion Effects in Axial Compressors", Transactions of the ASME – Journal of Fluids Engineering, Vol. 102, 1980, pp. 7-13.

25. Chen, F., Li, W., Wang, Z., and Cong, M., "An Experimental Investigation of a Turbojet Engine to Inlet Distortion", ASME Paper No. 85-GT-12, 1985.

26. Hynes, T.P. and Greitzer, E.M., "A Method for Assessing Effects of Circumferential Flow Distortion on Compressor Stability", Transactions of the ASME – Journal of Turbomachinery, Vol. 109, July 1987, pp. 371-379.

Stall Inception and Surge in High-Speed Axial Flow Compressors

T. Breuer, S. Servaty
MTU München
Dachauer Str. 665
80995 München
Germany

Summary

The results of experimental and numerical studies to examine the inception process of rotating stall and surge are presented.

Unsteady pressure measurements have been carried out in a 3-stage high speed compressor to reveal characteristic features of instability onset. Tests have been conducted with clean intake as well as a circumferential inlet distortion. Analysis of the data shows that instability starts from small amplitude disturbances rotating in rotor direction, finally leading to either rotating stall or surge.

A numerical model is used to calculate the instability onset in a compression system comprising of ducts, blade rows and volumes. The model is based on the unsteady two-dimensional Euler-equations in conservation law form. The influence of blade rows is simulated by source terms to account for pressure loss and energy input. Some results of computations are compared to the experimental results.

Introduction

One of the major challenging tasks for the designer of an aero-engine compressor is the necessity to find a compromise between the requirement to design an "efficient" compressor (in terms of weight, thermal cycle efficiency, ...) whilst at the same time to assure, that the engine can be operated safely even under adverse conditions without reaching the aerodynamic stability limit of the compressor. The resulting safety margin between compressor operating line and stability limit always leads to a waste of available pressure ratio, thereby affecting the weight and hence operating costs.

Despite these far-reaching implications, it was only at the begin of the eighties, that the work of Greitzer and Epstein stimulated new research efforts for a better understanding of the flow physics leading to compressor flow instability. During subsequent work (Garnier et al. /1/) rotating waves which precede the instability onset were found. The detection of rotating waves directly led to ideas to suppress compressor flow instability by controlling the amplification of those waves. The concept of active stability control, based on these considerations, turned out to be successful in extending the useable operating range of a compressor and in suppressing rotating stall or surge.

The majority of the work concerning active control, however, is based on results derived from low-speed compressor tests. Little is known, whether active stability control concepts developed for low-speed compressors are applicable to highly loaded transonic compressors. Furthermore, all active control concepts rely on the early detection of some kind of a stall precursor (usually a rotating wave). The transfer of such concepts to compressors representative for aero-engine applications requires the knowledge, whether a stall precursor can be identified in a high-speed compressor as well.

The following paper describes the results of a test series conducted at MTU which specifically aimed at looking for any kind of stall precursor present in the flow. A modern transonic IPC is used for the tests. Analysis of the data with an innovative analysis technique gives a clear indication that rotating pressure waves are identifiable from the data.

Furthermore, a numerical model, which has been specifically designed to allow the calculation of the flow field of a compressor operating within the unstable flow regime, is used in an effort to model the observed flow behaviour. The results obtained show a very good agreement with respect to characteristic features as surge overpressure and rotating stall frequency.

Compressor set-up

The compressor used for the test series was a 3-stage IPC with controlled diffusion airfoils, having a design pressure ratio of 2.5. Stage loading is representative of highly loaded transonic compressors. A cross-section of the compressor is shown in fig. 1. The IGV serves to

Paper presented at the AGARD PEP 85th Symposium on "Loss Mechanisms and Unsteady Flows in Turbomachines", held in Derby, United Kingdom, 8-12 May 1995, and published in CP-571.

produce an inlet swirl representative of inlet flow conditions for the installed compressor.

The compressor has been installed at one of MTU's compressor test-beds. Air is fed into the compressor from a settling chamber with a volume of 80 m^3. The compressed air is blown into a plenum with a volume of 2.5 m^3 and finally discharged via 2 choked throttle valves.

In front of each rotor, 8 KULITE pressure transducers have been installed, the circumferential distribution of which is given in table 1, a graphical representation is shown in fig. 1. Due to design constraints it was not possible to install the stransducers equally spaced around circumference.

stage / sensor	1	2	3
1	0°	26°	24° 28'
2	45°	64°	61° 55'
3	90°	122° 30'	122° 24'
4	120°	153°	159° 50'
5	180°	212°	205° 55'
6	240°	242° 30'	243° 21'
7	288° 15'	273° 30'	295° 12'
8	315°	332°	332° 38'

Table 1: Loacation of pressure transducers

Instability investigation tests have been conducted with clean intake flow at speeds between 40% and 100% of design speed. Those tests have been followed by a second test series with distorted inlet flow. The inlet distortion has been produced by a perforated plate, generating a circumferential sector distortion with a distortion level of DC_{60} = 0.7, the circumferential extent being 150°. The spoiler is located approximately 0.75 times rotor outer diameter upstream of the first rotor. Tests have been performed at 60%, 80% and 100% of design speed.

Data acquisition

All data output from the transducers has been stored using an analogue magnetic tape recorder. Tape speed has been set such to yield a cut-off frequency of 20 kHz. For the subsequent analysis, data has been digitized with a sampling rate of 80 kHz and transferred to a digital mass-storage device, where it was available for further analysis.

In order to assure that data can be retrieved undistorted and without any time shift from the tape, a 1 kHz square-wave signal has been fed into the tape recorder prior to the tests. The subsequent replay and analysis revealed a maximum time shift error of only a few µsec., which is of sufficient accuracy for the intended purpose. Furthermore, it has been successfully demonstrated that the signal can be recovered from the tape without distortions.

Data analysis technique

It was evident from the beginning, that the retrieval of an instability precursor would require the extraction of a very weak signal within a noisy environment. Furthermore, it had to be taken into account that the signal of interest may be available only for a very short period of time. Therefore, it has been anticipated that none of the more traditional analysis techniques were suited to provide all the features deemed necessary. Finally, after thorough evaluation, an analysis technique described by Kay and Marble /1/ has been adopted. The procedure is a least-squares fit of the data to a sum of exponentials in the following form

$$f(t,\Theta) = \Sigma A_m * e^{j(\beta_m t - \Theta_m)}, \text{ with}$$

j = complex unity
m = summation index
A_m = unknown complex coefficient
β_m = unkown complex argument
Θ_m = circumferential position

"A_m" accounts for amplitude and phase of the unkown pattern, whereas "β_m" determines frequency and damping of the pattern. Obviously, determination of the unkowns via a least-squares algorithm leads to a system of nonlinear equations, which has to be solved, a drawback which can partially be circumvented by using "Prony's method" as described in /1/. Several tests with generic functions exhibited that this method is actually able to extract signals from a very noisy background, even when the test function contains additional unmodeled signal contents.

Test results

The tests have shown that for the given test-bed configuration of the compression system, rotating stall ocurred at 40%, whereas surge can be found for all higher speeds tested.

From the variety of data, selected cases will be presented, representing different stage matching conditions at instability inception as well as different inlet conditions (clean intake/with inlet distortion). All data presented in this paper are derived from low-pass filtered time traces with a filter frequency of 400 Hz.

-N/N_0 = 0.6, clean intake:

In this speed regime, insufficient density increase throughout the compressor due to low stage pressure ratios leads to compressor instability induced by front-stage stall. Fig. 2 shows the signal of the sensor array installed in front of the first stage. Sensor signals are arranged (in vertical order) from bottom to top in direction of rotor rotation. The vertical displacement is proportional to the circumferential spacing of the sensors as given in table 1. The uppermost and the lowermost tracks are identical, thus providing a complete picture along circumference. Time axis is scaled in terms of rotor revolutions. On the left hand side, pressure development is shown over a period of approx. 200 rotor revolutions prior to surge. On the right hand side, an enlarged section is presented in order to give more details of the stall inception process.

A first uniqe indication of an emerging disturbance can be found at trace "6" (counted from bottom to top), which grows quite rapidly while rotating in circumferential direction. During its development, the disturbance can be found to consist of 3 cells with different amplitudes. The disturbance manifests itself as a sharp "spike" in the time traces. It was Day /2/ who first pointed to two different types of disturbances which he observed during his tests. One type has been termed a short-scale disturbance, exhibiting only a spike in the time traces. The other type has been termed modal (or long-length scale) disturbance, showing an almost sinussoidal time-dependent behaviour. For the case presented in fig. 2, the disturbance can be identified as "short-scale". The time, the disturbance needs for one revolution equals to about 1.8 times a rotor revolution. The point of interest with respect to the quest for a stall precursor is that it takes only about one revolution from the first apearance of the disturbance until surge occurs, giving practically no early warning. The enlarged section does not provide additional clues concerning the existence of pre-stall waves, either.

The situation renders totally different, however, if the data is analysed using the technique described beforehand. Analysis revealed that a rotating wave with a frequency close to the frequency of the observed rotating disturbance (deduced from the time traces) can be identified long before surge occurs. The analysis has been performed using data from a time window of 20 rotor revolutions for the parameter estimate. The number of modes to be calculated has been set to m = 3. The window is then shifted in time along the time traces with a certain increment of time steps, and a new set of parameters is calculated for the new instant of time. The parameter estimates as a function of time are displayed in fig. 3, providing a formal representation of the wave, represented by the parameter estimates of amplitude, (unwrapped) phase and frequency vs. time (time axis is scaled in terms of rotor revolution). The damping coefficient is close to zero over the whole period of time, it does not provide additional information and its presentation is therefore omitted. Phase unwrapping has been accomplished as follows: starting with the calculated phase at time t_0, the phase at time $t=t_0+\Delta t$ (Δt representing the increment in time from one calculation to the next) has been calculated by time integration of the frequency estimate. The result is compared to the phase determined independently by the parameter estimate for time $t=t_0+\Delta t$. If both figures do not deviate from each other by more than a preset value, phase unwrapping is assumed to be sensible and the phase angles at times t_0 and $t_0+\Delta t$ are connected by a line. Otherwise, a symbol is displayed in the phase angle plots.

Fig. 3 reveals that phase angles traces for all 3 sensor arrays line up along a line of almost constant slope, representing a constant frequency. The mean value of frequency derived from slope of phase angle vs. time agrees well with the frequency determined by the analysis procedure. Furthermore, comparison of phase angle derived from time integration of frequency with phase angles yielded by data analysis shows a good agreement as well. All in all, there is a strong indication of a rotating pressure wave to exist. The analysis also yielded that the 3rd harmonic of the calculated wave has the largest amplitude, also well corresponding to the observed behaviour.

The longest period of time, where a coherent phase unwrapping is possible, extends over some 50 rotor revolutions, corresponding to about 20 revolutions of the disturbance. Comparison of phase and amplitude traces highlights, that in cases where phase unwrapping is possible over longer periods of time the amplitude has a local maximum. The occurence of local maxima seems to indicate that compressor instability is not a sudden event but rather the result of a comparatively long process, where periods of amplification of small-scale disturbances are followed by periods of damping. During this

course of events, the temporal extent of damping periods shrinks, whereas periods of amplification grow. A sudden growth of amplitude of the wave, equivalent to a sudden "loss" of damping, finally leads to instability.

Fig. 4 shows a more illustrative comparison of measured and analysed pressure wave, providing a space-time representation of the measured pressure (lower part) as well as of the analysed wave (upper part). The figure shows the development of the circumferential pressure distribution in front of the first rotor, time axis is in the horizontal direction. The analysed wave has been reconstructed using the parameter estimates obtained. Please note, that both presentations have different scaling with respect to the function value in order to allow a meaningful graphical display. It can be seen that close to surge analysed *and* observed wave show the same behaviour with respect to frequency of the pre-stall wave (inclination of the wave with respect to the time axis) and phase. The presentation also de-monstrates that the pre-stall wave develops without discontinuities into the flow instability, also supporting the statement previously made that the analysed wave is of physical relevance.

It is recalled that tests have been conducted at a compressor test facility with a large plenum behind the compressor, leading to a "slow" response of of the compressor operating point to throttle area changes. Hence the compressor approaches the stability limit very slowly, leaving "plenty of time" for the instability to develop. It remains to de determined, whether such a long early warning time will be available in an engine application.

- N/N_0 = 0.8, clean intake:

In this case, stage matching is such that all stages stall almost simultaneously. Fig. 5 again presents the time traces recorded in front of the first stage. Whereas at 60% speed, the instability started as a short-scale disturbance, in this case the instability emerges from a modal disturbance. According to Day /3/, this difference may be attributed to the special stage matching situation at this speed. Consequently, modal disturbances have only been observed at 80% and 90% of design speed, where this matching situation is present. They can be identified from the time traces as wave-like structures which precede surge.

Apart from that difference, the fundamental behaviour is quite similar to the case discussed before. The time traces presented in fig. 5 exhibit the emergence of a rotating wave only a few rotor revolutions before surge. However, analysis of the data in the same way as described before leads to similar results as at 60% speed, showing the existence of a rotating wave long before instabiliy, as can be inferred from fig. 6 and 7. Also in this case, a rotating wave is identified remarkably long before surge.

- N/N_0 = 1, clean intake:

At this speed, surge is induced by stalling of the last stage. Consequently, data obtained in front of the last rotor is presented in fig. 8 in the same way as before. Disturbance starts as a short-scale disturbance, further backing the assumption that stage matching influences the type of disturbance occuring. Fig. 9 and 10 provide the data obtained from the analysis. Also in this case, the rotating wave is present within the data.

- N/N_0 = 1, with inlet distortion:

The tests with inlet distortion have been performed in order to assess their influence on the stall inception process. It is acknowledged that a pure circumferential distortion is seldomly encountered in practice. Nevertheless, due to its simple shape, it allows an easy analysis of the data by dividing the compressor into a part with clean inlet conditions and a part with distorted inlet flow. The large circumferential extent of the distortion also allows a simplified approach by neglecting transient phenomena present at the interface between undistorted and distorted sector (parallel compressor model assumptions).

The speed of N/N_0 = 1 has been chosen to present an interesting phenomen which is directly related to the presence of a circumferential inlet distortion. Fig. 11 presents the time traces recorded in front of the first rotor in the usual format. It can be seen that prior to surge some of the time traces exhibit short-scale disturbances which propagate in circumferential direction. The amplitude of those disturbances varies from one trace to the next, in the way that from sensor 4 to sensor 8 the disturbance grows and then decays, until it has travelled around the circumference to the position of sensor 4, where the process starts again. Comparing the region of growth of the disturbance with the position of the spoiler, which is indicated by a bar in front of the time traces, it turns out that growth occurs within the second half of the distorted section of the inlet flow. The term "second half" relates to the direction in which the rotor passes through the distorted flow segment, i. e. from bottom to top in fig. 11. The process observed is caused by the fact that due to the increased loading of the compressor within the distorted sector (enforced by the reduced inlet pressure), the

compressor already operates partially unstable, allowing small disturbances to grow. In the undistorted sector, however, the compressor still operates stable and is therefore able to damp the disturbances. A similar behaviour has also been observed by Longley /4/ as well as Greitzer and Hynes /5/. The amplification observed in the second half of the distorted sector is attributed to the fact, that the flow field of the rotor entering the distorted sector does not adjust instantaneously to the altered inlet flow conditions, but with a lag, which is roughly proportional to the time, a particle needs to travel through the rotor passage from entry to exit. It is only after this time, that the rotor experiences the full level of increased loading which finally leads to flow separation. Consequently, the adaption of the rotor to the undistorted flow also takes some time, therefore leading to the extension of the growth region into the undistorted sector of the flow.

In this case, the rotating wave is easily observed some ten rotor revolutions before stall. This behaviour is observed most pronounced for the speed line presented here. Nevertheless, the analysis of the data allows to track the wave even for a longer period of time, similar to the cases without inlet distortion. Fig. 12 and 13 once again present the results from the data analysis. In contrast to the results with clean intake condition, the frequency estimate as well as phase unwrapping indicate, that the wave is not present for the complete time intervall depicted in the figures, although first indications can also be observed some hundred rotor revolutions before surge. These findings hold true also for the other cases with inlet distortion. In general, it can be stated that for the cases with inlet distortion the frequency estimate of the pre-stall wave exhibits a larger scatter than in the cases with clean intake, making the detection of the wave pattern more difficult.

- Conclusion concerning test data:

All data presented as well as data for the remaining speed lines give a strong indication that rotating waves exist in high-speed compressors a "long" time before compressor instability occurs. This result is in line with results derived from low-speed compressors, and hence gives rise to the assumption that active control concepts developed for low-speed machines are viable for high-speed compressors as well. The tests also revealed that in cases with inlet distortion, the determination of rotating waves is more complicated than with clean inlet flow. It is not clear at the moment, whether this is to be attributed to a poor modeling of the wave structure, whose damping is not only dependent on time, but also on circumferential position, or to the physics of the flow. Furthermore, it was not possible to determine the cause of the rotating waves. Obviously, it seems plausible to relate the existence of the wave to a circumferential variation of loss and/or deviation, due to a variation of incidence. This will also change the "throttling" behaviour of those blade passages affected and will lead to an upstream redistribution of the flow similar to the mechanism first described by Emmons et al. /6/, increasing the incidence at the "back" end of the increased-blockage area and decreasing the incidence at the "front" end. This pattern of increased blockage will then rotate around the annulus. However, it seems not reasonable to assume massive flow separation to cause the blockage within the passages affected. The amplitudes of the waves observed are too small to allow such an assumption. Furthermore, it seems unlikely that a massive flow separation as well as reattachment can be achieved within such a short period of time as given by the passing of a disturbance.

Numerical modeling of compressor instability

In parallel to the experimental examination of compressor flow instability, development of a numerical model to allow the calculation of unstable compressor operation has started. The model is based on the solution of the time-dependent two-dimensional conservation laws of mass, momentum in meridional and circumferential direction, and energy:

$$\frac{\delta \varrho A}{\delta t} + \frac{\delta \varrho c_m A}{\delta m} + \frac{1}{r}\frac{\delta r \varrho c_\phi A}{r \delta \phi} = RHS1$$

$$\frac{\delta \varrho c_m A}{\delta t} + \frac{\delta (\varrho c_m^2 A + pA)}{\delta m} + \frac{1}{r}\frac{\delta r \varrho c_m c_\phi A}{r \delta \phi} = RHS2$$

$$\frac{\delta \varrho c_\phi A}{\delta t} + \frac{\delta \varrho c_m c_\phi A}{\delta m} + \frac{1}{r}\frac{\delta r (\varrho c_\phi^2 A + pA)}{r \delta \phi} = RHS3$$

$$\frac{\delta \varrho e_t A}{\delta t} + \frac{\delta \varrho c_m h_t A}{\delta m} + \frac{1}{r}\frac{\delta r \varrho c_\phi h_t A}{r \delta \phi} = RHS4$$

The terms on the right-hand side of the equations account for bleed-air extraction (RHS1), pressure change, flow turning and radial shift of streamlines (RHS2 and RHS3) and energy input (RHS4) due to the presence of compressor blades. The system of equations is solved with a time-accurate explicit solution procedure, which is first-order accurate in time. Spatial discretization follows the flux-filter method proposed by Vinckier /7/. The treatment of the flow variables at the inlet and exit boundary is based on local characteristic variables to distinguish between incoming and outgoing waves, as described by Veuillot and Meauze /8/. No special effort concerning the discretization has been made to distin-

guish between bladed and unbladed elements of the duct. This is somewhat in contrast to other approaches known to the authors (for instance, Escuret et al. /9/), where the blade rows are modeled by staggered 1-D cells. Nevertheless, the results achieved so far clearly indiciate that this approach is sensible, in the way that the obtained results compare very well to experimental data.

Most of efforts spent until now for the development of the numerical procedure focused on the problem to correctly model the unsteady behaviour of the compressor blades for stable as well as unstable operation of the compressor. Unsteady behaviour is modelled "conventionally" by use of first-order lag functions for loss and deviation to account for transient processes. In order to allow a sensible representation of the compressor response even at unstable operation, an extension of loss and deviation characteristics of the blades is required. The procedure adopted is based on works of Sugiyama /10/ who proposed an extension of the steady-state stage characteristics by two second-order polynomials to describe operation at positive mass flow beyond the stability limit as well as operation at reverse mass flow, hence covering the whole mass flow regime of interest. Given the steady-state blade row characteristics, the steady-state stage characteristics are calculated first (or vice versa, depending on the data available). Stage characteristics are then extended into the regime of unstable compressor operation. Finally, blade row characteristics are deduced for the unstable flow regime, making sensible assumptions concerning the split of losses between rotor and stator (for instance: constant ratio of rotor loss/stator loss). It turned out that this kind of representation allows a very useful modeling of blade row behaviour throughout the whole mass flow range.

During code development data from a surge event of a 3-stage transonic fan as well as data of a single transonic fan stage operating with rotating stall have been used to validate the procedure. It turned out that the model very accurately predicts the surge overpressure as well as the unsteady temperature rise during surge in front of the 3-stage fan. In the case of the single stage fan, the rotating stall frequency is very well captured.

Within the scope of this paper, it is obviously of interest to compare measured and calculated results for the 3-stage IPC described before. Calculations have been performed for the 100%-speedline. One (hypthetical) test case consists of the compressor together with a small volume, leading to rotating stall as the preferred type of instability. The second calculation has been performed with a large volume, comparable to the volume as given by MTU's compressor test facility. The results provide the frequency of the stall pattern as well as overpressure induced by surge, which can be compared with the experimental data. In both cases, data will be checked for the presence of pre-stall waves, using the same analysis technique as employed for the experimental test data. For the calculations, the system has been excited by random fluctuations of the values prescribed at the boundaries. Inlet and exit boundary conditions are allowed to vary randomly at 0.5% of their predefined value. Throttling is accomplished quite conventionally by simulating closing the exit throttle of the system.

Fig. 14 shows the calculated circumferential pressure distributions as a function of time in front of the rotors for the rotating stall case. The period of time displayed roughly equals to 20 rotor revolutions. Pressure distributions show the formation of a single-cell rotating stall system, the frequency of which has been determined as 0.45 times shaft frequency. This frequency compares well to the measured value of 0.5 times shaft frequency, as can be deduced from fig. 9. However, the graphical presentation as well as an analysis of the data does not give any indication of a pre-stall wave present in the data. Nevertheless, the data presented in fig. 14 show quite clearly, that the rotating stall cell grows out of a very small disturbance within approximately one revolution of the cell. This behaviour is very similar to the one observed in the experimental data, indicating a correct modeling of the system once the stability limit has been reached.

A data presentation similar to the one given for rotating stall is presented in fig. 15 for the surge case. Also in this case, no indications concerning a pre-stall wave have been found. The figure shows quite clearly the behaviour of a compressor stalling at the back end. Pressure rises in front of the first and second stage and drops in front of the third stage. A closer examination of fig. 15 also reveals 2-dimensional structures in the pressure traces prior to surge. An enlarged section of the region of interest concerning this behaviour is given in fig. 16. showing that a rotating disturbance is present immediately prior to surge. The rotational speed of the disturbance has been deduced (also with some ambiguity due to its very short existence) to be approx. 40% to 45% of rotor speed, hence coming close to the frequency determined in the rotating stall case as well as the measured value.

Finally, a comparison of measured and predicted pressure during surge in front of the stages is presented in fig. 17. Given the complexity of the flow the agreement

between measurement and predicted data can be regarded as being good.

In general, the calculation procedure has demonstrated its ability to capture the fundamental features of compressor instability. The procedure is well suited to assist compressor design concerning its mechanical integrity, allowing the prediction of unsteady aerodynamic and thermal loads during compressor flow instability.

Concluding remarks

Analysis of experimental data derived from tests with 3-stage transonic compressor allows the identification of rotating waves preceeding compressor instability. For the compression system under investigation, the waves are found to exist a long time before the fully developed instability. The analysis technique developed for instability identification provides a useful starting point and may guide future development work concerning identification techniques for real-time applications in connection with an active stability control device.

The theoretical approach to model compressor flow instability proves its capability to predict the basic behaviour of the unsteady flow. It shows that flow instability quite rapidly grows out of a small-scale disturbance.

The results presented also highlight that the current modeling approach does not produce pre-stall waves as observed during the tests. This deficit is attributed by the authors to a lack of knowledge concerning the nature and cause of the pre-stall waves, making them inaccessible for modeling. Future experimental work especially dedicated to this open question will help to solve the problem. The theoretical model, improved with this regard, should then be able to serve as a numerical test bed for active stability control strategies.

Acknowledgements

The experimental research programme as described in this paper has been supported by the Commission of the European Union under contract AER2-CT92-0039. The development of the numerical model as described above has been supported by the German Bundesministerium für Forschung und Technologie (BMFT) under the AG TURBO Turbotech project.

References

/1/ Garnier, V.H., Epstein, A.H., Greitzer, E.M.
"Rotating Waves as a Stall Inception Indication in Axial Compressors", ASME 90-GT-156

/2/ Day, I.J.
"Stall Inception in Axial Flow Compressors", ASME 91-GT-86

/3/ Day, I.J.
Private communication

/4/ Longley, J.P.
"Measured and Predicted Effects of Inlet Distortion on Axial Compressors"
ASME 90-GT-214

/5/ Greitzer, E.M., Hynes, T.P.
"A Method for Assessing Effects of Inlet Distortion on Compressor Stability"
ASME Journal of Turbomachinery, 1987, Vol. 109

/6/ Emmons, H.W., Pearson, C.F., Grant, H.P.
"Compressor Surge and Stall Propagation"
Transactions of the ASME, Vol. 79, 1955

/7/ Vinckier, A.
"An Upwind Scheme using Flux Filters Applied to the Quasi 1-D Euler Equations"
Zeitschrift für Flugwissenschaften und Weltraumforschung, Vol. 15, 1991, pp 311-318

/8/ Veuillot, J.P., Meauze, G.
"A 3D-Euler Method for Internal Transonic Flows computation with a Multi-Domain Approach", AGARD-LS 140

/9/ Escuret, J.F., Garnier, V.
"Numerical Simulation of Surge and Rotating Stall in Multi-Stage Axial-Flow Compressors"
AIAA-94-3202, 1994

/10/ Sugiyama, Y.
"Surge Transient Simulation in Turbo-Jet Engine"
Ph. D. Thesis, 1984, Unniversity of Cincinnati, Department of Aerospace Engineering and Applied Mechanics

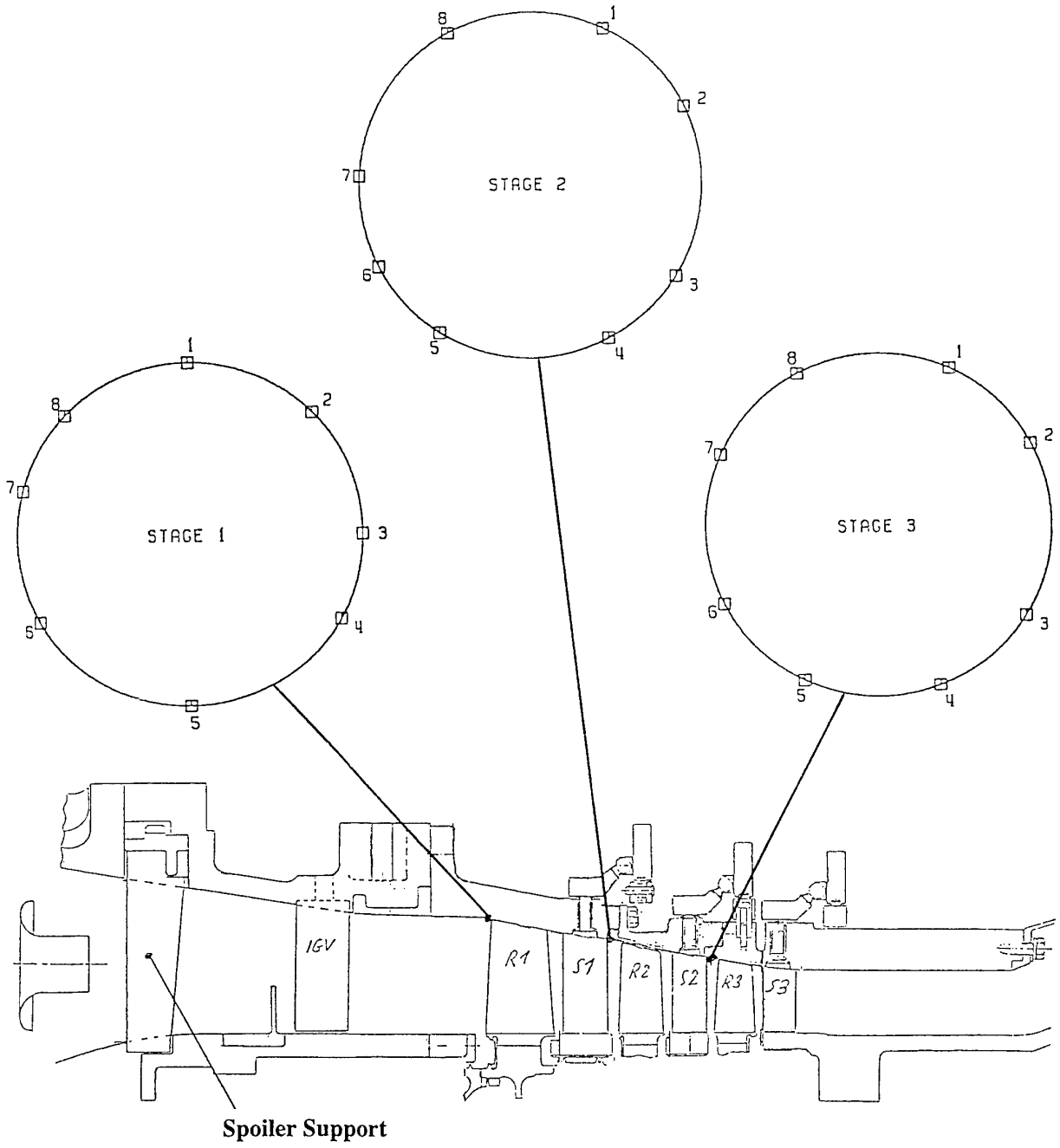

Fig. 1: Cross-section of compressor with location of pressure transducers

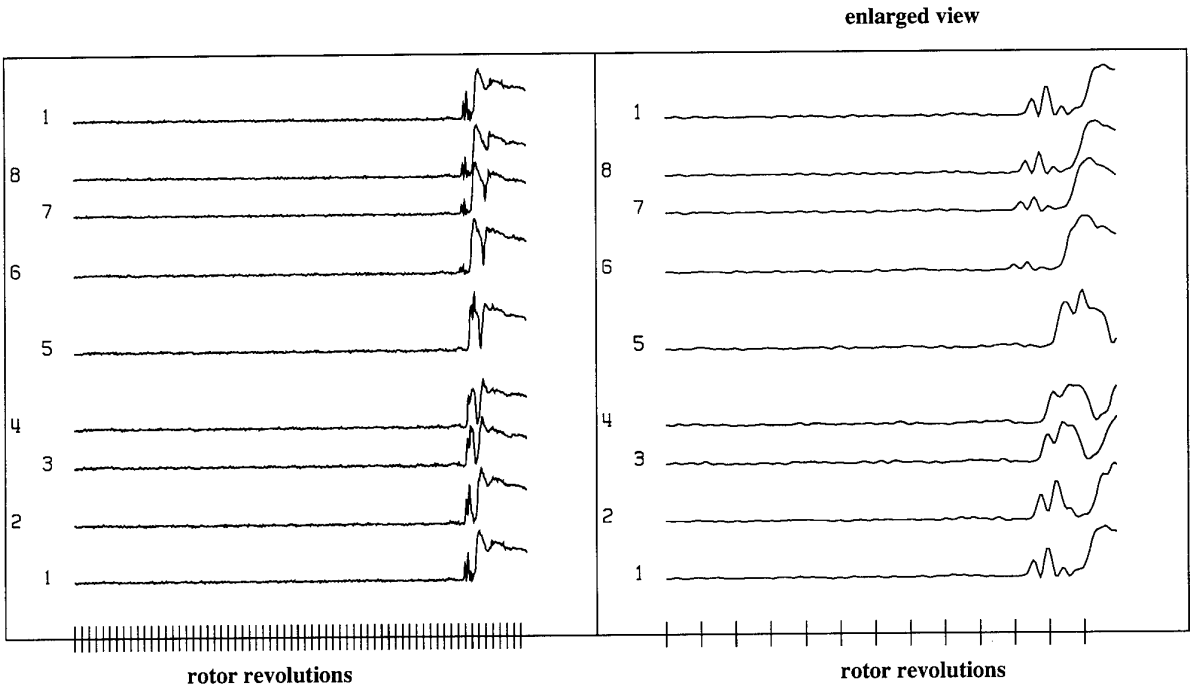

Fig. 2: $N/N_0 = 0.6$, pressure traces in front of 1st rotor

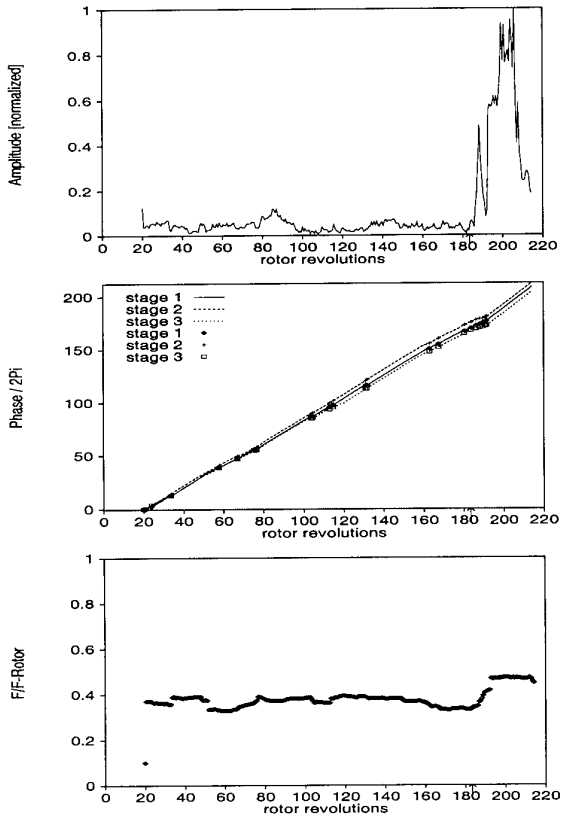

Fig. 3: $N/N_0 = 0.6$, estimate of wave parameter

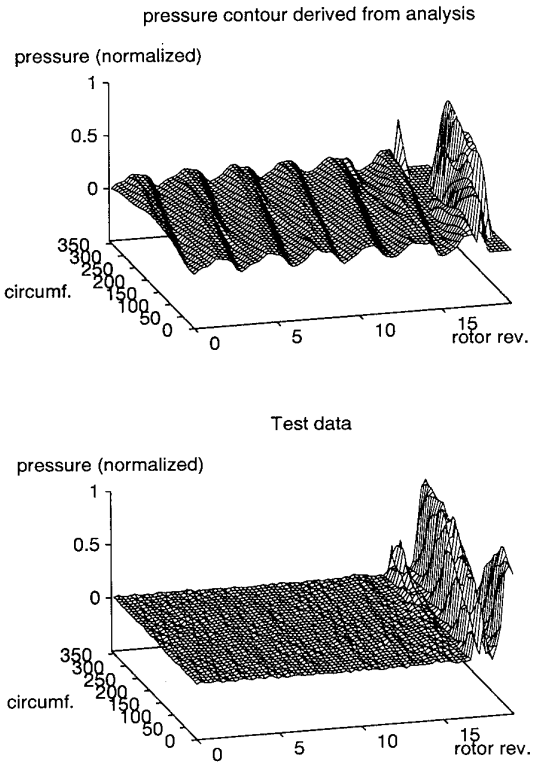

Fig. 4: $N/N_0 = 0.6$, measured (lower plot) and predicted distribution (upper plot)

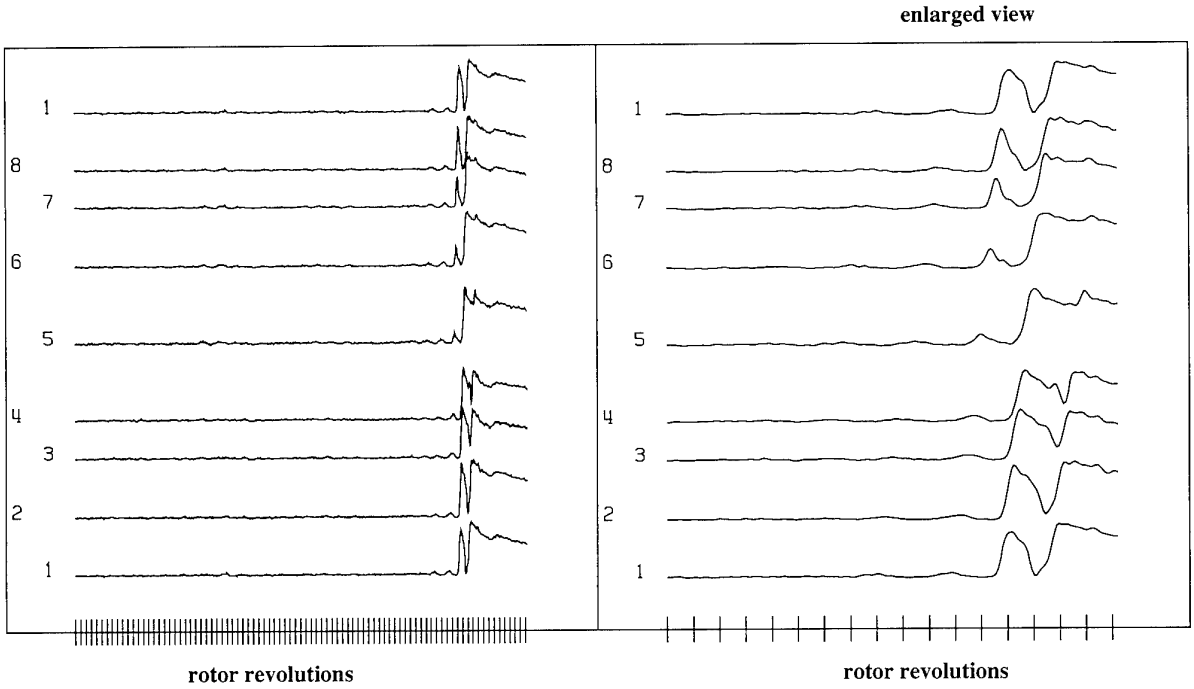

Fig. 5: N/N_0 = 0.8, pressure traces in front of 1st rotor

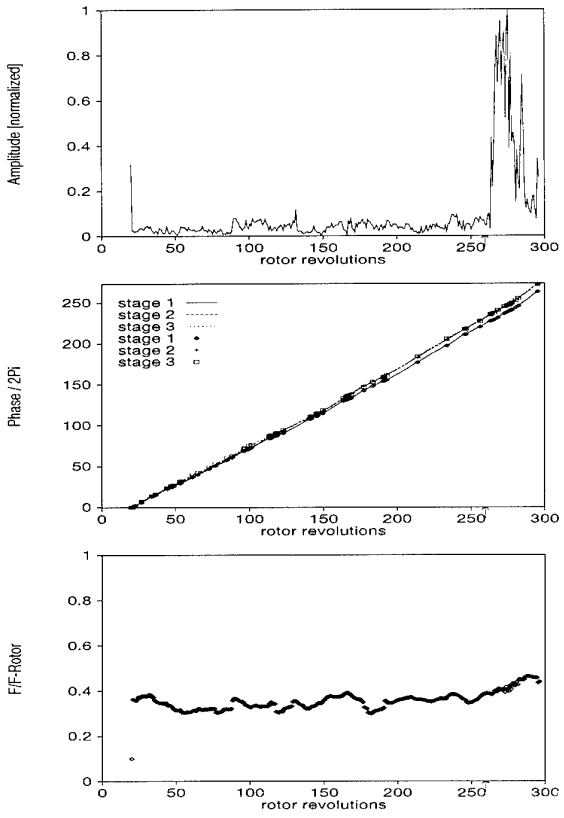

Fig. 6: N/N_0 = 0.8, estimate of wave parameter

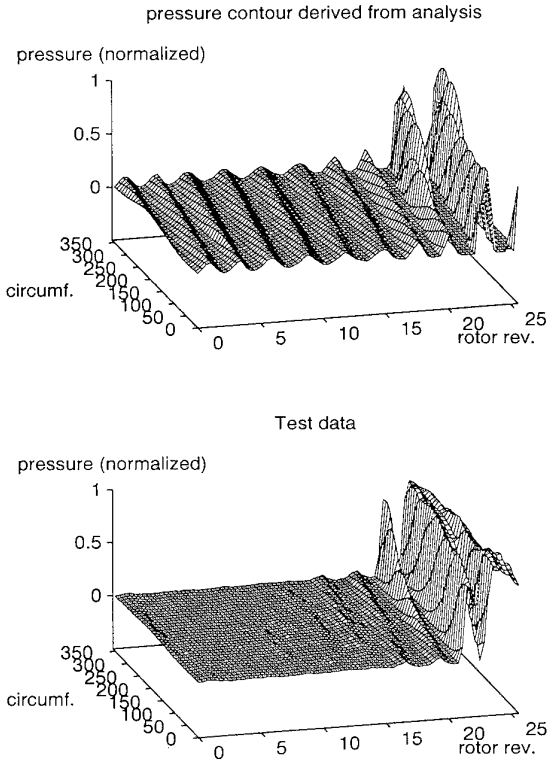

Fig. 7: N/N_0 = 0.8, measured (lower plot) and predicted distribution (upper plot)

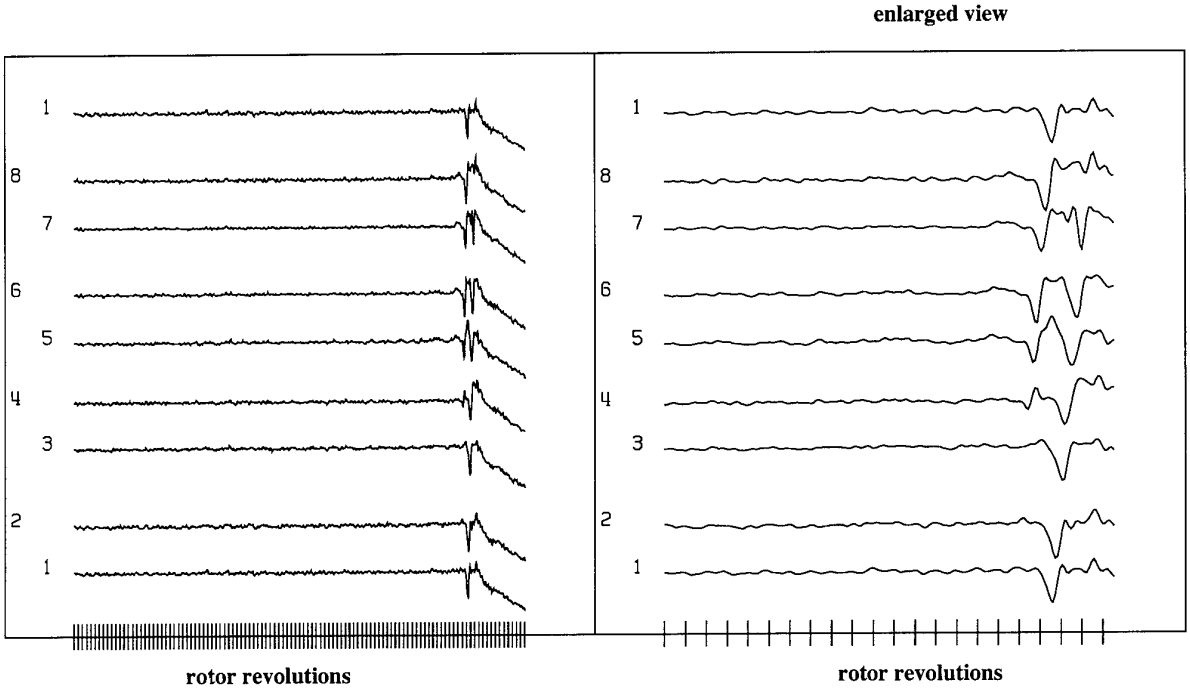

Fig. 8: $N/N_0 = 1$, pressure traces in front of 3rd rotor

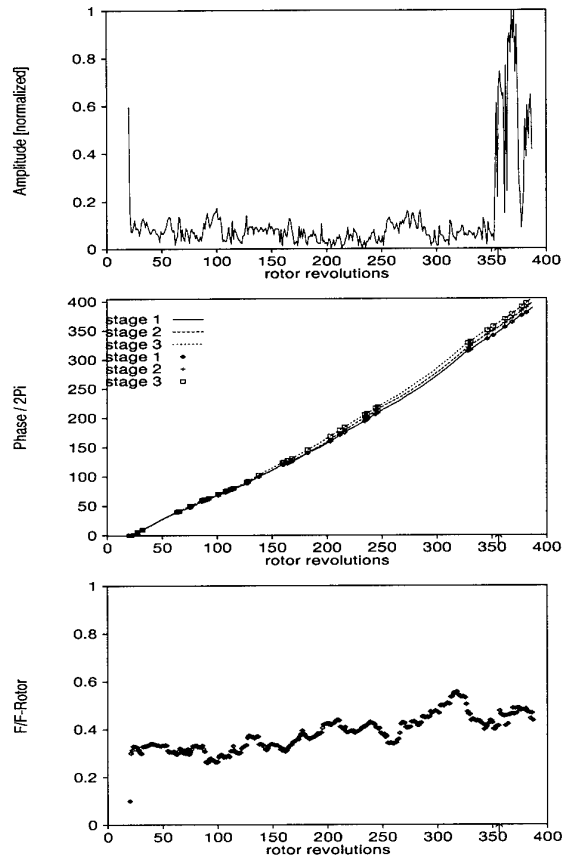

Fig. 9: $N/N_0 = 1$, estimate of wave parameter

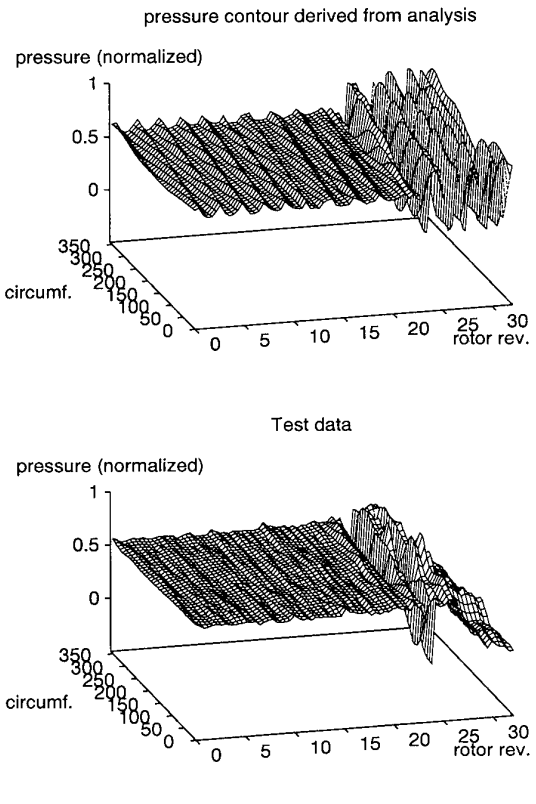

Fig. 10: $N/N_0 = 1$, measured (lower plot) and predicted distribution (upper plot)

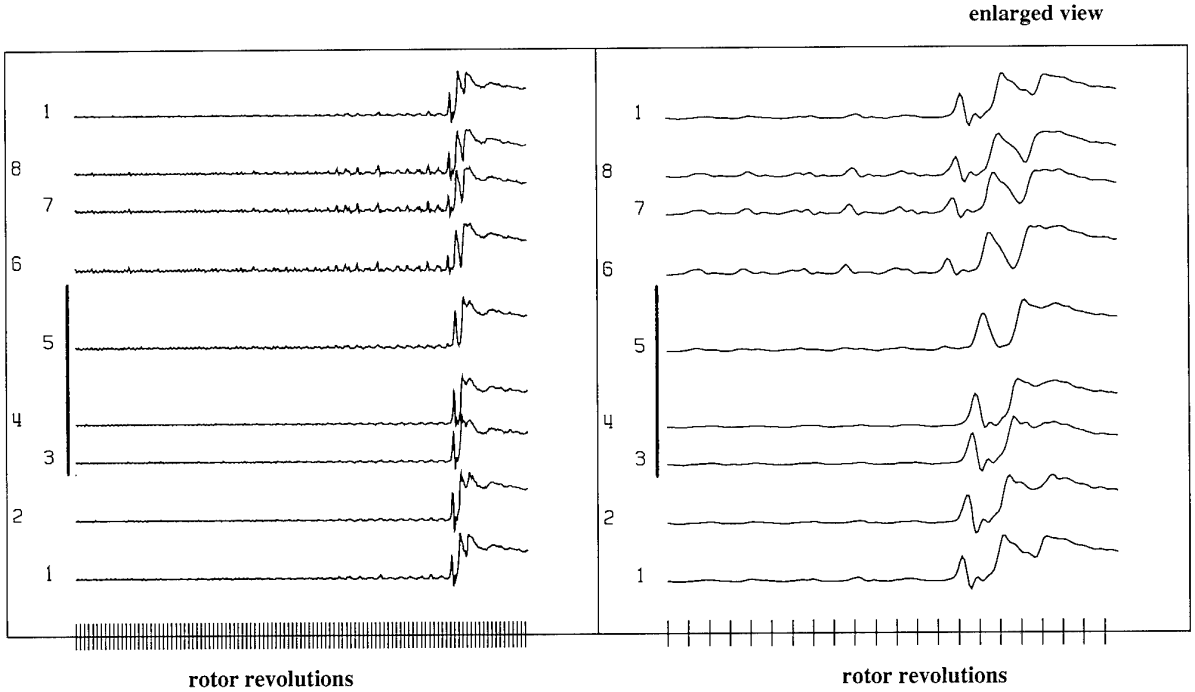

Fig. 11: $N/N_0 = 1$, with inlet distortion, pressure traces in front of 1st rotor

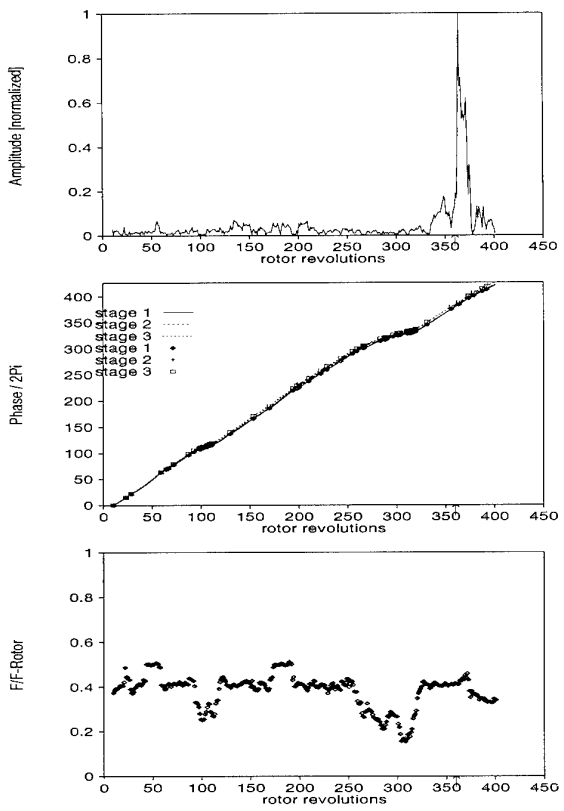

Fig. 12: $N/N_0 = 1$, with inlet distortion , estimate of wave parameter

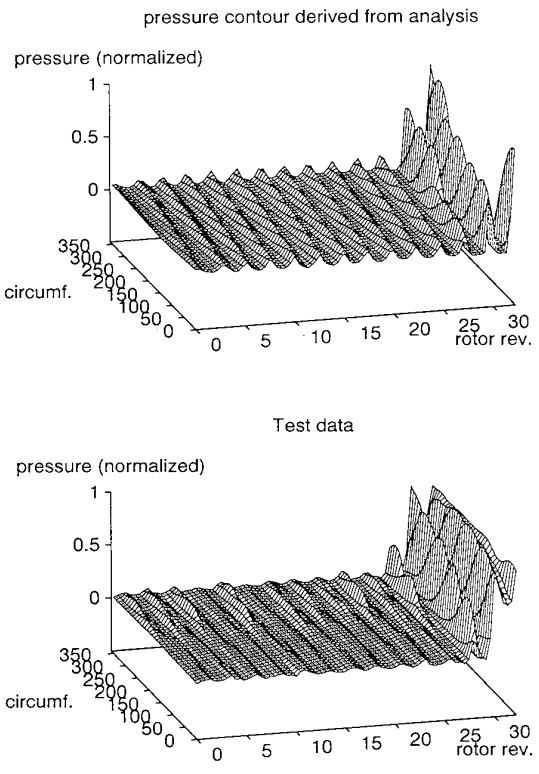

Fig. 13: $N/N_0 = 1$, with inlet distortion , measured (lower plot) and predicted distribution (upper plot)

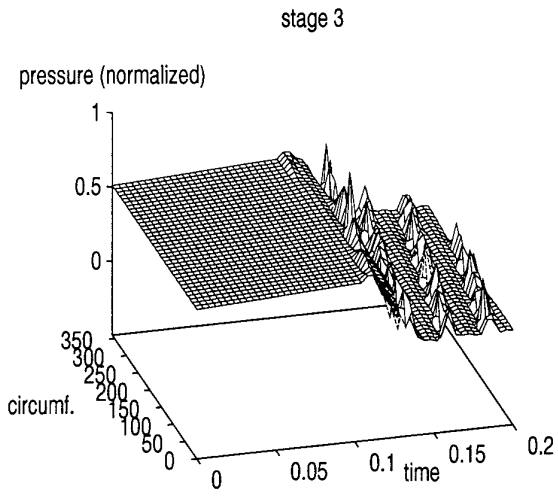

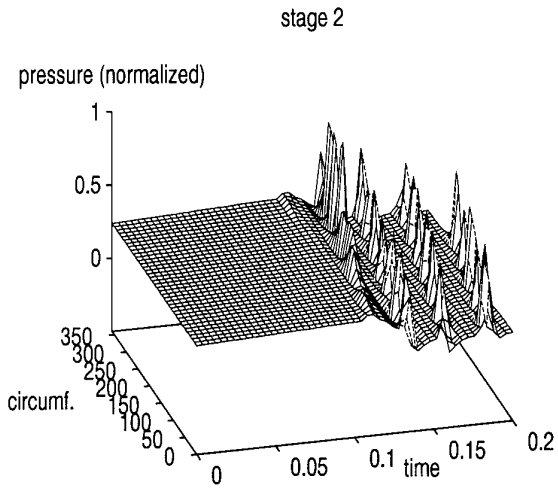

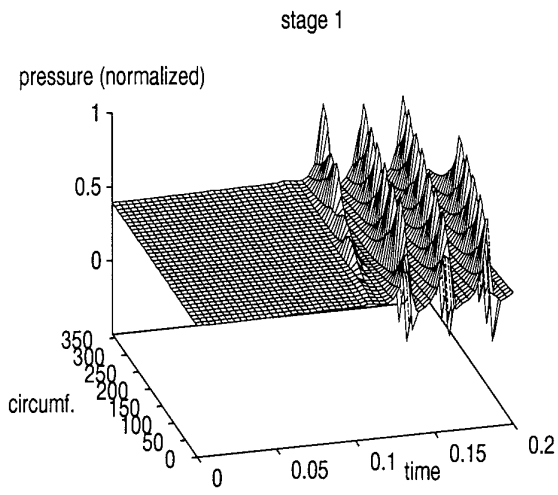

Fig. 14: calculated pressure during rotating stall

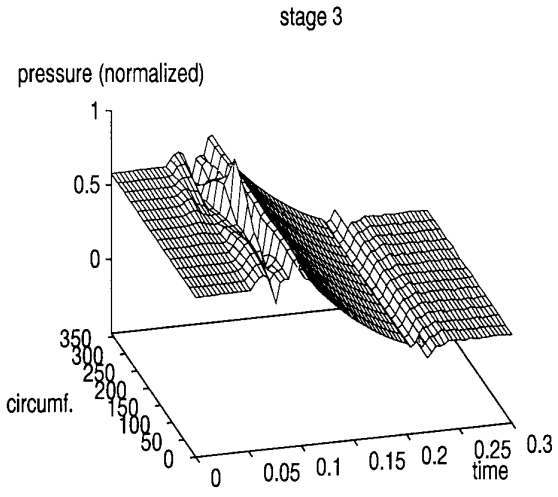

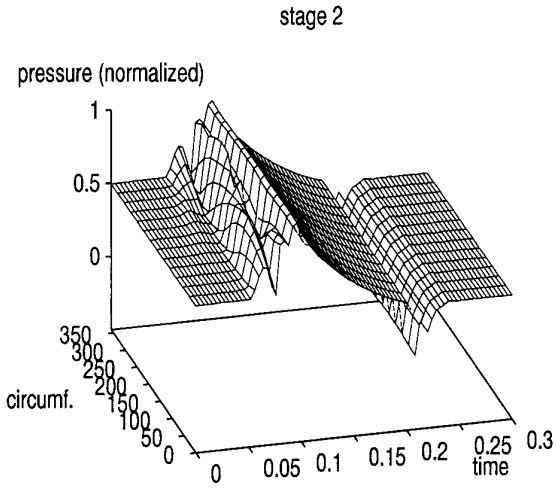

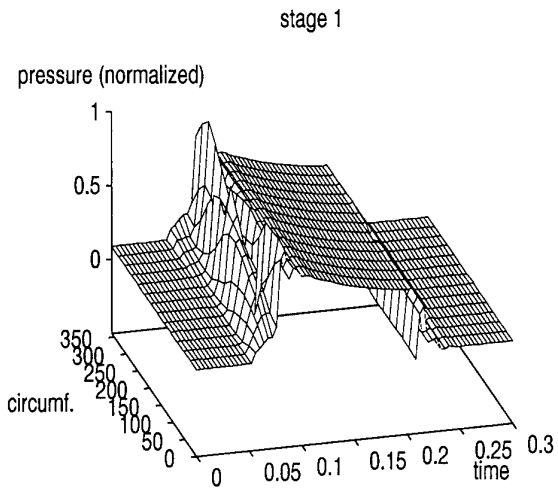

Fig. 15: calculated pressure during surge

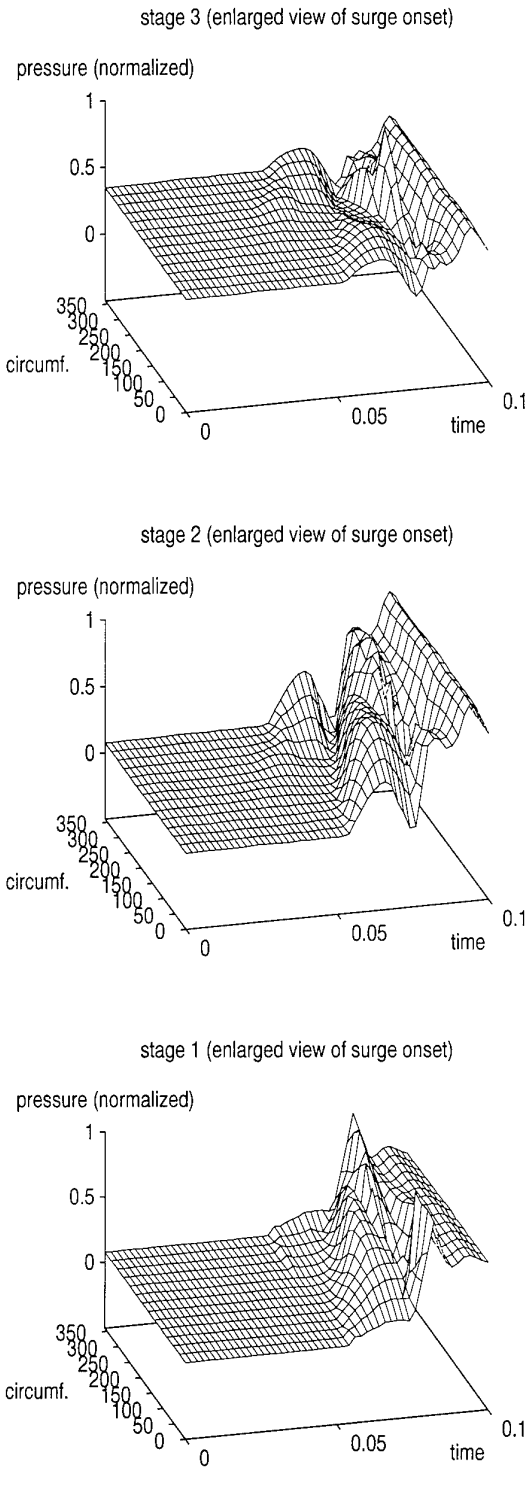

Fig. 16: enlarged section of fig.15, showing formation of a rotating disturbance

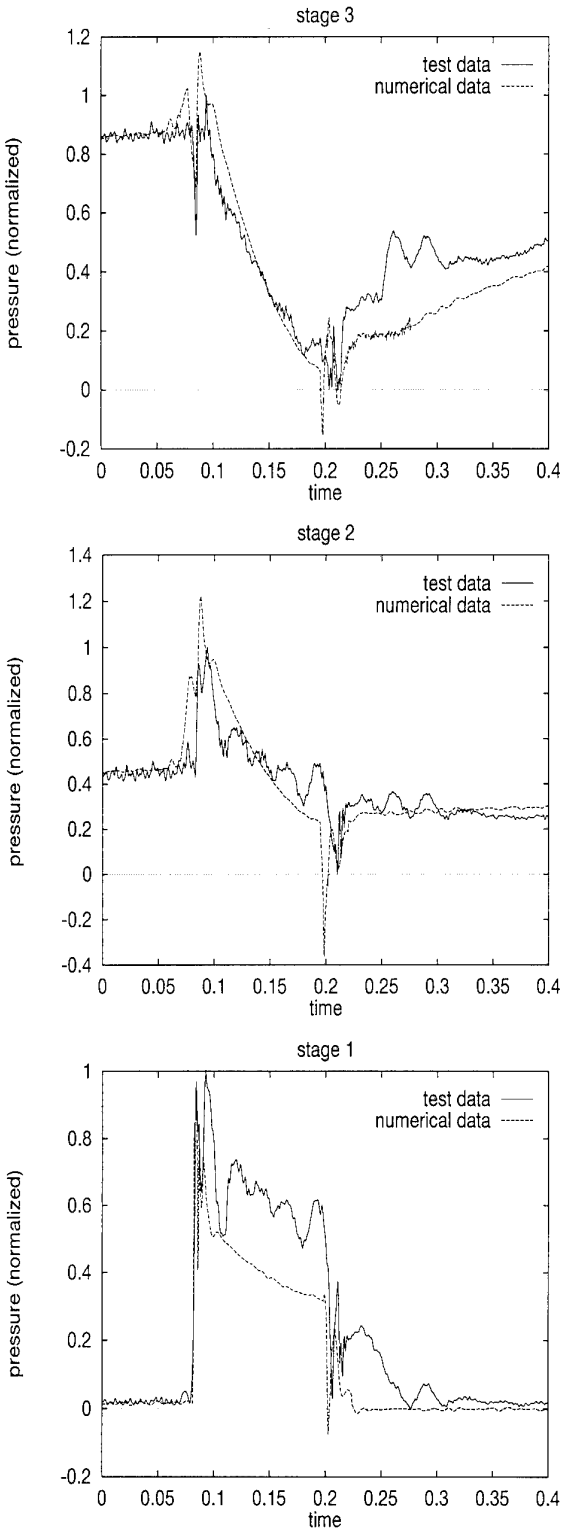

Fig. 17: comparison of measured and predicted surge overpressure

Questions to the authors:

F. Kameier, BRR:

1. Could you explain your surge inception manoeuvre?
2. Your operating conditions are not stable. I know that this way of surge evaluation is the standard in turbomachinery research, I. Day and others are also going this way. Frequency analysis with averaging the spectra for noise redcution and a sufficient frequency resolution are very difficult with these kind of manoeuvres. Have you analyzed your data in frequency domain?
3. The rotational potential flow field is not visible in your time domain data, does it depend on your transducer?
4. Did you calculate the wavelength of your pre-stall waves?

Answer:

Surge has been induced by allowing the compressor to settle at a stable operating point "close" to surge for some minutes. Starting from this point, the exit throttle is closed in very small steps until surge occurs, while data is recorded continuously. Due to the transient nature of the flow during this process, no thorough analysis of the data in the frequency domain has been performed. Collecting data for a stable operating point, regardless of its proximity to surge, was not the intention of the research programme. Rather the aim was to look for the *development* (which in itself is a transient process) of any kind of regular pattern leading to compressor flow instability. Therefore the use of any analysis technique which inherently requires data with almost constant spectrum contents was assumed inappropriate for the expected kind of data.

Due to low-pass filtering of the data no effect of rotor blades passing the sensor is visible in the time traces presented here.

The wavelength of the pre-stall waves has not been determined.

J. Durham, DRA:

How did you construct the stage characteristics of the compressor in the stalled operating region?

Answer:

The stage characteristics of the compressor which are (normally) available for the stable operating region are extended based on a procedure described by Sugiyama /10/. This procedure fits to second-order polynomials to the stable branch of the pressure rise characteristics to account for positive and negative mass flow, respectively. Efficiency is simply assumed to drop linearly to a preset value. In this way, the complete mass flow region of interest is covered. Stage characteristics are then splitted into blade row characteristics, following a simple rule, for instance constant ratio of rotor losses to stator losses.

Nicolas Piro, TURBOMECA:

Is the analysis procedure able to find which stage is responsible for surge onset in an axial multi-stage compressor?

Answer:

Looking at the amplitudes of the pre-stall waves, it is found that they are strongest in front of those stages, which induce surge, as deduced for instance from the pressure traces. Pressure traces show up a pressure spike for all stages in front of the stall-inducing stage and a drop for following stages.

REFERENCE NO. OF THE PAPER: 26

DISCUSSOR'S NAME: F. Kameier, BMW-RR, Germany

AUTHOR'S NAME: T. Breuer & S. Servaty

Q.: 1. Could you explain your surge inception manoeuvre?

2. Your operating conditions are not stable. I know that this way of surge evaluation is the standard in turbomachinery research and that I. Day and others are also going this way. Frequency analysis with averaging the spectra for noise reduction and a sufficient frequency resolution are very difficult with these kind of manoeuvres. Have you analyzed your data in frequency domain?

3. The rotational potential flow field is not visible in your time domain data; does it depend on your transducer?

4. Did you calculate the wavelength of your pre-stall waves?

A.: Surge has been induced by allowing the compressor to settle at a stable operating point "close" to surge for some minutes. Starting from this point, the exit throttle is closed in very small steps until surge occurs, while data is recorded continuously. Due to the transient nature of the flow during this process, no thorough analysis of the data in the frequency domain has been performed. Collecting data for a stable operating point, regardless of its proximity to surge, was not the intention of the research program. Rather the aim was to look for the *development* (which in itself is a transient process) of any kind of regular pattern leading to compressor flow instability. Therefore, the use of any analysis technique which inherently requires data with almost constant spectrum contents was assumed inappropriate for the expected kind of data.

Due to low-pass filtering of the data, no effect of rotor blades passing the sensor is visible in the time traces presented here.

The wavelength of the pre-stall waves has not been determined.

REFERENCE NO. OF THE PAPER: 26

DISCUSSOR'S NAME: D.J.Durham, DRA, U.K.

AUTHOR'S NAME: T. Breuer & S. Servaty

Q.: How did you construct the stage characteristics of the compressor in the stalled operating region?

A.: The stage characteristics of the compressor which are (normally) available for the stable operating region are extended based on a procedure described by Sugiyama /10/. This procedure fits second-order polynomials to the stable branch of the pressure rise characteristics to account for positive and negative mass flow, respectively. Efficiency is simply assumed to drop linearly to a preset value. In this way, the complete mass flow region of interest is covered. Stage characteristics are then split into blade row characteristics, following a simple rule, (for instance, constant ratio of rotor losses to stator losses).

REFERENCE NO. OF THE PAPER: 26

DISCUSSOR'S NAME: N. Piro, Turbomeca, France

AUTHOR'S NAME: T. Breuer & S. Servaty

Q.: Is the analysis procedure able to find which stage is responsible for surge onset in an axial multi-stage compressor?

A.: Looking at the amplitudes of the pre-stall waves, it is found that they are strongest in front of those stages which induce surge, as deduced for instance from the pressure traces. Pressure traces show up a pressure spike for all stages in front of the stall-inducing stage and a drop for following stages.

DYNAMIC RESPONSE OF A CRYOGENIC LOX PUMP TO PRESSURE AND MASSFLOW FLUCTUATION.

A. MUNARI
M. MOTTA

Fiat Avio S.p.A.,Direzione Progettazione,C.so Ferrucci 112, 10138 Torino, Italy

SUMMARY.

During the first stage flight many liquid propellant rockets have experienced longitudinal vibrations caused by interaction between the first launcher longitudinal mode and the dynamic of the propulsion system. This type of instability, called POGO, is closely related to the feeding pumps dynamic characteristics, expecially when working at the lowest suction pressure.
The knowledge of the pump dynamic response to pressure and massflow oscillations is essential for the prediction and analysis of the POGO phenomena. The necessary information can be represented in form of a pump-transfer-matrix, which relates the fluctuating pressure and massflow at pump inlet to the same quantities at pump discharge.
This work summarizes the results of the experimental activities performed to extract the dynamic transfer matrix of a liquid oxygen pump in both cavitating and non cavitating conditions.

LIST OF SYMBOLS.

A	pump flow gain [s]
C	pump compliance [Kg / Pa]
G(TAU+)	pump stability function [-]
I	pump inertia [1 / m]
Omega	pump rotational speed [rad / s]
PHI+	flow coefficient [m3]
PSI+	pressure rise coefficient [m2]
R	pump resistance [Pa * s / Kg]
TAU+	cavitation coefficient [m2]
TAU I	incipient cavitation coefficient [m2]
TAU R	rotating cavitation coefficient [m2]
Yi = s * C	pump admittance [Kg / Pa / s]
Zi = R + s * I	pump impedance [Pa * s / Kg]
m	pump pressure gain [-]
s	Laplace variable [1 / s]

1. INTRODUCTION.

Combustion in liquid rocket engines is never perfectly smooth, since fluctuations of temperature, pressure and velocity in the combustion chamber feeding line cannot be completely avoided.
According to ref. [1], combustion can be considered smooth if pressure fluctuations during steady state operation do not exceed +/- 5% of the mean chamber pressure.
If fluctuations are higher but random, combustion is considered rough.
If fluctuations are charachterized by organized oscillations which show periodical pressure peaks which may increase, this is the case of *combustion instability.*
According to ref. [1], main types of combustion instabilities can be listed in three different frequency ranges: 10 / 200 hertz , 200 / 1000 Hertz and above 1000 Hertz.
Low frequency instabilities are due to pressure interactions between the combustion chamber and propellant feeding system. Higher frequency instabilities are due to interactions between other parts of the missile or of other nature and they are not considered in this work.
If both the structure and the propulsion system have the same natural frequency, within the low frequency range, a closed loop interaction between the longitudinal structural vibration mode of the launcher and the propulsion system dynamics can occur and amplify itself. This phenomenon is commonly called POGO.
This problem can be solved adopting proper oscillation dumping devices but it is also possible to understand the phenomenon by means of analytical methods, as far as the vehicle and the main vehicle engine components are concerned.
In fact, a dedicated dynamic transfer function can be calculated to evaluate the response of the engine system to force pressure oscillations in the low frequency range.
According to the preliminary studies of the European launcher ARIANE 5, the necessity to know the dynamic transfer function of the liquid oxygen turbopump of VULCAIN engine was clear. Hence, S.E.P. (Societé Européenne de Propulsion, responsible for the overall rocket cryogenic main engine VULCAIN) and FIAT Avio (resposible for the LOX Turbopump component) decided to characterize the pump and its axial stage at component level before proceed ng with POGO tests at engine level.
As a consequence, a water test campaign was performed in FIAT test plant in Turin testing the pump in fluid dynamic similitude conditions, both in steady state performance and in cavitation..
Furthermore, results obtained during rotating cavitation test campaign have been considered to point out one of the main pump instabilities and the frequency range within which exciting pressure waves can derive from this phenomenon.
The possible way to reduce rotating cavitation effects is indicated as a future work.

2.TEST ARTICLE.

Testing activity exploited full scale pump components.
Tests were performed both on the pump axial stage plus deswirler stator alone and on the complete pump (axial stage called "inducer" plus deswirler stator and radial stage called "impeller")
Hereafter the main geometrical data of inducer, deswirler and impeller are reported together with a sketch of the inducer.

Inducer geometrical data:

Blade number: 4

Inlet tip diameter: 0.168 m
Inlet hub diameter: 0.072 m
Outlet tip diameter: 0.168 m
Outlet hub diameter: 0.0116 m
Average inlet blade angle: 78 deg
Hub axial length : 0.07 m

Paper presented at the AGARD PEP 85th Symposium on "Loss Mechanisms and Unsteady Flows in Turbomachines", held in Derby, United Kingdom, 8-12 May 1995, and published in CP-571.

Deswirler geometrical data:

Inlet outer diameter: 0.171 m
Inlet inner diameter: 0.114 m

Inlet blade angle: 60 deg.

Exit outer diameter: 0.140 m
Exit inner diameter: 0.102 m

Number of vanes: 19

Impeller geometrical data

Inlet blade nr.: 4
Outlet blade nr.: 8

Inlet tip diameter: 0.14 m
Inlet hub diameter: 0.108 m
Exit diameter: 0.218 m

Tip inlet blade angle: 71.8 deg
Hub inlet blade angle: 64.4 deg

3. TEST FACILITY.

The exploited water test facility allows the testing of single and multistage centrifugal and axial pumps.
It consists of a primary system and of several secondary systems like:
- heat removal system
- chiller unit
- demineralized water system
- raw cooling water system
- service gas system
- vacuum system.

Hereafter the main test facility data are listed:
- piping size: up tp 16"
- material: A 106 Gr B
- cold tank pressure: 20 Bar
- cold tank temperature: 373 K
- cold tank volume: 30 m3
- cold tank material: Fe510 - 2kW
- hot tank min. pressure: 1 Bar
- hot tank max. pressure: 20 Bar
- hot tank temperature: 473 K
- hot tank volume: 30 m3
- hot tank material: Fe510 - 2kW

4.MATHEMATICAL MODEL HYPOTHESYS.

In order to evaluate the pump dynamic transfer function, the fluid circuit in which the tested pump has to work must be excited by a flow disturbance.
The pumped fluid is hence subjected to a sinusoidal impulse obtained by means of a butterfly valve.
An accurate dynamic model of the test plant, including the pump itself and the excitation system, was realized in order to optimise the test campaign.
The above mentioned model is based on the following hypothesis:

1) A linear distributed parameter dynamic model can be adopted for the test plant. According to this, any hydraulic element can be described by means of a four pole matrix relating the input oscillating pressure and relative flow to the output ones.

2) The pipe resistence is negligible with respect to its inertia.

3) The speed of sound can be considered constant through the pipe (flow uniformity) and for every excitation frequency.

4) The pump (or its axial stage) and pipe models can be considered linear. This means that their dynamic response is considered indipendent from the excitation level and from the excitation position. This hypothesis can be applied only in case of oscillation around a steady state condition.

5) The pump pressure gain (m), the pump flow gain (A) and the pump compliance (C) depend only on the axial stage (called "inducer").

6) The rotational speed fluctuations during the flow modulation are considered small (< 0.1 %) with respect to the average value. As a consequence, for a cavitating pump or inducer a four pole model can be chosen which relates the inlet pressure and flow oscillations with the outlet ones by means of the matrix equation:

$$[OUT] = [Q]*[IN]$$

Where:

OUT11 = outlet pressure perturbation.

OUT21 = outlet flow perturbation.

IN11 = inlet pressure perturbation.

IN 21 = inlet flow perturbation.

$Q11 = 1 + m + Zi * Yi$

$Q21 = -Yi$

$Q12 = -Zi * (1-A*s)$

$Q22 = 1-A*s$

[Q] is a complex matrix, since its coefficients must take into account both the amplitude and the phase of fluid parameters oscillations.

7) The four [Q] matrix coefficients are a function of:
- oscillation angular frequency
- Net Positive Suction Pressure
- pump rotational speed
- fluid temperature

8) Hydropneumatic accumulator can be simply modelled as a compliance.

9) The exciting input is assumed to be a sinusoidal oscillating flow.

10) For the excitation system a non linear concentrated parameter model is adopted.

11) The system is considered indipendent from the excitation duration ("ergodicity").

5. TEST ACTIVITY TARGETS.

Test activity main objective was the determination of the [Q] matrix four coefficients in order to introduce the results in the overall Vulcain engine feeding system control model.
As a consequence, following parameters had to be evaluated experimentally:

m = pump pressure gain [-]

R = pump resistence [Pa*s/Kg]

A = pump flow gain [s]

I = pump inertia [1/m]

C = pump compliance [Kg/Pa]

To achieve the target, two independent sets of measurements of dynamic pressure and massflow at pump inlet and outlet interfaces are necessary
Two independent sets of data at a same operating point are obtained modifying the test plant impedance by means of different hydraulic accumulators connected to the main hydraulic pipe.

6.PERFORMED TESTS.

Two test campaigns were performed: the first testing the pump axial stage alone and the second testing the complete pump(axial + radial stages).
During the axial stage campaign, 144 different test conditions were adopted while during the complete pump campaign 36 different operating conditions were tested.
Hereafter the main test parameters are listed with their range.

Rotational speed.
Two different rotational speeds were selected for inducer campaign: 6500 and 10000 rpm.
The lower speed was chosen to allow the comparison with data collected during the complete pump campaign, since the maximum speed achievable with the complete pump is 6500 rpm (due to test facility power limitation).

Water temperatures.
In order to study the thermodynamic effect, three temperatures were chosen: 293 K, 348 K and 408 K. The last one was selected due to the existing similarity between liquid oxygen at TP operating conditions (91K) and water at 408 K.

Modulation frequency.
8 different values up to 80 Hz were selected. The adequacy of this frequency range selection is confirmed also by the results collected during a following water test campaign performed on the same test facility to study the effects of rotating cavitation on pump performance.
In the following, a chapter is dedicated to the problem of rotating cavitattion.

Net Positive Suction Pressure.
7 values of the corresponding cavitation coefficient TAU were selected, ranging from 1.27 e-4 to 5 e-4 m2.

Flow coefficient.
Four values, from 1.27 e-4 to 1.46 e-4 m3 were selected.
It is worth noticing that 80 among 144 and 14 among 36 tests were performed at design point flow coefficient (1.35 e-4 m3) respectively for inducer campaign and for complete pump campaign.
To verify the validity of simulation hypothesis, the influence of the oscillation level and excitation position (linearity and cavitation) and of the modulation duration was studied.

Two inducers of the same standard were used to verify the influence of the tested hardware to data dispersion.

In correspondence of each dynamic test condition, one steady state test (excitation frequency = 0) was performed, with the following goals:
- to check the accomplishement of selected test validation criteria;
- to collect preliminary dynamic charachteristics estimation, to be considered as a reference for very low frequency ranges.

7. STATIC TEST RESULTS.

Steady state test results allowed to verify that oscillations of pump rotational speed, water temperature, pump flow coefficient and inlet pump cavitation coefficient were within a narrow range of tolerance.

Then, steady state test results have been exploited to calculate two parameters of the [Q] pump characteristic matrix for excitation frequency = 0.

- pump pressure gain : m = d(PSI+)/ d(TAU+)

- pump resistence: R = - [d(PSI+)/d(PHI+)] * Omega

These two coefficients have been exploited deriving the obtained curves PSI+ vs. TAU+ and PSI+ vs. PHI+.
Two examples of such kind of curves are reported hereafter.

Fig. 1

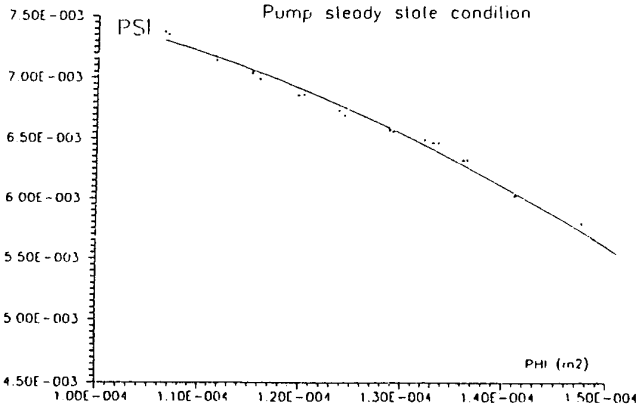

Fig. 2

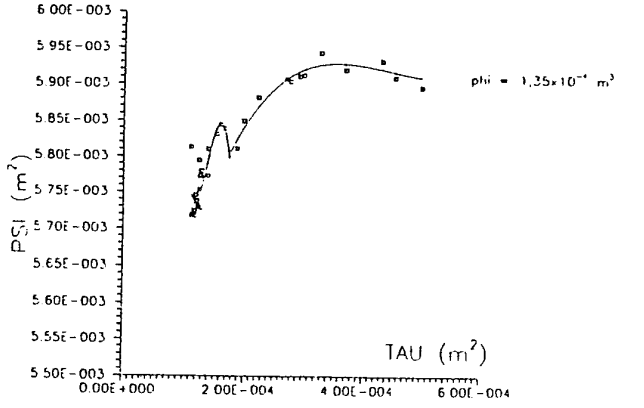

8. DYNAMIC TEST RESULTS.

Two sets of data were collected during dynamic tests:
the first during upstream (with respect to the pump) modulation tests, the second during downstream modulation tests at the same working points.

Pump matrix [Q] required coefficients have been characterized as it follows, plotted as function of excitation frequency.

Resistence.
Fig. 3

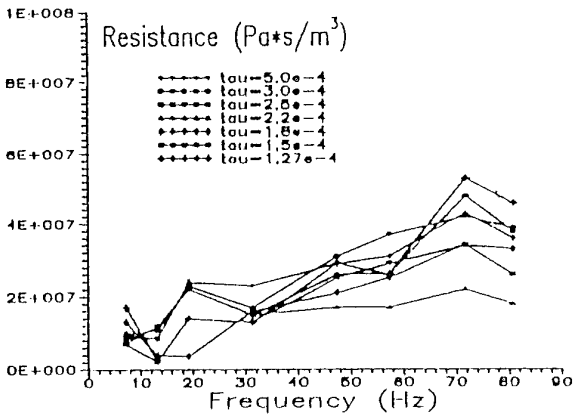

Fig. 4

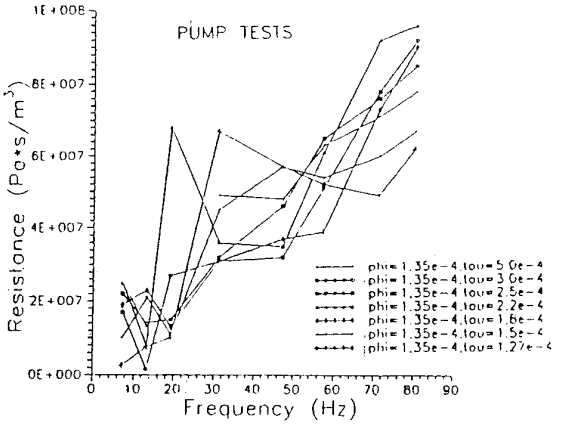

The inducer resistence (fig. 3, PHI+ = 1.35 e-4 m3) increases with frequency. Curve slope is higher for the overall pump (fig. 4).
- Rotational speed influence.
Direct dependence of resistence from rotational speed is detected all through the tested frequencies only at low flow coefficients values.
At higher one, for low frequencies (id est in quasi steady state conditions) the linear correlation is verified while for high frequencies the resistence decreases as the speed increases.
- Water temperature influence.
The effect of temperature is not worthy at 6500 rpm while the resistence increases with temperature at 10000 rpm, particularly at high flow coefficient values.
- Cavitation coefficient influence changes with the flow coefficient. For flow coefficient values lower than the design point one, the influence is not linear while, for higher flow coefficients, the resistence increases as the cavitation coefficient decreases.
- Flow coefficient influence.
Influence on resistence is scarce at 6500 rpm while at 10000 rpm the resistence decreases as flow coefficient increases.

Considering the overall pump tests, due to the selected working conditions only the influence of cavitation and flow coefficient could be determined.
Influence of the cavitation coefficient on the resistence is similar to the inducer case while the flow coefficient has a deeper influence.

Pressure gain.
Fig. 5

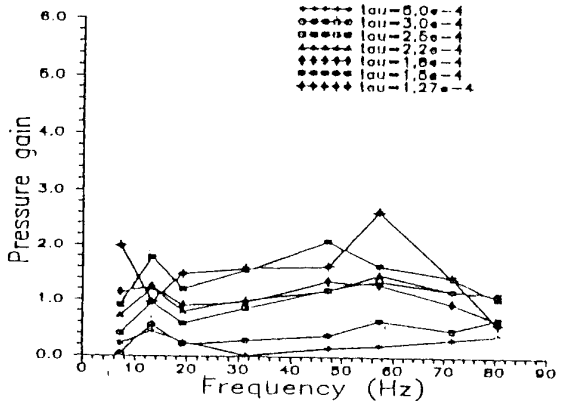

Fig. 6

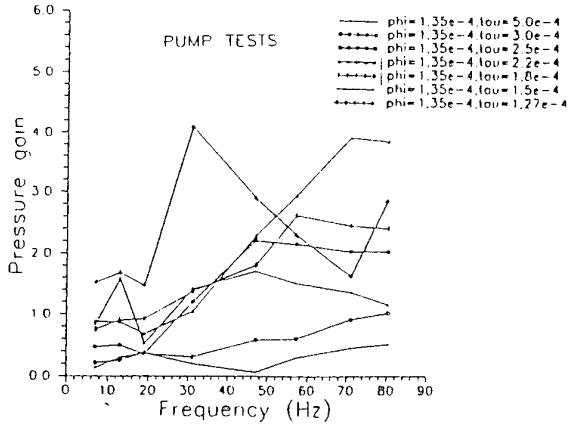

The inducer pressure gain (fig. 5, PHI+ = 1.35 e-4 m3) presents an increasing trend versus frequency as much as resistence does.
- Rotational speed influence.
The influence of rotational speed on the pressure gain is low.
- Fluid temperature influence.
It has the same influence as on resistance.

- Cavitation coefficient influence.
Pressure gain results low at high cavitation coefficients.
It increases while cavitation coefficients decrease.
- Flow coefficient influence.
It has a low influence.

Considering the overall pump tests, the influence of cavitation coefficient and flow coefficient is the same as for the inducer alone (fig. 6).

Compliance.
Fig. 7

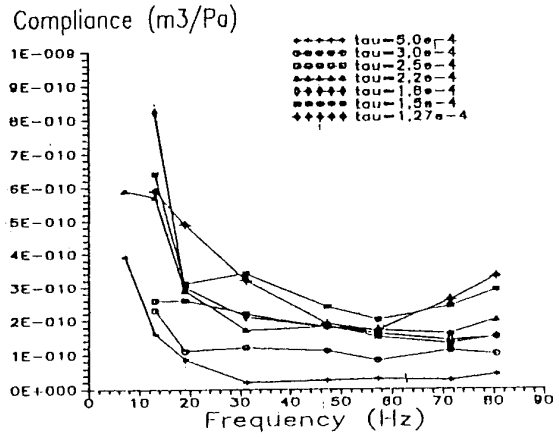

The inducer compliance decreases as the frequency increases, but this result can only be explained with the hypothesis that, at low excitation frequencies, the results are affected deeply by flow and pressure evaluation errors.
- Rotational speed influence.
Compliance increases as rotational speed increases.
- Temperature and flow coefficient influence.
These two parameters have scarce influence.
- Cavitation coefficient influence.
Compliace increases as cavitation level increases.

Flow gain.
Fig. 8

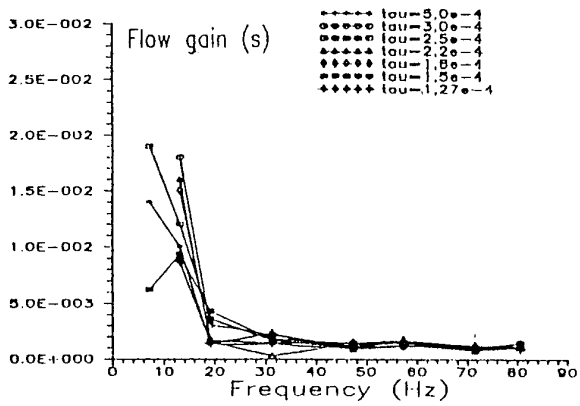

Influence of the test parameters on flow gain are exactly the same as for the compliace. It must only be added that a little influence of flow coefficient and rotational speed is detected.
In fig. 8, inducer flow gain is shown (PIII+ = 1.35 e-4 m3).

Inertia.
Fig.9

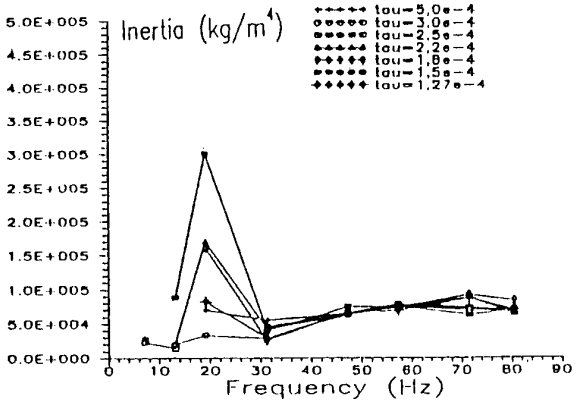

Rotational speed, fluid temperature, flow coefficient and cavitation coefficient do not influence inducer inertia (fig 9, PIII+ = 1.35 e-4 m3). An influence of cavitation coefficient seems to exist in low cavitation but it should only be due to problems with measures in these conditions.
A slight influence of frequency appear from the plot, were inertia increases slowly with frequency.

Main hypothesis verification dedicated tests.

- Analysis of data from dedicated tests confirmed the hypothesis of linearity, the inducer dynamic behaviour resulted indipendent from the exciting device position.

- One test performed with increasing modulation duration confirmed the system ergodicity hypothesis.

- Some tests were repeated with two different inducers of the same design and manufacturing standard so it was verified that the exploited hardware does not affect the matrix [Q] coefficient values.

9.ROTATING CAVITATION.

Rotating cavitation is a particular phenomenon which appears when Net Positive Suction Pressure is reduced below the incipient cavitation conditions and before the complete loss of pump performance. It makes the cavitation curve (PSI+ vs TAU+) present an instability window were d(TAU+) / d(PSI+) is minor than zero. In fact, while reducing the NPSP starting from incipient cavitation conditions, the pressure rise decreases in rotating cavitation conditions and then rises again to about the nominal pressure rise level. Afterwards, the total pressure rise performance drop is detected.
This phenomenon has been completely charachterized during a water test campaign performed on the same water test facility exploited to evaluate pump POGO matrix coefficients (8 tests were performed, at 7000 and 10000 rpm) and during the cavitation campaign performed, in winter 1993, at the Daimler Benz Aerospace LOX Turbopump test facility (P59.3) in Ottobrunn (Germany).

From the collected data it results that the rotating cavitation produces an exciting pressure oscillation in the pump circuit which is between f0 and 1.2 * f0 (were f0 is the rotor working frequency) with respect to the static parts of the pump, and can be between 0.2 * f0 and its multiples with respect to the rotating parts of the pump.
In addition to pump pressure rise fluctuation, rotating cavitation causes heavy radial loads acting on pump bearings.
In figure 10, the scheme of a typical inducer cavitation curve is represented:

Fig. 10

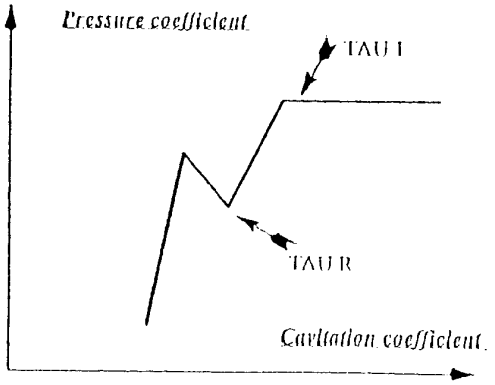

Today it is clear that the responsible for this behaviour is the pump axial stage. In fact the instability region is clearer on inducer cavitation curves than in overall pump cavitation ones. Following, a comparison between overall pump decay (R_DP) and axial stage decay (R_DPI) is shown for TAU+ values corresponding to rotating cavitation (data collected during LOX testing of VULCAIN LOX turbopump):

Rotational speed [rpm]	R_DP [%]	R_DPI [%]
12000	0.99	0.95
12000	0.995	0.955
12000	0.99	0.94
12800	0.99	0.96
12800	0.99	0.96
12800	0.99	0.95
14500	0.99	0.97
14500	0.985	0.965
14500	0.983	0.95
14500	0.983	0.96

Furtermore, the same behaviour has been shown by the Advanced Technoly Engine inducer designed and tested in water by FIAT Avio under a dedicated ESA contract and on other rocket inducers (for example on Japanese LE 7 turbopump inducer, see ref [2]).
A witness of the negative influence of rotating cavitation on pump stability is given by the evaluation of the stability function as defined on pump specification.
Stability function is defined as it follows:

$$G(TAU+) = [(PSI+) - (PSI+)0] / (PSI+)0$$

where PSI+ is the pressure rise coefficient calculated in cavitating conditions (function of both flow coefficient and cavitation coefficient), while (PSI+)0 is the pressure rise coefficient calculated in non cavitating conditions (function of the flow coefficient only).
The stability requirement is:

a) $G(TAU+) < 0$ or $G(TAU+) = 0$

or, if this condition is not verified, the following must be satisfied:

b) (b1): $G(TAU+) < 0.05$ or $G(TAU+) = 0.05$

and (b2): $dG(TAU+) / d(TAU+) > - 1 / (PSI)0$

The compliance with the stability requirement has been checked taking into account two LOX cavitation tests performed on the VULCAIN LOX turbopump. The first test was performed at high flow coefficient (1.5 e-4 m3) and the second one at low flow coefficient (1.21 e-4 m3).
The check was performed with particular attention to the range of TAU+ corresponding to rotating cavitation conditions.
Relationship a) was completely verified in the higher flow coefficient test (see fig. 11):

Fig. 11

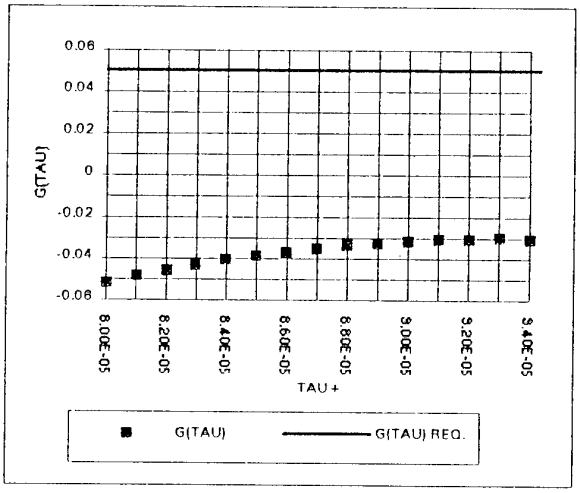

In the low flow coefficient test the relationship a) was not verified in the overall TAU + range 0.8 e-4 < TAU+ < 1 e-4 m2, which corresponds to rotating cavitation, but only for TAU+ > 0.9 e-4. As a consequence, the compliance with relationship b) was checked.
Relationship b1) was verified too, but b2) one was not satisfied in the range 0.89 e-4 < TAU+ <1 e-4 m2 (see fig. 12).

Fig. 12

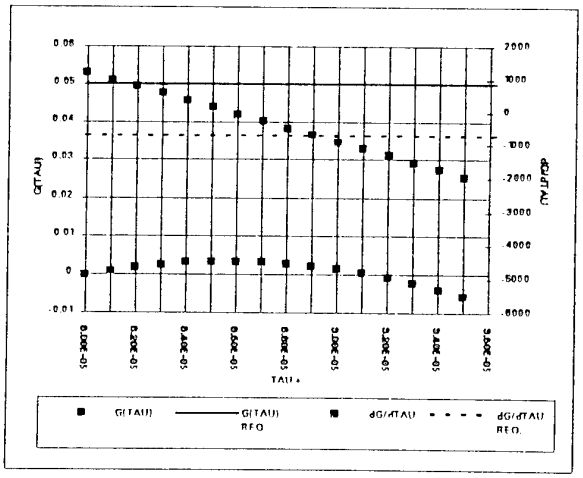

As far as the VULCAIN engine performance are concerned, this result was not considered dangerous due to the narrow TAU+ range in which the stability requirement is not satisfied; but this is a further assessment of the influence of rotating cavitation on engine feeding system instability.
Since the POGO phenomenon is essentially linked to oscillations in the rocket engine feeding system and in the combustion chamber, it is worth trying to reduce rotating cavitation effect.
As a consequence, a dedicated water test campaign will be performed by FIAT Avio exploiting a SEP rig in the next future to test new inducer liners designed taking into account the experience gathered by researchers in their report in ref [2], which should lead to dump totally the rotating cavitation effect.

10.CONCLUSIONS.

A theoretical LOX turbopump model has been prepared, which identify the dynamic respone to pressure exciting fluctuations in 0 to 80 Hz range by means of a complex dynamic response matrix.

FIAT water test facility, able to work both with cold (373 K) and with hot (473 K) water, has been exploited to test, in non cavitating and in cavitating conditions, both the axial stage alone and the complete pump in order to get the data necessary to calculate the pump dynamic response matrix coefficients.

Coefficients have been calculated and the influence of rotational speed, water temperature, modulation frequency, Net Positive Suction Pressure and flow coefficient on pump response has been evaluated.

Main results from rotating cavitation (one of the main instability reasons for the pump) tests have been listed.

11.FUTURE WORKS.

Results from the recent cavitation campaign performed in LOX on the complete Vulcain engine LOX Turbopump will be exploited to verify the POGO water test campaign achievements as far as pump pressure gain "m" and pump resistence "R" at zero exciting frequency are concerned.

A new water test campaign will be performed by FIAT and SEP to verify the effectiveness of criteria suggested in ref. [2] to reduce the rotating cavitation effects in Vulcain LOX pump axial stage.

12.REFERENCES.

1) Sutton \ Ross
Rocket propulsion elements _ 4th edition.
Wiley and Sons.

2) M. Yoshida \ S. Hasegawa \ T. Shimura \ K. Kamijo
Rotor vibration analysis of LE - 7 LOX Turbopump.
ISTS 94-0-11 Report.

3) A. Zocco \ A. Munari \ G. Malagnino
Radial load water test in cavitating conditions.
FIAT internal report nr. TPTP94025HMR.

4) M. Iacopozzi \ V. Lignarolo \ D. Prevel
POGO characterization of Ariane 5 turbopump LOX pump with hot water.
AIAA 93-2141 Report.

5) A. Munari
A.T.E. Inducer final report.
FIAT internal report nr. TPTP93075NPR.

7) M. Iacopozzi \ V. Lignarolo
HM60 pump POGO water tests exploitation report.
FIAT internal report nr. SCDS93036HMR

8) G. Malagnino
Synthesis report: TPOM5 test campaign.
FIAT internal report PRSPS95015HMR.

AKNOWLEDGEMENTS.

This work constitutes a natural complement to AIAA paper in ref. [4], hence thanks are due to M. Iacopozzi, V. Lignarolo and D. Prevel.
Furthermore, the authors thank their collegues G. Malagnino and A. Zocco for their fundamental contribution to experimental data analysis contained in ref. 3 and 8.
S.E.P. and Daimler Benz Aerospace are thanked for their contribution to water POGO test and to LOX cavitation tests respectively.

REFERENCE NO. OF THE PAPER: 27

DISCUSSOR'S NAME: L.A. Povinelli, NASA, USA

AUTHOR'S NAME: A. Munari, M. Motta

Q: Do the criteria given in the paper insure the elimination of main chamber oscillations, either in longitudinal or transverse modes? Is the injector face baffled?

A: The criteria that FIAT and SEP are going to validate are supposed to eliminate the pumped fluid pressure oscillations due to rotating cavitation, which means in a frequency range between f_o and $1.2xf_o$ (f_o being the rotor working frequency).

As far as the injector face design is concerned, this author does not have sufficient information to answer the question.

REFERENCE NO. OF THE PAPER: 27

DISCUSSOR'S NAME: J. Chauvin, Univ. of Paris VI, France

AUTHOR'S NAME: A. Munari, M. Motta

Q: Will you carry out your future tests on rotating cavitation in water or Freon? If in water, is it really representative of the phenomenon in cryogenic fluids?

A: Our future tests on rotating cavitation will be performed in water. We will be able to exploit the results for cryogenic fluids since we have deeply characterized the LOX thermal suppression head with respect to water during past experimental activities.

COMPARISONS BETWEEN UNSTEADY AERODYNAMIC EVENTS IN A GAS TURBINE GENERATOR AND AN IDENTICAL COMPRESSOR RIG

by
A. Karl Owen
U.S. Army Vehicle Propulsion Directorate
NASA Lewis Research Center, MS77-12
Cleveland, Oh, USA 44135-319139

1.0 SUMMARY

Extensive testing done on a T55-L-712 turboshaft engine compressor in a compressor test rig at TEXTRON/Lycoming (now Allied Signal Engines) is being followed by engine tests in progress at the NASA Lewis Research Center as part of the Army Non-Recoverable Stall Program. Goals include a greater understanding of the gas turbine engine start cycle and compressor/engine operation in the regions "beyond" the normal compressor stall line (rotating stall/surge). Rig steady state instrumentation consisted of 497 steady state pressure sensors and 153 temperature sensors. Engine instrumentation was placed in similar radial/axial locations and consists of 122 steady state pressure sensors and 65 temperature sensors. High response rig instrumentation consisted of 34 wall static pressure transducers. Rig and engine high response pressure transducers were located in the same axial/radial/circumferential locations in front of the first three stages. Additional engine high response instrumentation was placed in mach probes in front of the engine and on the compressor hub. This instrumentation allows for the generation of detailed stage characteristics, overall compressor mapping, and detailed analysis of dynamic compressor events..

2.0 INTRODUCTION

The TEXTRON/Lycoming T55-L-712 engine is the current powerplant for the US Army CH-47 "Chinook" helicopter. This powerplant/airframe combination can experience occasional difficulties in completing the start sequence. The US Army Vehicle Propulsion Directorate, in response to a request from the Aviation and Troop Command (ATCOM), initated the Army's Non-Recoverable Stall Program to investigate these difficulties. Program goals have been expanded to include: 1) the study of non-recoverable stall events, 2) the development of advanced dynamic engine and compressor models, and 3) the extension of compressor range with active compressor aerodynamic stabilization.

These program goals will provide 1) a characterization of normal and hung start events in the T55-L-712 engine, 2) recommendations to eliminate hung start events, 3) a characterization of rotating stall/surge and the events leading to their occurrence, 4) development/ demonstration of a control system that can

Paper presented at the AGARD PEP 85th Symposium on "Loss Mechanisms and Unsteady Flows in Turbomachines", held in Derby, United Kingdom, 8-12 May 1995, and published in CP-571.

delay the occurrence of rotating stall/surge, and 5) an enhancement of rig/engine relationships.

This paper addresses the last program goal. Often rig testing is used to supplement or replace full engine testing. Unique features such as repeatability and controllability can greatly ease the difficulties associated in obtaining component data on an engine. Further, rig testing provides a relatively low cost substitute. However, little information exists in the public domain addressing the similarities and differences of data acquired by these two different types of testing.

Finally, an ultimate goal of this program is the generation of a comprehensive dataset for academic and industry use in the development and assessment of dynamic engine models. Thus, knowing the impact of test methodology on the resultant data and, therefore, on the product models is of ultimate importance.

As a part of this program, extensive compressor rig testing was done at the AlliedSignal Engine Stratford, CT. facility. This testing generated complete performance maps for each stage of the compression system between 20% and 100% of design speed at increments of 10% and 85% and 95% of design speed. In addition, the compression system was instrumented to study rotating stall/surge events and was surged at all speeds between 20% and 100% of design with the exception of 95% speed.

The engine testing, begun the first calender quarter of 1995, will study, in detail, the dynamics of "hung start" events and rotating stall/surge events in an actual gas turbine engine. This phase of the test program includes a detailed sensitivity study of starting variables (such as bleed, starter motor torque, turbine inlet temperature, heat soak, and pressure altitude) on the T55-L-712 starting performance; detailed characterization of compressor start aerodynamics; and a detailed exploration of both low and high speed compressor dynamic events. Included will be the demonstration of a control system to delay the inception of rotating stall/surge.

Engine testing to date includes only testing to the ground idle range. This test configuration has a locked power turbine. Test facilities are currently being modified for testing up to design speed, which will begin the summer of 1995.

All data acquired during this program, both rig and engine, will be generally available to the research community from the VPD, within appropriate proprietary restraints.

3.0 APPARATUS AND FACILITIES

3.1 INTRODUCTION

Previous publications [1][2] contain detailed information concerning the the AlliedSignal rig test facility and preliminary rig test results. Thus, this section primarily discusses the engine test facility and only briefly reviews the rig test facility.

3.2 RIG TEST FACILITY

Rig testing occurred at the AlliedSignal Stratford, CT. facility in June of 1993. This sea level facility uses three T55-L-712 engines linked through a gearbox to power the test compressor rig. Airflow is measured by calibrated bellmouths in series and compressor loading is controlled with a butterfly valve downstream of the diffuser exit plenum. Bleed flow is attached to an altitude exhaust system to control the amount of bleed and was set for this test to simulate "nominal" bleed for any

given speed. Exit plenum volume was sized to match the engine combustor volume.

3.3 ENGINE TEST FACILITY

Engine tests are being conducted at the NASA Lewis Research Center (LeRC) on the Engine Component Research Laboratory (ECRL) side 2 test stand in Cleveland, OH. This facility is designed to accomodate turboshaft engines in the T700 size class and was recently upgraded to provide limited altitude capability to complete this test program. A detailed description of the engine test facility is provided in [3].

This altitude facility is capable of simulating pressure altitudes up to 5000 meters, however, temperature is not controlled. A dynamometer capable of absorbing up to 2500 shaft horsepower is available. Engine inlet airflow can be measured using a calibrated venturi with a limiting airflow of 5 Kg/sec.

For the low speed testing, the engine power turbine was locked and the dynamometer was not used. A waterbrake specifically designed for the T55 series engines will be used to accomplish the high speed portion of the test. Airflow for the high speed testing will be measured using a calibrated bellmouth. For the low speed testing (up to ground idle), massflow was calculated using total pressure/temperature rakes measurements and the continuity relation.

3.4 THE T55-L-712 COMPRESSOR

The T55-L-712 transonic compressor consists of seven axial and one centrifugal stage. It uses no variable geometry and has a single start bleed over the sixth stage stator.

The compressor design point operating conditions are a pressure ratio of about 8.0 and a massflow of about 12.0 Kg/sec. Compressor inlet radius ratio is about 0.36. Overall compressor design speed rotor tip clearances are normally less than 0.5% of the rotor blade span at the design operating conditions.

The operational engine inlet for the T55-L-712 engine was used during all tests. This inlet has four radial struts at equal circumferential spacing. The struts are placed approximately 1.5 blade chord lengths upstream of the first stage rotor and are large enough to contain shafting for the starter motor and the auxiliary power pull off shafts.

3.5 THE T55-L-712 TURBOSHAFT ENGINE

The T55-L-712 turboshaft engine is a gas turbine engine in the 12 Kg/sec class. The compression system is driven by a two stage gas generator turbine. The combustor is a reverse flow, annular type. The power turbine consists of two axial stages and its output shaft is positioned coaxially within the compressor shaft.

This engine and its compression system are described in much greater detail in [4].

3.6 INSTRUMENTATION

Instrumentation for this test was originally specified to fulfill data acquisition requirements for the U.S. Army investigation into the intermittent "hung start" condition exhibited by the T55-L-712 powered CH47D aircraft. Additional instrumentation was added to both the compressor rig and the full engine to explore in detail the unsteady aerodynamic compressor flow phenomena occurring during the approach and transition to surge.

3.6.1 Rig Instrumentation

Steady state compressor research instrumentation included shroud static pressures, vane

mounted total pressures, and thermocouples at each stator.Vane mounted pressures and temperatures were located at equal area radial locations There were 497 steady state pressure sensors, and 153 temperature sensors.

High response rig instrumentation consisted of 34 flush mounted wall static pressure transducers. This instrumentation included three sets of eight transducers located approximately one half chord upstream of each of the first three compressor rotors, a single pressure transducer located upstream of each of the first seven stators, and a set of three transducers located in the vaneless space downstream of the centrifugal compressor. The transducers were electrically ranged for best signal to noise ratio. Rig reference transducers were mounted similarly, but were blind to the flowpath in order to determine if transducer response was vibratory or aerodynamically induced. Additional information on rig instrumentation is provided in [1] [5].

3.6.2 Engine Instrumentation

Engine steady state instrumentation consisted of 122 pressure sensors and 65 temperature sensors. In addition to instrumentation placed in similar axial/radial locations to the rig, engine instrumentation included total pressure and temperature rakes in the bellmouth region upstream of the engine inlet.

Engine high response instrumentation consisted of 64 pressure transducers, twenty four of which were flush mounted in the same axial/radial/circumferential rig locations in front of the first three stages (three sets of eight). Additional engine high response pressure transducers were placed in six mach probes in front of the engine at 25%, 50%, and 75% span. Further, flush mounted hub transducers were placed in the first three stages and at one total pressure location for each stage. These total pressure sensors and the mach probe transducers are remotely mounted approximately 15 cm from the sensing tip using infinite line probes. This feature degrades frequency response for these remotely mounted probes and information thus acquired must be analyzed with caution.

Table I provides locations for the research instrumentation and Table II indicates transducer size. Instrumentation in similar positions on the rig are indicated with an asterisk Equivalent rig test tables are available in [1].

3.6.3 Summary of Instrumentation Differences, Rig and Engine

Reference [1] contains a detailed listing of instrumentation used during the rig testing and Tables I and II in this report provide similar information for the engine test. Nevertheless, it is appropriate here to note, in summary form, the differences in compressor instrumentation between rig and engine.

Upstream of the engine, in the research inlet, two sets of total pressure rakes and temperature rakes are used to measure inlet profiles and integrated massflow. The rig tests provided massflow using a calibrated bellmouth. Substantial other differences exist in the inlet area.

In front of the first stage rotor, the engine has Mach probes at 25%, 50%, and 75% span.

Steady state instrumentation on the stators is at identical span locations for stages 1, 2, and 3. For stages 4, 5, and 6, the rig has only three radial locations while the engine continues to have five radial locations. The rig stator instrumentation is at three circumferential locations while the engine has only one and the engine has hub static pressure readings for all axial stages, while the rig is instrumented for only the first three stages.

The high response pressure transducer locations for the shroud at the first three stages are the same. The engine has additional hub transducers in the first three stages not present on the rig. The other major difference between rig and engine high response pressure transducers is that an axial string of static pressure transducers exists on the rig that has been replaced by an axial string of total pressure transducers on the engine.

3.7 DATA AQUISITION/ REDUCTION

3.7.1 Introduction

Reference [1] describes in detail the rig test data reduction procedures, thus only engine data acquisition/reduction will be discussed in detail.

A total of 61 dynamic data sequences, including choke, load line and surge, were recorded during the rig testing. Steady state readings were acquired for each dynamic reading with the exception of the transitions into surge. For the surge dynamic events, a steady state reading was acquired at the steady operating condition that marked the start of the dynamic event.

During the engine testing, a total of 807 steady state readings were acquired and a total of 74 high response transient or dynamic events were also recorded. Start data was acquired at ground level and also at 5 km pressure altitude (0.84305×10^5 N/m^2) while all ground idle surge events were acquired at ground level. Sequential steady state (once per second updates) datasets were acquired during each start sequence. Normally a dynamic dataset was also acquired during each start, although not all were digitized. For constant speed transitions to surge at ground idle, a sequential steady state was acquired during each surge along with a dynamic dataset. To date, three surge events have been recorded.

3.7.2 Rig Steady State Data

Rig test steady state data were acquired using a TEXTRON/Lycoming data acquisition system which allowed all 556 steady state measurements to be simultaneously acquired, reduced and/or calculated, and updated every 4 seconds. Data were provided to the VPD by TEXTRON/Lycoming in flat ASCII format on 3.5 in floppy disks. A total of 180 operating points were acquired at 20, 30, 40, 50, 60, 70, 80, 85, 90, 95, and 100% design speed.

Data were reduced using a TEXTRON/ Lycoming in-house code. Data were processed by data ensemble averaging and a two pass data rejection technique and were corrected for wire corrections, probe geometry, velocity and density corrections, and humidity [5].

3.7.3 Rig Dynamic Data

All pressure transducers were AC coupled and uncooled. Data were recorded on a 28 channel analog recorder and transferred to LeRC for post processing. Tape speeds for low speed (80% and below) provided a bandwidth of 20 kHz/channel and for high speed (above 80%) provided a bandwidth of 40 kHz/channel.

The digital filtering and spectrum analysis of all transient (high response) data both rig and engine, were done using a commercially available software package, IDARS. Each finite impulse response (FIR) filter was designed with 16384 coefficients. All high response data was analyzed at the LeRC using the same Concurrent super-minicomputer. Data tape output was digitized at LeRC using the Creare IDARS and Scanalyzer systems. Data were initially low pass analog filtered at 3 kHz before digitizing at a rate of 9 kHz/channel to satisfy Nyquist criteria. All filtering of data

following the initial low pass analog filtering was digital.

3.7.4 Engine Steady State Data

Steady state pressure data is sensed using an electrically scanned pressure (ESP) system manufactures by Pressure Systems, Inc. ESP output is processed by signal conditioners and then sent to the Escort D system. All thermocouples are type K. Output from the thermocouples is also conditioned before being sent to the Escort D system.

The Escort D/D+ system provides real-time data acquisition, display, and control for the vast majority of test facilities at the Lewis Research Center (LeRC). The system includes a Digital Equipment Corporation (DEC) VAX microcomputer (microVAX 3100) located at the test facility, providing the bulk of the real time processing for the test, and a number of mainframe VAX computers (VAX 4000/200 systems) located at the central computing facility (RAC) for data storage and post-processing. The Escort system uses a distributed Ethernet system for intercomputer communications [6].

For this series of tests, the system scans and updates the readings every second. Start data was continuously acquired for 60 seconds after the initiation of data acquisition thus capturing the entire start sequence or the transition to rotating stall/surge.

3.7.5 Engine Dynamic Data

High frequency data from pressure transducers and thermocouples were acquired for all starts and for all rotating stall sequences.

A total of 64 pressure transducers, 26 thermocouples, and a once-per-rev (OPR) signal were recorded as high response instrumentation.

These data were recorded in three ways. Twenty six of the most critical channels were recorded on analog tape in the test facility, allowing a recorded bandwidth of up to 80 kHz/channel. All data was backed up on analog tape in the Research Analysis Center (RAC). This data was transmitted over land lines and bandwidth limited to approximately 12 kHz/channel by the landlines. All channels were also digitized during the data acquisition process. Two A to D convertors were available for digitization. Twenty-six pressure channels were digitized at a rate of 12685 samples/second/channel and the remainder of the data were digitized at the "low" rate of 4875 samples/second/channel. The higher sampling provides a frequency resolution of up to 5 kHz, resulting in resolution of the first stage blade passing at ground idle.

4.0 DATA ANALYSIS

4.1 Backround

Fundamental differences exist between a rig and an engine test. These differences can lead to discrepencies between data acquired in each of these environments. Discrepancies can result from differences in 1) hardware, 2) testing methodology, 3) thermal environment, and 4) control methods.

Hardware Differences. This program did not use the same compressor hardware for the rig and the engine testing. Rig tests were done on a compressor used only for rig testing. This compressor, while standard in configuration, had never been used in a complete engine. The T55-L-712 used for the engine testing was a rebuilt field engine acquired directly from the Corpus Christi Army Depot. While both the compressor rig and the engine meet "specs", differences in blade shapes, clearances, and surface finish certainly do exist.

Further differences exist in the components around the compression system. Figure 1 shows a non-dimensionalized meridional view of the flow paths for the rig (1a) and the engine (1b). Clearly, differences exist in the ducting upstream of the compressor. The hub contour for the rig extends well upstream while the engine hub contour is that of a bullet nose. Downstream of the compressor there exists a volume and an exit area. This is either a chamber and a choked valve (for the rig) or the combustor followed by the gas generator turbine. Meridional views of these components are shown in figure 2. Clearly, the reverse combustor of the engine is difficult, if not impossible, to duplicate in the rig. These system differences are likely to result in differences in compression dynamic performance characteristics.

Lastly, safety considerations restricted the instrumentation installed in the engine. Steady state instrumentation installed on the stator leading edges was restricted to one set (two vanes) per stage rather than sets of three that were installed in the rig. Conversely, this restricted instrumentation set reduced stator blockage in the engine, possibly modifying stage performance.

Differences in Testing Methodology. Clearly, the principal advantage to rig testing lies in its controllability (hence, repeatability). Rig operating conditions can be accurately set and maintained. It is normally a steady speed environment where steady state (speed line) and dynamic (rotating stall/surge) data are acquired.

Engine testing, on the other hand, is primarily an environmant where transient data is acquired. While steady state data can be acquired on a constant speed line and, with limitations, of the operating line with, for example, combustor inbleed, engine testing is more appropriately suited for the investigation of transient and overall system events.

Of course, another advantage to engine testing is the ability to more nearly replicate field engine operation.

Thermal Effects. One of the more obvious differences between rig and engine operation is the presence of a combustor downstream of the compressor. Heat soak effects can result in measurable performance differences between the rig and engine test results. Differences can result not only from system geometry changes due to heating but also due to changes in fluid (air) characteristics due to heat transfer. Additionally, the recverse flow, or blowdown, process during a surge cycle will transport very hot gases during the surge. This is not the case in a rig test.

Control Effects. Rig testing is a steady speed environment where the desired operating speed can be accurately maintained for both speed line mapping and for dynamic events such as surge. During engine testing, the engine will not continue to run following the occurrence of the first dynamic event (surge pulse). Thus, compressor speed will be changing during the surge.

Indeed, even at a steady operating point, the engine operation varies slightly due to combustor/fuel control unsteadiness.

The results presented below will explore differences between rig and engine tests up to ground idle. High speed engine testing is expected in the summer of 1995.

4.2 Comparisons of Steady State Results

Figure 3 shows overall pressure rise vs corrected massflow for all speeds between 20% and 70% of design speed. These data were

acquired during the Stratford rig testing. Also shown in this plot is a typical ground level engine start. Engine start data plotted is the steady state data acquired at 1 sample/second/ channel during the start. Start data is divided into speed ranges as shown in the table associated with the figure.

It is clear from this plot that a considerable amount of uncertainty exists in the massflow measurements at the lower flow/speed ranges. Variations of over 10% of design corrected massflow are calculated between adjacent points. As has been mentioned earlier, massflow is calculated by integrating massflow over the inlet using static to total pressure ratios and temperature measurements from rakes in the inlet. Considerable unsteadiness exists in the inlet during start, however, these uncertainties are probably the result of the low fluid velocities and calculation sensitivity to the measurements. Differences between static and total pressures early in the start are of the order of 0.003% of the measured value and such small differences are difficult to measure with certainty due to inherent measurement errors.

The most striking feature about the start shown in figure 3 is the fact that the engine is operating on the left side of the stall/surge line. Apparently the compressor is operating in rotating stall during most of the start. However, this does not mean that all stages are in rotating stall. Unfortunately, no rig test data were acquired in these operating regions because it was assumed that the engine would not operate here during the start sequence.

The stage matching at the ground idle point appears somewhat different. Notice that while the overall pressure ratio for the compression system fall on the 60% speed line, stage 7 appears to be operating below the speed line and, conversely, the centrifugal stage above its characteristic. An explanation for this observation has yet to be determined.

It must be noted that during the start testing, a starter disengagement parametric study was performed with the engine successfully completing the start sequence with the starter disengaged as low as 22% of design speed.

Figure 4 shows selected hub to shroud pressure profiles for the rig and engine testing at 60% of design speed. Clearly, no noticable differences exist between the rig and the engine compressor pressure rise, with the exception of the centrifugal stage. Here, the pressure profile for the engine reading shows substantial scatter. Whether this scatter is the result of instabilities in the combustor, a truly more non-uniform engine flow field due to hardware differences, or are merely data uncertainties remains to be determined.

Figure 5 shows the hub to shroud temperature profiles for the same stations as figure 4. It is difficult to make quantitative assessments of the data presented here. A number of engine thermocouples, such as the inner reading at the stage 7 may be inoperative. However, several observations can be made. The temperature rise, even for the stages not presented, is greater along the hub streamline than along the shroud. This is true for both rig and engine results. The temperature gradient from hub to shroud at the inlet is rather shallow. It is much more prominent at the exit of the diffuser (centrifugal stage) for both rig and engine. It appears larger for the engine test results but a review of the data indicates there is no substantial difference in temperature rise between the rig test and engine test results. Unfortunately, a direct comparison is not possible because at this location, the radial locations differ between the rig and engine test.

Figure 6a presents massflow vs time at ground idle and figure 6b shows measured variations in rpm vs time for the same period. Figure 6c shows the variations in pressure ratio for that

time interval. Variations in all parameters at ground idle are relatively small with massflow variations on the order of 4% of the ground idle massflow and pressure ratio variations less than 3% of the ground idle pressure rise. Notice that the normal engine sensor can only resolve the speed within 4.5 Hz or 2.38% of the ground idle speed. However, a once-per-rev sensor integrating over one second indicates that speed is remarkably steady, varying only 2 Hz at ground idle. Some slow cyclical variations may be occurring in pressure rise and massflow, but these conclusions await additional analysis.

4.3 Comparisons of Dynamic Results

Figure 7 shows a pressure trace vs time for a shroud wall static pressure transducer during a typical engine start. This transducer is located approximately one chord length upstream of the first stage rotor on the shroud and is one of eight circumferentially mounted transducers at the same axial location. Data from the same transducer has been presented in figures 7, 8, and 9. The large size of the pressure signal indicates that a dynamic event, such as rotating stall/surge is occurring in the compression system during much of the start sequence and grows in intensity as the start progresses. Indeed, as was indicated by the steady state data, the compression system operates in rotating stall from the beginning of the start sequence until approximately 50% of design speed. Ground idle is slightly over 60% of design speed.

An analysis of the transducer data indicates that this dynamic phenomena originates in the first stage of the compressor. A comparison of stage loadings indicates that the first stage is the most highly loaded of the axial stages. Earlier analysis of rig test data [7] has shown that in this compression system, the first stage initiates surge/rotating stall for all speeds from 60% speed to design speed. .

Figure 8 shows a pressure trace at approximately 11.5 seconds into the start or about 18% of design speed. Further analysis is needed to understand the dynamic nature of the phenomena and their effects on the start sequence but it appears, on close inspection, that the first stage remains critical at below ground idle speeds. However, the interactions between the axial stages have yet to be understood.

During the start sequence, the number and strength of the stall cells in the compression system vary. Initially, four stall cells exist. By 40% of design speed, this number has been reduced to three and immediately preceeding the end of the rotating stall phenomena at 50% of design speed, only a single stall cell is present in the first stage.

The dynamic behavior of the engine compression system was studied at ground idle to compare engine and rig operation. To surge the engine, the start bleed, which is normally open at ground idle, was closed.

Figure 9a shows the 60% surge event measured in the rig while figure 9b shows the ground idle (~61%) surge event induced in the engine. The cluster of five sharp spikes in figure 9a is the first surge pulse. Each of these sharp spikes is a rotating stall pulse passing the transducer. The large pulse shown at the extreme right of figure 9a is the beginning of the second surge pulse. The differences between figures 9a and 9b is striking. While the rig surge (9a) is marked by clearly separated patterns of rotating stall/surge and recovery, the engine event (9b) is notable for the fact that rotating stall never disappears from the system and no clear surge is discernable.

There are two possible explanations for this difference. The more likely cause of the discrepency is the difference in bleed opening size. For the rig test, the bleed was set to the

nominal open position and surge was induced by closing the exit throttle. For the engine test, the bleed valve was slowly closed to induce surge. This certainly changed the volume dynamics, although the extent is not clear.

Other possible causes for the discrepency are in the operation of the fuel control and combustor. In the case of the engine, the fuel control will attempt to maintain a constant operating speed by adjusting the fuel rate to the engine. It is unlikely that the bandwidth for this system is high enough for this to be the reason. It is possible that the dynamics of the combustion process and its interactions with the rapid air flow variations resulting from the surge are modifying the system response. Another possibility is the clear differences in the shape between the downstream rig dump and the engine combustor. Differences in the way the two volumes exhaust during the surge cycle may effect the event. Further, there is no clear surge in the engine dynamic event, which appears to be governed by the rotating stall. Rig test surge frequency is about 9 Hz.

The effect of the differing bleed areas must await the high speed testing, where surge will be induced using combustor inbleed rather than the stage six start bleed.

Notice, however, the similarities in the rotating stall cells that preceed the surge event for both rig and engine surge events. The shapes and rotational speeds (~61% of the rotor speed) are nearly identical for both. This is to be expected since rotating stall is much more a blade row than a system phenomena.

5.0 DYNAMIC MODELING

The T55-L-712 compression system has been modeled in a one dimensional dynamic model, DYNTECC [8]. Both geometries were modeled and are shown in figure 1. The code operational variables were adjusted for the rig geometry to provide a typical surge event signature for 60% of design speed. The engine event was then simulated using the same values for the operational variables.

figure 10 shows plots of compressor pressure ratio vs massflow and the overall compressor pressure ratio vs time for both geometries. figure 10 a provides rig geometry and figure 10b shows engine results. There exist few predicted differences between the two geometries. the most noticable difference is a difference in surge frequencies between the rig and engine geometries of 1 Hz. Whether such a difference exists will be resolved when engine testing resumes this summer.

Notice, the simulation indicates the engine should surge. This suggests that the change in geometry that results from using the start bleed to induced surge cause the discrepency between the measured rig and engine surge events.

6.0 SUMMARY OF RESULTS

The preliminary analysis can be summarized as follows:

1) Few steady state performance differences can be noted between compressor rig and engine data up to the ground idle point (60% of design speed).

2) During the start sequence, the engine compression system operates in rotating stall. The number of stall cells varies from four at low speeds to one near 50% of design speed. The stall cells are located in the first stage.

3) Fundamental differences exist between the rig surge event and the engine surge event at 60% of design speed. While it is likely that the different methods used to induce surge is the

cause, this cannot be verified without additional testing.

4) A one dimensional dynamic compression system model has been applied to both systems. Additional work will be required to properly tune this model.

5) At this point, it appears that rig testing can be successfully used for steady state and start transients, but perhaps not for surge behavior, due to burner, bleed or other differences.

7.0 SUMMARY

As part of the US Army's Non-Recoverable Stall program, complementary rig and engine testing has been accomplished on the Allied-Signal (formerly Lycoming) T55-L-712 axi-centrifugal turboshaft engine. This testing will continue for both the engine and rig. The program will result in one of the most complete sets of complimentary rig and engine data to ever be assembled in the open literature.

A preliminary analysis of rig and engine test data indicate that no substantial differences exist between the rig and engine data acquired. Substantial additional analysis of data must be done.

ACKNOWLEDGEMENTS

The author wishes to publicly recognize a number of persons and organizations crucial to the presentation of this paper and the continuation of this program. Mr. Stephen Etter, Dr. Arun Sehra, Mr. Sanjay Hingorani, and the entire engineering and technical staff at Allied-Signal/Stratford must be recognized for their professional and dedicated efforts. Mr. Tom Griffin, Ms. Kristy Csavina, Ms. Theresa Kline, Mr. Barry Piendl, and the entire engineering/technical staff in NASA Lewis' ECRL test facility. I wish to thank Mr. Vern Edwards, Mr. Gary Kellog and the Propulsion Systems Division of the U.S. Army's ATCOM for financial and programmatic support. Lastly, I wish to thank Mr. George Bobula whose encouragement was critical to the completion of this paper.

REFERENCES

1. Owen, A.K., "Analysis of Rig Test Data for an Axial/Centrifugal Compressor in the 12 Kg/Sec Class", AGARD Conference Proceedings 537, Technology Requirements for Small Gas Turbines, March 1994.
2. Owen, A.K, and Bobula, G.A., "Analysis of Dynamic Rig Test Data for an Axial/Centrifugal Compressor Operation at Design Speed", Presented at the American Helicopter Society 50th Annual Forum and Technology Display, May 11-13, 1994.
3. "The Engine Components Research Laboratory", Aeropropulsion Facilities and Experiments Division, Lewis Research Center, Aug 1993.
4. "Design Report for the T55-L-712 Turboshaft Engine", Report LYC 78-26, Jan, 1981.
5. Etter, S. and Hingorani, S., "T55-L-712 Start-Up Stall Investigation, Contract NAS3-26698, TEST PLAN", May 5, 1993,(Proprietary).
6. Blahe, R.J. (Editor), "ESCORT D/D+, Users Manual', NASA Lewis Research Center, First Edition, July 1993.
7. Owen, A.K. and Davis, M.W., "Modeling the Dynamic Behavior of an Axial-Centrifugal Compression System", AIAA Paper AIAA-94-2802,, June 27-29, 1994.

8. Hale, A.A. and Davis, M.W.,Jr., "DYNamic Turbine Engine Compressor Code: DYNTECC -- Theory and Capabilities", AIAA Paper 92-3190, Presented at the 28th Joint Propulsion Conference and Exhibit, Nashville, TN, July 1992

TABLE II
PRESSURE TRANSDUCER USE

Location	Type,Size
Rotor 1 Inlet Mach Probes	50Lbf/in^2, absolute
Rotor 2LE, shroud Rotor 3LE, shroud	50Lbf/in^2, absolute
Rotor 1LE, shroud	15Lbf/in^2, absolute
Stator 1 inlet, hub Stator 1 exit, hub Stator 2 inlet,hub Stator 3 inlet, hub	15Lbf/in^2, absolute
Stator 1 inlet, Stator 2 inlet, shroud	50Lbf/in^2, absolute
Inlet Totals, Stators 1,2,3,4,5,6,7	50Lbf/in^2, absolute
Rotor 1LE	15Lbf/in^2, absolute
Rotor 3LE	50Lbf/in^2, absolute
Stage 1LE Stator	5Lbf/in^2, gauge
Stage 2LE Stator	15Lbf/in^2, absolute
Stage 3LE, 4LE	25Lbf/in^2, absolute
Stage 5LE, 7LE	50Lbf/in^2, absolute

TABLE I
RESEARCH INSTRUMENTATION

STEADY STATE

TYPE	NUMBER	RADIAL LOCATION	AXIAL LOCATION
Inlet Total Pressure	18	2.5%,5%,10%, 20%,50%,80%, 95%,97.5% Span	Research inlet well upsteam of engine inlet
Inlet Total Temperature	18	2.5%,5%,10%, 20%,50%,80%, 95%,97.5% Span	Research inlet well upsteam of engine inlet
Inlet Static Pressure	4*	Shroud Hub	Same axial location as total pressures
Inlet Total Pressure (One Each Fore and Aft Facing)	2* 2* 2*	25% Span 50% Span 75% Span	Approximately 2 chord lengths upstream rotor 1
Inlet Total Temperature	2* 2* 2*	25% Span 50% Span 75% Span	Approximately 2 chord lengths upstream rotor 1
Endwall Static Pressures	2* 2*	Shroud Hub	One Chord length upstream of Rotor 1
Endwall Static Pressures	1 or 2* 1 or 2*	Shroud Hub	Leading Edge of all stators (1 for stages 1,2,3)
Endwall Static Pressures	1 1	Shroud Hub	Trailing Edge of Stators 1,2,6
Total Pressures	5	Equal radial areas between endwalls	At each stator leading edge
Total Temperatures	5	Equal radial areas between endwalls	At each stator leading edge
Total Pressures	3* 3* 3*	25% Span 50% Span 75% Span	At Centrifugal Diffuser Leading edge
Total Temperatures	3* 3* 3*	25% Span 50% Span 75% Span	At Centrifugal Diffuser Leading edge
Static Pressures	3*	Shroud	At Centrifugal Diffuser Leading edge
Static Pressures	12	Shroud	Bleed Orifice Static Pressures

*Approximately equally spaced circumferentially

HIGH RESPONSE TRANSDUCERS

TYPE	AXIAL LOCATION	CIRCUMFERENTIAL LOCATION
Forward/Aft Facing Total Pressures	Upstream of rotor 1 - 2 chordlengths	25% Span -0° and 180° 50% Span 60° and 240° 75% Span 120° and 300°
Static Pressure	Rotor 1 Inlet	11.733,58.65,103.78,150.68, 191.733,238.65,283.77,324.82
Static Pressure	Rotor 2 Inlet	3.783,50.45,103.78,143.78, 183.78,230.12,283.78,330.45
Static Pressure	Rotor 3 Inlet	4.33,51.0,117.67,151.0, 184.33,237.67,297.67,331.
Total Pressure	Stator 1 Inlet	Approximately 0°
	Stator 2 Inlet	
	Stator 3 Inlet	
	Stator 4 Inlet	
	Stator 5 Inlet	
	Stator 6 Inlet	
	Stator 7 Inlet	

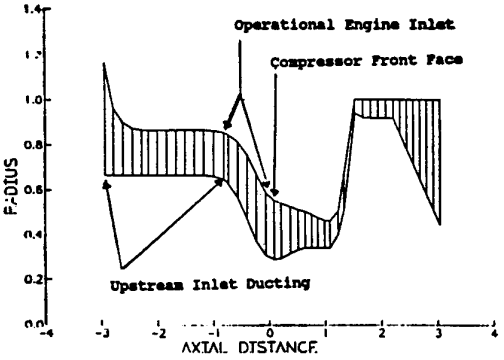

1a) Rig Configuration

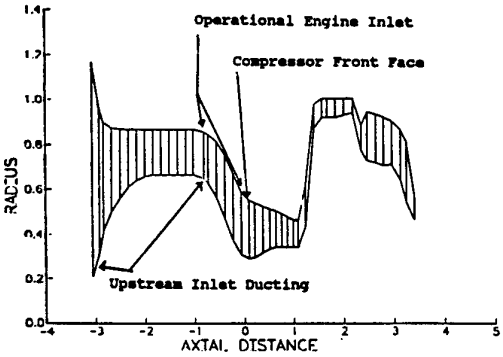

1b) Engine Configuration

Inlet Meridional Flow Paths
Figure 1

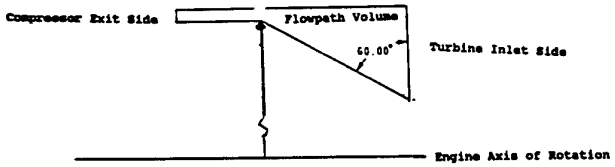

2a) Rig Configuration

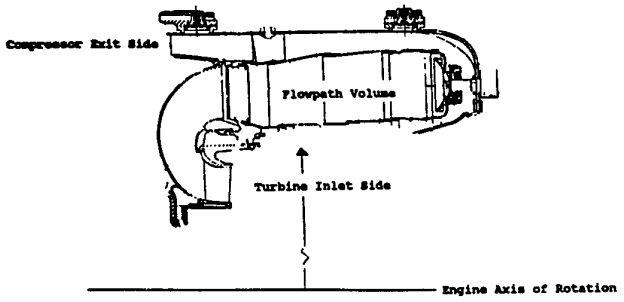

2b) Engine Configuration

Combustor Meridional Flow Paths
Figure 2

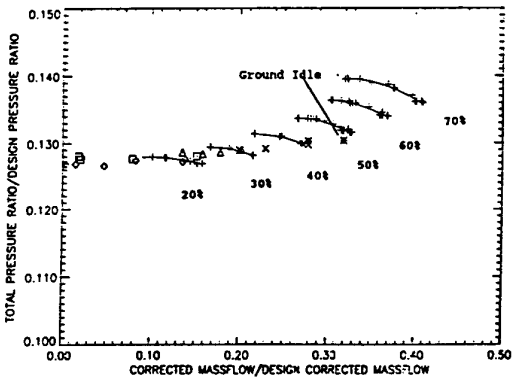

3g) Stage 7 Pressure Rise

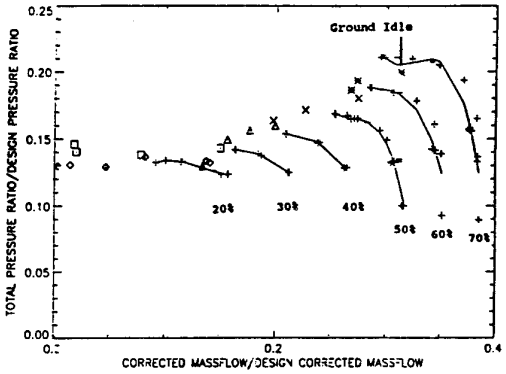

3h) Centrifugal Pressure Rise

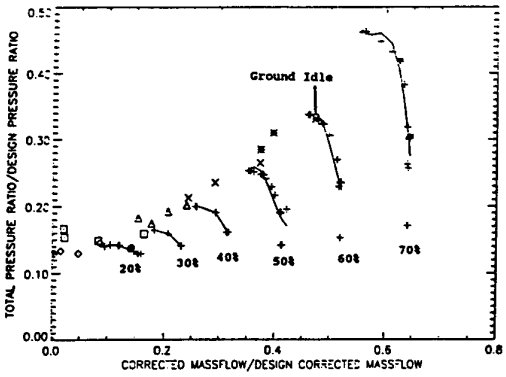

3i) Overall Compressor Pressure Rise

◇ >25% Design Speed
□ Between 25% and 35% Design Speed
△ Between 35% and 45% Design Speed
× Between 45% and 55% Design Speed
✱ Above 55% Design Speed

Compressor Pressure vs Massflow Map
Figure 3

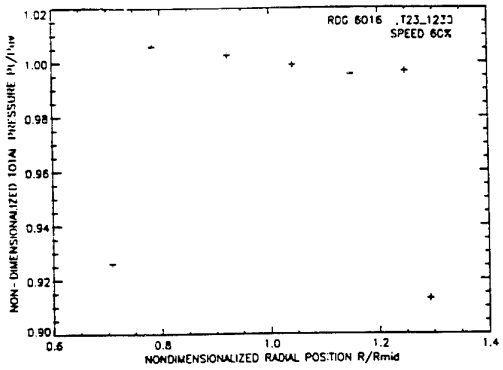

3e) Rig Test Stage One

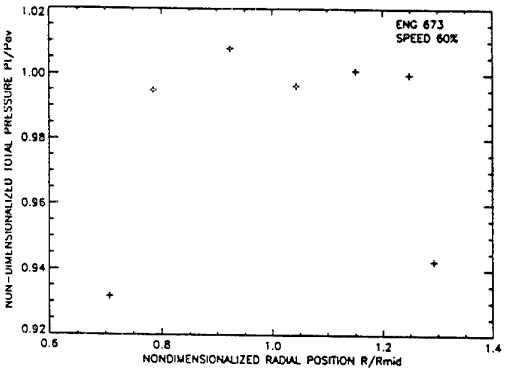

3f) Engine Test Stage One

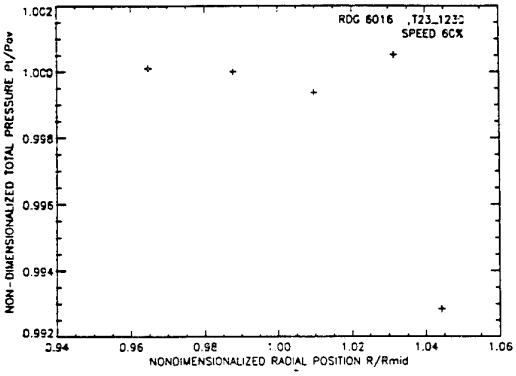

3a) Rig Test Centrifugal Stage

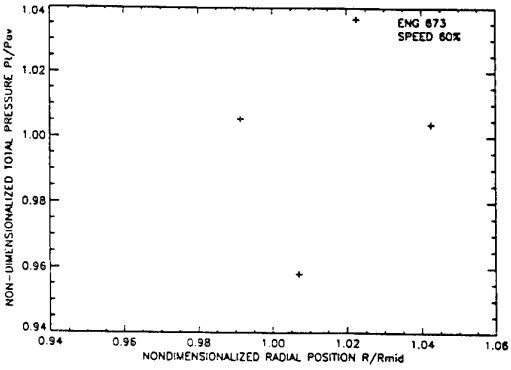

3b) Engine Test Centrifugal Stage

Rig and Engine Radial Profile Pressure Rise
Figure 4

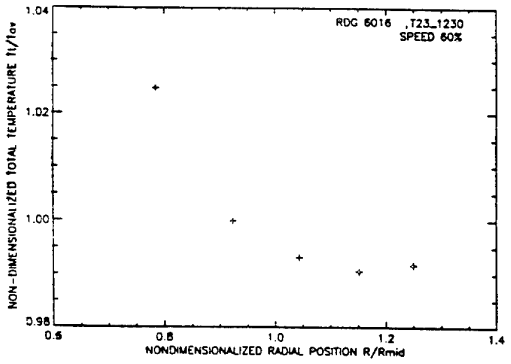

5e) Rig Test Stage One

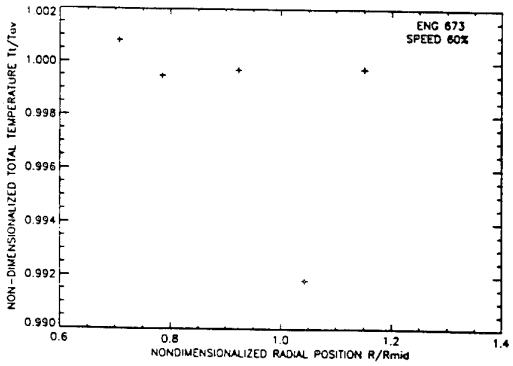

5f) Engine Test Stage One

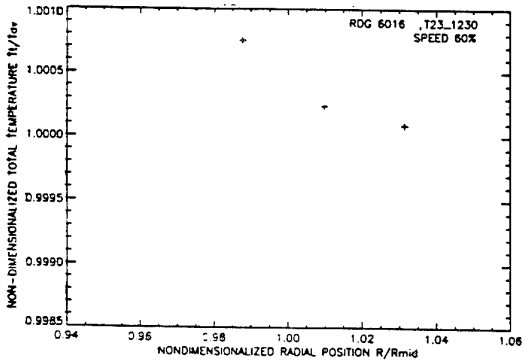

5a) Rig Test Centrifugal Stage

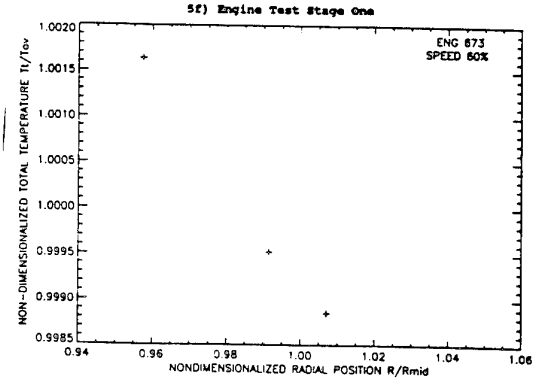

5b) Engine Test Centrifugal Stage

Rig and Engine Radial Profile Temperature Rise
Figure 5

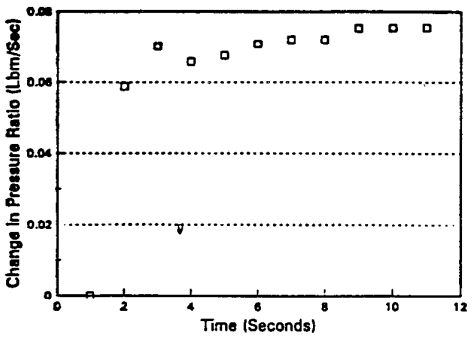

6c) Compressor Pressure Ratio vs Time

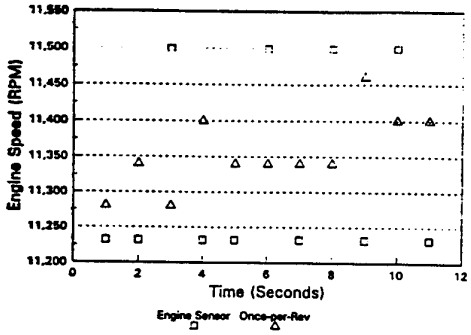

6b) Engine RPM vs Time

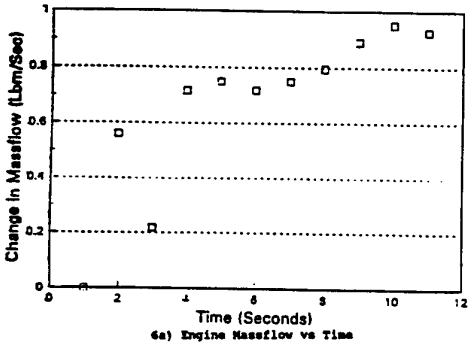

6a) Engine Massflow vs Time

Variations in Engine Parameters at Steady Ground Idle
Figure 6

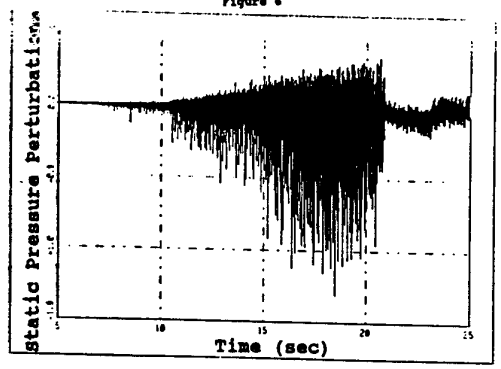

Typical Inlet Shroud Static Pressure Transducer
Static Pressure Transducer Start Trace
Figure 7

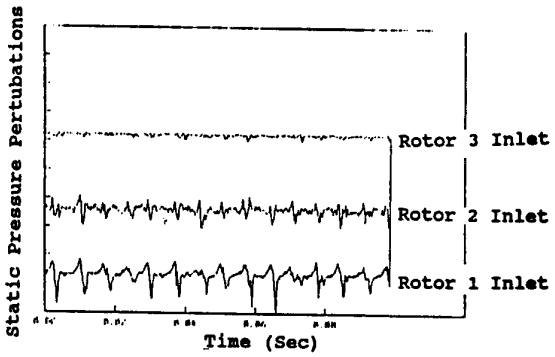

Static Pressure Transducers Start Trace - Axial String
Figure 8

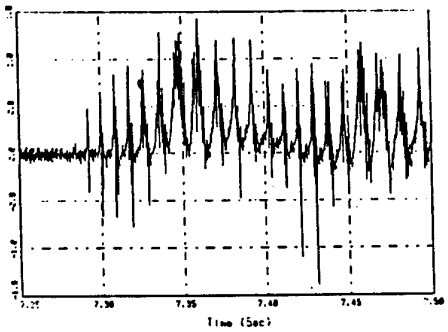

9b) Surge Event During Engine Testing

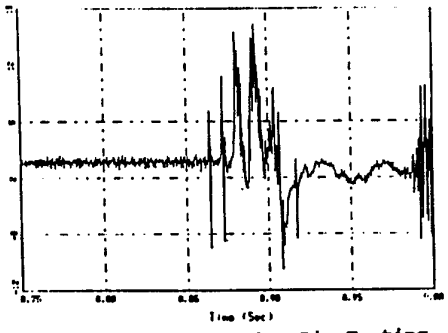

9a) Surge Event During Rig Testing

Typical Inlet Shroud Static Pressure Transducer
Static Pressure Traces for Surge at 60% of Design Speed
Figure 9

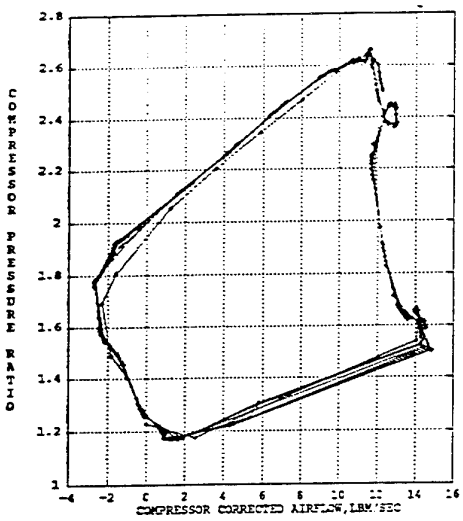

Pressure Ratio vs Massflow

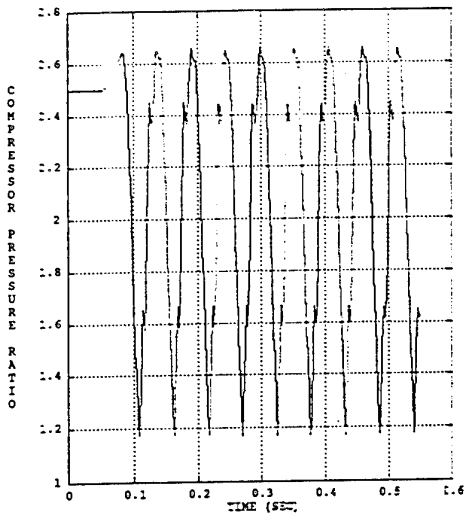

Pressure Ratio vs Time

10b) Engine

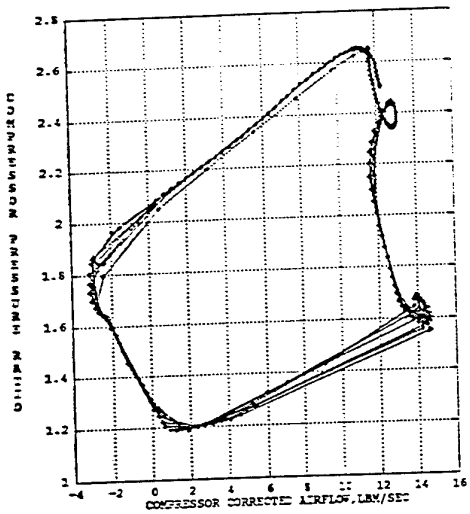

Pressure Ratio vs Massflow

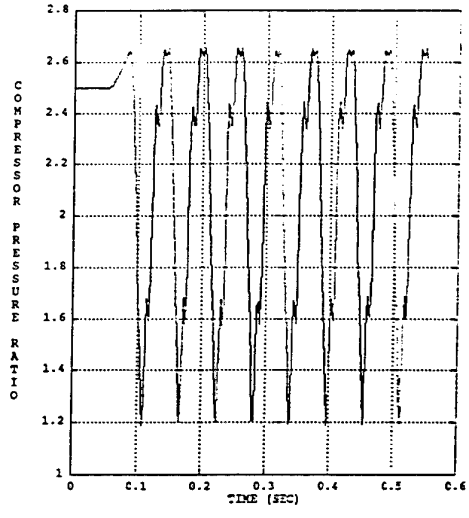

Pressure Ratio vs Time

10a) Rig

Simulations of Surge Events at 60% of Design Speed
Figure 10

REFERENCE NO. OF THE PAPER: 28

DISCUSSOR'S NAME: T. Breuer

AUTHOR'S NAME: A.K. Owen

Q: The author mentioned the application of an active stability control system at the end of the year '95. Could the author outline in more detail how to achieve this (instrumentation, hardware used, detection algorithm used)?

A: Specific hardware for the active stall/surge control is 8 high speed valves (450 Hz), eight jet ejectors 1 chord length in front of stage 1, max total injected mass flow for all 8 jets 5% of design. Detection algorithm could be either the MIT linearized analysis of an in-house algorithm. See papers by Mattern, D.L., "A Voice Coil Actuated Air Valve For Use in Compressor Forced Response Testing", and Bright, M.M., "Dimensional Determination of Precursive Stall Events in a Single Stage High Speed Compressor". Both presented at the Third Technical Conference on Nonlinear Dynamics (Chaos) and Full Spectrum Processing, July 10-14, 1995, American Institute of Physics and NUWC

REFERENCE NO. OF THE PAPER: 28

DISCUSSOR'S NAME: A.G. Wilson, Rolls-Royce, U.K.

AUTHOR'S NAME: A.K. Owen

Q: Greitzer - B type analysers suggests that compressor instability will be rotating stall-type at low speed and surge-type at high speed. At what speed did the changeover occur on the rig and on the engine?

A: In the rig, a clear surge occurred at all speeds from 60% up to design speed. 50% speed represented a very mild surge event. Speeds below 50% of design speed represented rotating stall type events.

In the engine, the compression system operated in rotating stall until about 51% of design speed - with the bleed fully open. When a dynamic event occurred at ground idle (61% of design speed) in the engine, it was induced by closing the bleed. As the plot (Fig. 96) would suggest, it appears to be a rotating stall. However, there are indications that some "surge-like" behavior is occurring.

Indeed, your question highlights differences between rig and engine operation that are likely the result of differences in bleed operation. Notice that all surge events began as rotating stall events in the first stage. Also note that the length of time the rotating stall event was present was inversely proportional to speed.

REFERENCE NO. OF THE PAPER: 28

DISCUSSOR'S NAME: C. Lam, Rolls-Royce GTE, Canada

AUTHOR'S NAME: A.K. Owen

Q: Given the difference in inlet geometry between the compressor rig and engine, did you attempt to simulate the engine profile on the rig? It appears to me that a difference in inlet profile could impact the characteristic of the highly-loaded rotor 1, and hence cause the rig-to-engine difference.

A: We did not attempt to duplicate the endwall boundary layer profiles from the rig test when doing the engine test. Indeed, differences between inlet configurations could make a difference in compression system performance, although we have yet to notice any significant difference. Unfortunately, instrumentation was not available to measure the rig's inlet boundary layer.

REFERENCE NO. OF THE PAPER: 28

DISCUSSOR'S NAME: R.G. Wells, E.G.T., U.K.

AUTHOR'S NAME: A.K. Owen

Q: Could you confirm the differences in bleed flows between the compressor rig testing and the engine tests. What percentage bleed flows were used?

A: Data have not been completely reduced at this point, and additional analysis of the bleed data must be done to quantify bleed flows for both. For the rig testing, bleed was set to a nominal 20% to match normal engine operation. The bleed was partially closed (to about 30% of its nominal opening) to induce surge in the engine. This does not, however, mean that the bleed flow was reduced a comparable amount.

Surge and Stall Characteristics of Axial-Centrifugal Compressors: The Enhancement to Engine Stability

W.T. Cousins
Engineering Specialist
AlliedSignal Engines
P.O. Box 52181, M/S 554-16
Phoenix, Arizona 85072-2181
USA

M.G. Jones
Manager
AlliedSignal Engines

T.L. Belling
Engineering
AlliedSignal Engines

SUMMARY

The characteristics of axial-centrifugal compressors in gas turbine engines that provide an enhanced tolerance to engine stall and surge are presented. The incipient, post-stall, and recovery behavior of axial-centrifugal compressors is described. Unique high-response measurements showing the pressure/flow characteristics of post-stall behavior are presented and the measurement techniques are discussed. Comparison of compressor stall and surge, with and without a centrifugal stage, shows the benefit of using axial-centrifugal technology in gas turbine engines.

A discussion is presented on the importance and the technique of detecting the compressor stage that has the potential to initiate instability under highly-loaded conditions. Data are presented from both compressor rigs and engines. An explanation of how to distinguish the stalling stage prior to surge in a compressor is included. The effect of interstage bleed on the axial-centrifugal stage match in the engine environment is shown, along with the changes in surge initiation due to speed mismatch that can occur at high altitude conditions.

INTRODUCTION

The stability characteristic of gas turbine compressors is one of the major operationally limiting factors in the design of the machine. Researchers have been examining the characteristics of stall and surge behavior of gas turbine engines for many years. Much research has been presented on the *characteristics* of stall and the *characteristics* of surge, but little has been discussed on the stall and surge differences inherent in various configurations of compressors. Different configurations of compression systems have different stall and recovery characteristics. Over the past 40 years, volumes of material have been written describing why stall and surge occur and what the characteristics look like. The original work by Emmons (1) in 1954 started the modeling of stall and surge. Model development continued for years and in the mid-1970's work by Greitzer (2) showed a system interaction and a system dependence on the development of rotating stall and surge. Moore (3) took a compressor map characteristic and defined an axisymmetric characteristic (on which the compressor would operate if it did not stall) as part of a system description of unstable operation. While the system approach to the understanding of stall and surge continued, a second approach to examining the phenomenon came about through the work by such individuals as Sexton (4), Cousins (5), Boyer (6), Kimzey (7), and Davis and O'Brien (8). Through these works and others, it was shown that to model compressor unstable operation, a system model is not enough. Observations in these publications show how the balance of blade row operational loading conditions, loss increases, and flow stability determine the stall and surge behavior of a compressor.

Data obtained in 1985 by Cousins (9) showed surge and rotating stall beginning in the same manner, through local flow separation of the blade row. This local separation grew into either a full rotating stall or grew large enough to disturb the overall pressure balance of the machine, causing a surge. In 1993, Day (10) presented data showing this effect, and stated that it shows that surge is always preceded by rotating stall. In a sense, this is not quite true because the flow disturbance is not yet a fully developed rotating stall and what is being observed is the local blade row separation that starts both rotating stall and surge. While this separation may rotate and exist over multiple rotations of the compressor, one must be careful about identifying it as "rotating stall" since this connotation is often thought of as being a nearly stable stalled condition.

The stall that is present prior to surge (and in fact, prior to the the quasi-stable fully-developed rotating stall) is a rapidly changing local blade row instability, growing in both the spanwise direction and in circumferential extent. It starts with only a few blades, then grows rapidly until it develops into a stable rotating stall or until the system energy balance is such that a surge occurs.

Recent work by many people in the area of "active stabilization" of compressors discuss "disturbance waves" upstream of the compressor. The authors of this paper believe that these "waves" are not a function of the system properties but rather an observation of the upstream flowfield disturbance caused by the same local blade row separation that initiates rotating stall and surge behavior. While measured in low-speed machines or in high-speed machines run at low speed, it is somewhat questionable whether this pressure disturbance would be sensed upstream of a properly designed high-speed compressor where the stage that initiates compressor instability is usually in the rear and the front of the compressor is operating near choke.

Paper presented at the AGARD PEP 85th Symposium on "Loss Mechanisms and Unsteady Flows in Turbomachines", held in Derby, United Kingdom, 8-12 May 1995, and published in CP-571.

The resolution to the ongoing dilemma of using the system approach or the blade row approach to understanding compressor instability is as simple as realizing that both approaches are in fact necessary and complementary to one another. The system approach to understanding stall and surge in compressors is of no value without the considerations of the detailed blade row aerodynamics. On the other hand, working with only the blade row aerodynamics is of no value without the considerations of the system behavior (upstream and downstream volumes, etc.). That is, the inception of instability in a compression system is governed by the individual blade rows, their loading, and their respective match points on their characteristics. The system does not come into play in determining stall inception, unless it itself is somewhat unstable (due to its energy storage capability, or lack thereof) and forces an unstable local blade-flow response and loading. But even in this case, the instability itself begins with a blade flow separation. Stall inception, therefore, is a function of the local blade loading and loss generation in the compressor. Once stall inception occurs, whether the compression system will exhibit rotating stall or surge behavior (or even become stable again) is a function of the system response, as shown by Greitzer (2) in his work performed in the mid-1970's.

What does this all mean to the design of a compression system? It means, that a thorough understanding of the blade loading and stage matching characteristics, *in addition* to understanding the overall system response due to the upstream and downstream energy storage capability of a compression system is necessary to design a machine with "good" stability characteristics. If care is taken while choosing a compression system during the design phase of an engine, the stability characteristics of the resulting engine can be enhanced.

The compression system most tolerant of flow disturbances is the multi-stage centrifugal compression system. This is due to the large percentage of total pressure rise obtained through the radial flow component of the velocity vector. Of course, whether an engine compression system is designed around a multi-stage centrifugal compressor, an axial compressor, or an axial-centrifugal compressor is a function of the size class of the engine. There is a range of compression system flow size where a multi-stage centrifugal compression system is clearly the best system to use in terms of efficiency, cost, weight and reliability. On the other end of the scale, at larger flows, there is a point at which centrifugal compressors become too heavy and the efficiency characteristics unacceptable for propulsion applications, and the axial compression system is the best choice. Between the appropriate size class for a multi-stage centrifugal compressor and that where an all axial machine is appropriate, there lies a class of axial-centrifugal compression systems that can be designed to provide the best of both worlds. When a multi-stage centrifugal compressor is clearly not the correct choice, the decision often must be made on whether to use an axial compressor or an axial-centrifugal compressor. Properly designed axial-centrifugal compression systems make use of the stability enhancing characteristics of the centrifugal compressor to enhance the characteristics of the axial portion of the machine and reduce the buildup of losses. In an aircraft, this provides a compression system with higher tolerance to stall and enhanced stall recovery characteristics.

The purpose of this paper is to present data to show the loss increases (through the pressure characteristics) in a compression system prior to reaching the stability limit and to show the stability-enhancing benefits of well designed axial-centrifugal compression systems in propulsion engines.

It is important to note that the acquisition of high-response data quickly results in quantities of data which are quite large. What is presented in this document is only a fraction of the data analyzed to arrive at the documented results. It is felt by the authors that presenting a reasonable quantity of data from several machines is better than presenting a large amount of data from a single compression system.

COMPRESSION SYSTEMS EXAMINED AND INSTRUMENTATION USED

Several configurations of axial-centrifugal compression systems were used to demonstrate the concepts presented in this work. These were a research compressor rig, the TFE1042 compressor rig, the TFE1042 engine, and the TFE731 engine. The TFE731 engine is of a split-core configuration, that is, the axial and the centrifugal compressors are on different spools. The other compression systems are designed with the axial and the centrifugal compressors on the same spool. These two configurations have some different characteristics, which will be discussed.

While there are many ways to examine the unsteady flows in a compression system, one of the better methods is the monitoring of the pressure field with high response transducers. These can be used to measure both steady-state pressure levels and the rapid pressure changes that occur during the stall and surge process. To arrive at good results, a high regard for the flow physics and an understanding of the flow in the compression system is necessary. Data signals from high response transducers can be easily mis-interpreted by well meaning analysts, if they are not familiar with instrumentation frequency response, effects of tape recording on data, and digital sampling theory. The results discussed here meet the criteria for good high-response data and are well within the accuracy and frequency requirements necessary for the analysis performed.

The measurement systems used to obtain the results of this work involve standard steady-state measurement systems normally used in compressor rigs and engines, and also high response transducers designed to measure either total or static pressure, depending upon the analysis requirements.

Measurement of Flow Through a Complete Surge Cycle

To examine the pressure/flow characteristics of a complete surge cycle, measurements capable of providing information through both forward and reverse flow in the compressor are necessary. Figure 1 shows a forward and aft facing probe that is used for this purpose. This special probe was designed to provide high-response data with a frequency response up to 5,000 Hz. The head of the probe contains two Kulite high-response pressure transducers, a high-response shielded thermocouple, and two steady state pressure measurements. The steady state pressure measurements were used as an in-place check of the pressure levels displayed by the high-response system. The probe is water cooled to keep the temperature of the transducers at a constant value, eliminating

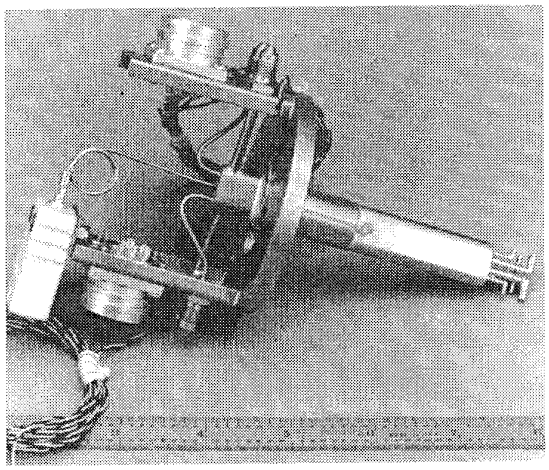

Fig. 1 Fore-Aft Probe Used for Measuring Full Surge Behavior

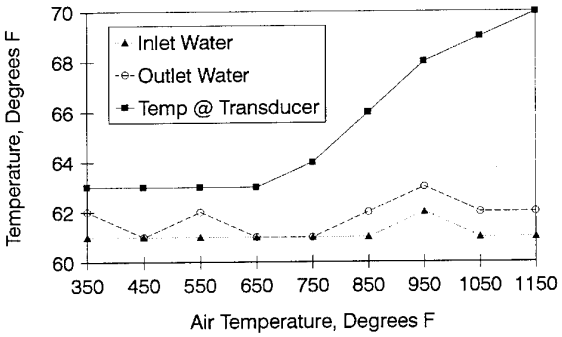

Fig. 2 Fore-Aft Probe Cooling Characteristics (water flowrate of 0.4 gal/min)

the worry of pushing the transducer past its compensated temperature range. While this is not a problem in the front of a compressor, use of this type of probe behind a compressor in the high-temperature environment or in an engine environment requires this special care. Figure 2 shows the results of a temperature test of the probe in a ceramic oven. Thermocouples specially built into the water passages of a development probe provided the temperature information near the transducer site, the inlet water temperature, and the exit water temperature. The water cooling passages in the probe were designed to pass volumes of water that could be easily obtained at a normal water faucet, eliminating the need for any special equipment.

Careful calibration of the fore-aft probe in a flow facility is required prior to use. While the forward-facing element reads total pressure during normal compressor operation, the aft-facing element reads a pressure value representative of the wake of the probe and is therefore neither total or static pressure, but is thought of as a "wake static." Using the total pressure, temperature, and the wake static pressure, a "pseudo Mach number" can be calculated. Using the true Mach number (calculated from the flow facility instrumentation) and the pseudo Mach number calculated from the probe values, a calibration curve can be drawn for forward flow over the probe. Figure 3 shows a typical calibration curve for the fore-aft probe. Also, knowing the flow values from the

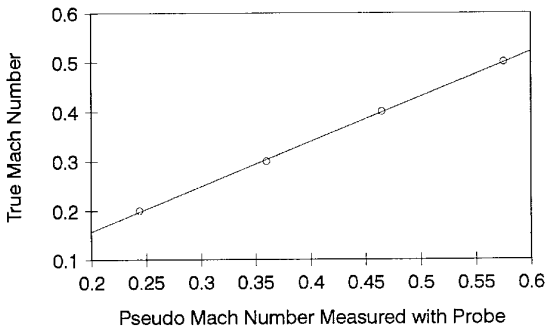

Fig. 3 Typical Mach Number Calibration for the Fore-Aft Probe

facility, a curve of Mach number versus flow per unit area can be developed. Once this information is obtained for the forward flow configuration of the probe, the probe must be turned around in the flow facility and the "reverse flow" configuration calibrated, developing the same information. During a compressor surge, the appropriate calibration curve must be applied depending upon the direction of flow at the probe. This is determined by a continuous comparison of the values of the two high-response pressure measurements. The element with the highest value is assumed to be facing into the flow.

For the probe described here, pitch and yaw calibrations were also performed in both the forward and reverse flow directions. It was found that the yaw acceptance of the probe was about 25 degrees for the forward facing element and about 15 degrees for the aft (wake-static measuring) element. Pitch angle acceptance of the probe was about 12 degrees, due to the large probe body that was necessary to provide the capability of a water-cooled probe. In many applications, water cooling is not necessary, depending upon the compensated characteristics of the high-response transducers, but during the development of this probe, knowing that it was going to run in both the engine and the rig during repeated surge tests, the decision to use water cooling was made.

Obtaining correct data using the fore-aft probe therefore requires proper probe design, calibration, and placement in the flowfield. This must be based upon a thorough understanding of the characteristics of the probe, knowledge of the local flow swirl angle, slope of the compressor flowpath, and an understanding of the environmental conditions under which the probe will operate.

Using the probe in a compressor where a good inlet flowrate measurement can be obtained by using a bellmouth or similar measuring device allows a curve of true Mach number versus actual inlet corrected flow to be developed during steady state measurements. This avoids using the Mach number versus flow per unit area calibration curve, reducing the chance for error. Of course, the assumption of relatively planar flow is made when using this type of probe, unless one is willing to use several probes around the circumference of the compressor and then averaging the result. Typically, the complexity of doing this is not worth the increased accuracy for the type of data being obtained. As it turns out, surge is a relatively planar event and for the type of time-dependent data being obtained, the use of multiple probes is not worth the effort and cost.

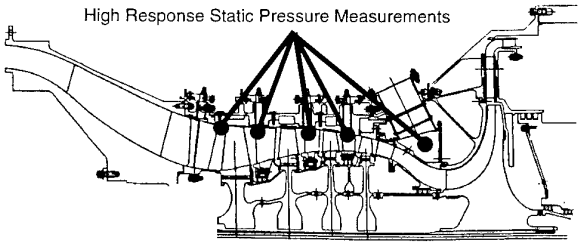

Fig. 4 Research Compressor Rig

The Research Compressor

The research compressor was developed as a high-technology 5-stage machine, with 4 axial stages and one centrifugal stage, as shown in Figure 4. Designed as a minimum-stage-count, maximum-performance machine, it has a design pressure ratio of about 15 at a corrected flow of 22 lbm/sec.

In addition to a full complement of steady-state instrumentation, flush-mounted high-response pressure transducers were located behind the inlet guide vane (IGV) and behind the first three axial rotors. A fourth transducer was located behind the fourth stator. This compressor rig was run both with and without the centrifugal stage, allowing the examination of the effect of the centrifugal stage on the axial compressor.

The TFE1042 Compressor Rig

The TFE1042 compressor rig also consists of a four stage axial compressor and a single stage centrifugal compressor mounted on the same shaft, as shown in Figure 5. This particular configuration of the rig has a movable IGV and fixed vanes. This compressor is different from the research compressor in that its design pressure ratio is about 6.5 at a corrected flow of 25 lbm/sec.

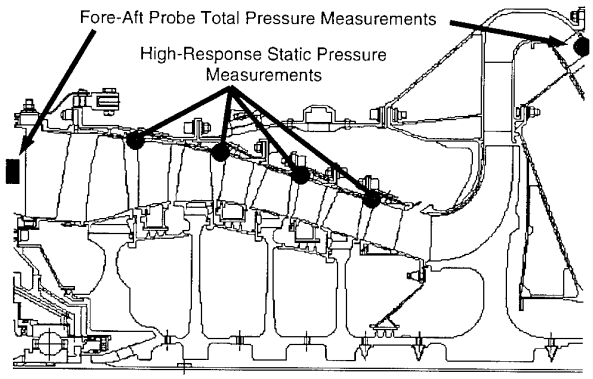

Fig. 5 TFE1042 Compressor Rig

In this compressor, in addition to the stage-based high-response static pressure transducers, two high-response fore-aft probes were installed. One was located at the inlet to the IGV at fifty percent span and the second was located at the centrifugal compressor diffuser exit. Through the use of these two probes, the complete surge cycle was obtained. The configuration of the centrifugal diffuser and deswirl vane system was different in this rig than in the engine which is described in the next section. The difference affects the post-stall behavior of the rig, and this will be shown later in this paper.

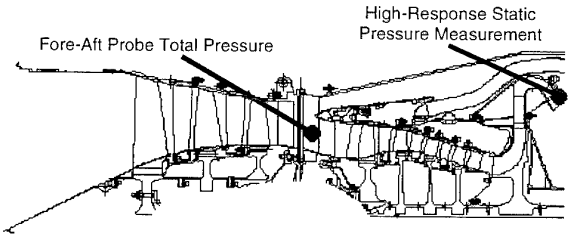

Fig. 6 TFE1042 Engine Configuration

The TFE1042 Engine

The TFE1042 is an afterburning turbofan engine in the 10,000 pound thrust class (during afterburner operation) with a bypass ratio of approximately 0.5. Since the overall stall and surge characteristics of an engine are a function of the fan and the core compressor match, some data will be presented to show the characteristics of both fan initiated and core compressor initiated surge behavior. The axial-centrifugal compressor in this engine (Figure 6) provides it with a unique stall tolerance and enhanced recovery capabilities.

In the engine, a fore-aft probe was installed at the compressor inlet location just in front of the splitter, as shown in Figure 6. At the compressor exit, the expansion differences in the engine internal and external case parts prohibited the use of the second fore-aft probe without some case modification for the instrumentation. Since this was not desirable in this test, a high-response static pressure was obtained at the compressor exit and used as though it were a total pressure, because the local flow velocity at the measurement station was approximately Mach 0.15.

The TFE731 Engine

The TFE731 engine has a core compressor that is slightly different than those already presented. This compressor is of a split core design, with the four stage axial compressor and the single stage centrifugal compressor on different spools, as shown in Figure 7. The spool shafts are concentric with the axial main shaft housed within the centrifugal spool. This compressor configuration, of which there are several variations, has been proven successful after many years of operation in the TFE731 engine line and demonstrates unique enhanced stability characteristics.

In this engine, the measurements used for the data presented herein were the static pressure at the axial compressor exit and the total pressure at the centrifugal stage exit.

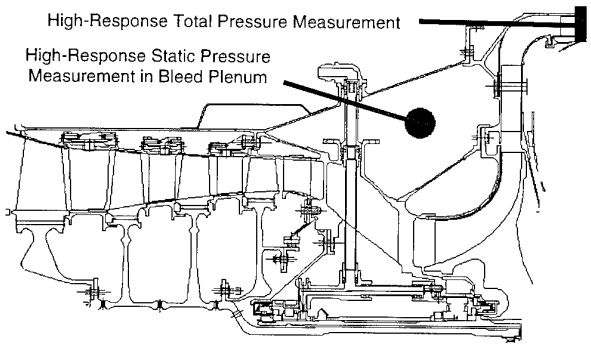

Fig. 7 TFE731 Split Core Configuration Compressor

TEST RESULTS AND BASIC CONCEPTS

Axial-Centrifugal Stage Matching

Proper stage matching between the axial compressor and the centrifugal compressor is critical to enhancing the stability tolerance of the compression system. As previously described, since the centrifugal compressor tends to be very tolerant of its inlet conditions, designing it so it "helps" the axial portion of the machine is possible. In well designed compression systems, the front stages of the compressor are designed to operate near their stability limit and the back of the compressor is designed to operate near choke when the machine is operating at low speed. At high speed, the reverse is true. The back end operates near it's stability limit while the front end is matched near choke. In general, this provides the most stable machine and is consistent with the physics of the flow as the compressor operating point moves toward high-speed operation. With an axial-centrifugal compression system, this general rule is the same, but if the centrifugal compressor is designed with enough range, it can be kept out of triggering the compressor instability. The centrifugal compressor stage then acts as a *stability enhancing* device to the axial compressor. Figure 8 shows the typical stage matching for an axial-centrifugal compression system where the stability is enhanced by the centrifugal stage. The following results will show the effect of the centrifugal stage on the stall and surge behavior of an axial compressor.

When observing the pressure field at the exit of a rotor, the flow stability over the rotor blade surface can be examined. As the flow over a rotor blade begins to separate, the local static pressure downstream of the blockage must drop since the local fluid has lower momentum. Upstream of the separated blade, the local static pressure rises. Using this as a guide, the *surge trigger* can be defined for a compressor operating at a particular speed. Figure 9 shows a pressure trace and the start of the blade row blockage (the surge triggering stage) as determined through the use of the high-response transducers on the TFE1042 compressor rig during a portion of the development test. In a well designed axial-centrifugal compressor, this surge trigger is controlled through the design configuration and the system operation such that the surge trigger remains in the axial portion of the compressor. The following results show the characteristics and the stability enhancing properties of a well-matched, well-designed system.

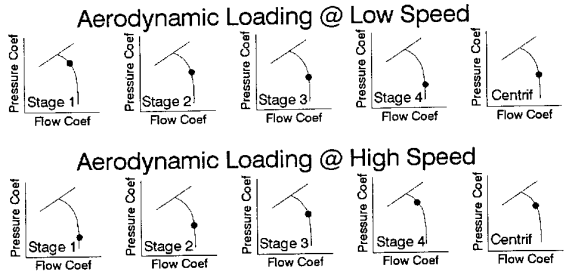

Fig. 8 Aerodynamic Loading of a Well-Designed Axial-Centrifugal Compressor for Enhanced Stability

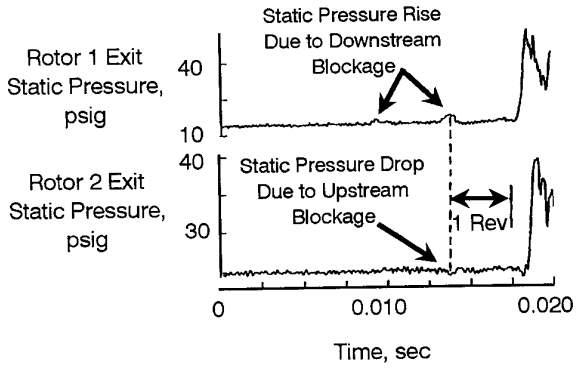

Fig. 9 Static Pressure Indication of Blockage in the 2nd Compressor Stage

Research Compressor Results

Figures 10 and 11 show the differences in the surge characteristic with and without the centrifugal compressor. The points that are labeled on the figure are as follows:

A Surge initiation at the stability limit of the compressor

B Point of maximum surge overpressure due to backflow of the compressor

C Point of minimum flow (seen as the maximum static pressure behind the IGV after the backflow)

D Point of minimum pressure, where the compressor starts to pump again

E Point at which the compressor has reached a steady-state condition again

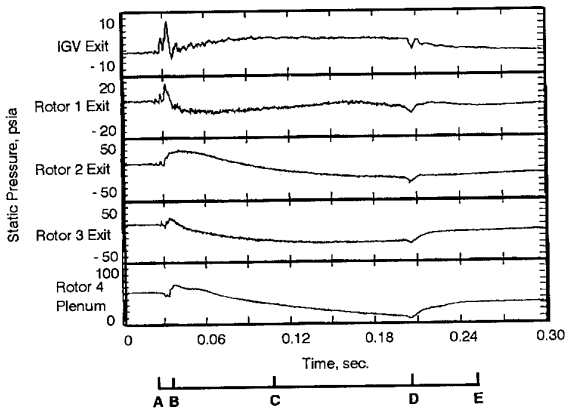

Fig. 10 Surge in the Research Compressor at 97.5% Corrected Speed with Centrifugal Stage

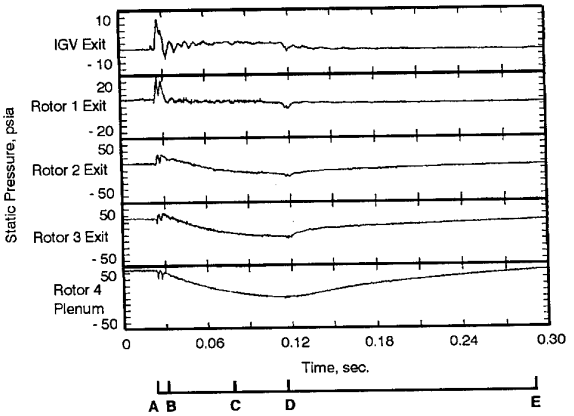

Fig. 11 Surge in Research Compressor at 97.5% Corrected Speed without Centrifugal Stage

During this test, the compressor was operating at 97.5 percent corrected speed. In Figure 10 at point D, the effect of the centrifugal stage's early pumping capability can be seen as the pressure throughout the axial stages drops due to the enhanced recovery effects of the centrifugal stage. In Figure 11, as the back of the axial begins to pump again, the pressure upstream can be observed dropping. Detailed examination of the time required to complete the surge cycle is as follows:

POINT	TIME WITH CENTRIFUGAL STAGE	TIME WITHOUT CENTRIFUGAL STAGE
A - B	11 ms	5 ms
B - C	70 ms	52 ms
C - D	99 ms	46 ms
D - E	38 ms	175 ms

The time to move from the stability limit of the compressor to the point of maximum backpressure (point A to B) is longer in the axial-centrifugal compressor than in the axial only compressor. This is to be expected because the centrifugal compressor chokes on backflow, limiting how fast the blowdown can occur. The same is true from B to C and from C to D, since this is part of the backflow portion of the surge cycle. The recovery portion of the cycle (from point D to E), is significantly faster with the centrifugal stage in place. This is because the centrifugal compressor stage recovers very quickly from a stalled condition since most of the pressure rise in the centrifugal stage comes from the radial flow. As long as the stage is rotating, it will try to pump. Examination of the data shows the compressor recovery with the centrifugal stage present is almost 5 times faster than the recovery with only the axial compressor. The inception and blowdown portion of the surge cycle (from A to D) takes 180 ms with the centrifugal stage present and 103 ms without the centrifugal stage. One might be lead to think that the faster the inception/blowdown portion of the cycle, the better off the system would be since the surge would be over faster. However, this is not true. Since the difference in the recovery time is so large, the total surge cycle is actually faster with the centrifugal stage in place (218 ms with the stage and 278 ms without the centrifugal stage).

There is another benefit to the centrifugal stage choking during the surge cycle, and while it can not be seen in Figures 10 and 11, it is important to mention here. When the centrifugal compressor chokes on backflow and the compressor is designed such that the surge trigger is in the axial portion of the machine, the surge overpressure that is experienced in front of the compressor is significantly reduced. This can not be seen in the research rig results since the two sets of data are at a different pressure ratio (and while this doesn't affect our time data already presented it does affect the overpressure level). This overpressure level dependence on the surge trigger will be shown later in this paper in the TFE731 results, where the surge trigger is intentionally changed from the axial to the centrifugal stage in the same compressor configuration.

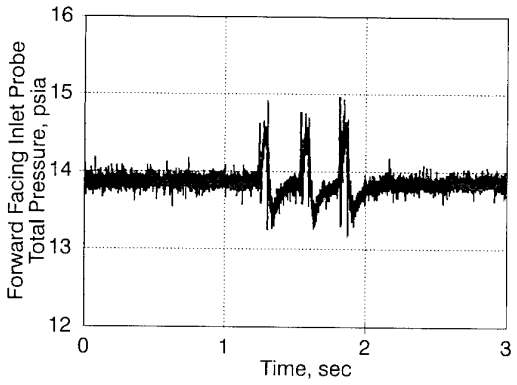

Fig. 12 Inlet Fore-Aft Probe Total Pressure

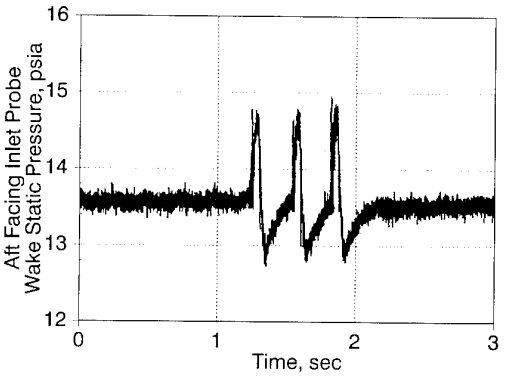

Fig. 13 Inlet Fore-Aft Probe Wake Static Pressure

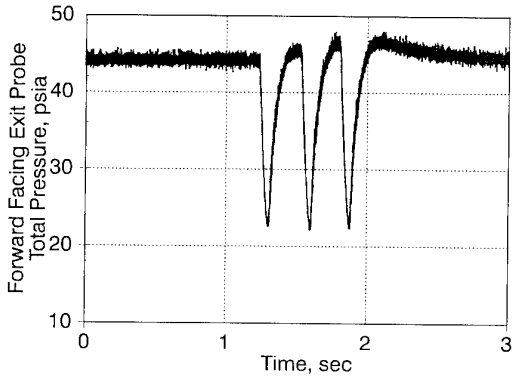

Fig. 14 Exit Fore-Aft Probe Total Pressure

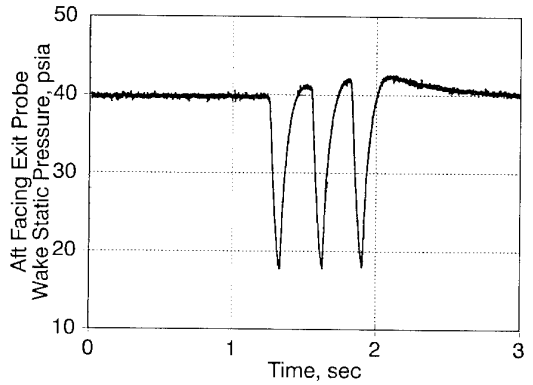

Fig. 15 Exit Fore-Aft Probe Wake Static Pressure

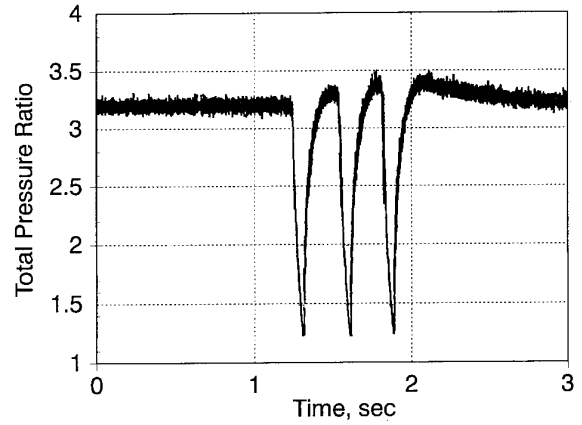

Fig. 16 Total Pressure Ratio Measured with Fore-Aft Probes

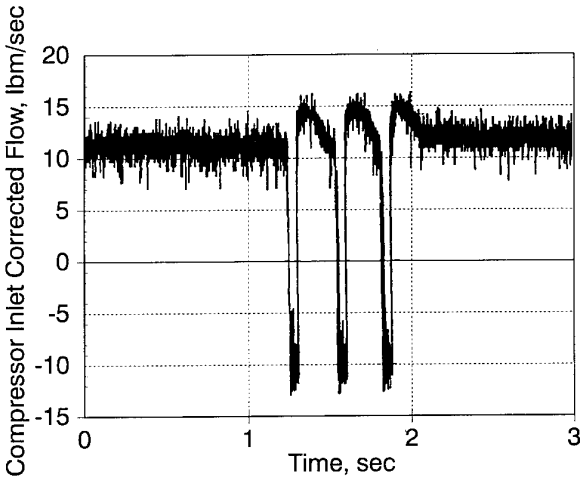

Fig. 17 Compressor Inlet Corrected Flow Measured with the Inlet Fore-Aft Probe

TFE1042 Rig Results

Data obtained in the TFE1042 compressor rig using the fore-aft probes previously discussed, allowed examination of the detailed surge behavior of the compressor rig through the complete surge cycle. Figures 12 through 15 show the individual data signatures from the inlet and exit high-response fore-aft probes, as the compressor goes through three surge cycles at 80 percent corrected speed. Figures 16 and 17 are calculated traces obtained by using the traces in Figures 12 through 15. The traces in Figures 12 through 15 are actually a display of the analog data traces that have been digitized at a rate of 5000 Hz. During the pressure ratio calculation (shown in Figure 16), the pressure difference across the individual probes is monitored such that the elements that are measuring total pressure (rather than wake static pressure) are being used. Of course this is critical to the calculation as the compressor goes into full reverse flow during the surge cycle. Figure 17 shows the compressor inlet corrected flow during the same three surge cycles. To obtain this trace, the calibration curve of pseudo-Mach number versus inlet corrected flow was used. As with the total pressure ratio, the Mach number calculation must be performed while monitoring which of the elements of the inlet probe is measuring total pressure (and therefore proper flow direction).

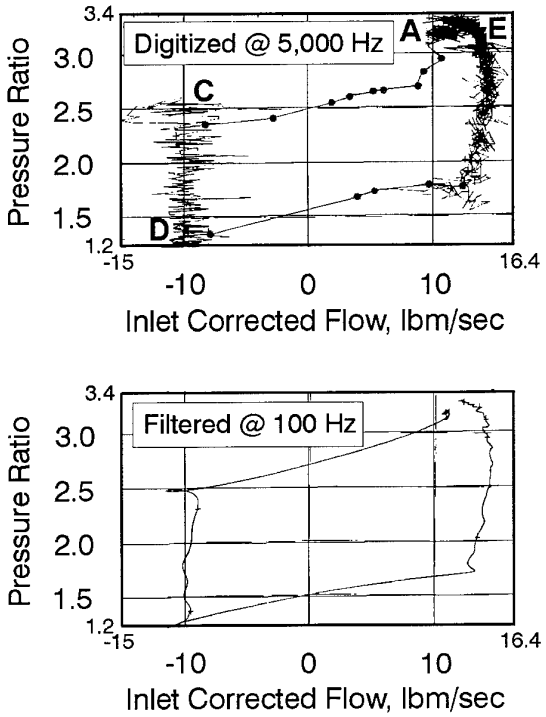

Fig. 18 Full Surge Cycle Measured on the TFE1042 Compressor Rig at 80% Corrected Speed

Examining only the first surge cycle and plotting the total pressure ratio and the compressor inlet corrected flow gives the surge cycle on a compressor map, as shown in Figure 18.

There are several observations that can be made about this surge cycle that need to be pointed out. First, the compressor pressure ratio gets fairly close to a value of 1.2, that is, the exit pressure get very close to the inlet pressure at the end of the blowdown cycle. Second, the actual flow reversal (going through zero flow) happens between the top of the total pressure trace and the minimum on the total pressure trace. Another way to see this would be to expand the traces from the inlet probe and plot the trace from the aft element on top of the trace from the forward element. Whenever the aft element pressure is higher than the forward element pressure, the flow is reversed.

Time to move through the surge cycle can be observed also. Since the digitizing rate of this data was 5000 Hz, the time between data points is 0.2 milliseconds. The points that correspond to the points in the research compressor discussion have been placed on Figure 18. The time to move from the stability limit to the start of the choked portion of the blowdown cycle is 1.6 milliseconds. The time to move from the bottom of the choked portion of the blowdown cycle across the bottom of the surge cycle to the start of the pressure recovery is 0.8 milliseconds. As was the case in the research compressor, the speed at which recovery occurs is quite fast, due to the centrifugal compressor enhancing the recovery. (These times cannot be directly compared to the research compressor times because the research compressor times include some of the unsteady inception time seen in Figure 18 at the stability limit where the surge starts. Also included is some of the repressurization time seen on the right side of the surge cycle. Exact comparison of the surge cycles of the two

compression systems could only be compared if there were a fore-aft probe in the research compressor, but the probe was developed only after the research compressor data was obtained.)

The last item of importance to note in the rig high-response surge cycle measurement is that the high-response data falls exactly on the steady-state measured stability limit. This was the case even if the downstream discharge valve on the compressor rig was closed in as rapid a manner as possible. Although not as fast as the effect of a fuel pulse in the engine, this test did provide some assurance that the core compressor on the engine (on which data was to be obtained after this rig test) could be mapped using high-response measurements in the core.

TFE1042 Engine Results

This turbofan engine, as with any turbofan, can have an engine surge initiated in the core compressor or in the fan. It is really quite easy to determine if an engine surge is triggered by either the fan or the core compressor, through the use of a high-response transducer behind the fan. Figure 19 shows an engine surge initiated by a stall in the fan section of the engine. The static pressure behind the fan falls off rapidly as the fan stalls. Once that happens, the core compressor experiences a drop in inlet pressure, and therefore suddenly sees a higher pressure ratio than it can sustain. The operating point on the core compressor is forced up the compressor characteristic to the stability limit of the compressor and a compressor surge occurs, driving the peak static pressure behind the fan up to a level higher than it was at the fan stall point. The backflow continues in both components as the engine surge progresses. On high bypass engines, it is possible to see the fan stall and undergo a backflow from the bypass only, while the core compressor keeps pumping. In this case, the spike seen in Figure 19 that is caused by the core compressor does not exist. If the core compressor initiates the engine surge, the fan stall indicated in Figure 19 does not occur. Instead, the compressor overpressure spike occurs as the first disturbance in time. This same behavior and general trace interpretation can be used in an axial-centrifugal compressor to identify a surge trigger as existing in the axial or in the centrifugal stage. This will be discussed to a greater extent in the next section.

Figures 20, 21, and 22 show a series of three surge cycles measured on the TFE1042 engine. These surge cycles were initiated by a fuel pulse at 80 percent compressor inlet corrected speed so they could be compared to those measured in the compressor rig. Many surges (over 80, with distorted and undistorted inlet conditions) were obtained and the data used to verify that the compressor rig was providing the same stability characteristics as the compressor in the engine. This was accomplished and the core compressor was "mapped" in the engine, proving that the compressor in the engine was responding in the same manner as the compressor rig. This technique was used to validate that the rig generated compressor maps that were being used in the performance computer model for the engine were in fact correct. The rig and the engine had the same stability limit (since that is governed by the blade row loading and the compressor match), while the post-stall behavior is slightly different. Examination of the post stall behavior shows that the engine surge cycle has

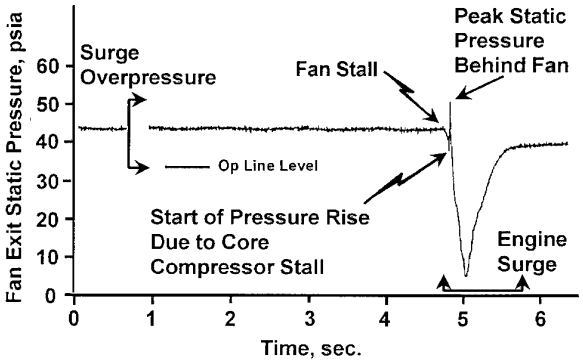

Fig. 19 Pressure Trace from TFE1042 Engine when Engine Surge is Initiated by a Fan Stall

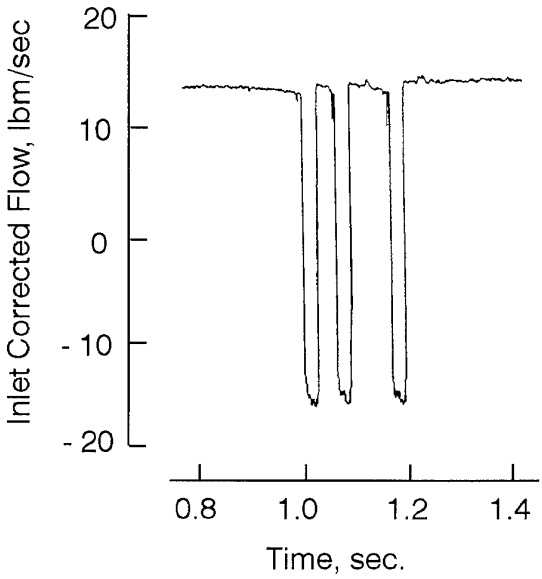

Fig. 20 Fluctuation in Flowrate for Three Surge Cycles on the TFE1042 Engine

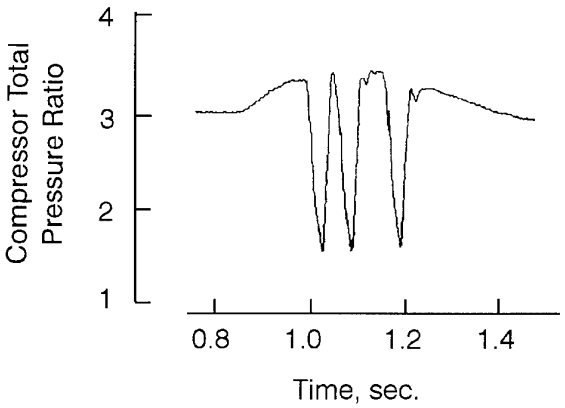

Fig. 21 Fluctuation in Pressure Ratio for Three Surge Cycles on the TFE1042 Engine

a "flatter" appearance and does not drop off in pressure as much as the rig (Figure 18). This could be caused by the change in the upstream and downstream effective volume between the rig and the engine and the effect of the fan and the bypass on the compressor inlet. Also of note is the difference in the post-stall choked blowdown portion of the cycle. The

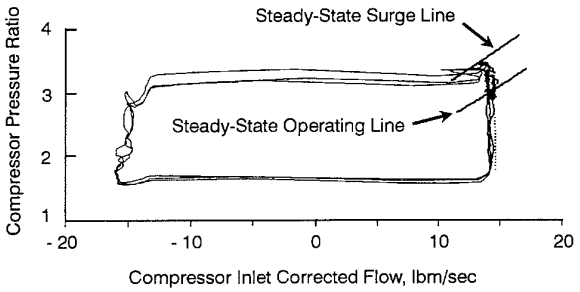

Fig. 22 Three Full Surge Cycles Measured on the TFE1042 Engine at 80% Corrected Speed (Filtered @ 100 Hz)

engine shows a choked blowdown at a larger reverse flowrate than the rig (Figure 18 vs. Figure 22). This is due to the difference in the centrifugal stage diffusion system in the two machines. Figure 22 also shows that the steady-state surge line measured in the rig. The high-response pressure and flow measurements in the engine reflect the same compressor surge line as in the rig.

TFE731 Engine Results

The TFE731 engine was tested in the base level test cell and at altitude on the AlliedSignal Boeing 720 test aircraft. This compressor, as mentioned previously, is a unique design in that it is constructed as a split spool machine, with the axial compressor on one spool and the centrifugal on another. Several different tests were performed, for the purpose of showing that a split spool configuration provides some unique challenges and that it is possible to move the surge trigger into the centrifugal stage using bleed, turbine temperature change, or speed mismatch. For the base level test cell, many tests were performed with different fuel and turbine temperature schedules, while performing snap accelerations. Figures 23 and 24 show two different surge triggers. Figure 23 shows the pressure trace when the surge trigger is in the centrifugal stage. The first indication that something is "wrong" is the rapid rise in overpressure between the axial and the centrifugal stages. Figure 24 shows an engine surge that is initiated in the axial compressor, the preferred location for axial-centrifugal compressors because of the inherent recoverability. The beginning of the centrifugal stage backflow can be seen in the trace. It is important to note that the surge overpressure (at the rear of the axial compressor) is higher when the centrifugal compressor is the surge trigger. When the axial compressor is the surge trigger, the local axial discharge pressure is reduced before the centrifugal compressor backflows, providing a buffer for the backflow of the high pressure downstream air.

During the flight test, surge behavior in the engine was initiated by fuel pulsing. The fuel pulse was performed during two different types of transients, as shown in Figures 25 and 26. The first technique was to heat soak the engine at 31,000 RPM on the centrifugal compressor (the speed consistent with the maximum climb power), and perform a snap deceleration, executing the fuel pulse when the engine speed reached the desired value. (The speeds of the centrifugal compressor are corrected to the engine inlet.) The second technique was to again heat soak the engine at 31,000 RPM on the centrifugal compressor and perform a snap deceleration. This time, the engine was allowed to decelerate to a speed point lower than

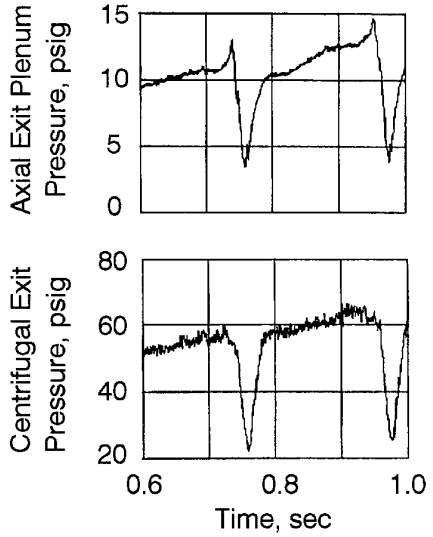

Fig. 23 Surge Pulse from the TFE731 at Sea Level with Centrifugal Compressor as the Surge Trigger

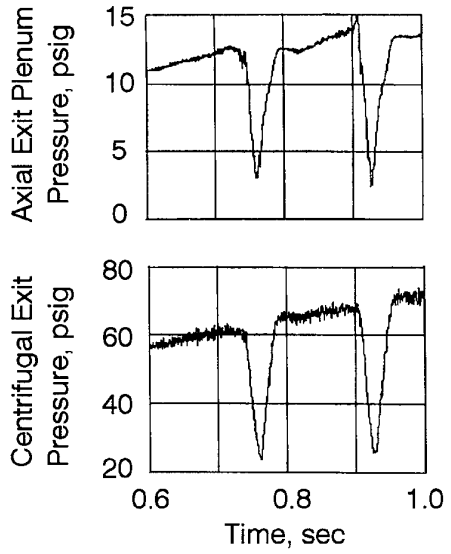

Fig. 24 Surge Pulse from the TFE731 at Sea Level with Axial Compressor as the Surge Trigger

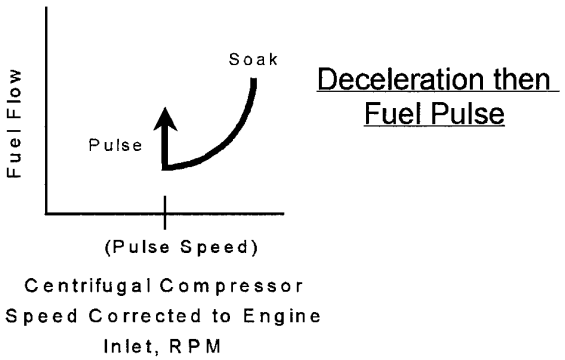

Fig. 25 First Method of Surging the TFE731 Engine During Testing - Deceleration then Fuel Pulse

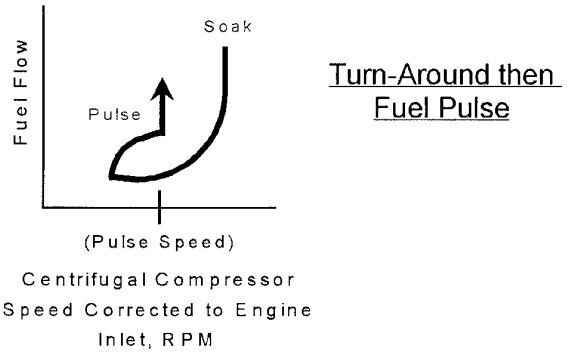

Fig. 26 Second Method of Surging the TFE731 Engine During Testing - Decel / Accel then Fuel Pulse

the intended fuel pulse point. The engine was then accelerated and the fuel pulse executed when the desired speed was reached. This forced a speed mismatch between the axial and the centrifugal compressors.

Figure 27 shows the results of performing a rapid deceleration and fuel pulsing to cause a surge, with and without bleed. This test was performed at 20,000 ft. altitude with the fuel pulse executed at 26,000 RPM on the centrifugal compressor. Without bleed between the axial and the centrifugal compressors, the axial compressor stalls, dropping the inlet pressure to the centrifugal compressor stage, forcing it to reach it's stability limit and then stall. The pressure trace is similar to that shown in Figure 19 for the core compressor and the fan, since the flowfield responds in the same manner. Opening the bleed causes the operating line on the axial compressor to drop so low that the surge trigger moves to the centrifugal stage. As the centrifugal stage begins to stall, it doesn't initiate surge right away, but as the stalling behavior of the centrifugal impeller gets more severe, the engine surges. The disturbances in the centrifugal impeller are picked up by the probe in the bleed plenum between the axial and the centrifugal compressors.

Figure 28 shows the effect of the speed mismatch on the surge trigger of the engine. This test was performed at 20,000 ft. altitude with the fuel pulse executed at a speed of 28,000 RPM on the centrifugal compressor. In the deceleration/fuel pulse test, the surge trigger is in the axial compressor. For this case, the axial speed is 16,681 RPM and the centrifugal speed is 28,160 RPM at surge. When performing a hot turn-around pulse (deceleration to below fuel pulse speed, then accelerate and fuel pulse), the centrifugal compressor stalls first (is the surge trigger). This time, the reason the surge trigger moved into the centrifugal stage is because the axial compressor, having more inertia, accelerates slower from the minimum speed point, and the centrifugal compressor picks up the load faster by accelerating faster. The axial compressor speed was 14,358 RPM and the centrifugal compressor speed was 28,848 RPM at surge. Therefore, when the centrifugal compressor was forced into being the stability limiting component of the compression system, the axial compressor was running 2,323 RPM slower and the centrifugal was running 688 RPM faster than in the previous case where the turn around was not performed and the axial compressor was the surge trigger.

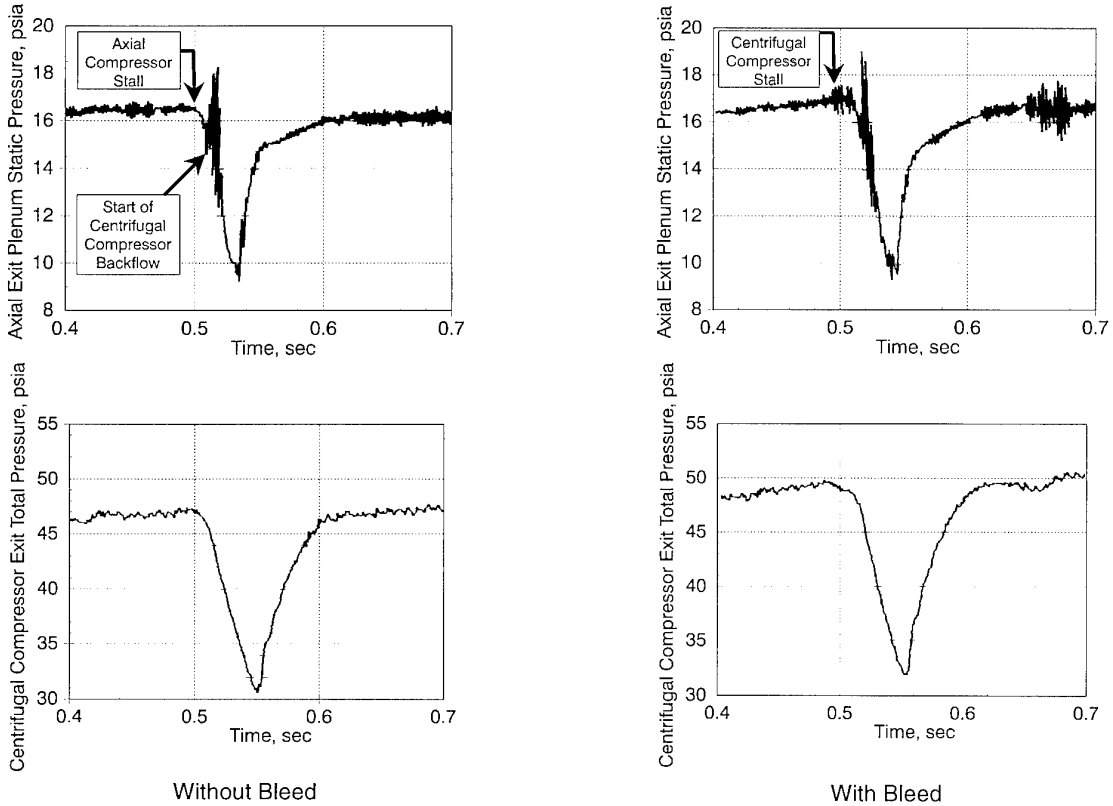

Fig. 27 Effect of Bleed on Surge Trigger After Deceleration

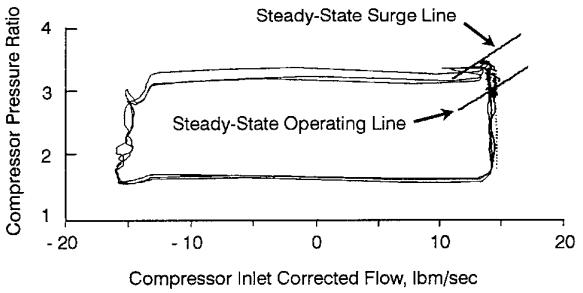

Fig. 22 Three Full Surge Cycles Measured on the TFE1042 Engine at 80% Corrected Speed (Filtered @ 100 Hz)

engine shows a choked blowdown at a larger reverse flowrate than the rig (Figure 18 vs. Figure 22). This is due to the difference in the centrifugal stage diffusion system in the two machines. Figure 22 also shows that the steady-state surge line measured in the rig. The high-response pressure and flow measurements in the engine reflect the same compressor surge line as in the rig.

TFE731 Engine Results

The TFE731 engine was tested in the base level test cell and at altitude on the AlliedSignal Boeing 720 test aircraft. This compressor, as mentioned previously, is a unique design in that it is constructed as a split spool machine, with the axial compressor on one spool and the centrifugal on another. Several different tests were performed, for the purpose of showing that a split spool configuration provides some unique challenges and that it is possible to move the surge trigger into the centrifugal stage using bleed, turbine temperature change, or speed mismatch. For the base level test cell, many tests were performed with different fuel and turbine temperature schedules, while performing snap accelerations. Figures 23 and 24 show two different surge triggers. Figure 23 shows the pressure trace when the surge trigger is in the centrifugal stage. The first indication that something is "wrong" is the rapid rise in overpressure between the axial and the centrifugal stages. Figure 24 shows an engine surge that is initiated in the axial compressor, the preferred location for axial-centrifugal compressors because of the inherent recoverability. The beginning of the centrifugal stage backflow can be seen in the trace. It is important to note that the surge overpressure (at the rear of the axial compressor) is higher when the centrifugal compressor is the surge trigger. When the axial compressor is the surge trigger, the local axial discharge pressure is reduced before the centrifugal compressor backflows, providing a buffer for the backflow of the high pressure downstream air.

During the flight test, surge behavior in the engine was initiated by fuel pulsing. The fuel pulse was performed during two different types of transients, as shown in Figures 25 and 26. The first technique was to heat soak the engine at 31,000 RPM on the centrifugal compressor (the speed consistent with the maximum climb power), and perform a snap deceleration, executing the fuel pulse when the engine speed reached the desired value. (The speeds of the centrifugal compressor are corrected to the engine inlet.) The second technique was to again heat soak the engine at 31,000 RPM on the centrifugal compressor and perform a snap deceleration. This time, the engine was allowed to decelerate to a speed point lower than

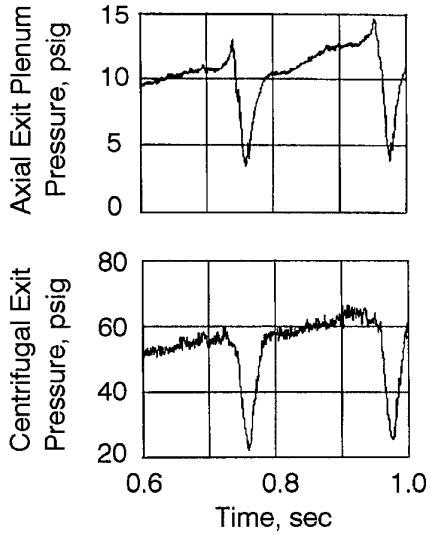

Fig. 23 Surge Pulse from the TFE731 at Sea Level with Centrifugal Compressor as the Surge Trigger

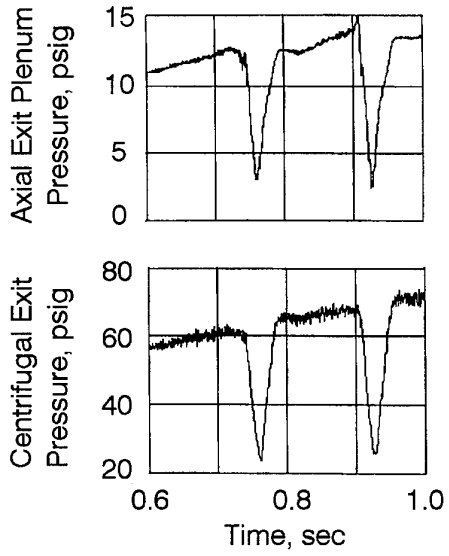

Fig. 24 Surge Pulse from the TFE731 at Sea Level with Axial Compressor as the Surge Trigger

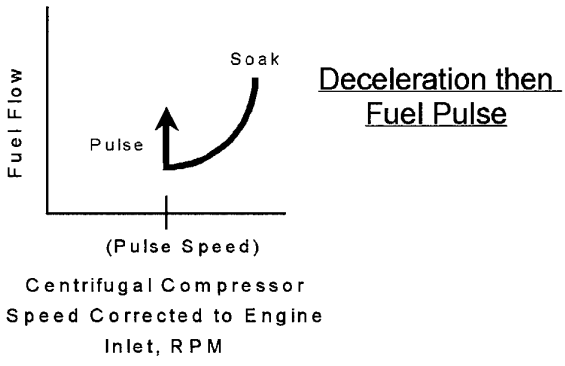

Fig. 25 First Method of Surging the TFE731 Engine During Testing - Deceleration then Fuel Pulse

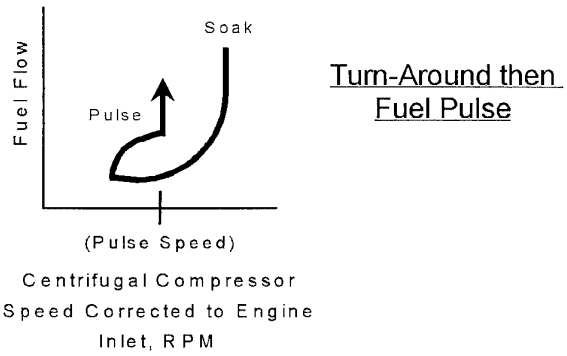

Fig. 26 Second Method of Surging the TFE731 Engine During Testing - Decel / Accel then Fuel Pulse

the intended fuel pulse point. The engine was then accelerated and the fuel pulse executed when the desired speed was reached. This forced a speed mismatch between the axial and the centrifugal compressors.

Figure 27 shows the results of performing a rapid deceleration and fuel pulsing to cause a surge, with and without bleed. This test was performed at 20,000 ft. altitude with the fuel pulse executed at 26,000 RPM on the centrifugal compressor. Without bleed between the axial and the centrifugal compressors, the axial compressor stalls, dropping the inlet pressure to the centrifugal compressor stage, forcing it to reach it's stability limit and then stall. The pressure trace is similar to that shown in Figure 19 for the core compressor and the fan, since the flowfield responds in the same manner. Opening the bleed causes the operating line on the axial compressor to drop so low that the surge trigger moves to the centrifugal stage. As the centrifugal stage begins to stall, it doesn't initiate surge right away, but as the stalling behavior of the centrifugal impeller gets more severe, the engine surges. The disturbances in the centrifugal impeller are picked up by the probe in the bleed plenum between the axial and the centrifugal compressors.

Figure 28 shows the effect of the speed mismatch on the surge trigger of the engine. This test was performed at 20,000 ft. altitude with the fuel pulse executed at a speed of 28,000 RPM on the centrifugal compressor. In the deceleration/fuel pulse test, the surge trigger is in the axial compressor. For this case, the axial speed is 16,681 RPM and the centrifugal speed is 28,160 RPM at surge. When performing a hot turn-around pulse (deceleration to below fuel pulse speed, then accelerate and fuel pulse), the centrifugal compressor stalls first (is the surge trigger). This time, the reason the surge trigger moved into the centrifugal stage is because the axial compressor, having more inertia, accelerates slower from the minimum speed point, and the centrifugal compressor picks up the load faster by accelerating faster. The axial compressor speed was 14,358 RPM and the centrifugal compressor speed was 28,848 RPM at surge. Therefore, when the centrifugal compressor was forced into being the stability limiting component of the compression system, the axial compressor was running 2,323 RPM slower and the centrifugal was running 688 RPM faster than in the previous case where the turn around was not performed and the axial compressor was the surge trigger.

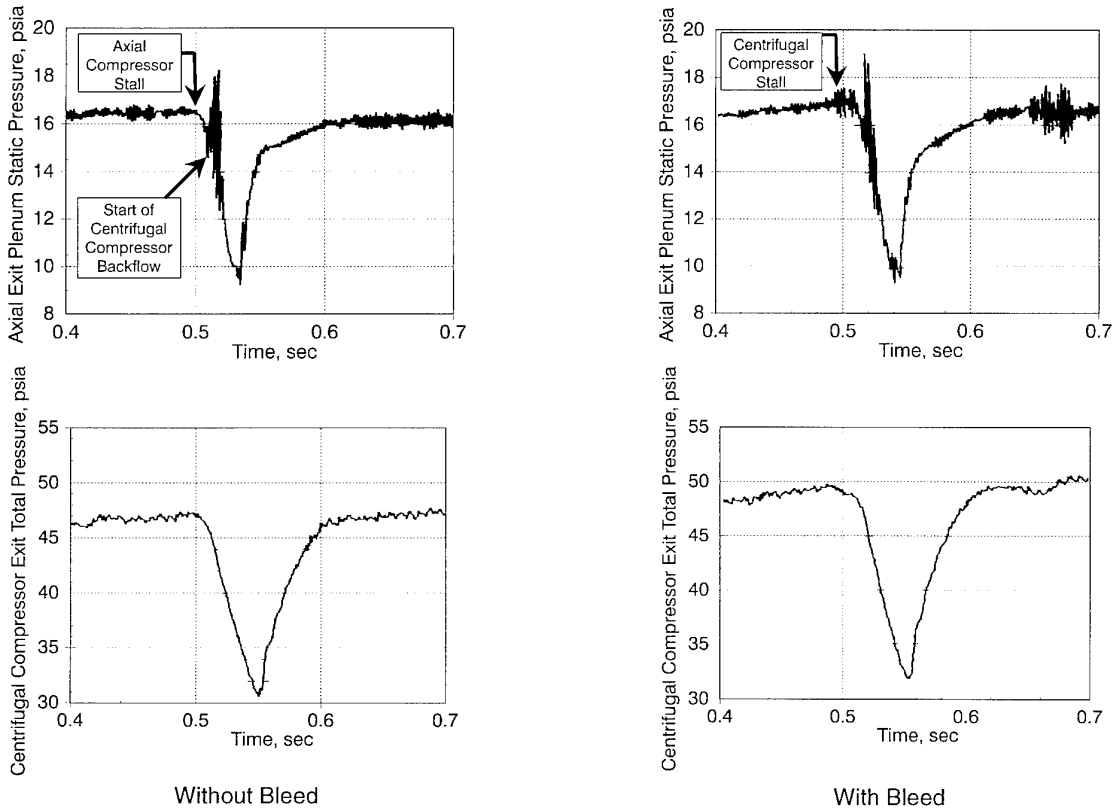

Fig. 27 Effect of Bleed on Surge Trigger After Deceleration

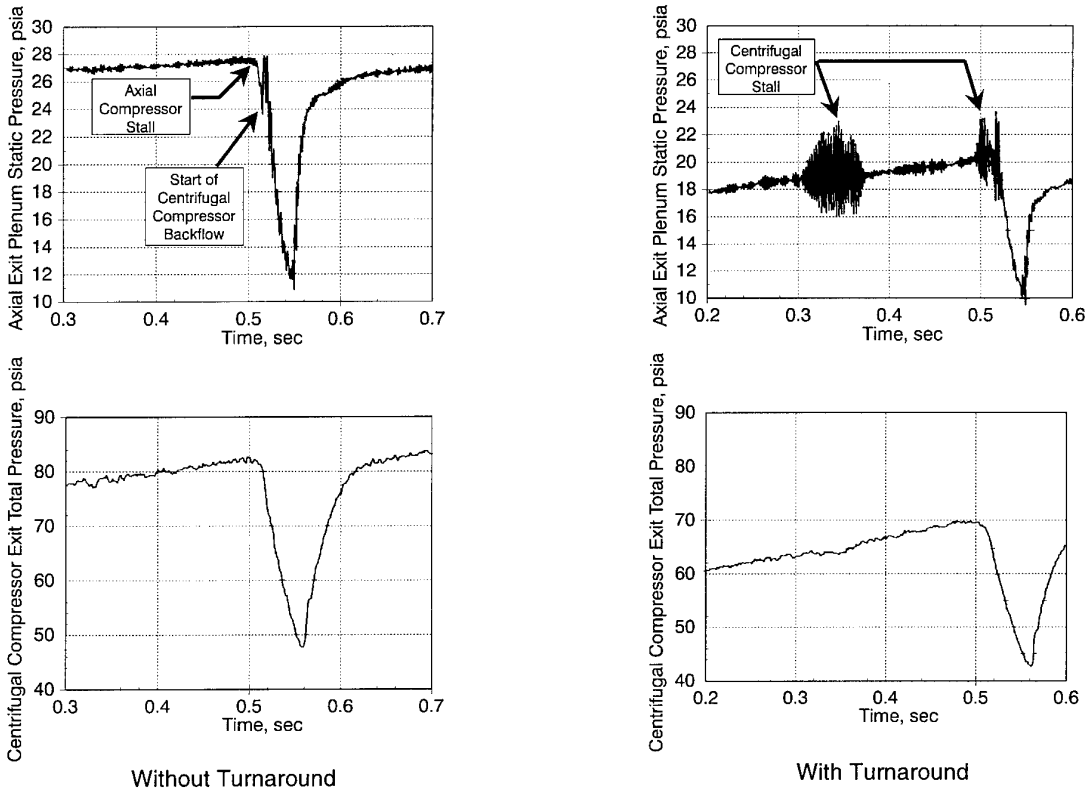

Fig. 28 Effect of Speed Mismatch on Surge Trigger Caused by Rapid Compressor Speed Turnaround

CONCLUSIONS

A significant number of high-response pressure measurements have been presented. This data, while a fraction of what has been gathered, is significant to furthering the understanding of the analysis techniques required for examination of the unsteady aerodynamic behavior in compressors. Identification of the compressor stage that limits the stability of the compressor (the *trigger*), is important to the designer. The work presented has shown that while the nature of compressor surge is a violent system flow oscillation, the instability really begins with a local blade row flow separation in some critical stage of the compressor that can be controlled by the designer. In addition, while rotating stall data has not been presented (due to space limitations), comparison of data from any rotating stall inception measurements to the dynamic data presented here just prior to surge (Figure 9) will show that the rotating stall local blade row separation has exactly the same characteristic. Whether the result of this separation takes the form of a surge or a rotating stall is a function of the system energy storage capability.

In the design of propulsion engine compression systems, in certain size class engines, there is a choice to be made as to use of an axial compressor or an axial-centrifugal compressor. One of the benefits of using an axial-centrifugal compression system is the enhanced stability that is acquired. The centrifugal stage helps to inhibit the inception of system instability due to the constant pumping of the centrifugal stage. If instability does occur, the centrifugal compressor stage forces recovery by pumping while the axial compressor stages have not yet recovered. This pumping forces the axial stages to recover. In design, to take advantage of this capability requires the design of a centrifugal stage with a lot of flow range. This means high efficiency, backswept impellers, balanced with the axial stages to provide the enhanced stability that is possible.

Designing to keep the stability trigger in the axial compressor as much as possible not only provides for a more stable axial-centrifugal compressor, but also reduces the inlet overpressure that occurs with surge. This reduction is due to the high-pressure centrifugal compressor discharge air flowing backwards into an axial compressor whose back stages are already at a significantly degraded pressure. While this may not seem all that important, it has major ramifications to the structural designer. In addition, the post-stall blowdown behavior is a function of the back end of the compressor, where the smallest area exists. This area limits the amount of backflow that the compressor will experience during the surge process.

Split-spool axial-centrifugal compressors have several unique characteristics with which both the engine control designer and the aerodynamic designer must be concerned. This stems from the ability to apply enough bleed between the axial and the centrifugal stages to force the stability trigger into the centrifugal stage. While this could be acceptable, if interstage bleed is typically used to resolve a stability problem and it is not recognized that the stability trigger is in the centrifugal stage, the stability problem can be aggravated, not helped. The split-spool axial-centrifugal compressor can also undergo a change in the location of the surge trigger through the speed mismatch that occurs during some types of aircraft

maneuvers.

Whether the axial-centrifugal compression system is of the split-spool configuration or not, knowledge of these operating characteristics is necessary for the controls designer, so that proper control bleed schedules, fuel schedules, and surge schedules can be developed.

Finally, enhancing the stability of a compression system requires that the designer be completely knowledgeable of the characteristics of the compressor. Compressor stability is not only system dependent, it is blade row based. Basic physics of airfoil separation are involved in addition to the system properties. This is important to remember as we pursue techniques for gaining surge margin through the manipulation of the compressor flowfield.

ACKNOWLEDGMENTS

The authors would like to thank AlliedSignal Aerospace for permission to publish these results. The authors would also like to thank the members of the Compressor Aerodynamics Department and of the Performance and Operability Department for their assistance in obtaining the data presented in this paper. In addition, thanks to the members of the Dynamics Laboratory, whose patience and assistance throughout the data reduction phase of the analysis made this work possible.

REFERENCES

1 Emmons, H.W., Pearson, C.E., amd H.P. Grant, "Compressor Surge and Stall Propagation," Transactions of the American Society of Mechanical Engineers, May 1955, pp. 455-469.

2 Greitzer, E.M., "Surge and Rotating Stall in Axial-Flow Compressors - Part 1: Theoretical Compression System Model," ASME Journal of Engineering for Power, Vol. 98, No. 2, April 1976, pp. 190-198.

3 Moore, F.K., "A Theory of Rotating Stall of Multistage Axial Flow Compressors," NASA CR-3685, Lewis Research Center, Cleveland, OH, July 1983.

4 Sexton, M.R. and W.F. O'Brien, "A Model for Dynamic Loss Response in Axial-Flow Compressors," ASME Paper 81-GT-154, March 1981.

5 Cousins, W.T., and W.F. O'Brien, "Axial-Flow Compressor Post-Stall Analysis," AIAA Paper No. 85-1349, July 1985.

6 Boyer, K.M. and W.F. O'Brien, "Model Predictions for Improved Recoverability of a High-Speed Ten-Stage Axial-Flow Compressor, AIAA Paper No. 89-2684, July 1989.

7 Kimzey, W.F., "An Analysis of the Influences of Some External Disturbances on the Aerodynamic Stability of Turbine Engine Axial Flow Fans and Compressors," AEDC-TR-77-80 (AD-A043543), August 1977.

8 Davis, Jr., M.W. and W.F. O'Brien, "Stage-by-Stage Poststall Compression System Modeling Technique," AIAA Journal of Propulsion and Power, Vol. 7, No. 6, November-December 1991, pp. 997-1005.

9 Cousins, W.T., "Summary of Some Applications and Analysis Techniques of High-Response Data," Internal AlliedSignal Presentation, December 1985.

10 Day, I.J., "The Unstable Behavior of Low and High Speed Compressors," ASME Paper 93-GT-26, June 1993.

REFERENCE NO. OF THE PAPER: 29

DISCUSSOR'S NAME: F. Kameier, BMW-RR, Germany

AUTHOR'S NAME: W.T. Cousins

Q: At the beginning of your speech you gave a critical comment on the accuracy of published transient data. I don't believe that data acquisition is an actual problem, although maybe 10 years old data have to be evaluated cautiously. I think that you didn't take the full information out of your data because you have only analyzed time domain data and not frequency spectra.

A: Yes, I did comment on the accuracy of some published dynamic data (not transient data). If one looks into the literature (even in the last two years), data presentations can be found that are not completely correct. The problems that often exist that are missed include amplifiers with a cutoff frequency less than the data being observed, recorded tape speeds that are too slow, improper use of windowing functions in analysis, or even improper transducer calibration. While this is not rampant among the literature, it does exist. The problem usually arises in observing the magnitude values of data. With a data system frequency response that is not high enough, the first thing lost are the proper magnitude values. In a frequency analysis, the frequencies of interest still show up in the data, but the magnitudes are incorrect. I mention this as a warning to researchers to be more careful, and as a warning to readers to be cautious when examining results.

As far as frequency analysis of the presented dat, some has been performed where necessary. Frequency analysis is useful only if it is necessary to obtain the required information. Much of the data that is presented is non-deterministic in nature and is therefore not applicable to many frequency analysis techniques. To be sure what is being observed relates to the true physics of the compressor unsteady flows, the time domain rather than the frequency domain is more appropriate. Pressure/flow values and changes in the time domain provide the desired information, so additional frequency analysis is not value added or beneficial to the problem presented.

INITIATION AND PROPAGATION OF FLOW INSTABILITIES IN MULTI-STAGE AXIAL COMPRESSORS

W. Rieß
M.Walbaum
Institut für Strömungsmaschinen
Universität Hannover
Appelstr. 9
30167 Hannover, Germany

SUMMARY

Axial Compressors for all the different applications are required to have an operating range as large as possible with high efficiency. The increase of aerodynamic stage loading renders, however, a distinct narrowing of the characteristic field. Broader and deeper knowledge of the mechanisms governing the initiation and propagation of flow instabilities near the stability limit of compressors would permit an optimised compressor design with full exploitation of the aerodynamic limits, which could result in a considerably increased operating range. In addition new methods for instability detection could be found, which would allow operation near the surge limit with the aid of on-line surge control.

The mechanisms of initiation and propagation of flow instabilities are investigated in a six-stage axial compressor with guide vane adjustment. By systematic modification of the aerodynamic loading of the different stages the propagation of disturbances and the interactions between disturbed and not disturbed flow in a multi-stage environment can be studied. Radial traverses with a six-hole probe and peripherally distributed pressure sensors render informations on instationary flow phenomena as local back-flows or transition from two-cell stall to single-cell stall. The results give the possibility to check different models for flow instability and develop methods for instability detection.

LIST OF SYMBOLS

t	time
p_{st}	static pressure
n	speed
n_N	speed of design point
v	velocity
v_a	axial velocity
v_c	circumferential velocity
w	relative velocity
ω	frequency
ε	load coefficient
φ	flow coefficient
ψ	isentropic coefficient

1. INTRODUCTION

The characteristic field of turbo-compressors is limited towards low volume flow by aerodynamic instabilities. It has been generally realised meanwhile, that compressor surge is a consequence of an essential primary instability and depends with regard of its specific character on the data of the complete system (compressor, reservoir volumes, pipe lengths). In multi-stage axial compressors with a stage pressure-ratio in industrial range the primary instability is a rotating stall - mostly of single cell type. It causes a considerable drop of the pressure ratio by a transient shift of the operating point on a second - lower - branch of the characteristic line and eventually triggers a surge cycle.

The flow disturbances, which cause the initiation of rotating stall, are described by different theories in literature. The flow phenomena in a developed stall cell in a multi-stage compressor are largely unknown in detail, similarly methods for reliable detection of incipient instability are lacking.

The continuous detection of the actual stability limit during operation would allow the application of on-line surge control systems. If would shift the usual surge-control-line, placed in the stable part of the characteristic field for safety reasons, towards the real stability limit and would open a part of the characteristic field with high efficiency for practical operation. Prerequisite is a reliable detection of instabilities during their initiation. Since the mechanisms of initiation depend on a number of different parameters, further investigations will be necessary to answer all open questions.

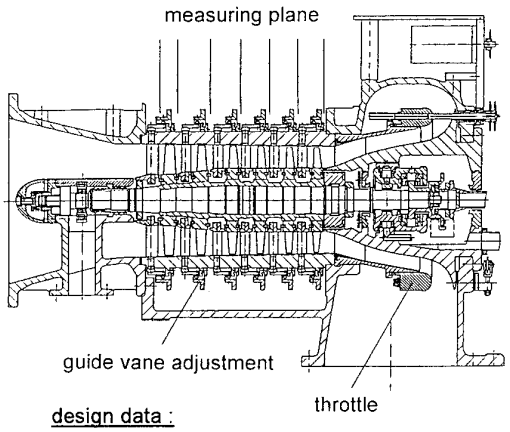

Fig. 1: Six Stage Compressor

2. EXPERIMENTAL SET-UP

The experimental investigations were carried out in a six-stage research axial compressor (fig. 1). All guide vane rows have variable setting and can be moved independently. Mass flow control is effected by a circular throttle in the exit diffusor. A computer controlled throttle drive allows exact reproduction of the variation of operating conditions during approach of the stability limit. The diffusor throttle encloses a

Paper presented at the AGARD PEP 85th Symposium on "Loss Mechanisms and Unsteady Flows in Turbomachines", held in Derby, United Kingdom, 8-12 May 1995, and published in CP-571.

much smaller pressure side volume than a throttle valve in the pressure pipe line. Therefore surge is avoided after passing the stability limit and stationary operation of the compressor with developed rotating stall on the second branch of the characteristic line is possible and allows detailed investigations of this type of operation. The small pressure side volume renders operation on parts of the characteristic line with positive slope near the stability limit at part speed possible. According to Schlamann /1/ a surge cycle is always initiated by rotating stall and - at least in multi-stage axial compressors - the stability limit is not influenced by the size of the pressure-side volume. Therefore experiments with large pressure-side volume - and surge - have been omitted.

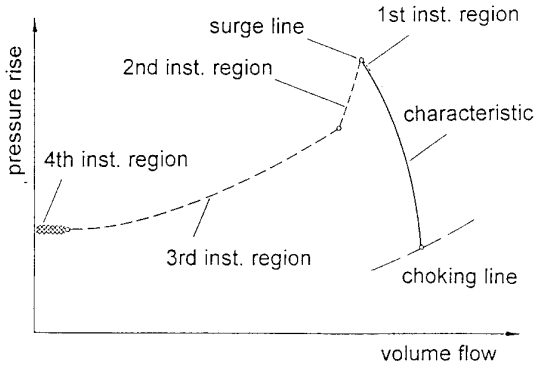

Fig. 2 : Complete Schematic Compressor Characteristic

2.1 Instationary measurement techniques

For detection of the flow effects during initiation and propagation of instabilities close to the stability limit the selection and placement of the instationary sensors is of utmost importance. Because of the guide-vane drive mechanisms on the compressor investigated here it was not possible to place sensors behind the guide-vane rows. The high-reaction blading effects most of the flow deceleration in the rotor, therefore instability initiation in the rotor blading seems probable.

The instrumentation of the test-compressor comprises three piezo-resistive pressure sensors, flush mounted in the casing wall and equally spaced around the circumference behind the inlet guide-vanes and behind each rotor blade row. The sensors have an naturalfrequency around 300 kHz, the maximum blade passing frequency is 4.13 kHz. Number and placement of the pressure sensors allows detection and identification of flow instabilities in the different instability regions acc. to fig. 2.

For measurement of instable flow phenomena within the compressor flow field hot-wire-probes and an instationary flow-vector-probe are applied. Hot-wire-probes are used for radial traverses behind the rotor blade-rows. By application of several probes simultaneous measurements behind all rotor blade-rows are possible. Single-wire-probes with radial wire orientation have been used, they measure the momentary flow velocity in a plane perpendicular to the wire and give informations on place, size and propagation of flow instabilities dependant on guide-vane setting and compressor speed.

For correct measurement of the magnitude of flow velocity a probe calibration in function of density and temperature of the fluid and the wire temperature ratio is necessary. In multi-stage compressors with compressible flow, however, rapid variations of fluid temperature and pressure occur during flow instabilities. Measurement of these fluctuations of fluid properties near the hot-wire-probe in the compressor is not possible. Exact determination of the flow velocity is practically not possible under these circumstances. Therefore a complete calibration of the hot-wire-probes was not made, the measured velocity-signals have a somewhat qualitative character. Nevertheless they are of great value for detection and interpretation of velocity fluctuations and show in detail the initiation of stall cells.

2.2 Development of an instationary flow-vector-probe

For a complete understanding of the origin of instabilities, their propagation and feed-back into regions of stable flow the development of velocity and pressure signals in space and time during the passage through the three phases of instability has to be determined. Quantitative measurement of the instationary flow velocity vector in a multistage compressor with high pressure ratio with hot-wire or hot-film probes meets severe limitations. Therefore an instationary flow-vector-probe on pneumatic basis has been developed.

The aims were:

- measurement of the flow velocity vector in a tangential plane in the compressor
- measurement range for flow angle ± 180°
- high temporal resolution
- small size

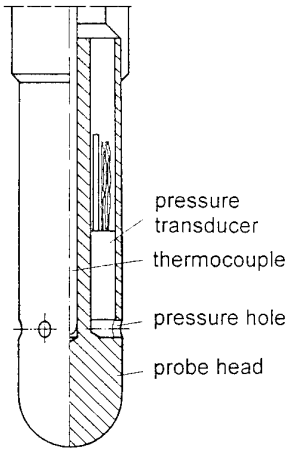

Fig. 3 : Flow-Vector-Probe

The cylindrical probe with 6 mm diameter has six pressure holes equally spaced around its circumference and for each an instationary pressure transducer placed directly adjacent (Fig. 3). Investigations in a shock-tube proved, that the dynamic characteristic of the system hole - enclosed volume - transducer is amply sufficient to follow the variations of the flow. Value and direction of the velocity vector can be determined from the six pressure signals with a special calibration and evaluation method /2/. In addition the instationary values of total and static pressure are delivered. The probe is sensitive enough to determine flow and pressure variations over each blade pitch behind a moving rotor blade row.

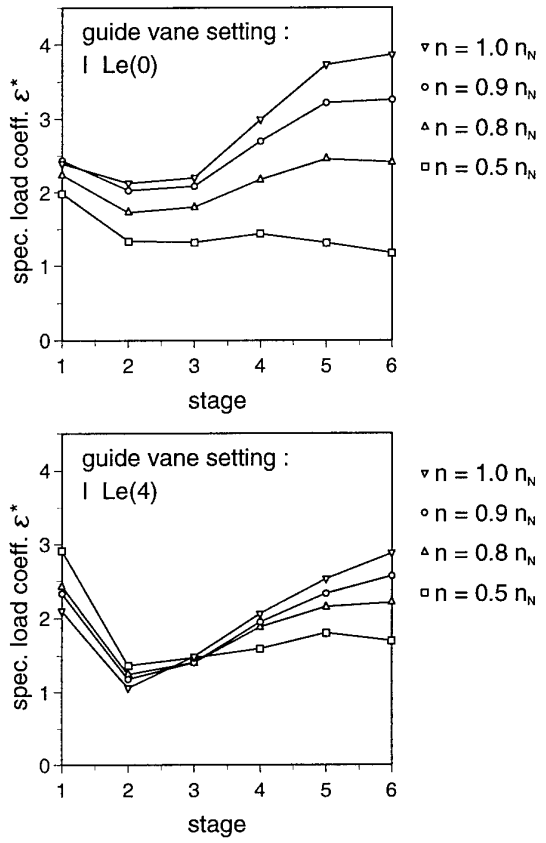

Fig. 4 : Load Distribution

3. EXPERIMENTAL CONDITIONS

The investigations in the compressor showed clearly, that the form of flow instabilities during their origin depends heavily on the aerodynamic loading of the stages near the stability limit. The possibility of individual setting of each guide vane row makes a variation of the aerodynamic load distribution over the stages possible, which has direct influence on the form of arising instabilities. The distribution and the value of stage loading in function of rotor speed and guide vane setting can be expressed with the

$$\text{load coefficient} \qquad \varepsilon = \psi / \varphi^2 \qquad (1)$$

Fig. 4 shows the load distribution over the stages for the nominal guide vane setting (I Le(0)) and for a closing of guide vanes decreasing from inlet to outlet (I Le(4)) for different rotor speed ratios (n_N design rotor speed) /3/. The specific load coefficient ε^* is the load coefficient ε of a specific stage near the stability limit divided by the mean value of the stage load coefficients of the compressor in the design point. The general increase of stage load towards the outlet near the stability limit and the load reduction resulting from speed decrease are clearly visible.

The highest values of specific load coefficient occur at nominal guide vane setting I Le(0) and nominal speed. The increased compressor pressure ratio near the stability limit causes an additional decrease of volume flow through the later stages and increases the aerodynamic load. Its value at the stability limit for the last stage is higher than that for the first stage by a factor of 1.6 and higher than the mean load coefficient at design point by a factor of 3.8. The inlet guide vanes are profiles without camber with a nominal axial position. Therefore the load characteristic of the first stage is different from the others for both guide vane settings. The influence of a speed variation on the stage loading near the stability limit is compensated to a large extent by the guide vane setting I Le(4).

Because of the great number of necessary probe positions a simultaneous collection of all data throughout the compressor is technically not possible. Nevertheless definite informations as to origin and propagation of instabilities can be acquired. The evaluation of the wall-pressure signal in front of the first rotor and the reproducible test conditions including the throttle movement insure sufficient identity of consecutive tests. Comparison of several test runs shows good reproducibility of the different phases of instability at high rotor speed-ratios. At lower rotor speeds varying forms of the first instability phase can be observed, but the general structures remain similar.

4. STABLE PART OF THE CHARACTERISTIC FIELD

Instationary flow disturbances in the stable part of the characteristic field are of central importance for the understanding of the initiation of rotating stall. Frequency analysis of the pressure signals from the transducers in the casing wall at an operating point with considerable distance from the stability limit shows amplitude maxima for the rotation frequency of the rotor - as expected - but also for the

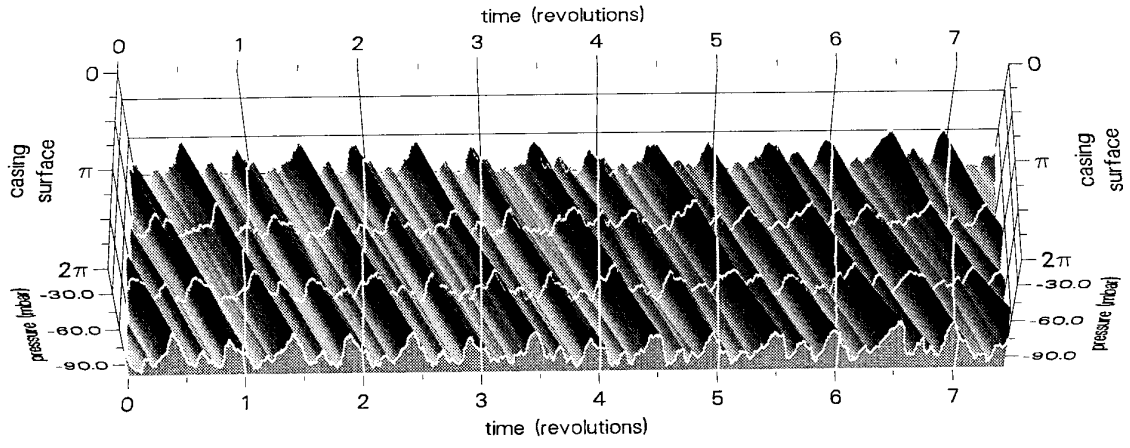

Fig. 5 : Pressure Distribution at the Casing in front of Rotor 1

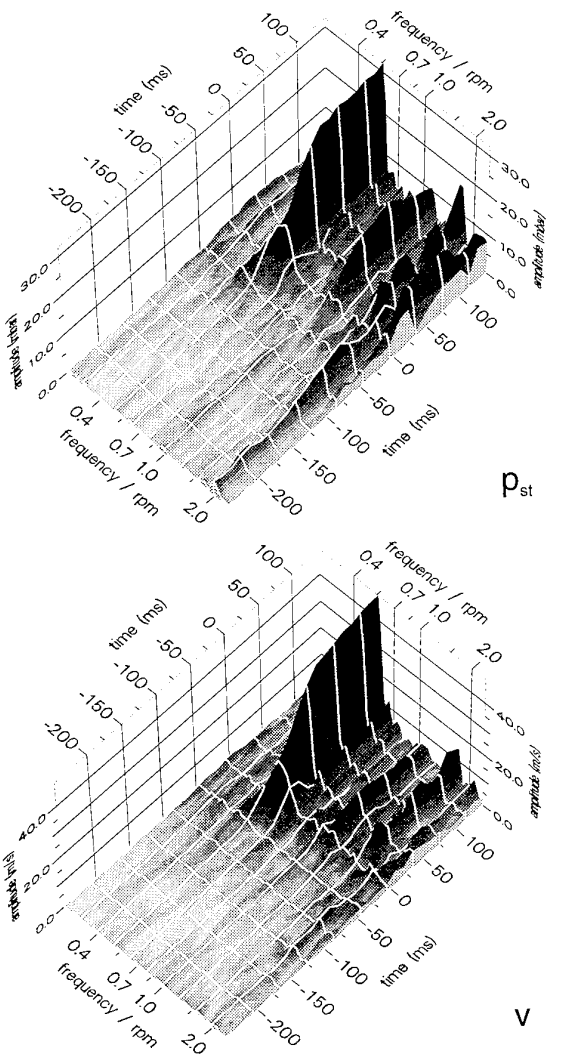

Fig. 6 : Sliding Frequency Analysis behind Rotor 1, at 75% of Blade Height, I Le(0), n = 0.9 n_N

double and, less pronounced, for the fourfold rotating frequency. The phase-shift between the three transducers on the circumference indicates a multi-phase disturbance rotating with the rotor. A plot of the instationary pressure signals at the casing in front of rotor 1 for nominal speed and nominal guide vane setting is given in fig. 5. The blade-to-blade pressure variations have been eliminated by calculation of temporal mean values over one rotor blade pitch. The plot shows clearly two disturbances, spaced about 180° and rotating with the rotor, which are rather persistent. Between them smaller disturbances are present, which vary considerably in amplitude and form.

This disturbance in the stable part of the characteristic field is present most clearly in the pressure signal. Radial traversing with the flow-vector-probe showed, that it is most pronounced in the front part of the compressor over the whole blade height. It is found as velocity variation, as well in the absolute as in the relative system, in an increased form in the second stage. Its intensity depends heavily on the guide vane setting nominal setting I Le(0) showed the highest values, rotor speed is of little importance. The exact cause for this type of rotating disturbance during stable compressor operation could not be determined up to now. Similar phenomena in compressors of different type might have led to the theory of modal disturbances.

5. FREQUENCY ANALYSIS OF FLUCTUATING PERIODIC SIGNALS

Frequency analysis is a suitable tool for detailed investigation of periodic signals. The representation of the signal by a Fourier series is permissible in an exact mathematical treatment only for a strictly periodic signal. For analysis of signals with temporally variable frequency components, as they occur during continuous throttling of the compressor over the stability limit, the classical Fourier analysis is not applicable. In order to achieve nevertheless detailed informations on the nature of pressure and velocity fluctuations during passage through the different instability regions, a "sliding frequency analysis" was developed. It is based on the Fourier integration, as it is used for Fourier transformation /4/, but the integration limits are reduced from $\pm\infty$, as in classical Fourier analysis, to a time interval T of 10 periods of the respective frequency ω.

The time-dependent coefficients for representation of the frequency spectrum are

$$a(\omega,t)=\frac{2}{T(\omega)}\int_{t-T(\omega)/2}^{t+T(\omega)/2} f(\tau)\cos(\omega\tau)d\tau \qquad (2)$$

$$b(\omega,t)=\frac{2}{T(\omega)}\int_{t-T(\omega)/2}^{t+T(\omega)/2} f(\tau)\sin(\omega\tau)d\tau \qquad (3)$$

They can be determined by "sliding" the integration interval over the measured signal and they describe the frequency spectrum of the analysed signal in the direct vicinity of the time t.

Fig. 6 shows the result of the sliding frequency analysis of the static pressure and the velocity signal acquired with the flow-vector-probe behind the first rotor at 75 % blade height and a rotor speed ratio of 0.9 during continuous throttling of the compressor over the stability limit. For better interpretation of the periodic parts of the signals all frequencies are referred to the rotating frequency of the rotor. For easier comparison of the different figures, the zero point of the time axis is placed in all cases at the transient drop of the compressor pressure ratio, i.e. in the moment of development of full rotating stall. After passing the stability limit the stall frequency with 56 % of the rotational frequency develops rapidly and distinctly. The frequency spectrum of the static pressure signal shows in the stable operating region a component with the double rotational frequency originating from the two-phase disturbance rotating with rotor, as described above. Closer to the stability limit its amplitude increases to the double value, directly at the limit it diminishes again. The frequency spectrum of the velocity signal has no distinct frequency at the beginning of the throttling. Nearer to the stability limit an increase of the signal amplitude at double rotational frequency can be distinguished simultaneously with the increase of the same component of the pressure signal. Approaching the limit the double-frequency velocity signal diminishes as the similar pressure signal but earlier. This is a result of the flow phenomena within the first instability region, where the stall cell begins to develop. This increase of the pressure and

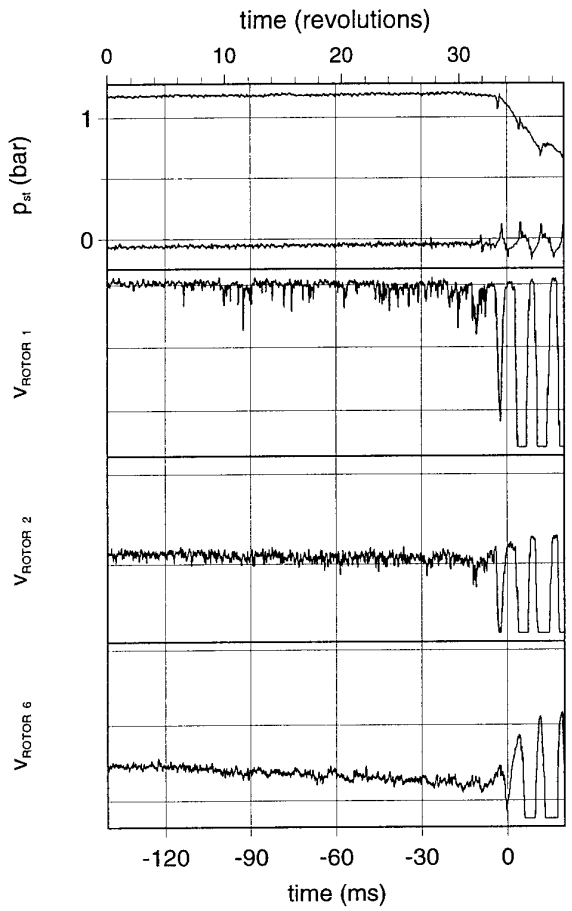

Fig. 7 : Hot-Wire-Measurements,
at 75% of Blade Height, I Le(0), n = n_N

velocity disturbances rotating with the rotor upon approach to the stability limit has been observed only in the upper region of the first stage blading at rotor speed ratios above 0.8. At lower rotor speeds a non-reproducible increase and decrease of this type of disturbance occurs in the whole operating range, a relation of the amplitude to certain parts of the characteristic field could not be established.

6. MECHANISMS OF INITIATION OF ROTATING STALL

The development of rotating stall has been explained with two different models, which have been deducted from observations in different axial compressors. The theory of Moore /6/ describes a global development of rotating stall by excitation of a modal wave, which is superimposed to the homogeneous distribution of the axial flow velocity in the compressor. Upon reduction of the volume flow the modal wave becomes instable because of the characteristic properties of the compressor and deforms to a rotating stall. A different description gives Day /5/, where an overloading of the blade row because of the reduced volume flow causes stochastic local flow separations at the profiles. The oncoming fluid is deflected then to the nearby parts of the blade row. This results for the adjacent blade at the pressure side to a reduced incidence angle and a stabilised flow. Contrary increases the incidence angle of the adjacent blade at the suction side and causes a flow separation, which moves further.

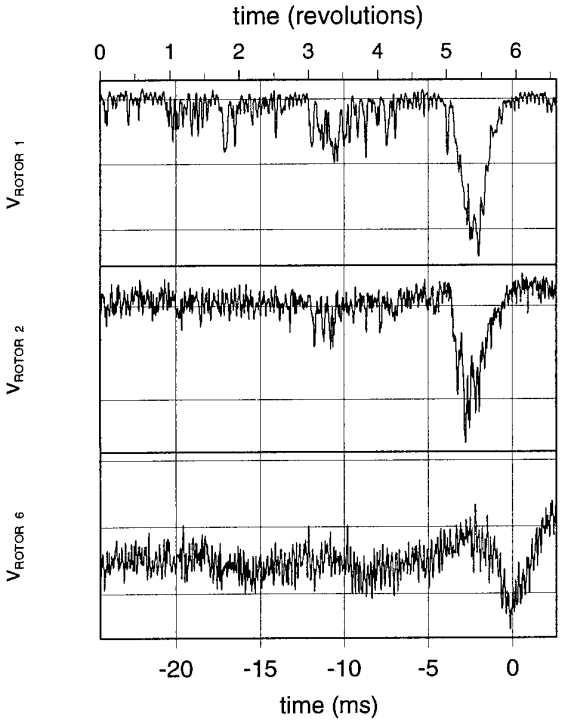

Fig. 8 : High Resolution of Hot-Wire Measurements,
at 75% of Blade Height, I Le(0), n = n_N

If this type of disturbance has stabilised, a rotating stall cell develops, which moves relative to the blade row in direction of the blade suction sides. In the test compressor investigated here, a global development of rotating stall resulting from excitation of a modal wave was never observed.

6.1 Operation at high rational speed

At a rotor speed ratio above 0.9 and with a guide vane setting acc. to I Le(0) the initiation of rotating stall could be observed in detail. Fig. 7 shows the development of wall static pressure in front of the first and the sixth rotor blade row and the - somewhat qualitative - flow velocity signal from a hot-wire probe at 75 % blade height behind the first, the second and the sixth rotor blade row. Time is scaled in ms and in rotor revolutions in order to allow coordination of the fluctuations with rotor speed. During evaluation the signals have been averaged over two blade pitches to eliminate the blade-passing frequency and accentuate the disturbances.

In the velocity signal behind the first rotor about 20 revolutions before the stability limit fluctuating sharp drops begin to occur. They result from local flow separations from the suction side of rotor profiles which extend over one or two blade pitches only. If they persist long enough they repeat after one revolution, this proves that these local flow disturbances rotate with the rotor.

Because of the interaction between local separation and flow around adjacent blade profiles described above, a local separation zone rotating with rotor speed cannot exist for longer time, this explains the heavy fluctuation. About 30 ms before the stability limit these separations become more numerous and regular, their intensity, however, diminishes up to the start of the rotating stall, which begins with increasing and broader drops of the velocity signal. These

flow phenomena appear in the first stage only. The velocity signals of later stages show smaller fluctuations, which extend over several blade pitches or even one or two revolutions, evidently they do not rotate with the rotor.

After decay of the co-rotating flow disturbances in the first stage the development of the stall cell in 75 % blade height can he observed in all stages practically simultaneously. The stall cell takes two to three rotor revolutions for full development, during the same interval the outlet pressure drops to a lower niveau. A higher temporal resolution of these signals in fig. 8 proves, that the rotating stall begins in the first stage. Because of the homogeneous state of the fluid in the first stage the velocity signal has highly quantitative character and makes clear separation of stable and disturbed regions of the flow possible. In later stages this differentiation is not possible.

The flow separations in the first stage cause only minor fluctuations in later stages. Only after full development of the stall cell in the first stage similar fluctuations arise in the last stage. Further proof for the initiation of the rotating stall in the first stage comes from measurements of the flow fluctuations over the blade height in the different stages. When comparing the flow phenomena in function of the blade height the last stage shows two or three passages of the developing stall cell over the whole blade height before the transient drop of the compressor pressure ratio, whereas in the first stage in the lower half of the blading no signs of a developing stall cell are visible at the same time (fig. 9). The measurements proved, that the rotating stall initiated in the upper half of the first stage, it extends during development radially inward through the following stages.

The place of the initiation of the stall being identified, the question remains as to the mechanisms of initiation. Fig. 10 shows the temporal-spatial distribution of static pressure at the casing wall in front of the first rotor at nominal speed and guide vane setting during development of the stall. In the later part of the diagram the single stall cell rotating with about 60 % of the rotor speed is clearly visible. It begins with a sharp pressure increase and a subsequent, more gradual drop to a minimum at the end of the cell. In the region of stable flow pressure rises continuously. The stall development begins at rotor revolution no. 2. Here a group of pressure peaks appears, which moves circumferentially with about 60 % of rotor speed. The pressure rise results probably from the blockage of blade passages of the rotor by the

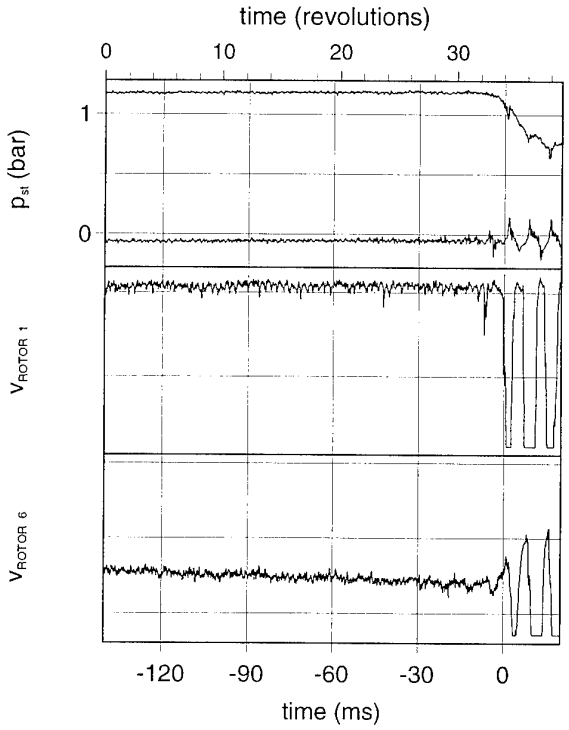

Fig. 9 : Hot-Wire Measurements,
at 50% Blade Height, I Le(0), n = n_N

developing flow separation.

The individual peaks within the group are not persistent, they disappear after about one revolution. New peaks form in a characteristic manner only at the side opposite to the rotor blade movement of the group. This shows clearly the development of a flow disturbance with relative movement from a local stochastic flow separation. After two or three further revolutions one of the peaks of the group grows considerably, while the others disappear. The stall cell has formed.

The same development is shown in fig. 11 by use of velocity signals measured with the flow-vector-probe. It comprises the absolute flow velocity with axial and circumferential component, the relative flow velocity and the static pressure, all measured behind the first rotor at 75 % blade height and rotor speed ratio of 0.9. At the begin of the time scale the

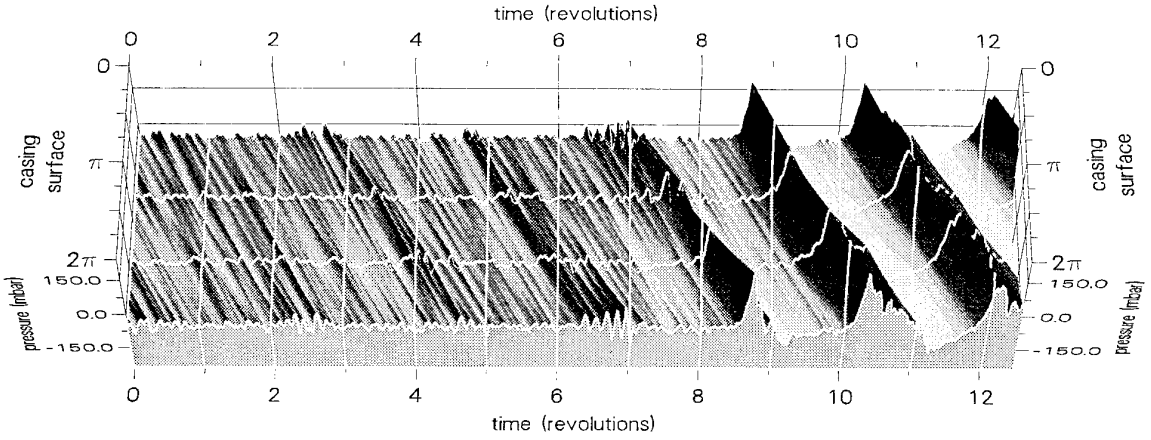

Fig. 10 : Pressure at the Casing in front of Rotor 1, I Le(0), n = n_N

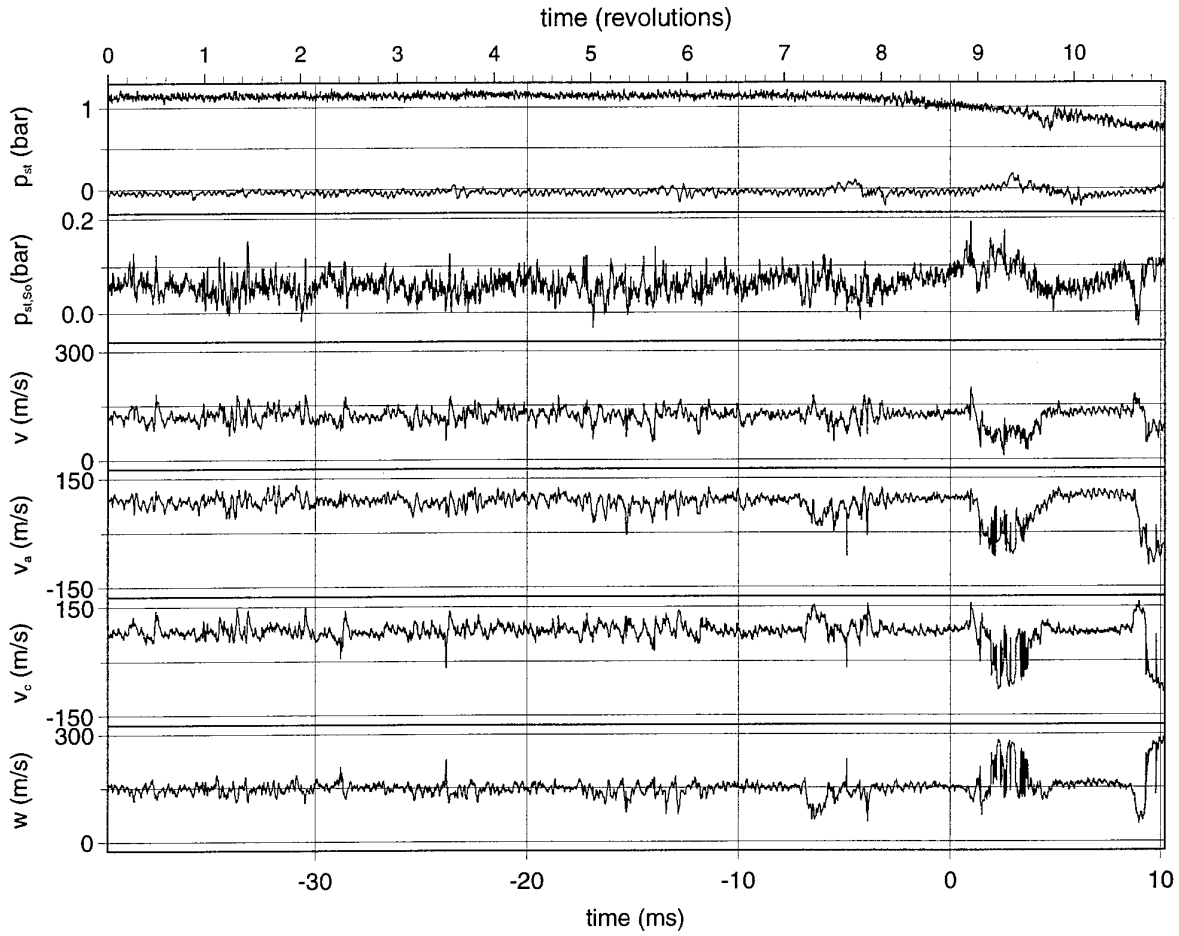

Fig. 11 : High Resolution of Flow-Vector-Probe Measurements, at 75% of Blade Height behind Rotor 1, I Le(0), n =0.9n_N

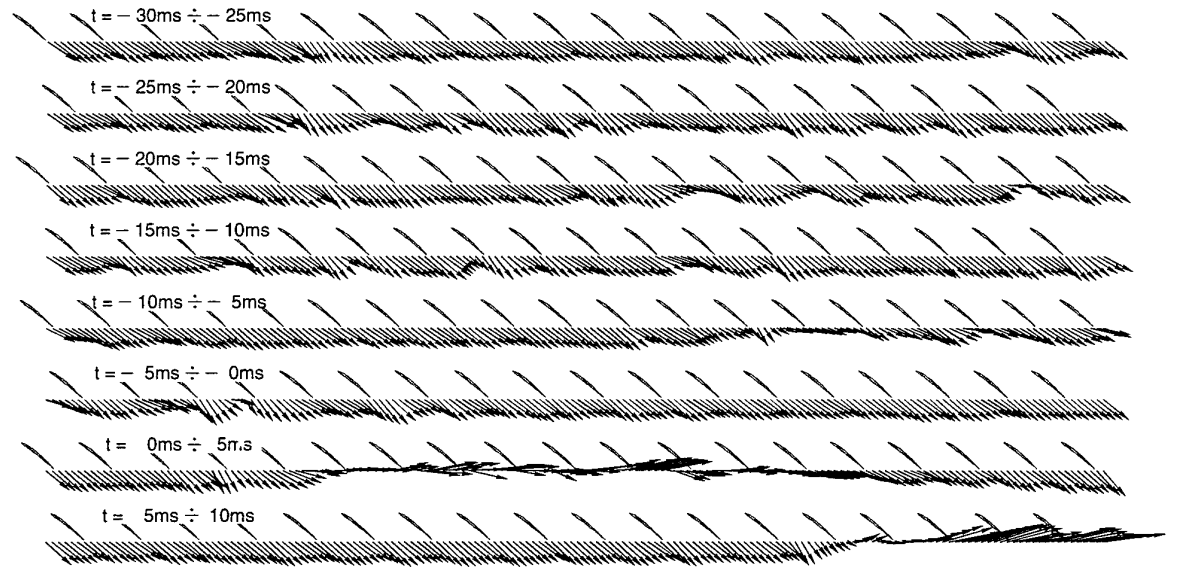

Fig. 12 : Relative Flow-Vector, at 75% of Blade Height behind Rotor 1, I Le(0), n = 0.9 n_N

initiation of a stall cell is visible, which rotates with stall frequency, i.e. it repeats after about two revolutions of the rotor. After three to four revolutions of the instability region the stall cell develops. The velocity curves show clearly the interaction between stable and instable regions of the flow. The growth of the instability and the consequent blockage of the blading causes a stabilisation of the stable flow part and a decrease or fluctuations there. After development of the full-span stall cell (time zero) the pressure and velocity curves between the cells are completely free of fluctuations.

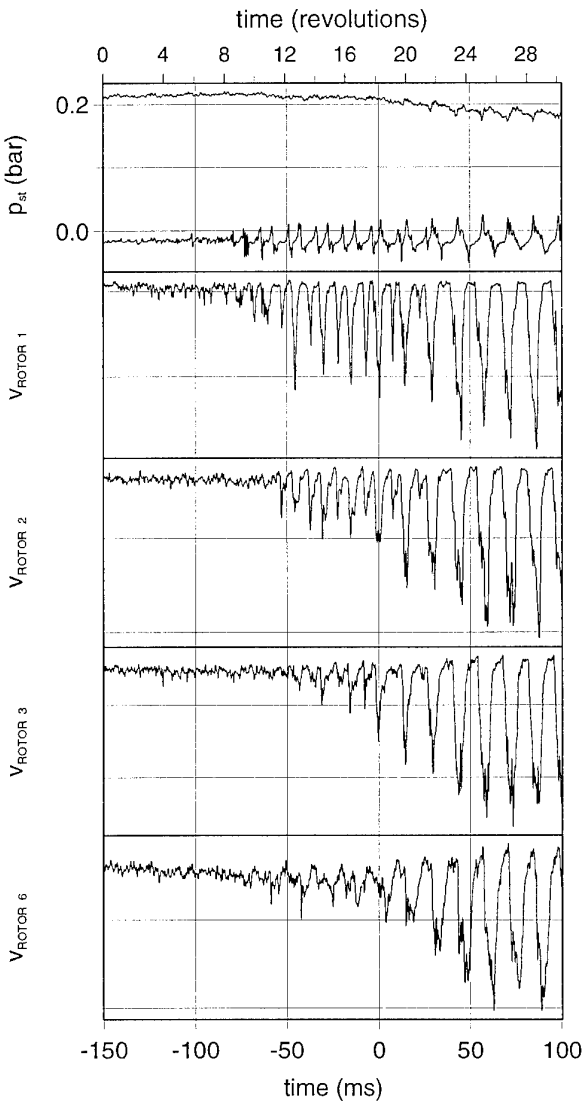

Fig. 13: Hot-Wire-Measurements, at 75% of Blade Height, I Le(0), n = 0.5 n_N

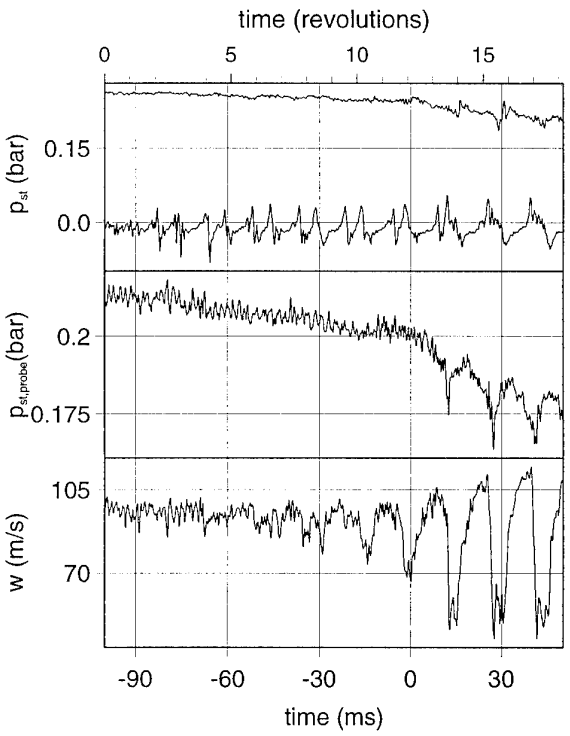

Fig. 14 : Static Pressure and relative Velocity in the Outlet, At 75% of Blade Height, I Le(0), n = 0.5 n_N

Similar measurements at 50 % blade height-during development of this instability show an increase of the axial velocity component below the instable region in the upper blade part. This points also to a local disturbance as origin of the rotating stall cell. Only after its complete development velocity drops occur also in the lower part of the blading.

The spatial correlation of the separation regions to the rotor blading is possible with a vectorial presentation of the relative velocity in fig. 12. At the beginning of the stall development (t = -24 ms to -21 ms) flow disturbances occur mainly on the suction side of the blade passage, a coherent flow separation over several blade pitches does not exist. In the time interval -17 ms to -11 ms a group of small disturbances forms combined with a regular flow separation on every second blade. After a region of rather stable flow (-11 ms to -7 ms) a complete flow break-down in two blade passages develops then into a rotating stall cell, which covers nearly ten blades.

6.2 Operation at low rotational speed

Investigations have been made in the rotor speed range from 50 % to 100 % nominal speed in order to detect correlations between development of instabilities and rotor speed, which determines the pressure ratio of the compressor. The rotor speed influences mainly the form of the instabilities during the first two phases of instability. The initiation mechanisms of instability show no dependency on rotor speed. They can be described in all observed cases by the model of local disturbance. A stall initiation by a modal wave of disturbances was never found also at lower rotor speeds.

While at rotor speed ratios above 0.9 always a single cell stall develops form a group of small instabilities, at lower speed stall configurations with two cells have been observed, which are stable over several revolutions.

Generally it was noticed, that with decreasing rotor speed the portion of measurements with short-time two cell configuration increases. The number of revolutions of the two cell stall varies even under identical operating conditions. With decreasing speed the mean time for formation of a stable single-cell stall increases.

An interesting feature is the obvious interaction of the "passive" back stages with the first stage, while instabilities develop. Fig. 13 shows the qualitative flow velocity signal measured with hot-wire probes at 75 % blade height behind the rotor blade rows 1, 2, 3 and 6. In addition the static wall pressure behind the inlet guide vanes and at the compressor outlet are shown. The curves show clearly the development of a two-cell stall in the front stages. Beginning in the first stage the instabilities propagate after one or two revolutions to the compressor outlet. While the two stall cells are well detectable in the first two stages over six revolutions a two-cell configuration is hardly present in the last stage.

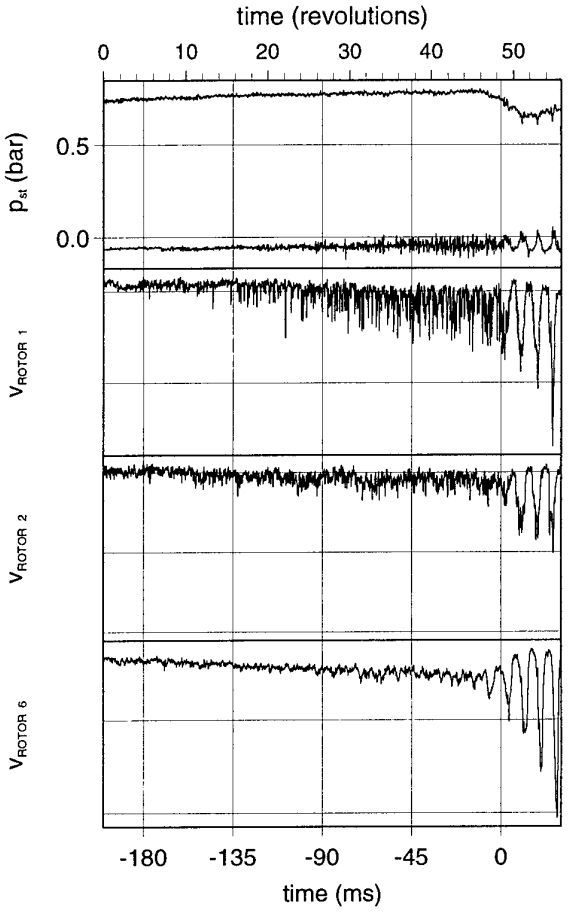

Fig. 15 : Hot-Wire-Measurements,
at 75% of Blade Height, I Le(4), n = n_N

Because of the low aerodynamic loading of the back stages at lower speed (fig. 4) the flow is stabilized again in this region. The stabilising effect of the development of a stall cell on the stable flow region in the same blade row suppresses the second cell is the development of a second one in the last stage. The single-cell stall of the back stages acts back on the front stages, the transition to a single-cell configuration there is evidently initiated by the back stages. The development of the single-cell stall intensifies the flow disturbances and causes finally a complete flow separation in all stages. The

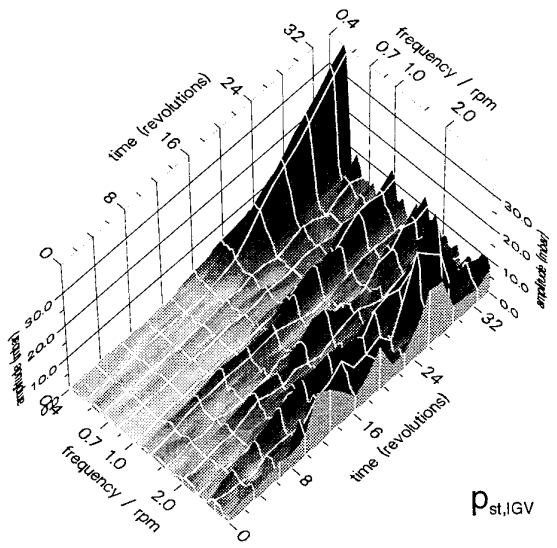

Fig. 17 : Sliding Frequency Analysis in front of Rotor 1,
I Le(4), n = n_N

transition of the cell configuration can be determined with the pressure graphs in fig. 14. The region of two-cell stall shows a continuous decrease of the pressure at the compressor outlet, which signals the begin of the transient drop of the pressure ratio. The two-cell stall in the first stage transforms into a single-cell configuration by gradual approach and finally merging of the two cells. Only then a full stall develops in the last stage, visible from the fluctuations of the outlet pressure signal.

6.3 Variation of aerodynamic load between the stages

Measurements of the flow in the compressor with nominal guide vane setting I Le(0) proved that stable flow conditions will not persist anywhere after onset of the first instability phase. A local flow disturbance grows after passage of the limit and leeds invariably to a break-down of stable flow in all stages. By changing the guide vane setting the aerodynamic load can be redistributed so, that instabilities remain limited to single stages. Fig. 15 shows the hot-wire velocity signal at 75 % blade height behind rotors 1, 2 and 6 and further static wall pressure after the inlet-guide vane and at the outlet at nominal speed. The guide vane setting I Le(4) creates a high aerodynamic load of the first stage compared

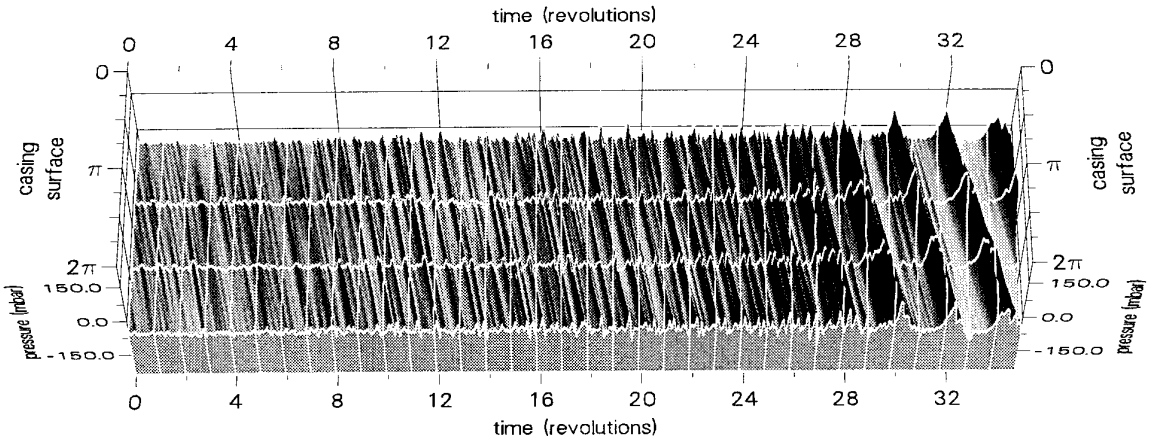

Fig. 16 : Pressure at the Casing in front of Rotor 1, I Le(4), n = n_N

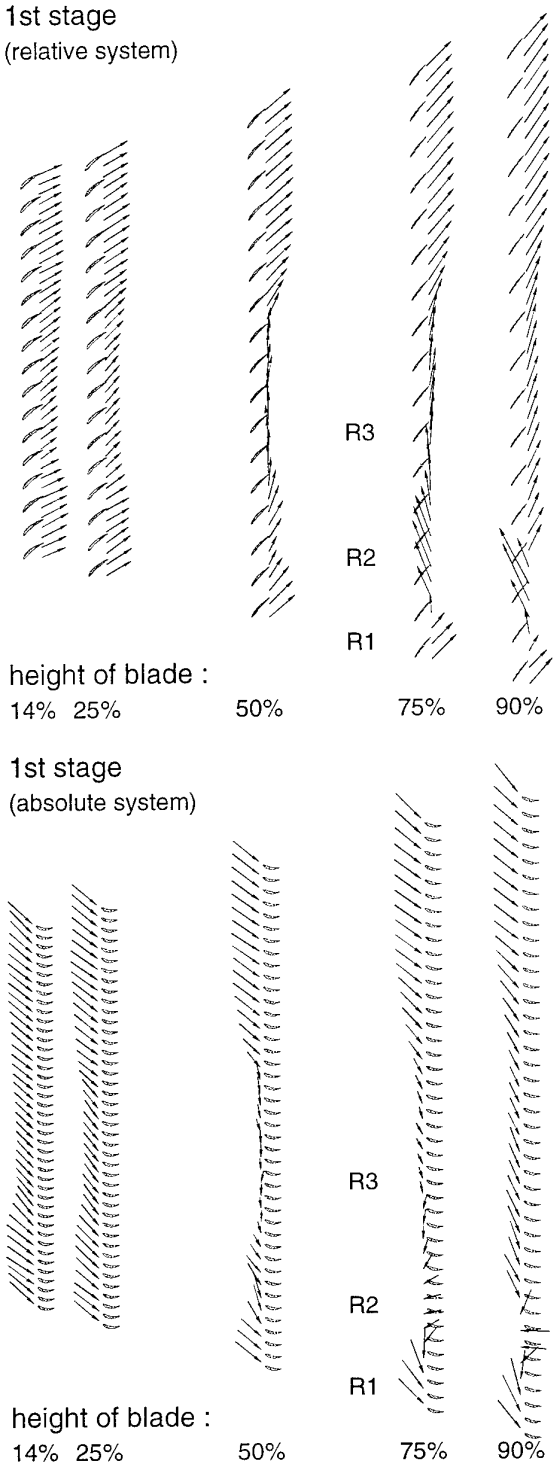

Fig. 18 : Flow-Vector around the Circumference

with the following (see fig. 4). This causes flow separations only in the upper part of the first rotor during the first instability phase. The numerous disturbances over the circumference of the first stage lead to mixing effects and thus to a homogenisation of the flow in the following stages. The velocity signal after the second rotor exhibits only minor fluctuations after onset of separations in the first stage. Only after further throttling of the compressor fluctuations arise at the outlet. The full development of a single-cell stall in the

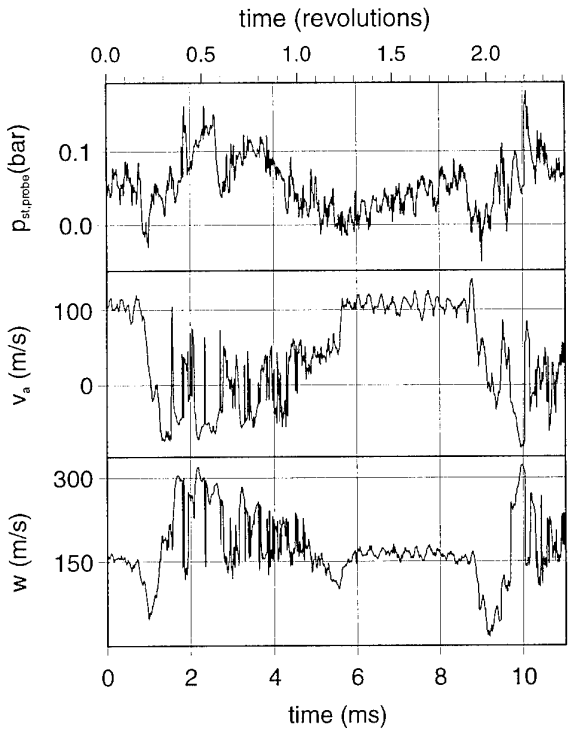

Fig. 19 : High Resolution of Measurement, during Stall, at 75% of Blade Height behind Rotor 1

first stage, combined with the transient drop of the pressure ration, propagates finally throughout the complete machine.

The character of the instabilities in the first stage during the first instability phase can be explained with the wall pressure transducers around the circumference. Fig. 16 shows the pressure distribution at the casing wall behind the inlet guide vane. The graph proves, that the disturbances move relative to the rotor blading. Number and intensity of the peaks vary in time. The time-dependent frequency spectrum in fig. 17 shows in the begin mainly excitation of the double, triple and four-fold stall-frequency due to the multi-cell character of the disturbance. The rotational speed of the instabilities diminishes during the first instability phase continuously from 60 % to 50 % of the rotor speed. Several experiments with guide vane setting I Le(4) showed considerable variations of the character of the instabilities during the first phase, number and intensity of the fluctuations vary continuously and irreproducibly. Usually a multi-cell stall forms under these operating conditions in the first stage directly before the stability limit. Sometimes the instability began with a single-cell stall, which changed into a multi-cell separation after some revolutions.

7. STRUCTURE OF STALL CELLS

The structure of the flow in the third instability phase (fully developed rotating stall, usually single-cell) was investigated behind the rotor blade rows with the flow-vector probe. The time-dependent, periodic flow phenomena were measured consecutively on the various radii of the different stages. A mean-value of the signals was calculated over several stall passages. The correct correspondence of the different measurements was assured by use of the wall pressure signal

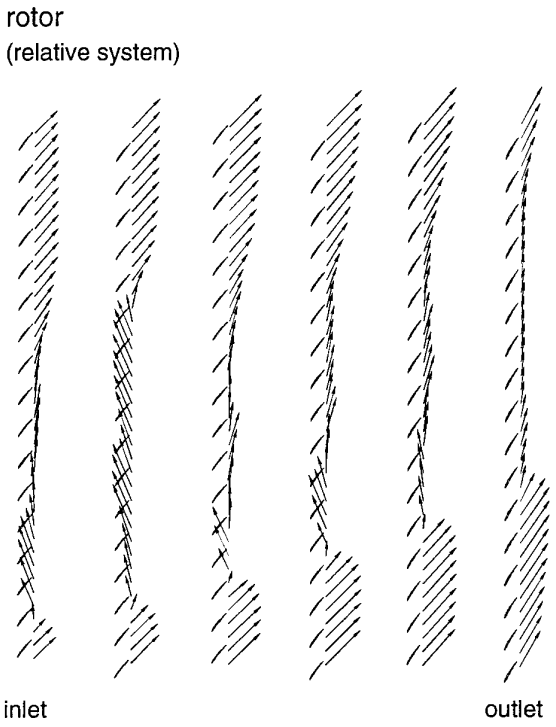

Fig. 20 : Flow-Vector through the Compressor

behind the inlet-guide vane as a trigger. Thus the numerous measurements in different places in the blading can be put together to a complete picture of the rotating stall cell.

Fig. 19 shows as an example the distribution of absolute and relative flow velocity of a single-cell rotating stall behind the first-rotor at nominal guide vane setting and rotor speed ratio of 0.9, over the blade height. The regions of disturbed and stable flow are clearly visible. The undisturbed flow is quite homogeneous and has a small deviation angle. Pressure and velocity curves of a stall cell at 75 % blade height in high temporal resolution are shown in fig. 19.

Within the stable flow region the wakes of the blades and the pressure increase from suction to pressure side are clearly visible. The stall cell, characterised by high fluctuations and local back-flow, covers nearly half of the circumference.

The instationary flow field within the stall cell can be subdivided in three regions R1 to R3 (fig. 18). Within region R1 the increased incidence angle at the guide vanes provokes a flow separation and consequently an increase of the circumferential component of the flow velocity. Region R2 exhibits intensive back-flow, which stretches through all stages (fig. 20). The reason for the back-flow is the different increase of static pressure in the stable and instable flow regions. Within the separated flow region the fluid will not receive the necessary supply of kinetic energy in the rotor blading to flow against the mean pressure increase of the stage.

The region R3 is the most extended an characterised by high velocity fluctuations. The instationary data in fig. 19 point to a complete flow separation. Strong vortices are created by the interaction of rotor blades and guide vanes at low flow rates.

A comparison of the velocity distribution diagrams for the different stages shows, that flow disturbances are more distinct in the first stage, were they concentrate on the upper part of the blade.

However, the circumferential extension of the stall cell increases towards the compressor outlet. The development of the stall cell through the stages gives fig. 20. The somewhat spiral form of the cell through the compressor results from the transport of the separated fluid, region R2, within the rotors. During their stay in the blade passage fluid particles with negative axial velocity are accelerated by the rotor blades circumferentially.

References:

1. Schlamann, U : "Experimentelle Untersuchung der Strömungsphänomene des Rotating Stall und des Pumpens bei mehrstufigen, hochbelasteten Verdichtern, VDI Forschungsberichte", Reihe 7, Nr. 91, 1985.

2. Rieß, W; Walbaum, M : "Meßtechnische Erfassung instationärer Strömungsvorgänge in mehrstufigen Axialverdichten", Mitt. Pfleiderer-Inst. 1, 1994 , W.H. Faragallah Verlag Braunschweig.

3. Kiesow, H.-J.: "Leitschaufelverstellung bei mehrstufigen Axialverdichtern", Dissertation, Universität Hannover, 1984.

4. Bronstein, I.N. : "Taschenbuch der Mathematik", Verlag Harri Deutsch, Thun 1981.

5. Day, I. J : "Stall Inception in Axial Flow Compressors", Journal of Turbomachinery 1993, Vol. 115, pp. 1-9.

6. Moore, F. K. : "A Theory of Rotating Stall of Multistage Axial Compressors, Part I, II, III", ASME Journal of Engineering for Gas Turbines and Power, 1984, Vol. 106, pp. 313-336 .

AMPLIFICATION DES INSTATIONNARITÉS GÉNÉRÉES PAR DES PERTURBATIONS AMONT OU AVAL

UNSTEADY FLOW AMPLIFICATION PRODUCED BY UPSTREAM OR DOWNSTREAM DISTURBANCES

P. FERRAND*
H. M. ATASSI**
S. AUBERT*

*Laboratoire de Mécanique des Fluides et d'Acoustique
URA CNRS 263
Ecole Centrale de Lyon,
Université Claude Bernard -Lyon I - BP 163
69131 ECULLY - FRANCE

**Department of Aerospace and Mechanical Engineering
University of Notre Dame
NOTRE DAME, IN 46556, USA

SUMMARY

In order to avoid or minimize the fluctuating forces resulting from unsteady flow-structure interaction, one tries to identify the important parameters which affect the level of these excitations. A subsonic and transonic convergent-divergent nozzle is used to analyze the unsteady flow near sonic conditions. Analytical and numerical computations using unsteady linear and nonlinear Euler equations are the carried out to analyze and quantify the upstream and downstream propagation of acoustic disturbances in the nozzle. The results show that, when the mean flow Mach number is close to unity, only upstream propagating acoustic disturbances are strongly amplified. It is therefore proposed to explain this phenomenon as resulting from the blockage of upstream propagating acoustic waves by near transonic mean flow. These results are confirmed on cascade configuration. A unsteady pressure bulge, near the sonic area, is found to be associated with the cut-on of a new acoustic mode in the upstream direction. The level of the pressure bulge is significantly reduced as a downstream propagating mode cuts on. These results confirm the phenomemon of acoustic blockage.

RÉSUMÉ

Pour réduire l'amplitude des forces fluctuantes provoquées par des problèmes d'interaction fluide-structure, on se propose d'essayer d'identifier les paramètres importants responsables de ces excitations. Une tuyère convergente-divergente a été utilisée pour analyser l'écoulement instationnaire pour des conditions d'écoulement stationnaire quasiment sonique. Des calculs analytiques et numériques ont été menés pour analyser et quantifier la propagation des ondes progressives et régressives dans la tuyère. Les résultats montrent que seules les ondes régressives sont amplifiées dans la zone proche de la ligne sonique. Ce résultat peut s'expliquer comme un effet de blocage acoustique dans la zone sonique des ondes remontant l'écoulement. Ces résultats sont confirmés par ceux obtenus sur une configuration de grille d'aube où une forte amplification des fluctuations de pression statique est observée près de la zone de plus haut nombre de Mach. Cette amplification n'est significative que lorsqu'un mode acoustique propagatif régressif supplémentaire apparaît à l'amont. Ce résultat confirme donc l'explication du blocage acoustique.

1. Introduction

La compréhension des mécanismes qui provoquent le flottement en écoulement transsonique n'est pas encore acquise malgré les potentialités des méthodes actuelles et les nouvelles capacités des moyens de mesure (1). Cette incompréhension tient à la complexité des géométries des turbomachines qui favorisent les multiples réflexions acoustiques rendant l'interprétation du champ instationnaire difficile. Par ailleurs, la dépendance du flottement vis à vis de mécanismes physiques complexes tels que le décollement instationnaire ou l'oscillation d'onde de choc accentue la difficulté de reproduction du flottement par les méthodes numériques.

La démarche que nous proposons repose sur la nécessité de dissocier les différents mécanismes qui rentrent dans l'organisation du flottement. Pour cette étude, nous nous appuierons principalement sur l'analyse de l'écoulement dans une tuyère convergente - divergente en régime haut subsonique et transsonique. Les résultats seront obtenus à l'aide d'une méthode de résolution des équations d'Euler non linéaires développée par Aubert et Ferrand (2,3). Sur la base de ces résultats, nous verrons comment étendre nos interprétations aux turbomachines en utilisant les résultats obtenus à l'aide d'une théorie linéarisée établie par Fang et Atassi (4,5).

2 Analyse de l'écoulement dans une tuyère à l'aide d'une méthode non linéaire

Pour étudier l'écoulement instationnaire dans une tuyère convergente - divergente, nous utilisons le logiciel PROUST (6) qui résout les équations d'Euler ou de Navier Stokes instationnaires bi ou tridimensionnelles. Le schéma numérique est du type volume fini avec formulation MUSCL, c'est à dire avec une extrapolation des variables du premier, deuxième ou troisième ordre pour définir les flux aux interfaces. Le schéma en temps est un schéma Runge Kutta à cinq pas précis au deuxième ordre. Le schéma en espace est du type mixte centré - à séparation de flux (3) ; la séparation de flux pouvant être basée sur celle de Van Leer, de Roe ou de Liou. Ce schéma en espace assure une optimisation de la précision numérique en tout point du domaine et à chaque pas de temps (7). Des relations de compatibilité sont introduites aux frontières du domaine par projection des caractéristiques sur les surfaces frontière. Sur

Paper presented at the AGARD PEP 85th Symposium on "Loss Mechanisms and Unsteady Flows in Turbomachines", held in Derby, United Kingdom, 8-12 May 1995, and published in CP-571.

le solide, des conditions de glissement sont imposées, à l'amont et à l'aval soit des conditions de non réflexion soit les grandeurs d'arrêt, et l'angle à l'entrée et la pression statique en sortie.

La géométrie de la tuyère est bidimensionnelle et similaire à celle expérimentée par Ött et al (8) pour étudier le mouvement d'une onde de choc droite en présence d'une fluctuation de pression statique à l'aval. Le code PROUST a été testé et validé sur cette expérience (9). La tuyère présente une convergence de veine de 10% entre l'entrée et le col. Le domaine de calcul est limité à une demi-tuyère avec une condition de symétrie sur l'axe. La longueur total du canal est de 2 avec une évolution de section sur 4/3 et pour une hauteur de 0.8. Différents maillages ont été utilisés suivant les conditions d'écoulements et les fréquences imposées. La figure 1 présente un maillage typique correspondant au cas légèrement transsonique.

Plusieurs conditions d'écoulements sont imposées pour obtenir un cas sans choc, un cas bloqué, enfin un cas avec un choc local faible qui ne traverse pas le conduit. Le nombre de Mach amont est de 0.64 dans le premier et le dernier cas et de 0.66 dans le cas bloqué. Les deux premières configurations se distinguent par la forme du col qui est continue alors que la dernière configuration est obtenue avec les mêmes conditions aérodynamique mais en modifiant légèrement la pente géométrique au col pour générer une accélération locale. La figure 2 présente les iso nombres de Mach du cas subsonique, avec un nombre de Mach maximum ($M_{max} = 0.97$). Pour le cas bloqué, le nombre de Mach maximum varie entre 1.24 à la paroi et 1.13 au centre du canal (figure 3). Enfin le cas légèrement transsonique présente un nombre de Mach maximum de 1.06 (figure 11). Deux sources d'excitation sinusoïdale ont été étudiées : soit une distorsion de pression totale à l'entrée δp_t^e, soit une distorsion de pression statique en sortie δp_s^s :

$$\delta p_s^s = a_s \sin \omega t \qquad \delta p_t^e = a_t \sin \omega t$$

La fréquence réduite, basée sur la demi-hauteur au col est égale à 0.3 pour tous les calculs présentés dans cet article sauf indication contraire :

$$k_1 = \frac{\omega d}{2U_{-\infty}}$$

L'amplitude de l'oscillation est fixée à 0.2% de la pression stationnaire pour se placer dans une configuration a priori où la réponse devrait être linéaire. Pour étudier le rapport d'amplification des fluctuations de pression statique δp_s, celles-ci sont normalisées par l'amplitude a_S à l'entrée ou à la sortie suivant le cas étudié.

La figure 4 montre une comparaison du rapport d'amplification $|\delta p_s|$ en fonction de la distance longitudinale pour trois lignes de maillage correspondant respectivement à des nombres de Mach maxima de 0.9, 0.95 et 0.97 pour une distorsion aval. On peut observer qu'au point où le nombre de Mach stationnaire est le plus élevé (donc au col en x=0.5), le rapport d'amplification est de 2.4, 8.75 et 13.5 pour les nombres de Mach maxima respectivement de 0.9, 0.95 et 0.97. Ces résultats montrent clairement que l'amplification des distorsions apparaît principalement dans la zone où le nombre de Mach est proche de l'unité et qu'en dessous d'une valeur de 0.9, l'amplification est négligeable. La non symétrie des courbes (le rapport d'amplification est inférieur à 1 à l'entrée) s'explique par la diffusion numérique importante dans la zone du col où l'amplitude des fluctuations est grande et où la longueur d'onde est faible (fonction de *u-a*, *a* étant la vitesse du son). Cependant cet effet reste suffisamment secondaire pour ne pas affecter les interprétations physiques.

La figure 5 complète ces résultats en comparant le rapport d'amplification pour une fluctuation imposée à l'entrée ou à la sortie, pour le nombre de Mach maximum de 0.97. Pour la distorsion amont le rapport d'amplification maximum n'est plus que de 2.75 comparé au 13.5 de la distorsion aval. La distorsion amont semble simplement convectée puis légèrement amplifiée au col. On peut remarquer d'autre part que la courbe reste symétrique, montrant que la dissipation numérique est plus faible ce qui est cohérent puisque cette fois la longueur d'onde est grande (fonction de *u+c*).

La figure 6 présente les mêmes évolutions du rapport d'amplification sous l'effet d'une excitation amont ou aval, pour le cas bloqué correspondant aux iso-nombres de Mach de la figure 3. Cette fois l'amplification est limitée à la traversée du choc, amplification provoquée par l'oscillation de celui-ci. On peut observer le même comportement qu'en subsonique, seules les perturbations provenant de l'aval ont un réel pouvoir d'amplification. On peut remarquer cependant une différence de comportement intéressante pour les perturbations provenant de l'amont. Alors que dans le cas subsonique la perturbation se trouvait amplifiée au col dans un rapport de 2.75, dans le cas transsonique, les fluctuations sont convectées sans amplification ni amortissement jusqu'au choc. Nous essayerons d'expliquer cette différence un peu plus loin.

L'interprétation des résultats des figures 4, 5 et 6 conduit à la définition du concept de blocage acoustique établi par Atassi et al. (10). Pour étayer ce concept, nous allons reformuler des solutions analytiques monodimensionnelles où il est possible de dissocier les influences amont et aval.

3 Analyse de solutions analytiques monodimensionnelles

Carrière avait montré qu'il était possible de déterminer des solutions analytiques des équations d'Euler instationnaires monodimensionnelles linéarisées (11). Nous nous proposons de reprendre une formulation équivalente mais adaptée à l'aspect que nous voulons analyser.

Soit les équations initiales de conservation et d'état :

$$\frac{\partial}{\partial t}(\rho A) + \frac{\partial}{\partial x}(\rho u A) = 0$$

$$\frac{\partial}{\partial t}(\rho u A) + \frac{\partial}{\partial x}(\rho u^2 A + pA) = p\frac{\partial}{\partial x}(A)$$

$$\frac{\partial}{\partial t}(\rho h_i A) + \frac{\partial}{\partial x}(\rho u h_i A) = A\frac{\partial}{\partial t}(p)$$

et

$$p = R\rho T \qquad p = \rho^{\gamma} e^{\frac{s}{C_v}}$$

A étant la section, *R* la constante des gaz, *s* l'entropie et h_i l'enthalpie totale.

L'ensemble des variables sont décomposées en partie stationnaire (ne dépendant que de l'abscisse x) et partie fluctuante de faible amplitude tel que :

$$Q(x,t) = \overline{Q}(x) + \delta q(x) e^{i\omega t} \qquad \text{avec} \quad \delta q << \overline{Q}$$

Un changement de variables est effectué pour faire apparaître des variables liées aux ondes progressives (se déplaçant dans le sens de l'écoulement stationnaire) et régressives (remontant l'écoulement stationnaire), ce qui

revient aux invariants de Riemann lorsque les gradients de l'écoulement stationnaire sont nuls.

Onde progressive :

$$\delta w^{+} = \frac{1+M}{\sqrt{M}} e^{i\omega\sigma} \left(\frac{a}{\gamma p}\delta p + \delta u\right)$$

Onde régressive :

$$\delta w^{-} = \frac{1-M}{\sqrt{M}} e^{-i\omega\tau} \left(\frac{a}{\gamma p}\delta p - \delta u\right)$$

Avec le déphasages en temps respectivement pour les ondes progressives et régressives :

$$\sigma = \int_{x_0}^{x} \frac{dx}{a+u} \quad \text{et} \quad \tau = \int_{x_0}^{x} \frac{dx}{a-u}$$

Il est alors possible de faire apparaître un paramètre ν qui caractérise la forme de la géométrie ; son expression peut être donnée en fonction de l'évolution de la section A ou du nombre de Mach :

$$\nu = \frac{2M}{1-M^2} \frac{(1+\frac{\gamma-1}{2}M^2)^{1/2}}{1-\frac{\gamma-1}{2}M^2} \left(\frac{dM}{dx}\right)^{-1}$$

Si l'on admet que le paramètre ν est constant, il est possible de trouver une solution analytique. Pour notre étude, cette hypothèse n'est pas pénalisante car on peut toujours admettre sa constance sur une partie de l'abscisse. Et comme nous voulons étudier l'amplification éventuelle des fluctuations entre deux points d'une tuyère, il suffira d'effectuer une étude paramétrique en fonction de ce coefficient.

Les variables s'expriment alors entre les abscisses x_0 et x_1 sont la forme matricielle suivante :

$$\begin{pmatrix} \delta w^{-} \\ \delta w^{+} \end{pmatrix}_1 = \begin{pmatrix} N_{11} & N_{12} \\ N_{21} & N_{22} \end{pmatrix} \begin{pmatrix} \delta w^{-} \\ \delta w^{+} \end{pmatrix}_0$$

Avec :

$$\varphi = \tfrac{1}{2} ln\left(\frac{M_0}{M_1}\frac{1+\frac{\gamma-1}{2}M_1^2}{1+\frac{\gamma-1}{2}M_0^2}\right)$$

$$r = \sqrt{1-\nu^2\omega^2}$$

$$N_{11} = \left(ch(r\varphi) - \frac{i\omega\nu}{r} sh(r\varphi)\right) e^{i\omega\nu\varphi}$$

$$N_{12} = \frac{1}{r} sh(r\varphi) e^{i\omega\nu\varphi}$$

$$N_{21} = N_{12}$$

$$N_{22} = \left(ch(r\varphi) + \frac{i\omega\nu}{r} sh(r\varphi)\right) e^{-i\omega\nu\varphi}$$

Cette solution est obtenue en supposant r réel. Si r est complexe, il faut changer celui-ci par $r = \sqrt{\nu^2\omega^2 - 1}$ et remplacer les sinus et cosinus hyperboliques par des sinus et cosinus trigonométriques. Dans tous les cas, un simple changement de variables permet de remonter à une expression matricielle qui relie les fluctuations de pression statique et de vitesses entre les abscisses x_0 et x_1 :

$$\begin{pmatrix} \delta p \\ \delta u \end{pmatrix}_1 = \begin{pmatrix} Q_{11} & Q_{12} \\ Q_{21} & Q_{22} \end{pmatrix} \begin{pmatrix} \delta p \\ \delta u \end{pmatrix}_0$$

Avec :

$$Q_{11} = \frac{p_1}{p_0}\frac{a_0}{2a_1}\sqrt{\frac{M_1}{M_0}}\left\{Q_{11}' + Q_{12}' + Q_{21}' + Q_{22}'\right\}$$

$$Q_{12} = \frac{\gamma p_1}{2a_1}\sqrt{\frac{M_1}{M_0}}\left\{-Q_{11}' + Q_{12}' - Q_{21}' + Q_{22}'\right\}$$

$$Q_{21} = \frac{a_0}{2\gamma p_{01}}\sqrt{\frac{M_1}{M_0}}\left\{-Q_{11}' - Q_{12}' + Q_{21}' + Q_{22}'\right\}$$

$$Q_{22} = \frac{1}{2}\sqrt{\frac{M_1}{M_0}}\left\{Q_{11}' - Q_{12}' - Q_{21}' + Q_{22}'\right\}$$

$$Q_{11}' = \frac{1-M_0}{1-M_1} N_{11} e^{-i\omega\tau_1}$$

$$Q_{12}' = \frac{1+M_0}{1-M_1} N_{12} e^{-i\omega\tau_1}$$

$$Q_{21}' = \frac{1-M_0}{1+M_1} N_{21} e^{-i\omega\sigma_1}$$

$$Q_{22}' = \frac{1+M_0}{1+M_1} N_{22} e^{-i\omega\sigma_1}$$

A partir de cette formulation générale, plusieurs configurations peuvent être étudiées : onde progressive ou régressive nulle, col sonique,... Dans tous les cas, ces configurations se traduisent par une condition qui lie les fluctuations de vitesse et de pression. Cette condition établit une dépendance linéaire entre les fluctuations de vitesse et de pression et si l'on appelle K ce coefficient, la relation s'écrit :

$$\delta u = K \frac{a}{\gamma p} \delta p$$

Si l'on impose cette condition à l'abscisse x_0, la fluctuation de pression statique peut alors s'exprimer entre les points d'abscisses x_0 et x_1 par une relation dépendant des nombres de Mach locaux et du coefficient K :

En remarquant que : $$\frac{p_1}{p_0} = \frac{a_1}{a_0}\left(\frac{1+\frac{\gamma-1}{2}M_0^2}{1+\frac{\gamma-1}{2}M_1^2}\right)^{\frac{\gamma+1}{2(\gamma-1)}}$$

Alors,

$$\delta p_1 = \tfrac{1}{2}\sqrt{\frac{M_1}{M_0}}\left(\frac{1+\frac{\gamma-1}{2}M_0^2}{1+\frac{\gamma-1}{2}M_1^2}\right)^{\frac{\gamma+1}{2(\gamma-1)}} \times$$

$$\left\{(1-K_0)\left(Q_{11}' + Q_{21}'\right) + (1+K_0)\left(Q_{12}' + Q_{22}'\right)\right\}\delta p_0$$

L'amplification des fluctuations de pression entre les points d'abscisses x_0 et x_1 peut être étudiée pour le cas où seule une onde progressive existe et inversement en présence uniquement d'une onde régressive. Dans le cas d'une onde progressive seule, $\delta w^{-} = 0$ et $K = 1$. Le module d'amplification s'écrit :

$\delta p_1 = CGP \times \delta p_0$

avec :

$$CGP = \sqrt{\frac{M_1}{M_0}}\frac{1+M_0}{1+M_1}\left(\frac{1+\frac{\gamma-1}{2}M_0^2}{1+\frac{\gamma-1}{2}M_1^2}\right)^{\frac{\gamma+1}{2(\gamma-1)}} \times$$

$$\left|\left(chr\varphi+\frac{i\omega v}{r}shr\varphi\right)e^{-i\omega(v\varphi+\sigma_1)}\right|$$

Et dans le cas d'une onde régressive seule, $\delta w^+ = 0$ et $K = -1$, le module d'amplification s'écrit :
$\delta p_1 = CGM \times \delta p_0$
avec :

$$CGM = \sqrt{\frac{M_1}{M_0}}\frac{1+M_0}{1-M_1}\left(\frac{1+\frac{\gamma-1}{2}M_0^2}{1+\frac{\gamma-1}{2}M_1^2}\right)^{\frac{\gamma+1}{2(\gamma-1)}} \times$$

$$\left|\left(chr\varphi-\frac{i\omega v}{r}shr\varphi\right)e^{-i\omega(v\varphi+\tau_1)}\right|$$

Les premiers facteurs du membre de droite des expressions *CGP* et *CGM* sont indépendants de la fréquence et ne dépendent que des nombres de Mach locaux. Ces coefficients ont été mis en évidence par Candel (9) dans le cadre d'une modélisation des termes de hautes fréquences uniquement, mais sans hypothèse sur la loi d'évolution de la section de la tuyère. Les second facteurs sont, par contre, liés à la fréquence et au gradient du nombre de Mach et par conséquent de la vitesse stationnaire à travers le coefficient *v*. Pour les hautes fréquences ou les faibles gradients de vitesse (*v* grand), *r* devient imaginaire, les fonctions hyperboliques deviennent trigonométriques. L'influence de ce terme n'agit plus alors que sur le déphasage. Les figures 7 et 8 présentent respectivement l'évolution des modules des coefficients d'amplification *CGM* et *CGP* en fonction des nombres de Mach M_0 et M_1, ceux-ci variant entre 0.03 et 0.97. La fréquence réduite est de 0.5 et le coefficient *v* de 1, ce qui correspond à une valeur réelle de *r*. Les figures 9 et 10 montrent les mêmes évolutions mais pour une fréquence réduite de 2 correspondant à une valeur imaginaire de *r*. Ces figures confirment les interprétations qui découlent des expressions analytiques:

1- Les ondes régressives sont fortement amplifiées lorsque le nombre de Mach M_1 tend vers 1, limite de validité de la théorie, et ce d'autant plus que le nombre de Mach M_0 est faible. Par contre les ondes progressives sont plus sensibles à une faible valeur de M_0 qu'à une forte valeur de M_1.

2- A un degré moindre (évolution en racine carrée), les ondes progressives et régressives sont amplifiées au voisinage d'un nombre de Mach M_0 nul, situation correspondant par exemple à un bord d'attaque.

3- L'influence de la fréquence sur l'amplification des perturbations est modérée, celle-ci agissant surtout sur le déphasage, principalement lorsque *r* devient imaginaire. Cependant la comparaison des figures 8 et 10 montre l'effet d'amortissement que produisent les hautes fréquences ainsi qu'une sensibilité plus réduite aux faibles valeurs de M_0. Par ailleurs, le facteur d'amplification *CGP* présente un maximum pour un nombre de Mach M_1 qui diminue quand la fréquence augmente, passant de 0.63 pour la fréquence réduite égale à 0.5 à 0.35 pour la fréquence réduite égale à 2. Cependant dans tous les cas ce maximum reste modéré, passant respectivement de 5 à 2.7.

4- L'analyse des expressions analytiques des solutions montrent que la fréquence apparaît toujours en produit avec le coefficient d'évolution de la section *v*. Par conséquent, le coefficient étant inversement proportionnel au gradient de vitesse, résultat intéressant, l'inverse du gradient de vitesse a le même effet que la fréquence. Donc, les faibles valeurs du gradient de vitesse stationnaire tendent à limiter l'amplification des fluctuations. La solution limite est obtenue pour une valeur nulle du gradient, ce qui correspond à la constance des invariants de Riemann, où seuls les déphasages apparaissent.

Tous ces résultats confirment ceux obtenus avec la méthode non linéaire. Ils apportent la confirmation que ni la fréquence, ni les gradients de vitesse stationnaire, ni la forme de la tuyère ne modifient fondamentalement l'interprétation du concept de blocage acoustique : les ondes progressives sont évacuées rapidement sans amplification importante dans tout le domaine, par contre les ondes régressives se trouvent bloquées, s'accumulent dans la région proche du nombre de Mach sonique générant ainsi une très forte amplification des fluctuations de pression statique.

4 Rôle du col sonique

Lorsque l'écoulement stationnaire devient sonique, le système différentiel se dénature en équations algébriques liant les variables instationnaires. La vitesse de l'écoulement au col n'est pas sonique en instationnaire, mais une relation (13) lie les fluctuations des grandeurs aérodynamiques:

$$\left\{-\frac{\gamma+1}{\gamma}\frac{\partial ln(u)}{\partial x'}-\frac{\partial ln(A)}{\partial x'}-i\frac{4}{\gamma}k_1\right\}\frac{\partial\rho}{\rho}+$$

$$\left\{\frac{2}{\gamma}\frac{\partial ln(u)}{\partial x'}+i\frac{2}{\gamma}k_1\right\}\frac{\partial\rho u}{\rho}+$$

$$\left\{-\frac{\partial ln(u)}{\partial x'}-\frac{\partial ln(A)}{\partial x'}-i\frac{2}{\gamma}k_1\right\}\frac{(\gamma-1)}{\gamma R}\partial S=0$$

x' étant l'abscisse adimensionnalisée par la distance *d*.

En considérant que le gradient de la section *A* est nul au col puisque la section est minimum, la relation précédente peut s'écrire après quelques manipulations et en tenant compte de l'égalité de la vitesse du son et de la vitesse de l'écoulement en stationnaire :

$$\left\{\frac{\partial ln(u)}{\partial x'}+ik_1\right\}\partial u_{col}=\left\{\frac{\gamma-1}{2}\frac{\partial ln(u)}{\partial x'}+ik_1\right\}\frac{a}{\gamma p}\partial p_{col}$$

Lorsque l'écoulement reste subsonique, le gradient de vitesse stationnaire est nul et une relation simple, indépendant de la fréquence relie les fluctuations de vitesse et de pression :

$\partial u_{col}=\frac{a}{gp}\partial p_{col}$ correspondant à $K=1$

Cette relation reste valable en écoulement transsonique si le gradient de vitesse reste modéré comparativement à la fréquence réduite ou si la fréquence réduite est élevée. Cette condition revient à garantir la nullité de l'invariant de Riemann correspondant à l'onde régressive : $w^-=0$. La condition au col, en imposant la nullité des ondes régressives, établit un filtre qui empêche l'amplification des perturbations. Cette condition n'apparaît réellement que lorsque le point sonique est atteint, néanmoins plus le nombre de Mach est proche de l'unité, plus cette condition tend à s'imposer, minimisant donc la contribution des ondes régressives. Cette condition montre

qu'une valeur bornée existe et donc que l'amplification théoriquement infinie des ondes régressives est en réalité finie, conformément aux résultats de la solution non linéaire (figure 5).

On peut observer que dans le cas d'un gradient de vitesse stationnaire élevé et d'une fréquence réduite faible, la relation au col est différente, K étant égal cette fois à $\frac{\gamma-1}{2}\frac{a}{\gamma p}$. Cette condition revient à filtrer au col les fluctuations de vitesse au bénéfice des fluctuations de pression. En fait, le couplage de cette condition avec les conditions aux limites amont modifie la solution de l'écoulement amont au col. Ainsi, la différence d'amplification observée au col entre le cas subsonique et le cas transsonique pour une perturbation amont (respectivement figure 5 et 6) peut s'expliquer par cette condition différente. En effet dans le cas subsonique, le gradient de vitesse est nécessairement nul au col, alors que dans le cas transsonique, le gradient de vitesse est près de dix fois la valeur de la fréquence réduite. Dans le cas transsonique, la deuxième condition est applicable, ce qui se traduit par une convection sans amplification des fluctuations de pression statique.

Entre ces conditions extrêmes, seule la condition générale est applicable, le coefficient K est complexe, et le passage d'une condition à l'autre s'effectue par glissement progressif du déphasage entre les fluctuations de vitesse et de pression.

5 Écoulement localement transsonique

Lorsque l'écoulement est bidimensionnel et localement transsonique sous l'effet de la courbure, les trois conditions monodimensionnelles précédentes vont être présentes localement le long de la ligne sonique :

1 - La pointe, où ligne sonique et choc se rejoignent, présente un gradient de vitesse nul, cette région sera donc amplificatrice,

2 - la ligne de courbure maximum le long de la paroi est caractérisée par un gradient de vitesse important, cette zone sera, au contraire, atténuatrice,

3 - les positions intermédiaires seront régies par la formulation générale et par conséquent responsables d'un déphasage évolutif vitesse - pression.

Il est clair que la région sonique joue un rôle déterminant dans les mécanismes d'amplification des fluctuations.

Pour confirmer cet effet, la tuyère précédente a été testée avec une pression statique aval donnant un nombre de Mach légèrement supersonique à la paroi (M_{max}=1.06). Les iso-nombres de Mach stationnaires obtenus avec le code PROUST présentent une région étendue autour d'un nombre de Mach égal à 1 (figure 11). Le code non linéaire a ensuite été utilisé pour simuler l'écoulement instationnaire sous l'effet d'une fluctuation de pression statique aval d'amplitude légèrement plus importante que dans les cas précédents (0.4% contre 0.2%).

La figure 12 montre les iso-amplitudes de fluctuation de pression statique pour des valeurs supérieures à 3. Les flèches des figures 11 et 12 correspondent à la position stationnaire du choc sur la paroi. Il est remarquable de constater que la zone amplifiée se situe à l'aval du col, d'une part juste à l'aval du choc stationnaire et d'autre part, plus vers le centre, dans la zone où le nombre de Mach est élevé. Contrairement à ce qui est couramment admis, l'amplitude des fluctuations à travers le choc n'est pas importante et l'amplitude du mouvement du choc reste faible malgré l'importance plus élevée de l'excitation. On peut vérifier qu'il existe une poche d'amplification (d'un facteur 5) à l'intersection de l'onde de choc et de la zone sonique. Cependant l'amplification majeure se situe près de la paroi et après l'onde de choc.

La figure suivante nous donne l'explication de cette amplification. En fait, compte tenu du rapport d'amplification élevé (facteur 15) et du nombre de Mach stationnaire important (de l'ordre de 0.95), le mécanisme amplificateur est essentiellement non linéaire et s'explique par l'apparition d'une deuxième onde de choc durant une partie du cycle. C'est ce que montre la figure 13 qui présente l'évolution du nombre de Mach instantané au cours d'une période : au temps zéro, les isovaleurs sont proches du cas stationnaire, le choc étant très légèrement reculé et l'isovaleur 0.97 plus étendu. Une fluctuation apparaît ensuite à l'aval de l'onde de choc et s'amplifie au point de devenir une onde de choc à partir de T=3/8. Cette onde de choc va s'intensifier et s'étendre tout en remontant l'écoulement. A l'approche de l'onde de choc principale (T=5/8 et 6/8), cette onde va remonter plus lentement avant d'impacter l'onde principale (T=7/8) puis va fusionner avec elle (T=0/8), ce qui explique le léger recul de l'onde de choc par rapport au cas stationnaire. Cette onde de choc secondaire concentre les fluctuations provenant de l'aval et en protège l'onde de choc principale jusqu'au moment de l'impact et de la fusion qui provoque alors un léger mouvement de l'onde principale. Parallèlement, on peut observer de fortes fluctuations de la zone correspondant à la 'pointe' de l'isovaleur 0.97, zone non protégée par l'onde de choc secondaire. Les mêmes calculs ont été effectués pour une fréquence plus élevée et le même mécanisme s'est produit. Seulement la longueur d'onde étant plus courte, cette fois ce sont deux ondes de choc secondaires, l'une derrière l'autre, qui sont apparues. L'ensemble de ces résultats confirme le rôle déterminant des ondes régressives qui traverse une région à haut nombre de Mach subsonique, même lorsque des non linéarités apparaissent.

6 Transposition aux turbomachines

Ces mécanismes peuvent être transposés aux turbomachines en considérant chaque canal interaube comme une tuyère. Cependant la présence des bords d'attaque et des bords de fuite, l'existence d'une périodicité circonférentielle rendent l'écoulement plus complexe et les interprétations plus délicates. Pour approfondir les notions précédentes, une méthode linéarisée a été utilisée sur la 10ème configuration (14). Le code CASGUST développé par Fang et al. (4, 5) résout les équations d'Euler linéarisées en décomposant en partie potentielle et partie rotationnelle. Une distorsion instationnaire est imposée à l'amont et la réponse de l'écoulement est alors étudiée. Le mécanisme est notamment différent de la tuyère par le fait que la distorsion amont rencontre la grille d'aubes et génère alors des réflexions acoustiques dans tout le domaine.

La figure 14 présente la géométrie de la 10ème configuration standard correspondant à un profil NACA 0006 ainsi que l'évolution du nombre de Mach stationnaire. La valeur maximum du nombre de Mach sur l'extrados est de 0.99 pour retrouver des conditions de blocage sonique sans onde de choc stationnaire. La figure 15 présente l'amplitude maximum de la fluctuation de pression statique sur le profil en fonction de la fréquence réduite k_1. Dans ce cas aussi, on observe, suivant la valeur de la fréquence

réduite, une amplification élevée, pouvant être supérieure à 8. L'observation de la figure 16 montre que ce maximum est obtenu dans la zone où le nombre de Mach stationnaire est maximum. L'ensemble de ces résultats confirment ceux obtenus sur la tuyère. Cependant, cette grande sensibilité vis à vis de la fréquence réduite n'avait pas été observée dans le cas de la tuyère, l'amplification étant très forte pour une valeur de k_1 comprise entre 1.4 et 2.6. Par contre l'écoulement instationnaire dans la tuyère était très sensible au sens de propagation des ondes, seule l'excitation provenant de l'aval étant amplifiée. Si l'on transpose ce résultat au cas de la grille d'aube, l'excitation provenant de l'amont, l'amplification ne peut s'expliquer que par la présence d'ondes réfléchies régressives. En fait l'existence d'une périodicité circonférentielle lie la fréquence réduite aux modes circonférentiels de propagation acoustique. Ainsi, en fonction de la fréquence réduite, certains modes acoustiques vont se propager hors du domaine sans amortissement. La fréquence de coupure correspond au passage d'un mode amorti à un mode propagatif. Ces modes propagatifs vont correspondre à des ondes progressives à l'aval et à des ondes régressives à l'amont. L'étude des modes acoustiques à l'amont et à l'aval permet de déceler la présence de modes propagatifs, donc d'ondes progressives ou régressives. Cette analyse montre que, dans le cas de cette grille, jusqu'à une fréquence réduite k_1=1.4, il n'existe qu'un mode propagatif à l'amont comme à l'aval. Au delà de 1.4, un deuxième mode propagatif régressif apparaît à l'amont pour toujours un seul mode propagatif progressif à l'aval. Enfin à partir d'une fréquence réduite k_1=2.6, un deuxième mode propagatif progressif se déclenche à l'aval, rééquilibrant l'amont et l'aval. Cette observation montre que pour une valeur de k_1 comprise entre 1.4 et 2.6, il y a un mode propagatif (régressif) de plus à l'amont. Dans cet intervalle, les ondes acoustiques se trouvent bloquées vers l'aval alors qu'elles peuvent s'évacuer vers l'amont, ce qui va favoriser la propagation des fluctuations de l'écoulement de l'aval vers l'amont. Cependant ces ondes régressives vont s'accumuler et se trouver bloquées en traversant la zone presque sonique, d'où la forte amplification observée. Ces résultats, en mettant en évidence le rôle de la fréquence réduite sur le sens de propagation des modes acoustiques, confirment aussi les résultats obtenus sur la tuyère et qui mettaient en évidence le rôle majeur des ondes régressives.

7 Conclusion

L'écoulement instationnaire a été étudié paramétriquement dans une tuyère convergente-divergente en fonction du nombre de Mach stationnaire et du sens de propagation des ondes acoustiques. Cette étude a permis de développer un modèle de blocage acoustique qui explique la forte amplification des fluctuations de pression statique qui apparaît dans certaines configurations. Le modèle est basé sur l'idée que lorsque le nombre de Mach stationnaire est proche de l'unité, les perturbations acoustiques qui remontent l'écoulement se trouve bloquées et sont fortement amplifiées. Ce concept a pu être vérifié sur une configuration de turbomachine en introduisant une relation directe avec les fréquences de coupure des modes acoustiques circonférentiels. Ainsi l'amplification se retrouve lorsqu'il y a plus de modes propagatifs à l'amont qu'à l'aval, les ondes acoustiques se déplacent alors préférentiellement vers l'amont et sont amplifiées à travers la zone sonique.

Ces fluctuations de pression instationnaires peuvent affecter de façon significative les limites de flottement ou provoquer des contraintes pouvant provoquer une rupture par fatigue. C'est pourquoi il est essentiel de comprendre les mécanismes générateurs pour pouvoir, dès le stade du dessin, réduire l'amplitude de ces fluctuations.

Les auteurs remercient l'OTAN qui a soutenu ce travail par le biais d'une bourse de recherche.

Références

1 - Y Tanida, M Namba. 7th International symposium on Unsteady Aerodynamics and Aeroelasticity of turbomachines, Fukuoka, Japan, 25-29 sept. 94

2 - S. Aubert, Etude de schémas à haute précision pour la simulation d'écoulements transsoniques instationnaires ou visqueux. Application aux turbomachines. *PH. D. Ecole centrale de Lyon,* 1993

3 - P. Ferrand and S. Aubert. A New Mixed Van Leer's flux splitting for transonic viscous flow. *AIAA paper 94-1876,* 1994

4 - J. Fang and H. M. Atassi. Compressible flows with vortical disturbances around a cascade of laoded airfoils, Unsteady Aerodynamics, Aeroacoustics, and Aeroelasticity of turbomachines and Propellers, *Ed. H. M. Atassi, Spring-Verlag*, pp 149-176, 1993

5 - J. Fang and H. M. Atassi. Numerical solutions for unsteady subsonic vortical flows around loaded cascades, J. of Turbomachinery, vol 115, pp 810-816, 1993

6 - S. Aubert, L. Hallo, P.Ferrand and M. Buffat Numerical Behaviour of Unsteady Waves. *AIAA journal*, à paraître, 1995

7 - P. Ferrand and S. Aubert. A New Mixed AUSM$^+$ Liou scheme, an extention of the mixed Van Leer Flux Splitting, proposé pour le *Compte Rendu de l'Académie des Sciences*

8 - P. Ött, A. Bölcs and T. H. Fransson. Experimental and numerical study of the time dependent presure response of a shock wave oscillating in a nozzle, *ASME paper 93-GT-139*, 1993

9 - S. Aubert and P.Ferrand. Study of Unsteady Transonic Flow with a new Mixed Van Leer Flux Splitting Method, *7th International symposium on Unsteady Aerodynamics and Aeroelasticity of turbomachines*, Fukuoka, Japan, 25-29 sept. 94

10 - H. M. Atassi, J. Fang and P. Ferrand. A Study of the Unsteady Pressure of a Cascade near Transonic Flow Condition, *ASME paper* 94-GT-476, 1994

11 - P. Carrière. Petites perturbations instationnaires d'un écoulement monodimensionnel permanent. *La Recherche Aérospatiale*, n° 6, pp 307-321, 1976

12 - S. M. Candel. Acoustic conservation principles and application to plane and modal propagation in nozzles and diffusers. *J. of Sound and Vibration*, vol. 41, n° 2, pp 207-232, 1976

13 - P. Ferrand. Etude théorique des écoulements instationnaires en turbomachine axiale. Application au flottement de blocage, *Thèse d'Etat es sciences, université Claude Bernard Lyon I*, mars 86

14 - T. H. Fransson and J. M. Verdon. Panel discussion on standard configurations for unsteady flow through vibrating axial flow turbomachine cascades. Unsteady Aerodynamics, Aeroacoustics, and Aeroelasticity of turbomachines and Propellers, *Ed. H. M. Atassi, Spring-Verlag*, pp 859-889, 1993

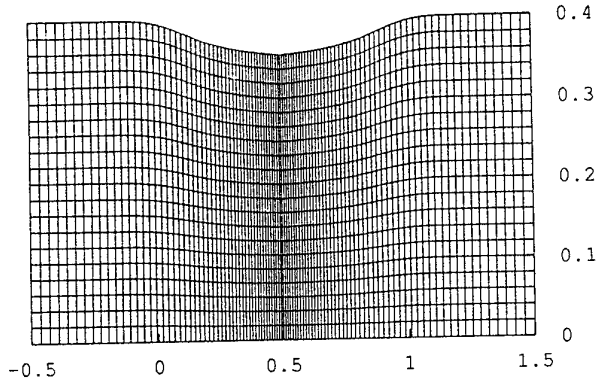

Figure 1 - Maillage de la tuyère

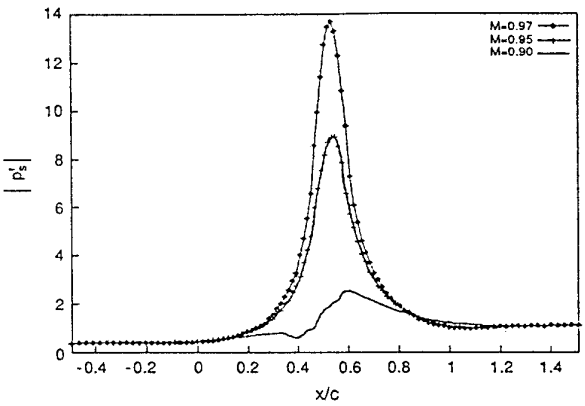

Figure 4 - Distribution de l'amplitude de la fluctuation de pression statique sous l'effet d'une perturbation aval

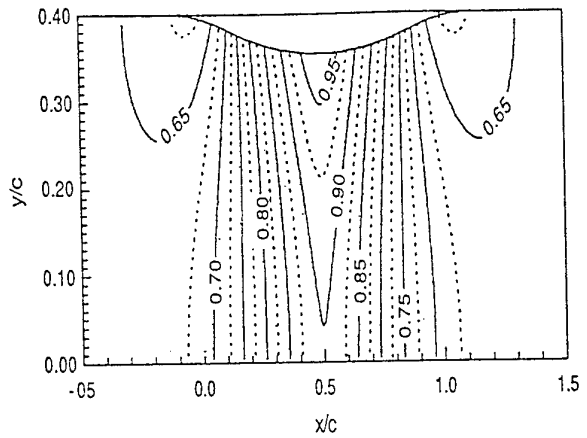

Figure 2 - Iso nombre de Mach pour le cas subsonique

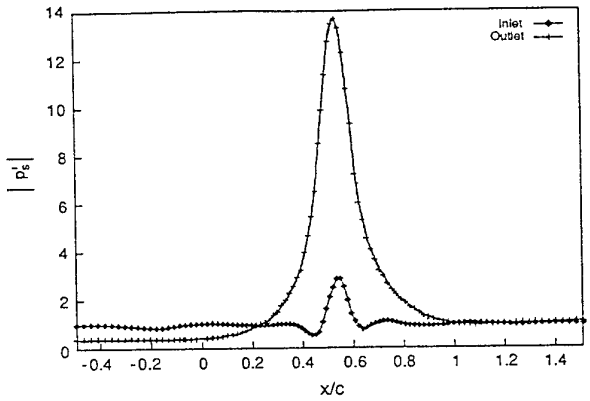

Figure 5 - Comparaison des distributions de fluctuation de pression statique sous l'effet d'une perturbation amont ou aval, M_{max}=0.97

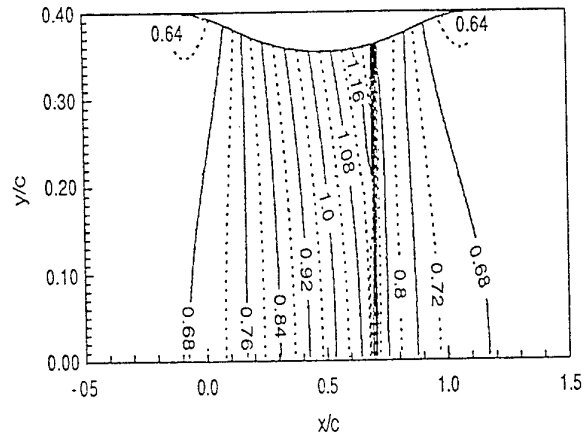

Figure 3 - Iso nombre de Mach pour le cas transsonique

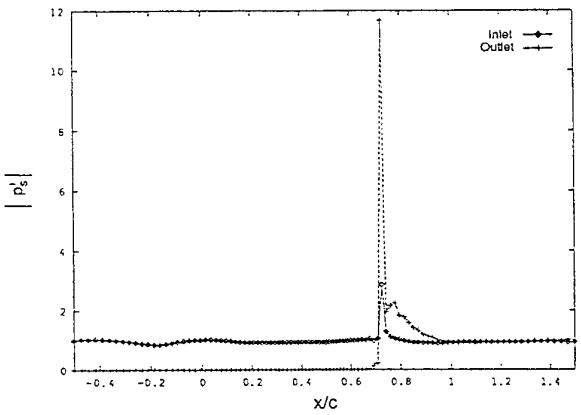

Figure 6 - Comparaison des distributions de fluctuation de pression statique sous l'effet d'une perturbation amont ou aval, cas transsonique

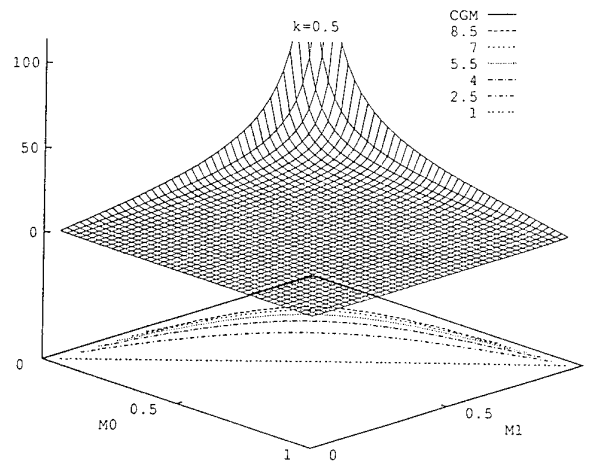

Figure 7 - Distribution de l'amplification des ondes régressives en fonction des nombres de Mach M_0 et M_1

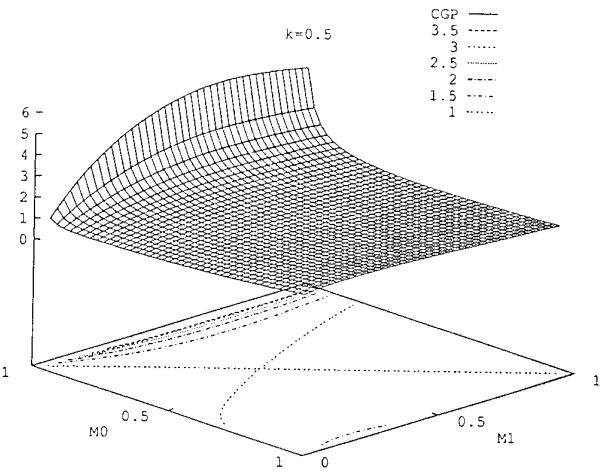

Figure 8 - Distribution de l'amplification des ondes progressives en fonction des nombres de Mach M_0 et M_1

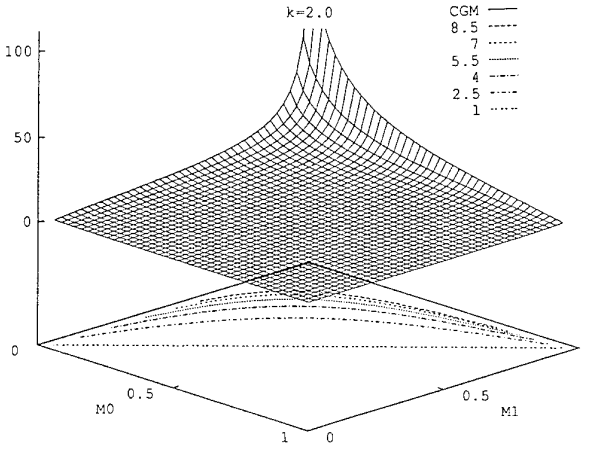

Figure 9 - Distribution de l'amplification des ondes régressives en fonction des nombres de Mach M_0 et M_1

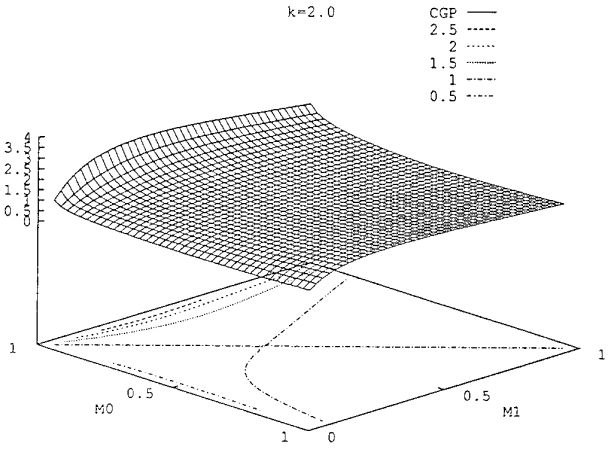

Figure 10 - Distribution de l'amplification des ondes progressives en fonction des nombres de Mach M_0 et M_1

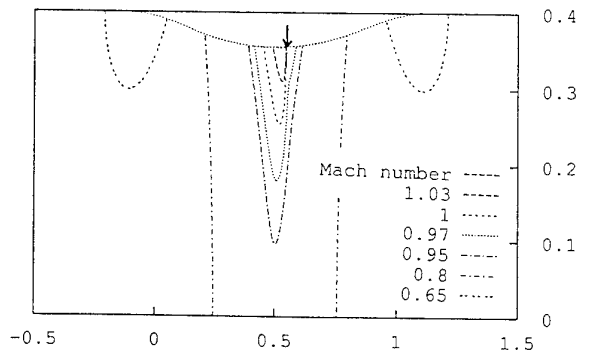

Figure 11 Iso nombres de Mach stationnaires, cas faiblement transsonique

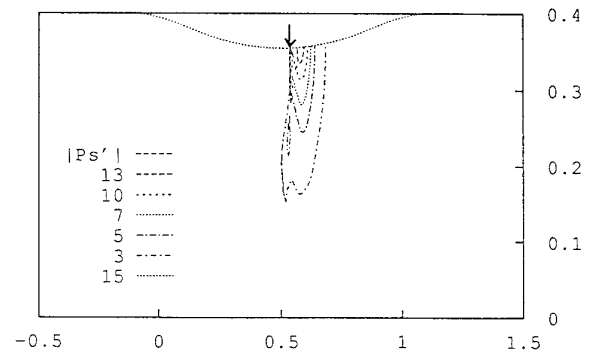

Figure 12 - Iso-fluctuations de pression statique sous l'effet d'une perturbation aval

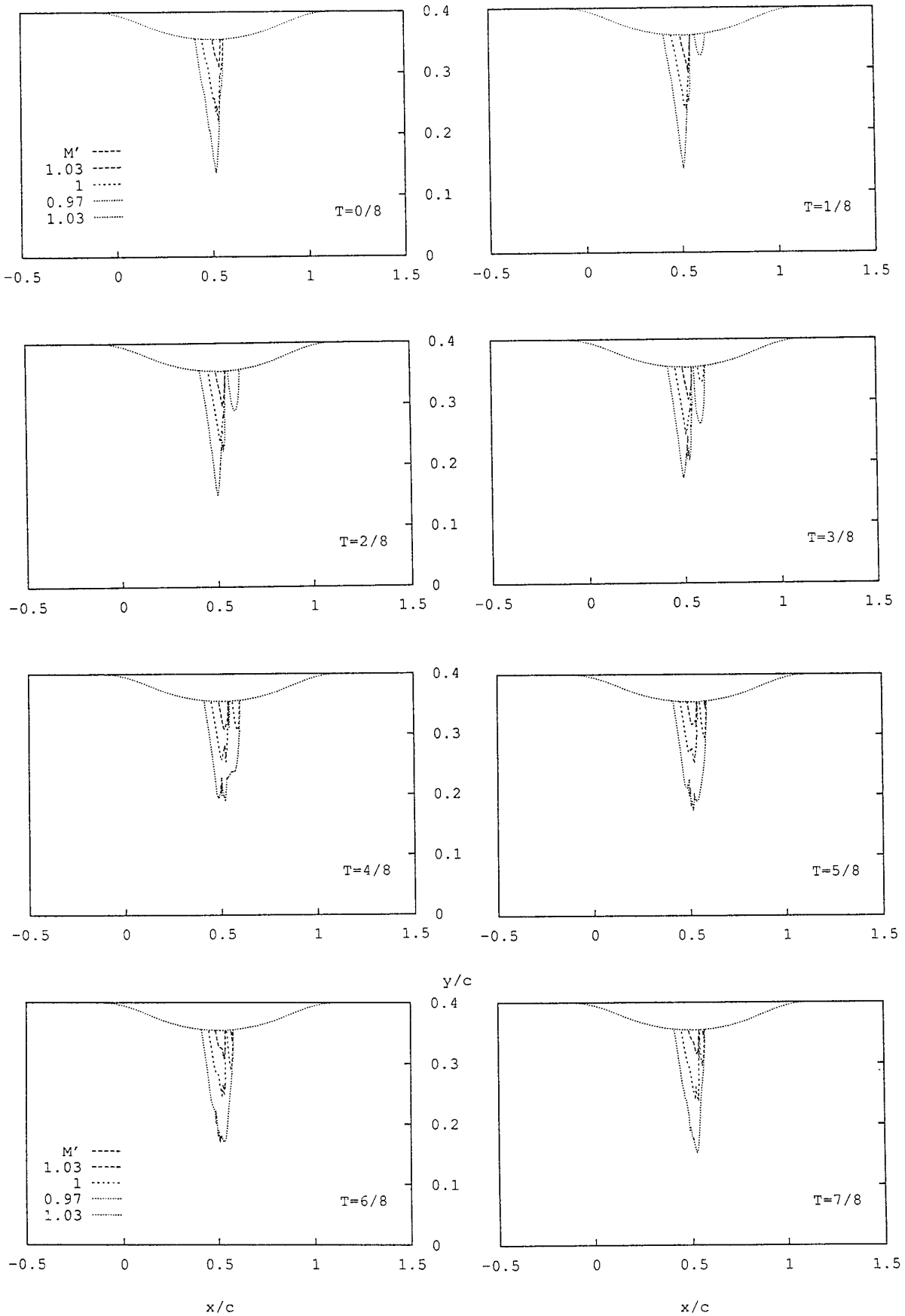

Figure 13 - Iso nombre de Mach instantané sous l'effet d'une perturbation aval

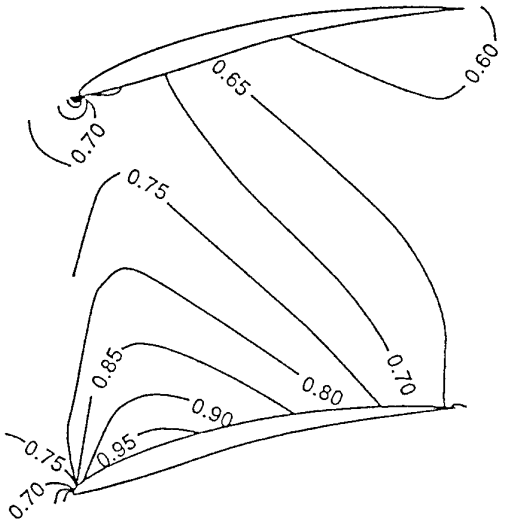

Figure 14 - Géométrie et iso-nombre de Mach de la 10ème configuration standard

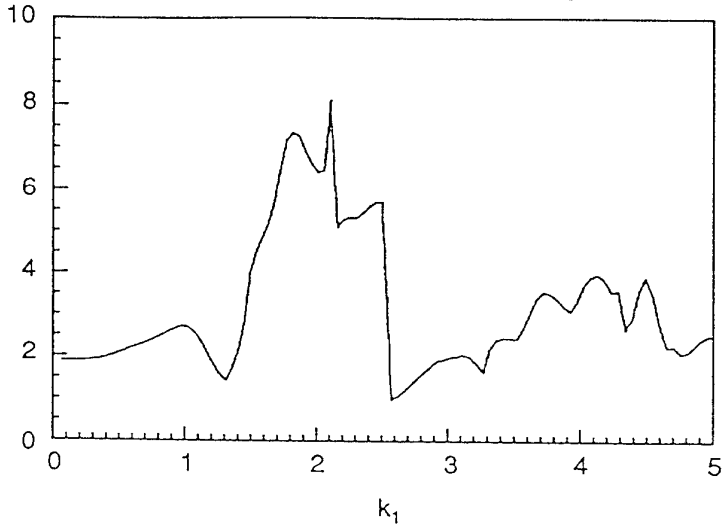

Figure 15 - Amplitude maximum de la fluctuation de pression statique en fonction de la fréquence réduite k_1

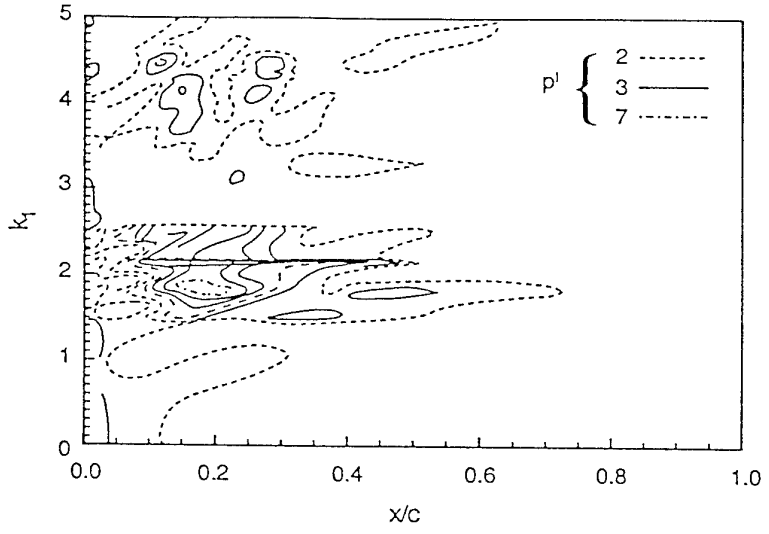

Figure 16 - Iso-amplitude de fluctuation de pression en fonction de la fréquence réduite k1 et de l'abscisse, coté extrados

MODELES POUR LE CALCUL DE FLUCTUATIONS SPATIALES TRIDIMENSIONNELLES DANS LE CADRE D'UNE APPROCHE MÉRIDIENNE EN TURBOMACHINE

G. PERRIN, F. LEBOEUF

École Centrale de Lyon
Laboratoire de Mécanique des Fluides et d'Acoustique
URA CNRS 263
36 av. Guy de Colongue
69131 ECULLY Cedex, France
Tel (33) 78 33 81 27, Fax (33) 78 64 71 45

1. RESUME

La compatibilité entre les calculs tridimensionnels résolvant les équations d'Euler ou de Navier-Stokes, et les calculs méridiens, repose sur l'introduction de termes de fluctuations spatiales dans les équations de conservations moyennes de la quantité de mouvement et d'énergie. Cette démarche constitue une approche peu explorée du calcul des différents mécanismes de génération de perte de charge et de travail dans une machine.
Un modèle de calcul de ces termes est présenté pour des écoulements stationnaires. Un écoulement en grille de turbine est utilisé pour la validation.

SUMMARY

The compatibility between tridimensional simulations with Euler or Navier-Stokes equations, and through-flow computations, may be satisfied by taking into account spatial fluctuation terms in the conservation equations of momentum and energy. This method has been little explored in order to determine the losses or work variations in a machine.
A model for the computation of these spatial fluctuation terms is presented. The test of the model is performed for a steady flow in a low speed turbine cascade.

2. INTRODUCTION

Le calcul de l'écoulement dans les turbomachines multiétagées constitue une difficulté sérieuse à la fois pour l'analyse et le dessin des machines ; ceci résulte de l'importance des mécanismes instationnaires dans le processus d'échange d'énergie entre le fluide et la machine. Le principal problème réside dans la taille considérable des volumes de calcul qui sont nécessaires pour tenir compte de toutes les échelles spatio-temporelles.
Pour un étage formé par une grille fixe et une grille mobile, il est possible de réaliser un calcul résolvant les équations de Navier-Stokes tenant compte d'interactions instationnaires entre grilles ; des conditions de périodicité spatio-temporelles particulières sont très utiles à ce niveau (GILES, 1987, 1992, CHAPIN, 1993). Cette technique ne peut pas s'étendre au-delà d'un étage. A l'heure actuelle, il n'est pas possible de traiter plus de deux grilles d'aubes consécutives sans introduire à un certain niveau une hypothèse forte que seule la confrontation avec des résultats issus d'expériences permet de justifier.
L'hypothèse principale réside dans la moyenne spatiale effectuée selon la direction circonférentielle, à l'aval d'une grille, afin que l'écoulement entrant dans la grille suivante soit stationnaire. Une telle technique est couramment employée sous diverses formes pour le calcul de machines multiétagées (DENTON, 1990, ADAMCZYK, 1989, DAWES, 1990). A ce niveau, il importe de souligner que la précision des calculs tridimensionnels pour des grilles intermédiaires dépend fortement des conditions aux limites moyennées imposées sur les faces amont et aval des domaines de calcul. ADAMCZYK (1984, 1994) a ainsi proposé plusieurs moyennes spatiales et temporelles permettant d'assurer un transfert correct d'informations entre grilles.
Plus classiquement, le modèle de calcul dans le plan méridien d'une machine a été employé depuis longtemps pour traiter les machines multiétagées. La forme originelle proposée par WU en limitait l'emploi

Paper presented at the AGARD PEP 85th Symposium on "Loss Mechanisms and Unsteady Flows in Turbomachines", held in Derby, United Kingdom, 8-12 May 1995, and published in CP-571.

en forçant l'écoulement à suivre une surface de courant méridienne particulière. Il a été montré qu'une forme équivalente pouvait être introduite à partir d'une moyenne des équations de transport selon la direction circonférentielle (HIRSCH et DRING, 1987). Le système d'équations obtenu n'est pas fermé, par suite de la présence de termes induits par la nature tridimensionnelle de l'écoulement. Certains sont liés aux aubages (force de pression, de frottement, flux de chaleur). D'autres résultent de la non-linéarité des termes de transports convectifs et sont nommés "fluctuations spatiales". La fermeture de ce système d'équations demande la connaissance de l'évolution de l'écoulement selon la direction circonférentielle. Elle peut être obtenue en réalisant un calcul sur des surfaces aube-à-aube, ce qui constitue le modèle quasi-tridimensionnel. L'hypothèse d'axisymétrie de ces surfaces aube-à-aube est une restriction très forte pour l'emploi pratique de l'approche quasi-tridimensionnelle. Aussi des modèles ont souvent été employés pour restituer une partie de l'information manquante. Les modèles de mélanges radiaux appartiennent à cette catégorie (ADKINS et SMITH, 1982, GALLIMORE et CUMPSTY, 1986).

Le présent travail propose la gestion rationnelle de l'information moyennée dans une machine. L'objectif est de définir un environnement en moyenne azimutale en amont et en aval d'une grille intermédiaire qui contienne la totalité de l'information.Il vise aussi à améliorer les modèles de calculs méridiens.
Nous allons tout d'abord souligner les caractéristiques essentiels d'un écoulement moyenné, et en particulier des équations qui le régissent. Puis, nous décrirons les équations de transport des fluctuations spatiales. Enfin nous proposerons une méthodologie permettant de fermer les équations. Le test des modèles sera réalisé pour une grille de turbine subsonique.
Afin d'analyser le champ moyenné, et valider nos modèles, nous avons employé une base de données issue d'une simulation numérique à l'aide des équations de Navier-Stokes tridimensionnelles pour une grille de turbine.

3. LE CAS TEST ET LA SIMULATION À L'AIDE DES ÉQUATIONS DE NAVIER-STOKES

Seule une brève description du cas test et des conditions de simulations sont données ici ; plus de détails sont fournis par PERRIN et LEBOEUF (1993). Nous avons utilisé les données issues des mesures réalisées sur une grille de turbine par DENTON, HODSON et DOMINY (1990). La turbine est une section de pied d'une roue mobile d'un étage à basse pression. Elle a été testée dans une grille linéaire (Figure 1). Les conditions expérimentales sont : angle de déflexion 92.4°, nombre de Mach à l'amont 0.5, nombre de Mach isentropique en sortie 0.71, nombre de Reynolds en entrée 2.3 10^5. La simulation a été réalisée à l'ONERA avec le code CANARI (CAMBIER, COUAILLER, VEUILLOT, 1988, ESCANDE et CAMBIER, 1991). Le domaine de calcul a été partagé en un domaine maillé en O entourant l'aube, et deux domaines maillés en H situés en amont et en aval. De l'amont à l'aval, les domaines ont respectivement 28875, 262605 et 42875 noeuds pour une demi-envergure de l'aube. Le modèle de turbulence emploie une longueur de mélange due à MICHEL, QUEMARD et DURAND (1969).

4. LA MOYENNE DANS LA DIRECTION AUBE-À-AUBE

Les résultats de la simulation tridimensionnelle ont été moyennés dans la direction z. Pour un repère cartésien, cette direction z prend la place de la direction circonférentielle q dans un repère cylindrique. La direction axiale est notée x, et la direction considérée selon l'envergure de l'aube est notée y.
Nous rappelons ici les formules de moyennes massiques. Nous notons $\bar{A}(x, y)$ la moyenne massique d'une grandeur A(x, y, z), et A'(x, y, z) l'écart de A par rapport à $\bar{A}$. Dans la suite, A' sera appelé le champ fluctuant.

$$A(x,y,z) = \overline{A}(x,y) + A'(x,y,z) \qquad (1)$$

$$\overline{\rho A} = \overline{\rho}^{\,a}\,\overline{A} = \frac{1}{b}\int_0^b \rho A \, d(z/g) \qquad (2)$$

où g est le pas interaube, et b est la distance entre deux aubages selon z. Les équations (1) et (2) sont valables pour toutes les variables, exceptées pour la masse volumique ρ, la pression P et les contraintes de cisaillement τ pour lesquelles une simple moyenne géométrique est appliquée. Ainsi :

$$\rho(x,y,z) = \overline{\rho}^{\,a}(x,y) + \rho''(x,y,z)$$

$$P(x,y,z) = \overline{P}^{\,a}(x,y) + P''(x,y,z)$$

Appliquée sur un gradient ∇, la formule (2) génère une différence Δ entre l'intrados et l'extrados des aubes, notés respectivement ici 'ps' et 'ss', selon la formule (3) :

$$\overrightarrow{\nabla \bar{A}} = \frac{1}{b}\overrightarrow{\nabla}\left(b\bar{A}\right) + \frac{1}{b}\Delta\left[\vec{A}\,\vec{n}\right]_{ps}^{ss} \qquad (3)$$

Cette différence Δ est à l'origine de la force d'aubage de pression et de cisaillement dans la conservation pour le champ moyenné de la quantité de mouvement, et des flux de chaleur dans la conservation de l'énergie.
La moyenne des termes non-linéaires apparaissant dans les termes convectifs des équations de transport introduisent des inconnues supplémentaires du point de vue du champ moyen, sous la forme :

$$\overline{\rho AB} = \bar{\rho}^{a}\overline{A\,B} + \overline{\rho A'B'} = \bar{\rho}^{a}\overline{A\,B} + \overline{\rho}^{a}\overline{A'B'} \qquad (4)$$

Le dernier terme de la relation (4) traduit la non-uniformité spatiale dans la direction aube-à-aube z. Il sera nommé dans la suite 'corrélation spatiale'.

5. INTERACTIONS ENTRE LE CHAMP MOYEN $\bar{A}$ ET LE CHAMP FLUCTUANT A'

Nous résumons ici l'essentiel des résultats présentés par PERRIN et LEBOEUF (1993), et par PERRIN (1994). Il est tout d'abord utile de quantifier la contribution des fluctuations spatiales, et particulièrement de l'énergie cinétique $\bar{K}$ des fluctuations, sur le champ moyen. Pour cet aubage, $\bar{K}$ atteint 1.6% de l'énergie cinétique moyenne ; il en résulte une correction de 1.2 degré sur la valeur de la température statique moyenne $\bar{T}$.
L'action du champ fluctuant est particulièrement spectaculaire pour l'équation de quantité de mouvement moyennée, projetée selon la direction y, qui joue ici le rôle de la direction radiale R dans une machine. Pour cette grille d'aube, le gradient de pression statique moyenne selon y est entièrement donné par le gradient selon y de la corrélation spatiale $\overline{\rho V_y'^2}$. Pour apprécier cet effet, nous l'avons comparé à celui de la force centrifuge dans la grille supposée disposée en machine, à un rayon R=0.5m. L'équation d'équilibre radial se réduit à la relation suivante, avec les mêmes conditions de fonctionnement que la grille étudiée :

$$\frac{\partial \bar{P}}{\partial R} = \frac{\bar{\rho}^{a}\bar{V}_{\theta}^{2}}{R} - \frac{\partial}{\partial R}\left(\bar{\rho}^{a}\overline{V_R^2}\right) \qquad (5)$$

La figure 2 donne l'évolution des deux termes du second membre selon R, pour une position axiale située à x/c=1.10, soit10% à l'aval du bord de fuite. Quoique la valeur choisie pour R soit arbitraire, et sous-évalue sans doute un peu l'effet centrifuge moyen, il est clair que pour cette aube supposée placée en machine, l'équilibre radial est fortement influencé par le terme de corrélation spatiale.

Le lien étroit entre la pression statique P et l'énergie cinétique K du champ fluctuant peut être observé sur la figure 3 qui présente des cartes de P et K dans un plan situé à x/c=0.75. Le maximum de K observé au voisinage de l'extrados de l'aube accompagne le minimum de P dans la même région. Cette évolution de la valeur locale de K est fortement influencée par le tourbillon de passage. De même, la valeur moyenne $\bar{K}$ évolue fortement sous l'influence des différents mécanismes tourbillonnaires. Nous donnons sur la figure 4, une carte de l'énergie cinétique $\bar{K}$ du champ fluctuant, dans le plan (x, y) 'méridien' ; la frontière inférieure de la figure correspond à la paroi latérale, et la frontière supérieure à la mi-envergure. A partir de l'analyse locale de l'écoulement, quatre régions remarquables ont été identifiées : (1) la trace du tourbillon en fer à cheval, qui résulte de l'enroulement de la couche limite amont autour du bord d'attaque (BA) de l'aube, (2) un tourbillon de coin qui se développe du côté de l'extrados de l'aube, (3) le tourbillon de passage, dont la trace s'étend largement au-delà du bord de fuite (BF), (4) le sillage de l'aube. L'importance de la zone influencée par le tourbillon de passage (3) permet d'expliquer le comportement particulier observé pour la part selon y de l'énergie cinétique moyenne présentée sur la figure 2.
La force de pression sur l'aubage joue un rôle dominant dans les composantes de la conservation de la quantité de mouvement projetées selon la direction axiale x et aube-à-aube z. Pour la composante selon z de l'équation moyennée, la figure 5 donne l'évolution selon y des principaux groupes de termes, pour une position située à x/c=0.75. Nous constatons le rôle dominant joué par la force de pression d'aubage F_p dans la balance de l'équation. Les termes de fluctuations spatiales sont de l'ordre de 12 à 30% de F_p dans la zone de paroi. En les négligeant, il en résulte une surestimation significative de l'effet convectif. Leur contribution dans la composante selon x de l'équation de conservation de la quantité de mouvement atteint 40% de F_p à mi-envergure.
Par comparaison, la contribution des termes de cisaillement reste globalement très faible ; hormis dans une couche d'épaisseur minime (2% de l'envergure), à proximité de la paroi latérale, où ils contrebalancent l'influence de F_p (figure 5). Ce dernier résultat est important car il souligne le caractère essentiellement non-visqueux du champ moyen dans presque tout le domaine.
De cette analyse, nous tirons les conséquences suivantes. Dans le cadre d'un calcul méridien, il est nécessaire de tenir compte des corrélations spatiales pour reproduire correctement les évolutions radiales de la pression. La force d'aubage est dominée par la pression, ce qui permet de la supposer normale à la paroi solide. Son effet est cependant fortement compensé par les fluctuations spatiales. Dans le cadre d'un transfert dans l'espace intergrille entre une roue mobile et une roue fixe, lors d'un calcul tridimensionnel stationnaire par roue, il est justifié de traiter uniquement des phénomènes non-visqueux. De

même, des informations moyennes étant échangées entre roues, l'emploi sur les faces amont et aval des domaines tridimensionnels de relations de compatibilités issues des équations d'Euler est raisonnable. Ces remarques sont évidemment à corriger dans une zone où la viscosité domine très près de la paroi latérale. Enfin, il est important de tenir compte lors du transfert intergrille de l'énergie cinétique radiale du champ fluctuant $\overline{\rho V_y'^2}$, les autres corrélations spatiales semblant assez faibles dès x/c=1.10 au-delà du bord de fuite pour cette grille.

6. COMPORTEMENT DU CHAMP FLUCTUANT

Nous donnons ci-dessous l'équation de transport (6) des corrélations spatiales $\overline{\rho V_j' V_k'}$.

$$
\begin{aligned}
&\text{(a)} \quad \frac{\partial}{\partial x_i}\left(b\overline{V_j}\,\overline{\rho\, V_j' V_k'} \right) \\
&\text{(b)} \quad + b\,\overline{\rho\, V_i' V_j'}\frac{\partial \overline{V_k}}{\partial x_i} + b\,\overline{\rho\, V_i' V_k'}\frac{\partial \overline{V_j}}{\partial x_i} \\
&\text{(c)} \quad + \frac{\partial}{\partial x_i}\left(b\,\overline{\rho\, V_i' V_j' V_k'} \right) \\
&\text{(d)} \quad + b\,\overline{V_j'}\frac{\partial \overline{P}^{\,a}}{\partial x_k} + b\,\overline{V_k'}\frac{\partial \overline{P}^{\,a}}{\partial x_j} \\
&\text{(e)} \quad - b\,\overline{P'\frac{\partial V_j'}{\partial x_k}} - b\,\overline{P'\frac{\partial V_k'}{\partial x_j}} \\
&\text{(f)} \quad + \frac{\partial}{\partial x_k}\left(b\,\overline{V_j' P''} \right) + \frac{\partial}{\partial x_j}\left(b\,\overline{V_k' P''} \right) \\
&\text{(g)} \quad + \overline{V_j}\,\Delta[\, P'' n_k \,]_{ps}^{ss} + \overline{V_k}\,\Delta[\, P'' n_j \,]_{ps}^{ss} \\
&\text{(h)} \quad - \frac{\partial}{\partial x_i}\left(b\,\overline{V_j' \tau_{ik}} \right) - \frac{\partial}{\partial x_i}\left(b\,\overline{V_k' \tau_{ij}} \right) \\
&\text{(i)} \quad + b\,\overline{\tau_{ik}\frac{\partial V_j'}{\partial x_i}} + b\,\overline{\tau_{ij}\frac{\partial V_k'}{\partial x_i}} \\
&\text{(j)} \quad - \overline{V_j}\,\Delta[\, \tau_{ik} n_i \,]_{ps}^{ss} - \overline{V_k}\,\Delta[\, \tau_{ij} n_i \,]_{ps}^{ss}
\end{aligned}
\qquad (6)
$$

Les différents termes de l'équation (6) ont la signification suivante : (a) transport par le champ moyen de la corrélation spatiale, (b) production par le champ moyen, (c) transport par le champ fluctuant ou diffusion par les corrélations triples, (d) effet de compressibilité, (e) corrélation pression-déformation, (f) diffusion par la pression, (g) travail de la force de pression d'aubage avec le champ moyen, (h) diffusion par les contraintes de cisaillement, incluant les effets turbulents, (i) dissipation, (j) travail de la force de cisaillement sur l'aube.

Nous résumons ici l'essentiel des résultats présentés par PERRIN et LEBOEUF (1994), et par PERRIN (1994). Nous considérons le transport de l'énergie cinétique moyenne, $\overline{K}$ qui est obtenue en écrivant j=k dans l'équation (6), puis en sommant sur les directions x, y et z.

$$\overline{K} = \overline{K_x} + \overline{K_y} + \overline{K_z} = \frac{1}{2}\left(\overline{V_x'^2} + \overline{V_y'^2} + \overline{V_z'^2} \right) \qquad (7)$$

La production de l'énergie cinétique moyenne est assurée par les termes (b) et (g) dans l'équation (6). Ceci constitue une différence majeure par rapport aux équations de transport des tensions de Reynolds pour un champ turbulent. En fait, le travail de la force de pression d'aubage est de 3 à 10 fois plus important que le terme (b). Il faut noter que le terme (g) n'est nul que dans l'approximation d'un nombre d'aube infini, elles-mêmes infiniment minces. Il est particulièrement élevé dans la zone du tourbillon de passage, suite à la surdéflexion de l'écoulement moyen observé sur la paroi latérale. Il change de signe dans la zone externe de la couche limite par suite du transfert en retour de l'extrados vers l'intrados dans cette zone (figure 6). Assez curieusement, ce terme est positif à la paroi, ce qui provoque une décroissance de l'énergie cinétique du champ fluctuant. En pratique la forte croissance de l'énergie cinétique moyenne $\overline{K}$ dans la zone du tourbillon de passage résulte de l'ensemble des termes de pression (d+e+f+g) (figure 7), et particulièrement du terme de diffusion par la pression (f) ; sa valeur est négative à la paroi, et excède de 10% le terme de travail des forces de pression d'aubage (g). Ainsi alors que la force de pression d'aubage est à l'origine du tourbillon de passage, le terme de diffusion par la pression (g) accroît la non-uniformité de l'écoulement selon la direction aube-à-aube.

Le terme de diffusion (c) traduit l'action du champ fluctuant sur lui-même. Son évolution est fortement corrélée avec l'évolution du tourbillon de passage. Il est de l'ordre de grandeur de la somme des termes de pression (d+e+f+g) dans la zone de paroi, mais avec un signe opposé. Ainsi, le champ fluctuant tend à réduire son énergie cinétique dans cette zone, selon un processus d'auto-homogénéisation. Un phénomène similaire est observé dans le sillage de l'aube.

La figure 8 donne les évolutions des termes de contraintes de cisaillement τ selon l'envergure, pour x/c=0.75. Nous notons que le travail de la force de frottement sur l'aubage (j) est toujours négatif, ce qui traduit bien l'accroissement de l'énergie cinétique du champ fluctuant ; ce résultat résulte de l'adhérence du fluide sur les parois des aubes. Ainsi la force de frottement d'aubage est toujours opposée au vecteur vitesse du champ moyen ; ceci est conforme à l'hypothèse largement employée dans les modèles de calcul méridien, due à HORLOCK (1971). Le terme de diffusion par les contraintes (h) est négligeable, sauf dans une couche très mince y/h<1%. Enfin, la dissipation (i) est constamment positive, ce qui traduit bien une décroissance de l'énergie cinétique du champ fluctuant. Le terme de dissipation (i) assure donc la disparition du champ fluctuant, au terme d'un processus

d'échange d'énergie entre les champs moyen et fluctuant qui rappelle le transfert turbulent. Notons cependant que l'énergie est échangée entre le champ moyen et le champ fluctuant en grande partie de manière réversible, et cela même dans la zone de sillage.
Sur la figure 8, la somme des effets des contraintes a été calculée également à partir d'une part de la somme des termes (h), (i) et (j), et d'autre part en effectuant la balance des termes de l'équation (6). Nous constatons une légère différence, qui résulte des erreurs de troncatures lors des différentes interpolations dans la base de données.
L'ensemble de ces résultats est résumé sur la figure 9, qui présente les évolutions des différents termes de l'équation de transport de la corrélation $\overline{\rho V_y'^2}$.
Rappelons que cette corrélation joue un rôle particulier dans l'équilibre du champ moyen (équation 5). Les aubes n'étant pas vrillées, le terme de travail des forces de pression d'aubages (g) est ici nul. Nous constatons en outre que le terme de production par le champ moyen (b) est négligeable. La croissance de la corrélation $\overline{\rho V_y'^2}$ est alors assurée par le terme diffusion par la pression (f), qui joue ici un rôle de redistribution entre les composantes de vitesse du champ fluctuant. Ce terme est cependant fortement compensé par la corrélation pression-déformation (e) ; notons que ce dernier terme joue un rôle faible dans le bilan de l'énergie cinétique moyenne, où il traduit un effet de compressibilité pour le champ fluctuant. Le terme de diffusion par le champ fluctuant (c) s'oppose à la résultante des termes de pression, et joue encore son rôle homogénéisant. Au total, le terme de convection est positif, essentiellement dans la zone externe du tourbillon de passage.

Pour conclure, nous avons montré que les mécanismes de dissipation jouaient essentiellement un rôle au niveau du champ fluctuant. La pression est un acteur essentiel dans l'échange qui s'établit entre le champ moyen et le champ fluctuant, en grande partie d'ailleurs de manière réversible. Le champ fluctuant a tendance à s'auto-homogénéiser ; il s'oppose en général à l'effet global de la pression. Il existe une forte anisotropie du champ fluctuant. Alors que V'_y est négligeable à mi-envergure, elle joue un rôle dominant dans la zone du tourbillon de passage. Il en résulte que la modélisation des différents termes dans les équations de transports des corrélations du champ fluctuant peut difficilement employer une hypothèse de pseudo-viscosité turbulente, telles que dans les modèles classiques de mélanges radiaux (ADKINS et SMITH, 1982).

7. MODÉLISATION DE L'ÉQUATION DE TRANSPORT DES CORRÉLATIONS SPATIALES

L'analyse précédente de l'évolution de l'énergie cinétique moyenne $\bar{K}$ a soulignée une certaine analogie entre le comportement du champ fluctuant et celui du champ turbulent considéré en moyenne statistique. La dissipation joue un rôle significatif au niveau du champ fluctuant uniquement, et très peu pour le champ moyen. Les corrélations de pression-déformation et de diffusion par les corrélations triples de vitesse s'opposent au mouvement convectif, et tendent donc à isotropiser le champ fluctuant. Par contre, contrairement au mouvement turbulent, les termes de production liés au gradient de vitesse moyenne jouent un rôle très faible dans l'alimentation du champ fluctuant. Au contraire, le travail des forces de pression d'aubage est une source importante qui alimente le champ fluctuant. Enfin, la diffusion par la pression joue un rôle essentiel de redistribution. Au total, l'effet global de la pression est d'augmenter l'énergie cinétique du champ fluctuant dans la zone de paroi.

Nous avons donc suivi la modélisation traditionnellement employée pour le traitement des champs turbulents (LAUNDER, 1984).
Le terme de corrélation pression-déformation (terme (e) de l'équation 6) peut être séparé en trois parties. Une première, notée (1) qui traduit l'action du champ turbulent sur lui-même, et souligne son action dans le retour à l'isotropie. Pour le champ fluctuant, ce mécanisme s'observe en particulier dans la zone de proche paroi où ce terme est négatif (figure 9). Nous écrirons donc :

$$\Phi_{ij}^{(1)} = \left(-b\,P'' \overline{\frac{\partial V'_i}{\partial x_j}} \right)^{(1)} = -b\,C_1 \frac{\overline{V'_i V'_j} - \frac{2}{3}\delta_{ij} K}{T_s} \qquad (8)$$

Pour un champ turbulent, Ts est une échelle de temps caractéristique assimilée à K/ε, où ε est la dissipation turbulente. Pour le traitement du champ fluctuant spatial, nous devons tenir compte du caractère réversible d'une grande partie de l'échange entre les champs moyen et fluctuant ; ceci exclue d'employer une échelle de dissipation dans la définition de Ts. Sachant que la génération du tourbillon de passage est la principale cause de l'accroissement local de $\bar{K}$, et que les aubages jouent un rôle important dans ce mécanisme, nous avons bâti Ts à partir de la distance b entre les aubes selon la direction z :

$$T_s = \frac{b}{\sqrt{\bar{K}}} \qquad (9)$$

La deuxième partie du terme de corrélation pression-déformation est constituée par une influence de gradient de vitesse moyenne. LAUNDER suggère un modèle d'isotropisation (IPM), qui introduit la production P_{ij} par le champ moyen (terme (b) de l'équation (6)) sous la forme :

$$\Phi_{ij}^{(2)} = \left(-b\,P'' \overline{\frac{\partial V'_i}{\partial x_j}} \right)^{(2)} = -b\,C_2 \left(P_{ij} - \frac{1}{3}\delta_{ij} P_{kk}\right) \qquad (10)$$

Pour le cas considéré ici, ce terme introduit une contribution minime, étant donné le faible niveau de la

production via le gradient de vitesse moyenne (b). La troisième partie du terme de corrélation pression-déformation concerne la contribution de la paroi, qui a été ignorée dans ce travail.
La diffusion par le champ fluctuant (terme (c) de l'équation 6) a été traitée à l'aide d'un modèle de DALY et HARLOW (1970). Par rapport au modèle d'HANJALIC et LAUNDER (1972), ce modèle présente l'avantage de comporter un nombre assez faible de termes à traiter, tout en donnant un résultat acceptable.

$$\overline{V'_i V'_j V'_k} = - C'_s T_s \overline{V'_k V'_L} \frac{\partial \overline{V'_i V'_j}}{\partial x_L} \qquad (11)$$

Le terme de diffusion par la pression (terme (f) de l'équation 6) a une évolution similaire à celle du terme de diffusion par les corrélations triples. Nous l'avons modélisé par :

$$\overline{P'' V'_i} = - C_3 \rho \overline{V'_k V'_k V'_i} \qquad (12)$$

Les constantes qui interviennent dans les relations (8) à (12) ont été ajustées aux valeurs suivantes : C_1=2., C_2=0.5, C'_S=0.20, C_3=2.0. Par comparaison, les constantes utilisées pour le calcul d'un champ turbulent sont :C_1=1.8, C_2=0.55, C'_S=0.18, C_3=0.2. Nous remarquons que le choix de la nouvelle échelle de temps Ts permet de conserver des constantes similaires dans les deux champs, hormis pour le terme de diffusion par la pression (équation 12).
Nous avons testé ce modèle pour l'équation de transport de la corrélation $\overline{\rho V_y'^2}$, dont la balance exacte a été présentée dans la figure 9 pour x/c=0.75.
Conformément aux résultats présentés dans cette figure, nous avons ignoré le terme de production par le champ moyen ce qui conduit également à éliminer la contribution "rapide" de la corrélation pression-déformation (équation 10). Les termes de contraintes de cisaillement n'ont pas été considérés, et nous rappelons que la production par les forces de pression d'aubage (terme g de l'équation 6) est nul pour cette équation de transport de $\overline{\rho V_y'^2}$.

Considérons tout d'abord le comportement des corrélations triples impliquées dans la balance de l'équation de $\overline{\rho V_y'^2}$. Selon le modèle décrit par l'équation (12), le terme de diffusion par la pression s'écrira :

$$\overline{P'' V'_y} = - C_3 \overline{\rho^a} \left(\overline{V'^2_x V'_y} + \overline{V'^3_y} + \overline{V'^2_z V'_y} \right) \qquad (13)$$

Le terme de diffusion par le champ turbulent (c) de l'équation (6) s'écrit :

$$\frac{\partial}{\partial x_i} \left(b \overline{\rho^a} \overline{V'_i V'^2_y} \right) =$$

$$\frac{\partial b \overline{\rho^a} \overline{V'_x V'^2_y}}{\partial x} + \frac{\partial b \overline{\rho^a} \overline{V'^3_y}}{\partial y} \qquad (14)$$

Les figures 10 à 13 présentent les cartes dans le plan méridien (x, y) des corrélations triples intervenant dans les relations (13) et (14) comme résultats du modèle (équations 9 et 11), et de la simulation tridimensionnelle.
Concernant la corrélation pression-déformation, la corrélation triple $\overline{\rho V_y'^3}$ joue un rôle dominant ; sa valeur est 5 à 10 fois plus importante par rapport aux deux autres corrélations triples intervenant dans (13). A partir des figures 10 à 13, nous pouvons conclure qu'un modèle de type DALY et HARLOW donne des résultats qualitativement acceptables pour cette turbine.
La figure 14 présente les résultats de la modélisation pour la balance de l'équation de transport de $\overline{\rho V_y'^2}$.
Nous observons que le modèle donne une production globale de la corrélation qui est assez bien en accord avec le résultat de la simulation tridimensionnelle (figure 9). Un écart assez significatif est observé dans la zone de paroi, pour laquelle le modèle donne des termes de pression qui tendent vers zéro. Cependant, l'effet global de la pression dans cette zone est bien négatif, c'est-à-dire qu'il tend à accroître la convection. Au contraire, le terme de diffusion par les corrélations triples de vitesse à un comportement inverse.

8. CONCLUSIONS

L'analyse du résultat d'une simulation tridimensionnelle à l'aide des équations de Navier-Stokes a été présentée sous la forme de moyenne selon la direction aube-à-aube.
Nous avons montré que le champ moyen se comportait de manière essentiellement non-visqueuse. Le champ fluctuant spatial joue un rôle significatif dans le bilan global des équations de quantité de mouvement. Le niveau de son influence s'élève à 10 à 50% de la force de pression d'aubage. Lors du transfert de l'information entre grille, il est essentiel de tenir compte de la corrélation radiale $\overline{\rho V_y'^2}$, qui conduit à une forte correction du champ de pression statique.
L'analyse du comportement du champ fluctuant a souligné une certaine analogie avec celui d'un champ turbulent. La dissipation exerce son influence sur le champ fluctuant essentiellement. Cependant, une grande part de ce champ fluctuant retourne dans le champ moyen selon un processus réversible d'échange. A ce niveau le travail de la force de pression d'aubage avec le champ de vitesse moyenne joue un rôle essentiel, puisqu'il intervient à la fois dans l'équation de transport de l'énergie cinétique pour le champ moyen, et pour le champ fluctuant. La pression joue un rôle dominant dans le développement du champ fluctuant. En particulier, le terme de diffusion par la pression

réalise un transfert à partir de la zone externe vers la paroi de l'énergie cinétique du champ fluctuant. L'effet global de la pression est compensé par l'action des corrélations triples de vitesse, qui ont tendance à auto-homogénéiser le champ fluctuant. La principale différence avec le champ turbulent réside dans l'influence très faible de la production via les gradients de vitesse moyenne, qui sont négligeables par rapport en particulier au travail des forces de pression d'aubages. Il faut enfin noter la très forte anisotropie du champ fluctuant. Ce dernier point ne plaide pas en faveur de modèles basés sur l'emploi de pseudo-viscosité turbulente, tels ceux définis dans les modèles de mélanges radiaux (DE RUYCK et HIRSCH, 1992). Nous avons proposé une modélisation simplifié des termes de corrélation pression-déformation, et des diffusions par les corrélations triples de vitesse et liées à la pression. L'analogie avec la modélisation d'un champ turbulent a été largement employée. L'objectif étant essentiellement ici de valider qualitativement une approche, nous pouvons considérer que les résultats sont encourageants. Avant d'envisager une utilisation de ce type de modèle dans un cadre par exemple de calcul méridien, il est nécessaire d'adjoindre l'influence de paroi dans la modélisation des termes de pression. La dissipation doit être ajoutée. Enfin, nous n'avons rien dit sur les termes liés aux forces de pression d'aubages. Dans le cadre d'un calcul méridien, ces termes ne sont pas des inconnues. LARREY (1991) a en effet montré qu'il est possible de déterminer directement la pression sur les parois des aubes, à l'aide d'une méthode d'éléments frontières, sans faire appel aux calculs aube-à-aube classiques.

Remerciements

Les auteurs remercient Ms. G.MEAUZE et G.BILLONNET de ONERA pour avoir permis la réalisation de la simulation tridimensionnelle ayant servi de base à ce travail. Nous remercions également EDF, SEP, SNECMA et TURBOMECA pour avoir contribué au financement de la bourse de thèse de G.PERRIN, dans le cadre du FIRTECH EMM.

Références

Adkins, G.G., Smith, L.H. Jr., 1982, "Spanwise mixing in Axial-flow Turbomachines," ASME J. of Engineering for Power, Vol. 104, pp 97-110

Adamczyk, J.J., 1984, "Model equation for simulating flows in multistage turbomachinery", NASA TM 86869, nov.

Adamczyk, J.J., Celectina, M.L., Beach, T.A., Barnett, M., 1989, "Simulation of Three-dimensional Viscous Flow within a Multi-stage Turbine", ASME Journal of Turbomachinery, Vol. 112, PP. 370-376.

Adamczyk, J.J., Celectina, M.L., Jen Ping Chen, 1994, "Wake-induced unsteady flows : Their impact on rotor performance and wake rectification", ASME Paper 94-GT-219, to appear in Tr. ASME.

Cambier, L., Couaillier, V., Veuillot, J.P., 1988, " Résolution numérique des équations de Navier-Stokes à l'aide d'une méthode multigrille", La Recherche Aérospatiale, n° 1988-2, pp 23-42.

Chapin, V., 1993, "Contribution à la Simulation Numérique de l'Interaction Aérodynamique de deux Roues Ailetées", Thèse de Doctorat, Université Pierre et Marie Curie, Janvier 1993.

Daly, B.J., Harlow, F.H., 1970, "Transport Equations in Turbulence", Phys. Fluids, Vol. 13, pp. 2634-2649.

Dawes, W.N., 1990, " Towards improved Throughflow Capability : The Use of 3D Viscous Flow Solvers in A Multistage Environnement", ASME Paper 90-GT-19, June.

Denton, J.D., 1990, " The Calculation of Three-Dimensional Viscous Flow through Multistage Turbomachines", ASME Paper 90-GT-19, June.

Denton, J.D., Hodson, H.P., Dominy, R.G., 1990," Test case E/CA-7: subsonic turbine cascade LA", in "Test Cases for Computation of Internal Flows in Aero-Engine Components", AGARD-AR-275, ed. Fottner, pp-124-138.

De Ruyck, J.,Hirsh, CH., 1992, " A Radial Mixing Computation Method", ASME paper n° 88-GT-68, Amsterdam, June.

Escande, B., Cambier, L., 1991, " Validation du Code CANARI par le Calcul de l'Ecoulement Tridimensionnel Turbulent dans un distributeur de Turbine", AGARD CP 510, San Antonio, USA.

Gallimore, S.J., Cumpsty, N.A., 1986, "Spanwise Mixing in Multistage Axial Flow Compressors: Part I - Experimental Investigations, "and "Part II - Through Flow Calculations Including Mixing, "ASME J. of Turbomachinery, Vol. 108, pp 2-16.

Giles, M.B., 1987, " Calculation of Unsteady Wake-Rotor Interaction", AIAA Paper 87-0006.

Giles, M.B., 1992, " An Approach for Multi-satge Calculation Incorporating Unsteadiness", ASME Paper 92-GT-282, Cologne, Germany.

Hanjalic, J., Launder, B.E., 1972, " A Reynolds Stress Model for Turbulence, and its Application to thin Shear Flows", JFM, Vol. 52, Part 4, pp. 609-698.

Hirsch, Ch., Dring, R.P., 1987 "Through Flow Models for Mass and Momentum Averaged Variables ", ASME paper n° 87-GT-52, Anaheim, 1987.

Horlock, J.H., Marsh, H., "Flow models for Turbomachines", J. of Mechanical Engineering Science, Vol. 13, pp. 358-368.

Launder, B.E., 1984, "Second-Moment Closure Methodology and Practice", in "Turbulence Models and their Applications", Vol.2, Ed. Eyrolles, 1984.

Larrey, E., "Résolution de l'équation de Pression par la méthode des éléments frontières. Application aux turbomachines multiétagées", Thèse de Doctorat, Ecole Centrale de Lyon, 1991.

Michel, R., Quemard, C., Durant, R., 1969, "Application d'un schéma de longueur de mélange à l'étude des couches limites turbulentes d'équilibres", ONERA NT n° 154.

G. Perrin, F. Leboeuf, 1993 " Investigation of Through-Flow Hypothesis in a Turbine Cascade Using a 3D Navier-Stokes Computation" , ASME paper 93-GT-21, Cincinnati. To be publishedin 1995, ASME Transactions.

G.Perrin, F.Leboeuf, 1994 "On the Transport of Spatial Fluctuations Correlations in a Turbine Stator", ASME 94-GT-330, LA HAYE, Juin 1994.

G.Perrin, 1994 "Expérimentation numérique tridimensionnelle en vue de la modélisation et du calcul des écoulements secondaires dans les tubromachines", Thèse de doctorat, Ecole Centrale de Lyon, Décembre 1993.

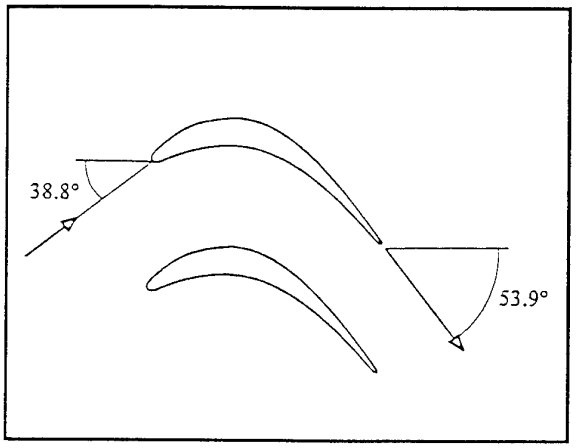

Figure 1 : Géométrie de la grille de Turbine

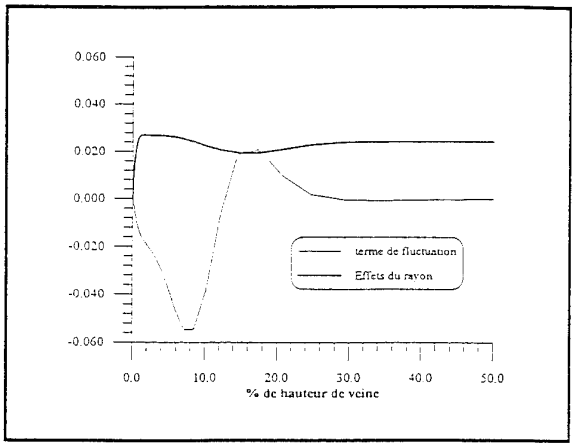

Figure 2 : Influence du terme de fluctuations dans l'équation d'équilibre radial à l'aval d'une roue fictive. (x/c=1.10)

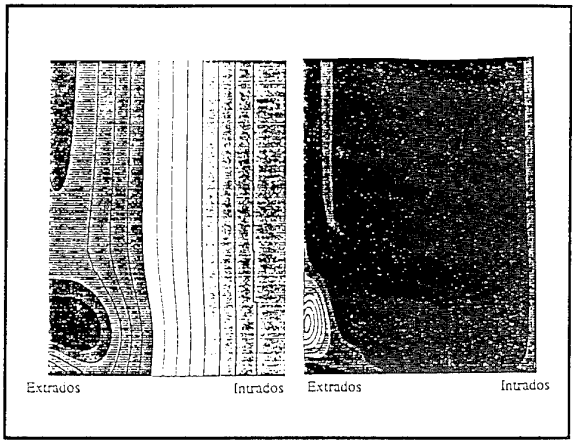

Figure 3 : Pression statique (figure de gauche), et énergie cinétique des fluctuations locales (figure à droite) (x/c=0.75)

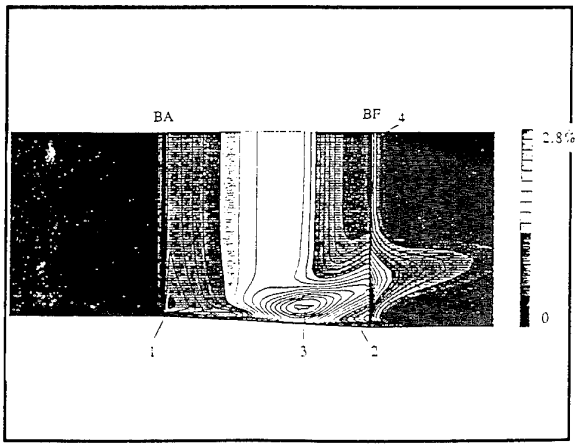

Figure 4 : Energie cinétique moyenne $\bar{K}$ des fluctuations spatiales dans le plan (x, y). BA et BF sont respectivement le bord d'attaque et le bord de fuite de l'aube. La paroi latérale est située en bas de la figure.

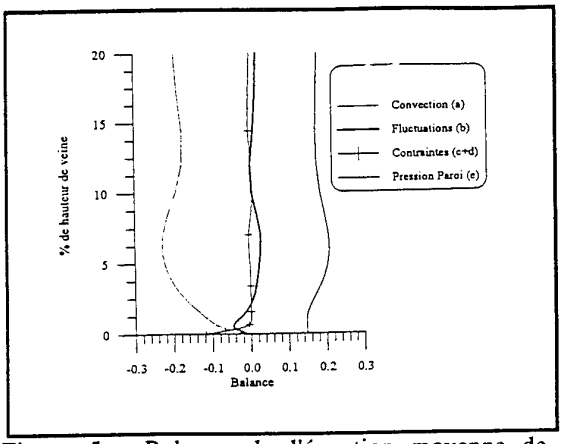

Figure 5 : Balance de l'équation moyenne de conservation de quantité de mouvement selon z. (x/c=0.75).

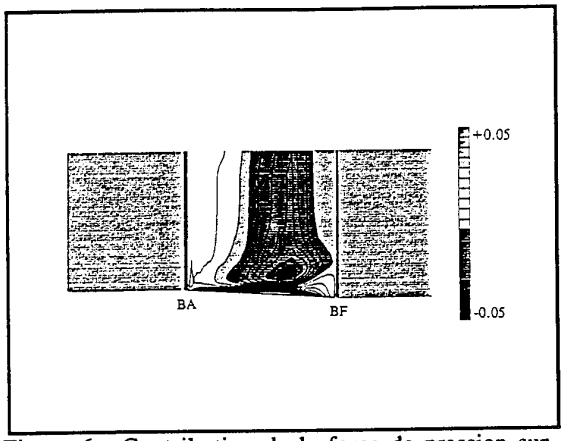

Figure 6 : Contribution de la force de pression sur l'aube dans l'équation de transport de $\bar{K}$. (vue dans le plan (x, y)).

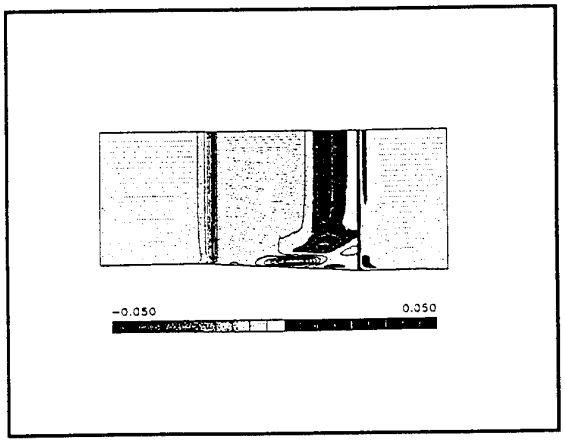

Figure 7 : Somme de tous les termes de pression dans l'équation de transport de $\bar{K}$. (vue dans le plan (x, y)).

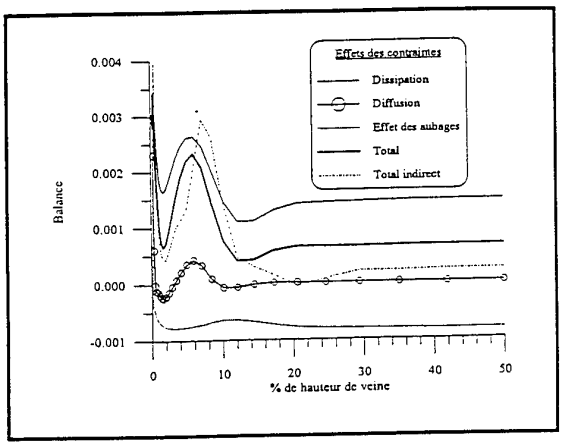

Figure 8 : Evolutions selon y des différents termes traduisant les effets de contraintes. (x/c=0.75).

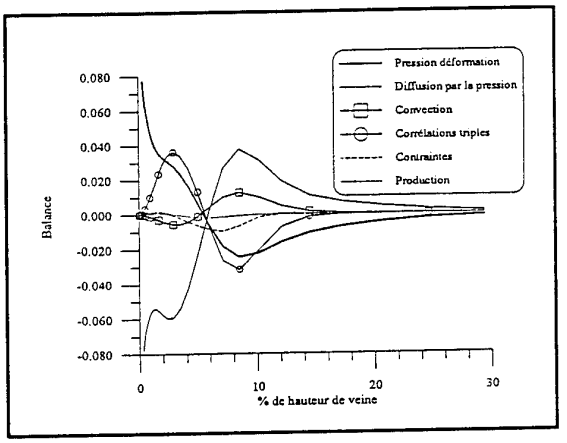

Figure 9 : Balance de l'équation de transport de la corrélation $\overline{\rho V'_y{}^2}$: résultats de la simulation tridimensionnelle

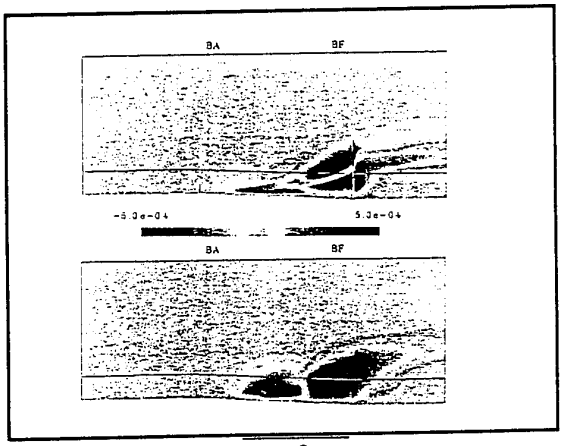

Figure 10 : Corrélation $\overline{\rho V'_y{}^2 V'_x}$ (en haut = résultat du modèle, en bas = résultat de la simulation tridimensionnelle)

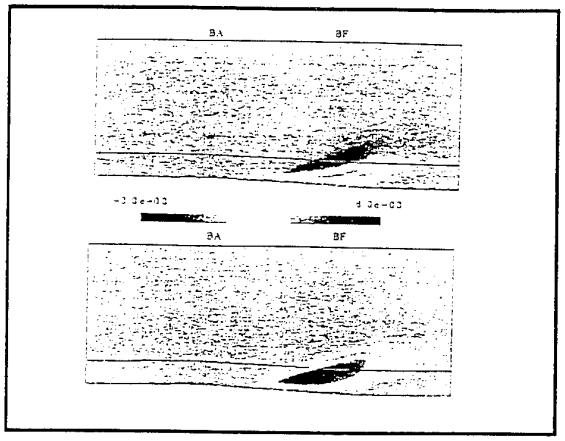

Figure 11 : Corrélation $\overline{\rho V'_y{}^3}$ (voir figure 10)

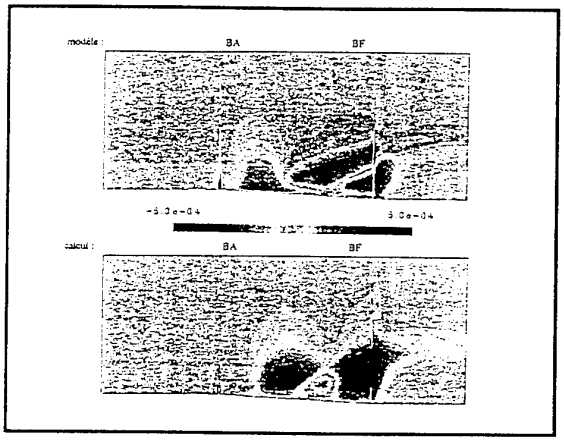

Figure 12 : Corrélation $\overline{\rho V'_x{}^2 V'_y}$ (voir figure 10)

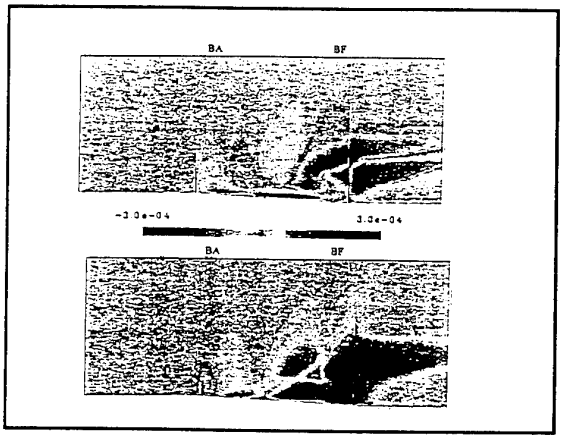

Figure 13 : Corrélation $\overline{\rho V'_z{}^2 V'_y}$ (voir figure 10)

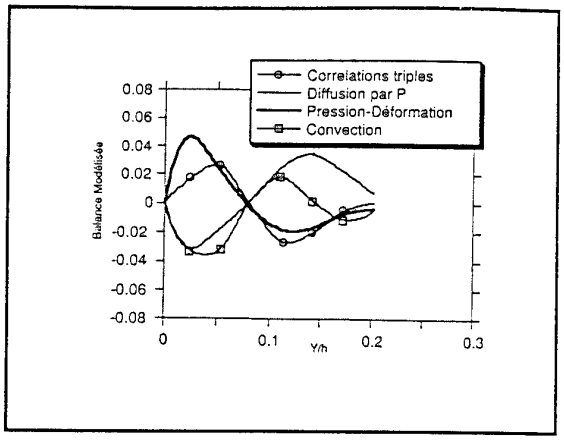

Figure 14 : Balance de l'équation de transport de la corrélation $\overline{\rho V'_y{}^2}$: résultats de la modélisation

Euler Modeling Techniques for the Investigation of Unsteady Dynamic Compression System Behavior*

M. W. Davis, Jr.
A.A. Hale
K.A. Shahrokhi
G.D. Garrard
Sverdrup Technology, Inc., AEDC Group, MS-9103
Arnold Engineering Development Center
Arnold Air Force Base, Tennessee 37389-9013
USA

SUMMARY

The development of advanced turbine engine simulations is a necessity for the analysis of turbine engine dynamic events such as compressor surge, rotating stall, and inlet distortion. Simulations can fill information gaps and extend the range of test results to areas not tested. In addition, once a simulation has been validated, the model can become a numerical experiment and the analysis engineer can conduct "what-if" studies to determine possible solutions to performance or operability problems. Turbine engine simulations can range from the one-dimensional cycle codes to the most complex computational fluid dynamics formulations. For dynamic events, the full Navier-Stokes solution is not feasible. However, CFD solutions using the Euler equations have achieved a good measure of success. This paper discusses both one-dimensional and three-dimensional Euler solution techniques that have been developed at the Arnold Engineering Development Center (AEDC) and applied to dynamic simulations for gas turbine engine compressors and the extension of the one-dimensional technique to the full turbine engine.

LIST OF SYMBOLS

A Area

Cp Specific heat at constant pressure

E Energy function

e Internal energy

F Matrix of diffusion terms in the governing equations

FX Axial component of compressor blading and casing force acting on fluid

G Matrix of turbomachinery source terms in the governing equations

H Total enthalpy

I Characteristic-based weighting term

$\dot{M}_T$ Mass flow function

P Pressure

PR Pressure ratio

Q Rate of heat addition to control volume

SW Rate of shaft work

T Temperature

TR Temperature ratio

t Time

u Axial velocity

U Matrix of dependent variables in the governing equations

W Mass flow rate

x Axial coordinate

ρ Density

Subscripts

B Bleed

des Design

ref Reference condition

s Static condition

ss Steady-state condition

x Axial direction

T Total conditions

INTRODUCTION

Today's military turbine engines are the most reliable aircraft power plants produced to date. This reliability has been obtained through extensive testing prior to introduction into the military fleet. To aid in the analysis of engine performance and operability, turbine engine mathematical models have been developed that can provide insight into a physical phenomenon that may not be understood by test data alone. Models can fill information gaps and extend the range of test results to areas not tested. In addition, once a model has been validated, the model can become a numerical experiment and

* The research reported herein was performed by the Arnold Engineering Development Center (AEDC), Air Force Materiel Command. Work and analysis for this research were done by personnel of Sverdrup Technology, Inc., AEDC Group, technical services contractor for the AEDC propulsion test facilities. Further reproduction is authorized to sastisfy the needs of the U. S. Government.

Paper presented at the AGARD PEP 85th Symposium on "Loss Mechanisms and Unsteady Flows in Turbomachines", held in Derby, United Kingdom, 8-12 May 1995, and published in CP-571.

the analysis engineer can conduct "what-if" studies to determine possible solutions to performance or operability problems.

Unsteady dynamic turbine engine simulations have branched in two directions: (1) component models, and (2) full simulations. Component models have mainly dealt with the compression system since it is that system which experiences the most violent types of dynamic instabilities and subsequently is the most damaging to engine operability. Compression system models range from one-dimensional lumped system models to stage-by-stage systems able to handle three-dimensional inlet distortion.

To obtain the fidelity and dynamic capability, the modeling technique must handle compressible gas dynamics. Current turbine engine cycle models use a lumped volume technique and in general are not able to simulate gas flow dynamics. A technique that does satisfy the dynamic requirement uses the Euler equations with turbomachinery source terms solved with efficient finite-difference or finite-volume schemes. This paper will present one-dimensional and three-dimensional compression system Euler modeling techniques developed at the Arnold Engineering Development Center (AEDC) by the JDAPS (Joint Dynamic Airbreathing Propulsion Simulations) partnerships, along with example applications.

DYNAMIC COMPRESSION SYSTEM MODELING TECHNIQUES

To illustrate the Euler compression system modeling technique, this paper will draw upon the techniques developed and coded in the one-dimensional **DYN**amic **T**urbine **E**ngine **C**ompressor **C**ode, **DYNTECC,** extensions of the one-dimensional methodology, **A**erodynamic **T**urbine **E**ngine **C**ode, **ATEC** (Refs. 1 - 3) and the three-dimensional **T**urbine **E**ngine **A**nalysis **C**ompressor **C**ode, **TEACC** (Ref. 4).

One-Dimensional Technique – DYNTECC and ATEC

DYNTECC is a one-dimensional, stage-by-stage, compression system mathematical model which is able to analyze any generic compression system. DYNTECC uses a finite-difference numerical technique to simultaneously solve the mass, momentum, and energy equations with turbomachinery source terms (mass bleed, blade forces, heat transfer, and shaft work). The source terms are determined from a complete set of stage pressure and temperature characteristics provided by the user.

Illustrated in Fig. 1 is a representative, single-spool, multistage compressor and ducting system. The compressor and ducting system are modeled by an overall control volume. Acting on the fluid control volume is an axial-force distribution, FX, attributable to the effects of the compressor blading and the walls of the system. Appropriate inlet and outlet boundary conditions are applied at the inflow and outflow boundary locations. Energy supplied to the control volume includes the rate of heat added to the fluid, Q, and shaft work done on the fluid, SW. Mass-transfer rates across boundaries other than the inlet or exit (such as the case of interstage bleeds) are represented by the distribution, W_B.

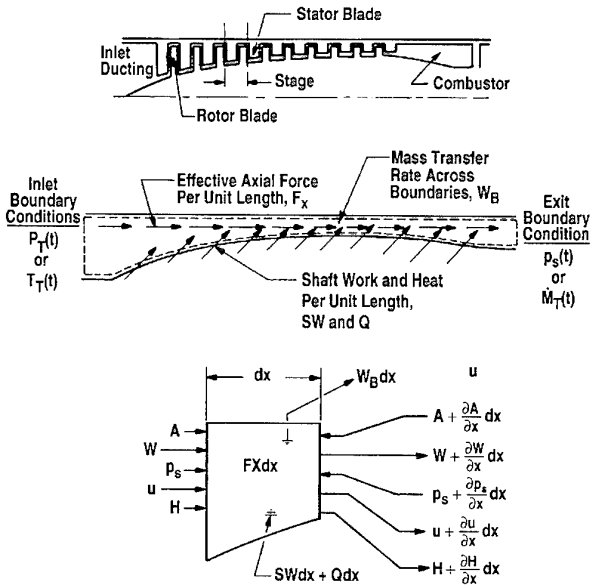

Figure 1. DYNTECC control volume technique.

The overall control volume is subdivided into a set of elemental control volumes. Typically, the compressor section is subdivided by stages either as rotor-stator or vice versa, depending on the way experimental stage characteristics may have been obtained. All other duct control volumes are divided to ensure an appropriate frequency response. The governing equations are derived from the application of mass, momentum, and energy conservation principles to each elemental control volume. These equations can be expressed as:

$$\frac{\partial \mathbf{U}}{\partial t} + \frac{\partial \mathbf{F}}{\partial x} = \mathbf{G} \qquad (1)$$

where

$$\mathbf{U} = \begin{Bmatrix} \rho A \\ \rho u A \\ e A + \frac{1}{2} u^2 A \end{Bmatrix} \quad \mathbf{F} = \begin{Bmatrix} \rho u A \\ \rho u^2 A + P A \\ \rho u A \left(e + \frac{P}{\rho} + \frac{1}{2} u^2 \right) \end{Bmatrix} \quad \mathbf{G} = \begin{Bmatrix} -W_B \\ FX \\ Q + SW - H_B \end{Bmatrix}$$

To provide stage force, FX, and shaft work, SW, inputs to the momentum and energy equations, a set of quasi-steady stage characteristics must be available for closure. The stage characteristics provide the pressure and temperature rise across each stage as a function of steady airflow. Using pressure rise, temperature rise, and airflow, a calculation can be made for stage steady-state forces and shaft work. A typical set of stage characteristics is presented in Fig. 2.

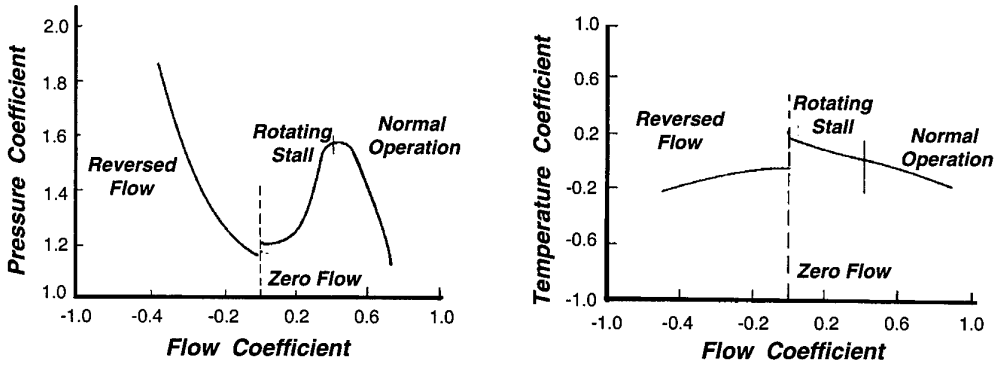

Figure 2. Typical set of stage characteristics.

The above discussion centers on the steady characteristic. During transition to surge and development of rotating stall, the steady stage forces derived from the steady characteristics are modified for dynamic behavior via a first-order lag equation of the form:

$$\tau \frac{d(FX)}{dt} + FX = FX_{SS} \qquad (2)$$

The time constant, τ, is used to calibrate the model to provide the correct post-stall behavior. The inflow boundary during normal forward flow is the specification of total pressure and temperature. The exit boundary condition is the specification of exit Mach number or static pressure. During reverse flow the inlet is converted to an exit boundary with the specification of the ambient static pressure. Therefore, both the inlet and exit boundary function as exit boundaries during a surge cycle.

Explicit 1-D Algorithm

An explicit split flux finite-difference algorithm is used to numerically solve the area weighted quasi-one-dimensional Euler equations. The quasi-one-dimensional Euler equations with source terms [Eq. (1)] are written in conservation Cartesian form and applied to a fixed grid. A finite-difference representation of Eq. (1) can be applied over an interval between grid points j and j+1 with the fluxes evaluated at the nodes and the sources evaluated at the center of the volume given by

$$\left(\frac{\Delta U}{\Delta t}\right)_j = I^+_{j-\frac{1}{2}} \left(\frac{\Delta U}{\Delta t}\right)_{j-\frac{1}{2}} + I^-_{j+\frac{1}{2}} \left(\frac{\Delta U}{\Delta t}\right)_{j+\frac{1}{2}} \qquad (3)$$

where

$$\left(\frac{\Delta U}{\Delta t}\right)_{j-\frac{1}{2}} = \left[G_{j-\frac{1}{2}} - \frac{(F_j - F_{j-1})}{(x_j - x_{j-1})} \right];$$

$$\left(\frac{\Delta U}{\Delta t}\right)_{j+\frac{1}{2}} = \left[G_{j+\frac{1}{2}} - \frac{(F_{j+1} - F_j)}{(x_{j+1} - x_j)} \right]$$

Characteristic theory is used to develop weighting terms (I^+, I^-) for splitting the time derivatives to the adjacent nodes as illustrated in Fig. 3.

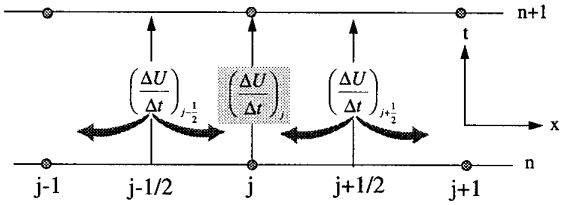

Figure 3. Schematic of the explicit split flux differencing scheme used in DYNTECC.

The time derivatives at the nodes can be obtained by summing the left characteristic-weighted time derivative from an upstream interval and the right characteristic-weighted time derivative from the downstream interval. A solution is now obtainable at the n+1 time step by a forward Euler time integration procedure.

Extensions of the One-Dimensional Technique

Extensions of the basic one-dimensional modeling technique include the modeling of some three-dimensional effects and the coupled relationship to engine components. The following section will discuss the extension for analyzing distorted inflow using a modified parallel compressor theory and extensions to include additional components of the gas turbine engine, including the full turbine engine (Ref. 3).

Modified Parallel Compressor Extension

When circumferential inlet distortion effects are important, DYNTECC can be operated as a parallel compressor model (See Fig. 4) with or without circumferential and radial crossflow approximations. The overall compression system control volume is sub-divided into a series of circumferential and parallel tubes. Each segment/tube then acts in parallel with each other segment, exiting to the same exit boundary condition. Different magnitudes of inlet total pressure and/or temperature can then be imposed upon each segment of the

parallel compressor. In the purest sense, each segment is independent of all other segments, except through the exit boundary condition. For complex distortion patterns, circumferential and radial crossflow terms are approximated. System instability occurs when any one segment becomes unstable as a result of the inlet and exit conditions imposed upon it.

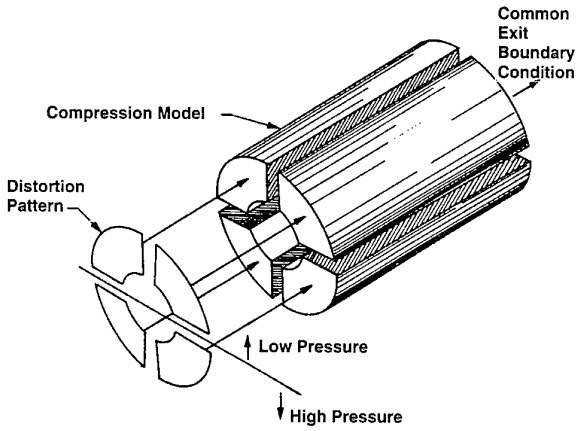

Figure 4. Example of compressor with circumferential segments with an applied inlet distortion.

Parallel compressor theory is generally valid if the segment arc is greater than 60 deg, also known as the critical angle. Secondary flow mechanisms become more significant for segments with arcs less than the critical angle. The parallel compressor theory's predictive capabilities deteriorate when segments of less than the critical angle are used. DYNTECC was recently modified to approximate the effects of circumferential crossflow during distorted flow (Ref. 5). Inlet pressure distortions with circumferential nonuniformities can generate mass flow in the circumferential direction. The static pressure difference between two segments driving a flow in the circumferential direction is illustrated in Fig. 5. The flow occurs in the gap between the compressor rotor and stator.

The circumferential mass flow within the rotor-stator gap can be approximated using a simple orifice flow analogy, a concept developed by Kimzey (Ref. 6). In the analogy, the high and low static pressure regions are seen as pressure reservoirs and the rotor-stator gap as an orifice. Thus, the flow can be approximated utilizing a simple algebraic expression based on a classic orifice flow.

Extension to Other Components

The most recent version of DYNTECC has been upgraded to include a combustor model. This new feature permits the user to study dynamic compressor/combustor interactions. The combustor flammability limits are determined by using steady-state engineering correlations developed by Herbert (Ref. 7). In order for stable combustion to occur, the primary zone equivalence ratio must fall within a rich and lean limit. Based on experimental data, Herbert defined a Combined Air Loading Factor to calibrate the light- off and blow-off data. A

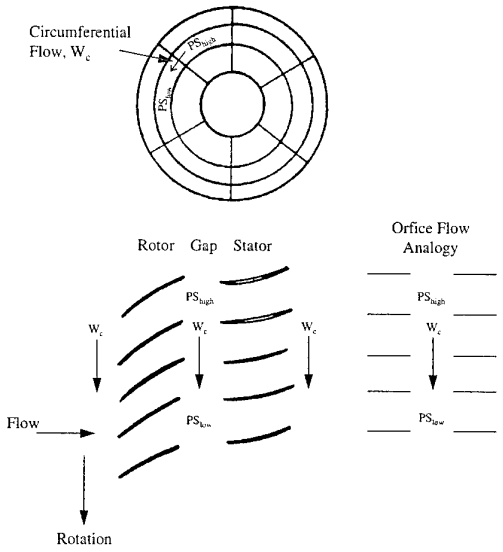

Figure 5. Illustration of the circumferential crossflow model.

polynomial curve fit of Herbert's flammability data for a generic can-type combustor is used in the combustor model. Combustion efficiency is determined by using steady-state engineering correlations developed by Lefebvre (Ref. 8). Lefebvre assumed that the overall combustion efficiency is limited by the efficiency of fuel evaporation and the reaction efficiency.

Because of the dynamic operation of the combustor, it is possible for heat release to occur for a short period of time, even though the combustor equivalence ratio may lie outside the steady-state flammability limits. Likewise, the heat release process may not resume immediately after the combustor equivalence ratio re-enters the flammability bounds. To account for these effects, a first-order lag on the heat release rate as proposed by Davis (Ref. 9) is incorporated in the model:

$$\tau \frac{dQ}{dt} + Q = Q_{SS}(t)$$

Extension to the Overall Turbine Engine

With the inclusion of a combustor model into the DYNTECC program, the extension to a gas turbine engine model could be developed by the addition of routines representing the turbine. The extension of DYNTECC to the full gas turbine engine has produced a code known as the Aerodynamic Turbine Engine Code, ATEC (Ref. 3).

ATEC is currently configured to support two gas generator turbines coupled to compressor systems through up to two shafts and one power turbine. Because of the modularity of the DYNTECC coding, integration of the turbine model into the existing code required specifying the performance characteristics in a fashion similar to the compressor performance (shaft work and blade forces). To determine the amount of work extracted across a given turbine during the initial conditions

calculations, the gas generator turbine is assumed to exactly provide the power required by the compressor system. Work output from the power turbine is initially specified by the user. Once the time integration starts, energy extraction is given by the pressure ratio across the turbine and the turbine inlet flow function.

Applications of the One-Dimensional Technique

To verify the Euler methodology, DYNTECC was applied to a ten-stage high-pressure compressor for post-stall behavior and to a two-stage low-aspect-ratio fan for circumferential distortion. In both instances, there existed a set of experimental results for which comparisons could be made and conclusions as to the accuracy of the model results verified.

Compressor Post-Stall Simulation

DYNTECC was configured by Boyer and O'Brien (Ref. 10) to aid in the analysis of a ten-stage compressor rig test conducted at the Compressor Research Facility to investigate the boundary between surge and rotating stall for high-pressure-ratio compressors. The model was executed at the experimentally determined stall/surge boundary where recovery hysteresis was most severe. DYNTECC was calibrated at the stall/surge boundary by ad usting calibration constants to produce rotating stall. The constants were held fixed for subsequent analysis investigating possible hardware modifications to reduce the sensitivity of the compressor to rotating stall.

Calibration of DYNTECC with experimental data matched the overall performance and individual stage performance of the 10-stage compressor rig. As illustrated in Fig. 6, the compressor initially experiences a partial surge cycle, then transitions to rotating stall. DYNTECC individual stage performance is also compared to that obtained experimentally. For both overall and individual stage behavior, DYNTECC reproduced the experimental results fairly accurately during the dynamic event.

Compressor Distortion Analysis

DYNTECC can be configured to analyze inlet total pressure distortion. Using the modified parallel theory, DYNTECC was used to analyze the effects of inlet distortion on a two-stage, low-aspect-ratio fan similar to the compression system examined by Gorrell and Davis (Ref. 11). The model was initially calibrated against the experimental clean inlet performance of the compressor. The modified model was then validated using the compressor performance with a pure circumferential inlet distortion pattern.

The inlet distortion pattern was generated from a 1/rev circumferential distortion screen shown in Fig. 7. This screen produces a total pressure inlet distortion that is purely circumferential. The simulation was run with the model

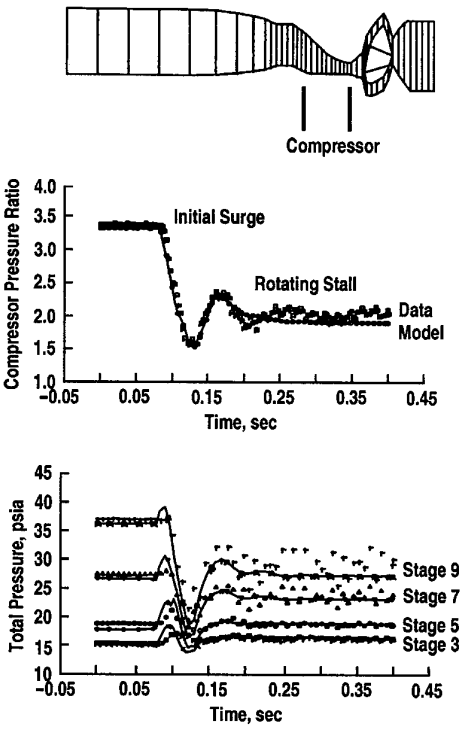

Figure 6. Post-stall dynamic event – DYNTECC predictions and comparison to experimental results.

modifications, as well as with the pure parallel compressor theory for comparison purposes. Shown in Fig. 8 is the model prediction compared to the experimental results at 98.6-percent speed. The inlet distortion pattern has a significant impact on both compressor performance and operability.

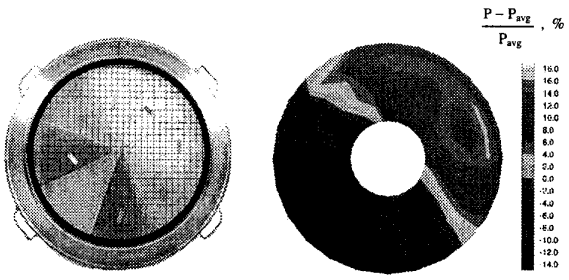

Figure 7. Imposed distortion pattern produced by distortion screen.

Full Turbine Engine Dynamic Behavior

The full turbine engine dynamic code, ATEC, was configured to the T-55 helicopter engine (schematically illustrated in Fig. 9) and operationally verified that it would exhibit surge cycles during a rapid fuel pulse. For this case, two turbines are modeled. The first turbine is the gas generator turbine which is coupled to the compressor system, and the second turbine is the power turbine. The shaft work and blade forces in each turbine were equally distributed across multiple control volumes, however, to keep the overall length of any given

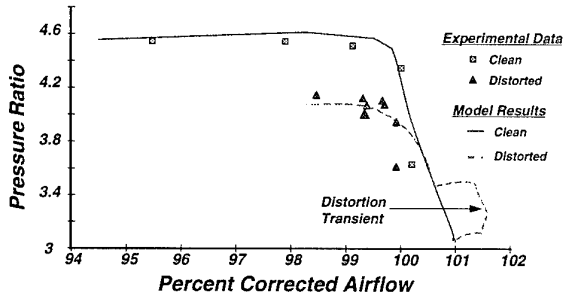

Figure 8. Model prediction and comparison to experimental results for distorted inflow.

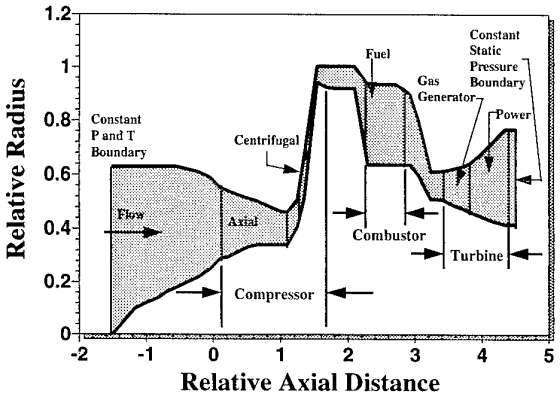

Figure 9. Computational schematic of the T55 ATEC simulation.

control volume on the same order as the rest of the grid. This helps maximize model dynamic fidelity and, with the explicit flow solver routine, numerical stability.

The combustor fuel was rapidly increased and held constant for a short time, which forced the compressor into surge. Steady-state operation was not reestablished until the fuel flow rate was returned to the original flow rate.

Relative mass flow rate in the engine as a function of time is shown in Fig. 10. During each of the surge cycles, the mass flow rate in the front section of the engine reverses and becomes negative. In the back section of the engine, the flow rate is greatly reduced, but it does not reverse.

THREE-DIMENSIONAL TECHNIQUE – TEACC

An alternate approach to parallel theory for distorted inflow is being developed at AEDC and is known as **TEACC** (Ref. 4). **TEACC** allows for circumferential and radial control volumes to interact directly with each other via Euler equations with body forces representing the forces associated with a blade row. This technique allows the direct

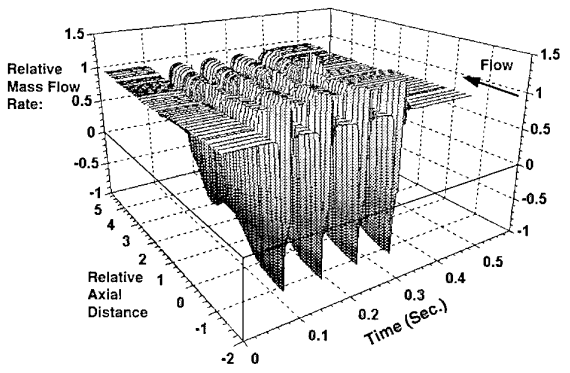

Figure 10. Relative mass flow rate during dynamic engine event.

exchange of mass, momentum, and energy. The overall technical approach for the development of TEACC is illustrated in Fig. 11.

A three-dimensional computational fluid dynamics algorithm was chosen which solves the inviscid Euler equations:

$$\frac{\partial \mathbf{U}}{\partial t} + \nabla \cdot \mathbf{F} = \mathbf{G}$$

$$\mathbf{U} = \begin{pmatrix} \rho \\ \rho u \\ \rho v \\ \rho w \\ E \end{pmatrix} \quad \mathbf{F} = \begin{bmatrix} \rho u & \rho v & \rho w \\ \rho u^2 + P & \rho uv & \rho uw \\ \rho uv & \rho v^2 + P & \rho vw \\ \rho uw & \rho vw & \rho w^2 + P \\ (E+P)u & (E+P)v & (E+P)w \end{bmatrix} \quad \mathbf{G} = \begin{pmatrix} W \\ Fx \\ Fy \\ Fz \\ SW \end{pmatrix}$$

$$E = \rho e + \frac{1}{2}\rho q^2 \qquad P = (\gamma - 1)\rho e$$

The H vector provides the source terms to model the effects of turbomachinery. These turbomachinery source terms of mass bleed, blade forces, and shaft work are supplied by a streamline curvature code called **CPAC**, (**C**ompressor **P**erformance **A**nalysis **C**ode, a derivative of a code known as HTO300). The streamline curvature code, CPAC, is based on radial

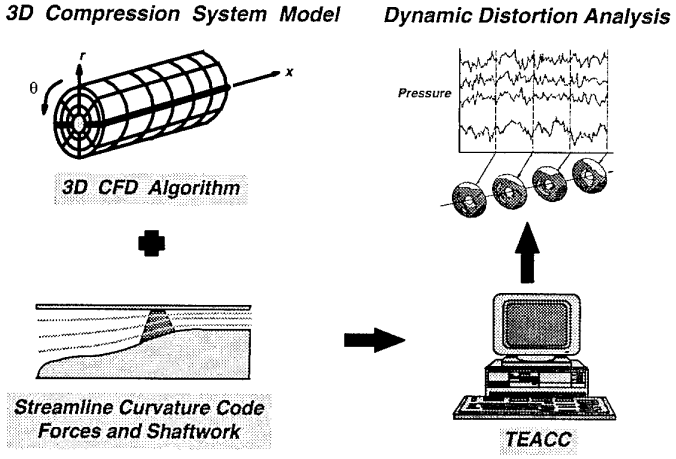

Figure 11. TEACC overall technical approach.

redistribution of blade force and shaft work for axisymmetric flow. Necessary inputs include overall geometry, blade geometry, and loss and deviation correlations. In general, these correlations are based upon NASA SP-36 (Ref. 12). An excellent reference for the derivation of the equations used in the streamline curvature method can be found in Ref. 13.

The cell-centered MacCormack algorithm was selected to integrate the Euler equations. The MacCormack algorithm is an explicit predictor-corrector algorithm which is based on a two-stage Runge-Kutta method, and is second-order accurate in time and space. This method is used to solve the Euler equations for new temporal values of the dependent variables

TEACC is a time-dependent, numerical algorithm requiring a set of initial conditions. A set of initial conditions is obtained from a converged solution of the streamline curvature code, CPAC, for the full geometry (i.e., inlet duct, compressor, and exit duct). An axisymmetric segment of the three-dimensional grid is used as the geometry of the streamline curvature code. A complete set of conditions (ρ, ρu, ρv, ρw, E, and turbomachinery source terms) is provided for every control volume within TEACC by CPAC for undistorted, steady flow. Inlet boundary conditions for CPAC are specification of uniform total temperature, uniform total pressure, overall mass flow, and inlet and exit curvature equal to zero.

Proper specification of boundary conditions is necessary for establishing steady-state convergence and uniqueness. Four types of boundaries are modeled in TEACC: wall, cyclic wrap around (periodic), inflow, and outflow. Wall boundary conditions use a phantom cell concept, typically used with cell centered finite-volume approaches. Cyclic wrap around or periodic boundary conditions also use phantom cells. The grid is rotated around the longitudinal axis such that the circumferential boundary planes coincide (Planes at the 1^{st} and n^{th} location). Inflow boundary conditions are calculated using a finite-difference implementation of reference plane characteristics on the inflow grid. The flow is assumed to be parallel to the centerline at the inflow plane. The specified inflow boundary conditions are total pressure, total temperature, and no velocity components in the y and z directions (i.e., $v = w = 0$). Outflow boundary conditions specify the total mass flow at the exit plane. The other properties are allowed to float by specifying a zero derivative in the axial direction. The values at the outflow plane are set equal to those immediately upstream. The outflow conditions are updated during both the predictor and corrector steps of the interior algorithm.

Calculation Procedure

A streamline curvature code delivers a velocity flow field in the form of streamlines. CPAC has been further modified to calculate turbomachinery source terms at the blades within each stream tube. Each of the sketches in Fig. 12 represents the same streamline curvature control volume. The inlets and exit of these control volumes represent the leading and trailing edge of a blade. The top and bottom of the control volume is

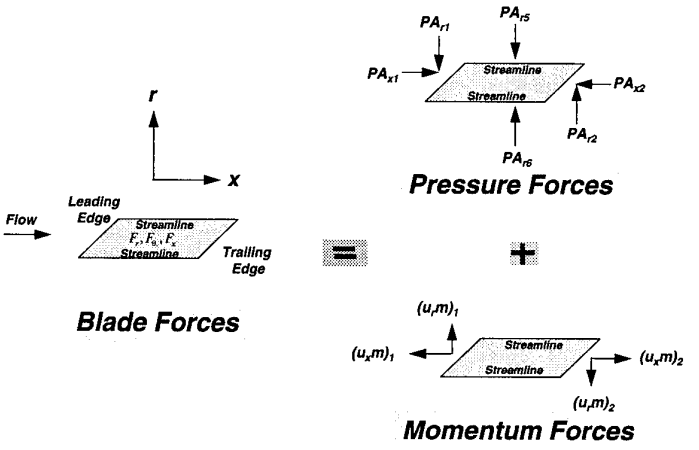

Figure 12. Turbomachinery blade force calculation technique.

defined by streamlines from a converged solution of the streamline curvature code.

For steady-state conditions, blade forces are equal to the pressure forces plus momentum forces. The pressure forces are accounted for on all surfaces, but momentum forces are not included across the streamline surface since flow is not allowed to cross a streamline by definition. The blade forces represented in Fig. 12 are a portion of the turbomachinery sources which are implemented into the three-dimensional computational fluid dynamics algorithm. The other turbomachinery source terms are the shaft work and bleed flows. Shaft work is obtained by applying the same control volume analysis for the energy equation, and the bleed flows are specified by the user.

For dynamic behavior it is necessary that the streamline curvature code calculate turbomachinery source terms across individual blades. Boundary conditions illustrated in Fig. 13 are obtained from the latest time step of the three-dimensional integrator. CPAC inlet boundary conditions are curvature, total pressure, total temperature, and swirl angle as a function of radius along with integrated mass flow. The only exit boundary condition specified is curvature as a function of radius. Curvature is calculated directly from the transient velocity field and its gradients.

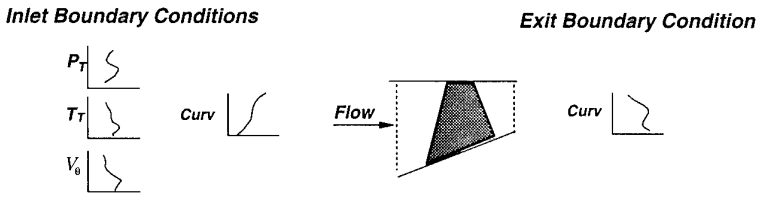

Fig. 13. Blade force update scheme for dynamic behavior.

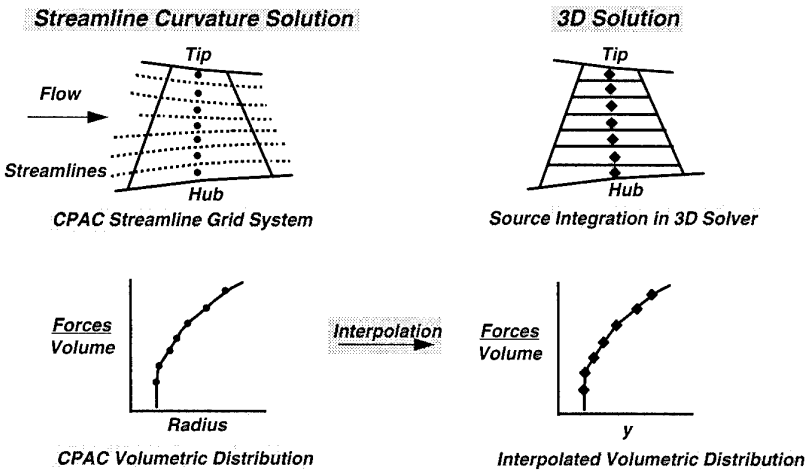

Figure 14. Radial interpolation scheme for blade forces and shaft work.

Integration of Turbomachinery Source Terms into the 3-D Solver

The streamline curvature code and the three-dimensional integrator code use the same axial stations in front of and behind the bladed region. However, there is a different radial distribution within the 3D control volume. The three-dimensional MacCormack integrator uses a fixed grid. The streamlines produced by the streamline curvature code are a function of flow conditions and are thus used to construct a grid to calculate turbomachinery source terms. Interpolation procedures have been constructed for passing information between the streamline curvature code and the three-dimensional integrator.

Figure 14 represents the radial interpolation procedure by which forces generated by the streamline curvature code are integrated into the 3-D solver. From any solution of CPAC volumetric distribution of forces and shaft work are calculated as a function of radius. The turbomachinery source terms are calculated at the CPAC radial control volume centers. The radial locations of the fixed control volume centers for the three-dimensional integrator are then identified, and the new turbomachinery source terms, forces, and shaft work distributions can be interpolated and then implemented in the three-dimensional integrator. A similar interpolation process is used to pass total pressure, total temperature, and curvature from the 3D integrator to CPAC.

APPLICATION OF THE THREE-DIMENSIONAL TECHNIQUE

TEACC was operationally verified using a single transonic rotor, R2D (Ref. 14). For this rotor there were no inlet guide vanes to direct the flow into the rotor, or a stator row to turn the flow back to the centerline. R2D is a medium-aspect-ratio transonic rotor with a hub-tip ratio of 0.5.

CPAC was configured to simulate R2D by providing the correct annulus and blade geometry along with a calibration procedure which adjusted the loss and deviation correlations until simulation results matched experimental results. Comparisons of TEACC to CPAC are made for overall rotor performance, radial pressure distributions (static and total), and resultant velocity vectors. The following results were obtained at 100-percent speed.

Geometric boundaries representing the hub, tip, inlet, and exit are similarly represented by TEACC and CPAC grids, respectively, and are presented in Fig. 15. R2D blade inlet and exit are specified at the same axial location in both grids. Internal grid selection was optimized for accuracy to support the specific numerical needs of each code.

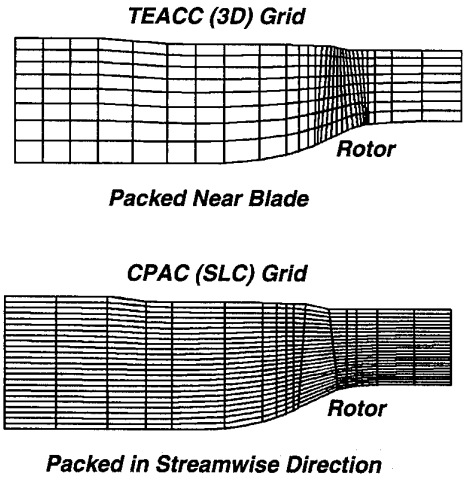

Figure 15. Single rotor geometric boundaries and grids for CPASC and TEACC.

Overall rotor performance obtained from the converged steady-state solution of the TEACC code compared extremely well for the single design point. TEACC predicted an average pressure and temperature ratio of 1.76 and 1.21, respectively, compared to that obtained by CPAC and experimental data of 1.83 and 1.21, respectively.

Static pressure calculations from TEACC are compared to those from CPAC in Fig. 16. TEACC's static pressure field compares very well to CPAC's static pressure field. The most obvious difference is that TEACC's solution indicates some errors at the hub. Some of this error can be explained by numerical errors associated with abrupt geometry changes that can occur with the MacCormack algorithm.

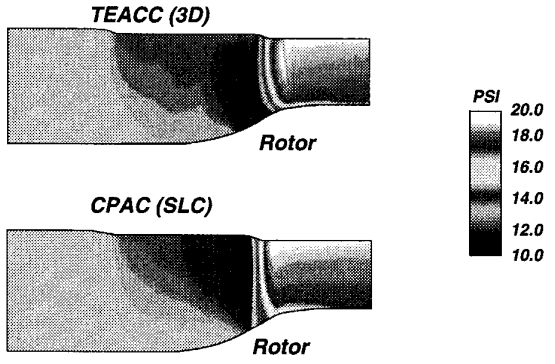

Figure 16. Comparison of TEACC calculated static pressure to that obtained with CPAC.

Velocity vectors are compared to those obtained from CPAC in Fig. 17. The grids have been rotated to one side so that the velocity vectors project up at an angle to clearly demonstrate swirling magnitude and direction. The overall velocity vectors of TEACC compare well to CPAC in magnitude and direction.

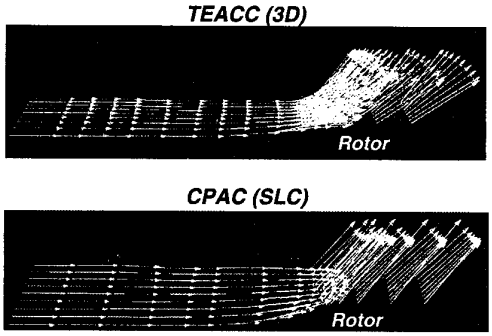

Figure 17. Comparison of TEACC calculated resultant velocity vectors to those obtained by CPAC.

CONCLUSIONS

A basic technical approach for analyzing turbine engine compression system dynamic behavior using analytical simulations based upon the solution of the Euler equations has been presented and verified. A one-dimensional technique was presented and shown to be viable for dynamic behavior which included surge and rotating stall. Extensions of this technique were developed which could handle inlet distortion effects and full turbine engine behavior during dynamic behavior. A three-dimensional technique which implements turbomachinery source terms into a Euler solution algorithm was also presented and operationally verified.

ACKNOWLEDGMENTS

This work is part of the continuing Joint Dynamic Airbreathing Propulsion Simulation, JDAPS, Partnership, and was supported by AEDC/DOT, the Compressor Research Facility of Wright Laboratory, NASA Lewis Research Center, and the Army Vehicle Propulsion Directorate.

REFERENCES

1. Hale, A. A. and Davis, M. W., Jr. "DYNamic Turbine Engine Compressor Code: DYNTECC – Theory and Capabilities." AIAA-92-3190, 28th Joint Propulsion Conference and Exhibit, Nashville, TN, July 1992.

2. Davis, M. W. , Jr. and O'Brien, W. F. "Stage-by-Stage Poststall Compression System Modeling Technique." *Journal of Propulsion and Power*, Vol. 7, No. 6, November-December 1991, pp. 997-1005.

3. Garrard, G. D., Davis, M. W., Jr., and Hale, A. A. "Recent Advances in Gas Turbine Engine Dynamic Models Developed Through JDAPS." ASME Paper to be given at the 40th ASME International Gas Turbine & Aeroengine Congress & Exposition, Houston, Texas, June 1995.

4. Hale, A. A., Davis, M. W, Jr., and Kneile, K. R. "Turbine Engine Analysis Compressor Code: TEACC – Part I: Technical Approach and Steady Results." AIAA-94-0148, 32nd Aerospace Sciences Meeting and Exhibit, Reno, NV, January 1994.

5. Shahrohki, K. A., and Davis, M. W., Jr., "Application of a Modified Dynamic Compression System Model to a Low-Aspect Ratio Fan: Effects of Distortion." AIAA-95-0301, 33rd Aerospace Science Meeting, Reno, NV, January 1995.

6. Kimzey, W. F. "An Analysis of the Influence of Some External Disturbances on the Aerodynamic Stability of Turbine Engine Axial Flow Fans and Compressors." AEDC-TR-77-80, August 1977.

7. Herbert, M. V. "A Theoretical Analysis of Reaction Rate Controlled Systems - Part 1." Chapter 6 in *Combustion Research and Reviews, 1957*, Agardograph No. 15, Butterworths Scientific Publications, London, February, 1957.

8. Lefebvre, A. H. "Fuel Effects on Gas Turbine Combustion - Ignition, Stability, and Combustion Efficiency." *Journal of Engineering for Gas Turbines and Power*, Vol. 107, January 1985, pp. 24-37.

9. Davis, M. W. "A Stage-by-Stage Post-Stall Compressor System Modeling Technique: Methodology, Validation, and Application." Ph.D. Dissertation, Virginia Polytechnic Institute and State University, August 1986.

10. O'Brien, W. F., and Boyer, K. M. "Stall and Recovery in Multi-stage Axial-Flow Compressors." AGARD 74th Specialist Meeting of the Propulsion and Energetics Panel, Luxembourg, August 1989.

11. Gorrell, S. E. and Davis, M. W., Jr., "Application of a Dynamic Compression System Model to a Low-Aspect Ratio Fan: Casing Treatment and Distortion," AIAA-93-1871, 29th Joint Propulsion Conference and Exhibit, Monterey, CA, June 1993.

12. Johnsen, I. A. and Bullock, R. O., eds. *Aerodynamic Design of Axial-Flow Compressors.* NASA-SP-36, NASA LeRC, 1965.

13. Novak, R. A. "Streamline Curvature Computing Procedures for Fluid-Flow Problems. *Journal of Engineering for Power*, October 1967, pp. 478-490.

14. Gostelow, J. P., Krabacher, K. W. and Smith, L. H., Jr., "Performance Comparison of High Mach Number Compressor Rotor Blading." NASA-CR-1256, December 1968.

UTILISATION DE CALCULS 2,5 D et 3D D'ECOULEMENTS INSTATIONNAIRES POUR LE CHOIX DE L'INSTRUMENTATION D'UN BANC D'ESSAI DE TURBINE

G. BILLONNET
A. FOURMAUX
J. HUARD
A. OCCHIONIGRO*
Office National d'Etudes et de Recherches Aérospatiales
29, avenue de la Division Leclerc
92320 CHATILLON (France)
*Société Nationale d'Etudes de Construction de Moteurs d'Aviation
Centre de Villaroche
77550 MOISSY CRAMAYEL (France)

RESUME

L'instrumentation d'une maquette de turbomachine est à la fois délicate et coûteuse dès lors que des mesures instationnaires sont envisagées dans les parties tournantes.

Une simulation numérique "prévisionnelle" de l'écoulement peut alors apporter à l'expérimentateur des informations précieuses sur le nombre et l'emplacement des capteurs.

Le défi à relever consiste donc à qualifier et quantifier le caractère tridimensionnel et instationnaire de l'écoulement dans la machine, par un calcul prenant en compte les effets visqueux dûs aux couches limites, aux sillages et au jeu en tête de la roue mobile.

Un tel calcul, s'il était mené dans l'étage complet, exigerait des ressources informatiques considérables, pour le moment inaccessibles. Actuellement, seul un calcul approximatif dans une fraction réduite d'étage (un canal ou deux de chaque roue) peut être envisagé de façon réaliste, fournissant ainsi des résultats dont le caractère instationnaire est biaisé par les hypothèses utilisées.

Ce papier poursuit donc un triple objectif :

- valider l'approche 3D (fraction d'étage) du point de vue instationnaire grâce à des calculs 2D ou 2.5D pour lesquels le rapport des nombres d'aubes peut être très proche du rapport réel,

- présenter les résultats d'un calcul 3D instationnaire de fluide visqueux en étage,

- montrer comment ces résultats peuvent être une aide à la définition de l'instrumentation de la maquette.

Il constitue la première étape d'une validation future du code de calcul pour la prévision des effets instationnaires visqueux.

ABSTRACT

The equipment of a turbomachinery test rig is at one critical and the same time expensive as soon as that unsteady measurements are placed in rotating parts of the machine.

A predicting numerical simulation can then provide to the research worker useful informations concerning the number of pressure sensors and their locations.

Then, the challenge consists of predicting 3D unsteady aspect of the flow in a turbine, by using a flow computation which take into account viscous effects due to boundary layers, wakes and rotor blade tip clearance.

Such computation in a whole stage would require a great deal of computer memory and time. At the present time, this is not possible and only the computation in a reduced stage (one or two blades of each row) can be considered. This computation induces some approximations in the description of the unsteady flow phenomena.

The objectives of this study are the following :

- the validation of the 3D approach (in a reduced stage) with respect to the unsteady phenomena, by means of 2D calculations for which the calculated blade number ratio is very closed to the actual blade number ratio ;

- setting out the computations results of unsteady 3D viscous flow in a turbine stage ;

- showing how these results can help to the choice of the pressure sensors.

This study is the first step of the code validation in the field of 3D viscous unsteady flows in turbomachinery.

INTRODUCTION

Le développement de programmes de calculs puissants, induit par la mise à disposition d'ordinateurs aux capacités en constante croissance, permet d'envisager la prise en compte des phénomènes instationnaires dans les codes de calculs des écoulements dans les turbomachines. Cette perspective implique la mise en oeuvre de moyens d'essais appropriés, propres à valider les résultats de calculs délivrés par ces programmes. Dans le cadre de la validation du code de calcul Navier-Stokes 3D instationnaire "CANARI" développé depuis 1987 à l'ONERA, une grille annulaire distributrice de turbine (opération VEGA 1) a été insérée dans un circuit en dérivation de la soufflerie transsonique S5 du Centre de Chalais-Meudon. Ces études se sont achevées en 1992 [1]. Dans le prolongement de ces travaux, et dans le cadre de la mise en oeuvre de moyens d'essais de recherche sur les turbines, il a été proposé de concevoir une roue mobile qui, associée à l'aubage fixe existant, pourrait constituer un étage complet adapté à la validation des codes.

Paper presented at the AGARD PEP 85th Symposium on "Loss Mechanisms and Unsteady Flows in Turbomachines", held in Derby, United Kingdom, 8-12 May 1995, and published in CP-571.

Cette opération est appelée "VEGA 2", elle consiste donc à implanter un étage de turbine représentatif d'un étage HP de moteur, en vue d'étudier les phénomènes d'interaction aérodynamique entre distributeur fixe et roue mobile. Ce banc d'essais qui est en cours de réalisation, devrait être opérationnel en 1996, il est le fruit d'une coopération exemplaire entre l'ONERA et trois partenaires industriels (SNECMA, TURBOMECA, EDF). Ce banc d'essais de turbine, dédié à la validation des codes et à une meilleure compréhension des phénomènes complexes d'interaction, apparaît également comme un outil remarquable pour l'adaptation et la maîtrise des techniques de mesures les plus modernes, on pense en particulier à l'étendue des possibilités offertes par les mesures non intrusives.

Cependant, l'instrumentation d'une maquette de turbomachine est à la fois délicate et coûteuse dès lors que des mesures sont envisagées dans les parties tournantes. La simulation numérique des écoulements peut trouver dans ce contexte une application originale : aider l'expérimentateur à optimiser l'instrumentation de la maquette, afin que les mesures les plus significatives puissent être obtenues avec les plus grandes chances de réussite.

Au cours des essais futurs, il est prévu de quantifier l'importance des effets instationnaires dûs à l'interaction entre le distributeur et la roue mobile. Ceci implique de disposer sur les aubages (fixes et mobiles) des capteurs de pression à court temps de réponse. Pour des considérations tant technologiques qu'économiques, leur nombre doit être limité.

L'objectif de cet article est de présenter la méthodologie employée pour évaluer numériquement ces effets instationnaires en vue du but final : fournir à l'expérimentateur des informations lui permettant de choisir au mieux le type de capteurs devant être installés, et d'en optimiser le nombre et la position.

DESCRIPTION DE LA MAQUETTE EXPERIMENTALE

Comme mentionné précédemment, il s'agit d'un étage transsonique représentatif d'un étage HP de moteur. Cependant la géométrie a été conçue avec une veine cylindrique de rayon externe Re = 0,245 mm et de rayon intérieur Ri = 0,190 mm, afin de minimiser les effets tridimensionnels (fig. 1). Il s'agit d'un banc froid, les conditions génératrice étant de Ti_o = 400 K et Pi_o = 0,8 bar. Le distributeur possède 23 aubes. La roue mobile a été définie à partir de deux coupes à 10 % et 90 % de hauteur de veine afin d'éviter le vrillage du profil et faciliter l'instrumentation. A partir de ces deux coupes de définition, l'aube est générée sur la hauteur. Cette aube résulte de plusieurs itérations aéro-mécaniques qui nous ont conduits, pour des raisons de tenue en vibratoire sur l'ensemble du champ, à diminuer la corde en tête et à épaissir le profil en pied par rapport à la version initiale. C'est pour cette raison que l'on observe une forte évolution du pas relatif sur la hauteur (0,6 en pied à 0,9 en tête). La roue mobile possède 37 aubes, elle tourne à 13000 tr/mn et sa puissance est absorbée par un frein hydraulique. Le jeu périphérique en fonctionnement est de 0,7 % de la hauteur de l'aube. La distance axiale entre le distributeur et la roue mobile peut être modifée pour évaluer son influence sur les effets instationnaires. Un collecteur tournant permet la transmission des mesures embarquées.

Les conditions de fonctionnement nominales de la turbine sont les suivantes :

$\Delta H/Ti_o$ = 265 J/kg.K
$\Delta H/2U^2$ = 0,603
$D\sqrt{Ti_o}/2U^2$ = 77,2 kg. $\sqrt{K}$/S.bar
Pi_o/Pi_s = 3,3

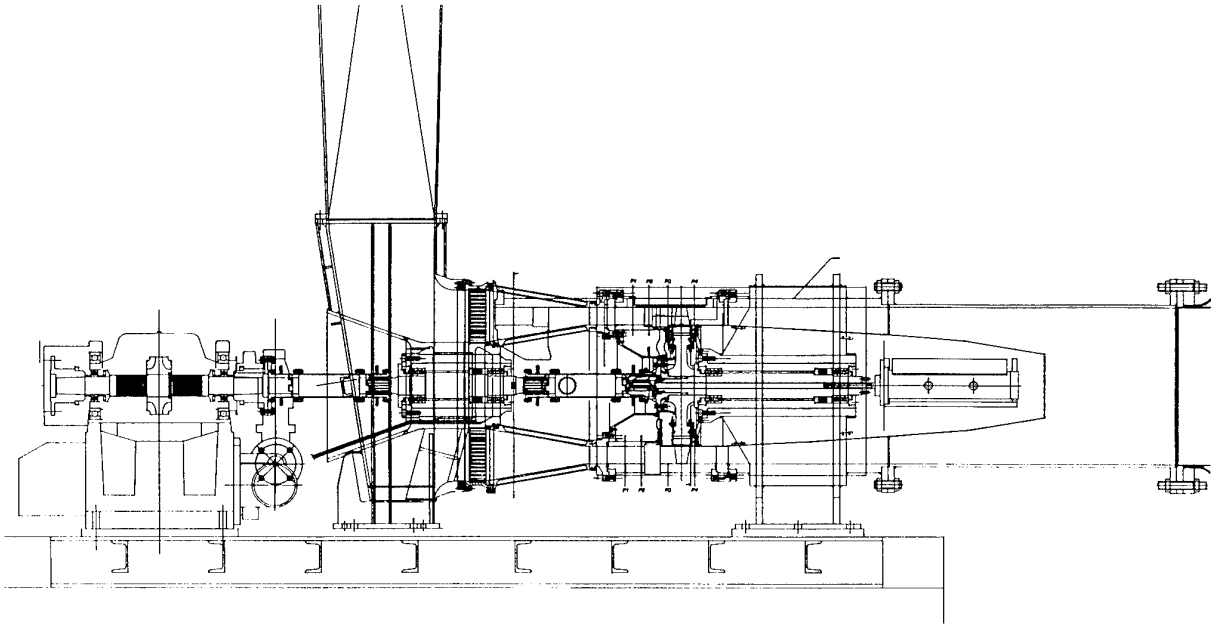

Figure 1 : Schéma du banc VEGA 2

L'étage est alimenté à l'aide d'une culotte (fig. 1) suivie d'un convergent symétrique qui assure un écoulement homogène à l'entrée du distributeur (vérifié par un calcul NS 3D et confirmé par des essais sur maquette). En amont du distributeur, des grillages de différentes perméabilités pourront être insérés pour étudier l'influence du taux de turbulence. A l'aval de l'étage un plénum permet d'homogénéiser et de contrôler les conditions de sortie de l'écoulement. La maquette expérimentale a été conçue pour permettre une investigation très fine de l'écoulement dans tous les plans de l'étage, en particulier les techniques les plus modernes de diagnostics optiques par laser seront utilisées.

Il est envisagé après avoir expérimenté la turbine en conditions nominales, de réaliser les mêmes essais pour différents points du champ, en particulier en faisant varier la vitesse de rotation et la charge de l'étage.

ECOULEMENT DANS LA ZONE D'INTERACTION

Dans l'étage de turbine considéré, un écoulement supersonique est amorcé dans le distributeur, sur la plus grande partie de la hauteur de l'aube. Il se forme donc à partir du bord de fuite et de la partie aval de l'extrados, un système d'ondes de choc et de détente. Ces ondes atteignent le rotor, s'y réfléchissent et reviennent sur le distributeur, où elles sont à nouveau réfléchies. Tout ce réseau traverse de plus les sillages et tourbillons secondaires et forme finalement un écoulement instationnaire complexe.

Dans le distributeur, la partie de l'extrados située entre le col aérodynamique et le bord de fuite doit donc probablement être fortement instrumentée. Par contre, dans la roue mobile, les phénomènes instationnaires sont beaucoup plus délicats à cerner, ce qui justifie une simulation numérique préliminaire aux essais donnant par exemple une analyse harmonique des fluctuations de la pression statique sur les profils.

REDUCTION DU DOMAINE DE CALCUL

Le rapport des nombres d'aubes de chaque roue a évidemment une importance fondamentale dans la description des phénomènes instationnaires. Comme les nombres d'aubes mentionnés ci-dessus sont premiers entre eux, un résultat exact pourrait être obtenu soit par le calcul dans l'étage complet (ce qui exigerait, en 3D, des ressources informatiques considérables), soit par diverses autres techniques (par exemple, utilisation des propriétés de déphasage espace-temps).

On a préféré, dans le cadre de cette étude, employer la technique développée à l'ONERA dans les années 80, pour des calculs "Euler" [2,3]. Elle est basée sur la prise en compte d'un groupe plus ou moins restreint de canaux de chaque roue. Elle présente l'avantage de respecter la géométrie des canaux interaubes, mais induit en contrepartie un certain degré d'approximation sur l'aspect instationnaire des résultats. Cette technique a également été utilisée pour des calculs "Navier-Stokes" [4]. Par ailleurs, il a été montré [3,4] que cette approximation, qui dépend notamment des nombres de canaux dans lesquels l'écoulement est effectivement calculé, peut être ramenée à un niveau raisonnable. Les lignes suivantes rappellent brièvement la façon de procéder.

Soit un étage comportant N1 aubes dans la première roue et N2 dans la seconde. On souhaite calculer l'écoulement dans une fraction de cet étage, fraction ne comprenant que K1 et K2 canaux.

On choisit donc K1 et K2 aussi petits que possible, mais tels que K1/K2 soit proche du rapport réel N1/N2. Dans chaque groupe de canaux, l'écoulement sur les frontières azimutales extrêmes n'est en général pas périodique. Il existe un déphasage d'autant plus petit que K1/K2 et N1/N2 sont proches l'un de l'autre. Ici, on annule simplement ce déphasage, et on applique sur ces frontières la condition de périodicité, très simple à mettre en oeuvre.

Par ailleurs, le lien entre les deux groupes de canaux s'effectue grâce à de légères contractions ou dilatations des gradients azimutaux, caractérisées par les paramètres suivants :

$\lambda_1 = e_c/e_1 \qquad \lambda_2 = e_c/e_2$

avec

$e_1 = 2\pi\, K1/N1 \quad e_2 = \pi\, K2/N2 \quad e_c = (e_1+e_2)/2$

Les références 3 et 4 présentent cette technique en détail, ainsi que ses effets prévisibles sur les résultats numériques.

APPROCHES NUMERIQUES PROPOSEES

Compte tenu de l'objectif visé (où les aspects qualitatifs et quantitatifs ont chacun leur importance), le problème a été considéré de plusieurs points de vue (fig. 2) :

Approche instationnaire NS 2D

Celle-ci consiste à analyser l'écoulement sur une coupe de l'étage tridimensionnel. Les ressources informatiques nécessaires pour cette approche sont assez faibles pour pouvoir choisir un rapport des nombres des canaux calculés très proche du rapport des nombres d'aubes réel. Les effets 3D y sont évidemment ignorés.

Approche instationnaire NS 3D

C'est a priori la plus satisfaisante, car elle tient compte de la complexité de la réalité physique : jeu en tête de la roue mobile, moyeu à parties fixe et mobile, etc... Elle seule permet de restituer totalement l'aspect tridimensionnel visqueux (écoulements secondaires). Cependant, pour des raisons pratiques (taille-mémoire et temps de calcul), elle est actuellement limitée à des configurations très réduites (1 canal du stator contre 2 canaux du rotor, ou 2 contre 3, selon le raffinement des maillages).

Approche mixte instationnaire Euler 3D

Cette approche découple les deux roues. Un premier calcul NS 3D stationnaire sur le distributeur isolé fournit le champ sur un secteur équivalant à un pas, juste à l'aval du bord de fuite. Ce champ est ensuite dupliqué dans la direction azimutale, afin de remplir un secteur correspondant à plusieurs canaux. La technique décrite précédemment pour le calcul en étage est à nouveau utilisée pour mener maintenant un calcul Euler dans la roue mobile, les conditions-limites amont, stationnaires dans l'espace absolu, devenant instationnaires dans l'espace tournant. Il s'agit donc en quelque sorte de la prise en compte d'une distorsion d'entrée.

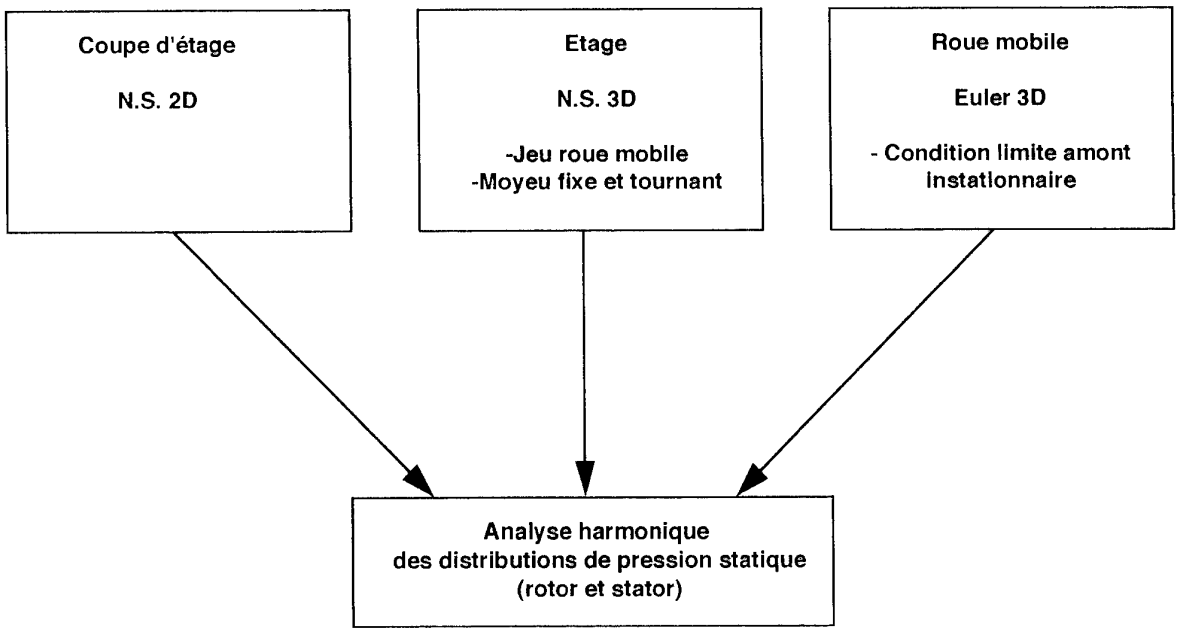

Figure 2 : Schéma de la méthodologie

Compte tenu de leurs hypothèses propres, et des conditions variées de leur application (maillages...), ces différentes approches ne donneront pas les mêmes informations. Néanmoins, il est permis d'espérer que la confrontation des résultats qu'elles fourniront permettra de mieux cerner le problème, et d'apporter à l'expérimentateur des éléments fiables en réponse aux questions posées.

OUTILS NUMERIQUES

Les deux codes (2D et 3D) sont très proches l'un de l'autre. Ils résolvent les équations de Navier-Stokes moyennées en temps à l'aide d'un schéma de Runge Kutta à quatre pas de type volumes finis, sur des maillages structurés multi-domaines. Le modèle de turbulence est algébrique (de type "longueur de mélange"). Une phase implicite de lissage des résidus permet l'établissement rapide de la solution périodique, grâce à des valeurs élevées du nombre de CFL. Les codes de base, à l'origine prévus pour le calcul d'écoulements stationnaires [5], ont été considérablement remaniés pour intégrer les aspects "instationnaires" des calculs en étage de turbomachine.

RESULTATS NUMERIQUES ET COMPARAISONS

Calculs NS 2D

Ils ont été effectués sur la coupe située au rayon moyen (217.5 mm). Les nombres d'aubes réels étant 23 et 27, les quatre configurations suivantes ont été calculées :

K1 = 1	K2 = 2	$\lambda 1 = 1.1216$	$\lambda 2 = 0.9022$
K1 = 3	K2 = 5	$\lambda 1 = 1.0180$	$\lambda 2 = 0.9826$
K1 = 5	K2 = 8	$\lambda 1 = 0.9973$	$\lambda 2 = 1.0027$
K1 = 2	K2 = 3	$\lambda 1 = 0.9662$	$\lambda 2 = 1.0362$

Chaque canal interaube comprend deux domaines de calcul (fig. 3). Un maillage en "O" entoure le profil et permet une très bonne définition de la géométrie dans les régions de bords d'attaque et de fuite. Le reste du canal est rempli par un maillage en "H" de l'amont à l'aval. Une optimisation "multi-blocs" régularise la forme et la taille des mailles. Ces maillages se raccordent sur des frontières où les points coïncident.

Les dimensions des maillages sont :

- distributeur	maillage "O" :	161x21,
	maillage "H" :	109x25
- maillage	maillage "O" :	121x21,
	maillage "H" :	89x21

Ces dimensions de maillage sont, pour une coupe, les mêmes que celles retenues pour le maillage 3D.

Les résultats comparés des quatre calculs 2D (fig. 4) permettent de juger de la validité de la technique de réduction du domaine de calcul. On y présente la distribution de pression statique sur une aube du rotor (valeur moyenne en temps), qui est pratiquement indépendante du choix de K1 et K2, ainsi que les distributions extrados et intrados du premier et du second harmonique des fluctuations instationnaires de la pression. Les trois meilleures approximations (3:5, 5:8 et 2:3) sont très proches les unes des autres. Ceci permet d'affirmer qu'un calcul exact aurait fourni le même résultat. La configuration 1:2 apparaît globalement moins bonne, particulièrement sur l'intrados et pour le premier harmonique. Par conséquent, il conviendra d'être prudent pour analyser les résultats de calcul NS 3D sur cette configuration.

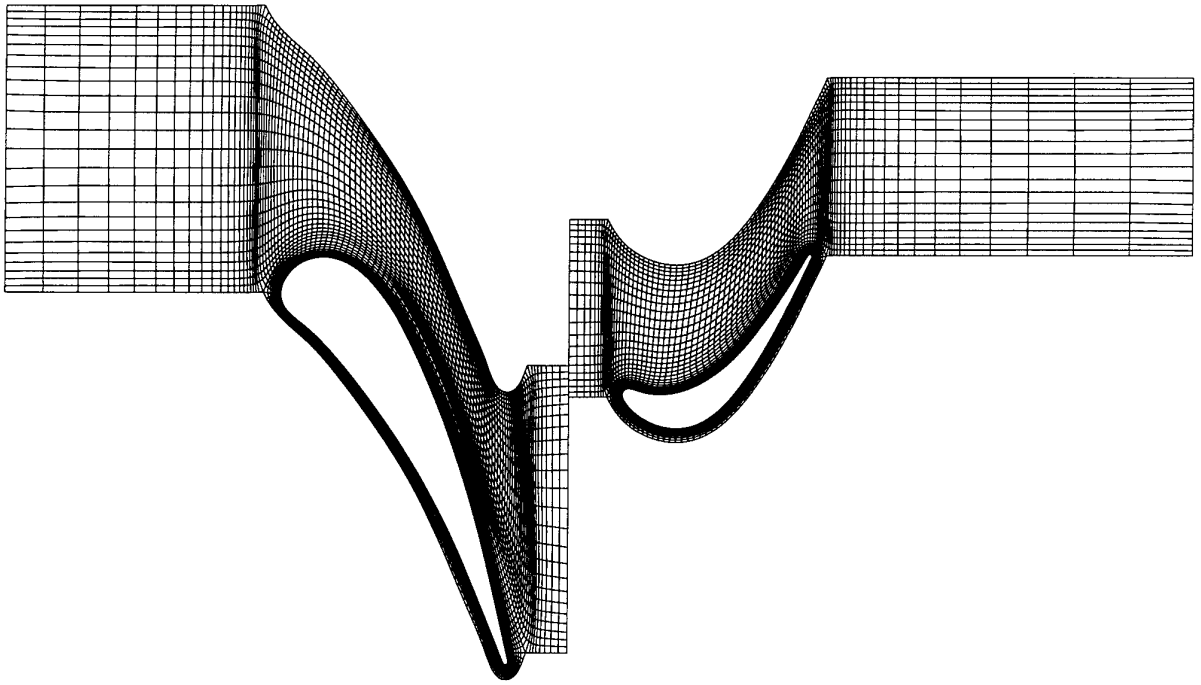

Figure 3 : Maillage de la coupe moyenne

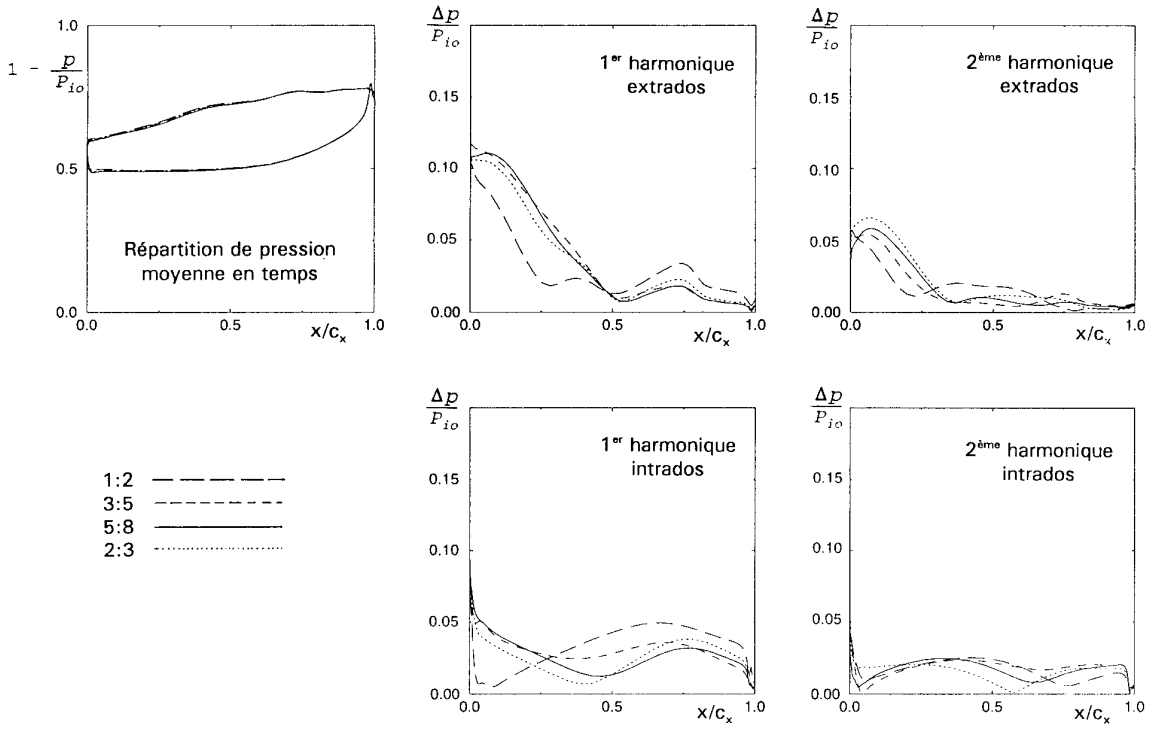

Figure 4 : Analyse harmonique sur la roue mobile (calculs NS 2D)

Calculs NS 3D

Comme on l'a mentionné ci-dessus, les différentes coupes du maillage 3D ont les mêmes caractéristiques que le maillage 2D. Suivant la direction radiale, 46 mailles ont été disposées sur l'envergure de la roue mobile, et 10 dans le jeu (0.385 mm), ce qui donne 57 coupes et un nombre de points proche de 900 000 en configuration 1:2.

Une attention particulière a été portée au maillage de la zone de jeu (fig. 5), décomposée en deux domaines : un maillage "O" épousant le contour interne de l 'aube, et un maillage "H" à l'intérieur du maillage "O". Comme pour le maillage du canal, les raccords sont à points coïncidents.

Sur CRAY YMP 128, la mémoire requise pour un calcul sur ce maillage est de l'ordre de 80 Mw. Quant au temps, de calcul nécessaire à l'établissement de la solution périodique établie, il a été évalué à partir des performances en 2D, estimé à environ 150 heures à partir d'un champ initial algébrique.

A la fois pour réduire le coût et le délai de restitution, il a été décidé de mener un calcul sur un maillage très lâche, incluant un point sur deux (dans chaque direction) du maillage décrit précédemment, afin de disposer d'un champ initial permettant d'atteindre plus rapidement la solution établie.

Par ailleurs, à la vue des résultats obtenus en 2D, où la configuration 1:2 semble insuffisante pour la prévision correcte des effets instationnaires, deux calculs ont été accomplis sur le maillage 3D lâche (configurations 1:2 et 2:3). Seule l'exploitation de la configuration 2:3 sera présentée ici, conformément aux observations formulées précédemment à propos des calculs 2D.

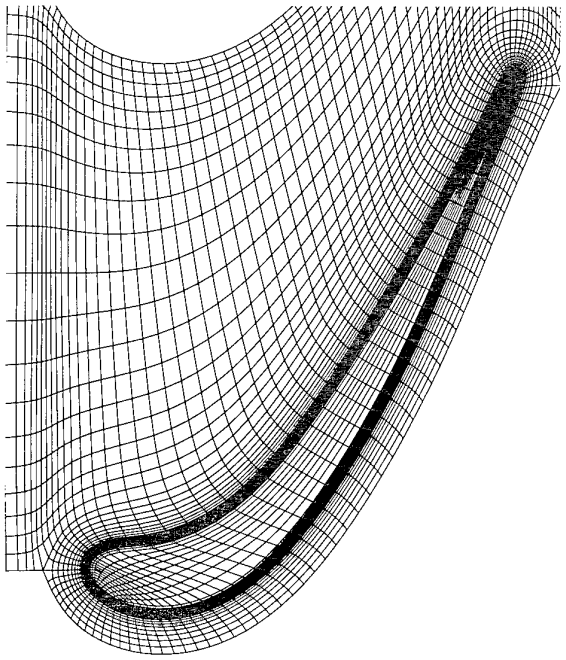

Figure 5 : Maillage de la zone de jeu

Les résultats, toujours en termes d'analyse harmonique de la pression instationnaire sur une aube de rotor, sont présentés sur la figure 6, sur laquelle on compare les amplitudes des deux premiers harmoniques sur la coupe moyenne entre le calcul 2D et le calcul 3D. A première vue, l'atténuation marquée des effets instationnaires pourrait être attribuée à la différence de densité des maillages. On verra cependant par la suite que cette analyse est insuffisante.

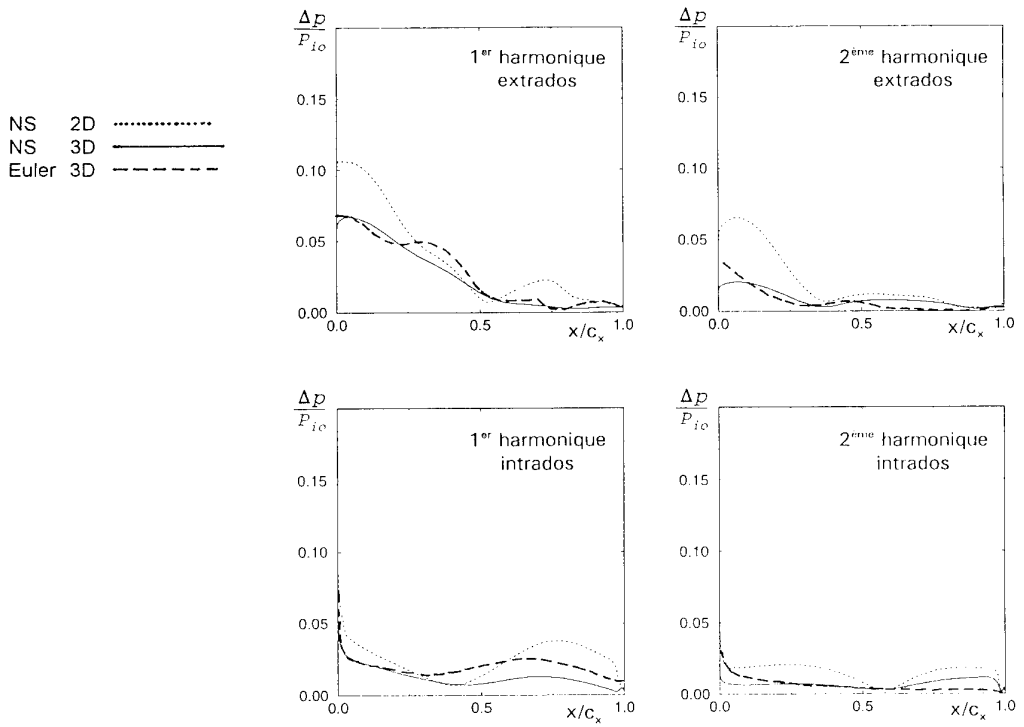

Figure 6 : Analyse harmonique sur la coupe moyenne de la roue mobile (calculs NS 2D, 3D et Euler 3D)

Calcul Euler 3D instationnaire

Le calcul NS 3D stationnaire sur le distributeur isolé fournit un champ, que l'on peut traduire en pression et température d'arrêt, deux directions de vitesse et nombre de Mach. Seules les quatre premières grandeurs sont imposées sur la frontière amont de la roue mobile, conformément à la théorie des caractéristiques sur laquelle est basé le traitement des conditions aux limites. Comme c'est un calcul "Euler" qui est mené dans la roue mobile, une légère modification de ce champ est faite dans les régions proches du moyeu et de carter (où le calcul NS donne des vitesses nulles aux parois). Cette modification ne concerne qu'une partie de la couche limite et n'est destinée qu'à éviter les ennuis numériques près des parois de la veine traitées avec une condition de glissement dans la roue mobile.

Ce calcul a été effectué dans les configurations 1:2 et 5:8 sur un maillage de topologie dite "H-C" (fig. 7). Seuls les résultats de cette seconde configuration sont présentés ici. Pour la coupe moyenne (fig. 6), on a déjà établi une comparaison entre les calculs NS 3D et 2D (configuration 2:3) ; celle-ci est complétée par le calcul Euler 3D et montre le bien-fondé de cette approche mixte. Les calculs 3D donnent des distributions des deux harmoniques très proches l'une de l'autre et relativement éloignées de celles fournies par le calcul 2D. Comme on l'a mentionné ci-dessus, les différences entre les maillages ne peuvent expliquer ces écarts, ceux-ci proviennent sans doute du caractère tridimensionnel de l'écoulement dans la zone d'interaction.

Pour deux autres coupes, l'une en pied, l'autre en tête, on peut confronter les deux calculs 3D (fig. 8 et 9). On note encore que les tendances sont les mêmes, bien que les niveaux soient assez peu comparables. Ici, on peut sans doute attribuer en partie ces écarts aux différences entre les maillages.

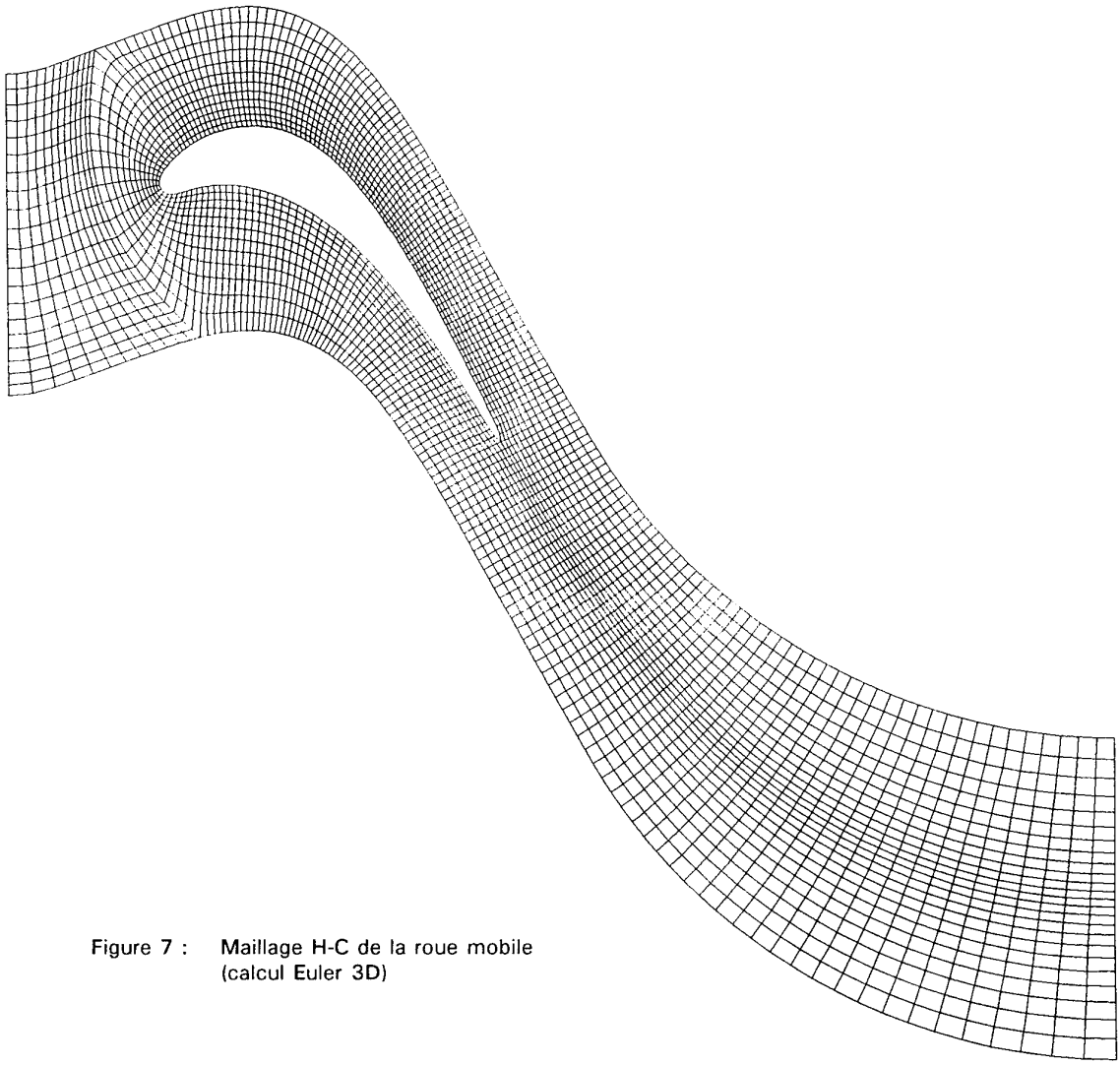

Figure 7 : Maillage H-C de la roue mobile (calcul Euler 3D)

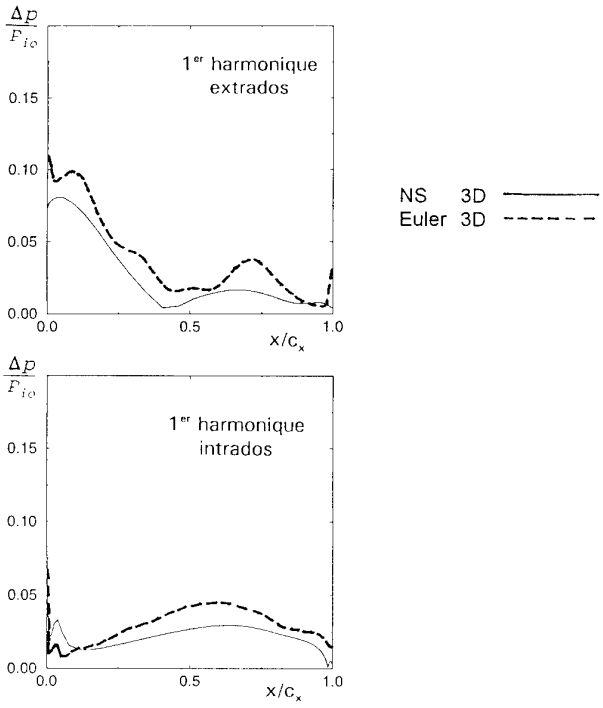

Figure 8 : Analyse harmonique sur la coupe de pied

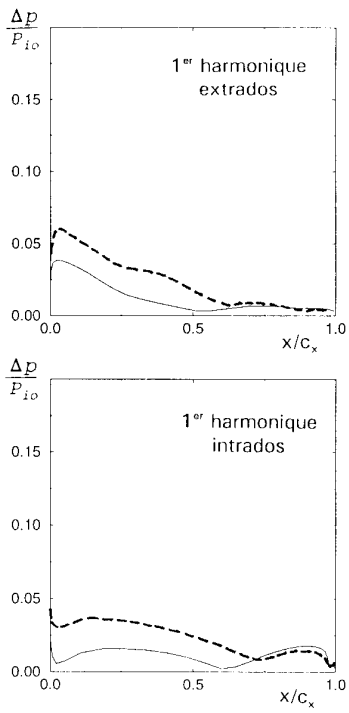

Figure 9 : Analyse harmonique sur la coupe de tête

SYNTHESE DES RESULTATS

L'aspect global de l'importance des effets instationnaires et leur localisation sur la surface d'une aube mobile est obtenue par une visualisation de l'amplitude du premier harmonique. On présente (fig. 10 et 11) ces visualisations pour les cas NS et Euler. On peut constater que les maxima sont obtenus sur la partie inférieure de l'extrados de l'aubage. Ceci est sans doute lié au fait que c'est dans cette région que l'écoulement de sortie du distributeur est supersonique. Ces cartes permettent d'affiner le choix de la répartition surfacique des capteurs instationnaires.

Jusqu'à présent, l'accent a été mis sur l'acquisition de renseignements concernant la roue mobile. Une analyse de même type, quoique moins approfondie a été faite sur une aube du stator. Pour cette roue, on ne présente que la visualisation extrados de l'amplitude du premier harmonique (fig. 12), pour le cas NS (configuration 2:3). Comme pour l'aube mobile, cette carte se révèle être une aide intéressante pour la localisation des capteurs.

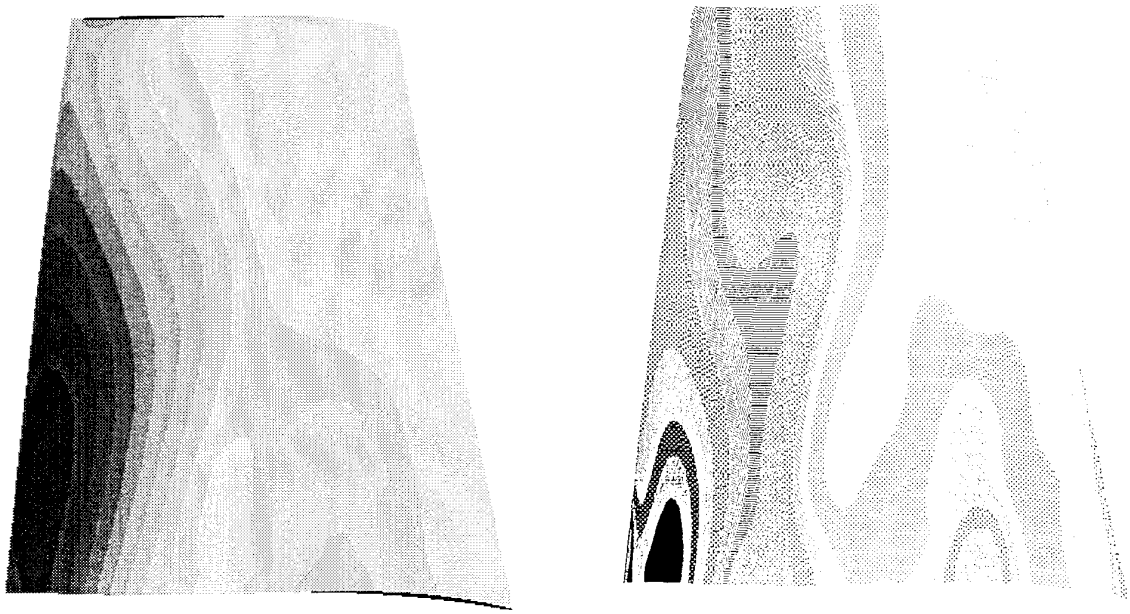

Figure 10 : Amplitude du 1er harmonique sur l'extrados de la roue mobile (calculs NS 3D et Euler 3D)

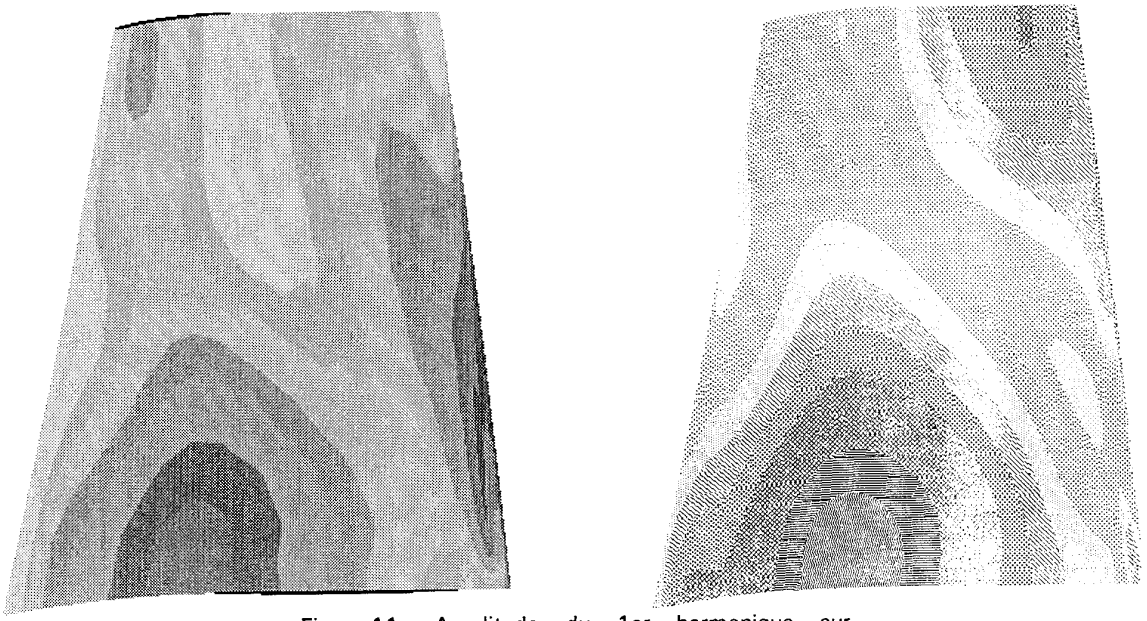

Figure 11 : Amplitude du 1er harmonique sur l'intrados de la roue mobile (calculs NS 3D et Euler 3D)

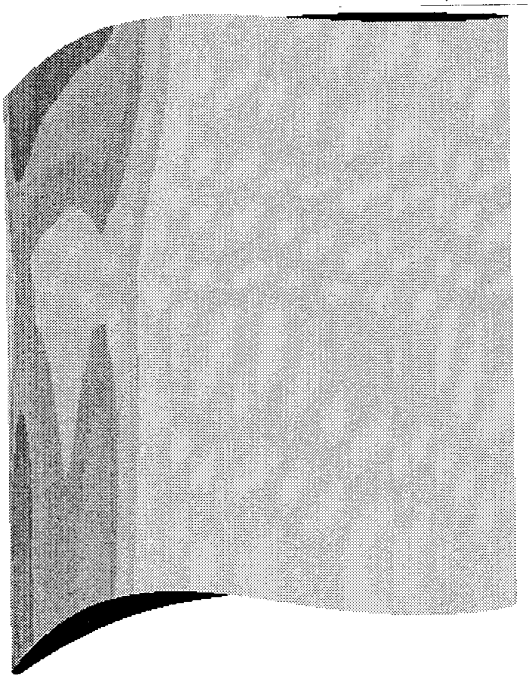

Figure 12 : Amplitude du 1er harmonique sur l'extrados du distributeur (calcul NS 3D)

CONCLUSIONS ET PERSPECTIVES

Le problème concret de la préparation de l'instrumentation d'un banc d'essai a pu trouver des éléments de réponse grâce à une série de simulations numériques.

Différentes approches ont été utilisées. Chacune d'entre elles possède sa marge d'incertitude, due aux hypothèses de base et aux conditions d'application. La comparaison des divers résultats révèle les limites de ces approches et permet de déceler les points à améliorer dans le futur, du strict point de vue numérique.

En particulier, il semble que la prise en compte d'au moins deux canaux dans le distributeur et de trois dans la roue mobile soit nécessaire pour une évaluation correcte des effets instationnaires. Ceci implique de revoir la densité du maillage pour l'approche NS 3D, afin de trouver le meilleur compromis entre la précision des résultats et les capacités informatiques actuellement disponibles.

Par ailleurs, sur ce cas précis d'étage isolé, l'approche chorochronique (utilisation des propriétés de déphasage espace-temps) offre l'avantage de supprimer l'approximation sur le rapport des nombres d'aubes. Elle pourraît être employée pour valider le bien-fondé de la technique de réduction du domaine de calcul, qui reste une voie simple pour la prise en compte de plusieurs étages.

Par rapport à l'objectif initial, le travail accompli est très riche d'enseignements : l'ordre de grandeur des amplitudes des fluctuations de la pression statique confirme les informations déjà recueillies sur des cas expérimentaux similaires. D'autre part, avant l'obtention des résultats présentés dans cet article, le choix de la position des capteurs ne pouvait s'appuyer sur aucune base sûre. On dispose maintenant de données concrètes.

Finalement, on est en droit d'espérer que cette étude préliminaire contribuera à obtenir des données expérimentales de qualité optimale et que la confrontation future "calcul-expérience" n'en sera que plus fructueuse pour la validation des codes de simulation numérique présents et à venir.

REFERENCES

Compte-rendu de Conférence

[1] ESCANDE B., CAMBIER L., "Validation du code CANARI par le calcul de l'écoulement tridimensionnel turbulent dans un distributeur de turbine", 77th PEP AGARD "CFD Techniques for Propulsion Applications", San Antonio (USA), 27-31 mai 1991.

Compte-rendu de Conférence

[2] VEUILLOT J.P., MEAUZE G., "A 3D Euler method for internal transonic flows computation with a multi-domain approach", AGARD Lecture Series n° 140, "3D computation techniques applied to internal flows in propulsion systems"

Compte-rendu de Conférence

[3] FOURMAUX A., BILLONNET G., LE MEUR A., LESAIN A., "Simulation numérique des écoulements tridimensionnels et instationnaires dans les turbomachines", 74-A PEP/AGARD "Phénomènes d'aérodynamique instationnaire dans les turbomachines", Luxembourg, 4-6 septembre 1989

Compte-rendu de Conférence

[4] FOURMAUX A., "Assessment of a low storage technique for multi-stage turbomachinery Navier-Stokes computations", 1994 ASME Winter Annual Meeting, Chicago, IL (USA), November 6-11, 1994

Compte-rendu de Conférence

[5] HEIDER R., DUBOUE J.M., PETOT B., BILLONNET G., COUAILLIER V., LIAMIS N., "Three-dimensional analysis of turbine rotor flow including tip clearance", Presented at the International Gas Turbine and Aeroengine Congress and Exposition, Cincinnati, OH (USA), May 24-27, 1993

On the Computation of Unsteady Turbomachinery Flows Part 2 — Rotor/Stator Interaction using Euler Equations

G.A. Gerolymos, D. Vinteler, R. Haugeard, G. Tsanga, I. Vallet
LEMFI, URA CNRS 1504, Bldg. 511, Université Pierre & Marie Curie, 91405 Orsay, Paris, France

Abstract

The purpose of this paper is to present a methodology for the prediction of unsteady flow resulting from rotor/stator interaction in multistage axial compressors. The methodology consists of a time-averaged multistage flow computation, which is used to initialize unsteady flow computations, dealing with a single stage and using chorochronic periodicity. Currently, time-marching Euler solvers are used for the time-averaged multistage computation, and for rotor/stator interaction computations, which can be coupled to an assumed-modes mechanical model. The development of a 3-D time-linearized Euler solver is also described. Typical results are presented and the methodology is validated through comparison with available data, both theoretical (analytical) and experimental. The updating of the methodology to Navier-Stokes solvers is discussed in detail, and some preliminary results are presented. The urgent need for reliable and detailed unsteady aeromechanical experimental data is stressed as a major pacing-item in methodology development.

1 Introduction

Understanding and predicting unsteady flow is a major pacing-item in modern turbomachinery development [2][9] [38][44][52][53]. Although the analysis of unsteady multistage flow is the ultimate objective, several phenomena can be understood by examining the simplified case of an isolated stage (rotor/stator or counter-rotating propellers). In this case the flow is characterized by a chorochronic periodicity, probably first introduced in the work of Kemp & Sears [36][37]. Erdos & Alzner & McNally [10] were the first to implement this method in a modern computational code (Euler solver for the blade-to-blade surface Euler equations in a compressor-stage). Lewis & Delaney & Hall [41] developed a similar method and applied it to a turbine-stage. Giles [30] developed a similar method, based on the inclined-plane implementation of chorochronic periodicity. Koya & Kotake [39][40] developed a 3-D Euler code for computing rotor/stator interaction using chorochronic periodicity.

In this work the concept of chorochronic periodicity is analyzed in detail, resulting in a clear relationship between chorochronic harmonics in the rotor and the stator frames-of-reference. This analysis allows for the simple and computationally efficient implementation of chorochronic periodicity in a 3-D Euler code. It is also the basis for the development of a time-linearized method, with harmonics matching at the rotor/stator interface. The method is validated using a number of simple well-documented distorsion/blade-row interaction cases. The extension of the method to multistage turbomachinery and to viscous flow solvers is discussed in detail.

2 Chorochronic Periodicity

2.1 Blade-Row Interaction

Consider 2 blade-rows (1) and (2), with rotation velocities Ω_1 and Ω_2, respectively, positive in the positive θ-direction of an (x, R, θ) frame-of-reference, x being the engine-axis (Fig. 1). Provided that $\Omega_1 - \Omega_2 \neq 0$ the flow in each frame is periodic with frequency the blade-passing-frequency of the adjoining row, and each blade has a phase-shift with respect to its neighbour that is uniquely determined by the number of blades of the rows and the direction of relative rotation (Gerolymos & Chapin [13])

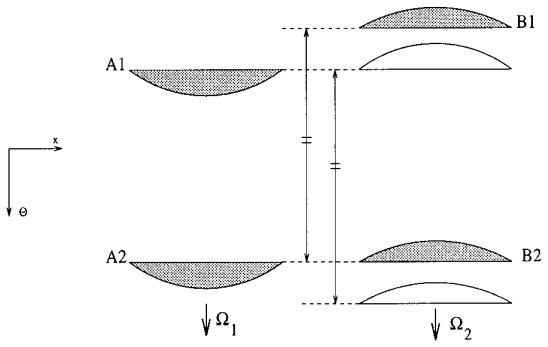

Figure 1: Schematic representation of rotor/stator interaction

$$f_1 = N_2 \frac{|\Omega_1 - \Omega_2|}{2\pi} \quad ; \quad \Delta\phi_1 = -2\pi \mathrm{sign}(\Omega_1 - \Omega_2) \frac{N_1 - N_2}{N_1} \tag{1}$$

$$f_2 = N_1 \frac{|\Omega_1 - \Omega_2|}{2\pi} \quad ; \quad \Delta\phi_2 = -2\pi \mathrm{sign}(\Omega_1 - \Omega_2) \frac{N_1 - N_2}{N_2} \tag{2}$$

where N_1 and N_2 are the numbers of blades (Fig. 2).

This periodicity suggests the possibility of computing the unsteady flow due to the interaction by modelling 1 interblade-channel per blade-row, applying the chorochronic periodicity conditions at the permeable

Paper presented at the AGARD PEP 85th Symposium on "Loss Mechanisms and Unsteady Flows in Turbomachines", held in Derby, United Kingdom, 8-12 May 1995, and published in CP-571.

pitchwise boundary, in a manner analogous to flutter computation procedures [11][14][15]. The new problem is the exchange of information between the 2 blade-rows at the interface of the computational domain.

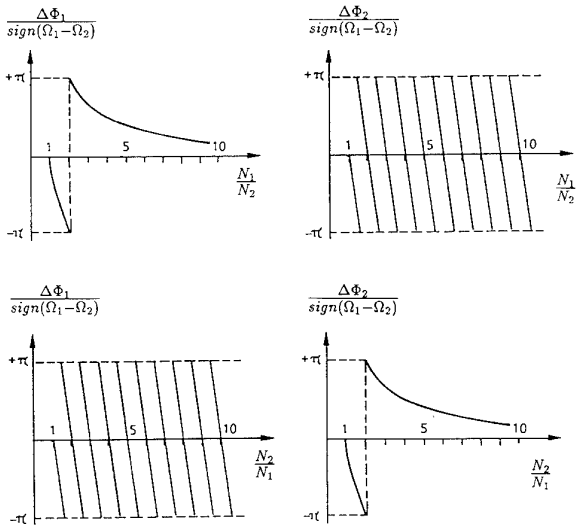

Figure 2: Interblade-phase-angle in rotor/stator interaction (a) $N_1 \geq N_2$ (b) $N_1 \leq N_2$

2.2 Chorochronic Harmonics

Previous work on the subject used a signal-storage-and-reconstruction technique to exchange information at the interface between the 2 blade-rows. This technique is rather cumbersome and was not used in this work. Instead the flow quantities are expressed using a 2-D-Fourier-series method (in time and azimuth). Let $F_1(x, R, \theta_1, t) \in \mathbb{R}$ be a flow quantity in the frame of blade-row (1). If x, R are such that the point considered lie outside the meridional projection of the blades, the flow periodicity is such that F_1 is a doubly periodic function, of period f_1^{-1} in t and 2π in θ_1. The angles θ_1 and θ_2 are the angles in the frames relative to each blade-row (Fig. 1)

$$\theta = \theta_1 + \Omega_1 t = \theta_2 + \Omega_2 t \quad \forall t \tag{3}$$

As a consequence F_1 can be expanded in appropriate double-Fourier-series

$$F_1 = \sum_{n=-\infty}^{+\infty} \sum_{m=-\infty}^{+\infty} \left\{ {}^{nm}\hat{F}_1 e^{i(2\pi n f_1 t + m\theta_1)} \right\} \tag{4}$$

where ${}^{nm}\hat{F}_1 \in \mathbb{C}$ are the chorochronic harmonics. Most of these harmonics are 0, because of the chorochronic periodicity. Indeed the phase-shift between adjacent blades requires that

$$F_1(x, R, \theta_1, t) = F_1(x, R, \theta_1 + \frac{2\pi}{N_1}, t - \frac{\Delta\phi_1}{2\pi f_1}) \quad \forall \theta, t \tag{5}$$

Replacing F_1 in Eq. (5) by its Fourier-series (Eq. 4) and introducing the value of $\Delta\phi_1$ (Eq. 1) yields

$$\sum_{n=-\infty}^{+\infty} \sum_{m=-\infty}^{+\infty} \left\{ {}^{nm}\hat{F}_1 e^{i[2\pi n f_1 (t - \frac{\Delta\phi_1}{2\pi f_1}) + m(\theta_1 + \frac{2\pi}{N_1})]} \right\} =$$

$$\sum_{n=-\infty}^{+\infty} \sum_{m=-\infty}^{+\infty} \left\{ {}^{nm}\hat{F}_1 e^{i(2\pi n f_1 t + m\theta_1)} \right\} \quad \forall \theta, t \Longrightarrow$$

$$\sum_{n=-\infty}^{+\infty} \sum_{m=-\infty}^{+\infty} \left\{ {}^{nm}\hat{F}_1 e^{i(2\pi n f_1 t + m\theta_1)} [e^{i(n\Delta\phi_1 - m\frac{2\pi}{N_1})} - 1] \right\}$$

$$= 0 \quad \forall \theta, t \Longrightarrow$$

$${}^{nm}\hat{F}_1 = 0 \quad \forall n, m : -n\Delta\phi_1 + m\frac{2\pi}{N_1} \neq 2\ell\pi \quad \ell \in \mathbb{Z} \tag{6}$$

Taking into account this relation (Eq. 6), and replacing $\Delta\phi_1$ from Eq. (1), F_1 can be expanded, ignoring harmonics that are identically equal to 0, as

$$F_1 = \sum_{n=-\infty}^{+\infty} \sum_{\ell=-\infty}^{+\infty} \left\{ {}^{nm_{1_{n\ell}}}\hat{F}_1 e^{i(2\pi n f_1 t + m_{1_{n\ell}}\theta_1)} \right\};$$

$$m_{1_{n\ell}} = \ell N_1 - n(N_1 - N_2)\text{sign}(\Omega_1 - \Omega_2) \quad \ell \in \mathbb{Z} \tag{7}$$

with an analogous relation for quantities in the frame relative to blade-row 2

$$F_2 = \sum_{n=-\infty}^{+\infty} \sum_{\ell=-\infty}^{+\infty} \left\{ {}^{nm_{2_{n\ell}}}\hat{F}_2 e^{i(2\pi n f_2 t + m_{2_{n\ell}}\theta_2)} \right\};$$

$$m_{2_{n\ell}} = \ell N_2 - n(N_1 - N_2)\text{sign}(\Omega_1 - \Omega_2) \quad \ell \in \mathbb{Z} \tag{8}$$

Using only the relevant chorchronic harmonics is necessary for computational efficiency of the method.

2.3 Interface Matching

At the computational interface between the 2 blade-rows, both expressions (Eqs. 7, 8) hold on either side. Denoting the characteristic variables, in the absolute frame, by

$$\underline{X} = [\rho, V_x, V_R, V_\theta, p]^T \in \mathbb{R}^5 \tag{9}$$

where ρ is the density, $\vec{V}$ the absolute flow velocity, and p the static pressure, the continuity at the interface $\mathfrak{S}_{int}$ requires

$$\underline{X}_1(x, R, \theta, t) = \underline{X}_2(x, R, \theta, t) \quad \forall \theta, t \quad \forall x, R \in \mathfrak{S}_{int} \tag{10}$$

where the subscripts $(1, 2)$ denote quantities computed on each side of the interface. This equality can be expressed using the corresponding Fourier series

$$\underline{X}_1 = \sum_{n=-\infty}^{+\infty} \sum_{\ell=-\infty}^{+\infty} \left\{ {}^{nm_{1_{n\ell}}}\underline{\hat{X}}_1 e^{i(2\pi n f_1 t + m_{1_{n\ell}}\theta_1)} \right\} =$$

$$= \underline{X}_2 = \sum_{n=-\infty}^{+\infty} \sum_{\ell=-\infty}^{+\infty} \left\{ {}^{nm_{2_{n\ell}}}\underline{\hat{X}}_2 e^{i(2\pi n f_2 t + m_{2_{n\ell}}\theta_2)} \right\}$$

$$\forall \theta, t \quad \forall x, R \in \mathfrak{S}_{int} \tag{11}$$

where ${}^{nm}\underline{\hat{X}}_1 \in \mathbb{C}^5$ and ${}^{nm}\underline{\hat{X}}_2 \in \mathbb{C}^5$ are the chorochronic harmonics on each side. Using Eq. (3) to replace θ_1 and

θ_2, and the relations for $m_{n\ell}$ (Eqs. 7, 8) yields after some algebra the interface-matching conditions

$$ {}^{n_1 m_{1_{n_1\ell}}}\underline{\hat{X}}_1 = {}^{n_2 m_{2_{n_2\ell}}}\underline{\hat{X}}_2 $$

$$ \forall m_{1_{n_1\ell}} = m_{2_{n_2\ell}} \Longleftrightarrow n_1 - n_2 = \ell \text{sign}(\Omega_1 - \Omega_2) \quad \ell \in \mathbb{Z} \quad (12) $$

In particular these relations include the fundamental matching conditions

$$
\begin{aligned}
{}^{0,0}\underline{\hat{X}}_1 &= {}^{0,0}\underline{\hat{X}}_2 \quad (13)\\
{}^{0,\pm N_1}\underline{\hat{X}}_1 &= {}^{\mp\text{sign}(\Omega_1-\Omega_2),\pm N_1}\underline{\hat{X}}_2\\
{}^{\pm\text{sign}(\Omega_1-\Omega_2),\pm N_2}\underline{\hat{X}}_1 &= {}^{0,\pm N_2}\underline{\hat{X}}_2\\
{}^{\pm 1,\mp(N_1-N2)\text{sign}(\Omega_1-\Omega_2)}\underline{\hat{X}}_1 &= {}^{\pm 1,\mp(N_1-N_2)\text{sign}(\Omega_1-\Omega_2)}\underline{\hat{X}}_2\\
{}^{\pm 1,\pm(N_1+N_2)\text{sign}(\Omega_1-\Omega_2)}\underline{\hat{X}}_1 &= {}^{\mp 1,\pm(N_1+N_2)\text{sign}(\Omega_1-\Omega_2)}\underline{\hat{X}}_2
\end{aligned}
$$

3 Rotor/Stator Interaction

3.1 Numerics

The flow is computed in 1 interblade-channel for each blade-row (Fig. 3). Each of the 2 domains is discretized on a classical H-grid. The flow is modelled using the 3-D Euler equations, written in a reference frame relative to each blade-row, using a perfect-gas thermodynamic approximation

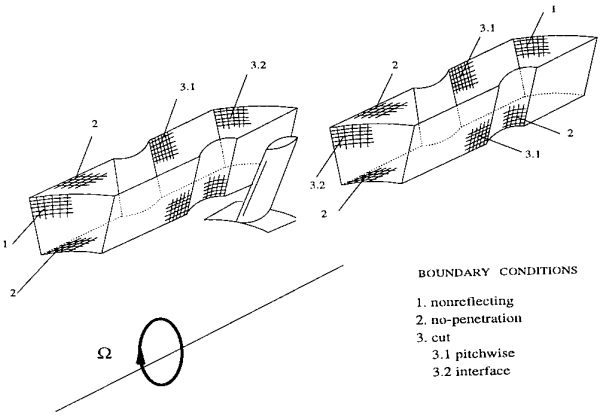

Figure 3: Computational domain and boundary-conditions

$$ p = \rho R_g T = \rho \frac{\gamma - 1}{\gamma} h = \rho(\gamma - 1)e \quad (14) $$

$$ \frac{\partial \rho}{\partial t} + \text{div}(\rho \vec{W}) = 0 \quad (15) $$

$$ \frac{\partial \rho \vec{W}}{\partial t} + \text{div}(\rho \vec{W} \otimes \vec{W} + p\boldsymbol{I}) + $$
$$ + 2\rho\vec{\Omega} \times \vec{W} + \rho \text{grad}(-\frac{\Omega^2 R^2}{2}) = 0 \quad (16) $$

$$ \frac{\partial \rho H_R - p}{\partial t} + \text{div}(\rho \vec{W} H_R) = 0 \quad (17) $$

where t is the time, ρ the density, p the static pressure, T the static temperature, $R_g = 287.04$ m^2 s^{-2} K^{-1} the gas-constant, $\gamma = 1.4$ the isentropic exponent, h the static enthalpy, e the internal energy, $\vec{W}$ the relative flow velocity, $\vec{\Omega} = \Omega \vec{e}_x$ the rotation velocity of the blade-row, $R = \sqrt{y^2 + z^2}$ the radius from the engine-axis x, and $H_R \doteq h + \frac{1}{2}W^2 - \frac{1}{2}\Omega^2 R^2$ the rothalpy. The equations are integrated in time using a standard centered 5-stage Runge-Kutta scheme, which is described in detail in Gerolymos [15]. The following boundary-conditions are applied at each iteration:

- no-penetration on the solid boundaries
- nonreflecting inflow and outflow conditions [35]
- chorochronic periodicity at permeable-pitchwise boundaries
- interface-matching at the interface

Details for the implementation of the boundary-conditions are given elsewhere [15][24] [25].

3.2 Post-Processing

Post-processing of the computations is based on the computation and storage of the first 4 time-harmonics at each grid-point. The harmonics are computed using the moving-averages technique described in Gerolymos & Vinteler [25].

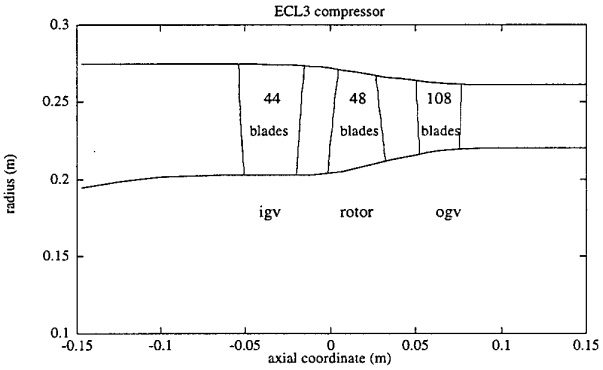

Figure 4: ECL-3 $1\frac{1}{2}$-stage

Table 1: Characteristics of ECL-3 compressor

RPM	16090	
π_{T-T}	1.84	
$\dot{m}$	18.1	kg s^{-1}
R_{tip}	275–264	mm
R_{hub}	203–216	mm
N_{IGV}	44	
N_R	48	
N_S	108	

3.3 Results

3.3.1 ECL-3 Compressor

The configuration studied is the ECL-3 compressor (Fig. 4), designed by SNECMA and tested at the Ecole

Centrale de Lyon. Details on the design of this compressor are given by Goutines & Navière [31]. It consists of an IGV with 44 blades, a rotor with 48 blades, and a stator with 108 blades. Its basic characteristics are given in Tab. 1.

3.3.2 Steady Multistage Computation

The steady multistage computation is performed using the classical Denton-Dawes averaging at the interface [7][8]. Thus each blade-row is influenced by the meridional average (in time and azimuth) of its neighbours. Results for the ECL-3 compressor, at the design point were obtained using a $3 \times (101 \times 17 \times 33)$ grid, which is sufficiently fine for an Euler computation. (Fig. 5).

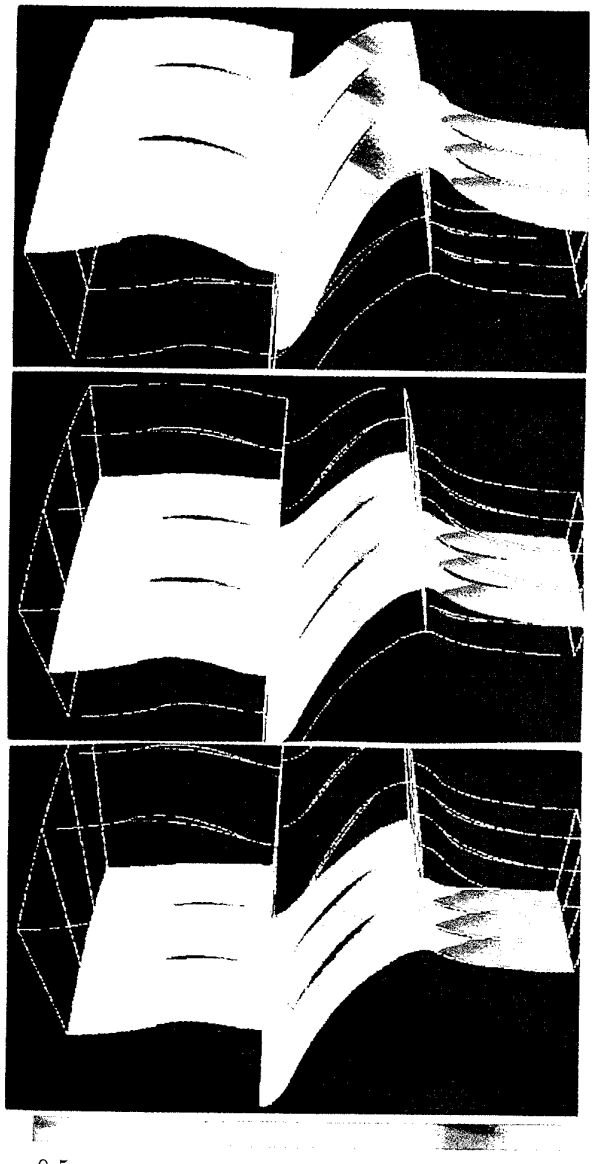

Figure 5: Steady multistage computation isothlipts

The computed results are in tolerable agreement with experimental measurements (Fig. 6). There is naturally unsatisfactory agreement with measurements in the end-wall-boundary-layers region. The important viscous losses in the stator cannot be predicted by an inviscid method.

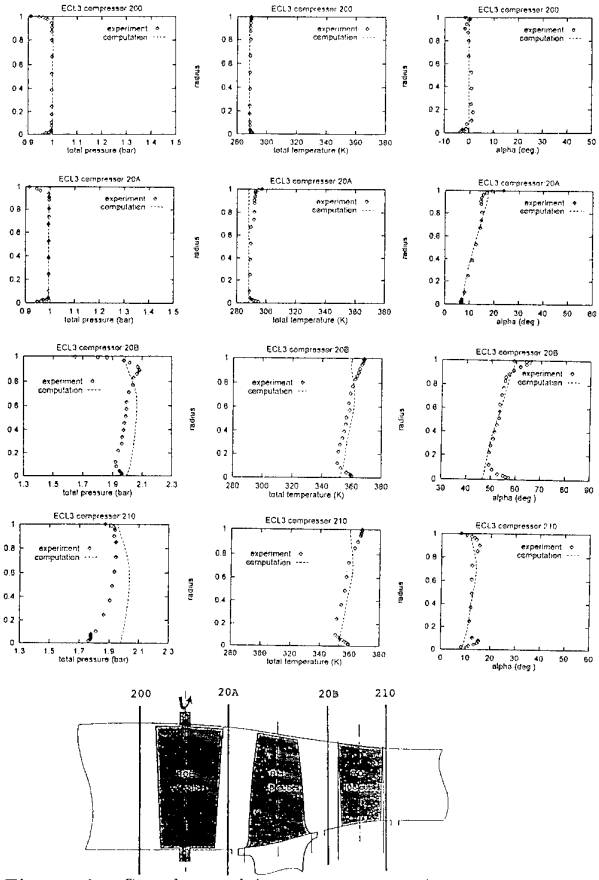

Figure 6: Steady multistage computation comparison with measurements

3.3.3 Unsteady Multistage Computation

Initially an unsteady multistage computation was performed. Due to $\frac{1}{4}$-symmetry of the configuration (all numbers of blades are divisible by 4) it is possible to compute only $\frac{1}{4}$ of the interblade-passages. Thus a preliminary computation was run where were discretized

- 11 interblade-channels of the IGV
- 12 interblade-channels of the rotor
- 27 interblade-channels of the stator

A rather coarse $61 \times 17 \times 17$ was used in each interblade channel. The final permeable pitchwise boundaries are treated with an instantaneous space-periodicity condition. The interface is treated using a $1 - D$ Fourier-series in θ. Some preliminary results of instantaneous pressure distributions on all computed blades are compared with the corresponding steady computation (Fig. 7). It is seen that the steady computation corresponds approximately to the mean value of the instantaneous results.

This computation is important because the correct multistage periodicity is used, at the expense of simulating many interblade passages. The detailed analysis of the results, especially with respect to multistage chorochronic

periodicity information is not yet finished, and will be presented elsewhere. When considering 2 isolated blade-rows, the use of chorochronic periodicity allows to compute only 1 interblade-channel per blade-row.

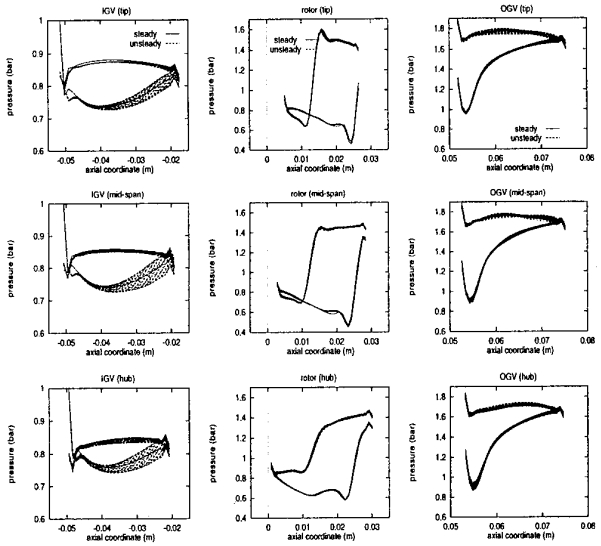

Figure 7: Unsteady multistage computation static pressures on the blades

Table 2: Chorochronic harmonics for ECL-3 IGV/Rotor interaction

n_{IGV}	m_{IGV}	n_R	m_R	n_R	m_R	n_{IGV}	m_{IGV}
-2	-80	-4	-80	-2	-88	0	-88
-2	-36	-3	-36	-2	-40	-1	-40
-2	8	-2	8	-2	8	-2	8
-2	52	-1	52	-2	56	-3	56
-2	96	0	96	-2	104	-4	104
-1	-84	-3	-84	-1	-92	1	-92
-1	-40	-2	-40	-1	-44	0	-44
-1	4	-1	4	-1	4	-1	4
-1	48	0	48	-1	52	-2	52
-1	92	1	92	-1	100	-3	100
0	-88	-2	-88	0	-96	2	-96
0	-44	-1	-44	0	-48	1	-48
0	0	0	0	0	0	0	0
0	44	1	44	0	48	-1	48
0	88	2	88	0	96	-2	96
1	-92	-1	-92	1	-100	3	-100
1	-48	0	-48	1	-52	2	-52
1	-4	1	-4	1	-4	1	-4
1	40	2	40	1	44	0	44
1	84	3	84	1	92	-1	92
2	-96	0	-96	2	-104	4	-104
2	-52	1	-52	2	-56	3	-56
2	-8	2	-8	2	-8	2	-8
2	36	3	36	2	40	1	40
2	80	4	80	2	88	0	88

3.3.4 IGV/Rotor Interaction

In this case the blade-passing-frequencies in each frame, and the corresponding interblade-phase-angles are

$$f_{IGV} = 12800 \text{ Hz} \qquad \Delta\phi_{IGV} = -32.72^o \tag{18}$$

$$f_R = 11733 \text{ Hz} \qquad \Delta\phi_R = -30.00^o \tag{19}$$

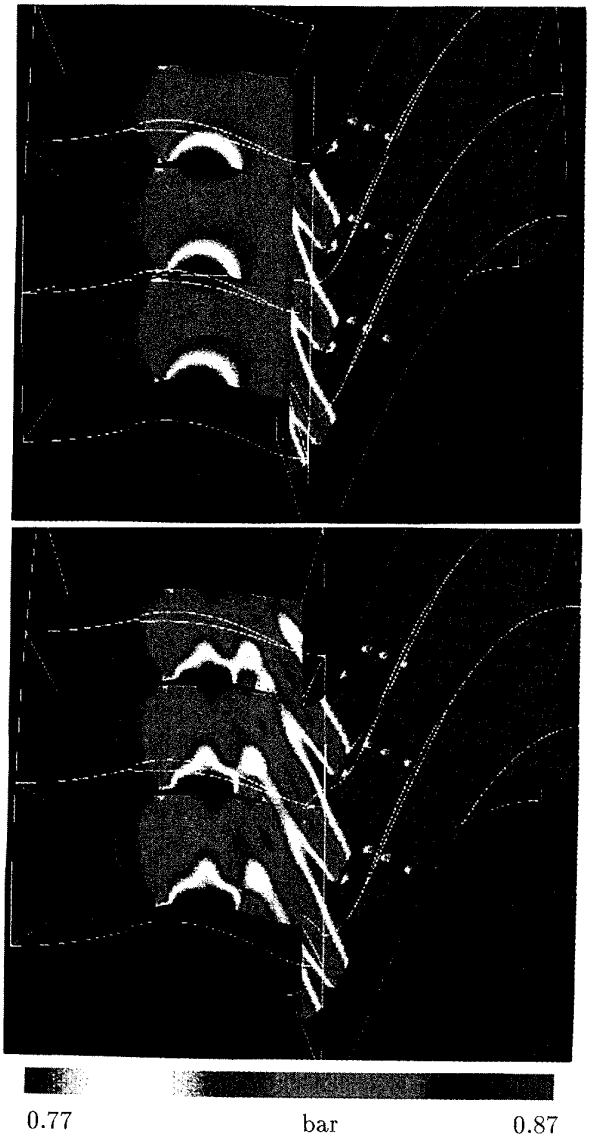

Figure 8: Instantaneous isothlipts for ECL-3 IGV/Rotor interaction at midspan

The corresponding chorochronic harmonics that are not identically 0 are given in Table 2 for $-2 \leq n \leq +2$ and $-2 \leq \ell \leq +2$. The left-side corresponds to the harmonics in the IGV-frame, and their matches in the rotor-frame. The right-side corresponds to the harmonics in the rotor-frame, and their matches in the IGV-frame. Numerical computations are presented using a $2 \times (101 \times 17 \times 33)$

grid, which is sufficiently fine for an Euler computation. The computation is well converged after the simulation of $\frac{1}{2}$ shaft-rotation. Instantaneous isothlipts show that the leading-edge-wave-system of the rotor strongly interacts with the stator (Fig. 8). For the purpose of comparison are also shown the corresponding "steady" isothlipts, obtained on the same grid using a classical Denton-Dawes averaging at the interface [7][8]. It is seen that the steady approach completely filters the upstream interaction.

The amplitude of the 1-harmonic on the blade-surface of both the rotor ($f_R = 11733$ Hz) and the IGV ($f_{IGV} = 12800$ Hz) shows the importance of the unsteady pressure fluctuations generated by the interaction (Fig. 9).

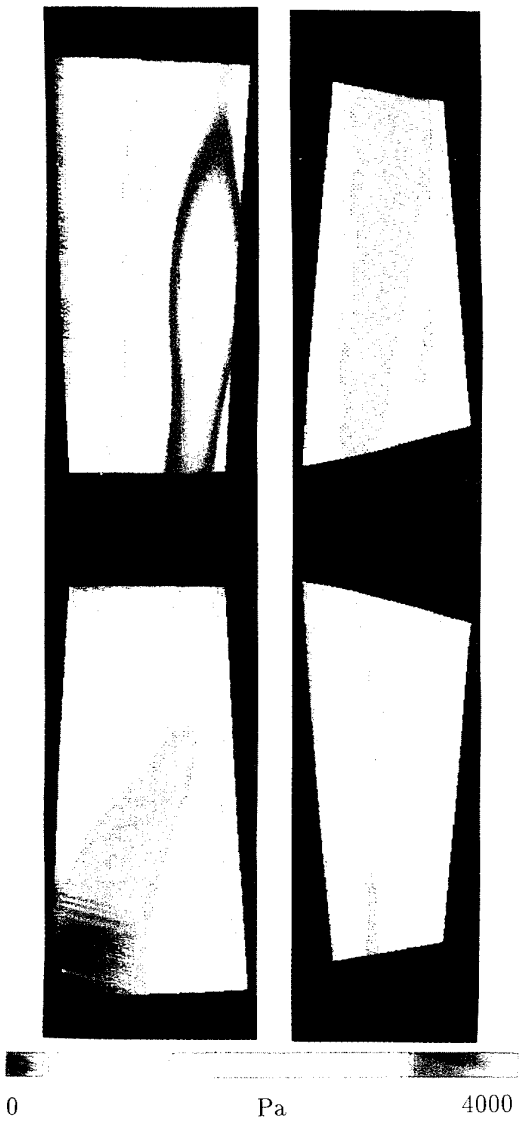

Figure 9: Amplitude of 1-harmonic on the blade-surface for ECL-3 IGV/Rotor interaction

3.3.5 Rotor/Stator Interaction

In this case the blade-passing-frequencies in each frame, and the corresponding interblade-phase-angles are

$$f_R = 28800 \text{ Hz} \qquad \Delta\phi_{IGV} = +90^o \tag{20}$$

$$f_S = 12800 \text{ Hz} \qquad \Delta\phi_R = -160^o \tag{21}$$

Table 3: Chorochronic harmonics for ECL-3 Rotor/Stator interaction

n_R	m_R	n_S	m_S	n_S	m_S	n_R	m_R
-2	-216	0	-216	-2	-336	-4	-336
-2	-168	-1	-168	-2	-228	-3	-228
-2	-120	-2	-120	-2	-120	-2	-120
-2	-72	-3	-72	-2	-12	-1	-12
-2	-24	-4	-24	-2	96	0	96
-1	-156	1	-156	-1	-276	-3	-276
-1	-108	0	-108	-1	-168	-2	-168
-1	-60	-1	-60	-1	-60	-1	-60
-1	-12	-2	-12	-1	48	0	48
-1	36	-3	36	-1	156	1	156
0	-96	2	-96	0	-216	-2	-216
0	-48	1	-48	0	-108	-1	-108
0	0	0	0	0	0	0	0
0	48	-1	48	0	108	1	108
0	96	-2	96	0	216	2	216
1	-36	3	-36	1	-156	-1	-156
1	12	2	12	1	-48	0	-48
1	60	1	60	1	60	1	60
1	108	0	108	1	168	2	168
1	156	-1	156	1	276	3	276
2	24	4	24	2	-96	0	-96
2	72	3	72	2	12	1	12
2	120	2	120	2	120	2	120
2	168	1	168	2	228	3	228
2	216	0	216	2	336	4	336

The corresponding chorochronic harmonics that are not identically 0 are given in Table 3 for $-2 \leq n \leq +2$ and $-2 \leq \ell \leq +2$. The left-side corresponds to the harmonics in the rotor-frame, and their matches in the stator-frame. The right-side corresponds to the harmonics in the stator-frame, and their matches in the stator-frame. Numerical computations are presented using a $2\times(101\times17\times33)$ grid, which is sufficiently fine for an Euler computation. The computation is well converged after the simulation of 1 shaft-rotation. The reason why this case converges much slower is the greater difference in the number of blades between the 2 rows. Instantaneous isothlipts (Fig. 10) show that the unsteady effects are mainly caused by the inhomogeneous rotor outflow (variation of incidence and entropy) affecting the stator. There is virtually no upstream influence of the stator on the rotor, presumably because of the great distance (almost 1 stator chord). For the purpose of comparison are also shown the corresponding "steady" isothlipts, obtained on the same grid using a classical Denton-Dawes averaging at the interface [7][8], illustrating the importance of unsteady effects.

The amplitude of the 1-harmonic on the blade-surface of both the rotor (f_R = 28800 Hz) and the stator (f_S = 12800 Hz) shows the importance of the unsteady pressure fluctuations generated by the interaction on the stator (Fig. 11). On the contrary the unsteady pressure fluctuations on the rotor are negligibly small by comparison.

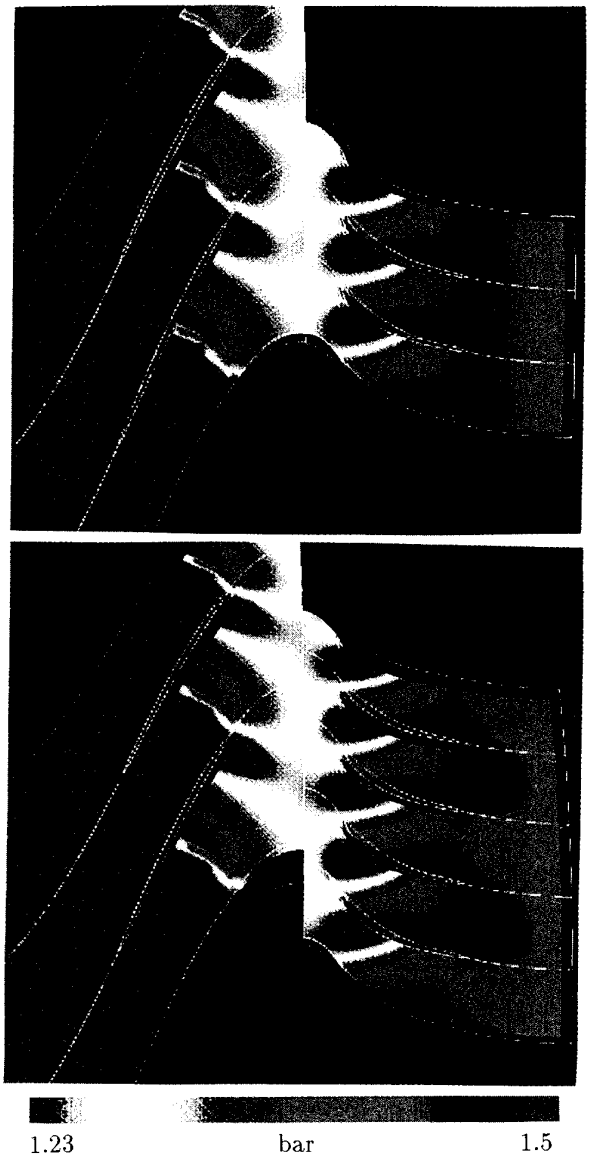

Figure 10: Instantaneous isothlipts for ECL-3 Rotor/Stator interaction at midspan

3.3.6 Further Work

There is a number of questions that still need to be answered:

- what is the effect of unsteadiness on mean flow performance?
- how do the isolated 2-blade-rows computations compare with the multistage computations?
- is it possible to use several 2-blade-rows computations, after developing an adequate theoretical analysis, to reconstruct multistage effects?
- what is the effect of axial gap on the unsteady pressures on the blades?

These problems are currently investigated using the methodology presented above.

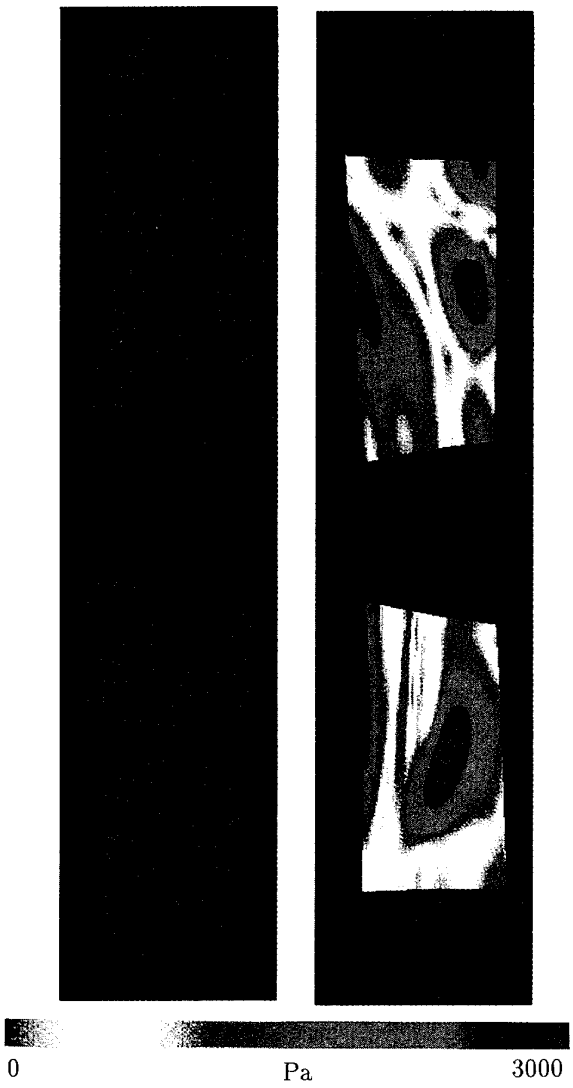

Figure 11: Amplitude of 1-harmonic on the blade-surface for ECL-3 Rotor/Stator interaction

4 Time-Linearized Method

4.1 Methodology

Recently, Lindquist & Giles [42] have shown that it is possible to develop shock-capturing time-linearized methods for unsteady transonic aerodynamics using Euler equations. Such methods have been developed and validated for the analysis of flow in vibrating cascades [32][33][34][23]. To the authors' knowledge the only

rotor/stator interaction analysis in the literature is the work of Suddhoo & Stow [47], who used a finite element time-linearized potential flow solver [51], in an uncoupled procedure to compute 2-D rotor/stator interaction in a turbine stage. In this work the unsteady effect in each blade-row was produced by the rotation of the steady flow in the adjoining blade-row, and the full unsteady flow was obtained by superposition. The interface matching analysis (Eqs. 13) shows that there is an unsteady matching (the last 2 Eqs.) which should be taken into account in a complete 1-order analysis.

A rotor/stator interaction time-linearized method has been developed. The flow is linearized in the neighbourhood of an underlying steady flow, computed using the Denton-Dawes interface-averaging, which corresponds to the condition ${}^{0,0}\underline{\hat{X}}_1 = {}^{0,0}\underline{\hat{X}}_2$. Defining

$$\underline{w} \doteq [\rho, \rho W_x, \rho W_y, \rho W_z, \rho H_R - p]^T \in \mathbb{R}^5 \qquad (22)$$

the steady flow satisfies, in each frame the steady Euler equations

$$\mathrm{div}[\underline{\vec{F}}({}^0\underline{w}_1)] + \underline{S}({}^0\underline{w}_1) = 0 \qquad (23)$$

$$\mathrm{div}[\underline{\vec{F}}({}^0\underline{w}_2)] + \underline{S}({}^0\underline{w}_2) = 0 \qquad (24)$$

in each computational subdomain, where ${}^0\underline{w}_1$ and ${}^0\underline{w}_2$ are defined by Eq. (22) for the flow relative to each blade-row. The time-linearized flow is obtained by considering small unsteady perturbations around the underlying steady flow

$$\underline{w}_1(\vec{x},t) = {}^0\underline{w}_1(\vec{x}) + \Re[{}^1\underline{\hat{w}}_1(\vec{x})\, e^{i2\pi f_1 t}] \qquad {}^1\underline{\hat{w}}_1 \in \mathbb{C}^5 \qquad (25)$$

$$\underline{w}_2(\vec{x},t) = {}^0\underline{w}_2(\vec{x}) + \Re[{}^1\underline{\hat{w}}_2(\vec{x})\, e^{i2\pi f_2 t}] \qquad {}^1\underline{\hat{w}}_2 \in \mathbb{C}^5 \qquad (26)$$

and satisfies

$$i2\pi f_1\, {}^1\underline{\hat{w}}_1 + \mathrm{div}[\frac{\partial \underline{\vec{F}}}{\partial \underline{w}}\, {}^1\underline{\hat{w}}_1] + \frac{\partial \underline{S}}{\partial \underline{w}}\, {}^1\underline{\hat{w}}_1 = 0 \qquad (27)$$

$$i2\pi f_2\, {}^1\underline{\hat{w}}_2 + \mathrm{div}[\frac{\partial \underline{\vec{F}}}{\partial \underline{w}}\, {}^1\underline{\hat{w}}_2] + \frac{\partial \underline{S}}{\partial \underline{w}}\, {}^1\underline{\hat{w}}_2 = 0 \qquad (28)$$

The boundary conditions are (Fig. 3)
- no-penetration at solid walls
- nonreflecting inflow and outflow boundary-conditions
- chorochronic periodicity at permeable pitchwise boundaries
- interface-matching (Eqs. 13) at the interface

The time-linearized Eqs. (27, 28) are discretized using an upwind scheme, based on the time-linearization of van Leer's scheme [49][50][1] [48][17], developed by Gerolymos & Haugeard [21] [22][23]. The resulting linear system is solved by successive underrelaxation.

4.2 IGV/Rotor Interaction

In this case the blade-passing-frequencies in each frame, and the corresponding interblade-phase-angles are given in Eqs. (18, 19), and the interface matching conditions up to 1-order (Eqs. 13) are (*cf.* Tab. 2)

$$\begin{aligned} {}^{0,0}\underline{\hat{X}}_1 &= {}^{0,0}\underline{\hat{X}}_2 \\ {}^{0,\pm 44}\underline{\hat{X}}_1 &= {}^{\pm 1,\pm 44}\underline{\hat{X}}_2 \\ {}^{\mp 1,\pm 48}\underline{\hat{X}}_1 &= {}^{0,\pm 48}\underline{\hat{X}}_2 \\ {}^{\pm 1,\mp 4}\underline{\hat{X}}_1 &= {}^{\pm 1,\mp 4}\underline{\hat{X}}_2 \\ {}^{\pm 1,\mp 92}\underline{\hat{X}}_1 &= {}^{\mp 1,\mp 92}\underline{\hat{X}}_2 \end{aligned} \qquad (29)$$

Time-linearized results agree well with time-nonlinear ones (Fig. 12). It is remarkable that just 1 θ-harmonic of the steady flow is sufficient to reproduce the essentials of the interaction. The slight discontinuity at the interface is due to higher θ-harmonics matching that is neglected. More details, and systematic comparison with nonlinear results are presented in Gerolymos & Haugeard [21].

Figure 12: Instantaneous isothlipts for ECL-3 IGV/Rotor interaction at midspan, obtained using the time-linearized method and the time-nonlinear method

5 Distorsion/Blade-Row Interaction

5.1 Methodology

Few well documented experimental data exist. Most are concerned with distorsion/blade-row interaction, where an upstream or downstream distorsion produces an unsteady flow. The distorsion, is in a 1. approximation considered steady in its frame of reference, which rotates relative to the blade-row. The flow is modelled using the blade-to-blade surface Euler equations

$$\frac{\partial(\rho bR)}{\partial t} + \frac{\partial(\rho bRW_m)}{\partial m} + \frac{\partial(\rho bRW_\theta)}{R\partial\theta} = 0 \quad (30)$$

$$\frac{\partial(\rho bRW_m)}{\partial t} + \frac{\partial(\rho bRW_m^2 + bRp)}{\partial m} + \frac{\partial(\rho bRW_mW_\theta)}{R\partial\theta} - p\frac{dbR}{dm} - \rho b(W_\theta + \Omega R)^2\frac{dR}{dm} = 0 \quad (31)$$

$$\frac{\partial(\rho bRW_\theta)}{\partial t} + \frac{\partial(\rho bRW_mW_\theta)}{\partial m} + \frac{\partial(\rho bRW_\theta^2 + bRp)}{R\partial\theta} + \rho bW_m(W_\theta + 2\Omega R)\frac{dR}{dm} = 0 \quad (32)$$

$$\frac{\partial(\rho bRH_R - bRp)}{\partial t} + \frac{\partial(\rho bRW_mH_R)}{\partial m} + \frac{\partial(\rho bRW_\theta H_R)}{R\partial\theta} = 0 \quad (33)$$

where m is the meridional coordinate ($dm = \sqrt{dx^2 + dR^2}$), and b the streamtube thickness. It is assumed that the thickness and radial position of the streamtube are axisymmetric.

The cases studied include:

- upstream distorsion due to incoming wakes or pressure waves (3 boundary-conditions at the inflow- boundary)
- downstream distorsion due to upstream propagating pressure waves (1 boundary-condition at the outflow-boundary)

In each case the distorsion is a rotating frozen signal (or signals). If θ_D is the azimuth in the frame where the distorsion is stationary, θ_{BR} the azimuth in the frame relative to the blade-row, and θ the azimuth in the absolute frame

$$\theta = \theta_D + \Omega_D t = \theta_{BR} + \Omega_{BR} t \quad (34)$$

the distorsion signal can be expressed as

$$F(\theta_D) \equiv F(\theta - \Omega_D t) \equiv F(\theta_{BR} + (\Omega_{BR} - \Omega_D)t) \quad (35)$$

The interest of this methodology lies in comparing with a number of experimental test-cases. Computational results have been compared with measurements or analytical theory in 4 test-cases, presented in the following. A detailed description of the code is given in Gerolymos & Tsanga & Vinteler [27].

5.2 Results and Comparison with Experiment

5.2.1 Hodson Turbine

This test-case, experimentally and computationally (using a similar method) studied by Hodson [28] is a turbine rotor attacked by the wakes of an upstream nozzle. Typical parameters are given in Tab. 4. Computations were run using a 301 × 61 grid. The measurements and computations are at the midspan section of the rotor, where the flow is considered 2-D (Fig 13). The 1-harmonic of unsteady pressures on the blades' surface compares well with measurements, if a fine grid is used (Fig 14).

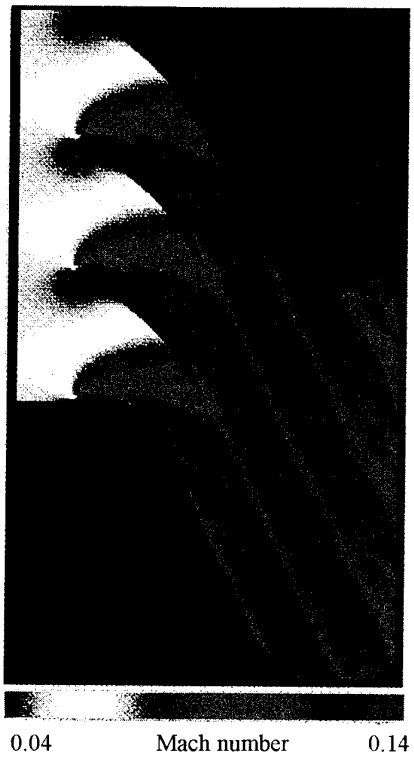

Figure 13: Steady flow for Hodson turbine

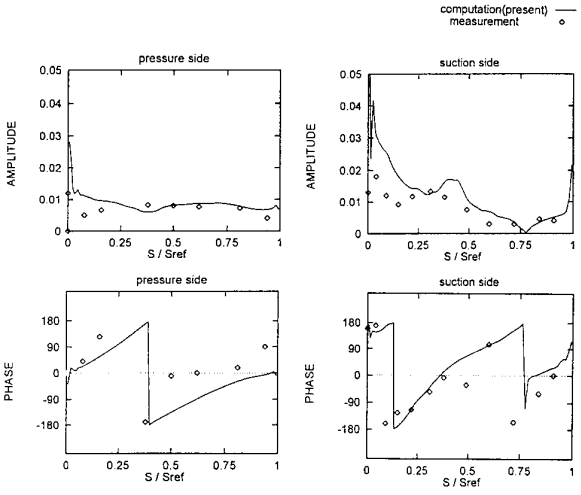

Figure 14: Comparison of computed and measured unsteady pressures for Hodson turbine

Entropy-perturbation contours at 4 different instants

illustrate the interaction of the wakes with the rotor (Fig 15).

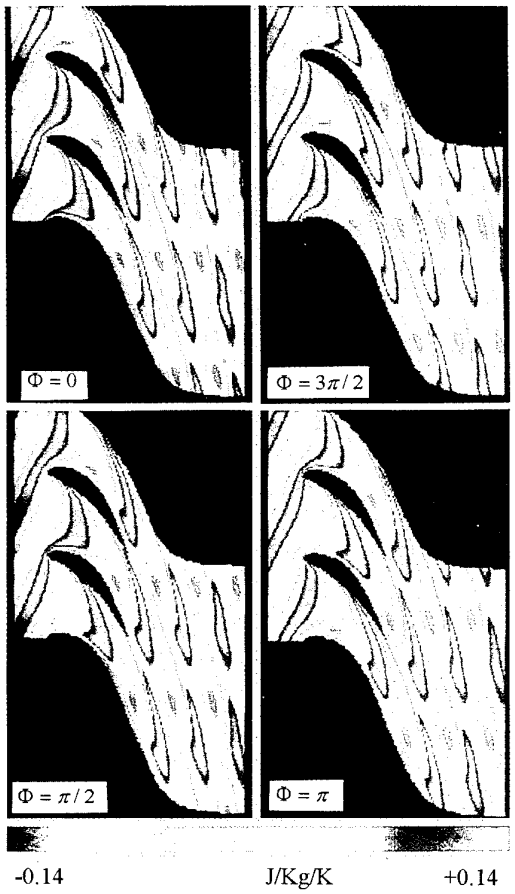

Figure 15: Instantaneous entropy-perturbation contours for Hodson turbine

Table 4: Characteristics of Hodson turbine

RPM	530	
M_{BR_1}	0.05	
N_D	36	
N_{BR}	51	
σ_{BR}	1.435	
f_{BR}	318	Hz
$\Delta\phi_{BR}$	-105.88^o	

Table 5: Characteristics of Giles flat-plate cascade

RPM	3030	
M_{BR_1}	0.7	
N_D	100	
N_{BR}	90	
σ_{BR}	2	
f_{BR}	5050	Hz
$\Delta\phi_{BR}$	40^o	

5.2.2 Giles Cascade

This test-case is a linear flat-plate cascade (Tab. 5) attacked by prescribed sinusoidal wakes. It has been studied by Giles [29]. Computations were run using a 401×81 grid. Comparison of unsteady pressures on the blades with linear theory is quite satisfactory (Fig. 16). Instantaneous entropy-perturbation contours show the interaction of the wakes with the flat-plates (Fig. 17).

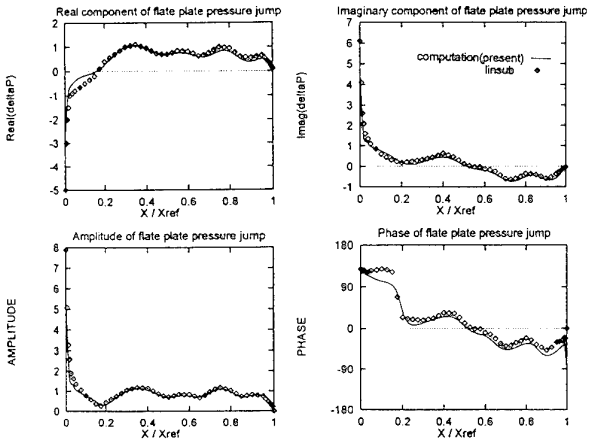

Figure 16: Comparison of computed and analytical unsteady pressures for Giles flat-plate cascade

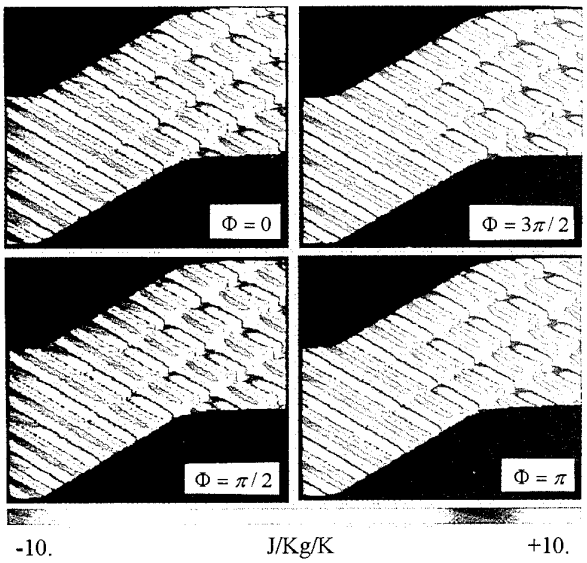

Figure 17: Instantaneous entropy-perturbation contours for Giles flat-plate cascade

5.2.3 VKI Centrifugal Compressor

This test-case (Tab. 6) is a volute/impeller interaction studied experimentally by Sideris & Van den Braembussche [46] (Fig. 18). A volute can be modelled, for chorochronic periodicity purposes as a blade-row with 1 blade. Steady pressure taps provide the pressure signal, in the absolute-frame which corresponds to a rotating

outflow-pressure distorsion in the impeller-frame. Computational and experimental results, at mid-height, do not compare so well as previous cases (Fig. 19). A possible reason is the 3-D nature of the flow at the impeller outlet. Presumably a coupled 3-D impeller/volute computation is necessary for predicting satisfactorily this test-case. The instantaneous pressure-perturbation contours indicate the strong unsteadiness of the flow (Fig. 20).

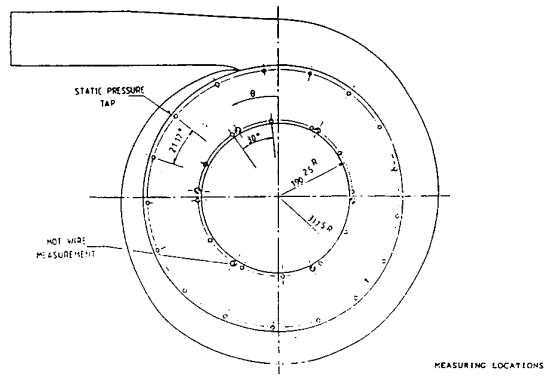

Figure 18: Schematic representation of VKI centrifugal compressor

Table 6: Characteristics of VKI centrifugal compressor

RPM	10000	
M_{BR_1}	0.4	
N_D	1	
N_{BR}	20	
σ_{BR}	3.6	
f_{BR}	167	Hz
$\Delta\phi_{BR}$	-18^o	

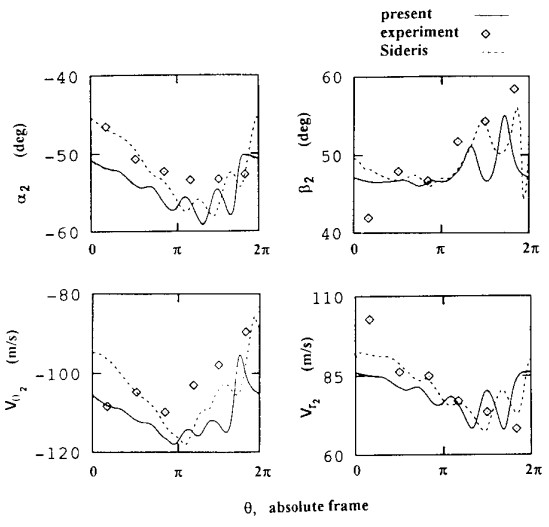

Figure 19: Comparison of computed and experimental results for VKI centrifugal compressor

5.2.4 SHF Centrifugal Pump

Another test-case is a 7-blade SHF pump (Tab. 7) interaction with its volute [6]. Details are given in Geroly-

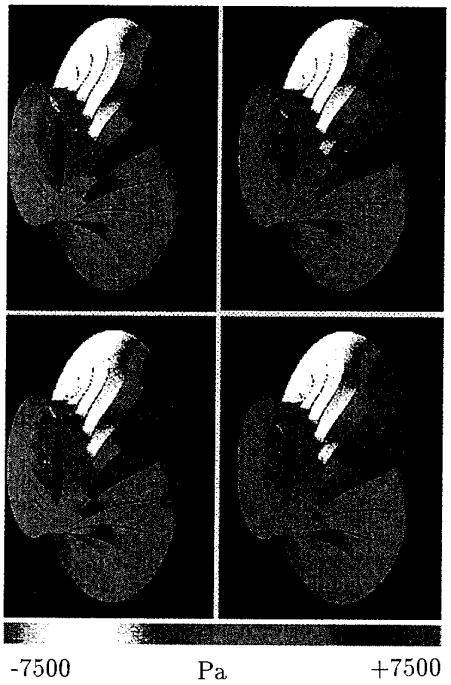

Figure 20: Instantaneous unsteady pressure-perturbation contours for VKI centrifugal compressor

Table 7: Characteristics of SHF centrifugal pump

RPM	3957	
M_{BR_1}	0.1	
N_D	1	
N_{BR}	7	
σ_{BR}	1.155	
f_{BR}	66	Hz
$\Delta\phi_{BR}$	-51.43^o	

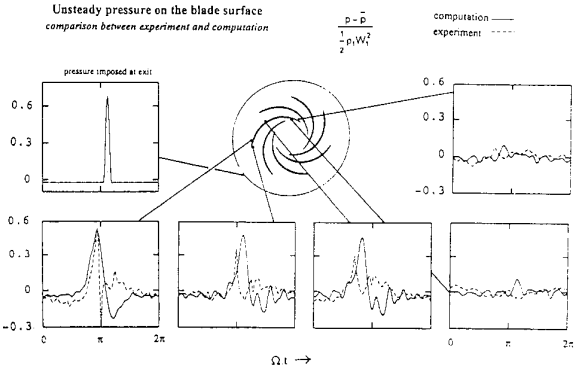

Figure 21: Comparison of computed and experimental results for SHF centrifugal pump

mos & Tsanga & Vinteler [27]. Computed and measured

pressure signals on the impeller blades compare quite well (Fig. 21). The difficulty of the computation suggests however that a coupled impeller/volute computation would be preferable.

5.2.5 Extension to 3-D

The distorsion/blade-row methodology has been extended to 3-D and used for computing forced-response of the blading, by Berthiller & Dhainaut & Burgaud & Garnier [5].

6 Extension to Navier-Stokes

6.1 Introduction

The Euler results presented above validate the methodology as far as chorochronic periodicity is concerned. The extension of the flow solver to Navier-Stokes equations is necessary to predict accurately complex unsteady flows in turbomachinery. A numerical method has been developed for this purpose, and validated for steady and unsteady flow in transonic nozzles.

6.2 Numerics

The flow is modelled by the compressible 3-D Navier-Stokes equations

$$\begin{aligned}
\frac{\partial \rho}{\partial t} + \mathrm{div}\rho\vec{V} &= 0 \\
\frac{\partial \rho\vec{V}}{\partial t} + \mathrm{div}[\rho\vec{V}\otimes\vec{V} + p\boldsymbol{I}] - \mathrm{div}\boldsymbol{\tau} &= 0 \\
\frac{\partial(\rho h_t - p)}{\partial t} + \mathrm{div}[\rho\vec{V}h_t] - \mathrm{div}[\vec{V}\cdot\boldsymbol{\tau} - \vec{q}] &= \\
= -P_k + \rho\epsilon + 2\mu(\mathrm{grad}\sqrt{k})^2 &
\end{aligned} \tag{36}$$

where the viscous stresses and heat-fluxes are

$$\begin{aligned}
\boldsymbol{\tau} &= (\mu+\mu_T)[2\boldsymbol{D} - \frac{2}{3}\mathrm{div}\vec{V}\boldsymbol{I}] - \frac{2}{3}\rho k\boldsymbol{I} \\
\vec{q} &= -k(1 + \frac{\mu_T}{0.9\mu})\mathrm{gradT}
\end{aligned} \tag{37}$$

where $\boldsymbol{D}$ is the rate-of-deformation tensor, k the turbulence kinetic energy, and μ_T the eddy viscosity, computed using the Launder-Sharma turbulence model

$$\begin{aligned}
\frac{\partial \rho k}{\partial t} + \mathrm{div}[\rho\vec{V}k] &= \mathrm{div}[(\mu+\mu_T)\mathrm{grad}k] + \\
&+ P_k - \rho\epsilon - 2\mu(\mathrm{grad}\sqrt{k})^2 \\
\frac{\partial \rho\epsilon}{\partial t} + \mathrm{div}[\rho\vec{V}\epsilon] &= \mathrm{div}[(\mu + \frac{\mu_T}{1.3})\mathrm{grad}\epsilon] + \\
\frac{\epsilon}{k}[1.44P_k - 1.92(1-0.3e^{-Re_T^2}]\rho\epsilon) &- 2\nu\mu_T(\nabla^2\vec{V})^2 \\
\mu_T = 0.09\mu Re_T e^{-\frac{3.4}{(1+0.02Re_T)^2}} &\;;\; Re_T \doteq \frac{k^2}{\nu\epsilon}
\end{aligned} \tag{38}$$

The molecular viscosity and heat conductivity coefficients are computed using Sutherland's law

$$\mu(T) = \mu_{273}\left[\frac{T}{273.15}\right]^{\frac{3}{2}}\frac{110.4+273.15}{110.4+T}$$

$$k(T) = k_{273}\frac{\mu(T)}{\mu_{273}}(1+0.00023\,T)$$

$$\mu_{273} = 17.11\times10^{-6}\ \mathrm{Pa\ s}\ ;\ k_{273} = 0.0242\ \mathrm{Wm^{-1}K^{-1}} \tag{39}$$

These equations (Eqs. 36, 38) are discretized in a structured grid using a finite-volume technique, with vertex-storage. The Navier-Stokes (Eq. 36) and turbulence-transport (Eq. 37) equations can be written

$$\frac{\partial \underline{w}}{\partial t} + \mathrm{div}[{}^C\vec{\underline{F}}(\underline{w}) + {}^V\vec{\underline{F}}(\underline{w})] + \underline{S}(\underline{w}) = 0 \tag{40}$$

where $\underline{w} = [\rho, \rho u, \rho v, \rho w, \rho h_t - p, \rho k, \rho\epsilon]^T \in \mathbb{R}^7$ is the vector of unknowns at each grid-point, ${}^C\vec{\underline{F}} \in \mathbb{R}^7\otimes\mathbb{R}^3$ the convective fluxes, ${}^V\vec{\underline{F}} \in \mathbb{R}^7\otimes\mathbb{R}^3$ the viscous fluxes and $\underline{S}(\underline{w}) \in \mathbb{R}^7$ the source-terms. The divergence of convective fluxes is discretized using the flux-vector-splitting method of Van Leer [50] with 3-order MUSCL interpolation [49] and Van Albada limiters [48]. Details for the particular implementation, and boundary approximations are given in Gerolymos & Bréus [17]. The divergence of viscous fluxes is computed using the centered scheme described in Arnone [3]. Viscous stresses are computed using a centered 2-order finite-difference scheme. More details can be found in Gerolymos et Vallet [18][19]. Denoting by $\underline{\mathcal{L}}_{i,j,k}$ the discretized form of the space-operator (divergence and source temrs), the semi-discrete equation at grid-point (i,j,k) gives

$$\frac{d\underline{w}_{i,j,k}}{dt} + \underline{\mathcal{L}}_{i,j,k} \cong 0 \quad \forall\, i,j,k \tag{41}$$

Assembling the unknowns and space-operators in global vectors, $\mathfrak{w} = [\underline{w}_{1,1,1}, \underline{w}_{1,1,2}, \cdots, \underline{w}_{Ni,Nj,Nk}]^T \in \mathbb{R}^{7\times Ni\times Nj\times Nk}$ et $\mathfrak{L} = [\underline{\mathcal{L}}_{1,1,1}, \underline{\mathcal{L}}_{1,1,2}, \cdots, \underline{\mathcal{L}}_{Ni,Nj,Nk}]^T \in \mathbb{R}^{7\times Ni\times Nj\times Nk}$, the semi-discrete equations (Eq. 41) are written

$$\frac{d\mathfrak{w}}{dt} + \mathfrak{L} \cong 0 \tag{42}$$

The time-discretization of the semi-discrete scheme uses a 1-order implicit scheme, and can be written between instants n and $n+1$

$$(\mathcal{I} + \Delta t\frac{\partial \mathfrak{L}}{\partial \mathfrak{w}})({}^{n+1}\mathfrak{w} - {}^n\mathfrak{w}) = -\Delta t\,{}^n\mathfrak{L} \tag{43}$$

where $\mathcal{I} \in \mathbb{R}^{(7\times Ni\times Nj\times Nk)\times(7\times Ni\times Nj\times Nk)}$ is the identity-matrix. The resulting linear system is solved after approximate factorization of the jacobian matrix of convective and viscous fluxes and source-terms. The 4 successive linear systems are solved using banded LU factorization. The bandwidth of the system is reduced using a 1-order accurate in space approximation for the implicit term. Viscous terms are treated using a spectral radius approximation [19].

The stability time-step is based on a combined convective (Courant) and viscous (von Neumann) criterion

$$\Delta t \le CFL\Delta t_{stab} = CFL\min\left\{\frac{\ell}{V+a}, \frac{\ell^2}{2\nu_{eq}}\right\} \quad \forall i,j,k \tag{44}$$

where ℓ is the grid-cell-size, V the flow velocity, a the sound velocity, et ν_{eq} the equivalent diffusivity, computed by MacCormack [43]

$$\nu_{eq} = \max\left\{\frac{4}{3}\nu, \frac{k}{\rho R_g(\gamma-1)}\right\} \tag{45}$$

for steady computations a $CFL = 50$ is used with local-time-strepping. For unsteady computations a $CFL = 500$ is used with spatially homogeneous Δt.

6.3 Ott-Nozzle

6.3.1 Experimental Set-up

This test-case was studied experimentally by Ott & Bölcs & Fransson [45]. The experimental set-up (Fig. 22) is a Laval nozzle, with transonic flow, where an unsteady back-pressure fluctuation can be produced by the rotation of a rod with elliptical cross-section at outflow. Steady and unsteady pressure measurements were obtained at the sidewall on the horizontal plane of symmetry of the nozzle. The nozzle characteristics are summarized in Tab. 8.

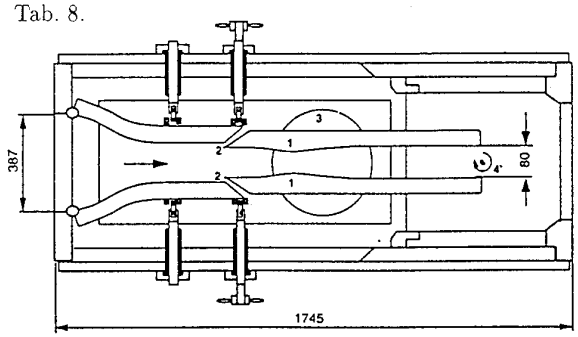

Fig. 1(b) Schematic view of the nozzle used: (1) nozzle liner; (2) boundary layer bleed; (3) Schlieren window; (4) rotating exciter

Figure 22: Ott & Bölcs & Fransson experimental set-up

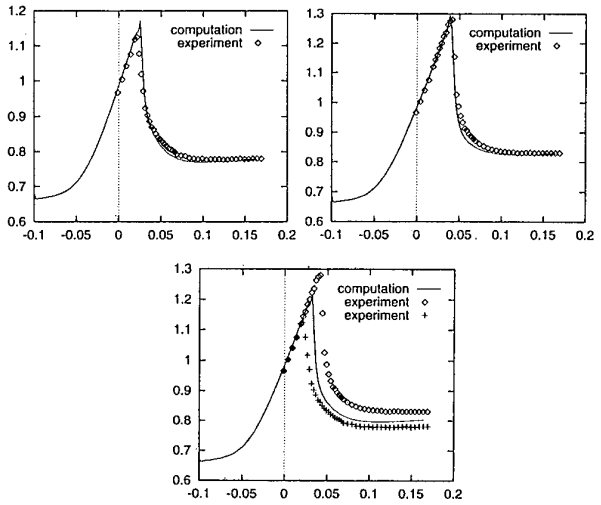

Figure 23: Steady computations and comparison with experiment for Ott nozzle

6.3.2 Steady Flow

Steady computations compare favourably with measurements (Fig. 23). The 2 experimental configurations correspond to horizontal and vertical position of the stationary rod. The intermediate back-pressure corresponds to the mean flow for the unsteady case. For the steady computations a $121 \times 67 \times 67$ grid was used. The 1 grid points away from the wall are at $y^+ \cong 0.5$.

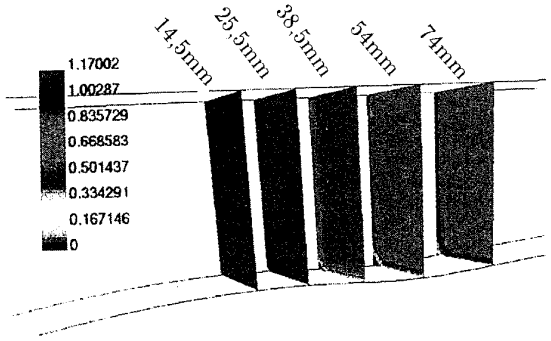

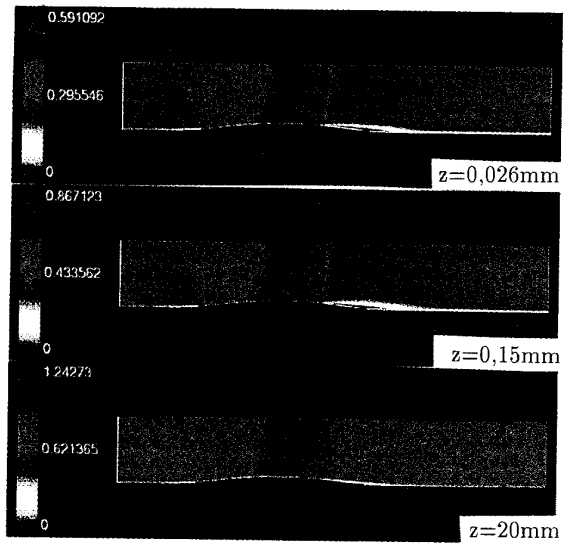

Figure 24: IsoMachs for Ott nozzle

Table 8: Characteristics of Ott nozzle

p_{t_1}	168600	Pa
T_{t_1}	323	K
inflow-height	80	mm
throat-height	71	mm
width	40	mm

The flow has strong 3-D effects because of the small width of the nozzle (Fig. 24), and the fact that the sidewall boundary-layers were not removed in the experiment. Accordingly, in the computations, a 5mm boundary layer thickness was assumed on the sidewall (at inflow). The inflow boundary-layer thickness on the bottom and top walls was 0.5mm. The shock-wave/boundary-layer interaction at the nozzle corner induces a highly 3-D flow (predictions using 2-D computations at the nozzle plane of symmetry are completely off the mark [18][19]).

6.3.3 Unsteady Flow

Unsteady flow computations were run on a coarser grid ($121 \times 57 \times 49$) but with the same 1 grid points away from the wall ($y^+ \cong 0.5$). This is necessary because

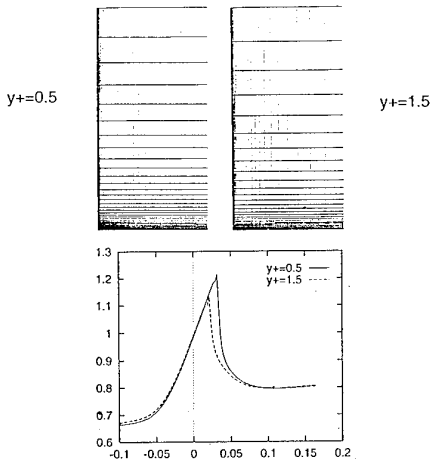

Figure 25: Influence of near-wall resolution on steady results

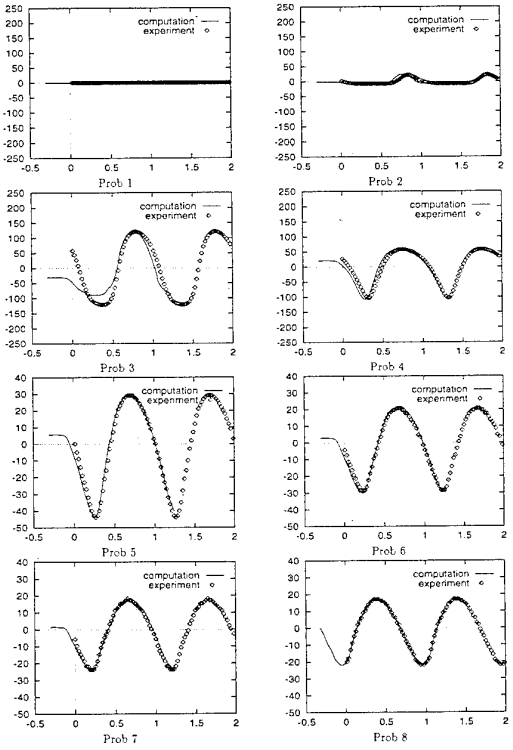

Figure 26: Comparison of computed and measured unsteady pressures on the sidewall for Ott nozzle at $f = 180$ Hz

using coarser near-wall resolution (which would dramatically reduce CPU-time) yields unsatisfactory steady results (Fig. 25). The CPU time for a steady computation is $\sim$ 10 h. For an unsteady computation, at 180 Hz, requires $\sim$ 400 h. Results for an unsteady computation at 180 Hz compare quite well with measurements (Fig. 26), illustrating the predictive capability of the unsteady Navier-Stokes computation.

7 Conclusions

In this paper the chorochronic periodicity that governs the interaction of 2 blade-rows in relative rotation was analyzed in detail, and used for developing 3-D Euler codes for rotor/stator interaction which compute only 1 interblade channel per blade-row, without any loss of unsteady information. Comparisons of computed and experimental results corroborate the validity of the methodology.

This methodology is currently upgraded to a 3-D Navier-Stokes solver, using $k - \epsilon$ turbulence closure. Preliminary steady and unsteady results for transonic flow in a Laval nozzle are encouraging.

Acknowledgments

Parts of this work were supported by contracts with SNECMA and EDF, and by FIRTech, and are published with their permission. The time-linearized method was developed under contract with SNECMA and is published by permission.

The computations presented in this work were run at the Centre de Calcul pour la Recherche de l'Université Pierre-et-Marie-Curie (CCR-Jussieu), and the Institut pour le Développement des Ressources en Informatique Scientifique (IDRIS).

References

[1] Anderson W.K. & Thomas J.L. & Rumsey C.L *AIAA J.* **27** (1989) 673–674
[2] Arndt N. *ASME J. Turbom.* **115** (1993) 137–146
[3] Arnone A. *ASME J. Turbom.* **116** (1994) 435–445
[4] Beam R. & Warming R.F. *J. Comp. Phys.* **22** (1976) 87–110
[5] Berthiller M. & Dhainaut M. & Burgaud F. & Garnier V. *ASME Paper* 94-GT-293 (1994)
[6] Caignaert G. *Private Communication* (1992)
[7] Denton J.D. *ASME J. Turbom.* **114** (1992) 18–26
[8] Dawes W.N. *ASME J. Turbom.* **114** (1992) 8–17
[9] Dunn M.G. *ASME J. Turbom.* **112** (1990) 531–538
[10] Erdos J.I. & Alzner E. & McNally W. *AIAA J.* **15** (1977) 1559–1568
[11] Gerolymos G.A. *AIAA J.* **26** (1988) 1483–1492
[12] Gerolymos G.A. *AIAA J.* **28** (1990) 1707–1717
[13] Gerolymos G.A. & Chapin V. *Rech. Aéro.* **1991**:5 (1991) 69–73
[14] Gerolymos G.A. *510. AGARD Conf.* (1991)
[15] Gerolymos G.A. *ASME J. Turbom.* **115** (1993) 781–790
[16] Gerolymos G.A. *ASME J. Turbom.* **115** (1993) 791–800
[17] Gerolymos G.A. & Bréus J.P. *ASME Paper* 94-GT-91 (1994)
[18] Gerolymos G.A. & Vallet I. *12. Cong. Franç. Méc.* (1995)
[19] Gerolymos G.A. & Vallet I. *AIAA J.* (1995) sub jud.
[20] Gerolymos G.A. & Vallet I. & Ott P. & Bölcs A. *3-D Complex Flows IMACS-COST Conf.* (1995)
[21] Gerolymos G.A. & Haugeard R. *AIAA J.* (1995) sub jud.
[22] Gerolymos G.A. & Haugeard R. *AIAA J.* (1995) sub jud.
[23] Gerolymos G.A. & Haugeard R. in writing
[24] Gerolymos G.A. in writing
[25] Gerolymos G.A. & Vinteler D. in writing
[26] Gerolymos G.A. & Haugeard R. in writing
[27] Gerolymos G.A. & Tsanga G. & Vinteler D. in writing
[28] Hodson H.P. *ASME J. Eng. Gas Turb. Power* **107** (1988) 337–344
[29] Giles M.B. *J. Prop. Power* **4** (1988) 356–362
[30] Giles M.B. *J. Prop. Power* **6** (1990) 621–627
[31] Goutines M. & Navière H. *421. AGARD Conf.* (1987)

[32] HALL K.C. & LORENCE C.B. *ASME J. Turbom.* **115** (1993) 800–809
[33] HALL K.C. & CLARK W.S. *AIAA J.* **31** (1993) 540–550
[34] HALL K.C. & CLARK W.S. & LORENCE C.B. *ASME J. Turbom.* **116** (1994) 477–488
[35] HEDSTROM G.W. *J. Comp. Phys.* **30** (1979) 222–237
[36] KEMP N.H. & SEARS W.R. *J. Aero. Sci.* **20** (1953) 585–597, 612
[37] KEMP N.H. & SEARS W.R. *J. Aero. Sci.* **20** (1955) 478–483
[38] KERREBROCK J.L. & MIKOLAJCZAK A.A. *ASME J. Eng. Power* **92** (1970) 359–368
[39] KOYA M. & KOTAKE S. *Int. J. Turbo Jet Eng.* **2** (1985) 44–55
[40] KOYA M. & KOTAKE S. *ASME J. Eng. Gas Turb. Power* **107** (1985) 945–952
[41] LEWIS J.P. & DELANEY R.A. & HALL E.J. *ASME J. Turbom.* **111** (1989) 387–393
[42] LINDQUIST D.R. & GILES M.B. *AIAA J.* **32** (1994) 46–53
[43] MACCORMACK R.W. *AIAA J.* **20** (1982) 1275–1281
[44] OKIISHI T.H. & HATAHAWAY M.D. & HANSEN J.L. *ASME J. Eng. Gas Turb. Power* **107** (1985) 549–551
[45] OTT P. & BÖLCS A. & FRANSSON T.H. *ASME J. Turbom.* **117** (1995) 206–114
[46] SIDERIS M.T. & VAN DEN BRAEMBUSSCHE R.A. *ASME J. Turbom.* **109** (1987) 48–54
[47] SUDHOO A. & STOW P. *AIAA Paper* 90-1916 (1990)
[48] VAN ALBADA G.D. & VAN LEER B. & ROBERTS W.W.JR. *Astron. Astroph.* **108** (1982) 76–84
[49] VAN LEER B. *J. Comp. Phys.* **32** (1979) 101–136
[50] VAN LEER B. *Lect. Notes Phys.* **170** (1982) 507–512
[51] WHITEHEAD D.S. *Int. J. Num. Meth. Fluids* **10** (1990) 13–34
[52] ZESCHKY J. & GALLUS H.E. *ASME J. Turbom.* **115** (1993) 128–136
[53] ZIERKE W.C. & OKIISHI T.H. *ASME J. Eng. Power* **104** (1982) 479–488

Numerical Simulations of Stator-Rotor Interactions on Compressor Blade Rows

N. Liamis, J.L. Bacha and F. Burgaud
Snecma
Compressor Aerodynamics Department
77550 Moissy Cramayel
France

1. ABSTRACT

A numerical analysis of the unsteady flow field in a single stage axial transonic compressor is presented, with the aim of exhibiting typical unsteady phenomena resulting from the rotor-stator interactions. Firstly, a 3D Euler solver is used to investigate the unsteady effects generated by the inlet guide vane-rotor-stator relative motion, for several operating points of the compressor. Various features of the unsteady compressor flow field are examined : the non-uniformity of the flow in the stator, the influence of the operating point, and the location of the unsteadiness on each blade surface. A quasi-3D Navier-Stokes analysis of the inlet guide vane-rotor interaction is then conducted and shows the large influence of moving oblique shocks on the inlet guide vane instantaneous outlet angles and velocities.

2. INTRODUCTION

The need for lighter and high performance aeroengines has led to compressors with high levels of aerodynamic loading and increased compactness. These trends have made compressor designers more and more interested in the unsteady aerodynamic phenomena occurring in close coupled blade rows, especially those due to the relative motion of rotors and stators. A clear and detailed understanding of the flow physics as well as a precise quantitative estimation of the unsteady effects should help to decrease aerodynamic losses and to minimise vibratory stresses on the blades. Large amounts of experimental work [1], [2] have been performed in order to determine some characteristic flow features and gather unsteady data. At the same time numerical simulations of the unsteady compressor flow field are becoming available for the designers.

The use of advanced computational methods is an efficient and powerful way to improve the performance of turbomachinery components and to reduce both design and development time and cost. Until recently, turbomachinery component design was based on steady-state flow calculations, while the unsteady effects were taken into account using empirical laws and large safety margins. Now that flow calculations within single blade rows are commonly used in the design process, the next step to gain further accuracy is the prediction of the unsteady flow in the entire stage. This type of simulation is currently becoming accepted practice in industry. However it is not as widely used as single row calculations because solving the fully non-linear unsteady equations leads to a large increase in computational cost, especially for complex viscous flows.

In the last several years, Snecma in cooperation with ONERA has developed solvers for turbomachinery applications. Considerable efforts have also been devoted to include new design and analysis codes in the engine component development methodology [3]. In the aerodynamic design, an early and systematic use of quasi-3D and 3D Euler and Navier-Stokes solvers has proved particularly helpful for the design of compressor and turbine blades. This experience and the increase in computer capabilities now allow the use of these solvers for rotor-stator interaction studies.

Many authors have already used 3D Euler [4], [5], [6], and 2D, quasi-3D or 3D Navier-Stokes [7], [8], [9], [10], [11], [12], [13], [14] approaches in order to simulate rotor-stator interactions. These efforts were related to the use of explicit [4], [5], [6], [7], [12] or implicit [8], [9], [10], [11], [13], [14] solvers. The use of explicit solvers, which are characterised by time step limitations (for stability reasons), results in important computational costs. Therefore implicit solvers able to use large time steps without any serious accuracy alteration seem more attractive for industrial use.

In the study presented hereafter, a 3D Euler and a quasi-3D Navier-Stokes implicit solvers developed at ONERA [15], [16], [8] are used to investigate the unsteady flows in a single stage axial transonic compressor. Two kinds of simulations are performed. The first one concerns simulations of the entire compressor (inlet guide vane-rotor-stator) by using the 3D Euler solver. The second one is the simulation of the inlet guide vane-rotor interaction by using the quasi-3D Navier-Stokes solver.

3. NUMERICAL METHOD

The physical models are the unsteady compressible 3D Euler [15] and quasi-3D Navier-Stokes [16] equation systems. For each row, the equations are formulated in a conservative manner and are solved in the frame of reference in which the blading is fixed. The 3D Euler equations are written in the cartesian coordinate system. The quasi-3D Navier-Stokes equations are written in the axisymmetric stream surface coordinate system where the radius and the stream surface thickness are taken to be known functions of the meridional coordinate. The turbulent closure of the Navier-Stokes equations is obtained from the algebraic mixing-length turbulence model of Michel et al. [17], validated in [18].

The solvers use a cell-vertex approach for multi-domain structured meshes. The numerical method is an implicit, finite volume, time marching, multi-step scheme. The method is presented in detail in [15], it will only be briefly mentioned in this paper.

Each step of the method is a combination of three stages : an explicit stage, an artificial dissipation stage, and an implicit stage. The explicit stage is the space-centred explicit Runge-Kutta scheme introduced by Jameson [19]. The artificial dissipation stage being based on space-centred difference operators of second and fourth order is analogous to that introduced by Jameson [19]. The implicit stage is a variable coefficients residual smoothing obtained by an extension of the Lerat implicit stage [20].

The explicit and the artificial dissipation stages are the same for the Euler and the Navier-Stokes equations, while the implicit stage is modified for the Navier-Stokes equations for stability reasons by the introduction of one additional term.

Paper presented at the AGARD PEP 85th Symposium on "Loss Mechanisms and Unsteady Flows in Turbomachines", held in Derby, United Kingdom, 8-12 May 1995, and published in CP-571.

This term being first order accurate in time affects the time accuracy of the scheme, which is of second order for the Euler case and becomes of first order for the Navier-Stokes case. Nevertheless it appears after a error analysis that for large time steps (high CFL numbers), usual refined meshes and low or moderate turbulence intensity levels, the first order temporal error generated by the extra term is comparable to the second order temporal error of the scheme. Furthermore, the temporal error introduced is small compared to the error generated by the use of a stationary turbulence model. Consequently, in practice, the temporal accuracy of the scheme can be considered of second order even for the Navier-Stokes case. The space accuracy of the scheme is of second order. The scheme being unconditionally stable, allows large time steps (high CFL numbers) to be used during the unsteady simulations.

The numerical method is similar to the method presented by Chima [10]. Their differences mainly consisted on the definition of the variable coefficients for the residual smoothing and the extra term introduced for the Navier-Stokes case. However the present scheme allows larger time steps to be used (see paragraph 4.2). Moreover with the present method it is possible to use such large time steps as with the Rai [11], [13] method but for a lower computational cost, because the implicit stage of the present method consist on the resolution of "simple" tridiagonal instead of "block" tridiagonal linear systems.

The sub-domain coupling as well as the non-reflecting treatment of the inlet and outlet boundary conditions are based on the use of characteristic relations as proposed in [21]. For the coupling of boundaries with non-coincident points, a bilinear (on the quasi-3D case) or trilinear (on the 3D case) interpolation is used. When coupling stationary and rotating rows, a transformation of the conservative variables from one reference frame to the other is also required.

4. COMPRESSOR DESCRIPTION

The ECL4 is a single stage experimental compressor representative of the first stage of an highly loaded HP compressor. This compressor has been designed by SNECMA in 1990 and its specifications at the design point are :

- Pressure ratio 2.25
- Isentropic efficiency 0.855
- Flow rate 18.54 kg/s
- Relative tip velocity 380 m/s
- Rotational speed 14590 rpm

The compressor is composed of a non-radially stacked inlet guide vane (igv), a rotor, and a variable stator (the flow path is shown on Fig. 1). The hub and the casing have a significant amount of convergence, especially at the igv and rotor locations producing some radial components. The gaps between the blade rows represent 45% of the axial rotor mid-span axial chord allowing non negligible interactions, whose consequences on global performances are to be investigated. Due to the temporary lack of unsteady measurements on this compressor, numerical results will be considered only from a qualitative point of view.

5. NUMERICAL RESULTS

The computations for the compressor stage previously described are performed as follows.

The unsteady interaction solutions are started from either initial states obtained from through-flow calculations or steady-state solutions. The steady solutions are calculated using the same code but with constant inter-row boundary conditions prescribed at the igv outlet, rotor inlet, rotor outlet and stator inlet. These conditions are evaluated from a "steady" coupling between the rows by using a peripheral averaging treatment at the interface planes. The periodic unsteady solution is independent from the initial state, but the transient is slightly shorter when a steady-state solution, instead of a through-flow calculation, is used as initial state.

The standard boundary conditions used for single blade row calculations are also applied at the stage inlet and outlet during the unsteady computations : total temperature and total pressure are imposed at the inlet of the stage along with the flow direction and the static pressure is prescribed at the stage exit. Some preliminary tests showed that the use of non-reflecting boundary conditions instead of standard boundary conditions yields to shorter transient but modifies slightly the compressor operating conditions. Therefore, although non-reflecting boundary conditions are usually considered more appropriate for unsteady computations, the following simulations use standard boundary conditions. On the blades profiles, tangency conditions are prescribed for inviscid flows and no-slip conditions for viscous flows.

The blade number for each row has been modified from (42,50,78) to (50,50,75). Consequently the rotor geometry is preserved, while the igv and stator angular spacings are modified. With this technique an angular sector containing two igv blades, two rotor blades and three stator blades is enough to describe the unsteady flow field in the whole compressor, while an angular sector containing one igv blade and one rotor blade is enough to describe the unsteady flow field in the first two rows. At each time step, the flow is the same between each angular sector (as described above) and its "neighbours" all around the considered rows. Then spatially periodic conditions can be used along the angular sector grid circumferential boundaries.

5.1 3D inviscid case : inlet guide vane-rotor-stator

In order to investigate the interaction phenomena in the entire compressor, a 3D Euler analysis is first performed. The computational domain contains two igv passages, two rotor passages and three stator passages and is discretised by using a multi-domain approach and an H type grid for each blade row (see Fig. 2). The upstream and downstream boundaries are set about one axial chord length away from the blades. The characteristics of the considered grids are :

	Grid points
H igv	2x(90 x 31 x 25)
H rotor	2x(120 x 31 x 25)
H stator	3x(90 x 21 x 25)
Total of mesh points	467250

Table 1 : 3D Euler mesh characteristics

For this configuration, the characteristic unsteady perturbation frequency (corresponding to two igv or two rotor or three stator blades passing frequency) is equal to 6100 Hz (244 Hz x 25 angular sectors), and the reduced frequency calculated by using the igv inlet total sound speed and the rotor mid-span axial chord is equal to 0.93.

For the simulation, 64 time steps per period are considered (which corresponds to a maximum CFL number roughly equal to 30). It is numerically possible to use fewer time steps per period than 64, but this case degrades accuracy. The variations in time (normalised by the period) of the igv, rotor and stator dimensionless forces are represented on Fig. 3. As expected, it can be seen that they become periodic after a transient. The periodic phenomenon can be obtained within 50 periods (i.e. two rotor revolutions) which correspond

approximately to 6 CPU hours (on a single processor CRAY YMP computer).

Several points on the compressor map were simulated, all with the same rotational speed (nominal speed) and the same inlet conditions. For each back-pressure level, unsteady calculations were performed until a periodic solution was obtained. On Fig. 4, the time-averaged pressure ratios and efficiencies (calculated at the rotor outlet and at the stator outlet) for each computation are plotted. All operating points have almost the same flow rate, the rotor being everywhere started.

The evolution of the compressor flow field at the mid-span section during a period (after the establishment of the periodic unsteady flow) for the lowest back-pressure (operating point 0) is represented on Fig. 5. In this case, both rotor and stator are started. Therefore flow fields are identical in all igv blade passages and in all rotor passages upstream of the normal shocks. On these graphs, it appears that the oblique shocks generated at the leading edge of the rotor become weaker upstream and finally degenerate in the igv passage into pressure waves which are reflected at the igv blade surfaces. At the same time, the stator is strongly influenced by the rotor passing and the unsteady effects are clearly different between the three stator blade passages.

A view of the instantaneous compressor flow field at the mid-span section for operating points 1, 2, 3, 4 and 5 is represented on Fig. 6. From Fig. 5 and Fig. 6, it appears that for operating points 0, 1 and 2 the stator is blocked and the shock in the stator blade passage moves upstream with increasing back-pressure, while the flow in the rotor remains unchanged. For operating points 3, 4, and 5 the stator is unstarted and the shock in the rotor blade passage starts to move upstream when the back-pressure is increased. This behaviour confirms the fact that for operating points 0, 1 and 2, the compressor pressure ratio and isentropic efficiency are controlled only by the stator (see Fig. 4). For all operating points, the flow fields are identical in the two igv blade passages, identical but out of phase in the two rotor blade passages, and quite different in the three stator blade passages.

On Fig. 7 are plotted at the mid-span the unsteady absolute angles and velocities at the igv outlet, versus the tangential location. The flow angles experience a 5° local variation and the flow velocities change by an amount of 25m/s, due to the passing of the weak oblique shocks. Fig. 8 show at the stator inlet, a 10° flow angle variation which is due to both "wakes" emanating from rotor blades moving downstream and stator potential disturbances moving upstream. Unsteadiness of the velocities (up to 25m/s) is uniformly distributed on a time-averaged distribution reproducing the stator periodicity ; the small variations in inlet conditions between two neighbouring stator blade passages are enough to produce significant differences on the forces acting on the blades.

It is important to notice that those results are valid only for operating point 0, where back-pressure is the lowest, and which simulates a rather mismatched configuration (the stator profiles operate at negative incidence). In fact, the unsteady angle and velocity amplitudes at the stator inlet are the smaller, the higher is the back-pressure (i.e. the closer we are of a good matching between rotor and stator flows). Mid-span conditions for operating point 5 present only a 4° angle unsteady variation and 12m/s velocity perturbation (see Fig. 9). Concerning the radial evolution of those variations, a general trend is noticed whatever the operating point. At the igv outlet, angle variations decrease with increasing spanwise location, and velocity amplitudes are maxima around mid-span ; at the stator inlet, angle variations increase with increasing radius and, again, maximum velocity variations occur around mid-span.

If one is interested in the global interaction between the three blade rows, one may look at the unsteady forces acting on each blade. For every operating point, an harmonic analysis is performed on the forces related to each blade of the angular sector.

The 2nd and 4th harmonics of the igv forces (corresponding to once and twice the frequency of rotor blade passing) are constant versus the operating point, except for the last, where the rotor is slightly unstarted (see Fig. 10). Fig. 11 shows that at mid-span, unsteady pressures are concentrated in the trailing edge region of the igv pressure side, where the rotor leading edge shocks mainly impact ; the reflection of those shocks give some local maximum pressure coefficient on the suction side.

On the rotor, the harmonics of interest are the 2nd and the 4th corresponding to the igv passing, and the 3rd, corresponding to the stator periodicity. The 2nd harmonic gradually increases with the back-pressure (quite similarly to the mean value of the force, representing the increasing load), whereas the 3rd and 4th harmonics decrease for the last operating point (see Fig. 12). Fig. 13 shows how the pressure harmonics are located on the mid-span blade surface (for operating point 5 where the shock is the more upstream positioned in the rotor blade passage). One must first notice that levels of unsteady pressures are much lower than in the igv or in the downstream stator (see Fig. 11 and Fig. 15). The 2nd harmonic is concentrated at the leading edge and on the strong inter-blade shock, the 3rd harmonic (revealing the influence of the stator) has its higher values around the trailing edge and the 4th harmonic has a quite uniform level on the pressure side. An examination of the upper part of the blade would reveal that higher levels of 2nd harmonics appear with increasing radial position (the shock getting stronger), while 3rd harmonic decrease. Investigating the hub region leads to opposite trends ; higher levels of 3rd harmonic indicate the induced effect of the stators (more loaded near the hub), and lower levels of 2nd harmonics, corresponding to the smearing of the rotor shock. Of course, all these comments need to be connected with the operating point chosen, which fixes the stator transonic zone which influences the unsteady pressures on the rotor blades.

On the stator, where only the 2nd and 4th harmonics are significant, one interesting feature is the substantially different behaviour of each of the three blades of the reference angular sector (the blades numbering is presented on Fig. 2). As shown on Fig. 14, the stator blades 1 and 2 experience respectively the lower and higher level of unsteadiness till we reach operating point 5. The discrepancy between blades 1 and 2 is nearly constant (30% of the maximum value) until the rotor shock configuration begins to be unstarted (operating point 5). When operating point 5 is reached, the lower and higher level of unsteadiness appear on the stator blades 2 and 3 respectively. For this point, the local 2nd harmonic of pressure for the three stator blades are plotted on Fig. 15. The time-averaged local pressure distributions being very similar, the disparity does not affect individual stator blades performances, but is quite remarkable since it reveals a pitchwise non-uniformity concerning stator unsteady inlet conditions. This, of course, needs to be confirmed by experimental evidence (the present simulation doesn't take into account all viscous effects such as corner stalls, strong trailing edge wakes, leakage effects...). However the interest of such a study remains, as it could lead to an optimum positioning of the blades of a fixed row versus the

blades of an upstream fixed row (here the igv), with the aim of minimising unsteady forces on the blades.

5.2 Quasi-3D viscous case : inlet guide vane-rotor

In order to investigate more precisely the inlet guide vane-transonic rotor interaction, a quasi-3D Navier Stokes analysis is also performed. The stream surface selected was initiated by a preliminary through-flow calculation, positioning the operating point near the peak efficiency. The mean stream surface radius is approximately 80% of the tip rotor radius. The computational domain contains one igv passage and one rotor passage. It is discretised using a multi-domain approach and an H-C-H type grid for each row (see Fig. 16). The upstream and downstream boundaries are set about one and half axial chord length away from the blades. The characteristics of the considered grids are :

	Grid points
H upstream igv	59 x 57
C around igv	161 x 21
H upper igv	72 x 77
H upstream rotor	21 x 193
C around rotor	279 x 35
H upper rotor	131 x 31
Total of mesh points	30167

Table 2 : 2D Navier-Stokes mesh characteristics

For this configuration, the characteristic unsteady perturbation frequency (corresponding to one igv or one rotor blade passing frequency) is equal to 12200 Hz (244 Hz x 50 angular sectors), and the reduced frequency calculated by using the igv inlet total sound speed and the rotor axial chord length is equal to 1.86. The Reynolds number computed on the basis of the rotor chord length and upstream stagnation conditions is roughly equal to 4,000,000.

For the simulation, 192 time steps per period are considered (which gives a maximum CFL number roughly equal to 650). As in the 3D inviscid case it is also possible to use fewer time steps per period than 192, but this results in poorer accuracy. The variations in time (normalised by the period) of the igv and rotor dimensionless force are represented on Fig. 17. As expected, it can be seen that they become periodic after a transient. The duration of the transient mainly depends on the reduced frequency of the unsteady phenomenon and on the nature of the flow. For an inviscid flow, the dynamics of the unsteady phenomenon are only controlled by the fluid inertia, while for a viscous flow the influence of viscous damping terms is also important. The viscous case being characterised by damping effects and a larger frequency requires a longer transient than the inviscid case. The unsteady phenomenon can be completely described within 150 periods (i.e. three rotor revolutions) which correspond approximately to 3 CPU hours (on a single processor CRAY YMP computer).

The evolution of the flow field around the blade during a period (after the establishment of the periodic unsteady flow) is represented on Fig. 18-19. The axial momentum contours are used in order to show at the same time shocks, boundary layers and wakes. On these graphs, it appears that the oblique shocks generated at the leading edge of the rotor become weaker upstream and finally degenerate in the igv passage into pressure waves which interact with the boundary layers and are reflected at the igv blade surfaces. At the same time, the wakes generated by igv blades interfere with the moving oblique shocks.

The igv unsteady pressure distribution (see Fig. 20) shows the fluctuations due to the impact and reflections of the shocks : these fluctuations are larger than in the 3D Euler case, and this is mainly due to the shock intensity, to the shock-boundary layer interaction and to the much better adapted mesh. The pressure variations on the rotor (see Fig. 20) are much smaller than the pressure variations on the igv.

The passing of the oblique shocks and the shock-wake interaction modify significantly the flow angles and velocities at the igv outlet. The outlet angles experience up to 8° variation and velocities vary up to 80m/s (see Fig. 21). One might summarise the time-evolution of those values by a time-averaged value (seen in the absolute frame) plus an unsteady variation, steady in the relative frame. Fig. 22 shows the igv outlet flow angle and velocity perturbations, seen in the rotor frame. The sharp gradient corresponding to the crossing of the oblique shock appears clearly.

On Fig. 23 is plotted the radial igv outlet angle distributions, as given by a steady 3D Navier-Stokes computation, and by steady azimutaly averaged experimental data. Three-hole probes were used at different radial locations to give total pressure and flow angle data. The discrepancy appearing between the two distributions, especially in the 50%-80% span region, can be due to the unsteady igv-rotor interaction. The numerical simulation has shown that sharp pressure gradients (corresponding to large angle and velocity gradients) are moving with the rotor blade, and this may disturb the angle measurements. Of course, this assumption has to be confirmed by further measurements, in particular using a non-intrusive unsteady measurement technique such as laser anemometry. Moreover, the unsteady phenomena previously described need to be validated with unsteady data.

6. CONCLUSION

Rotor-stator interactions in a single stage transonic compressor have been numerically investigated, with two codes resolving the unsteady 3D Euler and quasi-3D Navier-Stokes equations. These solvers use an implicit scheme which allows large time steps (thus reducing calculation costs) while keeping enough accuracy and robustness for the industrial treatment of interactions problems in highly loaded compressor blade rows. These properties make the method particularly attractive for industrial use.

The mutual influences of the moving and fixed rows of the 3D compressor has been discussed, considering several operating points, and the harmonic analysis of the unsteady pressures and forces has shown different behaviours between neighbouring stator blades. Then, the igv-rotor interaction has been simulated with the viscous code, and it was noticed how much the igv outlet angles can be disturbed by oblique shocks emanating from the rotor leading edges.

All the previous results qualitatively correspond to the behaviour observed in experiments with similar configurations. The natural step following this numerical investigation is a quantitative validation against unsteady experimental data, and this will be the subject of future work.

Another point of interest is the use of the code for different configurations in order to determine the influence of design parameters (axial gap, igv stager, blade number...). This type of study will allow compact stage geometries to be designed while preserving compressor design point characteristics and safety margins.

However, some efforts are still needed in order to improve the turbulence model used in the unsteady computations. The two transport equations k-ε turbulence model coupled with the quasi-3D equation system seems a more appropriate approach for this type of simulation, because it describes more accurately the turbulence kinetic energy transfer from one blade row to the other. Nevertheless the inclusion of this

model will significantly increase the computation time and probably will adversely affect the solver robustness (stability).

7. ACKNOWLEDGMENT

The authors wish to thank Snecma for permission to publish this paper. Their most sincere gratitude goes to M. Villain for his contribution to this work.

8. REFERENCES

1. Cherrett, M.A., Bryce, J.D. and Ginder, R.B. : "Unsteady 3D Flow in a Single-Stage Transonic Fan. Part I : Unsteady Rotor Exit Flow Field", ASME Paper 94-GT-223, 1994.
2. Cherrett, M.A., Bryce, J.D. and Ginder, R.B. : "Unsteady 3D Flow in a Single-Stage Transonic Fan. Part II : Unsteady Rotor Exit Flow Field", ASME Paper 94-GT-223, 1994.
3. Vuillez, C. and Petot, B. : "New Methods, New Methodology Advanced CFD in the Snecma Turbomachinery Design Process", AGARD Lecture Series 195, 1994.
4. Ni, R.H. and Sharma, O. : "Using 3D Euler Flow Simulations to Assess Effects of Periodic Unsteady Flow Through Turbines", AIAA Paper 90-2357, 1990.
5. Saxer, A.P. and Giles, M.B. : "Predictions of Three-Dimensional Steady and Unsteady Inviscid Transonic Stator/Rotor Interaction With Inlet Radial Temperature Nonuniformity", ASME Paper 93-GT-10, 1993.
6. Trepanier, J.Y., Paraschivoiu, M. and Reggio, M. : "Euler Computations of Rotor-Stator Interaction in Turbomachinery Cascades using Adaptive Triangular Meshes", AIAA Paper 93-0386, 1993.
7. Engel, K., Eulitz, F., Faden, M. and Pokorny, S. : "Numerical Investigation of the Rotor-Stator Interaction in a Transonic Compressor Stage", AIAA Paper 94-2834, 1994.
8. Fourmaux, A. : "Assesment of a Low Storage Technique for Multi-Stage Turbomachine Navier-Stokes Computations", AD Vol. 40, Unsteady Flows in Aeropropulsion, ASME 1994.
9. Hah, C., Puterbaugh, S.L. and Copenhaver W.W. : "Unsteady Aerodynamic Flow Phenomena in a Transonic Compressor Stage", AIAA Paper 93-1868, 1993.
10. Jorgenson, P. and Chima, R. : "An Unconditionally Stable Runge-Kutta Method for Unsteady Flows", AIAA Paper 89-0205, 1989.
11. Rai, M.M. and Madavan, N.K. : "Multi-Airfoil Navier-Stokes Simulations of Turbine Rotor-Stator Interaction", AIAA Paper 88-0361, 1988.
12. Rao, K.V., Delaney, R.A. and Dunn, M.G. : "Vane-Blade Interaction in a Transonic Turbine, Part I : Aerodynamics", Journal of Propulsion and Power, vol. 10, no. 3, 1994.
13. Yang, R.J., Lin, S.J. and Rai, M.M. : "Unsteady Aerodynamics of Rotor-Stator Interaction in a Turbine Stage", AIAA Paper 88-0360, 1988.
14. Yang, R.J. and Lin, S.J. : "Numerical Solutions of Two-Dimensional Multistage Rotor/Stator Unsteady Flow Interactions", Journal of Propulsion and Power, vol. 10, no. 6, 1994.
15. Liamis, N. and Couaillier, V. : "Unsteady Euler and Navier-Stokes Simulations with an Implicit Runge-Kutta Method", Proceedings of the Second European Computational Fluid Dynamics Conference, September 5-8 1994, Stuttgart, Germany, John Wiley & Sons, 1994.
16. Vuillez, C. and Veuillot, J.P. : "Quasi-3D Viscous Flow Computations in Subsonic and Transonic Turbomachinery Bladings", AIAA Paper 90-2126, 1990.
17. Michel, R., Quemard, C. and Durant, R. : "Application d'un schéma de longueur de mélange à l'étude des couches limites turbulentes d'équilibre", ONERA NT no. 154, 1969.
18. Cambier, L. and Escande, B. : "Calculation of a Three-Dimensional Shock Wave - Turbulent Boundary Layer Interaction", AIAA Journal, vol. 28, no. 11, 1990.
19. Jameson, A., Schmidt, W. and Turkel, E. : "Numerical Solution of the Euler Equations by Finite Volume Methods Using Runge-Kutta Time-Stepping Schemes", AIAA Paper 81-1259, 1981.
20. Lerat, A., Sides, J. and Daru, V. : "An Implicit Finite-Volume Method for Solving the Euler Equations", Lecture Notes in Physics, vol. 170, Springer Verlag, 1982.
21. Viviand, H. and Veuillot, J.P. : "Méthodes pseudo-instationnaires pour le calcul d'écoulements transsoniques", ONERA Publication no. 1978-4, (English translation, ESA TT 561) , 1978.

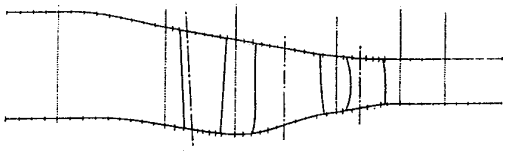

Figure 1 : ECL4 flowpath

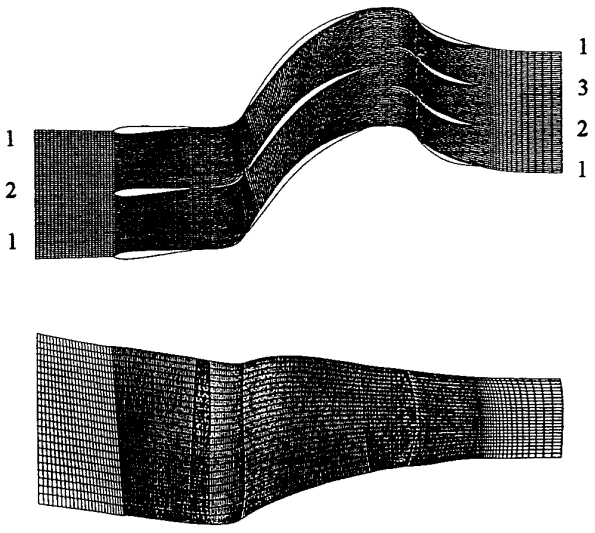

Figure 2 : Multidomain decomposition and overall view of the grid

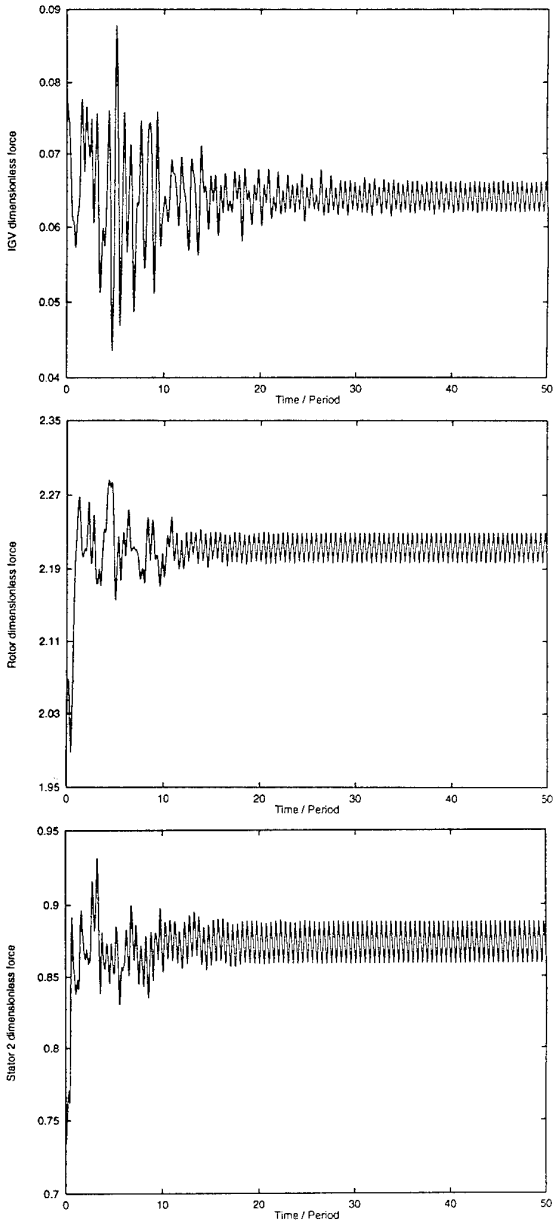

Figure 3 : Blade forces variation in time

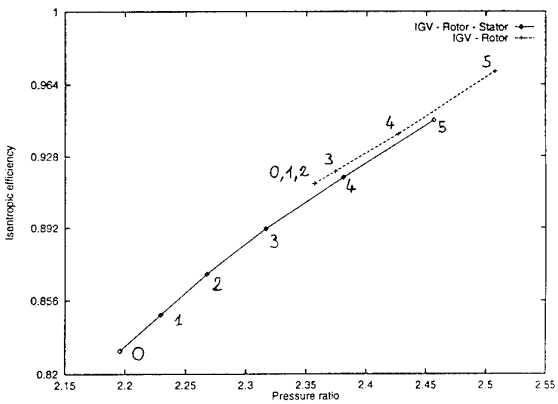

Figure 4 : Operating points location

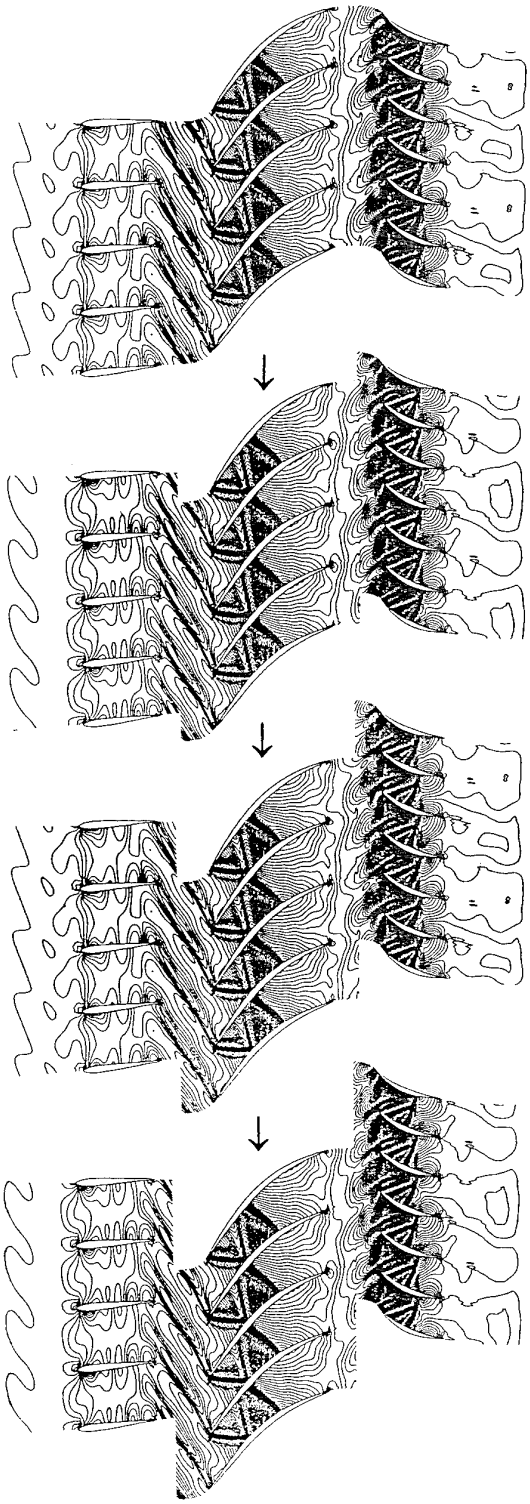

Figure 5 : Compressor instantaneous pressure contours at mid-span for operating point 0 during a period

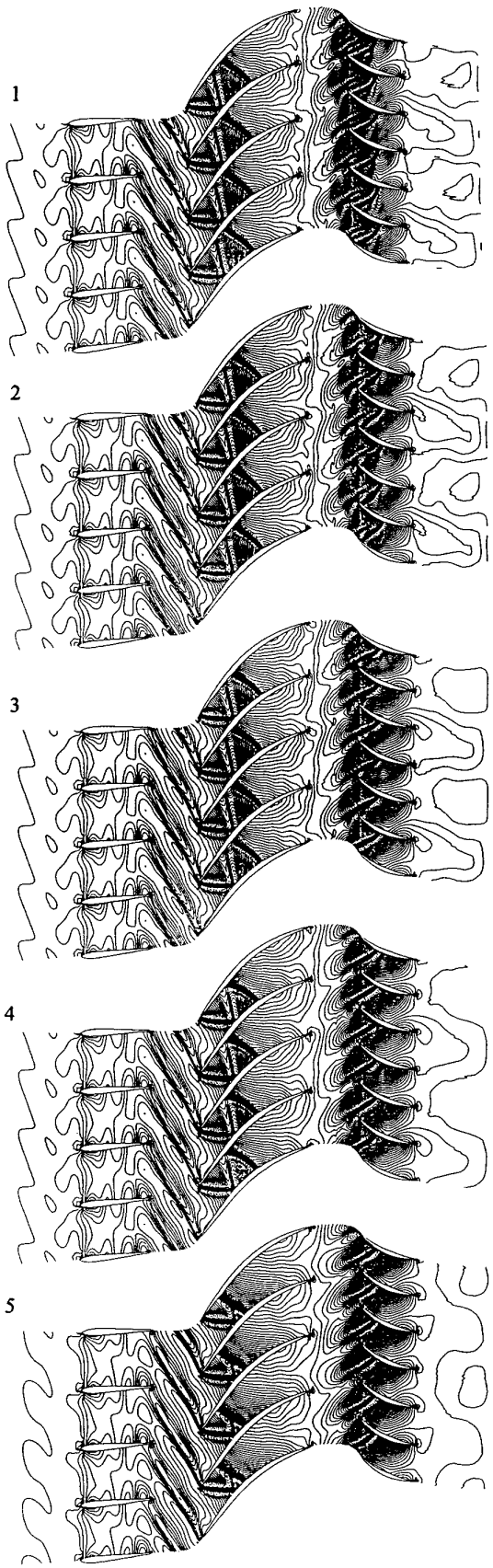

Figure 6 : Compressor instantaneous pressure contours at mid-span for operating point 1, 2, 3, 4 and 5

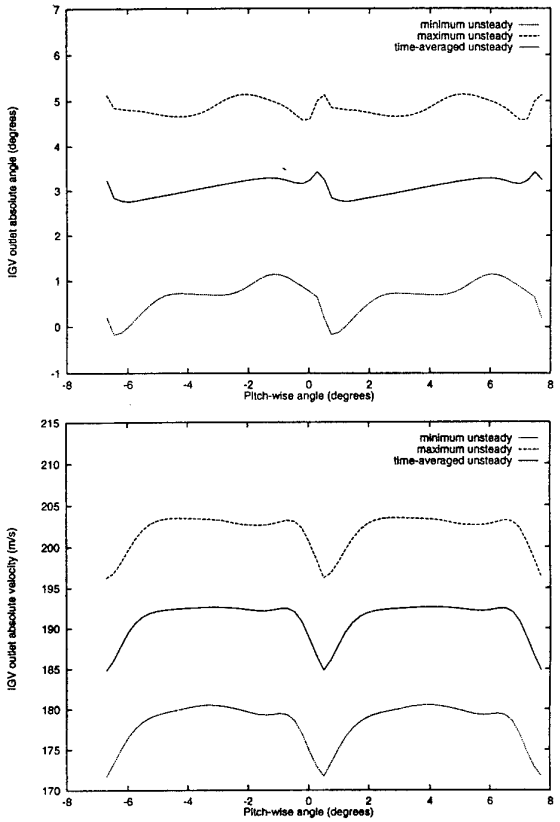

Figure 7 : IGV outlet absolute angle and absolute velocity variations at mid-span for operating point 0

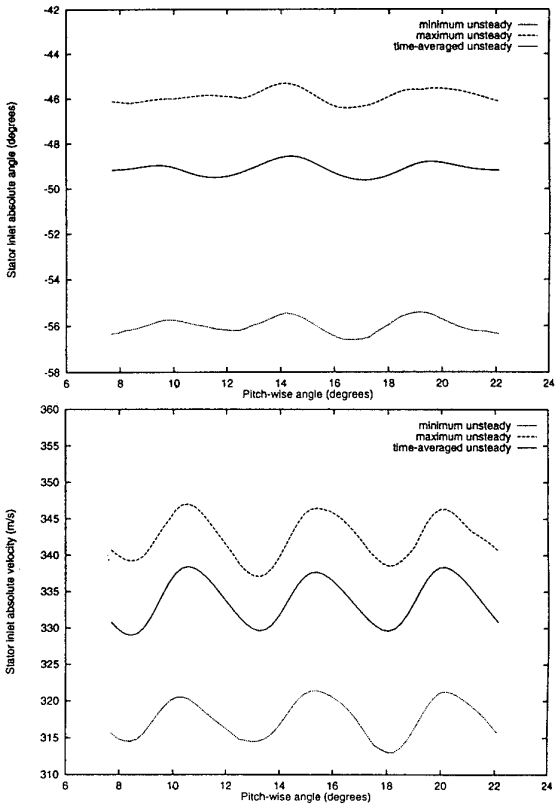

Figure 8 : Stator inlet absolute angle and absolute velocity variations at mid-span for operating point 0

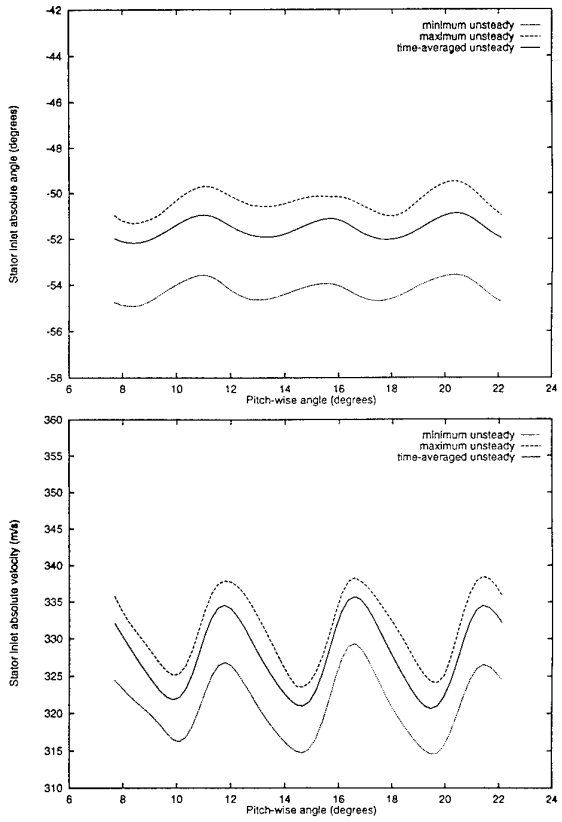

Figure 9 : Stator inlet absolute angle and absolute velocity variations at mid-span for operating point 5

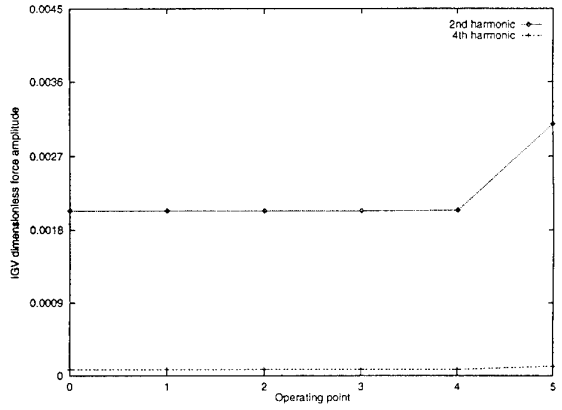

Figure 10 : Harmonic amplitudes of IGV forces versus the operating point

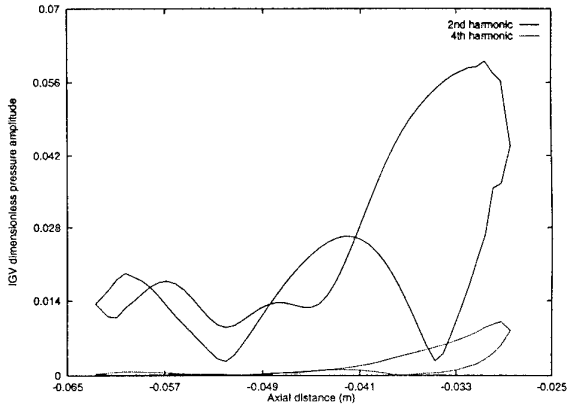

Figure 11 : Pressure harmonics at the IGV mid-span for operating point 5

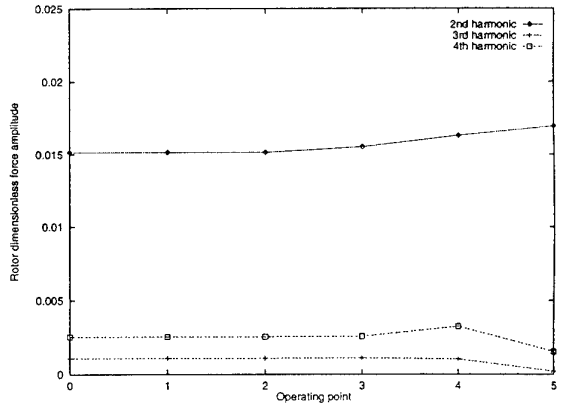

Figure 12 : Harmonic amplitudes of Rotor forces versus the operating point

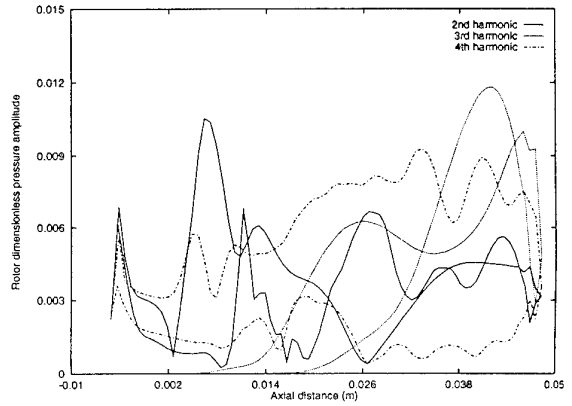

Figure 13: Pressure harmonics at the Rotor mid-span for operating point 5

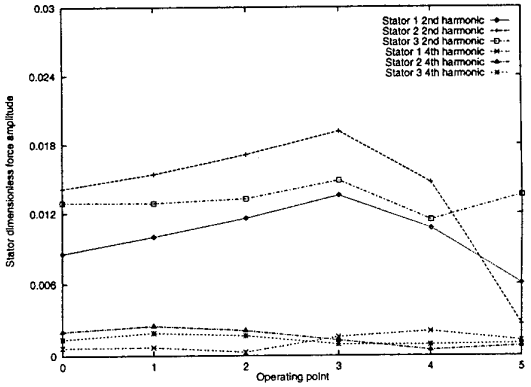

Figure 14 : Harmonic amplitudes of Stator forces versus the operating point

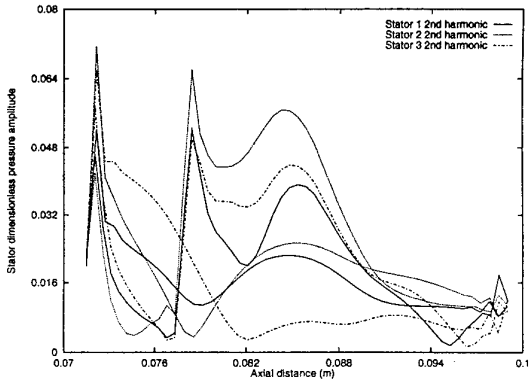

Figure 15 : Pressure harmonics at the Stator mid-span for operating point 5

Figure 16 : Multidomain decomposition and overall view of the grid

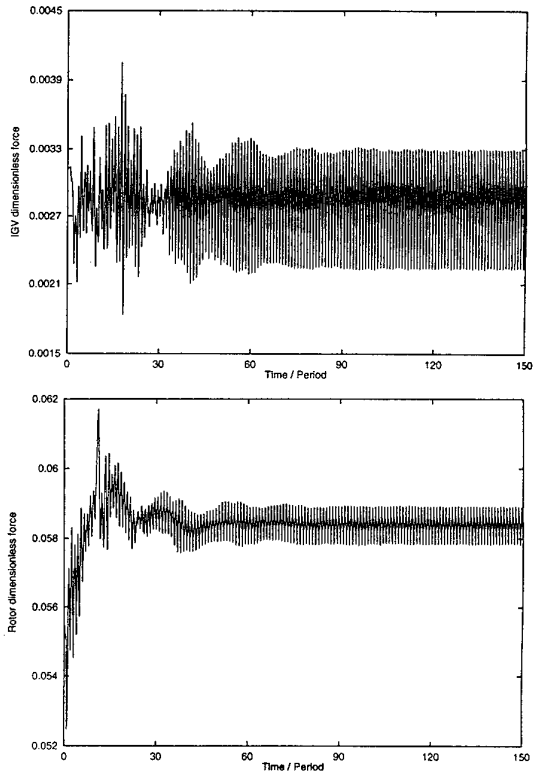

Figure 17 : Blade forces variation in time

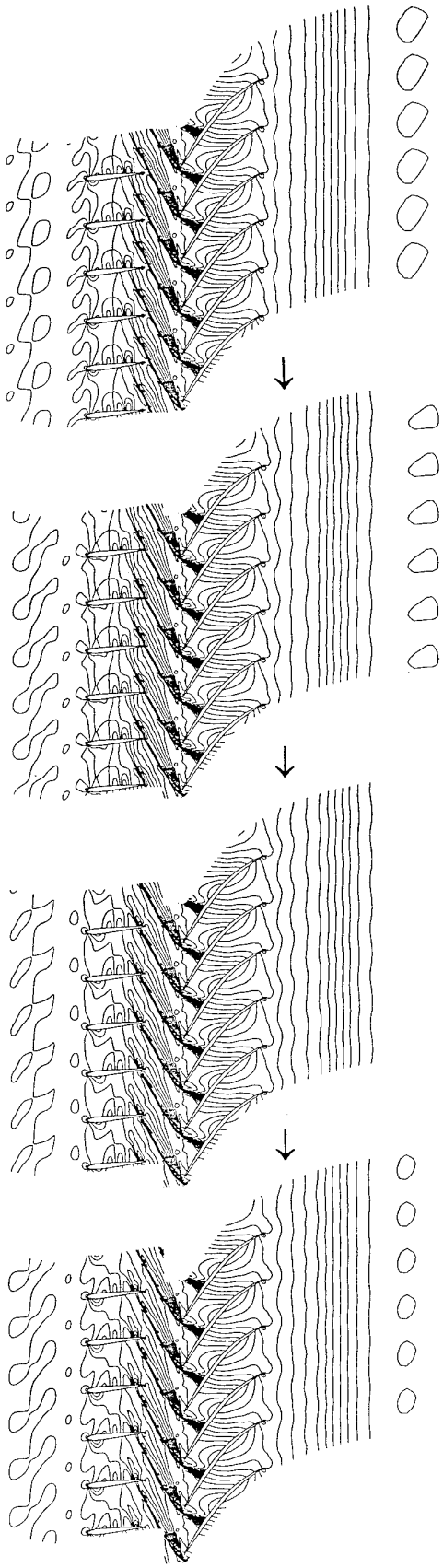

Figure 18 : Instantaneous pressure contours variation during a period

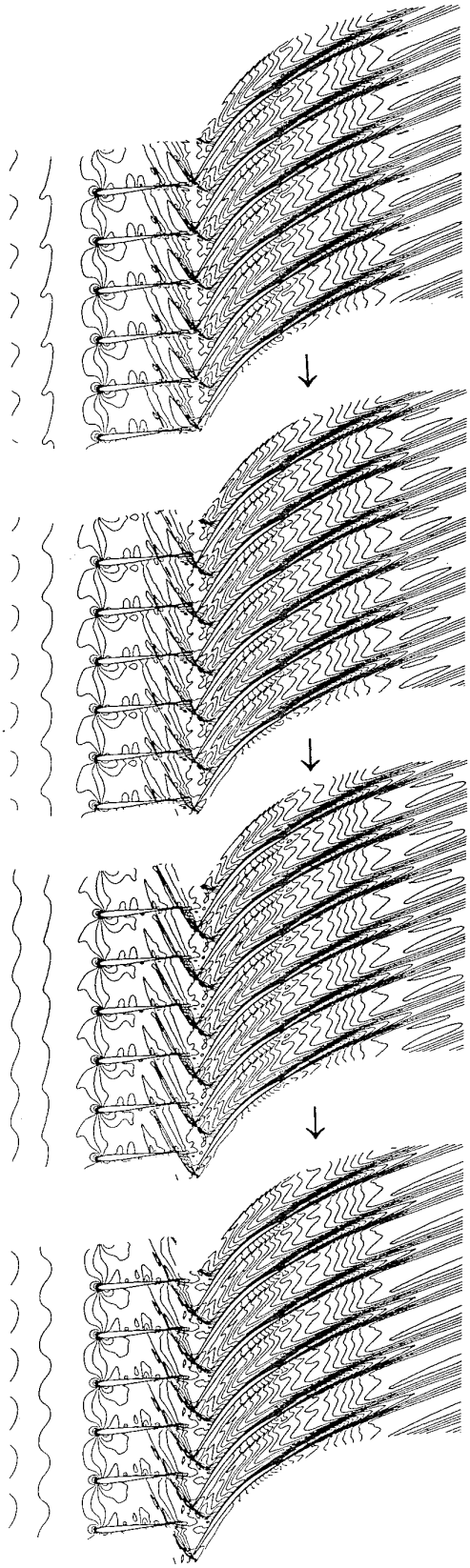

Figure 19 : Instantaneous axial momentum contours variation during a period

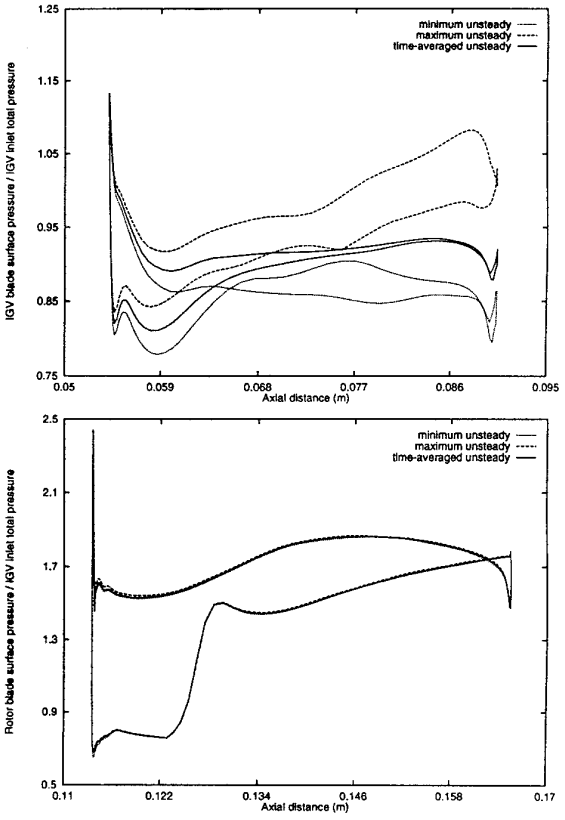

Figure 20 : Pressure variation on IGV and Rotor blade surfaces

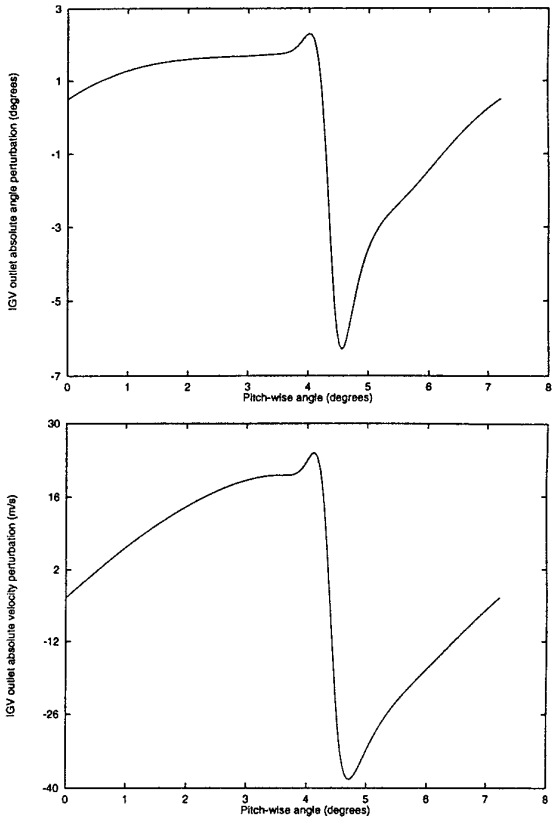

Figure 22 : IGV outlet absolute angle and absolute velocity perturbations (seen in the rotating frame)

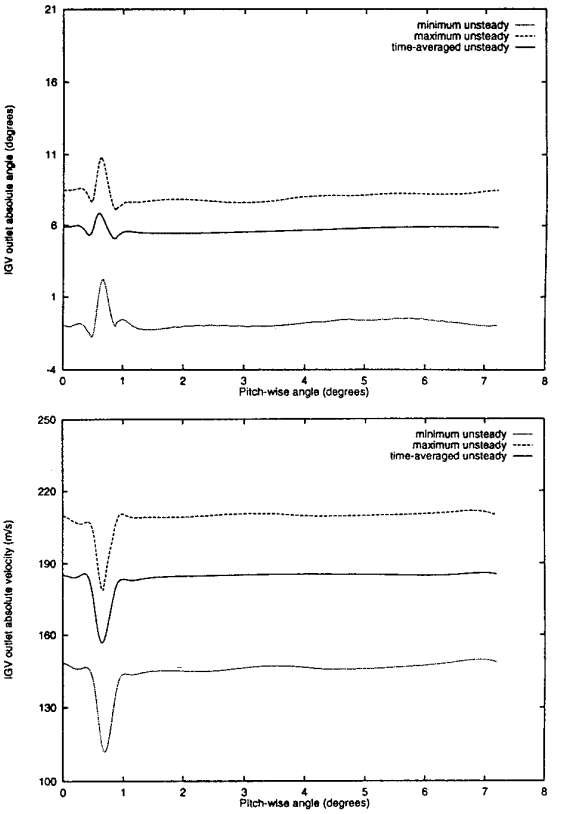

Figure 21 : IGV outlet absolute angle and absolute velocity variations

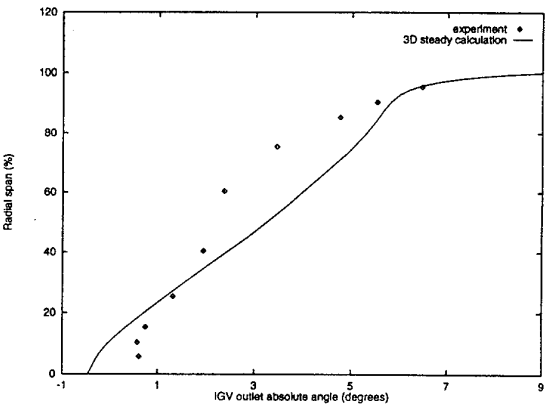

Figure 23 : IGV outlet absolute angle radial distribution

UNSTEADY FLOW AND LOSS PRODUCTION IN CENTRIFUGAL AND AXIAL COMPRESSOR STAGES

W.N. Dawes
University of Cambridge
Whittle Laboratory, Madingley Road
Cambridge, CB3 0DY
UK

Abstract

The aim of this paper is to help advance our understanding of the complex, three-dimensional, unsteady flows associated with the inter-blade row interactions in compressor stages. To achieve this, time-resolved, 3D, unsteady Navier-Stokes simulations were performed for two contrasting stages: a splittered centrifugal compressor with a vaned diffuser; and a transonic axial flow compressor. The interest in the first stage is the interaction with the diffuser blades of the jet-wake flow emerging from the wheel. In the second stage the focus is on the interaction of the rotor overtip leakage vortex with the downstream stator row.

The predicted flowfields were interrogated from the perspective of loss production to try and determine any contribution of the unsteady flow to the loss levels and, hence, to the time-average performances of the stages. Specifically, the time-averaged entropy production rate was compared with the entropy production rate of the time-averaged flow. Thereby, any contribution to loss production directly associated with unsteadiness could be identified.

Introduction

The first study was concerned with a centrifugal compressor stage. The background to this is as follows. The performance of a centrifugal impeller is often very good but when the wheel is combined with a vaned diffuser the performance of the overall stage is often disappointing. The diffuser performance is known to be very sensitive to inlet blockage distribution and distortion and so it seems likely that the performance of the diffuser is adversely affected by the jet-wake phenomena emerging from the wheel. The extent to which this performance degradation is due to unsteady interactions or to the time-mean axially distorted inlet flow is not known.

An experimental investigation of the nature of impeller - vaned diffuser interaction was published by Krain (1981). Substantial periodic flow unsteadiness was observed in the entry zone to the vaned diffuser with large temporal variations of swirl angle, of the order of 10-15 degrees, and large spanwise variations from hub to shroud, of the order of 20-25 degrees. However, and perhaps because the diffuser inlet Mach numbers were not supersonic, the presence of the vaned diffuser was observed to cause little unsteady variation in the impeller internal flow. In a subsequent lecture Krain (1984) presented some measurements downstream of the diffuser vane throat which showed that despite the large periodic unsteadiness in the entry zone, levels of unsteadiness decreased rapidly downstream of the throat.

Inoue (1980) published a similar investigation, albeit for a much more lightly loaded stage than that of Krain and with a lower solidity diffuser, and found the same large periodic flow unsteadiness in the diffuser vane entry zone. He too found that the magnitude of this periodic unsteadiness diminished rapidly downtream of the throat so that in the outer part of the diffuser no periodic unsteadiness could be observed.

In neither investigation did the impeller flow mix out before arriving at the diffuser vane leading edges as is sometimes assumed in design (see for example Johnston & Dean (1966)). For vaneless diffusers Senoo (1977) reports that spanwise (hub-tip) distortions mix out less rapidly than circumferential distortions and there is a suggestion that this is true also for vaned diffusers in both Krain's and Inoue's work. In any case this calls into doubt much of the current basis for design of vaned diffusers.

Paper presented at the AGARD PEP 85th Symposium on "Loss Mechanisms and Unsteady Flows in Turbomachines", held in Derby, United Kingdom, 8-12 May 1995, and published in CP-571.

The flowfield in the centrifugal stage predicted in the present study, validated against experimental data, displayed a complex, unsteady interaction especially in the neighbourhood of the diffuser entry zone which experiences large periodic flow unsteadiness. Downstream of the throat, although the magnitude of this unsteadiness diminishes rapidly, the flow had a highly distorted three-dimensional character. The rather high loss levels in the diffuser were then investigated and also comparedwith the levels expected from "equivalent" steady flow analysis performed by using the circumferentially averaged exit flow from the impeller as inlet to the diffuser. It was concluded that in fact little loss could be attributed directly to unsteady effects but rather that the principle cause of the high losses observed in the diffuser was the strong spanwise distortion in swirl angle at inlet which initiated a strong hub/corner stall.

The second and contrasting simulation was of the unsteady flow in a transonic compressor stage. The focus in the simulation was the endwall flow, its contrast with the mid-span flow and, in particular, the interaction of the rotor overtip leakage flow with the downstream stator.It is well-known that compressor rotor performance is affected by the size of the clearance and the associated overtip leakage flow. Many studies have been published over the years concentrating on rotors in isolation (see for example Hunter et al (1982), Lakshminarayana et al (1982), Inoue et al (1986), Chen et al (1991) and Storer (1991)) and these have contributed greatly to our understanding of the role of the rotor leakage flow both as a loss mechanism and a destabilising influence on the endwall flow. However, rather less is known about the impact of the rotor overtip leakage on the downstream stator where it is imagined that the axial velocity deficit associated with the rotor clearance flow is likely to put the stators at extreme and circumferentially varying incidence towards the casing. In addition it seems likely that the rotor overtip leakage vortex will interact with the stators; this may in itself be an important unsteady loss mechanism (Denton (1993)).

The inspiration for the present study is derived from a paper by Howard et al (1993) who reported an experimental study on a low speed, four stage axial compressor in which the performance of the third stage rotor and stator was measured for two different rotor clearances. The measurements took the form of radial and circumferential traverses downstream of the rotor and downstream of the stator using conventional pneumatic probes; no time-resolved measurements were attempted. Two rotor clearances were used, 1.2% and 3.0% of tip chord length. The circumferentially averaged rotor loss was observed to be substantially larger over the outboard 15% of the span for the larger clearance case - much as expected. The circumferentially averaged stator loss was also observed to be substantially larger over the region from 70% to 90% of the span for the larger rotor clearance case. Just near the casing, however, the stator loss seemed to be lower with the increased rotor clearance; this was attributed to some kind of "secondary flow redistribution mechanism". Although the magnitude of the observed effects was large, it is difficult to infer from "averaged" pneumatic probe data the various possible physical mechanisms and their relative contributions. The authors' tentatively concluded that gross axisymmetric effects (especially the large levels of mean flow incidence on the stators near the casing) were more important that any unsteady interaction; however, it is hard to sure.

The successful design of multistage compressors relies critically on our ability to model the flow in the endwall regions. It is therefore of great relevance to establish the physical mechanisms at play in the endwall region. Three classes of model have been persued to date with a range of modelling requirements. Classic axisymmetric throughflow methods like that of Howard et al (1992) rely on correlated loss and deviation angles, especially near the crucial endwall, and are at their mercy. Fully 3D steady flow Navier-Stokes solvers (see for example Denton (1992) & Dawes (1992)) can be coupled blade row to blade row by circumferentialy averaging the intra-blade flow. This removes the need to correlate loss and flow angle but forcing the flowfield to be axisymmetric at an arbitrary plane between rows introduces errors of unknown magnitude (see discussion in Fritsch et al (1993)). The more sophisticated approach of Adamczyk et al (1992) attempts to include correlations relating to circumferentially averaging the unsteady flow but the origin and magnitude of these correlations is not clear.

The endwall region of both the rotors and the stators was predicted to be proportionally responsible for much more loss production than the mid-span sections of the blading. Unsteady effects were predicted

to be responsible for rather more of the total loss production in the rotors than in the stators but the unsteady loss production in the rotors did not seem to be associated with the endwall flow but rather occurred over the bulk of the blade span caused by unsteady shock motion. By contrast, the rotor overtip leakage flow was shown to cause a considerable degradation of the stator performance near the casing. In the stators nearly a third of the loss production near the endwall was predicted to be directly due to unsteady effects associated with the rotor vortex interaction and a number of individual physical loss generating mechanisms were identified.

The numerical approach

Equations of motion

The equations solved are the fully 3D unsteady, compressible, Reynolds-averaged, Navier-Stokes equations expressed in strong conservation form. The full stress tensor is retained, including the full viscous energy equation. Turbulence is modelled via k-ε transport equations (Patel et al. (1985)) together with appropriate low Reynolds number terms (Lam et al. (1981)) to handle smoothly the approach to the blade surfaces should the mesh be sufficiently fine. The application to mixed rotating-stationary frames is greatly eased if the equations are cast in the absolute frame and this is done here. This necessitates detail changes to impermeable surface boundary conditions but otherwise presents no analytic or algorithmic difficulty.

Mesh

An unstructured mesh system was adopted consisting of a set of tetrahedra. The generation of the mesh is based on a simple multi-block procedure described in detail in Dawes (1992). The mesh generated for the subject of the present study, a splittered centrifugal impeller followed by a vaned diffuser, is shown in Figure 1. This initial mesh contained around 100,000 nodes; for these exploratory simulations advantage was not taken of the solution-adaptive capability. It is recognised that the number of nodes is rather low but nevertheless effected a good compromise between accuracy and solution time. Solutions obtained in the past with of order 40,000 nodes per blade element (for example Krain at al.(1989)) have been able to capture sufficient flow physics and be in sufficiently good agreement with data to make the exercise worthwhile.

During the simulation the impeller mesh rotates at a specified rate whilst the diffuser mesh remains fixed. Once the impeller has rotated through whatever is the periodic unit the whole mesh is then indexed back and the rotation restarted. The surface between the rotating and stationary frames is referred to as the "sliding surface". The flow variables must be interpolated across this sliding surface each time step during the simulation. To ensure conservation, a volume weighted interpolation procedure is adopted. This type of moving-to-fixed block interpolation is well-known and described in more detail in Rai (1985) and Rao & Delaney (1990) amongst others. It must be stressed that the sliding surface is intended to act as a transparent internal boundary between the rotating and stationary frames transferring any axial and circumferential distortions in the flow without modification; circumferential averaging is not employed to mix out the flow across the sliding surface.

The strategy in the current approach is to model the nearest convenient integer multiple of blades in the impeller and diffuser. In this case it meant matching 14 impellor blades plus 14 splitter blades to 28 diffuser vanes (instead of the 27 in the true geometry). This strategy was adopted because of its simplicity and the advantages with respect to convergence rate and solution and post-processing storage requirements when compared with the other available methods of handling non-integer blade ratios. In particular; the "time-tilting" method of Giles (1990) has a limited range of applicability and in practical use has to be supplemented by computing an integer ratio of blades but the solution then has to be reconstructed by Fourier analysis of a large number of storage-intensive solution levels throughout the cycle; the phase-shifted periodic boundary method of Erdos (see Hodson (1984)) leads to slow convergence rates and again to unacceptably large storage requirements for 3D simulations.

The solution algorithm

The solution algorithm will be described here only in outline ; for further details see Dawes (1991,1992 & 1993). The seven equations of motion are discretised in finite volume form on each of the tetrahedral

control volumes with vertex variable storage. The primary variables are assumed to have a piecewise linear variation over cell faces between the vertices so that the flux sum for a given cell is evaluated to second order accuracy in space. The derivative terms in the viscous stresses are piecewise constant over the cell (since the primary variables are piecewise linear) and are computed by simple application of the Gauss divergence theorem. Using all the cells surrounding each individual node as a control volume then allows the evaluation of the viscous stress terms at that node. Artificial diffusion is added to control shock capture and solution decoupling. The smoothing consists of a classical blend of fourth derivatives as a general background and second derivative terms controlled in magnitude by the local strength of the pressure gradient.

At inflow boundaries the total pressure, total temperature, turbulent kinetic energy and dissipation rate and two flow angles are specified and the derivative of static pressure in the streamwise direction set to zero; at the outflow boundaries the static pressure is specified and the other variables extrapolated from the interior. At present the inflow boundary is not treated in a truly non-reflecting manner; however, the outflow uses a simple one-dimensional non-reflecting treatment based on the work of Giles (1988,1990). On solid surfaces zero normal fluxes of mass, momentum and energy are imposed. The wall shear stress can be computed either from the laminar sublayer or log law wall functions depending on whether the local value of the wall coordinate Y^+ is less than or greater than 10 respectively.Similarly the wall heat flux can be computed either from the wall normal temperature derivative if Y^+ is less than 10 or from a wall function based on Reynolds analogy. In a similar spirit if Y^+ is less than 10 the turbulent kinetic energy and the normal gradient of dissipation rate are set to zero on the surface ; otherwise k and ε are set to be consistent with the assumed log law at values of $u_\tau^2 / \sqrt{c_1}$ and $u_\tau^3 / \kappa Y_w$ respectively with Y_w the normal distance to the wall. For the present simulations the relative coarseness of the mesh means that wall Y^+ values were in the range 30 to 70 and so all viscous boundary conditions were implemented via the various wall functions.

The net flux imbalance into each cell is used to update the flow variables themselves via a four step Runge-Kutta time marching algorithm with residual smoothing inspired by the pioneering work of Jameson et al. (1987). Standard fractional step coefficients of 1/4, 1/3, 1/2 and 1 are used, conferring second order time accuracy (fourth order for linear equations). Residual smoothing (Jameson et al. (1987)) is applied after each fractional step to extend the stability domain of the algorithm. For calculations with a steady state solution as the objective the algorithm is run with spatially varying time steps (i.e., a constant CFL number imposed everywhere) and correspondingly with a spatially constant residual smoothing coefficient selected. Clearly, unsteady simulations must use a spatially constant time step which will invariably be limited by the very fine mesh in the viscous dominated regions near wetted surfaces. To alleviate this limit and make numerical simulation practical, a spatially varying residual smoothing is used, as suggested by Jorgenson et al (1989), which has the effect that in the inviscid part of the flow no residual smoothing is used and the algorithm reduces to a simple explicit time accurate integration. In the viscous dominated regions near wetted surfaces the allowable time step is increased substantially beyond the local explicit limit; nevertheless the formal second order temporal accuracy is not disrupted provided the magnitude of the residual smoothing coefficient is carefully controlled.

As well as interpolating the basic flow variables across the "sliding surface" between the rotating impeller mesh and the stationary diffuser mesh as described earlier, all the fluxes, viscous stress terms and artificial smoothing terms are also interpolated in an attempt to ensure no loss of time accuracy across this interior boundary.

Post-processing

To aid the interpretation of the unsteady simulation certain unsteady statistics are extracted:

time-average

$$\tilde{D} = \frac{1}{N} \sum_{n}^{n+N} D(n)$$

rms fluctuation

$$D_{rms} = \sqrt{\left[\frac{1}{N} \sum_{n}^{n+N} \{D(n)-\tilde{D}\}^2 \right]}$$

where D(n) is the instantaneous value at time step n of a selected variable, D, and N the number of time steps in a period. Thus plots can be made of instantaneous values, either averaged quantity or the (instantaneous - averaged) value at a selected instant during the simulation.

The averages are extracted on-the-fly as the computation proceeds such that during a given period the current time-average is that from the previous period and the current rms fluctuation is based on the instantaneous values in the previous period and the time-average of the next previous period. Limitations of computer storage have prevented the accumulation of ensembled averages.

Application to the centrifugal impeller-vaned diffuser simulation

Background

The pioneering paper by Krain (1981) seems to contain the only public-domain stage geometry and experimental data concerning centrifugal impeller - vaned diffuser interaction.The geometry he studied consisted of a splittered, radial discharge impeller, with 14 main blades and 14 splitter blades, together with a straight channel diffuser containing 27 blades. The key details of the vaned diffuser's geometry are:

radius ratio of diffuser LE/impellor exit	1.1
radius ratio of diffuser discharge/impeller exit	1.905
throat aspect ratio	1.6
length/width ratio of the channel diffuser	11.46
channel divergence angle	7.54°
diffuser vane stagger angle	17.32°

Detail measurements were made at the DFVLR using laser-two-focus velocimetry within the impeller and diffuser vane entry zone at the following operating point:

rotational speed	14000 rpm.
mass flow	5.8 kg/s
total-total pressure ratio (nominal)	2.

The unstructured mesh generated for the present numerical simulation was shown in Figure 1. For economy the number of diffuser blades was increased to 28 to allow a periodic unit of 1 main impeller blade per 2 diffuser vanes; the alternative of modelling the entire annulus was considerd excessive for a preliminary study of this nature. The impeller overtip leakage gap was not known; nominal clearances are 1.1 mm at zero rpm and 0.2 mm at 22,500 rpm.(Krain (1993)). Assuming that clearance scales with rotational speed squared (which might be true for radial clearance but not necessarily for the axial clearance at the impeller exit) suggested setting the clearance to 0.8 mm for the simulations and this was done with three nodes across the gap. The resulting mesh contains roughly 100,000 nodes and with the maximum CFL number set to around 3 required of order 1000 time steps per periodic blade passing scale. The code was run on a simple IBM RISC/6000 workstation at a processing rate of around 0.8 ms/node/time step. The boundary conditions to the simulation consisted of the rpm., inlet boundary conditions to the impellor and the diffuser exit static pressure. Some difficulty was experienced in finding a matched operating point, nevertheless the following:

rotational speed	14000 rpm.
mass flow	5.6 kg/s
static-total pressure ratio	1.70
total-total pressure ratio	1.85
total-total stage efficiency	71.2%

was predicted to be a converged, periodic solution. Convergence was judged by monitering velocity levels in the most sensitive part of the flowfield - the diffuser leading edge. Figure 2 shows the variation with time from the start of the simulation of predicted velocities in mid-pitch of the diffuser vane leading edge plane at 10%, 50% and 90% span. About 14 blade passing periods were required to produce a solution judged to be acceptably periodic over the last three to four cycles.

The impeller flow

The predicted impeller flow exhibits, by the exit from the blading, the expected development of the jet-wake structure. Figure 3 summarises the rotor flow by showing predicted time-averaged relative velocity vectors near the casing, predicted time-averaged mid-passage relative Mach numbers and a comparison of predicted and measured

time-averaged meridional velocities in a cross-flow plane towards the wheel exit at 87% of the streamwise distance through it. The predicted wake is slightly larger and pushed somewhat further over to the suction sides of the passages than in the measurements; the wake depth is nevertheless well represented. Clearly, a finer mesh and more sophisticated turbulence modelling might reduce these discrepancies somewhat. Nevertheless, in the context of the current effort aimed at advancing our understanding of the flow physics, the predicted wake structure was judged acceptable, particularly as the wake deficit itself was well predicted and it is primarily this which produces the expected velocity and flow angle variations in the diffuser entry zone.

To assess the level of unsteadiness induced in the impeller by the interaction with the diffuser the rms averaged static pressure fluctuation was derived. It was found that the majority of the impeller experienced very low levels of periodic flow fluctuation except over the last 10% of the flow passage towards the suction side where the rms pressure fluctuations were of order 5% of the local time-mean level. This lack of influence of the diffuser on the impeller was observed by Krain (1981) who measured very similar meridional velocity distributions in the 87% meridional distance plane when the impeller was tested both with and without the diffuser.

The flow in the vaned diffuser: the entry zone

Next the flowfield in the "entry zone" of the vaned diffuser (i.e., the zone from impeller discharge to diffuser throat) will be considered. The jet-wake discharge from the impeller sweeps periodically over the diffuser and induces a very strongly varying, periodic flow in the entry zone.

The variation with time of predicted meridional velocity at mid-pitch of the diffuser vane leading edge plane is compared with Krain's laser measurements in Figure 4 for about three periodic time scales. The amplitude of the periodic variation is very large: around $\pm$ 5% near the hub but nearer $\pm$ 10% at mid-span and near the casing. The agreement between predicted and measured amplitude is good. The Krain data has been ensemble averaged over 28 blades whereas in fact the flow emerging from the two different passages of the impeller is not identical (see Figure 3) and so the correct time scale for averaging should have been that associated with the number of main blades, ie.14 blades. In terms of phase, the agreement between prediction and measurement near the hub and near the casing is also good. In mid-span there is a small phase shift between the predicted and measured variations and this is associated with the slightly different locations of the wake in the prediction and the experiment discussed in the previous section.

Figure 5 shows the variations with time of predicted meridional velocity at mid-pitch of the diffuser vane throat plane and compares them with Krain's measurements. The flow is still strongly periodic in the diffuser throat in terms of blade passing time scales but the amplitudes of the variations are noticeably reduced. At mid-span and near the casing the predicted amplitude agrees well with that measured although there is disagreement over the mean level of meridional velocity near the casing and the mid-span phase shift referred to earlier still persists. The only serious discrepancy between measurement and prediction is near the hub; the reason for this has not yet been determined but is believed to be associated with uncertainty as to the precise location of the onset of the highly three-dimensional distorted flow in the diffuser downstream of the throat (to be described in the next section). The noticeable phase shifts between all the data in the throat when compared with the corresponding locations in the vane leading edge plane are simply associated with the time taken for the phenomena to convect from one location to the next.

Associated with the substantial periodic variations of meridional velocity described above are large variations of the absolute swirl angle at diffuser entry. Figure 6 plots the variations with time of predicted swirl angle at mid-pitch of the diffuser vane leading edge plane compared with Krain's measurements. The amplitude of the angle variation is very large being as high as $\pm$ 7 degrees in mid-span and around $\pm$ 5 degrees near the hub and the casing. The agreement between prediction and measurement is good near the casing and in mid-span and fair near the hub. It is very noticeable both in the predictions and the measurements that considerable flow angle variations exist from hub to casing. Near the casing the flow vector has a mean angle roughly equal to the blade inlet angle; in mid-span the mean angle corresponds to around 5 degrees negative incidence (i.e., flow direction closer to radial) onto the vanes; and near the hub the mean

incidence angle is about 10 degrees negative incidence. These are large flow incidences for vanes such as these, with very sharp leading edges, and as the next section describes a large stall is provoked in the hub-pressure side corner of the diffuser main passage.

It is clear from the previous observations that the jet-wake flow emerging from the impeller gives rise to substantial circumferential and spanwise distortions. These distortions do not mix out before arriving at the diffuser vanes' entry zone. This mixing is assumed in some design theory (eg. Dean & Senoo (1960) and Johnston & Dean (1966)); doubt must therefore be placed on the validity of design procedures of this type.

It seems reasonable to conclude from this section that good qualitative and quite fair quantitative agreement has been achieved between the predicted and measured flowfields in the entry zone to the diffuser. The next section concerns the development of this flowfield downstream of the throat in the diffuser passage as a whole.

The flow in the vaned diffuser; the passage as a whole

The predicted flow pattern in the diffuser was quite similar near the shroud and in mid-span but dramatically different towards the hub where a substantial hub-pressure side corner stall was predicted. Figure 7 shows contours of predicted time-averaged total velocity on slices through the diffuser flow near the hub, in mid-span and near the casing. The contours show the corner stall to be initiated just downstream of the vane throat; the vanes run near the hub with a flow incidence varying from 5 to 12 degrees with a mean level of around 10 degrees. The stalled zone expands rapidly downstream extending all across the vane passage before the trailing edge is reached. There is evidence of the corner stall even in the mid-span plane which is in fact virtually tangential to the separated zone over the aft half of the passage. Krain (1984) has presented some extra data for two stations downstream of the throat. In these, a zone of blockage is measured developing in the hub/pressure side corner with velocity levels fallen as low as around 25% of the passage mean value The measurements do not indicate reverse flow however, nor are they made far enough downstream to see if the low velocity zone develops into a reversed flow as predicted. The observations of Inoue (1980) also support the likelihood of the development of a corner blockage aft in the diffuser passages. It seems safest to conclude that a substantial blockage does develop in the hub/pressure side corner at this operating point but that its extent is somewhat overpredicted in the current effort.

Also of some interest is the extent to which the periodic, highly unsteady flow in the diffuser entry zone propagates downtream. The behaviour is illustrated in Figure 8 which shows two plots of (instananeous - averaged) velocity vectors in the mid-span slice a quarter of a blade-passing time period apart. The magnitudes of the velocity fluctuations decay rapidly away from the entry zone; this is already happening quite strongly by the throat region (compare also Figures 5 and 6). This sort of behaviour was observed by Inoue (1980) who found that the magnitude of the periodic flow unsteadiness in the diffuser vane entry zone diminished rapidly downtream of the throat so that in the outer part of the diffuser no periodic unsteadiness could be observed. The physical mechanism seems to be as follows. The unsteady perturbation flow takes the form in the blade-blade plane of train of vortices which can be seen quite clearly emanating from the entry zone. Vortices "A" and "B" are propagating downstream and vortex "C" is the next one forming. This pattern of propagation is periodic and locked to the blade passing time scale. Also clear in the Figure is way the vortices are damped as they propagate, seemingly being absorbed into the irregular fluctuations associated with the edge of the corner stall. The large corner stall with its relatively large natural time scale seems not to respond quickly enough to the rapid fluctuations in the entry zone but rather absorbs them and acts to damp them away.

A final point related to Figure 8 is that the time-averaged flow in alternate diffuser passages is not identical. This is because the averaging is conducted on-the-fly over a single blade passing period whereas in fact the diffuser flow was predicted to be slowly varying over a time scale of the order of 5 to 7 blade passing periods. This may be a result of conducting a simulation with a relative blade count of 14:28 instead of the true 14:27. Nevertheless it is quite plausible in a flow such as this that there could be a variety of time scales present: short scales associated with trailing edge vortex shedding phenomena, medium ones associated with the blade passing time scale and large ones

associated with the large separated zone in the long duct-like diffuser passages.

Overall the diffuser flow is characterised by the growth of a substantial corner blockage/stall and a rapid decay of periodic unsteadiness downstream of the throat. It seems likely that the corner stall is initiated by the very unfavourable flow incidence near the hub at this operating point. The spanwise variation of flow property, especially swirl angle, seems to exert a more significant influence on the diffuser performance than does the unsteady, circumferential variation in flow. There is some evidence to support this view from Senoo et al (1977), who found that spanwise (axial) distortions persisted further downstream than did circumferential distortions in vaneless diffusers.

Unsteady loss production; average vs. steady operating point;

Finally, the predicted flow field was interrogated from the perpective of loss production to try to determine the contribution of the unsteady flow to the loss levels in and hence to the time-average performance of the stage.

The only scientific measure of loss in an unsteady flow is entropy. The unsteady transport equation for entropy, s, takes the following form for adiabatic flow:

$$\rho \frac{Ds}{Dt} = \frac{1}{T} \tau_{ij} \frac{\partial u_i}{\partial x_j} + \frac{k}{T^2} \frac{\partial T}{\partial x_i} \frac{\partial T}{\partial x_i}$$

where τ_{ij} is the stress tensor, ρ the density, u_i the velocity field, x_i the space coordinate and k the thermal conductivity. The right hand side can be interpreted as the source of entropy; the left hand side represents the unsteady convection of that entropy. All the entropy produced within the flowfield will eventually pass through the exit boundary from the stage and be perceived as the "stage" loss. For a periodically varying flow the instananeous rate of entropy production will also vary periodically.

The dominant production term is the tensor product of the stress and the strain and this is quadratic in velocity. If the velocity is represented by the sum of a time-averaged and a fluctuating part , $u=\tilde{u} + u'$ then the time-average of a quadratic velocity "production" term is

$$\widetilde{u^2} = \tilde{u}^2 + \widetilde{u'^2}.$$

The first term on the right hand side represents the loss production associated with the time-averaged flow; this may be indirectly affected by unsteadiness in that the time-averaged flow may differ from an "equivalent steady flow". The second term represents the non-linear contribution to loss production directly attributable to the unsteady flow itself.

For comparative purposes an "equivalent steady flow simulation" was performed by modelling just the diffuser and with the circumferentialy averaged impellor exit flow used as inlet boundary conditions (in particular modelling the spanwise variation of flow incidence). Running to the same back pressure as the stage the diffuser was predicted to pass the same mass flow (i.e., the basic operating point did not change). The resulting predicted contours of velocity are shown in Figure 9 which should be compared with the time-averaged velocities in Figure 7. A hub/corner stall is seen to be present also in the "equivalent steady flow". The extent of the corner blockage is not quite as great as in the time-averaged flow and the reason would seem to be that in the unsteady flow the corner stall is absorbing the unsteadiness propagating from the entry zone, as discussed earlier, and this acts to increase the time-averaged size of the stalled zone.

A comparison is now made of the time-averaged entropy production rate, the production rate which would be associated with the time averaged flow and the production rate of the "equivalent steady flow". The first represents the actual performance of the stage. The difference between the first two should correspond to

loss production directly attributable to the unsteady flow itself. The result is shown below:

	impeller	diffuser
time-averaged entropy production	8.15	11.13
entropy production of the time-averaged flow	8.13	10.63
entropy production of the "equivalent steady flow"	-	9.47

($kW/m^3kg\ K$)

This shows little loss directly attributable to unsteady effects in the rotor. The diffuser is seen to contribute nearly two thirds of the overall loss. In the diffuser vanes, despite the highly unsteady flow in the entry zone, only around 5% of the loss production could be directly associated with the unsteady flow (and this is really the impeller discharge mixing out in the diffuser entry zone rather than diffuser loss per se). The principle cause of the rather high loss levels observed in the diffuser seems to be the strong hub/corner stall which is initiated by the strong spanwise distortion in swirl angle at inlet. The bulk of this loss (85% of the predicted actual time-averaged total) is in fact captured by the "equivalent steady flow" simulation. The mixing loss arising from the circumferential averaging of the rotor flow was not included in the equivalent steady flow loss above. The difference therefore between the time-averaged losses and the equivalent steady result gives a measure of the magnitude of the mixing loss itself (about 6% of the total stage loss).

Kirtley et al. (1991) simulated a low-speed centrifugal stage with a steady flow Navier-Stokes solver using the passage averaging approach of Adamczyk (1985) to model deterministic unsteadiness arising from blade row interactions. Their simulations also showed that whilst in the entry zone to the diffuser deterministic unsteadiness was important, aft of the throat only the spanwise incidence variation onto the diffuser was important. A very useful future exercise would be to use the present unsteady simulations to help in the formulation of such passage averaged models.

Application to the axial compressor stage

Background

The stage selected for the second and contrasting study is the first stage of a five stage NACA research compressor tested and reported by Sandercock et al (1963). This particular stage was selected because the geometry is in the public domain and since the author has accumulated experience with the Sandercock stage in earlier Navier-Stokes studies (for example Dawes (1992)). The characteristics of the first stage are:

tip radius	0.254 m.
hub-to-tip ratio	0.50
rotational speed	12605 rpm.
rotor tip relative Mach number	1.4.

The unstructured mesh of tetrahedral computational control volumes generated for the stage is shown in Figure 10 and contains around 100,000 nodes. The number of nodes per blade row was the same as in earlier studies (Dawes (1992)) and the same rotor clearance gap was used.This mesh is sufficient to resolve the rotor boundary layers down to log law scale which was considered acceptable since the main function of the rotor is to generate a realistic overtip leakage flow to sweep periodically over the stators. The stator mesh was somewhat finer resolving the suction side boundary layer down to near sublayer scale in the endwall region. Starting from an initial guess, the simulation converged to an acceptably periodic solution in around 8-10 blade passing periods, each one of which required around 500 time steps. The simulation took around 2 cpu-days on an inexpensive IBM RISC/6000 workstation

The overall flowfield

To set the scene for the remainder of this paper, the overall character of the flow in the compressor stage will now be described. Figure 11 shows predicted instantaneous relative Mach numbers near the casing, just inboard of the rotor tip, and in mid-span. The Mach numbers are plotted relative to the rotor in the rotor mesh block and relative to the stator in the stator block and so are not continuous across the sliding plane. The operating point of the compressor has been chosen to be near choke and the strong rotor shock sits aft in the passage. A comparison

of the predicted and measured (Sandercock (1963)) stage performance is shown below:

	predicted	measured
mass flow	31.52 kg/s	31.81 kg/s
total pressure ratio	1.384	1.375
total-total efficiency	89%	88%

This was considered acceptable.

In mid-span the stator flow is well ordered with near-optimum incidence and thin, attached boundary layers. Near the casing the rotor overtip leakage vortex flow is clearly visible as the large distortion in the Mach number contours downstream of the shock wave. This particular plotting plane slices through the vortex and since the shape of the vortex is, roughly speaking, a flattened cone the plot slices an elliptical section through it. The stator flow, near the casing is not well ordered with much thickened blade boundary layers and a highly distorted flow along the suction sides of the blades.

To give a more three-dimensional feel to the flowfield, Figure 12 shows predicted instantaneous velocity vectors just near the casing (through the rotor clearance gap) relative Mach numbers in the rotor TE (trailing edge) plane and streamwise vorticity in the stator LE (leading edge) plane. The overtip leakage vortex occupies about three quarters of the rotor pitch and around the last 10% of the span near the casing. The overtip leakage represents a considerable axial flow deficit which means that the stator row sees, via the velocity triangles, a strongly circumferentially varying flow incidence: the mean incidence is approximately 11 degrees and the amplitude of the variation about ± 10 degrees. The extent of this large variation in flow angle can be judged from the plot of the streamwise vorticity in the stator leading edge plane; as the rotor moves past the stators this vortex sweeps periodically over the stator blades. The stator responds to the large flow incidence angle with much thickened boundary layers compared to mid-span. The suction side boundary layer separates at around mid-chord with the location of the separation varying with time in sympathy with the varying incidence. It should be noted that even though the incidence variation is roughly from zero to 20 degrees, the stator boundary layer does not vary between fully attached (at zero degrees) and badly stalled (at 20 degrees) as might be expected from quasi-steady arguements but remains separated throughout the cycle. Finally, the stator loading varies in sympathy with the incidence and this results in vortex shedding from the trailing edges.

Before proceeding to discuss in more detail the fluid mechanics of the unsteady rotor-stator interaction it is convenient to describe the performance of the compressor.

Predicted performance: loss production

The predicted flow field was interrogated from the perpective of loss production to try and determine the relative contribution of the unsteady flow to the loss levels in and hence to the time-average performance of the stage.

A comparison is now made of the time-averaged entropy production rate and the production rate which would be associated with the time averaged flow; these statistics are processed on-the-fly as the simulation proceeds. The time-averaged entropy production rate represents the actual performance of the stage. The difference between the two production rates should, following on from the discussion above, correspond to loss production directly attributable to the unsteady flow itself. The result for the overall flow is shown below:

	time-averaged entropy production	entropy production of the time-averaged flow
rotor	1.56	1.25
stator	1.71	1.49

(kJ / kg K)

It is interesting to break out of this the production rates associated with the the "endwall" defined as the 10% of the span near the casing (since this is roughly the extent of the flow affected by the rotor

vortex). The result is as follows:

	time-averaged entropy production in the "endwall"	entropy production of the time-averaged flow in the "endwall"
rotor	0.35	0.32
stator	0.28	0.20

(kJ / kg K)

Two observations may be made. Firstly, the "endwalls" are responsible for a disproportinate amount of the overall loss (as is well known of course): 22% of the rotor overall time-averaged loss and 16% of the stator loss is produced in the endwall 10% of the span. This means that the rotor endwall loss production rate per unit span is a factor 2.2 greater than the loss production rate per unit span over the rest of the blade. Similarly, the stator endwall losses per unit span are a factor of 1.8 greater than over the bulk of the blade.

Secondly, the loss production directly associated with the unsteady flow behaves quite differently in the rotor compared to the stator. In the rotor 19% of the overall loss but only 9% of the endwall loss is derived directly from the unsteady flow. This suggests that unsteady shock motion is responsible since the shock extends over most of the span; this will be explored in the next section. By contrast, in the stator only 12% of the overall loss is derived directly from the unsteady flow but as much as 29% of the endwall loss. The unsteady interaction between the rotor overtip leakage vortex with the stators is obviously a strong factor in determining the endwall loss production rate. This too will be explored on a later section.

The simulation of such stages using individual 3D Navier-Stokes simulations in each blade row coupled by circumferentially averaging the intra-blade flow (eg. Denton (1992) and Dawes (1992)) needs more thought. Two issues arise: firstly, since for the stage as a whole the difference between the time-averaged loss production and the loss production asssociated with the time-averaged flow is 16% the circumferential averaging approach may underpredict the stage inefficiency. Secondly, and more seriously, because there is such a large "unsteady" loss the circumferential averaging approach may not even be able to replicate the time-mean operating point of the real stage in terms of a compatible pressure ratio-blockage-mass flow-efficiency combination.

The predicted mid-span flow

The motives for describing the detail of the mid-span flow first are twofold. Firstly, there is some experimental data in this region from similar compressor stages which can establish the basic realism of the present simulation. Secondly, the mid-span flow provides a useful reference with which to contrast the endwall flow.

The general pattern of the mid-span flow is illustrated in Figure 13 which shows predicted instantaneous entropy variations, relative Mach numbers and (instantaneous-averaged) velocity vectors. The plot shows a "classic" wake interaction with the rotor wakes "chopped" by the stators before convecting onwards through the passage. The rotor wake appears, as is well known, in the stator frame as a relative jet directed away from the suction surface towards the pressure surface and this is visible in the plots of (instantaneous-averaged) velocity vectors. (In fact since the plot is of (instantaneous-averaged) velocity rather than the more usual (instantaneous-"steady flow without wakes") in between the wakes the relative flow is directed towards the suction side; this is simply a question of offset: the overall effect of the wakes is to produce net relative transport towards the pressure side). The relative jet in this three-dimensional simulation is not only directed from blade to blade but also driven radially inwards by the bulk pressure field asociated with the swirling flow. Much less "bowing" of the rotor wakes is observed than in turbines since the blade loading is much lower with much less difference in velocity level across the passage to distort the wake. This type of behaviour is observed in experimental data and Figure 14 shows the motion of the rotor wakes, flagged by measured instantaneous turbulence intensities, in the mid-span plane of a very similar compressor stage with similar relative blade numbers (Dunker et al (1983)).

An interesting periodic variation of velocity level is observed over the fore part of the suction side of the stators. Figure 15 shows predicted instantaneous Mach numbers in mid-span at intervals throughout the periodic cycle. The Mach numbers are

plotted in the relative frame for the rotor and the absolute frame for the stator; the rotor wake centre-line is shown by a dotted line. As the rotor wake arrives the zone of highest velocities in the stator row suction side starts to divide into two distinct parts. Once the rotor wake has passed these two parts coalesce and the process repeats on the other stator. This is exactly the behaviour measured by Dunker et al (1983) in a very similar transonic compressor stage with similar relative blade count. Figure 16 shows their measured instantaneous absolute velocities in the mid-span plane of the stator row at three times during the periodic cycle; the same splitting of the high velocity zone along the suction side into two by the arrival of the rotor wake is clearly observed. The origin of this effect appears to be the relative jets associated with the chopped rotor wakes, illustrated in Figure 13. Fluid is entrained into these relative jets as they convect through the rotor row. On the suction side of the stators there is a kind of relative stagnation point in the relative velocity field between the wakes. Upstream of this point the relative flow is entrained into the upstream wake, downstream of this point the relative flow is into the downstream wake. This relative stagnation point lies rather closer to the upstream wake than the downstream one and its location corresponds to the area between the two parts of the divided high velocity zone.

As a final indication of the extent and character of the observed unsteady efects in mid-span, Figure 17 shows the predicted time averaged and rms averaged static pressure fields. The largest pressure fluctuations by far in mid-span are predicted to be in the rotor and are associated with oscilation of the rotor shock with an amplitude of about ±5% of chord. The shock motion is probably driven by the circumferentially varying static pressure field from the downstream stators but also a self-excited motion coupled to unsteady blade circulation is possible. Unsteady shock motion has important implications for both blade stressing and aerodynamic loss production. Essentially the non-linearity in the shock jump equations mean that the increased entropy generation rate when the shock is moving upstream will be greater than the reduction when it is moving downstream (Denton (1993)).This type of behaviour has also been observed by Ng et al (1984) in two dimensions.

Three basic unsteady flow mechanisms are observed to be at play in mid-span. In the stators: firstly, the rotor wakes are chopped and convected through but with little distortion as they slowly mix out; and secondly, the negative jet associated with the rotor wakes causes a periodic distortion to the stator suction side boundary layer. In the rotor the shock is observed to be in periodic unsteady motion. In terms of predicted loss production, the analysis in the previous section showed that most of the "unsteady" loss associated with the rotor was produced in mid-span whereas in the stators the converse was true and very little of the mid-span loss could be directly associated with unsteady effects. It must be concluded, therefore, that despite the evident complexity of the stator mid-span flow, there do not seem to be any implications of this unsteadiness for predicting the blade performance (subject to possible influences of the rotor wake/stator suction-side boundary layer interaction on the state of turbulence in these boundary layers which may not be adequately modelled by the present approach). By contrast, the rotor shock motion does seem to have important implications for performance predictions and it would seem worthwhile to take this into account in design methods. The very simple one-dimensional model analysis of Ng et al (1984) showed that the extra entropy generated from an oscilating shock is strongly dependent on the amplitude of the shock motion since it is the product of the amplitude and its frequency which is directly related to the increased relative upstream Mach number. They studied a particular case where a shock amplitude of only around 0.5% chord led to an efficiency decrease of about 0.15 percentage points. In the present simulations the predicted shock amplitude is much higher and there will therefore be much more loss generation directly associated with the shock itself. Nevertheless, this does not seem sufficient in itself to explain the observation that the "unsteady" inefficiency in mid-span is nearly a fifth of the total. It seems very likely, therefore, that much of the "unsteady" loss is generated by a non-linear shock-boundary layer interaction and this should be a focus for further study.

The predicted flow near the endwall in the stator row

In this stage at this operating point nearly a third of the loss production near the endwall in the stator row was predicted to be

directly due to unsteady effects. The purpose of this final section is to examine in more detail the stator flowfield near the endwall to determine which unsteady mechanisms are present.

The predicted endwall flow is presented in Figures 18, 19 & 20 which show for a blade-to-blade slice near the casing (in fact at 5% span slicing through the rough centre of the rotor overtip vortex) the variations at intervals through a periodic cycle of: Mach number, streamwise vorticity and (instantaneous-averaged) velocity vectors respectively. Marked on each plot is the approximate centre-line of the rotor vortex taken from Figure 19; each figure should be examined in periodic sequence starting from top left and proceeding in a clockwise direction. Time "**t**" is the arbitrary start of the periodic cycle.

The rotor overtip leakage puts the stators at large and circumferentially varying incidence and the Mach numbers in Figure 18 show much thickened blade boundary layers and wakes compared to mid-span; this in itself is responsible for augmented blade losses relative to the optimum incidence case (as identified by Howard et al (1993)). The blade-to-blade flow is very distorted and time-varying and localised zones of elevated Mach number can be seen "tied" to the propagating portions of the rotor vortex. The boundary layer on the suction side of the stators is found to be extensively separated with the size and location of the separated zone varying with time. The approximate edge of the separated zone is marked on Figure 19. Vortices can be seen to be shed alternately from the stator trailing edges; these are associated with the time-varying blade loading. The vortex shedding is particularly well resolved in the plots of (instantaneous-averaged) velocity vectors in Figure 20. This vortex shedding is dissipative and might well be counted as representing augmented base loss for the profile.

The progress of the rotor overtip vortex through the stators can be seen from the plots of streamwise vorticity in Figure 19. The vortex is chopped by the stators, after some distortion at the leading edges, and then convected through the blade passage. The circumferential extent of the rotor vortex is effectively terminated by interaction with the stator boundary layers and wake. As the chopped vortex segments pass downstream the magnitude of the vorticity is seen to decay as the secondary kinetic energy is converted into loss. The rotor vortex does not seem to stretch much, still less burst, as was observed by Binder (1984) in studies in a turbine stage and this is presumably due simply to the much lower blade loading levels in the compressor case. The (instantaneous-averaged) velocity vectors associated with the vortex, Figure 20, are interesting in that they show that the principle perturbation introduced by the rotor vortices over most of the blade passage is a pattern of negative (suction side to pressure side) and positive jets (vice versa). (As discussed before, the perturbation flow is defined by "instantaneous - average" rather than the more common "instantaneous - wake free" and so both positive and negative excursions are inevitable).This implies that the main effect of the rotor overtip leakage flow is in fact exerted by its associated axial velocity deficit rather than by its angle variation as perhaps might have been expected. This is clear from the way the velocity perturbations lie roughly parallel to the vortex axis; if the dominant effect of the vortex were angle pertubations then the velocity perturbations would lie roughly transverse to the jet axis. Only near the suction side are the velocity perturbations more transverse to the vortex axis suggesting that here, at least, the expected angle perturbations are more dominant.

As the chopped vortex segments sweep over the stator suction surfaces an unexpected unsteady loss producing feature is predicted. Rather abruptly, at time "**t**" in the figures, just as the vortex segment reaches mid-chord a zone of opposite sign streamwise vorticity is formed at around 25% chord on near the suction side (Figure 19; "opposite sign" with respect to the sign of the rotor vortex). Associated with this is a sudden thickening of the separated zone on the blade. Figure 21 shows detail views, just at time "**t**", showing the formation of this "opposite sign" vortex. In successive frames during the cycle this zone of opposite sign streamwise vorticity becomes much more intense (with peak levels roughly twice in magnitude than those in the rotor vortex) as it convects along the edge of the separated layer before dissipating its secondry kinetic energy into loss before the trailing edge plane is reached. The observation that the created zone has streamwise vorticity, even though it emanates from a boundary layer (which has little streamwise vorticity), implies that it is produced from a three-dimensional separation which occurs upstream of that in the plotted location outboard nearer the casing and

downstream of this location inboard; this is in fact found to be the case here. The separation is caused by the very strong negative jet associated with the velocity deficits in the rotor overtip leakage flow. When one of the negative jets arrives at around 25% chord (see Figure 21) it sucks boundary layer fluid off the blade surface and towards the free stream; more vortical fluid is entrained by the negative jets as they convect downstream. The following postive jet tends to push the flow back onto the blade surface and limit the upstream spread of the separation zone itself. The three-dimensionality of the separation is simply due to the rapid spanwise variation of the rotor vortex/boundary layer interaction - particularly the angle perturbations observed towards the suction side which obviously change sign from zero to underturning to overturning moving over only 10% of the span outboard to the casing. This novel and unexpected loss mechanism may be the three-dimensional equivalent of the B-vortices predicted by Valkov et al (1993) in a two-dimensional simulation which was notable for using much larger wake deficits than is usual for such 2D simulations but in fact more representative of the size of deficit observed here in the present simulations.

In summary, the stator blades experience elevated loss levels in the endwall region partly due to the highly unfavourable flow incidence but also around a third of the losses are associated directly with the unsteady flow itself. Three unsteady loss mechanisms were identified: blade trailing edge vortex shedding derived from the time-varying blade load; unsteady boundary layer separation; and most significantly the novel "sucking off" of blade boundary layer fluid into an intense vortical structure which quickly dissipates. The rotor vortex is also observed to dissipate in the stator row and whilst this might be debited to the rotor the mixed out loss associated with it depends on the environment in the stator in which the mixing out takes place.

Conclusions

The following summarises the contrasting conclusions which may be drawn from the present study.

Centrifugal compressor stage:

• Except over the critical zone near the impeller trailing edges, the impellor flow was observed to be essentially steady; this result might change if the diffuser entry velocities were supersonic.

• The highly distorted jet-wake flow emerging from the impeller did not appear to mix out before arriving at the diffuser vanes' entry zone as assumed in some design methods.

• Very large periodic variations of velocity and flow angle were observed in the entry zone to the diffuser.

• Good qualitative and quite fair quantitative agreement was achieved between the predicted and measured flowfields both in the impeller and in the entry zone to the diffuser.

• Flow unsteadiness at blade passing scale in the vaned diffuser was confined largely to the entry zone and diminished rapidly further outboard in the diffuser. Outboard although the flow was predicted to be unsteady, the unsteadiness did not appear to be periodic on blade passing time scales and in any case was much lower in magnitude that in the entry zone.

• The flow pattern in the diffuser downstream of the throat was quite similar near the shroud and in mid span but dramatically different near the hub where a substantial hub-pressure side corner stall was predicted; this corner stall seems largely to be caused by the spanwise variation of flow angle at diffuser inlet.

• The irregular fluctuations associated with the corner stall seem to overwhelm and damp out any periodic, propagating unsteadiness emmanating from the entry zone.

• The spanwise variation of flow property, especially swirl angle, seems to exert a more significant influence on the diffuser performance than does the unsteady, circumferential variation in flow.

• A comparison was made of the time-averaged entropy production rate with the production rates which would be associated with the time averaged flow and with the "equivalent steady flow". This showed little loss directly attributable to unsteady effects. The principle cause of the rather high loss levels observed in the diffuser seems to derive from the strong spanwise distortion in

swirl angle at inlet which initiates a strong hub/corner stall.

• It is very important therefore that design methods which mix out the impeller flow before entry to the diffuser should only perform such mixing circumferentially so that the crucial spanwise variation of flow property be preserved and passed on to impact the diffuser performance.

Axial compressor stage:

• The endwall region of both the rotors and the stators was predicted to be proportionally responsible for much more loss production than the mid-span sections of the blading.

• Unsteady effects were predicted to be responsible for rather more of the total loss production in the rotors than in the stators.

• The unsteady loss production in the rotors did not seem to be particularly associated with the the endwall flow but rather occurred over the bulk of the blade span and caused by unsteady shock motion. Higher loss levels near the casing were obviously caused by the overtip leakage flow.

• In the stator row losses near the casing were found to be augmented by the unfavourable flow incidence which led to badly thickened and separated suction side boundary layers. In addition, nearly a third of the loss production near the endwall was predicted to be directly due to unsteady effects associated with the rotor vortex interaction; a number of individual unsteady loss mechanisms were identified.

• The simulation of such stages using individual 3D Navier-Stokes simulations in each blade row coupled by circumferentially averaging the intra-blade flow needs more thought since on the basis of the present predictions this approach may underpredict the inefficiency but more seriously may not even be able to replicate the same time-mean operating point.

References

Adamczyk JJ "Model equation for simulating flows in multistage turbomachinery" ASME Paper 85-GT-226, 1985

Dawes WN "The simulation of three-dimensional viscous flow in turbomachinery geometries using a solution adaptive unstructured mesh methodology" J.of Turbomachinery, ASME Paper 91-GT-124, 1991

Dawes WN "The extension of a solution-adaptive 3D Navier-Stokes solver towards geometries of arbitrary complexity" J.of Turbomachinery, ASME Paper 92-GT-363, 1992

Dawes WN "Simulating unsteady turbomachinery flows on unstructured meshes which adapt both in time and space" ASME Paper 93-GT-104,1993

Dean RC & Senoo Y "Rotating wakes in vaneless diffusers" ASME J.of Basic Engineering, Vol. 82, pp. 563-570, 1960

Giles MB "Calculation of unsteady wake/rotor interaction" AIAA J.of Propulsion and Power, 4(4), pp 356-362, July 1988

Giles MB "Stator/rotor interaction in a transonic turbine" AIAA J.of Propulsion and Power, 6(5), Sept.1990

Holmes DG & Connell SD " Unstructured, adaptive, finite volume solution methods for fluid dynamics" 7th IMACS Conference on the Computer Simulation of pde's, Rutgers, NJ, July 1992

Hodson HP "An inviscid blade-to-blade prediction of a wake generated unsteady flow" ASME Paper 84-GT-43, 1984

Inoue M "Centrifugal compressor diffueser studies" PhD Dissertation, Cambridge University, 1980

Jameson A & Baker TJ " Improvements to the aircraft Euler method" AIAA Paper 87-0452, Reno, Nevada, Jan.1987

Johnston JP & Dean RC "Losses in vaneless diffusers of centrifugal compressors and pumps" ASME J.of Eng.for Power, Vol.8, pp.49-60, 1966

Jorgensen P & Chima R "An unconditionally stable Runge-Kutta method for unsteady flows" AIAA Paper 89-0205, 27th Aerospace Sciences Meeting, Jan.9-12, Reno, 1989

Kirtley KR & Beach TA "Deterministic blade row interactions in a centrifugal stage" ASME Paper 91-GT-273, 1991

Krain H "A study on centrifugal impellor and diffuser flow" ASME Paper 81-GT-9, 1981

Krain H "Experimental observations of the flow in impellers and diffusers" VKI Lecture Series 1984-07, 1984

Krain H & Hoffmann W "Verification of an impeller design by laser measurements

and 3D viscous flow calculations" ASME Paper 89-GT-159, 1989

Krain H Private communication, 1993.

Lam CKG & Bremhorst KA "Modified form of the k-e model for predicting wall turbulence" Journal of Fluids Engineering, vol.103, 1981

Patel VC, Rodi W & Scheuerer G "Turbulence models for near-wall flows and low Reynolds numbers : a review" AIAA Journal vol.23, no.9,Sept.1985

Rai MM "Navier-Stokes simulations of rotor-stator interaction using patched and overlaid grids" AIAA-85-1519, AIAA 7th CFD Conference, Cincinnati, July 1985

Rao K & Delaney R "Investigation of unsteady flow through transonic turbine stage Part I: analysis" AIAA-90-2408, AIAA/SAE/ASME/ASEE 26rd Joint Propulsion Conference, Orlando, July 1990

Senoo Y, Kinoshita Y & Ishida M "Asymmetic flow in vaneless diffusers of centrifugal blowers" ASME J.of Fluids Eng., Vol.99, pp.104-114 ,1977

-oOo-

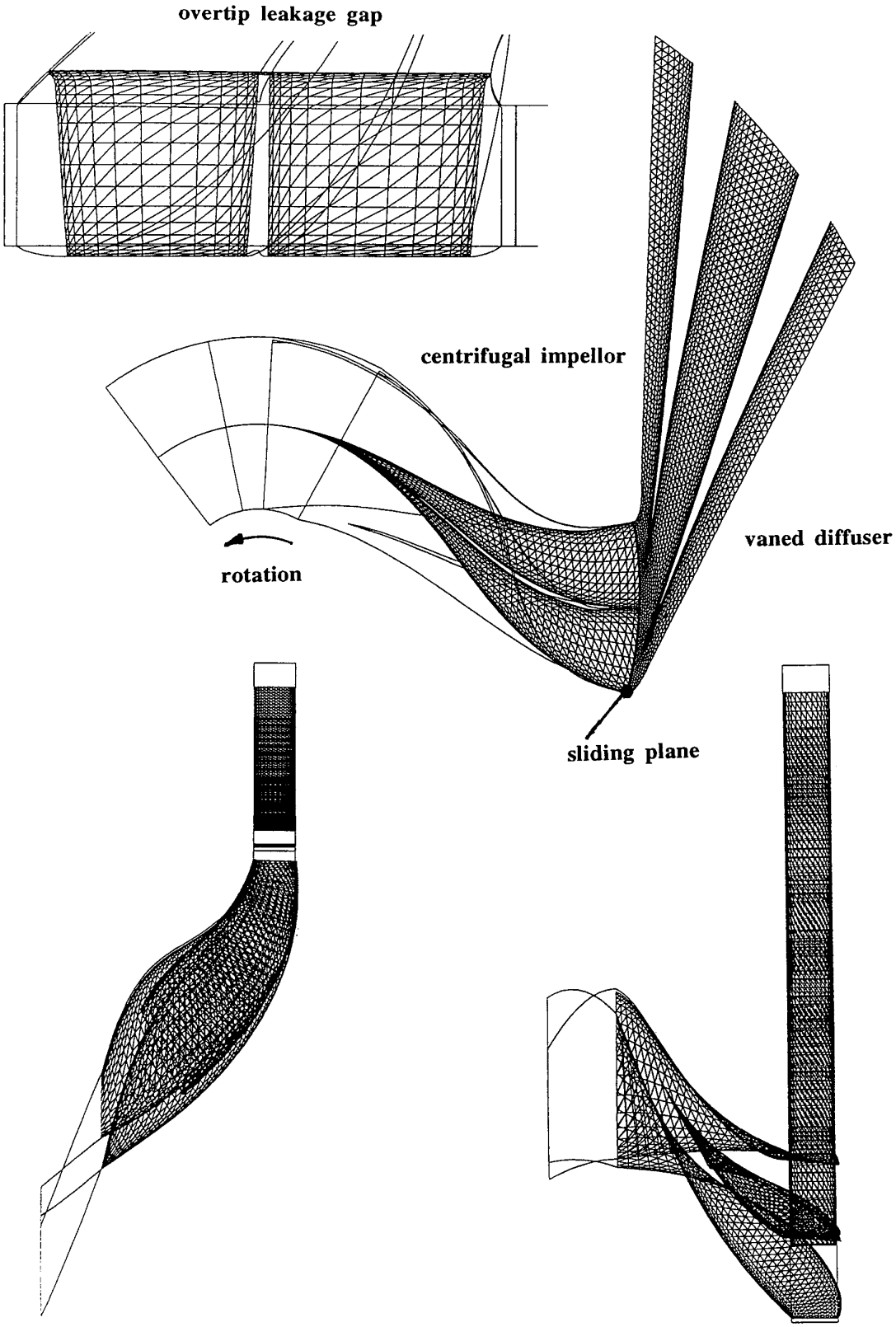

Fig.1 The unstructured mesh generated for the splittered centrifugal impellor-vaned diffuser stage.

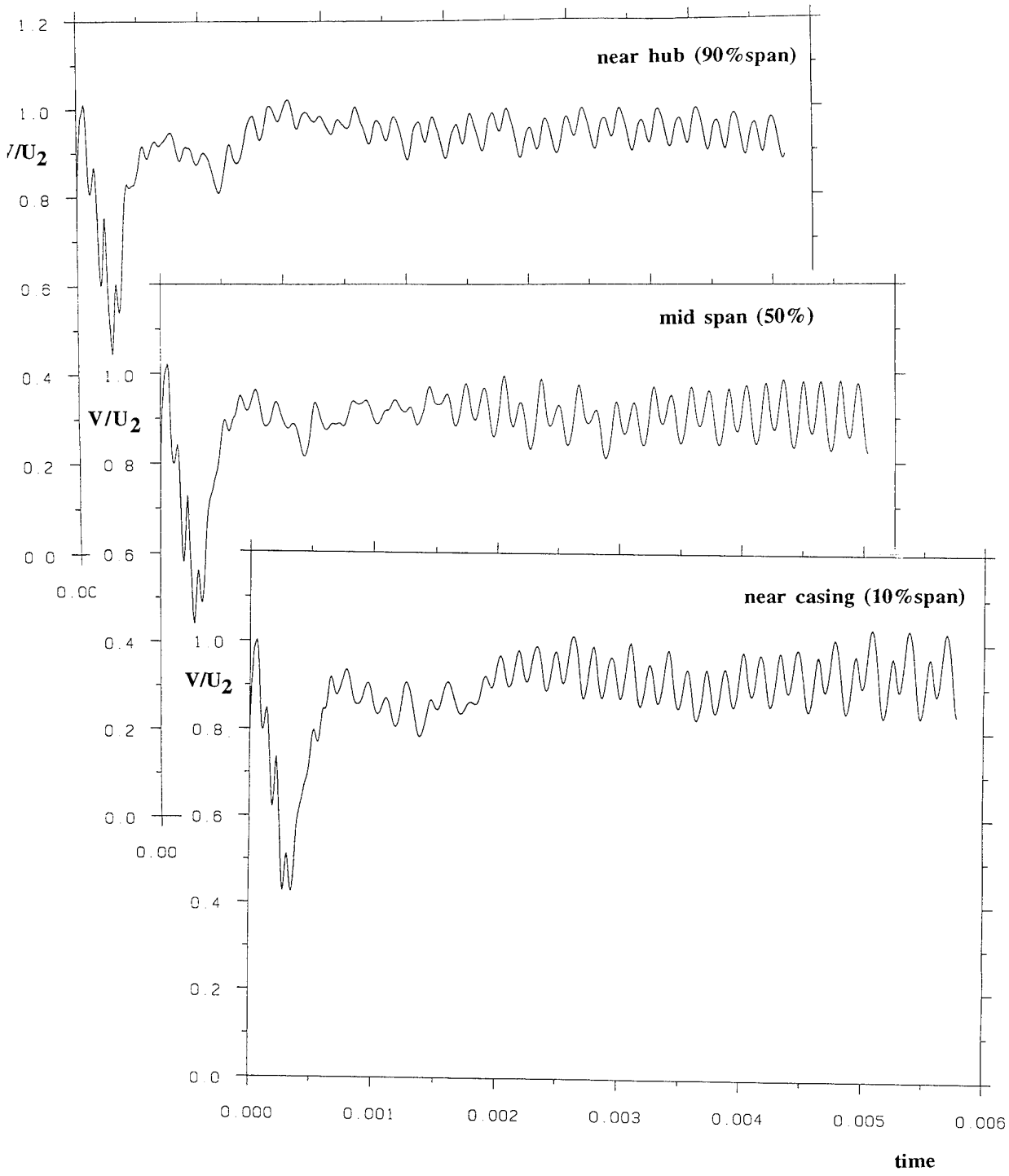

Fig.2 Variation with time of predicted velocities in mid-pitch of the diffuser vane leading edge at 10%, 50% and 90% span.

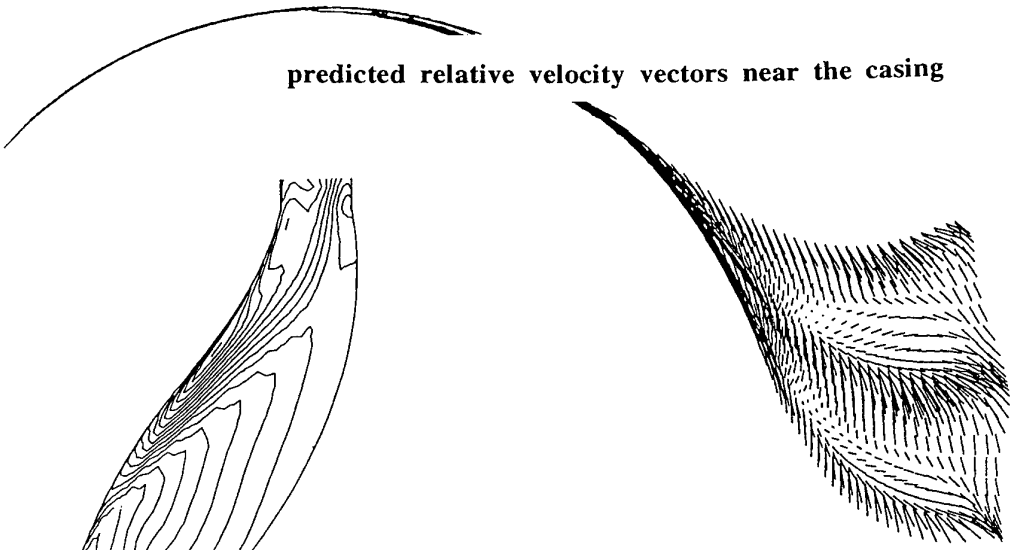

predicted relative velocity vectors near the casing

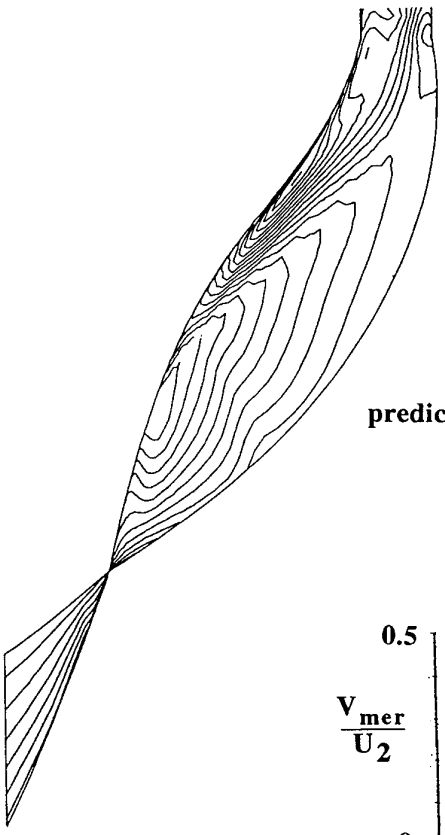

predicted mid-passage relative Mach numbers

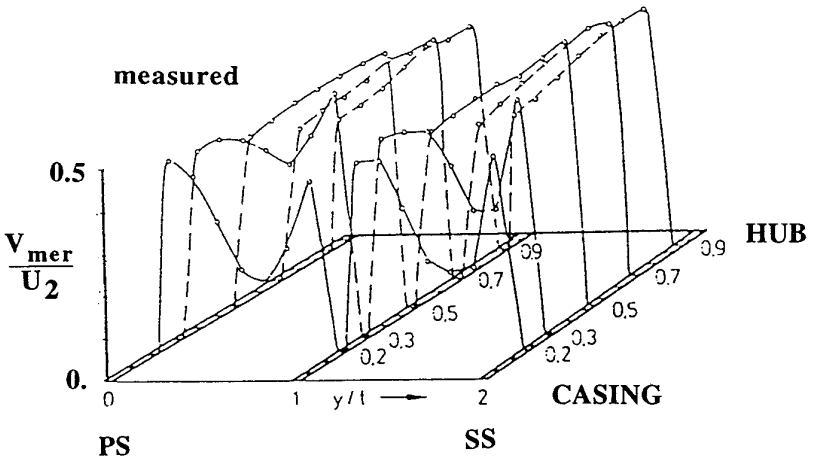

a comparison of predicted and measured meridional velocities in a cross-flow plane towards the wheel exit at 87% of the streamwise distance through it (Plane IV)

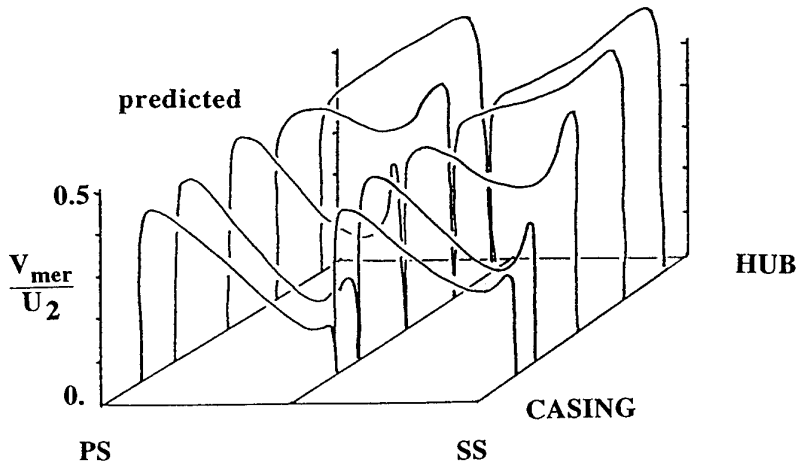

Fig.3 A summary of the rotor flow showing the development of the jet-wake.

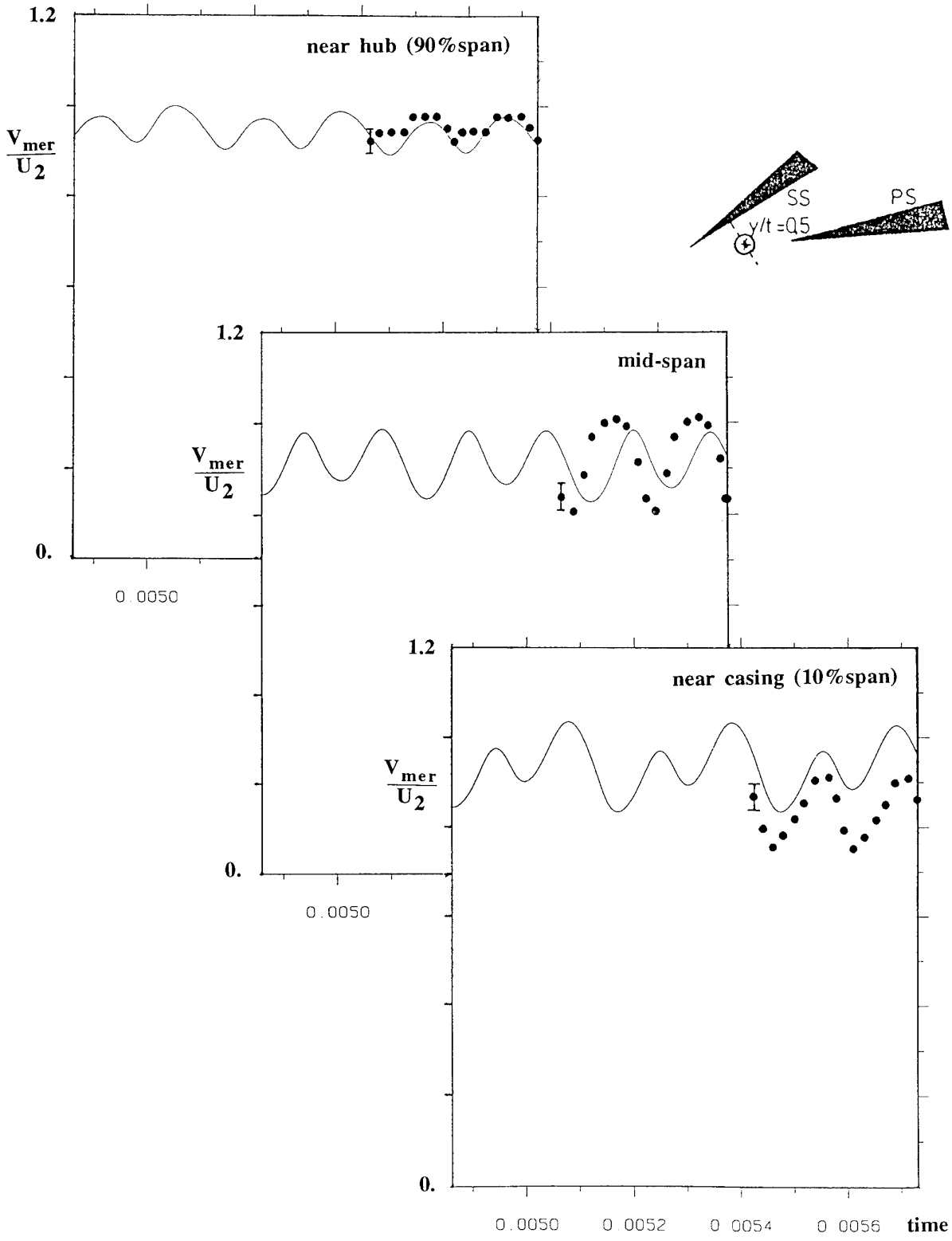

Fig.4 The variation with time of predicted meridional velocity at mid-pitch of the diffuser vane leading edge plane compared with measurements (line=prediction; symbol=experiment).

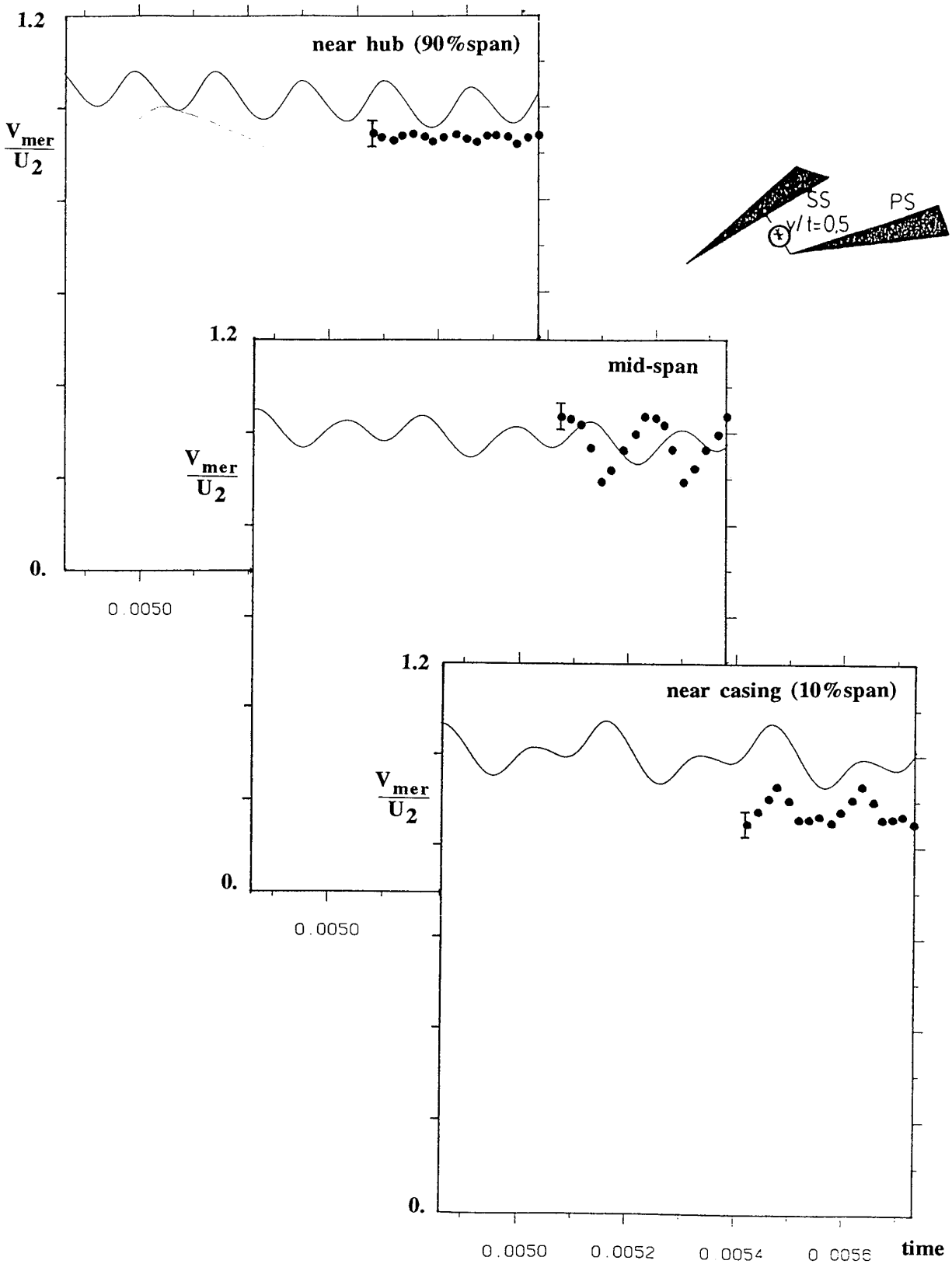

Fig.5 The variation with time of predicted meridional velocity at mid-pitch of the diffuser vane throat plane compared with measurements (line=prediction; symbol=experiment).

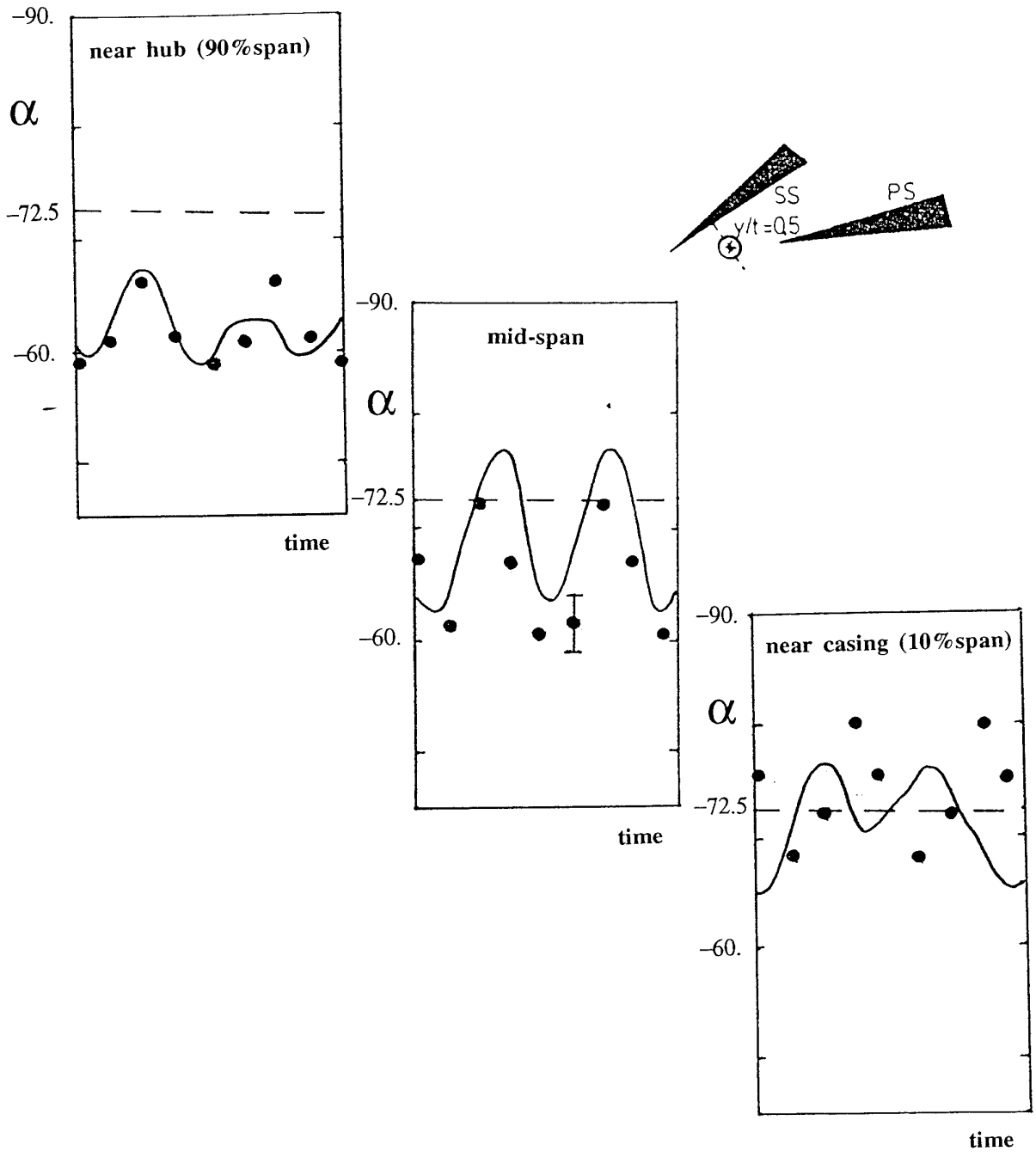

Fig.6 The variation with time of predicted swirl angle at mid-pitch of the diffuser vane leading edge plane compared with measurements (line=prediction; symbol=experiment).

Fig.7 Predicted time-mean velocities on slices through the diffuser flow near the hub, in mid-span and near the casing.

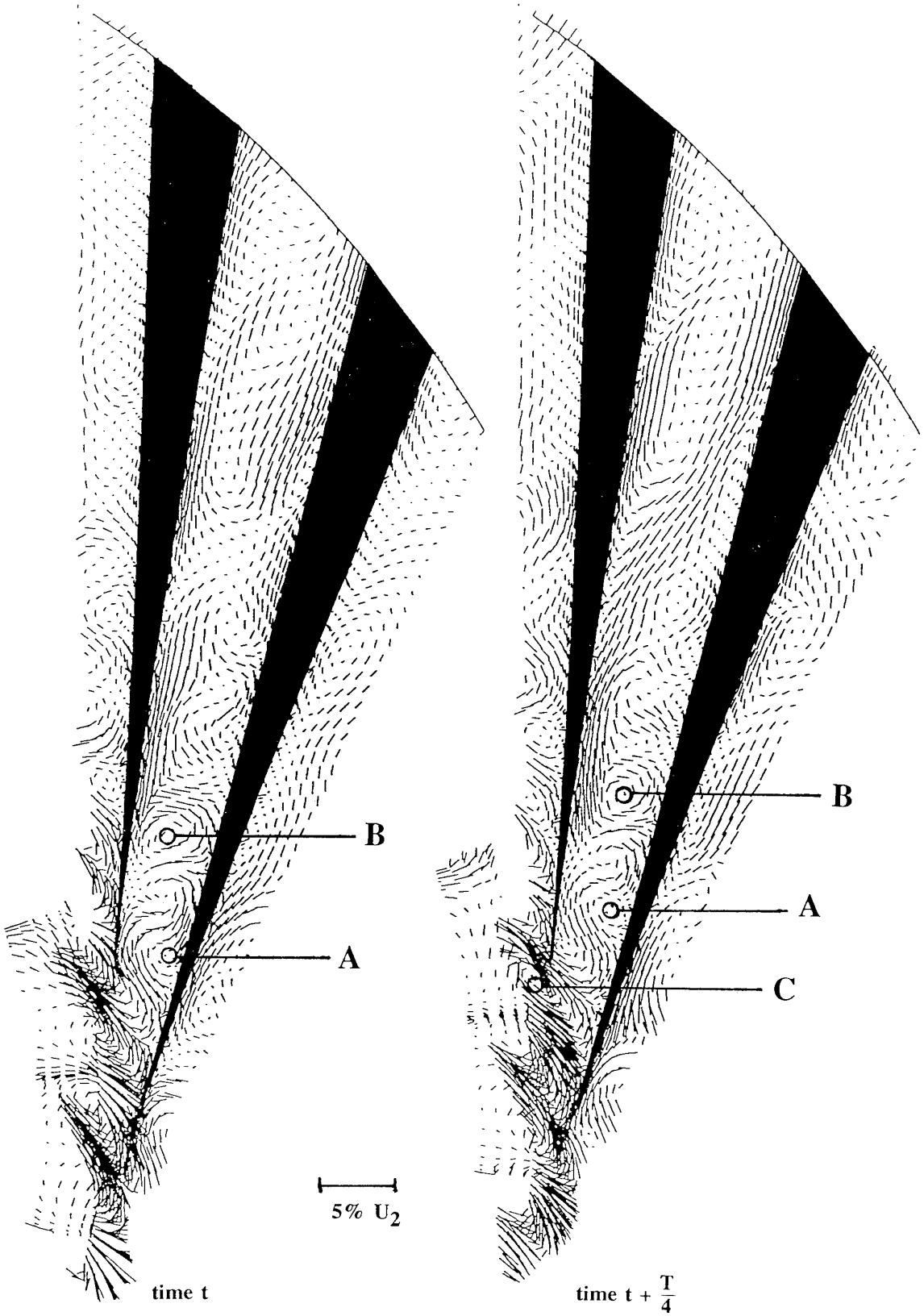

Fig.8 (Instananeous - averaged) velocity vectors in the mid-span slice a quarter of a blade-passing time period apart.

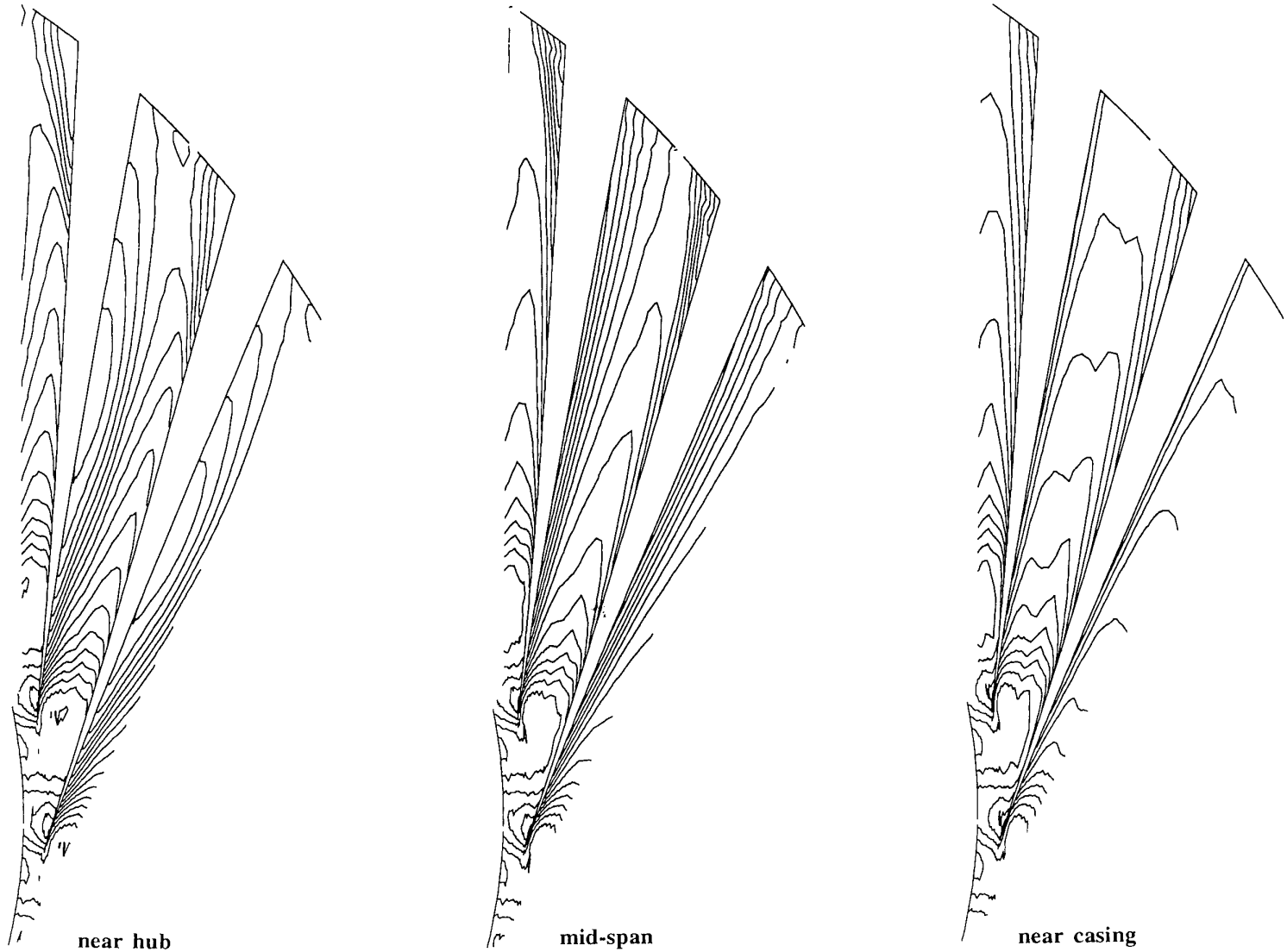

Fig.9 Predicted velocities on slices through the diffuser flow near the hub, in mid-span and near the casing for the "equivalent steady flow".

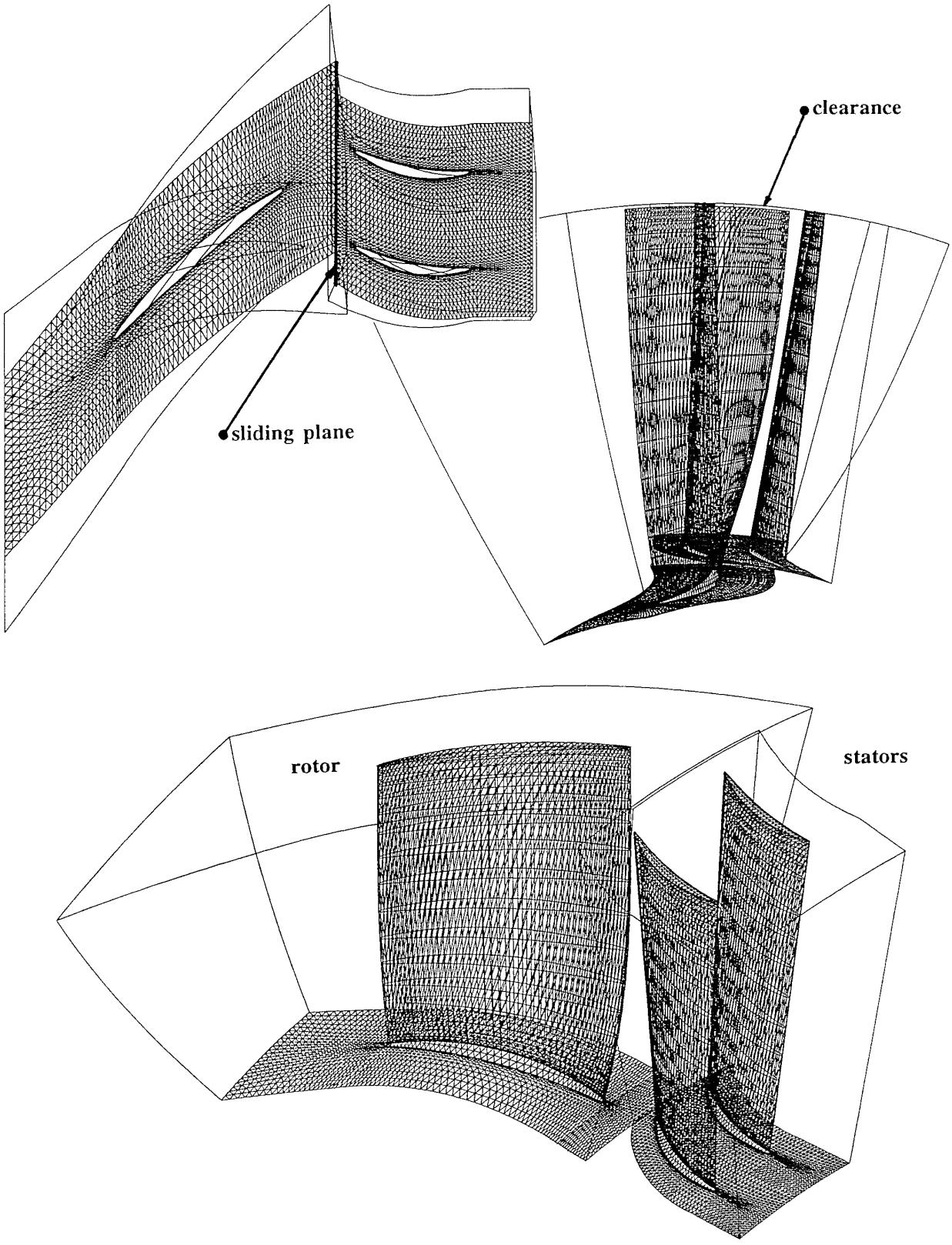

Fig.10 The unstructured mesh generated for the transonic fan stage.

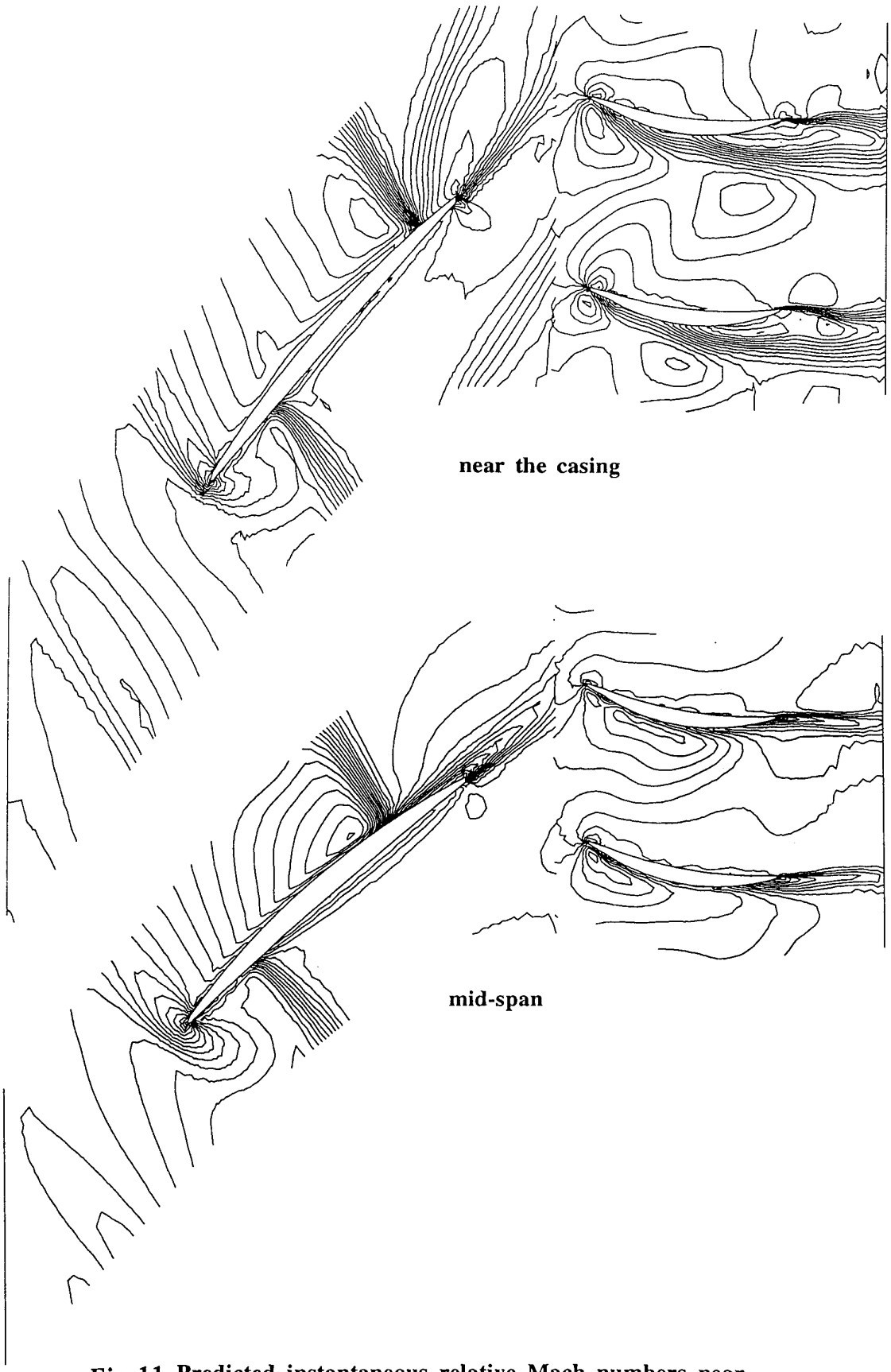

Fig.11 Predicted instantaneous relative Mach numbers near the casing, just inboard of the rotor tip, and in mid-span (interval 0.05).

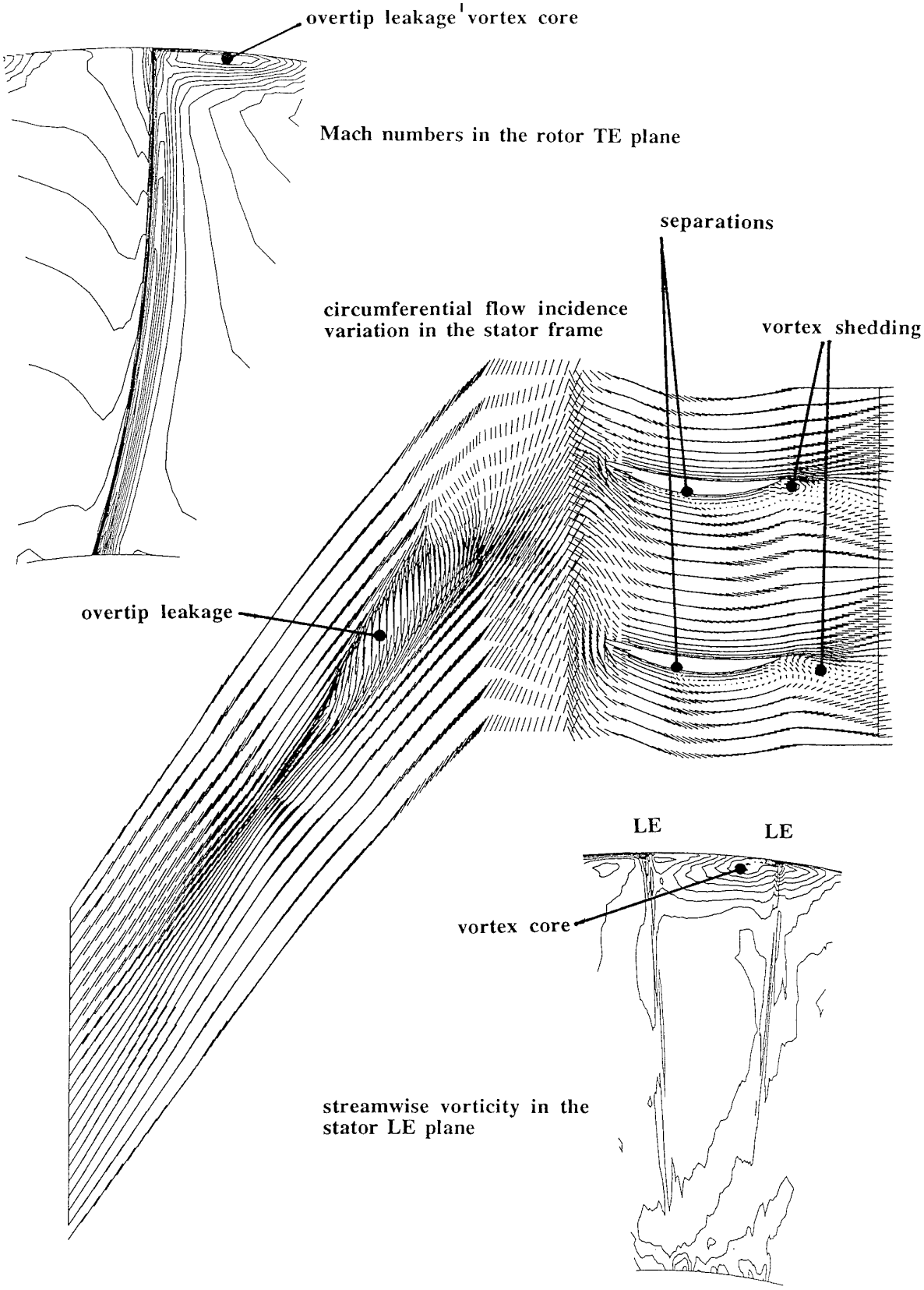

Fig.12 Predicted instantaneous velocity vectors just near the casing (through the rotor clearance gap) relative Mach numbers in the rotor TE plane and streamwise vorticity in the stator LE plane.

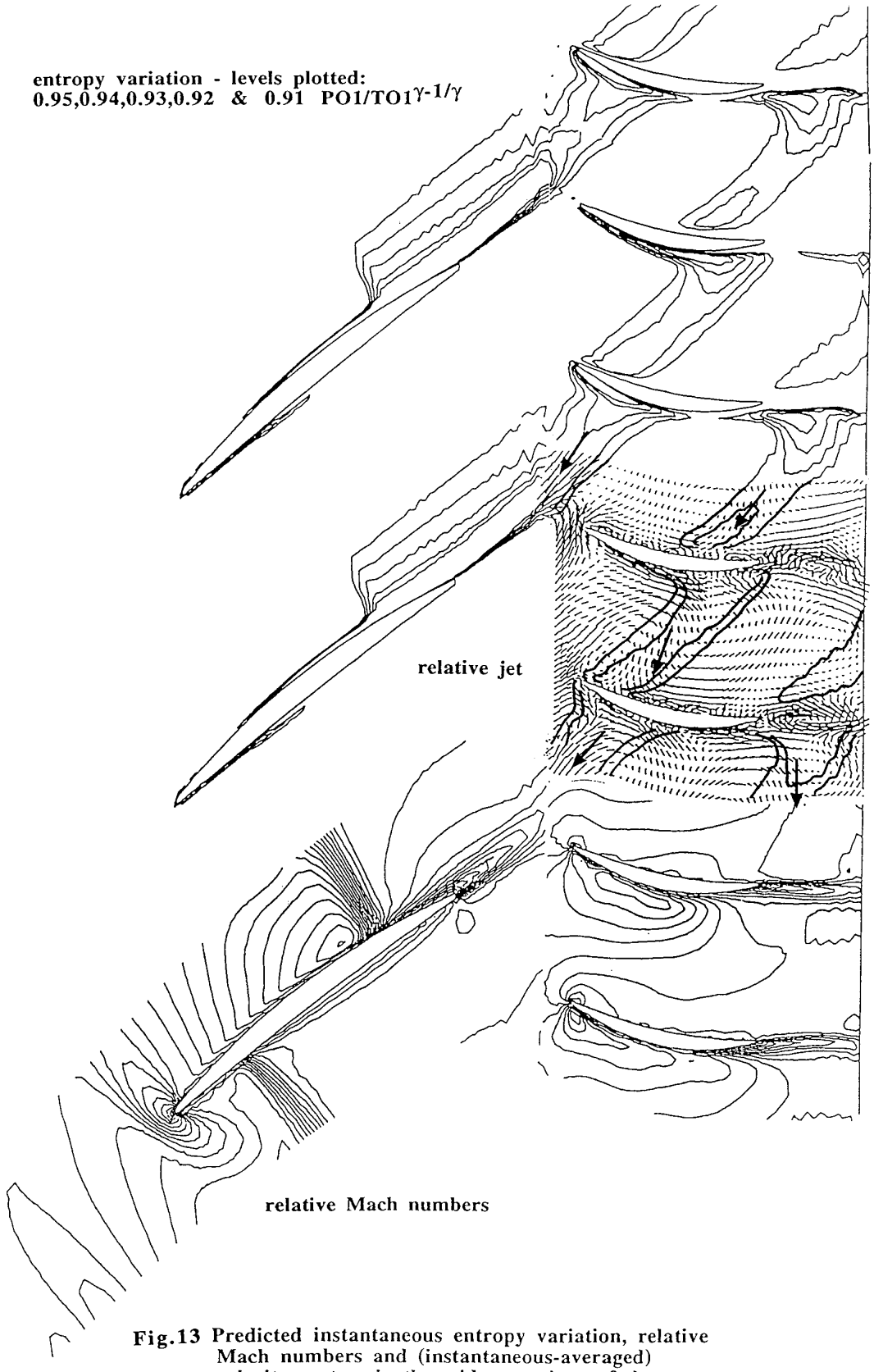

Fig.13 Predicted instantaneous entropy variation, relative Mach numbers and (instantaneous-averaged) velocity vectors in the mid-span plane of the compressor stage.

rotor

— — — wake centre-line

t

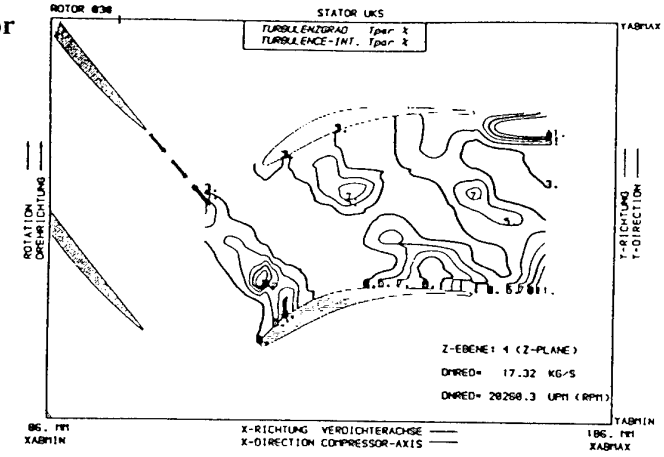

$t+\frac{1}{3}T$

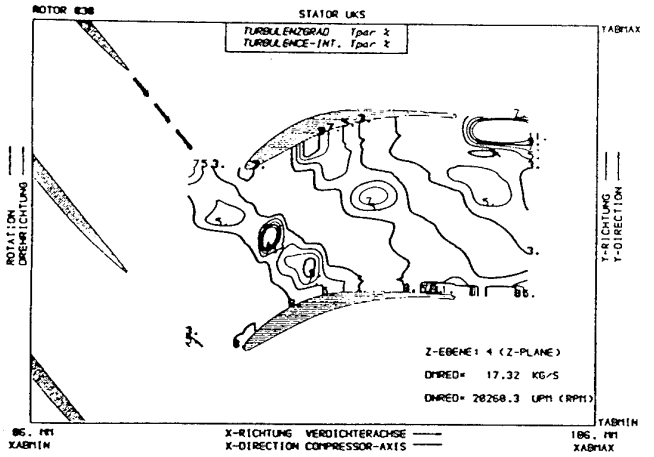

$t+\frac{2}{3}T$

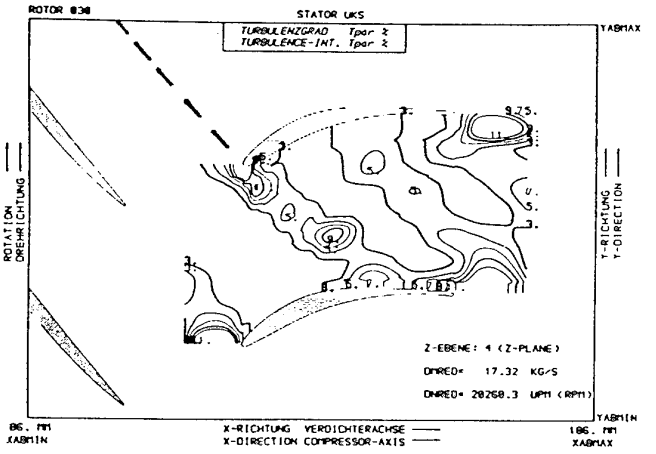

Fig.14 Measured instantaneous turbulence intensity in the mid-span plane of the DFVLR compressor stage.

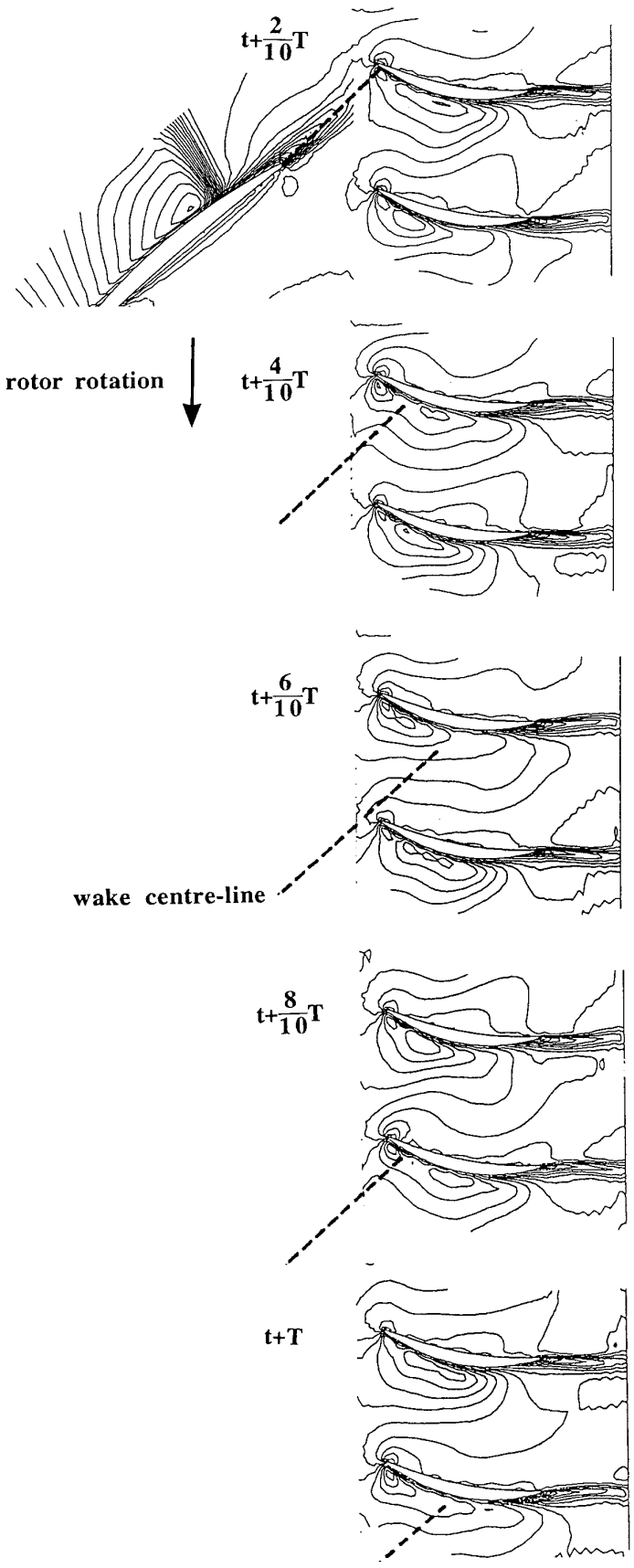

Fig.15 Predicted instantaneous Mach numbers in the mid-span plane of the compressor stage.

rotor

— — — wake centre-line

t

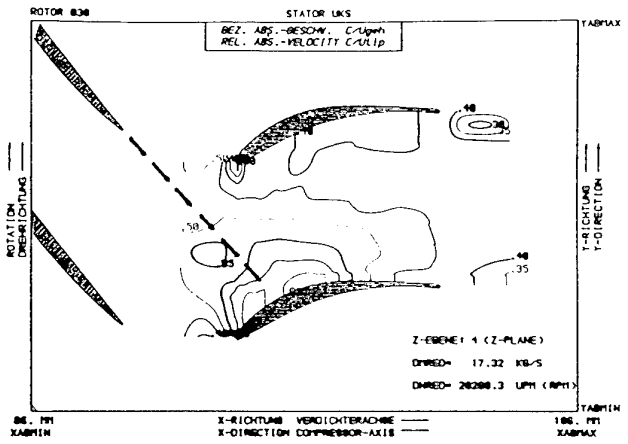

$t+\frac{1}{3}T$

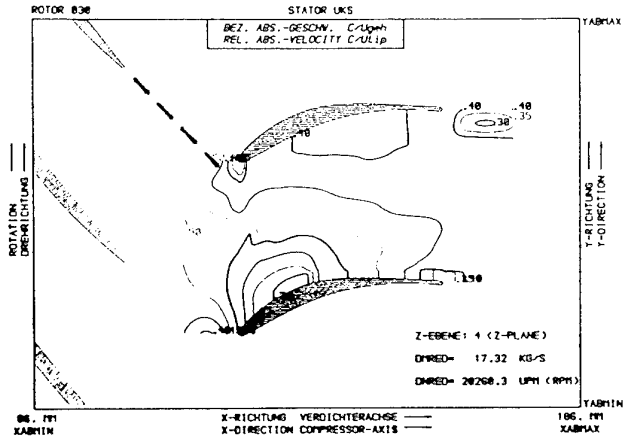

$t+\frac{2}{3}T$

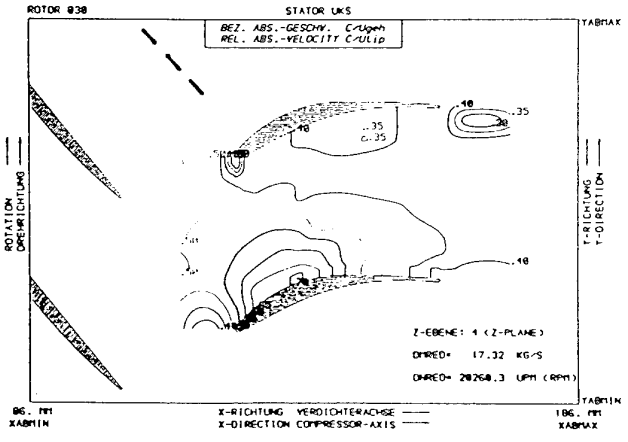

Fig.16 Measured instantaneous absolute velocities in the mid-span plane of the DFVLR compressor stage.

time averaged static pressure; interval 2%PO1

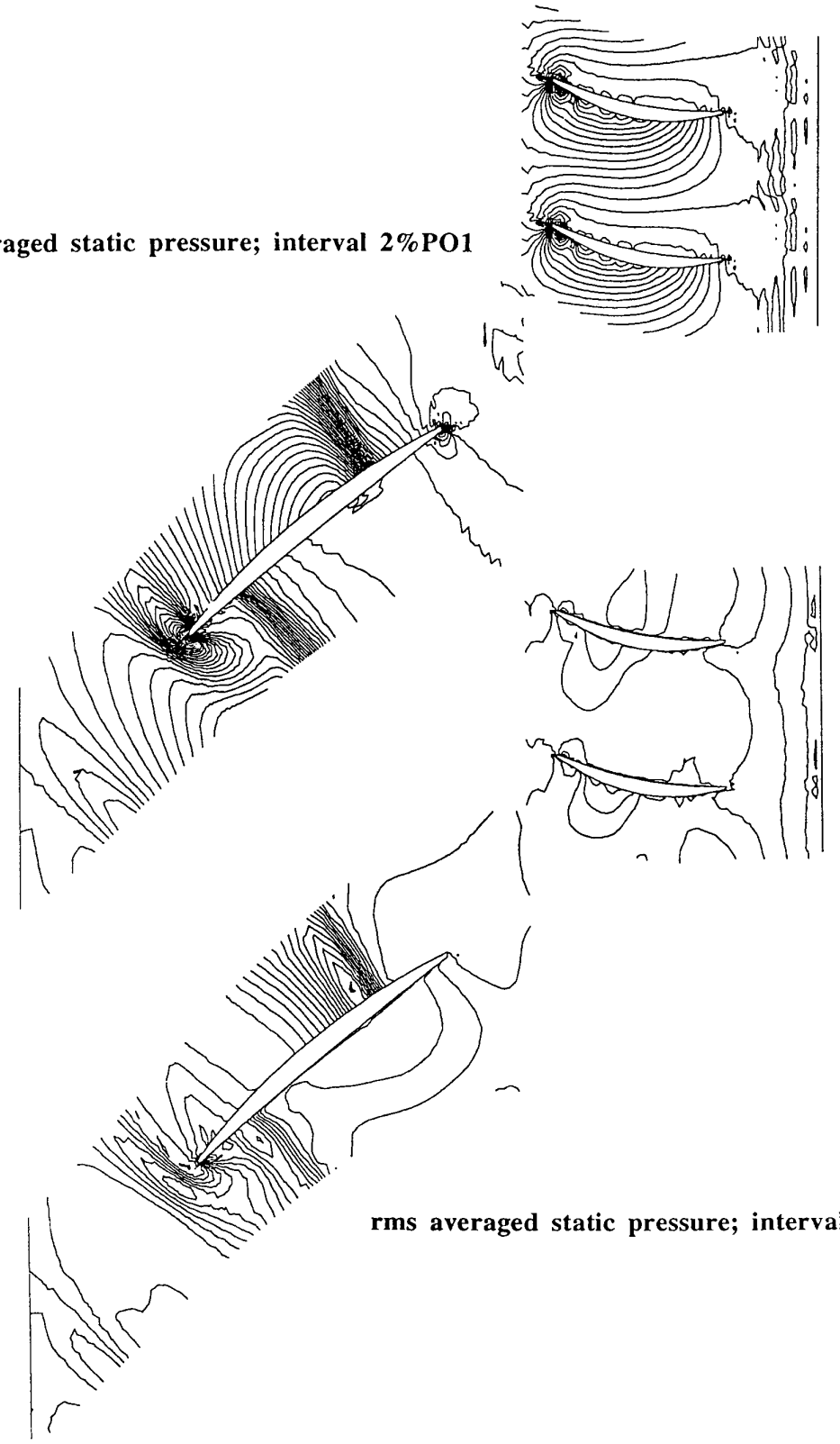

rms averaged static pressure; interval 1%PO1

Fig.17 Predicted time averaged and rms averaged static pressure in mid-span of the compressor stage.

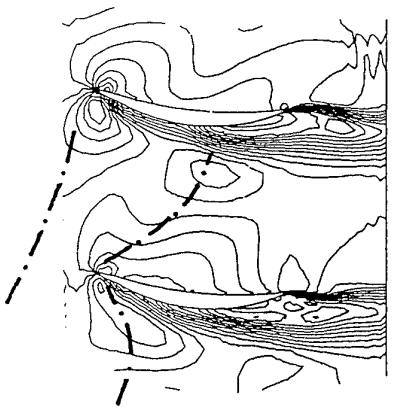

t

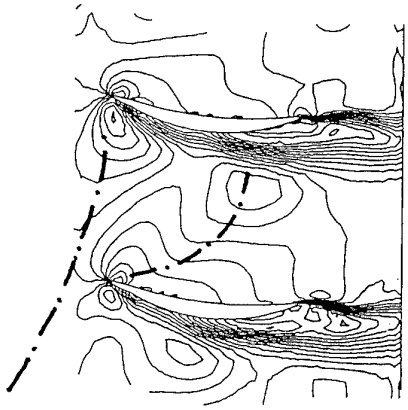

$t+\frac{2}{10}T$

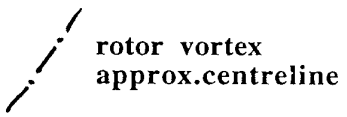

rotor vortex
approx.centreline

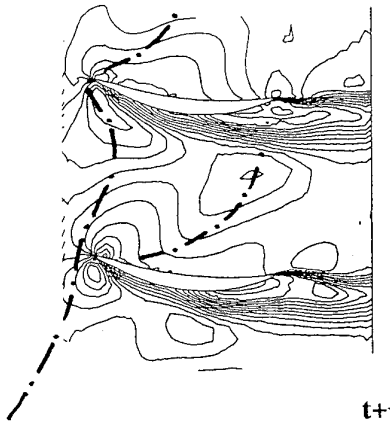

$t+\frac{4}{10}T$

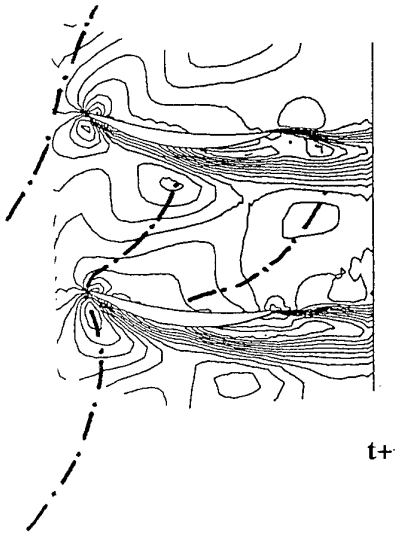

$t+\frac{8}{10}T$

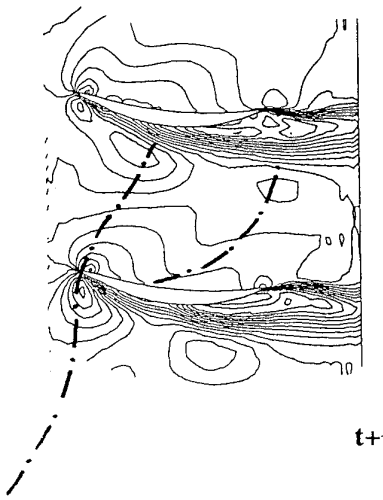

$t+\frac{6}{10}T$

Fig.18 Predicted Mach number at intervals throughout the cycle in a slice just near the casing ($\Delta M=0.05$).

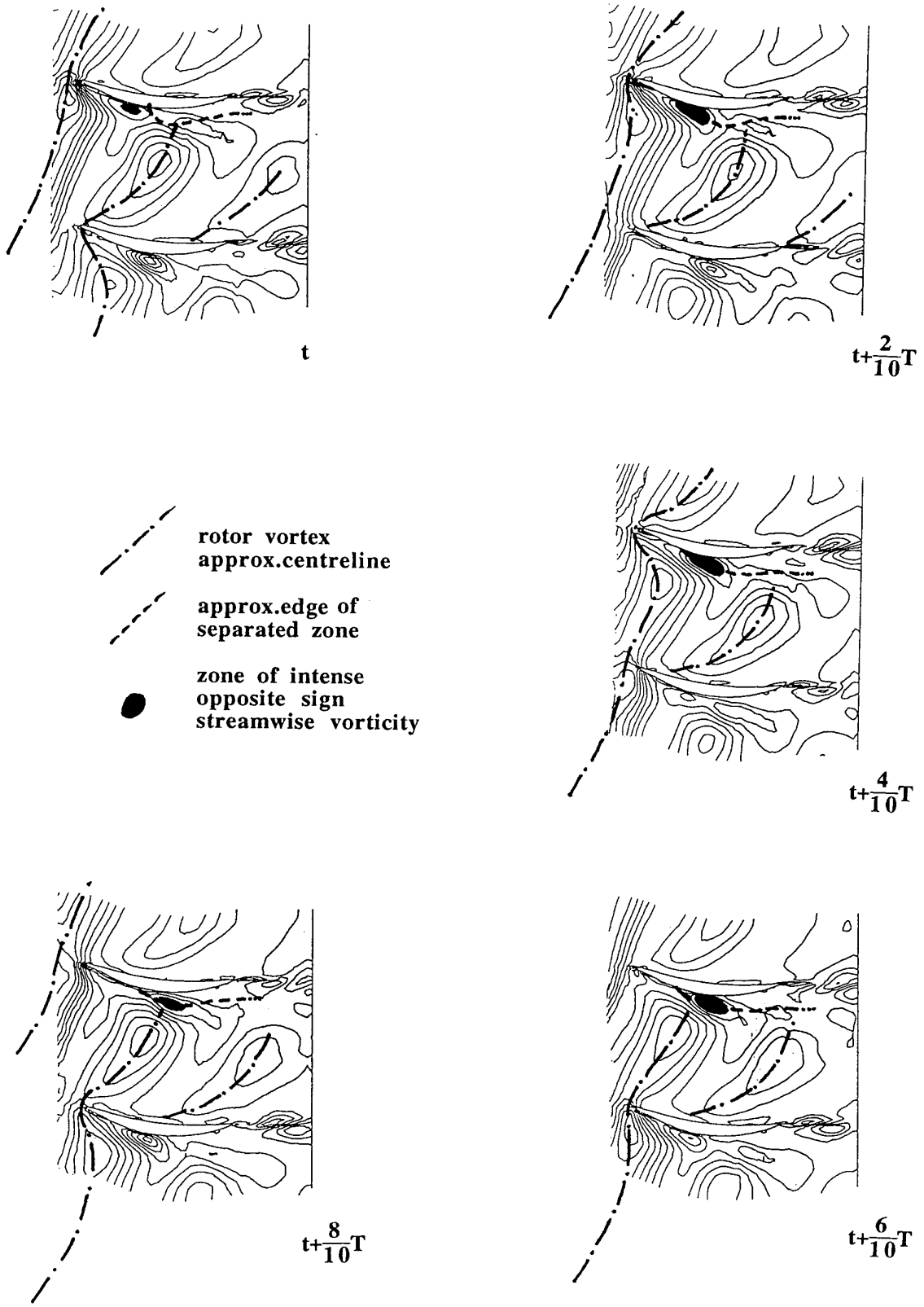

Fig.19 Predicted streamwise vorticity at intervals throughout the cycle in a slice just near the casing.

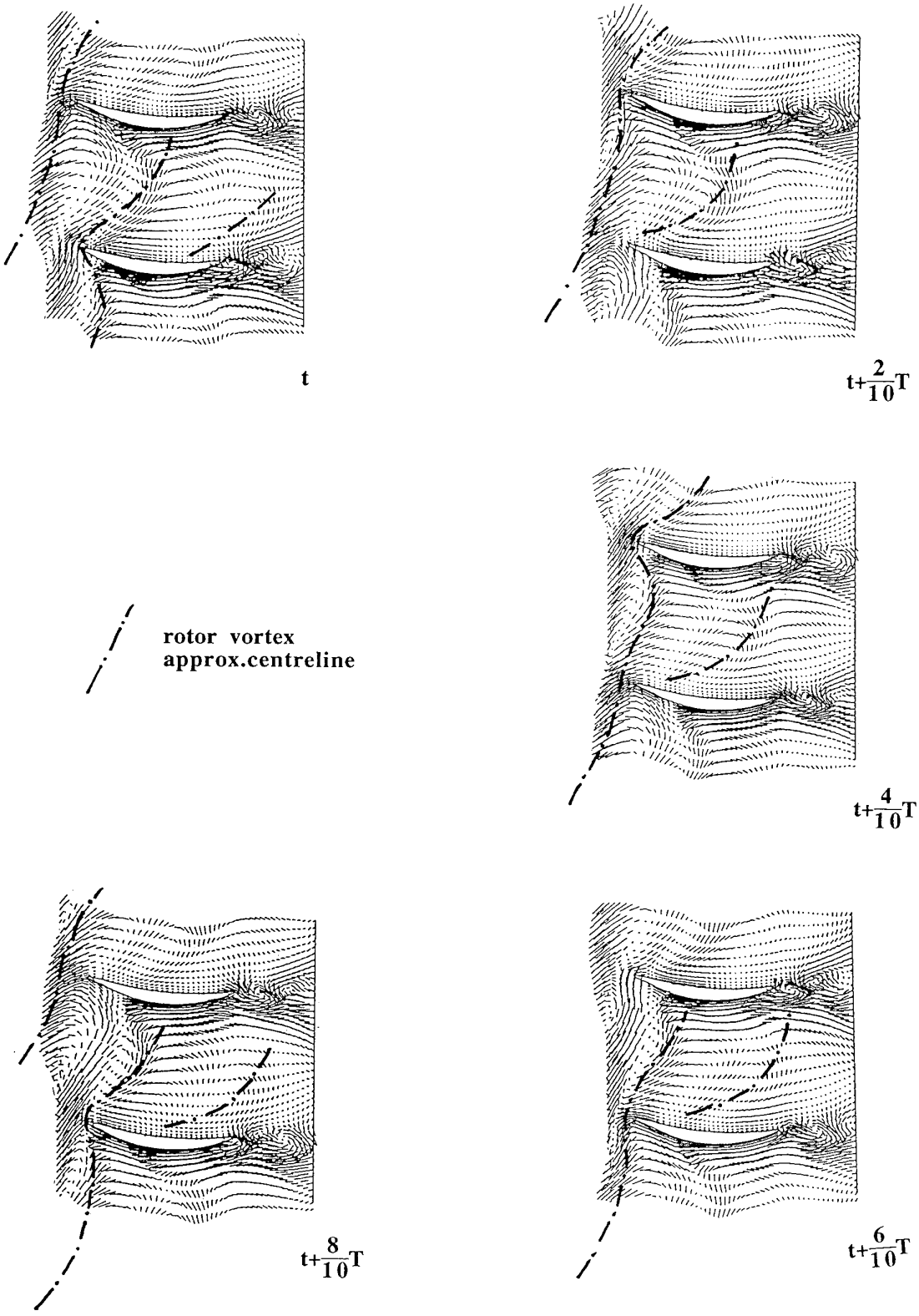

Fig.20 Predicted (instantaneous-averaged) velocity vectors at intervals throughout the cycle in a slice just near the casing.

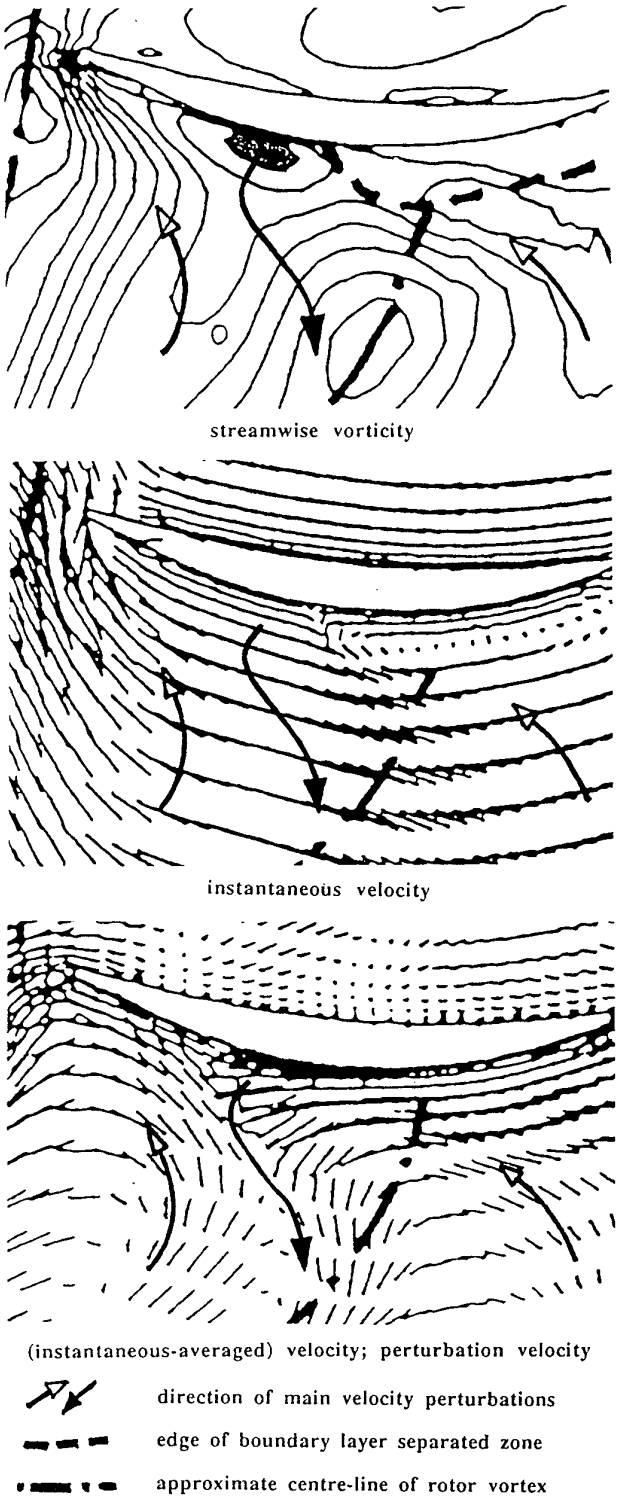

Fig.21 Detail view at time"t" showing the interaction of the rotor vortex with the stator boundary layer.

Numerical Investigation of Inviscid and Viscous Interaction in a Transonic Compressor

Frank Eulitz, Karl Engel
DLR, Institut für Antriebstechnik
Postfach 90 60 58
51147 Köln
Germany

Stefan Pokorny
DLR, Department for High-Performance Computing

1. SUMMARY

The paper presents inviscid and viscous results of unsteady flow calculations for a stator-rotor configuration of a transonic compressor. The calculations were run on a massively parallel hardware architecture. A second-order upwind total-variation diminishing scheme is employed in combination with a second order Runge-Kutta time integration method. The in- and outflow boundaries are treated with non-reflecting boundary techniques. The validity of the numerical method for time accurate calculations is thoroughly assessed by comparison to linear theory and experiments. In the analysis part of the paper, emphasis is on the stage interaction physics. A Fourier analysis of the stator blade pressure reveals fluctuations with a maximum amplitude close to 10% of the time-average. In the viscous case, the interaction of the observed propagating pressure waves with the boundary layer induces unsteady flow separation. Turbulence is accounted for by using either the Baldwin-Lomax or Spalart-Allmaras model. The influence of the turbulence model on the viscous solution is taken into account.

2. LIST OF SYMBOLS

α	Runge-Kutta coefficient, angle of attack
γ	specific heat ratio
c_p	pressure coefficient = $(p-p_{t1})/\left(0.5\rho_{t1}a_{t1}^2\right)$
d	wall normal distance
J	Jacobian transformation
h	streamtube thickness
κ	MUSCL control parameter
L	limiter function
ν	(laminar) molecular viscosity
ν_t	turbulent eddy viscosity
$\hat{\phi}$	flux function
Ω	vorticity
Pr	(laminar) Prandtl number
Pr_t	turbulent Prandtl number
R	gas constant
$\hat{R}, \hat{R}^{-1}$	right, left eigenvector matrix
Re	Reynolds number
t,τ	time
T	time-period
τ_w	shear stress at wall
$\vec{u}$	velocity vector
u_τ	friction velocity, $u_\tau = \sqrt{\tau_w/\rho_w}$
ξ, η	curvilinear coordinates
y	coordinate normal to solid surface
y^+	law-of-the-wall coordinate, $y^+ = \frac{\rho_w u_\tau}{\mu_w} y$

Subscripts

t	turbulent
w	at the wall

3. INTRODUCTION

Modern compressor and turbine design trends are towards size and weight reduction. As a result of less stages with less blades per row and a narrowing of the axial spacing between the blade rows, the aerodynamic loading of the blades increases. In particular, unsteady effects will gain in magnitude and in importance for the design.

Adamcyk et al. [2] distinguish between three different length scales to categorize unsteady turbomachinery flow effects. Wake turbulence or shock boundary-layer interaction, for example, are grouped into the "small scale" category as these are unsteady phenomena which are at least an order of magnitude smaller than the blade chord. "Medium scale" effects are of roughly the size of the blade chord or a passage. This category includes all types of stage interaction due to upstream potential effects or wake velocity distributions. Consequently, unsteady phenomena which extend over more than one passage, e.g. rotating stall, compressor surge or low frequency blade flutter, are "large scale" effects. It is the kind of "medium scale" phenomena which are in focus of the present work. More specifically, the upstream influence of rotor passage shocks on the stator blade row of a transonic compressor stage is studied based on the numerical solution of the unsteady inviscid or viscous flow equations. In a viscous calculation, the shock-induced interaction is superposed by a wake interaction. In this case, the turbulence model needed for closure of the Reynolds-averaged Navier-Stokes equations is a critical issue since the solution will contain no more turbulence physics than incorporated by the model.

Whereas steady-state calculations of the flow through a single rotor or stator passage have become a common tool in the on- and off-design, unsteady simulations are not as widely spread. The reason for this is not the lack of accurate numerical models but rather the handling problem. The time accurate simulation of a highly unsteady flow problem requires considerably more computation time and memory. A natural architecture for the solution of the hardware problem is a massively parallel computer since, from the theoretical point of view, it can be scaled arbitrarily with the problem size presuming that the code is fully scalable. For more passages to compute simply more processors with independent memory have to be added.

Paper presented at the AGARD PEP 85th Symposium on "Loss Mechanisms and Unsteady Flows in Turbomachines", held in Derby, United Kingdom, 8-12 May 1995, and published in CP-571.

Based on this, a parallel and interactive flow simulation system has been developed. Similar to a test facility, the interactive system enables the user to alter physical parameters and to request information about the current state of the system during run-time [23]. The flow solver along with a data processing unit has been implemented on a massively parallel computer using the message passing programming model. Parallelization of the code is achieved by virtue of domain decomposition and shown to be fully scalable [11]. Roe's upwind scheme has been implemented to ensure high resolution shock capturing and low numerical dissipation in smooth and viscous flow regions.

4. FLOW SOLVER

The two-dimensional Reynolds-averaged Navier-Stokes equations are solved for the compressible ideal gas in conjunction with a turbulence model. Three-dimensional effects are included through the specification of a streamtube thickness in the third dimension. The equation system to be solved reads in strong conservation form for a moving grid in body-fitted coordinates

$$h\frac{\partial \hat{Q}}{\partial t} + \frac{\partial h(\hat{F}-\hat{F}_v)}{\partial \xi} + \frac{\partial h(\hat{G}-\hat{G}_v)}{\partial \eta} = \hat{S} \qquad (1)$$

with

$$\begin{aligned} \hat{Q} &= Q/J\,, \\ \hat{F} &= (\xi_x F + \xi_y G + \xi_t)/J\,, \\ \hat{G} &= (\eta_x F + \eta_y G + \eta_t)/J\,, \\ J^{-1} &= x_\xi y_\eta - x_\eta y_\xi\,. \end{aligned} \qquad (2)$$

The conservative solution vector and the convective fluxes are written as

$$Q = \begin{bmatrix} \rho \\ \rho u \\ \rho v \\ e \end{bmatrix},\quad F = \begin{bmatrix} \rho u \\ \rho u^2 + p \\ \rho uv \\ u(e+p) \end{bmatrix},\quad G = \begin{bmatrix} \rho v \\ \rho vu \\ \rho v^2 + p \\ v(e+p) \end{bmatrix}. \qquad (3)$$

The variables t, ρ, u, v, e, p, T denote the non-dimensional time, density, Cartesian velocity components, specific total energy, pressure and temperature, respectively. The specific total energy is given by

$$e = \rho\left[\varepsilon + \frac{1}{2}\left(u^2 + v^2\right)\right] \qquad (4)$$

and the pressure is determined from the equation of state

$$p = \rho RT. \qquad (5)$$

The viscous fluxes read

$$F_v = \frac{1}{Re}\begin{bmatrix} 0 \\ \tau_{xx} \\ \tau_{xy} \\ \tau_{xx}u + \tau_{xy}v + q_x \end{bmatrix},\quad G_v = \frac{1}{Re}\begin{bmatrix} 0 \\ \tau_{xy} \\ \tau_{yy} \\ \tau_{xy}u + \tau_{yy}v + q_y \end{bmatrix} \qquad (6)$$

with the shear stresses and the heat terms including the Reynolds-averaged turbulent contribution,

$$\begin{aligned} \tau_{xx} &= \frac{\mu+\mu_t}{Re}\frac{2}{3}(2u_x - v_y)\,, & q_x &= \left(\frac{\gamma\mu}{Pr} + \frac{\gamma\mu_t}{Pr_t}\right)T_x\,, \\ \tau_{xy} &= \frac{\mu+\mu_t}{Re}(u_y + v_x)\,, & q_y &= \left(\frac{\gamma\mu}{Pr} + \frac{\gamma\mu_t}{Pr_t}\right)T_y\,. \\ \tau_{yy} &= \frac{\mu+\mu_t}{Re}\frac{2}{3}(2v_y - u_x)\,, \end{aligned} \qquad (7)$$

The non-dimensional molecular viscosity is calculated from Sutherland's formula,

$$\mu = T^{3/2}\frac{1 + 110/\tilde{T}_0}{T + 110/\tilde{T}_0}, \qquad (8)$$

where $\tilde{T}_0$ is the dimensional total temperature. The source term on the right hand side of (1),

$$\hat{S} = \begin{bmatrix} 0 \\ p\left(\xi_x\frac{\partial h}{\partial \xi} + \eta_x\frac{\partial h}{\partial \eta}\right) \\ p\left(\xi_y\frac{\partial h}{\partial \xi} + \eta_y\frac{\partial h}{\partial \eta}\right) \\ 0 \end{bmatrix} \qquad (9)$$

accounts for a streamtube of varying thickness.

4.1 Numerical Model

Different flux-difference-splitting schemes with total variation diminishing (TVD) properties are implemented in the code for the discretization of the inviscid equation part [9]. This allows for more flexibility during different phases of the simulation, e.g. calculation of the rotor acceleration phase or time-periodic operating point.

For the present flow problem, the convective fluxes are discretized using Roe's upwind scheme [26] which is combined with van Leer's [19] MUSCL extrapolation (monotonic upstream scheme for conservation laws) to obtain second order accuracy in space. The numerical flux at the cell interface is expressed as a function of the conservative states left and right of the interface:

$$\begin{aligned} \hat{F}_{j+\frac{1}{2}} = \frac{1}{2}\Bigg(& \left(\frac{\xi_x}{J}\right)_{j+\frac{1}{2}}\left[F^L_{j+\frac{1}{2}} + F^R_{j+\frac{1}{2}}\right] \\ & + \left(\frac{\xi_y}{J}\right)_{j+\frac{1}{2}}\left[G^L_{j+\frac{1}{2}} + G^R_{j+\frac{1}{2}}\right] \\ & + \left(\frac{\xi_t}{J}\right)_{j+\frac{1}{2}}\left[Q^L_{j+\frac{1}{2}} + Q^R_{j+\frac{1}{2}}\right] - \frac{1}{J}\hat{D}_{j+\frac{1}{2}}\Bigg). \end{aligned} \qquad (10)$$

The $\hat{G}$-flux is assembled correspondingly. The last of the numerical flux constituents is the upwind dissipation term which is defined at the cell interface $j + 1/2$ as

$$\hat{D} = \hat{R}\Lambda\hat{R}^{-1}\left(Q^R - Q^L\right), \qquad (11)$$

where the right eigenvector matrix is evaluated at Roe's average and Λ is a diagonal matrix containing the entropy-corrected eigenvalues of the inviscid part of equation system (1). According to Yee [32], one is free to choose the type of variable set to extrapolate. Here, the left and right *primitive* states $U = [\rho, u, v, p]^T$ are MUSCL-extrapolated, i.e.

$$U^R_{j+\frac{1}{2}} = U_{j+1} - \frac{1}{4}\left[(1-\kappa)\,\Delta'_{j+\frac{3}{2}} + (1+\kappa)\,\Delta''_{j+\frac{1}{2}}\right],$$
$$U^L_{j+\frac{1}{2}} = U_{j} + \frac{1}{4}\left[(1-\kappa)\,\Delta''_{j-\frac{1}{2}} + (1+\kappa)\,\Delta'_{j+\frac{1}{2}}\right]. \quad (12)$$

By variation of the parameter κ, the space discretization can be made fully upwind (κ=-1), upwind biased (κ=1/3 or 0) or central (κ=1). The mark indicates limited differences of the flow quantities,

$$\Delta'_{j+\frac{1}{2}} = L\left(\Delta_{j+\frac{1}{2}}, \omega\Delta_{j-\frac{1}{2}}\right),$$
$$\Delta''_{j+\frac{1}{2}} = L\left(\Delta_{j+\frac{1}{2}}, \omega\Delta_{j+\frac{3}{2}}\right), \quad (13)$$

where L denotes a nonlinear limiter function. Here, the van Albada limiter in quadratic form [20], is employed and the weighting factor ω is chosen to be unity,

$$L(\Delta_{j-\frac{1}{2}},\Delta_{j+\frac{1}{2}}) = \frac{2\Delta^2_{j-\frac{1}{2}}\Delta^2_{j+\frac{1}{2}} + \varepsilon}{\Delta^4_{j-\frac{1}{2}} + \Delta^4_{j+\frac{1}{2}} + \varepsilon}, \quad \left(\varepsilon = 10^{-5}\right) \quad (14)$$

The viscous fluxes are discretized using central differences.

The solution is advanced in time by a second-order accurate Runge-Kutta four-stage scheme using the upwind-tuned Runge-Kutta coefficients [20] for κ=0 in equation (12), α_1=0.11, α_2=0.255, α_3=0.46, and α_4=1.

4.2 Boundary Conditions

The treatment of the computational domain boundaries deserves special attention for time-accurate flow calculations since inappropriate boundary conditions may distort the solution considerably if not give non-physical solutions. Prone to unwanted artificial reflections, the inflow and outflow boundaries were found to be the most critical for the quality of the unsteady flow field. Two formulations of non-reflecting boundary conditions are implemented and used in different phases of the simulation. One is based on the linear approach by Acton, Cargill [1] and Giles [12] and generalized by the authors for curvilinear coordinates [7]. The formulation is non-reflecting in the sense of linear perturbations about a (prescribed) mean flow. In the present application, it is used to reach the desired operating point of the compressor stage. The other non-reflecting formulation is based on the nonlinear approach originally developed by Hedstrom [16] for the one-dimensional and later extended by Thompson [29] for the multi-dimensional case. The nonlinear method is of benefit during the rotor acceleration phase where, in the inviscid case, the flow is prone to numerical instability due to non-zero incidence at the leading edge of the rotor blades [7]. Contrary to its non-reflecting linear counterpart, it is not possible to prescribe any flow quantities. Consequently, the resulting flow field depends only on the initialization and the motion of the blades. Hence, the physical perturbations which evolve in the compressor stage are allowed to leave the computational domain with a minimum of artificial reflections.

At the intergrid boundary (between the stator grid and the moving rotor grid), the sheared-cell technique according to Giles [13] is adopted.

4.3 Treatment of Turbulence

Turbulence effects are accounted for by either an algebraic or a one-equation model. The first is the classic Baldwin-Lomax model (BL) [3]. The later has been developed by Spalart and Allmaras (SA) [28] recently and its application to unsteady turbomachinery flow is rather new. Unlike many early one-equation models, as for instance by Prandtl [24], which solve for the transport of the turbulent kinetic energy, the SA model directly solves for the eddy viscosity. The version which is used for the stage interaction problem reads

$$\frac{\partial\tilde{\nu}}{\partial t} + \vec{u}\nabla\tilde{\nu} = c_{b1}|\tilde{\Omega}|\tilde{\nu} - c_{w1}f_w\left(\frac{\tilde{\nu}}{d}\right)^2 + \frac{1}{\sigma}\left[\nabla\left((\tilde{\nu}+\nu)\nabla\tilde{\nu}\right) + c_{b2}(\nabla\tilde{\nu})^2\right], \quad (15)$$

where $\tilde{\nu}$ is the working variable and related to the eddy viscosity ν_t by

$$\tilde{\nu} = \nu_t f_{v1},$$
$$f_{v1} = \frac{\chi^3}{\chi^3 + c^3_{v3}}, \quad \chi = \frac{\tilde{\nu}}{\nu}. \quad (16)$$

Relationship (16) accounts for the flow behavior in the viscous sublayer. The negative term in (15) is a wall destruction term and defined as

$$f_w = g\left[\frac{1+c^6_{w3}}{g^6+c^6_{w3}}\right]^{1/6},$$
$$g = r + c_{w2}\left(r^6 - r\right), \quad (17)$$
$$r = \frac{\tilde{\nu}}{|\tilde{\Omega}| + \kappa^2 d^2},$$

where $\tilde{\Omega}$ is given by

$$\tilde{\Omega} = \Omega + \frac{\tilde{\nu}}{\kappa^2 d^2} f_{v2}. \quad (18)$$

Here, additional terms which provide control over laminar regions and smooth transition to turbulence are omitted as the present compressor flow is assumed to be all-turbulent. The model's constants are as given by Spalart and Allmaras, c_{b1} = 0.1355, σ = 0.667, c_{w1} = 3.239, c_{b2} = 0.622, κ = 0.41, c_{w2} = 0.3, c_{w3} = 2, c_{v1} = 7.1. The following boundary conditions for the eddy viscosity are prescribed

$$\nu_t = 0, \quad \text{at the wall},$$
$$\frac{\partial^2\nu_t}{\partial\xi^2} = 0, \quad \text{at outflow boundary } \eta = const, \quad (19)$$
$$\frac{\partial^2\nu_t}{\partial\eta^2} = 0, \quad \text{at outflow boundary } \xi = const.$$

So far, numerical studies indicate a fair insensitivity of the model to the initial condition making a precalculation with an algebraic model unnecessary. The time integration of the model is started by setting the eddy viscosity to a freestream value of 10^{-4} everywhere in the flow field.

The above one-equation model has been implemented as a first step towards accounting for turbulence history effects. A comparison of several one-equation models and the standard $k-\varepsilon$

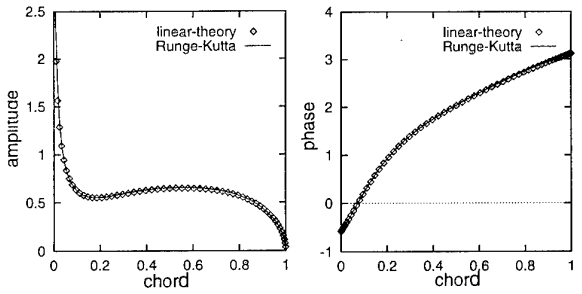

Fig. 1 - Amplitude and phase distribution of pressure jump on flat plate due to sinusoidal time variation of the exit pressure (reduced frequency = 1.086).

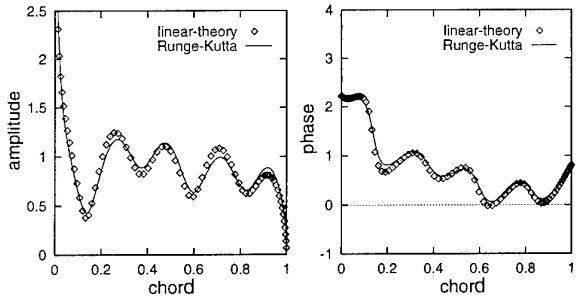

Fig. 2 - Amplitude and phase distribution of pressure jump on flat plate due to time varying inlet velocity distortion (reduced frequency = 12.56).

model led Birch [4] to the conclusion that one-equation models which solve for the eddy-viscosity itself "give overall performances close to that of a standard $k-\varepsilon$ model". The better numerical robustness of a model equation for only a single variable is obvious. The Gallilean invariance property qualifies the SA model for application to moving grid problems. Due to its local character, the numerical solution of the model on a massively parallel architecture raised no additional problem. The wall destruction term and viscous sublayer damping merely have to be evaluated on processors bordering a solid boundary. In the free shear flow region, both damping terms approach zero. At the wall, the model does not require any finer mesh resolution than most algebraic models. For a detailed discussion of the SA model, the reader is referred to the original work of Spalart and Allmaras [28]. In their work, the model is validated for various test cases and a robust implicit method for the solution of the model is proposed. More applications of the model can be found in [4] and [21].

5. VALIDATION

In a recent paper by the authors [8], three test cases with relevance for unsteady turbomachinery flow were presented and applied to test various flux difference splitting schemes. Here, an extended validation is presented for the above MUSCL-scheme combined with Runge-Kutta time stepping.

5.1 Inviscid Flat Plate Cascade

First, the flow through a flat plate cascade excited by an unsteady perturbation is considered. For a sufficiently small amplitude of the perturbation, nonlinear effects are negligible and a comparison of the numerical results to a linear, inviscid theory as by Smith [27] is possible. Similar to thin airfoil theory, the linear analysis leads to an integral equation which is solved computationally according to Whitehead [30]. The

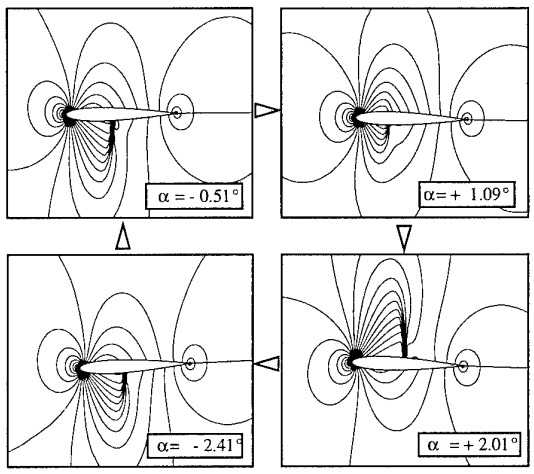

Fig. 3 - NACA-0012 airfoil at oscillatory pitch: Instantaneous iso-pressure contours during an oscillation period are shown, the frequency is 62.5 Hertz (reduced frequency = 0.08) and the mean angle of attack is 0.016.

linear analysis has been previously applied by Giles [14] for the validation of his unsteady flow solver in the linear regime.

The flat plate cascade considered here has a pitch to chord ratio of 1/2, a stagger angle of 30 degrees and is discretized using a 130 x 50 nodes mesh. The mean flow condition of the cascade is given by a Mach number of 0.7. Convergence of the numerical solution to the periodic state is generally obtained after computation of three perturbation periods. Two kinds of perturbations which are of relevance for stage interaction are enforced. In a first case, a sinusoidal variation of the back pressure is imposed at the exit boundary. The reduced frequency of the pressure variation is 1.068. The first Fourier harmonic of the pressure jump across the flat plate is compared to the corresponding linear results in terms of its amplitude and phase distribution along the chord, as shown in figure 1. For this low frequency case, perfect agreement of the nonlinear numerical results with linear theory can be observed. In a second case, a high frequency wake perturbation is imposed at the entry boundary. The reduced frequency of the variation amounts to 12.56 and its angle relative to the cascade is -30 degrees. The mean flow conditions are the same as in the first case. Again, the results shown in figure 2 compare well with the exact data. The wave length of the unsteady flow is roughly 1/4 of the chord. Similar disturbances, i.e. a combination of pressure waves and vorticity waves of moderate amplitudes, can be observed in the stage interaction process as will be seen in the final chapter.

5.2 Oscillating Airfoil

In a second case, the transonic flow past a NACA-0012 profile oscillating about the quarter-chord point is considered to evaluate the numerical method in the nonlinear regime. Depending on the incidence, shock-waves develop and vanish in turn on either side of the airfoil as can be seen in figure 3 which shows iso-pressure lines at various instants during the oscillatory pitch. The numerical results are compared to measurements by Landon [18] for a freestream Machnumber of 0.75 and a frequency of 62.5 Hertz (corresponding to a reduced frequency of 0.08). The angle of attack oscillates between -2.49 degrees and +2.52 degrees. Although the oscillation frequency is rather low, when compared to typical frequencies of "medium scale"

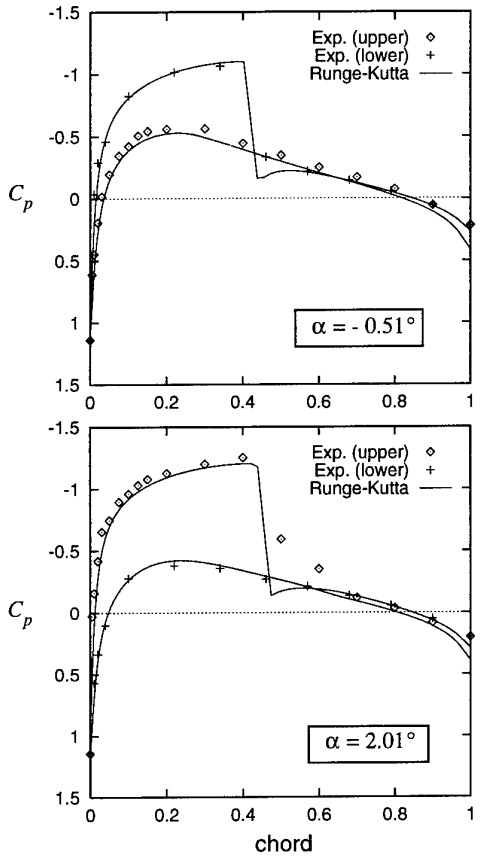

Fig. 4 - Distribution of pressure coefficient on oscillating NACA-0012 airfoil at two selected angles of attack. Symbols denote experimental data on upper and lower side.

turbomachinery unsteady phenomena (see introduction), the flow clearly exhibits a dynamic behavior, i.e. a hysteresis, as can be concluded from the obvious time lag of shock position and angle of attack in figure 3. Comparison of the experimental data with the inviscid numerical data at two selected time instants are provided in figure 4 in terms of the non-dimensional pressure coefficient.

5.3 Turbulent Shock Boundary-Layer Interaction

The SA turbulence model has been validated by Spalart and Allmaras for the Samuel-Joubert flow and the flow past the RAE2822 airfoil at transonic flow conditions [28]. To test the model for unsteady flow, a double-circular-arc profile (DCA) in a two-dimensional channel is considered at transonic flow conditions. Self-excited flow oscillation, due to the interaction of the shock system with the wake, can be observed if the specified channel exit pressure lies within an unstable range. The case has been studied both experimentally and numerically by Yamamoto and Tanida [31]. For the simulation of the unsteady flow, a fully converged steady-state solution is necessary. It can be easily obtained by prescribing a stable exit pressure. The Reynoldsnumber is 1 Million and the Machnumber at the channel entry is 0.72. In figure 5, the iso-density lines of the steady-state calculation, which has been obtained on a 310x62 nodes grid, is shown. The unsteady calculation is presently under work by the authors.

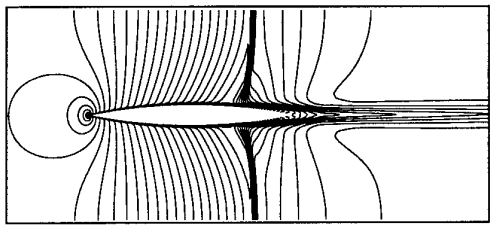

Fig. 5 - Distribution of iso-density lines of transonic flow past DCA profile in a two-dimensional channel.

6. RESULTS

The shock induced interaction between a stator and a rotor of a transonic compressor is in focus of the present investigation. At certain operating conditions of the compressor, rotor passage shocks may interact with the upstream stator row. The interaction mechanism as sketched in figure 6 looks predominantly inviscid and one therefore expects an inviscid computation to already produce the essential interaction features. As, in reality, the wave interaction is superposed by viscosity effects such as vortex shedding, wake shock interaction, and boundary layer separation the viscous solution will, however, differ from an inviscid one. It is the second purpose of the following investigation to discuss the difference between the inviscid and viscous results.

The inviscid results are discussed in detail and compared to the viscous results. The latter are presented in a more qualitative manner. Doing this, the level of the turbulence modelling is taken into account.

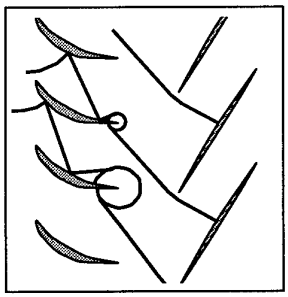

Fig. 6 - Schematic of shock-induced stator-rotor interaction according to Bölcs [5]. Rotor passage shocks (right) interact with the upstream stator blades (left).

The computational domain as shown in figure 11 includes three stator passages and two rotor passages, i.e. the pitch ratio of stator versus rotor is 3:2. For the stator passages, a varying streamtube thickness, corresponding to an axial velocity density ratio of 1.3, is assumed. The grid shown is for the viscous calculation. For the inviscid calculation, C-blocks instead of O-blocks are used to enforce the Kutta-Joukowski condition. The inviscid mesh contains approximately 80,000 nodes. The integration domain is decomposed into 220 subdomains subject to acceptable load balancing for use of 220 processors of a GCel-1024 transputer system.

6.1 Simulation Procedure

The operating point is defined by a relative inflow Machnumber of 1.1 in the rotor corresponding to a non-dimensional rotor-speed of 0.9744 and a pitch-averaged back pressure of 0.96. The reduced blade passing frequency equals 3.07. The parameters for the inflow and outflow boundary and the rotor-speed are estimated by one-dimensional flow analysis. Starting from the guessed steady flow field, the rotor is accelerated and

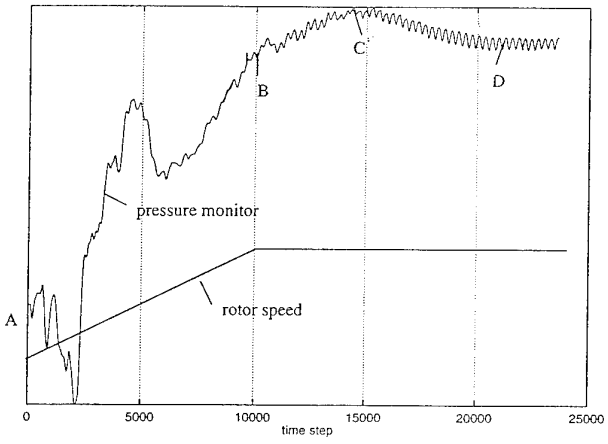

Fig. 7 - Log of simulation procedure for calculation of inviscid stator-rotor interaction: The rotor-exit pressure in the mid-passage and the rotor speed is plotted versus the time step.

the mean back pressure is increased accordingly to ensure non-zero incidence at the leading edge. Thus, the subsequent overshooting of the flow variables, prone to numerical instability, can be avoided. The computational start-up procedure is logged in figure 7 where the rotor exit pressure in the mid-passage and the rotor speed is plotted versus the time step. Due to acceleration of the rotor, there is a pressure rise at the rotor exit (A-B). To reach the operating point of the stage, a further increase of the pressure is prescribed at the exit boundary after the rotor has reached its nominal rotation speed (C). The time-periodic operating point (D) is obtained after calculation of 20,000 explicit time steps. A period T, which is resolved by approximately 1700 time steps, equals the time taken by a rotor blade to pass one and a half stator passages. The non-reflecting boundary conditions of the nonlinear Thompson type have been employed during the start-up phase (A-B). To reach and maintain the operating point (B-D), the linear non-reflecting approach according to Giles is used [8].

6.2 Inviscid Rotor-Stator Interaction

In figure 12, instantaneous iso-pressure contours provide a representative overview of the flow field during time-periodic operating point. From the pitch ratio of 3:2 follows a 120-degrees phase shift of the flow history in the stator passages. The unsteady flow details in the stator row are described using the four iso-pressure snap-shots of figure 13 focussing on a selected stator passage and a time period. The rotor-passage shock interacts with the trailing edge of the upstream stator blade. This causes upstream propagating reflections on either side of the blade. While propagating upstream, the pressure wave of the pressure side crosses the stator passage and is then reflected a second time on the suction side of the neighboring blade. The secondary reflection continues its way upstream and again crosses the passage inducing another reflection, this time on the pressure side. Eventually, the pressure wave leaves the computational domain, and owing to the non-reflecting boundary condition practically without any artificial reflections at the inflow boundary. The multiple reflections along the stator profile correspond to the fact that pressure waves of 4 generations coexist in a stator passage as can be realized after careful examination of the instantaneous isobar snap-shots in figure 13. To make the point clear, the temporal origin, i.e. the generation, of the observed wave patterns are distinguished by different shading in the schematic of figure 8.

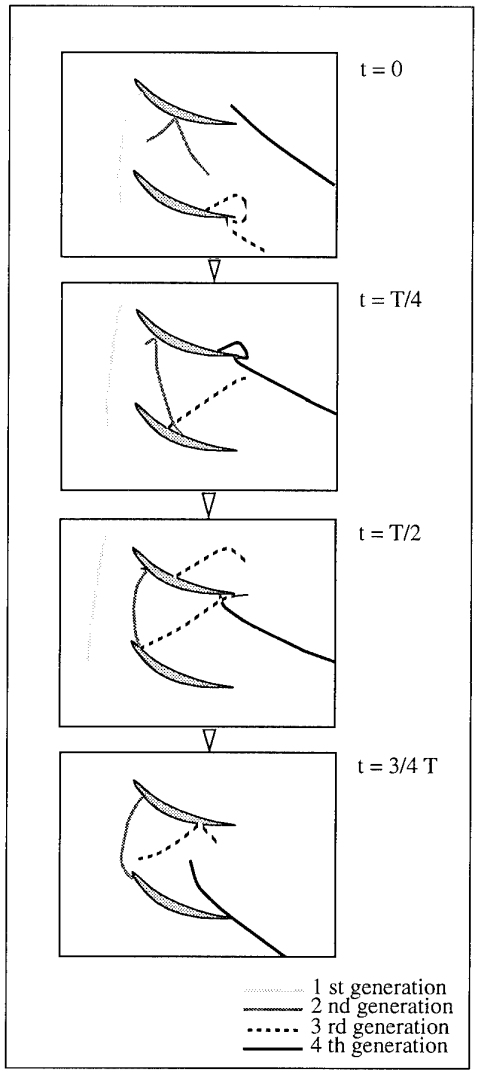

Fig. 8 - Observed flow dynamics in a stator-passage during a period T due to rotor-passage shock induced interaction. For the present case, 4 generations of pressure waves coexist in a stator passage, i.e. the 1st generation disturbance has been induced 3 time-periods previously by a rotor-passage shock (solid lines). The schematic has been derived from the computational results in figure 13.

The dynamics of wave propagation and reflection explains two dominant unsteady flow features. The first feature is the obvious phase lag between the surface pressure peaks of the suction and pressure side (the pressure peaks can be identified by a V-shape in the pressure iso-contours). The second feature can be observed from a Fourier analysis of the stator blade surface pressure. Results of the Fourier analysis in terms of the rotor blade passing frequency are shown in figure 9 where the amplitudes of the surface-pressure harmonics are plotted versus the chord of the stator blade. On the pressure side, the first three harmonics exhibit two distinct maxima, one not far from the leading edge and the other near the trailing edge. Opposed to this, the harmonics of the suction side show only one dominant maximum near mid-chord. Comparison of the maximum amplitude values with the zeroth harmonic, i.e. the time average, shown in figure 10, reveals that the peak amplitude amounts to nearly 10% of the mean flow values. Except for the bubble on the suction side near the leading edge, the time averaged distribution is in qualitative accordance with what one

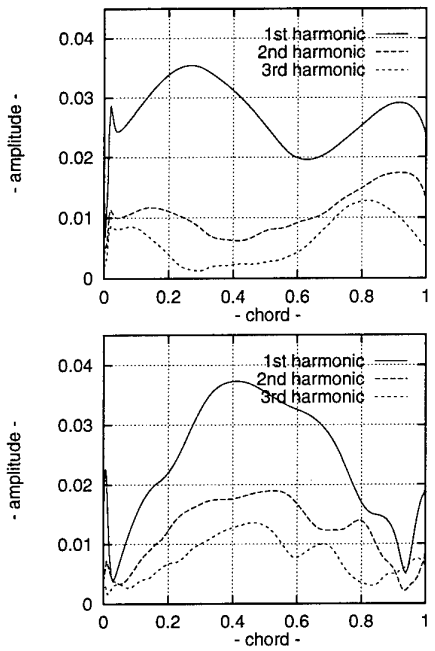

Fig. 9 - Amplitude distributions of non-dimensional stator-blade surface pressure harmonics due to shock-induced stage interaction (upper pressure side, lower: suction side).

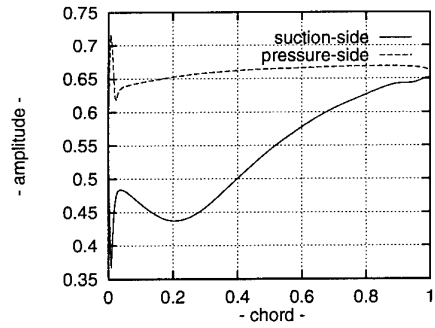

Fig. 10 - Distribution of time-averaged non-dimensional stator-blade surface pressure due to shock induced stage interaction.

expects from an inviscid steady-state solution. The pressure bubble is possibly a manifestation of the rotor-passage shock interacting with the trailing edge of a stator blade (compare with figures 8 and 13).

6.3 Viscous Stator-Rotor Interaction

In the following, the influence of the pressure disturbances on the boundary layer in the stator and the effects of the wake are discussed. Two viscous computations with different turbulence models and mesh refinements were done for a qualitative study of viscosity effects on the shock-induced interaction: In a first computation, the Baldwin-Lomax model (BL) is employed on a coarse grid for exactly the same geometry (pitch ratio 3:2, figure 11) and operating point as in the inviscid case. The second computation is performed on a finer mesh for a pitch ratio of 1:1 (figure 16) using the Spalart and Allmaras model (SA). Here, the higher level of grid refinement is achieved by reducing the number of passages to compute instead of adding grid nodes. Reducing thus the computational costs the price to be paid is that of reduced comparability which is accepted for the following qualitative study. In both cases, the boundary layer of the rotor-blade is not resolved assuming that its existence has negligible upstream effect on the stator flow and the wake, that is, the rotor-blade is modelled as an inviscid solid boundary.

6.3.1 Coarse-Grid Results with BL Turbulence Model

For the coarse-grid solution, the same multiblock grid as for the inviscid investigation is used except for the O-blocks around the stator-blades where more nodes are introduced for a coarse boundary layer resolution. The average y^+-value for the first nodes from the wall is about 3 and the boundary layer at mid-chord is resolved by 7 to 8 grid points. Therefore, the viscous BL results can only be considered to be of preliminary nature. The Reynolds number with respect to the stator pitch and sonic speed at stagnation point is 400,000. Due to the displacement of the boundary layer the back pressure is slightly corrected in order to obtain roughly the same flow conditions as in the inviscid case. All the other flow parameters remain the same. Although time consuming, the above initialization procedure has been employed. In figure 14, an isobar plot of the viscous calculation using the BL is shown. Principally new is the interference of shear layers with the pressure waves. In the stator passages, the upstream running pressure waves are reflected at the outer boundary layer and at the same time induce massive flow separation. This interaction gives rise to the generally more complex flow field. An additional viscous flow feature can be observed from the corresponding iso-entropy contours (figure 15). This is the vortex shedding from the trailing edge of the stator blades. As the wake is convected downstream it interacts with the rotor shock-wave and eventually breaks up. Further downstream, the wake is cut by the rotor-blade and an irregular, though time-periodic, entropy distribution develops. Thus, turbulent wake portions are distributed into the mid-passage. The results indicate that proper turbulence modelling is of crucial importance for the physical content of the computation not only near the wall but in the entire flow field. The simple algebraic Baldwin-Lomax model which is of wall-bounded nature can only be of limited use. It does not account for turbulence history effects in space and time. It is admitted that the mesh resolution is not fine enough for the specific application and that the determination of the maximum of the important function $f(y) = y|\Omega|\left[1 - \exp\left(-y^+/A^+\right)\right]$ (using same notation as in Baldwin, Lomax [3]) may be unsafe if not wrong. The massive boundary-layer separation zones may look less severe with a finer mesh or more refined turbulence model. It is concluded, that here the minimum would be a one- or two-equation transport model

6.3.2 Fine-Grid Results with SA Turbulence Model

Results obtained with the one-equation SA turbulence model at a comparable operating point of a similar stage on the fine grid are presented in the figures 17 to 21. Figure 17 shows an instantaneous iso-pressure distribution. Due to the reduced pitch ratio of 1:1 the wave pattern in the stator passage generated by the moving rotor-shock appears less complex as for the previous configuration with a 3:2 pitch. The unsteady interference of the stator-wake with the rotor-shock leads to a wake structure very similar to a von Karman vortex street which is well visible in the instantaneous iso-entropy plot of figure 18. In this regard, the SA simulation is in qualitative agreement with the BL case. The entropy gradient parallel to the flow direction is due to the Q3d source term in equation (1). An instantaneous distribution of the iso-eddy-viscosity is given in figure 19. An overview of the flow in the stator pas-

sage during a time-period is provided in figure 20 where instantaneous iso-pressure distributions are shown. Again, the interaction of the rotor-shock with the upstream trailing edge of the stator-blade leads to a reflection on the pressure side which propagates upstream as it crosses the stator passage. After the reflected wave has crossed the passage (bottom picture in figure 20 at time instant 3/4T) a secondary reflection is induced on the suction side of the next blade. Different from the previous case (compare with figure 13), however, it is not visible as it merges with the shock-wave of the next rotor-blade. At the same instant, the shock-wave passes the wake as can be detected from its double-S shaped deformation. The corresponding velocity vector snap-shots of figure 21 illustrate the effect of the upstream propagating waves on the boundary layer. At the instant the reflection of the rotor-shock on the pressure side is strongest (t=0) a small separation bubble evolves and a substantial deviation of the vectors from the unperturbed flow direction can be observed. As the reflection migrates further upstream (t=T/4 to T/2) the separation bubble decays gradually and vanishes altogether at t=3/4T. On the suction side where the shock-wave itself interacts with the boundary layer the effect is accordingly stronger. Here, the upstream moving shock induces a steadily growing separation zone with a maximum length of about 40 percent chord length. After a moment of reattachment (at about t=T/2) the next shock-wave restarts the separation process (at about t=3/4T) allover again.

7. CONCLUSIONS

Inviscid and viscous unsteady flow interaction in a transonic compressor stage is studied numerically with a massively parallel and interactive flow solver using 220 processors.

Main features of the numerical method are a second order MUSCL flux-difference-splitting scheme, an explicit Runge-Kutta time-stepping and two formulations of non-reflecting boundary conditions. The numerical method has been validated using various unsteady test cases. The predicted results for a flat-plate cascade excited by a linear perturbation are in practically perfect agreement with linear theory. For the oscillating NACA-0012 airfoil, the numerical method produced results in good agreement with experimental data.

Inviscid and viscous transonic interaction phenomena are discussed for two stator-rotor configurations. The inviscid interaction due to the moving rotor-shock can be characterized by upstream propagation and multiple reflection of pressure waves. A Fourier analysis of the stator-blade surface pressure reveals fluctuations with a peak amplitude close to 10% of the mean flow value. The pitch ratio has a drastic effect on the wave pattern in the stator-passage.

In the viscous case, the pressure disturbances induce unsteady flow separation. Separation bubbles evolve and vanish in the course of a time-period. The unsteady interference of the stator-wake with the downstream rotor-shock leads to a flow structure similar to a van Karman vortex street. Turbulent flow portions are spread into the midpassage region of the rotor. The algebraic turbulence model by Baldwin-Lomax has been found difficult to apply to the specific flow problem. The results obtained with the one-equation model by Spalart and Allmaras show physically plausible content which encourage further and more detailed investigation of viscous rotor-stator interaction.

8. REFERENCES

[1]Acton, E., and Cargill, M., "Non-Reflecting Boundary Conditions for Computations of Unsteady Turbomachinery Flow," *Proceedings of the Fourth International Symposium Unsteady Aerodynamics and Aeroelasticity of Turbomachines and Propellers,* pp. 211-228, 1988.

[2]Adamcyk, J.J., Greitzer, E.M., Wisler, D.C., "Unsteady Flow in Turbomachines: Where's the Beef?", AD-Vol. 40, Unsteady Flows in Aeropropulsion, ASME 1994.

[3]Baldwin, B., and Lomax, H., "Thin Layer Approximation and Algebraic Turbulence Model for Separated Turbulent Flow," AIAA Journal, No. 78-257, 1978.

[4]Birch, S.F., "One Equation Models Revisited", AIAA-93-2903, 1993.

[5]Bölcs, A., Suter, P., "Transsonische Turbomaschinen", G. Braun Karlsruhe, 1986.

[6]Dannenhofer, J.F., and Giles, M.B., "Convergence Acceleration Through the Use of Time Inclining", AIAA Journal 28(8), 1990.

[7]Engel, K., Faden, M., Pokorny, S., "Implementation of Non-Reflecting Boundary Conditions into an Unsteady Flow Simulation System" *3rd International Conference on Numerical Methods for Fluid Dynamics*, ICFD92, 7-10 April, Reading U.K, 1992

[8]Engel, K., Eulitz, F., Faden, M., Pokorny, S., "Numerical Investigation of the Shock Induced Interaction in a Transonic Compressor Stage", ASME Symposium, 6-11 November, Chicago, U.S.A., 1994.

[9]Engel, K., Eulitz, F., Faden, M., Pokorny, S., "Validation of Different TVD Schemes for the Calculation of the Unsteady Turbomachinery Flow", ICNMFD 94, 11-15 July, Bangalore, India, 1994.

[10]Erdo, J.I., Alzner, E., and McNally, W., 1977, "Numerical Solution of Periodic Transonic Flow Through a Fan Stage", AIAA Journal, 15(11).

[11]Faden, M., Pokorny, S., and Engel, K. 1993, "Unsteady Flow Simulation on a Parallel Computer", 11*th AIAA Computational Fluid Dynamics Conference*, July 6-9th, Orlando FL, U.S.A.

[12]Giles, M.B., "Non-Reflecting Boundary Conditions for the Euler Equations", CFDL-TR-88-1, 1988.

[13]Giles, M.B., "UNSFLO: A Numerical Method for the Calculation of the Unsteady Flow in Turbomachinery", GTL Report #205, Gas Turbine Laboratory, MIT, 1990.

[14]Giles, M.B., Haimes, R., "Validation of a Numerical Method for Unsteady Flow Calculation", ASME, 91-GT-271, 1991.

[15]Harten, A, "On a Class of High-Resolution Total-Variation-Stable Finite-Difference Schemes", *SIAM Journal Numerical Analysis*, Vol 21, pp 1-23, 1984.

[16]Hedstrom, G., W., "Non-reflecting boundary conditions for non-linear hyperbolic systems" *J. Comp. Phys.,* 30, pp. 222-23, 1979.

[17]Hirsch, C., "Numerical Computation of Internal and External Flows", John Wiley & Sons Ltd. NY 10158-0012, USA., 1990.

[18]Landon, R.H. "Oscillatory and Transient Pitching", in AGARD Report No. 702, *Compendium of Unsteady Aerodynamics Measurements,* 1977.

[19]van Leer, B., "Towards the Ultimate Conservation Difference Scheme V, A Second-Order Sequel to Godunov's Method", J. Comp. Phys., Vol. 32, pp. 101-136, 1979.

[20]von Lavante, E., Yao, J., "Simulation of Flow in Exhaust Manifold of an Reciprocating Engine", AIAA 93-2954, 1993.

[21]Liu, C.H., "Vortical Structures of Aircraft Wakes", in *Vortex Flow in Aeronautics*, International Colloq., 12-14 October, Aachen, Germany, 1994.

[22]von Lavante, E., El-Miligui, A., Cannizario, F., E., "Simple Explicit Upwind Schemes For Solving Compressible Flows", *Proceedings of the Eighth GAMM-Conference on Numerical Methods in Fluid Mechanics,* Vieweg, Braunschweig Vol. 29, 1990.

[23]Pokorny, S., Faden, M., Engel, K., "An Integrated Flow Simulation on a Parallel Computer Part I: Basic Idea, Part II: The Flow Solver", *7.th International Conference on Numerical Methods in Laminar and Turbulent Flow,* July 15-17th, Stanford, CA, U.S.A., 1991.

[24]Prandtl, L., "Über ein neues Formelsystem für die ausgebildete Turbulenz", Nachr. Akad. Wiss., Göttingen, Math.-Phys., p.6, 1945.

[25]Pulliam, T.H., and Steger, L., "Recent Improvements in Efficiency, Accuracy, and Convergence for Implicit Approximative Factorization Algorithms", AIAA-85-0360, 1985.

[26]Roe, P.L., "Approximative Riemann Solvers, Parameter Vector and Difference Schemes", *J. Comp. Phys.,* 43, pp. 357-372, 1981.

[27]Smith, S.N., "Discrete Frequency Sound Generation in Axial Flow Turbomachines", Aeronautical Research Council Reports and Memoranda, R. & M. No. 3709, 1973.

[28]Spalart, P., R., Allmaras, S., R., "A One-Equation Turbulence Model for Aerodynamic Flows", AIAA-92-0439, 1992.

[29]Thompson, K.W., "Time Dependent Boundary Conditions for Hyperbolic Systems", *J. Comp. Phys. 68*, pp. 1-24, 1986.

[30]Whitehead, D.S., ,"Classic Two-Dimensional Methods in Aeroelasticity in Axial Flow Turbomachines, AGARD-AG-298, Vol.1 , 1987.

[31]Yamamota, K., Tanida, Y., "Self-Excited Oscillation of Transonic Flow around an Airfoil in a Two-Dimensional Channel", 34th ASME, 1989.

[32]Yee, H.C., "A Class of High-Resolution Explicit and Implicit Shock Capturing Methods", *VKI-Lecture Notes in Computational Fluid Dynamics,* 1989.

9. FIGURES

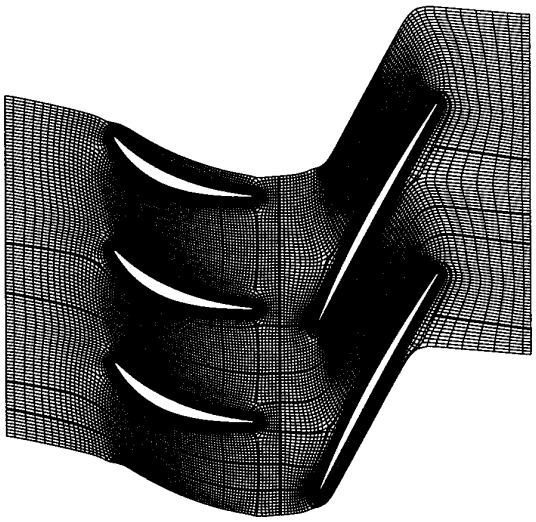

Fig. 11 - Configuration (A): Grid for a stator-rotor configuration of 3 stator passages and 2 rotor passages with 100,000 nodes.

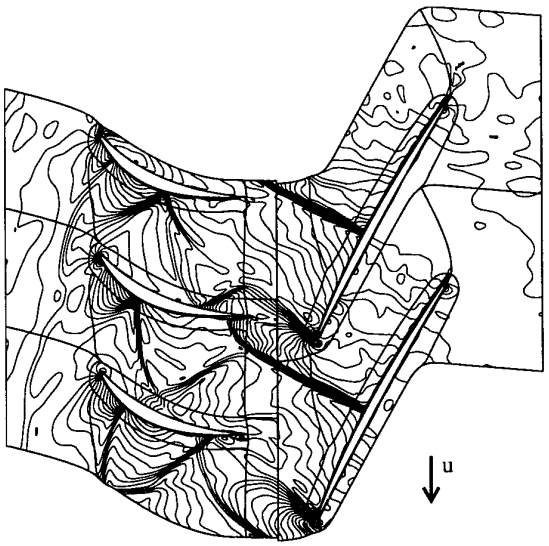

Fig. 12 - Instantaneous iso-pressure contours in a transonic compressor stator-rotor configuration (A) - inviscid calculation. The stator is on the left side and the rotor on the right. Also shown are the the block boundaries of the inviscid grid.

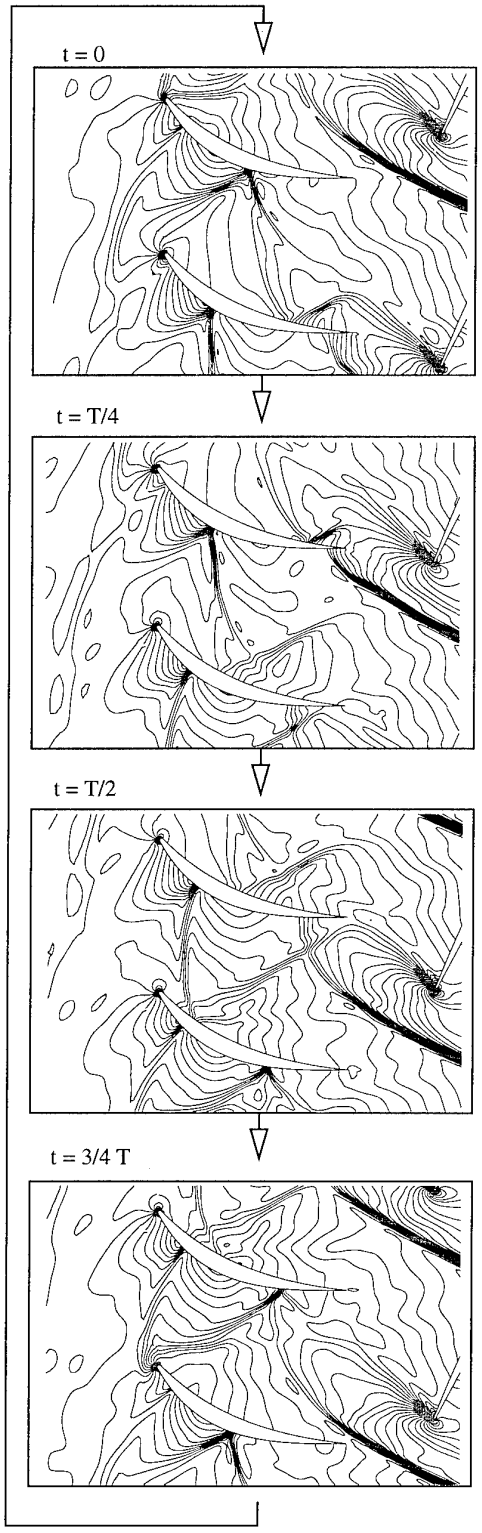

Fig. 13 - Close-ups of instantaneous iso-pressure contours in a chosen stator-passage during a period T - inviscid calculation, configuration (A). On the right side of the close-ups part of the rotor blades and the rotor shock-waves are visible.

Fig. 14 - Instantaneous iso-pressure contours, Re =400000, configuration (A). Turbulence model used: Baldwin Lomax.

Fig. 15 - Instantaneous iso-entropy contours, Re = 400000, configuration (A). Turbulence model used: Baldwin-Lomax.

Fig. 16 - Cnfiguration (B): Grid for a stator-rotor configuration of 1 stator passage and 1 rotor passage with 50000 nodes.

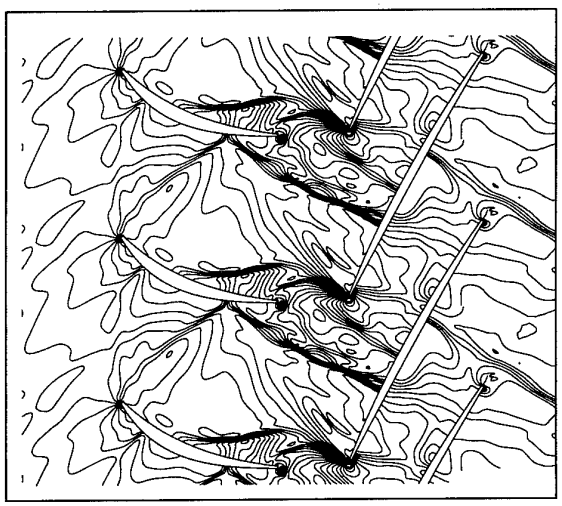

Fig. 17 - Instantaneous iso-pressure contours at t=0, configuration (B), Re = 400000. Turbulence model used: Spalart-Allmaras.

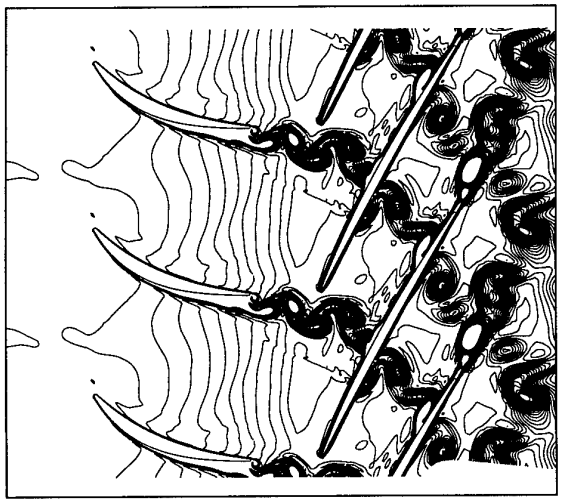

Fig. 18 - Instantaneous iso-entropy contours at t=0, configuration (B). Re = 400000. Turbulence model used: Spalart-Allmaras.

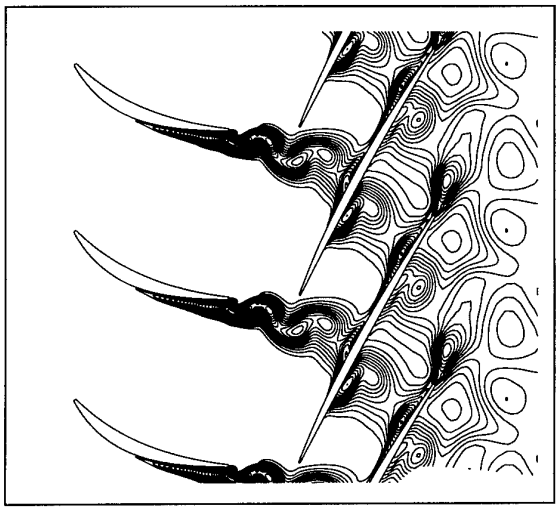

Fig. 19 - Instantaneous iso-eddy-viscosity contours at t=0, configuration (B), Re = 400000. Turbulence model used: Spalart-Allmaras.

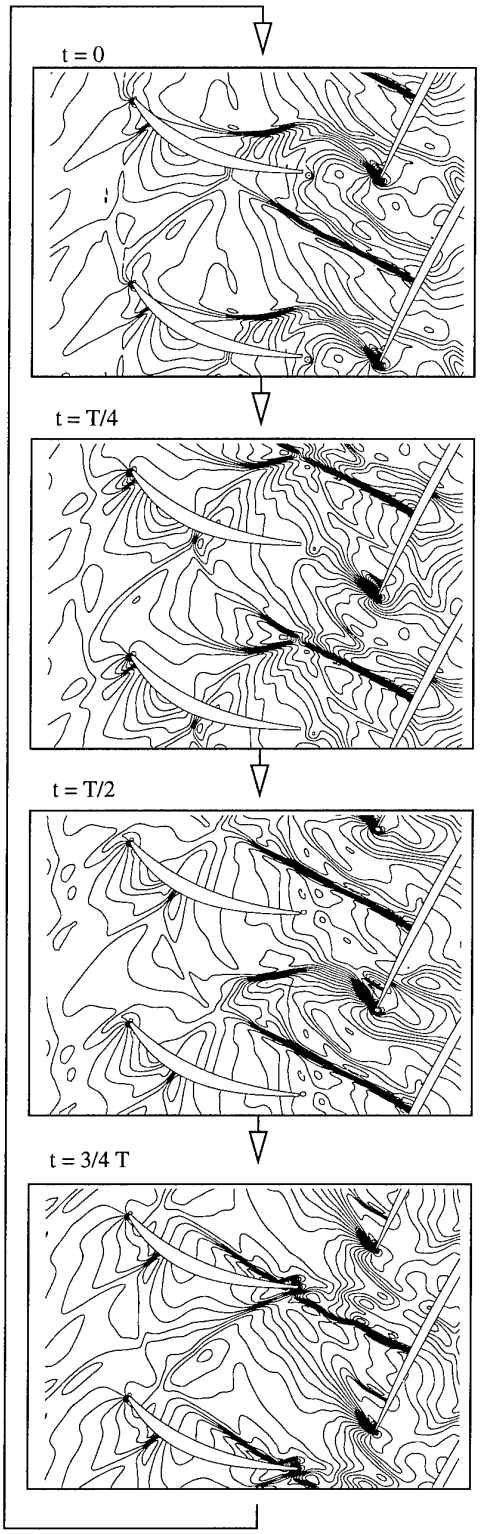

Fig. 20 - Close-ups of instantaneous iso-pressure contours during a period, Re = 400000, configuration (B). On the right sides of the close-ups, part of the rotor blades and rotor shockwaves are visible.

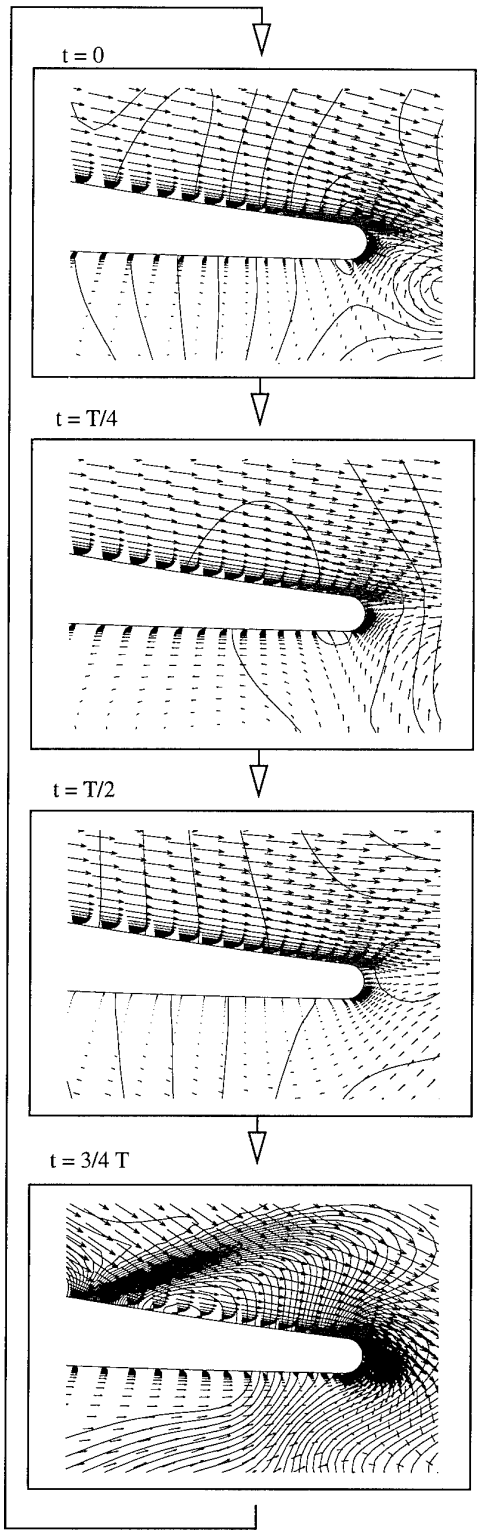

Fig. 21 - Close-ups of instantaneous velocity vectors near trailing edge of a stator blade during a period, Re = 400000, configuration (B). In the background, the instantaneous iso-pressure lines are plotted.

REFERENCE NO. OF THE PAPER: 38

DISCUSSOR'S NAME: F. Burgaud, SNECMA, France

AUTHOR'S NAME: K. Engel

Q: What did motivate your choice of the SA Turbulence model? Was it accuracy in treating separated flowfields, numerical robustness, simplier implementation vs. 2-equation models, etc?

A: The SA model is a one-equation transport model for the eddy viscosity, and in several publications is reported to be numerically robust and easy to implement. The model is insensitive to a specified initial condition. Evaluation of the SA model for unsteady separated flows is currently underway. As the model includes history effects, it is expected to have some advantage over algebraic models.

Q: Do you think the Reynolds number and/or the periodicity imposed by the rotor had any influence on the vortex shedding aft of the stator trailing edge?

A: As could be seen in the video-animation, the rotor shocks in fact trigger the vortex shedding. This indicates a periodicity phenomenon. A significant influence of the Reynolds number in a given range is therefore unlikely.

Q: Could you comment on the "backward travelling pressure wave" observed in the films, for both viscious and inviscid calculations?

A: In general, the periodic upstream influence of the rotor induces upstream propagating pressure waves. In the present case, particularly strong waves are generated by the rotor shock and its interaction with the upstream stator trailing edge. Both the inviscid and viscous results show multiple wave reflections on the stator blades. A Fourier analysis of the viscous stator surface pressure data will tell how far the reflections are dampened by the existence of the boundary layer, since the boundary layer represents an elastic buffer zone for waves impinging on the blade.

STATOR-ROTOR-STATOR INTERACTION IN AN AXIAL FLOW TURBINE AND ITS INFLUENCE ON LOSS MECHANISMS

R.E. Walraevens
H.E. Gallus

Institut für Strahlantriebe und Turboarbeitsmaschinen
RWTH Aachen, University of Technology
Templergraben 55
D-52062 Aachen, Germany

SUMMARY

Detailed measurements have been carried out to investigate in particular the development of the rotor wakes and vortices, entering, passing and leaving the second stator. Pneumatic measurements in the axial gaps behind all blade rows provided information about the steady flow behaviour. Hot-wire measurements with double- and triple-wire probes have been performed behind rotor and second stator to acquire the time dependent three-dimensional velocity vector. Surface mounted hot film gages and highly sensitive subminiature pressure transducers were used to get information about the boundary layer behaviour of the stator blades. This paper concentrates on the rotor flow and its time dependent influence on the flow behind the second stator.

Results will be discussed mainly from figures showing time dependent secondary flow. Typical passage vortices dominate the rotor exit flow in the relative and absolute frame. It will be shown that the vortices leaving the rotor passage influence strongly the second stator exit flow. This leads to highly three-dimensional unsteady effects. Even time averaged quantities show rotor flow phenomena in the exit flow of the second stator.

NOMENCLATURE

M	Mach number
Tu	Turbulence intensity
c	Absolute velocity
w	Relative velocity
u	Circumferential velocity
u',v'	stochastic velocity fluctuations
h,H	Span
t,T	Pitch
s	Chord
rel	relative
abs	absolute
TI	"TimeIndex"
POR	Point of reference

Greek symbols

α	Yaw angle
β	Relative Yaw angle
γ	Pitch angle
λ	Stagger angle

Subscripts

0	First stator inlet
1	Rotor inlet
2	Rotor exit, second stator inlet
3	Second stator exit
sec	secondary (flow vector)
loc	local (flow vector)
avrg	averaged (flow vector)

1. INTRODUCTION

To improve performance and design of turbomachines currently being developed further understanding of the physical basics is essential. Most of the present analysis and design methods are based on steady aerodynamics. But unsteady flow associated with blade row interaction causes highly three-dimensional flow fields which change periodically with time. It is necessary to check the influence of the periodic unsteadiness on loss generation and extend the design process, taking in account time-dependent flow features.

One most important source of unsteadiness is the relative motion of blade rows. Turbine rotor flow is influenced by the non-uniform exit flow of the first stator and the periodically incoming wakes induced by the upstream stator blades. In addition passage vortices and the tip clearance vortex develop during the flow passes the rotor. The strongly distorted three-dimensional rotor exit flow now enters the passage of the second stator. Entering this passage, rotor wakes and vortices are cut off by the vanes of the second stator. The already unsteady flow has to follow blade curvature thereby inducing the stator passage vortices. A strongly disturbed, three-dimensional and highly unsteady second stator exit flow is the consequence. To understand, describe and model these complex phenomena detailed experimental investigations in rotating turbomachines are necessary.

A number of experimental studies have been carried out in recent years. Joslyn et al. (1983) demonstrated that the rotor outlet flow at midspan of a turbine changes remarkably as the rotor interacts periodically with the stator wakes. The three-dimensional flow through a large-scale turbine was measured by Hunter (1982), Sharma et al. (1985) and Joslyn and Dring (1992). They detected considerable variations of flow angles, velocity and pressure distributions for different rotor-stator positions. Binder et al. (1985) measured a sudden increase of turbulence energy when the rotor cut off the passage vortices of the upstream stator row. Extensive studies of the unsteady rotor flow were carried out by Zeschky and

Paper presented at the AGARD PEP 85th Symposium on "Loss Mechanisms and Unsteady Flows in Turbomachines", held in Derby, United Kingdom, 8-12 May 1995, and published in CP-571.

Gallus (1993). They proved that the development of the rotor secondary flow, the rotor wake and the outlet flow angles is strongly influenced by the non uniform stator exit flow and the periodically unsteady rotor inlet flow respectively. Sharma et al. (1988) showed the impact of unsteadiness on the characteristics of secondary flows in the downstream rotor and stator passages. They proposed a semi-elliptical model to provide improved estimates of losses in the midspan regions of turbine rotors. Morphis and Bindon (1994) described the response of the second stator to the complex tip clearance flow in a 1.5 stage low speed axial turbine. Investigations on the unsteady flow before, within and behind the second stator passage in a 1.5 stage turbine were performed by Yamamoto et al. (1993). A large axial gap between first stator and rotor was installed to minimize the effects of the wakes of the first stator on the rotor inlet flow. His results indicate that the stator passage and stator exit flow mainly depend on the rotor exit flow and the secondary flow generated within the stator passage. Some computational studies of flow associated with blade row interaction have been carried out e.g. by Hah et al. (1993), Valkov and Tan (1993), and Gallus, Zeschky and Hah (1994). The latter conclude that accurate predictions of the secondary flows at the exit of turbine stages requires numerical approaches which account for three-dimensional as well as unsteady effects.

All investigations described above have been performed to understand unsteady flow phenomena and/or to improve prediction methods. According to Denton (1993) some loss mechanisms are well understood, but in other cases the loss mechanisms are still not clearly understood. He emphasizes that the use of correlations should not be a substitute for trying to understand the origins of loss.

The present paper concentrates on the three-dimensional highly unsteady flow conditions within and behind the rotor and behind the second stator of a 1.5 stage axial flow turbine. Results from earlier research by Zeschky (1991) on the flow conditions within the rotor of the same turbine will be used additionally to describe the formation of typical flow phenomena in the rotor passage and their effects on losses.

2. EXPERIMENTAL FACILITIES AND TECHNIQUE

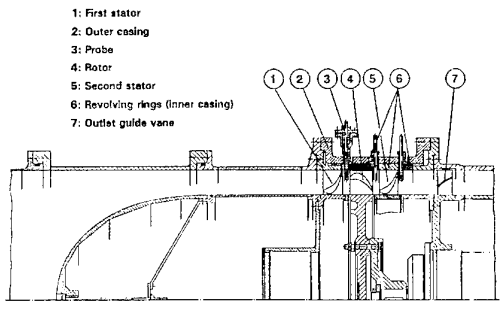

Fig. 1: Turbine Test Facility

Experimental data behind the rotor and second stator was acquired in a 1.5-stage axial turbine shown in Fig. 1. The casing construction consists of a fixed mounted outer ring and 3 revolving inner rings. Measurements with independent circumferential probe positions behind the blade rows can therefore be performed at the same time. For both stators the Traupel profile is used (Utz, 1972). Profile geometry, number of blades and stagger is identical for the first and the second stator. A modified VKI-profile is used for the rotor. Both stators and the rotor consist of untwisted blades. Stator vanes are stacked in the trailing edge, rotor blades in the center of gravity. A cross section of the turbine with mid-span velocity triangles and definitions of the flow angles is shown in Fig. 2.

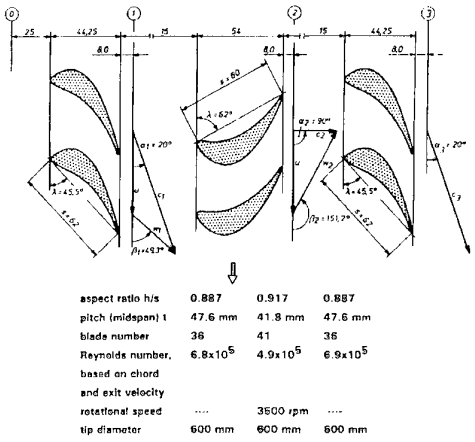

Fig. 2: Turbine Geometry and Design Data

Results presented in this paper have been acquired at the design point of the turbine. This is at a rotational speed of 3500 rpm. The shaft speed variation was less than 0.2 percent. Total temperature at turbine inlet was maintained in the range of 308 K +/-0.5 K by cooling the supplying air at the compressor outlet. With a fixedly mounted five-hole probe the rotor inlet Mach number (absolute frame) was measured and adjusted to Ma=0.45. Accuracy achieved is about 0.5 percent.

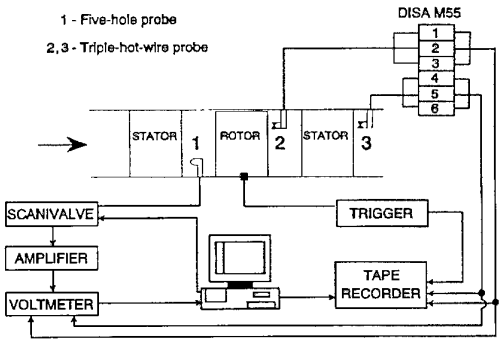

Fig. 3: Data Acquisition Scheme

Flow field properties behind rotor and second stator have been measured with pneumatic five-hole probes, pneumatic boundary layer probes, triple-hot-wire probes and cross-wire probes 8mm behind the blade rows. Pneumatic probes only were used behind the first stator but currently 3D-hot wire measurements are under the way to investigate the potential upstream influence of the rotor on the first stator exit flow. All pressures were logged in the same way as shown bottom left in Fig. 3 (fixedly mounted five-hole probe to control rotor inlet Mach number). The

remaining sketch shows the data acquisition method which has been used to log the unsteady real time data. A triple-hot-wire probe behind rotor and second stator respectively was traversed in a radial-circumferential array covering 9% to 91% span in the radial direction (20 positions) and one first stator vane pitch (17 positions) in the circumferential direction. Each wire was connected to a DISA M55 hot-wire bridge. During the test the fluctuating output signal has been stored with a special multi-channel tape recorder on usual video cassettes. The trigger signal was recorded at the same time and stored on the tape as well. All devices were controlled by a personal computer which stored also the time-averaged voltages, logged with the voltmeter. This was to calculate steady values of velocity and flow angles which were used to check the quantities during the test.

The operational costs are remarkably reduced with this data acquisition method. Only a fraction of rig-running time is necessary in comparison to conventional methods.

To evaluate the data stored on tape a multi-channel data acquisition device was connected to the tape recorder. Playing the tape 512 real-time samples were recorded for each of 128 revolutions. This covers more than 8 blade passing periods. Using the phase-locked ensemble average method the data was reduced and calibrated to 64 time-dependent flow vectors for each probe position. Considering that time-dependence is equal to rotor movement, flow properties are available at 64 different rotor/stator positions *along one rotor pitch*. A more detailed description of probe calibration and data reduction is given by Poensgen and Gallus (1991).

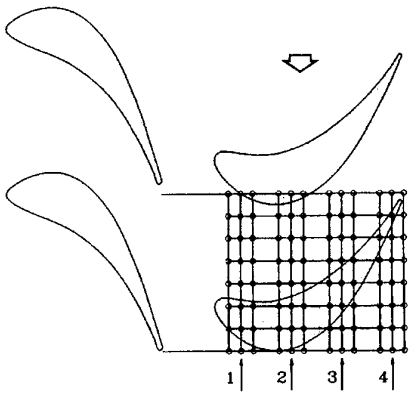

Fig. 4: Location of LDV-Measurements within the Rotor Passage

LDV-measuring-technique has been used by Zeschky (1991) to acquire the two-dimensional velocity vector and turbulence data within the passage of the rotor. Measurements have been carried out in 4 axial planes. Each plane had 7 circumferential positions covering one first stator pitch and each circumferential position had 22 spanwise locations (Fig. 4). 256 real-time samples for 256 consecutive rotor revolutions have been recorded covering 4 blade passing periods. Data reduction and evaluation follows the same scheme as used for the hot-wire data which is described in the previous paragraph.

3. RESULTS AND DISCUSSION

All figures presented are rear views and shown without boundary layers. The pitchwise flow angle α starts at circumferential direction and its counter clockwise rotation is positive (Fig. 2). Spanwise flow angles γ have positive values when directing to the casing. Thus a steady three-dimensional flow vector is given as

$$\vec{c}_{loc}=f(c,\alpha,\gamma)_{loc} \tag{1}$$

and a three-dimensional time-dependent flow vector as

$$\vec{c}(t)_{loc}=f(c(t),\alpha(t),\gamma(t))_{loc} \tag{2}$$

A secondary flow vector is the difference vector between the local flow vector and an averaged flow vector. The latter is calculated using the total local velocity $|c|$, the radially averaged yaw angle α and the circumferentially averaged pitch angle γ:

$$\vec{c}_{sec}=\vec{c}_{loc}-\vec{c}_{avrg} \tag{3}$$

with

$$\vec{c}_{avrg}=f(|\vec{c}_{loc}|,\bar{\alpha}_{radial},\bar{\gamma}_{circumferential}) \tag{4}$$

Secondary flow vectors *in the rotor passage* show the difference between local flow vector and time averaged flow vector:

$$\vec{c}_{avrg,ROTOR}=f(\bar{c}_{time},\bar{\alpha}_{time},\bar{\gamma}_{time}) \tag{5}$$

Unsteady results will be presented in showing secondary flow fields and some flow quantities at different rotor positions relative to the first stator. The unsteady rotor exit flow and the second stator exit flow is shown at six different rotor/stator positions. As mentioned above data has been acquired at 64 different rotor positions distributed along one rotor pitch. Each data set is numbered with an index which can be seen in the figures as "TimeIndex" (TI). The following table shows the reference between "TimeIndex" (TI) and rotor position.

TI	Movement*	TI	Movement*
1	0.0%	34	51.6%
12	17.2%	45	68.8%
17	25.0%	49	75.0%
23	34.4%	56	85.9%
33	50%		

* Rotor movement in percent of rotor pitch starting at a point of reference (POR)

Table 1: Reference of "TimeIndex" and rotor movement

POR is the point of reference either in a time- or in a location-coordinate system. Both systems are equivalent. Here the point of reference is equal to TI 1 which is the moment when the data-logging-device got the trigger signal. Time-dependent results presented in more than two figures should be analyzed in the counterclockwise direction which is equivalent to positive circumferential movement of the rotor.

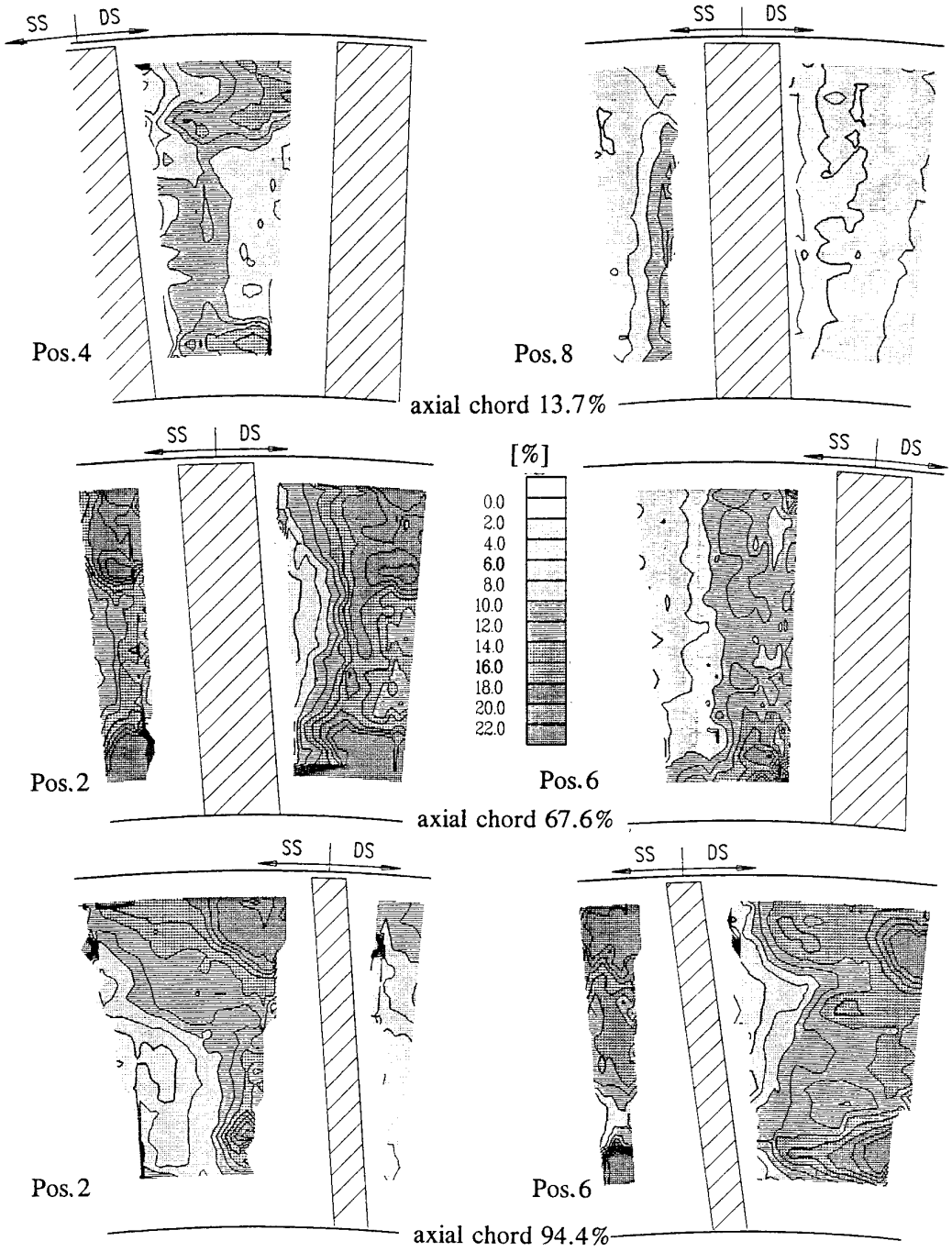

Fig. 5: Time-Dependent Turbulence Distribution in 3 Axial Planes within the Rotor Passage

Fig. 6: Time-Dependent Secondary Flow and Turbulence Distribution in a Radial Plane at 72.7% Span within the Rotor Passage

3.1 Unsteady flow within the rotor passage

Figure 5 presents the time dependent turbulence intensity measured in the axial planes 1, 3 and 4 (Fig. 4) within the rotor passage. This is at 13.9%, 67.6% and 94.4% axial chord of the rotor blade. Flow properties have been measured at 8 different stator/rotor positions. Two selected positions in each plane will be presented here. Equation (6) gives the definition of the turbulence intensity:

$$T_u = \sqrt{\frac{u'^2+v'^2}{2*\bar{c}_2^{\,2}}} \qquad (6)$$

The totally averaged rotor exit velocity c_2 has been chosen as reference speed. The upper two figures show the turbulence at 13.9% axial chord at two stator/rotor positions (difference between 2 positions is 50% rotor pitch). Low turbulence levels between 2% and 8% can be observed at position 8, whereas at position 4 a sharply contoured area of increased turbulence appears. The level is about twice as high as at position 8. This area marks the wake of the stator vane and the higher turbulence is generated by the mixing process between low energy wake fluid and surrounding fluid. Two clear areas at about 15% and 85% span show maximum turbulence values of about 16% to 18%. This corresponds with the loss cores due to the stator passage vortices. Further downstream in the plane 67.6% axial chord away from inlet the stator wake is still detectable (pos. 6), but appears wider and a bit tattered. The reason is the continuing mixing process and influence due to the pressure gradient. Strong turbulence of about 20% can be seen in the corner between casing and suction side (pos. 2). Near casing this is due to interaction between tip clearance flow and developing rotor casing passage vortex, near hub it is the first indication of the hub passage vortex.

Close to the rotor exit, at 94.4% axial chord, the stator wake is not clearly detectable. Only the higher turbulence values of about 16%, spreading nearly from pressure side to suction side at 20% and 80% span respectively (pos. 6), indicate in comparison to position 2 a strong interaction between the diminishing stator wake and the rotor passage vortices. Location of the latter must be in the areas of maximum turbulence (20%-22%) which remains nearly unchanged during rotor movement from position 2 to position 6.

A significant effect of the rotor flow is the fluid transport to the suction side when stator wakes pass the rotor passage. This is indicated in Fig. 6, showing secondary flow and turbulence distribution in a plane with constant radii at 72.7% span. The passing stator wake can be identified by the strong secondary flow directing to the suction side (pos. 2 at about 70% axial chord, pos. 8 at about 45% axial chord). Accumulation of higher turbulence levels in the same area due to transport of the low energy fluid (wake) confirms this observation. Secondary flow at the rotor inlet, directing outwards against the mean flow direction, shows the entering stator wake. Speed in the wake is much lower than time-averaged speed at the same location. Considering equation 3 it follows that secondary flow for this case points outward in the direction mentioned above.

Position 6 shows in the front half of the passage a secondary vortex rotating clockwise. It can be observed more distinctive in the lower half at position 8 with the center a little further downstream. The downstream part of the vortex transports low energy material against the pressure gradient from the suction side into the main flow in the middle of the passage. A similar secondary flow field at midspan of a turbine rotor showing the same vortex has been calculated by Hodson (1985).

3.2 Unsteady flow behind the rotor

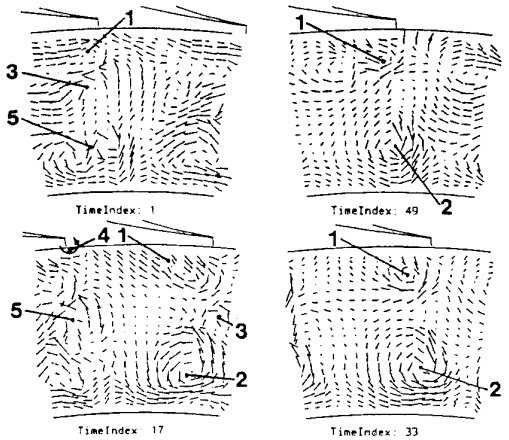

Fig. 7: Time-Dependent Secondary Flow Field at Rotor Exit in the Relative Frame

The time-dependent secondary flow field in the relative frame at rotor exit is shown in Fig. 7. The arrows represent the components of the secondary flow vector viewed from the downstream direction which is given by the design angle at outlet of the blade row. This is valid for all following figures showing secondary flow. Values in the relative frame have been calculated from data acquired in the absolute frame. Each flow vector is reduced to its components. The difference between circumferential component and circumferential speed delivers the circumferential component of the relative velocity. Relative axial and radial components are equal to their absolute counterparts. The relative flow vector then has been recalculated from its components. Secondary flow phenomena to be seen in the figures have been numbered. A reference list is given in table 2.

At TI 33 (Fig. 7) the flow field leaves a balanced impression showing clearly casing (1) and hub vortex (2). Also the lower part of the tip clearance vortex (4) seems to appear behind the rotor blade trailing edge. Because the tip clearance is only of 0.6% of span the corresponding vortex cannot be expected to be bigger than 10% of h/H (Zeschky and Gallus, 1993), which is just in the range of measurements. Between 60% and 70% span the flow vectors show, initiated by the passage vortices, on nearly constant radii a transport of low energy material from the suction to the pressure side. This low energy fluid is originated in the suction side boundary layer. Top right in Fig. 7 the casing passage vortex moves in the circumferential direction and becomes wider but also disturbed by some inward leading flow (5). On the right hand the casing passage vortex of the next blade passage appears.

No	Meaning
1	Casing passage vortex
2	Hub passage vortex
3	Trailing edge vortex
4	Tip clearance vortex
5	Influence due to first stator
6.1	Rotor casing passage vortex
6.2	Rotor hub passage vortex
6.3	Rotor trailing edge vortex
7	Combi vortex (second stator)

Table 2: Reference for secondary flow figures

When the rotor is at the point of reference, which is equal to TI 1, the shape of the upper passage vortex has changed completely in comparison to TI 33. It appears now flattened and stretches slanted from the trailing edge inward.

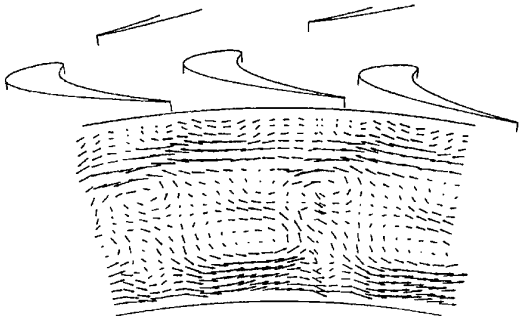

Fig. 8: Time-Averaged Secondary Flow Field at Rotor Exit in the Absolute Frame

Second stator inlet flow is equivalent with rotor exit flow in the absolute frame. To understand the unsteady flow behaviour behind the second stator it is therefore necessary to discuss the results obtained in the absolute frame at rotor exit. Figure 8 gives an impression of the time averaged secondary flow field. Close to the hub a distinctive flow from pressure side to suction side, forming the lower part of the hub passage vortex, can be observed. At approximately h/H=0.75 flow in the opposite direction from suction to pressure side forms the lower side of the casing passage vortex. The upper side cannot be detected in this figure. Behind the trailing edge a little above midspan another vortex structure can be seen. It is the upper trailing edge vortex which develops from the shear layer in the wake some distance behind exit of the cascade. Figure 9 illustrates this mechanism. Further down it is shown that this vortex plays an important role in the interaction between rotor and second stator.

Time-dependent secondary flow fields behind the rotor in the absolute frame are shown in Fig. 10 at six different rotor/stator positions. Except at TI 1 and TI 12 casing passage vortex (1) and hub passage vortex (2) are the domina-

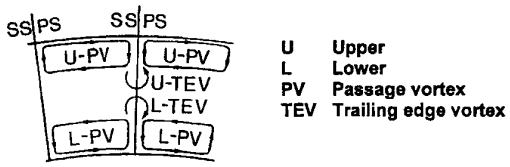

Fig. 9: Development of Trailing Edge Vortices

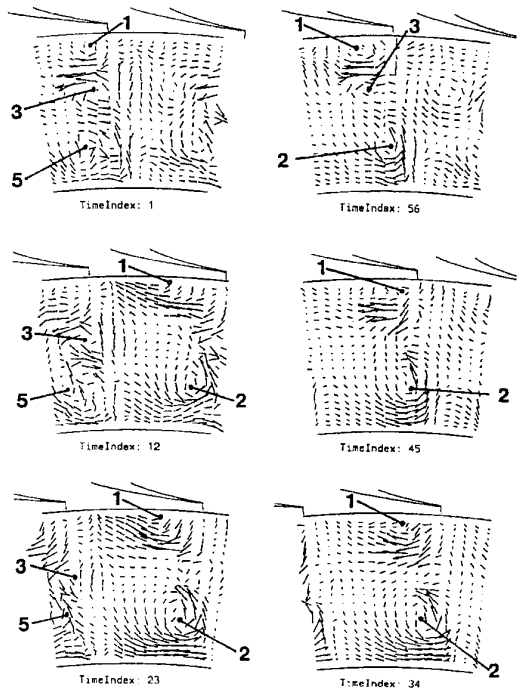

Fig. 10: Time-Dependent Secondary Flow Field at Rotor Exit in the Absolute Frame

ting flow features. Biggest differences are found between TI 1 and TI 34. The latter leaves an overall balanced impression of a typical blade exit flow containing the distinctive passage vortices. On the other hand at TI 1 a flow distortion due to the first stator (5) appears in the area of the hub passage vortex. The formerly rotational sense in the counterclockwise direction is disturbed and at TI 12 only a diagonal inward directed slanted structure is left. Together with the appearance of the described distortion at approximately 70% span another vortex (3) can be seen rotating in the counterclockwise direction as well. Its upper part seems to go together with the lower part of the casing passage vortex. Location and rotational sense conclude that this structure is the upper trailing edge vortex of the just passing rotor blade. At TI 12 the same structure can be detected. The extended trailing edge of this blade shows the corresponding wake. Nearly all flow vectors directing from suction to pressure side undergo a strong turning radial upwards forced by the high pressures induced on the pressure side of the blade. Note that the measurements took place 8mm behind the rotor exit plane so that the flow undergoes strong mixing processes in the plane of measurement.

The circumferentially mass-averaged stator inlet velocity and yaw angle is documented in Fig. 11. Inlet velocity is

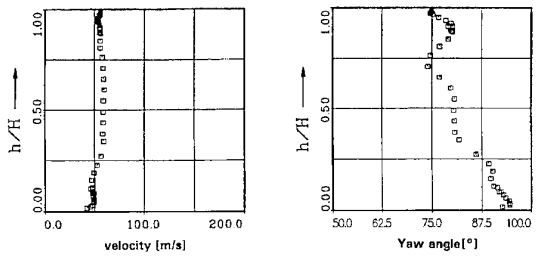

Fig. 11: Rotor Exit/Stator Inlet Velocity and Yaw Angle - Absolute Frame (Circumferentially Mass-Averaged Values)

of about 50m/s and nearly constant with radius. The yaw angle lays in a range of about 75 degrees near casing and 90 degrees near hub. The incidence at all radii except the hub area is therefore of negative values (design angle: 90 degrees). Only the hub area consists of incidences around 0 degrees.

3.3 Unsteady flow behind the second stator

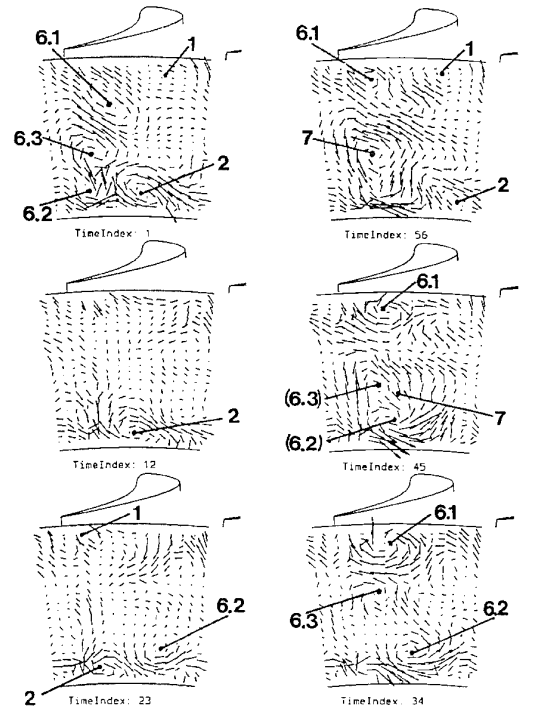

Fig. 12: Time-Dependent Secondary Flow Field at Second Stator Exit

Time-dependent secondary flow fields behind stator two are shown in Fig. 12 at six different rotor/stator positions. At TI 1 several vortex structures can be distinguished. Taking in account the rotational sense of each vortex, their location and their behaviour with time their origin can be detected. The vortex (6.1) close to casing and suction side of the stator blade rotates in the clockwise direction whereas the weak vortex structure (1) on the right hand side rotates counterclockwise. This is the rotational sense of the stator casing vortex but the location (casing, pressure side) does not fit. Observing the top right corner of TI 34 to TI 1, it can be seen that a structure rotating counterclockwise (as the casing stator passage vortex) appears. It is distinctive at the beginning (TI 34) and diminishing with rotor movement until the weak vortex structure already mentioned appears (TI 1). At TI 12 the stretched vortex (6.1) has disappeared and been replaced by the casing passage vortex (1) of the second stator.

Considering the structure of the rotor exit flow in the absolute frame, the radial inward directing and stretched looking vortex (6.1) must be the rotor casing passage vortex. At TI 34, at the same location, this vortex has the same structure and rotational sense as its counterpart behind the rotor. Its sudden appearance at TI 34, the change of its shape with time followed by complete disappearance points clear to a rotor vortex chopped by the stator vanes.

A similar but more complex vortex system (2, 6.2, 6.3) can be seen bottom left at TI 1, filling nearly half the figure. It consists obviously of three different vortices, where the one located bottom left (6.2), shows only a bit more than half of the usual circular shape. Looking at the rotational sense it is found that the two vortices on top of each other (6.3, 6.2) do have the same rotational sense (counterclockwise). The third vortex (2) rotates clockwise. Moving with the rotor to TI 12 this structure becomes very weak but is still detectable. Further on at TI 23 the hub passage vortex (2) is clearly to recognize. Following the way from TI 1 to 23 it is found that structure (2) has moved from pressure to suction side and must be identical with the hub passage vortex of stator two.

Bottom right at TI 23 a new vortex structure, rotating clockwise, seems to appear. Comparing this with TI 34 the small hub passage vortex has been removed completely by the sudden appearance of a large vortex structure (6.2) rotating in the opposite direction. The sudden appearance and the rotational sense leads to the conclusion that this vortex is originated in the rotor and identical with the rotor hub passage vortex. A little above midspan and left of the center of the figure (TI 34) a vortex rotating counterclockwise as well (6.3) can be seen. Rotational sense and location indicate together with Fig. 9 that this is a trailing edge vortex coming from the rotor exit. It is also detectable that there is some transport of material from the lower (6.2) to the upper vortex (6.3). The amplification of two vortices leads to the huge vortex (7) which can be seen at TI 45 filling more than half the area representing this figure. TI 56 shows bottom right a diagonally inward directed new vortex structure (2) which is barely detectable at TI 45. It causes an indentation in the vortex structure (7). This disturbance together with the diminishing rotor hub passage vortex leads to the separation of structure (7) which can be seen at TI 1. The flow values Mach number, yaw angle and pitch angle measured behind the second stator are shown in Fig. 13, 14 and 15. Time-dependent secondary flow vectors have been calculated based on these flow properties.

The corresponding time averaged secondary flow field is shown in figure 16. A clear casing vortex structure and a clear hub vortex structure rotating in the sense of the rotor passage vortices dominate the flow field. Quite small stator passage vortices seem to appear close to hub and

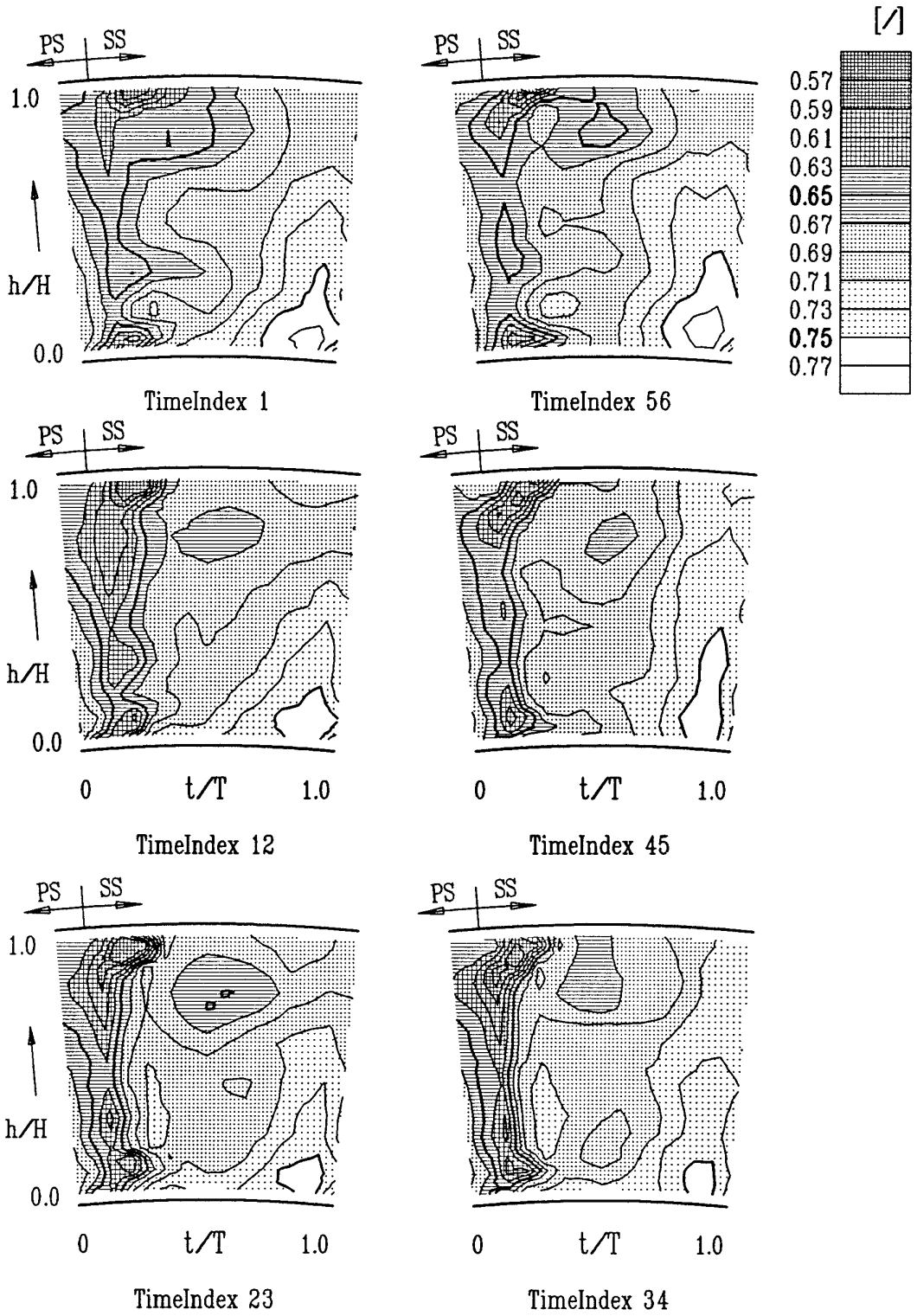

Fig. 13: Mach Number at Second Stator Exit - 6 Different Rotor/Stator Positions

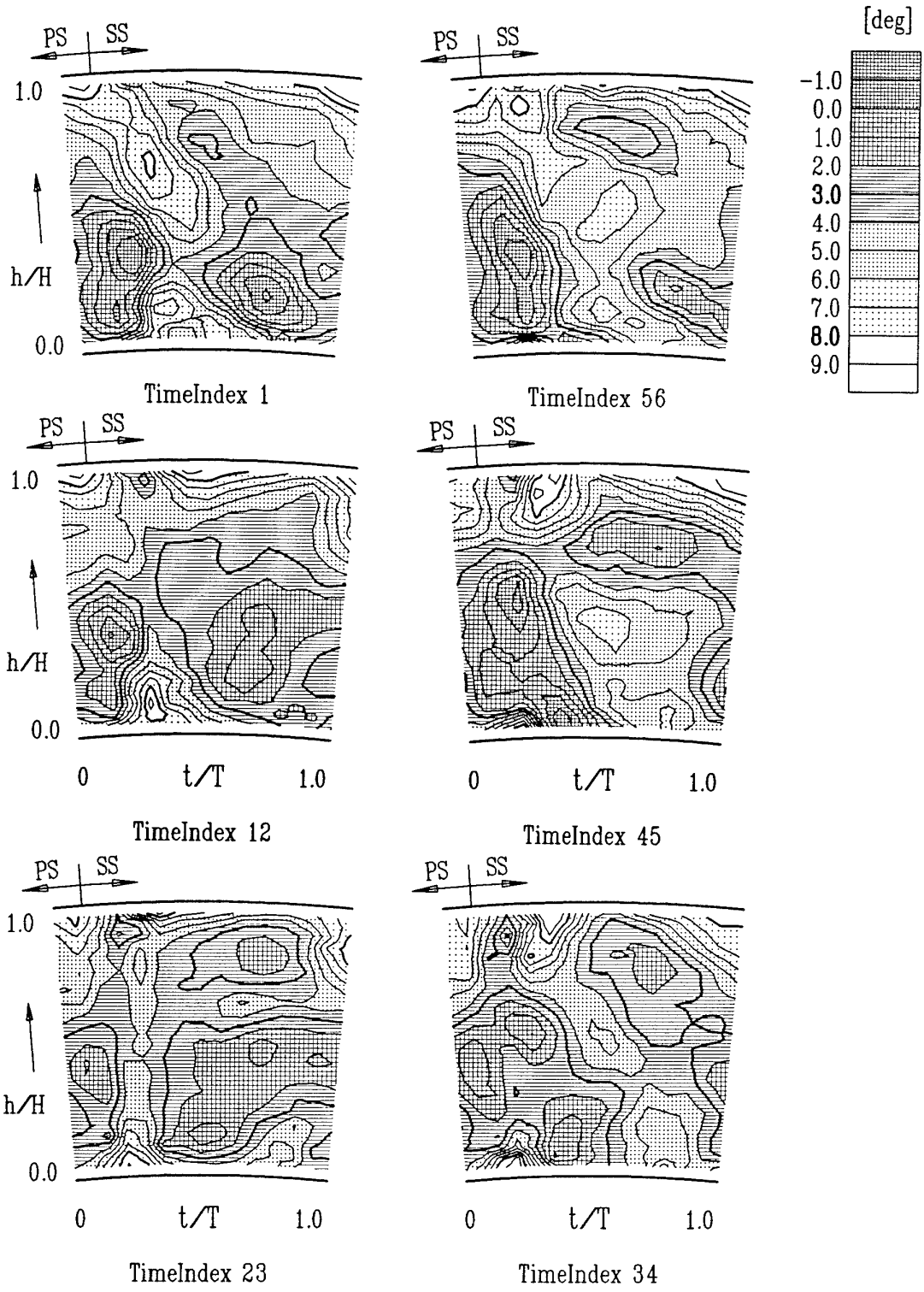

Fig. 14: Yaw Angle at Second Stator Exit - 6 Different Rotor/Stator Positions

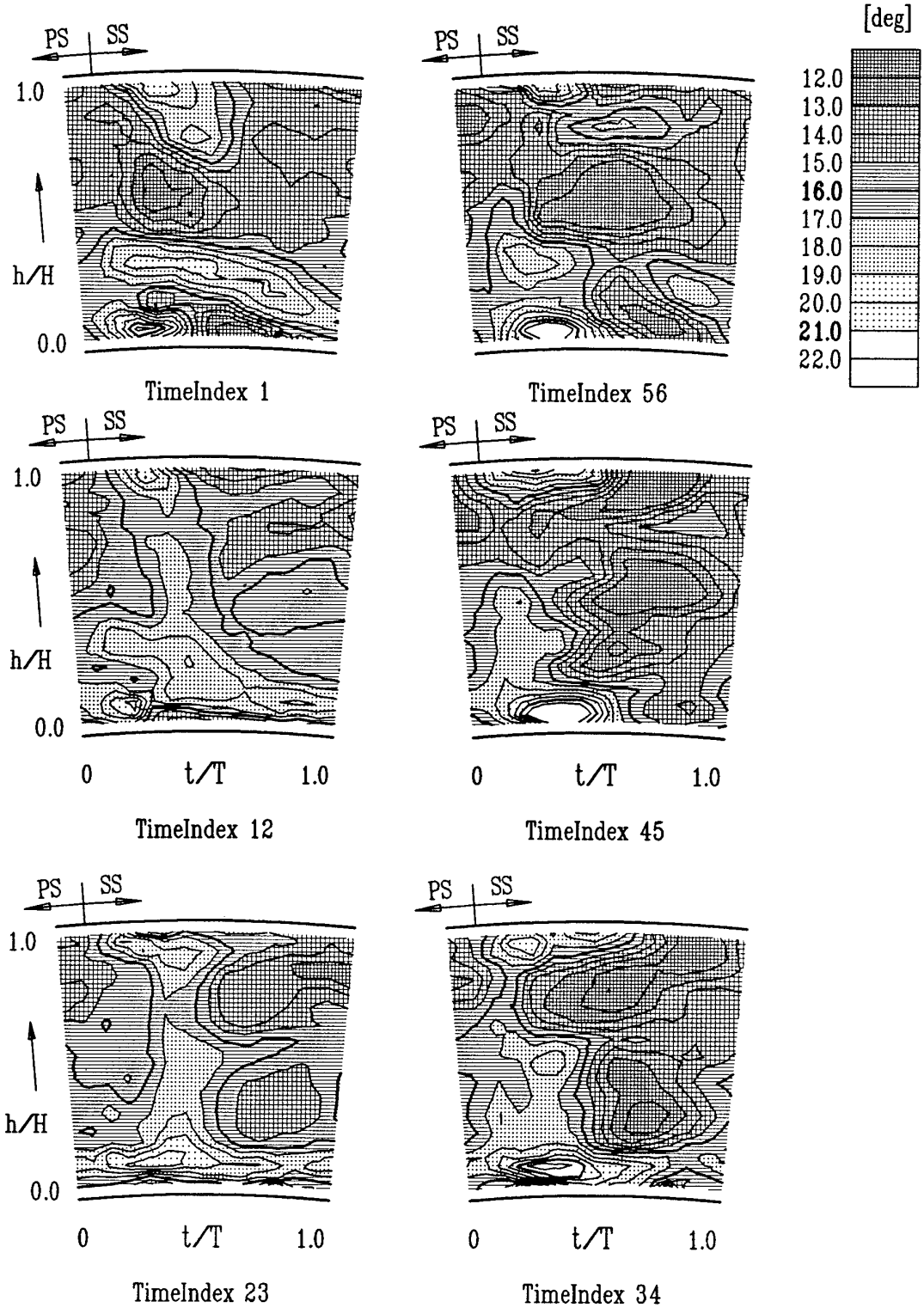

Fig. 15: Pitch Angle at Second Stator Exit - 6 Different Rotor/Stator Positions

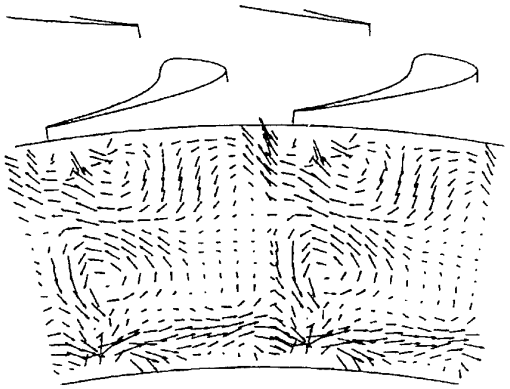

Fig. 16 Time-Averaged Secondary Flow Field at Second Stator Exit

casing. Only the lower part (casing) and the upper part of the vortices can be seen in the range of measurements.

4. CONCLUSIONS

To investigate stator/rotor/stator interaction unsteady measurements have been performed within the passage of the rotor (LDV-measurements in single stage configuration carried out by Zeschky, 1991) and in the axial gaps of a 1-1/2 stage axial flow turbine. Time-dependent secondary flow fields and other flow properties measured at these locations have been presented in this paper. Results lead to the following conclusions:

- First stator wakes strongly influence the flow field of the rotor passage. The wake and the "chop off" of the stator passage vortices cause high turbulence levels and strong crossflow towards the suction side of the rotor passage.
- Rotor exit flow shows at several rotor/stator positions influence due to the exit flow of the first stator (see Fig. 7 and Fig. 11, No. 5).
- Typical passage vortices in the relative and absolute frame have been found to be the dominating flow features in the rotor exit flow.
- Trailing edge vortices could be detected in the plane behind the rotor.
- All vortices leaving the rotor passage influence strongly the second stator exit flow. Upper and lower rotor passage vortex and also the upper rotor trailing edge vortex have been visualized in the stator exit plane.
- Highly three-dimensional unsteady effects are main features in the flow behind the second stator.
- Time averaged hot wire data behind the second stator show clearly that rotor vortices are dominant in the exit flow of the second stator.

Additional measurements of the steady and unsteady flow field have been performed within the passage of the second stator. Yet the results are not fully evaluated and analyzed. When completed it should be possible to develop a model which helps to understand unsteady flow behaviour in multistage turbines. This will be subject of another paper.

ACKNOWLEDGEMENT

The experimental work was supported by the Forschungsvereinigung Verbrennungskraftmaschinen e.V. (FVV) which is gratefully acknowledged. The help of Mr. J. Laschet, Mr. M. Plohr and Ms. G. Schaffrath in preparing the diagrams is also gratefully recorded.

REFERENCES

Binder, A., Förster, W. ,Kruse, H. and Rogge, H., "An Experimental Investigation into the Effect of Wakes on the Unsteady Turbine Rotor Flow", ASME Journal of Engineering for Gas Turbines and Power, Vol. 107, pp. 458-466, 1985.

Denton, J.D., "Loss Mechanisms in Turbomachines", ASME 93-GT-435, May 1993.

Gallus, H.E., Zeschky, J. and Hah, C., "Endwall and Unsteady Flow Phenomena in an Axial Turbine Stage", ASME 94-GT-143, June 1994.

Hah, C., Copenhaver, W.W. and Puterbauch, S.L., "Unsteady Aerodynamic Flow phenomena in a Transonic Compressor Stage", AIAA Paper AIAA-93-1868, 1993.

Hodson, H.P., "An Inviscid Blade-to-Blade Prediction of Wake-generated Unsteady flow", J. Engineering for Power, Vol. 107, pp 337-344, 1985.

Hunter, I.H., "Endwall Boundary Layer Flows and Losses in an Axial Turbine Stage", ASME Journal of Engineering for Power, Vol. 104, pp. 184-193, 1982.

Joslyn, H.D., Dring, R.P. and Sharma, O.P., "Unsteady Three-Dimensional Turbine Aerodynamics", ASME Journal of Engineering for Power, Vol. 105, pp. 322-331, 1983.

Joslyn, D. and Dring, R., "Three-Dimensional Flow in an Axial Turbine: Part 1 - Aerodynamic Mechanisms; Part 2 - Profile Attenuation", ASME Journal of Turbomachinery, Vol. 92, pp. 61-78, 1992.

Morphis, G. and Bindon, J.P., "The Flow in a Second Stage Nozzle of a Low Speed Axial Turbine and its Effect on Tip Clearance Loss Development", ASME 94-GT-145, June 1994.

Poensgen, C. and Gallus, H.E., "Three-Dimensional Wake Decay Inside of a Compressor Cascade and its Influence on the Downstream Unsteady Flow Field: Part 1 - Wake Decay Characteristics in the Flow Passage", ASME Journal of Turbomachinery, Vol. 113, pp. 180-189, 1991.

Sharma, O.P., Butler, T.L., Joslyn, H.D. and Dring, R.P., "Three-Dimensional Unsteady Flow in an Axial Flow Turbine", Jet Propulsion, Vol. 1, No. 1, pp. 29-38, 1985.

Sharma, O.P., Renaud, E., Butler, T.L., Milsaps, K., Dring, R.P. and Joslyn, H.D., "Rotor-Stator Interaction in Multi-Stage Axial-Flow Turbines", AIAA-88-3013, July 1988.

Utz, C., "Experimentelle Untersuchung der Strömungsverluste in einer mehrstufigen Axialturbine", Dissertation Nr.4894, ETH Zürich, Switzerland, 1972.

Valkov, T. and Tan, C.S., "Control of the Unsteady Flow in a Stator Blade Row Interacting with Upstream Moving Wakes", ASME 93-GT-23, May 1993.

Yamamoto, A., Mimura, F., Tominaga, J., Tomihasa, S., Outa, E. and Matsuki, M., "Unsteady Three-Dimensional Flow Behavior due to Rotor-Stator Interaction in an Axial-Flow Turbine", ASME 93-GT-404, May 1993.

Zeschky, J. and Gallus, H.E., "Effects of Stator Wakes and Spanwise Nonuniform Inlet Conditions on the Rotor Flow of an Axial Turbine Stage", Transactions of the ASME, Vol. 115, pp. 128-136, January 1993.

Zeschky, J., "Experimentelle Untersuchung der dreidimensionalen instationären Rotorströmung einer axialen Kaltluftturbine", Dissertation, RWTH Aachen, July 1991.
ary

REFERENCE NO. OF THE PAPER: 39

DISCUSSOR'S NAME: MG Rose, Rolls-Royce, U.K.

AUTHOR'S NAME: RE Walraevens, HE Gallus

Q: Could you please explain the origin of your "trailing edge vortex"?

A: Figure 9 in the paper shows the development of an upper and lower trailing edge vortex. Due to the passage vortices (e.g. at the casing) in adjacent passages, the suction side boundary layer flow close to the trailing edge points radially inward, whereas the pressure side boundary layer flow of the same blade points radially outward. Both boundary layers now leave the blade surface and form a shear layer with strong mixing due to the pressure gradient. Some distance behind the trailing edge the continuing mixing process and settling of the flow forms the trailing edge vortex.

REFERENCE NO. OF THE PAPER: 39

DISCUSSOR'S NAME: P. Came, PCA Engineers, U.K.

AUTHOR'S NAME: RE Walraevens, HE Gallus

Q: The figure showing secondary flow vectors at Stator 1 exit indicated quite low secondary flows, but the secondary loss levels were quite high. Could the author comment on the Stator 1 secondary flow, and also the thickness of the inlet boundary layers?

A: The main flow behind the first stator actually shows little secondary flow. But close to the hub and casing, strong secondary flow forming the quite flat passage vortices can be seen. This is due to the relatively thick inlet boundary layer (hub BL-thickness about 4% span, casing BL-thickness about 10% span) which is transported nearly completely to the suction side of the stator vane. Therefore most of the low energy fluid of the inlet boundary layer concentrates in the trailing edge suction surface area of the exit plane, and this leads to a loss coefficient of about 0.2 in the loss cores, up to a coefficient of about 0.35. The totally averaged loss coefficient is 0.049.

REFERENCE NO. OF THE PAPER: 39

DISCUSSOR'S NAME: H.B. Weyer, DLR, Germany

AUTHOR'S NAME: RE Walraevens, HE Gallus

Q: How did you manage to identify a vortex generated in the rotor behind the outlet stator just by time averaging?

A: Time-averaging has been done locally for each flow vector in the exit plane of the second stator. Time-averaged secondary flow vectors then have been calculated using eq. 3 and eq. 4. Plotting these leads to figure 16. Analyzing the time-dependent secondary flow (figure 12), showing the periodic appearance and disappearance of the rotor passage vortices, it is found that rotor vortices can clearly be detected in four of the six secondary flow figures. This covers more than 65% of a rotor blade passing period. Therefore, a time-averaged plot containing a full blade passing period must show activity of rotor vortices.

ROTOR-STATOR INTERACTION IN A HIGH-SPEED AXIAL COMPRESSOR

M A Cherrett
Propulsion Technology Department,
Defence Research Agency,
Pyestock,
Farnborough,
GU14 OLS
United Kingdom

1.0 SUMMARY

Detailed unsteady aerodynamic measurements have been taken in a single-stage transonic fan with a very high stage hub-loading. 2D dynamic yawmeters were traversed at rotor and stator exit, while dynamic pressure sensors and heated thin-film gauges were fitted to the stator at mid-span. This paper concentrates largely on analysis and interpretation of the on-stator measurements supplemented by consideration of some of the stator exit measurements and an inviscid-viscous prediction of the flow about the stator. These data show that at mid-span the rotor wakes augmented an incipient stator suction surface separation, causing a transient (larger) separation and re-attachment. This gave rise to an acoustic disturbance which propagated upstream, where it interacted with subsequent rotor wakes. At these points of interaction, large amplitude static pressure fluctuations were induced. Wake convection was seen in both pressure and thin-film gauge data taken on the suction surface, although there was a complex relationship between both data sources. However, rotor wake convection was absent from the pressure surface pressure-field data despite evidence of 'negative-jet' effects convecting the rotor wake fluid toward the pressure surface of the stator.

2.0 INTRODUCTION

It is required that future aeroengines be lighter and have a reduced cost of ownership, while achieving improved levels of performance. When applied to compressors, these goals dictate that designs become more compact and that higher levels of aerodynamic loading and Mach numbers are used, particularly for military applications. These trends increase greatly the complexity of the compressor flow field and make it more difficult to design machines that achieve their design performance with adequate stability margin. Therefore, it is anticipated that future design methods will need to take account of aspects of the flow field ignored currently. In particular, that the effects of blade row proximity and flow field unsteadiness will need to be modelled. However, there is an acute lack of measurements detailing unsteady flow fields in engine-relevant machines. Hence, fundamental understanding of the complex unsteady flows, and how they interact, is poor and there is little data to assess the integrity of predictions made by the growing number of time-accurate CFD codes.

DRA are engaged in a programme to address this problem by taking detailed steady and unsteady aerodynamic measurements in high-speed axial compressors. These are being used to improve understanding of the important flow phenomena and subsequently to contribute to the development and evaluation of steady and time-accurate CFD codes. This paper is the third in a series reporting measurements taken in a transonic fan known as C148. Although this paper is intended to be self sufficient, the reader is referred to these earlier publications (ie. Cherrett *et al* (1994 a & 1994b)) reporting other aspects of the same data set.

Number of rotor blades	25
Rotor pitch/ chord ratio (mid span)	0.65
Number of stator blades	52
Stator pitch/ chord ratio (mid span)	0.55
Corrected mass flow (kg/s)	53.3
Stage pressure ratio	1.807
Stage temperature rise ratio ($\Delta T/T$)	0.214
Stage hub loading ($\Delta H/U^2$)	1.21
Rotor tip speed (m/s)	442
Rotor inlet tip diameter (mm)	633
Stage inlet hub/tip ratio	0.39
Stage exit hub/tip ratio	0.62
Mid-span stator Reynolds number	1.0×10^6

TABLE 1 C148 INFORMATION

3.0 THE C148 TRANSONIC FAN

3.1 Rig Performance

The C148 single stage transonic fan is illustrated in Fig 1, while geometric and aerodynamic information relevant to this paper are given in Table 1. C148 was derived from an existing Rolls-Royce multi-stage fan designed in the early 1980's and its design concept and major aerodynamic features are described by Bryce *et al* (1993). The fan was designed to have a rotor tip inlet relative Mach number of 1.5 and a high aerodynamic stage loading at the hub which resulted in near sonic Mach numbers at inlet to the stator hub and high deflection through the stator (>57° turning to axial at stator exit).

Bryce *et al* showed, using the surface oil-flow visualization reproduced in Fig 2 (and pneumatic stator exit traverse measurements), that the stator hub flow was dominated by a large endwall corner stall. A significant high loss region was associated with the corner stall, and a region of high total pressure (and Mach number) was found between adjacent high loss regions. A smaller corner stall was also evident at the stator casing. Cherrett *et al* (1994 a & 1994b) reported detailed unsteady measurements taken with 2D dynamic yawmeter probes traversed at rotor and stator exit. The first of these references showed the salient features of the rotor flow, including a

Paper presented at the AGARD PEP 85th Symposium on "Loss Mechanisms and Unsteady Flows in Turbomachines", held in Derby, United Kingdom, 8-12 May 1995, and published in CP-571.

significant hub corner stall, and how they varied with changing compressor operating conditions. Cherrett *et al* (1994a) showed the effects of rotor passing on the temporal development of the stator hub and casing corner stalls, and showed that stagnation pressure levels within the stator passage were also subject to large variations within the rotor passing period. The behaviour of the stator corner stalls were apparently closely linked to passing of the viscous corner-stall and tip-leakage flow shed from the upstream rotor.

3.2 Specialised instrumentation

Because C148 was a major research vehicle for studying unsteady flow development, the unit was designed to contain a range of instrumentation not normally associated with high-speed research compressors. Multi-sensor dynamic yawmeters were traversed at rotor and stator exit, and these probes have been reported by Cherrett *et al* (1994a). However, the rig was also provided with two removable double-stator cassette ports which facilitated the rapid fitting and removal of stators containing different instrumentation.

One of these double-blade cassettes was fitted with dynamic pressure sensors at mid-span. Six miniature semiconductor pressure transducers were embedded in the suction surface of one blade and six in the pressure surface of the other blade. The blades were assembled so that the instrumented pressure and suction surfaces were adjacent to each other, allowing the unsteady pressure field on both sides of the same passage to be measured simultaneously. The technique used to mount the transducers was developed at Oxford University (Ainsworth *et al*) and 1.2mm square transducers were used. The effective measurement bandwidth, based on this length scale and a perturbation speed corresponding to the pressure surface free-stream velocity, was approximately 100kHz.

The transducers were calibrated over a range of pressures and temperatures at Oxford to determine the effect of temperature on the transducer null-pressure outputs and pressure sensitivities. However, the temperature compensation was not employed when taking the measurements and the transducer sensitivities were derived from the predicted temperature field about the stator, while a similar cassette containing pneumatic pressure tappings was used to measure the dc pressure levels. The pneumatic cassette contained eight tappings on the suction surface and five on the pressure surface.

A further double blade cassette was constructed (at Oxford University for DRA) with 12 thin-film gauges mounted on both pressure and suction surfaces. The platinum gauges were applied using vapour deposition through a photolithographic mask, and measured 2.0 mm by 0.2 mm. The gauges were run as hot films using constant current analogue circuits developed at Oxford University for use with heat transfer gauges mounted on semi-infinite thermal substrates in short duration test facilities (Oldfield *et al*). However, as the gauges used in C148 were mounted on enamelled metal blades in a continuously running compressor, the electrical analogue circuitry allowing the signals to be processed to yield quantitative wall shear stress measurements was not applicable. Hence only qualitative information could be obtained from these measurements, although this has been used to good effect by Hodson *et al*. The bandwidth of the heated thin-film sensors was expected to be of the order of 20-30kHz.

3.3 Data acquisition and processing

All of the unsteady aerodynamic signals were amplified at the rig and transmitted over 20m cables to the facility control room. Here, the data were recorded on a high-speed digital data acquisition system and the data were sampled in two modes. That is, either as continuous records, or as multiple 'discontinuous' records captured in response to a once-per-revolution trigger signal. The latter were processed on-line to determine the following parameters.

a) Ensemble averaged signal:

$$\tilde{P}_{(t)} = \frac{1}{N}\sum_{n=1}^{N} P_{(n,t)}$$

b) Average random unsteadiness:

$$\tilde{p}'_{(t)} = \sqrt{\frac{1}{N}\sum_{n=1}^{N} \left(P_{(n,t)} - \tilde{P}_{(t)}\right)^2}$$

Where: $P_{(n,t)}$ is an instantaneous signal captured in response to a once-per-rev trigger pulse.

N is the number of consecutive rotor revolutions during which phase-locked data capture was carried out in response to a once-per-revolution pulse, normally 128.

t is the temporal duration of each of the segmented data records (typically 512 or 2048 samples depending on the recorder module capacity).

Processing data in this manner is a well established technique that accentuates the periodic unsteadiness correlated with the rotor. As the data are captured in response to a once-per-revolution signal, the rotor is in the same position each time the recording cycle is initiated and differences in the flow field associated with individual rotor passages are retained.

4.0 MID-SPAN STATOR SURFACE PRESSURE MEASUREMENTS

4.1 Time-averaged measurements

Pneumatic measurements. The static pressure distribution measured using the pneumatic stator cassette is shown in Fig 3, along with the results predicted by the S1-S2 model reported by Bryce *et al* (1993). The positions of the dynamic pressure sensors are also indicated. Generally, the S1-S2 model predicts less lift on the aerofoil than that measured, due to an under-prediction of mid-span rotor work. However, the predicted pressure distribution on the pressure surface is in good qualitative agreement with the measurements, although agreement is not so good on the suction surface. Here the S1-S2 model predicts greater acceleration over the first 60% of the blade than inferred from the measurements.

The S1-S2 prediction is used in this paper primarily to provide estimates of free-stream velocity (U_∞) about the aerofoil, in

order to estimate the convection velocity of perturbations measured by the pressure sensors and thin-film gauges. To this end, the S1-S2 data provide a good first order estimate of (U_∞), and better predictions carried out subsequently using 3D viscous modelling have not altered significantly the conclusions drawn from using the S1-S2 data for this purpose. The S1-S2 model was also used to construct a Q3D inviscid model of chopped wake behaviour (see Cherrett 1994). As an aside, it is interesting to note that the point transition boundary layer model coupled to the S1 calculation predicted that the boundary layer would separate at approximately 85% of the chord on the suction surface. This is in good agreement with the flow visualization results. Although phenomenologically incorrect, the boundary layer calculation predicted transition to fully turbulent flow on the suction and pressure surfaces at approximately 5% of the chord. The Reynolds number based on mid-span stator chord was approximately $1x10^6$.

Averaged unsteady measurements. The amplitudes of the ensemble-average and random unsteady pressure fluctuations on both stator surfaces are shown in Fig 4. Figs 4a & 4b show the steady-state pressure distribution with the time-averaged RMS of the ensemble-average and random unsteadiness data superimposed. Both data have been normalized with respect to the fan delivery stagnation pressure, and an indication of the maxima and minima in the data are also included. However, it should be noted that these refer to the phase-locked processed data, and larger values would be found in the instantaneous `raw' data.

Fig 4a also includes an indication of the magnitude of the dynamic head at stator inlet, as shown by the vertical arrow. Comparison of the ensemble-average and random unsteadiness data on both sides of the stator with this, and the steady-state pressure distribution, shows that the pressure field is highly unsteady and influenced strongly by passing of the upstream rotor. RMS ensemble-average pressure fluctuations of 30% to 40% of inlet dynamic head were recorded. It is also evident that the fluctuations are more vigorous on the suction surface than on the pressure surface. On the pressure surface, both ensemble-average pressure and random unsteadiness tend to decrease with increasing chord, with the largest amplitudes being found near the leading edge. On the suction surface, the ensemble-average fluctuations are also high near the leading edge, although even higher levels are found locally at 58% of axial chord. The reasons for this behaviour are discussed in the following sections. Toward the suction surface trailing edge ie, at 89% of axial chord, the ensemble-averaged average amplitude falls markedly.

4.2 Unsteady pressure measurements (suction surface)

Time-histories. The time-histories from which the suction surface measurements were derived are shown in Fig 5, where they are expressed as a percentage of the local steady-state static pressure. For brevity, only the suction surface data are shown in this form in this paper, although both suction and pressure data will be shown as space-time diagrams later. From careful consideration of Fig 5, and similar data phase-locked on a once-per-blade basis (not shown here), it is apparent that the suction surface is influenced by two disturbances. Both of these disturbances have a wavelength corresponding to one rotor passing period, although the phase angle between the disturbances changes along surface.

That two disturbances exist, is most readily seen in the transducer S3 data at 37% of axial chord, where they are marked A and B, and are almost 180° out of phase. In the random unsteadiness measurements the A-type disturbances are manifest as sharp high amplitude perturbations. The type-B disturbances are less repeatable from passage-to-passage and they appear to be less distinct and are of lower amplitude than the type-A perturbations. These events correlate temporally with features in the ensemble averaged data, although at transducer S3 they are manifest as disturbances of similar size and amplitude. It is not easy to chart the development of these perturbations as they propagate along the suction surface because they are less easy to distinguish at other chord-wise positions. For instance, at transducer S4 (54% of axial chord) the two disturbances are superposed. Where the two disturbances are superposed the net amplitude of the ensemble-averaged average pressure fluctuations increases greatly. This explains the behaviour of the ensemble-averaged RMS pressure fluctuations shown in Fig 4a. Finally, further evidence that the flow is separated near the trailing edge is suggested by the marked decrease in the amplitude of the blade-passing events.

Random unsteadiness space-time diagram. Fig 6 presents the suction surface random pressure unsteadiness measurements, which have been annotated to aid their interpretation. The red overlay demarks the boundaries of the type A and type B disturbances, while the yellow overlay depicts the trajectories of disturbances moving at different speeds derived from the S1-S2 prediction. It is evident that the two disturbances identified in Fig 5 propagate in opposite directions along the suction surface.

The first disturbance (type B in Fig 5) propagates from the leading edge to the trailing edge, and is therefore attributed to rotor wake convection. The leeward side of the disturbance travels slower (ie. $0.4U_\infty$) than the windward side (ie. $0.7U_\infty$), and is consequently enveloped by the windward side of the next wake-disturbance close to transducer S5.

The second disturbance (type A in Fig 5) propagates in the opposite direction (ie. upstream). Between transducers S5 and S4 the disturbance appears to travel at rate derived from the sum of U_∞ and an acoustic wave originating at the trailing edge. Upstream of transducer S4 the disturbance appears to correlate with the acoustic propagation rate alone. The phenomenon giving rise to this disturbance is not so easy to identify, although the following hypothesis is suggested.

It has already been noted that the steady-state flow appears to have separated from the suction surface by transducer S6 during the entire rotor passing period. However, the data recorded at transducer S5 appears to indicate that the separation point momentarily moves upstream following interaction between the windward side of the `first' wake and the leeward side of the `second' wake. That is, the S5 data are characterized by juxtaposed low and high unsteadiness levels which are thought to be due to separation and re-attachment of the boundary layer near this point. There is corroborating evidence to support this hypothesis in the traverse probe measurements taken downstream

of the stator reported by Cherrett et al (1994b). That is, computer based animations of these data showed that, near mid-span, there was a sudden increase in unsteadiness when the rotor wakes swept past the stator wake and that the rotor wakes appeared to be retarded on exit from the stator passage close to the stator suction surface at mid-span.

In this paper, this is illustrated by viewing the traverse measurements (taken 36% of axial chord downstream of the stator trailing edge, plane Y in Fig. 1) as rθ-T diagrams on constant radii planes. The random unsteadiness data are presented in this way for the measurements taken at 35% and 50% of span, in Fig 7. The wake trajectories predicted by the S1 model (see Cherrett, 1994) are superimposed on these data as pairs of parallel lines, although the separation of the lines is arbitrary and not meant to represent the rotor wake thicknesses.

At 35% and 50% span the rotor wakes are retarded (relative to the predicted trajectories) close to the suction surface, where viscous flow field interactions are dominant. However, the extent of the retardation is more severe at mid-span. That is, it is clear that at 35% span the chopped rotor wakes arrive on the suction surface side of the stator wake before the pressure surface side. However, at mid-span, the rotor wake is so retarded close to the suction surface side of the stator wake, that the pressure surface side of the wake arrives at the traverse plane before the suction surface side. (Note that the fact that the unsteadiness on either side of the stator wake originates from the same rotor wake is illustrated by the correlating the positions of the weaker rotor wake filaments either side of the stator wake in Fig 7).

Given the above evidence for a transient augmentation of the separation and its subsequent re-attachment, it is thought likely that this gives rise to the acoustic disturbance propagating upstream. The author is not aware of published data indicating similar phenomena in a compressor cascade, although Dring *et al* identified such disturbances on the vane of a low-speed turbine stage as the rotor swept past the trailing edge. If such a disturbance were to originate at the mid-span near the trailing edge it would propagate upstream at U_∞-a. This seems reasonable for the C148 stator at mid-span where relatively thin, attached, boundary layers are thought to cover most of the blade. However, it is difficult to explain why the disturbance accelerates to -a upstream of transducer S4. One possible explanation might be that over the forward portion of the aerofoil, the disturbance trajectory becomes inclined relative to the pseudo-streamline on which the transducers are arranged. If the disturbance strikes the transducers obliquely the propagation rate could be perceived as being faster than the actual rate. For example, a wavefront passing all the transducers at the same time would appear to be travelling at infinite velocity.

As well as showing that the mid-span rotor wakes are retarded near the stator suction surface, Fig 7 also shows that the chopped rotor wakes broaden as they approach the pressure surface side of the passage and that the unsteadiness between the rotor wakes is greatest on the pressure side of the passage. This is a manifestation of the negative jet effects hypothesized by Kerrebrock & Mikolajczak to explain temperature excesses near the pressure surface sides of high-speed compressor stator passages, ie. the wake fluid is convected across the stator passage due to the slip velocity in the wake.

Ensemble-averaged pressure space-time diagram. While it seems relatively easy to make an intuitive interpretation of the random unsteadiness data, this is less easy for the ensemble-average pressure data in Fig 8.

Relating the ensemble-average and random unsteadiness measurements using the red overlay, it is evident that the ensemble-average pressure field associated with the acoustic wave is largely in phase with local maxima in the ensemble-average field. However, the random unsteadiness associated with the wake-disturbance does not occur where the associated random unsteadiness levels are highest. Rather, the point where the locally increasing ac-coupled pressure data cross the ac-coupled zero level correlate more reasonably with the wake-disturbance centre, as indicated by the asterisks in Fig 8.

Although much of the behaviour noted in Fig 8 is too complex to explain fully, it is interesting to note that where the transient separation and re-attachment occurs at transducer S5, the ensemble-averaged average pressure oscillates between a localized minimum and maximum. This is largely in phase with the cycle of low and high random unsteadiness. This reinforces the interpretation, drawn from the random unsteadiness data, that a transient separation and re-attachment is taking place.

4.3 Unsteady pressure measurements (pressure surface)

Turning attention to the pressure surface random unsteadiness and ensemble-average pressure in Fig 9 and 10 respectively, it is clear that there is little indication of wake convection in either data. This is surprising as the negative jet effects (illustrated in Fig 7) transport fluid from the suction surface side of the passage toward the pressure surface. Therefore, it might be expected that this would result in high levels of random pressure unsteadiness correlated with rotor wake passing. While it is not possible to understand fully the lack of blade passing activity in the pressure surface data, it is plausible that the significant mixing which accompanies the cross-passage convection of the chopped wake fluid dissipates the perturbations close to the pressure surface.

The main features in the pressure surface data are disturbances convected downstream apparently faster than the local sonic velocity. These are manifest as broad ridges of high unsteadiness in Fig 9, and as a narrow pressure troughs in Fig 10. Due to the limited extent of the stator-surface measurements, it is not possible to ascertain whether these features are due to genuine perturbations originating at the leading edge and travelling downstream, or whether they originate elsewhere in the stator passage and only appear to travel at faster than the local sonic velocity because the disturbance passes over the transducers obliquely. Certainly, the stator exit flow field traverses presented by Cherrett *et al* (1994b) showed that the region of high stagnation pressure adjacent to the stator pressure surface expanded and contracted rapidly during the rotor passing period, and that this activity was particularly vigorous near the pressure surface side of the passage. It is feasible that the pressure field on the pressure surface of the stator is more strongly influenced by this behaviour than by rotor wake convection.

Finally, the other features worthy of discussion in Fig 9 are the regions of high unsteadiness in the region of transducer P5. These are largely in phase with the low-to-high unsteadiness perturbations seen on the suction surface which have been attributed with the transient separation and re-attachment. However, it is not possible to prove conclusively that the pressure surface activity is a manifestation of the same phenomenon.

5.0 MID-SPAN THIN-FILM GAUGE MEASUREMENTS

5.1 Pressure surface measurements

Because of the difficulty in interpreting the pressure measurements on the pressure surface, attention is first turned to the corresponding thin-film measurements in Fig 11. These data have been derived from continuously sampled recordings which were subsequently phase-lock processed on a once-per-blade passage basis. That is, the instantaneous 'raw' data were spliced into portions equivalent to one blade passage, and processed using the methods defined in section 3.3. Therefore, each blade passage is an identical copy of its neighbour. As noted in section 3.2, quantitative analysis of the measurements could not be carried out without introducing large errors into the shear stress (τ_w) data. Therefore, the data have been presented in normalized form, ie. with the maximum-to-minimum variation set to unity.

Although wake convection was indistinguishable in the pressure field measurements, it is immediately evident in the thin-film data. In the random unsteadiness measurements, Fig 11, the wakes travel at close to the predicted value of U_∞ and they show no tendency to broaden as they travel along the pressure surface. That is, there is no evidence to suggest that turbulent patches are formed under the wakes in the manner identified in by Dong & Cumpsty, and the effect of the wakes seems to be limited to locally raising the randomness in the τ_w measurements. Similarly, it is curious that there is no evidence to suggest boundary layer transition in between the passing wakes either. While the conditions on the pressure surface should be amenable to sustaining an appreciable portion of laminar/transitional boundary layer over the first 50% of the aerofoil, it is not plausible to expect this to extend over the entire surface. Even if this were the case, a laminar/transitional boundary layer would be even more likely to sustain the formation of wake-induced turbulent patches which broaden as the travel downstream. The reasons for the lack of parity with other low-speed and high-speed turbomachinery experiments is not easy to understand.

The normalized ensemble-average τ_w measurements are shown in Fig 12. Although there is some evidence to suggest the presence of perturbations due to wake convection, the strongest disturbances seem to travel faster than the local sonic velocity. In this respect the data reflect the observations made when discussing the corresponding pressure field data in Fig 10. However, none of the features travelling at this speed are in phase with the pressure field data.

5.2 Suction surface measurements

The thin-film measurements taken on the suction surface are shown in Fig 13, where it can be seen that they were compromised by failure of most of the gauges between 45% axial chord and the trailing edge. However, there is clear evidence of wake convection in the random unsteadiness measurements over the first half of the surface. The red overlay determined during analysis of the corresponding pressure field measurements has been reproduced to allow direct comparison of the data. The predicted U_∞ and sonic velocity trajectories are also included. Consequently it can be seen that the wake disturbances in Fig 13 travel at close to U_∞ between gauges Ts1 and Ts6. Beyond this they apparently slow down, which is shown by the fact that the high random unsteadiness seen at gauge Ts11 does not lie on the U_∞ trajectory. Initially the perturbations due to wake convection in both the pressure and τ_w data are in phase. However, the τ_w data show no tendency to broaden as they move downstream, and as such they are different to the limited body of similar measurements taken elsewhere. The data do however exhibit regions of low random unsteadiness between the wakes at gauges Ts1 and Ts3, while the inter-wake regions at gauge Ts3 are considerably more active. This may suggest that transition to a fully turbulent boundary layer occurs naturally between gauges Ts3 and Ts4. However, the spacing between these gauges, and the aforementioned lack of evidence to support the formation of broadening turbulent patches in the upstream boundary layer make it difficult to be certain of this interpretation.

Additional features are visible in these data, which may due to the acoustic wave travelling upstream. However, it is clear from comparison with the red overlay that there is not a simple phase relationship between the perturbations measured in the pressure field and the τ_w field.

The normalized ensemble-average τ_w measurements are shown in Fig 14. Like the pressure surface measurements these are far more complex than the random unsteadiness data, and in that respect are far more complex than data published elsewhere. Given the presence of the acoustic wave propagating upstream identified in the pressure field data, this is not surprising, although it is not possible to identify the features attributable to the acoustic wave because of the complex phase relationship between the pressure field and the τ_w data.

6.0 DISCUSSION

The data presented in the paper are thought to be the most detailed of their kind to be published to date illustrating the transient pressure distribution and boundary layer development in a high-speed compressor. Generally, the measurements have proven more complex than the limited amount of relevant data published elsewhere. In addition, much of the interpretation of the pressure field data reported in this paper has relied on analyses of the random unsteadiness in the measurements. This has proven particularly fruitful, yet the author is unaware of similar analyses being carried out elsewhere; therefore it is not possible to compare these data with other measurements directly. Indeed it is noteworthy that analyses of unsteady pressure field measurements taken on low-speed compressor aerofoils elsewhere (eg. Schulz *et al*, Sugeng & Fiedler, Franke & Henderson) concentrate on the ensemble-averaged pressure fluctuations. As seen in the equivalent C148 data, it is difficult to identify the phenomena responsible for the fluctuations without making reference to the random unsteadiness data.

It is also noteworthy that the pressure fluctuations recorded in these low-speed aerofoil studies (often utilizing `rotating bar rotors' to simulate the wakes) documented monotonic decays in perturbation amplitude with increasing stator chord. The C148 data were quite different, because of the interactions between the acoustic wave and wake disturbances. Therefore, caution should be exercised when applying the lessons learnt from such idealized studies to high-speed turbomachinery. However, the low-speed turbine measurements taken by Dring *et al* displayed similar characteristics to the C148 pressure field perturbations.

The behaviour of the pressure field measurements on the suction surface showed the wake disturbances to spread as they progressed downstream because the windward and leeward sides of the rotor wakes moved at different speeds. In this respect, the interpretation of the wake-type disturbance behaviour resembles closely that of wake induced turbulent patches seen in the work reported by Dong & Cumpsty. However, these cited data were taken using intra-boundary layer hot-wire anemometry, ie. velocity field measurements. Therefore, it should not be interpreted prematurely that the observed random pressure unsteadiness data depict wake-induced transitional/turbulent patches in the suction surface boundary layer.

Indeed, it is curious that although the pressure field data displayed the aforementioned behaviour, the thin-film measurements on the suction and pressure surfaces showed no evidence for the development and propagation of turbulent patches due to wake passing. The reasons for this are not clear. Similarly, it was not possible to identify unambiguously where natural transition took place using the data; there was certainly no evidence to suggest point transition occurring at 5% of the surface length, as modelled by the boundary layer code coupled to the S1 calculation. Even so, the latter predicted full separation of the suction surface boundary layer at approximately 85% surface length, and this agreed well with evidence from the surface mounted pressure sensors and the oil flow visualization.

7.0 CONCLUSIONS

Detailed unsteady aerodynamic measurements have been taken in a single-stage transonic fan with a very high stage hub-loading. 2D dynamic yawmeters were traversed at rotor and stator exit, while dynamic pressure sensors and heated thin-film gauges were fitted to the stator at mid-span. This paper has concentrated on analysis and interpretation of the on-stator measurements supplemented by consideration of some of the stator exit measurements and an inviscid-viscous prediction of the flow about the stator. The following detailed conclusions are drawn from the measurements.

1) Suction surface (pressure data). The suction surface pressure field was influenced strongly by two phenomena. i) Disturbances due to rotor wake convection, which travelled downstream becoming broader with increasing surface length. The front-edge of these disturbances travelled at approximately 70% of the free stream velocity, while the rear-edge propagated at approximately 40% of the free stream velocity. ii) Disturbances travelling upstream were also present. These propagated at the local acoustic velocity over much of the surface, although toward the trailing edge they appeared to move more slowly. These were attributed to augmentation of the suction surface boundary layer separation by the passing rotor wakes, causing a transient (larger) separation and subsequent re-attachment. Evidence to support this hypothesis was obtained from the downstream stator exit traverse measurements. These showed heightened levels of unsteadiness near the mid-span suction surface side of the stator wake, and that the passing rotor wakes were retarded in this region.

Because the wake and acoustic disturbances travel at different speeds on the suction surface, and in opposite directions, they interacted near 58% axial chord to yield large amplitude perturbations in the local static pressure levels.

2) Suction surface (thin-film data). The gauges on the first half of the surface showed clear evidence of wake convection. These disturbances were initially in-phase with the corresponding pressure field disturbances, although unlike the pressure disturbances they continued to travel at close to the free stream velocity and showed no tendency to broaden as they travelled downstream. As such, the disturbances did not behave like the wake induced turbulent patches measured in low-speed and high-speed flows elsewhere. The data did not illustrate conclusively where natural transition occurred on the stator during the periods between rotor wake passing.

3) Pressure surface (pressure data). The pressure surface pressure measurements showed no sign of rotor wake convection despite evidence from the exit traverse measurements to suggest that `negative jet' effects were convecting chopped rotor wake fluid toward the pressure surface. The strongest influence on the pressure surface pressure field was a disturbance that travelled downstream, apparently faster than the local sonic velocity. The origin of this disturbance was not as easy to identify as those seen on the suction surface in the absence of additional measurements. However, it was thought to be linked to the rapid expansion and contraction of a high-pressure fluid within the stator passage; this was revealed in the stator exit traverse measurements reported by Cherrett *et al* (1994b).

4) Pressure surface (thin-film data). Wake convection was strongly evident in the thin-film gauge data, although it had been absent from the corresponding pressure field measurements. The wakes travelled at close to the free stream velocity without broadening; again this behaviour was unlike that reported elsewhere.

5) The thin film measurements on both pressure and suction surfaces did not indicate where natural transition occurred on the aerofoil, ie. in-between the regions affected by wake convection.

6) The measurements reported in this paper, and in previous works on C148 (ie. Bryce et al, Cherrett (1994) and Cherrett et al (1994a & b), illustrate one of the most comprehensive data sets of its type to be published to date. C148 represents a particularly challenging test case for CFD modelling, being characterized by a transonic, highly 3D viscous and unsteady flow field. These data will be used to evaluate and develop steady and time-accurate methods, and this activity will be reported in future work.

ACKNOWLEDGEMENTS

The C148 research programme reported in this paper was supported by the UK Ministry of Defence's Strategic Research Programme and by the Aerospace Division of the UK Department of Trade and Industry. The success of the C148 measurement programme owed much to the enthusiasm and input of John Bryce, who has now retired from DRA. Thanks are also due to Peter Lyes.

REFERENCES

Ainsworth, R.W., Deitz, A.J., Nunn, T. *The use of semiconductor sensors for blade surface pressure measurements in a model turbine stage.* ASME 90-GT-346 (1990)

Bryce, J.D., Cherrett, M.A., Lyes, P.A., *Three-dimensional flow in a highly loaded single-stage transonic fan.* ASME 93-GT-3. Subsequently reproduced in Trans. ASME Journal of Turbomachinery, Vol. 117, Jan. 1995, pp. 22-28 (1993)

Cherrett, M.A., Bryce, J.D., Ginder, R.B., *Unsteady 3D flow in a single-stage transonic fan. Part I: Unsteady rotor exit flow field.* ASME 94-GT-223 (1994a)

Cherrett, M.A., Bryce, J.D., Ginder, R.B., *Unsteady 3D flow in a single-stage transonic fan. Part II: Unsteady stator exit flow field.* ASME 94-GT-223 (1994b)

Cherrett, M.A., *Unsteady flow in high-speed axial compressors.* PhD Thesis, Imperial College, London University (1994)

Dring, R.P.,Joslyn, H.D., Hardin, L.W. Wagner, J. H., *Turbine rotor-stator interaction.* ASME Journal of Engineering for Power, Vol. 104,pp. 84-95 (1982)

Dong, Y., Cumpsty, N.A., *Compressor blade boundary layers: Part II Measurements with incident wakes.* ASME 89-GT-51 (1989)

Dring, R.P, Joslyn, H.D, Hardin, L.W, Wagner, *J.H, Turbine Rotor-Stator interaction.* ASME Journal of Engineering for Power, Oct. 1982, Vol. 104, pp. 729-742 (1982)

Franke, G.F, Henderson, R. *E, Unsteady stator response to upstream rotor wakes.* Journal of Aircraft, Vol. 17, No. 7 (1980)

Hodson, H.P, Huntsman, I, Steele, A.B, *An investigation of boundary layer development in a multi-stage LP turbine.* ASME Paper 93-GT-310 (1993)

Kerrebrock, J.L, Mikolajczak, A.A, *Intra-stator transport of rotor wakes and its effect on compressor performance.* Trans. ASME Journal of Engineering for Power, pp. 359-369, (1970)

Oldfield, M.G.L, Burd, H.J, Doe, N.G, *Design of wide bandwidth analogue circuits for heat transfer instrumentation in transient tunnels.* Heat & Mass Transfer, Hemisphere Publications Corp. (1984)

Schulz, H. D, Gallus, H.E, Lakshminarayana, *B, Three-dimensional separated flow field in the endwall region of an annular compressor cascade in the presence of rotor-stator interaction: Part 2 Unsteady flow and pressure field.* Trans. ASME Journal of Turbomachinery, Vol 112, pp. 679-690 (1990)

Sugeng, F, Fiedler, *K, An experimental investigation into unsteady blade forces and blade losses in an axial compressor cascade.* ASME Paper 85-GT-132 (1985)

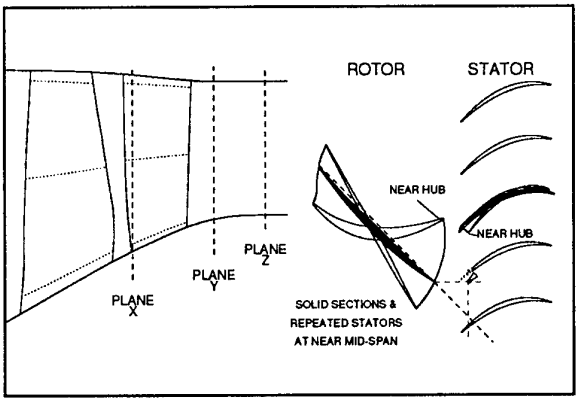

FIG 1 THE C148 TRANSONIC FAN

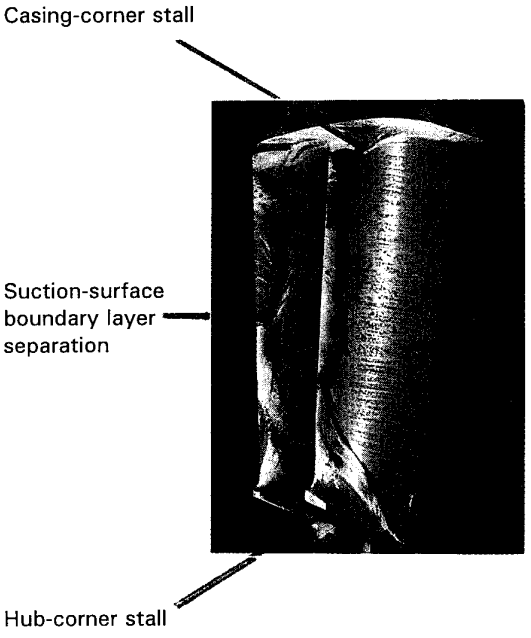

FIG 2 SUCTION SURFACE OIL FLOW VISUALIZATION

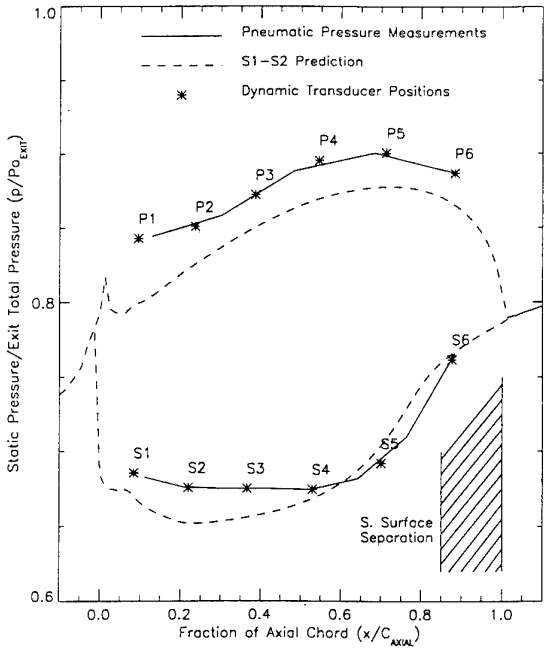

FIG 3 THE MID-SPAN STATOR STATIC PRESSURE DISTRIBUTION

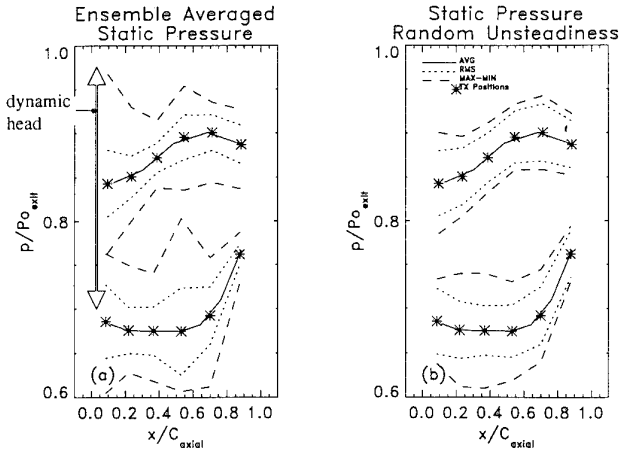

FIG 4 THE MID-SPAN TIME-AVERAGED UNSTEADY PRESSURE MEASUREMENTS

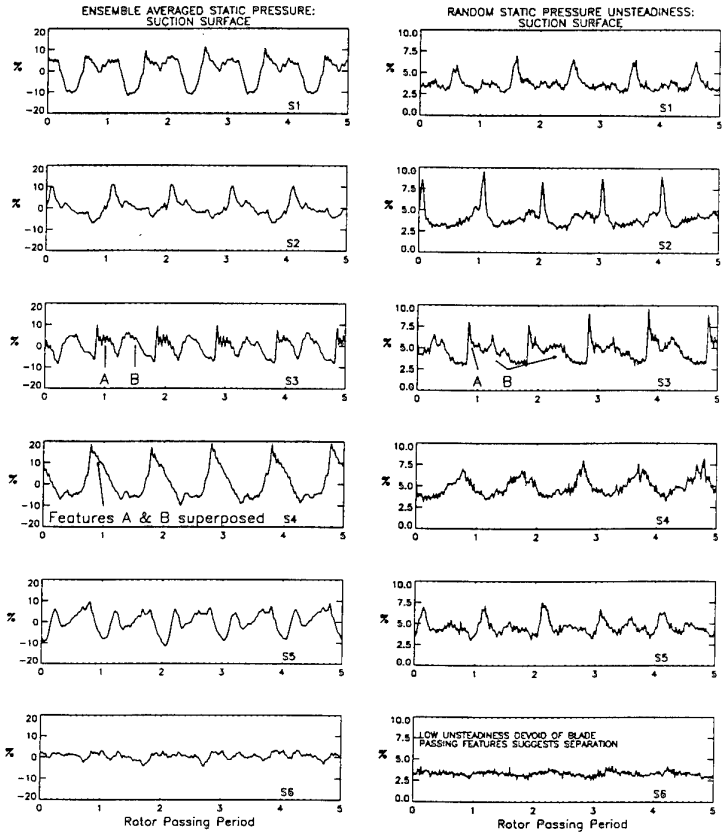

FIG 5 THE PRESSURE FIELD TIME-HISTORIES FOR THE MEASUREMENTS TAKEN ON THE SUCTION SURFACE AT MID-SPAN

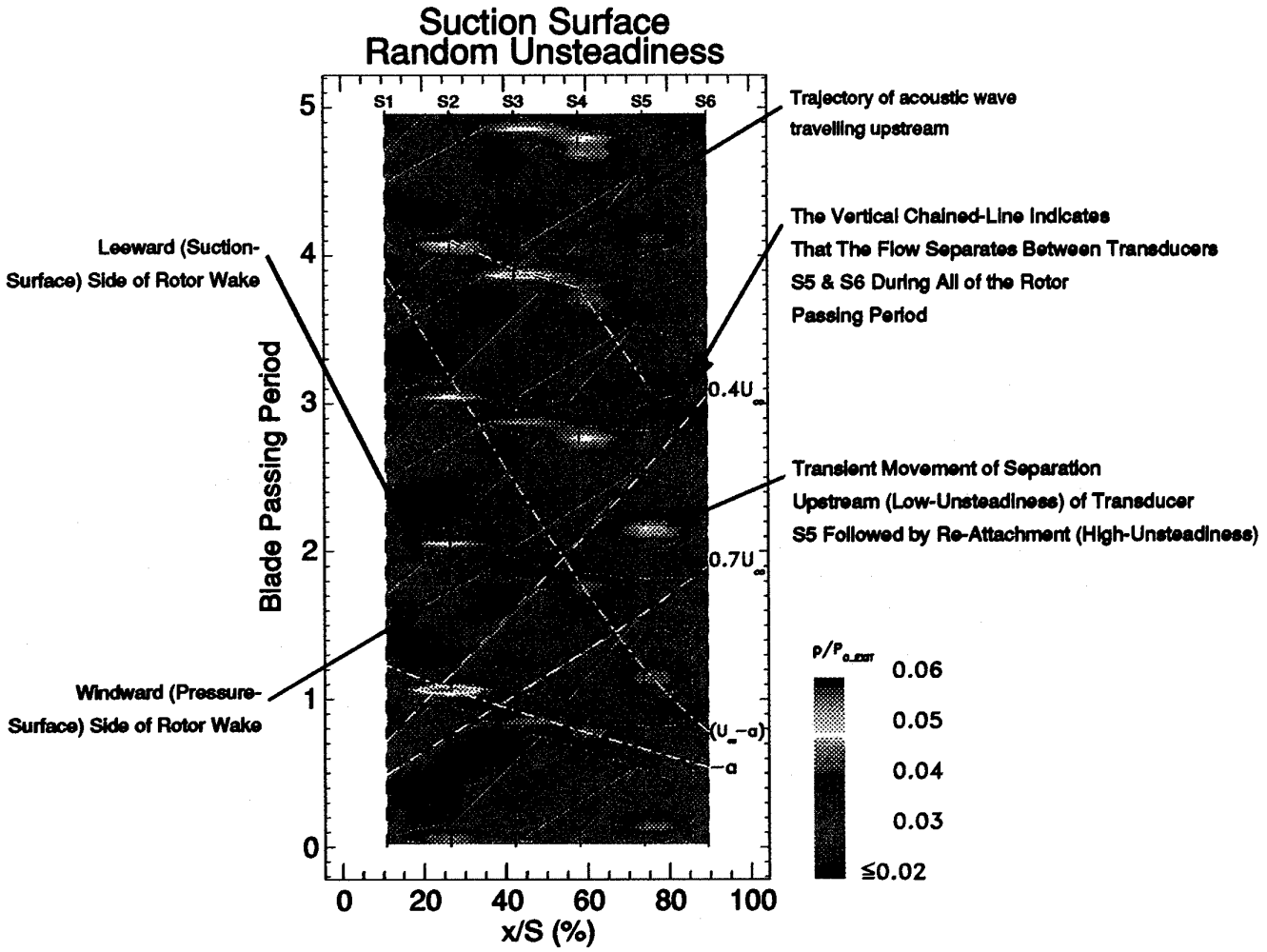

FIG 6 A RANDOM UNSTEADINESS SPACE-TIME DIAGRAM SHOWING THE PHENOMENA EFFECTING THE STATOR SUCTION SURFACE PRESSURE-FIELD

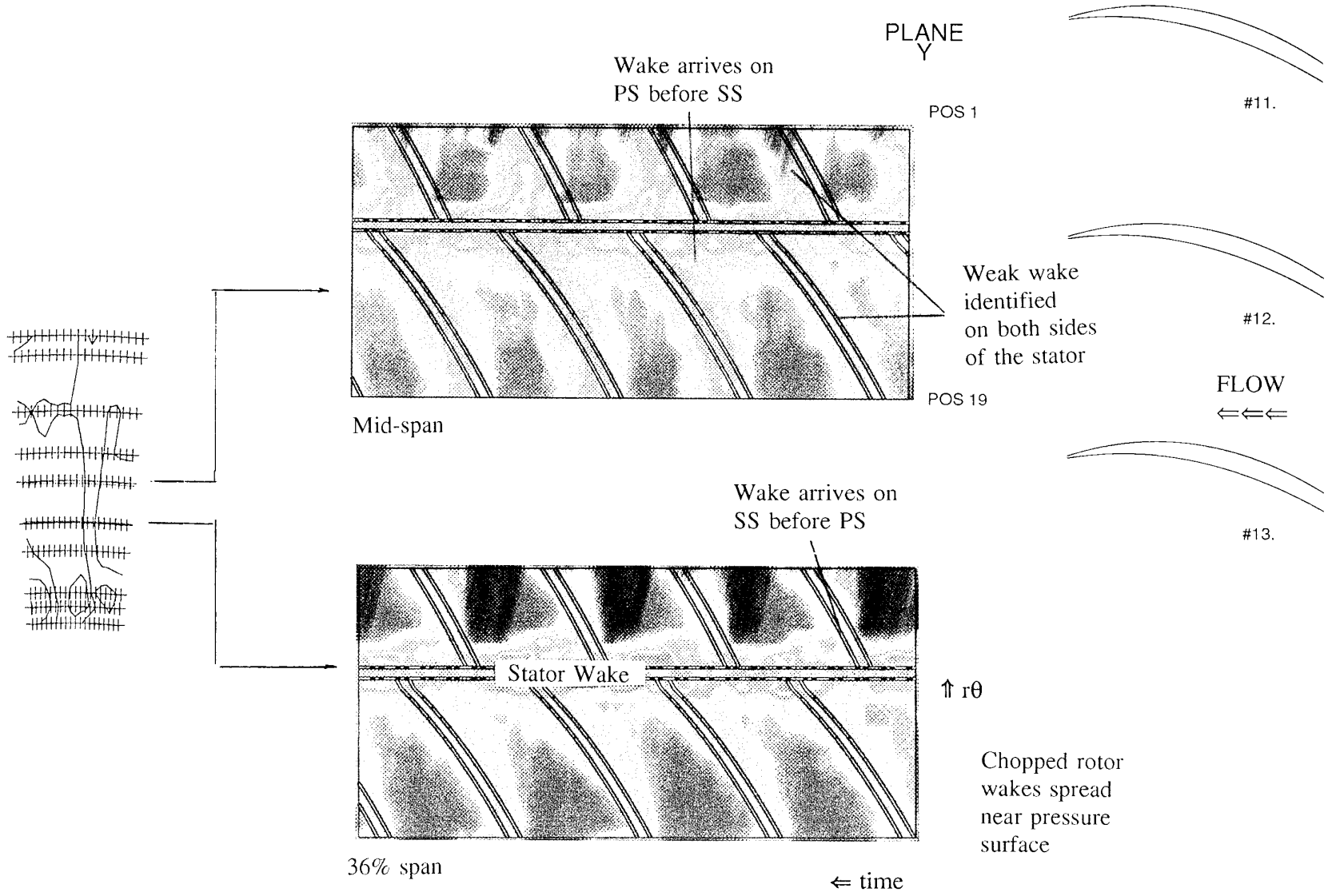

FIG 7 A SPACE -TIME (rθ-t) DIAGRAM SHOWING THE ROTOR WAKE BEHAVIOUR AT THE TRAVERSE PLANE 36% CHORD DOWNSTREAM OF THE STATOR TRAILING EDGE

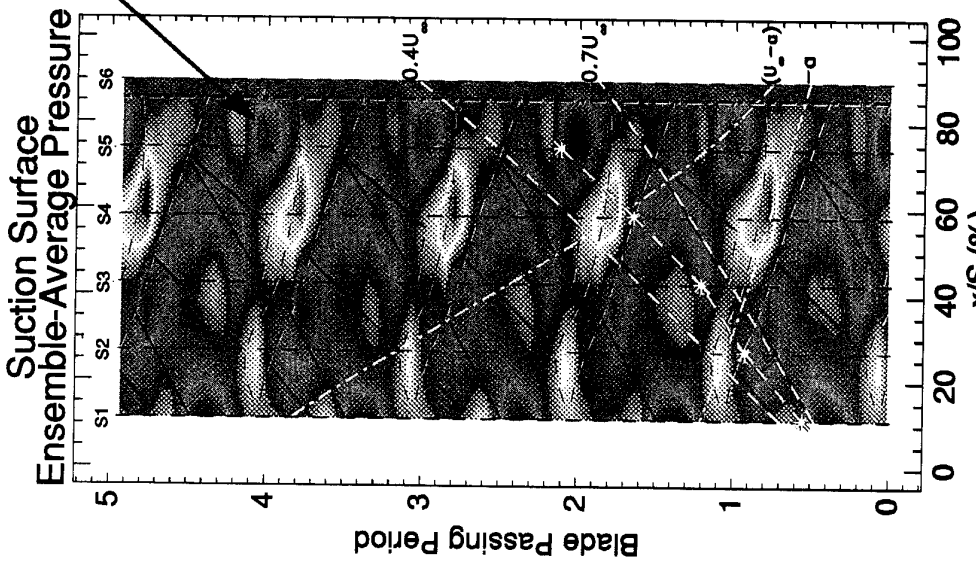

FIG 8 ENSEMBLE-AVERAGED PRESSURE-FIELD MEASUREMENTS ON THE SUCTION SURFACE

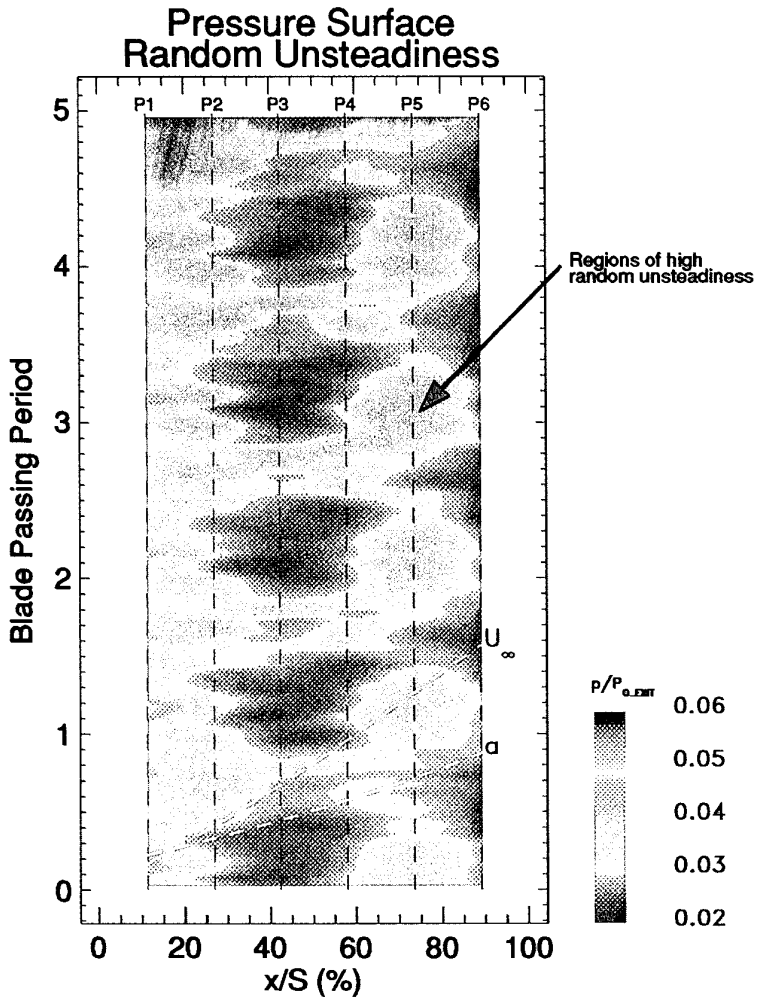

FIG 9 RANDOM UNSTEADINESS IN THE PRESSURE SURFACE PRESSURE-FIELD MEASUREMENTS

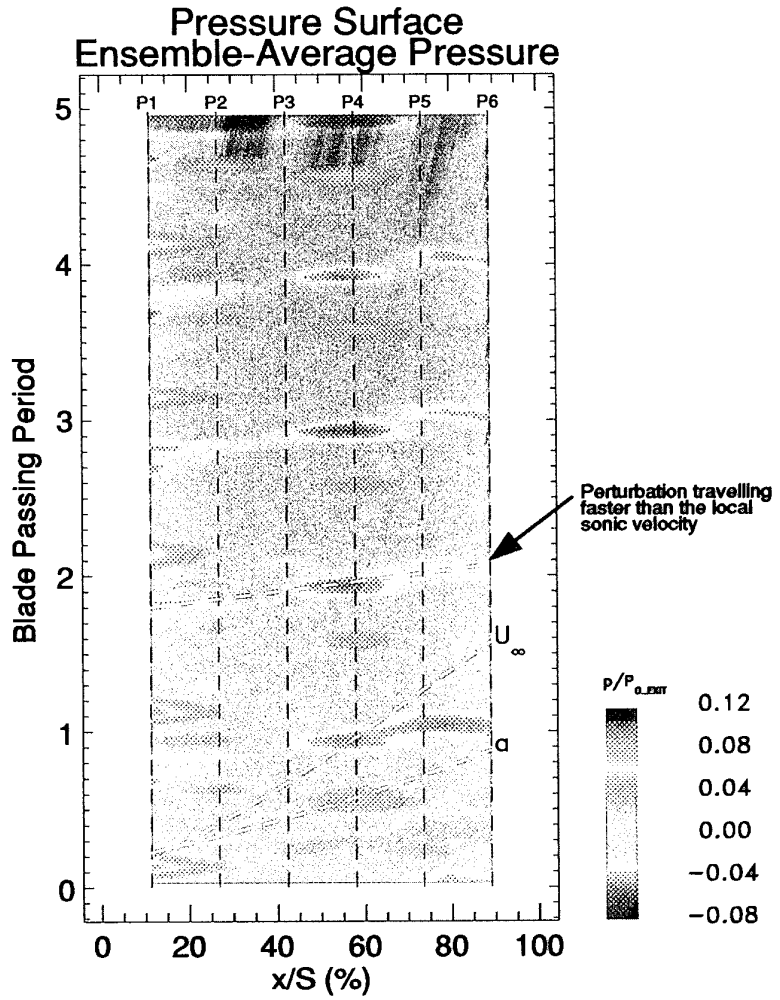

FIG10 ENSEMBLE-AVERAGE PRESSURE-FIELD MEASUREMENTS ON THE PRESSURE SURFACE

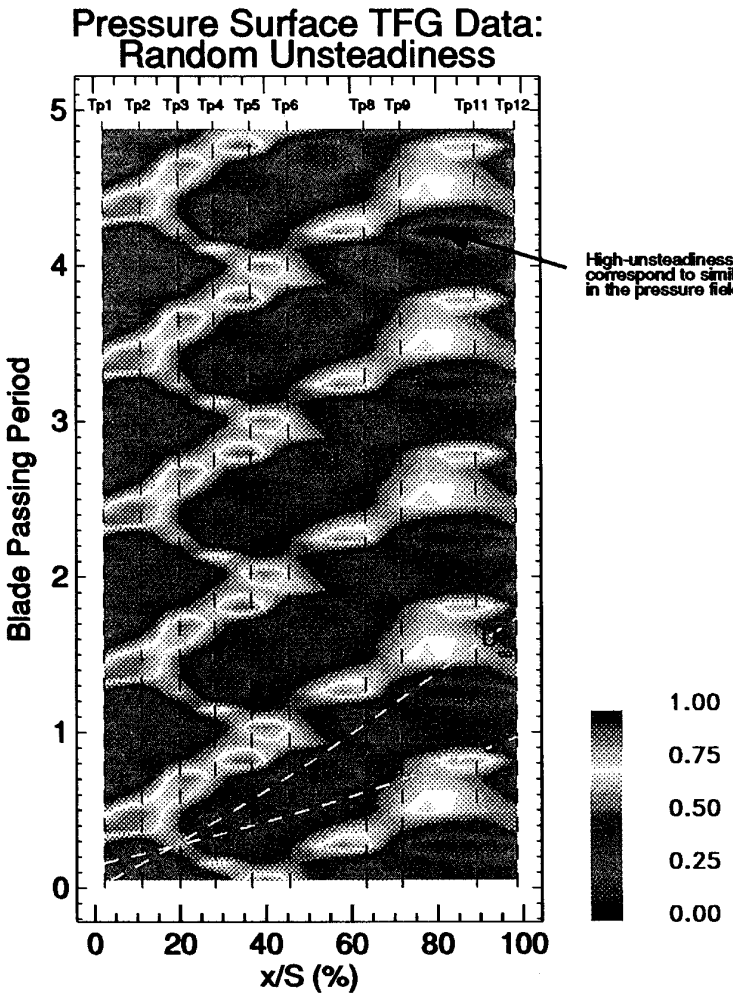

FIG 11 RANDOM UNSTEADINESS IN THE THIN-FILM GAUGE MEASUREMENTS ON THE PRESSURE SURFACE

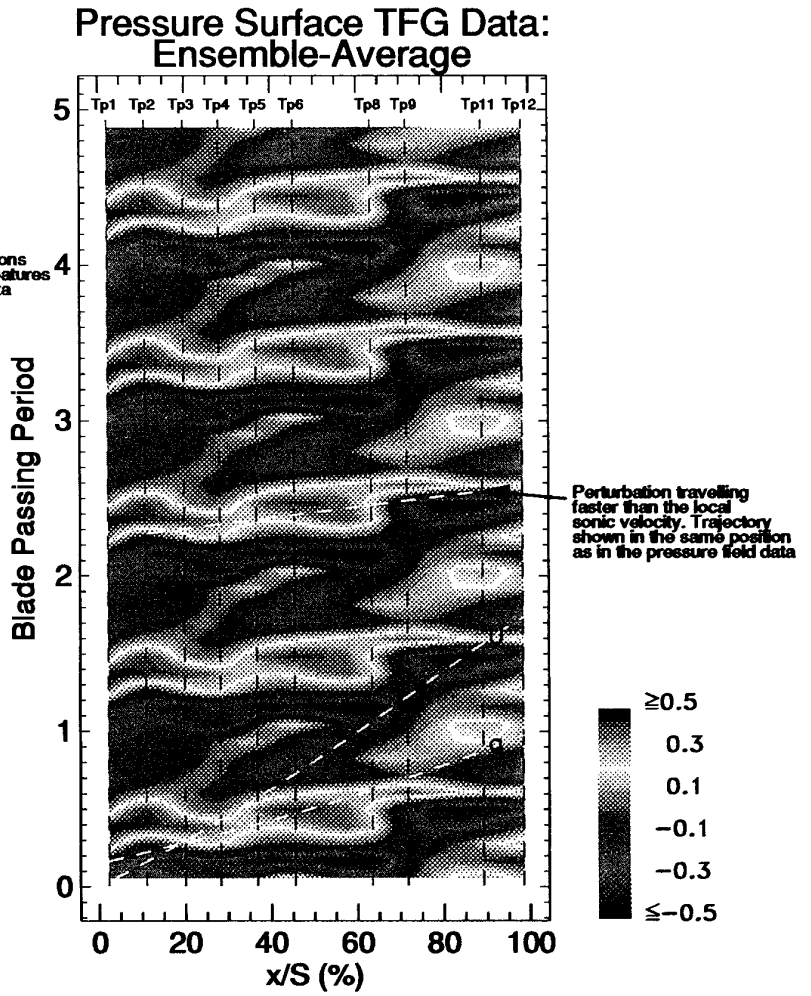

FIG12 ENSEMBLE-AVERAGE THIN-FILM GAUGE MEASUREMENTS ON THE PRESSURE SURFACE

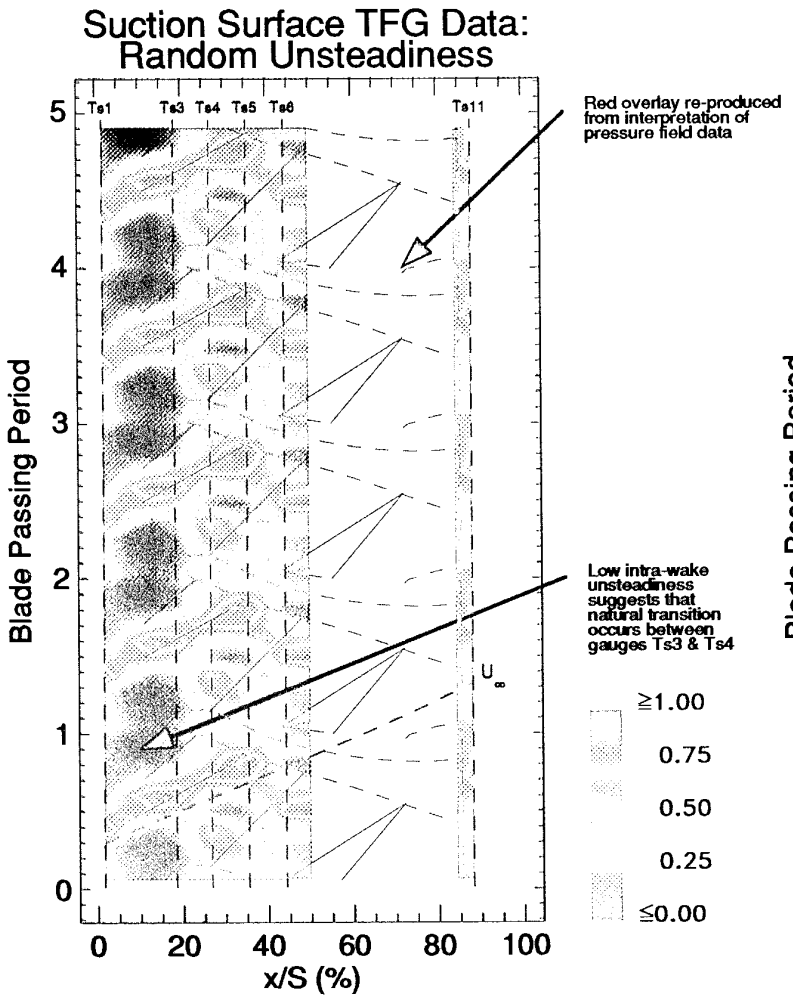

FIG 13 RANDOM UNSTEADINESS IN THE THIN-FILM GAUGE MEASUREMENTS ON THE SUCTION SURFACE

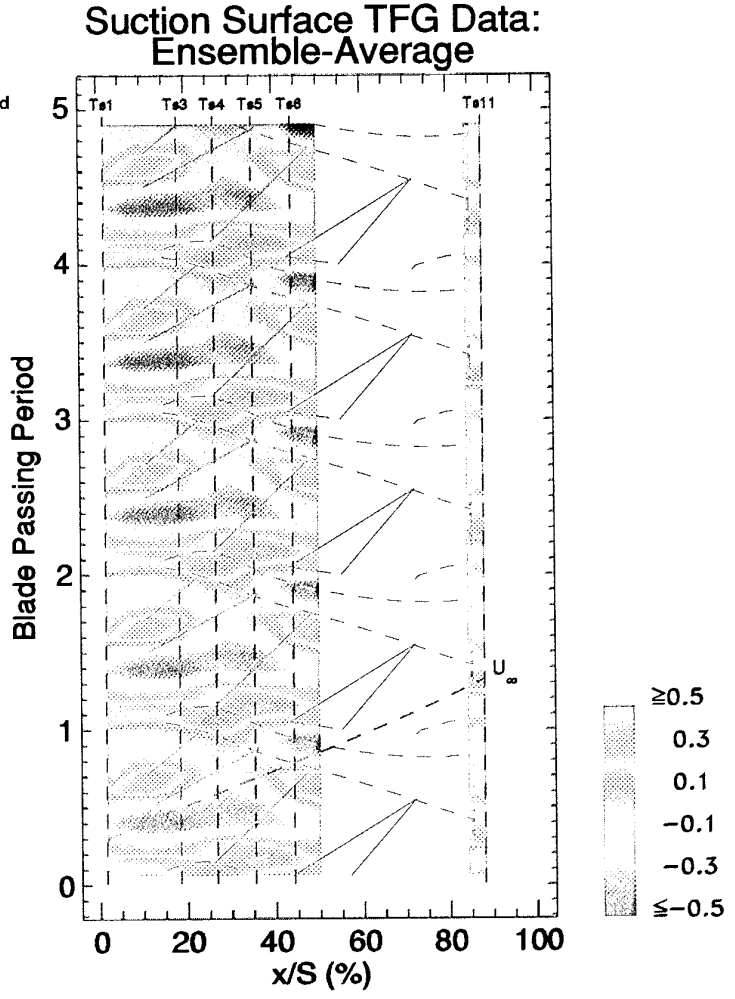

FIG14 ENSEMBLE-AVERAGE THIN-FILM GAUGE MEASUREMENTS ON THE SUCTION SURFACE

EXPERIMENTAL INVESTIGATION OF FLOW STRUCTURE AND LOSSES IN A HIGH LOAD TRANSONIC TURBINE STAGE

A.V. Granovskii
A.M. Karelin
K.M. Popov
Central Institute of Aviation Motors
2, Aviamotornaya Street, Moscow 111250, Russia

SUMMARY

The investigation of a loss mechanisms and flow pattern in a high load transonic single stage high pressure turbine is presented. The part of real vane row (vane sector) and midspan plane blade cascade were tested to obtain the flow structure and the level of losses for a wide range of outlet isentropic Mach -number from 0.7 to 1.4. During these tests flow visualization, total and static pressure and wake measurements were made. An inviscid and viscous computer codes and Bezier polynomials were used to the blade design by interactive technique. These experimental and calculated data were used for the stage design and analysis. The experimental stage was tested with changing of a tip clearance. The blade tip clearance values were measured by optical system. Comparison between measured and calculated performance of the experimental stage was carried out.

LIST OF SYMBOLS

a	-	Throat width.
h	-	Static enthalpy or blade height.
c	-	Chord length, velocity in absolute motion.
w	-	velocity in relative motion
h_0	-	Stagnation enthalpy.
i	-	Incidence.
M	-	Mach number.
s	-	Pitch.
u	-	Rotational speed.
ζ	-	Enthalpy loss coefficient.
ε	-	Blade turning angle.
χ	-	Blade stagger angle.
d_1	-	Leading Edge Thickness.
d_2	-	Trailing Edge Thickness.
D	-	Profile Maximum Thickness.
δ	-	Tip Clearance Value.
G_a	-	Mass flow of cooling air.
$\overline{S}$	-	Relative curvilinear coordinate.
S	-	Curvilinear coordinate.
P	-	Airfoil perimeter.
p	-	Pressure.
η	-	Efficiency.
T	-	Temperature.
n	-	Speed.

Subscript

0	-	Stagnation.
1	-	Inlet to the cascade and stage.
2	-	Outlet from the cascade.
3	-	Outlet from the stage.
s	-	Isentropic.
e	-	Endwall.
x	-	Axial.
av	-	Average.
pr	-	profile

1 INTRODUCTION

Lately the single stage transonic high load turbines are used as a high pressure turbine for transport and industrial gas turbine units [1,2]. The high exit stream swirl behind the rotor of such turbines is usually taken by the next contra-rotating stage.

The main problem for a high load turbine is the keeping of a high efficiency. The large pressure ratio and a high loading coefficient in such turbines cause complicated transonic flow pattern with the shock waves and the separate zones, especially in the blades having the large blade turning angles $\varepsilon = \beta_2 + \beta_3 = 125^\circ - 135^\circ$. These all cause the increase of the losses, especially shock wave losses. Therefore preliminary the computational and experimental investigation of the vane sector and the midspan blade cascade was carried out and these data were used for the experimental stage design.

The special attention was paid to the design of the blade. The aim of such design was to receive moderate level of losses in the blade row for the exit supersonic Mach-number and the large blade turning angle.

The experimental high load stage was prepared for the investigation of the working properties and the tip clearance's influence on the stage efficiency. The vane row from an existing turbine was used to reduce the cost and to simplify the testing.
Some parameters of this stage are given in Table 1.

Table 1: Parameters of experimental stage.

Pressure Ratio	$PR = \frac{p_{01}}{p_{03}}$	3.2
Mean Dia.Loading Coefficient	$\frac{\Delta h}{u^2}$	2.3

Paper presented at the AGARD PEP 85th Symposium on "Loss Mechanisms and Unsteady Flows in Turbomachines", held in Derby, United Kingdom, 8-12 May 1995, and published in CP-571.

Mean Dia.Flow Coefficient	$\frac{c_x}{u}$	0.52
Mean Dia.Reaction	$\rho = \frac{h_2 - h_3}{h_{01} - h_3}$	0.51
Blade Number	Vane Rotor	42 90
Mean Dia. Blade Speed		286 m/s
Vane Height		52 mm
Exit Blade Height		64 mm
Exit Vane Angle	$\alpha_2 = \cos^{-1}\left(\frac{a}{s}\right)$	74°
Inlet Blade Flow Angle	β_2	59°
Exit Blade angle	$\beta_3 = \cos^{-1}\left(\frac{a}{s}\right)$	69°
Exit Stage angle	α_3	47°
Mean Dia.Exit Vane Mach-number		1.045
Mean Dia.Exit Rotor Mach-number		1.27
Aspect ratio	Vane Blade	0.68 2.0
Zweifel Coefficient	Vane Blade	0.55 0.89
Mass flow	G_g	21.2 kg/s

2 VANE ROW INVESTIGATION

The experimental vane sector has seven real cooling vanes, it is shown in Fig.1.

The basic geometrical parameters of the vane sector are given in Table 2.

Table 2: Mean diameter geometry of the vane row annulus sector.

α_1^0	α_2^0	$\frac{s}{c}$	$\frac{D}{c}$	$\frac{d_1}{c}$	$\frac{d_2}{a}$	χ	a	c
0°	73.6	0.67	0.18	0.11	0.115	41.5°	13.95 mm	76.45 mm

The investigation was carried out on the test rig, the scheme and detailed description is given in [3]. Air pressure and temperature before the cascade were practically equal to the atmospheric ones, inlet turbulence intensity was 0.04-0.06. The vane chord Reynolds number was more than 6×10^5. In detail the experimental results were described in the paper[4].

For transonic vane sector cascade tests the real exit radial pressure gradient may be achieved by using a tip annular segment behind the vane cascade as shown in Fig.2. The annular segment is sunk into the flow to form an annular flange on the tip endwall. By changing the height of this flange the necessary radial pressure gradient can be achieved. As a result there is no distortion of the flow pattern in the traverse plane which is placed near the trailing edges.

Since the vane row works for Mc2s = 1.045 the level of the flow nonuniformity behind the experimental vane sector is estimated along the circular and radial directions.
The relative static pressure distributions along the circular direction on the different distance from the hub are shown in Fig.3. The pressure measurements were carried out with the help of the static pressure probe and of the static pressure taps on the tip (18 points) and on the hub (14 points). These measurements permitted to define the external shock wave intensity and its position. The experimental mean diameter distributions of the exit vane flow angle in circular direction are shown in Fig.4,a. One can see the flow angle variation may be 6-8 degrees within of the pitch range. The radial distributions of the exit vane flow angle averaging along the circular direction are shown in Fig.4,b for M_{c2s} =0.95, 1.1, 1.23 .
When the flow passes through the external shock wave the exit vane flow angle and flow velocity are decreased. Therefore inlet blade flow angle is decreased too and it may be distinguished from the design inlet blade angle very strong. The such inlet blade flow angle decrease causes the negative incidence in the blade row. The negative incidence may cause separate bubble on the pressure surface in leading edge region.

The cooling air is discharged through the holes in the vane and the pressure surface slots near trailing edge. Besides the cooling air is discharged through the holes in the tip (see Fig.2) and the hub endwalls. The experimental loss distributions along the height for full cooling air discharge and without cooling air discharge through the holes in the endwalls are shown in Fig. 5. One can see that additional discharge of the cooling air through the holes in the tip endwall equal to Gae = 0.013 causes increase of the losses

by 0.015. The loss distribution behind the vane sector for full cooling air discharge was used for the calculated estimate of the stage efficiency.

3 ROTOR DESIGN AND ANALYSIS

Before the blade design and the manufacture a preliminary computational and experimental investigation was carried out. Especially the level of the blade losses was estimated . These estimates were made by procedure statistic process of the experimental data for 177 plane turbine cascades [5]. The calculated estimate showed the level of the blade profile losses about $\zeta pr = 0.06$--0.07 at the design point.

The blade row was designed by means of the interactive technique with the application of Bezier polynomials [6] and time marching method [7].

The computations of flow by Navier-Stokes equations were carried out for the more detail information about the flow pattern and the loss mechanisms in the blade cascade for Mw3s = 0.8, 0.95, 1.10, 1.27, 1.38 and i = 0. Besides the computations were made for Mw3s = 1.27 and i = ±10°. The computer method for solution of Navier-Stokes equations was designed by M. Ja. Ivanov and V. G. Krupa [8]. The midspan blade Mach number distributions by Euler and Navier-Stokes are shown in Fig. 6,a. The computational flow pattern (Mach number contours) for Mw3s = 1.27 and i = 0 is shown in Fig. 6,b. One can see the flow decelerates by the weak internal shock wave. Outside the passage the flow decelerates by the external shock wave. It is shown in Fig.6,b.

The computational flow pattern (Mach number contours) for Mw3s = 1.27 and i = 10° is shown in Fig. 6,c. One can see the flow accelerates on the short part of the leading edge on the suction surface. Then flow decelerates by strong shock wave. As a result of the shock wave and boundary layer interaction the flow is separated on the suction surface. The spacious separate zone on the suction surface causes the increase of the losses in the blades with a large blade turning angles for positive incidence.

For decrease of the secondary and the tip clearance losses the region of the flow weak deceleration on the leading part of the suction surface (Fig. 6,a) was designed. The such design reduces inlet pressure difference between the pressure side and the suction side. Therefor the secondary flow region displaces into the passage.

The midspan plane blade cascade was manufactured to investigate flow pattern and to determine the level of losses in cascade . It has 8 blades with height h = 125 mm and chord length c = 70.11 mm. In order to drain boundary layers being accumulated on wind tunnel walls the cutting off plates were installed in the cascade as shown in Fig.8. The tests were carried out in a wide range of exit isentropic Mach-number of M_{w3s} = 0.7-1.4 and with incidence $i = \pm 10^{\circ}$. Taking into account that blade had a meridional opening at a hub region the experimental investigation was carried out with parallel and divergence relative position of the cutting off plates. The flow was traversed after the cascade in blade to blade and radial directions.

The flow visualization was carried out according to the technique suggested in [9]. Fig.7a shows a flow pattern in the cascade with parallel endwalls colored by paint. On the suction surface tracks of paint are parallel and are laid out along streamlines. The trace of the weak internal shock wave (Figure 7a) is seen on the suction side. This shock wave does not separate the boundary layer. Fig.7b shows the forming of a secondary flow on the cutting off plate before the leading edges. The point of the three-dimensional separation before the leading edge may be seen very well. Due to the inlet compression zone on the suction surface the flow on the endwall surface at first is not pressed to suction side by lateral pressure gradient. The place of the interaction of the suction side boundary layer with endwall boundary layer is displaced from the inlet into the passage. This phenomenon allows to decrease secondary flow zones and secondary losses.

The meridional opening of the flowpath changes the character of secondary flow along the suction surface (Figure 8a) and loss distribution along the blade height. The loss distributions along radial direction for tested cascades with parallel and diverging endwalls for M_{w3s} = 1.2 are compared on Fig.8b. The cascade with parallel endwalls has greater inlet to exit blade channel area ratio (1.42) than cascade with diverging endwalls (1.24). The secondary loss coefficient is about 0.006 in the cascade with parallel endwalls . In the cascade with diverging endwalls it increases up to 0.018.

Fig.9a shows the experimental and the calculated variation of the profile loss coefficient in this cascade for exit Mach-number range M_{w3s} = 0.7-1.4. The profile loss coefficient makes up 0.06-0.065 for design point. One can see the calculated losses agree with the experimental satisfactorily . The influence of the incidence on the profile losses is shown in Fig.9b. The level of profile losses decreases a little for incidence angle of $i = -10^{\circ}$. If incidence is more than 5° the profile losses increase rapidly.

It is necessary to take into account the influence of positive incidence and meridional opening of the flowpath for transonic rotor cascades with a large turning angles.

4 STAGE INVESTIGATION

The preliminary investigation of the vane and blade cascades indicated on the strong influence cooling air discharge through the holes in the vane tip endwall, blade positive incidence and meridional opening of the flow path on the losses. It is difficult beforehand to predict as these factors will act in the real stage conditions. The tests of the stage must show how the data about loss mechanisms in the cascades correlate with the stage efficiency.

The experimental stage was tested in an aerodynamic warm air test rig, shown schematically in Fig.10a.

Inlet Press.	(kPa)	450-500
Inlet Temp.	(K)	750-780
Pressure Ratio		2.7-3.4
Speed range	(rpm)	6000-9000

Cooling air was released from the vanes into the flow path. The blades were uncooled. The output power was measured by a water brake.

Fig.10b presents a schematic of the instrumentation. The measurements were carried out at three planes; plane A_1 before the stage (the fields of total pressure P_{01} temperature T_{01} and static pressure P_1 on the endwalls), plane A_2 behind the stator (static pressure P_2 on the

endwalls) and plane A_3 behind the rotor (the fields of total pressure P_{03} and temperature T_{03}, exit angle and static pressure P_3 on the endwalls).

The turbine efficiency was evaluated by the formula :

$$\eta_t^* = \frac{N_T}{G_g(h_{0t} - h_{02s})} \quad ,$$

where η_t^* is an total to total overall turbine efficiency,

N_T is a stage output power,

G_g Is a mass flow through the vane row .

Taking into account that the data about influence of the tip clearance on the stage efficiency are contradictory it was decided to investigate the tip clearance influence on the stage efficiency.

The rotor tip clearance was measured during the tests by the optical system (Figure 10a). The tip clearance value changed due to temperature deformations of turbine case above the blades. As an illustration Fig.11 presents photographs of different tip clearances and corresponding parameters of stage. The variation of the stage efficiency with tip clearance value is shown in Fig.12.

The increase of tip clearance by 1% at the design point for the high loading turbine without blade shroud causes the drop of efficiency by 3%.

The averaged exit total pressure distributions and the exit angle distribution along blade height are shown in Fig.13 for three speeds: $n/\sqrt{T_{0t}}$ = 82%, 100%, 110%. High level of the hub reaction (ρ = 0.44 - 0.45) provides the flow to be without separation in this region.

The variation of stage efficiency with speed for PR=2.9-3.2 is shown in Fig.14. The level of efficiency at the design point for the relative tip clearance of δ = 0.4% equals η_t^* = 0.863. The predicted level of the efficiency equals 0.875.

It is interesting that for the loading coefficient of $\Delta H/u^2 = 2.3$ and flow coefficient of $c_x/u = 0.52$ the level of stage efficiency on the modified Smith Chart [1] with the allowance for tip clearance losses equals to 0.838. The same chart without the allowance for tip clearance losses [10] equals to 0.88. Experimental values of efficiency for tip clearance range from 0 to 1.1% fall within those levels of efficiency (Figure 12).

Calculation of this stage for PR = 3.25 was carried out using the Quasi-3D time marching method based on solution of the Euler equations [11] with the allowance for flow path losses. The behavior of some stage parameters along the radial direction is shown in Fig.15. There is a good correspondence of the calculation results with the experimental data.

CONCLUSION

Combination of the various experimental and computational methods permitted to investigate in more detail the flow structure and to determine the losses in the vane and blade rows of the high load stage with a high accuracy. The difference between calculated and experimental efficiency is connected with not accuracy prediction of influence of the tip clearance and of the unsteady effects.

Investigation of the loss mechanisms in the vane and blade cascades and the experimental stage showed that cooling air discharge through the vane endwalls, blade positive incidence and tip clearance might influence on the efficiency in the high load turbine stages very strong.

Using the interactive technique with the application of the Bezier polynomials the supersonic blade with large flow turning angle without strong compression zones and with moderate profile and secondary losses was designed.

REFERENCES

1. Hannis, J. M., Maali, R. and Woollatt,G., " The Design and Development of a High Work Transonic Turbine Stage", Proceeding of the Institution of Mechanical Engineer.Turbomachinery: Latest Developments in a Changing Scene. European Conference, London, 1991, pp. 33-45.

2. Moustapha, S.N., Okapuu, U. and Williamson, R.G., "Influence of rotor Blade Aerodynamic Loading of the Performance of a Highly Loaded Turbine Stage", Energeticheskiye Mashiny i Ustanovky, Mir, Moskva, N 2, 1988, pp. 100-108.

3. Abiants, V.X., Aero Gas Turbine Theory Machinostroeniye, Moskva, 1979, 246p.

4. Venediktov, V.D., Granovskii, A.V. and Kolesov, A.N., "Experimental Investigation of the Sector Nozzle Cascades", CIAM, Proceedings N 1280, 1991, pp. 116-126.

5. Venediktov, V.D., Granovskii, A.V., Karelin, A.M., Kolesov, A.N., Muhtarov M.H. " Atlas of the experimental characteristics of 2D cooled gas turbine cascades " CIAM , 1990., 393 p.

6. Karelin, A.M., " The Design of a Turbine Cascade by Rational Parametric Curves " , Trudy CIAM, Moskva, N 1234,

7. Bogod, A.V., Granovskii, A.V. and Karelin, A.N., "The Rise of Accuracy and Decrease of Time for the Numerical Investigation of Transonic Flow in Turbomachine Cascades" , Teploenergetica, Moskva, N 8, 1986, pp. 48-52.

8. Ivanov M.JA., Krupa V.G. " Solution of Navier-Stokes equations using high accuracy monotone schemes " , AGARD - lecture series, N 198.1994.,LS - 198.

9. Venediktov, V.D., Granovskii, A.V. and Gurov, V.I., "The Flow Visualization Technique in Turbomachines", Avtorskoe Svidetelstvo, N 1651123,· Bulluten Izobretatelja, Moskva, 1991 , N 19

10. Wilde, G.L. and Picherell, D.I., 1968, " The Rolls -Royce Three Shaft Turbofan Engine", Aircraft Engng., 11, Vol.40, N 2, pp. 19-29.

11. Ivanov, M.Ja., Nigmatullin, R. Z., Quasi-3D Numerical Model of a Flow Passage of the Aviation Gas Turbine Engines. ISABE 91-7029, pp.299-305.

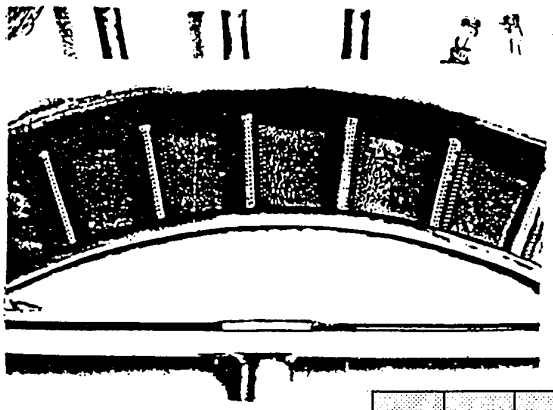

Fig.1 Vane sector

α_1^0	α_2^0	$\frac{s}{c}$	$\frac{D}{c}$	$\frac{d_1}{c}$	$\frac{d_2}{a}$	χ	a	c
0°	73.6°	0.67	0.18	0.11	0.115	41.5°	13.95 mm	76.45 mm

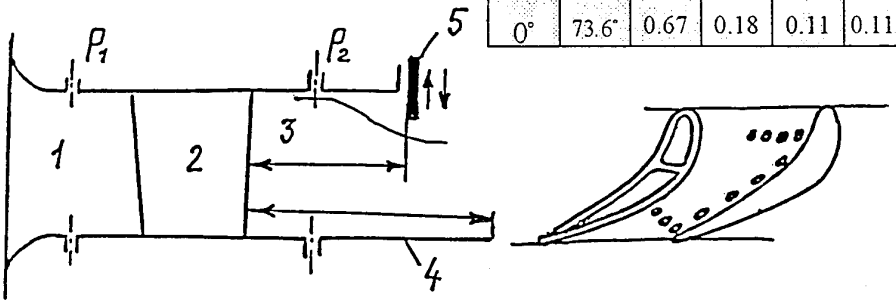

Fig.2 Test rig schematic for vane cascade.
1. inlet facility, 2. vanes, 3. exit facility,
4. hub, 5. annulus flange.

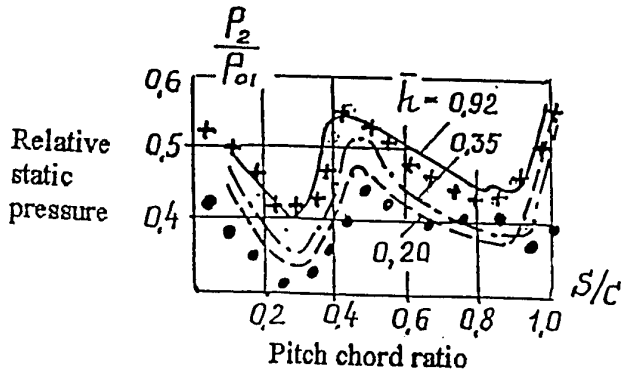

Fig.3 Pitchwise relative static pressure variation behind vane sector with h = var. (Mc2s = 1.1)
• - hup static pressure taps
+ - tip static pressure taps
—
—·— } - static pressure probe
– –

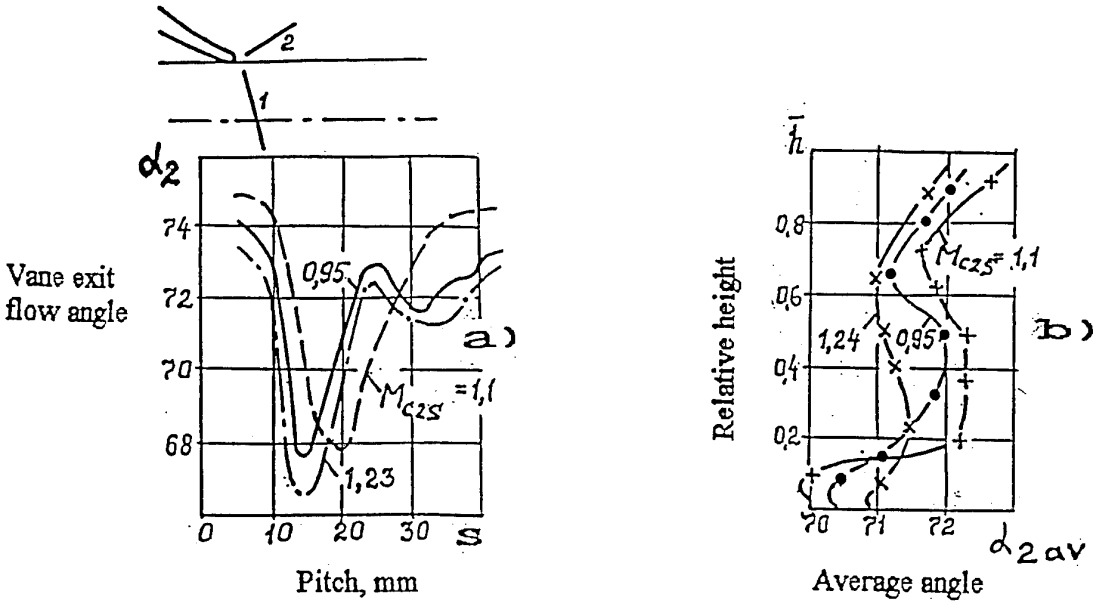

Fig.4 Vane exit angles
a) Vane mid-span pitchwise exit angle variations
1 - external trailing edge shock wave
2 - internal trailing edge shock wave
b) Exit average angle distribution along flowpath height.

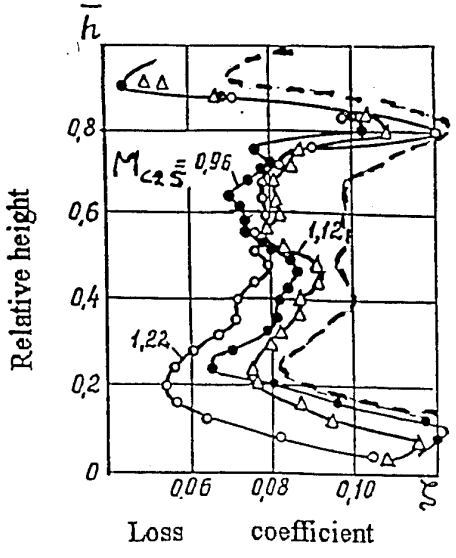

Fig.5 Vane radial loss profiles.
Δ , •, o - cooling mass flow through endwalls of Gae = 0.
——— - Gae = 0.013.

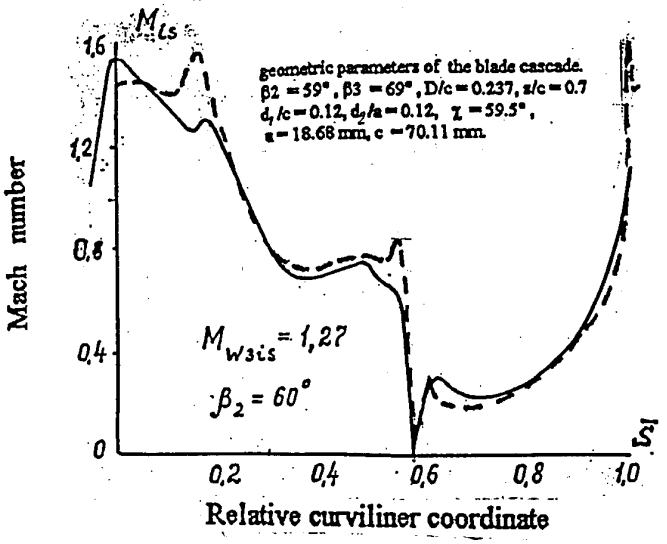

a)

b)

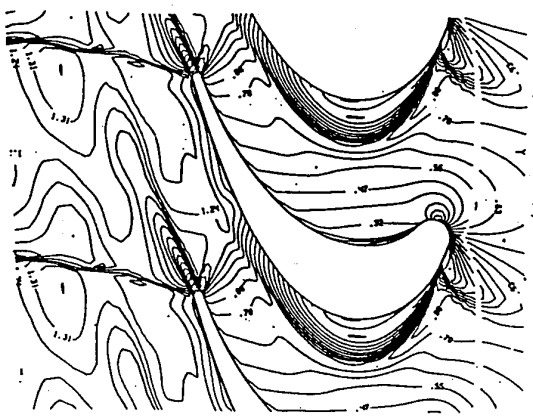

c)

Fig.6 Calculated flow pattern for the midspan blade cascade for Mw3s = 1.27

a) Midspan Mach number distribution
— computation by Euler
--- computation by Navier-Stokes
b) Much nurmber contours for i=0 ,
c) Much nurmber contours for i=10°.

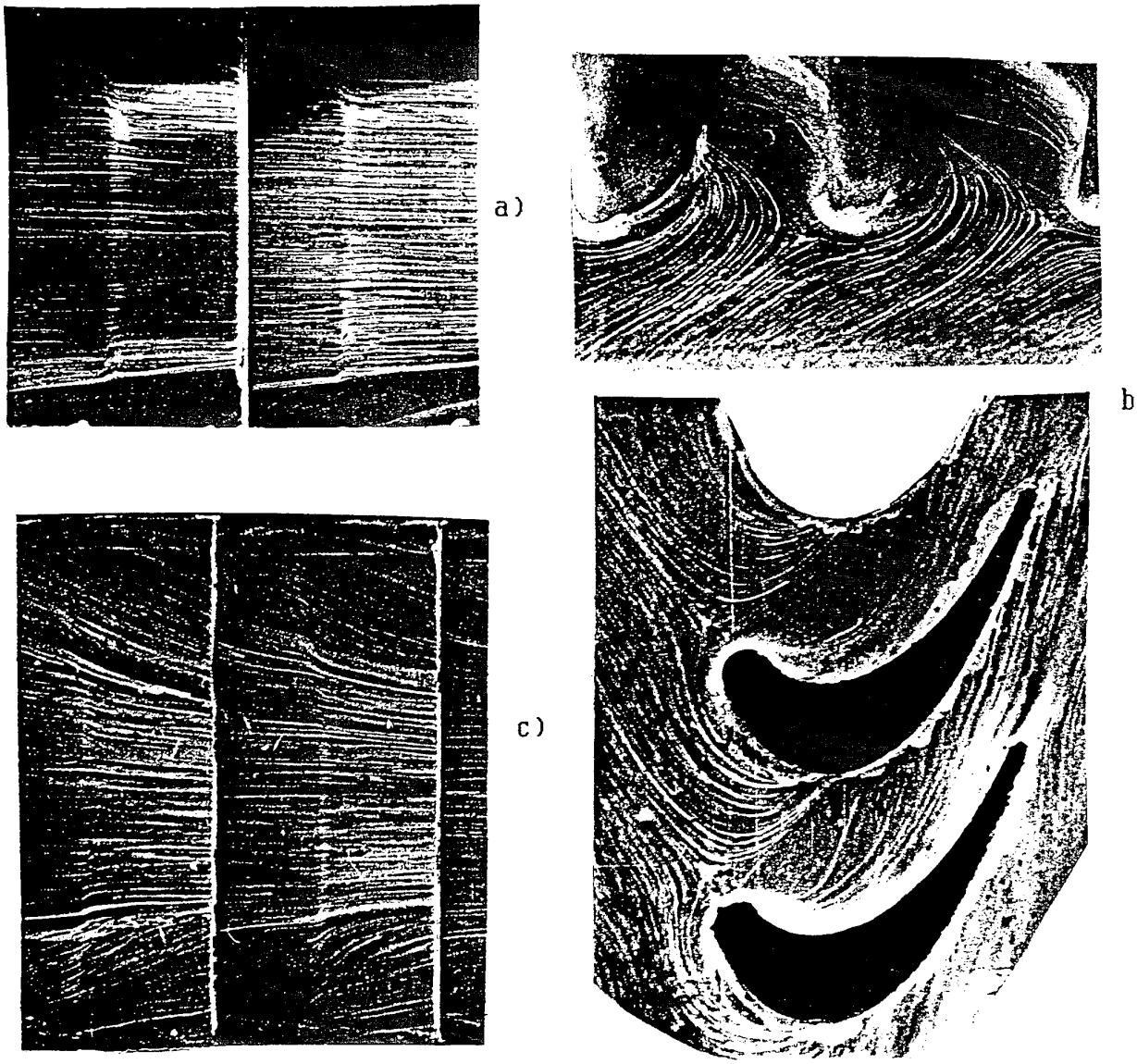

Fig.7 Visualization in the blade cascade $\beta 2 = 60°$, Mw3s = 1.25.
a) Suction side paint flow pattern: parallel endwalls
b) Endwall surface paint flow pattern
c) Suction side paint flow pattern: meridional opening.

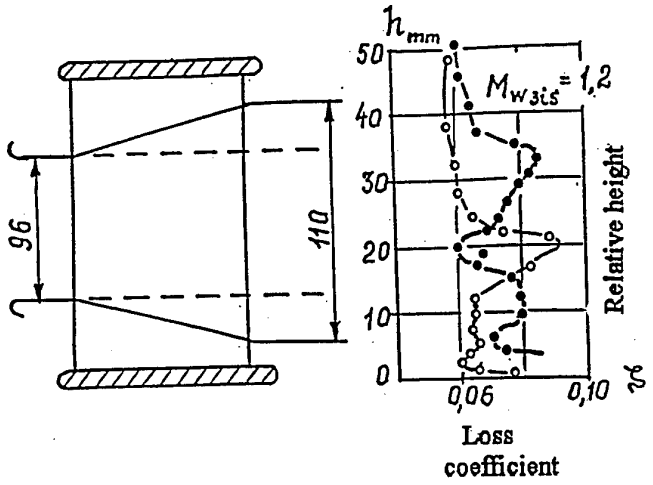

Fig.8 Loss variations along height behind the blade cascade.
-o-o- - parallel endwalls;
-●-●- - meridional opening.

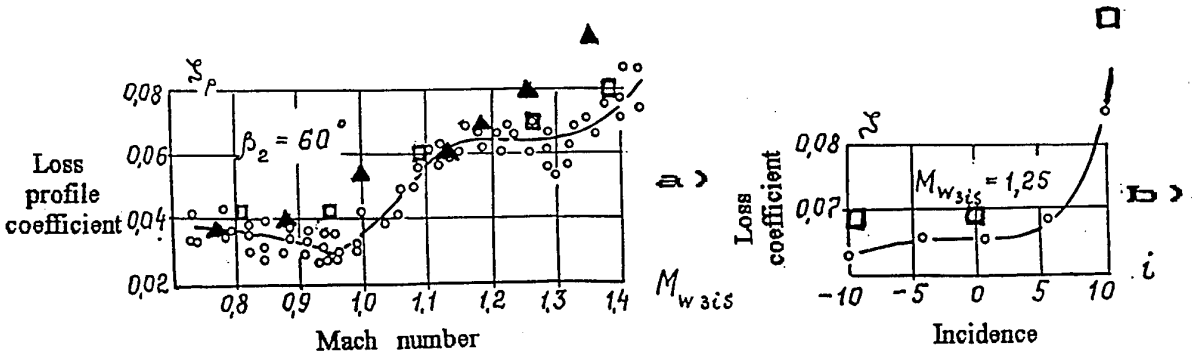

Fig. 9 Profile loss coefficient in the blade cascade.
a) loss coefficient variation with Mw3s .
b) loss coefficient variation with i .

o - experiment
□ - computation by Navier-Stokes
▲ - computation by statistics procedure

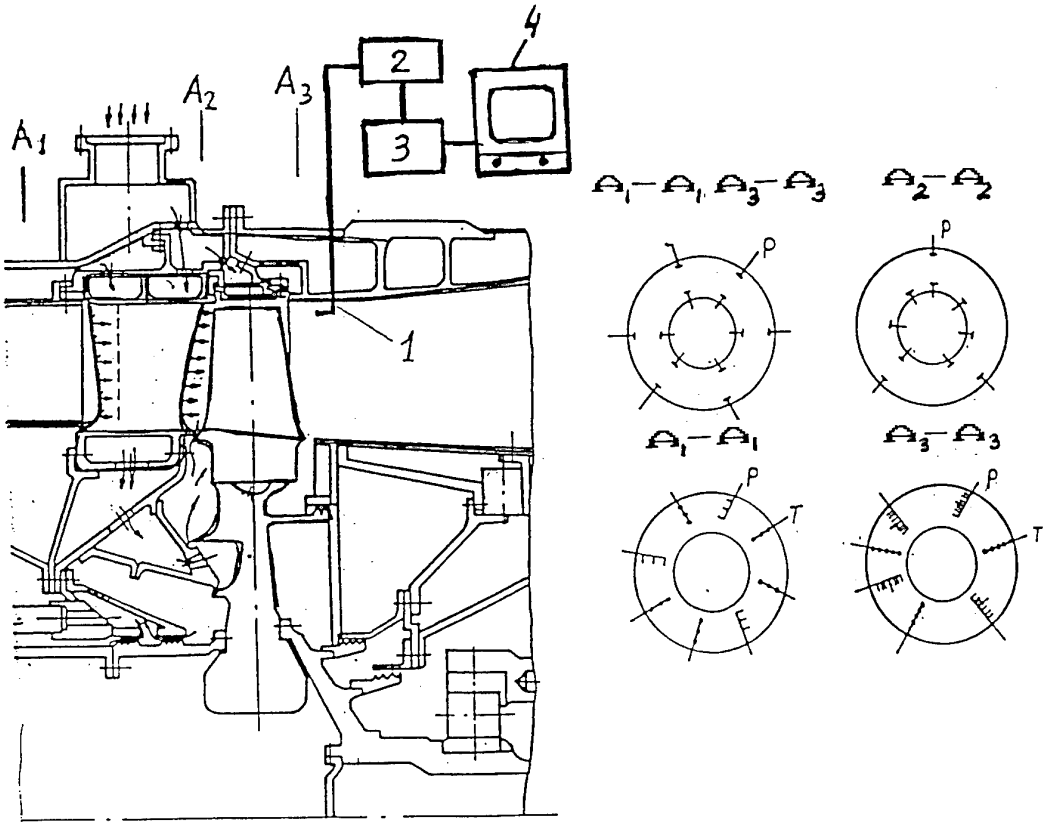

Fig. 10 Test rig and instrumentation schematic.
1 - endoscope, 2 - videochamber, 3 - videotape,4 - monitor.

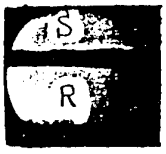

← 1.1 mm. Erection Tip Clearance

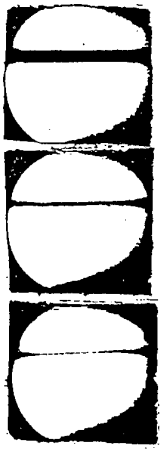

$\bar{\delta}$, %	η_t^*	p_{01}, KPa	T_{01}, K	$n/\sqrt{T_{01}}$, %
1,05	0,843	500	750	100
0,55	0,857	500	753	100
0,25	0,867	500	755	100

Fig. 11 Tip clearance influence to efficiency

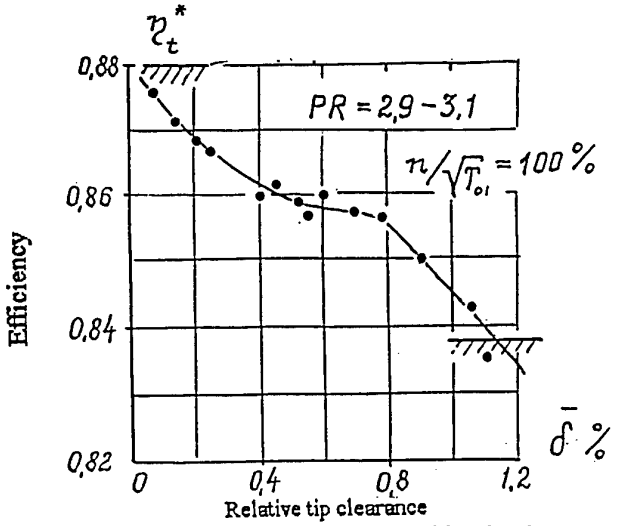

Fig. 12 Efficiency variation with tip clearance

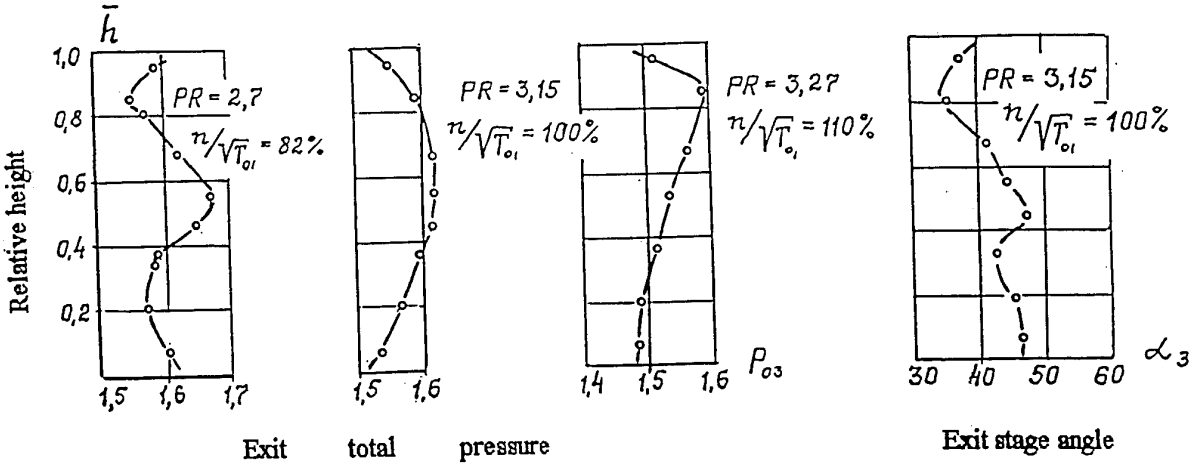

Fig. 13 Exit total pressure and exit flow angle

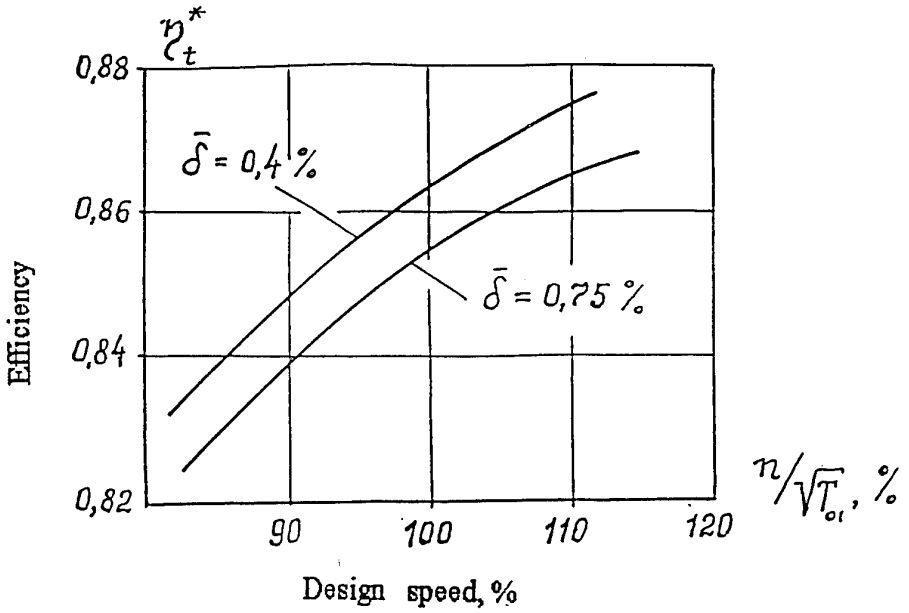

Fig. 14 Efficiency variation with speed and tip clearance

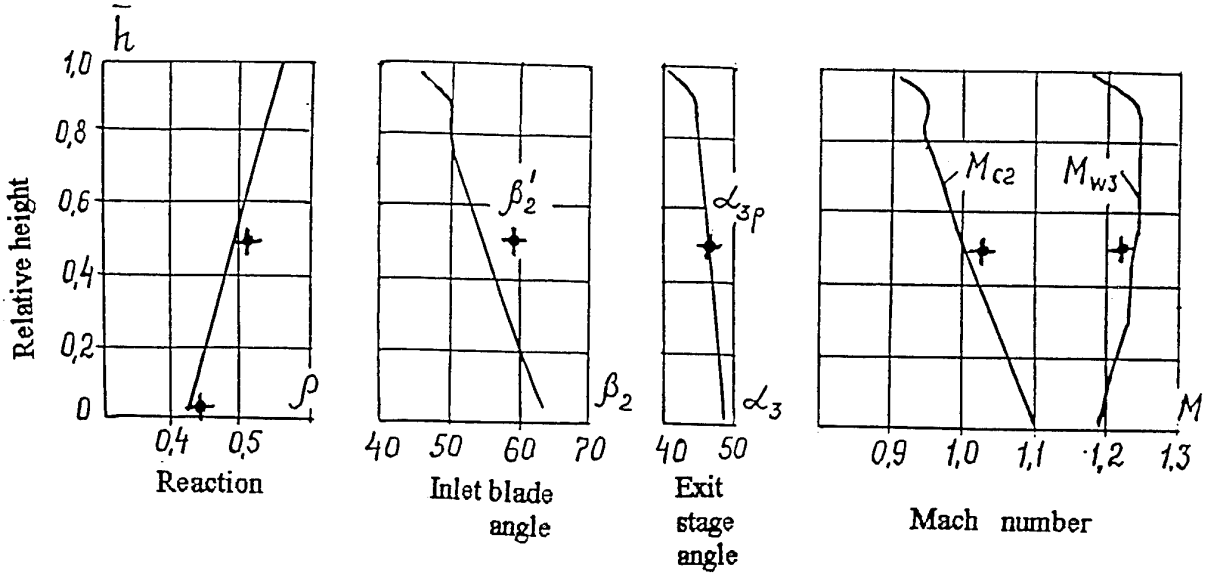

Fig. 15 Quasi-3D stage analysis in design point
✦— mean diameter design parameters

REFERENCE NO. OF THE PAPER: 41

DISCUSSOR'S NAME: G. Schulze, Technische Hoehschule Darmstadt, Germany

AUTHOR'S NAME: A.V. Granovskii

Q: Why is there virtually no difference between the inviscid and viscid prediction of the cascade flow?

A: Fig. 6a shows distributions of isentropic Mach number along the airfoil. These distributions were computed by inviscid (Euler equations) and by viscous (Navier-Stokes equations) methods. The difference between these methods is in those places where there is strong viscous effects. For example, there are places of the separation and shock wave boundary layer interaction, etc. There on fig. 6A one can see that maximum difference between these methods takes place for shock wave boundary layer interaction on the suction side and farther right up to the trailing edge.

On the other hand, on the part of the suction side where there is a large negative gradient of pressure and thin boundary layer, Mach number distribution by Euler coincides with Mach number distribution by Navier-Stokes.

REFERENCE NO. OF THE PAPER: 41

DISCUSSOR'S NAME: K. Broichhausen, MTU, Germany

AUTHOR'S NAME: A.V. Granovskii

Q: In your vane test the influence of hub cooling has been studied. How did you take into account the cooling air energy in your determination of the losses?

A: In our tests of the real vanes the cooling air was discharged through holes in the vane, through pressure side slots near the trailing edge and through holes in the endwalls. The mass flow of the cooling air corresponded to the real engine's conditions. The relative mass flow of the cooling air through the tip endwall was equal to 0.008 and through the hub endwall was equal to 0.005. At first we carried out the test with the full cooling air discharge. As a result, we determined the experimental loss distribution along the span for the full cooling air discharge. Then we filled up the holes on the endwalls with mastic very thoroughly. We repeated the test without cooling air discharge through the endwalls. Accordingly, we have an experimental loss distribution along the span of the vane for the full cooling air discharge and without cooling air discharge through the holes in the endwalls. The cooling air energy was taken into account automatically in this case.

CASCADE SIMULATION OF MULTIPLE SHOCK PASSING FROM UPSTREAM BLADE ROWS

R. L. Doughty
Mechanical Engineering
J. A. Schetz
Aerospace and Ocean Engineering
Virginia Polytechnic Institute and State University
Blacksburg, VA USA 24061-0203

SUMMARY

Shock waves shed from the trailing edges of current high pressure turbine blades for aircraft engines are believed to cause a decrease in the efficiency of downstream stages. A simulation of the effects of unsteady shock waves is developed here, using a shock tube with multiple outlets to produce three shock waves. Time delays between the shocks are introduced using a duct length differential. The three shocks are passed upstream of a cascade of turbine blades, traveling tangentially along the cascade leading edge. Shock periods of 0.055 msec and 0.200 msec are used. Shadowgraphs of the shock diffraction in the blade passages are presented. The shocks are also found to have a significant effect on unsteady blade static pressures and forces.

1 INTRODUCTION

Current aircraft gas turbines extract large amounts of work from the high pressure turbine stage(s), resulting in relative supersonic exit speeds from the stators and rotors. Significant trailing edge shock strengths result, and the shocks propagate downstream from both the blade suction side and pressure side (after a reflection from the suction side of the lower blade). Recent three-dimensional unsteady, inviscid calculations of turbine stage flow[1-3] indicate significant fluctuations in unsteady blade heat transfer and surface pressures resulting from impinging shocks and wakes from upstream blade rows.

In a recent case[4], a single-stage high pressure (HP) turbine was coupled with a low pressure (LP) turbine and the combined efficiency was much less than expected. It was suggested that the reduction in efficiency could be caused by the strong shocks from the HP turbine rotor, as they are "chopped" by the LP turbine stator, or by poor 3D design of the rotor blades. The aim of the current experiment is to investigate the effects of the moving shock waves on a downstream blade row. This simulation is unique since only shock waves are used, rather than combined shocks and wakes typical of other cascade experiments[5-8] and rotating rig tests (which also include mean flow effects). No attempt is made to simulate the correct inlet velocity triangle for the cascade.

A shadowgraph of a typical high-speed exit flow is found in Figure 1. This picture was taken in the cascade facility used in the current experiment. The blade profile is an HP turbine blade, modified to have an axial inlet (turning was decreased). The design exit Mach number for the cascade is M=1.2. The static pressure distribution at design is shown in Figure 2, as both computed and measured values. Note that the throat for this blade occurs on the suction side(SS) at about 50% of axial chord. The leading edge of the blade is clearly unloaded, since there is negative lift until 20% of axial chord.

Two different shock/blade interactions are possible. With a single stage HP turbine, the first interaction is between the shocks shed from the upstream stator row and the rotating rotor blades. The second interaction is between the shocks shed from the upstream rotating rotor and the stationary downstream LP nozzles. Both of these interactions are fundamentally the same, when relative motions are considered.

While the shock wave effects are unsteady, the steady blade design parameters have a significant effect on the strength of the trailing edge shocks.[11] The basic geometry factors influencing the shock strength are: 1) amount of suction side turning downstream of the passage throat, 2) trailing edge thickness, and 3) the angle between the pressure side (PS) and SS at the trailing edge (wedge angle). Indicators of a good geometry choice include little suction side diffusion downstream of the impinging PS shock, small Mach number difference at the trailing edge between the PS and SS, and good flow uniformity across the pitch. Converging-diverging (CD) passages are known to be useful to accelerate the PS Mach number and minimize the Mach number difference across the trailing edge. Trade-offs exist, however the use of CD passages can lead to poor off-design performance (near Mach 1), and decreased suction side shock strength implies increased PS shock strength for a fixed blade loading. Note that the static pressure distribution of Figure 2 exhibits small SS diffusion, a CD passage, and little difference in Mach number across the trailing edge, yet the shock strength for this blade at design conditions is significant.

The suction side shock strength for the test blade is estimated in Figure 3. The blade was tested in the cascade at different exit Mach numbers, and end-wall static pressure data at 17% of axial chord downstream of the blade was taken. The resolution of the static pressure data was ten points per blade pitch. By forming the ratio of maximum pitchwise static pressure to the minimum pressure, a simple estimate of suction side shock strength is obtained. The results are shown in the figure, with a shock static pressure ratio of about 1.2 at the design exit Mach number. This figure serves to illustrate the importance of the shock strength issue. Current HP turbines for commercial engines have exit Mach numbers of about 1.2, but military engines are

Paper presented at the AGARD PEP 85th Symposium on "Loss Mechanisms and Unsteady Flows in Turbomachines", held in Derby, United Kingdom, 8-12 May 1995, and published in CP-571.

Figure 1. Shadowgraph

now approaching M=1.5 for the HP turbine. Commercial engines can be expected to follow suit in the future. From the figure it is clear that shock strengths can therefore be expected to increase in the future, contributing to possible interaction problems.

An important parameter in the shock passing problem is the time between the arriving shock waves, as seen by a blade in the cascade. The several possibilities are: 1) shocks are isolated events, 2) one shock is incident on the blade passage at a time (but more than one influences the passage flow at a time), or 3) more than one shock arrives before the previous incident shock(s) leave the blade passage. For an equal number of stators and rotors in a stage, only one shock crosses a blade passage at a time. A typical high pressure turbine for a commercial engine has upstream to downstream blade count ratios in the range 0.5 to 1, corresponding to case 2).[4]

The present experiment used multiple shocks at two different passing periods. A single shock case was

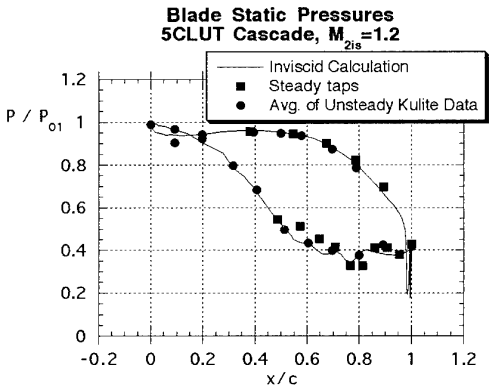

Figure 2. Blade Static Pressures

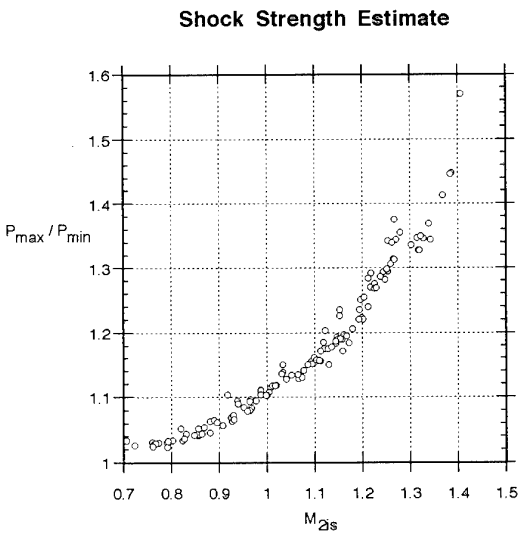

Figure 3. Shock Strength Estimate

also done for comparison purposes. The case which most closely represents similarity with engine conditions is a shock period of 0.200 msec. The second case, not typical of current commercial engine conditions, is a shock period of 0.055 msec, resulting in two shocks crossing a blade passage at a time. That is, before the first shock has left a blade passage, the second shock enters the passage. The 0.055 msec period, while not typical of current practice, certainly represents an interesting possible engine condition.

Similarity with engine conditions is indicated by the Strouhal number:

$$St = \frac{fc_{ax}}{W_{z1}}$$

where f is the upstream blade passing frequency, c_{ax} is the blade axial chord, and W_{z1} is the blade inlet relative velocity. For a typical LP nozzle the Strouhal number is 2.25, and for a typical HP rotor the Strouhal number is 1.80.[4] For the simulation here, the Strouhal numbers are 10.4 (0.055 msec case) and 2.9 (0.2 msec case).

2 EXPERIMENTAL METHOD

To simulate the effects of unsteady shock waves on turbine blades, a source of unsteady shocks is needed. For the current experiment, the shocks are produced with a shock tube. The shock tube is used to get a single traveling shock wave (in the tube driven section), which is then split into three parts. The split is done at the end of the shock tube, where a cap with three outlets is located. Part of the incident shock is transmitted into each of the three outlet ducts, and part is reflected back into the shock tube. The three resulting shocks are then conveyed to the test section

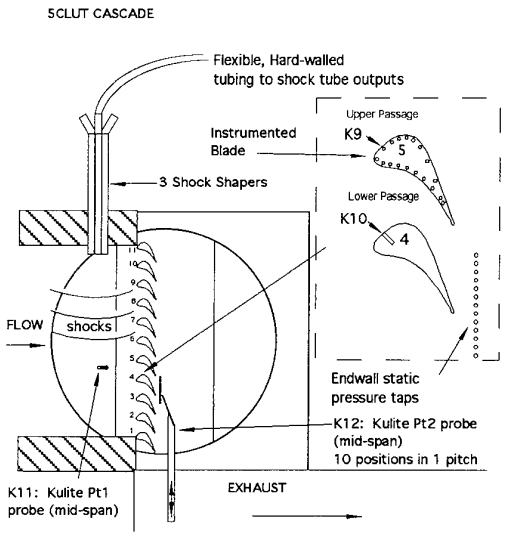

Figure 4. Facility and Instrumentation

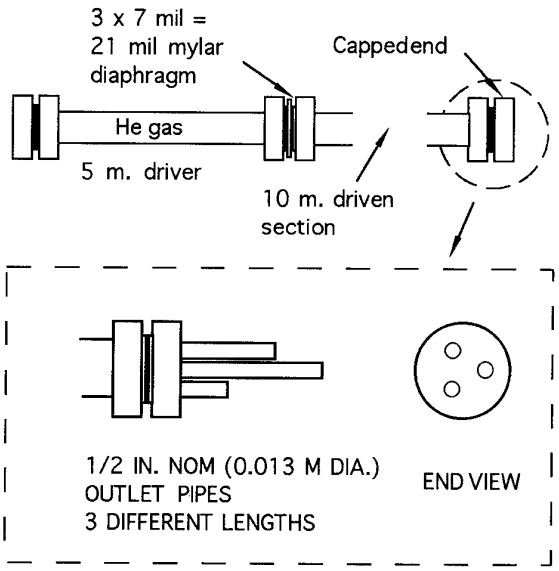

Figure 5. Shock Tube Geometry

through separate round ducts. By changing the relative lengths of the three ducts, we get time delays between the three shock waves as they arrive at the test section. Transition between the round ducts and the span of the test section is provided by three "shock shapers" to be described below.

The cascade facility is diagrammed in Figure 4. There are eleven blades in the cascade, with a total turning of 68 degrees. The blade chord is 38mm, with an aspect ratio of 4. Blade pitch to chord ratio is about 1, and the Reynolds number based on the throat is 340,000. A typical throat Reynolds number for an LP nozzle on a large commercial engine is 75,000, and for an HP rotor, Re=112,000.[4] Compressed air for the blow-down tests is provided at about 10kg/s by a four-stage compressor with storage tanks. Capability for heated runs exists, but all of the tests described here are unheated. The run time is 20 seconds, with a total pressure of 200 kPa and a total temperature of 273K. Different exit Mach numbers are obtained with different upstream total pressures. More information on the test facility can be found elsewhere.[9-12]

In the facility diagram (Figure 4), a system of three traveling shocks is shown propagating tangentially (down) along the cascade leading edge. At the top of the figure, an example duct from one of the three shock tube outlets is shown, leading to a channel in the shock shaper. The instrumentation is also indicated on the diagram. The magnified section of the figure shows the endwall static pressure taps used for estimating shock strength (as in Figure 3), and for calculating the isentropic exit Mach number. Also, the large-scale insert shows the unsteady pressure instrumentation on blades 4 and 5.

Unsteady pressures were measured with Kulite XCQ-062-50 miniature semiconductor transducers, capable of absolute static and dynamic measurements. The transducers are 1.6mm in diameter and 6.5mm long, and they have a screen installed to protect the diaphragm. The transducer mounted in blade 4 is located with the screen flush with the blade surface. Even though the transducers are small, putting more than a few of them on a single blade necessitates mounting the axis of the transducers in the spanwise direction, as on blade 5. In this case, small taps were drilled in the blade surface to expose the transducer diaphragm to the flow. A frequency response investigation showed that the spanwise mounting of the transducers did not decrease the maximum frequency response of 23kHz. The transducers on blade 5 were used to estimate the unsteady blade forces from the measured static pressures. Also shown in Figure 4 are unsteady transducer probes for measurement of upstream and downstream total pressure. Results from these measurements are not reported here.

2.1 SHOCK TUBE

Shock tube flow is well understood and easily calculated[13]. The shock tube for this experiment is shown in Figure 5. There is a 2:1 ratio of driver to driven lengths, and the tube diameter is 75mm. The tube was constructed from Extra Heavy (Sch. 120) steel pipe. The diaphragm material was Mylar sheet of 7mil thickness. Three separate thicknesses were combined to get a total of 21 mils, for a bursting pressure of 3445 kPa. Helium was used as the driver gas to maximize the shock strength, and the driver section was evacuated before charging. The cap on the driven section is illustrated in the figure, and the end view of the cap shows the hole pattern for the three exit ducts. Also, the three output pipes of different lengths are shown. Flexible, hard-walled vinyl conduit, which connects the shock tube output pipes to the shock shapers, can be

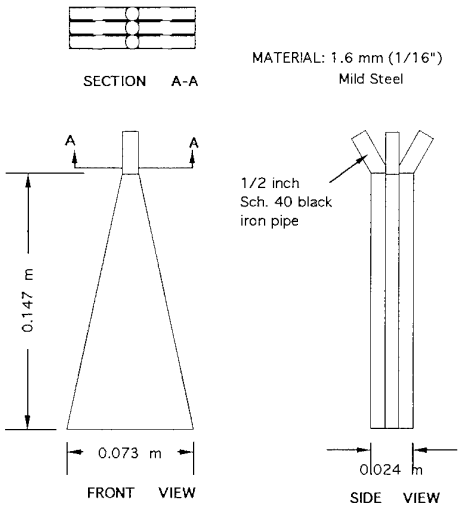

Figure 6. Shock Shaper Geometry

slid on the output pipes for fine adjustment of the time delay between the three shock waves.

2.2 SHOCK SHAPER

The details of the shock shaper are shown in Figure 6. The basic purpose of the shock shaper channels (one for each shock) is to smoothly transition the moving shock waves from the round ducts to the full span (152mm) of the cascade blades. Good transition is necessary to get two-dimensionality in the cascade inlet flow (planar shock fronts), and to minimize reflected disturbances behind the shock waves as they enter the test section. Each shaper channel was welded from steel sheet to the same geometry. The divergence angle of the shaper sides (24 degrees) has been shown in the literature to minimize the reflected disturbances for the large shock strengths used here. Initial attempts with sudden-expansion shock shapers were unsuccessful because of strong side-wall reflections. Similarly, shock shapers with exit widths less than the blade span caused strong reflections at the shaper exit. Reflected disturbances are inevitable for shocks traveling through area changes, but they can be minimized with the correct choice of geometry.

2.3 SHOCK PREDICTIONS

To understand the inlet flow to the cascade behind a moving shock wave, it is necessary to turn to some simple results from shock dynamics. During the development of this experiment, simple models for predicting transmitted shock strengths in area changes were used. These models and their usefulness will be reviewed. Most importantly, the decay rate of flow properties and velocity behind the shocks needs to be understood. To address this problem, an analytical solution from "blast wave" literature was used.

There are three main area changes in the shock path from the shock tube to the test section blades. The first is at the shock tube cap, the second through the shock

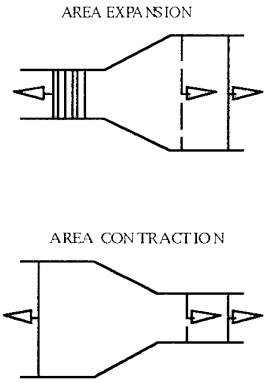

Figure 7. Example of Steady Flow Models

shaper, and the third when the shock enters the large test section. The first two cases are shocks traveling in ducts, while the third case is basically a shock traveling in free air.

The simplest method for dealing with shock propagation through an area change, called the steady-state method, is attributed to Chester[14]. Two examples of models proposed by Chester are shown in Figure 7, one each for an expansion and a contraction. In the models, traveling shocks are indicated by single solid (arrowed) lines, expansion waves by a series of solid lines, and contact surfaces by dashed lines. Contact surfaces, or lines of discontinuous entropy (temperature), are necessary to get closure on the models. The existence of contact surfaces is verified by experiments. In both models, the transmitted shock wave enters on the left and exits on the right. For an area expansion, an expansion wave is reflected, while a shock wave is reflected for an area contraction. By simultaneously solving the shock jump conditions and the expansion characteristics (using pressure and velocity constant across the contact discontinuity), the transmitted and reflected wave strengths can be calculated, given the input shock strength. This method was used to calculate the transmitted shock strength at the shock tube cap, for a given shock tube driver pressure (using the shock tube relations).

A similar method, also due to Chester, uses the same idea as the steady-state method, but with differential changes in duct area. The solution is[14]

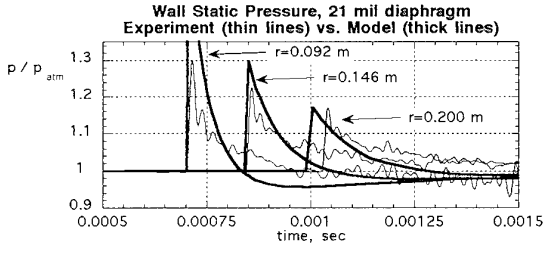

Figure 8. Wall Static Pressures

$$\frac{\delta A}{A} = \frac{-2M(\delta M)}{(M^2-1)K(M)}$$

where K(M) is a complicated function of Mach number and γ, the ratio of specific heats. For γ=1.4, K(M) varies only slightly from 0.52 for a sonic shock to 0.39 for infinite Mach number. The above solution rigorously applies only to differential changes in area, but the method is often applied to finite area changes in ducts. Integrating, the solution to the differential equation for finite area changes is[15]

$$Af(M) = const.$$

where f(M) is again a complicated function of Mach number and specific heat ratio. Given the initial and final areas in a duct and the initial shock Mach number, the final shock Mach number is easily found. The shock Mach number at the shock shaper exit was calculated using this second method.

Each shock, as it enters the test section at the shaper exit, has a nearly planar, rectangular shape. After exiting the shock shaper, the shocks will propagate in a roughly cylindrical shape down toward the instrumented blade. Because of this fact, an analytical solution[16] for the decay of cylindrical blast waves can be used to predict the behavior of the flow behind the traveling shocks.. The solution, which is general for planar, cylindrical, or spherical shock propagation, couples the steady flow equations with the Rankine-Hugoniot conditions (shock jump conditions) at the shock front. Additional information required to solve the equations includes a power law density profile assumption, and use of the energy equation to specify the decay of the shock front with distance from the origin of the blast. The result is two coupled partial differential equations which can be solved numerically using the Runge-Kutta method. However, the solution is singular at the origin, so a power series method must be used to start the solution. The result of the solution is the decay of flow properties and induced velocity behind the propagating shock as a function of initial blast (shock) energy.

The only difficulty in applying this model to the current situation is determination of the initial shock energy. Since the energy of a traveling shock includes the energy of the flow behind it (which has been influenced by the shock), determination of the absolute energy of a shock exiting the shock shaper is difficult. It is easy to estimate the energy per unit time, but not the absolute energy. To get around this problem, a simplifying assumption was made. The shock was assumed to immediately become perfectly cylindrical at the shock shaper exit with the same diameter as the shaper height, and the induced velocity was assumed entirely radial. The shock energy was taken to be completely enclosed by the volume defined by the shock front and the shaper exit plane. Using these assumptions, the shock energy for air (ideal gas) is formulated as follows:

$$E = p_1\left(\frac{\tau}{2}\right)^2 s\left[\frac{35}{24}\left(\frac{M^4+M^2-2}{M^2+5}\right)\right]$$

where τ is the shock shaper height (17 mm) and s is the shaper width (152 mm). Thus, the shock energy is determined only by the shock Mach number at the shaper exit and the pressure ahead of the shock (P_1). The initial shock energy for the cylindrical propagation model could then be estimated, and the solution completed for the known distance (radius) of the instrumented blade passage. A similar assumption was used by Heilig to calculate the energy of shock waves in mine explosions[17].

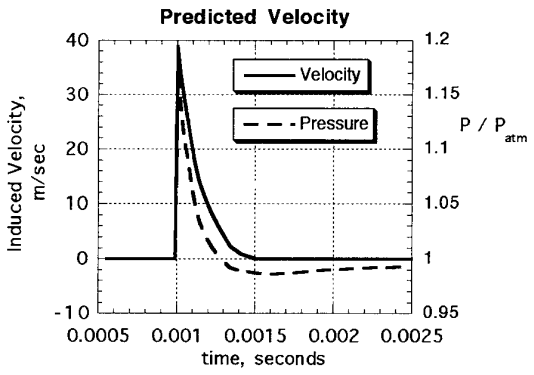

Figure 9. Predicted Induced Velocity

2.4 VERIFICATION OF PREDICTIONS

To test the validity of the prediction method described above, a simple experiment was done. The cascade was removed from the test section, and there was no mean flow of air in the tunnel. A single shock was produced by the apparatus and propagated into the test section. Unsteady wall static pressure measurements were made at the blade leading edge plane for different distances (radii) from the shock shaper exit. Static pressures were measured at radii of 0.092m, 0.146m and 0.200m from the shaper exit. These corresponded to the leading edges of blades 5, 7 and 9, where blade 5 is the instrumented blade.

Some results of the validation experiments are shown in Figure 8. The plot shows results for a single run with a single shock. The experimental static pressures at each radius are shown as thin lines, while the predictions for the same shock tube driver pressure are the thick lines. Atmospheric pressure is used to normalize the results, since there is no tunnel flow. For the smallest radius, the prediction of overpressure and underpressure is not good, which is to be expected because the shock is not actually cylindrical in shape (an assumption) near the exit. For the largest radius, corresponding to the leading edge of the test blade, the prediction of the pressure decay rate is good, although the shock arrival time is missed. The original idea in using the model, however, was to understand the decay of flow conditions behind the shock, and it was successful in this regard.

The predicted magnitude and decay of the induced velocity behind the shocks is of most interest, since it cannot be easily measured. The predicted induced

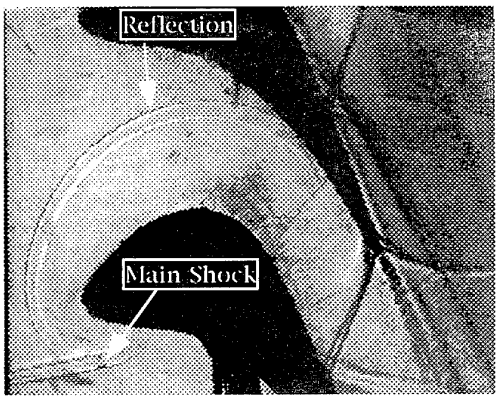

Figure 10. Shadowgraph - Single Shock

velocity at the test blade radius is shown in Figure 9 compared with the predicted pressure. Both the pressure and velocity decay back to ambient values in the same amount of time (about 0.5 msec). Thus for closely spaced multiple shocks, the induced velocity and pressure do not decay back to ambient conditions between the arriving shocks. Also, the magnitude of the induced velocity is on the order of the cascade inlet velocity, which is 60 m/s. Thus, large negative incidences are induced by the passage of the shocks. Experience suggests that the blade tested is insensitive to significant negative incidences because of the thick leading edge. Note that the peak level of induced velocity can be calculated using a normal shock assumption (since the shocks are relatively weak), but the model is necessary to predict the decay rate. Temperature and density behind the shock wave are predicted to change by only 5% and 15%, respectively.

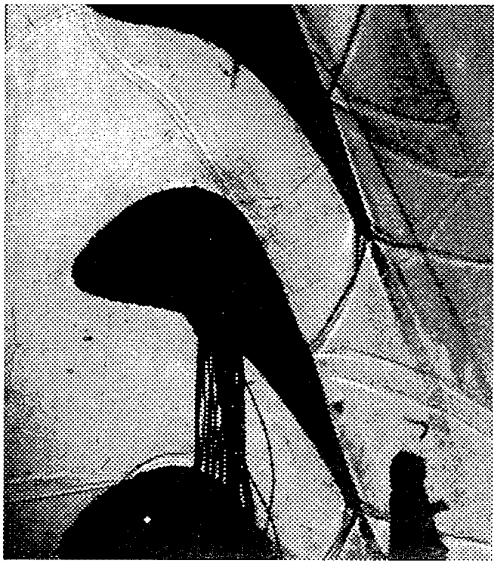

Figure 11. Shadowgraph - Single Shock

3 RESULTS

Some results from the three different test cases are discussed below. The three test cases are: 1) single shock, 2) three shocks at 0.055 msec period, and 3) three shocks at 0.2 msec period (engine typical). Shadowgraphs and unsteady blade surface pressures are the basic results.

3.1 SHADOWGRAPHS

The single shock case was done as a benchmark, and is a repeat of previous results,[6, 18] but at a shock Mach number more typical of engine conditions. Two example shadowgraphs are in Figures 10 and 11. In the figures, the incident shock is traveling downwards, impacting first the blade suction side, then the pressure side. The second picture (Figure 11) was taken 50 microseconds later than the first (relative to a trigger signal), but in separate tunnel runs. An animation of the shock reflection in the blade passages is found in Figure 12, which was drawn with reference to a series of shadowgraphs. Figures 10 and 11 correspond to frames A and B on the animation. In frame A, the primary shock reflection from the blade suction side ("b") is propagating up towards the pressure side of the adjacent blade. In frame B, shock "b" is split into two parts by reflection from the pressure surface. Piece "b" continues across the leading edge into the upper blade

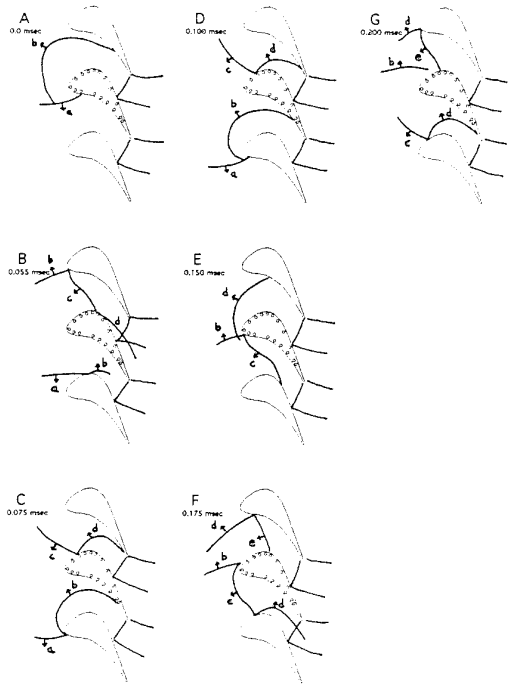

Figure 12. Animation of Shock Reflections, Single Shock

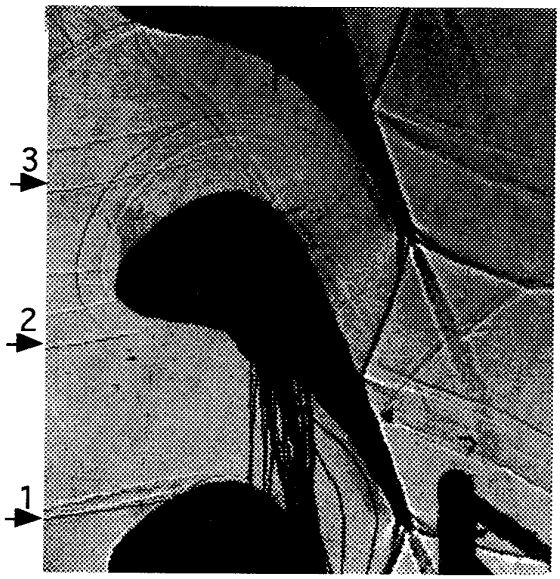

Figure 13. Shadowgraph - 3 Shocks, 0.055 msec period

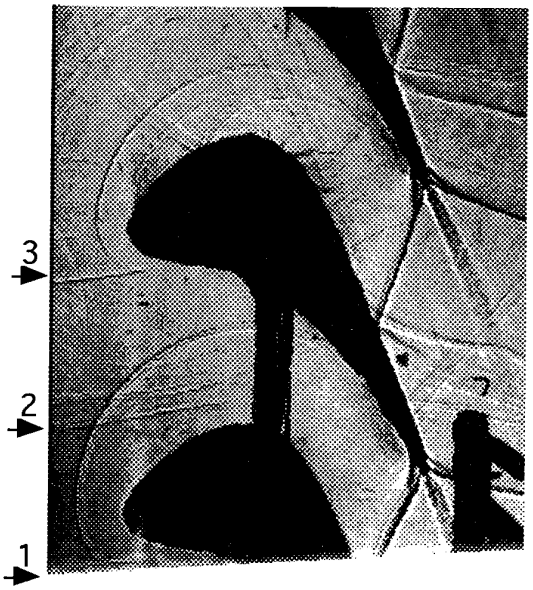

Figure 14. Shadowgraph - 3 Shocks, 0.055 msec period (0.05 msec later than Figure 13)

passage while piece "c" heads forward on the suction side. Most importantly, the original incident shock has left the top blade passage by frame B, but the reflections continue in the top passage until frame G and beyond, 0.2 msec later. The shock velocity, calculated from the time required to cross from blade 4 to blade 5 (see Figure 4) is 418m/s, corresponding to a shock Mach number of 1.26.

Shadowgraphs are also useful for studying the development of the 0.055 msec period multiple shock case. The small time delay between the shocks allows all three to be captured in one frame, as shown in Figures 13 and 14. The second shadowgraph was taken 50 microseconds later than the first, relative to an arbitrary trigger signal. Note that in both pictures, two shocks can be seen crossing a single blade passage at the same time. The multiple images for the second and third shocks are believed to be either Mach waves or contact surfaces caused by repeated crossing of shock waves, since pressure traces for these shocks show only single pressure rises. Each subsequent wave reflects in the same manner as the first, with no apparent interaction between the shocks. Significant interactions are not expected, because of the relative weakness of the shock waves. The shock velocity is 418m/s for the first shock, and 463m/s for the subsequent shocks. Since the pressure and induced velocity do not completely decay between shocks, the resulting shock Mach numbers are all about 1.3 (obtained by solving the Rankine-Hugoniot equations relative to the shock iteratively).

The lack of interactions between the shocks allows a simple method for interpreting the multiple shock shadowgraphs in this case. Assuming each shock reflects in the same way as the first, the animation of Figure 15 was drawn. Frame B corresponds to Figure 13, and frame D to Figure 14. A different line type is used for each shock and its reflections. In frame C, note the proximity in the top passage of reflection "d" (see Figure 12) from the first shock and reflection "b" from the third. The two reflections are distinct and mometarily propagate in parallel with the same shape. Later, at frame D, the two reflections have different shapes. In frame G, the combined reflections from all three incident shocks still exist and continue to propagate through the blade passages, forming complicated patterns long after the incident shocks have left the blade passages.

3.2 BLADE STATIC PRESSURES

The blade static pressure traces for the single shock case are shown on Figure 16, all to the same scale but at different average pressure levels. The noise spikes seen on some of the plots are crosstalk from the shadowgraph light source trigger. Each trace is an ensemble average of eleven runs. However, different traces are not averages of the same eleven runs due to the rotation of transducers (not enough transducers were available for simultaneous measurements at each location). Ensemble averaging can be done since the test conditions are repeated, even though the data is transient.[19] Each trace is synchronized using tap S1 as a trigger to allow comparison. The pressure peak at the shock arrival does not match the expected value for the known shock velocity because of the limited pressure response of the transducers. However, the shock velocity is known from the time to cross the instrumented passage, and the 23kHz response of the transducers accurately captures the pressure signal except at the shock impulse.

First, note that the strong second pressure peak at about 0.7 msec on the blade suction side is from the passage of shock "c" at its reflection point (see Figure 12) heading toward the blade leading edge. The

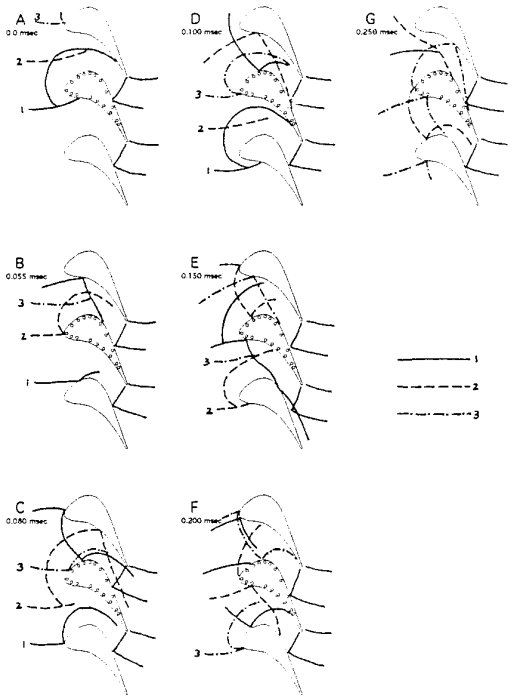

Figure 15. Animation of Shock Reflections, 0.055 msec Period

pressure side tap P1 shows three peaks: the first is from the incident shock (0.5 msec), the second from reflection "b" moving in the opposite direction (0.7 msec), and the third from reflection "d" (0.85 msec). Taps P2-P5 also show three peaks. On both sides of the blade, the pressure signals damp out toward the trailing edge due to multiple reflections. The geometry of the blade passage prevents any incident shocks or their reflections from impacting taps S6 to S9 directly, because the blade surface faces away from the passage opening.

At the suction side tap S9 near the trailing edge, the pressure rise occurs before the pressure rise at tap 0 (leading edge tap) and is followed by a rapid drop in pressure. The individual pressure records for tap S9 vary widely because of the oscillations of the "steady" trailing edge shock from the adjacent upper blade, which impacts and reflects near tap S8, but all show this trend. A possible mechanism is disturbance by shock "b" (Figure 12, frame C) of the steady trailing edge shock attached to the upper blade pressure side, leading to movement of the steady shock. In fact, the shock is seen to be concave in frame B. The disturbance may cause the shock to momentarily move downstream of tap S9, decreasing the pressure at that location. However, this does not explain how a pressure rise is seen at tap S9 before it is seen at the blade leading edge. A possible explanation for that fact is given later.

The blade static pressure data for the 0.200 msec case are shown in Figure 17. The shock velocities for

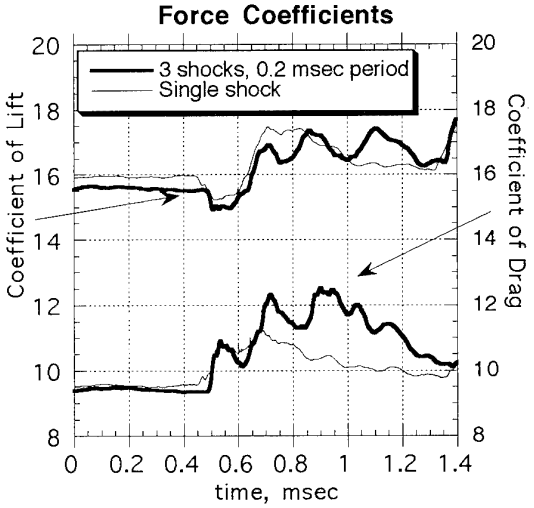

Figure 18. Force Coefficients

this case are the same as for the 0.055 msec case. However, since the shocks are more widely spaced (more decay of flow variables), the resulting Mach numbers are 1.3, 1.4 and 1.4 for the three shocks. The leading edge (tap 0) clearly shows the incidence of the three shocks at 0.5, 0.7 and 0.9 msec. Note the difference between tap 0 and tap S1. The pressure trace at S1 ramps upwards as further shocks arrive, but it does not at tap 0. Evidently, this is due to the induced velocity behind the shock waves, which would have a component perpendicular to tap S1 (increasing dynamic pressure) but none at the leading edge. The distinction between the three shocks disappears towards the trailing edge on the suction side, although it can be detected at taps S8 and S9. The arrival of all three shocks is clear at tap P8 (0.6, 0.8 and 1.0 msec) because reflection "b" impacts the blade along the whole pressure side. The early rise (relative to tap 0) in pressure again occurs at tap S9.

A possible interaction of the main reflected shock ("b" in Figure 12) with the steady pressure side trailing edge shock was briefly described above. The idea that the reflected shock could influence the strength, location or shape of the steady trailing edge shock comes from the phenomena of blast/bow wave interactions for blunt bodies in supersonic flow. When a blast wave passes head on through a bow wave, the bow wave is momentarily moved closer to the blunt body, and the pressure on the body is temporarily increased. The best argument in support of the proposed shock interaction is the observed blade static pressure at the suction side tap S9. The observed pressure rise at tap S9 occurs before the incident shock reaches the leading edge of the same blade, but coincident with the arrival of the main reflected shock at tap P5 on the pressure side of the adjacent upper blade. This is observed for all three test cases. None of the other suction side taps, which are all upstream of the impinging trailing edge shock, exhibit this behavior.

3.3 BLADE FORCES

Integrating the unsteady blade static pressures found in Figures 16 and 17 versus surface distance, the transient unstready blade forces can be estimated. Note that the steady value of base pressure was used in the integration since no unsteady instrumentation could be located at the trailing edge. When the unsteady forces are resolved as lift and drag, the results are as shown in Figure 18. The thin line is for the single shock case, and the thick line for the engine typical, 0.200 msec multiple shock case.

In the single shock case, the shock arrives at the blade leading at at t=0.5msec. As the shocks reflect off first the suction side and then the pressure side, the lift first decreases and then increases before decaying back to the steady value. The drag shows only an increase, a slight dip, and a further increase before the decay. In the three shock case (0.200 msec period), the shocks arrive at the blade leading edge at t=0.5, 0.7 and 0.9 msec. The lift appears to begin oscillating as a result of the characteristic increasing-decreasing behavior shown in the single shock results. We suspect that with more shock events the oscillation would be definite. The peak to peak variation of lift for the 0.200 msec case is about 6%, with little change in average level of lift. The drag, on the other hand, increases in average level by about 20%, with peak to peak fluctuations of about 8%.

4 CONCLUSIONS

The unsteady shock wave simulation described is capable of simulating different passing periods of shock waves, with no wakes present. While the experiment is transient in nature, the spacing between shock waves can be easily varied. More than three shock waves could be used in principle. The effects of the negative incidence of the cascade inlet flow behind the incident shocks cannot be de-coupled from the shock effects, but the aerodynamic effects are expected to be small. Shadowgraphs showed complicated shock reflection patterns for some single and multiple shock cases. Blade static pressures for the single shock and engine typical multiple shocks cases (0.200 msec period) were used to estimate the unsteady blade forces. The onset of oscillations in the blade forces caused by shock waves was demonstrated, which has significance for blade mechanical design. Also, a possible mechanism for the unsteady shocks influencing the steady PS trailing edge shock was discussed.

5 ACKNOWLEDGMENTS

The work of the first author was supported by General Electric Aircraft Engines in Cincinnati, Ohio. The work of the second author was supported in part by AFOSR.

6 REFERENCES

1 Abhari, Guenette, Epstein, and Giles. "Comparison of Time-Resolved Turbine Rotor Blade Heat Transfer Measurements and Numerical Calculations." Journal of Turbomachinery 114 (October 1992): 818-827.

2 Saxer, A. P. and Giles, M. B. "Predictions of Three-Dimensional Steady and Unsteady Inviscid Transonic Stator/Rotor Interaction with Inlet Radial Temperature Nonuniformity." Journal of Turbomachinery 116 (July 1994): 347-357.

3 Giles, M. G. "Stator/Rotor Interaction in a Transonic Turbine." Journal of Propulsion 6 (1990): 621-627.

4 Shelton, M. L. Personal communication.

5 Johnson, A. G., Rigby, M. J. and Oldfield, M. L. G. "Unsteady Aerodynamic Phenomena in a Simulated Wake and Shock Wave Passing Experiment." AGARD-CP-468.

6 Johnson, A. B., Oldfield, M., Rigby, M., and Giles, M. "Nozzle Guide Vane Shock Wave Propagation and Bifurcation in a Transonic Turbine Rotor." ASME Paper 90-GT-310.

7 Ashworth, D., LaGraff, J., Schultz, D. and Grindrod, K. "Unsteady Aerodynamic and Heat Transfer Processes in a Transonic Turbine Stage." Journal of Engineering for Gas Turbines and Power 107 (October 1985): 1022-1030.

8 Johnson, A., Rigby, M., Oldfield, M., Ainsworth, R. and Oliver, M. "Surface Heat Transfer Fluctuations on a Turbine Rotor Blade Due to Upstream Shock Wave Passing." ASME Journal of Turbomachinery 111 (1989): 105-115.

9 Doughty, R. L. and Moses, H. L. "The Effect of Blade Solidity on the Aerodynamic Loss of a Transonic Turbine Cascade." AIAA Paper 92-0393.

10 Kiss, T., Schetz, J. A. and Moses, H. L. "Experimental and Numerical Study of Transonic Turbine Cascade Flow." AIAA Paper 93-3064.

11 Shelton, M. L., Gregory, B. A., Lamson, S. H., Moses, H. L., Doughty, R. L. and Kiss, T. "Optimization of a Transonic Turbine Airfoil Using Artificial Intelligence, CFD and Cascade Testing." ASME Paper 93-GT-161.

12 Shelton, M. L., Gregory, B. A., Doughty, R. L., Kiss, T., and Moses, H. L. "A Statistical Approach to the Experimental Evaluation of Transonic Turbine Airfoils in a Linear Cascade." Journal of Turbomachinery 115 (July 1993): 366-375.

13 Anderson, John D. Modern Compressible Flow . New York: McGraw-Hill, 1990 (206-240).

14 Chester, W. "The Propogation of Shock Waves along Ducts of Varying Cross Section." Advances in Applied Mechanics VI (1960): 119-152.

15 Chisnell, R. F. "The Motion of a Shock Wave in a Channel, with Applications to Cylindrical and Spherical Shock Waves." Journal of Fluid Mechanics Volume 2 Part 3 (May 1957): 286-298.

16 Bach, G. G. and Lee, J. H. S. "An Analytical Solution for Blast Waves." AIAA Journal 8 (February 1970): 271-275.

17 Heilig, Werner H. "Propagation of Shock Waves in Various Branched Ducts." Modern Developments in Shock Tube Research -- Proceedings of the Tenth International Shock Tube Symposium, 1975 (273-283).

18 Collie, J. C., Moses, H. L., Schetz, J. A. and Gregory, B. A. "Recent Advances in Simulating Unsteady Flow Phenomena Brought About by Passage of Shock Waves in a Linear Turbine Cascade." ASME Journal of Turbomachinery 115 (October 1993): 687-698.

19 Bendat, J. S. and Piersol, A. G. Engineering Applications of Correlation and Spectral Analysis . New York: Wiley (1993).

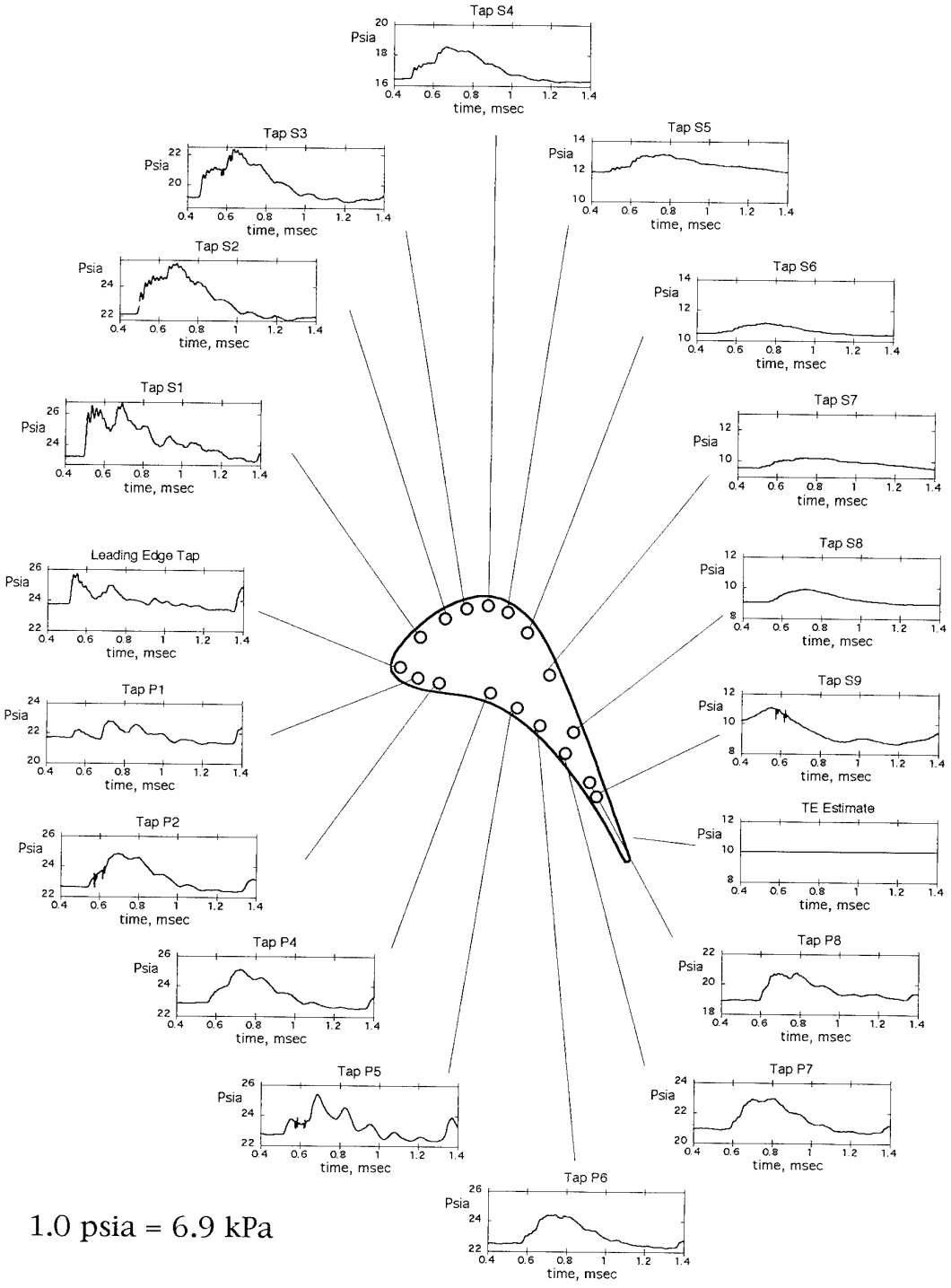

Figure 16. Blade Static Pressures, Single Shock

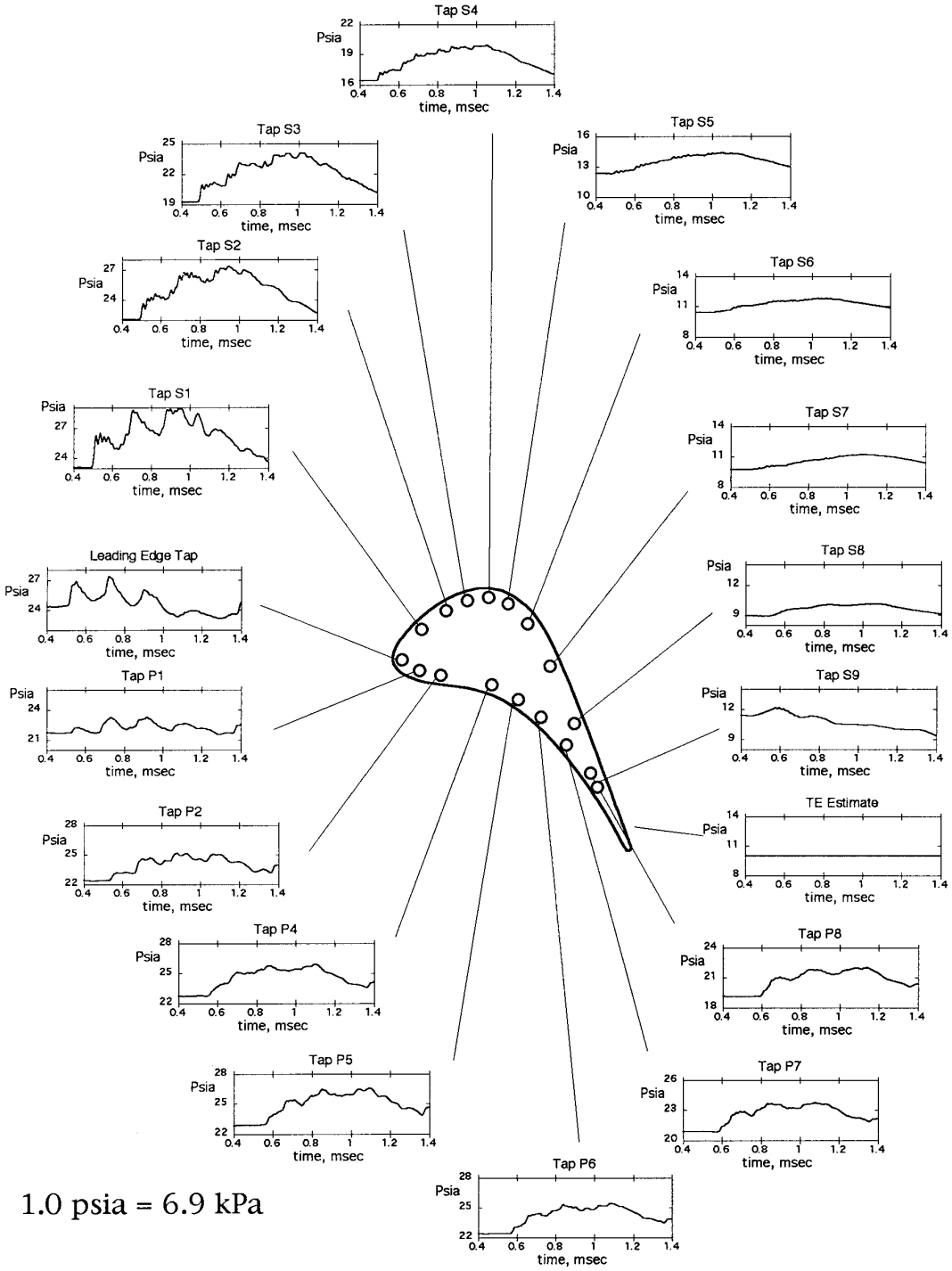

Figure 17. Blade Static Pressures, 0.200 msec period

REFERENCE NO. OF THE PAPER: 42

DISCUSSOR'S NAME: D.W. Bechert, DLR, Germany

AUTHOR'S NAME: R.L. Doughty, J.A. Schetz

Q: Would the added mass in the shock generation contribute to the measured losses in your system?

A: The upstream total pressure was measured at an axial location which was directly in the path of the added mass jet from the shock tube. Ideally, the upstream conditions should be measured at a location downstream from the jet entrance. We tried to avoid getting too much effect from leading edge shock reflections on the upstream total pressure measurement by locating the probe well upstream of the cascade leading edge. The probe location was therefore a compromise, but most of the effect from the added mass should be included.

REFERENCE NO. OF THE PAPER: 42

DISCUSSOR'S NAME: M.G. Rose, Rolls-Royce, U.K.

AUTHOR'S NAME: R.L. Doughty, J.A. Schetz

Q: I am intrigued by your data showing the aft part of the suction surface responding before the shock reaches the leading edge. Does this mean that information was propagated down the exit of the cascade faster than the super-sonic speed of the incident shock? Note that the fluid at exit is already traveling in this direction at a near sonic speed. Any propagating wave would surely travel faster behind the cascade than in front, as shown by your data.

A: As you noted, the tangential flow behind the cascade is travelling at roughly the same speed as the travelling shock in front of the cascade. We do not feel, then, that flow speed explains the early detection of the shock on the aft portion of the suction surface. Instead, we have reason to believe that the steady pressure side trailing edge shock strength is influenced by the passing shock (specifically the main passage reflection). The change in the steady shock is then felt soon afterwards across the whole passage exit, impacting the suction surface of the lower adjacent blade. This hypothesis applies only to this particular type of blade geometry, because the main passage reflection hits the pressure side trailing edge of the upper blade before the main shock crosses the leading edge of the lower blade, as observed in shadowgraphs. This idea merits further study.

REFERENCE NO. OF THE PAPER: 42

DISCUSSOR'S NAME: D.J. Dunham, DLR, U.K.

AUTHOR'S NAME: R.L. Doughty, J.A. Schetz

Q: Did you define drag with respect to the net Pt_1 (after allowing for the time-average shock loss)? If you were to do so, what change in loss coefficient would result from the analysis?

A: Due to the compressible nature of the flow, no direct correlation between lift and loss is possible. We defined drag using the standard form for supersonic coefficient of pressure, or

$$CD = \frac{\text{Drag per Unit Area}}{\gamma P_\infty M^2_\infty/2}$$

where the subscript infinity quantities were replaced by the time average upstream values.

REPORT DOCUMENTATION PAGE

1. Recipient's Reference	2. Originator's Reference	3. Further Reference	4. Security Classification of Document
	AGARD-CP-571	ISBN 92-836-0020-7	UNCLASSIFIED/ UNLIMITED

5. Originator Advisory Group for Aerospace Research and Development
North Atlantic Treaty Organization
7 rue Ancelle, 92200 Neuilly-sur-Seine, France

6. Title

Loss Mechanisms and Unsteady Flows in Turbomachines

7. Presented at/sponsored by

The Propulsion and Energetics Panel 85th Symposium held in Derby, United Kingdom, 8-12 May 1995.

8. Author(s)/Editor(s)	9. Date
Multiple	January 1996
10. Author's/Editor's Address	**11. Pages**
Multiple	598

12. Distribution Statement There are no restrictions on the distribution of this document. Information about the availability of this and other AGARD unclassified publications is given on the back cover.

13. Keywords/Descriptors

Turbomachinery	Experimental data
Computational fluid dynamics	Aircraft engines
Steady flow	Turbine blades
Unsteady flow	Loss mechanisms
Boundary layer flow	Off-design conditions

14. Abstract

The Conference Proceedings contains 42 papers presented at the Propulsion and Energetics Panel 85th Symposium on Loss Mechanisms and Unsteady Flows in Turbomachines which was held from 8-12 May 1995, in Derby, UK.

Sessions: Cascade Steady Flow Mechanisms and Losses (9 papers); Steady Flow Clearance and Injection Flow Mechanisms and Losses (6); Steady Secondary Flows and Shock Boundary Layer Interaction (3); Blade Section-Wake Boundary layer Interaction (6); Management of Unsteady Flows (10); Blade Interactions (8).

The Symposium contributes to improving the efficiency and operation of turbomachinery also in off-design conditions by application of experimental and computational fluid dynamics methods. Multi-stage methods and positive loss management in the design stage have been identified as next steps.

This will yield optimized engines of high efficiency for expanded flight envelopes including active control of the plane movement at high reliability levels.

AGARD

NATO OTAN

7 RUE ANCELLE • 92200 NEUILLY-SUR-SEINE

FRANCE

Télécopie (1)47.38.57.99 • Télex 610 176

DIFFUSION DES PUBLICATIONS

AGARD NON CLASSIFIEES

Aucun stock de publications n'a existé à AGARD. A partir de 1993, AGARD détiendra un stock limité des publications associées aux cycles de conférences et cours spéciaux ainsi que les AGARDographies et les rapports des groupes de travail, organisés et publiés à partir de 1993 inclus. Les demandes de renseignements doivent être adressées à AGARD par lettre ou par fax à l'adresse indiquée ci-dessus. *Veuillez ne pas téléphoner.* La diffusion initiale de toutes les publications de l'AGARD est effectuée auprès des pays membres de l'OTAN par l'intermédiaire des centres de distribution nationaux indiqués ci-dessous. Des exemplaires supplémentaires peuvent parfois être obtenus auprès de ces centres (à l'exception des Etats-Unis). Si vous souhaitez recevoir toutes les publications de l'AGARD, ou simplement celles qui concernent certains Panels, vous pouvez demander à être inclu sur la liste d'envoi de l'un de ces centres. Les publications de l'AGARD sont en vente auprès des agences indiquées ci-dessous, sous forme de photocopie ou de microfiche.

CENTRES DE DIFFUSION NATIONAUX

ALLEMAGNE
Fachinformationszentrum Karlsruhe
D-76344 Eggenstein-Leopoldshafen 2

BELGIQUE
Coordonnateur AGARD-VSL
Etat-major de la Force aérienne
Quartier Reine Elisabeth
Rue d'Evere, 1140 Bruxelles

CANADA
Directeur, Services d'information scientifique
Ministère de la Défense nationale
Ottawa, Ontario K1A 0K2

DANEMARK
Danish Defence Research Establishment
Ryvangs Allé 1
P.O. Box 2715
DK-2100 Copenhagen Ø

ESPAGNE
INTA (AGARD Publications)
Pintor Rosales 34
28008 Madrid

ETATS-UNIS
NASA Headquarters
Code JOB-1
Washington, D.C. 20546

FRANCE
O.N.E.R.A. (Direction)
29, Avenue de la Division Leclerc
92322 Châtillon Cedex

GRECE
Hellenic Air Force
Air War College
Scientific and Technical Library
Dekelia Air Force Base
Dekelia, Athens TGA 1010

ISLANDE
Director of Aviation
c/o Flugrad
Reykjavik

ITALIE
Aeronautica Militare
Ufficio del Delegato Nazionale all'AGARD
Aeroporto Pratica di Mare
00040 Pomezia (Roma)

LUXEMBOURG
Voir Belgique

NORVEGE
Norwegian Defence Research Establishment
Attn: Biblioteket
P.O. Box 25
N-2007 Kjeller

PAYS-BAS
Netherlands Delegation to AGARD
National Aerospace Laboratory NLR
P.O. Box 90502
1006 BM Amsterdam

PORTUGAL
Força Aérea Portuguesa
Centro de Documentação e Informação
Alfragide
2700 Amadora

ROYAUME-UNI
Defence Research Information Centre
Kentigern House
65 Brown Street
Glasgow G2 8EX

TURQUIE
Millî Savunma Başkanliği (MSB)
ARGE Dairesi Başkanliği (MSB)
06650 Bakanliklar-Ankara

Le centre de distribution national des Etats-Unis ne détient PAS de stocks des publications de l'AGARD.
D'éventuelles demandes de photocopies doivent être formulées directement auprès du NASA Center for AeroSpace Information (CASI) à l'adresse ci-dessous. Toute notification de changement d'adresse doit être fait également auprès de CASI.

AGENCES DE VENTE

NASA Center for
AeroSpace Information (CASI)
800 Elkridge Landing Road
Linthicum Heights, MD 21090-2934
Etats-Unis

ESA/Information Retrieval Service
European Space Agency
10, rue Mario Nikis
75015 Paris
France

The British Library
Document Supply Division
Boston Spa, Wetherby
West Yorkshire LS23 7BQ
Royaume-Uni

Les demandes de microfiches ou de photocopies de documents AGARD (y compris les demandes faites auprès du CASI) doivent comporter la dénomination AGARD, ainsi que le numéro de série d'AGARD (par exemple AGARD-AG-315). Des informations analogues, telles que le titre et la date de publication sont souhaitables. Veuiller noter qu'il y a lieu de spécifier AGARD-R-nnn et AGARD-AR-nnn lors de la commande des rapports AGARD et des rapports consultatifs AGARD respectivement. Des références bibliographiques complètes ainsi que des résumés des publications AGARD figurent dans les journaux suivants:

Scientific and Technical Aerospace Reports (STAR)
publié par la NASA Scientific and Technical
Information Division
NASA Headquarters (JTT)
Washington D.C. 20546
Etats-Unis

Government Reports Announcements and Index (GRA&I)
publié par le National Technical Information Service
Springfield
Virginia 22161
Etats-Unis
(accessible également en mode interactif dans la base de
données bibliographiques en ligne du NTIS, et sur CD-ROM)

Imprimé par le Groupe Communication Canada
45, boul. Sacré-Cœur, Hull (Québec), Canada K1A 0S7

AGARD

NATO OTAN

7 RUE ANCELLE • 92200 NEUILLY-SUR-SEINE

FRANCE

Telefax (1)47.38.57.99 • Telex 610 176

DISTRIBUTION OF UNCLASSIFIED

AGARD PUBLICATIONS

AGARD holds limited quantities of the publications that accompanied Lecture Series and Special Courses held in 1993 or later, and of AGARDographs and Working Group reports published from 1993 onward. For details, write or send a telefax to the address given above. *Please do not telephone.*

AGARD does not hold stocks of publications that accompanied earlier Lecture Series or Courses or of any other publications. Initial distribution of all AGARD publications is made to NATO nations through the National Distribution Centres listed below. Further copies are sometimes available from these centres (except in the United States). If you have a need to receive all AGARD publications, or just those relating to one or more specific AGARD Panels, they may be willing to include you (or your organisation) on their distribution list. AGARD publications may be purchased from the Sales Agencies listed below, in photocopy or microfiche form.

NATIONAL DISTRIBUTION CENTRES

BELGIUM
Coordonnateur AGARD — VSL
Etat-major de la Force aérienne
Quartier Reine Elisabeth
Rue d'Evere, 1140 Bruxelles

CANADA
Director Scientific Information Services
Dept of National Defence
Ottawa, Ontario K1A 0K2

DENMARK
Danish Defence Research Establishment
Ryvangs Allé 1
P.O. Box 2715
DK-2100 Copenhagen Ø

FRANCE
O.N.E.R.A. (Direction)
29 Avenue de la Division Leclerc
92322 Châtillon Cedex

GERMANY
Fachinformationszentrum Karlsruhe
D-76344 Eggenstein-Leopoldshafen 2

GREECE
Hellenic Air Force
Air War College
Scientific and Technical Library
Dekelia Air Force Base
Dekelia, Athens TGA 1010

ICELAND
Director of Aviation
c/o Flugrad
Reykjavik

ITALY
Aeronautica Militare
Ufficio del Delegato Nazionale all'AGARD
Aeroporto Pratica di Mare
00040 Pomezia (Roma)

LUXEMBOURG
See Belgium

NETHERLANDS
Netherlands Delegation to AGARD
National Aerospace Laboratory, NLR
P.O. Box 90502
1006 BM Amsterdam

NORWAY
Norwegian Defence Research Establishment
Attn: Biblioteket
P.O. Box 25
N-2007 Kjeller

PORTUGAL
Força Aérea Portuguesa
Centro de Documentação e Informação
Alfragide
2700 Amadora

SPAIN
INTA (AGARD Publications)
Pintor Rosales 34
28008 Madrid

TURKEY
Millî Savunma Başkanliği (MSB)
ARGE Dairesi Başkanliği (MSB)
06650 Bakanliklar-Ankara

UNITED KINGDOM
Defence Research Information Centre
Kentigern House
65 Brown Street
Glasgow G2 8EX

UNITED STATES
NASA Headquarters
Code JOB-1
Washington, D.C. 20546

The United States National Distribution Centre does NOT hold stocks of AGARD publications.
Applications for copies should be made direct to the NASA Center for AeroSpace Information (CASI) at the address below. Change of address requests should also go to CASI.

SALES AGENCIES

NASA Center for
AeroSpace Information (CASI)
800 Elkridge Landing Road
Linthicum Heights, MD 21090-2934
United States

ESA/Information Retrieval Service
European Space Agency
10, rue Mario Nikis
75015 Paris
France

The British Library
Document Supply Centre
Boston Spa, Wetherby
West Yorkshire LS23 7BQ
United Kingdom

Requests for microfiches or photocopies of AGARD documents (including requests to CASI) should include the word 'AGARD' and the AGARD serial number (for example AGARD-AG-315). Collateral information such as title and publication date is desirable. Note that AGARD Reports and Advisory Reports should be specified as AGARD-R-nnn and AGARD-AR-nnn, respectively. Full bibliographical references and abstracts of AGARD publications are given in the following journals:

Scientific and Technical Aerospace Reports (STAR)
published by NASA Scientific and Technical
Information Division
NASA Headquarters (JTT)
Washington D.C. 20546
United States

Government Reports Announcements and Index (GRA&I)
published by the National Technical Information Service
Springfield
Virginia 22161
United States
(also available online in the NTIS Bibliographic
Database or on CD-ROM)

Printed by Canada Communication Group
45 Sacré-Cœur Blvd., Hull (Québec), Canada K1A 0S7

ISBN 92-836-0020-7